

Preface

The 21st International Symposium on Space Terahertz Technology was held at The Said Business Center of Oxford University and The STFC Rutherford Appleton Laboratory in the United Kingdom, on March 23-35, 2010. The Symposium was attended by about 140 scientists and engineers from the European Union, USA, Japan, Russia, Chile and China.

The organizers would like to thank the scientific committee and the authors who made the symposium such an interesting and enjoyable event. Special thanks are due to Vanessa Ferraro-Wood from Oxford Astrophysics and Jane Porter from RAL who worked many hours, often outside normal office hours, organizing the college accommodation, registration and numerous other logistical items.

All submitted papers have been included in these proceedings. In total, 5 plenary presentations and 106 ordinary presentations were made, 55 of them as oral presentations and 51 posters. The breakdown in terms of technology category was as follows:

Astronomical telescopes	6
Earth and planetary observations	9
Receivers and THz systems	15
HEB Mixers	5
SIS mixers	9
Direct detectors	15
Schottky diodes and mixers	12
Local Oscillators and THz sources	13
Novel devices	5
Optics and waveguide components	14
Calibration and measurements	3

The 22nd International Symposium on Space THz Technology will be held on April 2011 in Tucson, Arizona. Further details are available at <http://isstt2011.events.asu.edu/isstt/>

The 23rd International Symposium on Space THz Technology will be held in 2012 in Japan.

– Ghassan Yassin and Brian Ellison

ISSTT 2010 Scientific Organising Committee:

Victor Belitsky (Chalmers University of Technology, Sweden)
Ray Blundell (Harvard-Smithsonian Center for Astrophysics, USA)
Tom Crowe (VDI / University of Virginia, USA)
Brian Ellison (Rutherford Appleton Laboratory, UK)
Ghassan Yassin (University of Oxford, UK)
Gregory Goltsman (Moscow State Pedagogical University, Russia)
Karl Jacobs (KOSMA, Germany)
Tony Kerr (NRAO, USA)
Teun Klapwijk (TU Delft, the Netherlands)
Alain Maestrini (Paris University France)
Imran Mehdi (JPL, USA)
Yutaro Sekmoto (NAOJ, Japan)
Sheng-Cai Shi (Purple Mountain Observatory, China)
Jan Stake (Chalmers University of Technology)
Wolfgang Wild (ESO)
Stafford Withington (Cambridge University)
Neal Erickson (University of Massachusetts)
Arthur Lichtenberger (University of Virginia, USA)
Christopher Walker (University of Arizona, USA)
Alexandre Karpov (Caltech, USA)
Eric Bryerton (NRAO, USA)
Doris Maier (IRAM, France)
Herbert Eisele (University of Leeds)

ISSTT 2010 Local Organising Committee:

Prof. Ghassan Yassin (Dept. of Physics, University of Oxford)
Prof. Brian Ellison (Rutherford Appleton Laboratory)
Dr. Peter Huggard (Rutherford Appleton Laboratory)
Dr. Jamie Leech (Dept. of Physics, University of Oxford)
Dr. Paul Grimes (Dept. of Physics, University of Oxford)
Boon Kok Tan (Dept. of Physics, University of Oxford)
Yangjun Zhou (Dept. of Physics, University of Oxford)
Vanessa Ferraro-Wood (Dept. of Physics, University of Oxford)
Jane Porter (Rutherford Appleton Laboratory)
Matthew Emery (Rutherford Appleton Laboratory)
Ashling Morris (Dept. of Physics, University of Oxford)

Table of Contents

Session 1: THz Telescopes

ID	Presenting Author	Title	Page
S1.1	Robert Gehrz	The Stratospheric Observatory for Infrared Astronomy (SOFIA)	18
S1.2	Hiroshi Matsuo	Far-infrared Interferometry from Antarctica	28
S1.3	Willem Jellema	The Herschel/HI-FI OD-81 Anomaly	33
S1.4	David Teyssier	Herschel/HIFI In-flight Commissioning and Performance	40
S1.5	Chris Walker	The Stratospheric THz Observatory (STO): 1 st Test Flight	46

Session 2: THz Sources

ID	Presenting Author	Title	Page
S2.1*	Iván Cámara Mayorga	Photonic local oscillators for terahertz radio astronomy	52
S2.2*	Manju Henry	GaAs varactor multipliers based on transferred substrate technology	53
S2.3*	Michael Wanke	Effect of Feedback on Quantum Cascade Laser Performance	54
S2.4	Robert Lin	Development of Local Oscillators for CASIMIR	55
S2.5	Heribert Eisele	Superlattice Electronic Devices as Compact Terahertz Sources	60
S2.6*	Heiko Richter	A compact, continuous-wave radiation source for local oscillator applications based on a quantum-cascade laser	64

* Paper not submitted. These proceedings instead contain the abstract from the ISSTT programme.

Session 3: Direct Detectors I

ID	Presenting Author	Title	Page
S3.0*	Stafford Withington	Towards Ultra-low-noise Transition Edge Sensors for Millimeter-Wave and Far-infrared Space Telescopes (<i>Invited Talk</i>)	67
S3.1	Leonid Kuzmin	Superconducting Thermo-Electric Bolometer for Cosmology Instruments	68
S3.2	Marcus Roesch	Development, Fabrication and Characterization of Lumped Element Kinetic Inductance Detectors for NIKA	72
S3.3	Damian Audley	Performance of a Microstrip-coupled TES Imaging Module for CMB Polarimetry	76
S3.4	David Goldie	Transition Edge Sensor Thermometry for On-chip Materials Characterization	85
S3.5	Boris Karasik	Demonstration of Multiplexed Operation of Hot-Electron Detectors Using MSQUIDS	91
S3.6	Pieter de Visser	Hysteretic thermal switching due to readout power heating in kinetic inductance detectors	96

Session 4: Optics and Waveguides

ID	Presenting Author	Title	Page
S4.1*	Sheng-Cai Shi	A THz FTS for Site Testing at Dome A	103
S4.2	Christopher Thomas	Electromagnetic Simulations of the Partially Coherent Optical Behaviour of Resistive Film TES Detectors	104
S4.3	Jamie Leech	Measured performance of a 230 GHz prototype focal-plane feedhorn array made by direct drilling of smooth-walled horns	114
S4.4*	Takeshi Manabe	Measurements of the Offset-Cassegrain Antenna of JEM/SMILES Using a Near-Field Phase-Retrieval Method in the 640 GHz Band	120
S4.5	Stig Sørensen	Analysis of the ALMA Telescopes and Front-ends	121

Session 5: THz Systems and Receivers

ID	Presenting Author	Title	Page
S5.1	Christian Leinz	A 1THz Receiver System at APEX	130
S5.2*	Wenlei Shan	A 9-Beam 2SB Receiver for Millimeter-Wave Radio Astronomy	136
S5.3*	Bhushan Billade	ALMA Band 5 cartridge performance	137
S5.4*	Jacob Kooi	Measurement Results of the Caltech Submillimeter Observatory 230 GHz and 460 GHz Balanced Receivers	138
S5.5	Michael Edgar	CASIMIR: A high resolution, far-IR/submm spectrometer for airborne astronomy	139

Session 6: Schottky Diodes and Mixers

ID	Presenting Author	Title	Page
S6.1	Neal Erickson	TeraHertz Schottky-Diode Balanced Mixers	150
S6.2*	Tom Crowe	Full Waveguide Band Schottky Mixers for Terahertz Applications	154
S6.3	Bertrand Thomas	An 874 GHz fundamental balanced mixer based on MMIC membrane planar Schottky diodes	155
S6.4	Hugh Gibson	183 GHz Mixer on InGaAs Schottky Diodes	159
S6.5	Bertrand Thomas	A 530-600 GHz silicon micro-machined integrated receiver using GaAs MMIC membrane planar Schottky diodes	161
S6.6*	Jesús Grajal	Electro-thermal Model for the Design of Schottky Diode Based Circuits	165

Session 7: Calibration and Measurements

ID	Presenting Author	Title	Page
S7.1	Yoonjae Lee	ALMA Front-End Verification Using a Dry Cold Load	168
S7.2*	Axel Murk	Development of Conical Calibration Targets for ALMA	172
S7.3	Hugh Gibson	Harmonic Mixers for VNA extenders to 900GHz	173

Session 8: Earth Observations

ID	Presenting Author	Title	Page
S8.1	Satoshi Ochiai	Performance of JEM/SMILES in orbit	179
S8.2*	Brian Moyna	ISMAR: Towards a Sub Millimetre-Wave Airborne Demonstrator for Observation of Precipitation and Ice Clouds	185
S8.3	Chris Groppi	Laboratory and Ground Testing Results from ATOMMS: the Active Temperature, Ozone and Moisture Microwave Spectrometer	186
S8.4	Manfred Birk	TELIS: TERahertz and subMMW Limb Sounder - Project Summary After First Successful Flight	195

Session 9: Superconducting Mixers

ID	Presenting Author	Title	Page
S9.1*	Alexandre Karpov	1.4 THz SIS mixer using Nb and Al tuning circuit	203
S9.2	Boon-Kok Tan	Design of Broadband Unilateral Finline SIS Mixers Employing 15 μm Silicon-On-Insulator Substrate at THz Frequencies	204
S9.3	Yangjun Zhou	An SIS unilateral finline mixer with an ultra-wide IF bandwidth	212
S9.4*	Jonathon Kawamura	A 1.5 THz waveguide HEB mixer using silicon-on-insulator substrates for Stratospheric Terahertz Observatory	217
S9.5*	Anna Maslennikova	Gain bandwidth and noise temperature of NbN HEB mixers with simultaneous phonon and diffusion cooling	218
S9.6	Wen Zhang	Noise Temperature and Beam Pattern of a Quasioptical Heterodyne Receiver based on NbN Hot Electron Bolometer Mixer at 5.25 THz	220

Session 10: THz Systems and Planetary Missions

ID	Presenting Author	Title	Page
S10.1*	C. M. Bradford	The Background-Limited Infrared Submillimeter Spectrograph (BLISS) for SPICA	228
S10.2	Yuan Ren	Gas cell measurement using a 2.9 THz heterodyne receiver based on a quantum cascade laser and a superconducting hot electron bolometer	229
S10.3*	Paul Goldsmith	A flexible quasioptical input system for a submillimeter multi-object spectrometer	233
S10.4	Erich Schlecht	Wide-band heterodyne submillimetre wave spectrometer for planetary atmospheres	234
S10.5*	Brian Ellison	ORTIS - Orbiter Terahertz Infrared Sounder	243

Session 11: Direct Detectors II

ID	Presenting Author	Title	Page
S11.1	Philip Mausekopf	A TES Focal Plane for SPICA-SAFARI	246
S11.2	Mikhail Tarasov	Cold-Electron Bolometer Array Integrated with a 350 GHz Cross-Slot Antenna	256
S11.3*	Stefan Heyminck	Development of a MKID camera for APEX	262
S11.4	Matt Hollister	An Update on MUSIC: A Kinetic Inductance Detector Camera for Sub/Millimeter Astrophysics at the Caltech Submillimeter Observatory	263
S11.5*	James Schlaerth	Design and readout of large MKID arrays for submillimeter astronomy	270

Poster Session 1: Astronomical Telescopes

ID	Presenting Author	Title	Page
P1.1*	Dominic Benford	Pico Veleta Atmospheric Noise Limits At Millimeter Wavelengths	273

Poster Session 2: Direct Detectors

ID	Presenting Author	Title	Page
P2.1	Dorota Glowacka	Comparative Performance of Mo/Cu vs. Mo/Au Transition Edge Sensors for Space Science Applications	276
P2.2	Ernst Otto	Cold-Electron Bolometer Integrated with a Unilateral Finline	279
P2.3	Andrew Beyer	Ultra-sensitive Transition-edge Sensors for Far-Infrared Spectroscopy on SPICA	285
P2.4	Boris Karasik	Optical NEP in Hot-Electron Nanobolometers	291
P2.5*	Sumedh Mahashabde	Focal Plane Arrays of Thermo-Electric Bolometers	298

Poster Session 3: Earth Observation

ID	Presenting Author	Title	Page
P3.1*	Gert de Lange	TELIS SIR Channel Performance Analysis	301
P3.2*	Manju Henry	High Performance component development at RAL for the ISMAR instrument	302
P3.3*	Peter Vogt	Charaterisation of the TELIS autocorrelator spectrometer	303

Poster Session 4: Novel Devices and Measurements

ID	Presenting Author	Title	Page
P4.1	Michael Cyberey	On-Wafer Penetration Depth Measurements of Superconducting Films	306
P4.2*	Spas Spasov	Terahertz imaging with a highly-sensitive quantum dot detector	311
P4.3	Enrique Carrion	Single Wall Carbon Nanotube (SWCNT) Devices as THz Detectors and Mixers	312
P4.4	Jeffrey Hesler	THz Vector Network Analyzer Measurements and Calibration	318
P4.5	Lei Liu	Development of Microwave and Terahertz Detectors Utilizing AlN/GaN High Electron Mobility Transistors	321

Poster Session 5: Optics and Waveguides

ID	Presenting Author	Title	Page
P5.1	Alessandro Navarrini	A Waveguide Orthomode Transducer for 385-500 GHz	328
P5.2	Chris Groppi	Automated CNC micromachining for integrated THz waveguide circuits	338
P5.3	Choonsup Lee	Silicon Micromachining Technology for Passive THz Components	342
P5.4*	Jin Zhang	Performance of Planar Ortho-Mode Transducers for CMB satellite missions	345
P5.5	Huan Zhao	VNA-Calibration and S-Parameter Characterization of Submillimeter Wave Integrated Membrane Circuits	346
P5.6	Pablo Zorzi	Revisiting the ALMA Band 1 Optics Design	348
P5.7	Nick Ridler	Towards Standardized Waveguide Sizes and Interfaces for Submillimeter Wavelengths	353
P5.8	Jeffrey Hesler	THz Waveguide Couplers Using Quartz Micromachining	358
P5.9	Hansheng Su	Design and Analysis of Active Frequency Selective Surfaces with Organic Semiconductor	360

Poster Session 6: Receivers

ID	Presenting Author	Title	Page
P6.2	Patricio Mena	Construction of a Heterodyne Receiver for Band 1 of ALMA	366
P6.3	Chris Groppi	Testing and Integration of Supercam, a 64-Pixel Array Receiver for the 350 GHz Atmospheric Window	368
P6.4	Olle Nyström	Integrated Setup for THz Receiver Characterization	374
P6.5	Oliver King	SNS: Analytic Receiver Analysis Software Using Electrical Scattering Matrices	379
P6.7*	Serguei Cherednichenko	Water Vapor Radiometer for ALMA: optical design and verification	389
P6.8	Ronan Higgins	Calibration of the Herschel HIFI Instrument using Gas Cell Measurements	390

Poster Session 7: Schottky Diodes

ID	Presenting Author	Title	Page
P7.1	Diego Pardo Santos	Harmonic Generation and Noise in GaAs and GaN Schottky Diodes	400
P7.2	José Siles	Physics-Based Modeling Aspects of Schottky Diodes for Circuit Design Above 1 THz	404
P7.3*	José Siles	Design and Fabrication of 190-GHz Dual-Chip Single-Waveguide Schottky Doublers	411
P7.4*	Aik Yean Tang	Parameter Extraction and Geometry Optimisation of Planar Schottky Diodes	412
P7.5*	Paul Wilkinson	A 664 GHz Sub-Harmonic Schottky Mixer	413
P7.6	Jeanne Treuttel	Design of a Combined Tripler-Subharmonic Mixer at 330 GHz for Multipixel Application Using European Schottky Diodes	414

Poster Session 8: Superconducting Mixers

ID	Presenting Author	Title	Page
P8.1	Yury Lobanov	Microwave-assisted Measurement of the Frequency Response of Terahertz HEB mixers with a Fourier Transform Spectrometer	420
P8.2	Jose Luis Giordano	Superconducting devices for radioastronomy; First steps in Chile: SNS-junction fabrication	424
P8.3	Abigail Hedden	Upgrading the SMA 600 GHz Receivers	428
P8.4*	Ronald Hesper	Implementing a Modular 650 GHz Sideband-Separating Mixer	433
P8.5	Doug Henke	Modeling SIS junction arrays with application to APEX Band 3 (390-500 GHz)	434
P8.6*	Valery Koshelets	Superconducting Integrated THz Receivers	442
P8.7*	Alwin Brettschneider	Wideband receiver based on AlN Barriers	443
P8.8	Hiroyuki Masezawa	Development of a 1.9 THz Band Hot-Electron Bolometer Heterodyne Receiver with a Quantum Cascade Laser	444

Poster Session 9: THz Sources

ID	Presenting Author	Title	Page
P9.1*	Heiko Richter	Frequency stabilization of a THz quantum-cascade laser to a molecular absorption line	452
P9.2*	Heiko Richter	A 4.7 THz gas laser local oscillator for GREAT on SOFIA	453
P9.3	Johanna Liljedahl	Development of a HBV tripler for 0.6 THz	454
P9.4	Ernest Michael	Vertically Illuminated TW-UTC Photodiodes for Terahertz Generation	460
P9.5	Konstantin Kalashnikov	Phase-locking of Flux-Flow Oscillator by Harmonic Mixer based on SIS junction	464
P9.6	Yuan Ren	3.5 THz surface emitting distributed feedback QCL operated at 70 K as local oscillator	468
P9.7*	Tom Crowe	Development and Characterization of a 1.9THz LO Source	472

List of Registered Participants – p474

Session S1: THz Telescopes

The Stratospheric Observatory for Infrared Astronomy (SOFIA)

R. D. Gehrz^{2,*} and E. E. Becklin²

¹*Department of Astronomy, 116 Church Street, S. E., University of Minnesota, Minneapolis, MN 55455, USA*

²*Universities Space Research Association, NASA Ames Research Center, MS 211-3, Moffett Field, CA 94035, USA*

*Contact: gehrz@astro.umn.edu, Phone 1-612-624-7806

Abstract— The Stratospheric Observatory for Infrared Astronomy (SOFIA) is a joint U.S./German Project to develop and operate a 2.5-meter infrared airborne telescope in a Boeing 747-SP that flies in the stratosphere at altitudes as high as 45,000 and is capable of observations from 0.3 μm to 1.6 mm with an average transmission greater than 80 percent. SOFIA will be staged out of the NASA Dryden Flight Research Center aircraft operations facility at Palmdale, CA and the SOFIA Science Mission Operations Center (SSMOC) will be located at NASA Ames Research Center, Moffett Field, CA. First science flights will begin in 2010 and a full operations schedule of more than 100 8 to 10 hour flights per year will be reached by 2014. The observatory is expected to operate until the mid 2030's. SOFIA will initially fly with eight focal plane instruments that include broadband imagers, moderate resolution spectrographs that will resolve broad features due to dust and large molecules, and high resolution spectrometers capable of studying the kinematics of molecular and atomic gas lines at km/s resolution. We describe the SOFIA facility and outline the opportunities for observations by the general scientific community, future instrumentation developments, and operations collaborations. The operational characteristics of the SOFIA first-generation instruments are summarized and we give several specific examples of the types of scientific studies to which these instruments are expected to make fundamental scientific contributions. Additional information about SOFIA is available at <http://www.sofia.usra.edu>.

I. INTRODUCTION: PROJECT OVERVIEW AND STATUS

NASA's Stratospheric Observatory for Infrared (IR) Astronomy (SOFIA) will soon join the Spitzer Space Telescope [1,2], Herschel Space Observatory [3], and James Webb Space Telescope (JWST) [4] as one of the premier observatories for IR/Submillimeter astronomy during the next 25 years. SOFIA, a joint project of NASA and the German Space Agency (DLR), is a 2.5-meter telescope in a Boeing 747SP aircraft (Figure 1) designed to make sensitive IR measurements of a wide range of astronomical objects. SOFIA will fly at altitudes up to 45,000 feet (13.72 km), above 99.8% of the obscuring atmospheric H₂O vapor. It will enable observations at wavelengths from 0.3 μm to 1.6 mm with $\geq 80\%$ transmission, concentrating especially on the obscured region between 30 and 300 μm (Figure 2). At this altitude, the precipitable water column depth is typically less than 10 μm .

Science support for the SOFIA user community will be provided by the SOFIA Science Mission Operations Center (SSMOC) at NASA Ames Research Center, Moffett Field,



1. (Left) The NASA/DLR SOFIA observatory flying with its observatory door opened to full aperture for the first time on Dec. 18, 2009. (NASA Photo / Carla Thomas).

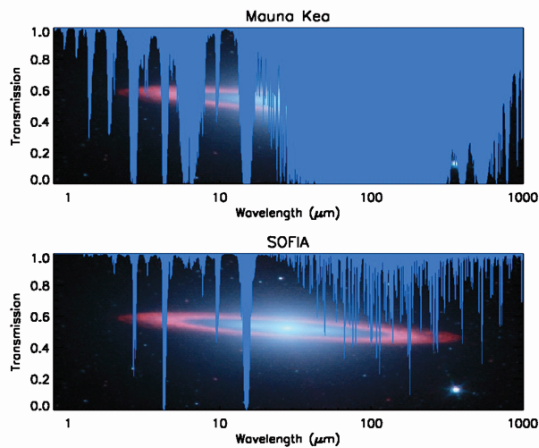


Fig. 2. The typical atmospheric transmission at an altitude of 45,000 feet as compared to the transmission on a good night at Mauna Kea (13,800 ft. MSL). From 1 to 1000 μm , the average transmission is $\geq 80\%$ except in the center of absorption lines due to mostly H_2O , CO_2 , and O_2 . Background image: IRAC false color image of the Sombrero Galaxy, courtesy of NASA/JPL-Caltech.

California and the Deutsches SOFIA Institut (DSI) at the University of Stuttgart, Stuttgart, Germany. The home base for flight operations of the SOFIA aircraft, Clipper Lindbergh, will be NASA's Dryden Aircraft Operations Facility (DAOF) in Palmdale, California. SOFIA will also operate from other bases world wide, including some in southern hemisphere, to enable observations at any declination in the sky and to facilitate timely observations of transient events such as variable stars, comet apparitions, occultations, exoplanet transits, novae, and supernovae.

SOFIA will provide community-wide opportunities for forefront science, invaluable hands-on experience for young researchers, and an extensive and unique education and public

outreach program. With observing flexibility and the ability to deploy new and updated instruments, the observatory will make important contributions towards understanding a variety of astrophysical problems well into the 21st century.

First test flights of the observatory began in April 2007 at L-3 Communications in Waco, Texas after which it was ferried to DAOF where further flight testing and development has been conducted. Closed door testing was completed in January, 2008. The first flight of the DAOF open door test series occurred on December 9, 2009, and the door was opened to expose the full aperture of the telescope a week later on December 18, 2009. SOFIA will see first light in April of 2010, and by 2014, is expected to begin making more than 100 8-10 hour scientific flights per year until the mid 2030s.

II. THE SOFIA TELESCOPE

The SOFIA telescope (Table 1 and Figures 3 and 4), supplied by DLR under an agreement with NASA in exchange for observing time on SOFIA, is a bent Cassegrain with a 2.7m (2.5m effective aperture) parabolic primary mirror and a 0.35m diameter hyperbolic secondary mirror with a $f/19.6$ Nasmyth infrared focus fed by a 45° gold coated dichroic mirror.

The infrared Nasmyth focus is 300mm behind the instrument flange. The dichroic mirror allows transmitted optical light to be reflected by a second tertiary behind the dichroic to a visible Nasmyth focus where it is fed into an optical focal plane guiding camera system, the [Focal Plane Imager](#) (FPI). Two other imaging and guiding cameras, independent of the FPI, are available: the [Wide Field Imager](#) (WFI) and the [Fine Field Imager](#) (FFI). The WFI and the FFI are attached to the front ring of the telescope. The dichroic tertiary mirror can be replaced by a fully reflecting tertiary for applications requiring maximum throughput at the shorter wavelengths.

Table 1. Characteristics of the SOFIA Observatory and Telescope

Nominal Operational Wavelength	0.3 to 1600 μm	Diffraction Limited Wavelengths	$\geq 15 \mu\text{m}$
Primary Mirror Diameter	2.7 meters	Optical Configuration	Bent Cassegrain with chopping secondary mirror and flat folding tertiary
System Clear Aperture Diameter	2.5 meters	Chopper Frequencies	1 to 20 Hz for 2-point square wave chop
Nominal System f-ratio	19.6	Maximum Chop Throw on Sky	+/- 4 arcmin (unvignetted)
Primary Mirror f-ratio	1.28	Pointing Stability	= 1.0" rms at first light = 0.2" rms in operations
Telescope's Unvignetted Elevation Range	20 to 60 degrees	Pointing Accuracy	= 0.5" with on-axis focal plane tracking
Unvignetted Field-of-View Diameter	8 arcmin	Total Emissivity of Telescope (Goal)	15% at 10 μm with dichroic tertiary 10% at 10 μm with aluminized tertiary
Image Quality of Telescope Optics at 0.6 μm	1.5 arcsec on-axis (80% encircled energy)	Recovery Air Temperature in Cavity (and Optics Temperature)	= 240 K
Diffraction Limited Image Size	$0.1'' \cdot \lambda \mu\text{m}$ FWHM		

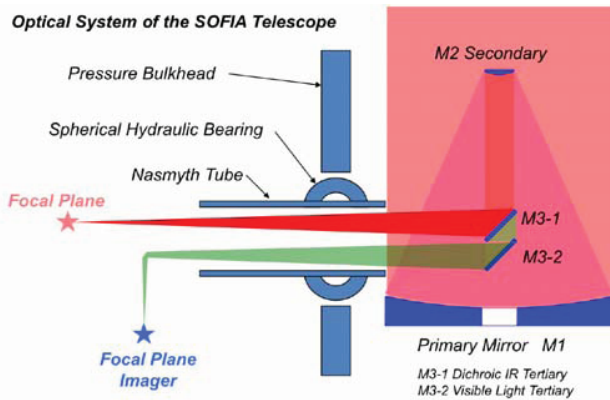


Fig. 3. (left) The bent Cassegrain-Nasmyth optical configuration of the SOFIA 2.5-meter infrared telescope. (right) Main cabin looking aft toward the pressure bulkhead and telescope assembly (courtesy of the NASA Dryden Flight Research Center Photo Collection.).

The secondary mirror is attached to a chopping mechanism providing chop amplitudes of up to ± 4 arcmin at chop frequencies between 0 and 20 Hz, programmable by either a user supplied wave-form or by the telescope control electronics.

III. SOFIA'S FIRST GENERATION INSTRUMENTS

SOFIA's eight first generation Science Instruments (SIs, Table 2) cover a much wider range of wavelengths and spectral resolutions than those of any other observatory (Figure 5). These include three Facility Class Science Instruments (FSIs) that will be maintained and operated by

the SOFIA Science Mission Operations (SMO) staff: the High-resolution Airborne Wideband Camera (HAWC), the Faint Object InfraRed Camera for the SOFIA Telescope (FORCAST), and the First Light Infrared Test Experiment CAMERA (FLITECAM). FSI pipeline-reduced and flux calibrated data will be archived for general access by the astronomical community after a one year exclusive access (proprietary) period.

The remaining five SIs are Principal Investigator (PI) class instruments are maintained and operated by the PI teams at their home institutions. These instruments are designed to be less general in their potential applications than FSIs. They are more likely to undergo upgrades between flight series so that they can be maintained at the state-of-the-art, albeit at the expense of not having fixed capabilities. General investigators will be able to propose for PI instruments in collaboration with the PI team. Present development plans are for pipeline reduced data from the US PI instruments to be added to the science archive after a one year exclusive access period. Two PI-class instruments are being developed in Germany. It is planned that the German PI instrument

Fig. 4. (Below) Cutaway view of the SOFIA Observatory showing the locations of the critical components

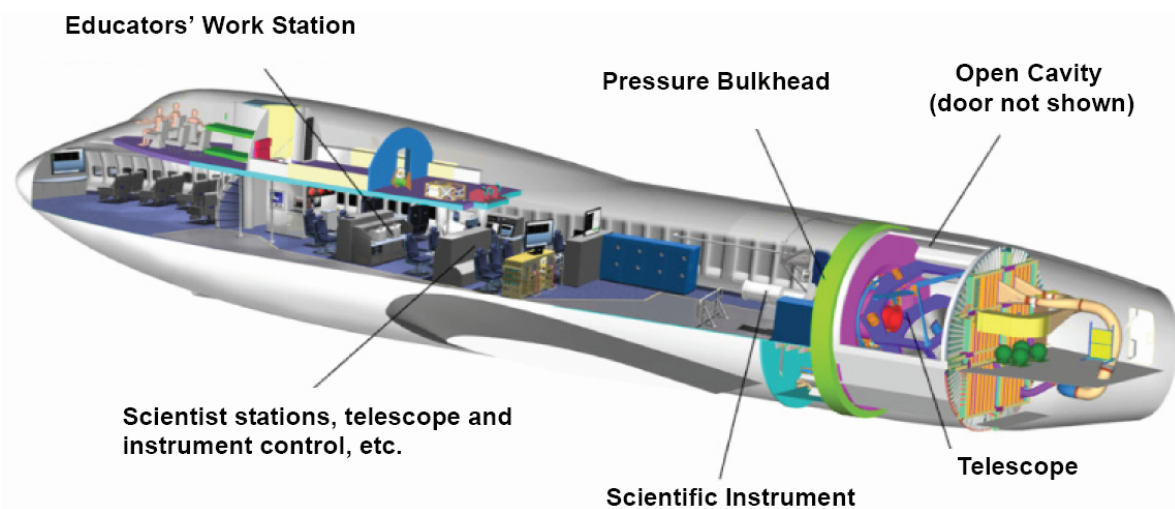


Table 2. SOFIA First Generation Instrument Summary

SOFIA Instrument	Description	Built by / PI	λ range (μm) spec res ($\lambda_r/\Delta\lambda$)	Field of View Array Size	Available
FORCAST	Faint Object InfraRed CAMera for the SOFIA Telescope Facility Instrument - Mid IR Camera and Grism Spectrometer	Cornell T. Herter	5 - 40 R ~ 200	3.2' x 3.2' 256 x 256 Si:As, Si:Sb	2010
GREAT	German Receiver for Astronomy at Terahertz Frequencies PI Instrument - Heterodyne Spectrometer	MPIfR, KOSMA DLR-WS R. Güsten	60 - 200 R = 10^6 - 10^8	Diffraction Limited Single pixel heterodyne	2010
FIFI LS	Field Imaging Far-Infrared Line Spectrometer PI Instrument w/ facility-like capabilities - Imaging Grating Spectrometer	MPE, Garching A. Poglitsch	42 - 210 R = 1000 - 3750	30"x30" (Blue) 60"x60" (Red) 2 - 16x5x5 Ge:Ga	2010
HIPO	High-speed Imaging Photometer for Occultation Special PI Instrument	Lowell Obs. E. Dunham	.3 - 1.1	5.6' x 5.6' 1024x1024 CCD	2012
FLITECAM	First Light Infrared Test Experiment CAMera Facility Instrument - Near IR Test Camera and Grism Spectrometer	UCLA I. McLean	1 - 5 R~2000	8.2' x 8.2' 1024x1024 InSb	2012
CASIMIR	CAItech Submillimeter Interstellar Medium Investigations Receiver PI Instrument - Heterodyne Spectrometer	Caltech J. Zmuidzinas	200 - 600 R = 3×10^4 - 6×10^6	Diffraction Limited Single pixel heterodyne	2012
HAWC	High-resolution Airborne Wideband Camera Facility Instrument - Far Infrared Bolometer Camera	Univ of Chicago D. Harper	50 - 240	Diffraction Limited 12x32 Bolometer	2013
EXES	Echelon-Cross-Echelle Spectrograph PI Instrument - Echelon Spectrometer	UT/UC Davis NASA Ames M. Richter	5 - 28 R = 10^5 , 10^4 , or 3000	5" to 90" slit 1024x1024 Si:As	2013

The Field Imaging Far-Infrared Line Spectrometer (FIFI LS) will be available to the US science community as a Facility-like instrument under special arrangement with the FIFI LS team. The FIFI LS data will be pipeline-reduced and flux-calibrated before it is placed in the data archive.

Information about all the first-generation instruments is at:

<http://www.sofia.usra.edu/Science/instruments/index.html>.

IV. EARLY SCIENCE WITH FORCAST AND GREAT

Early science programs during 2010-2011 will be conducted with the Cornell FORCAST imager and the German spectrometer GREAT (see Figure 5).

FORCAST is a facility class, mid-infrared diffraction-limited camera with selectable filters for continuum imaging

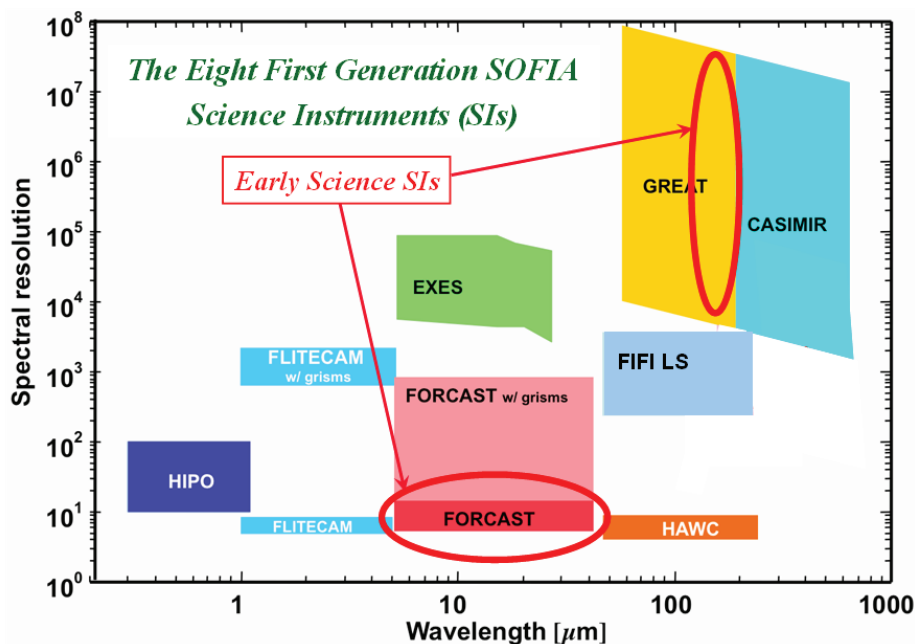


Figure 5. (Right) SOFIA's first generation instruments shown in a plot of log spectral resolution vs. log wavelength. FORCAST and GREAT will operate in the regimes indicated by the large red ovals at first light and during early science operations

in two 4-25 μm and 25-40 μm bands, and also incorporates low resolution ($R = 200\text{-}800$) grism spectroscopy in the 4-8, 16-25 μm and/or 25-40 μm regions. It will provide the highest spatial resolutions possible with SOFIA, enabling detailed imaging of protostellar environments, young star clusters, molecular clouds, and galaxies. Simultaneous high-sensitivity wide-field imaging can be performed in the two-channels using 256x256 Si:As and Si:Sb detector arrays which sample at 0.75 arcsec/pixel giving a 3.2 arcmin x 3.2 arcmin field-of view. For small objects, chopping can be performed on the array to increase sensitivity.

GREAT, a PI-class instrument, will investigate a wide range of astronomical questions requiring the highest spectral resolution. These include observations of the 158 μm fine-structure transition of ionized carbon (CII), which is the most important cooling line of the cold interstellar medium and is a sensitive tracer of the star forming activity of a galaxy. Observations of the 112 μm rotational ground-state transition of HD will allow the derivation of the abundance profile of deuterium across the galactic disk and nearby galaxies, thereby providing unique information on the chemical evolution and star formation history of these systems. GREAT is a 2-channel heterodyne instrument that offers observations in three frequency bands with frequency resolution down to 45 kHz (3.74×10^{-6} μm). The lower band, 1.4-1.9 THz (157.89 -214.29 μm), covers fine-structure lines of ionized nitrogen and carbon. The middle band is centered on the cosmologically relevant 1-0 transition of deuterated molecular hydrogen (HD) at 2.6 THz (112 μm) and the rotational ground-state transition of OH. A high-frequency band includes the 63 μm transition of OI. The receivers employ sensitive superconducting mixer elements, SIS tunnel junctions and hot electron bolometers. A polarizing beam splitter allows simultaneous measurements of two lines at the same time.

V. PERFORMANCE SPECIFICATIONS OF SOFIA WITH ITS FIRST GENERATION INSTRUMENTS

SOFIA's first generation SIs will initially provide for high-resolution spectroscopy ($R \geq 10^4$) at wavelengths between 5 and 600 μm , and the 8 arcminute diameter field of view (FOV) allows use of very large format detector arrays. Despite the relatively large thermal IR background at SOFIA's operational altitude, the 2.5-meter aperture of the SOFIA telescope will be capable of measurements with an order of magnitude better photometric sensitivity than IRAS (Figure 6) and a factor of > 3 better linear spatial resolution than that of the *Spitzer* Space Telescope (Figure 7). It will be comparable in sensitivity to the European Space Agency (ESA) Infrared Space Observatory (ISO). SOFIA's capability for diffraction-limited imaging beyond 15 μm will produce the sharpest images of any current or planned IR telescope operating in the 30 to 60 μm region (Figure 5). SOFIA's performance for line flux measurements with various first generation instruments is shown in Figure 8. Each instrument will have an exposure time calculator on the

SOFIA website to enable prospective observers to evaluate the feasibility of the programs they propose to conduct. See <http://www.sofia.usra.edu> for details.

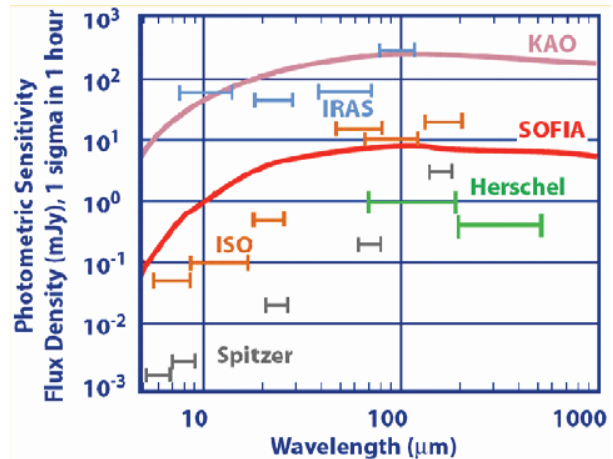


Fig.6. SOFIA's photometric sensitivity will be comparable to that of ISO.

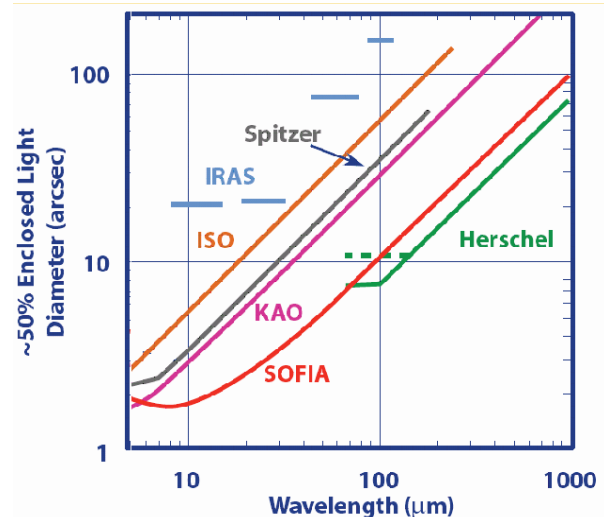


Fig.7. SOFIA's high angular resolution will make it a premier IR imaging facility.

VI. UNIQUE ADVANTAGES OF SOFIA

Key advantages of the SOFIA Observatory concept promise to make it a unique asset for astronomy in the coming decades. First, SOFIA is an observatory operating in a near-space environment that comes home after every flight. Thus, its SIs can be exchanged regularly to respond to changing science requirements and new technologies that need not be space qualified. Second SOFIA can accommodate large, massive, complex instruments requiring substantial power and heat dissipation. Third, simple repairs and adjustments to SIs can be performed in flight to optimize

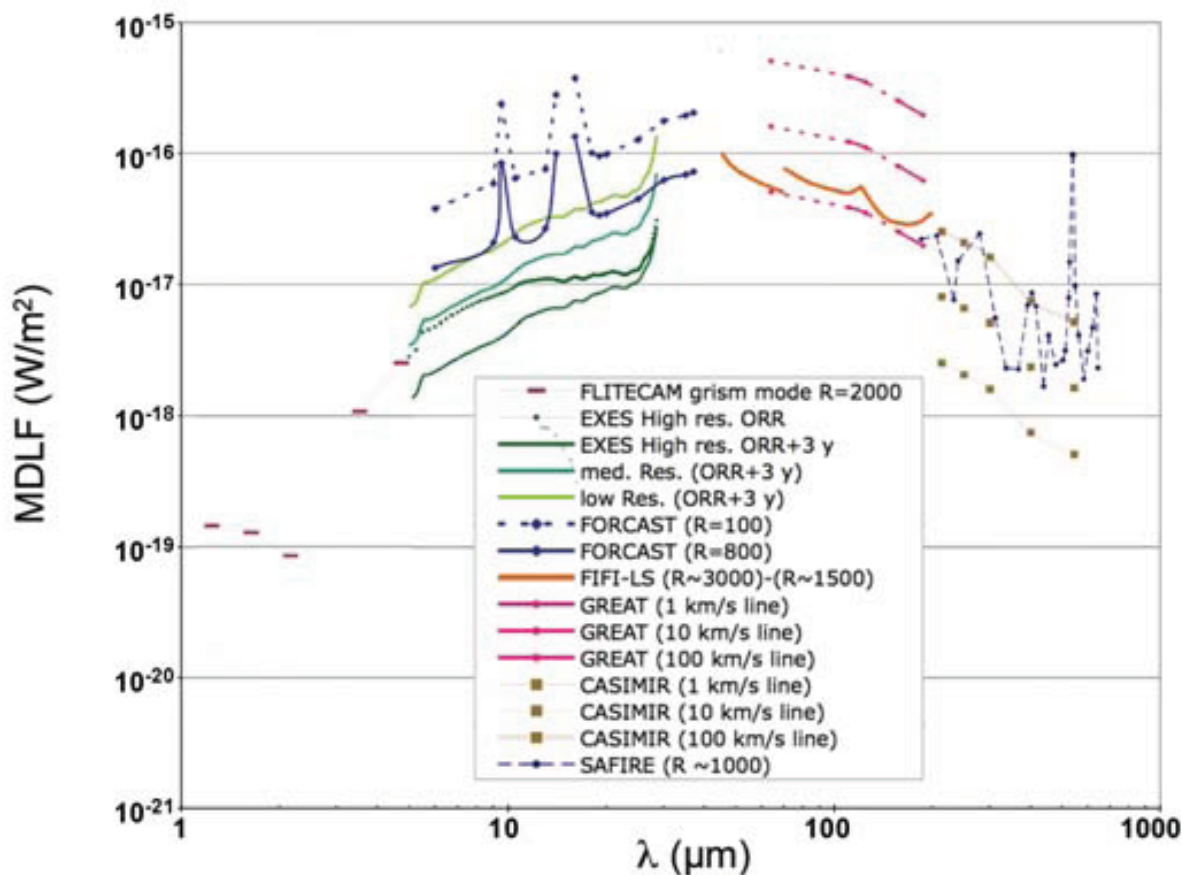


Fig. 8 (Above) The expected line sensitivity of SOFIA spectrometers at the time of full operational capability. Shown is the 10σ minimum detectable line flux (MDLF) in watts per meter squared for 900 seconds of integration on source. Observing and chopper efficiency have not been included.

SOFIA's science productivity. Fourth, SOFIA is a unique platform for studying transient events because it can operate from airbases worldwide on short notice to respond to new discoveries at all declinations. SOFIA can respond to such diverse events as supernova/nova explosions, cometary impacts, comet apparitions, eclipses, occultations, near-Earth objects, activity in Active Galactic Nuclei, and activity in luminous variable stars. Fifth, SOFIA's versatile complement of SIs will facilitate a coordinated panchromatic science program on specific targets. No other observatory operating in SOFIA's wavelength range has such a large variety of SIs for such a long period of time. Sixth, SOFIA will be able to access events that many space observatories cannot view because of the constraints imposed by their orbits. For example, SOFIA can observe objects close to the sun, enabling temporal monitoring of supernovae, novae, and variable stars, throughout the year. It will be the only infrared mission that can view the inner planets and bright, active comets during perihelion passage when they are brightest and most active.

Finally, SOFIA's 20-year operational lifetime will enable long-term temporal studies and follow-up of work initiated by SOFIA itself and by other observatories.

VII. TRAINING STUDENTS AND DEVELOPING TECHNOLOGY WITH SOFIA

The US and German science communities have identified the continuous training of instrumentalists as a high priority. SOFIA will contribute to this objective by enabling the training of students and faculty in instrument hardware and software development. It provides an optimal environment for students to participate in the hands-on, development of forefront technologies, an opportunity generally not available to students working on satellite projects. SOFIA will inspire the next generation of young experimental astrophysicists to develop their talents in many different areas of science and engineering. Just as was the case with the Kuiper Airborne Observatory (KAO)⁵, SOFIA graduate and post-doctoral students will form a rich reservoir of talent that will become the next generation of Principal Investigators and Instrument Scientists.

SOFIA will facilitate the early deployment of new detector and instrumentation technology applicable to space-

flight. Unlike space borne observatories, which must use technologies qualified for space-flight years in advance of launch, SOFIA will always be able to utilize the latest state-of-the-art technology in terms of sensitivity, detector response time, observation technique, spectral resolution and more, by conducting an ongoing instrument development program. As noted above, SOFIA instruments can be more complex, larger in volume and weight, and require higher power consumption than instruments typically flown on space-based observatories.

VIII. SCIENCE OPERATIONS AND SCHEDULE

The SOFIA Science and Mission Operations Center (SSMOC) is located at NASA Ames Research Center in Moffett Field, CA. The Universities Space Research Association (USRA) and the Deutsches SOFIA Institut (DSI) in Stuttgart, Germany manage science and mission operations for NASA and DLR. The SOFIA Program will support approximately 50 investigation teams per year, selected by a peer reviewed proposal process. An on-going instrumentation development program will ensure that the facility is operating at the state-of-the-art during its flight lifetime.

IX. GENERAL OBSERVER OPPORTUNITIES WITH SOFIA

Three Early Short Science (ESS) flights with FORCAST and GREAT will occur in 2010. ESS flights, limited in scope, will call for collaboration with the Principle Investigators (PIs) of FORCAST and GREAT. Routine observations will begin in 2011. A first call to the astronomical community for proposals for a fifteen flight Early Basic Science (EBS) Program will occur on April 19, 2010, with proposals due on July 2, 2010. The ~ 15 flight EBS program will be executed during 2011. The first call for General Investigator (GI) science proposals will occur in 2011. There will be future GI science calls at least every 12 months. The first GI flights will occur in 2012. GI science flights conducted annually on a shared risk with the SI PI's. There will be additional GO flight opportunities with Facility Instruments. The annual flight rate will ramp up to at least 100 8-10 hour flight by 2014. SOFIA's

X. INSTRUMENTATION DEVELOPMENT PROGRAM

With observing flexibility and the ability to deploy new and updated instruments, the observatory will make important contributions towards understanding a variety of astrophysical problems well into the 21st century. The SOFIA instrumentation development program will include the development of new science instruments (both FSIs and PSIs), upgrades existing SIs, and studies of instruments and technology. The second call for SOFIA science instruments is expected to be in 2011, and there will be additional calls for new instrumentation development every 3 years and the

Project anticipates that there will be one new instrument or upgrade per year. The approximate funding level for the new science instrument development program will be ~\$10 M/yr.

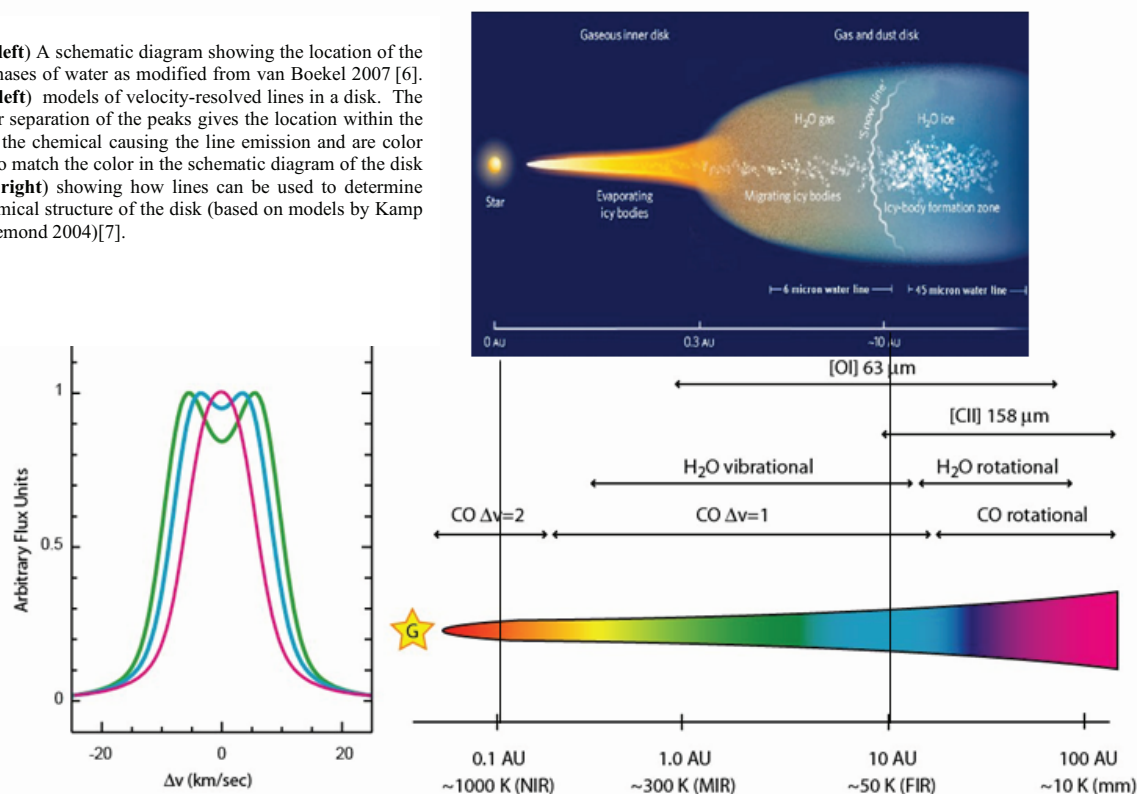
XI. SELECTED EXAMPLE SCIENCE OPPORTUNITIES WITH SOFIA

SOFIA science emphasizes four major themes: 1) The formation of stars and planets, 2) The Interstellar Medium (ISM) of the Milky Way, 3) galaxies and the Galactic Center, and 4) planetary science. Many of these studies involve objects that are hidden from view by dense layers of obscuring dust and gas. Others are at very low temperatures. SOFIA, with its diverse complement of instruments, is uniquely suited to study cool and deeply embedded objects and to determine their role in the evolution of the universe. Below, we describe detail a selected sample of the science problems from these themes that we expect will be studied to advantage with SOFIA during the early years of its mission.

A. Studies of Protoplanetary Disks

Much of our understanding about the origin of the Solar System will be gained by studying circumstellar disks in which planets may be forming around young stars. Such studies involve obtaining the spectral energy distributions (SEDs) and direct images at IR and submillimeter wavelengths. SOFIA's spectrometers will provide data on circumstellar disks that will reveal their kinematics, composition, and evolution. It is generally believed that water (H₂O) plays a major role in the formation and early evolution of planetary systems. Water is the dominant reservoir of oxygen under nebular conditions so that water ice condensation will dominate the mass budget of newly-formed planetesimals. It is thought that the cores of giant planets are formed beyond the "snow line": the boundary in a disk where the temperature falls below the 170K sublimation temperature of water ice[5]. Thus, the origin and distribution of water in the inner proto-planetary disks is crucial to our understanding of the abundance of water on terrestrial planets in the habitable zones around stars. While the spatial resolution of SOFIA will be limited, the resolved line profile provides, in combination with Kepler's law, will yield the distribution of the water and other biogenic molecules in the emitting layers of the disk (see Figure 9). Observations of water lines in the 2.0 to 2.4 μ m window have revealed the power of such molecular line studies, but these are of course limited to very hot gas close to the protostar. The 6 μ m region, on the other hand, is sensitive to the warm gas in the terrestrial planet zone and near the snow line. We note that studies of the pure rotational lines (at submillimeter wavelengths) are hampered by either severe beam dilution or by telluric absorption. The strength of the lines will provide direct measurements of the temperature and column density of water in these disks.

Fig.9. (left) A schematic diagram showing the location of the three phases of water as modified from van Boekel 2007 [6]. (lower left) models of velocity-resolved lines in a disk. The Doppler separation of the peaks gives the location within the disk of the chemical causing the line emission and are color coded to match the color in the schematic diagram of the disk (lower right) showing how lines can be used to determine the chemical structure of the disk (based on models by Kamp & Dullemond 2004)[7].



B. Star Formation and the Interstellar Medium of Galaxies

The interstellar medium (ISM) plays a central role in the evolution of galaxies as both the birth site of new stars and the repository for old stellar ejecta as shown schematically in Figure 10. The formation of new stars slowly consumes the ISM, locking it up for millions to billions of years. As these stars age, the winds from low-mass, asymptotic giant branch stars (AGB) and high-mass, red supergiants (RSG), novae, and supernovae inject products of stellar and explosive

nucleosynthesis into the ISM, slowly increasing its metallicity. This constant recycling and the associated enrichment drives the evolution of a galaxy’s visible matter and changes its emission characteristics. To understand this recycling, we must study the physical processes of the ISM, star formation, mass-loss from evolved stars, and the relationships of these processes on a Galactic scale. Dust and gas play a major role in these processes. SOFIA with its wide wavelength coverage and high spectral resolution capabilities is destined to play a dominant role in this field.

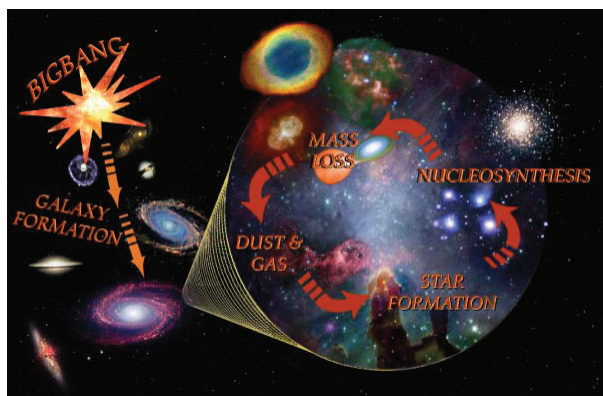


Fig. 10 Chemical Evolution of the universe (after Gehrz 2008 [8])

The 5-1000 μm spectral region accessible to SOFIA contains atomic forbidden lines, molecular ro-vibrational lines, and dust emission features that are critical for understanding the physical processes at work in regions of star formation. A typical sample of these is shown in Figure 11. At the spectral resolutions available to SOFIA, these lines can be used to study the mineralogy of the dust, abundances of elements in the gas and dust, and the kinematics of the gas phase elements.

C. The Interstellar Deuterium Abundance

Deuterium in the universe was created in the Big Bang and the primordial deuterium abundance provides the best constraint on the mass density of baryons in the universe. Its abundance provides strong constraints on the physical

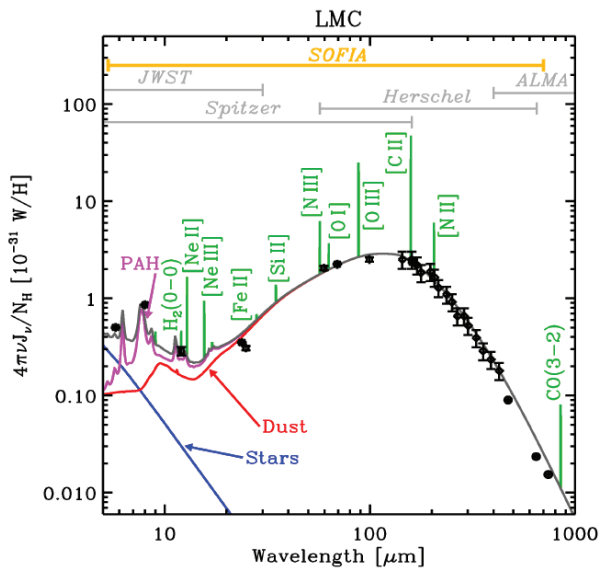


Fig.11. The spectral energy distribution of the entire LMC, based on data from Spitzer, IRAS and FIRAS [9]. SEDs are fitted with the dusty PDR model of Galliano et al. [10]. Spitzer and Herschel will provide good photometric coverage of a galaxy's spectral energy distribution (SED) over a portion of the wavelengths. SOFIA will provide excellent wavelength coverage and spectroscopic capability across the entire SED. In the future, JWST and ALMA will provide complementary wavelength coverage and work on nearby galaxies and the most distant Universe. Figure courtesy of Galliano.

conditions during the first few minutes of the universe's expansion. However, this record of the Big Bang has subsequently been modified by stellar nuclear burning as material has been cycled from stars to the interstellar medium and back to stars during the chemical evolution of the universe by the cycle of stellar evolution (see Figure 12). Deuterium is thus potentially a key element for probing the origin and evolution of the universe as well as the star

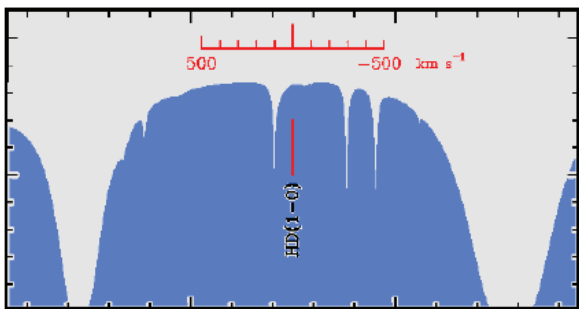


Fig. 12. Schematic representation of the atmospheric transmission around the 2.6 THz (112 μm) HD line at 40,000 feet

formation history of the universe. As pointed out by Neufeld et al. [11], HD is a proxy for the cold molecular hydrogen component of the ISM in the Galaxy, and the distribution of

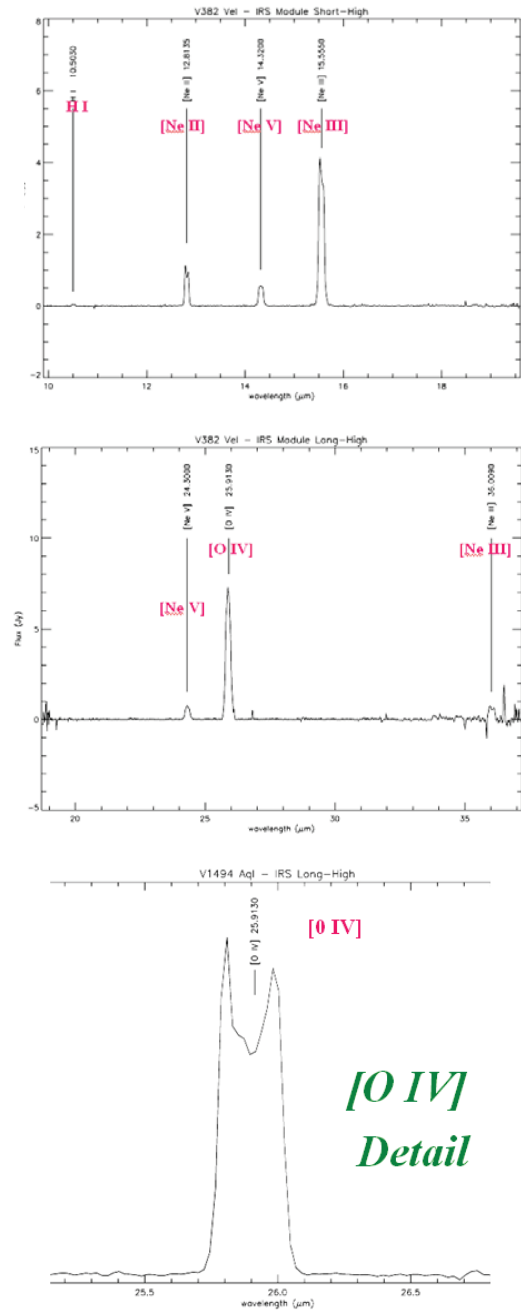


Fig. 13. (Right) Nova explosions caused by thermonuclear runaways on the surfaces of white dwarfs accreting matter in close binary systems lead to the production of Ne and O as shown the top and middle panels above in Spitzer Space Telescope IRS Short and Long-High Resolution Spectra. Abundances and kinematics (see lower panel) can be determined from the high spectra. Data from NASA/JPL/Caltech/R. D. Gehrz

deuterium in the Galaxy thus probes both stellar processing and the efficiency with which the debris of stellar evolution is mixed into the interstellar medium. HD has a much lower

excitation temperature than molecular hydrogen and a dipole moment that essentially compensates for the higher abundance of molecular hydrogen. Measuring the amount of cold HD ($T < 50\text{K}$) and therefore the deuterium abundance throughout our Galaxy can best be done by observing the 2.6 THz (112 μm) ground state (1-0) rotational transition line of deuterated molecular hydrogen (HD) at with SOFIA (Figure 9).

The 112 micron line can also be observed at high spectral resolution ($R > 10^5$ or $< 3\text{km/s}$) with SOFIA's GREAT spectrometer to determine the velocity structure across the Galaxy.

D. Nucleosynthesis in Classical Nova Explosions

The astrophysical thermonuclear runaways that produce classical nova explosions may play an important part in producing some of the isotopic anomalies that are present in the meteoritic and cometary debris that represent the remains of the primitive solar system [8]. Metal abundances in nova ejecta can be deduced from IR dust emission features and IR forbidden emission lines from highly ionized metals. Recent IR observations with ground-based telescopes and the Spitzer Space Telescope (Figure 13) have shown that some recent novae ejected shells that were extremely overabundant in CNO, Ne, Mg, Al, and Si. These novae also produced every known type of astrophysical dust. SOFIA will be a superb platform for observing nova explosions on several counts. First, its mobility will enable the timely monitoring of the temporal development of nova events. This requires observational capabilities that cover all possible declinations and the capability of following events that develop on time-scales of days, weeks, and months.

SOFIA's ability to observe objects close to the sun by flying a path that places the sun below the horizon will enable a continuous record of the temporal development of such events to be recorded. Second, the spectroscopic capabilities of SOFIA will enable the recording of many

forbidden lines obscured by the atmosphere from ground-base observatories and unavailable to the spectrometers of other space missions.

ACKNOWLEDGMENTS

We thank the entire SOFIA team for their tireless work on the SOFIA project. R. D. G. was supported by USRA, NASA, and the US Air Force.

REFERENCES

- [1] Werner, M. W., et al., "The Spitzer Space Telescope Mission," *Astrophys. J. Supp. Series* 154, 1-9, 2004.
- [2] Gehrz, R. D., et al., "The NASA Spitzer Space Telescope," *Rev. Sci. Instrum.*, 78 (011302), 2007.
- [3] Pilbratt, G. L., "Herschel Space Observatory mission overview," *Proc. SPIE*, 4850, 586, 2003.
- [4] Gardner, J. P., et al. "The James Webb Space Telescope," *Space Science Reviews*, 123,485, 2006.
- [5] D. D. Sasselov and M. Lecar, "On the snow line in dusty protoplanetary disks," *Astrophys. J.* 558, 995-998,
- [6] van Boekel, R., "Water worlds in the making," *Nature* 447, 31, 2007.
- [7] Kamp, I., Dullemond, C. P., "The Gas Temperature in the Surface Layers of Protoplanetary Disks," *Ap. J.* 615, 991, 2004
- [8] R. D. Gehrz, "Infrared Studies of Classical Novae," in "Classical Novae," 2nd Edition, eds. M. F. Bode and A. Evans, Cambridge University Press: Cambridge, Ch. 8, 2008.
- [9] Bernard, J - P, et al., "Spitzer Sage Survey of the Large Magellanic Cloud. III. Star Formation and ~1000 New Candidate Young Stellar Objects." *Ap. J.* 136, 919., 2008.
- [10] Galliano, F., Madden, S., Tielens, A.G.G.M., Peeters, E., Jones, A.P., "Variations of the Mid - IR Aromatic" Features inside and among Galaxies." *Ap. J.* 679, 310, 2008..
- [11] D. A. Neufeld, J. D. Green, D. J. Hollenbach, et al., "Spitzer Observations of Hydrogen Deuteride," *ApJL*, 647, L33-L36, 2006. van Boekel, R., "Water worlds in the making," *Nature* 447, 31, 2007. Kamp, I., Dullemond, C. P., "The Gas Temperature in the Surface Layers of Protoplanetary Disks," *Ap. J.* 615, 991, 2004.

Far-Infrared Interferometry from Antarctica

Hiroshi Matsuo

Advanced Technology Center, National Astronomical Observatory of Japan, Mitaka, Tokyo 181-8588, Japan

Contact: h.matsuo@nao.ac.jp, phone +81-422-34 3915

Abstract— Future high-angular resolution far-infrared interferometers and their possible implementation plans on high altitude sites such as Dome Fuji or Dome A in Antarctica is presented. Importance of observing far-infrared atomic fine-structure lines is discussed referring to recent AKARI observations of a high mass star-forming region.

I. INTRODUCTION

Astronomy in terahertz frequency region is advancing rapidly owing to the development of detector technologies, large aperture telescopes on high mountains and cryogenic telescopes in space. Variety of astronomical sources is probed in this frequency range by molecular and atomic lines and dust continuum emissions. Those are also important probes of distant galaxies as well as the Sunyaev-Zel'dovich effects for distant galaxy cluster searches.

In far-infrared region, Japanese satellite *AKARI* has made all sky survey in six bands [1]. A Fourier transform spectrometer was installed in the far-infrared surveyor (FTS/FIS) which made imaging spectroscopic observations [2]. Here, an observation of interstellar material around a massive star, Eta Carinae is presented as an example.

To study more detail of the source distribution or observe distant objects, higher angular resolution observations by space-based far-infrared interferometer is needed, but this required technology developments of detectors and interferometers. In this paper I discuss on far-infrared interferometry from high altitude plateau in Antarctica. I will compare the performance of heterodyne and direct detector interferometers and show that direct detector interferometers can achieve wide-field and high angular resolution imaging.

As an example of direct detector interferometry, experimental performance of a double input Martin-Puplett type interferometer that realized multiplying interferometer is reviewed in the last section.

II. PROBES OF DISTANT UNIVERSE

Here I'd like to summarize astronomical probes of distant universe. Following three components are important in millimetre, submillimeter and far-infrared astronomy.

- Interstellar dust in starburst galaxies observed by thermal emission.
- Hot plasma in galaxy clusters observed by Sunyaev-Zel'dovich effects.
- Photo-dissociation and ionized regions observed by atomic fine-structure lines.

Firstly, high-redshift starburst galaxies are observed by wide field surveys. One example is millimetre-wave survey by AzTEC bolometer array on ASTE telescope toward *AKARI* deep field south [3]. Because of its large negative K-correction, millimetre-wave observations selectively sampled galaxies at high redshifts.

Secondly, Sunyaev-Zel'dovich effects have been a probe to measure the Hubble constant and also to identify thermal structure of the plasma [4]. Because Sunyaev-Zel'dovich effects are interaction of hot plasma with cosmic background radiation, the intensity does not decline as a function of redshift.

Thirdly, far-infrared atomic forbidden emission lines play an important role as coolants of PDRs and HII regions. The emission could be probes of starburst activities of high-redshift universe. But, we still do not understand into detail the physical conditions each atomic line probes, mostly due to the limited imaging capabilities and angular resolutions.

The following figure illustrate the importance of observing in terahertz frequencies, where variety of emission can be observed as distortion of background or as foreground emission in Wien part of the cosmic background radiation in all the redshift range. This frequency region can be called as 'Terahertz Cosmic Window' to the distant universe.

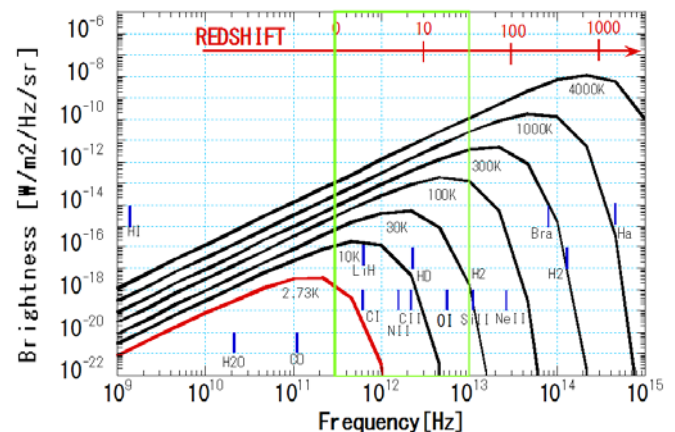


Fig. 1 The Terahertz Cosmic Window.

III. FIR LINES OF INTERESTS

There are a number of far-infrared forbidden transition lines from ionized and neutral atomic species such as [OI] 63 μm , 145 μm , [OIII] 52 μm , 88 μm , [NII] 122 μm , 205 μm and [CII] 158 μm . These lines are major coolants of photo-dissociation and ionized regions [5]. To postulate importance

of atomic fine structure line, I present *AKARI* observation of interstellar material around one of the most massive star in our galaxy, Eta Carinae [6]. It is known that Eta Carinae is a binary with the primary Luminous Blue Variable with mass of about $100 M_{\odot}$ and a companion of $30 M_{\odot}$, both with violent mass loss activities [7]. Distance to the star is only 2.3 kpc and extinction toward the star and Carinae Nebula is small and detailed studies have been made by optical emission lines [8]. Studies of interstellar environments of the most massive stars in local universe are also linked to the understanding environments of massive stars in the early universe, Pop III stars.

A. Observations with *AKARI*

Seven pointed observation was made using FTS/FIS in 2007. Observational details, data reduction and analysis is given in [6, 9]. Figure 1(a) and (b) shows the distribution of [CII] $158 \mu\text{m}$ and [OIII] $88 \mu\text{m}$ lines around Eta Carinae. Referring to the $\text{H}\alpha$ emission in figure 1(c), west from Eta Carinae with ionized emission and molecular gas in front is called the Keyhole Nebula. The head of the Keyhole Nebula, with the arc-like emission that is aligned with the stellar wind axis, is thought to be related to the past activity of Eta Carinae [9].

The [CII] emission seems to peak around the head of the Keyhole where ionized nitrogen line [NII] $122 \mu\text{m}$ is also observed. Toward the opposite side of the stellar wind axis to the south-east, [CII] emission is also observed. In this region there is no indication of ionized gas, but the area is where stellar wind interacts with molecular clouds. The apparent alignment of the [CII] emission peaks seems to indicate that it is related to the past stellar wind activities. The current mass loss rate of Eta Carinae is estimated to be $10^{-4} - 10^{-3} M_{\odot}$ /yr with velocity of about 600 km/s. Assuming the same velocity it takes about 5000 year for the stellar wind to interact with the ionized region or molecular clouds, which are 3-5 pc away from Eta Carinae

The [OIII] emission, on the other hand, has strong emission to the west of Eta Carinae. Intensity of the [OIII] emission is more than ten times stronger than [CII] emission peak at Keyhole and strong EUV ionization source is required to ionize oxygen with ionization potential of 35 eV. The strong [OIII] emission come from the edge of ionized arc and the clump 4 or the feature called defiant finger [10]. From analysis of optical emission lines, ionization sources of the region are thought to be W25 and O4 If-type star Tr16-244 that are at the south-west corner of $\text{H}\alpha$ image in figure 2(c). Since critical density of [OIII] $88 \mu\text{m}$ is $5 \times 10^2 \text{ cm}^{-3}$, it can be efficient coolant of low density ionized gas. Combination with [OIII] $52 \mu\text{m}$ emission with different critical density can be used to estimate density of the ionized gas.

B. Requirements to Future Observations

Far-infrared spectroscopic observations by *AKARI* FTS/FIS revealed some physical condition of interstellar material around a massive star, which shows variety of activities related to the stellar activities and highly ionizing

UV flux within the region. To identify the physical condition and comparing with observation at other wavelength region, it is important to make higher angular resolution observations. Higher angular resolution observations by Herschel Space Observatory will provide more details of ionization and density structure.

The Carina Nebula is the nearest high mass star-forming region where we can observe into detail. To conduct observation in other star-forming regions and also in nearby galaxies, still higher angular resolution observations are required. Space based far-infrared interferometry will be the next step, but developments of detector and interferometer technologies are still on the way. In the next section I discuss what we can start in a short time scale to realize far-infrared interferometry on Antarctica Plateau.

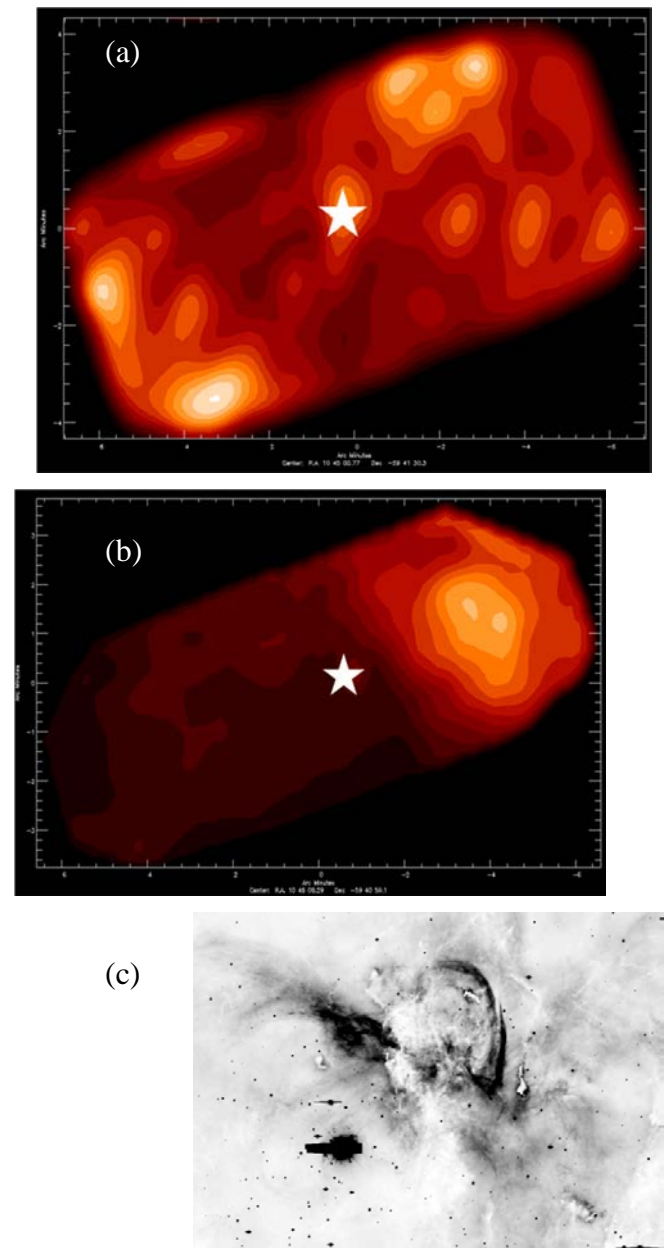


Fig. 2 Eta Carina and its surroundings observed by *AKARI*. (a) [CII] $158 \mu\text{m}$, (b) [OIII] $88 \mu\text{m}$, and (c) $\text{H}\alpha$ image by Smith et al. (2002) as a reference to the Keyhole Nebula. Coordinates are R.A.-Dec, and scale is identical.

IV. ANTARCTIC TERAHERTZ INTERFEROMETER

Observing condition of terahertz frequencies in Antarctica, sensitivity requirements and realization method will be discussed.

A. Atmospheric Transmission

Since terahertz radiation is absorbed by water vapour, high altitude site and/or cold sites are preferred for astronomical observations in millimetre and submillimeter-waves, such as Hawaii, Atacama and South Pole in Antarctica. High plateaus in Antarctica, such as Dome A or Dome Fuji, will be the ultimate site for astronomical observations, and that are unique sites for terahertz astronomy from ground.

Figure 3 shows calculated atmospheric transmission from high altitude site in Antarctica using 'am' program [11] assuming precipitable water vapour of 75 μm .

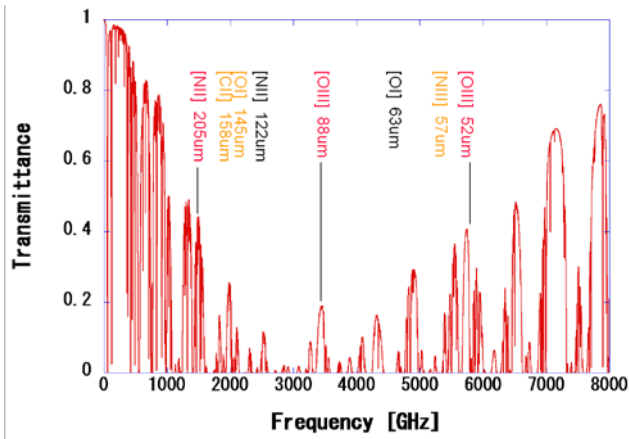


Fig. 3 Atmospheric transmission calculated for 75 μm precipitable water vapour from 4100 m altitude in Antarctica using 'am' program [11].

Under this condition, some fine structure atomic lines can be observed through atmospheric windows at terahertz frequencies. [NII] 205 μm have been observed by the SPIFI instrument at South Pole [12]. Doubly ionized oxygen lines, [OIII] 52 μm and 88 μm , could be observed with a transparency of better than 10% whereas [CII] 158 μm , [OI] 145 μm and [NIII] 57 μm with lower transparencies from high plateau in Antarctica.

B. Sensitivity of THz interferometers

First I compare heterodyne and direct detector interferometry. For ground based observations, sensitivity of heterodyne and direct detector interferometry is almost identical if the observing system is background and quantum noise limited. However, under low background condition in millimetre-wave or at high frequencies more than a few THz direct detector observations can be more sensitive. In terms of observing bandwidth, atmospheric windows will limit observing bandwidth up to several 10 GHz.

Heterodyne interferometry is a matured technology and many telescope apertures can be combined to make large arrays. On the other hand, direct detector interferometry is still under development and telescopes have to be optically connected and the number of antennas is limited.

TABLE I
SENSITIVITY OF TERAHERTZ INTERFEROMETERS

	Direct detectors	Heterodyne
Aperture diameter	1 m	1 m
Element number	2	10
Base line	50 m	50 m
Wavelength	200 μm	200 μm
NEP/ η or T_{sys}	10^{-15} W/Hz ^{0.5}	500 K
Bandwidth	10 GHz	10 GHz
Focal plane array	1000	1
Synthesized beam	1 "	1 "
Field of view	0.25 deg ²	0.5 arcmin ²
NEFD	20 mJy (1 σ , 12h)	10 mJy (1 σ , 12h)

The bandwidths can be wider for direct detectors and narrower for heterodyne detectors. For continuum study wider bandwidth is advantageous but background limited NEP will be degraded. For spectroscopic observations, heterodynes are advantageous for their high frequency resolution, but direct detector sensitivity also improves by limiting observing bandwidth.

Field of view would be a large factor in favour of direct detector interferometry. Current technologies enable focal plan array of more than 1000 elements. Signals from the direct detector interferometers can be sampled relatively slowly, and data recording systems are not limiting factors. On the other hand heterodyne interferometer required fast sampling and processing is required that limit number of detectors, hence the observing field of view.

C. Configuration

Direct detector interferometry requires input aperture mirrors and a beam combiner. Simplest configuration will be like figure 4(a). Aperture mirror can be on a straight boom or on a round track as shown in the figure. Mirrors on the track reflect signal from astronomical sources to a beam combiner at the center. For installation in high plateau in Antarctica it is better to make the interferometer as simple as possible. All components except a round track can be compact with sizes of about 1 m. To make beam combiner compact, beam diameter at combiner should be decreased to about 100 mm, which should also accommodate with focal plane detector arrays.

Figure 4(b) shows possible configurations of the four-beam interferometer. One Martin-Puplett type beam combiner that uses wire grid can make interferograms from linearly polarized signal. Four beam combiners can make use of dual polarization beams from four input mirrors. For compensation of different optical path between two sets of mirrors, optical delay should be implemented that is schematically shown in figure 4(b) at the bottom.

Since Martin-Puplett interferometer is polarizing interferometer, combination of polarizer angles gives measurements of different polarization state; parallel combination gives measurements of I and Q, orthogonal combination for U and V.

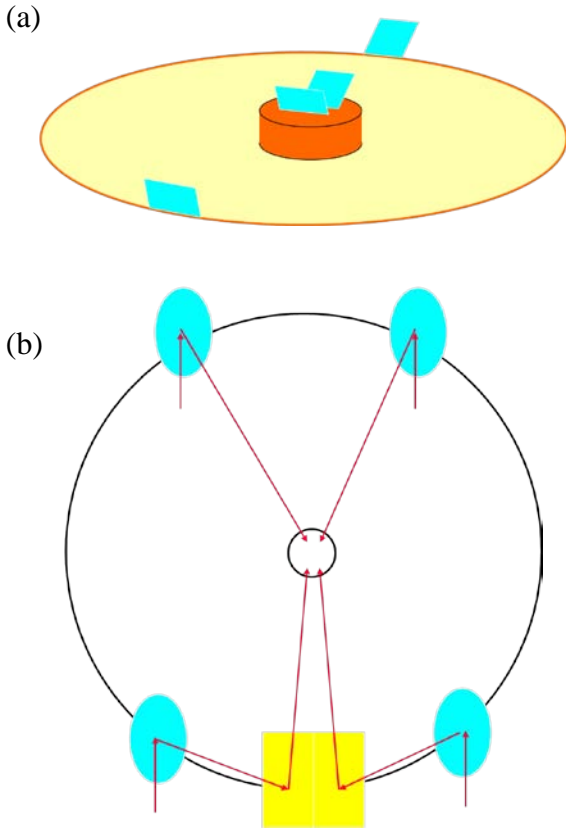


Fig. 4 Possible configurations of far-infrared interferometers. Top figure shows two-element interferometer on a round track. A beam combiner is at the center. Bottom figure shows four-element interferometer. There is additional delay line compensation optics.

D. Technology developments

There are two types of millimetre and submillimetre-wave bolometric interferometers under study. One uses a Fizeau type interferometer [13] and another used Michelson type interferometer [14, 15]. Here I review the performance of a Michelson type, especially the one using wiregrid as beam combiner, which is called as Martin-Puplett type interferometers.

Martin-Puplett type Fourier transform spectrometers have been used for wide band measurements in millimetre and submillimetre-waves [16]. To measure spectra of sources, both input and output polarizers are used. Polarity of output signal depends on the configuration of the input and output polarizers. By subtracting parallel configuration signal from that of orthogonal, DC component and common fluctuations are subtracted. This is very useful for two aperture interferometer, since this subtract all common fluctuation such as atmospheric fluctuation. This is the merit of multiplying type interferometer realized by Martin-Puplett type bolometric interferometers. Experimental demonstration was made in [17, 18] by measuring interferogram of the moon in millimetre-wave. Figure 6 shows the measured interferogram and its Fourier transformation that clearly

shows atmospheric fluctuation is subtracted by measuring two output ports of the Martin-Puplett interferometer.

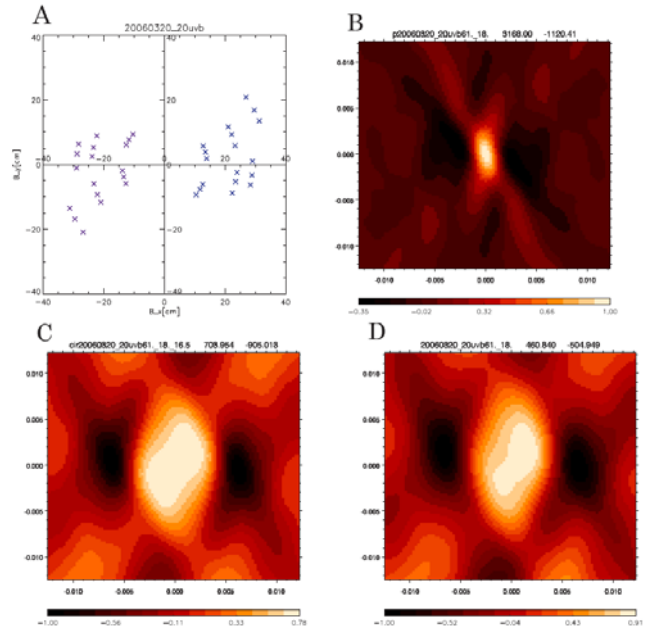


Fig. 5 Synthesized image of the sun by bolometric interferometer [17, 18]. Measurement was made with 5 cm aperture and 35 cm baseline, and 150-350 GHz frequency range was used for image reconstruction. Ge composite bolometer at 1.5 K is used for observation. A: baseline coverage, B: synthesized beam, C: simulated image, D: synthesized image of the sun.

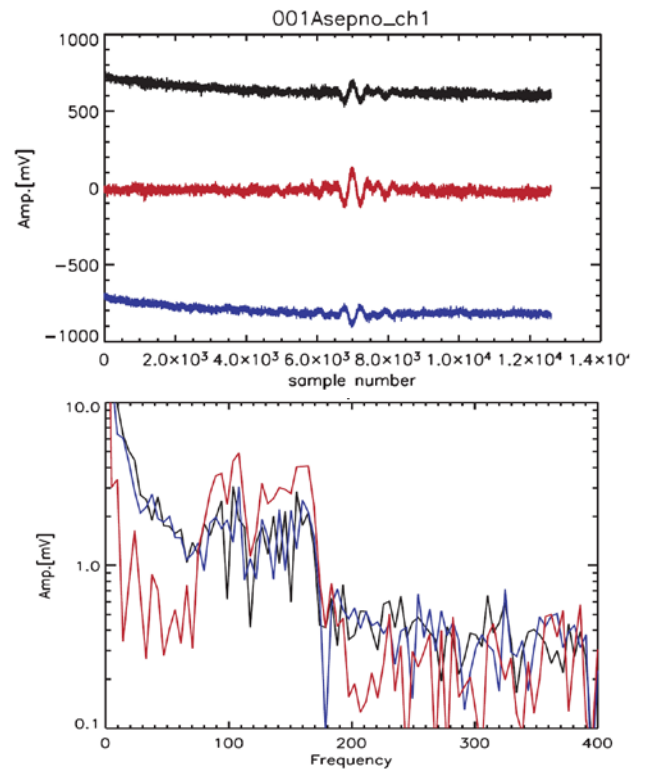


Fig. 6 Demonstration of multiplying interferometer by observing the moon [17, 18]. Top figure shows interferograms at two output ports in black and blue, and subtracted interferogram in red. Bottom figure shows Fourier transformation of the interferograms. The output signal in red clearly shows that atmospheric fluctuation is cancelled.

V. CONCLUSIONS

Results on far-infrared observations of a massive star-forming region by *AKARI* show a complex nature of interstellar material. For more detailed study of the region or observing massive star-forming region in nearby galaxies, higher angular resolution capability is required. Interferometry on a high plateau in Antarctica offers opportunities for high angular resolution observations in the far-infrared using either heterodyne or direct detectors. Direct detector interferometers can be more sensitive and achieve wider field of view than heterodyne system. Performance of a Martin-Puplett type double input interferometer was reviewed that can subtract common fluctuations of atmospheric emission.

ACKNOWLEDGMENT

Part of this research is based on observations with *AKARI*, a JAXA project with the participation of ESA. HM thank Scott Paine of Harvard Smithsonian Center for Astrophysics for supplying atmospheric model over Antarctica.

REFERENCES

- [1] H. Murakami et al., "The Infrared Astronomical Mission *AKARI*", *PASJ* 59, S369-S376 (2007)
- [2] M. Kawada, H. Takahashi, N. Murakami, H. Matsuo et al., "Performance of an Imaging Fourier Transform Spectrometer with Photoconductive Detector Arrays: An Application for the *AKARI* Far-Infrared Instrument", *PASJ* 60, S389-S397 (2008)
- [3] B. Hatsukade, K. Kohno, Y. Tamura et al. "AzTEC/ASTE Deep Survey: 1.1-mm Map and Source Catalogue of the *AKARI* Deep Field South and Number Counts", in preparation
- [4] E. Komatsu, H. Matsuo, T. Kitayama, M. Hattori et al., "Substructures Revealed by the Sunyaev-Zel'dovich Effect at 150 GHz in the High Resolution Map of RX J1347-1145", *PASJ* 53, 57-62 (2001)
- [5] A.G.G.M. Tielens, "The Physics and Chemistry of the Interstellar Medium", Cambridge University Press (2005)
- [6] H. Matsuo, A. Kosaka, T. Arai, N. Nitta, "Far-Infrared Spectroscopic Imaging of Interstellar Material around Eta Carinae", *ASP Conference Series*, Vol. 418, pp. 451-454 (2009)
- [7] A. Okazaki, S.P. Owocki, C.M.P. Russell, M.F. Corcoran, "Modelling the *RXTE* light curve of η Carinae from a 3D SPH simulation of its binarywind collision", *MNRAS* 388, L39-L43 (2008)
- [8] N. Smith, "Near-infrared and optical emission-line structure of the Keyhole Nebula in NGC 3372", *MNRAS* 331, 7-12 (2002)
- [9] H. Matsuo, A. Kosaka, T. Arai, N. Nitta, M. Tanaka, "Far-Infrared Spectroscopic Imaging of Interstellar Material around Eta Carinae", in preparation
- [10] N. Smith, R.H. Barba, N.R. Walborn, "Carina's defiant Finger: HST observations of a photoevaporation globule in NGC 3372", *MNRAS* 351, 1157-1470 (2004)
- [11] S. Paine, "The *am* Atmospheric Model", *SMA Technical Memo #152-Revision 3* (2004), <http://www.cfa.harvard.edu/sma/memos/152-03.pdf>
- [12] T.E. Oberst, S.C. Parshley, G.J. Stacey, T. Nikola et al., "Detection of the 205 μm [NII] line from the Carina Nebula", *ApJ* 652, L125-L128 (2006)
- [13] G.S. Tucker, J. Kim, P. Timbie, S. Ali, L. Piccirillo, C. Calderon, "Bolometric interferometry: the millimeter-wave bolometric interferometer", *New Astronomy Reviews* 47, 1173-1176 (2003)
- [14] I.S. Ohta, M. Hattori, H. Matsuo, "Development of multi-Fourier transform interferometer: fundamentals", *Applied Optics* 45, 2576-2585 (2006)
- [15] I.S. Ohta, M. Hattori, H. Matsuo, "Development of multi-Fourier transform interferometer: imaging experiment: imaging experiments in millimeter and submillimeter waveband", *Applied Optics* 46, 2881-2892 (2007)
- [16] D.H. Martin, E. Puplett, "Polarized interferometric spectrometry for the millimetre and submillimetre spectrum", *Infrared Physics* 10, 105-109 (1969)
- [17] I.S. Ohta, M. Hattori, Y. Chinone, Y. Luo, Y. Hamaji, J. Takahashi, H. Matsuo, N. Kuno, "Astronomical testing observation in Multi-Fourier transform interferometer: Aperture synthesis technique and CMB", *Conference Digest of IRMMW-THz 2007*, 335-336 (2007)
- [18] Y. Luo, M. Hattori, I. S. Ohta, Y. Chinone, J. Takahashi, Y. Hamaji, H. Matsuo, N. Kuno, "Realization of multiplying type interferometer with 2-elements 0.3K bolometer detectors", *IEEE conference proceedings, Global Symposium on Millimeter Waves*, 213-215 (2008)

The HIFI OD-81 Anomaly

Willem Jellema^{1,2,*}, Herman Jacobs¹, Bert-Joost van Leeuwen¹, Piotr Orleanski³, Witold Nowosielski³, Martin Stokroos¹, Malgorzata Michalska³, Thomas Klein⁴, Albrecht de Jonge¹, Anna di Giorgio⁵, David Teyssier⁶, Christophe Risacher¹, Pieter Dieleman¹, John Pearson⁷, Michael Olberg¹, Tony Marston⁶, Peter Roelfsema¹, and Frank Helmich¹

¹SRON Netherlands Institute for Space Research, Groningen, the Netherlands

²Kapteyn Astronomical Institute, University of Groningen, Groningen, the Netherlands

³Space Research Center (SRC), Warsaw, Poland

⁴Max Planck Institute for Radio Astronomy (MPIfR), Bonn, Germany

⁵Istituto di fisica dello Spazio Interplanetario (IFSI), Rome, Italy

⁶European Space Astronomy Center (ESAC), Madrid, Spain

⁷Jet Propulsion Laboratory (JPL), Pasadena, USA

*Contact: W.Jellema@srn.nl, phone +31-50-363 4058

Abstract— On Monday 3rd of August 2009 the Mission Operation Center (MOC) reported that Herschel-HIFI was found in an undocumented state since 22:43Z on August 2nd during otherwise nominal execution of a red-shifted C+ observation in band 7b. The instrument no longer responded to HK requests and commands for the LO subsystem and communication between the Instrument Control Unit (ICU) and the Local Oscillator Control Unit (LCU) had clearly been lost. At the same time the HEB mixer in band 7 had changed from a nominally pumped to a completely under-pumped state and the primary power consumption of the LCU had dropped from a nominal current of 2.5A to 0.36A only.

In this paper we present the results of the HIFI OD-81 anomaly investigation from early symptoms to a fully consistent failure scenario offering an explanation for what most likely had happened in space. This paper summarizes the key findings obtained from a detailed telemetry analysis and timing reconstruction, electrical circuit simulations, laboratory tests on a representative hardware model and component level tests, as well as software code analysis and simulation. We conclude by a description of the identified recovery solution and the implementation of risk mitigation measures protecting the instrument during future operations.

I. INTRODUCTION

A. HIFI Block Diagram

The Heterodyne Instrument for the Far-Infrared (HIFI)[1] on board of ESA’s cornerstone mission Herschel[2] launched on the 14th of May 2009 is a high resolution spectrometer operating in the 480-1910 GHz frequency range. A schematic block diagram is shown in Fig. 1. The Instrument Control Unit (ICU) interfaces with the spacecraft bus and divides up the telecommands received from the spacecraft into unit level commands distributed over a serial interface and collects housekeeping from all units and science data from a High Resolution Spectrometer (HRS) and Wide Band Spectrometer (WBS). The spectrometers operate on two orthogonal polarizations H and V whose inputs are connected to the IF amplifier outputs of mixer units (SIS and HEB) where the astronomical signal has been down-converted to a 4-8 GHz IF band. The Local Oscillator (LO) signal is generated in the Local Oscillator Unit (LOU) which is based on direct multiplication and power amplification of a Ka-

band synthesizer referred to as the Local oscillator Source Unit (LSU). The LO subsystem (LOU + LSU) is controlled via the Local oscillator Control Unit (LCU) providing the bias supplies for the LO hardware and secondary power to the LSU.

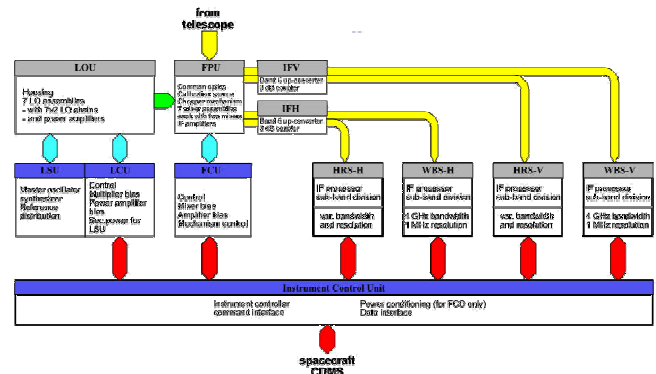


Fig. 1 Schematic block diagram of HIFI illustrating the functional division between the Local Oscillator and Focal Plane Unit subsystems, the spectrometers and the control units.

B. Local oscillator Control Unit (LCU) Breakdown

The primary power to the LCU is supplied through the spacecraft Power Distribution Unit at a bus voltage of +28V. The prime and redundant circuits of the LCU as well as the ICU can be selected by a dedicated Latching Current Limiter (LCL) that connects the spacecraft bus to the desired unit and provides over-current protection from the spacecraft point of view. It is worth mentioning here that it is not possible to configure the instrument in a hybrid mode where prime and redundant units are in mixed use. Either all prime or all redundant units can be switched on. The redundancy of the FPU and spectrometers are implemented in the H and V polarization and do not have separate prime and redundant interfaces with the spacecraft.

The LCU electronics contain four groups of DC/DC converters generating all the necessary supply voltages for the digital electronics, bias circuits, relays, heaters, and secondary power circuits. The LCU contains a micro-controller in which the LCU software runs and safety tables for LO tuning are maintained. A schematic block diagram is

shown in Fig. 2. In the upper left corner the spacecraft primary power interface is shown followed by a low-frequency ripple filter which was added during spacecraft integration to reduce current ripple as a result of primary current oscillations between the LCL and LCU. Within the LCU the +28V is filtered and further distributed to four groups of DC/DC converters. One of those groups, consisting of convertors DCDC1, DCDC2, DCDCHRS1 and DCDCHRS2 is only powered when the LO is providing RF power. In standby mode these units are off reducing the overall power consumption of the unit. Mode transitions between nominal and standby can be controlled through a standby switch/relay.

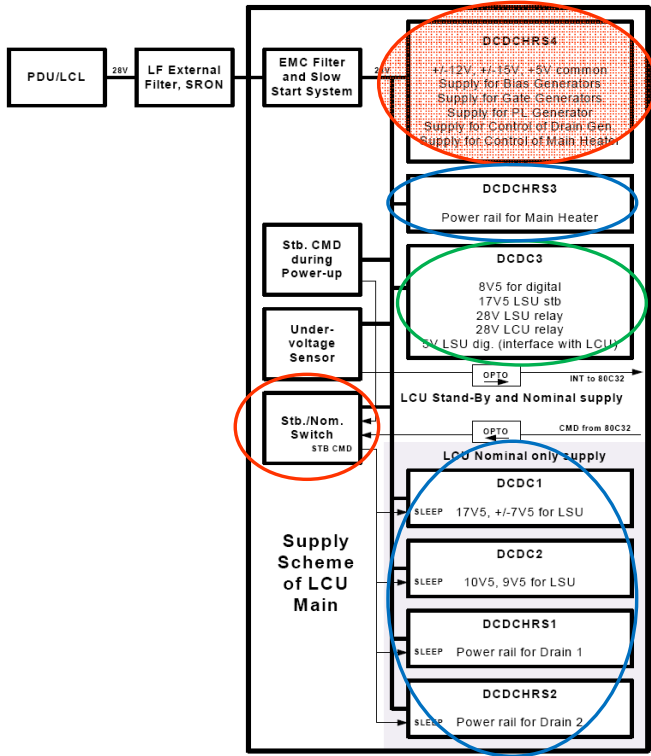


Fig. 2 Electrical block diagram of the Local oscillator Control Unit (LCU) showing the groups of DC/DC convertors.

II. EVENT RECONSTRUCTION

A. LCU Failure 2009-08-02 T22:43:00Z

During DTCP (daily ground contact) of August 3rd (OD81) the LCU was found in an unknown mode 14 since 2009-08-02 T22:43:00Z (Fig. 3 and 4). From that moment on no response from the LCU to periodic HK requests (0xEEEE) and commands was received anymore (See Fig. 3). The LCU, LOU and LSU temperatures started to drop immediately. Spacecraft heaters were immediately switched on in an attempt to compensate the drop in temperature. The primary supply current dropped from 2.5A, corresponding to nominal operation of the LCU, to 0.36A from one to the next periodic HK reading, whereas the primary supply voltage remained constant all the time. The active band at the time of failure was band 7b tuned at a frequency of 1893.16 GHz in an on-the-fly mapping observing mode.

Time	HL_Mode S	HL_LCU Status	HL_checksum	HL_17P5 V	HL_S_17P5 V
-12	normal	10670	34380	17.9214072	17.95438484
-8	normal	10670	34380	17.9240355	17.94258956
0	normal	10670	34380	17.9240355	17.94652132
4	<-INVALID TEXT CONVERSION FOR RAW VALUE 14>	61166	61166	NaN	NaN
8	<-INVALID TEXT CONVERSION FOR RAW VALUE 14>	61166	61166	NaN	NaN
12	<-INVALID TEXT CONVERSION FOR RAW VALUE 14>	61166	61166	NaN	NaN

HL_17P5 C	HL_S_17P5 C	HL_VS_5P V	HL_VS_15P V	HL_VS_15M V	HL_REF_2P5 V	HRH_3P3 C	HRV_3P3 C
0.2973404	0.185086215	5.112370678	14.74865963	-14.70854488	2.494832301	2.31	2.28
0.2973404	0.185406537	5.112777795	14.74865963	-14.70796503	2.494832301	2.31	2.29
0.29725782	0.185406537	5.112370678	14.74865963	-14.70854488	2.495035554	2.31	2.28
NaN	NaN	NaN	NaN	NaN	NaN	2.32	2.28
NaN	NaN	NaN	NaN	NaN	NaN	2.30	2.26
NaN	NaN	NaN	NaN	NaN	NaN	2.30	2.26

- Anomaly event at t = 0 (periodic HK every 4s)
- No LCU response: all HK reads 0xEEEE
- H/V mixers under-pumped
- HRS 3P3 currents drop slightly

Fig. 3 No response from LCU to periodic HK requests

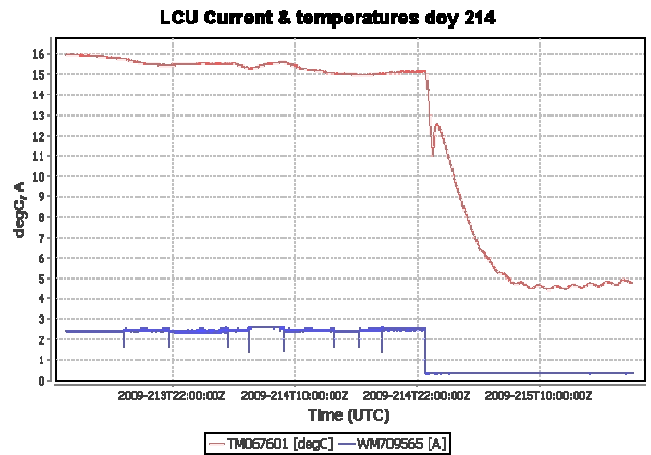


Fig. 4 Graphical illustration of the event recorded on OD-81. In blue the primary current consumption is shown, whereas the LCU temperature profile is indicated in red.

Inspection of the periodic LCU HK revealed that the LO power dropped from one to the next HK reading leaving the HEB mixer in an unpumped state (see Fig. 5). Prior to the event the conditions of the LO hardware as mimicked by the LCU HK were stable at the bit resolution level. The change occurred within one HK cycle of 4s. The drop in LO power was also confirmed by the HRS 3P3 current HK reading which is indicative of the IF power level of the mixer which in turn depends on the LO power received by the mixer. Just prior to the event the conditions at the LO hardware were completely stable (at the bit resolution level), reflected by very stable LCU analogue HK readings, primary supply current readings as well as HEB mixer and HRS 3P3 current HK readings. No action directed to the LO chain was going on at the time of the event.

B. LCU Switch-off 2009-08-04 T15:20:00Z

During DTCP of the 4th of August 2009 (OD83) the LCL for the LCU was opened removing the primary power from the unit. This was done in between the switching points of the thermal regulation cycle of the spacecraft. From the LCU and LSU temperature profiles with respect to time it was concluded that the dissipation of the LCU as well as the LSU had dropped. This was concluded on the basis of the changed temperature slope and duty cycle of the thermal regulation loop as shown in Fig. 6. When switching the LCU off the HRS 3P3 current increased from 2.2 to 2.6A yielding a

yellow flag for the HRS as can be seen in the upper plot of Fig. 6. In turn the HRS-H and -V were switched off as well. The increase of 3P3 current was assigned to the loss of the 10 MHz reference signal supplied by the LSU. HIFI was hence left in a hybrid state with the all units powered except for the LCU, LSU and HRS.

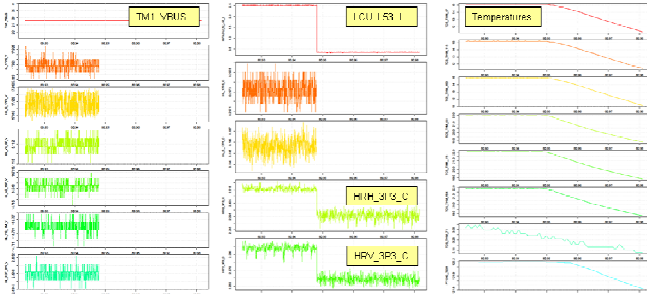


Fig. 5 HK traces illustrating the sudden drop of primary supply current (top-middle) whereas the bus voltage remains unchanged (upper-left). The change of mixer current and IF power level was also detected by the HRS 3P3 current HK (IF processor). In the right column the change of temperatures following the event can be seen.

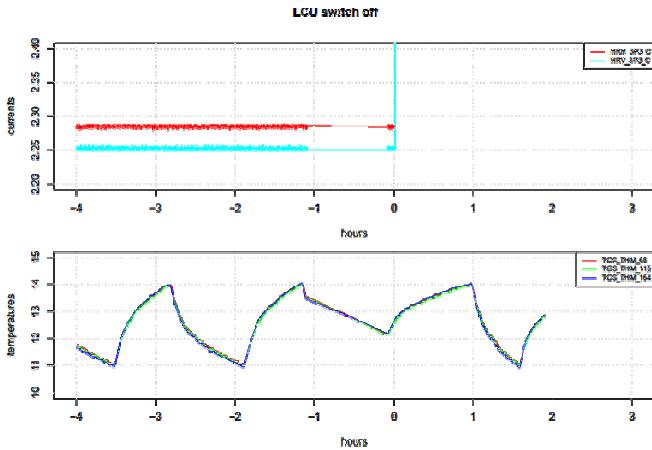


Fig. 6 Change of the HRS IF processor current consumption (3P3) and changed temperature profile of the LSU spacecraft panel when the LCU was switched off.

C. HIFI Switch-off 2009-08-07 T15:15:00Z

For spacecraft thermal management reasons it was finally decided to switch off HIFI entirely during DTCP of the 7th of August (OD86). The final LOU, LCU and LSU temperature levels showed to be consistent with the values observed during the initial switch-on of HIFI after launch on May 24th.

D. Initial Evaluation LCU Power Consumption

Using the refurbished QM model of the LCU (IMD-3) an initial evaluation of the power consumption of the electronic modules was made in order to explain the low primary power consumption of the LCU (0.36A in Fig. 4). The main conclusion was that only a failure in DC-DC convertor HRS-4 in combination with a switched standby relay as shown in Fig. 2 would explain such low power consumption. All other combinations of single failures in DC-DC convertors would lead to higher power consumption than observed. Simulating

a failure in HRS-4 in the lab setup and switching the LCU off and on again showed that the communication would be restored, analogue HK would be missing (zero readings, fixed raw values ADC) and a current below 0.4A would be drawn.

E. HIFI Restart 2009-08-10 T15:30:00Z

During DTCP of August 10th (OD89) a HIFI restart attempt was made. After closing the LCL for the LCU the primary supply current stabilized at 0.36A as shown in Fig. 7. The 10 MHz reference supplied by the LSU re-appeared reflected by the expected drop in the HRS 3P3 currents. Communication was fully restored and the LCU was found in standby mode after the boot procedure. The LCU checksum was in agreement with the expected value for the firmware (0x8D04) loaded from the on-board PROM confirming the integrity of the LCU memory. The analogue HK values were zero with a fixed raw value of 0x4000 in agreement with a non-powered ADC.

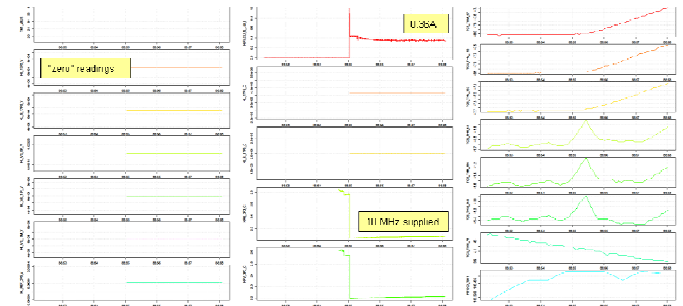


Fig. 7 HK charts centered on the HIFI restart attempt. In the left column "zero readings" of all analogue HK channels are shown. In the middle column the top plot the primary current consumption converges at 0.36A and the 10 MHz signal is provided again as shown by the 3P3 current profiles. In the right column the rising unit temperatures are shown.

Time	HK_Messg_B	HL_LCU_Status	HL_checksum	HL_TTYPE_V	HL_B_TTYPE_V	HL_TTYPE_C	HL_B_TTYPE_C
-39	<<NO MEASURE>>	9.22337E+18	9.22337E+18	NaN	NaN	NaN	NaN
-37	failure	86636	81188	NaN	NaN	NaN	NaN
-36	failure	86636	81188	NaN	NaN	NaN	NaN
0	<<RAW VALUE 14>>	81188	81188	NaN	NaN	NaN	NaN
1	failure	86636	86636	NaN	NaN	NaN	NaN
2	failure	86635	86635	NaN	NaN	NaN	NaN
3	failure	86636	86636	Firmware CRC (0x8D04)	NaN	NaN	NaN
4	failure	86636	86636	Memory not damaged	NaN	NaN	NaN
5	failure	86635	38100	6.57E-04	6.56E-04	4.10E-05	2.00E-05
6	standby	4088	38100	6.07E-04	6.06E-04	4.13E-05	2.00E-05
30:00	standby	4088	38100	6.57E-04	6.56E-04	4.13E-05	2.00E-05

| HL_VS_DP_V |
|------------|------------|------------|------------|------------|------------|------------|------------|
| NaN | NaN | NaN | NaN | NaN | NaN | 2.68 | 2.57 |
| NaN | NaN | NaN | NaN | NaN | NaN | 2.68 | 2.57 |
| NaN | NaN | NaN | NaN | NaN | NaN | 2.68 | 2.57 |
| NaN | NaN | NaN | NaN | NaN | NaN | 2.68 | 2.57 |
| NaN | NaN | NaN | NaN | NaN | NaN | 2.68 | 2.57 |
| NaN | NaN | NaN | NaN | NaN | NaN | 2.22 | 2.20 |
| NaN | NaN | NaN | NaN | NaN | NaN | 2.22 | 2.20 |
| NaN | NaN | NaN | NaN | NaN | NaN | 2.22 | 2.20 |
| 2.04E-04 | 6.00E-04 | 6.00E-04 | 1.02E-04 | 2.22 | 2.22 | 2.20 | 2.20 |
| 2.04E-04 | 6.00E-04 | 6.00E-04 | 1.02E-04 | 2.22 | 2.22 | 2.20 | 2.20 |
| 2.04E-04 | 6.00E-04 | 6.00E-04 | 1.02E-04 | 2.24 | 2.24 | 2.20 | 2.20 |

Fig. 8 HK table extract near the HIFI restart attempt. At t = -37s the HK is activated, but the unit is still off and no valid HK is available, at t = 0 the unit is switched on and after the boot procedure the correct firmware CRC is echoed at t=5. From t=6 the LCU responds to HK requests in standby mode and "zero" readings for the analogue HK are observed. During the boot procedure the 3P3 current of the HRS IF processor drops indicating the presence of the 10 MHz signal provided by the LSU.

F. Timing reconstruction

In addition to the periodic HK, collected every 4s, a number of specific HK readings from the LCU were made as part of the observing mode at the time of the failure. At the start of

each spectrometer integration a specific sequence of LCU commands and HK requests was sent to fill the start-frame packet of the science data. It was found that communication was lost before power was lost. At the start of each spectrometer integration the commands as shown in Fig. 9 are sent to the LCU with 3ms separation in time. The moment where communication was lost could be confined to a time interval of 6 ms connected to the execution of a specific command (F30A CC7A) and following housekeeping request (B33A). From that moment in time the HEX pattern 0xEEEE was found in the data which is the default HK value substitution by the ICU for an uncompleted HK request.

- Tests on QM/IMD-3 using S/S monitor revealed that in addition to periodic HK (1/4s) additional LCU HK is contained in Science Start Frame Packets:
 - B086 HK request of LSU frequency telemetry voltage
 - F30A CC7A Command setting 7A page address
 - B33A HK request reading from specific RAM page address
 - F30A CC7A Command setting 7A page address
 - B33C HK request reading from specific RAM page address
 - F30A CC7A Command setting 7A page address
 - B33E HK request reading from specific RAM page address

Time	Specification	HL Frequency	Min	Offset	Description
1627944393.142675	Time = obsltime	0x0000	0x23EE	0x010E4	Periodic HK
1627944393.376840	Reported latched time	0x61D0	0xEEEE	0xEEEE	HRS H start frame HK
1627944393.376840	Reported latched time	0xEEEE	0xEEEE	0xEEEE	HRS V start frame HK
1627944397.826100	Time = obsltime	0xEEEE	0xEEEE	0xEEEE	Periodic HK

Fig. 8 Sequence of commands associated with a start science frame packet. It was found that in between execution of the command F30A CC7A and HK request B33A communication had been lost confining the moment of the event to a time interval of only 6 ms.

Making use of the data collected by the HIFI spectrometers during the integration interval where loss of LO power took place it could furthermore be reconstructed that permanent loss of communication happened 1.6s before the LO power was lost. The observing mode consisted of 3s integrations: 3 times 1s integrations for the HRS and one 3s integration for the WBS.

By considering the total power in an IF spectrum for A) a fully pumped mixer prior to the event, B) an integration during which drop of LO power occurred and C) a fully underpumped mixer after the event a linear interpolation scheme was used to reconstruct the time of the event relative to the start of the integration sequence (see Fig. 9). For the WBS as well as the HRS a consistent number of 1.58s was found. The validity of the method was verified by using the lab setup consisting of the QM/IMD-3 LCU unit, a so-called subsystem bus monitor which was used to monitor and trigger on traffic on the serial interface between the ICU and control units and a noise source connected to a fast switch.

We therefore came to the important conclusion that the whole sequence of events connected to the LCU failure started with loss of communication and only 1.6s later with loss of LO power. This strongly suggested that loss of communication was not caused by a failure and reversed the intuitive order of cause and effect.

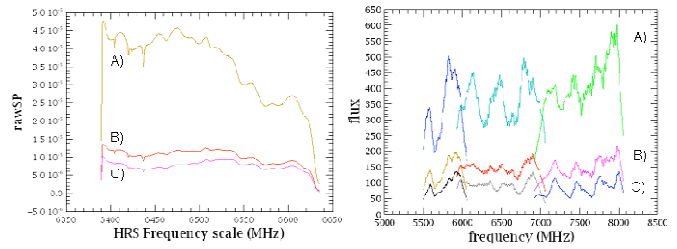


Fig. 9 Raw HRS and WBS spectra corresponding to A) fully pumped mixer, B) integration during which failure occurred and C) completely underpumped mixer.

G. Key Symptoms of the LCU Event

Reconstruction of the LCU event showed that the failure scenario must be consistent with all of the following key symptoms:

- After the event the LCU was found in a state with low power consumption drawing 0.36A primary supply current
- After the event the LCU was found in a state where the standby relay had been switched
- During the sequence of events eventually leading to the LCU failure communication was lost and only 1.6s later the RF power was lost.

III. HARDWARE INVESTIGATIONS

A systematic Failure Mode and Effect Analysis (FMEA) was made on the basis of available electrical circuit diagrams. This FMEA focussed on the main effects summarized above in II.G. The FMEA included the effect of the LCU interfaces as well as environmental conditions (temperature, radiation). The failure of DC/DC convertor HRS-4 has been analysed in several ways:

- Design inspection by DC/DC convertor experts from ESA (Ferdinando Tonicello) and JPL (Ted Fautz)
- Part stress analysis by JPL supported by SRON
- Circuit simulations by SRON

The FMEA showed that there is a group of component failures that may cause the failure effect for DC/DC convertor HRS-4 as observed in the mission. This group of components contains all secondary rectifier diodes, an UC1825 PWM controller and some resistors and capacitors.

Extensive testing was undertaken on the QM/IMD-3 unit in the lab to simulate the effect of these potential component failures and to determine the corresponding electrical conditions. Many partial failure scenarios starting with a component failure in DC/DC convertor HRS-4 have been considered but have all been rejected because:

- Loss of communication could not be explained within hardware constraints

- Loss of LO power would be rather immediate ($\ll 1.6s$) or precede the moment of loss of communication

A scenario starting with a component failure was therefore considered not to be consistent with the observed behaviour and a component failure leading to failure of DC/DC converter HRS-4 appeared to be a consequence and not the root cause of the anomaly.

Design inspection by Ferdinando Tonicello and subsequent tests finally revealed that a group of diodes of type 1N5819 were subject to electrical conditions that exceeded their absolute maximum ratings. There are 16 diodes in the HRS-4 DC/DC converter and 4 in the DCDC2 converter. All these diodes are secondary rectifier diodes that were identified in the FMEA as possible causes of the failure effect as observed in the mission. No other components were found with any electrical or thermal stresses outside acceptable ranges.

In Fig. 10 we show the secondary diode configuration. Diodes D1 and D2 are of type 1N5819. It was found that the leakage inductance of the transformer in series with the diode capacitance formed a resonant LC circuit resulting in a very short spike/overshoot every time the diodes switch from forward conduction to reverse operation. The 16 diodes in the HRS-4 converter are nominally subjected to reverse voltage peaks of $\sim 54V$, while their absolute maximum reverse voltage is specified as 45V. The duration of the voltage peaks is ~ 50 ns at a repetition rate of 65 kHz (0.3% duty cycle).

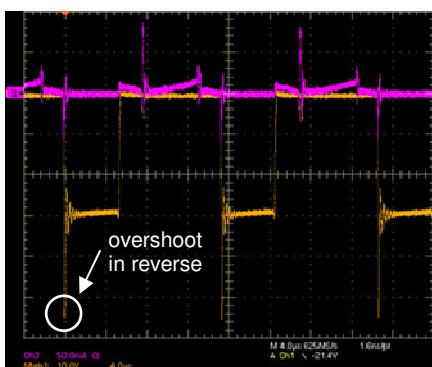
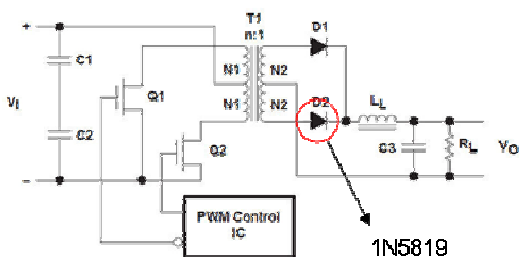


Fig. 10 Reverse voltage overshoot across the 1N5819 secondary rectifier diode.

The level of the peak voltage only depends on the input voltage of the HRS-4 converter. This voltage is usually 27V due to voltage loss across cables and LCU Ripple Filter. An overshoot on the HRS-4 input voltage occurs when the

current drawn by the LO subsystem changes significantly (i.e. during mode transitions, band changes, etc). Generally these overshoots are about 2V (planned cases), only in case of a sudden transition from nominal to stand-by mode (unplanned) the overshoot can be as high as 4V. The voltage peaks across the diodes reach 58V or 62V respectively.

Tests performed on a limited number of diodes showed an average reverse breakdown voltage of 59V, so it is likely that breakdown occurs during such changes in LO subsystem activity. Breakdown is considered as the primary cause for damage and ultimately failure of these diodes.

For that reasons dedicated component level tests have been performed on representative flight quality devices (see Fig. 11). An endurance test of over 2000 hrs with short repetitive reverse current pulses up to 1A avalanche current did not kill any Schottky diode. On the other hand tests on commercial diodes immediately killed one device at only moderate conditions whereas another could not be killed at all. All of this suggests a failure mode in which the reverse current finds a local destructive path in contrary to a global thermal breakdown of the entire junction. Evidence was furthermore found in literature that the failure mechanism is threshold driven and can be avoided by reverse energy screening of flight devices.

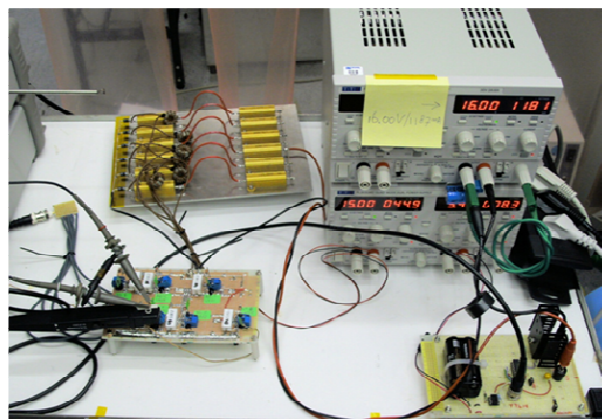


Fig. 11 Repetitive pulsed-stress setup addressing failure mechanism of 1N5819 diodes.

IV. SOFTWARE INVESTIGATIONS

In parallel of hardware investigation a thorough software investigation program was set up. The program concentrated on:

- routines in the LCU software that invoke the standby relay
- identification of program execution paths taking 1.58s before switching the standby relay
- possible ways to loose communication

It was found that only a limited number of software routines actually invoke the standby relay:

- in the start procedure (software reset) which is initiated when:

- the LCU is powered on
- executing a reset command from the ICU
- returning from an undervoltage protection (emergency shutdown) interrupt service
- in the undervoltage protection (emergency shutdown) interrupt service
- in the procedure of executing the standby command from the ICU (standby transition)
- in diagnostic testing procedures still present in the program memory but not being used

Regarding the delay between loss of communication and LO power it was identified that only the start procedure takes considerable execution time and could add significantly to the 1.6s delay observed during the mission. This procedure takes about 1.2 to 1.3s during which the LCU firmware in the PROM is copied into RAM and the standby relay is switched in the end as a final initialization step.

Regarding the loss of communication many analyses and tests have been executed trying to simulate permanent loss of communication. Only in two cases permanent loss of communication was demonstrated:

- When the 28V voltage is interrupted (removed) internally for a specific duration such that the system restarts. This is however not compatible with the observed 1.6s delay as the undervoltage protection interrupt service would have acted immediately removing the LO power with virtually with zero delay. Moreover the LCL would have tripped in view of the required duration.
- When the program makes an unexpected “jump to zero”. If program execution somehow jumps to address zero, the start procedure is being executed, which leads to a switch of the standby relay after 1.2 to 1.3s, but in this case also to permanent loss of communication.

During the confined time interval where loss of communication was observed either a command was being handled or a HK request was being executed. A detailed analysis of the code and subroutines executed as part of handling the command (F30A CC7A) and the HK request (B33A) was made. In the code related to handling the command a memory area was identified whose corruption could have lead to an unexpected jump in the program eventually leading to a jump to address zero. Single bit-flips in that memory were simulated by patching the LCU software and executing the command and HK request sequence. Of order 40 bitflips out of 800 tested cases could lead to the observed sequence of permanent loss of communication and a standby relay switch after more than one second (1.3-1.6s). The statistics also showed that in 5 individual bit-flip cases both the observed sequence as well as the 1.6s delay could be reproduced.

A Single Event Upset (SEU) analysis confirmed that the SEU rate for the memory chip used is approximately once per 5 days. The probability that a SEU causes the observed

behaviour ranges from once per year to once per 90 years (and even once per 700 years when the delay of 1.6s is exactly to be reproduced).

V. PROPOSED FAILURE SCENARIO

Putting all investigation results together we found only one consistent scenario that could explain the full sequence of events as observed on OD-81:

- A single event upset corrupted the memory at the location of the program code of a particular command or HK request.
- This bit-flip caused loss of communication when that specific code was called as part of a scientific integration sequence.
- Eventually the processor resumed program execution at address 0 where the start procedure was activated
- After 1.6s the standby relay was switched
- The corresponding load transient caused a voltage overshoot on the 28V bus.
- In the presence of the intrinsic pulsed-stress condition on the secondary rectifier diodes, this overshoot became fatal for one of the devices taking DC/DC HRS-4 down.
- The whole sequence of events left the unit in standby mode, with permanent loss of communication and low primary current consumption of 0.36A.

VI. RISK MITIGATION MEASURES AND FUTURE OPERATIONS

Since further use of the HIFI prime units appeared pointless it was recommended to continue preparations for switching on and using the redundant units of HIFI. Before this could be done the following risk mitigation measures had to be taken in order to avoid a repetition of a similar component failure:

- Reduce load steps, avoid significant and unnecessary primary current transients associated with instrument mode transitions by changing the operational procedures and a modified LCU state definition
- Avoid a cold start of the LCU, operate the unit between 10 and 30°C to keep the stress on the rectifier diodes within tested ranges
- Disable the LCU program code that can switch the standby relay after execution of the boot procedure
- Perform explicit and regular checksum calculations after each observation verifying the integrity of the LCU memory in order to timely capture a SEU. Abort operations when a corruption is detected.

At the time of reporting and after implementation and verification of modified operational procedures, HIFI redundant has meanwhile been successfully switched on again. See the paper by Teyssier et al in the proceedings of this conference[3]. Current work involves refinement of (autonomous) recovery procedures reducing the loss of observing time in case of future SEU's.

VII. ACKNOWLEDGEMENT

The authors would like to thank all persons that contributed either directly or indirectly to the anomaly investigation. The joint and parallel effort of the HIFI system

team, the ESA senior investigation team and the support from NASA-JPL has significantly accelerated the investigation process and formed the basis for the success in finding a consistent scenario and explanation for the anomaly and relatively fast recovery of Herschel-HIFI.

REFERENCES

- [1] T. de Graauw et al., "The Herschel-Heterodyne Instrument for the Far-Infrared (HIFI)", *Astronomy & Astrophysics*, 2010, in press.
- [2] G. Pilbratt, et al., "The Herschel Mission Status and Highlights", *Proc. Int. Symp. Space Terahertz Technology*, 2010, this volume.
- [3] D. Teyssier et al., "Herschel/HIFI In-flight Commissioning and Performance", *Proc. Int. Symp. Space Terahertz Technology*, 2010, this volume.

Herschel/HIFI In-flight Commissioning and Performance

David Teyssier^{1,*}, Christophe Risacher², Pieter Dieleman², Wouter Laauwen², A. de Jonge², J. Braine³, M. Caris⁴, O. Coeur-Joly⁵, B. Delforge⁶, F. Helmich², F. Herpin³, R. Higgins⁷, W. Jellema², T. Klein⁴, J. Kooi⁸, C. Leinz⁴, K. Edwards², A. Marston¹, P. Morris⁹, M. Olberg¹⁰, V. Ossenkopf¹¹, J. Pearson¹², P. Roelfsema², R. Shipman²

¹European Space Astronomy Centre, ESA, Madrid, Spain

²SRON Netherlands Institute for Space Research, Groningen, the Netherlands

³Universite de Bordeaux, Laboratoire d'Astrophysique de Bordeaux, 33000 Bordeaux, France

⁴Max Planck Institute für Radio Astronomie, Auf dem Hügel 69, 53121 Bonn, Germany

⁵Centre d'etude Spatiale des Rayonnements, Universite de Toulouse [UPS], 31062 Toulouse Cedex 9, France

⁶Laboratoire d'Etudes du Rayonnement et de la Matière en Astrophysique, UMR 8112 CNRS/INSU, OP, ENS, UPMC, UCP, Paris, France

⁷National University of Ireland, Maynooth, Department of experimental physics, County Kildare, Ireland

⁸Physics Department, California Institute of Technology, Pasadena, California, USA

⁹Infrared Processing and Analysis Center, California Institute of Technology, MC 100-22, 770 South Wilson Avenue, Pasadena, CA 91125 USA

¹⁰OSO, Chalmers University of Technology, SE-412 96 Göteborg, Sweden

¹¹KOSMA, I. Physik. Institut, Universität zu Köln, Zùlpicher Str. 77, D 50937 Köln, Germany 29

¹²Jet Propulsion Laboratory, 4800 Oak Grove Drive, MC 264-782, Pasadena, CA 91109 USA

*Contact: David.Teyssier@esa.int, phone +34-91-813 1355

Abstract— The Herschel Space Observatory was successfully launched on the 14th of May, 2009, lifting into space the Heterodyne Instrument for the Far-Infrared (HIFI). After the standard early orbit operations on the Space-craft, the instrument was switched on for the first time on the 24th of May, kicking off an instrument Commissioning period of more than a month and a half. We present here the outcome of this Commissioning campaign, including the measured in-flight performance of the instrument. Among the challenges encountered during this period was the need to optimize the stability of the signal provided by the Local Oscillator (LO) chains in some of the frequency bands, in particular that covering the singly Ionized Carbon (C+) line at the upper edge of the HIFI range, and one of the backbones of the science program of the instrument. The same concept also allowed significant improvements in the upper end of the 3b LO chain. Another noticeable achievement was the very good co-alignment measured between the mixer beams in the respective H and V polarizations offered by HIFI, allowing for more than a simple build-in redundancy, as the observing efficiency will really benefit from the combination of the two mixers.

I. INTRODUCTION

Herschel [1] is the fourth ‘cornerstone’ mission in the ESA science programme. With a 3.5 m Cassegrain telescope it became on the 14th of May 2009 the largest space telescope ever launched. It allows photometry and spectroscopy observations in approximately the 55-672 μ m range, bridging the gap between earlier infrared space missions and ground-based facilities. Aboard Herschel, the Heterodyne Instrument for the Far-Infrared (HIFI [2]) offers very high-resolution (up to $R > 10^7$) spectroscopy with a continuous coverage between 488 and 1272 GHz (SIS mixers), and 1430 and 1902 GHz

(HEB mixers), as well as a simultaneous coverage of up to 4 GHz with its two backend spectrometers (an Acousto-Optic Spectrometer, and a Digital Auto-correlation Spectrometer).

HIFI is suitable for investigating interstellar gas, for example in star-forming areas and in the gas expelled by dying stars. In the far-infrared and the submillimetre areas where HIFI is working, a wide range of molecules absorb radiation, including water. HIFI is suitable for capturing this radiation and can unravel it into a spectrum in which the characteristic fingerprints of all the different molecules can be seen. This instrument can be used to determine exactly what the gases are composed of and the temperature and pressure they are at. Furthermore, HIFI is highly suitable for measuring the speed of gas.

In this paper, we present the early phases of the HIFI operations that focussed on the Commissioning of the instrument, and the assessment of its performances.

II. THE HIFI COMMISSIONING CAMPAIGN

A. The Early Mission Phases

Immediately after its successful launch on the 14th of May 2009, Herschel entered the so-called Launch and Early Operation Phase (LEOP) during which most of the Spacecraft functionalities are verified. HIFI was switched on exactly 10 days after the launch, and started a Commissioning Phase which, shared with the other two instruments on-board Herschel (PACS and SPIRE), took about almost two months. About 440 hours of instrument data were collected during this phase.

The Commissioning Phase was immediately followed by a Performance Verification (PV) Phase, which concentrated on the validation of the various observing modes. This campaign was unexpectedly interrupted on August 2nd by a fatal failure of one of the warm electronic units controlling the Local Oscillator (LCU). We refer to [3] for more details about the mechanisms that lead to the loss of this unit. It took about 5 months of deep laboratory investigations, and preparation of an alternative operation scheme, before HIFI was started again on the 10th of January 2010, using its redundant electronics. A short regression-Commissioning campaign was performed, which confirmed the perfect health of the newly started instrument. As of today, HIFI is working nominally and the operation scheme designed to recover from similar upsets as the one that occurred on the Prime LCU has proven to be fully adequate.

B. The HIFI Commissioning Phase

The Commissioning campaign was broken down in the following way:

- **Instrument functional and health checks:** those tests were done immediately after the instrument power-on, and were dedicated to checking that all units had survived the launch. Of particular importance were the functional checks of the mechanical components of HIFI, namely the Martin-Pupplett assemblies used in the diplexer bands, and the internal chopper, which allows to observe various lines-of-sight on the sky at a fast rate, but also to couple the mixer beams to the internal calibration loads. Those activities were run in real-time contact with the instrument, from the European Space Operation Centre (ESOC) located in Darmstadt, Germany. The rest of the operations was run off-line, based on time-tagged sequences of telecommands uploaded on-board on a daily basis.
- **Instrument characterisation:** those measurements focussed on the characterisation of the instrument operation settings for optimum heterodyne performance (IF chain settings, mirror and diplexer settings, LO power tables, etc).
- **Instrument performances:** those measurements focussed on the parameters defining the figures of merit of HIFI as a heterodyne system (sensitivity, stability, standing waves, direct detection, etc). Those numbers are presented in the following section.
- **Instrument Astronomical Observing Template (AOT) pre-validation:** although the bulk of the observing mode validation was encompassed in the PV campaign, a subset of the so-called Astronomical Observing Templates (AOT) was needed in order to map the loci of the instrument apertures with respect to the Spacecraft pointing unit (i.e. the star trackers).
- **Focal Plane Geometry (FPG):** those measurements are necessary in order to relay the HIFI beam positions on the Herschel Focal Plane to the position of the Spacecraft boresight, and eventually derive all alignment parameters needed to adequately point on astronomical sources. These measurements offered HIFI its first-light spectra (Fig. 1).

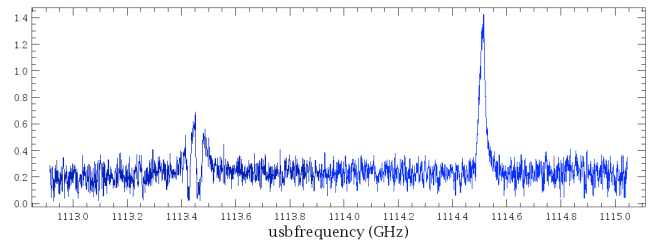


Fig. 1 One of HIFI first-light measurements in one of the polarization channels connected to the Wide-Band Spectrometer (WBS). The intensity scale is not fully calibrated in this plot.

III. INSTRUMENT IN-FLIGHT PERFORMANCES

A. Instrument sensitivity

The HIFI sensitivity was assessed using the standard Y-factor technique, measured towards the two internal loads with respective physical temperatures of 100 K (Hot load) and 10 K (Cold load). Because of the absence of atmosphere, and thanks to a telescope forward efficiency near to unity, the receiver noise temperatures obtained in this fashion offer sensitivity figures very close to the system noise temperature. Fig. 2 summarizes the distribution of the DSB receiver noise temperatures as measured over the full HIFI tuning range.

All mixers offer state-of-the-start sensitivity, in line with the performances reported by the various mixer groups at the time of delivery to the PI institute. While the SIS bands feature some variations over their operating ranges, the HEB mixers show a relatively flat noise distribution over almost 500 GHz of frequency coverage. There is some LO power shortage observed at isolated frequencies, but the bulk of the targeted range has been achieved.

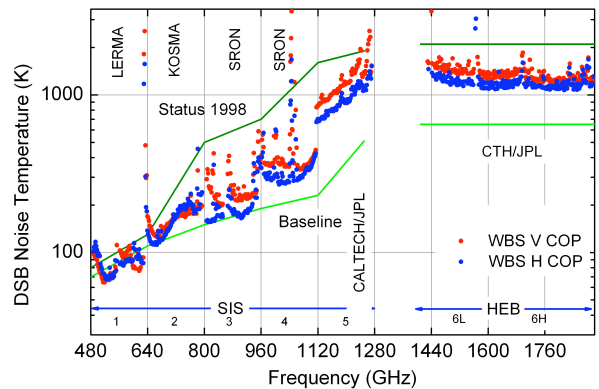


Fig. 2 HIFI Double-Side-Band receiver noise temperatures, together with an indication of what institute manufactured and provided the corresponding mixers. Also shown are the temperatures as measured 10 years before launch, as well as the baseline values at the time of the instrument proposal.

B. Instrument stability

The instrument stability performance was measured using the Allan variance technique (e.g. [4]). This is a standard technique to characterise the stability of spectroscopic instruments used in astronomical observations. In particular, the period for switching between source and reference measurement is often derived from the Allan minimum time.

We used the unified Allan variance computation scheme proposed by [5], which allows to trace total-power and spectroscopic fluctuations within the same framework. This definition of the instrument stability time allows to characterise the instrument even in the case of a fluctuation spectrum shallower than $1/f$, as measured for the total power fluctuations in high-electron-mobility transistors.

In order to map all switching cycles involved in the HIFI observing modes, the following Allan times were mapped across the HIFI tuning range:

- Total power Allan times
- Spectroscopic (or System) Allan times
- Differential Allan times for *i)* measurements between the two internal loads, *ii)* measurements between two positions on the sky (in use in the so-called *Double-Beam-Switching* (DBS) mode), *iii)* measurements between the sky and the internal cold load (in use in the so-called *Load-Chop* mode), and *iv)* measurements taken in *Frequency-Switching* (FSW) mode

Because of the long durations needed for those measurements (at least twice the expected Allan time), the number of frequency points sampled for a given mixer band remains limited, so that isolated stability degradations are difficult to fully cover. In general, it is observed that gain fluctuations represent the main cause of instrumental instabilities, leading to large differences between the stability times relevant for measurements aiming at an accurate determination of the continuum level and for purely spectroscopic measurements. Fast switching loops (using the internal chopper – up to 4 Hz) are needed for a reliable determination of the continuum level, while most spectroscopic measurements can be set up in such a way that baseline residuals due to spectroscopic drifts are at a lower level than the radiometric noise.

Total power Allan times are found to be of the order of 10-30s at a resolution of 1 MHz, although in some areas of the HEB bands, they can be less than 2-3s. In bands using diplexers for the LO injection, a degradation is observed at both ends of the IF, due to a higher contribution from the LO excess noise. Spectroscopic Allan times are in the range 60-400s at the best location of the IF, and usually 3-4 times worse when considering the whole IF. Finally, differential Allan times are in most of the cases longer than the measurement times (1800s) setting a lower limit on the real figure. There are some exceptions to this when using the FSW referencing scheme, especially in HEB bands.

C. Standing Waves

Standing waves are one of the main artefacts that can result from gain drifts as they generally arise from the non-cancellation of the band-pass power modulation when combining the on-source and references phases of an astronomical measurement. Those power modulations can take place between optics (e.g. between horns, loads, mirrors, or combinations of those latter) or within electronics (e.g. impedance mismatch). See also [6].

For HIFI, as on most radio-telescopes, the main optical paths susceptible to give rise to noticeable standing wave systems are:

- 1) Between the mixer horn and the secondary mirror: the measurements have shown that this standing wave is hardly seen in any of the HIFI spectra – it was only detected to a very low level in dedicated measurements done in the band with the largest beam. This positive effect is very likely due to the presence of a dedicated scatter cone added in the centre of the Herschel secondary mirror (see Fig. 3).

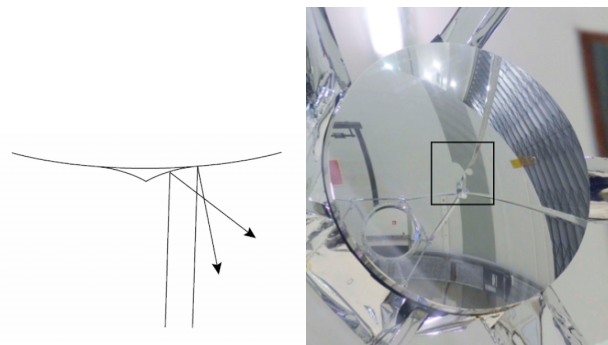


Fig. 3 *Left*: simple sketch depicting the shape of the scatter cone implemented on the Herschel secondary mirror. *Right*: picture of the Herschel secondary mirror, with its scatter cone. The location of the cone is indicated by the square in the centre.

- 2) Between the mixer horn and the internal loads: despite of the absorption coating (~ -45 dB) covering the internal Hot and Cold loads, residual standing waves can be seen especially when observing strong continuum sources. This standing wave, of period around 100 MHz, is however relatively well behaved and can usually be removed with standard sine-wave fitting at data-processing level
- 3) Between the mixer horn and LO horn: although this standing wave does not show up directly on the spectral baseline, it provokes a modulation of the LO power feeding the mixer and can affect in a similar fashion the side-band gain ratio of DSB measurements. Its characteristics can be measured by sweeping the LO frequency with a fine granularity and measure the variation of the mixer current (a direct measure of the LO pumping power). Such a measurement is illustrated in Fig. 4.
- 4) Between the mixer horn and the edge of some of the roof-top mirrors in the band using diplexers, giving rise to a weak ripple of period around 650 MHz.

On top of those, an electrical standing wave is generated in the HEB bands, most likely because of the absence of isolators between the mixer and the low noise amplifier. Unlike the optical standing wave, this ripple cannot be described as a simple sine wave. It appears with a main period of about 320 MHz, but its structure shows more skewed wave morphology, together with a period modulation. The amplitude of this standing wave scales with the difference in mixer currents between two observing phases (impedance mismatch), and can therefore be worse for FSW observations. A full description of this effect, and its possible cures, has been presented in [7].

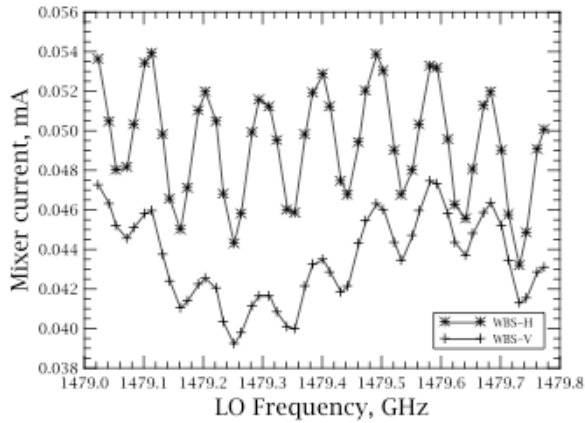


Fig. 4 Example of a measurement of the LO power modulation due to standing waves between mixer and LO horns.

D. Spectral purity

There are several frequencies in HIFI where the local oscillator has been shown to produce more than one frequency, leading to the presence of potential lines at unknown and possibly unstable frequencies. Those impurities are believed to be due to oscillations in the first, and sometimes, second stage multipliers of the Local Oscillator.

1) Oscillation theory

All multipliers that use a capacitor to terminate the bias port at the RF frequencies can oscillate if the RLC of the capacitor and attaching lead and its phase shift are a sub-harmonic of the input frequency. Simplistically this is an analog of the famous mechanical problem of small pendulum forcing a large pendulum. It will work very well if the frequency of the large pendulum is a sub harmonic of the small one.

The RF works as a charge pump for the RLC circuit. The amount of charge pumped depends on the bias point with bias closer to zero generally producing more current. This would be a monotonic function if the input match of the multiplier were independent of bias, however the input match degrades away from the optimal bias condition so there is often a peak in the RF pumped IV curve. The bias circuit oscillation has the effect of moving the bias point at the oscillation frequency allowing for there to be substantial gain in the oscillation. Fig. 5 shows the IV curve of a 200 GHz doubler in oscillation and not in oscillation. Note that the IV curve has the same shape but is compressed in the oscillating case.

2) Purification of the LO signal

The HIFI Local Oscillator chains were designed in order to leave a full control on the multiplier and gate bias settings. The following two options have been considered to purify the affected frequency areas:

- force the multiplier to operate in a varactor mode with a sub-threshold level of rectified current. Ideally the mode would be pure varactor with zero current; however, due to non-ideality in the diodes this really never possible. Fortunately several of the doublers in use (e.g. band 7b) are varactors and were

designed to have little current at its optimal bias point. A major concern to reverse biasing the multiplier is allowing the RF voltage swing to probe the reverse breakdown region. In this case it was known that the IV characteristics of the diode will change and this change will not be reversible. The HIFI design approach was to avoid all hints of reverse current and not take any chances with a degradation process that was poorly understood

- force the multiplier to work in a varistor mode, i.e. well in the second hump of the IV curve (e.g. first stage multiplier in bands 5a/5b)

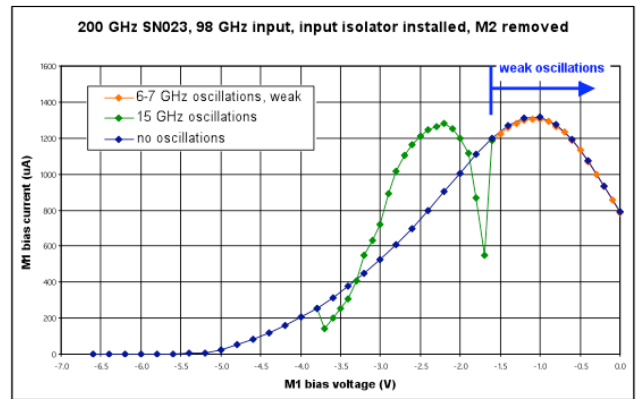


Fig. 5 IV curve of oscillating and non-oscillating 200 GHz doubler

E. Spurious Signals

The LO multiplier oscillations can also give rise to free-running spurious signals which will appear in the calibrated spectra as strong spikes and can in the worst case saturate all pixels of one spectrometer sub-band.

While the weakest and narrowest spurs can usually be eliminated at data processing levels, some other spurs have been treated at the multiplier level by changing their bias settings. Fig. 6 shows the example of a strong spur in band 1a close to one very important water line, and how biasing the first multiplier more negative significantly helped in reducing the spur intensity. It is noted however that a compromise must often be found as such changes on the multiplier biases can reduce the available LO output power, and therefore jeopardize the mixer pumping.

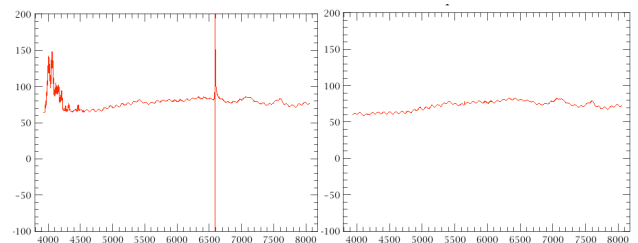


Fig. 6 Example of an LO spur removal by multiplier bias change in band 1a at 551 GHz. Left: receiver noise temperature at the nominal bias, featuring a strong spur. Right: same with a more negative multiplier bias, showing the removal of the spurious signal.

IV. POINTING PROPERTIES

The pointing performance offered by the instrument is the combination of two contributions. On the one hand, the capability of the Spacecraft to accurately stare at a targeted line-of-sight is fully driven by the performance of its star-tracker system. On Herschel, the so-called *Absolute Pointing Error* (APE) was measured to be of the order of 2 arcsec on the sky, i.e. fully within the specifications. On the other hand, the capability of the instrument to get its beam well coupled to the targeted source depends on the accuracy with which the positions of its aperture are known with respect to the frame defined by the Star-tracker. Ensuring the latter is the purpose of the Focal Plane Geometry (FPG) measurements.

A. HIFI FPG campaign

The in-flight assessment of the HIFI aperture was highly relying on the very accurate measurements that had been performed on the ground during the Instrument-Level Test (ILT) campaign, see e.g. [8], [9]. During those measurements, the aperture positions were measured with respect to a reference (alignment cube) belonging to a common reference frame, but most importantly, the various bands were paired in clusters for which the relative positioning was measured with an accuracy better than 0.7 arcsec on the sky. The results of this campaign are illustrated in Fig. 7.

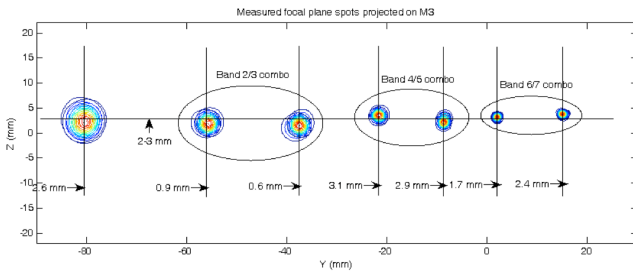


Fig. 7 Projection of the beam intensity distribution onto the HIFI pick-up mirror (M3) as measured during the Instrument-Level Tests.

This legacy results allowed to starting the in-flight FPG measurements with only one aperture per cluster. The measurements were done in two steps:

- A coarse mapping was performed over an area around the expected aperture location on the sky, allowing for mis-pointing margins. For this, a sampling slightly worse than a Nyquist sampling was used. Only one aperture per cluster was considered at the time
- After correcting the offset measured from the coarse mapping, a finer mapping was repeated with a smaller sampling and extent. This time, all 7 bands were measured.

The typical map sizes and sampling for the above steps are illustrated on Fig. 8. Fig. 9 shows an example of such measurements on Saturn in bands 1 and 6.

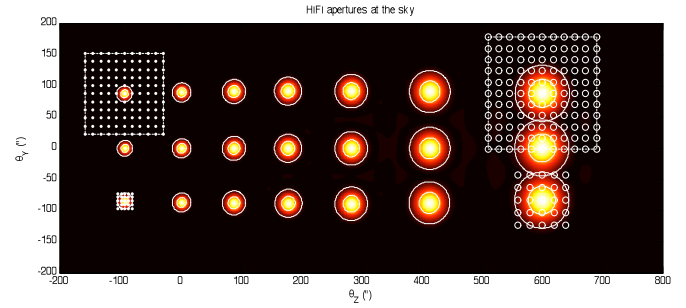


Fig. 8 Illustration of the HIFI aperture positions on the sky, together with the footprints of the raster map pixels performed in the framework of the coarse (upper coverages) and fine (lower coverages) focal plane geometry measurement campaigns.

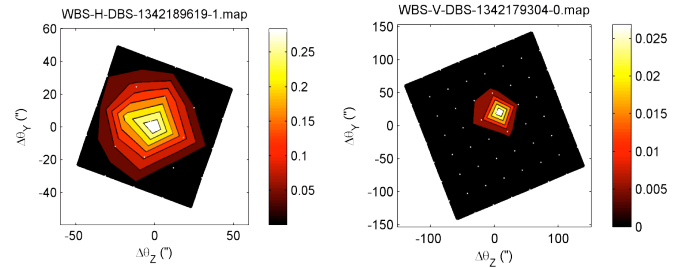


Fig. 9 Example of Saturn measurements in band 1 (491 GHz) and 6 (1625 GHz), used to determine the offsets of the corresponding HIFI apertures.

B. Beam co-alignment

HIFI offers for each receiver two polarisation channels that can be measured simultaneously. While they provide a hardware redundancy to cover contingency failures, they can also be combined to decrease the noise level achieved in spectral measurements by a factor $\sqrt{2}$. This assumes that both polarisations are looking at the same point on the sky. Because they correspond to two physically different mixers and their associated optics, the co-alignment of the respective apertures on the sky adds a potential error.

The co-alignment was measured using the map information collected in the respective polarisation channels. The results are summarized in Table 1. The co-alignment is found to be very good, and in perfect agreement with what was measured pre-launch. However, in order to mitigate the global pointing error when combining the two polarisations, it was decided to not favour any of the channels and rather use an synthetic aperture located in the centre of the two polarisation beams. The resulting coupling losses in such an approach are limited, and listed in Table 1.

TABLE I
BEAM CO-ALIGNMENT RESULTS

Band	F (GHz)	FWHM (")	ΔHV_{ILT} in Y;Z (")	ΔHV_{CoP} in Y;Z (")	Coupling loss (%)
1	480	44.3	-4.5;+1.5	-6.2;+2.2	0.8
2	640	33.2	-4.3;-1.5	-4.4;-1.3	0.7
3	800	26.6	-5.1;-4.3	-5.2;-3.5	1.9
4	960	22.2	-1.5;-2.2	-1.2;-3.3	0.9
5	1120	19.0	+1.5;+3.6	0.0;+2.8	0.8
6	1410	15.2	+0.7;0.0	+0.7;+0.3	0.1
7	1910	11.2	+0.7;-1.5	0.0;-1.0	0.2

C. Chopper angle calibration

In one of HIFI's most used observing modes (DBS), the internal chopper mirror is used to move the beam to a reference Off position on the sky within 3 arc minutes away from the On-target position. Since moving the internal mirror changes the light path for the incoming waves the possibility of residual standing waves exists. By slewing the telescope so that the source appears alternatively in both On and Off chopped positions, the impact of standing wave differences is eliminated to a first order.

The whole scheme assumes that there is a perfect match between the distance on the sky involved between the two chopper positions, and the distance involved in the telescope slew. Since the FPG measurements have been taken in the DBS mode, it is possible to create two separate maps corresponding to each telescope position, and therefore derive any offset between the source positions in each coverage. This offset is used to recalibrate the exact telescope slew distance needed to match the intrinsic chopper angle on the sky. This is particularly important since there is some curvature involved when chopping away from the on-axis line-of-sight and this effect varies with the HIFI band. Fig. 10 illustrates this result, showing an excellent agreement between measured and theoretical throws on the sky.

V. CONCLUSIONS

The HIFI in-flight Commissioning campaign has taken about 2 months and involved a team of more than 40 scientists, with a short regression test period following the HIFI re-start after the LCU failure in August 2009. The instrument performances are similar or better than pre-launch, meeting all top-level specifications. The science data quality is very good, albeit more challenging in the higher frequency bands (HEBs), and data artifacts are similar to those encountered in other radio-telescopes on the ground. On-going efforts in the area of spectral purity is made possible by a system design flexible enough to allow the last-fine tunings in space.

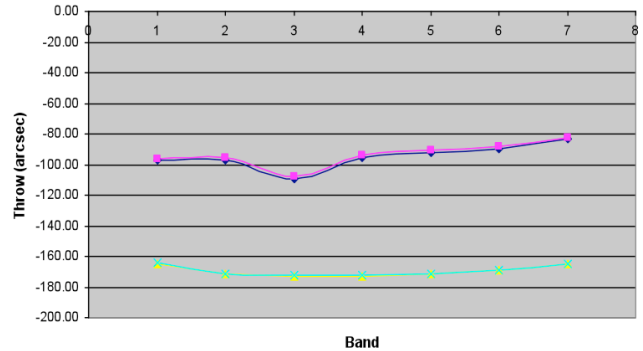


Fig. 10 Chopper throw distances on the sky. *Upper curves*: theoretical (diamonds) and measured (squares) distances for a so-called half-throw, i.e. a chopper throw between the secondary (M2) centre and one of the borders of M2. *Lower curves*: theoretical (triangles) and measured (crosses) distances for a so-called full-throw, i.e. a chopper throw between the two opposite borders of M2.

ACKNOWLEDGMENT

Herschel is an ESA space observatory with science instruments provided by European-led Principal Investigator consortia and with important participation from NASA. The HIFI instrument has been constructed, tested and prepared for operations by a large set of teams of dedicated engineers, scientists and managers, from 12 European and North American countries, with additional funding by grants from their national Space agencies. A part of this research was carried out at the Jet Propulsion Laboratory, California Institute of Technology, under contract with the National Aeronautics and Space Administration.

REFERENCES

- [1] G. Pilbratt, et al., *The Herschel Mission Status and Highlights, 2010*, this volume.
- [2] T. de Graauw et al., *The Herschel-Heterodyne Instrument for the Far-Infrared (HIFI)*, 2010, *Astronomy & Astrophysics*, in press.
- [3] W. Jellema et al., *The HIFI OD81 Anomaly*, 2010, this volume.
- [4] D. W. Allan, *Statistics of atomic frequency standards*, 1966, *Proc. IEEE*, 54, 221
- [5] V. Ossenkopf, *The stability of spectroscopic instruments: an unified Allan variance computation scheme*, 2008, *Astronomy & Astrophysics* 479, 915
- [6] R. D. Higgins et al., *Calibration of the Herschel HIFI Instrument using Gas Cell Measurements*, 2010, this volume.
- [7] R. D. Higgins and J. W. Kooi, *Electrical standing waves in the HIFI HEB mixer amplifier chain*, 2009, in *Society of Photo-Optical Instrumentation Engineers (SPIE) Conference Series*, vol. 7215
- [8] W. Jellema et al., *The HIFI Focal Plane Beam Characterization and Alignment Status*, 2008, *Proc. of the 19th International Symposium on Space Terahertz Technology*
- [9] P. Dieleman et al., *HIFI Flight Model Testing at Instrument and Satellite Level*, 2008, *Proc. of the 19th International Symposium on Space Terahertz Technology*

The Stratospheric THz Observatory (STO): 1st Test Flight

C. Walker¹, C. Kulesa¹, J. Koostermann¹, T. Cottam¹, C. Groppi², P. Bernasconi³, H. Eaton³, N. Rolander³, D. Neufeld³, C. Lisse³, A. Stark⁴, D. Hollenbach⁵, J. Kawamura⁶, P. Goldsmith⁶, W. Langer⁶, H. Yorke⁶, J. Sterne⁶, A. Skalare⁶, I. Mehdi⁶, S. Weinreb⁷, J. Kooi⁷, J. Stutzski⁸, U. Graf⁸, C. Honingh⁸, P. Puetz⁸, C. Martin⁹, D. Lesser⁹, Mark Wolfire¹⁰

¹Steward Observatory, University of Arizona, Tucson, AZ 85721 USA

²School of Earth and Space Exploration, Arizona State University, Tempe, AZ 85287 USA

³Johns Hopkins Applied Physics Laboratory, Laurel, MD 20723 USA

⁴Smithsonian Astrophysical Observatory, Cambridge, MA 02138 USA

⁵SETI Institute, Mountain View, CA 94043 USA.

⁶Jet Propulsion Laboratory, Pasadena, CA 91109 USA

⁷California Institute of Technology, Pasadena, CA 91125 USA

⁸University of Cologne, Cologne, D-50937 Germany

⁹Oberlin College, Oberlin, OH 44074 USA.

¹⁰University of Maryland, College Park, MD 20740 USA

*Contact: cwalker@as.arizona.edu, +01-520-621-8783

Abstract— The Stratospheric TeraHertz Observatory (STO) is a NASA funded, Long Duration Balloon (LDB) experiment designed to address a key problem in modern astrophysics: understanding the Life Cycle of the Interstellar Medium (ISM). STO will survey a section of the Galactic plane in the dominant interstellar cooling line [C II] (1.9 THz) and the important star formation tracer [N II] (1.46 THz) at ~1 arc minute angular resolution, sufficient to spatially resolve atomic, ionic and molecular clouds at 10 kpc. STO itself has three main components; 1) an 80 cm optical telescope, 2) a THz instrument package, and 3) a gondola [1]. Both the telescope and gondola have flown on previous experiments [2,3]. They have been re-optimized for the current mission. The science flight receiver package will contain four [CII] and four [NII] HEB mixers, each with its own digital spectrometer. The first engineering test flight of STO was from Ft. Sumner, NM on October 15, 2009. Test flight instrumentation was used to evaluate STO's ability to point and track using gyroscopes/star cameras with a load-varying, cryogenic system onboard. The science flight receiver electronics and control system were also tested.

I. INTRODUCTION

STO is a Long Duration Balloon (LDB) experiment designed to address a key problem in modern astrophysics: understanding the Life Cycle of the Interstellar Medium (ISM). During its upcoming science flight STO will survey a section of the Galactic plane in the dominant interstellar cooling line [C II] (158 μm) and the important star formation tracer [N II] (205 μm) at 1 arcminute angular resolution, sufficient to spatially resolve atomic, ionic and molecular clouds at 10 kpc. The goals for the survey are to:

- [1] Determine the life cycle of Galactic interstellar gas.

- [2] Study the creation and disruption of star-forming clouds in the Galaxy.
- [3] Determine the parameters that affect the star formation rate in the galaxy.
- [4] Provide templates for star formation and stellar/interstellar feedback in other galaxies

On Oct. 15, 2009 STO had its test flight from Ft. Sumner, NM. During its 12 hours at float altitude (~126,000 ft.) key components of STO were tested to help ensure the system would meet the objectives of the upcoming science flight. STO consists of 3 major components; a gondola, an 80 cm telescope, and a THz heterodyne receiver system. The gondola and telescope have been refurbished from the successful Flare Genesis Experiment. The gondola was upgraded by APL to use 3 gyroscopes for inertial guidance and an optical tracker for absolute pointing. The telescope was light-weighted and its primary and secondary mirrors re-aluminized. A room temperature receiver system and a cryostat were constructed and flown on the test flight. A computer-controlled, sliding weight was added to dynamically compensate for cryogen evaporation during flight.

2. TEST FLIGHT INSTRUMENT

The STO flight from New Mexico was designed to provide a complete and faithful test of the full Antarctic gondola, telescope, and key elements of the science instrumentation.

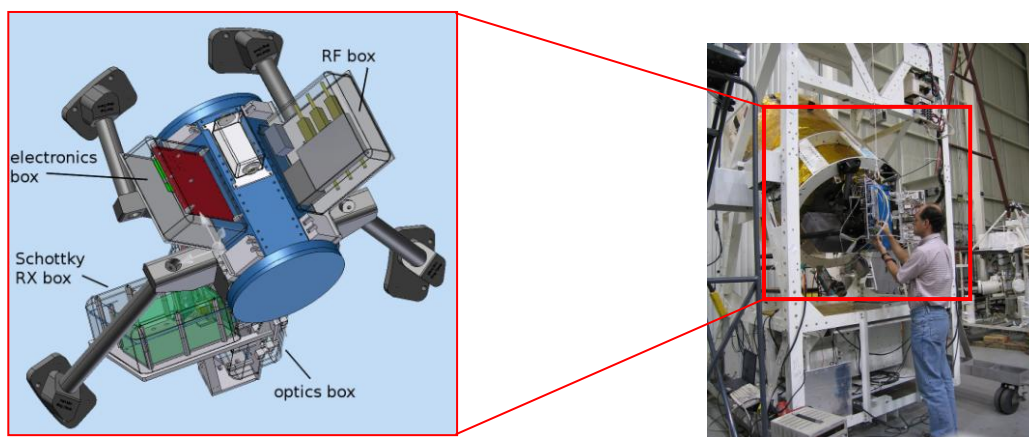


Figure 1: STO test-flight telescope and instrument package configuration, as conceptualized (left) and being integrated at Fort Sumner in early October, 2009 (right).

Antarctic ready versions of the telescope/gondola systems, instrument electronics, computing, control, and data storage systems were flown. To faithfully characterize the performance of the telescope drives and pointing system, the test flight instrument was designed with the same CG and weight as the full Antarctica flight instrument. The STO test flight carried a test cryostat and an un-cooled Schottky receiver. The receiver was used to point on the ^{13}CO J=3-2 line. The dewar was used to test the ability of a sliding weight to compensate for the loss of cryogenics during flight.

Figure 1 shows the STO telescope and instrument package as it was configured for the test flight. The instrument flight system as deployed contained the following subsystems:

- an *optics box* containing relay optics for the 330 GHz receiver and actuators to direct the telescope beam into calibration loads.
- an *electronics box* containing the instrument control computer, bias electronics for the Schottky and future HEB receivers, housekeeping temperature monitors, analog multiplexers, and solid state relays for calibration actuators.
- a *RF box* containing the LO drive synthesizers, amplifiers for the HEB mixers, and a downconverter for the Schottky mixer receiver.
- a 330 GHz *Schottky mixer receiver* from JPL, kept at ambient temperature and pressure.
- a 4K *dewar*, the nitrogen and helium cryogenic vessels were pressure-regulated to approximately sea level pressure, to maintain a helium bath temperature of 4.2K.
- A *pressure vessel* containing the FFT spectrometer, data control computer, and Cisco router to isolate the instrument network traffic from the gondola. Figure 2 shows the pressure vessel contents just before they were sealed and installed onto the gondola mezzanine level.

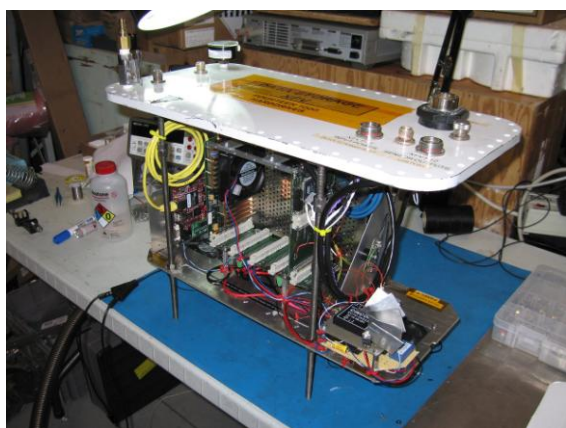


Figure 2: Pressure vessel containing the data acquisition and control computer, solid state storage, network router, and Omnisys FFT spectrometer.

Figure 3 depicts the subsystem contents in a block diagram.

End-to-end testing of the complete system was performed on the ground using the ambient temperature Schottky receiver. A 330 GHz test tone was emitted by an outdoor transmitter through the telescope and instrument optics (Figure 4).

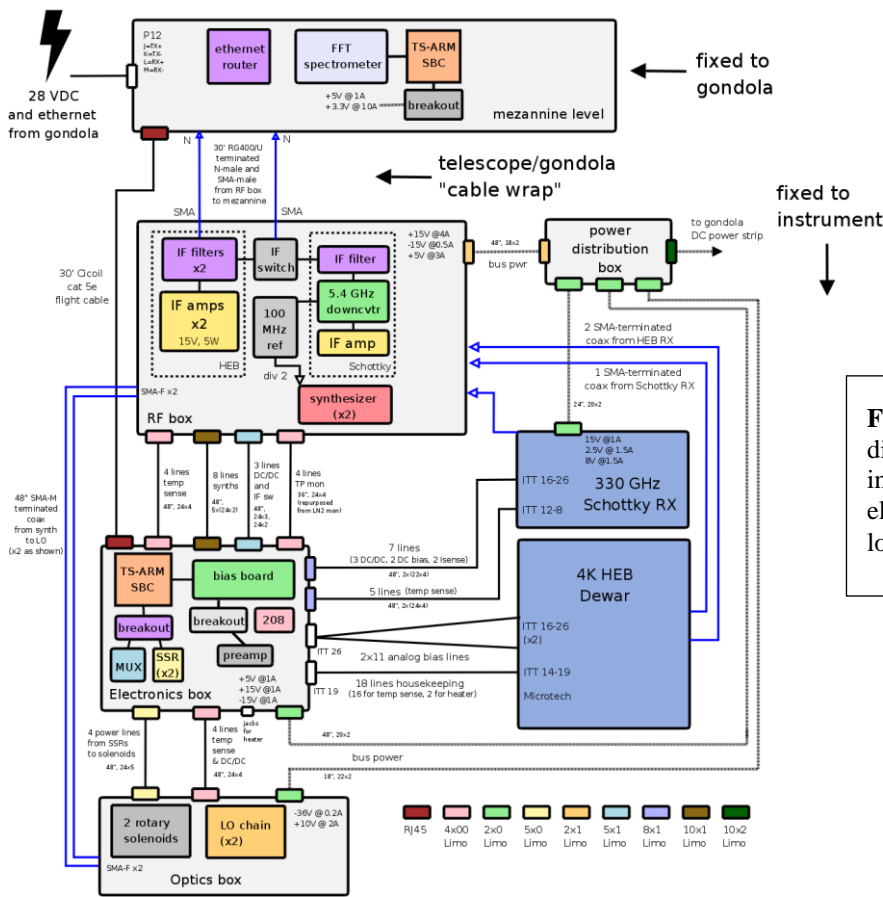


Figure 3: Detailed block diagram of the instrument control electronics and their location on the gondola.

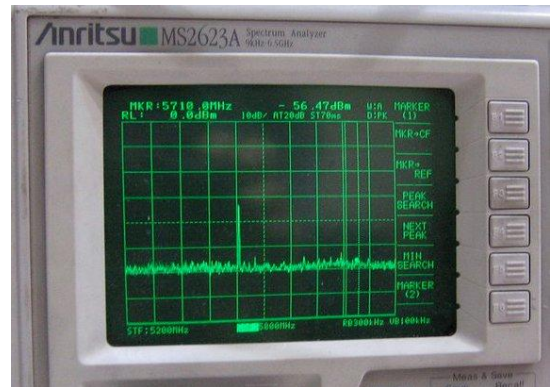
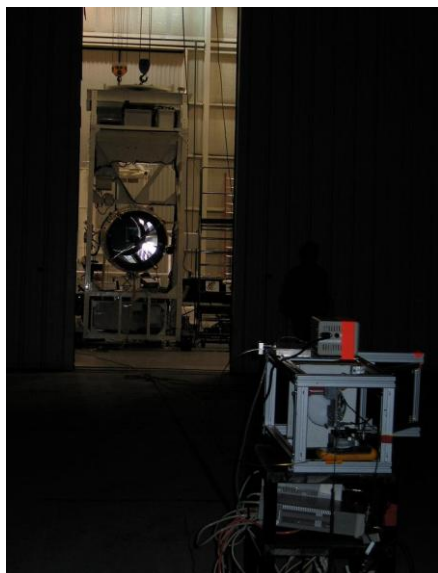


Figure 4: (Left) End-to-end testing of the entire STO instrument using the ambient temperature Schottky receiver and a 330 GHz test transmitter placed ~50m away from the telescope. (Right) Spectrum analyzer view of the Schottky receiver IF, showing the test transmitter tone passing through all telescope and instrument optics and downconverted and amplified by the IF processor. This test represented the final “go” for launch.

3.0 TEST FLIGHT RESULTS

STO was uneventfully launched at 10:03 AM MDT on 15 October, 2009 from the NASA facility at Fort Sumner, New Mexico under excellent launch conditions (Figure 5).

The primary results from the test flight were:

- 1) The gyros performed well, allowing the telescope/gondola to track at the 5 arcsecond level (rms) after settling from a slew or a momentum transfer.
- 2) The star tracker demonstrated it can provide absolute pointing knowledge that meets mission requirements.
- 3) The sliding weight successfully controlled the telescope CG during all phases of flight.
- 4) The room temperature receiver, instrument control electronics, IF processor, and spectrometer performed well throughout the flight.
- 5) Control of the telescope, gondola, and instrument was maintained throughout the flight.
- 6) As an end-to-end test of the system, a ^{13}CO J=3-2 spectrum of the Orion molecular cloud was obtained by STO at float altitude (see Figure 6).



Figure 5: (Left) Balloon inflation is nearly complete at 9:50 AM on 15 October. (Center) STO launches at 10:03 AM, and reaches float altitude two hours later, hanging overhead (Right) for nearly the entire flight, and landing < 100 miles away at 1:15 AM on 16 October.

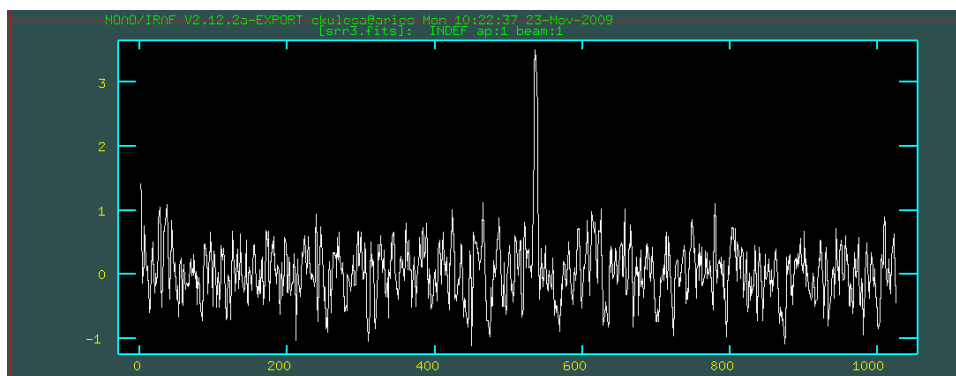


Figure 6: STO first-light spectral observation of the ^{13}CO J=3-2 line toward Orion taken from float altitude.

4.0 FUTURE PLANS

STO is scheduled to have its first LDB science flight from McMurdo, Antarctic in December 2011. For the science flight STO will employ a long (~28 day) hold time cryostat built by Ball Aerospace. STO's four 1.9THz and four 1.45THz HEB mixers and their L-band IF amplifiers will reside in an insert thermally strapped to the Ball cryostat's helium vessel. Optical and electrical connections to the mixer arrays will be made through the insert. The solid-state local oscillators and associated Fabre-Perot diplexer will reside in an ambient temperature optics box bolted to the top of the cryostat. The optics box will also contain reimaging mirrors and a calibrated black body load. There will be eight, 1GHz wide FFT spectrometers in the pressure vessel to process the IF signals.

REFERENCES

- [1] Walker, C. K., Kulesa, C. A., Groppi, C. E., Young, E. T., McMahon, T., Bernasconi, P., Lisse, C., Neufeld, D., Hollenbach, D., Kawamura, J., Goldsmith, P., Langer, W., Yorke, H., Sterne, J., Sklare, A., Mehdi, I., Weinreb, S., Kooi, J., Stutzki, J., Graf, U., Honingh, N., Puetz, P., Martin, C., Wolfire, M., 2008, "The Stratospheric TeraHertz Observatory" in Proceedings of 19th International Symposium on

- Space Terahertz Technology, ed. Wolfgang Wild, Groningen, 28-30 April 2008, (https://www.sron.nl/files/LEA/ISSTT2008/Proceedings_ISSTT2008.pdf), p.28.
- [2] Bernasconi, P.N., Rust, D. M., Eaton, H. A. C., Murphy, G. A. A., 2000, "A Balloon-borne Telescope for high resolution solar imaging and polarimetry", in Airborne Telescope Systems, Ed. By R. K. Melugin, and H. P. Roeser, SPIE Proceedings, 4014, 214.
- [3] Bernasconi, P.N., Eaton, H. A. C., Foukal, P., and Rust, D. M., 2004, "The Solar Bolometric Imager", Adv. Space Res., 33, 1746.

Session S2: THz Sources

Photonic local oscillators for terahertz radio astronomy

Iván Cámara Mayorga^{*}, Andreas Schmitz, Christian Leinz, Thomas Klein, Alfred Dewald[†] and Rolf Güsten

^{*}Max Planck Institut für Radioastronomie
Email: imayorga@mpifr-bonn.mpg.de

[†]Institut für Kernphysik, University of Cologne

Abstract

We report on recent improvements of photomixing technology and the realization of a photonic local oscillator (LO) at 1.05 THz for the Atacama Pathfinder Experiment (APEX) radiotelescope in the Atacama desert, Chile. Experiments with state-of-the-art photomixers operated in a cryogenic environment demonstrate pumping of an astronomical heterodyne receiver at 1050 GHz with a superconductor-insulator-superconductor (SIS) mixer. The system noise temperature of the heterodyne receiver was compared with that of the same system using a conventional solid-state LO, revealing similar noise temperatures. A self-made optical comb generator served as a relative frequency reference to which one laser was phase-locked. Under the phase lock condition, the 3 dB linewidth of the THz signal was below 3 KHz and could be continuously tuned within a range of 500 MHz -the overall tunability of the system was determined by the photomixer antenna resonance bandwidth, which was roughly 200 GHz. We installed the laser system in the telescope pedestal, whose output, the frequency-stabilized laser signal, was fed into the photomixer through a 20 meters long single-mode fiber optic.

In addition, preliminary results achieved with photomixers at 2.5 THz will be reported. The work on these devices is aimed for the implementation of a photonic LO in the GREAT instrument onboard of the Stratospheric Observatory for Infrared Astronomy (SOFIA).

GaAs varactor multipliers based on transferred substrate technology

M. Henry^{*}, B. Alderman^{*}, H. Sanghera^{*}, P. Maagt[†] and D. Matheson^{*}.

^{*} Space Science and Technology Department
Rutherford Appleton Laboratory, Chilton, Oxfordshire OX11 7RQ
Email: manju.henry@stfc.ac.uk

[†] Antenna and Sub-millimetre Wave Section
Electromagnetics & Space Environments Division European Space Agency,
NL 2200 AG Noordwijk
The Netherlands

Abstract

There is a demand for millimetre wave and sub-millimetre wave power sources to be used as local oscillators in heterodyne radiometers for remote sensing, atmospheric physics and radio astronomy. An ideal source for most of these applications should exhibit high output power, efficiency, large bandwidth and high thermal stability.

We report here on the design and evaluation of high efficiency frequency doublers which provide useful power at millimetre and sub-millimetre wavelengths. The active device is a single GaAs chip consisting of a linear array of 4/6 planar schottky varactors which have been subsequently transferred on to Aluminium Nitride in order to improve the power handling capability and hence the efficiency. The so-called transferred substrate multipliers improves the efficiency of the component by around 15% compared to similar designs on the original GaAs substrates. The varactor chip and quartz microstrip circuit are embedded in a split waveguide block. The transferred substrate multipliers exhibit an efficiency of around 30 % at 160 GHz for an input power of 60 mW, and a 20% efficiency at 332 GHz for an input power of 40 mW.

Effect of Feedback on Quantum Cascade Laser Performance

M.C. Wanke*, M.Lee*, C.D. Nordquist*, M.J. Cich *, C.T. Fuller* , A.D. Grine[†] and J.L. Reno*

* Sandia National Laboratories
Email: mcwanke@sandia.gov

[†] LMATA Government Services

Abstract

THz quantum cascade lasers are promising solid-state sources for use as local-oscillators in THz heterodyne receiver systems especially when frequencies higher than 2 THz or power exceeding mW are needed. Recent phase locking measurements of THz QCLs to high harmonics of microwave frequency reference sources as high as 2.7 THz [[1], [2]] demonstrate that the linewidth and frequency stability of QCLs can be more than adequate for astrophysical measurements.

Using a novel transceiver with a Schottky diode monolithically integrated into a THz QCL, we have begun to explore the sensitivity of the laser performance on feedback due to retroreflections of the THz laser radiation. The transceiver allows us to monitor the beat frequency between internal Fabry-Perot modes of the QCL or between a QCL mode and external radiation incident on the transceiver. When feeding back the radiation from a Fabry-Perot type QCL with quasi-static optics we observe reproducible fluctuations of the difference frequency between the QCL modes as either the alignment of or distance to the reflector is changed.

We have also explored the behavior when the difference frequency of the internal laser modes is locked to an ~ 13 GHz microwave reference source (as done in ref. [[3]]) with a linewidth less than 10 Hz. The narrow linewidth allowed us to observe sidebands with a few hundred Hz separation when the retroreflector was vibrated at a fixed frequency. In some cases these sidebands were only 3dB down from the central peak at the locked frequency.

This work was supported by the LDRD program office at Sandia National Labs. Sandia is a multiprogram laboratory operated by Sandia Corporation, a Lockheed Martin Company, for the United States Department of Energy's National Nuclear Security Administration under contract DE-AC04-94AL85000.

REFERENCES

- [1] D. Rabanus, U. U. Graf, M. Philipp, O. Ricken, J. Stutzki, B. Vowinkel, M. C. Wiedner, C. Walther, M. Fischer, and J. Faist, "Phase locking of a 1.5 Terahertz quantum cascade laser and use as a local oscillator in a heterodyne HEB receiver," *OPTICS EXPRESS*, vol. 17, pp. 1159–1168, FEB 2 2009.
- [2] P. Khosropanah, A. Baryshev, W. Zhang, W. Jellema, J. N. Hovenier, J. R. Gao, T. M. Klapwijk, D. G. Paveliev, B. S. Williams, S. Kumar, Q. Hu, J. L. Reno, B. Klein, and J. L. Hesler, "Phase locking of a 2.7 THz quantum cascade laser to a microwave reference," *OPTICS LETTERS*, vol. 34, pp. 2958–2960, OCT 1 2009.
- [3] A. Baryshev, J. N. Hovenier, A. J. L. Adam, I. Kasalynas, J. R. Gao, T. O. Klaassen, B. S. Williams, S. Kumar, Q. Hu, and J. L. Reno, "Phase locking and spectral linewidth of a two-mode terahertz quantum cascade laser," *APPLIED PHYSICS LETTERS*, vol. 89, JUL 17 2006.

Development of Local Oscillators for CASIMIR

R. Lin, B. Thomas, J. Ward¹, A. Maestrini², E. Schlecht, G. Chattopadhyay,
J. Gill, C. Lee, S. Sin, F. Maiwald, and I. Mehdi

*Jet Propulsion Laboratory, California Institute of Technology,
4800 Oak Grove Drive, Pasadena, CA, 91101, USA. Email: Robert.H.Lin@jpl.nasa.gov*

¹ *now with Raytheon Company, Fort Wayne, Indiana*

² *Observatoire de Paris, LERMA, University P&M Curie, Paris-VI. 77 Avenue Denfert-Rochereau 75014 Paris, France*

Abstract— We present the development of three local oscillator chains to be used on the CASIMIR (Caltech Airborne Submillimeter Interstellar Medium Investigations Receiver) instrument onboard the SOFIA (Stratospheric Observatory for Infrared Astronomy) aircraft. All three chains use all solid-state GaAs-based components to amplify and multiply a ~1-3 mW input signal at W band. At room temperature, the 900 GHz source produces 50-100 μ W of power from 800 to 930 GHz. The 1 THz source produces 50-120 μ W of power from 960 to 1045 GHz. The 1.4 THz source produces 10-70 μ W of power from 1320 to 1470 GHz. When cooled to 120 K, the 1.4 THz chain's output power increases by approximately 3 dB with a peak power of 129 μ W at 1395 GHz.

Index Terms – CASIMIR, local oscillator, terahertz source, frequency multiplier, cascaded multipliers, GaAs Schottky diode, submillimeter wavelengths.

I. INTRODUCTION

The Caltech Airborne Submillimeter Interstellar Medium Investigations Receiver (CASIMIR) is a multi-band, far infrared and submillimeter, high resolution, heterodyne spectrometer designed for high sensitivity observations of warm interstellar gas [1]. Multiple bands are being developed to study the transition lines of various molecular species. Of special interest are lines from H_2^{18}O , H_2D^+ , and N^+ around 1 THz and 1.4 THz. The detectors for the receivers use advanced Superconductor-Insulator-Superconductor (SIS) mixers, pumped by solid-state local oscillator (LO) sources.

We present here the development and characterization of three LO sources which cover 800-930 GHz, 970-1040 GHz, and 1320-1470 GHz, respectively. The first two sources will serve as local oscillators for the spectroscopic lines in the 800-1040 GHz range [2], while the 1.4 THz source will enable the study of the H_2D^+ line at 1.37 THz and the N^+ line at 1.46 THz [3]. Each chain is composed of cascaded frequency multipliers driven by WR10 or WR8 power amplifiers. The multipliers are based on GaAs substrateless and membrane device technologies, which have been successfully demonstrated on the Herschel HIFI instrument [4],[5]. Measurements of SIS and HEB heterodyne mixers pumped by these LO chains prove that they are low noise and produce power at the correct frequency [6],[7].

II. 900 GHz LO CHAIN

The 900 GHz LO is driven by a few milliwatts of power in the 88-105 GHz range. Three cascaded power amplifiers amplify the input signal to ~100 mW. This is then followed by a wideband isolator, built by Millitech, and two stages of frequency triplers as shown in Fig 1.

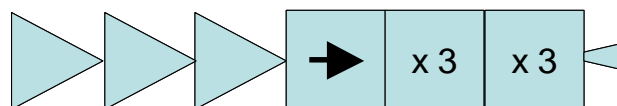


Fig.1: Schematic block diagram and photo of the 900 GHz LO chain, including power amplifiers, an isolator, two stages of frequency triplers, and a corrugated output horn.

The first stage tripler provides output power in the 265-325 GHz range. Its circuit is based on a GaAs Monolithic Membrane Device (MoMeD) with beamleads for electrical connections and handling [8]. The tripler, previously described in [9], has an efficiency of about 7-9% across the band, with average output power ~7-9mW. The second stage tripler (M2) uses a 3 μ m GaAs MoMeD with 4 anodes in a balanced configuration. Its design and characterization were previously reported in [10].

The output power of the complete chain was measured using an Erickson PM2 calorimeter by removing the corrugated output horn and attaching a custom-made 300x150 μ m to WR10 waveguide transition. At fixed bias voltages for both tripler stages, there is a strong standing wave due to the lack of isolation between the two triplers. By tuning the bias voltages of the frequency multiplier diodes, we were able to obtain a smooth frequency vs. power sweep that still meets the required minimum 50 μ W of output power across the full 800-930 GHz band. Figure 2 shows the results of the measurements, uncorrected for the loss due to the waveguide transition.

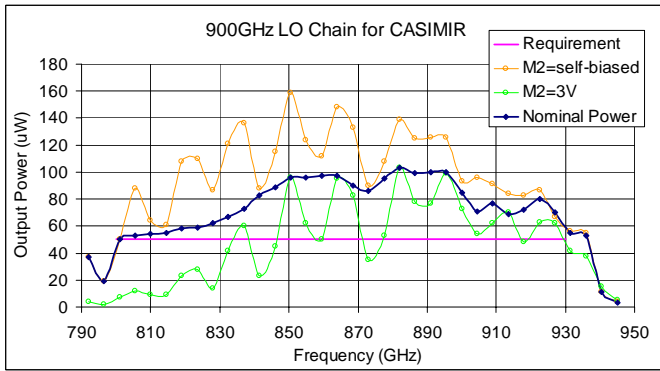


Fig.2: Performance of the 900 GHz LO Chain at room temperature. At fixed bias conditions, a standing wave pattern exists in the frequency sweep. By tuning the bias voltages properly, the nominal output power shown in dark blue is obtained.

III. 1 THz LO CHAIN

The 1 THz LO is driven by a few milliwatts of power in the 107-117 GHz range. Four cascaded power amplifiers amplify the input signal to ~ 80 -100 mW. This is then followed by two stages of frequency triplers as shown in Fig. 3. Due to the lack of a low-loss wide bandwidth isolator at WR8 frequencies, no isolation exists between the amplifier and the first stage tripler. The final stage tripler has a diagonal horn integrated into the block described in [11]. The CASIMIR horn is scaled such that the dimension of the square on the output flange is 1.86 mm.

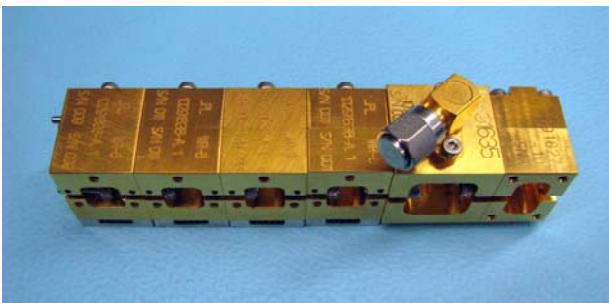
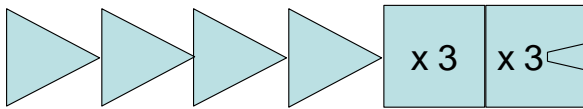


Fig.3: Schematic diagram and photo of the 1 THz LO Chain, including four power amplifier stages and two stages of frequency triplers.

The first stage tripler gives output in the 325-350 GHz range. Its circuit is a scaled version of the 265-325 GHz tripler used in the 900 GHz LO chain. This tripler produces about 6-11 mW of power across the band. The second stage tripler uses a $3 \mu\text{m}$ thick GaAs MoMeD with 2 anodes in a biasless configuration. The same device has been previously used on the Herschel HIFI instrument for the Band 5 (1.2 THz) receivers [12]. For the CASIMIR chain, the waveguides were redesigned for optimal efficiency in the 970-1040 GHz range.

The output power of the complete chain was measured using an Erickson PM2 calorimeter by attaching a circular to WR10 waveguide transition directly to the output face of the last stage tripler. With fixed bias voltages for both the power amplifier and tripler, the output power of the chain is shown in Figure 4. The required $50 \mu\text{W}$ of power across 970 to 1040 GHz is met at room temperature even without correcting for the waveguide transition loss. Peak measured power was $120 \mu\text{W}$ at 980 GHz. The compact nature of this chain, combined with the excellent output power performance without mechanical or electrical tuning, makes this chain very robust and easy to use.

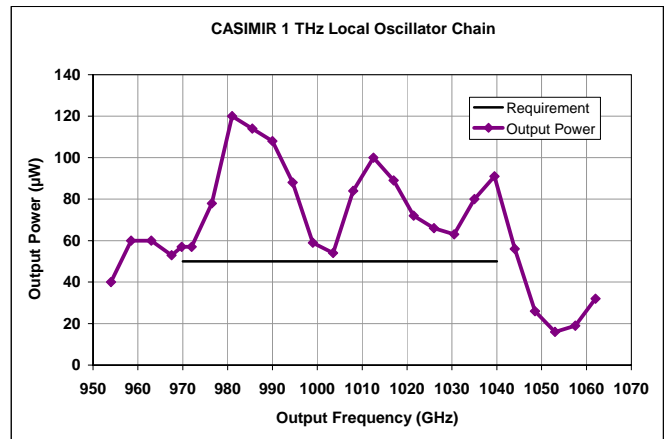


Fig.4: Performance of the 1 THz LO Chain. Measured with Erickson PM2 calorimeter, uncorrected for waveguide transition loss.

IV. 1.4 THz LO CHAIN

The 1.4 THz LO features three amplifier blocks, an isolator, and three stages of frequency multiplication. It is driven by a few milliwatts of power in the 72-82 GHz range. First, three cascaded power amplifiers amplify the input signal to ~ 130 mW. This is then followed by a wide-band isolator, a frequency doubler, and two additional stages of frequency triplers as shown in Fig 5.



Fig.5: Schematic diagram and photo of the 1.4 THz LO Chain, including three power amplifier stages, one doubler stage and two tripler stages.

The first stage multiplier is a frequency doubler that gives output in the 144-164 GHz range. The circuit is based on the substrate-less device technology used on Herschel / HIFI [12], scaled to ~150 GHz. This doubler produces about 40 mW of power across the band with a fixed bias voltage of -6V.

The second stage multiplier is a frequency tripler operating from 430 to 495 GHz, with ~4 mW of power across 445 to 490 GHz. The bias voltage is mostly fixed at +12V except at output frequencies below 445 GHz, where it prefers to be biased closer to 0V. The circuit uses a 5 μm GaAs MoMeD which is a scaled version of the 265-325 GHz tripler discussed earlier in this paper.

The final stage frequency tripler features a 2-anode biasless MoMeD device on a 3 μm thick GaAs membrane, shown in Figure 6. It operates from 1320 to 1470 GHz, and has an integrated diagonal horn [11]. The horn dimensions are scaled such that the output square dimension is 1.35 mm.



Fig.6: Photo of the 1.4 THz tripler device mounted in its waveguide block, featuring 2 anodes on 3 μm GaAs membrane in a biasless configuration.

A. Investigation and Management of Signal Purity

The photo in Figure 5 shows the presence of an extra waveguide shim between the second and third multiplier stages. This is inserted to suppress a spurious signal that was found after an investigation into the spectral purity of the chain, as described below.

The spectral purity of the 1.4 THz chain output signal was analysed with a Fourier Transform Spectrometer (FTS) based on a simple Michelson interferometer. With an input signal at $f_0=80$ GHz, the chain is expected to produce $f_0 \times 2 \times 3 \times 3 = 18f_0$, the 18th harmonic, at 1440 GHz. However, when the output spectrum is analysed with the FTS system, we find an additional signal at 1280 GHz that is stronger than that at 1440 GHz.

To investigate this spurious signal, the output of the first stage doubler was analysed with the FTS. It was found that a strong 4th harmonic ($4f_0 = 320$ GHz) was present in addition to the nominal 2nd harmonic ($2f_0 = 160$ GHz). When this 4th harmonic enters the second stage multiplier, it gets tripled to the 12th harmonic ($12f_0 = 960$ GHz), and at the same time, some of the 4th harmonic leaks through to the third stage multiplier. The last stage tripler takes these two additional inputs, the 12th harmonic and the 4th harmonic, and *mixes* them to produce the 16th harmonic at 1280 GHz. Additional signals at $12f_0$ and at $10f_0$, from mixing the $6f_0$ and $4f_0$ signals, are also present. The signal flow diagram and frequency spectrum are shown in Figure 7.

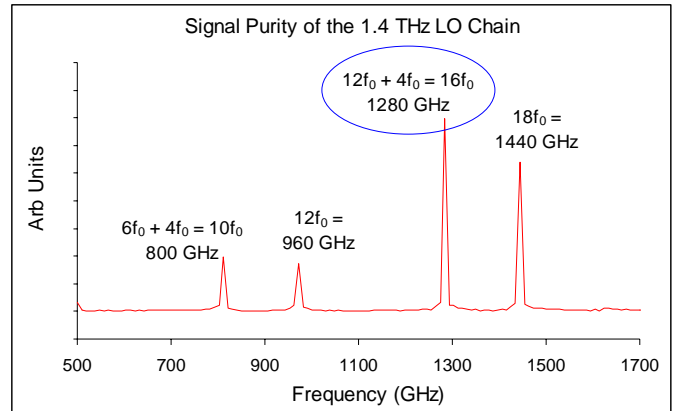
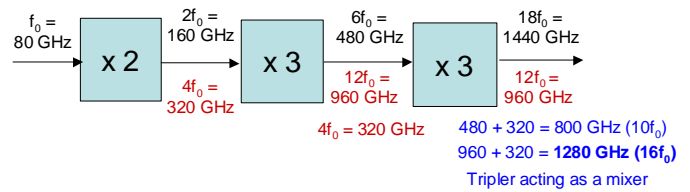


Fig.7: FTS spectrum of the 1.4 THz chain at 1440 GHz. The extra signals can be traced to the presence of a fourth harmonic at the output of the first stage doubler. This fourth harmonic propagates through the second multiplier as well as getting tripled before going into the third multiplier. The final stage tripler then acts as a mixer, producing the 10th and 16th harmonics in addition to the nominal 18th harmonic.

The solution to removing the spurious signal at $16f_0$ is to cutoff the $4f_0$ signal from going into the last stage tripler, thereby eliminating the mixing action. An extra waveguide shim with dimensions 432 μm x 216 μm x 1.5 mm, whose cutoff frequency is at 350 GHz, was machined and inserted between the second and third stage multipliers. FTS measurements of the output spectrum of the second stage multiplier before and after insertion of this waveguide confirm that the $4f_0$ signal is effectively cancelled after the extra waveguide section. With this waveguide shim inserted, the FTS spectrums of the chain at 1.36 THz and at 1.46 THz are shown in Figure 8. It is observed that in addition to the 18th harmonic, the 12th and 24th harmonics are still present due to mixing of the 18th and 6th harmonics. However, their power levels are much lower than the nominal signal, and the frequencies are far enough away from the main signal that they will not affect the LO pump into the SIS mixer.

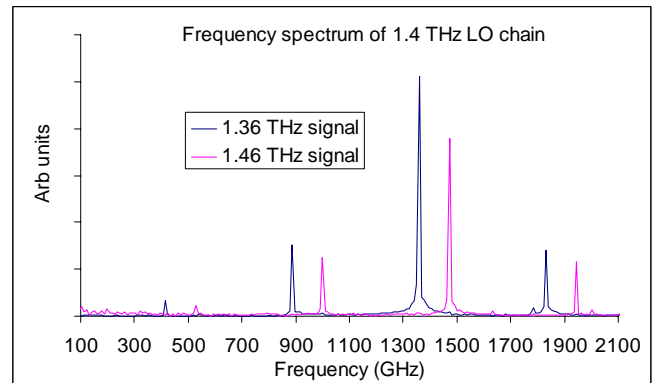


Fig. 8: Frequency spectrum of the 1.4 THz LO chain at 1.36 THz and 1.46 THz. The 16th harmonic has been removed by placing an extra waveguide shim between the second and third stage multipliers.

B. Frequency Sweep at Room Temperature

The output power of the complete 1.4 THz chain, including the extra waveguide shim, is measured by placing a Thomas Keating meter at Brewster's angle of 57 degrees to the axis, located ~10 cm away from the output horn. With nominally fixed bias voltages for the power amplifier and both stage multipliers, the output power of the chain is shown in Figure 9. The chain meets the required 10 μ W of power across 1320 to 1470 GHz. A strong atmospheric absorption line due to water vapour is present at 1410 GHz, which could account for the dip seen in the frequency sweep. Peak measured power was 70 μ W near 1350 GHz and 1395 GHz.

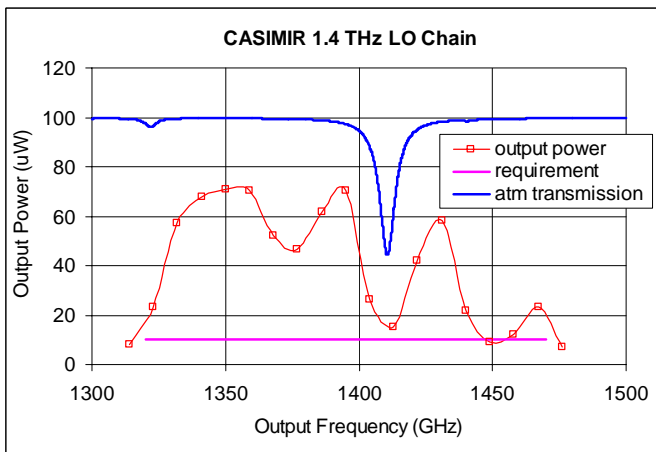


Fig.9: Performance of the 1.4 THz LO chain operated at room temperature, measured with a Thomas Keating meter, uncorrected for atmospheric losses from water vapour absorption. Atmospheric transmission is courtesy of Scott Paine's AM model [13] calculated with 25% relative humidity and 10 cm path length.

C. Frequency Sweep at 120K and Comparison with HIFI

We have also made measurements at the cryogenic temperature of 120K and compared the results with the Herschel / HIFI Band 6A (1.5 THz) LO chain. The multiplier blocks of the 1.4 THz chain were placed in a cryostat at 120K, while the amplifiers and isolator driving the multipliers remained at ambient temperatures outside the cryostat. Measurements were made with the Keating meter under the same bias conditions as at room temperature. Compared with room temperature results, the output power increased by a factor of approximately 3 dB across the band (see Figure 10). Output power was over 50 mW from 1325 GHz to 1445 GHz except around the water line at 1410 GHz. Peak output power was 129 μ W at 1395 GHz. To the best of the authors' knowledge, this is the highest reported power by an all-solid state source in this frequency range.

In Figure 11, the performance of the CASIMIR chain at 120K is plotted against data from the Herschel / HIFI chain. The peak power of the CASIMIR chain is higher than the peak power of the HIFI chain by a factor of 6.

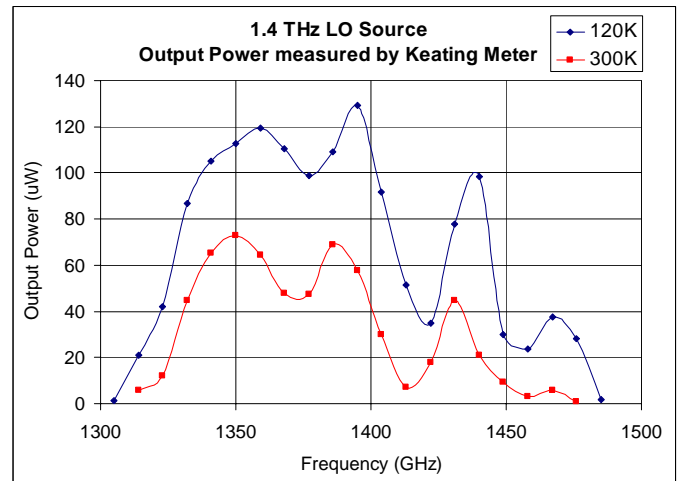


Fig. 10: Performance of the 1.4 THz LO chain at ambient and cryogenic temperatures. The output power at 120K is a factor of 3 dB better than at 300K.

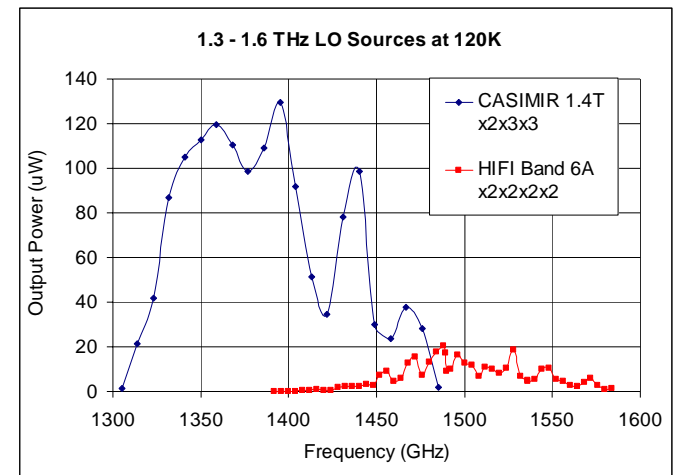


Fig. 11: Performance of the 1.4 THz LO chain compared to the Band 6A LO chain of Herschel HIFI.

V. CONCLUSIONS

The fabrication, development, and characterization of three local oscillator chains for CASIMIR have been presented. The 900 GHz and 1 THz LO chains meet and exceed the required performance in terms of output power and frequency range. The 1.4 THz LO chain exhibits state-of-the-art performance at room temperature and when cooled to 120 K. Compared with Herschel / HIFI, the results are impressive: more than a factor of 10 better at room temperature and a factor of 6 improvement at 120K.

ACKNOWLEDGMENT

The authors wish to acknowledge the help and support of Dr. Peter Siegel of the Submillimeter Wave Advanced Technology group at JPL. We thank Peter Bruneau of the JPL Space Instruments Shop for fabrication of the multiplier blocks.

This work was funded by the California Institute of Technology and carried out at the Jet Propulsion Laboratory, California Institute of Technology, under contract from NASA.

REFERENCES

- [1] M. Edgar *et al.*, "CASIMIR: A high resolution, far-IR/submm spectrometer for airborne astronomy," to appear in Proceedings of the 21st ISSTT 2010, Oxfordshire, UK, March 2010.
- [2] A. Karpov, *et al.*, "Broadband SIS mixer for 1 THz Band", Proceedings of the 20th ISSTT, Charlottesville, Virginia, April 20-22, 2009.
- [3] A. Karpov *et al.*, "Low Noise 1.4 THz SIS mixer for SOFIA," Proceedings of the 19th ISSTT, Groningen, The Netherlands, April 28-30, 2008.
- [4] J. Ward, *et al.*, "Local Oscillators from 1.4 to 1.9 THz," Proceedings of the 16th ISSTT, Göteborg, Sweden, May 2005.
- [5] J. Ward *et al.*, "1400 - 1900 GHz Local Oscillators for the Herschel Space Observatory," Proceedings of the 14th ISSTT, pp. 94-101, Tucson, Arizona, 2003.
- [6] G. Lange *et al.*, "Performance of the HIFI Flight Mixers," Proceedings of the 19th ISSTT, Groningen, The Netherlands, April 28-30, 2008.
- [7] S. Cherednichenko *et al.*, "Hot-electron bolometer terahertz mixers for the Herschel Space Observatory," *Rev. Sci. Instrum.*, 79, Issue 3, 2008.
- [8] S. Martin *et al.*, "Fabrication of 200 to 2700 GHz multiplier devices using GaAs and metal membranes," *Microwave Symposium Digest*, 2001 IEEE MTT-S, Vol. 3, pp.1641 – 1644, 2001.
- [9] A. Maestrini *et al.*, "A High Efficiency Multiple-Anode 260-340 GHz Frequency Tripler," Proceedings of the 17th ISSTT 2006, Paris, France, May 10-12, 2006.
- [10] A. Maestrini *et al.*, "A 780-950GHz frequency tripler for radio astronomy," proceedings of the 18th ISSTT 2007, Pasadena, California, March 21-23, 2007.
- [11] J. Johansson and N. Whyborn, "The Diagonal Horn as a Sub-Millimeter Wave Antenna," *MTT* vol. 40, no. 5, May 1992.
- [12] F. Maiwald *et al.*, "THz Frequency Multiplier Chains Based on Planar Schottky Diodes," Proceedings of SPIE: International Conference on Astronomical Telescopes and Instrumentation, vol. 4855, pp. 447-458, Waikoloa, Hawaii, August 22-28, 2002.
- [13] <http://www.cfa.harvard.edu/~spaine/am/>

Superlattice Electronic Devices as Compact Terahertz Sources

Heribert Eisele*, Suraj P. Khanna, and Edmund H. Linfield

*Institute of Microwaves and Photonics, School of Electronic and Electrical Engineering,
University of Leeds, Leeds LS2 9JT, United Kingdom*

*Contact: h.eisele@leeds.ac.uk, phone +44-113-343-7074

Abstract—Negative differential resistance devices were fabricated from four epitaxial wafers with different GaAs/AlAs superlattices and evaluated in resonant-cap full-height WR-15 and WR-10 waveguide cavities. These devices on integral heat sinks generated output powers in the fundamental mode between 62–108 GHz. The best RF powers (and their corresponding dc-to-RF conversion efficiencies) were 58 mW (3.5%) at 66 GHz, 42 mW (2.6%) at 78 GHz, and 28 mW (1.8%) at 94 GHz. The RF power of 15 mW at 101 GHz constitutes a 30-fold improvement over previous results; the highest fundamental oscillation frequency was 108 GHz. In a second-harmonic mode, one device yielded 2.0 mW at 216 GHz, the highest second-harmonic frequency to date for a GaAs/AlAs superlattice.

I. INTRODUCTION

Compact, reliable, and efficient sources of radiation are a prerequisite for many emerging systems applications at terahertz frequencies, such as wideband wireless communications, material analysis, imaging, chemical and biological sensing, and space exploration. High spectral purity is also imperative for these sources to be used as transmitters or local oscillators in such applications [1]. In their seminal paper of 1970, Esaki and Tsu proposed a device structure “with virtually no frequency limitation” where the Bragg reflection of electrons in an engineered semiconductor superlattice (SL) gives rise to energy minibands and regions of negative differential velocity [2] in the velocity-electric field characteristics. At sufficiently high electric fields across a doped SL, traveling domains may then form in the SL [3] and, similar to domains in Gunn devices, cause a negative differential resistance (NDR) to occur between the device terminals. When a superlattice electronic device (SLED) with such an NDR is connected to a suitable resonant RF circuit, RF power is generated.

SLEDs have attracted much attention since the 1990s because the underlying physical process, the Bloch effect, has relevant time constants that are much shorter than those of the transferred-electron effect in, for example, GaAs Gunn devices [4], [5]. SLEDs with sufficiently wide minibands in the GaAs/AlAs and InGaAs/InAlAs material systems have been demonstrated as millimeter-wave oscillators [4]–[7]. As examples, fundamental-mode operation up to 103 GHz (with an RF output power of 0.5 mW) was demonstrated for a GaAs/AlAs SL [4], and a high dc-to-RF conversion efficiency of 5% at 64.4 GHz was obtained with a SLED in a cavity micromachined using SU-8 [7]. More recently, the use of selective etching technologies [8], and improved thermal

management with substrateless devices, yielded RF output powers of more than 80 mW and dc-to-RF conversion efficiencies up to 5.1% around 63 GHz [9]. This paper reports the demonstration of SLEDs as high-performance millimeter-wave oscillators above 75 GHz.

II. EXPERIMENTAL PROCEDURE

Four different SL structures were grown in an Oxford Instruments (VG Semicon) V80-H molecular beam epitaxy growth chamber at a substrate temperature of 580 °C and with a V/III flux ratio of approximately 7. In this MBE system, the substrate temperature is determined using a k-Space Associates calibrated BandiT spectrometer, whereas the flux ratio is determined by a beam monitoring ion gauge. The growth conditions for the four wafers were similar to those used at the time to grow high electron mobility transistor structures with mobilities exceeding $10^6 \text{ cm}^2 \text{ V}^{-1} \text{ s}^{-1}$ at 1.2 K. Doping levels were assessed by growing separate bulk GaAs layers for Hall effect measurements.

Table I lists the structural properties of the four wafers and their estimated miniband widths [11]. To increase the operating frequency slightly from previously evaluated devices [9], the total lengths of these SL structures were reduced for Wafers 2–4 by approximately 12–15%, and, for Wafer 4, a wider miniband width was also chosen. In all four wafers, and as before [9], the SLs were sandwiched between graded transition layers and thin buffer layers on both sides. A 0.5- μm -thick $\text{Al}_{0.55}\text{Ga}_{0.45}\text{As}$ layer was grown between the substrate and the SLED layers to allow for complete substrate removal during device fabrication [8], [9], [12], [13].

TABLE I: NOMINAL DEVICE STRUCTURES OF THE WAFERS USED FOR MILLIMETER-WAVE SUPERLATTICE ELECTRONIC DEVICES

Wafer	Number of periods	Number of GaAs MLs	Number of AlAs MLs	Nominal doping [cm^{-3}]	Miniband width [meV]
1	120	12	3	1.5×10^{17}	85
2	102	12	3	1.6×10^{17}	85
3	102	12	3	1.9×10^{17}	85
4	110	12	2	1.5×10^{17}	150

Device fabrication followed the same process steps described in [9] except that the top ohmic contacts were defined by etching in a wet etchant [12] for all fabrication runs, and somewhat smaller SLEDs, with nominal diameters

of 30–55 μm , were selected for packaging and RF testing. SLEDs were mounted in the same type of package that has been employed previously in the evaluation of different types of active two-terminal devices on integral and diamond heat sinks in the GaAs and InP material systems [8], [12]–[15], including SLEDs [9].

SLEDs fabricated from each of the four wafers were evaluated in the fundamental mode and in higher harmonic modes. For fundamental-mode operation, the same types of resonant-cap full-height WR-15 and WR-10 waveguide cavities were employed, as previously used in the evaluation of various two-terminal devices in the GaAs and InP material systems at *V*-band (50–75 GHz) frequencies [8], [9] and *W*-band (75–110 GHz) frequencies [8], [12]–[15], respectively. RF output powers and oscillation frequencies were measured in calibrated WR-15 (*V*-band) and WR-10 (*W*-band) waveguide test setups that each have a precision attenuator, a precision direct-reading frequency meter, a thermistor power head, and a directional coupler to connect to a harmonic mixer [8].

For operation in a second-harmonic mode below approximately 190 GHz, the SLEDs had to be mounted in a different package, which fitted the highly tunable waveguide mount of Figure 1. This mount previously yielded state-of-the-art results from InP Gunn devices above 180 GHz [14] and SLEDs around 130 GHz [9]. Therefore, the SLEDs for this mount were not evaluated in the fundamental mode. Conversely, the SLEDs with fundamental oscillation frequencies above 100 GHz were also evaluated for second-harmonic power extraction, and the waveguide configuration of Figure 2 was employed. It is one of the configurations that were used previously for the same purpose with GaAs tunnel injection transit-time (TUNNETT) diodes [14].

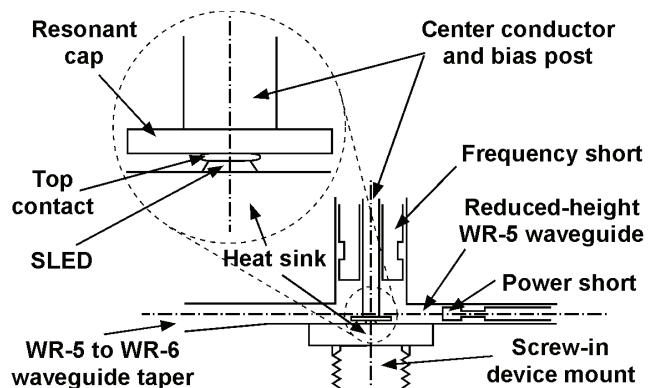


Figure 1: Schematic of the waveguide oscillator mount for second-harmonic power extraction from SLEDs from Wafers 1–3 below 190 GHz.

III. RESULTS

The current-voltage characteristics of SLEDs from Wafers 1–4 are very similar to that reported previously [9] and typically show the onset of a negative slope at a dc bias voltage of approximately 0.8 V. SLEDs from Wafer 1 yielded RF powers (and corresponding dc-to-RF conversion efficiencies) of 52 mW (4%) and 58 mW (3.5%) at 62.7 GHz

and 66.4 GHz, respectively, and these values are comparable to those typical for the SLEDs of [9]. In a second-harmonic mode, one SLED from Wafer 1 generated an RF power of 5 mW around 150 GHz in the mount of Figure 1.

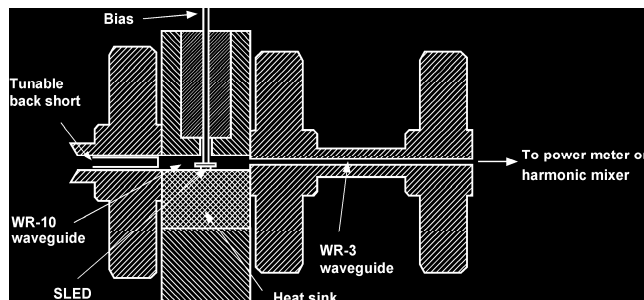


Figure 2: Schematic of the WR-10 waveguide oscillator cavity and WR-3 output waveguide for second-harmonic power extraction from SLEDs from Wafer 4.

Contrary to the SLEDs of [9] however, SLEDs from Wafer 1 could be operated easily in a WR-10 waveguide cavity and at fundamental frequencies above 75 GHz. They then produced RF powers of 31 mW and 20 mW at 75.2 GHz and 87.1 GHz, respectively. RF powers of 20–25 mW around 75 GHz were measured with SLEDs from Wafer 2 in a WR-15 waveguide cavity whereas SLEDs from Wafer 3 yielded much higher RF powers (and corresponding dc-to-RF conversion efficiencies) of 47 mW (3%) at 66.6 GHz and 42 mW (2.6%) at 77.8 GHz in the same cavity.

The spectral purity of the fundamental-mode oscillations in *V*-band was verified with an Agilent E4407B spectrum analyzer and an Agilent 11970V waveguide harmonic mixer connected to the *V*-band waveguide setup. Typical dc bias voltages of the SLEDs from the four wafers are below 3 V. At such bias voltages, even small noise signals (less than 1 mV) from the power supply were found to cause appreciable frequency modulation and broadening of the line width of the oscillators. As a consequence, the same bias filter as for the 480-GHz oscillator with an InP Gunn device [16], consisting of a series resistor of 1 Ω and a parallel capacitor of more than 50 mF, was connected between the power supply and the SLED under test. The spectral purity of the SLEDs was found to be as good as or better than that reported in [9].

The SLEDs from Wafer 4 were first tested in a WR-10 waveguide cavity and instantly achieved the highest oscillation frequencies of the four wafers of Table I. Therefore, they were not tested in a WR-15 waveguide cavity. The best results to date are RF powers (and corresponding dc-to-RF-conversion efficiencies) of 28 mW (1.8%) at 94.5 GHz and 15 mW (1.0%) at 101.0 GHz.

The employed WR-15 and WR-10 waveguide cavities generally do not support the operation of devices in a second-harmonic mode at 50–75 GHz and 75–110 GHz, respectively. Nonetheless, two types of additional experiments were carried out to confirm that the SLEDs from Wafer 4 were operating in the fundamental mode. The tunable back short in the waveguide greatly changes the impedance seen by the active two-terminal device and,

consequently, its oscillation frequency when the device is operating in the fundamental mode. As a result, active two-terminal devices in the fundamental mode commonly show monotonic tuning behavior and a wide tuning range when the position of the back short is changed [8], [14]–[15]. Conversely, the oscillation frequency of an active two-terminal device in a second-harmonic mode is hardly affected by the tunable back short such as the power short in the waveguide of the mount of Figure 1.

As can be seen from Figure 3, the SLED from Wafer 4 can be tuned monotonically (and virtually linearly) by more than 6 GHz, that is, from 101.1 GHz to 107.7 GHz, when the position of the back short is changed by 0.7 mm. No mode or frequency jumps occur over the full tuning range, and an RF output power of more than 11 mW is available over a smaller tuning range, which still exceeds 4 GHz. Such a wide tuning range is a clear indication of operation in the fundamental mode.

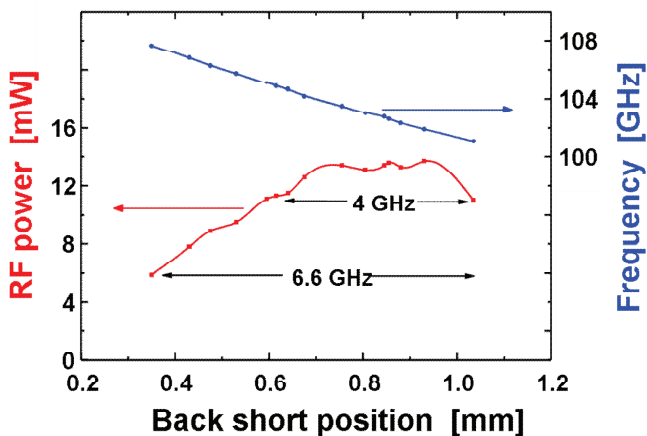


Figure 3: RF output power and oscillation frequency as a function of backshort position for a GaAs/AlAs SLED from Wafer 4 operating in the fundamental mode on an integral heat sink.

SLEDs are well known to generate strong signals at higher harmonic frequencies [7], [9], [17]. Therefore, the same SLED whose tuning characteristics were presented in Figure 3 was also evaluated for its performance in the configuration of Figure 2. For different positions of the back short, RF powers of 2.2 mW and 1.3 mW were measured at 207.7 GHz and 212.3 GHz, respectively and confirm again that the results presented in Figure 3 correspond to operation in the fundamental mode.

The excellent spectral purity of SLEDs from Wafer 4 at the fundamental and second-harmonic frequencies was ascertained using a Rohde & Schwarz FSU-46 spectrum analyzer either with a *W*-band harmonic mixer connected to the WR-10 waveguide setup or a *J*-band (170–325 GHz) mixer connected to the output waveguide of Figure 2. The same bias filter as before with a series resistor and a parallel capacitor [16] was used. Figure 4 shows the spectrum of the SLED for an RF power of 8 mW at 106.2 GHz and Figure 5 the spectrum of the same SLED for an RF power of 1.3 mW at 212.3 GHz. Both figures show the two traces that are

produced by the IDENTIFY function of the spectrum analyzer.

The SLED of Figures 3–5 was removed from its WR-10 cavity to allow for testing of other SLEDs from Wafers 3 and 4. It was then tested again after reassembly with the same resonant cap as before and the aforementioned RF power of 15 mW was measured at 101.0 GHz. For the same resonant cap, but different positions of the tunable back short, it also yielded RF powers of 24 mW at 96.4 GHz in the fundamental mode and 2.0 mW at 216.3 GHz in a second-harmonic mode. Figure 6 summarizes the best results from Wafers 1, 3, and 4 of Table I in the fundamental mode over the frequency range 60–110 GHz. The RF power of 15 mW at 101.0 GHz constitutes a 30-fold improvement over previous results [4] and this performance improvement confirms the importance of suitable thermal management in SLEDs [9], as already known from other active two-terminal devices [8], [12]–[15]. Furthermore, RF powers of 2.2 mW at 207.7 GHz and 2.0 mW at 216.3 GHz are several orders of magnitude higher than those reported before. The oscillation frequency of 107.7 GHz is the highest reported to date from GaAs/AlAs SLEDs operating in the fundamental mode and also much higher than the highest reported to date for GaAs Gunn devices operating in the fundamental mode (87 GHz) [8].

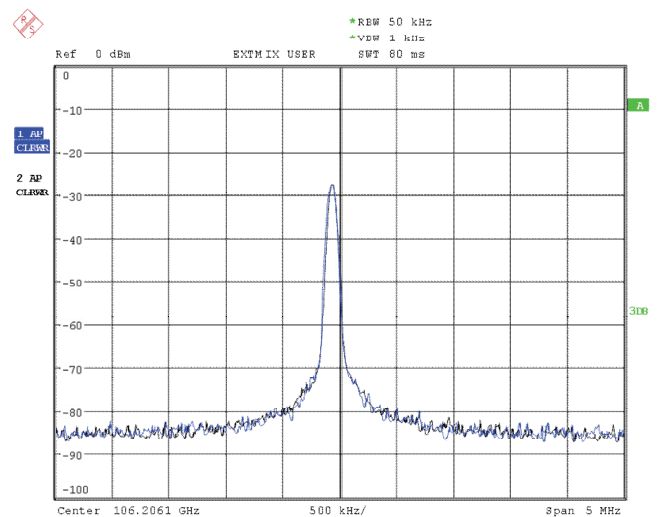


Figure 4: Spectrum of a free-running oscillator with a SLED from Wafer 4 in the fundamental mode; RF power: 8 mW, center frequency: 106.21 GHz, vertical scale: 10 dB/div., horizontal scale: 500 kHz/div., resolution bandwidth: 50 kHz, video bandwidth: 1 kHz.

IV. CONCLUSIONS

The experimental results reported in this paper show that shorter SL structures and wider miniband widths lead to higher operating frequencies. They are also a very good indication of the strong potential of SLEDs as high-performance fundamental sources for millimeter-wave and submillimeter-wave frequencies up to 1 THz. Further performance improvements are expected not only from fully optimized thermal management, but also from SL structures designed for higher operating frequencies or more efficient

harmonic operation. In addition, approaches to efficient third-harmonic power extraction that have already been demonstrated with GaAs TUNNETT diodes [18] and InP Gunn devices up to 480 GHz [16], [19] could be implemented.

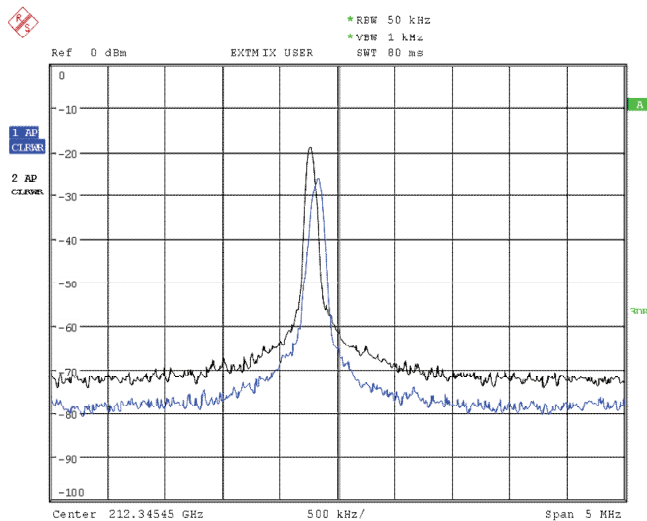


Figure 5: Spectrum of a free-running oscillator with a SLED from Wafer 4 in a second-harmonic mode; RF power: 1.3 mW, center frequency: 212.34 GHz, vertical scale: 10 dB/div., horizontal scale: 500 kHz/div., resolution bandwidth: 50 kHz, video bandwidth: 1 kHz.

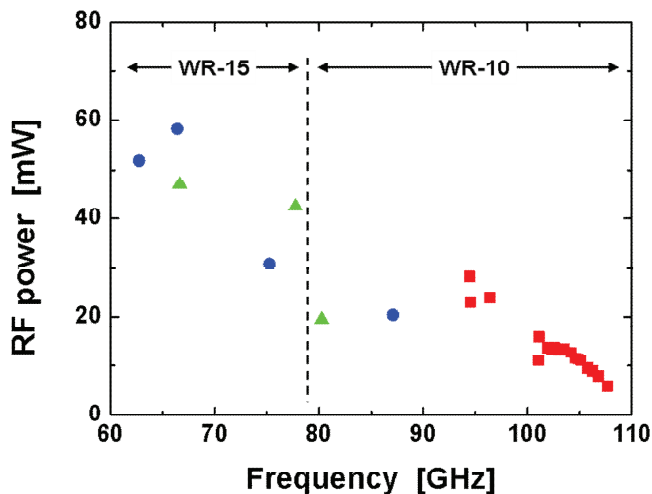


Figure 6: RF powers from SLEDs of Wafers 1 (●), 3 (▲), and 4 (■) in the fundamental mode over the frequency range 60–110 GHz.

ACKNOWLEDGMENT

The devices were fabricated in the Michigan Nanofabrication Facility. The authors thank George I. Haddad, University of Michigan, for providing access to these cleanroom facilities. This work was supported in part by the US Army, the UK Electro Magnetic Remote Sensing

Defence Technology Centre, and the UK Engineering and Physical Science Research Council.

REFERENCES

- [1] P. Siegel, "Terahertz technology," *IEEE Trans. Microw. Theory Tech.*, vol. 50, no. 3, pp. 910–928, Mar. 2002.
- [2] L. Esaki and R. Tsu, "Superlattice and negative differential conductivity in semiconductors," *IBM J. Res. Develop.*, vol. 14, no. 1, pp. 61–65, Jan. 1970.
- [3] H. Le Person, C. Minot, L. Boni, J. F. Palmier, and F. Mollot, "Gunn oscillations up to 20 GHz optically induced in GaAs/AlAs superlattice," *Appl. Phys. Lett.*, vol. 60, no. 19, 2397–2399, May 1992.
- [4] E. Schomburg, M. Henini, J. M. Chamberlain, P. Steenson, S. Brandl, K. Hofbeck, K. F. Renk, and W. Wegscheider, "Self-sustained current oscillation above 100 GHz in a GaAs/AlAs superlattice," *Appl. Phys. Lett.*, vol. 74, no. 15, pp. 2179–2181, Apr. 1999.
- [5] R. Scheuerer, E. Schomburg, K. F. Renk, A. Wacker and E. Schöll, "Feasibility of a semiconductor superlattice oscillator based on quenched domains for the generation of submillimeter waves," *Appl. Phys. Lett.*, vol. 81, no. 8, pp. 1515–1517, Aug. 2002.
- [6] E. Schomburg, R. Scheuerer, S. Brandl, K. F. Renk, D. G. Pavel'ev, Yu. Koschurinov, V. Ustinov, A. Zhukov, A. Kovsh, and P. S. Kop'ev, "An InGaAs/InAlAs superlattice oscillator at 147 GHz," *Electron. Lett.*, vol. 35, no. 17, pp. 1491–1492, Aug. 1999.
- [7] M. Häußler, E. Schomburg, J.-M. Batke, F. Klappenberger, A. Weber, H. Appel, K.F. Renk, H. Hummel, B. Ströbl, D.G. Pavel'ev and Yu. Koschurinov, "Millimetre-wave generation with semiconductor superlattice mounted in cavity fabricated by UV-photolithography and galvanofarming," *Electron. Lett.*, vol. 39, no. 10, pp. 784–785, May 2003.
- [8] H. Eisele and G. I. Haddad, "Active Microwave Diodes," in *Modern Semiconductor Devices*, S. M. Sze, Ed., Ch. 6, John Wiley & Sons, New York, 1997, pp. 343–407.
- [9] H. Eisele, I. Farrer, E. H. Linfield, and D. A. Ritchie, "High-performance millimeter-wave superlattice electronic devices," *Appl. Phys. Lett.*, vol. 93, no. 18, pp. 182105-1–182105-3, Nov. 2008.
- [10] H. Eisele, S. P. Khanna, and E. H. Linfield, "Superlattice electronic devices as high-performance oscillators between 60–220 GHz," *Appl. Phys. Lett.*, vol. 96, no. 7, pp. 072101-1–072101-3, Feb. 2010.
- [11] G. Bastard, "Superlattice band structure in the envelope-function approximation," *Phys. Rev. B*, vol. 24, no. 10, pp. 5693–5697, Nov. 1981.
- [12] H. Eisele, "Selective etching technology for 94 GHz GaAs IMPATT diodes on diamond heat sinks," *Solid-State Electron.*, vol. 32, no. 3, pp. 253–257, Mar. 1989.
- [13] H. Eisele and G. I. Haddad, "Two-terminal millimeter-wave sources," *IEEE Trans. Microw. Theory Tech.*, vol. 46, no. 6, pp. 739–746, Jun. 1998.
- [14] H. Eisele, A. Rydberg, and G. I. Haddad, "Recent advances in the performance of InP Gunn devices and GaAs TUNNETT diodes for the 100–300-GHz frequency range and above," *IEEE Trans. Microw. Theory Tech.*, vol. 48, no. 4, pp. 626–631, Apr. 2000.
- [15] H. Eisele and R. Kamoua, "Submillimeter-wave InP Gunn devices," *IEEE Trans. Microw. Theory Tech.*, vol. 52, no. 10, pp. 2371–2378, Oct. 2004.
- [16] H. Eisele, "480 GHz oscillator with an InP Gunn device," *Electron. Lett.*, vol. 41, no. 6, pp. 422–423, Mar. 2010.
- [17] E. Schomburg, J. Grenzer, K. Hofbeck, T. Blomeier, S. Winnerl, S. Brandl, A. A. Ignatov, K. F. Renk, D. G. Pavel'ev, Yu. Koschurinov, V. Ustinov, A. Zhukov, A. Kovsh, S. Ivanov, and P. S. Kop'ev, "Millimeter wave generation with a quasi planar superlattice electronic device," *Solid-State Electron.*, vol. 42, no. 7–8, pp. 1495–1498, Aug. 1998.
- [18] H. Eisele, "355 GHz oscillator with GaAs TUNNETT diode," *Electron. Lett.*, vol. 41, no. 6, pp. 329–331, Mar. 2005.
- [19] H. Eisele, "Third-harmonic power extraction from InP Gunn devices up to 455 GHz," *IEEE Microw. Wireless Compon. Lett.*, vol. 19, no. 6, pp. 416–418, Jun. 2009.

A compact, continuous-wave radiation source for local oscillator applications based on a THz quantum-cascade laser

H. Richter ¹⁾, M. Greiner-Bär¹⁾, S. G. Pavlov ¹⁾, A. D. Semenov ¹⁾, M. Wienold ²⁾, L. Schrottke ²⁾, M. Giehler ²⁾, R. Hey ²⁾, H. T. Grahn ²⁾, and H.-W. Hübers ^{1),3)}

¹⁾Institute of Planetary Research, German Aerospace Center (DLR), Rutherfordstr. 2, 12489 Berlin, Germany

²⁾Paul-Drude-Institut für Festkörperelektronik, Hausvogteiplatz 5–7, 10117 Berlin, Germany

³⁾Institut für Optik und Atomare Physik, Technische Universität Berlin, Hardenbergstraße 36, 10623 Berlin, Germany

Abstract

Heterodyne spectroscopy of molecular rotational lines and atomic fine-structure lines is a powerful tool in astronomy and planetary research. It allows for studying the chemical composition, the evolution, and the dynamical behaviour of many astronomical objects. As a consequence, current and future airborne as well as spaceborne observatories such as SOFIA, Herschel or Millimetron are equipped with heterodyne spectrometers.

A major challenge for heterodyne receivers operating above approximately 2 THz is the local oscillator, which should be a compact source requiring little electrical input power. THz quantum-cascade lasers (QCLs) have the potential to comply with these requirements. However, until now, THz QCLs operate at rather low temperatures so that cooling by liquid helium or using large cryo-coolers becomes necessary. While these cooling approaches might be acceptable for laboratory experiments, they either result in too many restrictions on airborne or spaceborne heterodyne receivers or are completely unacceptable.

We report on the development of a compact, easy-to-use source, which combines a QCL operating at 3.1 THz with a compact, low-input-power Stirling cooler. The QCL, which is based on a two-miniband design, has been developed for high output powers and low electrical pump powers [1]. Efficient carrier injection is achieved by resonant longitudinal-optical phonon scattering. At the same time, the operating voltage can be kept below 6 V. The amount of generated heat complies with the cooling capacity of the Stirling cooler of 7 W at 65 K with 240 W of electrical input power. Special care has been taken to achieve a good thermal coupling between the QCL and the cold finger of the cryostat. The whole system weighs less than 15 kg including cooler, power supplies etc. The output power is well above 1 mW at 3.1 THz. With an appropriate optical beam shaping, the emission profile of the laser becomes a fundamental Gaussian one. In addition to the performance of the QCL in the Stirling cooler, we will present results of the application of this source to high-resolution molecular spectroscopy.

REFERENCES

- [1] M. Wienold, L. Schrottke, M. Giehler, R. Hey, W. Anders, and H. T. Grahn, *Electron. Lett.* 45, 1030–1031 (2009).

Session S3:

Direct Detectors I

Towards Ultra-Low-Noise Transition Edge Sensors for Millimeter-Wave and Far-Infrared Space Telescopes

S. Withington^a, J.R.Gao^b, D. Glowacka^a, D. Goldie^a, D. Griffin^δ, P. Khosropanah^b, P. Mauskopf^γ,
D. Morozov^γ, A. Murphy^η, C. O'Sullivan^η, M. Ridder^β, N. Trappe^η

^aUniversity of Cambridge

Email: Stafford@mrao.cam.ac.uk

^βSRON Netherlands Institute for Space Research

^γUniversity of Cardiff

^δRutherford Appleton Laboratory

^ηNational University of Ireland

Abstract

Upcoming submillimetre-wave and far-infrared space telescopes will require a new generation of cryogenic (50mK) ultra-low-noise Transition Edge Sensors (TESs). For example, BPol is a submillimetre-wave (3.0-0.5mm) telescope dedicated to searching for B modes in the polarisation state of the CMB, whereas SPICA is a cooled-aperture infrared (210-35 μ m) telescope aimed at studying star formation in distant galaxies. Furthermore, the detector technology needed for these infrared missions is closely related to the calorimeter technology needed for the Cryogenic Imaging Spectrometer on the International X-ray Observatory, IXO.

In recognition of the importance of ultra-low-noise TES technology for experimental astrophysics, the European Space Agency (ESA) has established a program¹ to study the physics, materials science, and performance of ultra-low-noise submillimetre-wave and far-infrared TES imaging arrays. The central theme relates to understanding how the NEP can be reduced from $10^{-17}\text{WHz}^{-1/2}$ (typical of ground-based experiments) to $10^{-18}\text{WHz}^{-1/2}$ (needed for space-borne CMB experiments), $10^{-19}\text{WHz}^{-1/2}$ (needed for space-borne cooled-aperture infrared telescopes), and $10^{-20}\text{WHz}^{-1/2}$ (needed for space-borne infrared interferometers). Achieving ultra-low-noise operation is not in itself a major challenge, but achieving ultra-low-noise operation while maintaining high saturation powers (1pW for CMB astronomy, and 10fW for IR astronomy), fast response times (<10ms), and high optical sampling is a considerable problem. Moreover, the pixels must be packed into large multiplexed imaging arrays, and must be useable in space.

In this paper, we review the physics and technological challenges associated with developing ultra-low-noise TESs for space applications. We review the needs of typical missions, and address the fundamental device physics that limits the performance of single pixels. We consider issues such as power handling, noise, and response time, and discuss how these relate to the form and layout of the device. We also consider how the properties of the materials that make up the device affect performance, and how these can be chosen to achieve the specifications required. Finally, we consider the problems associated with packing TESs into large polarimetric and photometric imaging arrays, and touch on issues relating to uniformity of performance.

¹The authors would like to thank the European Space Agency for supporting this work through TRP Programme AO/1-5922/08/NL/EM.

Superconducting Thermo-Electric Bolometer for Cosmology Instruments

Leonid Kuzmin

Chalmers University of Technology, S-41296 Gothenburg, Sweden,

*Contact: leonid.kuzmin@chalmers.se, phone +46 31 7723608

Abstract— A novel type of the zero-biased thermo-electric bolometer (TEB) is proposed. The bolometer is based on a Charge-to-Voltage Converter (CVC) with a Superconductor-Insulator-Normal (SIN) Tunnel Junction and a superconducting absorber. The absorption of photons in the absorber leads to excitation of quasiparticles with some fraction of charge imbalance, tunneling through the SIN junction and generation of voltage. The thermoelectric voltage is determined by accumulation of tunneling charge in an external capacitance. Conversion efficiency is very high and voltage values comparable with a superconducting gap are easily achieved. The zero-biased CVC-TEB can be effectively used for creation of an array of bolometers.

I. INTRODUCTION

Recent Cosmology experiments have discovered that the Universe consists mainly of mysterious Dark Energy and Dark Matter [1]. There are several cosmology instruments that are being designed to measure the polarization of the Cosmic Microwave Background (CMB), in particular the B-mode polarization, which is generated by primordial gravitational waves.

A new design of antennas and a new generation of detectors are needed for these advanced telescopes. These detectors must achieve sensitivities better than $\sim 10^{-18}$ W/Hz^{1/2} and should be realized in large format arrays of detectors (up to 100x100 pixels). Several advanced concepts of bolometers, such as transition-edge sensor [2], cold-electron bolometer (CEB) [3,4], and kinetic-inductance detector, are in the stage of development. In scaling up today's detectors to a large format, we encounter serious problems with overheating of the detector system, which typically has to work at a low temperature. All these problems become even more severe for focal-plane arrays [4], where each pixel is replaced by an array of bolometers (up to 16x16). In a large-scale array with 104 pixels, one has to deal with several million bolometers, each of them contributing to overheating problems.

Here the zero-biased thermo-electric bolometer (TEB) is proposed in order to solve the problem by essentially eliminating the overheating due to the absence of DC bias dissipation. In addition, zero-biased bolometers help to avoid problems caused by complicated electrical circuitry, ground loops, and unwanted interferences. For ordinary metals and semiconductors, the thermo-electric Seebeck coefficient is dramatically decreased at low temperatures. In contrast, superconductors have been shown to have a rather large thermo-electric coefficient if they come in contact with a

normal metal or with a different superconductor. Classic experiments in the 1980s using a bulk bimetallic superconducting loop and a SQUID amplifier showed an unexpectedly large thermoelectric response (even reaching five orders of magnitude than that predicted by theory) [5-7]. This situation leads us to reconsider the fundamentals of thermoelectricity, and opens up an opportunity to use superconducting systems for creating a new class of thermoelectric bolometers.

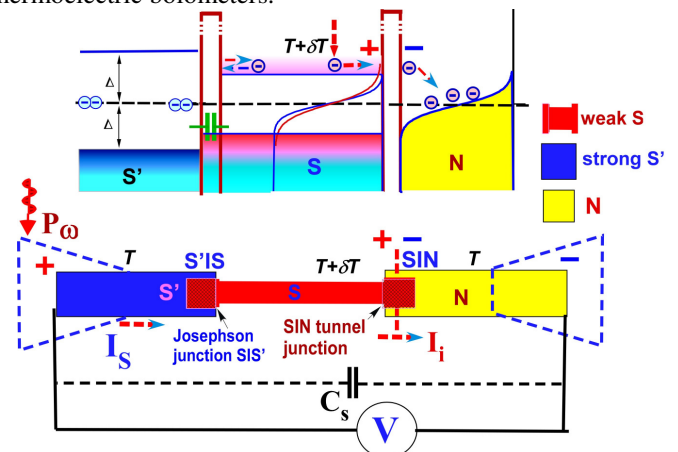


Fig 1. Sketch of the proposed **Thermo-Electric Bolometer based on a Charge-to-Voltage Converter (CVC-TEB)** with capacitive coupling to the antenna. The converter will work in a novel mode as an integrator of charge that has tunneled through the SIN junction to an external capacitor.

A novel type of the zero-biased thermo-electric bolometer (TEB) is proposed. The bolometer is based on a Charge-to-Voltage Converter (CVC) with a Superconductor-Insulator-Normal (SIN) Tunnel Junction and a superconducting absorber. The absorption of photons in the absorber leads to excitation of quasiparticles with some fraction of charge imbalance, tunneling through the SIN junction and generation of voltage. The thermoelectric voltage is determined by accumulation of tunneling charge in an external capacitance. Conversion efficiency is very high and voltage values comparable with a superconducting gap are easily achieved. The zero-biased CVC-TEB can be effectively used for creation of an array of bolometers.

The concept is based on the radically new principle of harvesting energy from the incoming signal, converting this energy to charge in a superconducting nano-absorber, and accumulating the imbalanced charge carriers, which tunnel through an SIN tunnel junction in an on-chip capacitance.

The tunneled quasiparticles are trapped in normal metal and could not return back if their energy is lower than the superconducting gap of the absorber. The SIN tunnel junction has proven to be self-biased in voltage by the energy accumulated in the capacitor. The built-up voltage would be used for read-out. The CVC allows a substantial increase in the dynamic range by removing incoming power from the absorber to normal electrode.

II. MODEL

The operation of a CVC with unbiased SIN tunnel junction has been analyzed in relation to the CEB with strong electrothermal feedback [3-4,9-12]. The system is described by a heat balance equation for a superconducting absorber coupled to a normal metal by an SIN tunnel junction:

$$P_{SIN}(T_e, T_{ph}) + P_{e-ph}(T_e, T_{ph}) = P_0 + \delta P(t) \quad (1)$$

Here, $P_{SIN}(V, T_e, T_{ph})$ is the cooling power of the SIN junction, $P_{e-ph}(T_e, T_{ph})$ is the heat flow from electron to phonon subsystems in the superconducting absorber; T_e and T_{ph} are, respectively, the electron and phonon temperatures of the absorber; P_0 and $P(t)$ are incoming RF power.

The current components through SIN junction (Fig. 2a) are described by a current balance equation:

$$I_{tot}(V, T_e, T_{ph}) = I_{SN} + I_{NS} + I_{leak} = 0 \quad (2)$$

Full expression for current is

$$I_{tot} = \frac{1}{eR} \int dE N_s(E) \left[f(E, T_e) - f(E - eV, T_{ph}) \right] - \frac{V}{R_j} \quad (3)$$

where $N_s(E) = |E|/\sqrt{E^2 - \Delta^2}$ is the normalized density of states in the superconductor, Δ is a superconducting gap, and $f(E, T) = 1/[\exp(E/T) + 1]$.

In the case of imbalance of quasielectrons and quasiholes, the SN current is modified to

$$I_{SN} = (1 + K_i)I_{e0} - (1 - K_i)I_{h0} \quad (4)$$

where I_{e0} and I_{h0} are current components without imbalance and K_i is imbalance coefficient

$$K_i = \frac{I_{e0} - I_{h0}}{I_{e0} + I_{h0}}.$$

A bolometer is characterized by its responsivity, and a noise equivalent power. In the self-biased mode, the responsivity, S_V , is described by the voltage response to an incoming power from Eq. 1

$$S_V = \frac{\delta V}{\delta P} \frac{\omega}{\omega} \quad (5)$$

We have made an analysis of a single CVC with power load of $P_0 = 20$ fW. Absorbed power would create some imbalance of quasielectrons and quasiholes in the absorber [14,15]. The CVC is working as an integrator of charge tunneled through the SIN junction in an external capacitance:

$$V = \int I_{tot} dt / C_s \quad (6)$$

The time constant is determined by a subgap resistance R_j

and an external capacitance C_s . After applying an RF signal, the voltage is linearly increased and C_s is charged by tunnelling current I_{SN} .

The dependence of current components through SIN junction on a self-biased voltage is shown in Fig. 2 for imbalance coefficient $K_i=0.5$, tunnel resistance $R=1$ kOhm, $T=100$ mK and $T_c=1.2$ K. The voltage is increased until saturation point, V_s , where the main tunneling current I_{SN} is compensated by a current through leakage resistance, I_{leak} , and a back current I_{NS} (Eq. 2).

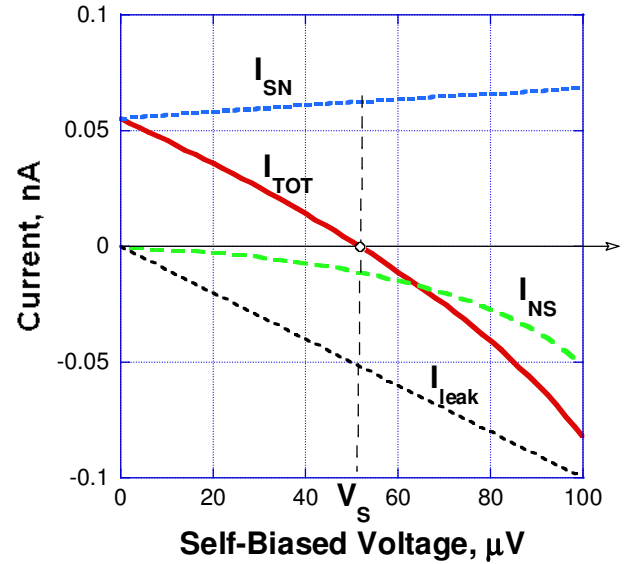
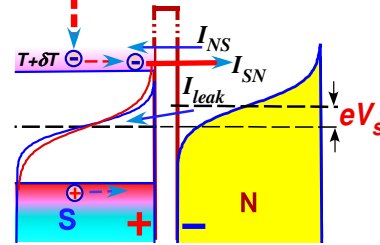


Fig. 2. Three contributions to the SIN tunneling current displayed in the occupancy diagram (a) and dependence of these components on a self-biased voltage. The saturation voltage, V_s , corresponds to current balance of these three components and total current $I_{TOT}=0$.

As a result, $I_{tot}=0$ in this point.

Some asymptotic expressions in the limit $V_s \ll \Delta/e$ can be obtained for the self-biased voltage as a reaction to the power P_0

$$V_s = I_{SN} * R_j \quad (8)$$

and voltage-to-power responsivity

$$S_V = K_i \frac{R_j * e}{\Delta} \quad (9)$$

Due to integration principle (6), the voltage can achieve quite high values. The proper tunnel resistance should be selected to get optimal noise properties with maximum response (9) and to avoid saturation when V_s is approaching to Δ . Noise properties are characterized by the noise equivalent power (NEP), which is the sum of three contributions:

$$NEP_{tot}^2 = NEP_{SIN}^2 + NEP_{e-ph}^2 + NEP_{AMP}^2. \quad (10)$$

Here NEP_{SIN}^2 is the noise of the SIN tunnel junctions. The SIN noise has three components: the shot noise $2eI/S^2I$, the fluctuations of the heat flow through the tunnel junction and the correlation between these two processes [9]:

$$NEP_{SIN}^2 = \frac{\delta I_{\omega}^2}{(S_V/R_d)^2} + 2 \frac{\langle \delta P_{\omega} \delta I_{\omega} \rangle}{S_V/R_d} + \delta P_{\omega}^2 \quad (11)$$

The second term in Eq.10 is the noise associated with electron-phonon interaction [10, 11] and the last term is due to the voltage δV and current δI noise of the amplifier (JFET), which is expressed in $nV/Hz^{1/2}$ and $pA/Hz^{1/2}$:

$$NEP_{AMP}^2 = \frac{\delta V^2 + (\delta I * R_d)^2}{S_V^2} \quad (12)$$

III. SIMULATION RESULTS

A self-biased voltage V_s and voltage response dV_s/dT was simulated using a heat balance equation (1), current balance equation (2) and full expression for SIN junction current.

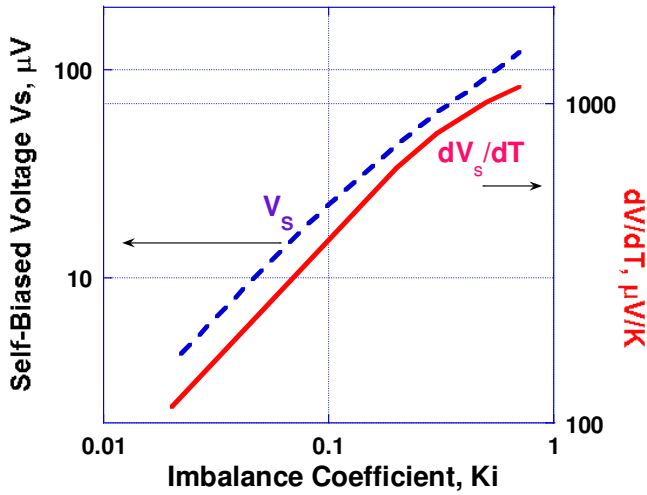


Fig. 3. Dependence of a self-biased voltage, V_s , and a thermopower responsivity, dV_s/dT , on the imbalance coefficient K_i .

In dependence on frequency, superconducting gap and energy dependence of transparency of SIN tunnel junction, the various imbalance coefficients (4) could be realized. The Fig. 3 shows dependence of voltage response and NEP components on the imbalance coefficient K_i in the range from 0.02 to 0.7. The parameters of the SIN junction are the same as used in Fig. 2: tunnel resistance $R=1k\Omega$, $T=100$ mK and $T_c=1.2K$.

The dependence of saturation voltage V_s and noise components on junction resistance R are shown in Fig. 4.

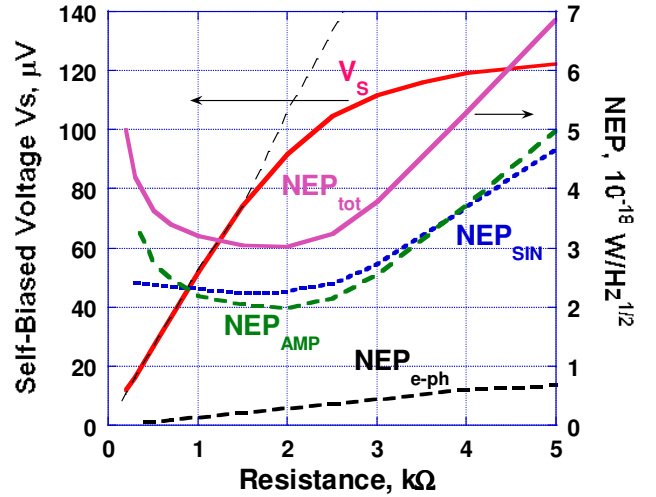


Fig. 4. Dependence of a self-biased voltage, V_s , and noise components on junction resistance R . Asymptotic dependence of V_s on R (Eq. 8) is shown by a dashed line.

The voltage V_s is deviating from linear asymptotic (8) when approaching to Δ . Responsivity S_V is decreased in this region that leads to increase of the bolometer noise. The optimal $NEP_{tot}=3*10^{-18}W/Hz^{1/2}$ is at $R=2k\Omega$. This value is comparable with the photon noise level of $NEP_{phot}=3.2*10^{-18}W/Hz^{1/2}$ for 350 GHz.

The noise is determined by the noise of SIN tunnel junction caused by transferring of incoming power P_o . Voltage response in this point is 92 μV . It is not reasonable to increase further this response because CVC is approaching to the saturation of responsivity near Δ . For a typical value of JFET noise of $2nV/Hz^{1/2}$, we estimate $NEP_{amp}=2*10^{-18}W/Hz^{1/2}$. Electron-phonon noise is at a very low level of $2*10^{-19}W/Hz^{1/2}$, which is typical for superconducting absorbers at low power load.

In dependence on frequency, the various imbalance coefficients could be realized. The Fig. 5 shows dependence of voltage response and NEP components on the imbalance coefficient K_i in the range from 0.02 to 0.7.

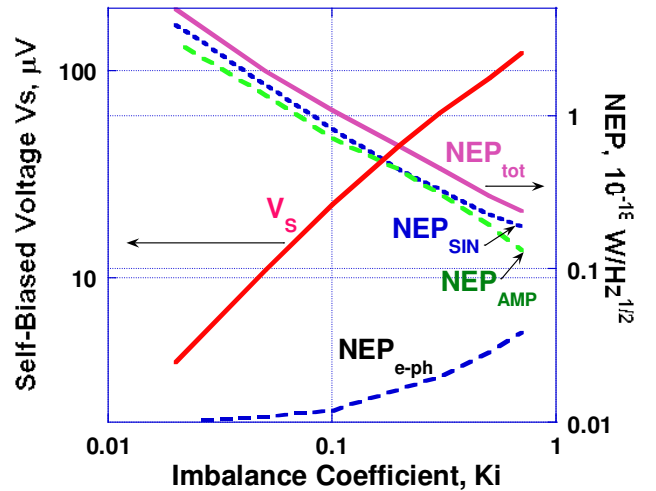


Fig. 5. Dependence of a self-biased voltage, V_s , and NEP components on the imbalance coefficient K_i .

Voltage V_S is increased approximately linearly when K_i is increased. Proportionally, NEP_{tot} is decreased due to the dependence of NEP_{SIN} and NEP_{AMP} on S_V . NEP_{e-ph} is practically not dependent on K_i . These dependences show the importance of high branch imbalance for the realization of the low noise TEB. The factors required to achieve high branch imbalance are: the involvement of self-biased SIN junction in process of absorption, application for frequencies comparable with Δ , and maximum use of energy dependent transparency of the SIN junctions [15].

IV. DISCUSSION

The analysed parameters of CVC are promising for the creation of series array of bolometers for effective matching to a JFET amplifier in analogy to a CEB array [13,16]. The series arrays with large number of bolometers (64 or 256) can be effectively used for focal plane antenna [5,16]. The typical applications are balloon and ground-based telescope with an expected power load of 5 pW. Power will be distributed between N bolometers, avoiding overheating of bolometers and leading to the increase of total responsivity. The great advantage is also the zero dc impedance of superconducting absorbers in the array of N bolometers in contrast to bolometers with resistive absorbers. Zero-biased CVC could overcome problems of overheating for large format arrays of detectors (up to 100x100 pixels) due to the absence of bias heating the cold stage.

V. CONCLUSIONS

In conclusion, a novel concept of the CVC-TEB with SIN tunnel junction and superconducting absorber provides important advantages. The CVC is acting in a new mode as an integrator of charge in an external capacitance and could give high voltage response and good noise performance. By operating in a zero-biased mode, it reduces power dissipation, simplifies schematic, and paves the way to large scale multi-pixel arrays. Practical limitations, including imbalance coefficient and role of an SIN tunnel junction in quasiparticle excitation, have yet to be determined.

The author thanks Dmitry Golubev, Tero Heikillä, Michael Titov and Mikhail Tarasov for useful discussions. The work was supported by SNSB, STINT and SI Swedish grants.

REFERENCES

- 1 C. Seife, *Science*, vol. 302, pp. 2038, Dec. 2003.
- 2 K. Irwin. *Applied Physics Letters*, **66**, (1995) 1998
- 3 L. Kuzmin, "Ultimate Cold-Electron Bolometer with Strong Electrothermal Feedback", *Proc. of SPIE conference*, vol. 5498, pp 349-361, June 2004.
- 4 L. Kuzmin, "Superconducting Cold-Electron Bolometer with Proximity Traps", *Microelectronic Engineering*, **69**, 309-316 (2003).
- 5 Peter K. Day et al., "Far-infrared imager-polarimeter using distributed antenna-coupled transition-edge sensors, 5498, pp 856-875, SPIE, 2004.
- 6 V. Ginzburg, *Rev. of Modern Physics*, **76**, 981 (2006).
- 7 D. J. Van Harlingen, *Thermoelectric Effects in the Superconducting State. Physica B+C*, **109**, 1710 (1982)

- 8 Y.M. Galperin et al., *Theory of Thermoelectric Phenomena in Superconductors*, *Physical Review B*, **65**, 064531 (2002)
- 9 Golubev D. and Kuzmin L., "Nonequilibrium theory of the hot-electron bolometer with NIS tunnel junction," *Journal of Applied Physics*. **89**, 6464 (2001).
- 10 J. Clarke, in *Nonequilibrium superconductivity*, ed. by D.N. Langenberg and A.I. Larkin, Elsevier Science Publishers B.V. (1986).
- 11 L.Kuzmin , P. Mauskopf, and D. Golubev "Superconducting Cold-Electron Bolometer with JFET Readout", Submitted to EUCAS-05, Vienna, September 2005; *Journal of Physics: Conference Series (JPCS)*, Volume 43, pp. 1298-1302 (2006).
- 12 Leonid Kuzmin, "A Superconducting Cold-Electron Bolometer with SIS' and Josephson Tunnel Junctions", *Journal of Low Temperature Physics*, **151**, pp. 292-297 (2008).
- 13 Leonid Kuzmin, "Array of Cold-Electron Bolometers with SIN Tunnel Junctions for Cosmology Experiments". *Journal of Physics: Conference Series (JPCS)*, vol. 97, 012310 (2008).
- 14 A.D. Smith, M. Tinkham, "New Thermoelectric effects in tunnel junctions". *PRB*, **22**, 4346 (1980).
- 15 J. E. Hirsch, *Phys.Rev.Lett.*, **72**, 558 (1994).
- 16 Leonid Kuzmin, "Distributed Antenna-Coupled Cold-Electron Bolometers for Focal Plane Antenna", *Proc. of the 19th ISSTT conference*, pp 154-158, Groningen, April 2008.

Development, Fabrication and Characterization of Lumped Element Kinetic Inductance Detectors for NIKA

M. Roesch^{1,*}, L. Swenson², A. Bideaud², A. Benoit², S. Doyle³, K.F. Schuster¹ and A. Monfardini² for the NIKA collaboration
¹IRAM, Institut de Radioastronomie Millimétrique, St. Martin d'Hères, France
²Institut NEEL, Grenoble, France
³Department of Physics and Astronomy, Cardiff, CF243AA
 *Contact: roesch@iram.fr

Abstract— Lumped-element kinetic inductance detectors (LEKIDs) have recently shown considerable promise as direct-absorption mm-wavelength detectors for astronomical applications. One major research thrust within the Néel Iram Kids Array (NIKA) collaboration has been to investigate the suitability of these detectors for deployment at the 30-meter IRAM telescope located on Pico Veleta in Spain. In order to optimize the LEKIDs for this application, we have recently probed a wide variety of individual resonator and array parameters through simulation and physical testing. This included determining the optimal feed-line coupling, pixel geometry, resonator distribution within an array (in order to minimize pixel cross-talk), and resonator frequency spacing. Based on these results, a 32-pixel Aluminum array was fabricated and tested in a dilution fridge with optical access, yielding an average optical NEP of $\sim 1 \times 10^{-15} \text{ W/Hz}^{1/2}$.

I. INTRODUCTION

Since 2003 kinetic inductance detectors (KID) are considered as promising alternative to classical bolometer for mm and sub-mm astronomy [2]. Photons, with energy higher than the gap energy ($E=h\nu > 2\Delta$), break Cooper pairs in a superconducting film. This leads to an increase in number of quasi particles, which changes the surface reactance of the superconductor (kinetic inductance effect) [6].

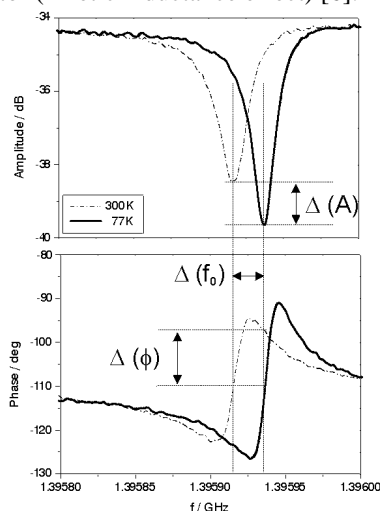


Fig. 2 Principle of KIDs. Solid lines: under dark conditions; dashed line: optical load of 300 K.

One possibility to make advantage of this effect is to use a superconducting resonant circuit as detecting element. A measurement of such a resonator coupled to a transmission line is shown in Fig. 1. An illumination of the detector leads to a shift in resonance frequency f_0 , which can be measured through a change in amplitude and phase. One advantage of KIDs is the easy fabrication process. Due to only one metallisation layer on a substrate, it is less complicated compared to bolometer fabrication. Another advantage of KIDs resides in the readout system. Frequency multiplexing allows the readout of a large number of resonators. Packed in a limited bandwidth, a single transmission line is sufficient to read out several hundreds of pixel.

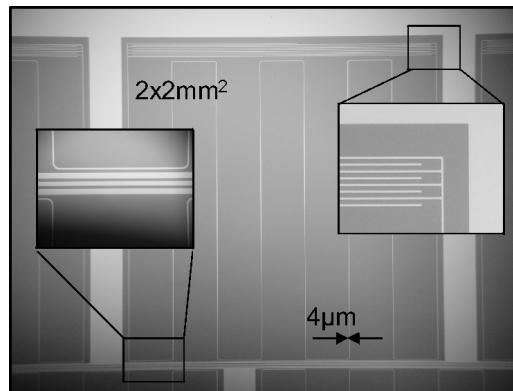


Fig. 1 LEKID geometry. Enlarged left hand side: coupling area; right hand side: interdigital capacitor.

In Fig 2, one resonator design, a so-called lumped element kinetic inductance detector (LEKID) is shown. Simon Doyle first proposed this type of resonator in 2008 [1]. Compared to other microwave resonators (quarter wavelength resonator [3]), this type consists of a long meandered line, the inductive part, and an interdigital capacitor. A very high and constant current density over the whole length of the meander makes this part a very sensitive direct detection area. The optical efficiency can be optimised by changing the geometry of the meander. Therefore, there are no lenses or antenna structures necessary to couple the incoming microwaves into the resonator.

The NEEL IRAM KIDS array (NIKA) is a collaboration of several groups to develop a multi pixel camera based on kinetic inductance detectors for the IRAM 30m telescope located in Spain [4]. Here we present the development of a LEKID array for NIKA. Measurement results of electrical (coupling, frequency distribution) and optical characterization (optical coupling, NEP) are presented in this paper.

II. CHARACTERIZATION OF LEKIDS

A. Electrical characterization

To test parameters like coupling strength and frequency tuning, several test arrays were designed. In Fig. 3 one of the 6-pixels test chip is shown. The samples were fabricated with a 60 nm Nb film that on top of a high resistance (>5kOhms) silicon substrate. The critical temperature of Nb ($T_c=9.2\text{K}$) allows measuring the samples in liquid Helium ($T=4.2\text{K}$). Due to a pumping system, connected to the cryostat, a minimum temperature of 2 K was reached for the measurements of the Nb-samples.

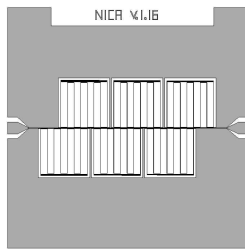


Fig. 3 Layout of a 6-pixel LEKID array for the el. characterization.

To investigate the coupling of a LEKID to a transmission line we varied the width of the ground plane between the transmission line and the meander (see Fig. 2). In Fig. 4 the measurement curves of two resonators with different couplings are shown. The resonance dip of the solid line is much deeper, due to a stronger coupling. The intrinsic quality factor, Q_0 , was calculated to be 10^5 for the 60 nm Nb film @ 2K. The coupling quality factor for the less coupled resonator was determined to be $\sim 150\,000$, for the stronger coupled $\sim 80\,000$.

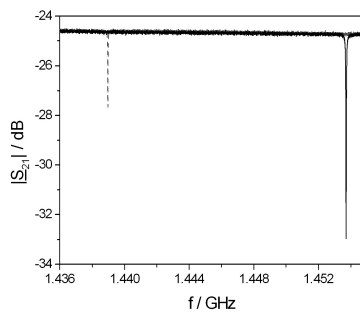


Fig. 4 Measurements of two LEKID arrays with different couplings (one resonator of each array). Dashed line: 20 μm ground plane; solid line: 10 μm ground plane.

Another important factor, in order to pack as many resonators as possible in a limited bandwidth, is the frequency spacing between the resonances. Therefore, it is necessary to be able to simulate the frequency tuning before making the design for a big array to avoid overlapping resonances. The simulations [8] showed a non-linearity in frequency tuning when the number of fingers of the capacitor is too low. In Fig. 5 the comparison of simulation and measurement is shown for two different arrays.

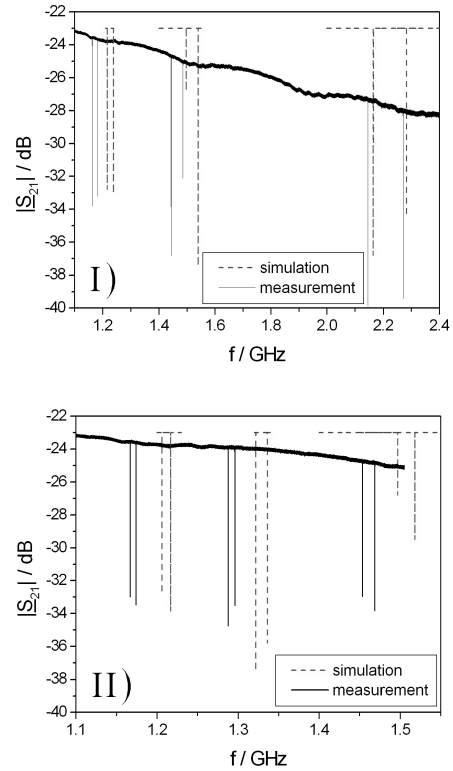


Fig. 5 Comparison of simulation (dashed lines)[8] and measurement (solid lines) to investigate the frequency tuning by changing the number and length of the capacitor fingers. I) bandwidth $\sim 1\text{ GHz}$; II) bandwidth: $\sim 300\text{ Mhz}$.

The resonances of sample (I) are distributed in a bandwidth of $\sim 1\text{ GHz}$. For the second array (II) a bandwidth of $\sim 300\text{ Mhz}$ was chosen. A shift of the simulated resonances to higher frequencies is due to the value of the kinetic inductance (L_s) in sonnet. In I), the highest two resonance frequencies are less shifted compared to the others, the reason for that is the limited bandwidth of the amplifier. Beside these explainable shifts, Fig. 5 shows a good agreement between simulation and measurement. Further is there a number of fingers that should not be decreased in order to avoid a shift of the resonances to much higher frequencies. In this case the number of fingers of the capacitor was varied from three to nine. In between, the length of the fingers was varied as well.

B. Optical characterization

Based on the measurement of the Nb test array, a 32-pixels array was designed for optical characterization of the LEKIDs. The arrays were fabricated and tested in a dilution

fridge with optical access. They were made with an aluminium film ($T_c=1.2K$) on a high resistance ($>5k\Omega$) silicon substrate. Two different arrays were fabricated, one with a metallization thickness of 40 nm, the second one with 60 nm thick film. A schematic of the optical measurement setup is shown in Fig. 6. On a XY-table, a so-called sky simulator is placed. It consists of a mirror (A), a chopper (B) and a box filled with liquid nitrogen (D). In the box there is an absorber material (C) with a hole of 1 cm in diameter in the centre. This configuration was built to be as close as possible to the background conditions at the telescope. The cryostat itself is a 3He - 4He -dilution fridge with a minimum temperature of $T=100$ mK. Between the focal plane (F), where the array is mounted, and the optical access, there are several filters allowing to cut the IR load and to define the bandwidth of 125-170 GHz.

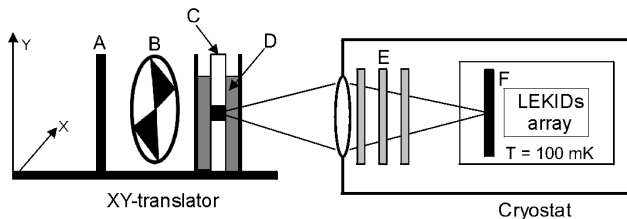


Fig. 6 Configuration of the cryostat and the XY-translator. A) Mirror, B) Chopper, C) Absorber with a hole of 1 cm of diameter, D) Liquid nitrogen, E) Optical filters for a bandwidth from 125 to 170 GHz, F) LEKID array in the focal plane at the 100 mK stage.

In Fig. 7 a schematic of the measurement configuration, including the readout electronics [5], [7], is shown. The frequencies are digitally created in the FPGA in a limited bandwidth of 45 MHz before they are DA-converted. To excite the resonators the frequencies are up-converted to the actual resonance frequencies using an IQ-mixer (C) and a synthesizer (A). After the signal has passed the cryostat, it is amplified (E) at 4K and at room temperature. To readout the signal, it has to be down-converted (C) to the original bandwidth of the FPGA. In the FPGA a Fast Fourier transformation is done to separate each resonator signal.

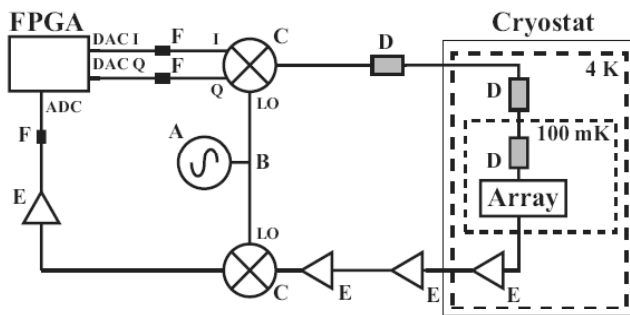


Fig. 7 Basic measurement schematic: A) High-frequency synthesizer, B) Splitter, C) IQ-Mixer, D) Attenuator, E) Amplifier and F) Low-pass filter.

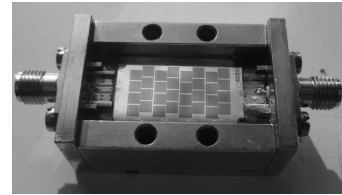


Fig. 8 Mounted 32-pixel array in a gold plated copper sample holder.

Fig. 8 shows the 32-pixel array mounted in a gold plated copper sample holder. To optimize the optical absorption, a back-short cavity was mounted in a calculated distance, $d = \lambda_{eff}/4$, to the array. To check the distribution of the resonances, a frequency scan was done, as shown in Fig. 9. Due to fabrication errors and parasitic magnetic fields, the resonances are not equally spaced. For this array 30 out of 32 resonators worked. We calculated an average intrinsic quality factor of $Q_0 \approx 10^5$ and a loaded quality factor of $Q_L \approx 50\,000$. After we did an optical scan, using the XY-table and the chopper, over the whole area of the array to determine the location of each pixel. During the scan, the phase response of each pixel changes, depending on the position of the table.

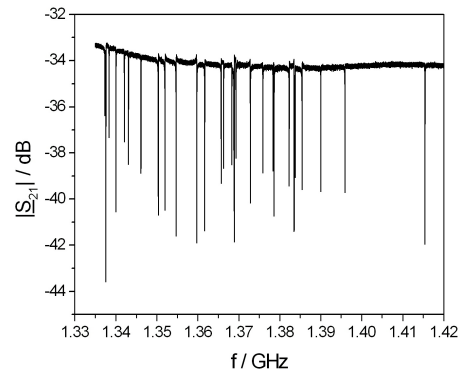


Fig. 9 Frequency scan (S_{21}) over all resonance frequencies of the array.

In Fig. 10 the location of the maximum response of each pixel is plotted over the fabricated array. This beam pattern shows a good agreement in pixel distribution compared to the real array. Double resonances can cause calculation errors in the FPGA, leading to a wrong location of the pixel in the XY-plane (as seen in Fig 10).

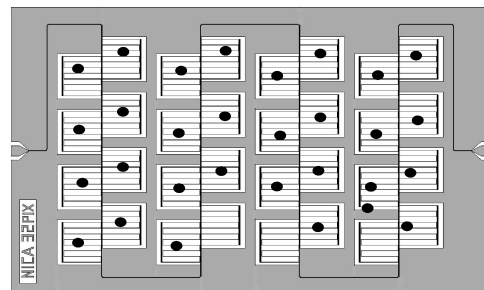


Fig. 10 Beam pattern of the 32-pixel LEKID array. Dots: Position of maximum optical response of each pixel

The spectrum of the phase noise of the array is shown in Fig. 11. The roll-off above 30 Hz is related to the read-out

electronics rate. We calculated an average detector phase noise at 1 Hz of $5 \text{ mdeg/Hz}^{1/2}$. With an average phase signal of 5 degree and

$$NEP = \frac{P}{S/N} \frac{1}{\sqrt{\tau}},$$

the optical Noise Equivalent Power (NEP) was determined to be around $1 \times 10^{-15} \text{ W/Hz}^{1/2}$ for the 40 nm thick film. With P the optical power on one pixel, the signal to noise ratio S/N and the integration time τ of the Fourier transformation. We gained a factor of 2 in NEP by reducing the film thickness from 60 nm to 40 nm. The kinetic inductance in the meander line increases due to a smaller volume of the line. A higher kinetic induction fraction α leads to a higher sensitivity.

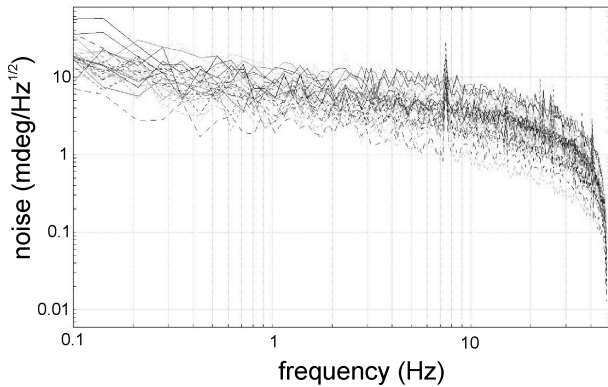


Fig. 11 Spectrum of the phase noise of each pixel without the chopper.

III. CONCLUSIONS

The promising measurement results presented in this paper show a high potential of the LEKIDs for mm and sub-mm detection. The easy fabrication and the Frequency-Multiplexing make them feasible for developing arrays with several hundreds of pixels. The good agreement between simulations and measurements makes it possible to simulate the design of a much bigger array.

In October 2009 a 30-pixel LEKID array was tested at the IRAM 30 m telescope in Spain and achieved first astronomical results [4].

REFERENCES

- [1] S. Doyle, "Lumped Element Kinetic Inductance Detectors," thesis, Cardiff University, Cardiff, Wales, April, 2008.
- [2] P.K. Day, H.G. LeDuc, B.A. Mazin, A. Vayonakis and J. Zmuidzinas, "A broadband superconducting detector suitable for use in large arrays," *Nature*, 425, 817, 2003.
- [3] B.A. Mazin, "Microwave Kinetic Inductance Detectors," thesis, California Institute of Tecnology, Pasadena, California, USA, 2004.
- [4] A. Monfardini, et al. NIKA: A Millimeter-Wave Kinetic Inductance Camera, *Astronomy & Astrophysics*, 2010, to be submitted.
- [5] L.J. Swenson, J. Minet, G.J. Grabovskij, et al., in *AIP Proc.*, 2009, paper 1185, p. 84.
- [6] M. Tinkham, *Introduction to Superconductivity*, Krieger Pub Co, 1975.
- [7] S.J.C. Yates, J.J.A. Baselmans, A.M. Baryshev, et al., in *AIP Proc.*, 2009, paper 1185, p. 249.
- [8] "Sonnet User's Guide-Manual of the Program Sonnet," Sonnet Software, Inc., 2007, 100 Elwood Davis Road, North Syracuse, NY13212, USA.

Performance of a Microstrip-coupled TES Imaging Module for CMB Polarimetry

Michael D. Audley^{1,*}, Dorota Glowacka¹, David J. Goldie¹, Vassilka Tsaneva¹, Stafford Withington¹, Lucio Piccirillo², Giampaolo Pisano², Paul Grimes³, Ghassan Yassin³, Peter A. R. Ade⁴, C. North⁴, Kent D. Irwin⁵, and Mark Halpern⁶

¹*Cavendish Laboratory, University of Cambridge, United Kingdom*

²*University of Manchester, United Kingdom*

³*University of Oxford, United Kingdom*

⁴*Cardiff University, Cardiff, United Kingdom*

⁵*National Institute of Standards and Technology, Boulder CO, United States of America*

⁶*University of British Columbia, Vancouver, Canada*

M.D. Audley is now with the Space Research Organization of the Netherlands

V. Tsaneva is now with the University of Cologne, Germany

*Contact: audley@physics.org

Abstract— We have developed a 16-element, 97GHz, low-noise Transition Edge Sensor (TES) module that can be packed easily into large-format polarimetric imaging arrays. The technology was developed originally for the low-frequency instrument of the CLOVER experiment, which was aimed at searching for the signature of primordial gravitational waves in the polarisation state of the Cosmic Microwave Background Radiation. Each module contains 16 slotline and microstrip-coupled TES bolometers, allowing eight polarimetric pixels with external waveguide OMTs, along with time-domain multiplexed SQUID readout. Here we describe the design of the modules, and explain how they were realised in practice, detailing some of the technology developed along the way. Performance was measured by following two parallel paths: (i) detailed characterisation of individual detectors using an exceedingly well understood, fully modelled, analogue SQUID readout system, and (ii) simultaneous measurements of the entire module using CLOVER's multichannel readout electronics. We describe the results of measurements on one of the modules, with an emphasis on uniformity of performance, and we assess the effect of non-uniformity on the operation of a complete array. Although the technology was developed in the context of CLOVER, the work has consequences for many instruments including future space telescopes such as BPol.

I. INTRODUCTION

A. Scientific Motivation

Thomson scattering of radiation in the early Universe can lead to linear polarization [1] in the cosmic microwave background (CMB). The polarization depends on density fluctuations, and thus carries cosmological information which is complementary to the well-studied temperature anisotropies of the CMB. The linear polarization may be decomposed into a curl-free part and a divergence-free part, denoted E- and B-mode respectively. The ratio of the E- to B-mode polarisation r is proportional to the energy scale of inflation. The CLOVER experiment aimed to detect the signature of primordial gravitational waves in the B-mode polarisation of the CMB [2], [3] or to place an upper limit on r of 0.026 in an angular multipole range of $20 < \ell < 1000$ (8° to 10°).

B. Overview of CLOVER

The CLOVER experiment, which was cancelled at an advanced stage, is described in detail elsewhere [4], [5]. CLOVER consists of two telescopes (see Fig. 1), each with compact range antenna optics that have been designed to have extremely low sidelobes and cross-polarisation [6]. One telescope (the low-frequency or LF instrument) observes at 97 GHz and the other (the HF instrument) has a mixed focal plane containing detector modules sensitive in the 150- and 220-GHz bands.

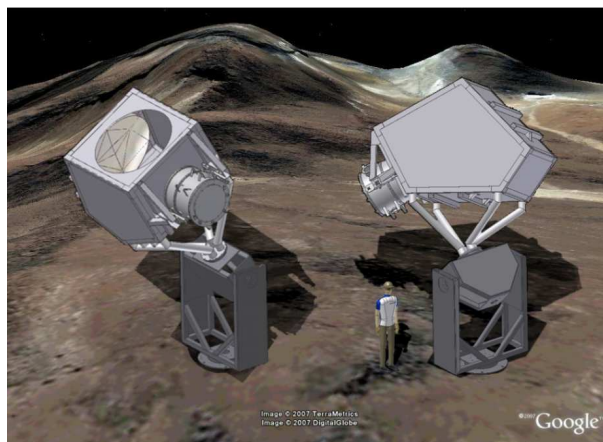


Fig. 1 Drawing of CLOVER at its site in the Atacama Desert.

To detect the extremely weak B-mode signal, CLOVER requires detectors with low enough NEP so that the instrument NEP is dominated by unavoidable sources of background photon noise ($\sim 3 \times 10^{-17}$ W/ $\sqrt{\text{Hz}}$ at 97 GHz). To achieve this sensitivity CLOVER uses bolometers with superconducting transition edge sensors (TES) [7] operating with a bath temperature of 100 mK. The detectors are cooled in two cryostats by a pulse-tube cooler, He-7 sorption fridge, and miniature dilution fridge [8]. The cryostat for the LF instrument is shown in Fig. 2.



Fig. 2 CLOVER's LF cryostat.

CLOVER's two focal planes are populated by hexagonal arrays of corrugated feedhorns (see Fig. 3).



Fig. 3 The full set of 96 corrugated feedhorns for the LF focal plane.

The low-frequency (LF) telescope's focal plane was to be populated with the detector modules discussed in this paper. The high-frequency (HF) telescope was to have a dual-frequency focal plane with a mixture of modules carrying detectors sensitive in the 150 or 220-GHz bands.

Orthomode transducers (OMT) separate the signal collected by each horn into two polarisations. In the LF telescope waveguide OMTs divide the two polarisations from each horn between two rectangular waveguides which each feed a finline-coupled detector [9]. Fig. 4 shows eight of these OMTs mounted on a LF detector module.

The high frequency channels use polarisation-sensitive detectors of a different architecture: four rectangular probes in a circular waveguide [10]. In this paper we concentrate on the LF instrument. The HF instrument was also at an advanced stage of readiness when the project was cancelled, although mass-production of the detector modules had not yet started.

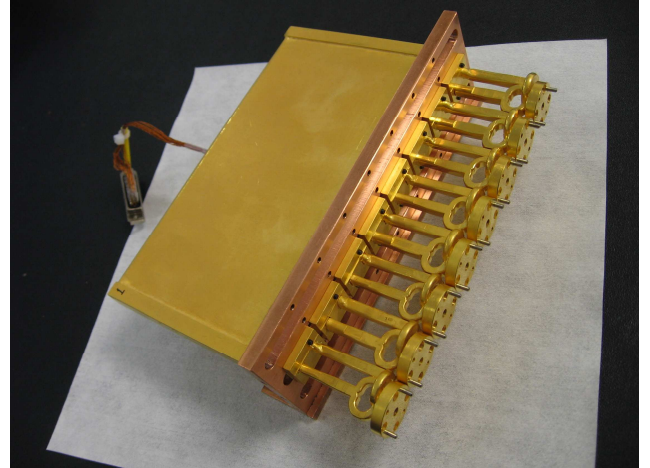


Fig. 4 LF detector module with OMTs.

Because of the large number of TESs to be read out (192 at each frequency) we use time-domain multiplexing in order to have a manageable number of wires from room temperature. The TESs are read out by 1×32 SQUID multiplexers [11], [12], [13] fabricated by the National Institute of Standards and Technology (NIST). Further amplification is provided at the cold end by SQUID series arrays [14], also fabricated by NIST.

All the multiplexer chips in each of CLOVER's two telescopes share address lines, significantly reducing the number of wires needed to room temperature. The Nyquist inductors, which provide antialiasing filtering, and the shunt resistors that provide voltage biasing, are contained in separate chips. All of these chips are mounted on a PCB at 100 mK and connections are made to the detectors by aluminium wire bonds. The SQUID series arrays are mounted in eight-chip modules which provide the necessary magnetic shielding. Because of their higher power dissipation ($1 \mu\text{W}$ per series array compared with 16 nW per multiplexer chip) these modules are heat-sunk to the still of the dilution refrigerator and they are connected to the multiplexer PCB with superconducting NbTi twisted pairs. Room-temperature multi-channel electronics (MCE) developed by the University of British Columbia, provides SQUID control and readout as well as TES bias [15]. CLOVER's MCE is similar to that used by SCUBA-2 [16].

II. DETECTOR DESIGN

A. Requirements

For maximum sensitivity, we require that the detectors be background-limited, i.e. the contributions to the noise equivalent power (NEP) from the detectors and readout must be less than the NEP due to unavoidable sources of photon noise:

$$\text{NEP}_{\text{det}}^2 + \text{NEP}_{\text{ro}}^2 \leq \text{NEP}_{\text{photon}}^2.$$

Once the detectors are background-limited, the only way to improve the sensitivity is to increase the number of detectors. 96 pixels are needed at each frequency to meet CLOVER's sensitivity requirements. The LF instrument has two finline detectors per pixel (one for each

polarisation). In the HF instrument there is one polarisation-sensitive OMT detector chip per pixel which measures both orthogonal polarisations. Thus, the LF instrument has 192 finline detectors and the HF instrument has a total of 192 planar OMT detectors. We require a detector time constant faster than 1 ms to satisfy the scanning requirements.

Also, the detectors must be able to absorb the power incident from the sky without saturation. This power is variable and depends on the weather. The power-handling requirement is for the detectors to be able to operate for 75% of the time at the site. We have allowed a 70% margin on this to account for uncertainties in the sky background at the site. This means that our target power handling for the LF detectors is 11.4 pW, rather than the predicted background level of 6.8 pW. The detector requirements are summarised in Table I.

TABLE I
CLOVER DETECTOR REQUIREMENTS AT THE THREE OPERATING FREQUENCIES.

Centre Frequency (GHz)	97	150	220
Band (GHz)	82—112	127—172	195—255
Number of pixels	96	96	96
NEP _{background} (10^{-17} W/ $\sqrt{\text{Hz}}$)	2.9	4.9	8.9
Power Handling (pW)	11.4	20	32

To meet these requirements we chose targets of $T_c = 210$ mK and $G \geq 215$ pW/K for the transition temperature and thermal conductance of the LF detectors. With those values of T_c and G the phonon NEP would be $\sim 2 \times 10^{-17}$ W/ $\sqrt{\text{Hz}}$. Table I shows that the sensitivity requirement is most strict on the 97-GHz detectors because of the lower sky background in the LF band. Meeting the sensitivity requirement for the 97-GHz detectors demonstrates our ability to meet the sensitivity requirement at the other two frequencies.

B. Detector Format

Rather than fabricating monolithic arrays we decided to make individual detectors so that we could guarantee a 100% functioning focal plane, which is important for meeting the sensitivity requirement. Having individual detector chips allows us to select the best ones for inclusion in the instrument. Also, because the detectors are much smaller than the horns in the focal plane, a monolithic array would have large, inactive areas between detectors, which would make fabrication of the detectors extremely inefficient. With hundreds of detectors needing to be mass-produced we decided to produce individual detectors that could be packed close together on a wafer to maximise processing efficiency.

C. TES Design

The TES films in CLOVER are Mo/Cu proximity-effect bilayers with normal copper banks to define the edges of the TES. The transitions of the bilayers can be made as sharp as 1—2 mK for high sensitivity. We can also tune the transition temperature (T_c) of the films to the desired value by choosing the film thicknesses. The transition temperature T_c and thermal conductance G of CLOVER's detectors are chosen to meet the NEP and power-handling requirements operating with a bath temperature of 100 mK.

CLOVER's bolometers are on low-stress silicon nitride islands suspended by four legs for thermal isolation (see Fig. 5). The nitride is 0.5 μm thick. The thermal conductance to the thermal bath is controlled by the four nitride legs. A microstrip carries RF power to the bolometer and is terminated by a 23- Ω AuCu resistor which dissipates the incoming power as heat that the TES can detect. A shunt resistor in parallel with the TES ensures that it is voltage biased so that it operates in the regime of strong negative electrothermal feedback. For example, if the temperature drops, so does the resistance of the TES. Since it is biased at constant voltage, this means that the current, and hence the Joule power, will increase, heating up the TES. Conversely, if the temperature increases the resistance will increase, reducing the current, and thus the Joule heating. This means that the TES operates at a bias point that is in a stable equilibrium. Thus, the TES is self-biasing, and the electrothermal feedback speeds up the response of the detector and cancels out temperature fluctuations, which has the effect of suppressing the noise.

Copper fingers extend from the normal copper banks most of the way across the TES from opposite edges (see Fig. 5). The purpose of these is to improve thermalisation of the TES film and suppress excess noise due to internal thermal fluctuations. The dark NEP we measure for these TESs is consistent with what we expect from the known Johnson and phonon noise sources [17].

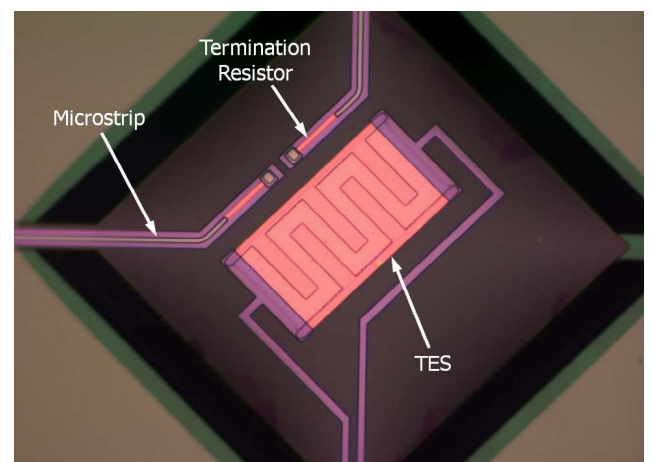


Fig. 5 CLOVER TES bolometer.

D. On-Chip Heaters

Fig. 5 shows two resistors terminating microstrips on the nitride island. One of these carries RF power from the

sky and the other is the on-chip heater which is used to inject DC power into the device.

The TES will be driven into the normal state or saturated when enough power is incident on it. This saturation power is the sum of the bias (and heater) and sky power. The sky power is variable and depends on the weather at the site. To operate efficiently CLOVER needs to be able to observe when the sky background power is high without losing the ability to observe in good weather when it is low. Also, for best performance the power incident on the detectors should be kept approximately constant so that their responsivity does not vary. The on-chip heaters are used to compensate for changes in the sky background. The heater power is increased in good weather when the sky opacity is low and decreased in bad weather when the sky background is high so that the total power incident on the detectors remains approximately constant. The on-chip heaters are also extremely useful for calibration because they allow us to inject a known amount of DC or pulsed power directly into the detectors.

E. RF Design

Fig. 6 shows one of CLOVER's 97-GHz detector chips. The chip sits in a rectangular waveguide that has small support slots cut in its walls. A unilateral finline transition [18] couples RF power from the waveguide to a slotline. A closer view of the transition is shown in Fig. 7. The slotline is coupled to a microstrip by a radial-stub transition. The microstrip is terminated on the silicon nitride island by a matched resistor where the RF power is detected by the TES. The finline has serrations where the chip sits in the support slots to prevent the propagation of higher-order modes. The measured optical efficiency of these detectors is about 60%.

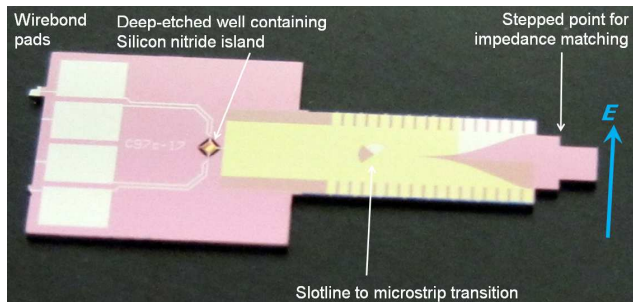


Fig. 6 CLOVER 97-GHz detector chip. The chip is 10 mm long.

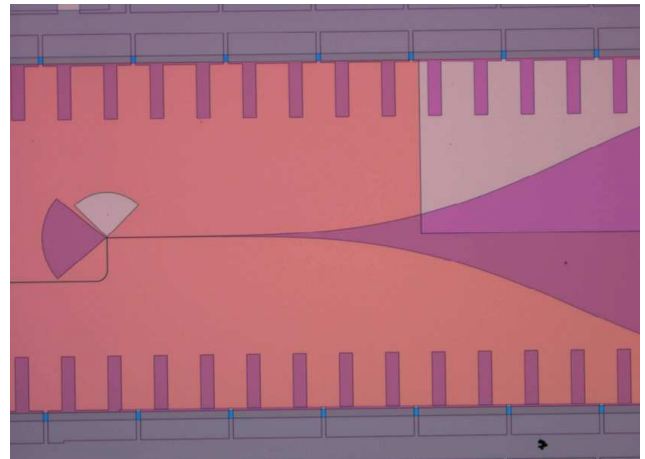


Fig. 7 The unilateral finline and the slotline to microstrip transition.

F. Detector Fabrication

The detectors are fabricated [19] on 2" silicon wafers that are 225 μm thick (see Fig. 8). The overall yield is very high and we have already mass produced all of the detectors needed to populate the LF focal plane. We have found no evidence of any change in the Mo/Cu TES properties on a timescale of years and after numerous thermal cycles.

The chip outline and the well in which the nitride island sits are defined by deep reactive ion etching (DRIE). All of the processing steps are carried out in the Detector and Optical Physics Group in the Cavendish Laboratory at Cambridge, except for the DRIE, which is done at the Scottish Microelectronics Centre in Edinburgh.

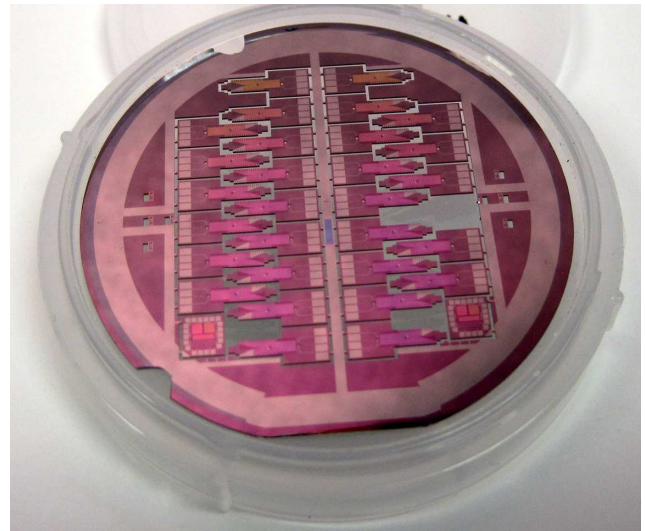


Fig. 8 30 detectors fabricated on a 2" wafer.

III. DETECTOR PACKAGING

A. Detector Mounting

In order to take advantage of the fact that we are using discrete detectors that can be replaced it is necessary to mount them in such a way that they can be easily replaced in a module without disturbing the others. We thus mounted each detector chip on its own individual

chipholder as shown in Fig. 9. The chipholders are made of gold-plated copper and are fixed to the detector block with brass screws. The detector chips are glued to the chipholders using Stycast 1266 epoxy. The chipholders have been carefully designed to prevent the adhesive spreading to places where it might cause problems.

With this mounting scheme it is possible to replace individual detectors in a module without disturbing the others. This means that once we have characterised the detectors we can rearrange them, replacing some if desired, according to their properties to optimise the performance of the array.

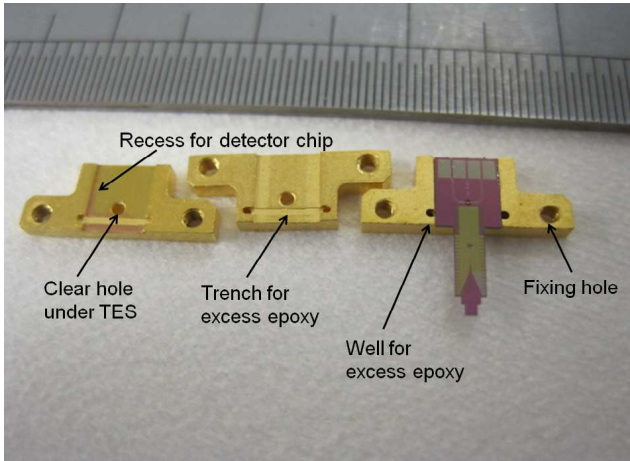


Fig. 9 Individual chipholders showing features for controlling spread of epoxy.

B. LF Module design

The finline detectors are packaged in linear modules containing 16 detectors (Fig. 10, Fig. 11). The detector block comes in two halves, upper and lower. When these are put together they form split-block waveguides (Fig. 12), into which the finlines protrude. The edges of the finlines stick into shallow slots in the sides of the waveguides for grounding. To prevent unwanted modes from propagating the WR10 waveguide is tapered to a reduced height of 1.1 mm (from 1.27 mm).

In the design of the detector module careful attention has been paid to protecting the detector chips from the effects of differential thermal contraction.

Aluminium wire bonds provide electrical connections from the detector chip to a PCB carrying the multiplexer, inductors, and shunt resistors. These three chips are held in place on the PCB with G-10 clamps. The PCB has gold-plated copper tracks and as much of the copper as possible is left on the board to help with heatsinking. The gold is deposited by electroplating in order to avoid the use of a nickel undercoat. The traces are tinned with solder to make them superconducting. The PCB is enclosed in a copper can (Fig. 13) and the module is covered with niobium foil for magnetic shielding.

This scheme has the apparent disadvantage that it under-uses the 1×32 multiplexer chips by a factor of two,

increasing the number needed. However, because we are not using all of the first-stage SQUIDs on a multiplexer chip, we can connect the detectors to those SQUIDs that have the most similar critical currents. This optimises the first-stage SQUID biasing, reducing the noise contribution from this stage of the readout. Reducing the number of detectors multiplexed by each multiplexer chip also reduces the aliased readout noise, improving the NEP. Another advantage of under-using the multiplexer chips is that we can use multiplexer chips in which not all of the first-stage SQUIDs are functioning.

Fig. 14 and Fig. 15 show how the detector modules fit together to populate the focal plane. Individual modules can be removed from the focal plane or replaced either for maintenance, or to reconfigure the experiment. The modules have detachable handles to make removal easier.

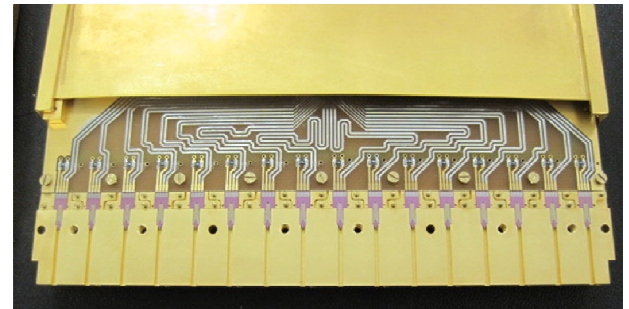


Fig. 10 LF detector module showing 16 detectors sitting in the lower block.

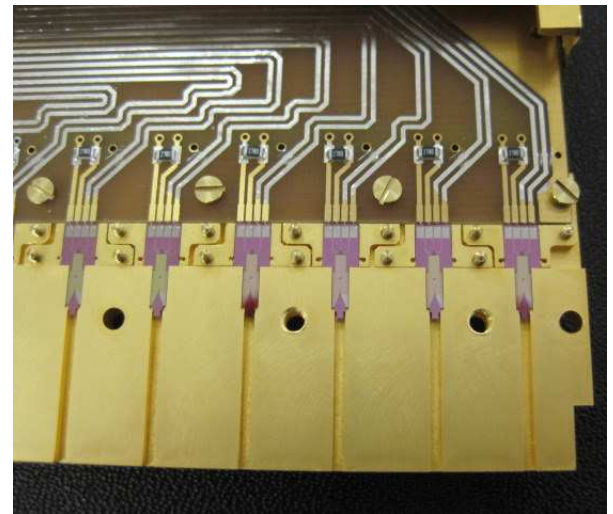


Fig. 11 Closer view of detector chips in LF module.



Fig. 12 Close-up view of assembled LF detector module showing split-block rectangular waveguides and circular alignment holes.

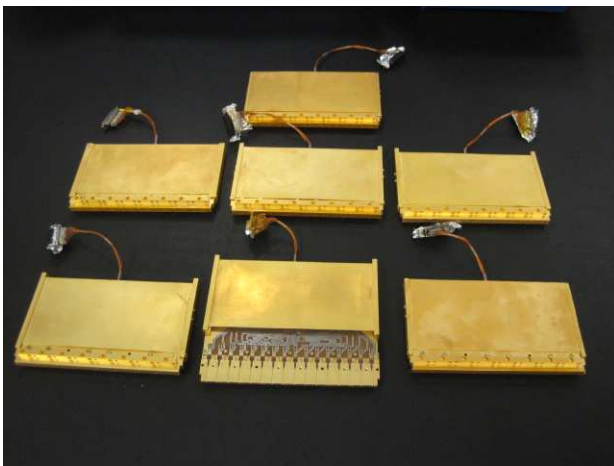


Fig. 13 Seven LF detector modules fully populated with a total of 112 detectors.

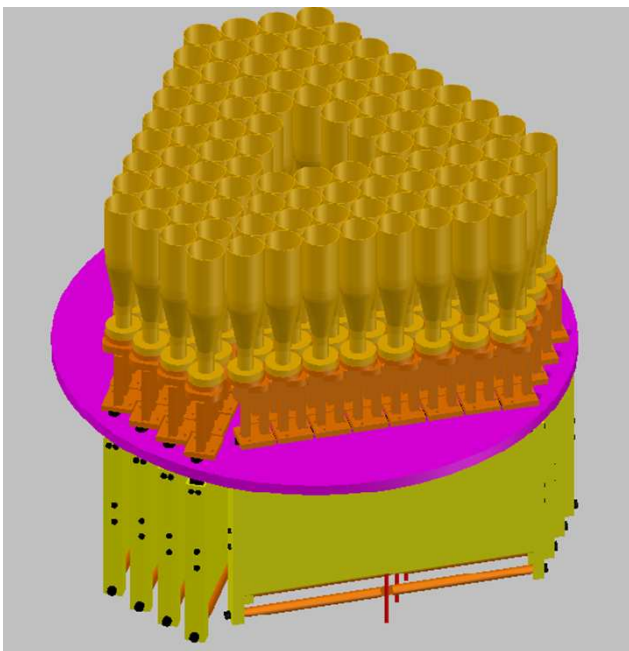


Fig. 14 Drawing of the LF focal plane populated with twelve detector modules.

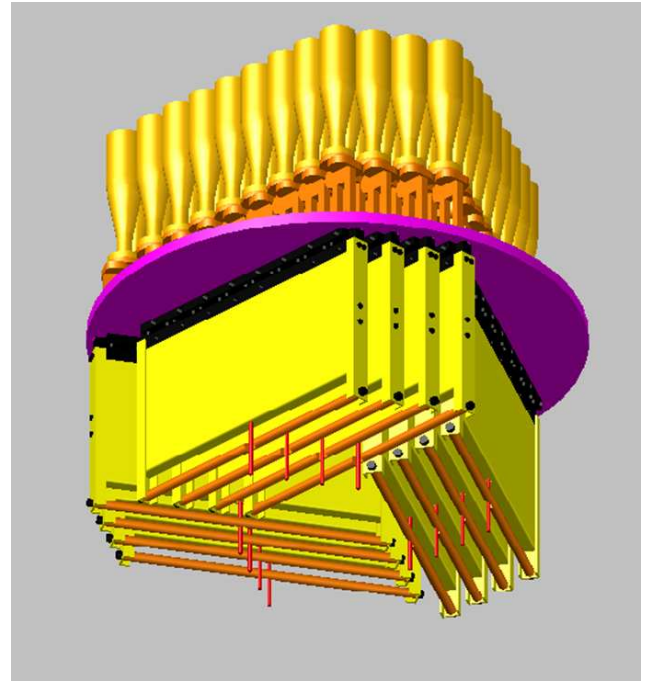


Fig. 15 Drawing of the LF focal plane viewed from the back showing how the twelve detector modules fit together.

IV. PERFORMANCE

A. Testing

We have a dedicated test cryostat for mass-testing the science-grade detector modules. The cryogenics are similar to those in the final instrument, comprising a pulse-tube cooler, He-7 sorption fridge, and miniature dilution fridge. This allows us to test the detectors under realistic conditions and to validate CLOVER's cryogenics. The refrigerator can be operated remotely, and can reach a temperature of about 70 mK with a hold time of about eight hours. The cryostat has a large test volume and contains SQUID series arrays and associated wiring to read out up to eight detector modules or 128 TESs at once.

There is an internal black-body illuminator for optical tests. This illuminator has a conical radiator for high efficiency and two low-pass filters for defining the bandpass. We have paid careful attention to the thermal design of this illuminator to minimise its effect on the thermal performance of the refrigerator. The filters are mounted on nested radiation shields and these shields are heatsunk at 350 mK and 1 K stages of the He-7 sorption fridge.

The test bed also has two parallel sets of warm readout electronics (the MCE and an analogue system) so that we can characterise fully the entire readout chain from the detectors up to room temperature. Unlike the MCE, the analogue electronics does not multiplex, but can be switched between three columns and three rows. However, it is more versatile and convenient for characterising the TESs and SQUIDs. For example, it can lock on any of the three SQUID stages, while the MCE is designed to lock on the first-stage SQUID only. In this

paper we present results obtained with both sets of electronics.

B. Results

We characterised all of the detectors in a LF module using both the analogue readout electronics and the MCE. It is important not only that the detectors have transition temperatures and conductances close to the targets of $T_c = 210$ mK and $G \geq 215$ pW/K but also that these parameters are uniform across the array. The TES bias and heater supplies are common. There are three of each for the whole array. This means that the detector parameters must be uniform enough for all of the detectors to be operated simultaneously with common TES bias and heater supplies. Fig. 16 shows the measured transition temperature for the module. The row number corresponds to the detector's position in the module. The average transition temperature is 207 ± 7 mK.

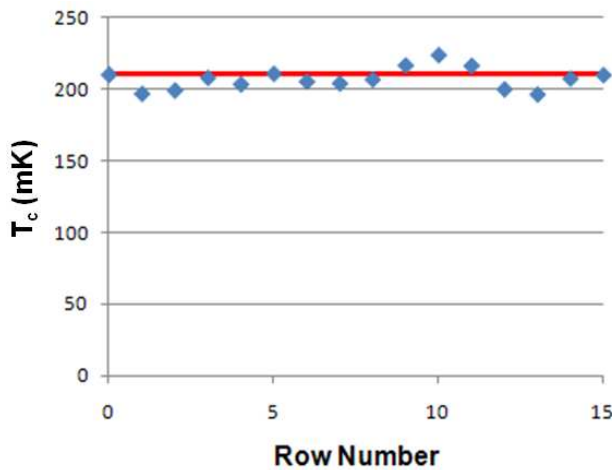


Fig. 16 Measured transition temperatures of TES detectors in module. The solid line represents the target of 210 mK

Fig. 17 shows the measured thermal conductances. The average value is $G = 229 \pm 34$ pW/K. The detector in position 6 has a conductance about half that of the other detectors. The reason for this is that this detector broke between the first and second thermal cycles of the module. Only two of its nitride legs were then intact so that its thermal conductance was halved. It should be noted that this is an extremely rare event: only two detectors out of hundreds have failed in this way. We have found that two thermal cycles will identify any detectors that should be replaced; no detector that survived two thermal cycles has ever failed even after numerous further cycles.

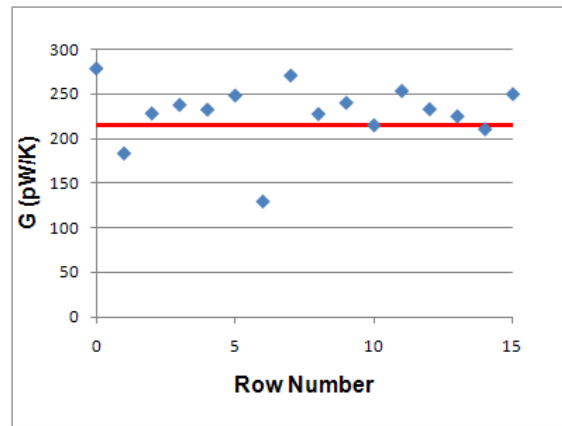


Fig. 17 Measured thermal conductances of TES detectors in module. The solid line represents the target of 215 pW/K.

Fig. 18 shows the heater power required to saturate the detectors in the module when operated with a bath temperature of 100 mK. The average value is $P_{100} = 13 \pm 2$ pW. When the optical efficiency of 60% is taken into account all of the detectors have power handling comfortably larger than 11.4 pW, except for the broken detector in position 6.

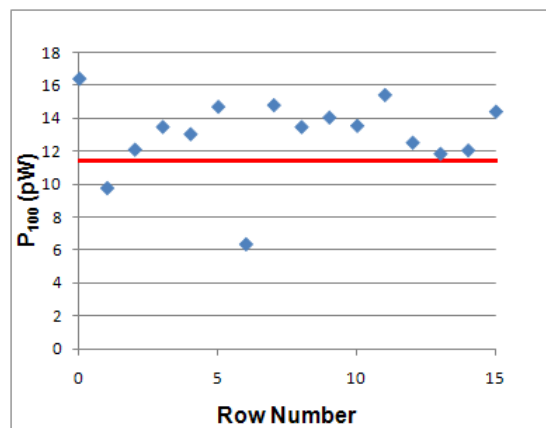


Fig. 18 Measured power handling of TES detectors in module. The solid line represents the target of 11.4 pW.

Fig. 19 shows the response of the detectors to power injected into the on-chip heaters. The heater power has been divided by the optical efficiency (60%) to show the response to incident radiation. The detectors were operated with a fixed bias of 191 nV and read out simultaneously with the MCE. The curve for each detector has a linear region where the TES is biased on its transition. The slope of this linear region is the responsivity of the detector. At higher powers the curves flatten out as each TES becomes saturated and the responsivity decreases to close to zero. The curves do not extend all the way down to zero heater power. This is because either the electrical circuit has become unstable low on the transition where the L/R time constant becomes long or the TES is in the superconducting state. The linear region of each curve shows the range of heater powers over which we can operate the detectors. The vertical solid line in Fig. 19 is the power handling target of 11.4 pW. Clearly the

detectors can be operated simultaneously over a comfortable range of heater powers around this target. We therefore conclude that the detectors are sufficiently uniform to be operated in an array.

It should be noted that we have made no attempt to select detectors with similar properties when populating this module; the 16 detectors were chosen at random before their properties were known. It has always been intended that before delivery to the telescope the detectors would be characterised and replacements made if necessary to optimise the sensitivity of the array. The fact that we obtain the required uniformity without any detector selection means that a 100% functional focal plane is readily achievable for CLOVER.

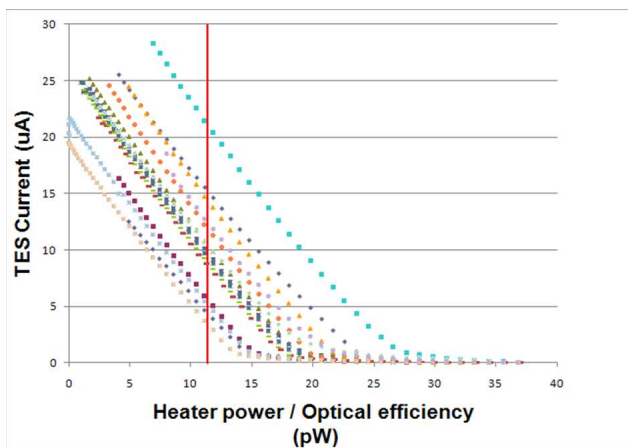


Fig. 19 Response of TES current to power injected into the on-chip heaters. The vertical line shows the 11.4-pW power-handling target.

V. CONCLUSIONS

We have successfully mass-produced all of the detectors for the LF focal plane and integrated them into detector modules. We have demonstrated that these detectors have the required power-handling, NEP, and optical efficiency for ground-based CMB polarimetry, with sufficient uniformity in the detector parameters that they can be operated simultaneously with common TES bias and heater lines.

While this paper has concentrated on the LF detector modules, it should be noted that the CLOVER team has produced an essentially complete instrument which would be expected to be very successful if deployed. Everything from detector modules, OMTs, feedhorns, filters, and readout electronics through to the mirrors and telescope mounts has been manufactured and tested and is ready for integration. Also, a large body of software has been produced for the automatic acquisition and analysis of data as well as extensive modelling work. All of this work will be relevant to any future CMB polarisation experiments.

ACKNOWLEDGMENT

This work was carried out for the CLOVER project, funded by the Science and Technology Research Council. The authors would like to thank Michael Crane for his contribution to device fabrication and process

development, Dennis Molloy for mechanical engineering, and David Sawford for electronic and software engineering. Finally, we would like to thank all of the members of the CLOVER team for their contributions to producing a world-class instrument.

REFERENCES

- [1] M.J. Rees, "Polarization and Spectrum of the Primeval Radiation in an Anisotropic Universe," *Astrophysical Journal*, vol. 153, pp. L1, 1968.
- [2] U. Seljak and M. Zaldarriaga, "Signature of Gravity Waves in the Polarization of the Microwave Background," *Physical Review Letters*, vol. 78, pp. 2054–2057, 1997.
- [3] M. Kamionkowski, A. Kosowsky, and A. Stebbins, "A Probe of Primordial Gravity Waves and Vorticity," *Physical Review Letters*, vol. 78, pp. 2058–2061, 1997.
- [4] L. Piccirillo, P. Ade, M.D. Audley, C. Baines, R. Battye, M. Brown, P. Calisse, A. Challinor, P. Ferreira, W. Gear, D.M. Glowacka, D. Goldie, P.K. Grimes, V. Haynes, B. Johnson, M. Jones, A. Lasenby, P. Leahy, S. Lewis, B. Maffei, L. Martinis, P.D. Mauskopf, S.J. Melhuish, C.E. North, D. O'Dea, G. Pisano, G. Savini, R.V. Sudiwala, A. Taylor, G. Teleberg, D. Titterington, V.N. Tsaneva, C. Tucker, and R. Watson, "The CLOVER experiment," *Proceedings of the SPIE*, vol. 7020, pp. 70201E–70201E-10, 2008.
- [5] P.K. Grimes, P.A.R. Ade, M.D. Audley, C. Baines, R.A. Battye, M.L. Brown, P. Cabella, P.G. Calisse, A.D. Challinor, P.J. Diamond, W.D. Duncan, P. Ferreira, W.K. Gear, D. Glowacka, D.J. Goldie, W.F. Grainger, M. Halpern, P. Hargrave, V. Haynes, G.C. Hilton, K.D. Irwin, B.R. Johnson, M.E. Jones, A.N. Lasenby, P.J. Leahy, J. Leech, S. Lewis, B. Maffei, L. Martinis, P. Mauskopf, S.J. Melhuish, C.E. North, D. O'Dea, S.M. Parsley, L. Piccirillo, G. Pisano, C.D. Reintsema, G. Savini, R. Sudiwala, D. Sutton, A.C. Taylor, G. Teleberg, D. Titterington, V. Tsaneva, C. Tucker, R. Watson, S. Withington, G. Yassin, J. Zhang, and J. Zuntz, "Clover - Measuring the Cosmic Microwave Background B-mode Polarization", *Proceedings of the 20th International Symposium on Space Terahertz Technology*, pp. 97-106, 2009.
- [6] G. Yassin, S.B. Sørensen, and P.K. Grimes, "Compact Optical Assemblies for Large-Format Imaging Arrays", *Proceedings of the 16th International Symposium on Space Terahertz Technology*, pp. 89-92, 2005.
- [7] K.D. Irwin, "Phonon-Mediated Particle Detection Using Superconducting Tungsten Transition-Edge Sensors", PhD thesis, Stanford University, Stanford, California, 1995.
- [8] G. Teleberg, S.T. Chase, and L. Piccirillo, "A miniature dilution refrigerator for sub-Kelvin detector arrays," *Proceedings of the SPIE*, vol. 6275, pp. 62750D, 2006.
- [9] G. Pisano, L. Pietranera, K. Isaak, L. Piccirillo, B. Johnson, B. Maffei, and S. Melhuish, "A Broadband WR10 Turnstile Junction Orthomode Transducer," *IEEE Microwave Compon. Lett.*, vol. 17, pp. 286-288, 2007.
- [10] P. Mauskopf, J. Zhang, P. Ade, S. Withington, and P. Grimes, "Clover Polarimetric Detector - A Novel Design of an Ortho-mode Transducer at 150 and 225 GHz", *Proceedings of Progress In Electromagnetics Research Symposium*, pp. 173-176, 2008.
- [11] J.A. Chervenak, K.D. Irwin, E.N. Grossman, J. Martinis, C.D. Reintsema, and M.E. Huber, "Superconducting multiplexer for arrays of transition edge sensors," *Applied Physics Letters*, vol. 74, pp. 4043–4045, 1999.
- [12] P.A.J. de Korte, J. Beyer, S. Deiker, G.C. Hilton, K.D. Irwin, M. Macintosh, S.W. Nam, C.D. Reintsema, L.R. Vale, and M.E. Huber, "Time-division superconducting quantum interference device multiplexer for transition-edge sensors," *Review of Scientific Instruments*, vol. 74, pp. 3807–3815, Aug. 2003.
- [13] C.D. Reintsema, J. Beyer, S.W. Nam, S. Deiker, G.C. Hilton, K. Irwin, J. Martinis, J., Ullom, L.R. Vale, and M. Macintosh, "Prototype system for superconducting quantum interference device multiplexing of large-format transition-edge sensor arrays," *Review of Scientific Instruments*, vol. 74, pp. 4500–4508, Oct. 2003.

- [14] R.P. Welty and J.M. Martinis, "Two-stage integrated SQUID amplifier with series array output," *IEEE Transactions on Applied Superconductivity*, vol. 3, pp. 2605–2608, 1993.
- [15] E.S. Battistelli, M. Amiri, B. Burger, M. Halpern, S. Knotek, M. Ellis, X. Gao, D. Kelly, M. Macintosh, K. Irwin, and C. Reintsema, "Functional Description of Read-out Electronics for Time-Domain Multiplexed Bolometers for Millimeter and Submillimeter Astronomy," *Journal of Low Temperature Physics*, vol. 151, pp. 908–914, 2008.
- [16] M.D. Audley, W.S. Holland, T. Hodson, M. MacIntosh, I. Robson, K.D. Irwin, G. Hilton, W.D. Duncan, C. Reintsema, A.J. Walton, W. Parkes, P.A.R. Ade, I. Walker, M. Fich, J. Kycia, M. Halpern, D.A. Naylor, G. Mitchell, and P. Bastien, "An update on the SCUBA-2 project," *Proceedings of the SPIE*, vol. 5498, pp. 63–77, 2004.
- [17] D.J. Goldie, M.D. Audley, D.M. Glowacka, V.N. Tsaneva, and S. Withington, "Modeling and reduction of excess noise in transition edge sensor detectors," *Proceedings of the SPIE*, vol. 7020, pp. 70200K-70200K-12, 2008.
- [18] G. Yassin, P.K. Grimes, O.G. King, and C.E. North, "Waveguide-to-planar circuit transition for millimetre-wave detectors," *Electronics Letters*, vol. 44, pp. 866-867, 2008.
- [19] D.M. Glowacka, D.J. Goldie, S. Withington, M. Crane, V. Tsaneva, M.D. Audley, and A. Bunting, "A Fabrication Process for Microstrip-Coupled Superconducting Transition Edge Sensors Giving Highly Reproducible Device Characteristics," *Journal of Low Temperature Physics*, vol. 151, pp. 249–254, 2008.

Transition Edge Sensor Thermometry for On-chip Materials Characterization

D. J. Goldie*, D. M. Glowacka*, K. Rostem*[†] and S. Withington*

*Detector and Optical Physics Group

Cavendish Laboratory
University of Cambridge
Madingley Road
Cambridge
CB3 0HE, UK

Email: d.j.goldie@mrao.cam.ac.uk

[†]Current Address

NASA-Goddard Space Flight Center
Greenbelt
MD 20771 USA

Abstract—The next generation of ultra-low-noise cryogenic detectors for space science applications require continued exploration of materials characteristics at low temperatures. The low noise and good energy sensitivity of current Transition Edge Sensors (TESs) permits measurements of thermal parameters of mesoscopic systems with unprecedented precision. We describe a radiometric technique for differential measurements of materials characteristics at low temperatures (below about 3 K). The technique relies on the very broadband thermal radiation that couples between impedance-matched resistors that terminate a Nb superconducting microstrip and the power exchanged is measured using a TES. The capability of the TES to deliver fast, time-resolved thermometry further expands the parameter space: for example to investigate time-dependent heat capacity. Thermal properties of isolated structures can be measured in geometries that eliminate the need for complicating additional components such as the electrical wires of the thermometer itself. Differential measurements allow easy monitoring of temperature drifts in the cryogenic environment. The technique is rapid to use and easily calibrated. Preliminary results will be discussed.

I. INTRODUCTION

The problem of characterizing the thermal properties of mesoscopic thin-film structures at low temperatures (below 3 K), in particular their thermal conductances and heat capacities as a function of temperature, remains one of the key challenges for designers of ultra-low-noise detectors. This problem is not confined exclusively to the detector community.[1] These measurements require small, easily fabricated, easily characterized thermometers. Techniques are already used such as Johnson noise thermometry (JNT) using thin film resistors as noise sources with dc-SQUID readout or measurements of thermal properties using Transition Edge Sensors (TESs) but both have practical limitations. JNT can perform measurements over a reasonable temperature range and is in principal a primary thermometer but is in practice secondary because of stray resistance in the input circuit to the SQUID that must be calibrated. The achievable measurement precision, σ_T , for a

source at temperature T_s is given by the radiometer equation

$$\sigma_T^2 = \frac{T_s^2}{t_m \Delta f} \quad (1)$$

where t_m is the measurement time and Δf is the measurement bandwidth.[2], [3] In practice the bandwidth is limited by the source resistance and the input inductance of the SQUID to a few 10's of kHz. This gives $\sigma_T \simeq 3$ mK for $T_s = 500$ mK with $t_m = 1$ s. This is the precision that we found in practice.[4] TESs can be used to determine conductances by measuring the power dissipated in the active region of the device where electrothermal feedback (ETF) stabilizes the TES at its transition temperature, T_c , as a function of the temperature of the heat bath, T_b . These measurements are widely reported particularly in the context of measurements of the thermal conductance of silicon nitride films, but a key limitation is that the technique measures thermal properties averaged over a large temperature difference (i.e. between T_c and T_b) and the films under study must support additional (generally superconducting) metalization to provide electrical connection. A problem arises if the thermal properties are themselves a function of temperature. A technique for measuring conductances or heat capacities of micron-scale objects rapidly over a reasonable temperature range without additional overlying films certainly seems to be required. The proposed technique permits true differential measurements of conductance (i.e with small temperature gradients), in a geometry without complicating additional metalization. Measurements of heat capacities are also possible. The technique is easy to implement, simple to calibrate and rapid to use.

We recently demonstrated highly efficient coupling of very broadband thermal power between the impedance-matched termination resistors of a superconducting microstrip transmission line.[5] The efficiency of a short microstrip ($l \simeq 2$ mm) was better than 97% for source temperatures up to 1.5 K. When the coupling efficiency is very high the power trans-

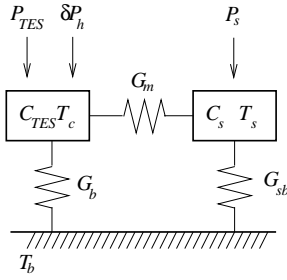


Fig. 1. Thermal circuit of a simple geometry.

ferred along a superconducting microstrip between a source and a TES can be used as a fast, accurate thermometer. [6] The practical temperature sensitivity is determined by the TES low-frequency Noise Equivalent Power, $NEP(0)$. The limiting temperature sensitivity is determined by the very-wide radio-frequency bandwidth of the microstrip coupling so that we substitute $\Delta f \rightarrow \Delta\nu$ in Eq. 1 and $\Delta\nu = 34.5/T_s$ GHz/K is the equivalent rf-bandwidth of a blackbody source at temperature T_s .

II. TES THERMOMETRY

We begin by reviewing the technique of TES thermometry for a simple geometry. In section II-B we describe the full thermal circuit used in the measurements of conductances. In sections II-C and II-D we describe how the conductances are determined experimentally.

A. A simple geometry

A thermal circuit for a simple geometry for TES thermometry is shown in Fig. 1. A source of total heat capacity C_s which could be a thermally isolated silicon nitride (SiN_x) island is connected to a TES also formed on a SiN_x island by a conductance formed from a resistively-terminated superconducting microstrip. Broadband power is transferred between the impedance-matched termination resistors of the microstrip which has thermal conductance G_m . Over a portion of its length the microstrip crosses the Si substrate so that any phonon conductance is efficiently heat sunk to the bath. G_m arises from conduction due to photons. The source and TES are connected to a heat bath at temperature T_b by conductances G_s and G_{sb} respectively which include the contribution from the phonon conductance of dielectric of the microstrip. Heaters permit the source temperature to be varied and the TES to be calibrated. Changes in the power coupling along the microstrip are measured using the TES which is in close proximity to its termination resistor. For low source temperatures $T_s \leq 3$ K, all of the power is contained within the pair-breaking threshold of the superconducting Nb, $2\Delta_{Nb}/h \simeq 760$ GHz where h is Planck's constant and Δ_{Nb} is the superconducting energy gap. The power transmitted between the source at temperature T_s and the TES at its transition temperature T_c is given by

$$P_m(T_s, T_c) = \int_0^{\frac{2\Delta_{Nb}}{h}} [P_\nu(T_s) - P_\nu(T_c)] d\nu, \quad (2)$$

where ν is the frequency, $P_\nu(T_i) = h\nu n(\nu, T_i)$ and $n(\nu, T_i)$ is the Bose-Einstein distribution, and we have assumed that the coupling is loss-less. If the source temperature is low $T_s \leq 3$ K all of the power is contained well-within the cut-off frequency of the microstrip and the upper limit of may be set to infinity. Eq. 2 then has the solution

$$P_m(T_s, T_c) = \frac{\pi^2 k_b^2}{6h} (T_s^2 - T_c^2). \quad (3)$$

The measurement conductance $G_m(T_s) = dP_m(T_s, T_c)/dT_s$ is $G_m(T_s) = \pi^2 k_b^2 T_s / 3h$. G_m determines how changes in source temperature affect power flow to the TES.

To calibrate the thermometry we need to know the low-frequency TES current-to-power responsivity, $s_I(0)$. This is measured by applying slowly-varying power, δP_h , to the known heater resistance on the TES island and measuring the change in detected current δI . The responsivity is then $s_I(0) = \delta I / \delta P_h$. As the source temperature is changed using the source heater, the power incident on the TES changes as given by Eq. 3. Measuring the change in the current flowing through the TES, δI , determines the change in detected power $\delta P_m = \delta I / s_I(0)$. Noting that $\delta P_m = P(T_s, T_c) - P(T_b, T_c)$, and since ETF fixed the TES's temperature at T_c , we can determine the source temperature to a good approximation as

$$T_s = \sqrt{\frac{\delta I}{s_I(0)} \frac{6h}{\pi^2 k_b^2} + T_b^2}. \quad (4)$$

The practical temperature measurement precision is determined by the low-frequency TES $NEP(0)$ so that[6]

$$\sigma_{T_s}^2 = \frac{NEP^2(0)}{2t_m G_m^2(T_s)}. \quad (5)$$

Here we have intentionally omitted thermal fluctuations of the source island which we consider a signal in this geometry. For $NEP(0) = 2 \times 10^{-17} \text{ W}/\sqrt{\text{Hz}}$ the achievable temperature precision is $30 \mu\text{K}$ for $t_m = 1$ s and $T_s = 500$ mK. This is two orders of magnitude better than JNT.

B. The measured geometry

In the full geometry two source islands S_1, S_2 are connected by the subject under test here a conductance, G_{12} . The subject may be more complicated. Each source island is connected to its own TES by a microstrip. Figure 2 shows the full thermal circuit. We measure the quiescent TES currents to monitor and subtract small drifts in the substrate temperature or the electronics. The measurement precision of the temperature of either source, σ_T , with a measurement time t_m is determined by the low-frequency TES $NEP(0)$ so that

$$\sigma_{T_{1,2}}^2 = \frac{NEP^2(0)}{2t_m} \left(\frac{1}{G_m^2(T_b)} + \frac{1}{G_m^2(T_{1,2})} \right) + \frac{k_b T_{1,2}^2}{C_{1,2}}, \quad (6)$$

and the temperature measurement precision for this differencing approach includes a contribution from the bath temperature measurement. We have also now explicitly included the effect of thermodynamic fluctuations in the temperatures of the sources of heat capacity $C_{1,2}$ since these fluctuations directly affect the precision with which the source temperature can be determined.

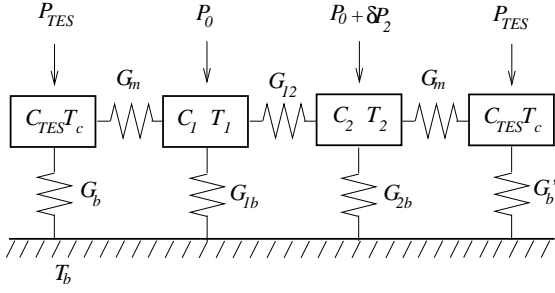


Fig. 2. Thermal circuit of the full measurement. The subject under test is shown here as a conductance G_{12} but may be more complicated.

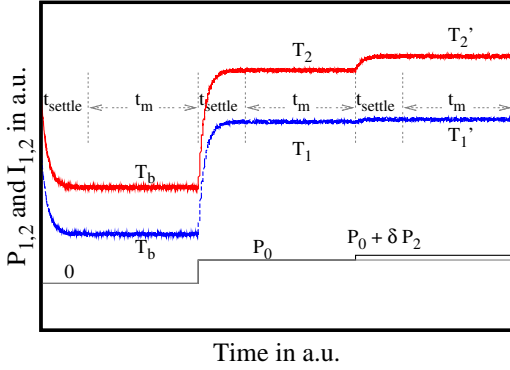


Fig. 3. Schematic showing the time variation of the input powers (lower traces) and output currents (upper traces) for one cycle of the measurement. The sequence of measurement and settling times is indicated. The full time-sequence represents a measurement frame. The measurement intervals determine the temperatures as shown.

C. Measurement of the conductance G_{12}

We measure the interconnect conductance G_{12} in a three step process. A schematic of the measurement cycle is shown in Fig. 3. In the first step the quiescent TES currents are measured. Then dc power P_0 is input to both source islands raising the temperatures from the bath temperature T_b to T_1, T_2 . We find $T_1 \cong T_2$ and we quantify the effect of $T_1 \neq T_2$ later. Finally power to S_2 is stepped by an additional small amount δP_2 raising the island temperatures to T_1' and T_2' . Since both $T_1' - T_1$ and $T_2' - T_2$ are small the measurement is differential. For the next temperature sample the process is repeated with incremented P_0 . The power steps are adjusted in software to give approximately constant increments and differences in temperature across the range of temperatures measured. One complete measurement cycle (i.e. $P = 0, P_0, P_0 + \delta P_2$), with a short settling time t_{settle} between each measurement step to accommodate thermal response times, defines a ‘frame’ time. The frame must be measured in a time less than the Allan time of the system.

The power flow across a conductance G connecting thermal reservoirs at temperatures T, T' can be written for notational convenience as

$$P(T', T) = \int_T^{T'} G(T) dT = \overline{G(T', T)}(T' - T), \quad (7)$$

where the over-set line denotes averaging. If $T' - T = \delta T$ is small then the power flow can be linearized so that

$P(T', T) = G(\overline{T})\delta T$. Ignoring for now the small conductance of the microstrips, the input powers and resultant temperatures are related by

$$P_0 = P_{1b}(T_1, T_b) - \overline{G_{12}(T_1, T_2)}(T_2 - T_1) \quad (8a)$$

$$P_0 = P_{2b}(T_2, T_b) + \overline{G_{12}(T_1, T_2)}(T_2 - T_1) \quad (8b)$$

$$P_0 = P_{1b}(T_1', T_b) - \overline{G_{12}(T_1', T_2')}(T_2' - T_1') \quad (8c)$$

$$P_0 + \delta P_2 = P_{2b}(T_2', T_b) + \overline{G_{12}(T_1', T_2')}(T_2' - T_1') \quad (8d)$$

Subtracting 8a from 8c, 8b from 8d and using, for example,

$$P_{2b}(T_2', T_b) - P_{2b}(T_2, T_b) = \int_{T_2}^{T_2'} G_{2b}(T) dT \quad (9)$$

$$= G_{2b}(\overline{T_2})\delta T_2,$$

where $\overline{T_2} = (T_2' + T_2)/2$ and the final equality follows since δT_2 is small, we find

$$\delta P_2 = 2G_{12}(\overline{T_{12}})(\delta T_2 - \delta T_1) + G_{2b}(\overline{T_2})\delta T_2 - G_{1b}(\overline{T_1})\delta T_1 \quad (10)$$

and $\overline{T_{12}} = (T_1 + T_1' + T_2 + T_2')/4$. Finally the effect of conductance along the microstrip needs to be included. The result is

$$G_{12}(\overline{T_{12}}) = \frac{\delta P_2 - (G_{2b}(\overline{T_2}) + G_m(\overline{T_2}))\delta T_2 + (G_{1b}(\overline{T_1}) + G_m(\overline{T_1}))\delta T_1}{2(\delta T_2 - \delta T_1)} \quad (11)$$

D. Measurement of the conductances G_{1b}, G_{2b}

The conductance to the bath at a given temperature is measured in a two-step procedure where we measure the quiescent TES current ($P = 0$) and the effect of applying equal power P_0 to both islands and measuring the changes in T_1 and T_2 . The next temperature sample uses incremented P_0 . This measurement is rapid. With $t_m = 0.82$ s, 500 data points are acquired in less than 15 minutes. In the analysis we use Eqs. 8a and 8b and assume $T_1 = T_2$. This introduces an inevitable error in the analysis and the magnitude is of order $\epsilon = |G_{12}(\overline{T_{12}})(T_2 - T_1)|/P_{1,2b}$. Experimentally the error is small $\ll 1\%$. A fifth-order polynomial is fitted to the $T_{1,2} - P_0$ data and the conductances G_{1b}, G_{2b} found by differentiation. Note that since the temperature difference $T_{1,2} - T_b$ may be large this measurement is temperature-averaged.

III. MEASURED DEVICE

An optical image of the device described here is shown in Fig. 4. The measured conductance labelled G_{12} is a long thin SiN_x bar of dimensions $500 \times 10 \times 0.5 \mu\text{m}^3$ formed by reactive ion and deep reactive ion etching of a nitride-coated Si wafer. G_{12} carries no additional films. G_{12} connects two larger $0.5 \mu\text{m}$ -thick nitride source islands S_1 and S_2 themselves isolated from the Si wafer by four supporting nitride legs, two of length $255 \mu\text{m}$ two of length $358 \mu\text{m}$ each of width $15 \mu\text{m}$. One of the longer legs also carries a Nb microstrip line. The microstrip is terminated by an impedance-matched AuCu termination resistor at each end. Each island

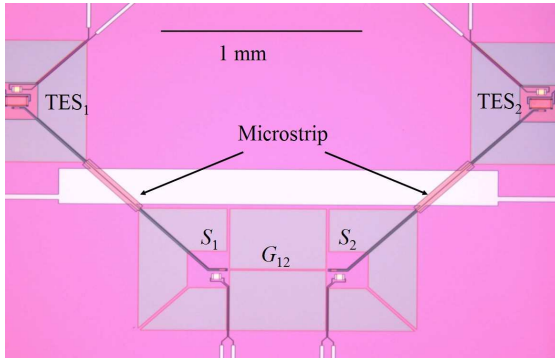


Fig. 4. Optical image of the device under test. The central nitride bar (labelled G_{12}) of length $500 \mu\text{m}$, width $10 \mu\text{m}$ connects the nitride source islands S_1 , S_2 . Resistively terminated microstrip lines run from the islands to TESs in the upper corners of the image. The conductance between each nitride island and the heat bath is formed from four nitride legs, two of length $285 \mu\text{m}$, two of $355 \mu\text{m}$ that run diagonally.

also supports a square AuCu resistor with Nb bias lines that can be used as a heater to modulate the temperature of the sources. The microstrips run over the Si wafer then onto nitride islands which support TESs. Routing of the microstrips in this way ensures that the phonon conductance associated with the microstrip dielectric is efficiently heat-sunk to the bath. The TES islands also include AuCu resistors with Nb bias lines that allow the power-to-current responsivity of the TESs to be measured.

AuCu resistors are 40 nm thick, Nb bias lines and the ground plane of the microstrip are 250 nm thick. The microstrip dielectric is sputtered SiO_2 and is 400 nm thick. The TESs use our standard higher temperature MoCu bilayer layout with 40 and 30 nm of Mo and Cu respectively. The fabrication route is identical with our usual process for MoCu TESs.[7] The TESs are voltage biased and read-out with SQUIDs. The device is measured in a He-3 refrigerator with a base temperature of 259 mK . The transition temperature of the TESs described here was $T_c \sim 485 \text{ mK}$ which is slightly higher than reported in our earlier work with the same Mo-Cu bilayer lay-up. As a result the conductance to the bath of the TESs is increased and the measured TES Noise Equivalent Power is $NEP(0) = 1.2 \times 10^{-16} \text{ WHz}^{-1/2}$.

IV. RESULTS AND DISCUSSION

The Allan variance statistic, $\sigma_A^2(\tau)$ where τ is the integration time, provides an exceptionally powerful diagnostic of system stability and a plot of the variance as a function of τ identifies the optimum time for signal averaging.[8], [9] In the Allan plot, a log-log plot of σ_A^2 as a function of τ , underlying fluctuations with frequency-domain power spectra varying as $1/f^\alpha$ show a $\tau^{(\alpha-1)}$ dependence. Hence white noise with $\alpha = 0$ has a τ^{-1} characteristic. $1/f$ noise shows no dependence on integration time and drift exhibits a dependence with $1 < \alpha < 3$. Figure 5 shows measured Allan variances for both SQUID systems with biased TESs and the bath temperature at $T_b = 259 \pm 0.5 \text{ mK}$. The measured characteristic indicates that white noise is reduced by time-integration up to a maximum of order $\tau_A \simeq 5 \text{ s}$. The dashed

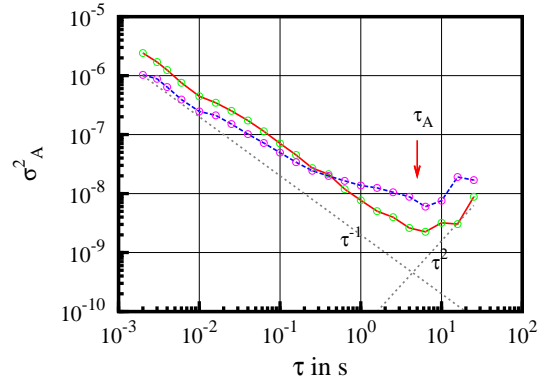


Fig. 5. Allan plot for the two SQUID systems with biased TESs and $T_b = 259 \pm 0.5 \text{ mK}$. The optimum integration time, identified as τ_A , is at the minimum of the statistic σ_A^2 .

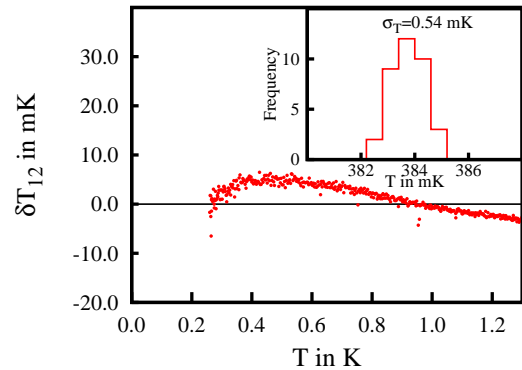


Fig. 6. Difference in temperature between the two islands as a function of average temperature for equal applied powers. Note the improvement in the measurement precision as the temperature increases. The inset shows the measured temperature precision for repeated measurements near 384 mK . The measured precision $\sigma_T = 0.54 \text{ mK}$ compares well with the calculated value from Eq. 6 which gives $\sigma_T = 0.47 \text{ mK}$ for the measurement time used $t_m = 0.82 \text{ s}$ and the measured $NEP(0) = 1.2 \times 10^{-16} \text{ WHz}^{-1/2}$.

lines show the expected behaviour for white noise with a slope τ^{-1} and for drift with a slope of τ^2 . This shows that drift limits these measurements. Guided by the Allan plot, we chose a sample time $t_m = 0.82 \text{ s}$ being 2^{14} data points sampled at 20 kHz and $t_{\text{settle}} = 100 \text{ ms}$. For the conductance measurements with three power steps the total frame time is 2.8 s at each sample temperature.

Applying equal power to both sources, G_{1b} and G_{2b} were determined. As discussed earlier the analysis introduces an unavoidable error in the measurement of G_{1b} and G_{2b} depending on $T_2 - T_1$. Figure 6 shows the difference in temperature $\delta T_{12} = T_2 - T_1$ for equal powers applied to both islands as a function of average island temperature. The difference is small and a maximum of about 5 mK at 500 mK . Since δT_{12} is small we will see that the error is negligible. The temperature difference implies a difference in conductance for the two notionally identical conductances G_{1b} , G_{2b} of about $\pm 2\%$ between 0.26 and 1.3 K . The temperature dependence of δT_{12} evident in Fig. 6 is also unexpected. It does not seem that the difference can be accounted for by experimental uncertainty (such as in the calibration of the TES responsivities). One possibility might be differences in the actual coupling efficiencies of the

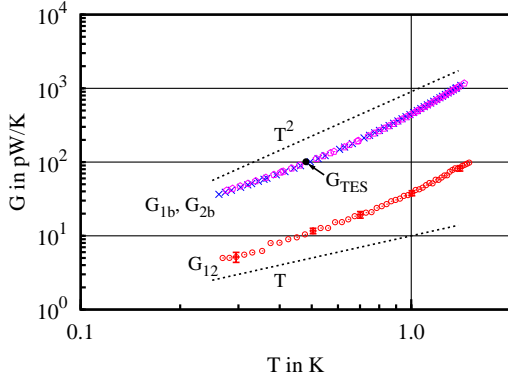


Fig. 7. Measured conductances to the bath G_{1b} , G_{2b} and calculated sample conductance G_{12} . Estimated errors for G_{12} are indicated. The dotted lines indicate dependencies proportional to T^2 and T . The single circle is the measured G_{TES} scaled by the A/l ratios to compare directly to G_{1b} and G_{2b} .

microstrip lines.

The inset of Fig. 6 shows a histogram of calculated temperatures for repeated measurements of a source temperature near 384 mK. The measured precision $\sigma_T = 0.54$ mK compares well with the value calculated from Eq. 6 which gives $\sigma_t = 0.47$ mK for the measurement time used $t_m = 0.82$ s and the measured $NEP(0) = 1.2 \times 10^{-16}$ $\text{WHz}^{-1/2}$.

Figure 7 shows measured conductances G_{1b} , G_{2b} and G_{12} as a function of temperature. Representative error bars for G_{12} determined from the variance of repeated measurements are indicated. We can now estimate the magnitude of the error in G_{1b} and G_{2b} . The maximum temperature difference occurs near 500 mK where $\delta T_{12} \simeq 5$ mK is greatest. We find $\epsilon \simeq 0.2\%$, but less than this over most of the temperature range. This is considered acceptable. We also show the variation with temperature if $G = kT^\beta$ with k a constant. The dotted lines show dependencies $\beta = 1$ and 2 . There is a strong suggestion here that a simple power law does not account for the conductance across this measurement range. At the highest temperatures $\beta > 2$, at the lowest $\beta < 2$. A reduction of the exponent may be expected at low temperatures if dominant phonon wavelengths start to become comparable to the nitride thickness. The single dot in Fig. 7 is the measured G_{TES} for one of the TESs obtained in the standard way by measuring the power plateau in the ETF region of the current-voltage characteristic as a function of the bath temperature. This single point represents approximately 2 hours of data taking. By contrast the conductances to the bath G_{1b} , G_{2b} plotted in Fig. 7 are found from 500 measurements of temperature acquired in 15 minutes. A comparable acquisition time measures G_{12} with 50 data points with additional signal averaging.

Figure 8 shows the ratio of G_{12} to G_{1b} as a function of temperature. The simplest model for power flow along, or the conductance of, a uniform bar would assume that the power scales as the ratio of cross-sectional area, A , to length, l . From the dimensions of the nitride support legs for the source islands and the dimensions of G_{12} we calculate a conductance ratio of 0.082. This ratio includes the conductance associated with the SiO_2 dielectric of the microstrip lines and

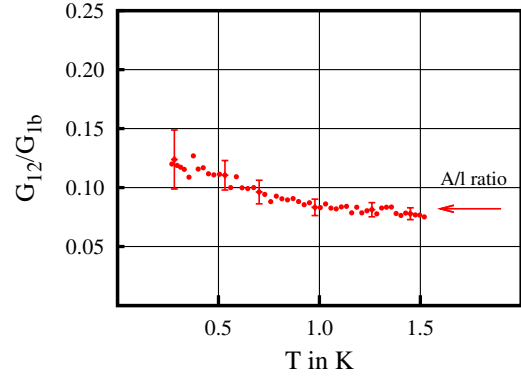


Fig. 8. Ratio of the measured conductance G_{12} to the conductance to the bath G_{1b} . The arrow indicates the expected ratio if the conductances scale as the area to length ratio of the structures.

the smaller contribution from the Nb wiring all of which we assume are equal to that of SiN_x . The variation of the ratio is experimentally significant and may already illustrate the difference between thermal properties averaged over a temperature range and the true differential measurement.

V. CONCLUSION

We have described our first true-differential measurements of thermal conductances of a micron-scaled object at low temperatures using microstrip-coupled TES thermometry. The temperature precision is already significantly greater than that achievable with JNT with the same measurement time. The measurements are rapid and easily calibrated. The achieved precision already strongly suggests that the thermal transport characteristics of the nitride structure are not described by a simple power-law across the temperature range 0.26 to 1.5 K. The device under test can be fabricated without additional metalization for wiring. It should be straight-forward to include specific layers on the nitride test structure to measure particular thermal properties in a controlled manner. In the future we expect to be able to explore the temperature dependence of heat capacities of thin films such as SiO_2 including possibly measurements of time dependent heat capacity. We will explore the effect on conductance of superposed layers: for example, does thermal conductance in thin multilayers really scale as total thickness? We also see the possibility of exploring the engineering of the nitride to realise phononic structures, to achieve reductions of the conductance in compact nitride structures needed for the next generation of ultra-low-noise detectors.

ACKNOWLEDGMENT

We would like to thank Michael Crane for assistance with cleanroom processing, David Sawford for software and electrical engineering and Dennis Molloy for mechanical engineering.

REFERENCES

- [1] F. Giazotto, T. T. Heikkilä, A. Luukanen, A. M. Savin, and J. P. Pekola, "Opportunities for mesoscopies in thermometry and refrigeration: Physics and applications," *Reviews of Modern Physics*, vol. 78, no. 1, p. 217, 2006.

- [2] J. D. Kraus, *Radio Astronomy*, 2nd ed. New York: McGraw-Hill, 1986.
- [3] D. R. White, R. Galleano, A. Actis, H. Brixy, M. D. Groot, J. Dubbeldam, A. L. Reesink, F. Edler, H. Sakurai, R. L. Shepard, and J. C. Gallop, "The status of Johnson noise thermometry," *Metrologia*, vol. 33, no. 4, pp. 325–335, 1996.
- [4] K. Rostem, D. Glowacka, D. J. Goldie, and S. Withington, "Technique for measuring the conductance of silicon-nitride membranes using Johnson noise thermometry," *J. Low Temp. Phys.*, vol. 151, pp. 76–81, 2008.
- [5] K. Rostem, D. J. Goldie, S. Withington, D. M. Glowacka, V. N. Tsaneva, and M. D. Audley, "On-chip characterization of low-noise microstrip-coupled transition-edge sensors," *J. Appl. Phys.*, vol. 105, p. 084509, 2009.
- [6] D. J. Goldie, K. Rostem, and S. Withington, "High resolution on-chip thermometry using a microstrip-coupled transition edge sensor." *Accepted for publication in J. Appl. Phys.*, 2010.
- [7] D. M. Glowacka, D. J. Goldie, S. Withington, M. Crane, V. Tsaneva, M. D. Audley, and A. Bunting, "A fabrication process for microstrip-coupled superconducting transition edge sensors giving highly reproducible device characteristics," *J. Low Temp. Phys.*, vol. 151, pp. 249–254, 2008.
- [8] D. W. Allan, "Statistics of atomic frequency standards," *Procs. IEEE*, vol. 54, pp. 221–230, 1966.
- [9] R. Schieder and C. Kramer, "Optimization of heterodyne observations using Allan variance measurements," *ASTRONOMY & ASTROPHYSICS*, vol. 373, pp. 746–756, 2001.

Demonstration of Multiplexed Operation of Hot-Electron Detectors Using MSQUIDS

Boris S. Karasik^{1*}, Peter K. Day¹, Jonathan H. Kawamura¹, Steve P. Monacos¹,
Bruce Bumble¹, Henry G. LeDuc¹, and Robin Cantor²

¹Jet Propulsion Laboratory, California Institute of Technology, Pasadena, California, CA 91109, USA

²STAR Cryoelectronics, 25-A Bisbee Court, Santa Fe, NM 87508, USA

*Contact: boris.s.karasik@jpl.nasa.gov, phone +1-818-393 4438

Abstract— We have demonstrated the multiplexed operation of titanium hot-electron nanobolometers (nano-HEB). Because of their low thermal conductance and small electron heat capacity nanobolometers are particularly interesting as sensors for far-infrared spectroscopy and mid- and near-IR calorimetry. However, the short time constant of these devices ($\sim \mu\text{s}$ at 300-400 mK) makes time domain or audio-frequency domain multiplexing impractical. The Microwave SQUID (MSQUID) approach pursued in this work uses dc SQUIDs coupled to GHz-band microresonators which are, in turn, coupled to a transmission line. We used a 4-element array of Ti HEBs operated at 415 mK in a He3 dewar with an optical fiber access. The microwave signal exhibited 10-MHz wide resonances at individual MSQUID frequencies between 9 GHz and 10 GHz. The resonance depth is modulated by the current through the bolometer via a change of the SQUID flux state. The transmitted signal was amplified by a cryogenic amplifier and downconverted to baseband using an IQ mixer. A 1-dB per $\Phi_0/2$ responsivity was sufficient for keeping the system noise at the level of $\sim 2 \text{ pA/Hz}^{1/2}$. This is more than an order of magnitude smaller than phonon noise in the HEB. The devices were able to detect single near-IR photons (1550 nm) with a time constant of 3.5 μs . A digital transceiver for simultaneous generation of 16 probing tones and for processing of 16 downconverting signals has been demonstrated as well.

I. INTRODUCTION

Multiplexed readouts are becoming very important for the transition-edge sensor (TES) arrays continuously growing in size. Along with the requirements for having the least number of wires connecting the detectors residing at sub-kelvin temperatures to the room temperature electronics, the large multiplexing bandwidth is crucial for accommodating a large number of the detector channels. The high multiplexing speed is especially important for the sensors whose inherent signal bandwidth is large. This is the case for the hot-electron nanobolometers (nano-HEB) [1] with the thermal time constant of the order of a microsecond at 300-400 mK. Along with the short relaxation time, the nano-HEB has a very low thermal conductance and a very low electron heat capacitance, both due to the extremely small sensor volume. Compared to traditional micromachined TES bolometers, nano-HEB has a large sensitivity margin. For example, the NEP $\approx 10^{-18} \text{ W/Hz}^{1/2}$ is achieved at 320 mK [2] compared to the 50-100 mK temperature range, which is required for other types of bolometers. Also, the ability to detect single photons down to THz frequencies makes the nano-HEB an interesting

candidate for sensitive FIR spectroscopic applications [1,3] and for infrared calorimetry.

In order to address the need for an adequately fast readout for nano-HEB, we have built and characterized a small-scale demo array using microwave SQUIDs (MSQUIDs) [4] for X-band frequency-domain multiplexing. In this technique, a dc SQUID is coupled to a high-frequency tank circuit with a relatively high Q-factor. The signal current from the bolometer causes a flux change through the SQUID, which changes the SQUID rf impedance and introduces the damping and/or frequency offset in the resonating circuit [5]. In our implementation, much larger resonator frequencies were used thus making possible the use of microfabricated resonators. The readout electronics for these microresonators are very similar to that used for the microwave kinetic inductance detectors [6].

II. THE MSQUID CHIP

We used a 4-element MSQUID chip introduced earlier in [4] (see Fig. 1). Each element consists of a dc SQUID capacitively coupled to a coplanar resonator, a signal coil, and a flux control/modulation coil. Each resonator is linked

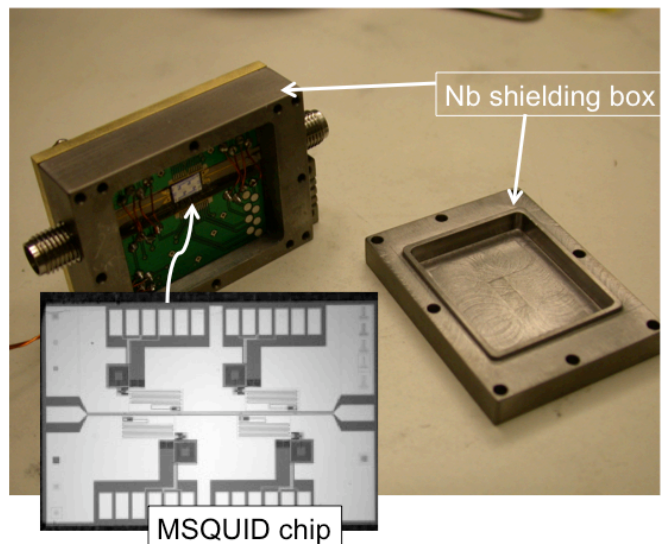


Fig. 1. A four-element Microwave SQUID chip in a Nb shielding enclosure. The coplanar transmission line runs horizontally across the chip; meander line shaped resonators are coupled to the line from the top and from the bottom.

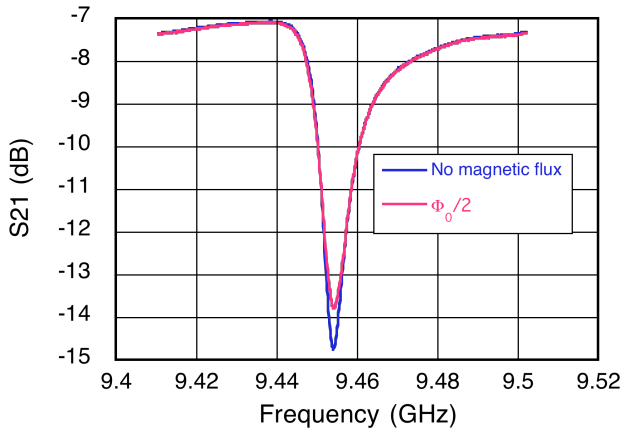


Fig. 2. A transmission of the coplanar line in the vicinity of the resonance frequency of one of the MSQUID resonators. A maximum change of the SQUID flux state ($\Phi_0/2$) causes an about 1-dB change of S_{21} . The phase shift for this MSQUID design was negligibly small.

to a common coplanar waveguide (CPW) transmission line through which the probing microwave signals was launched. The SQUIDS are biased by adjusting the transmitted signal power rather than by dc current. A separate common line connected to the flux control/modulation coils is used for tuning the SQUIDS flux bias points. The individual resonator lengths set the channel frequencies and their separation. For this particular design, all the resonator frequencies were between 9 and 10 GHz and separated by approximately 200 MHz. A typical microwave transmission of a single MSQUID resonator is shown in Fig. 2. The resonance width is about 10 MHz and its depth is decreasing by ~ 1 dB when the maximum flux ($\Phi_0/2$) is coupled to the SQUID. In these experiments, the SQUIDS were operated in open loop mode, therefore a periodic response was observed when the signal current exceeded $\Phi_0/2M$ (M is the mutual inductance of the signal coil).

III. THE TEST SYSTEM

The experimental system was built in an IR Labs HDL-8 He3 cryostat (see Fig. 3). The HEB sensors along with bias filters were placed on a shielded He3 cold plate. The MSQUID chip was enclosed in an Nb magnetic shield and placed on a 4K cold plate (in the future work, a more compact casing will be

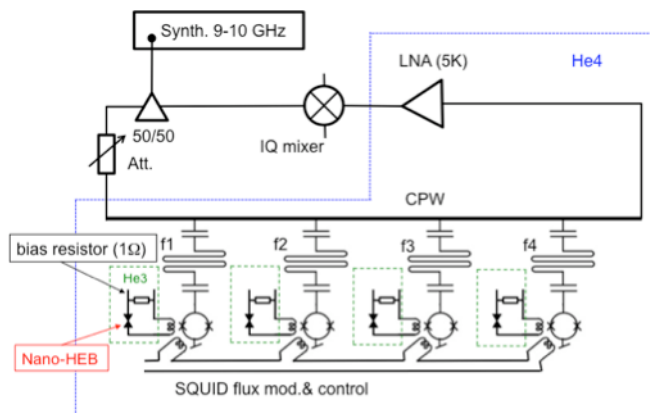


Fig. 3. A schematic of the test system. Components surrounded by the dotted blue line were on the He4 platform (4.3 K). The bolometer (dashed green line) were on the He3 platform.

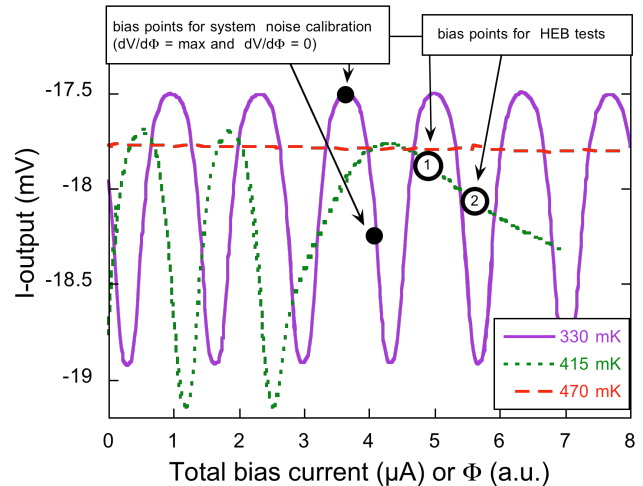


Fig. 4. Signal at the output of IQ-mixer as function of the total current through the HEB device in parallel with a 1-W resistor. When the HEB is in superconducting state, the total current is proportional to the SQUID magnetic flux. 330 mK: the HEB is in superconducting state. When the device was absent, a similar periodic response function was used for the system noise calibration. 425 mK: the device is in the resistive state. Bias points 1 and 2 were used for noise measurements of Fig. 6. 470 mK: the device is in the normal state.

used so the MSQUID chip can reside next to the detectors on the same millikelvin platform). The probe signal was generated by a microwave synthesizer and sent in the dewar through a tunable attenuator and stainless coax. We used a second synthesizer in order to simultaneously operate two pixels. The magnitude of the probe signal was tuned experimentally to provide the maximum sensitivity of the MSQUIDS to the magnetic flux. The probe signal was also fed to an IQ mixer. After passing through the MSQUID chip, the microwave signal was amplified by a broadband cryogenic low-noise amplifier (LNA) with noise temperature ≈ 5 K mounted next to the MSQUID housing and sent to the IQ mixer. We recorded both in-quadrature output signals but did not process the data to retrieve amplitude-phase coordinates. Only the signal exhibiting the largest response is discussed. The signal coils of MSQUIDS were connected to the HEB devices via 50- μ m dia NbTi superconducting twisted pairs shielded individually with NbTi thin-wall capillaries. Each bolometer was voltage biased using a 1- Ω shunt resistor. The bias lines were filtered using 3-stage RC-filters embedded in Eccosorb CRS-124 microwave absorber.

To calibrate the system noise performance and the bandwidth we measured the noise at the output of the mixer as function of the temperature of a 1- Ω resistor directly connected to the SQUID input coil. To obtain the maximum sensitivity, the flux bias point was tuned to region where the derivative $dV/d\Phi$ reaches maximum (V is the output voltage, see Fig. 4). In order to measure the system noise, the flux bias was chosen to be at its maximum or minimum value (where $dV/d\Phi = 0$). In either case the resistor noise is effectively prevented from reaching the SQUID input coil and the total noise contribution of the MSQUID and the LNA could be measured.

Figure 5 shows the noise spectra for 3 different experimental settings. From these data, assuming that the resistor generates only Johnson noise, the effective

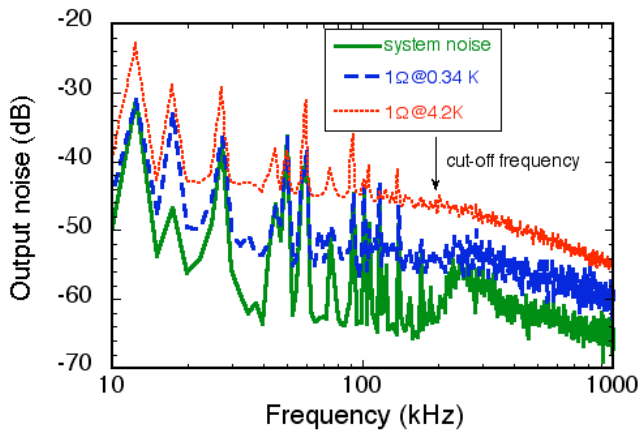


Fig. 5. System noise characterization using the Johnson noise of a 1-Ω resistor at 340 mK and at 4.2 K. The roll-off of the noise spectra is due to the low-pass L_s/R filter.

system noise is $\sim 2 \text{ pA/Hz}^{1/2}$. The roll-off of the noise spectrum is due to the L_s/R low-pass filtering at the input coil (L_s is the input coil inductance). The cut-off frequency of $\sim 200 \text{ kHz}$ agrees with L_s $\approx 1 \text{ μH}$.

IV. MSQUID TEST USING HEB DEVICES

Two Ti HEB devices (20μm × 1μm × 40 nm) were used. The devices exhibited a superconducting transition with T_C = 430 mK with nearly zero residual resistance. Figure 4 shows the output signal for one of the devices as function of the bias. Well below T_C (330 mK) the response is periodic, and corresponds to a monotonically increasing subcritical current through the device. Just below T_C (415 mK), the critical current value is achieved at about 3 μA of the total bias current. After that the current through the device increases slower (all changes are within the Φ₀/2M range), reaches its peak value at $\sim 4.2 \text{ μA}$ and then decreases, exhibiting an N-shaped IV characteristic typical for the voltage biased TES.

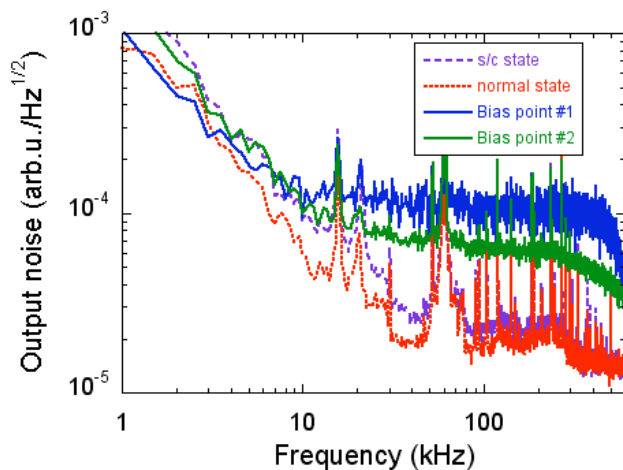


Fig. 6. Output noise from a Ti HEB device. When the detector device is biased to the points of high responsivity (two upper traces taken at points 1 and 2 in Fig. 4) its noise exceeds the system noise. The dotted line shows the noise when the device is in the normal state. The dashed line is the noise when the device is in superconducting state. The 1/f noise below 10 kHz is due to the TLS noise in the superconducting resonator.

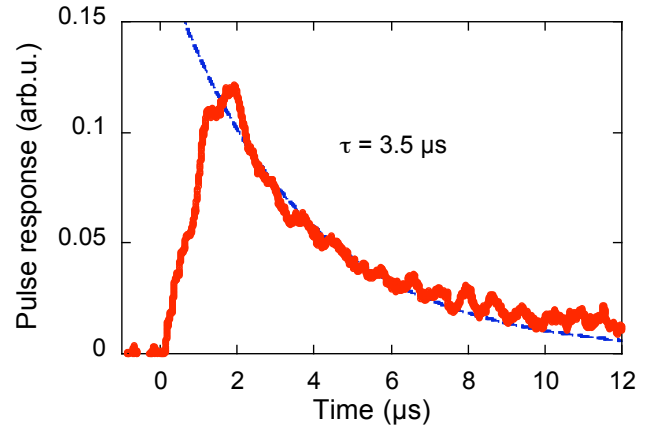


Fig. 7. Response of the HEB detector to a single NIR photon (λ = 1550 nm).

When the device is biased in the negative differential resistance region (bias points 1&2 in Fig. 4), the output noise increases reflecting the corresponding increase of the responsivity. This detector noise (traces “bias point 1” and “bias point 2” in Fig. 6) well exceeds the system noise except in the frequency range below 10 kHz where 1/f-noise is observed. This noise likely originates from the two-level system noise (TLS) observed in Nb superconducting resonators [7]. The presence of the TLS noise may represent a problem for slow bolometers. Fortunately, this is a minor problem for HEB detectors operating above 300 mK where the most of the signal bandwidth is above 10 kHz, and where some kind of modulation can be used to completely avoid the 1/f noise.

The detector’s white noise level agrees well with our recent measurements [2] where we found the output noise for Ti HEB at $\sim 320 \text{ mK}$ to be about 60-70 pA/Hz^{1/2}. The noise is dominated by thermal energy fluctuations (TEF or “phonon” noise). The devices studied in [2] are smaller in size, but, since the TEF noise does not depend on the HEB sensor volume, the same magnitude should be expected in the current experiments. Indeed, the detector noise exceeds the system noise by an order of magnitude in the current setup that proves the low-noise operation of the MSQUID readout. Finally, we measured the time constant of the HEB devices by detecting single NIR photons (1550 nm wavelength). Short pulses ($\sim 1 \text{ μs}$ duration) were generated by a fiber-coupled laser diode. The fiber was fed into the dewar and then through a cold (4.2 K) 25-dB attenuator to the HEB device. A room temperature variable attenuator was used to adjust the energy per pulse to a sufficiently low level so that only one photon per pulse was typically detected. The amplitude of the single-photon response was a small fraction of the total output of the IQ-mixer so the exponential shape of the pulse was preserved (see Fig. 7) despite the non-linearity of the used readout technique. The observed microsecond time constant originates mostly from the electron-photon relaxation in Ti HEB at this temperature [1,2]. The electrical time constant L_s/R should be noticeably less in this case as the total resistance R > 1 Ω (compare to the data of Fig. 5).

V. DIGITAL READOUT OF MSQUIDS

The prototype analog circuit of Fig. 3 allowed for reading of just one detector at a time. In order to demonstrate the real multiplexed operation all frequency tones corresponding to the superconducting resonators must be generated simultaneously. At the same time, all the signals passing the MSQUID must be downconverted and digitized fast enough to preserve the detector signal bandwidth and to maximize the signal-to-noise ratio of the system. In order to do this, we built and tested a circuit shown in Fig. 8. The general approach was proposed in [8]. Our particular implementation included generation of 16 frequency tones in a 80-MHz range (see Fig. 9) using an arbitrary waveform generator Tektronix AWG 5012B. The spectral purity of the individual tones was identical to that of a standard HP synthesizer. The entire frequency comb was upconverted to the GHz range and after passing the MSQUID array was downconverted to the baseband and fed into a broadband 16-bit ADC (Pentek 7852) which had the input bandwidth of 200 MHz (~ 100 MSPS) and a firmware core allowing for digital downconversion of the baseband signal into 32 output channels. The digital local oscillator (LO) frequencies have to be synchronized with the frequencies of the comb generated by AWG5012B. Each channel's bandwidth could be tuned between 20 kHz and 10 MHz. The system was tested using sinusoidal signals with the frequency set apart from the digital LO frequency by 500 Hz – 50 kHz (that is, within the output channel bandwidth). Spectral analysis of the processed signals did not reveal any significant spurious components.

VI. FOLLOW-ON DEVELOPMENT

The system setup is on-going and in the next phase we expect to test the entire system with up to 16 nano-HEB detectors operating at 650 GHz. Compared to the setup of Fig. 3 the nano-HEB array and the MSQUID chip will be at the same low temperature (He3) and be connected to the higher temperature (4.3K) platform via only 2 NbTi low thermal conductance coaxes, 2 detector bias wires and 2 SQUID modulation wires (Fig. 8). We plan to implement a

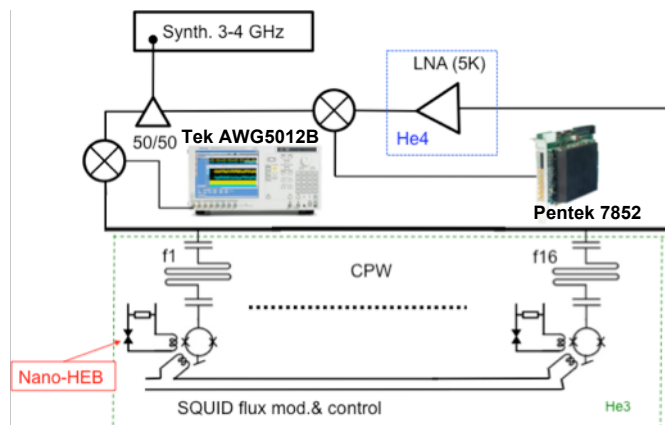


Fig. 8. A schematic of the test system with digital MSQUID readout. Components surrounded by the dotted blue line were on the He4 platform (4.3 K). Both the bolometers and the MSQUIDs (dashed green line) will be on the He3 platform.

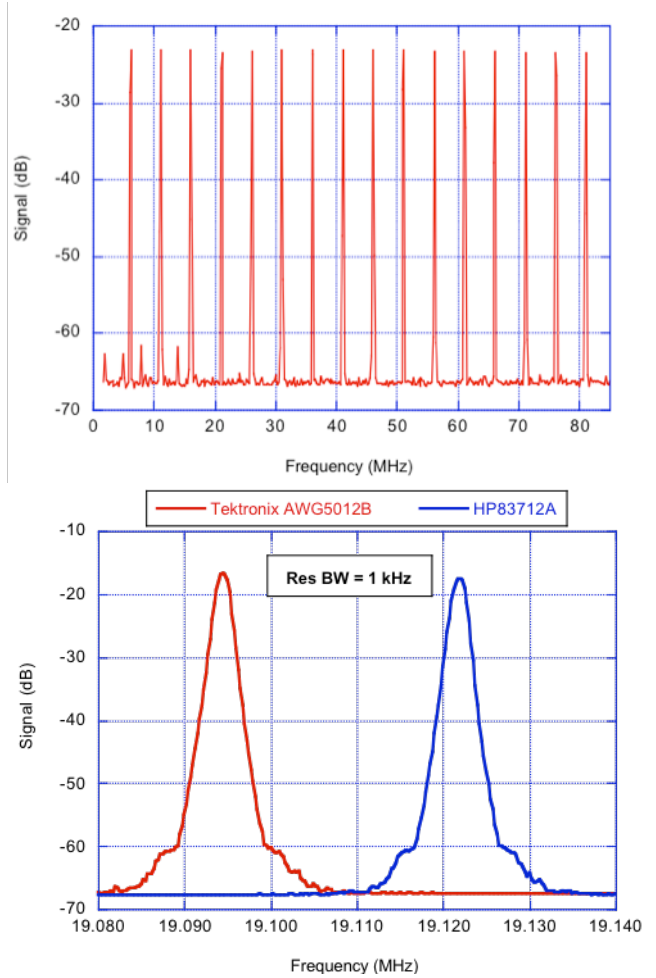


Fig. 9. Top panel: 16 digitally generated frequency tones for probing superconducting resonators. Bottom panel: comparison of the lineshape of one the tone to the frequency line produced by an HP synthesizer.

modification of the MSQUID chip in order to improve the overall system performance. The new prototype chip uses dissipationless MSQUIDs at 3-4 GHz [9] with lumped-element resonators, which should have a lesser 1/f noise [10]. Eventually the separation between the resonances should be tuned to ~ 1-2 MHz to allow for a maximum number of pixels per the ADC bandwidth without putting a limitation on the signal bandwidth or causing a crosstalk between pixels. We will also use antenna-coupled nano-HEB which have been recently tested in a separate optical setup having demonstrated an optical NEP below 10^{-17} W/Hz^{1/2} at 360 mK [11-12].

VII. CONCLUSIONS

The obtained results clearly demonstrate the feasibility of low-noise and broadband readout scheme using microwave dc SQUIDs. Both the system noise and the bandwidth were sufficient to operate Ti HEB detectors without degradation of the sensitivity and the detector response time. Given the progress with ADC and DAC electronics much larger number of pixels per ADC/DAC (up to ~ 1000) can be expected in the future. A combination of the high sensitivity along with the μ s response time and high operating

temperature requiring only a simple He3 sorption cryostat is attractive for using in ground based and suborbital submillimeter instruments

ACKNOWLEDGMENT

This research was carried out at the Jet Propulsion Laboratory, California Institute of Technology, under a contract with the National Aeronautics and Space Administration and funded in part through the internal Research and Technology Development program.

REFERENCES

[1] J. Wei, D. Olaya, B. S. Karasik, S. V. Pereverzev, A.V. Sergeev, and M. E. Gershenson, "Ultrasensitive Hot-electron Nanobolometers for Terahertz Astrophysics," *Nat. Nanotechnol.*, vol. 3, pp. 496-500, Aug. 2008.

[2] B. S. Karasik, S. V. Pereverzev, D. Olaya, J. Wei, M. E. Gershenson, and A. V. Sergeev, "Noise Measurements in Hot-Electron Titanium Nanobolometers," *IEEE Trans. Appl. Supercond.*, vol. 19, pp. 532-535, Jun. 2009.

[3] B. S. Karasik and A. V. Sergeev, "THz Hot-Electron Photon Counter," *IEEE Trans. Appl. Supercond.*, vol. 15, pp. 618-621, Jun. 2005.

[4] I. Hahn, P. Day, B. Bumble, and H. G. LeDuc, *J. Low Temp. Phys.* 15, 934-939 (2008).

[5] K. D. Irwin and K. W. Lehnert, "Microwave SQUID multiplexer," *Appl. Phys. Lett.*, vol. 85, 2107-2109, Sep. 2004.

[6] P. K. Day, H. G. LeDuc, B. A. Mazin, A. Vayonakis, and J. Zmuidzinas, "A broadband superconducting detector suitable for use in large arrays," *Nat.*, vol. 425, 817-821, Oct. 2003.

[7] J. S. Gao, M. Daal, A. Vayonakis, S. Kumar, J. Zmuidzinas, B. Sadoulet, B. A. Mazin, P. K. Day, and H. G. LeDuc, "Experimental evidence for a surface distribution of two-level systems in superconducting lithographed microwave resonators," *Appl. Phys. Lett.*, vol. 92, 152505, Apr. 2008.

[8] B. A. Mazin, P. K. Day, K. D. Irwin, C. D. Reintsema, and J. Zmuidzinas, "Digital readouts for large microwave low-temperature detector arrays," *Nucl. Instr. Meth. Phys. Res. A*, vol. 559, 799-801, Apr. 2006.

[9] J. A. B. Mates, G. C. Hilton, K. D. Irwin, and L. R. Vale, "Demonstration of a multiplexer of dissipationless superconducting quantum interference devices," *Appl. Phys. Lett.*, vol. 92, 023514, Jan. 2008.

[10] S. Doyle, P. Mauskopf, J. Naylor, A. Porch, and C. Duncombe, "Lumped Element Kinetic Inductance Detectors," *J. Low Temp. Phys.*, vol. 151, 530-536, Apr. 2008.

[11] B. S. Karasik, S. V. Pereverzev, D. Olaya, M. E. Gershenson, R. Cantor, J. H. Kawamura, P. K. Day, B. Bumble, H. G. LeDuc, S. P. Monacos, D. G. Harding, D. Santavicca, F. Carter, and D. E. Prober, "Development of the nano-HEB array for low-background far-IR applications," in *Proc. SPIE*, 2010, vol. 7741, paper 774119.

[12] B. S. Karasik, S. V. Pereverzev, R. Cantor, D. Olaya, and M. E. Gershenson, "Noise study and optical NEP in hot-electron nanobolometers," this *Symp. Proceedings*.

Hysteretic thermal switching due to readout power heating in kinetic inductance detectors

Pieter de Visser^{*†§}, Stafford Withington[‡] and David Goldie[‡]

^{*}*Kavli Institute of NanoScience, Faculty of Applied Sciences, Delft University of Technology, Lorentzweg 1, 2628 CJ Delft, The Netherlands*

[†]*SRON National Institute for Space Research, Sorbonnelaan 2, 3584 CA Utrecht, The Netherlands*

[‡]*Cavendish Laboratory, Cambridge University, JJ Thomson Avenue, Cambridge CB3 0HE, United Kingdom*

[§]Contact: p.j.devisser@tudelft.nl

Abstract—Kinetic Inductance Detectors (KIDs) consist of thin-film superconducting resonators. An incoming photon breaks Cooper pairs, and causes the surface impedance of the resonator to change. The resonant frequency shifts, and the absorption event is recorded by monitoring the change in microwave transmission amplitude and phase. In this paper, we show that the power deposited by the microwave readout signal can cause the temperature of the quasiparticles in the superconducting film to switch between well-defined states. Experimentally, the effect appears as a discontinuity in the resonance curve, but is actually a hysteretic switching between thermal states as the readout frequency is swept up and down. We present numerical simulations that predict, quite clearly, the existence of hysteretic switching in low T_c superconducting resonators. The switching occurs as a direct consequence of the relationship between the readout power absorbed by the resonator as a function of temperature, and the finite thermal impedance of the quasiparticle-phonon coupling. This work may lead to an improvement of the power handling in KIDs, which is the easiest way of noise reduction in these devices, and to a better understanding of electron-phonon coupling in superconductors.

I. INTRODUCTION

Kinetic Inductance Detectors (KIDs) consist of thin-film superconducting resonators ($<10\text{GHz}$) on sapphire, quartz, or silicon substrates. An incoming infrared, optical, or x-ray photon breaks Cooper pairs, and causes the surface impedance of the resonator to change. The resonant frequency shifts, and the absorption event is recorded by monitoring the change in microwave transmission amplitude and phase [1].

One of the key issues in improving KIDs for detector purposes is decreasing the amount of noise. Using phase readout, excess noise was found, which scales inversely with the amount of applied microwave readout power [2], [3]. Therefore increasing the power handling of resonators is one of the topics of current research. At certain power resonators start to show nonlinear behaviour, which gives the power limit for linear detection. On the other hand, a lot of research has been done on nonlinear effects in resonators, showing that vortices, thermal instabilities due to local hot spots [4] and a power dependent surface impedance [5], [6] can also cause strong nonlinearities in the resonator response. This kind of research focuses usually on superconductors with a high critical temperature and a high resistivity. Since the nonlinearities are used for amplification

and other purposes, easier operation at higher temperature is favourable. Thermal effects described in literature cause nonlinearities due to local spots where the superconductor is driven normal. Also quasiparticle heating was described, but neglected usually due to the relatively low heat resistances of high T_c superconductors [5], [7], which cannot set up a significant temperature gradient between the electron system and the phonon system.

In this paper we describe a nonlinear effect in superconducting resonators due to the temperature-dependent readout power dissipated in the resonator and the thermal resistance due to the limited electron-phonon coupling. We present simulations showing that these two processes together give rise to multiple temperature states of the quasiparticle system when solving the heat balance equation. These temperature states manifest themselves as switching, and hysteresis, in the resonance curve. The effect of bistability due to different solutions of the heat balance equation was described earlier [8], but in the context of local instabilities, switching around T_c . We note that other nonlinear effects can still be present in superconducting resonators, but the temperature state switching we describe here is likely to be dominant at low temperatures, and does not necessarily involve hot spots.

II. THEORY

The microscopic picture of the electrodynamic response of a superconductor was developed by Mattis and Bardeen [9]. The complex conductivity $\sigma = \sigma_1 - i\sigma_2$ describes the response of both Cooper pairs and quasiparticles to an applied electric field. The surface impedance of a superconductor can be calculated from the complex conductivity. For arbitrary thicknesses t , the surface impedance Z_s in the dirty limit is given by [10]

$$Z_s = \sqrt{\frac{i\mu_0\omega}{\sigma}} \coth(\sqrt{i\omega\mu_0\sigma}t), \quad (1)$$

where ω is the free space angular frequency, μ_0 the permeability of free space and σ the complex conductivity.

A quarter wave resonator consists of a shorted piece of transmission line. The input impedance for a shorted

transmission line Z_{line} is given by

$$\begin{aligned} Z_{line} &= Z_0 \tanh \gamma l = Z_0 \tanh(\alpha + i\beta)l \\ &= Z_0 \tanh\left(\frac{\beta}{2Q_i} + i\beta\right)l, \end{aligned} \quad (2)$$

where Z_0 is the characteristic impedance of the line, γ the propagation constant of the line and l the length of the line. To calculate the impedance of a superconducting microstrip line we follow the analysis by Yassin and Withington [11]. We leave out the very details of the specific calculations. For an ideal line $\alpha = 0$, so that at resonance when $l = \lambda/4$ the input impedance $Z_{line} \rightarrow \infty$. For a non-ideal line, we can define an internal quality factor $Q_i = \frac{\beta}{2\alpha}$, describing the losses in the transmission line. The ideal line case corresponds to an infinite Q_i .

To couple electromagnetic energy into the resonator, a small gap is introduced between the open end of the quarterwave resonator and the feedline. The capacitance of this gap loads the resonator. The impedance looking into the capacitance becomes

$$Z_{in} = \frac{1}{i\omega C_g} + Z_0 \tanh \gamma l, \quad (3)$$

where C_g is the capacitance of the gap, and the second term is the input impedance of the transmission line, taken from Equation 2.

In the case of a parallel circuit, the coupler can be seen as a 3 port system. Port 1 and port 2 are the left and right side of the feedline, and port 3 is at the resonator waveguide just under the coupler. What is typically measured is the transmission from port 1 to port 2, given by the transmission function or forward scattering matrix element S_{21} , which is given by

$$S_{21} = \frac{2}{2 + Z_0/Z_{in}}, \quad (4)$$

where Z_0 is again the impedance of the feedline and Z_{in} the impedance looking into the coupling capacitor as given by Equation 3. S_{21} can also be written in terms of its amplitude $|S_{21}|$ and phase θ by $|S_{21}|e^{i\theta}$, and the power transmission is given by $|S_{21}|^2$. The quality factor of the resonator can be defined as $1/Q = 1/Q_c + 1/Q_i$, where Q_c is the coupling quality factor.

A. Power dissipation

Although the resonator is made of a superconducting material, it has a small resistance and therefore dissipates power. The internal quality factor Q_i is a measure for the resistive losses in the resonator, which should decrease exponentially with decreasing temperature. However measurements show that the internal quality factor always saturates at values around 10^6 at $T/T_c \approx 0.2$, which means an additional loss. The source of this loss can be excess quasiparticles or loss at the surface or in the dielectric, but is not exactly known [12], [13]. To make a realistic estimate of the dissipated power we take this saturation into account by modifying the internal quality factor in Equation 2 in the following way

$$\frac{1}{Q_i} = \frac{1}{Q_{i,MB}} + \frac{1}{Q_{sat}}, \quad (5)$$

TABLE I
PARAMETERS OF A SIMULATED MICROSTRIP RESONATOR.

Parameter	Symbol	Value
Strip length	l	4 mm
Strip width	w	3 μm
Film thickness	t	200 nm
Dielectric height	h	200 nm
Gap capacitance	C_g	5 fF
Relative permittivity of dielectric	ϵ_r	11
Feedline impedance	Z_0	20 Ω

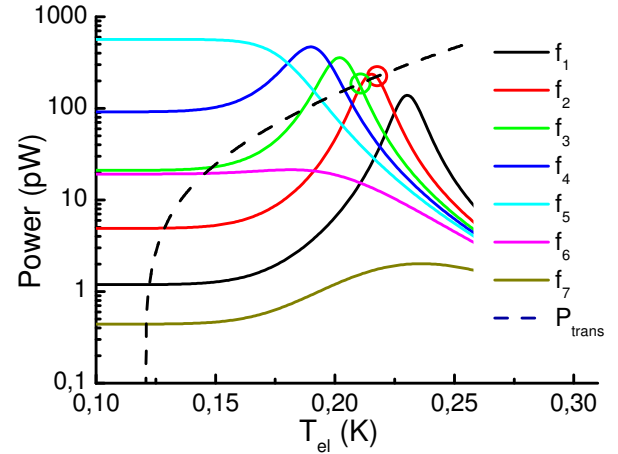


Fig. 1. Dissipated power in an Al microstripline resonator as a function of temperature for different readout frequencies. The readout power is -60 dBm. The dashed line shows the transported power due to electron-phonon coupling as a function of temperature according to $P_{trans} = -V\Sigma(T_e^5 - T_{ph}^5)$, for a phonon temperature of 120 mK.

where Q_{sat} is the saturation quality factor and $Q_{i,MB}$ the quality factor following the Mattis-Bardeen equations. In the calculations presented here we assume the additional loss to be due to quasiparticles. This is reasonable since we are interested in high readout power levels while dielectric losses saturate at a relatively low power level [13].

The dissipated power depends on how much power is coupled into the resonator, and therefore peaks at the resonance frequency. The resonance frequency is temperature dependent, and therefore the (peak in the) dissipated power is temperature dependent. Equally well we can define a resonance temperature for a particular frequency. The dissipated power is calculated for an Al microstrip resonator as a function of temperature and plotted in Figure 1 for different frequencies. The geometry properties are listed in Table I and material properties are $N_0V = 0.17$, $T_D = 420$ K and $\rho = 2.4 \mu\Omega\text{cm}$ [14]. The readout power is 2 nW (-57 dBm) and the bath temperature 120 mK.

We observe that the resonance temperature is lower for higher frequencies as expected. At the highest frequencies a plateau is reached where the zero-temperature resonance frequency is approached and the saturation in the quality factor (Eq. 5) comes into play.

B. Heat transport

The resistance that causes the energy dissipation in the resonator is due to quasiparticles. When energy is dissipated into the quasiparticles, the quasiparticle system heats up and will transfer energy to the colder phonon system, and from the phonon system of the superconducting film to the phonon system of the substrate. The energy transport from electrons to phonons can be described for a metal by a power law [15]:

$$P_{e-ph} = V\Sigma(T_e^5 - T_{ph}^5), \quad (6)$$

where T_e is the electron temperature, T_{ph} the phonon temperature and V the volume where the power is dissipated. Σ is a material constant with a value of $\Sigma = 0.2 \times 10^9 \text{ W m}^{-3}\text{K}^{-5}$ for Al, measured in a Coulomb-blockade electrometer [16]. The volume can be calculated by $V = wtl$, where w and l are the width and length of the microstrip and t is the thickness of the film. For an Al microstripline with dimensions as given in Table I we get $V\Sigma = 480 \text{ nW K}^{-5}$. In Figure 1, the power transported by electron-phonon coupling as a function of temperature is plotted as the dashed line, for a phonon temperature of 120 mK.

In calculating the transported power, we assumed implicitly that electron-phonon coupling is the limiting heat transport mechanism. Another transport limiting heat resistance can be the Kapitza coupling between the film and the substrate of the resonator. The Kapitza coupling can also be described by a power law

$$P_{Kap} = A\Sigma_{Kap}(T^4 - T_{bath}^4), \quad (7)$$

where $A = wl$ is the area of the microstrip and Σ_{Kap} a material parameter. From Ref. [17] we estimate Σ_{Kap} to be $850 \text{ Wm}^{-2}\text{K}^{-4}$ and $A\Sigma_{Kap} = 10 \mu\text{WK}^{-4}$ and therefore assume electron-phonon coupling being the limiting heat transport mechanism.

III. SIMULATIONS

Power is dissipated by the readout signal into the quasiparticle system of the superconducting film. This will increase the effective quasiparticle temperature. The phonon temperature of the film will be lower, so a temperature difference between the phonon- and electron system is set up, dependent on the strength of the electron-phonon coupling. From a steady state heat flow, the temperature of the electron system can be calculated by equating the dissipated power and the transported power. Finding the steady-state temperature for different readout frequencies and power levels is analogous to calculating the intersections of the dissipated power curve with the transported power curve in Figure 1. Steady state temperatures are calculated for every frequency using a root-finding algorithm which uses the steady state temperature of the previous frequency as an initial guess.

In Figure 2 the steady state temperature, and the resonator response of the same Al resonator, are plotted as a function of frequency for a set of readout powers. We observe that below 10 pW, the temperature rise is small and the resonance curve shows a deep symmetrical resonance. At 100 pW the electron temperature at resonance already rises 30 mK

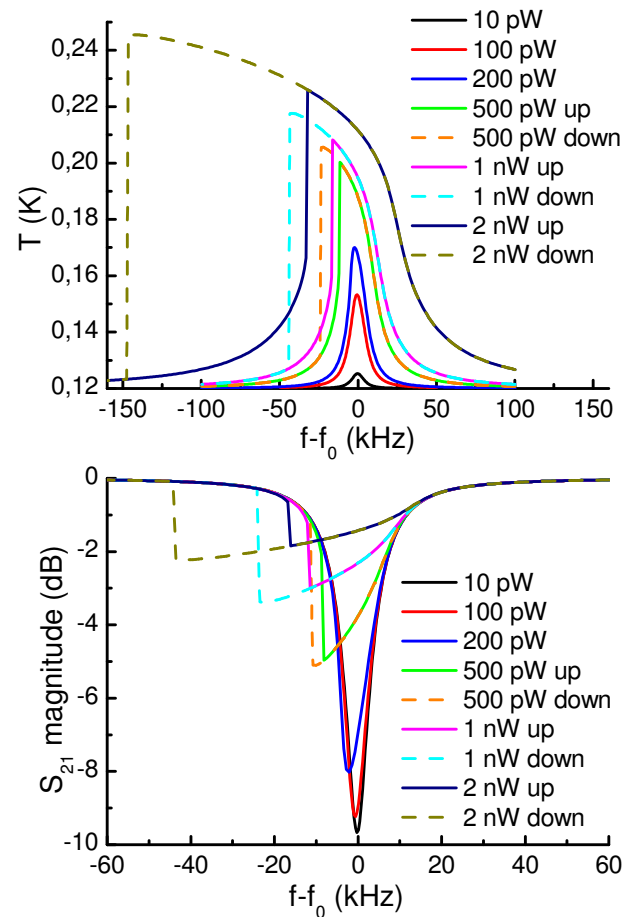


Fig. 2. Steady state temperature of the electron system (a) and the corresponding resonator response curve (b) for an Al microstripline resonator as a function of frequency for different readout power levels.

above the phonon temperature, making the resonance curve a bit less pronounced and introducing a frequency shift. Above 200 pW the resonance curve becomes asymmetrical as a result of a 50 mK temperature rise and at 500 pW there is clear switching with hysteresis. For even higher powers, the operating temperature rises and the amount of hysteresis increases.

IV. EXPERIMENT

A 100 nm thick Al film was sputter deposited on a R-plane sapphire substrate under ultra high vacuum. The critical temperature of the film T_c is 1.228 K, the low temperature resistivity ρ was $0.63 \mu\Omega\text{cm}$ and the residual resistance ratio was 5.2. The resonator pattern was created using wet etching. A coplanar waveguide (CPW) resonator was used in the experiment, and therefore we can only make a qualitative comparison with the presented simulations. The chip was cooled in a cryostat with an adiabatic demagnetization refrigerator to a bath temperature of 81 mK. The complex transmission S_{21} of the chip was measured using a vector network analyzer.

The S_{21} magnitude is plotted as a function of frequency in Figure 3 for a set of readout power levels. For power levels below -81 dBm the response stays the same, except for

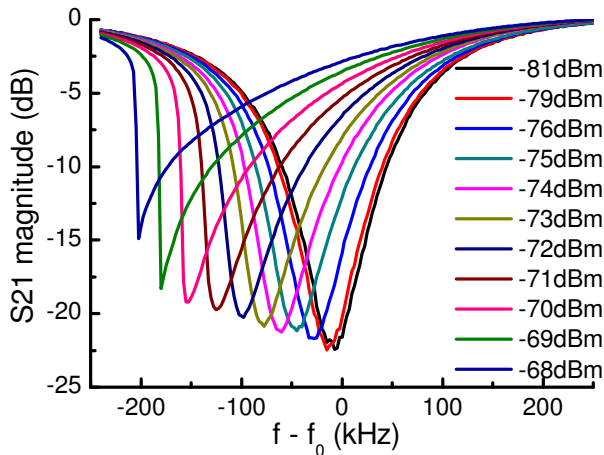


Fig. 3. Measured resonances curves of an Al coplanar waveguide resonator for different readout power levels. The bath temperature was 81 mK and $f_0 = 4.55929$ GHz.

the relative increase of noise. We observe that the resonance frequency decreases for increasing power, which is a sign of heating, because the resonance frequency shifts in the same way if the bath temperature is increased. Asymmetry in the resonance curve appears for a power of -75 dBm and true switching from -69 dBm, which is of the same order of magnitude as for the simulations in Figure 2.

V. COMPARISON ON INTERNAL POWER

The most common way to compare the power handling of resonators is comparing them on internal power, which takes into account the quality factor dependent coupling of the readout signal to the resonator. The internal power, the power of the travelling wave inside the resonator, is given by

$$P_{internal} = P_{readout} \frac{2 Q^2 Z_{feedline}}{\pi Q_c Z_{resonator}}, \quad (8)$$

where $Z_{feedline}$ and $Z_{resonator}$ are the impedances of the feedline and the resonator. Using Equation 8 combined with the simulations presented in Section III we calculate an internal power of -22 dBm where the response becomes nonlinear. From the experimental data presented in Section IV we obtain a limiting internal power value of -30 dBm, which is a value commonly measured in Al KIDs of this thickness [18]. It is only possible to compare the internal power of devices just before the resonance curve becomes asymmetric since the quality factor cannot be obtained from a highly nonlinear resonance curve.

VI. DISCUSSION

Experimental values for the limiting internal power before the resonator response becomes nonlinear are within an order of magnitude with the simulated values as presented above. This shows that thermal switching is a mechanism that is very likely to be present in resonators consisting of a low temperature superconducting film. However, there are other

mechanisms that can be responsible for nonlinear behaviour. More detailed experiments are needed to explore the nonlinear effects that are observed experimentally in relation with the proposed thermal effect. Additional simulations are underway to compare the predictions about the limit to the internal power to experimental values with varying film thicknesses and film properties.

The assumed electron-phonon coupling is taken for a metal in the normal state and we believe that it could very well be an order of magnitude weaker for a superconductor, especially at temperatures much lower than T_c . This would bring the simulated power values where nonlinear behaviour starts remarkably close to the experimental data. We also implicitly assumed that the losses that determine the internal resonator quality factor are fully due to quasiparticles. Although there are also known dielectric losses, this assumption is better justified at higher readout powers, which is the regime we are operating in.

The two stable temperature states, with one unstable state in between, suggest that rapid switching between those three states can give excess noise. This could happen when the temperature difference between these states is small. Experiments show that as soon as the resonator is driven nonlinear, the noise increases quite significantly. However, more involved simulations and experiments are needed to investigate if the temperature states and the measured excess noise are correlated.

VII. CONCLUSION

We modelled the heat dissipation and heat transport in superconducting thin film resonators. We solved the heat balance, given by the temperature and frequency dependent microwave readout power dissipation together with limited electron-phonon transport described by a power law. For certain readout power levels this leads to multiple solutions to the steady state temperature giving hysteretic two state switching in the resonance curve. Simulated resonance curves as a function of power show qualitatively the same behaviour as experimentally observed resonance curves. With some refinements, the model could explain the microwave power handling in KIDs and could lead to an improvement of their performance.

REFERENCES

- [1] P. K. Day, H. G. LeDuc, B. A. Mazin, A. Vayonakis, and J. Zmuidzinas, "A broadband superconducting detector suitable for use in large arrays," *Nature*, vol. 425, p. 817, 2003.
- [2] J. Gao, M. D. J. M. Martinis, A. Vayonakis, J. Zmuidzinas, B. Sadoulet, B. A. Mazin, P. K. Day, and H. G. LeDuc, "A semiempirical model for two-level system noise in superconducting microresonators," *Appl. Phys. Lett.*, vol. 92, p. 212504, 2008.
- [3] R. Barends, H. L. Hortensius, T. Zijlstra, J. J. A. Baselmans, S. J. C. Yates, J. R. Gao, and T. M. Klapwijk, "Noise in nbn, al and ta superconducting resonators on silicon and sapphire substrates," *IEEE Trans. on Appl. Supercond.*, vol. 19, p. 936, 2009.
- [4] B. Abdo, E. Sergev, O. Shtempluch, and E. Buks, "Escape rate of metastable states in a driven nbn superconducting microwave resonator," *J. Appl. Phys.*, vol. 101, p. 083909, 2007.
- [5] C. C. Chin, D. E. Oates, G. Dresselhaus, and M. S. Dresselhaus, "Nonlinear electrodynamics of superconducting nbn and nb thin films at microwave frequencies," *Phys. Rev. B*, vol. 45, p. 4788, 1992.

- [6] M. A. Golosovsky, H. J. Snortland, and M. R. Beasley, "Nonlinear microwave properties of superconducting nb microstrip resonators," *Phys. Rev. B*, vol. 51, p. 6462, 1995.
- [7] P. Lahl and R. Wördenweber, "Fundamental microwave-power-limiting mechanism of epitaxial high-temperature superconducting thin-film devices," *J. Appl. Phys.*, vol. 97, p. 113911, 1995.
- [8] A. Gurevich and R. Mints, "Self-heating in normal metals and superconductors," *Rev. Mod. Phys.*, vol. 59, p. 941, 1987.
- [9] D. C. Mattis and J. Bardeen, "Theory of the anomalous skin effect in normal and superconducting metals," *Phys. Rev.*, vol. 111, p. 412, 1958.
- [10] R. L. Kautz, "Picosecond pulses on superconducting striplines," *J. Appl. Phys.*, vol. 49, p. 308, 1978.
- [11] G. Yassin and S. Withington, "Electromagnetic models for superconducting millimetre-wave and sub-millimetre-wave microstrip transmission lines," *J. Phys. D: Appl. Phys.*, vol. 28, p. 1983, 1995.
- [12] R. Barends, J. J. A. Baselmans, J. N. Hovenier, J. R. Gao, S. J. C. Yates, T. M. Klapwijk, and H. F. C. Hoevers, "Niobium and tantalum high-q resonators for photon detectors," *IEEE Trans. on Appl. Supercond.*, vol. 17, p. 263, 2007.
- [13] J. Gao, M. Daal, A. Vayonakis, S. Kumar, J. Zmuidzinas, B. Sadoulet, B. A. Mazin, P. K. Day, and H. G. Leduc, "Experimental evidence for a surface distribution of two-level systems in superconducting lithographed microwave resonators," *Appl. Phys. Lett.*, vol. 92, p. 152505, 2008.
- [14] R. D. Parks, *Superconductivity*, 1st ed. Marcel Dekker Inc. New York, 1969, vol. 2.
- [15] F. C. Wellstood, C. Urbina, and J. Clarke, "Hot-electron effects in metals," *Phys. Rev. B*, vol. 49, p. 9, 1994.
- [16] R. L. Kautz, G. Zimmerli, and J. M. Martinis, "Self-heating in the coulomb-blockade electrometer," *J. Appl. Phys.*, vol. 73, p. 2386, 1993.
- [17] E. T. Swartz and P. O. Pohl, "Thermal boundary resistance," *Rev. Mod. Phys.*, vol. 61, p. 605, 1989.
- [18] J. J. A. Baselmans, "Optimizing kinetic inductance detectors for low background applications," 2nd Workshop on the Physics and Applications of Superconducting Microresonators, June 19-20, 2008.

Session S4: Optics and Waveguides

A THz FTS for Site Testing at Dome A

Sheng-Cai Shi^{*}, S. Paine[†], Q.J. Yao^{*}, X.X. Li^{*}, X.G. Zhang^{*}, Z.H. Lin^{*}, K.M. Zhou^{*}, Q.G. Huang^{*}, H. Matsuo[#], J. Yang^{*}, Q.Z. Zhang[†]

^{*}Purple Mountain Observatory
Email: scshi@mail.pmo.ac.cn

[†]Smithsonian Astrophysical Observatory
Email: spaine@cfa.harvard.edu

[#]National Astronomical Observatory of Japan
Email: h.matsuo@nao.ac.jp

Abstract

With an altitude of 4093m and temperatures as low as -80 celsius degree, Dome A in Antarctic is a very attractive site for astronomical observations, especially at frequencies beyond 1THz. Preliminary observation results by a radiometer at 661GHz, which was brought to Dome A in 2008 by Chinese Antarctic expedition team, have demonstrated that Dome A has the lowest PWV among those good THz sites (ALMA site, South Pole and Dome C, for example) on the earth which have been investigated. To have better understanding on the atmospheric condition at Dome A, we have developed a broadband THz FTS to be deployed to the site in Jan. 2010. The FTS will measure atmospheric emission in the frequency range of 0.75-15THz (split in two bands), from which atmospheric transmission is derived using an atmospheric propagation model. Broad spectral coverage helps make this derivation more accurate—this is particularly important at Dome A, where the extremely cold temperatures lie well outside the tested range of water vapor continuum models. The FTS mainly consists of a Martin-Puplett interferometer subsystem in rapid scan mode, which is fabricated by BlueSky and QMC, an outdoor subsystem for atmospheric signal coupling and calibration, and a data acquisition subsystem. Two room-temperature DLATGS detectors with respective filters (short- and long-wavelength ones) are employed since the FTS is designed for unattended and long-duration operation. The details of the FTS and preliminary measurement results will be presented.

Electromagnetic Simulations of the Partially Coherent Optical Behaviour of Resistive Film TES Detectors

Christopher N. Thomas^{*†} and Stafford Withington^{*}

^{*}*Detector and Optical Physics Group, Cavendish Laboratory, JJ Thompson Avenue, Cambridge, CB3 0HE*

[†]Contact: c.thomas@mrao.cam.ac.uk

Abstract— Resistive films are a commonly used absorber for free-space coupled TES detectors at sub-mm and far-infrared wavelengths. A formalism is presented for calculating the full partially coherent optical behaviour of such devices in a rigorous way. The scheme is based on a boundary condition on the resistive film, which takes into account the film's finite surface impedance and allows the incident field to be written in terms of the induced current. A Method-of-Moments-like (MoM) approach is then used to invert this relation to give the current in terms of the applied field. Rather than use a set of 'testing functions' as in traditional MoM approaches, a set of dual basis functions is used, leading to a particularly elegant formulation. Using the equation for ohmic power dissipation, it can then be shown the power absorbed by the detector is given by the total contraction of the coherence dyadic of the incident field with a second dyadic field, which will be referred to as the Detector Response Function (DRF). The DRF completely describes the optical behaviour of the detector. The scheme is easily applied to the modelling of arrays of films, allowing cross-talk between pixels to be investigated. We will discuss the details of our method, and present results for the intensity and polarisation response of resistive film TESs to plane wave radiation. In particular, we will concentrate on how the film's dimensions and surface impedance affect its behaviour.

I. INTRODUCTION

A common architecture for free-space-coupled THz detectors is the Transition Edge Sensor (TES), which comprises of a rectangular resistive film and superconducting bilayer on a micro-machined Si_3N_4 island. In operation, the bilayer is biased on its normal-superconducting transition and the island's temperature is kept constant by the resulting electro-thermal feedback. Incident radiation induces currents on the film, which dissipate power. The amount of power dissipated can then be measured from the changes in bilayer current needed to maintain island temperature, and this provides a measure of the power flux in the incident radiation.

To fully understand the optical behaviour of such devices, it is vital to understand the relationship between the incident electromagnetic field and the surface currents. The problem is complicated by the possibility of exciting several different current distributions incoherently on the same film. If this is the case the film will be incoherently sensitive to the power in a particular set of modes, with the responsivity of the device varying between the modes. It can be shown that the partially coherent optical behavior of such multi-moded detectors can be described by a two point dyadic response function [1],

which we will call the detector response function (DRF). The detector output is given by the total contraction, over some reference surface, of the DRF with the coherence dyadic of the incident radiation.

We have calculated the DRF for resistive film TES detectors rigorously for the first time using a new scheme described in [2]. The scheme is based on a boundary condition on the film, which takes into account the film's finite surface impedance and allows the incident field to be written in terms of the induced current. A Method-of-Moments-like (MoM) approach is then used to invert this relation to give the current in terms of the applied field, and subsequently this can be used to find the DRF from the equation for ohmic power dissipation. Rather than use a set of 'testing functions' as in MoM approaches, a set of dual basis functions is used, leading to a particularly elegant formulation. The scheme is easily applied to the modelling of arrays of films, allowing cross-talk between pixels to be investigated. We will discuss the details of our method, and present results for the intensity and polarisation response of resistive film TESs to plane wave radiation. In particular, we will concentrate on how the film's dimensions and surface impedance affect its behaviour.

The formalism that will be developed is also relevant for understanding the optical behaviour of Kinetic Inductance Detectors (KIDs). A KID is typically comprised of a superconducting microstrip circuit, which is resonant at microwave frequencies, connected to an optical absorber. The device is engineered so that an incident photon generates excess quasiparticles in the superconducting circuit by breaking Cooper pairs. The excess quasiparticles alter the electrical properties of the circuit, and the incident power flux is determined by probing the corresponding changes in the circuit's resonant behaviour. At sub-mm and far-infrared wavelengths a planar-antenna-like structure is commonly employed as the absorber. Quasiparticles are generated by the power dissipated by lossy currents flowing on the antenna. Instead of being lumped at the feed, the antenna load in these absorbers is, in effect, distributed over the entire structure. Consequently, they cannot be treated as conventional antennas, and full electromagnetic simulations must be used to determine the power absorbed. Antenna structures implemented as patterned thin films can be treated identically to the resistive film absorbers for TESs, and the methods outlined in this paper are directly applicable.

II. BASIC FORMALISM

The full formalism for the simulations has been discussed in detail by Withington[2]. This summary will concentrate on the analysis of a single film. The extension to arrays of films is straightforward, but leads to additional notational complexity. It will be discussed briefly at the end of the section, although interested readers should consult the original paper for the complete analysis[2].

In the derivation that follows the incident field will assumed to be temporally stationary, allowing the power absorbed at different wavelengths to be treated independently. Any vector fields introduced should be assumed to be the analytic signal representation of the particular frequency component of the field being considered. The values for the power dissipated represent the power dissipated *per unit bandwidth* at the radiation frequency. However, as we will only consider narrow band illumination and so they may be treated as the total power absorbed by the film.

A. Determining the induced currents

To determine the power absorbed by the resistive film in the TES, it is first necessary to deduce the currents which the incident field excites upon the thin-film absorber. Consider a thin resistive film occupying the region \mathcal{S} of the plane $z = z_0$. Let \mathbf{r}_t denote a point (x, y) on the film's surface, with the absolute position of the point in space given by $\mathbf{r} = \mathbf{r}_t + z_0\hat{\mathbf{z}}$. For simplicity, we will assume that the surface impedance of the film, in Ω , is given by the scalar function $Z_s(\mathbf{r}_t)$. Directional anisotropies in the surface impedance may be included by elevating $Z_s(\mathbf{r}_t)$ to a dyadic function $\tilde{\tilde{Z}}_s(\mathbf{r}_t)$, and non-local behaviour by elevating it to a two point function $\tilde{\tilde{Z}}_s(\mathbf{r}_{t1}, \mathbf{r}_{t2})$.

The incident electric field \mathbf{E}_I will excite surface currents on the film, and these currents in turn produce a scattered electric field \mathbf{E}_S . The current density associated with the induced currents is off the form

$$\mathbf{J}(\mathbf{r}_t, z) = \mathbf{J}_S(\mathbf{r}_t)\delta(z - z_0), \quad (1)$$

where we shall refer to \mathbf{J}_S as the surface current density. As the currents are confined to flow on the surface of the film, \mathbf{J}_S is tangential to the film surface at all points, and as a surface current density it has units Am^{-1} . Following Senior[3], we assume that over the surface of the film, the total electric field –incident plus scattered– and the surface current density satisfy the relation

$$\left[\tilde{\tilde{I}} - \hat{\mathbf{z}}\hat{\mathbf{z}}\right] \cdot \left[\mathbf{E}_I(\mathbf{r}_{t1}, z_0) + \mathbf{E}_S(\mathbf{r}_{t1}, z_0)\right] = Z_s(\mathbf{r}_{t1})\mathbf{J}_S(\mathbf{r}_{t1}). \quad (2)$$

The dyadic acting on \mathbf{E}_I and \mathbf{E}_S simply picks out the component tangential to the film. (2) is essentially the well-known conductivity equation for the current density applied to surface currents, and is used widely in the electromagnetic-modelling community as a starting boundary condition.

We assume now that in the space containing the film there exists a relationship between \mathbf{E}_S and \mathbf{J} in terms of a Green's dyadic of the form

$$\mathbf{E}_S(\mathbf{r}) = \int d^3\mathbf{r}' \tilde{\tilde{G}}(\mathbf{r}; \mathbf{r}') \cdot \mathbf{J}(\mathbf{r}'). \quad (3)$$

Substituting (3) and (1) into (2) gives

$$\begin{aligned} \left[\tilde{\tilde{I}} - \hat{\mathbf{z}}\hat{\mathbf{z}}\right] \cdot \mathbf{E}_I(\mathbf{r}_{t1}, z_0) &= Z_S(\mathbf{r}_{t1})\mathbf{J}_S(\mathbf{r}_{t1}) - \\ \left[\tilde{\tilde{I}} - \hat{\mathbf{z}}\hat{\mathbf{z}}\right] \cdot \int d^2\mathbf{r}_{t2} \tilde{\tilde{G}}(\mathbf{r}_{t1}, z_0; \mathbf{r}_{t2}, z_0) \cdot \mathbf{J}_S(\mathbf{r}_{t2}, z_0). \end{aligned} \quad (4)$$

This equation gives the tangential component of the incident field if the surface current is known, and must be inverted to give the current from the incident field. This is done by writing \mathbf{J}_S and $\left[\tilde{\tilde{I}} - \hat{\mathbf{z}}\hat{\mathbf{z}}\right] \cdot \mathbf{E}_I$ in decomposed form,

$$\mathbf{J}_S(\mathbf{r}_t) = \sum_n \alpha_n \mathbf{U}_n(\mathbf{r}_t) \quad (5)$$

and

$$\left[\tilde{\tilde{I}} - \hat{\mathbf{z}}\hat{\mathbf{z}}\right] \cdot \mathbf{E}_I(\mathbf{r}_t, z_0) = \sum_m \beta_m \mathbf{V}_m(\mathbf{r}_t). \quad (6)$$

The basis functions set used for the field and the current need not be the same, and the sets need not be individually orthogonal. Basis functions can be defined over a sub-region of the film (local) or defined over the entire film (global). Localised basis functions are useful for first determining the surface current distributions that can be excited on a film. For array simulations, where it is beneficial to use small basis sets, they may then be replaced with a reduced set of global basis functions chosen to best span the current distributions observed. Substituting (5) and (6) in (4) yields

$$\begin{aligned} \sum_m \beta_m \mathbf{V}_m(\mathbf{r}_{t1}) &= \sum_n \alpha_n \left(Z_s(\mathbf{r}_{t1})\mathbf{U}_n(\mathbf{r}_{t1}) - \right. \\ \left. \left[\tilde{\tilde{I}} - \hat{\mathbf{z}}\hat{\mathbf{z}}\right] \cdot \int d^2\mathbf{r}_{t2} \tilde{\tilde{G}}(\mathbf{r}_{t1}, z_0; \mathbf{r}_{t2}, z_0) \cdot \mathbf{U}_n(\mathbf{r}_{t2}) \right). \end{aligned} \quad (7)$$

In a traditional MoM approach[4], a set of so-called weighting and testing functions would now be introduced. The inner product of these functions with (7) is would then be taken to generate a matrix equation. Instead we will make use of the duals, $\{\tilde{\tilde{\mathbf{V}}}_m(\mathbf{r}_t)\}$, of the field basis functions, $\{\mathbf{V}_m(\mathbf{r}_t)\}$. The dual basis set is defined such that

$$\int d^2\mathbf{r}_t \tilde{\tilde{\mathbf{V}}}_m^*(\mathbf{r}_t) \cdot \mathbf{V}_n(\mathbf{r}_t) = \delta_{mn}, \quad (8)$$

and its explicit calculation is discussed in [5]. Left multiplying (7) by the conjugate of each dual basis function, then integrating, results in the matrix equation

$$\boldsymbol{\beta} = (\mathbf{Z} - \mathbf{G}) \cdot \boldsymbol{\alpha}, \quad (9)$$

where

$$Z_{mn} = \int d^2\mathbf{r}_t Z_S(\mathbf{r}_t) \tilde{\tilde{\mathbf{V}}}_m^*(\mathbf{r}_t) \cdot \mathbf{U}_n(\mathbf{r}_t), \quad (10)$$

and

$$G_{mn} = \int d^2\mathbf{r}_{t1} \int d^2\mathbf{r}_{t2} \tilde{\tilde{\mathbf{V}}}_m^*(\mathbf{r}_{t1}) \cdot \tilde{\tilde{G}}(\mathbf{r}_{t1}, z_0; \mathbf{r}_{t2}, z_0) \cdot \mathbf{U}_n(\mathbf{r}_{t2}). \quad (11)$$

Relation (2) has successfully been reduced to a matrix equation, and may be inverted by finding the pseudo inverse of the matrix on the left hand side. Letting, $\mathbf{M} = (\mathbf{Z} - \mathbf{G})^{-1}$, we have explicitly that

$$\boldsymbol{\alpha} = \mathbf{M} \cdot \boldsymbol{\beta}. \quad (12)$$

Using (6) and (8) it is straightforward to show that

$$\beta_m = \int d^2\mathbf{r}_t \tilde{\mathbf{V}}_m^*(\mathbf{r}_t) \cdot \mathbf{E}_I(\mathbf{r}_t, z), \quad (13)$$

This allows the decomposition coefficients for the incident field to be found, which may then be used with (12) and (5) to construct the induced current. Consequently once \mathbf{M} has been found for the particular film, we are able to calculate the current induced on it by any incident field at the relevant wavelength.

B. Determining the power dissipated in the absorbing film

Of principle interest to us is the total power P dissipated in the film, as it is to this that the TES as a whole is sensitive. The power dissipated by the currents is given by

$$P = \frac{1}{2} \int d^2\mathbf{r}_t \Re[Z_s(\mathbf{r}_t)] |\mathbf{J}_S(\mathbf{r}_t)|^2. \quad (14)$$

Substituting (5) into (14), we find that the P can be written in terms of the current decomposition coefficients as

$$P = \frac{1}{2} \boldsymbol{\alpha}^\dagger \cdot \mathbf{C} \cdot \boldsymbol{\alpha}, \quad (15)$$

where

$$C_{mn} = \int d^2\mathbf{r}_t \Re[Z_S(\mathbf{r}_t)] \mathbf{U}_m^*(\mathbf{r}_t) \cdot \mathbf{U}_n(\mathbf{r}_t). \quad (16)$$

The expression for P in terms of the field decomposition coefficients follows logically using (12):

$$P = \frac{1}{2} \boldsymbol{\beta}^\dagger \cdot \mathbf{M}^\dagger \cdot \mathbf{C} \cdot \mathbf{M} \cdot \boldsymbol{\beta}. \quad (17)$$

The power absorbed can now be calculated for a given incident field.

C. The Detector Response Function (DRF)

A very powerful result can be obtained by substituting (13) into (17). Letting

$$\mathbf{D} = \frac{1}{2} \mathbf{M}^\dagger \cdot \mathbf{C} \cdot \mathbf{M}, \quad (18)$$

we obtain

$$P = \sum_m \sum_n \int d^2\mathbf{r}_{t1} \int d^2\mathbf{r}_{t2} D_{mn} \left(\tilde{\mathbf{V}}_m^*(\mathbf{r}_{t2}) \cdot \mathbf{E}_I(\mathbf{r}_{t2}, z) \right)^* \left(\tilde{\mathbf{V}}_n^*(\mathbf{r}_{t1}) \cdot \mathbf{E}_I(\mathbf{r}_{t1}, z) \right). \quad (19)$$

The kernel of this integral may be written in a more instructive form by adopting double dot notation for dyadics:

$$\begin{aligned} & \sum_m \sum_n D_{mn} \left(\tilde{\mathbf{V}}_m^*(\mathbf{r}_{t2}) \cdot \mathbf{E}_I(\mathbf{r}_{t2}, z) \right)^* \left(\tilde{\mathbf{V}}_n^*(\mathbf{r}_{t1}) \cdot \mathbf{E}_I(\mathbf{r}_{t1}, z) \right) \\ &= \left(\sum_m \sum_n D_{mn} \tilde{\mathbf{V}}_m(\mathbf{r}_{t2}) \tilde{\mathbf{V}}_n^*(\mathbf{r}_{t1}) \right) \cdot \left(\mathbf{E}_I(\mathbf{r}_{t1}, z) \mathbf{E}_I^*(\mathbf{r}_{t2}, z) \right). \end{aligned} \quad (20)$$

Using (20) and then taking the ensemble average of (19) gives

$$\langle P \rangle = \int d^2\mathbf{r}_{t1} \int d^2\mathbf{r}_{t2} \bar{\mathbf{D}}^\dagger(\mathbf{r}_{t1}; \mathbf{r}_{t2}) \cdot \cdot \bar{\bar{\mathbf{E}}}(\mathbf{r}_{t1}; \mathbf{r}_{t2}), \quad (21)$$

where

$$\bar{\bar{\mathbf{E}}}(\mathbf{r}_{t1}; \mathbf{r}_{t2}) = \left\langle \mathbf{E}_I(\mathbf{r}_{t1}, z) \mathbf{E}_I^*(\mathbf{r}_{t2}, z) \right\rangle \quad (22)$$

is the correlation dyadic of the incident field, or EFC, and

$$\bar{\bar{\mathbf{D}}}(\mathbf{r}_{t1}; \mathbf{r}_{t2}) = \sum_m \sum_n D_{mn} \tilde{\mathbf{V}}_m(\mathbf{r}_{t1}) \tilde{\mathbf{V}}_n^*(\mathbf{r}_{t2}). \quad (23)$$

is the Detector Response Function, or DRF.

Equation (21) completely describes the optical response of the detector to partially coherent fields[1], [6]. The relationship between the DRF and the detector is analogous to that between an antenna and its reception pattern. However, whereas the reception pattern of a classical antenna is a fully coherent field, the DRF is a partially coherent field. It describes the state of coherence of the incident field in which the detector is sensitive to power. The amount of power absorbed by the detector depends on how well the actual state of coherence of the field, described by the ECF, ‘overlaps’ with the desired state. (21) is simply the inner product between these two state vectors in an abstract space. Like a reception pattern, the DRF can be back-propagated through an optical system to determine the responsivity of the detector to power on a different reference surface. As a partially coherent field, the DRF admits a decomposition in terms of coherent modes. These coherent modes, which are called the natural modes of the detector, correspond to the modes of incident field in which the detector is incoherently sensitive to power.

D. Extension to arrays of films

For an array of films, the boundary condition (2) must be satisfied on each film. Again the incident field and surface current density on each film are in expanded in a set of basis functions. A matrix equation is set up as in section II-A, remembering to take into account the cross terms between basis functions on different films (which are coupled by $\bar{\bar{\mathbf{G}}}(\mathbf{r}_{t1}, \mathbf{r}_{t2})$). The process of finding the induced currents then follows in the same way as in the case of the single film. When calculating the power absorbed, the currents over a sub-set of films - ranging from an individual pixel to an array sub-cell - can be considered and the appropriate DRF for that sub-assembly found. This formulation takes into full account the electromagnetic cross talk between members of the array when considering the behaviour of single elements.

III. SIMULATION DETAILS

A. Arrangement considered

As a first application of the scheme outlined above, we have studied the optical properties of square films in free space as a function of the film size and surface impedance. The simulations represent the behaviour expected for a single resistive film TES bolometer isolated from any scattering structure. This is an unlikely configuration in reality, as such devices are typically employed in imaging arrays where, at minimum, there will be scattering from adjacent pixels. Simulations of full arrays are computationally intensive, and it is desirable for efficiency to use the smallest possible basis set on each film that can adequately describe the current distributions that

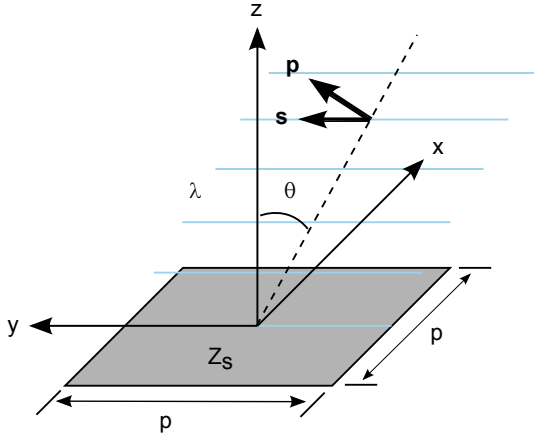


Fig. 1. Diagram showing the arrangement considered in the simulations and the notation used for the incident radiation.

may be excited. Simulations on a single detector are useful for determining these current distributions, and are therefore an important first step in the analysis of a full array. In addition, in a recent paper [7] we have proposed a simplified model for the electromagnetic behaviour of thin-film absorbers and investigated the resulting optical behaviour. Part of our motivation for performing simulations on single detectors was for comparison with this previous work. In particular, we were keen to determine the exact conditions under which the model is a good approximation to the actual behaviour. Finally, we are also interested in how the optical behaviour of the detector may be altered by patterning the absorbing film. This is best investigated initially without the additional complication of scattering from other structures.

Figure 1 illustrates the geometry considered. The film is assumed to a square of side length p lying at the centre of the plane $z = 0$. In subsequent sections we consider illuminating the film with a monochromatic plane wave of wavelength λ , and it is useful to consider the form the incident field takes. We restrict ourselves to waves whose direction of incidence is in the (x, z) plane, and will use θ to denote the angle the direction of travel makes with the positive z -direction. The functional form of the incident field over the film's surface is given by

$$\mathbf{E}(\mathbf{r}_t) = E_0 \exp[-ikx \sin \theta] \begin{cases} \cos \theta \hat{\mathbf{x}} - \sin \theta \hat{\mathbf{z}} & \text{p-polarised} \\ \hat{\mathbf{y}} & \text{s-polarised,} \end{cases} \quad (24)$$

where $k = 2\pi/\lambda$ and we adopted the normal p and s polarisation states. In the sections that follow we will concentrate on the optical behaviour of the film under these illumination conditions.

B. Implementation details

The film is assumed to be in free space, so the Green's dyadic $\bar{\bar{G}}(\mathbf{r}_{t1}, z_1; \mathbf{r}_{t2}, z_2)$ for the problem is

$$\bar{\bar{G}}(\mathbf{r}_{t1}, z_1; \mathbf{r}_{t2}, z_2) = i\omega\mu_0 \left(\bar{\bar{I}} + \frac{1}{k^2} \nabla_1 \nabla_1 \right) g(\mathbf{r}_{t1}, z_1; \mathbf{r}_{t2}, z_2), \quad (25)$$

with

$$g(\mathbf{r}_{t1}, z_1; \mathbf{r}_{t2}, z_2) = \frac{\exp \left[ik \sqrt{|\mathbf{r}_{t1} - \mathbf{r}_{t2}|^2 + (z_1 - z_2)^2} \right]}{4\pi \sqrt{|\mathbf{r}_{t1} - \mathbf{r}_{t2}|^2 + (z_1 - z_2)^2}}. \quad (26)$$

It is immediately obvious that the Green's dyadic is singular when both $\mathbf{r}_{t1} = \mathbf{r}_{t2}$ and $z_1 = z_2$, and that this complicates the numerical evaluation of the integrals in (11). We are free to choose to the current basis functions and field dual functions, and by careful choice we can to some extent alleviate these numerical problems. In our simulations we employed the same set of Rao, Wilson and Glisson (RWG) basis functions[8] defined on a square mesh for both sets for both functions. RWG basis functions are used extensively in the MoM community, and the evaluation the integral of their product with the free space Green's dyadic is well documented. The approach taken is to break the kernel of the integrals up into a singular and non-singular part, a procedure called extracting the singularity. The non-singular part is then handled numerically, whilst the singular part when RWG basis functions are used is simple enough that it may be evaluated analytically[9]. Using the same set of basis functions for the current basis and field duals also has the advantage $Z = C$, reducing the computations that must be performed.

C. Simple model for the excited current

Full electromagnetic simulations may be to cumbersome for some design problems. In these circumstances it is useful to have a simpler model for the film's behaviour, and to know the regimes in which its use is valid. As a first approximation to the full behaviour, the non-local response introduced by the scattered field can be ignored. The surfaced current, $\mathbf{J}_S(\mathbf{r}_t)$, induced at a point on the film then depends only on the incident field, $\mathbf{E}_I(\mathbf{r}_t)$, at that point. Naively, we might then assume that $\mathbf{J}_S(\mathbf{r}_t) \approx \mathbf{E}_I(\mathbf{r}_t)/Z_S(\mathbf{r}_t)$ will be a good model for the induced currents. However, it is unphysical as in the limit $Z_S \rightarrow 0$ the surface current density tends to infinity at all points.

For guidance we consider the analytically soluble problem of a plane wave incident normally on an infinite film. From the translational invariance of the problem, the wave must excite an infinite sheet current. It can be shown that the electric field radiated by an infinite current sheet lying in the plane $z = 0$ is given by

$$\mathbf{E}_S(z) = -\frac{Z_0}{2} \mathbf{J}_S \exp(ik|z|), \quad (27)$$

where Z_0 is the impedance of free space. Using (27) in (2) and rearranging gives

$$|\mathbf{J}_S| = \frac{|\mathbf{E}_I|}{Z_S + \frac{1}{2}Z_0}, \quad (28)$$

where the effect of scattering appears to be to increase the effective surface impedance seen on induction by $\frac{1}{2}Z_0$. Adopting this effective surface impedance as the proportionality constant, we have for our simple model

$$\mathbf{J}_S(\mathbf{r}_t) \approx \frac{1}{Z_S + \frac{1}{2}Z_0} \left(\bar{\bar{I}} - \hat{\mathbf{z}}\hat{\mathbf{z}} \right) \cdot \mathbf{E}_I(\mathbf{r}_t, z_0), \quad (29)$$

where the dyadic operator is there so the induced current only has components tangential to the surface. In the subsequent sections we shall compare this model with the simulation results to determine the limits of its application. The optical behaviour associated with this simple model is investigated in detail in [7].

IV. SIMULATION RESULTS

A. Current distributions excited by an *s*-polarised plane wave

In order to understand power absorption by the film, it is useful to first consider the spatial form of the induced currents. Figure 2 shows the current distribution induced on films of various size and surface impedance by an *s*-polarised plane wave incident from $\theta = 0^\circ$. Film size, p/λ , increases across the rows of the figure, and the surface impedance of the film, Z_s , down the its columns. In each plot the black line shows the current along the cut $(x, 0, 0)$, and the grey line the currents along the cut $(0, y, 0)$. For both cuts the magnitude of the dominant component J_y of the surface current is plotted, and it is normalised to the incident magnetic field intensity H to remove the dependence on incident field strength. For all the simulations, a 41×41 sub-domain mesh was used and convergence of the solution was checked. Where the approximate model (29) is valid, we expect the plots in fig. 2 to be straight lines at

$$\frac{|J_y|}{|H|} \approx \frac{2Z_0}{2Z_s + Z_0}. \quad (30)$$

The current distributions found for perfectly electrically conducting (PEC) films (top row of figure 2) are in agreement with those in the literature[8], providing validation of the code. Across the rows of figure 2, where $\frac{p}{\lambda}$ is increasing, the surface current distribution along both cuts are observed globally to flatten out. Flatten here is used to mean that the scale of any variation in $|J_y|$ decreases relative to the mean value. On local scales we see the development of standing wave like patterns in $|J_y|$, and these most likely result from the trapping of the scattered field between film edges. For fixed Z_s , as $\frac{p}{\lambda}$ is increased the mean current level is observed to remain approximately constant. However, this should not be taken as meaning the power absorbed will scale simply with the increased area. Remember that the local power dissipation scales with $|J_y|^2$, making P sensitive to the precise spatial current distribution. By the same principle, we see that in electrically small, low Z_s films, the edges are the regions of highest power dissipation. Down the columns of figure 2, where Z_s is increasing, the same flattening of the current distributions is observed. However, there is no accompanying development of fine scale structure and, for fixed $\frac{p}{\lambda}$, as Z_s is increased the mean current along each cut decreases.

Visually, the current distributions obtained agree best with the predictions of (29) when either $\frac{p}{\lambda}$ is larger than unity and/or Z_s is large compared with Z_0 . The numerical values for the current in these regimes are also in good agreement with the values expected from (30), which have been collated in table I. When Z_s is large, Z dominates the right-hand-side of (9). For a uniform impedance film we then have $M \approx Z_s l$, or

$ J_y / H_x $	Z_s/Z_0
0.00	2.00
0.50	1.00
1.00	0.67
2.00	0.40
10.0	0.10

TABLE I
VALUES OF $|J_y|/|H_x|$ AS A FUNCTION Z_s PREDICTED BY SIMPLE MODEL

$\mathbf{J}_S(\mathbf{r}_t) \approx \mathbf{E}_I(\mathbf{r}_t)/Z_s$. This is the same as (29) when $Z_s \gg Z_0$. Physically, when Z_s is high the induced currents are small so the scattered field is weak and can be ignored – this is the main assumption made in the simple model. When $\frac{p}{\lambda}$ is large, the edges only weakly effect the behaviour in the bulk of the film and it may essentially treated as being infinite in dimension. Since we used the case of an infinite film to guide our model, it is expected they will agree.

Figure 3 is the equivalent of figure 2 for a plane wave incident at angle $\theta = 90^\circ$, i.e. edge-on. The current distribution along the $(0, y, 0)$ cut is, in all cases, similar in shape to that observed for a normally incident wave. Along the $(0, x, 0)$ cut different behaviour is observed. When Z_s is less than Z_0 , in general the current distribution along $(0, x, 0)$ is peaked at the leading edge of the film, then decays exponentially in the direction of propagation of the wave across the film. This is the effect is a result of the currents on leading edge screening the bulk film. It means that for large, low Z_s , films the majority of the induced current is confined to a small strip near the edge when $\theta = 90^\circ$. This fact will become important in the next section when we discuss how the edge on absorption cross section scales with p .

Similar trends in the current distributions excited by the edge-incident wave are observed for increasing $\frac{p}{\lambda}$ and Z_s as for the normally-incident wave. One difference is that with Z_s fixed, the mean current now decreases as $\frac{p}{\lambda}$ increases due to the decay over the films surface. In the limit $\frac{p}{\lambda} > 1$ and $Z_s > Z_0$ the simulations for the edge incident wave are still in good numerical agreement with the simple model, even though it was formulated assuming a normally incident wave.

It is worth noting that since currents are excited on the film when an *s*-polarised wave is incident edge-on, power is dissipated and the TES is therefore be sensitive to radiation incident from edge-on. This is a fact which may not be immediately obvious, and is discussed in detail in the next sub-section. It has important implications for the stray-light sensitivity of thin film devices.

B. Effective area of the film as a function of θ and the polarisation

A useful measure of the ability of a film to extract power from the incident plane wave is the effective area, A_E . The effective area is ratio of the total power P dissipated in the film to the power flux in the incident wave:

$$A_E = \frac{2Z_0 P}{|E_0|^2}. \quad (31)$$

Obviously, A_E will be a function of both the direction of incidence and polarisation of the plane wave. Usually we plot

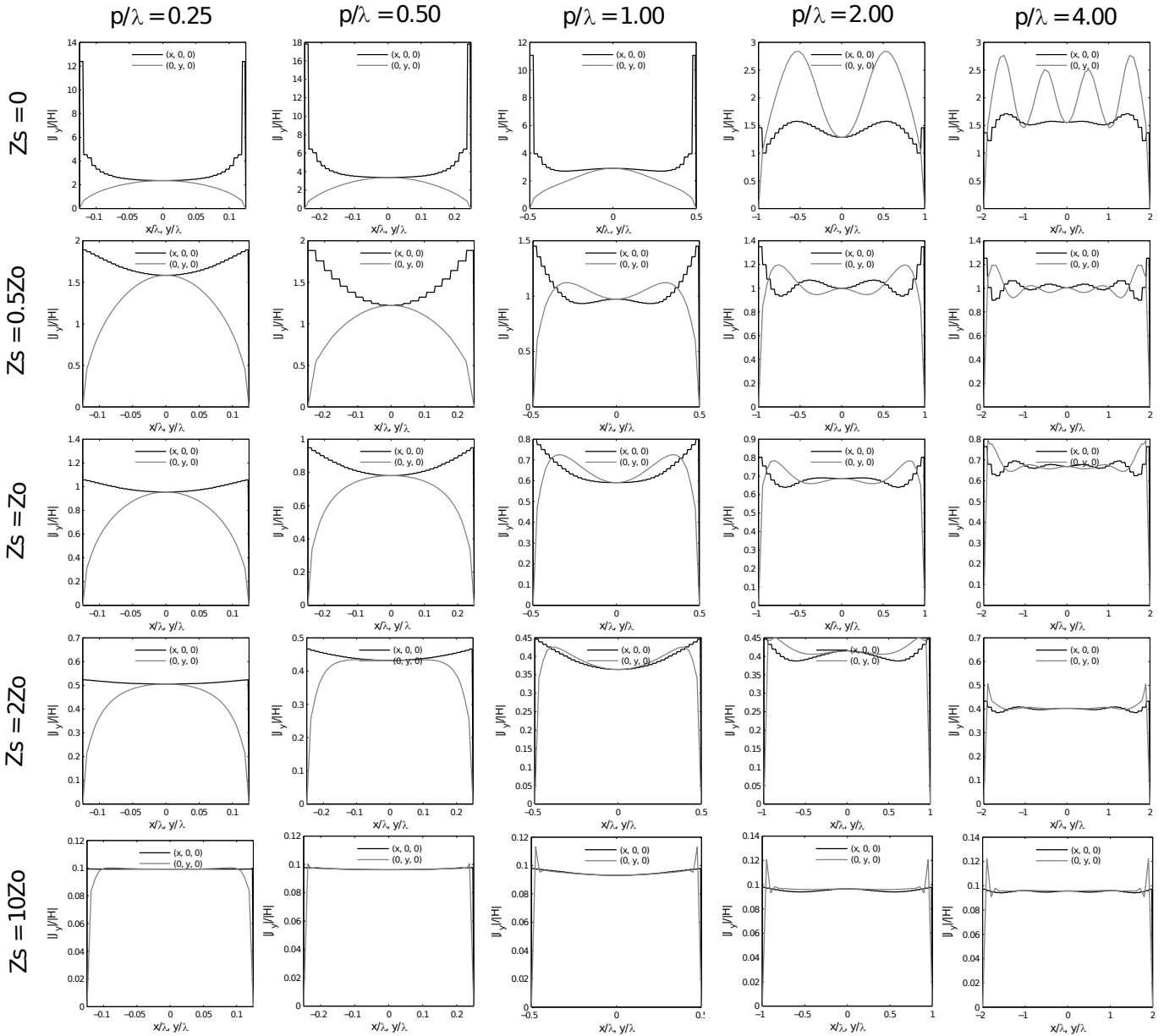


Fig. 2. Plots showing the current distributions excited by an s -polarised wave incident at an angle $\theta = 0^\circ$.

A_E/λ^2 and use $\frac{p}{\lambda}$, as this allows the scaling of the results from the simulation to any physical scale.

We will restrict ourselves to plane waves incident according to the restrictions in III-A. With the approximate model of the induced current, using (29), (14) and (24) gives

$$\frac{A_E(\theta)}{\lambda^2} = \frac{4Z_0Z_S}{(2Z_S + Z_0)^2} \left(\frac{p}{\lambda}\right)^2 \begin{cases} 1 & s\text{-polarised} \\ \cos^2 \theta & p\text{-polarised.} \end{cases} \quad (32)$$

Notice that the response to s -polarised waves is expected to be isotropic in the regime where the model is valid, i.e. the film should be as sensitive to plane waves incident edge on as it is face on. It may at first appear surprising that the film is sensitive to power incident edge-on, but remember that the \mathbf{E} -field when the wave is s -polarised and $\theta = 90^\circ$ is directed tangential to the film surface. It is, therefore, still able to excite a surface current and dissipate power. By contrast the \mathbf{E} -field

associated with the equivalent p -polarised wave is normal to film, is unable to force a current and so $A_E(90^\circ) = 0$. The normal and edge-on cross sections for p -polarised radiation are the same in the simple model as the currents excited by the two waves are identical. This is not the case in reality, as will be seen shortly.

Figure 4 shows polar plots of A_E as a function of θ and polarisation direction for films of several different values of $\frac{p}{\lambda}$ and Z_S . The size of film decreases down the rows of the array, and the surface impedance Z_S increases across the columns. These plots describe the angular response that would be expected from a resistive film bolometer.

At low Z_S the results for the $4\lambda \times 4\lambda$ film (first row of figure 4) are as we might have expected intuitively. $A_E(0^\circ)$ for both the p - and s -polarised wave is approximately half the physical pixel area (except at very low Z_S). For the s -polarised

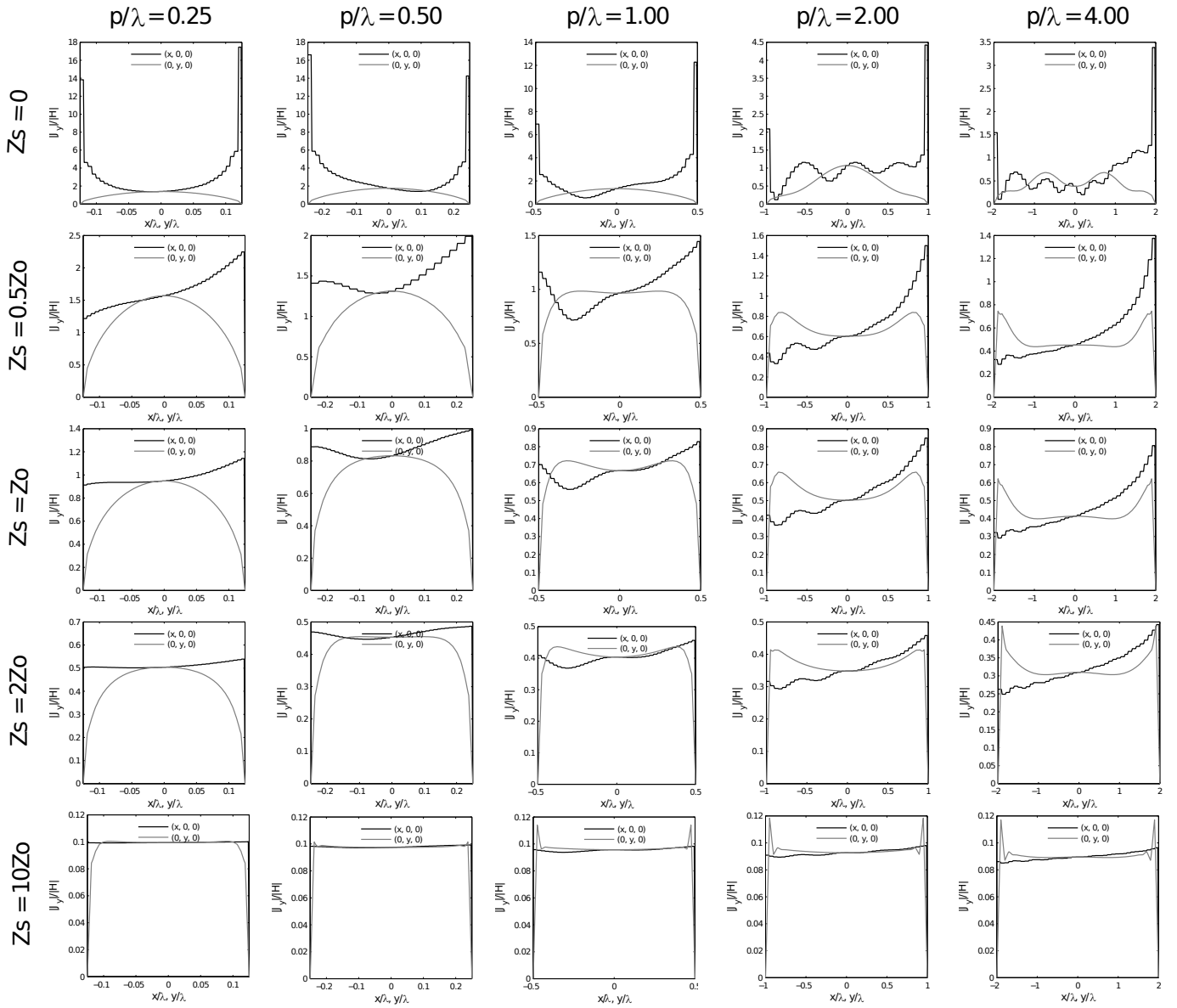


Fig. 3. Plots showing the current distributions excited by an s -polarised wave incident at an angle $\theta = 90^\circ$.

wave, $A_E(90^\circ)$ is zero for the reasons explained above. For the p -polarised wave $A_E(90^\circ)$ is finite, but still much smaller than the face-on cross section. Generally, for the p -polarised plane the film behaves as it is comprised of two Lambertian absorbers, one of which is orientated parallel to the film and the other normal to it. As Z_S is increased the response to the s -polarised wave becomes more forward directed, while $A_E(90^\circ)$ is seen to increase towards $A_E(0^\circ)$. At very low Z_S , the films absorption patterns exhibit lobe structure like an antenna.

The A_E curves for the $\lambda \times \lambda$ and $0.25\lambda \times 0.25\lambda$ film (rows two and three of figure 4) have a similar structure to those for the much larger film. However, for all Z_S the values of $A_E(0^\circ)$ and $A_E(90^\circ)$ for the p -polarised wave are more comparable. At low Z_S , $A_E(90^\circ)$ even exceeds $A_E(0^\circ)$, which is not intuitive. At high Z_S , the results for electrically small films are in excellent agreement with the behaviour predicted by (32).

It is worth considering how the effective area for a s -polarised edge-incident wave can exceed that for a normally incident wave of the same polarisation, as observed for the electrically small films in figure 4 when $Z_0 < Z_S$. This behaviour can be explained in terms of the current distributions observed in section IV-A. When an s -polarised plane is normally incident, the induced current can be approximated as a uniform sheet. The magnitude of the current is approximately independent of film size (figure 2), so we expect the total power absorbed, and thus $A_E(0^\circ)$, to scale as p^2 . For the equivalent edge incident wave, if $Z_S < Z_0$ the current is confined to a narrow strip at the leading edge of the film. Its value on the leading edge for fixed Z_S is approximately independent of the film size (figure 3), so we expect $A_E(90^\circ)$ to scale as p . This result also follows by noting that the narrow strip current at the edge should behave like a thin-wire antenna. These simple scaling rules can be seen to roughly hold for the

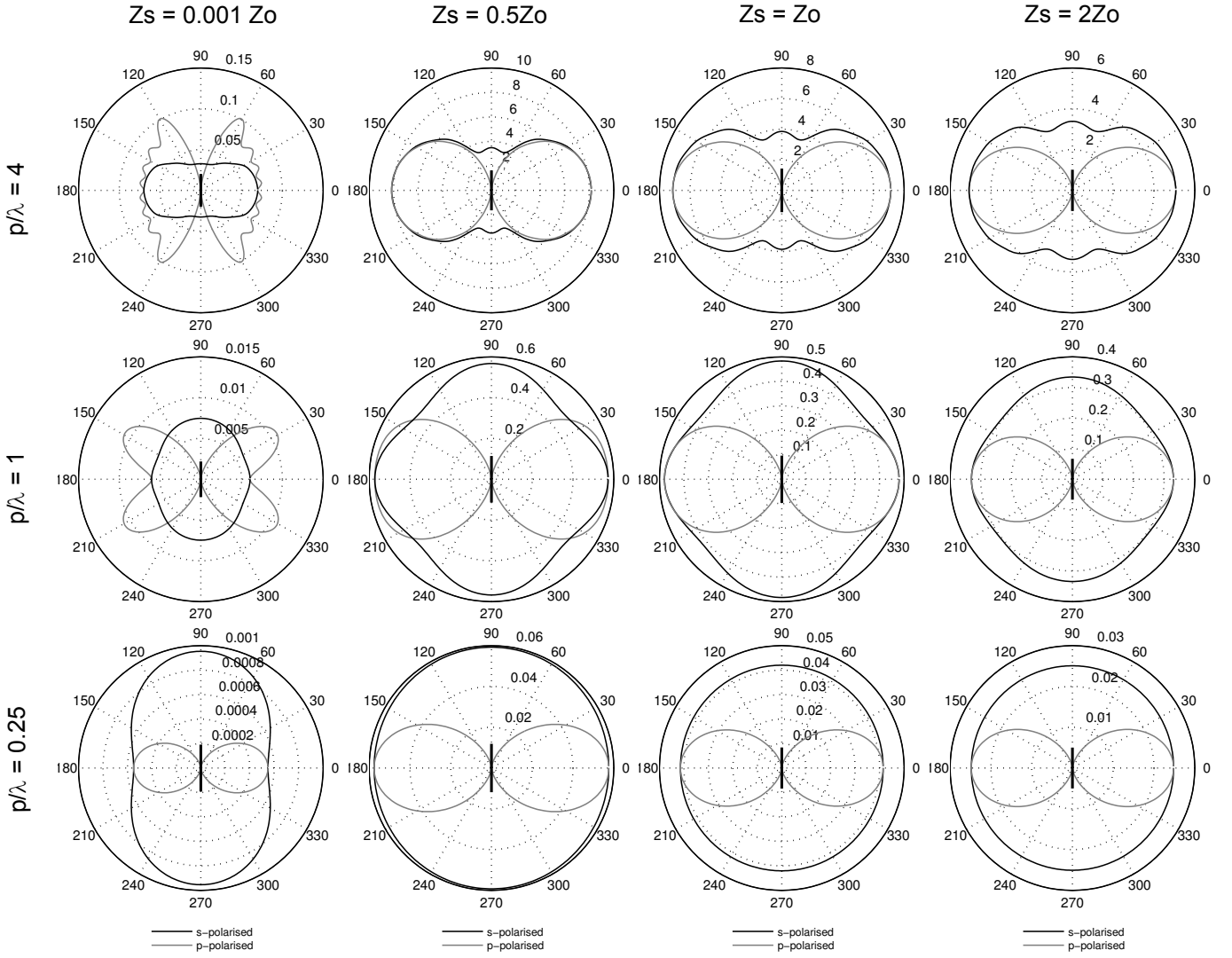


Fig. 4. Plots showing the effective area of the absorber as a function of polarisation and incidence angle. A_E/λ^2 is plotted on the polar axis.

values in table II, which are for a film with $Z_S = 0.5Z_0$. If $A_E(0^\circ) \propto p^2$ and $A_E(90^\circ) \propto p$ hold for all p , it is always possible to find a value of p below which $A_E(90^\circ)$ is greater than $A_E(0^\circ)$. This explains why, when $Z_S < Z_0$, the edge-incident value of A_E for an s -polarised wave exceeds the value for normal incidence only once the film falls below a certain size relative to the wavelength, e.g. figure 4.

Extrapolating in the other direction, for $Z_S < Z_0$ we would expect $A_E(90^\circ)$ to grow much faster with p than $A_E(0^\circ)$ for the p -polarised wave. For large, low impedance films, the A_E for a normal incident wave should therefore greatly exceed A_E for edge-on wave, as observed in the data. When $Z_S > Z_0$, from figure 3 we see that for edge-incident waves the current is less concentrated at the leading edge. In this circumstance, we would therefore expect $A_E(90^\circ) \propto p^2$. This should mean for high Z_S films that $A_E(0^\circ)$ and $A_E(90^\circ)$ should be comparable for all p , in agreement with the observed trends.

Finally it is traditionally assumed that a free-standing thin film is only able to absorb, at maximum, half of the power incident upon it. We would therefore expect A_E to always be less than or equal to half the film's geometric area, p^2 .

p/λ	$A_E(\theta = 0^\circ)$	$A_E(\theta = 90^\circ)$
0.25	0.06	0.06
0.50	0.17	0.20
1.00	0.60	0.60
2.00	2.00	1.5
4.00	8.00	3.5

TABLE II
 A_E/λ^2 AS A FUNCTION OF p FOR A WAVE INCIDENT NORMALLY AND EDGE-ON, $Z_S = 0.5Z_0$.

This indeed the case when $p > \lambda$ in figure 4, however for the electrically small films values of A_E almost equal to the physical area are observed. It is well known from antenna theory that the effective area of an electrically small antenna can exceed its physical area (e.g. the Hertzian dipole), and the observed behaviour is simply a manifestation of this effect.

C. Detector Response Function (DRF)

The DRF was introduced in section II-C and fully describes the response of the detector to partially coherent radiation. A

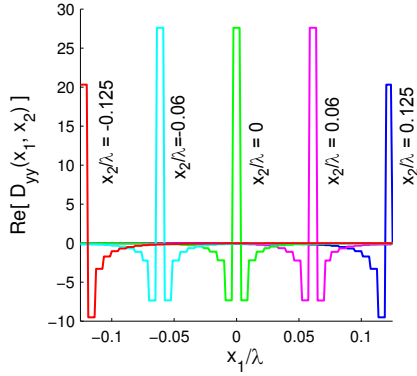


Fig. 5. Plot of part of the DRF for a 188.5Ω $0.25\lambda \times 0.25\lambda$ film. $y_1 = y_2 = 0$

useful physical picture of the DRF is as the correlation dyadic, (22), of the particular state of coherence of the incident field to which the detector is responsive. A natural terminology that then arises is to describe the detector response as coherent, partially-coherent or incoherent depending on the level of coherence in the field the DRF describes. As an example, consider the DRF predicted using the simple model for the electromagnetics of the field from III-C. Substituting (29) into (14), it is straightforward to show that

$$\bar{\bar{D}}(\mathbf{r}_{t1}, \mathbf{r}_{t2}) = \frac{Z_S}{2(Z_S + Z_0/2)^2} (\bar{\bar{I}} - \hat{\mathbf{z}}\hat{\mathbf{z}}) \delta(\mathbf{r}_{t1} - \mathbf{r}_{t2}), \quad (33)$$

which represents a fully incoherent response. Power detectors that use traditional antennas, for example a microwave radiometer, are an example of a fully coherent detector. Partially coherent detectors show intermediate behaviour, with the DRF taking non-zero for small values of $|\mathbf{r}_{t1} - \mathbf{r}_{t2}|$.

Space precludes a full discussion of DRFs calculated for the resistive films, but fig. 5 has been included to show the general behaviour. The data in the plot is for a $0.5\lambda \times 0.5\lambda$ film with uniform surface impedance $Z_S = 0.5Z_0$. There are two main problems that arise when trying to represent DRFs graphically. The first is that they function of two position vectors, which in this case results in a four-parameter function $\bar{\bar{D}}(x_1, y_1; x_2, y_2)$. For all the lines in fig. 5, y_1 and y_2 are zero, while each line represents results for a different value of x_2 (which are equally spaced along the cut $(x, 0, 0)$). This leaves x_1 as the dependent variable. The second difficulty is that the dyadic has multiple elements. In fig 5 only the yy component is shown. A sharp peak in each line is observed at point where $x_1 = x_2$. Further simulations have shown that these peaks behave like delta functions, and correspond to the incoherent part to the film's response. Unlike the behaviour predicted by (33), the incoherent response is non-uniform over the film's surface and is observed to decrease at the edges. Coherence is observed in the DRF over scales $|x_1 - x_2| < 0.05$, and so overall the response of absorber is partially-coherent. This coherence results from the ability of the induced current at one point to effect the current at a second point via the scattered field.

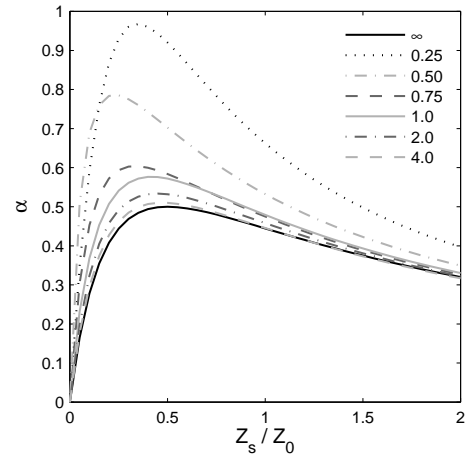


Fig. 6. $\alpha = A_E(\theta = 90^\circ)/p^2$ vs Z_S for various film sizes

D. Choosing Z_S to maximise the absorbed power

When designing a resistive film TES detector, the surface impedance of the film is usually chosen to maximise the absorbed power. For electrically large ($p \gg \lambda$) free-standing absorbers, it is usually assumed that the optimal value for Z_S is $0.5Z_0$ as a result of the analysis of the case of an infinite film (section III-C). However, there is no corresponding result or advice for electrically small films. In order to rectify this, we investigated the effect of Z_S on $\alpha = A_E(\theta = 0^\circ)/p^2$ for various size films and the results are shown in figure 6. For each size of film, the effective area has been normalised to the film's physical area so that the curves can all be shown on the same axes. Also included is the analytic result for an infinite film, and it is reassuring the simulations tend to this line when $\frac{p}{\lambda}$ is large. As $\frac{p}{\lambda}$ decreases the curve are observed to become increasingly sharply peaked, and the location of the maxima to move. There appears to be no definite rule about the value of Z_S needed to match the film to free space. In the range $\frac{p}{\lambda} = 4.0 - 0.5$, the value of Z_S at which α is maximised –i.e. the match value– is observed to decrease with decreasing p . However, by $\frac{p}{\lambda} = 0.25$ it seems to have increased again. Consequently, these curves demonstrate that for optically small devices, full electromagnetic simulations, of the type described, will most likely be needed at the design stage to find the optimum Z_S .

The code also allows us to investigate the effect that a non uniform surface impedance has on the devices optical behaviour. In particular, we have studied the effect of 'striping' the film, i.e. breaking into up into an array of parallel strips, as opposed to one continuous film. Figure 7 shows A_E as a function of θ for two $\lambda \times \lambda$ films made out of the same material with the same $Z_S = 30\Omega$ (well below the match point). The film in 7(a) is continuous, while the film in (b) has been patterned into an array three identical strips in the y -direction, separated by two gaps of the same width and occupying the same overall footprint. The striping is seen to direct the films response to p -polarised waves forward: $A_E(0^\circ)$ is increased and $A_E(90^\circ)$ decreased compared with (a). The trade-off is that response to s -polarised waves is strongly suppressed in (b) compared with (a), which depending on the situation this may

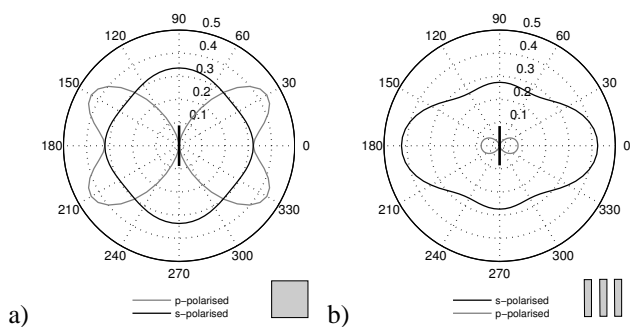


Fig. 7. Effect of striping the resistive film. Sub-figure (a) shows the results for a uniform $\lambda \times \lambda$ film with $Z_S = 30\Omega$. Sub-figure (b) shows results for identically sized film with the same Z_S , however the metallization has now been divided into three identical strips separated by gaps of equal width. The patterning of the film is shown in the bottom right-hand corner of each sub-figure.

or may not be beneficial. This behaviour can be explained in terms of the effective surface impedance of the striped film. To currents flowing parallel to the strip orientation, the film sections appear like a parallel array of lumped resistors. Adding more high resistance gaps will therefore push the effective film impedance in this direction up. For a low surface impedance material (e.g. $30\Omega/\text{sqr}$) this can bring the film's effective surface impedance closer to the match value. It is this effect that causes the increase in $A_E(0^\circ)$ for the s -polarised wave in 7(a). Currents attempting to flow perpendicular to the strips see a broken path and correspondingly a very high Z_S . This leads to the decrease in $A_E(90^\circ)$ for the p -polarised wave in 7(a). Striping offers the possibility of making resistive film detectors with highly polarised beams, or alternately a method of improving the matching of low Z_S films to free space.

V. CONCLUSIONS

It is possible to analyse the optical behaviour of certain classes of power detector in a rigorous way by using a method-of-moments like formulation to determine the power dissipated in the thin, resistive, films that comprise them. The far-field response, polarisation and natural detector can be calculated numerically, as well as the cross-talk between adjacent detectors in an array. To demonstrate the technique, full simulations of a single, isolated, resistive film TES detector were performed. The effect of the absorbing film's dimension and surface impedance have on the device's optical behaviour have been investigated rigorously, leading to the following recommendations:

- When the resistive film is electrically large and/or $Z_S \gg Z_0$, the optical behaviour of the TES is well described by the simple model described in section III-C and [7]. When

the absorbing film is electrically small and/or $Z_S < Z_0$, full electromagnetic simulations, as described here, must be performed to determine the value of Z_S required for a match, as well as other aspects of the optical behaviour.

- Resistive film bolometers are expected to be sensitive to stray light at high angles of incidence. This will not be so much of a problem in the centre of an imaging array, where the pixels shield each other. However it may be an issue for detectors at the edge. A possible solution is to introduce a guard ring around the array, which will also mitigate edge effects in the beams.
- By using a spatially varying surface impedance, the polarisation properties of the detector can be altered. A striped pattern can also be used to obtain a better match to free space when only low Z_S films can be fabricated. We have investigated the effect of 'striping' the film in detail, and hope to produce a paper with some design rules in the near future.

Future work will focus on analysing the interaction between the absorbing films in an imaging array. We have already determined how to include a ground plane in the simulations via the Green's dyadic. This will allow the analysis of a very common detector architecture, where a back-short is placed behind the film to improve absorption. Additionally, we are using the modelling scheme described in the paper as a tool in the development of a new class of end-fire absorber.

REFERENCES

- [1] S. Withington and G. Saklatvala, "Characterizing the behaviour of partially coherent detectors through spatio-temporal modes," *Journal of Optics A: Pure and Applied Optics*, vol. 9, pp. 626–633, 2007.
- [2] S. Withington and C. Thomas, "Optical theory of partially coherent thin-film energy-absorbing structures for power detectors and imaging arrays," *Journal of the Optical Society of America A*, vol. 26, no. 6, pp. 1382–1392, 2009.
- [3] T. Senior, "Backscattering from resistive strips," *IEEE Transactions on Antennas and Propagation*, vol. 27, pp. 808–813, 1979.
- [4] M. Ney, "Method of moments as applied to electromagnetic problems," *IEEE Transactions on Microwave Theory and Techniques*, vol. 33, no. 10, pp. 972–980, 1985.
- [5] S. Withington, M. Hobson, and R. Berry, "Representing the behavior of partially coherent optical systems by using overcomplete basis sets," *Journal of the Optical Society of America A*, vol. 21, no. 2, pp. 207–217, 2004.
- [6] G. Saklatvala, S. Withington, and M. Hobson, "Coupled-mode theory for infrared and submillimeter wave detectors," *Journal of the Optical Society of America A*, vol. 24, no. 3, pp. 764–775, 2007.
- [7] C. Thomas and S. Withington, "Modelling the intensity and polarisation response of planar bolometric detectors," *Accepted for publication in Journal of the Optical Society of America A*.
- [8] S. Rao, D. Wilton, and A. Glisson, "Electromagnetic scattering by surfaces of arbitrary shape," *IEEE Transactions on Antennas and Propagation*, vol. 30, no. 3, pp. 409–418, 1982.
- [9] X. Dardenne, "Method of moments simulation of infinite and finite periodic structures and application to high-gain metamaterial antennas," 2007.

Measured performance of a 230 GHz prototype focal-plane feedhorn array made by direct drilling of smooth-walled horns

J. Leech*, B. K. Tan*, G. Yassin*, P. Kittara†, A. Jiralucksanawong† and S. Wangsuya †

*Department of Physics

University of Oxford

Email: jxl@astro.ox.ac.uk

†Department of Physics

Mahidol University.

Abstract—We present the first, complete 230 GHz feedhorn array manufactured by direct drilling of smooth-walled horns into a single plate of aluminium. The horn design process, based on a genetic algorithm, is described and the fabrication process, via direct drilling using shaped drill bits, is presented. We present cross coupling and beam pattern measurements of a close-packed pair of the smooth-walled horns fabricated in a single block of aluminium. We also present a prototype 37 horn array, again fabricated by drilling into a single block. Our measurements show that our designs and fabrication techniques will be robust when applied to large focal arrays of horns consisting of hundreds or thousands of feedhorns. We expect our smooth-walled horn designs and novel manufacturing techniques will offer an attractive, low-cost alternate to traditional horn arrays consisting of electroformed corrugated horns.

I. INTRODUCTION

High quality feed horns for astronomical telescopes are usually *corrugated horns*, where the hybrid HE_{11} is made to propagate by fabricating many $\sim \lambda/4$ corrugations along the interior of the horns (Figure 1). While these horns offer excellent beam patterns with high circularity and low cross polarisations over wide ($\sim 50\%$) bandwidths, they suffer from the disadvantage of being time consuming and expensive to manufacture, particularly as the wavelength decreases into the submillimetre regime. Corrugated horns are usually manufactured by micromachining a mandrel which is then electroplated before the mandrel is dissolved in a process known as *electroforming*. This process is time-consuming and expensive and individual submillimetre horns made in this way can cost of order of 1000 USD each. This is not a problem when only a few horns are required, but for large format focal plane array receivers[1][2] requiring hundreds or thousands of horns, the cost of the feed horns themselves can become a large fraction of the entire cost of the instrument.

In this paper, we describe the design of smooth-walled feed horns which use discontinuities in flare angle near the throat of the horn to excite a balance of higher order modes which are then phased by choosing the length of the horn to give a uniform horn aperture illumination and hence a high quality far-field beam pattern. These horns are similar to Potter horns[3],[4], where a balance of TE_{11} and TM_{11}

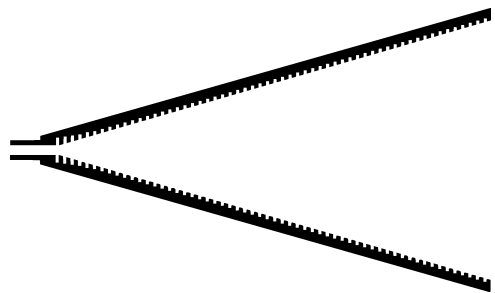


Fig. 1. The cross-section of a corrugated horn.

modes are excited by step or flare angle discontinuities near the throat. Traditionally, Potter horns have been difficult to design analytically since the throat discontinuities will in general excite a spectrum of higher order modes, which effect the aperture field distribution in complicated ways, especially as one moves away from the central design frequency. These higher order modes make it hard to produce broadband designs analytically and thus the problem suggests the use of numerical optimisation techniques. Here we use a combination of a *genetic algorithm*[5] and *modal matching*[6] to produce optimised broadband horn designs. We have previously reported the successful use of this technique to design Potter horns with both step and flare angle discontinuities[7].

The simplicity of the interior shape of our multi-flare angle horns means that they lend themselves well to novel fabrication techniques. In this paper we describe a “drilling” technique which uses a machine tool whose cutting edge is shaped to match the interior profile of the required horn. We present experimental beam pattern results measured for horns and horn arrays manufactured using this technique. We also measure the cross coupling between two horns and present new results from modelling these horns using the full 3D electromagnetic simulation package, Ansoft’s HFSS. Such HFSS modelling will be useful in understanding the effects of non-axisymmetric machining errors on the far-field beam patterns of the horns.

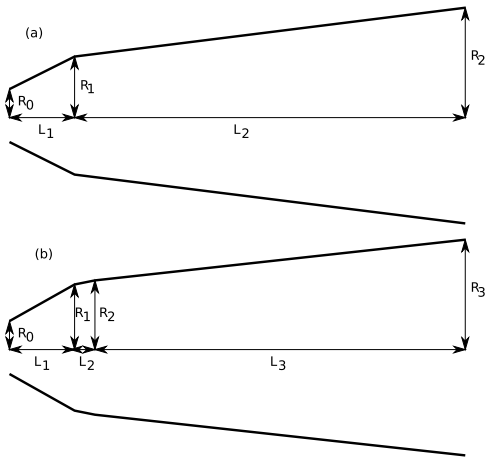


Fig. 2. A schematic of (a) a 2-section and (b) a 3-section smooth walled horn with one and two discontinuities in flare angle, respectively.

II. DESIGN WITH A GENETIC ALGORITHM

Genetic algorithms employ a “natural selection” process which is similar to biological evolution[5]. We begin by encoding the parameters which describe a certain horn design to form a “chromosome”. We then construct a random set of horn designs and their corresponding chromosomes to form a population. We then evaluate a cost (or quality) function for each design to measure its fitness. Our cost function incorporates weighted measures of beam circularity and cross-polarisation, calculated using modal matching[6], across the required frequency band [7][8]. The chromosomes forming the fittest half of the population are then randomly paired to form parents which produce offspring to form a new generation. When the offspring are generated, crossover and mutation are used to introduce variation into the next generation. The whole process is then repeated with the new population. After many iterations, this evolutionary process yields an increasingly fitter population, with the optimised design being the fittest individual. Once the position of the global cost function minimum has been approximately found using the genetic algorithm, the precise position of the minimum can be quickly found using a downhill simplex technique.

A careful choice of the cost function is important for efficient optimisation with the GA. Our cost function is chosen to maximise far-field beam circularity and minimise the peak cross-polar level. A Potter horn with good beam circularity and low cross-polarisation will also tend to exhibit low sidelobe levels and high beam efficiency, so we have not included the latter parameters explicitly in the cost function. The return loss for smooth walled Potter horns is usually low and does not depend strongly on the horn profile, so we have not explicitly included this parameter in the cost function. Our cost function, at single frequency f may be written as

$$\delta_f^2 = w_X \left[\sum_{P=-1}^{P=-30} \left(\frac{\sigma_P}{\sigma_P^{\text{av}}} \right)^2 w_P \right] \quad (1)$$

where P is the power level in dB, $w_P = 10^{P/15}$ is the weighting function for the beam circularity, w_X is the peak

TABLE I
GEOMETRICAL PARAMETERS FOR THE 3-SECTION 230 GHz DESIGN

Parameter	Length (mm)
R_0	0.62
R_1	1.486
R_2	1.812
R_3	3.652
L_1	1.479
L_2	1.212
L_3	24.0

cross-polar power relative to main-beam peak power, σ_P is the difference between the E and H-plane beamwidths at power level P dB and σ_P^{av} is the mean E and H-plane beamwidths at power level P dB. We calculate our final cost function across bandwidth $\sigma_f = f_U - f_L$ centred at frequency f_0 via

$$\delta^2 = \sum_f \delta_f^2 w_f \quad (2)$$

where $w_f = \exp(-(f - f_0)^2 / 2\sigma_f^2)$ is the frequency dependent weighting factor. While this cost function works well for our purposes, it should be emphasized that other cost functions can be easily incorporated into the design software, depending on the design requirements.

We have developed a fully automated suite of horn design software using a genetic algorithm for design synthesis and modal matching for pattern computation, and produced designs with excellent predicted patterns over a bandwidth of up to 20%. We have also successfully parallelized the code to run on multiple CPU Beowulf clusters using MPI messaging for communication between tasks. We are using this code to optimise designs with a larger number of discontinuities, and hope to produce designs with bandwidths of up to 50%.

III. A 3-SECTION, 230 GHz DESIGN

Table I shows the optimised parameters for a horn with 3 conical sections (2 flare angle discontinuities, Fig. 2(b)). The input waveguide radius, R_0 and the aperture radius R_3 were fixed prior to the optimisation of the remaining five parameters. The FWHM beam width is 14.7 degrees at 230 GHz.

IV. FABRICATION OF SINGLE HORNS BY ELECTROFORMING AND DRILLING

We have previously reported [9] the measured far-field beam patterns for electroformed horn prototypes with the design shown in Table I. We measured these beam patterns directly the far-field using a vector network analyser as a direct detector. These measured patterns agreed well with the expected far field patterns calculated using modal matching. This agreement with theory for these prototype horns demonstrates that the horns work well when constructed with the close tolerances typically obtained with electroforming ($\sim 5\mu\text{m}$).

Figure 3 shows the shaped cutting tool we use for machining our drilled horns. The tool is made from high speed steel, and has the form of the horn described in Table I in its upper cutting edge. We used this tool to manufacture three



Fig. 3. The machine tool used for the fabrication of the drilled horn prototype.

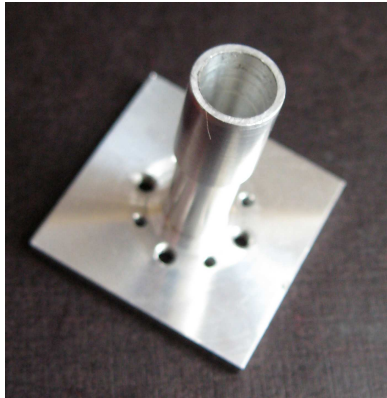


Fig. 4. A completed 230 GHz prototype drilled horn.

individual horns (Figure 4), measuring the beam patterns of two of the horns [10] while splitting the third horn to examine the machining quality of its interior (Figure 5). The measured beam patterns (presented in [10]) matched the expected beam patterns well, with good beam circularity, low sidelobes and low measured cross polar response (below -20dB across the 17% measured bandwidth). In particular each of the drilled horns gave a virtually identical beam patterns, an important result for the use of this horn construction method to make large format focal plane arrays. We observed some asymmetry (around 3 dB) in the sidelobe levels in each of the drilled horns. We expect that this might arise from non-axisymmetric machining errors, either in the positional or angular alignment of the axis of the input waveguide and horn itself. A close examination of Figure 5 shows that there is indeed a slight mismatch ($\sim 50\mu\text{m}$) between the axis of the waveguide drill tool and horn tool.

V. HORN SIMULATIONS IN HFSS

While modal matching is well suited for the analysis of axisymmetric horns, it is less useful for analysing horns with

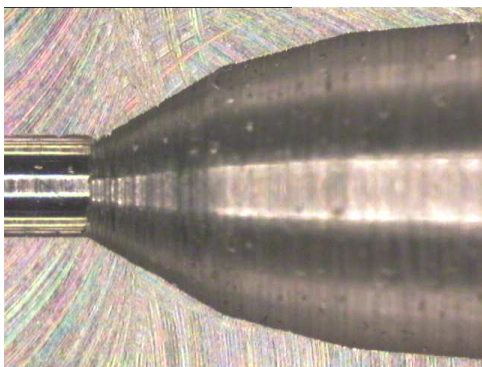


Fig. 5. The throat region of one half of the split drilled horn.

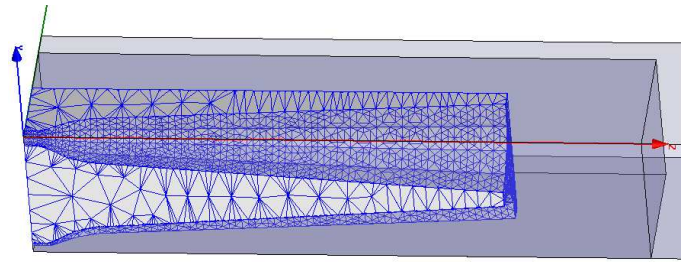


Fig. 6. A section of the HFSS model used to calculate the cross coupling between two horns, showing the mesh points used.

axial asymmetry, such as those that might arise from errors in the alignment of the horn and waveguide cutting tools. For circular waveguide sections with a common centre, the overlap integrals between waveguide modes can be expressed analytically, which is not the case when the waveguide sections are offset. In order to examine the effect of off-axis machining errors, as well as calculate the cross coupling between horns, we created a model of the 3-section horn described above in Ansoft's HFSS, a full electromagnetic simulation package. Unlike corrugated horns, which have many corrugations per wavelength, Potter-type horns with long, smooth phasing sections are much more amenable to analysis using HFSS, since these phasing sections do not require a large number of mesh points per wavelength for an accurate treatment. Nevertheless accurate HFSS models for these horns do require a relatively large number of mesh points and consequently a reasonably large amount of available RAM for analysis. The model whose meshing is shown in Figure 6 required 12 GB of RAM for analysis.

A comparison of the beam patterns calculated for a single 3-section horn using HFSS and modal matching are shown in Figures 7 and 8. The agreement down to the ~ -30 dB response level is seen to be very good indicating that HFSS is a promising tool for modelling this type of smooth walled horn. There are some slight disagreements in sidelobe levels around ~ -40 dB, which may be due to the automated HFSS meshing being slightly too coarse to capture the mode conversion at the discontinuities near the throat with sufficient accuracy. We are currently further investigating these slight differences between the HFSS and modal matching predicted patterns. Nevertheless, our results show that HFSS is a useful tool for investigating cross coupling between horns (discussed below) and also examining the effect of non-axisymmetric machining errors in tolerancing studies.

VI. A 2-HORN ARRAY PROTOTYPE

In order to investigate the suitability of our horns for use in an array, we produced a 2-horn array prototype with a horn centre separation of 8 mm, a packing density appropriate for focal plane arrays (Fig. 9). We measured the beam patterns for each horn in the array, using the far-field antenna test range described above. The results are shown in Figs. 10–13. The match between the theoretical patterns, calculated using modal matching, and the experimentally measured patterns is seen to

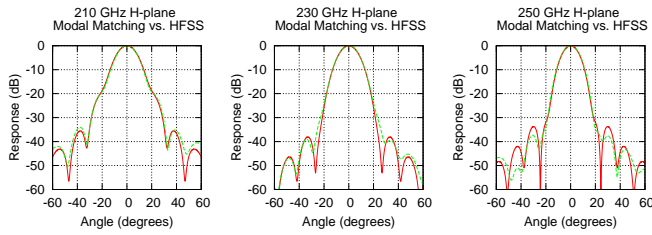


Fig. 7. A comparison of HFSS simulated H-plane beam patterns (green dashed line) and H-plane beam patterns calculated using modal matching (solid red line).

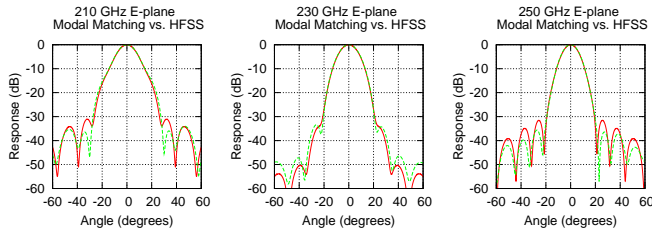


Fig. 8. A comparison of HFSS simulated E-plane beam patterns (green dashed line) and E-plane beam patterns calculated using modal matching (solid red line).

be very good. It should be noted that the slight asymmetries found in the patterns are very similar in magnitude for both horns and also that these asymmetries are oriented similarly for both horns. This indicates that they are very likely caused by a small axial misalignment, which would be of similar magnitude and orientation for both horns as they are machined in turn into a single plate.

We also used our two horn array prototype to measure the cross coupling between the two horns. We measured this coupling using a vector network analyser in an anechoic chamber, using an absorbing carbon loaded plastic cone in front of the two horn array. Our measured cross couplings should thus be viewed as upper limits, since some fraction of the coupling may be due to residual reflection from our absorbing cone. We also calculated the expected cross coupling for our horn array using HFSS. Figure 14 shows the measured and simulated cross coupling for our two horns across the operating bandwidth. The experimentally measured



Fig. 9. The two horn array prototype, made by repeated drilling into a single block of aluminium.

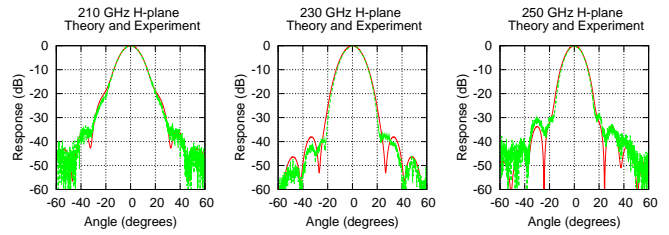


Fig. 10. A comparison of the theoretical beam patterns calculated using modal matching and the experimentally measured H-plane beam patterns for horn No.1 of the 2 horn block.

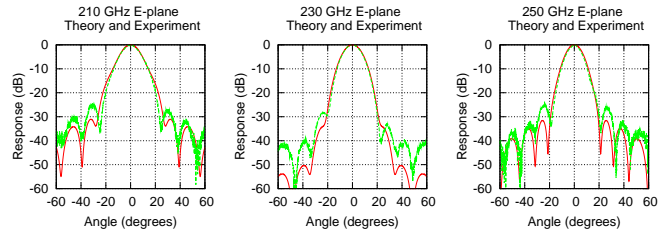


Fig. 11. A comparison of the theoretical beam patterns calculated using modal matching and the experimentally measured E-plane beam patterns for horn No.1 of the 2 horn block.

cross coupling is below -70 dB across the band, an excellent result for the use of these horns in focal plane arrays. The predicted HFSS cross coupling are also low, but only agree with the experimentally determined cross coupling to within 10 dB or so. We are currently investigating this disagreement, which may be due to a lack of numerical precision within HFSS when the calculated S-matrices become very low (~-60 dB). We are also investigating analytical approaches for calculating the cross coupling based on the methods presented

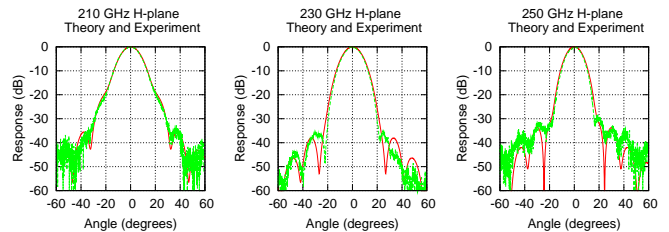


Fig. 12. A comparison of the theoretical beam patterns calculated using modal matching and the experimentally measured H-plane beam patterns for horn No.2 of the 2 horn block.

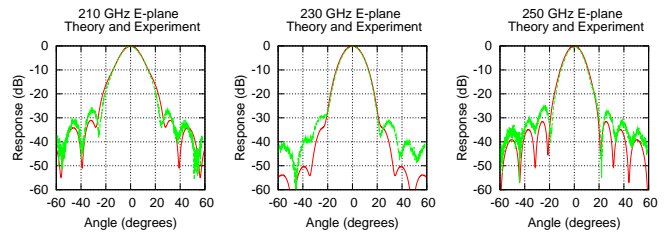


Fig. 13. A comparison of the theoretical beam patterns calculated using modal matching and the experimentally measured E-plane beam patterns for horn No.2 of the 2 horn block.

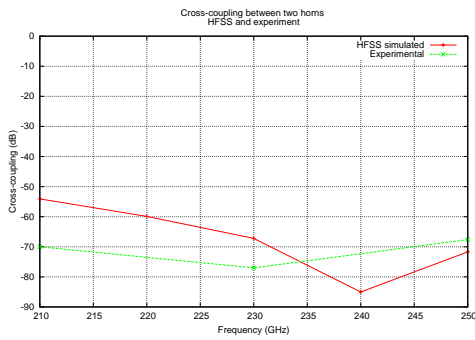


Fig. 14. Measured and HFSS simulated cross coupling between the two horns in the 2 horn prototype array.

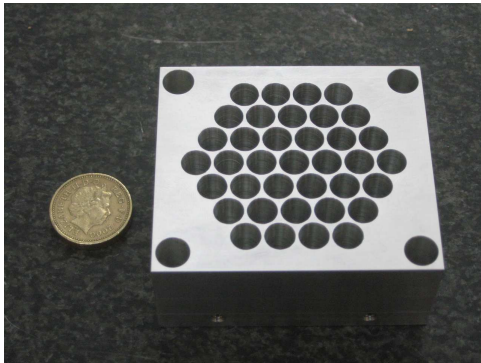


Fig. 15. The 37 horn array prototype, made by repeated drilling into a single block of aluminium.

in [6].

VII. A 230 GHz, 37 HORN ARRAY AND 700 GHz HORN PROTOTYPES

We have now constructed a prototype 37 horn hexagonally close packed horn array for use at 230 GHz (Figs. 15 and 16). We plan to measure the beam patterns for all of the individual horns in the array, as well as measuring the cross coupling between selected pairs of horns in the array. We are also extending our horn design to higher frequencies and have constructed an individual 700 GHz horn, with a design scaled from that presented above using the same drilling technique. We are currently constructing a custom far field test range with a 4K cooled bolometer detector (usable between 100 GHz – 1 THz) to test both the array and the 700 GHz horn prototype.

VIII. CONCLUSIONS AND FURTHER WORK

We have developed a technique, based on a genetic algorithm and modal matching for designing smooth walled horns with several discontinuities in flare angle. We have verified our design technique by constructing 230 GHz prototype horns to a high tolerance using traditional electroforming and measuring the beam patterns using a far-field test range. The beam patterns agreed well with theory, showing excellent beam circularity and low cross polarisation over the measured bandwidth of around $\sim 17\%$. We are currently using our design software to design 4 section horn with the hope of extending the bandwidth to around 50%.

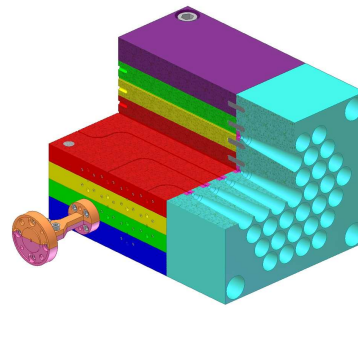


Fig. 16. The 37 horn array prototype showing a multiplate split block which enables power to be delivered to each of the horns from a split block waveguide at the side.



Fig. 17. The 700 GHz drilled horn prototype.

Our horns lend themselves well to the novel fabrication technique of repeated drilling using a shaped machine tool. We have constructed two separate horns using this technique, as well as a two horn close-packed array. The individual drilled horns and the horns in the 2-horn array exhibit high quality beam patterns, with excellent reproducibility between horns. We have seen slight asymmetries in these beam patterns which are likely to be due to small non-axisymmetric machining errors. We have successfully modelled our horns using the full 3D electromagnetic modelling package HFSS, which we intend to use to arrive at well understood target tolerances for the angular and positional alignment of the waveguide and horn drilling tools.

We have measured the cross-coupling of the close packed horns in the 2 horn prototype array and have found this to be below -68 dB across the operating bandwidth. We are also investigating the use HFSS and analytical techniques to characterise the expected cross coupling of close packed horns.

We have constructed a prototype 230 GHz, 37 horn close packed horn array by repeated drilling into a single aluminium plate, which we plan to test experimentally in the near future. We have also made a 700 GHz drilled horn, which we will test shortly. We are currently exploring the commercialization of this technology, including our design software, design methodology and horn fabrication techniques in collaboration with ISIS Innovation Ltd., the Oxford University technology transfer company.

ACKNOWLEDGMENTS

The construction and testing of the horn array prototypes, and horn software development work was supported using an STFC follow-on-find grant for the production of pre-commercialisation prototypes. The authors would like to thank Manju Henry, Jeunne Treuttel, Peter Huggard, Bertrand Thomans and Matthew Oldfield for their assistance in setting up and using the ABmm vector network analyser and 230 GHz antenna test range at the Rutherford Appleton Laboratories.

REFERENCES

- [1] H. Smith, J. Buckle, R. Hills, G. Bell, J. Richer, E. Curtis, S. Withington, J. Leech, R. Williamson, W. Dent, P. Hastings, R. Redman, B. Wooff, K. Yeung, P. Friberg, C. Walther, R. Kackley, T. Jenness, R. Tilanus, J. Dempsey, M. Kroug, T. Zijlstra, T. M. Klapwijk, 2008, "HARP: a submillimetre heterodyne array receiver operating on the James Clerk Maxwell Telescope", Society of Photo-Optical Instrumentation Engineers (SPIE) Conference Series, Vol 7020.
- [2] C. E. North, B. R. Johnson, P. A. R. Ade, M. D. Audley, C. Baines, R. A. Battye, M. L. Brown, P. Cabella, P. G. Calisse, A. D. Challinor, W. D. Duncan, P. G. Ferreira, W. K. Gear, D. Glowacka, D. J. Goldie, P. K. Grimes, M. Halpern, V. Haynes, G. C. Hilton, K. D. Irwin, M. E. Jones, A. N. Lasenby, P. J. Leahy, J. Leech, B. Maffei, P. Mauskopf, S. J. Melhuish, D. O'Dea, S. M. Parsley, L. Piccirillo, G. Pisano, C. D. Reintsema, G. Savini, R. Sudiwala, D. Sutton, A. C. Taylor, G. Teleberg, D. Titterton, V. Tsaneva, C. Tucker, R. Watson, S. Withington, G. Yassin and J. Zhang, 2008, "Detecting the B-mode Polarisation of the CMB with Clover". Proceedings of the XXXIIIrd Rencontres de Moriond "Cosmology".
- [3] Potter P., 1963. "A new horn antenna with suppressed sidelobes and equal beamwidths". *Microwave J.*, 6, 71-78.
- [4] Pickett H., Hardy J. & Farhoomand J., 1984. "Characterisation of a dual mode horn for submillimetre wavelengths". *IEEE Trans. Microwave Theory Tech.*, MTT32(8), 936-937.
- [5] Haupt R.L. and Haupt S.E. (1998). "Practical genetic algorithms". Wiley-Interscience Publication.
- [6] Olver A., Clarricoats P., Kishk A. & Shafai A., 1994. "Microwave horns and feeds". Bookcraft, Bath.
- [7] Kittara, P., Jiralucksanawong, A., Wangsuya, S., Leech, J. and Yassin, G., 2007 "The design of potter horns for THz applications using a genetic algorithm" *International Journal of Infrared and Millimeter Waves* (2007) 28: pp.1103-1114.
- [8] Yassin, G., Kittara, P., Jiralucksanawong, A., Wangsuya, S., Leech, J. and Jones, M.E. "A high performance horn for large format focal plane arrays", *Proc. of the 18th International Symposium Space Terahertz Technology*, Pasadena, USA, 2007.
- [9] Kittara, P., Leech, J., Yassin, G., Tan, B. K., Jiralucksanawong, A. and Wangsuya, S., 2008 "The fabrication and testing of novel smooth-walled feed horns for focal plane arrays" *Proc. 19th International Symposium on Space Terahertz Technology*.
- [10] J. Leech, G. Yassin, B.K. Tan, M. Tacon, P. Kittara, A. Jiralucksanawong and S. Wangsuya, 2009, "A new, simple method for fabricating high performance sub-mm focal plane arrays by direct machining using shaped drill bits.", *Proc. 20th International Symposium on Space Terahertz Technology*.

Measurements of the Offset-Cassegrain Antenna of JEM/SMILES Using a Near-Field Phase-Retrieval Method in the 640 GHz Band

Takeshi Manabe*, Toshiyuki Nishibori†, Kazuo Mizukoshi†, Fumiaki Ohtsubo‡, and Satoshi Ochiai§,

*Department of Aerospace Engineering
Graduate School, Osaka Prefecture University
Email: manabe@ieee.org

†Japan Aerospace Exploration Agency

‡Advanced Engineering Services Co., Ltd.

§National Institute of Information and Communications Technology

Abstract

SMILES, Superconducting Submillimeter-Wave Limb-Emission Sounder, is a highly sensitive limb-sounding spectrometric radiometer to observe altitude profiles of ozone and ozone-depletion-related molecules in the stratosphere in the submillimeter frequency bands, 624.32–626.32 GHz and 649.12–659.32 GHz. SMILES was launched aboard the H-II Transfer Vehicle by the H-IIB launch vehicle on September 11, 2009, and was attached to the Japanese Experiment Module (JEM), dubbed “*Kibo*,” of the International Space Station. The objective of the SMILES mission is to demonstrate highly sensitive submillimeter-wave soundings and to monitor global distributions of the stratospheric trace gases. For these requirements a superconductive low-noise receiver with a mechanical 4-K refrigerator is used in space for the first time.

In order to observe the stratospheric atmosphere with an altitude resolution of about 3 km from the ISS orbit about 2000 km away, a 400-mm×200-mm elliptical offset Cassegrain antenna with a high beam efficiency of 90% and low sidelobe levels below -20 dB is employed to vertically scan the atmosphere with an elliptical beam with half-power beam widths of 0.09° in elevation and 0.18° in azimuth.

In this paper, the results of the measurements made for the flight model of the offset Cassegrain antenna of SMILES are described. Although we have tried to make near-field measurements in which the amplitude and phase of the near field of the antenna aperture by using a submillimeter vector network analyzer at first, it did not work well because of its malfunctioning in the phase-lock circuit. Then, we have decided to employ a near-field phase retrieval method in which the aperture phase distribution is estimated only from the amplitude distribution measurements over two near-field planes. The far-field pattern estimated from thus estimated near-field pattern were compared with theoretical calculations based on physical optics in which the the surface errors measured for the main and sub reflectors were taken into account. As a result of the comparison, the far-field pattern estimated from the phase retrieval method were found to be in very good agreement with the physical optics calculations to the sidelobe levels as low as -55 dB. This demonstrates that the phase retrieval is an effective method to evaluate aperture antennas in the submillimeter-wave region where accurate phase measurement is rather difficult.

Analysis of the ALMA Telescope and Front-ends

S.B. Sørensen*, K. Pontoppidan
TICRA, Copenhagen, Denmark

*Contact: ticra@ticra.com, phone +45-33-12-4572

Abstract— The purpose of the present study is to provide a more detailed electromagnetic analysis of the telescope optics than previously performed, including support leg blockage effects, detailed reflector geometry, surface deformations and front-end analyses. Radiation patterns including these effects are calculated for all frequency bands.

I. INTRODUCTION

The ALMA (Atacama Large Millimeter Array) project is an array of 12-meter radio astronomy telescopes now being assembled in the high-altitude Atacama desert in Chile. A very large bandwidth is covered by the array since each telescope includes 10 receiver front-ends that operate from 30 to 950 GHz. TICRA became involved in ALMA through a contract with ESO. Our work started late in the ALMA project after the design of the telescope and most of the front-ends was established, so our role was to provide accurate verification of the optical design and to calculate the detailed performance of the total telescope system for all frequency bands. The paper will present a summary of the analysis of both the front-ends and the telescope with emphasis on the most challenging and critical aspects of the optics system. Further details can be found in [1] and [2]. All analyses have been carried out by the TICRA software tools GRASP [3] and CHAMP for reflector antennas and corrugated horns, respectively. These tools use accurate and well established numerical methods, such as Physical Optics, the Method of Moments and Mode Matching.

II. FRONT-END ANALYSIS

The total frequency bandwidth of the ALMA telescopes is extremely wide (from 30 to 950 GHz) which necessitates a complicated front-end with 10 separate receiver systems for different frequency sub-bands. The sub-bands are numbered from 1 to 10. As a typical example, the band 6 front-end is illustrated in Fig. 1 and operates in the range from 211 to 275 GHz. The optics is located in a cryostat and consists of a corrugated horn and two ellipsoidal mirrors. The apertures corresponding to two thermal filters and a cryostat window are also shown in the figure.

The design of such front-end optics is conveniently carried out by Gaussian beam techniques by which a number of beam parameters can be computed and optimized. More accurate methods are, however, needed for verification of the design.

The corrugated horn designs have for some bands been verified by the CHAMP mode-matching software by which the performance over the full frequency band can be

calculated with high accuracy, including cross polarization and return loss.

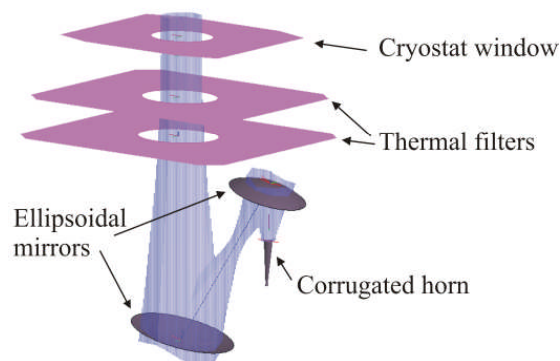


Fig. 1 Band 6 front-end optics.

A detailed analysis of the ellipsoidal mirrors was carried out for all bands by means of Physical Optics using the GRASP software. This gives an accurate prediction of the beam shape, cross-polarization, beam truncation and diffraction at the edges of the mirrors and spill-over loss. The filter and cryostat windows were treated as apertures in screens to determine possible beam truncation effects, whereas reflection and loss in the filter and window material was found from measured data.

A. Feed Lens Analysis

The band 3 front-end operates from 84 to 116 GHz and is shown in Fig. 2. Due to the relatively low frequency the mirrors become large and must be located above the filters and cryostat window and thus outside the cryostat. The limited space also necessitates a short corrugated horn supplemented with a phase correcting plano-convex dielectric lens. A close-up of the horn+lens is shown in Fig. 3.

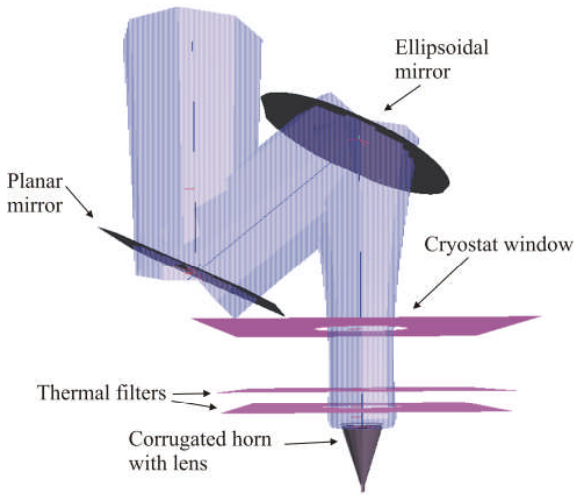


Fig. 2 Band 3 front-end optics.

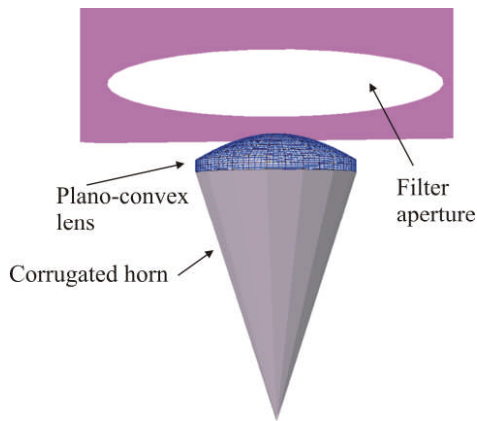


Fig. 3 Band 3 horn with lens.

The analysis procedure was mode-matching for the corrugated horn, a plane-wave expansion to transform the far field of the horn to the lower surface of the lens and then the Method of Moments for analysis of the lens. A special complication is the concentric grooves in the lens as shown in Fig. 4 which act as matching layers. Such grooves cannot be modelled with Physical Optics, but can be handled very accurately by the Method of Moments.

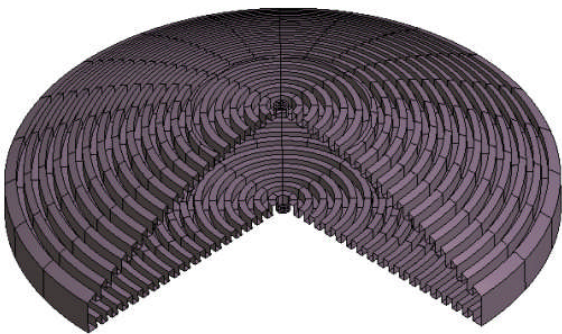


Fig. 4 Band 3 lens with grooves.

The effect of the grooves on the co-polar pattern is shown in Fig. 5 and the cross-polar pattern is shown in Fig. 6. It is seen that the grooves give a very significant reduction of the reflection from the lens, but that the cross-polar maximum is increased by app. 10 dB. It is also seen that such detailed modelling is very important for accurate prediction of the performance.

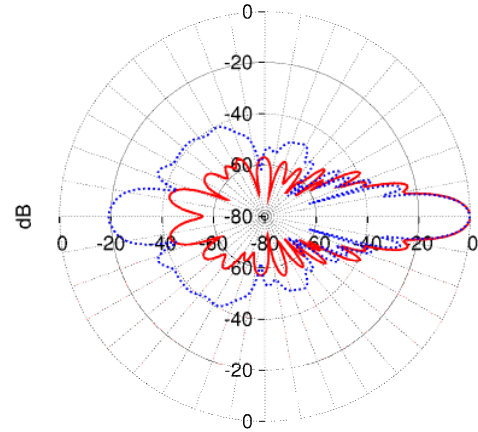


Fig. 5 Band 3 Feed+lens co-polar pattern
Blue curve: Smooth lens
Red curve: Lens with grooves

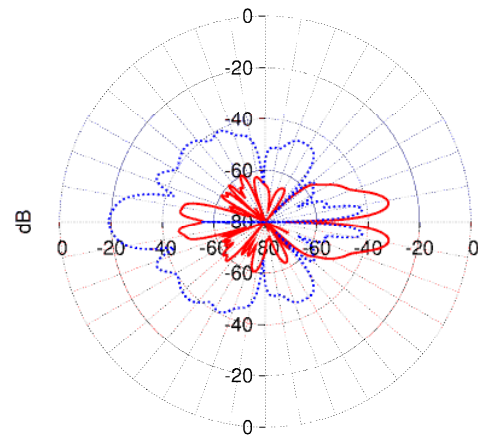


Fig. 6 Band 3 Feed+lens cx-polar pattern
Blue curve: Smooth lens
Red curve: Lens with grooves

B. Polarization Grids

In some of the front-ends, e.g. band 7, a polarization grid is used to split the incoming beam in two polarizations which are directed to two different corrugated horns. The geometry of band 7 is shown in Fig. 7.

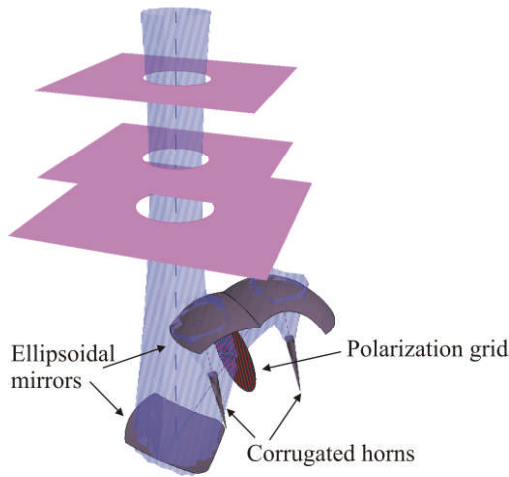


Fig. 7 Band 7 Front-end optics.

The polarization grid is constructed as thin strips located on a dielectric support layer. The maximum spacing of these strips must be app. $\lambda/20$ for good performance. In GRASP the analysis of such structures is carried out by means of plane-wave reflection and transmission coefficients. For simple layers (dielectrics, strip grids [4], etc.) the reflection and transmission coefficients are known and the total coefficients for a layered sandwich structure can be found by a cascade coupling of the reflection and transmission matrices (i.e. S-matrices [3]). Since the incident field on the grid is not a single perfect plane wave an accurate analysis requires expansion of the incident field in a spectrum of plane waves of the form

$$\mathbf{E}(\mathbf{r}) = \sum_i \mathbf{q}_i e^{-j\mathbf{k}_i \cdot \mathbf{r}} \quad (1)$$

where \mathbf{E} is the incident field, \mathbf{r} is the observation point, and \mathbf{q}_i and \mathbf{k}_i are the plane-wave amplitude and propagation vectors, respectively. The analysis proceeds by treating each plane wave separately such that reflection and transmission coefficients are computed for each plane wave. The resulting reflected and transmitted fields are then converted to equivalent electric and magnetic currents which can finally be added and integrated. This procedure is necessary for an accurate treatment of the grid and also reveals significant difference in performance of the two grid orientations shown in Fig. 8 and Fig. 9. The grid in Fig. 8, where the strips are orthogonal to the centre beam direction performs better than the other possibility in Fig. 9, where the grid lines are parallel to the plane define by the incident and reflected centre rays.

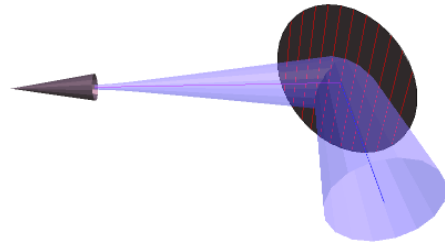


Fig. 8 Strip grid with orientation orthogonal to the plane of incidence.

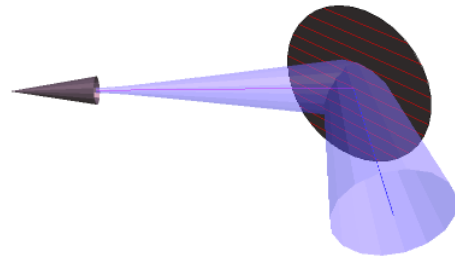


Fig. 9 Strip grid with orientation parallel to the plane of incidence.

C. Front-end Efficiencies

The final step in the front-end analysis was an efficiency calculation that turned out to be of great interest for ESO. Here the front-end performance is subdivided into a number of efficiencies, i.e. amplitude, phase, spill-over and polarization efficiency. In this way it becomes easier to overview the performance and point to possible weaknesses in the front-end. In some cases this has suggested minor modifications and fine-tuning of the optical systems.

The peak directivity of the telescope can be written as

$$\frac{4\pi A}{\lambda^2} \eta_{spill-over} \eta_{polarization} \eta_{amplitude} \eta_{phase} \quad (2)$$

where the first factor $4\pi A/\lambda^2$ is the ideal maximum directivity for an aperture of area A. The remaining four factors are efficiencies for spill-over, polarization, amplitude and phase, respectively. They can be calculated from

$$\begin{aligned} \eta_{spill-over} &= I_1 / (4\pi) \\ \eta_{polarization} &= I_2 / I_1 \\ \eta_{amplitude} &= I_3^2 / (\Omega I_2) \\ \eta_{phase} &= I_4^2 / I_3^2, \end{aligned} \quad (3)$$

where Ω is the solid angle subtended by the subreflector and the I's are the integrals

$$\begin{aligned} I_1 &= \int_{\Omega} |\mathbf{E}_{tot}|^2 d\omega \\ I_2 &= \int_{\Omega} |\mathbf{E}_{co}|^2 d\omega \end{aligned}$$

$$I_3 = \int_{\Omega} |\mathbf{E}_{co}| d\omega \quad (4)$$

$$I_4 = \left| \int_{\Omega} \mathbf{E}_{co} d\omega \right|$$

Here the integrals are calculated over the solid angle Ω , with $d\omega$ as the solid angle element and \mathbf{E}_{tot} and \mathbf{E}_{co} as the total and co-polar E-field, respectively, from the front-end.

As an example the efficiencies for band 7 are shown in Table I.

TABLE I
BAND 7 EFFICIENCIES

Band 7	$\eta_{spill-over}$	η_{pol}	η_{amp}	η_{phase}	η_{total}
324 GHz					
x-pol	0.9370	0.9932	0.9018	0.9996	0.8389
y-pol	0.9377	0.9932	0.9033	0.9995	0.8409
Gauss Beam	0.9399	1.0000	0.8624	1.0000	0.8106

It is seen that the front-end is well designed with high polarization and phase efficiencies, and a good compromise between spill-over and amplitude efficiency. It is also seen that the numbers obtained with the ideal Gaussian beam feed pattern (as used in the synthesis) deviates significantly from the realistic values. Although the Gaussian beam analysis is very useful in the design phase a detailed Physical Optics analysis is thus necessary for verification of the design.

III. TELESCOPE ANALYSIS

One of the telescopes is shown in Fig. 10. The main reflector is 12 m in diameter with a centre hole of 0.75 m and it consists of 120 or 264 panels, depending on the manufacturer. The subreflector is 0.75 m in diameter and it is supported by four struts. The front-ends are located 1.3 m behind the main reflector apex. The subreflector is supplied with a central tip corresponding to the hole in the main reflector.

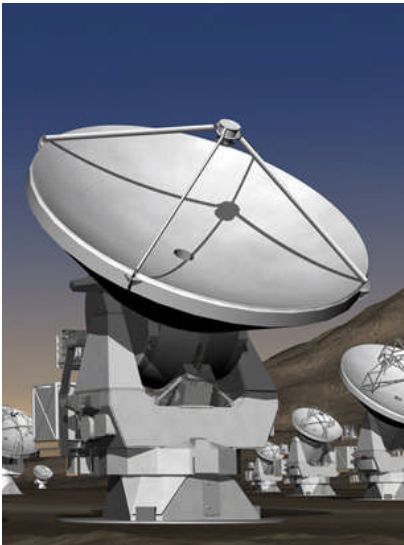


Fig. 10 ALMA telescope

Besides the nominal telescope performance TICRA also calculated a number of individual effects such as strut scattering (from the four support legs, see Fig. 10) and surface tolerance effects. This will be described in the following subsections.

A. Strut Effects

In Fig. 11 the scattering from a single strut is illustrated. An incident field from the telescope mirror (a nearly plane wave) will induce a set of currents on it, which in turn radiates a field illustrated by the red rays in Fig. 11. At each point on the struts the rays form a scattering cone with a half apex angle of $\nu = 62^\circ$. In the vertical direction these rays will be in opposite phase of the main beam and give a small reduction of the peak directivity. Most of the rays will hit the cold sky either directly or through reflection in the mirror as show in Fig. 11, but in a small angular region it is, however, possible that the rays hit the ground which generates noise.

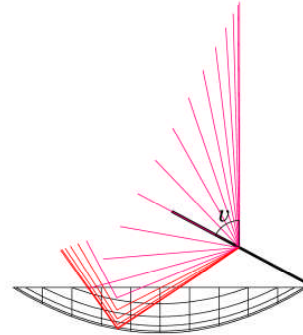


Fig. 11 Strut cross-section

The strut cross-section is elliptical and it is supplied with a cladding to improve the noise performance as shown in Fig. 12. This cladding is undesirable from a mechanical point of view and one task for TICRA was to determine how much it improves the noise performance in order to find out if the added mechanical complexity is justified.

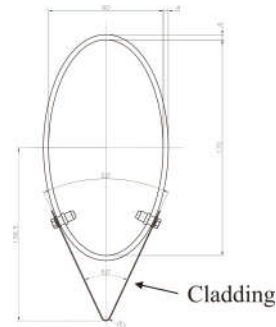


Fig. 12 Strut cross-section

The field from the scattered rays in Fig. 11 is shown in Fig. 13, with and without cladding. Both versions give the same shadowing effect near the boresight direction but away from this direction the elliptical strut gives an almost constant field of 15 dBi. However, the cladding gives rise to

two significant effects. The planar facets of the cladding generates high peaks at 50° on the diffraction cone and above this angle the field is about 10 dB lower than without cladding.

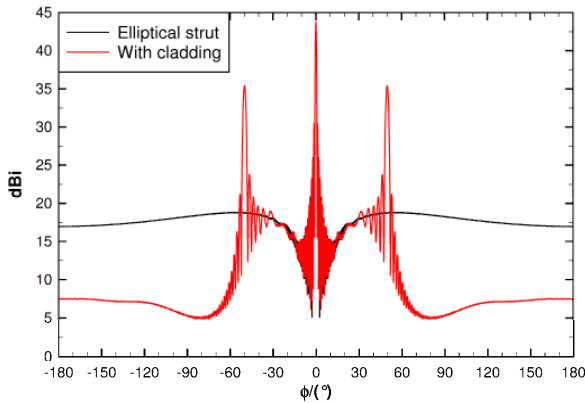


Fig. 13 Strut scattering and effect of the cladding

The angle ϕ in Fig. 13 is measured around the strut with $\phi=0^\circ$ as the boresight direction. With $\theta=0^\circ$ as the axis of the strut in a standard polar coordinate system it turns out that a significant noise contribution from the ground is only obtained in the interval from 106.4° to 147.5° in ϕ and from 61.9° to 62.1° in θ . For all struts this gives a noise contribution of 0.15°K with cladding and 1.72°K without cladding. From these results it was decided that the cladding was necessary.

B. Influence of Reflector Panels

This section describes the influence of the fact that the main reflector consists of a number of panels separated by a certain gap. The goal is to quantify the influence of the gaps. It is assumed that the surface of each panel is identical to that of the parent paraboloid and the feed is located at the focus of the antenna system.

A typical layout of the panels for the main reflector is shown in Fig. 14. The reflector consists of 120 panels located in 5 rings. The width of all gaps, both radial and circumferential, is 1.5 mm.

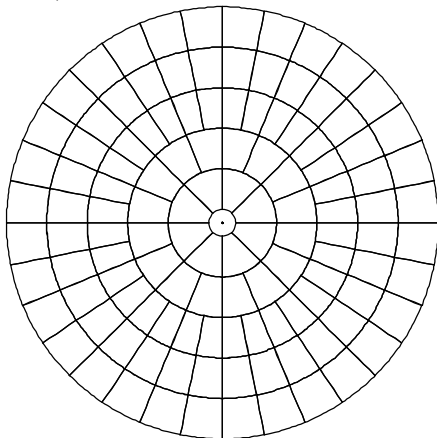


Fig. 14 Typical layout of the main reflector panels.

Fig. 15 shows the radiation patterns for the solid main reflector in black and for the reflector with panels in red. It is seen that the two patterns are almost identical and the

difference pattern in green shows that the influence of the panels is around 70 dB below peak everywhere, except in the beam direction where the panel influence is determined by the gap area, approximately 50 dB below peak. The panel gaps reduce the peak gain by only 0.03 dB.

This result shows that the influence from the panel gaps is very small. This is an important conclusion because it means that all calculations can be carried out for a solid main reflector. The only exception is where the panel mounting errors are investigated and where it is obviously necessary to perform the calculations on the individual panels.

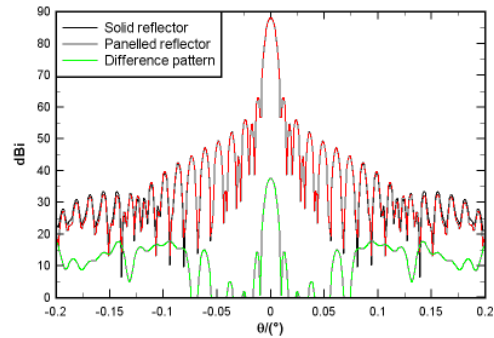


Fig. 15 The influence of the panels for the main reflector. 230 GHz.

C. Main Reflector Surface Errors

1) Gravitation Effects

The main reflector surface will deform due to gravitation, wind and thermal gradients. Here the deformations due to gravitation for 0° elevation are considered. Fig. 16 shows the deformed surface relative to the nominal paraboloid. The unit on the z-axis is mm. It is seen that there is a significant difference, in the order of 0.5 mm at the edge. From the deformed surface it is possible to find a best fit paraboloid. It has six degrees of freedom: the vertex position in x, y and z, the focal length and the axis direction.

Fig. 17 shows the best fit paraboloid relative to the nominal paraboloid and it is seen that most of the deviations in Fig. 16 are very well represented by the best fit paraboloid.

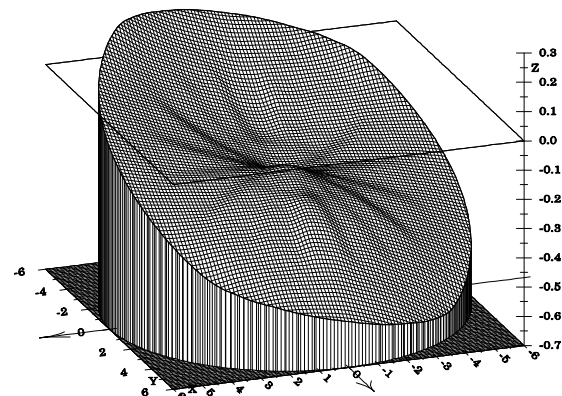


Fig. 16 The deviation between the nominal paraboloid and the reflector subject to gravitation, 0° elevation.

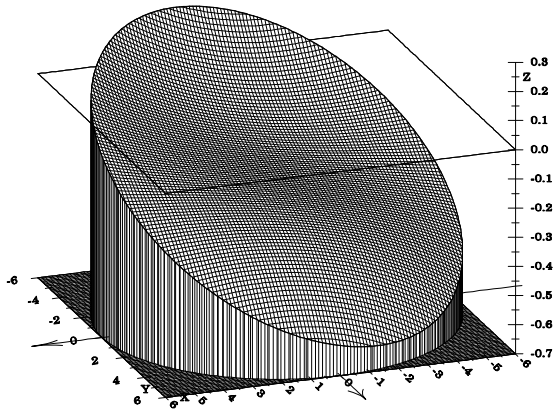


Fig. 17 The deviation between the nominal and the best fit paraboloid, 0° elevation.

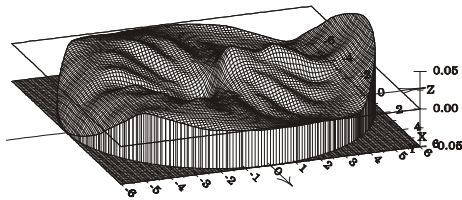


Fig. 18 The deviation between the deformed reflector and the best fit paraboloid, 0° elevation.

In other words, the reflector deformations change the nominal paraboloid into another paraboloid. Fig. 18 shows the remaining surface errors as the difference between the real deformed surface and the best fit paraboloid. The maximum deviation is here only about $50 \mu\text{m}$ and the rms error has been calculated to $12 \mu\text{m}$.

The following plots illustrate the influence from the gravitation effects on the radiated beam. Fig. 19 and 20 show, as an example, the contour plots both for the nominal antenna and for gravitation deformation at 0° elevation at 243 GHz. The four support struts for the subreflector are also included in these calculations and this is the reason for the four-fold symmetry in the contour plots.

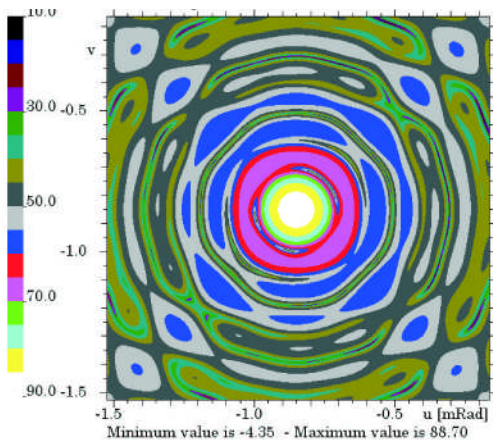


Fig. 19 Contour plot of the nominal beam at 243 GHz. Struts included.

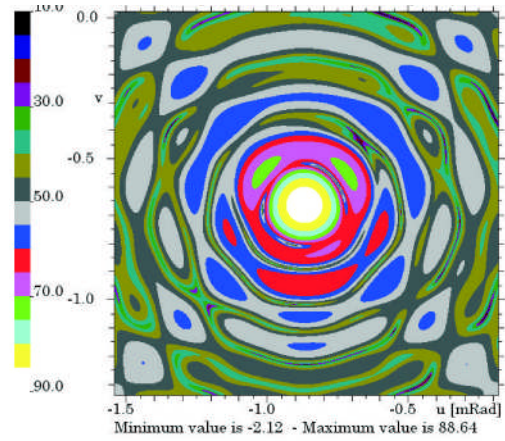


Fig. 20 Contour plot of the gravitation deformed beam at 243 GHz. Struts included.

The same type of plots is shown in Fig. 21 and 22 for 720 GHz. It is clearly seen that the surface deformations are much more critical at the highest frequency. The gain reduction is only 0.06 dB at 243 GHz whereas it increases to 0.50 dB at 720 GHz.

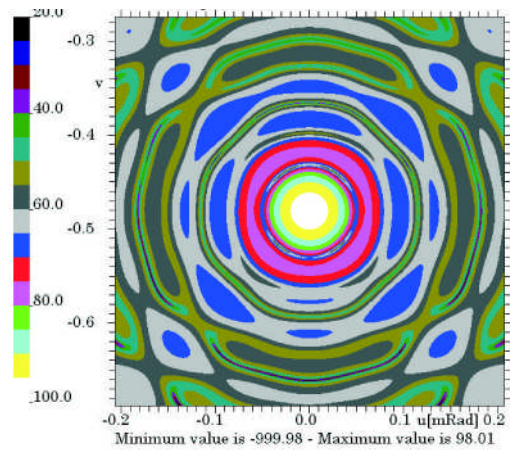


Fig. 21 Contour plot of the nominal beam at 720 GHz. Struts included.

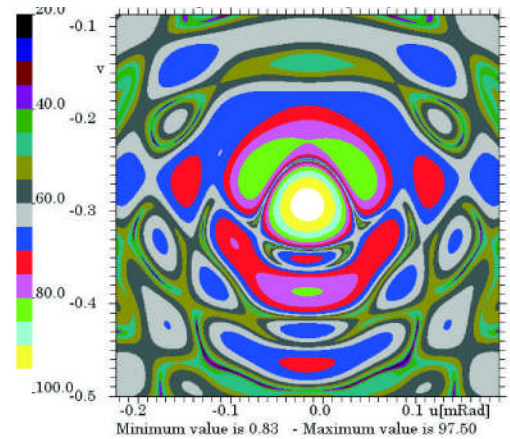


Fig. 22 Contour plot of the gravitation deformed beam at 720 GHz. Struts included.

2) Panel Surface and Alignment Errors

As mentioned earlier, the influence of the panel gaps is very small when the surface shape and alignment of the panels is ideal. In this section both panel deformation and panel alignment errors will be presented.

Based on information from the antenna supplier it was decided to model the panel shape error as a smooth random distortion all over the reflector with an rms error of 8 μm and a correlation distance approximately equal to the panel size.

Each panel is attached at five attachment points and the accuracy at these points is assumed to be 5 μm . A random number generator is used to model the errors at the attachment points. The alignment errors are modelled by tilting each panel individually, without changing its shape, such that it passes through the five points in the best possible way. The principle is illustrated in Fig. 23 where the errors are increased by a factor 10000.

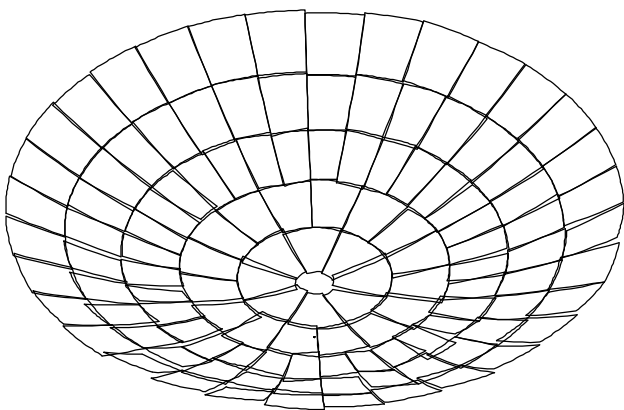


Fig. 23 Main reflector illustrating the panel alignment errors. The realistic errors are multiplied by 10,000 in this figure.

Figures 24 and 25 show contour plots and pattern cuts for the two types of panel errors separately: the manufacturing errors affecting the shape of the panels and the alignment errors affecting the orientation of the panels. Since the impact of these errors is quite small only the results for 720 GHz are presented. The reduction in gain at 720 GHz is 0.18 dB and 0.03 dB for manufacturing and alignment errors, respectively. The corresponding numbers at 243 GHz are 0.02 and 0.00 dB.

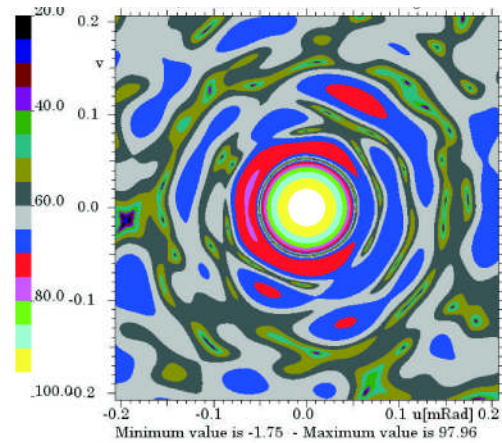


Fig. 24 Contour plot of the beam at 720 GHz for the antenna with panel manufacturing errors.

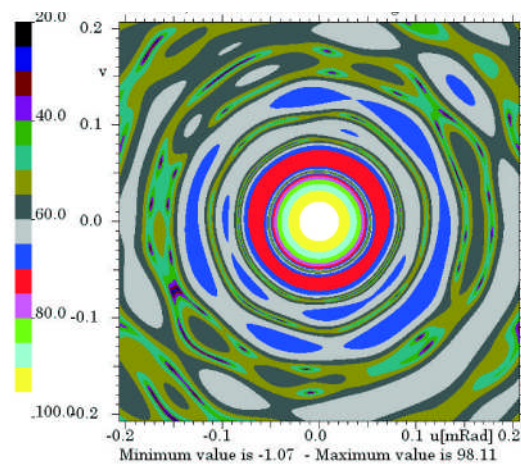


Fig. 25 Contour plot of the beam at 720 GHz for the antenna with panel alignment errors.

IV. CONCLUSIONS

In the present study it is demonstrated that it is possible to do a detailed electromagnetic analysis of the ALMA telescope optics with standard software tools. Detailed performance of the front-ends as well as the telescope mirrors can be computed by means of accurate diffraction methods, such as Physical Optics and the Method of Moments. It is also possible to take into account various distortion effects from e.g. struts and mirror surface errors.

REFERENCES

- [1] K. Pontoppidan, *Electromagnetic properties and optical analysis of the ALMA antennas and Front Ends*, TICRA report No. S-1430-02, ALMA doc. Number: ALMA-80.04.00.00-026-A-REP January 2008.
- [2] M. Carter, *ALMA Front-end Optics Design Report*, FEND-40.02.00.00-035-B-REP, June, 2007.
- [3] K. Pontoppidan, *GRASP Technical Description*, Downloadable from www.ticra.com
- [4] K. Nakamura and M. Ando, *A Full-wave Analysis of Offset Reflector Antennas with Polarization Grids*, IEEE trans. Antennas Propagat., Vol. 36, No. 2, pp. 164-170, 1988.

Session S5: THz Systems and Receivers

A 1THz Receiver System at APEX

C. Leinz^{1*}, M. Caris¹, T. Klein¹, G. de Lange², T. Zijlstra³, T.M. Klapwijk³, H.J. Wunsch¹ and R. Güsten¹

¹Max-Planck-Institut für Radioastronomie, Auf dem Hügel 69, 53121 Bonn, Germany

²SRON Netherlands Institute for Space Research, Postbus 800, 9700 AV Groningen, The Netherlands

³Delft University of Technology, P.O. Box 5046, 2600 GA Delft, The Netherlands

*Contact: cleinz[at]mpifr-bonn.mpg.de

Abstract— We present a two channel heterodyne receiver system operating simultaneously in the 300 μ m and 625 μ m atmospheric windows. For the design of the THz channel, we make use of the technological spin-off of HIFI, the heterodyne instrument on board of the HERSCHEL space telescope. The system concept includes a co-aligned 460GHz channel, to establish a pointing reference and to increase therefore the efficiency of the astronomical operation.

I. INTRODUCTION

Successful ground based astronomical observations in the THz regime are depending on several important factors, the most dominant is the atmospheric transmission, that allows our view into space in a few windows only. The APEX telescope (Fig. 2) with its 12 meter dish, located at an altitude of 5100m in the high Chilean Andes is one of the few places where observations of such short wavelength are possible [1]. Under very good weather conditions an atmospheric transmission of up to 35% (Fig. 1) in the 300 micron window is possible, where statistics show that only in about 5% of the nights the atmosphere is transparent enough for reasonable THz measurements [2].

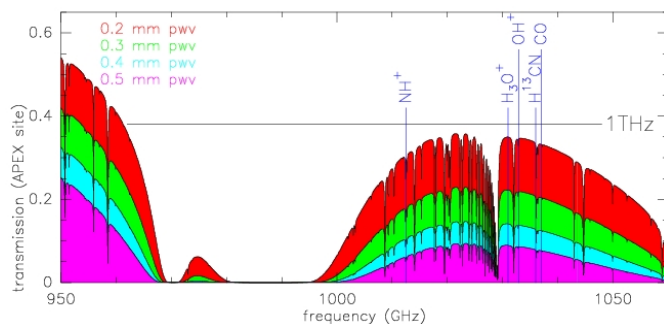


Fig. 1 The atmospheric transmission at APEX in the 300 micron window for different precipitable water vapor values and the RF tuning range of the 1THz Rx.

But not only the atmosphere plays an important role, the telescope itself with its surface accuracy, and pointing capabilities must be able to handle the rather small beams of THz receivers and produce good beam efficiencies on sky. In order to get all these uncertainties included, a robust calibration scheme must also be in place.

The design of the THz receiver fell into the late phase of satellite integration and testing of HIFI [3], which made it possible to use the technological spin-off in mixer and local oscillator (LO) development of band IV. Operating the 1THz RX at APEX will act as a valuable test bed, it allows to study the long term behavior of the used HIFI components, to gain

further knowledge in handling spurious signals and to optimize the operation conditions of the used LO components [4].

A complex system as the 1THz receiver requires a modern infrastructure for operation, like fast data network, broad band IF and backend processing and fast telescope beam switching, all these requirements are provided by APEX.

The instrument was designed as a dual-frequency system. Both channels use SIS mixers, the 1THz channel operates a copy of HIFI band IV ([5],[6]) while the second channel, designed for pointing purposes, uses a 460GHz mixer from the de-commissioned CHAMP array [7]. Two different LO systems are installed. The state-of-the art band IV solid-state active multiplier chain, is feeding the 1THz mixer, while a GUNN oscillator followed by self biased multipliers builds up the 460GHz LO chain.

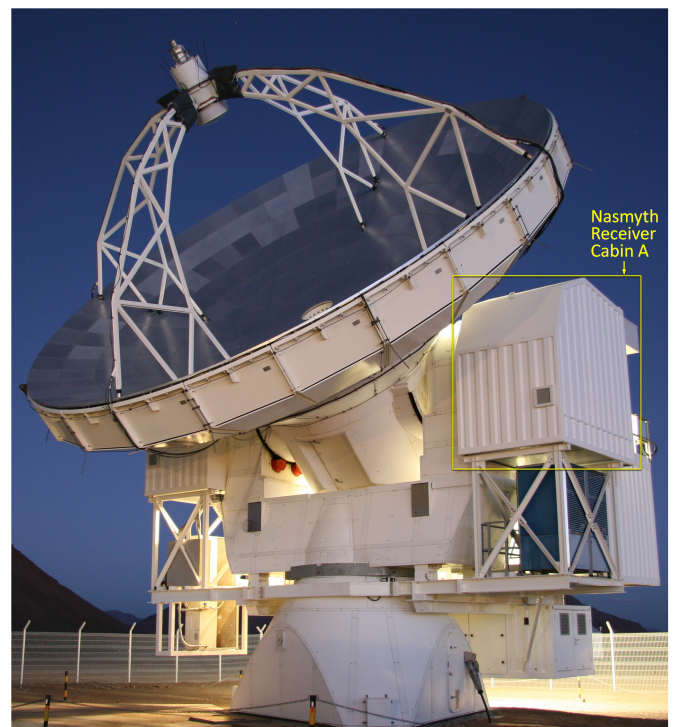


Fig. 2 The APEX telescope short after sunset – marked: Nasmyth receiver cabin A

With the ongoing development of local oscillator sources in the terahertz regime, demanding for high spectral purity, signal stability and sufficient output power, the receiver system also perfectly acts as a test bed for the photonic local oscillator developments at MPIfR [11].

II. SYSTEM DESCRIPTION

In the following paragraphs we will outline the system layout, beginning with the local oscillator systems, followed then by details of the receiver cryostat and an overall system description.

A. 460GHz LO system

The 460GHz LO is a PLL locked GUNN oscillator in W-band, followed by a self-biased multiplier chain. There are no special environmental conditions to take into account, making the LO from a mechanical and electrical point of view rather comfortable to use. All required RF-signals are generated by commercial synthesizers. During telescope operation, the APEX control system [10] commands the synthesizers for the LO frequency and Doppler-shift correction. Therefore, frequency changes can be commanded remotely but require, depending on the covered span, a final re-tuning of the micrometers of GUNN and multiplier waveguide back-shorts to recover LO power.

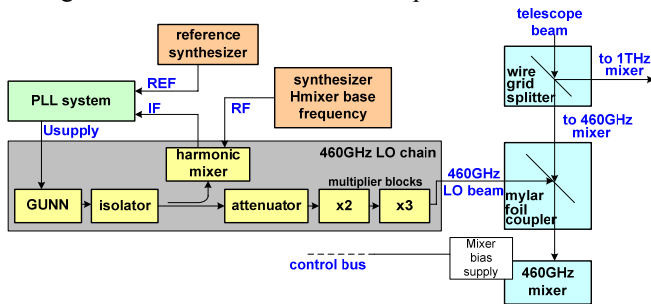


Fig. 3 Schematic of the 460GHz LO subsystem and the LO signal path to the 460GHz mixer

B. 1THz LO system

In contrast to the 460GHz LO layout, output power and foremost lifetime issues make it necessary to operate the 1THz LO chain cold. An additional cryostat increases the mechanical complexity of the system.

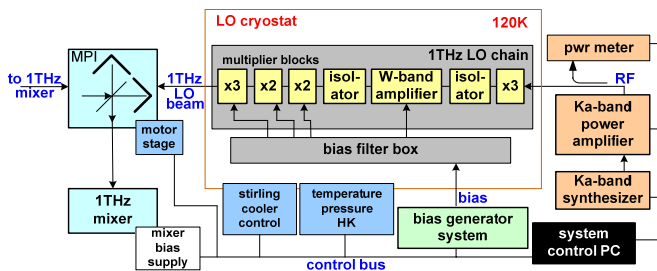


Fig. 4 Schematic of the 1THz LO subsystem and the LO signal injection path to the 1THz mixer

The solution is based on a very compact cryostat design that contains a bias filter box and the LO chain, stacked together in sandwich form. The typical LO chain DC power dissipation of about 3 to 4Watts demands for a cooling system with sufficient power to cool to 120K. In order to have sufficient cooling capacity to compensate for the heat dissipation inside the W-band amplifier, which changes with LO output power, we use a cooler that is capable of handling 6W@77K.

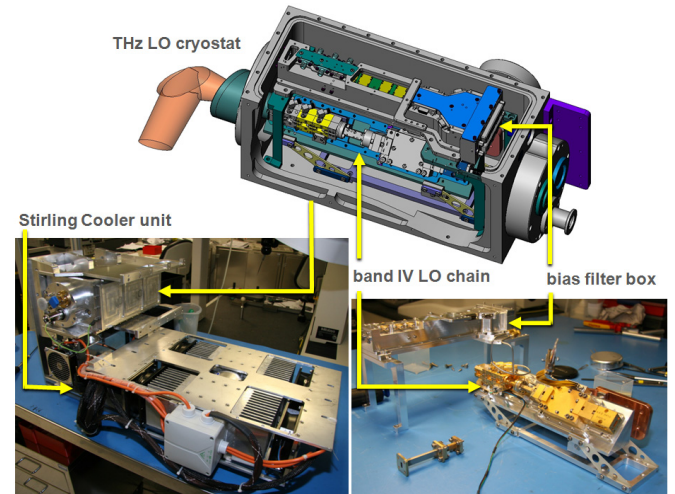


Fig. 5 The 1THz LO cryostat. Left: LO cryostat linked to the Stirling Cooler, the cooler with its radiator system takes most of the space. In the upper right corner is the opened cryostat visible and gives an impression of the very compact design achieved by placing the local oscillator chain and the bias filter box in a stacked way.

Since most of the LO chain's components are actively biased, 7 voltage supplies and additional monitoring of the currents are required to safely operate the chain. We make use of the HIFI LO operation philosophy and strategy, from software as well as from hardware side [8],[9]. Fig. 4 gives a schematic of the 1THz LO subsystem components. The heart of it is the band IV HIFI local oscillator chain. A commercial synthesizer generates the fundamental frequency in Ka-band which is amplified to drive a Ka- to W-band frequency tripler. Output power leveling of the LO chain is achieved by regulating the drain voltage of the second stage of the W-band amplifier. Starting from a safe, low drain voltage with almost no LO chain output power, the drain bias is ramped up to the setting where the mixer is pumped at its optimum level or to the maximum allowed drain voltage value. The Ka-band RF power level, the frequency setting and also the current and voltage housekeeping of the LO chain are monitored. In case that a parameter moves out of predefined ranges, the system takes appropriate measures to bring it back into the safe range or to stop the frequency tuning and set the drain bias voltage or Ka-band drive power to a safe state. The chain produces a peak power level of about 200 μ W, with a lower limit of ca. 40 μ W over the range 967GHz to 1042GHz.

C. The Receiver System

Fig. 6 gives insights into the system configuration. On the cryostat cover plate the warm optic components and both local oscillator systems are mounted. The incoming telescope beam is split by a wire grid into the two signal paths. For the 460GHz channel, we couple the LO signal to the mixer by use of a 10% Mylar foil coupler. On the 1THz side a Martin-Puplett interferometer, used as a diplexer, serves for the LO injection.

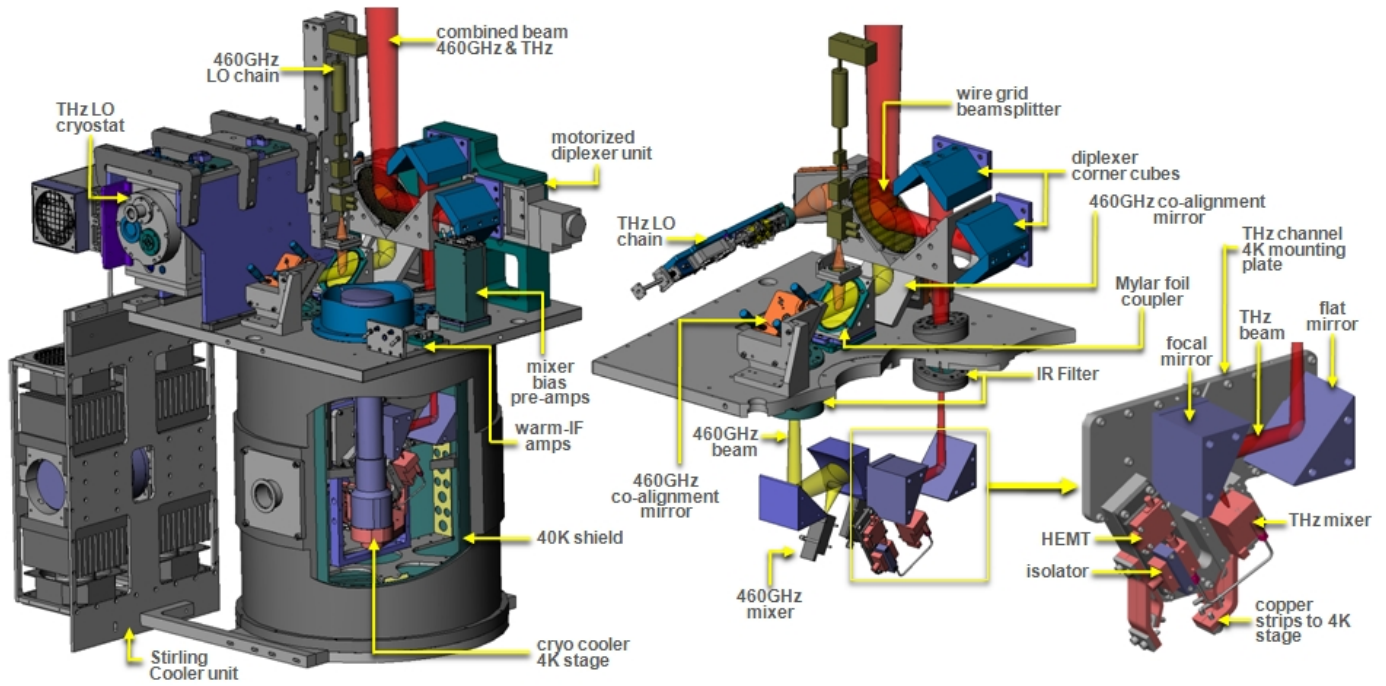


Fig. 6 CAD pictures of the receiver cryostat, generated with the 3D mechanical design software. Left: full integrated system; middle: beam paths with optical components; right: THz channel 4K mounting plate

Although the output power of the solid-state chain is comparably high, we use the Martin-Puplett Interferometer to allow integration of weak LO sources (e.g. the photonic LO source [11]).

For frequency tunings, the moveable arm of the interferometer is motorized to adjust for the correct optical path-length difference with a resolution of 0.1 micron. For the THz beam no adjustable optical elements are foreseen, here we make use of the strict mechanical tolerances achievable in our workshop. In order to co-align the 460GHz pointing channel to the THz beam, two adjustable flat mirrors with micrometer screw drives allow for a tilt and offset move.

We use a 2 stage cryocooler, providing a 40K and 4K temperature level. The cooler's 40K stage is connected to a thermal shield to minimize the radiative thermal load at the 4K stage. Thermally connected to this temperature stage, there are two mounting plates, one for the 460GHz channel and the other for the 1THz channel (Fig. 6 right). Basically these are precision manufactured aluminum plates that carry the mixer, a low noise and high gain HEMT amplifier and two aluminum made mirrors. To improve the signal matching between mixer and HEMT amplifier an RF isolator, useable under cryogenic temperatures and thermally linked to 4K, is additionally inserted in the 1THz IF path. We gained a low thermal resistance path between the channel mounting plates and the 4K stage of the cryocooler by using packets of copper strips, resulting in an operational temperature of the mixer of 3.9K.

The first optical element behind the mixer is an aspheric mirror, followed by a flat mirror to direct the beam towards the warm optic plate. Infrared stray radiation in the beam path is blocked by IR-filters on the 40K and 4K stage. This reduced the mixer's physical temperature by ~0.4K but also

introduces optical loss of 6%. Both cryostat windows use Mylar foils of appropriate thickness to minimize for Fabry-Perot effects.

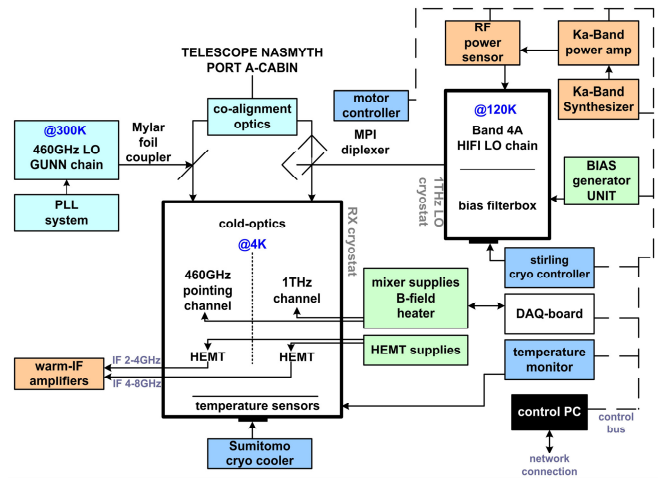


Fig. 7 Schematic of the full system layout

A major benefit of the receiver system is its capability of full remote operation. The control PC connects via a standard instrument bus to the relevant devices and keeps track of important housekeeping parameters on a periodic time base. Tuning requests are accepted via network UDP socket protocol from the APEX telescope control system (APECS).

III. TEST ACTIVITIES

A. Receiver Tests

The system was thoroughly characterized in our laboratory prior to its shipment to APEX. Optimum operation of the receiver is achieved by using look-up tables, where relevant data for the optimum LO bias voltages, synthesizer power

level, diplexer position are stored as a function of frequency. Therefore, a single frequency entry contains more than fifteen parameters. Between two frequency entries, a linear interpolation scheme is in place, but an adequate distribution in frequency is required to get good receiver performance. Fig. 8 gives a simplified overview of the test setup.

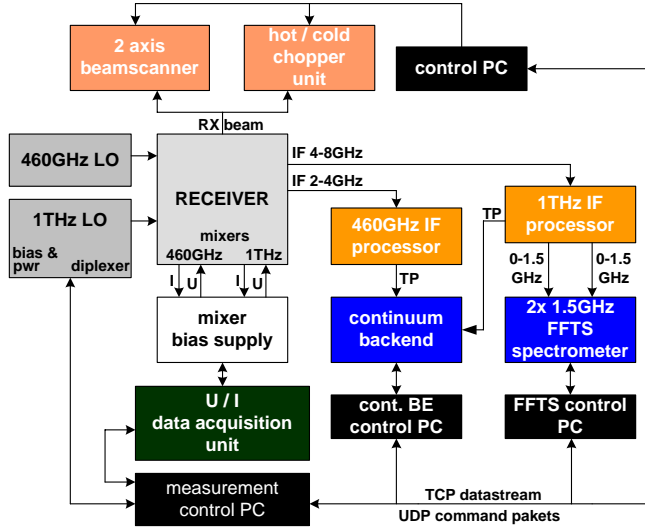


Fig. 8 Laboratory Test Setup

B. Receiver Noise Performance

The receiver noise has been measured with the y-factor method using 290K and 78K absorber loads. A typical measurement is shown in Fig. 9. For the un-pumped device, the total power vs. mixer bias in the shot noise region yields an IF noise temperature $T_{IF} = 16K$. From the hot – and cold traces at the optimum bias point, we derive a total conversion loss $L = 2.9$, resulting in an upper limit of 45K contribution of the IF to the total noise temperature $T_{RX} = 454K$. A successive break-down of the system noise is given in Table 1: Starting from the y-factor measurement at 2.8GHz IF bandwidth, we get 430K at the IF center, explained by the increase of diplexer filter losses at offsets from the IF center. We then subtract the various optical contributions and end up with 292K in front of the mixer. Assuming $L_{mixer}=1$, T_{mixer} would be less or equal 276K, which nicely fits to the mixer's EIDP.

Loss Component	Loss [% ,K]	$T_{ambient}$ [K]	T_{Noise} [K]
y-Factor (2.8GHz IF)			455 K
Diplexer Filter Curve	25 K	290 K	430 K
70cm air	50 K	290 K	380 K
Diplexer insertion	1%	290 K	373 K
Window	10%	290 K	312 K
IR Filter	3%	50 K	301 K
IR Filter	3%	6 K	292 K
Mixer	0%	4 K	276 K

TABLE 1 RECEIVER NOISE CONTRIBUTIONS FROM VARIOUS COMPONENTS

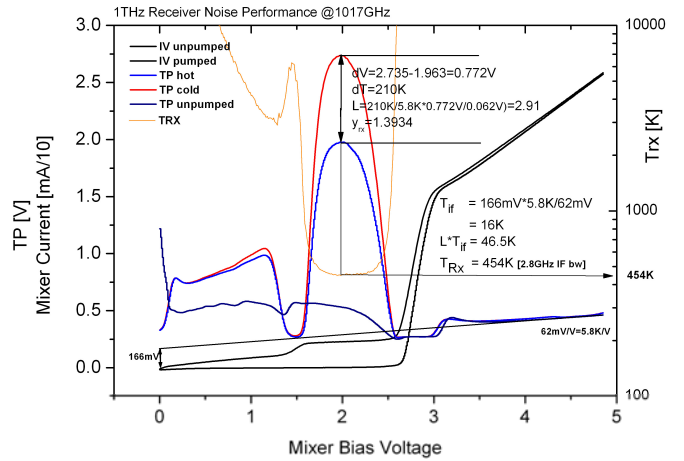


Fig. 9: Receiver noise measurement at 1017GHz. The total power signal contains the IF signal bandwidth of 2.8GHz

D. Local Oscillator Noise

As mentioned above, the total power signal refers to the 2.8 GHz wide IF. Fig. 10 shows T_{RX} vs. IF band frequency and reveals the LO diplexer's filter characteristic pass-band. The black curve of this figure represents the receiver noise temperature for a 120K blackbody¹ LO (physical LO temperature), whereas the red curve has been calculated assuming an equivalent temperature of 350K to fit to the measured T_{RX} . A comparison shows that obviously a significant noise contribution apart from the LO physical temperature is generated by the LO in the range 4.6 - 7.4 GHz offset to its carrier. We have compared this to the HIFI band 4a noise measurements, taken during the HIFI commissioning phase and got to a very similar result.

To eliminate the uncertainty in knowing the exact blackbody temperature of the cooled LO chain, we repeated this test operating the LO at room temperature. Fig. 11 shows the measured T_{RX} and two traces, red and black, representing the calculated T_{RX} for 460K and 290K black body temperature loads at the diplexer LO port. We conclude that the local oscillator signal noise in this configuration is 170K higher than its physical temperature, confirming the above considerations for the cooled LO.

Tuning the LO diplexer to the appropriate path-length difference gets more critical the more LO noise is in excess at the diplexer's LO port. The significant impact of a detuned diplexer on the receiver performance is shown in Fig. 12. Adjusting the tuning mirror position in steps of 6 microns immediately increases the noise temperature, and detuning it more, reveals an excess noise feature at about 600MHz below the IF center. We obviously make use of the diplexer's property, to act as a filter of LO noise in the signal frequency range. Regardless of the sign of the detuning, the noise feature appears at the same IF frequency, because the mixer is a DSB mixer and the LO noise is symmetric wrt. to the

¹ We define the LO physical blackbody temperature of 120K as a lower limit for the noise contribution. A more realistic value would be 150K, as the chain front-side absorber is IR heated. The thermal noise of the window at 290K adds another 30K.

carrier. The only difference appears to be that the higher LO frequency tuning (negative detuning) favored an optical standing wave manifested in an IF ripple. An outmost important conclusion is that only a very precise model to predict the interferometer’s mirror adjustment over the whole RF range can ensure an optimum noise suppression by this filter, when it is operated remotely at the telescope-site.

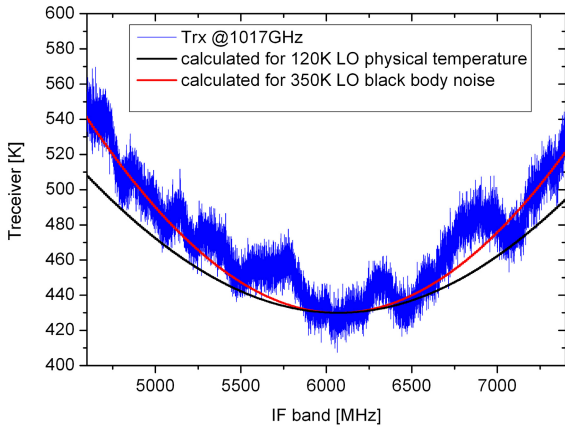


Fig. 10: Measured receiver noise vs. IF band frequency, showing the noise contribution of the local oscillator diplexer pass-band. The black curve indicates the expected noise by the local oscillator port at a physical temperature of 120K, the red curve fits to the measured data assuming 350K LO port load, indicating excess noise of the solid state local oscillator chain.

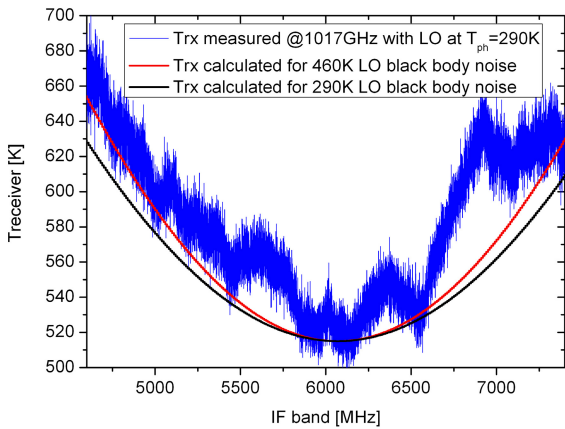


Fig. 11 Measured receiver noise vs. IF band frequency with LO chain operated at room temperature. The black curve represents the calculated noise temperature assuming 290K for the LO, whereas the red curve, assuming 460K, fits to the data. The LO noise is 170K higher than its physical temperature.

C. Beam Measurements

We used a computer controlled two axis motorized moving stage to move a chopped cold load aperture in front of the receiver’s field of view and monitored the total power signals of both receiver channels in parallel. Beside the verification of the telescope beam waist (size and position), the co-alignment of both channels is of outmost importance. Only an excellent relative pointing accuracy can ensure that the 460GHz channel guides the 1THz system in tracking the

weak astronomical source with a 6 arcsecond footprint on sky at 1THz.

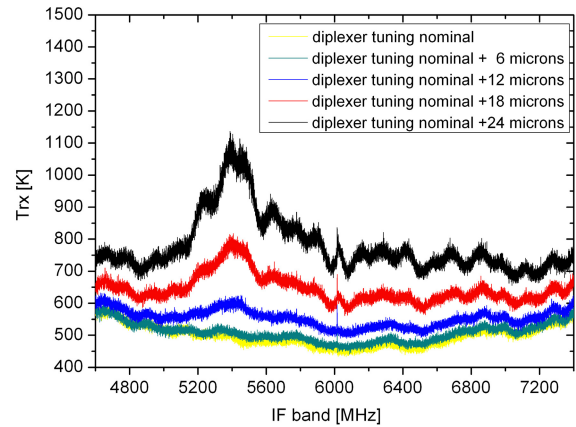
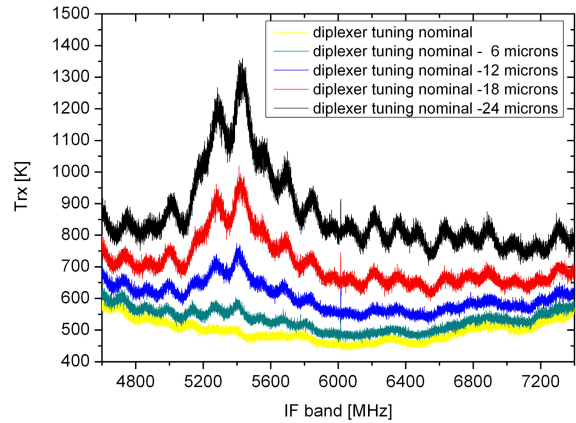


Fig. 12: Trx for various diplexer tunings around the optimum path-length difference. Top and lower figures show the LO noise contribution for negative and positive corner cube mirror movement, respectively. The spike at the band center at the IF center (6GHz) due to the overlay of adjacent backends will be blanked in the calibration pipeline.

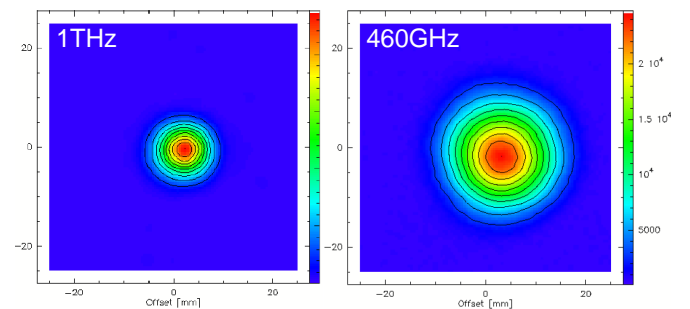


Fig. 13: Beam patterns measured in the laboratory. After de-convolution with the absorber-moon diameter, the waist sizes agree with the telescope nasmyth waist.

IV. RECEIVER AT APEX

The system was installed at the APEX telescope (Fig. 2, Fig. 16) Principle Investigator position #2 of the Nasmyth A flange in mid 2009 for the MPIIR observation periods in August and November.

After first integration tests and fine tunings on the look-up tables, we have been able to reproduce good receiver noise temperatures over the IF range as measured in the laboratory setup. Fig. 14 gives the receiver noise for a remotely invoked tuning by the APEX control system at the CO(9-8) rest frequency. The data was measured by using the telescope's internal calibration load inside the A cabin and the APEX signal processing chain.

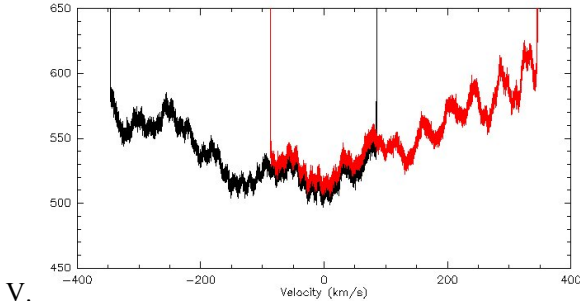


Fig. 14: Receiver noise temperature at the CO(9-8) line USB tuning, LO at 1030.91GHz

By pointing scans on planets we determined the beam size on sky for the 460GHz to be 12.7 arcsec and for the THz channel to be 6 arcsec. At that time Mars was rather small in diameter, 5.4 arcsec only, Jupiter 47.3 arcsec, respectively. These results match pretty well to the telescope's diffraction limited beams.

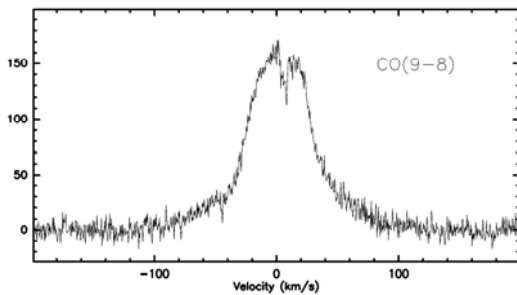


Fig. 15: A CO(9-8) spectrum towards Orion-KL, with PWV ≥ 0.4 mm, main beam brightness of ~ 170 K

Despite of rather bad atmospheric conditions throughout the full observation period, we could make use of nights with PWV values of 0.4mm, just at the edge where useful THz observations are possible. Fig. 15 shows a spectrum towards the star forming region of Orion-KL, centered on the frequency of the CO(9-8) transition. The main beam brightness temperature of ~ 170 K is comparable with those measured with CHAMP+ for the CO(7-6) transition.

VI. CONCLUSIONS

We have presented the system layout and technical details of a dual channel heterodyne instrument, operating in the 300 and 625 micron atmospheric windows at APEX. The 1THz and 460GHz beams are optically co-aligned which allows to guide the 1THz observation with the 460GHz channel (at 1THz there are very few pointing sources available). Unusually bad weather conditions with high PWV during the observation periods in 2009 made challenging observations impossible. After establishing a pointing model, we managed to take a few spectra towards the star forming region of

Orion-KL. This, at least, proved the robustness of our data pipeline and the pointing procedure. The receiver will return to APEX for the 2010 observing season.

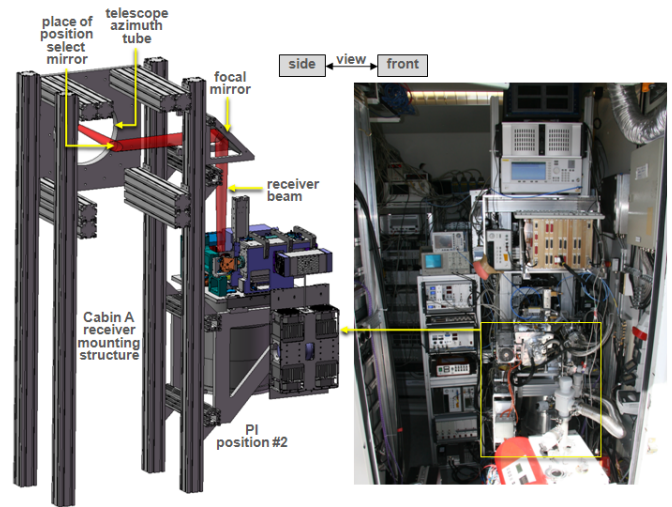


Fig. 16: Receiver installed in A-cabin at APEX, with all the electronics for operation the receiver consumes quite an amount of space

ACKNOWLEDGMENT

We thank the MPIfR mechanical workshop for excellent machining, C. Kasemann (MPIfR) for his contributions, and the APEX telescope staff for the support during installation and operation phase at the telescope.

REFERENCES

- [1] R. Güsten, et. al.: "APEX, The Atacama Pathfinder Experiment", in Proc. SPIE, 2006, 6267, 626714.
- [2] Atmospheric transmission calculator for Llano de Chajnantor, <http://www.apex-telescope.org/sites/chajnantor/atmosphere/>
- [3] T. de Graauw, et. al.: "The Herschel-Heterodyne Instrument for the Far-Infrared (HIFI): instrument and pre-launch testing", Proc. SPIE 7010, 701004, 2008
- [4] J. Pearson, R. Güsten, T. Klein, N. Whyborn: "Local Oscillator System for the Heterodyne Instrument for FIRST", Proc. SPIE, vol. 4013, p. 264, UV, Optical and IR Telescopes and Instruments, 2000.
- [5] G. de Lange, B.D. Jackson, M. Hochemsen, et. al.: "Performance of the flight model HIFI band 3 and 4 mixer units", Proc. SPIE 6275, 2006
- [6] B.D. Jackson, G. de Lange, T. Zijlstra, et al.: "Low-noise 0.8-0.96 and 0.96-1.12THz Superconductor-Insulator-Superconductor Mixers for the Herschel Space Observatory", IEEE transaction on microwave theory and techniques, vol 54, no. 2, 2006
- [7] R. Güsten, G. Ediss, F. Gueth, K. Gundlach, H. Hauschildt, C. Kasemann, T. Klein, J. Kooi, A. Korn, I. Kramer, R. LeDucc, H. Mattes, K. Meyer, E. Perchtold, M. Pilz, R. Sachert, M. Scherschel, P. Schilke, G. Schneider, J. Schraml, D. Skaley, R. Stark, W. Wetzker, H. Wiedenhöver, W. Wiedenhöver, S. Wongsowijoto, F. Wyrowski: "CHAMP - The Carbon Heterodyne Array of the MPIfR", Proc. SPIE Vol.3357, 1997, p.167-177
- [8] P. Orleanski, M. Ciechanowicz, M. Michalska, W. Nowosielski, M. Rataj, M. Winkler: "LCU: the control unit dedicated for local oscillator subsystem in ESA HIFI/Herschel project", Proc. SPIE 6159, 2006
- [9] M. Michalska, G. Juchikowski, T. Klein, C. Leinz, W. Nowosielski, P. Orleanski, J. Ward: "Safe Operation of HIFI Local Oscillator Subsystem on Herschel Mission", COSPAR, Symposium E, session 16 (poster). Paper Number: E16-0034-08.
- [10] D. Muders, et. al.: "APECS - The Atacama Pathfinder Experiment Control System", A&A, 2006, vol. 454, pp L25.
- [11] I. Cámara Mayorga, A. Schmitz, T. Klein, C. Leinz and R. Güsten: "Photonic Local Oscillator for Terahertz Heterodyne Astronomy", these proceedings

A 9-beam 2SB Receiver for Millimeter-wave Radio Astronomy

W.L. Shan^{*}, J. Yang^{*}, S.C. Shi^{*}, Q.J. Yao^{*}, Y.X. Zuo^{*}, S.H. Chen^{*}, Q. G. Huang^{*}, A.Q. Cao^{*}, Z.H. Lin^{*},
X. G. Zhang^{*}, W.Y. Duan^{*}, S. Li^{*}, P. Yang^{*}, J.Q.Zhong^{*†}, Z.Q. Li^{*†}, J. Liu^{*†} and K. Liu^{*†}

^{*}Purple Mountain Observatory
Chinese Academy of Sciences
Email: shan@pmo.ac.cn

[†]Graduate School
Chinese Academy of Sciences

Abstract

A 3X3 multi-beam receiver is being developed for Delingha millimeter telescope, the major open facility for millimeter-wave radio observation in China, aiming to significantly enhance the mapping capability in millimeter-wave line observation. The receiver employs sensitive SIS mixers, working over 85-116GHz frequency range. Sideband separation (2SB) scheme is adopted to enable high-precision calibration procedure and to reduce the idle sideband noise especially when the atmosphere transparency is not good in some seasons. The SIS mixers were designed to have nearly constant dynamic resistance and uniform conversion gain, allowing stable bias and direct connection of the SIS mixer and the cryogenic low noise amplifier without an IF isolator. Besides, low noise and stable digital SIS bias circuit has been designed to operate the SIS mixer efficiently. The nine 2SB mixers are driven by a single LO signal source. Two stages of cascaded power dividers realized by 6-branch line directional couplers distribute the LO signal with good isolation between paths. The LO is generated by a frequency synthesizer followed by an amplifier-multiplier module providing output power not less than 10mW across the RF band. The IF band is centered at 2.64GHz and bandwidth 1GHz allowing simultaneously observing three CO lines ($C^{18}O$, ^{13}CO and ^{12}CO), which has been proved to be an efficient observation mode in probing a broad range of gas density. The nine pixels yield 18 independent IF outputs. Each of them is processed by a digital FFT spectrometer with 200MHz-1GHz reconfigurable bandwidth and 16384 channels, which has obvious merits over the present analog AOS system to form a compact and reliable backend system for focal array receiver. In this symposium the design and the performance of this multi-beam receiver will be presented.

ALMA Band 5 cartridge performance.

Bhushan. Billade*, I. Lapkin*, O. Nystrom*, E. Sundin*, M. Fredrixon*, R. Finger[†], H. Rashid*, V. Desmaris*, D. Meledin*, A. Pavolotsky*, and Victor Belitsky*

*Dept. of Radio and Space Science
Chalmers University of Technology, Gothenburg, Sweden.
Email: bhushan.billade@chalmers.se

[†]University of Chile, Santiago, Chile.

Abstract

Work presented here concerns the design and performance of the ALMA Band 5 cold cartridge, one of the 10 frequency channels of ALMA project, a radio interferometer under construction at Atacama Desert in Chile.

The Band 5 cartridge is a dual polarization receiver with the polarization separation performed by orthomode transducer (OMT) [1]. For each polarization, Band 5 receiver employs sideband rejection (2SB) scheme based on quadrature layout, with SIS mixers covering 163-211 GHz with 4-8 GHz IF. The LO injection circuitry is integrated with mixer chip and is implemented on the same substrate, resulting in a compact 2SB assembly.

Amongst the other ALMA bands, the ALMA Band 5 being the lowest frequency band that uses all cold optics, has the largest mirror. Consequently, ALMA Band 5 mirror along with its support structure leaves very little room for placing OMT, mixers and IF subsystems. The constraints put by the size of cold optics and limited cartridge space, required of us to revise the original 2SB design and adopt a design where all the components like OMT, mixer, IF hybrid, isolators and IF amplifier are directly connected to each other without using any co-ax cables in-between. The IF subsystem uses the space between 4 K and 15 K stage of the cartridge and is thermally connected to 4 K stage. Avoiding co-ax cabling required use of custom designed IF hybrid, furthermore, due to limited cooling capacity at 4 K stage, resistive bias circuitry for the mixers is moved to 15 K stage and the IF hybrid along with an integrated bias-T is implemented using superconducting micro-strip lines.

The E-probes for both LO and RF waveguide-to-microstrip transitions are placed perpendicular to the wave direction (back-piece configuration). The RF choke at the end of the probes provides a virtual ground for the RF/LO signal, and the choke is DC grounded to the chassis. The on-chip LO injection is done using a microstrip line directional coupler with slot-line branches in the ground plane. The isolated port of the LO coupler is terminated by floating wideband elliptical termination. The mixer employs two SIS junctions with junction area of $3 \mu m^2$ each, in twin junction configuration, followed by a quarter wave transformer to couple it to the signal probe. A quarter-wave high impedance line on an extra layer of SiO_2 is used to extract the IF by separating from RF [2].

At the conference, we plan to present details of the cartridge design and results of the experimental characterization of the ALMA Band 5 cold cartridge.

REFERENCES

- [1] The actual Band 5 OMT uses slightly modified design suggested by Dr. S. Asayama for Band 5 and based on the ALMA Band 4 cartridge OMT.
- [2] Bhushan Billade, "Design of Dual Polarization Sideband Separation Mixer for ALMA Band 5", Thesis for the degree of licentiate of engineering, ISBN/ISSN:1652-9103, Gothenburg 2009.

Measurement Results of the Caltech Submillimeter Observatory 230 GHz and 460 GHz Balanced Receivers

J. W. Kooi*, R. R. Monje *, B. L. Force*, F. Rice*, D. Miller*, and T. G. Phillips*.

*Dept. of Physics
California Institute of Technology
Email: kooi@caltech.edu

Abstract

The Caltech Submillimeter observatory (CSO) is located on top of Mauna Kea, Hawaii, at an altitude of 4.2km. The existing suite of heterodyne receivers covering the submillimeter band is rapidly aging, and in need of replacement. To this extend we have developed a family of balanced receivers covering the astrophysical important 180-720 GHz atmospheric windows.

For the CSO, wide IF bandwidth receivers are implemented in a balanced receiver configuration with dual frequency observation capability^{1, 2}. This arrangement was opted to be an optimal compromise between scientific merit and finite funding.

In principle, the balanced receiver configuration has the advantage that common mode amplitude noise in the LO system is canceled, while at the same time utilizing all available LO power. Both of these features facilitate the use of commercially available synthesized LO system. In combination with a 4 GHz IF bandwidth[†], the described receiver layout allows for rapid high resolution spectral line surveys.

Dual frequency observation is another important mode of operation offered by the new facility instrumentation. Two band observations are accomplished by separating the H and V polarizations of the incoming signal and routing them via folded optics to the appropriate polarization sensitive balanced mixer.

Scientifically this observation mode facilitates pointing for the higher receiver band under mediocre weather conditions and a doubling of scientific throughput (2 x 4 GHz) under good weather conditions.

Not only do these changes greatly enhance the spectroscopic capabilities of the CSO, they also enable the observatory to be integrated into the Harvard-Smithsonian Submillimeter Array (eSMA) as an additional baseline.

The upgrade of the 345 GHz/650 GHz dual band balanced receivers is not far behind. All the needed hardware has been procured, and commissioning is expected the summer of 2010.

[†]The SIS junctions are capable of a 2-12 GHz bandwidth.

REFERENCES

- [1] J. W. Kooi, A. Kovacs, B. Bumble, G. Chattopadhyay, M. L. Edgar, S. Kaye, R. LeDuc, J. Zmuidzinas, and T. G. Phillips, "Heterodyne Instrumentation Upgrade at the Caltech Submillimeter Observatory," in Proc. SPIE, 21-25 Jun., Glasgow, Scotland, United Kingdom, (2004).
- [2] J. W. Kooi, A. Kovacs, M. C. Sumner, G. Chattopadhyay, R. Ceria, D. Miller, B. Bumble, R. LeDuc, J. A. Stern, and T. G. Phillips, "A 275-425 GHz Tunerless Waveguide Receiver Based on AIN SIS Technology", in IEEE Trans. Microwave Theory and Techniques, Vol. 55, No. 10, pp. 2086-2096, Oct. (2007).

CASIMIR: A high resolution, far-IR/submm spectrometer for airborne astronomy

M. L. Edgar^{*}, M. Emprechtinger[†], A. Karpov[†], R. Lin[‡], S. Lin[‡], F. Maiwald[‡], I. Mehdi[‡],
D. Miller[†], S. J. E. Radford[†], F. Rice[†], J. Ward^{‡§} and J. Zmuidzinas[†]

^{*} California Institute of Technology,
MS 301-17,
Pasadena, CA, 91125
U.S.A.

Email: mick@submm.caltech.edu

[†]California Institute of Technology

[‡]Jet Propulsion Laboratory

Pasadena, CA 91109

[§]Currently at Raytheon Company,
Fort Wayne, Indiana, USA

Abstract—CASIMIR, the Caltech Airborne Submillimeter Interstellar Medium Investigations Receiver, is a far-infrared and submillimeter heterodyne spectrometer, being developed for the Stratospheric Observatory For Infrared Astronomy, SOFIA. CASIMIR will use newly developed superconducting-insulating-superconducting (SIS) mixers. Combined with the 2.5 m mirror of SOFIA, these detectors will allow observations with high sensitivity to be made in the frequency range from 500 GHz up to 1.4 THz. Initially, at least 5 frequency bands in this range are planned, each with a 4-8 GHz IF passband. Up to 4 frequency bands will be available on each flight and bands may be swapped readily between flights. The local oscillators for all bands are synthesized and tuner-less, using solid state multipliers. CASIMIR also uses a novel, commercial, field-programmable gate array (FPGA) based, fast Fourier transform spectrometer, with extremely high resolution, 22000 (268 kHz at 6 GHz), yielding a system resolution $> 10^6$. CASIMIR is extremely well suited to observe the warm, ≈ 100 K, interstellar medium, particularly hydrides and water lines, in both galactic and extragalactic sources. We present an overview of the instrument, its capabilities and systems. We also describe recent progress in development of the local oscillators and present our first astronomical observations obtained with the new type of spectrometer.

I. INTRODUCTION

CASIMIR[1], the Caltech Airborne Submillimeter Interstellar Medium Investigations Receiver, is a far-infrared (FIR) and submillimeter, very high-resolution, heterodyne spectrometer. It is being developed as a first generation, Principal Investigator class instrument for the Stratospheric Observatory For Infrared Astronomy, SOFIA [2]-[4]. Observations with CASIMIR on SOFIA are expected to begin in 2013 and the instrument should be available to guest investigators soon after. It is anticipated SOFIA will eventually achieve a flight rate of up to 160 flights per year, with a lifetime of 20 years.

Species	Transition	Frequency (GHz)	E_{lower} (K)	Atmospheric Transmission	
				1 mm H ₂ O	SOFIA
CH	$F_1 \rightarrow F_2; J = 3/2^- \rightarrow 1/2^+$	536.76	0.0	0 %	97 %
H ₂ ¹⁸ O	$1_{10} \rightarrow 1_{01}$	547.68	34.2	0 %	81 %
NH ₃	$1_0 \rightarrow 0_0$	572.50	0.0	0 %	94 %
H ₂ ¹⁸ O	$2_{11} \rightarrow 2_{02}$	745.32	100.6	0 %	82 %
NH	$N = 1 \rightarrow 0; J = 2 \rightarrow 1$	974.48	0.0	0 %	96 %
H ₃ O ⁺	$0_0^- \rightarrow 1_0^+$	984.66	7.5	0 %	65 %
NH ⁺	$3/2^+ \rightarrow 1/2^-$	998.90	0.0	0 %	95 %
HF	$1 \rightarrow 0$	1232.48	0.0	0 %	30 %
H ₂ D ⁺	$1_{01} \rightarrow 0_{00}$	1370.09	0.0	0 %	94 %
N ⁺	$^3P; J = 1 \rightarrow 0$	1461.13	0.0	0 %	92 %
¹⁶ OH	$^2\Pi_{1/2}; J = 3/2^+ \rightarrow 1/2^-$	1837.82	181.9	0 %	94 %
C ⁺	$^2P; J = 3/2 \rightarrow 1/2$	1900.54	0.0	0 %	88 %
CH ₂	$1_{10} \rightarrow 1_{01}$	1917.66	22.4	0 %	99 %
CO	$18 \rightarrow 17$	1956.02	751.7	0 %	90 %

Fig. 1. Comparison of atmospheric transparency for a selection of significant astronomical lines between good conditions on Mauna Kea and within the stratosphere

Initially, CASIMIR will cover a frequency range from 500 GHz up to 1.4 THz. The frequency coverage may eventually be expanded up to 2 THz. It will be capable of covering this range at a resolution of $> 10^6$.

The FIR/submm is extremely important for the investigation of both the galactic and extragalactic warm ($T \sim 100$ K), interstellar medium. This material is heated by shock waves or UV radiation, phenomena that are often associated with star formation or other high energy events, e.g. supernovae or active galactic nuclei. This excited material then re-emits either as dust continuum radiation or gas line emission. CASIMIR will be able to utilize recent advances in the sensitivity of superconducting mixers to study the fundamental rotational transitions of many astronomically significant molecules, which cannot be observed with ground based telescopes, see Figure 1.

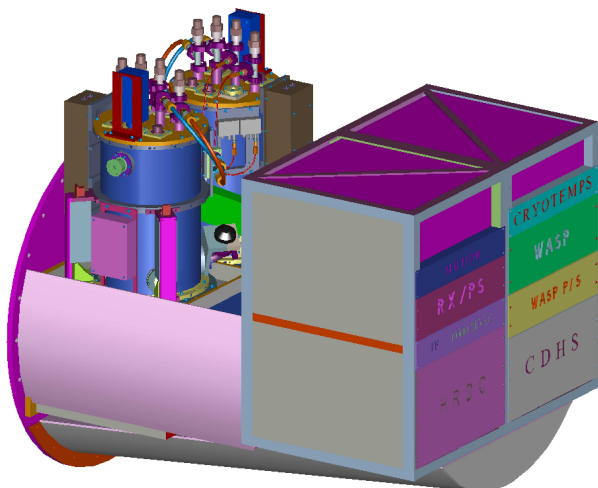


Fig. 2. The CASIMIR instrument. The instrument is mounted to the telescope via the round flange at extreme left of the figure. This flange forms the pressure interface between the telescope cavity and the aircraft's cabin. The portion of the instrument shown is located in the cabin, with the observers. The telescope beam enters the instrument through the center of this round flange, about 150 mm below the bases of the cryostats. The instrument structure is constructed almost exclusively of aluminum. It is approximately 1.5 m long by 1 m square. It weighs approximately 550 kg, including 150 kg of electronics mounted in the racks, at the right of the figure. Approximately 150 kg more of ancillary electronics are located elsewhere in the aircraft cabin.

II. INSTRUMENT CONFIGURATION AND STRUCTURE

The general layout of the CASIMIR instrument is shown in Figure 2. Two cryostats are mounted side by side on top of a box, which contains the relay optics, see Section II-A.

Two 19-inch racks are mounted directly behind this box. All the critical electronics components are mounted in these racks, eg. the LO drive electronics and the microwave spectrometers. This ensures very short cable runs to the cryostat and prevents any differential rotation. All electronic systems for the instrument are packaged as 19-inch bins, which will allow easy replacement of any unit and reconfiguration of the electronics.

A. Optics Box

Figure 3 shows a 3D model of the Optics Box, which is the mount for the cryostats and contains all the optics common to all frequency bands. The central feature is a plane mirror, which can be commanded to rotate through $\pm 180^\circ$ in the plane of the telescope and up to $\pm 5^\circ$ in tilt. This rotating mirror directs the telescope beam to one of the four elliptical mirrors mounted on the two cryostats, selecting the frequency band.

The calibration system consists of a chopper wheel at ambient temperature plus hot and ambient temperature loads. Moving the rotating mirror by $\sim 180^\circ$, allows any of the frequency bands to be first illuminated with the sky signal and then the signal from a known temperature calibration load.

CASIMIR will use the fully reflective tertiary mirror on SOFIA's telescope. As a result, none of the observatory's guiding cameras will be able to image the telescope's focal

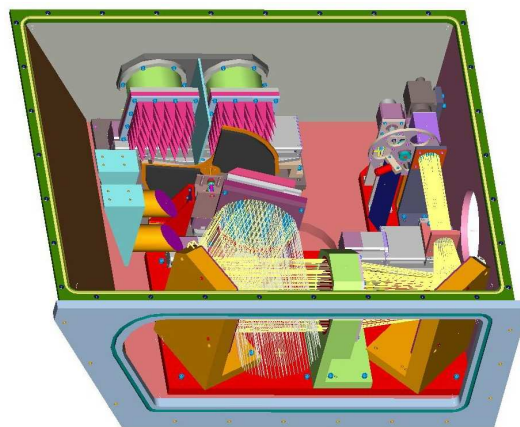


Fig. 3. The Optics Box. The cryostats are bolted directly to the lid of this box, which has been removed for this image. The elliptical mirrors mounted on the base of the cryostats protrude through an aperture in the lid and are located in the plane of the telescope beam. The two elliptical mirrors for one of the cryostats are shown in the left part of the image. The telescope beam enters from the front of the figure. In this image, the rotating mirror, at the center of the figure, directs the telescope beam to the optical boresight, at the far right rear corner. The calibration chopper wheel and the two loads are shown in the rear of the figure. The box forms part of the pressure interface between the aircraft cabin and the exterior, i.e. the box interior is exposed directly to the telescope cavity, so that at altitude, the pressure inside is ~ 200 Tr. The wall thickness varies between 0.5 and 0.75 in.

plane. Therefore, we have included an optical boresight camera, inside the Optics Box, for alignment and beamfinding. The boresight can also be used as a pupil imager by moving a biconcave lens into the optical path. The camera has a $6' \times 6'$ field of view and uses a 1024×1024 pixel, optical wavelength CCD. The rotating mirror also selects this camera.

Stepper motors are used to move all the optical components. All of these motors are mounted inside the Optics Box and are controlled remotely via software. There are only electronic feedthroughs mounted in the sides of the box, without any mechanical motions through the pressure boundary. Physical access to the Optics Box will not be required at any time during the flight.

B. Cryostats

The cryostats are of conventional design with LN_2 and LHe reservoirs, see Figure 4. For frequencies below 1 THz, the mixers will operate at ~ 4 K. At higher frequencies, we will pump on the LHe reservoir to operate the receivers at ~ 2.5 K.

There will be two cryostats per flight and up to two frequency bands in each cryostat, so there will be up to four bands available per flight. Observations can be made with only one band at a time. Any one of the four bands can be selected at anytime during the flight. This selection is made by software alone, and does not require caging of the telescope, any mechanical adjustment or physical access to the instrument.

As shown in Figures 4 and 5, all the components specific to an individual frequency band are integrated directly onto the cryostat, eg. the LOs, IF systems and relay optics. All systems mounted elsewhere on the instrument are used for all of the bands. Therefore, the selection of the four bands which

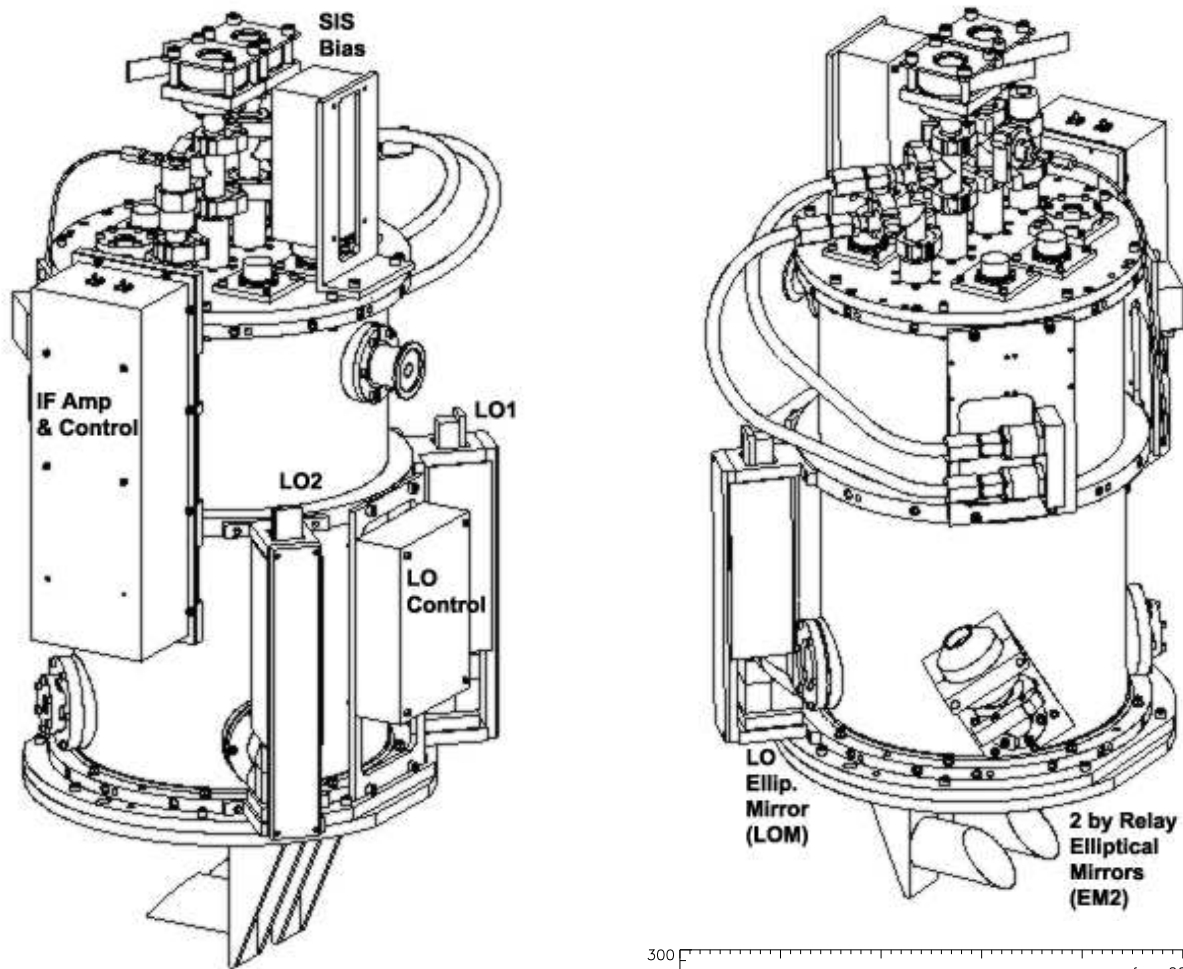


Fig. 4. The CASIMIR Cryostat. The cryostat contains 5 liters each of LN₂ and LHe and has a 250 mm diameter cold-work-surface. This is the maximum, practical diameter for cryostats that can be used in the side-by-side configuration for SOFIA. It is 600 mm high and weighs ~40 kg. The LOs, IF system, receiver and LO bias electronics are mounted directly to the side of the cryostat. The electronics for the cryogenic amplifier bias and mixer electromagnet current are also mounted on the cryostat but are not shown in this view. The two elliptical mirrors of the relay optics, mounted on the base of the cryostat, can be seen at the extreme bottom of the image.

are to be used on a given flight is determined by the choice of cryostats. Swapping of cryostats could easily be carried out between flights. Also, any upgrades and improvements to the bands could be accomplished independently of the rest of the instrument. This will allow continuous upgrades to the frequency bands, throughout the life of the instrument.

C. Optics

Figure 5 shows a schematic of the relay optics, which uses two off-axis, elliptical mirrors to match the incoming telescope beam to the output beam of the mixer. Including the three telescope mirrors, there are five mirrors at ambient temperature and one cryogenically cooled mirror, EM1, in the optical train.

The window in the base of the cryostat is the only pressure boundary in the optical path from the telescope. Therefore, this window and a lens in the mixer assembly are the only

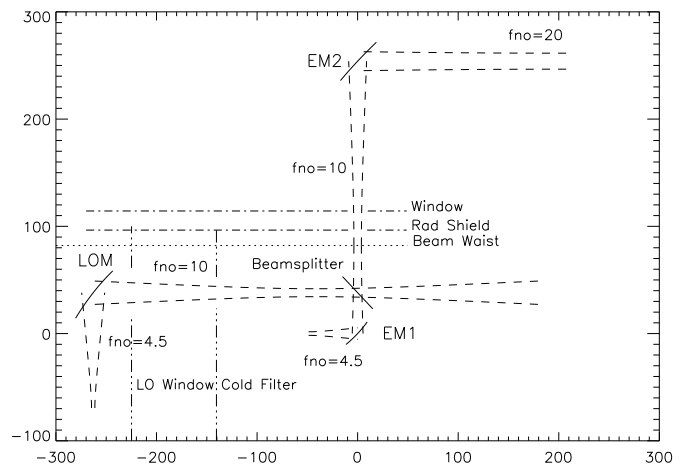


Fig. 5. CASIMIR Relay and LO Injection Optics. The top image shows the location of the elliptical mirrors mounted on the cryostat. The bottom part of the image shows a schematic of the optics. In the lower image, the up down orientation is reversed and the units on the scale are mm, with the origin at the center of EM1, the elliptical mirror mounted on the cryostat cold-work surface. EM2 is the elliptical mirror mounted below the base of the cryostat, visible in the upper image. EM2 is in the plane of the telescope beam, it converts the incoming, diverging $f/\# \sim 20$ telescope beam into an intermediate $f/\# \sim 10$ beam and reflects it through 90°, through a window in the base of the cryostat. LOM is the LO elliptical mirror, which matches the LO output beam to the incoming intermediate beam. EM1 converts the intermediate beam to a converging $\sim f/\# 4.5$ beam, which matches the output beam of the mixer.

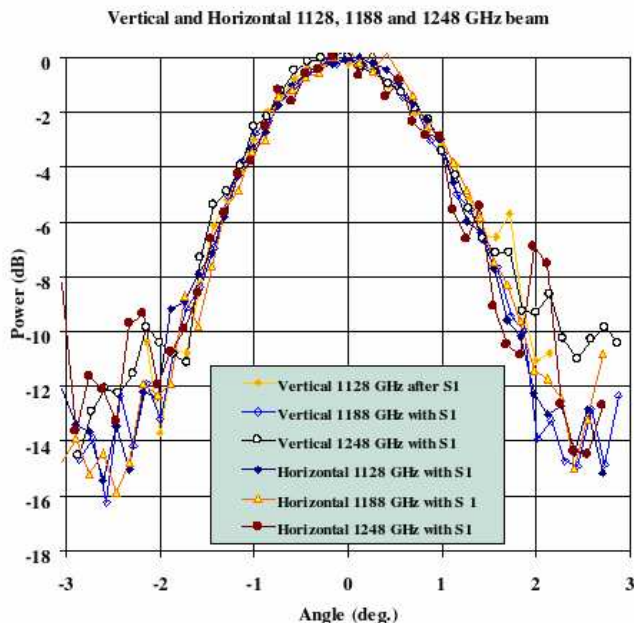


Fig. 6. Measurements of the output beam profile of the 1.2 THz mixer. The image consists of 6 curves overlaid on each other. These curves are vertical and horizontal scans through the output beam after the second elliptical mirror, EM2 in Figure 5. These scans were taken at three separate frequencies across the 1.2 THz band.

transmissive elements in the entire optical train from the telescope to the receiver.

The optical designs for all bands have an edge taper of 10 dB. Aperture and main beam efficiencies are calculated to be 0.71 and 0.77, respectively. The largest beam size is 0.8 arcmin, at 550 GHz.

Figure 6 shows measurements of the mixer beam after the second elliptical mirror. There is little evidence of distortion or chromatic aberration. The measured $f/\#$ is >18 , as opposed to the design point of 20.7. This is the first iteration of our mixer optics. This faster beam would reduce our aperture efficiency on the telescope, but is suitable for continued lab testing. Further iterations should remedy this. These measurements are discussed in detail elsewhere in these proceedings[5].

D. Mixers

The mixers for all 5 bands will be Nb/AlN/NbTiN, quasi-optically coupled, superconducting-insulating-superconducting (SIS), twin-slot mixers. The development of these mixers is discussed elsewhere in these proceedings[6].

III. MICROWAVE BACK END SPECTROMETER

We have acquired a field-programmable gate array (FPGA) based, fast Fourier transform (FFT), microwave backend spectrometer from Omnisys Instruments[7], see Figure 7. The spectrometer consists of a variable number of modules covering an IF band of 4 GHz each.

Each of these modules consists of three cards;

- two FPGA digitizer and correlator cards, each with a 2 GHz bandwidth,

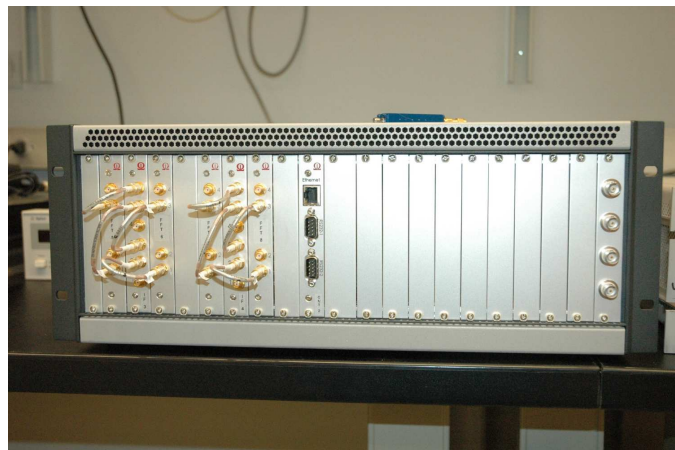


Fig. 7. Omnisys FPGA based FFT microwave spectrometer. In this image, the rack bin is only half populated, with two 4 GHz IF modules, i.e. two sets of three cards, giving a total IF coverage of 8 GHz. The center card in each set of three, is the IF processor. The cards have a single height Eurocard format and are mounted in a 4U, 19" rack bin. As displayed, the system weighs 12.5 kg and dissipates less than 200 W. During initial flights on SOFIA, only a single module would be used. If both halves of the rack were populated, a single unit could cover an IF passband of 16 GHz. Therefore, depending on the number of installed modules, this single rack bin can be readily configured to cover an IF range of 4, 8, 12 or 16 GHz.

- and an integrated IF downconverter and processor card, which uses IQ mixers to distribute the 4-8 GHz IF passband to the two digitizer cards.

There is some overlap in the outputs from the digitizer cards, and the total useful IF bandwidth of the spectrometer has been measured to be 3.8 GHz. Efforts are underway to reduce this overlap and to recover the full 4 GHz IF coverage.

The frequency resolution has been measured to be 268 KHz, i.e. over 14,000 usable channels. At 1 THz, this corresponds to a resolution greater than 3×10^6 , or 800 m/s.

A. Tests at CSO

In October, 2009, the spectrometer was used to carry out observations at the Caltech Submillimeter Observatory (CSO), using the 230 GHz wide band receiver, aka Frank's Receiver[8]. During these observations, we used two of the digitizer correlator cards and an external IF processor which yielded a IF bandpass of 4-8 GHz. Figures 8 and 9 show examples of the spectra obtained during this run.

We expect to take a spectrometer with 8 GHz of IF coverage to the CSO in the middle of this year.

IV. LOCAL OSCILLATORS AND FREQUENCY BANDS

The Local Oscillators (LOs) for all bands are tunerless and use solid state devices exclusively. LOs for the lower frequency bands, below 900 GHz, have been acquired from Virginia Diodes Inc. (VDI)[9]. LOs for the higher frequency bands were developed at JPL for CASIMIR. The development of the LOs at JPL is discussed elsewhere in these proceedings[10].

As shown in Figure 4, up to two LOs can be mounted directly to the side of the cryostat. The LO output is via a feedhorn. The output divergent beam is reflected through 90° and converted into a $\sim f/\#10$ converging beam, by an off-axis, elliptical mirror, mounted directly below the feedhorn,

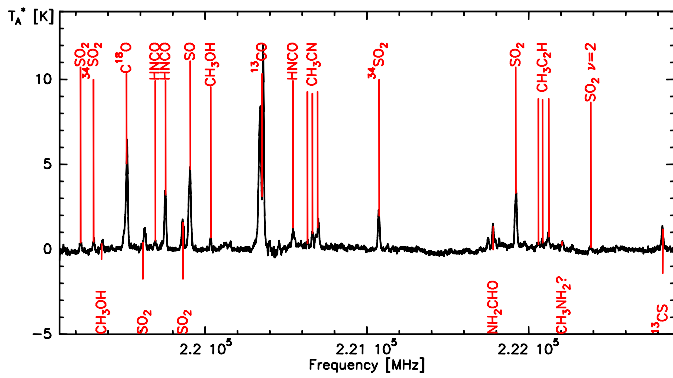


Fig. 8. Spectrum of the Galactic Center, centered on 221 GHz. This spectrum displays the full usable 3.8 GHz IF bandwidth of the spectrometer. This data was obtained with position switching under marginal conditions, $\tau = 0.18$.

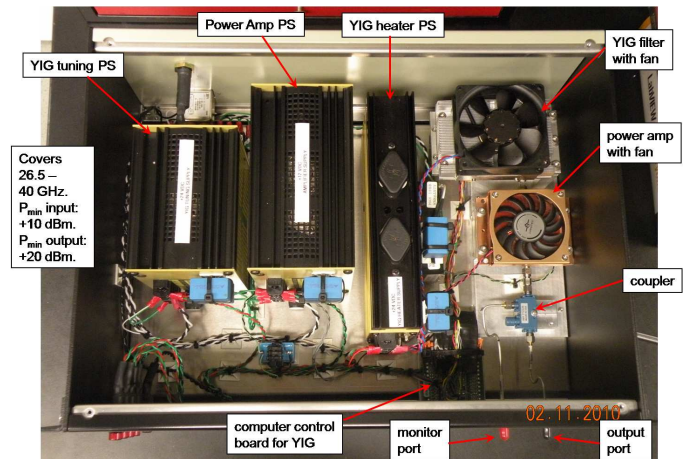


Fig. 10. The LO Drive Unit (LDU). This unit contains a single YIG Filter and power amp. It is located immediately adjacent to the microwave frequency synthesizer. The LO drive signals for all four frequency bands, on a given flight, will be routed through this unit. This is a lab prototype, completely filling a 4U 19" rack bin. Significant effort will be required to produce a lighter, more compact flight unit.

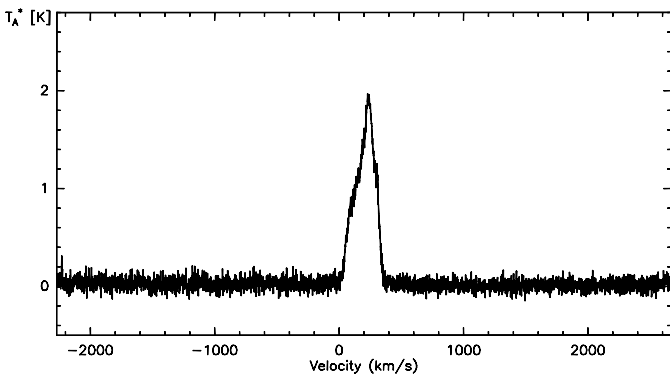


Fig. 9. Spectrum of M82 observed in the ^{12}CO 2-1 line. The line width is approximately 400 km/s. Note the extremely flat continuum.

see Figure 5. The beam passes through a window in the cryostat wall to a mylar beamsplitter mounted directly below the receiver elliptical mirror, EM1. The beamsplitter directs a portion of the LO signal power towards the cryostat cold work surface, combining it with the incoming, astronomical signal.

A. LO Drive System

1) *LO Drive Signals and Conditioning.*: All bands are driven from a single, commercial, microwave synthesizer, an Anritsu MG3694[11], at a frequency in the range 26-40 GHz. Immediately after the synthesizer, the LO drive signals are conditioned via the LO Drive Unit (LDU), containing a single YIG filter and power amplifier, see Figure 10.

Figure 11 compares the IF output from a mixer pumped by the same LO, with and without the LDU. The artifacts from the microwave frequency synthesizer are completely removed by the YIG filter.

Figure 12 compares the mixer noise temperature of a mixer pumped by a synthesized, solid state, tunerless LO and a Gunn Diode based LO. With the YIG filtering on the synthesizer output, we obtain equivalent performance for these two types of LOs.

The output from the LDU will be used to drive all the four LO chains, on any given flight. Only one chain will be driven at any given time. Any one of four bands can be selected completely via software at anytime during the flight, without any mechanical adjustment.

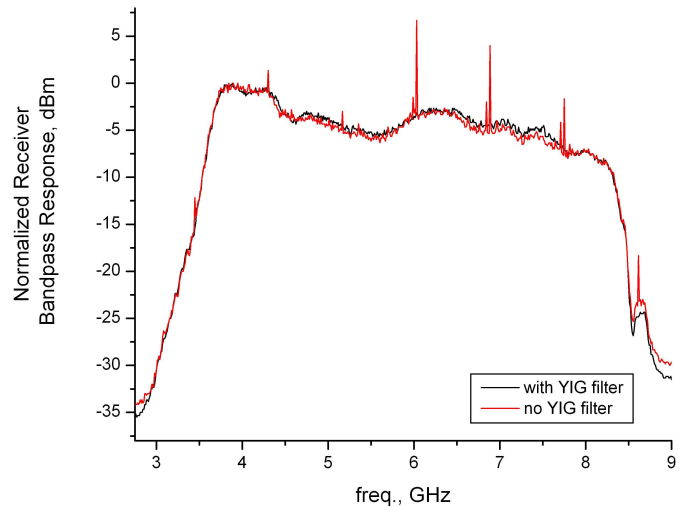


Fig. 11. Comparison of the IF output from an SIS mixer driven by a solid state 500 GHz LO, with and without the LDU. The same LO drive signal, from the microwave frequency synthesizer, was used for both curves. The lighter line does not use the YIG filter and the dark line does.

2) *The First Stage of the LO Chains:* On the aircraft, the first stage will be the same for each LO multiplier chain. One of these first stages will be dedicated to each chain. This first stage will have an output of 78-120 GHz and consists of;

- 1) a VDI tripler,
- 2) a W10 isolator,
- 3) a W10 Spacek amplifier,
- 4) a W10 isolator.

At present, each of our existing LO chains uses this first stage, except the 750 GHz LO, see Section IV-C. Figure 13 shows an example of a full LO multiplier chain.

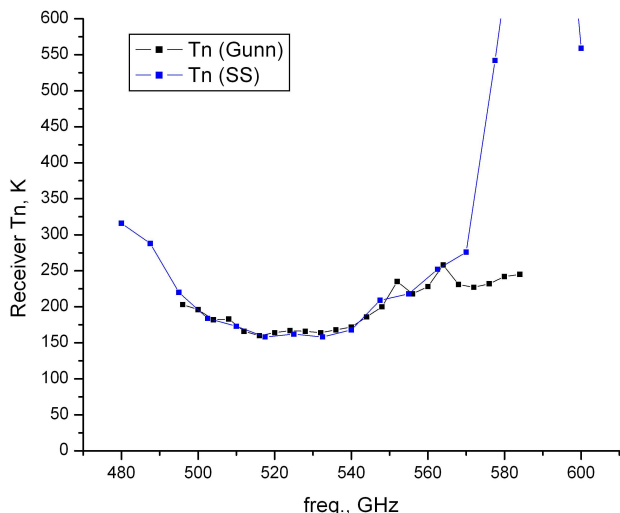


Fig. 12. Comparison of the receiver noise temperature from a SIS mixer pumped by a synthesized, solid-state LO and a Gunn diode based LO. The increase in noise at the high frequency end of the bandpass, for the solid state LO, is not due to the LO drive signal. It is due to bandpass limitations on the high frequency multiplier, see Section IV-B.

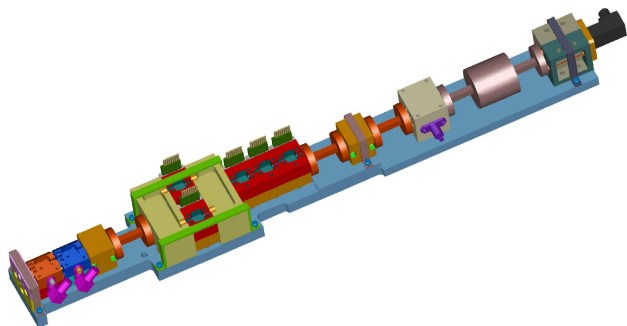


Fig. 13. The complete LO Chain for the 1.2 THz band. The first stage of the multiplier chain occupies the right half of the diagram. The high frequency part of the chain, i.e. frequency multiplication above 120 GHz, is shown in the left half of the figure and is also shown in Figure 16. This chain is expected to be the longest used on the instrument. It will be approximately twice as long as the LO assemblies shown in Figure 4, and will extend slightly beyond the top of the cryostat itself.

B. 500 GHz

The 500 GHz channel is intended to cover the 500 to 640 GHz passband. The most important line in this region is the H_2O^{18} line at 547 GHz. The other interesting lines are CH (532 and 536 GHz), NH_3 (572 GHz) and CO (576 GHz).

At present, we are using a single VDI quintupler as the high frequency multiplication stage. However, its output is limited to ~ 570 GHz. We are now investigating using a 2×3 combination of VDI multipliers, in order to extend the coverage up to 640 GHz.

C. 750 GHz

We have acquired a 750 GHz LO from VDI. Figure 14 shows the the output power spectrum and the LO itself. The 750 GHz LO is intended to cover the 690 to 840 GHz frequency range. The coverage of this large fractional bandwidth, $\sim 20\%$, requires two parallel chains, for the low and high frequency parts of the band. The input from these chains is fed into a common, final multiplier, via a microwave switch. This arrangement provides good power levels across the band of interest, with up to $\sim 80 \mu\text{W}$ at the most interesting line, H_2O^{18} at 745 GHz.

D. 1 THz

Figure 15 shows the output power and multiplier chains for the LOs covering the 1 THz band. These LOs were manufactured at JPL for CASIMIR.

The frequency range for this band covers 800 to 1050 GHz. Such a large fractional bandwidth, 27%, cannot be covered by a single multiplier chain. So the band must be split into two sub-bands, nominally 900 GHz and 1 THz, with a separate multiplier chain for each of them.

The lines of most astronomical interest, e.g. CH_2 (946 GHz), NH (975 GHz), H_3O^+ (985 GHz), H_2O^{18} (995 GHz) and CO (1037 GHz) are all located in the upper sub-band. The 1 THz LO has good coverage, $> 50 \mu\text{W}$ for most of these lines.

Many of the frequencies in the lower sub-band are observable from the ground, so there may be relatively little demand for this sub-band on SOFIA. We intend to fly the 1 THz sub-band in the default configuration for CASIMIR. If there is a request to observe in the 900 GHz sub-band, we would use the same mixer, but replace the 1 THz LO with the 900 GHz chain. At this stage, we do not intend to have both of these sub-bands available on any one flight.

E. 1.2 THz

Figure 16 shows the output power for the multiplier chain for the 1.2 THz LO. This chain was developed at JPL. The frequency range for this band is 1.1-1.2 THz, and it is covered with power levels from 30-90 μW . The most significant frequencies, the four H_2O^{18} lines, are well covered with LO power levels $> 60 \mu\text{W}$ for all of them. The next most interesting line, HF at 1.23 THz, may be difficult to observe due to the relatively low LO power, $< 30 \mu\text{W}$, and the high atmospheric absorption at that frequency.

F. 1.4 THz

Figure 17 shows the output power for the multiplier chain for the 1.4 THz LO. This chain is still under development at JPL. At present, the power output over the region of interest is in the range 40 – 70 μW . However, it is possible that this may improve. The most important frequency in this band is the H_2D^+ line at 1.37 THz, which is well covered with LO power levels $> 50 \mu\text{W}$. The next most interesting line, N^+ at 1.46 THz, lies at the extreme high frequency end of the LO's output and probably cannot be observed.

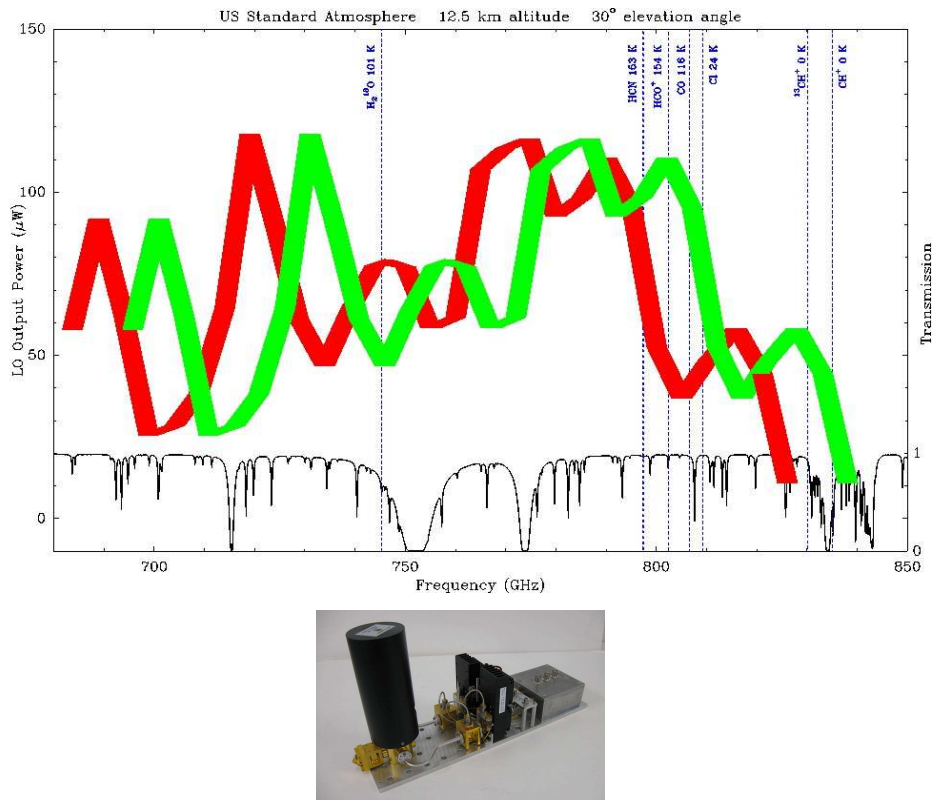


Fig. 14. Frequency coverage of the 750 GHz band and the existing complete 750 GHz LO. The plot shows the LO output power superimposed on the atmospheric absorption at SOFIA's operating altitude. The significant astronomical, spectral lines are also shown. The light and dark LO output power curves, respectively, represent the upper and lower side bands, for a given frequency tuning. The large black object at the left of the photograph of the LO, is the microwave switch for selecting the high or low multiplying chain. Some effort will be required to reconfigure this LO for flight.

V. CONCLUSIONS

CASIMIR is a FIR/Submm, heterodyne spectrometer for SOFIA. It is well suited for the studies of the warm ($T \sim 100\text{K}$) interstellar medium, particularly water, measuring many significant lines unobservable from the ground. Initially, the instrument will cover 5 bands in the frequency range from 0.5 to 1.4 THz.

A very high resolution backend spectrometer has been successfully tested. It provides continuous coverage of 3.8 GHz of IF bandwidth with a resolution $> 10^6$, across the whole frequency range of the instrument.

LO chains suitable for flight are available for the three frequency bands of 1 THz or higher and candidate chains are available for the two lower frequency bands. With conditioning of the LO drive signals, the synthesized, solid state LOs will provide performance equivalent to those based on Gunn diodes.

The instrument design is extremely modular. CASIMIR will be able to continuously incorporate new hardware, to accommodate future improvements in mixer, LO and backend spectrometer technology, for some time to come.

VI. ACKNOWLEDGMENTS

Various subsystems of the CASIMIR instrument have been, or continue to be developed, by a number of people at several institutions: J. Stern and H. G. LeDuc, Micro Devices Lab, JPL (mixer fabrication), M. R. Haas, NASA Ames (optics), the Kosma I/O Team, U. of Koln and S. W. Colgan, NASA

Ames (software), and S. Lin, Caltech/JPL (mechanical design). The development of CASIMIR is supported by NASA/USRA SOFIA Instrument Development Fund.

REFERENCES

- [1] M. L. Edgar, A. Karpov, S. Lin, D Miller, S. J. E. Radford & J. Zmuidzinas, "CASIMIR, The Caltech airborne submillimeter interstellar medium investigations receiver", *SPIE*, **7020**, 702012 (2008).
- [2] E. E. Becklin, A. A. G. M. Tielens, R. D. Gehrz & H. H. S. Calis, "Stratospheric Observatory for Infrared Astronomy", *SPIE*, **6678**, 667880A, 2007.
- [3] S. C. Casey, "The SOFIA program: astronomers return to the stratosphere", *SPIE*, **6267**, 2006.
- [4] E. E. Becklin, A. A. G. M. Tielens & H. H. S. Callis, "Stratospheric Observatory for Infrared Astronomy (SOFIA)", *Mod. Phys. Lett. A*, **21**, 2551-2560, 2006.
- [5] A. Karpov, D. Miller, M. Emprechtinger, M. Edgar, F. Rice, A. Harris, J. A. Stern, H. G. LeDuc & J. Zmuidzinas, "Characterization of 1.2 THz SIS receiver for CASIMIR", *these proceedings*.
- [6] A. Karpov, D. Miller, J. A. Stern, F. Rice, H. G. LeDuc & J. Zmuidzinas, "1.4 THz SIS mixer using Nb and Al tuning circuit", *these proceedings*.
- [7] Omnisys Instruments AB, Gruvgatan 8, SE-421 30 Vastra Frolunda, SWEDEN, www.omnisys.se
- [8] F. Rice, M. Sumner, J. Zmuidzinas, R. Hu, H. LeDuc, A. Harris & D. Miller, "SIS mixer design for a broadband millimeter spectrometer suitable for rapid line surveys and redshift determinations", *SPIE*, **4855**, 301-311, 2002.
- [9] Virginia Diodes Inc., 979 Second St. S.E., Suite 309, Charlottesville, VA 22902-6172, USA, virginiadiodes.com
- [10] R. Lin, B. Thomas, J. Ward, A. Maestrini, E. Schlecht, J. Gill, C. Lee, S. Sin, F. Maiwald & I. Mehdi, "Development of Local Oscillator Sources for CASIMIR", *these proceedings*.
- [11] Anritsu Company, 490 Jarvis Drive Morgan Hill, CA 95037-2809, USA, www.us.anritsu.com

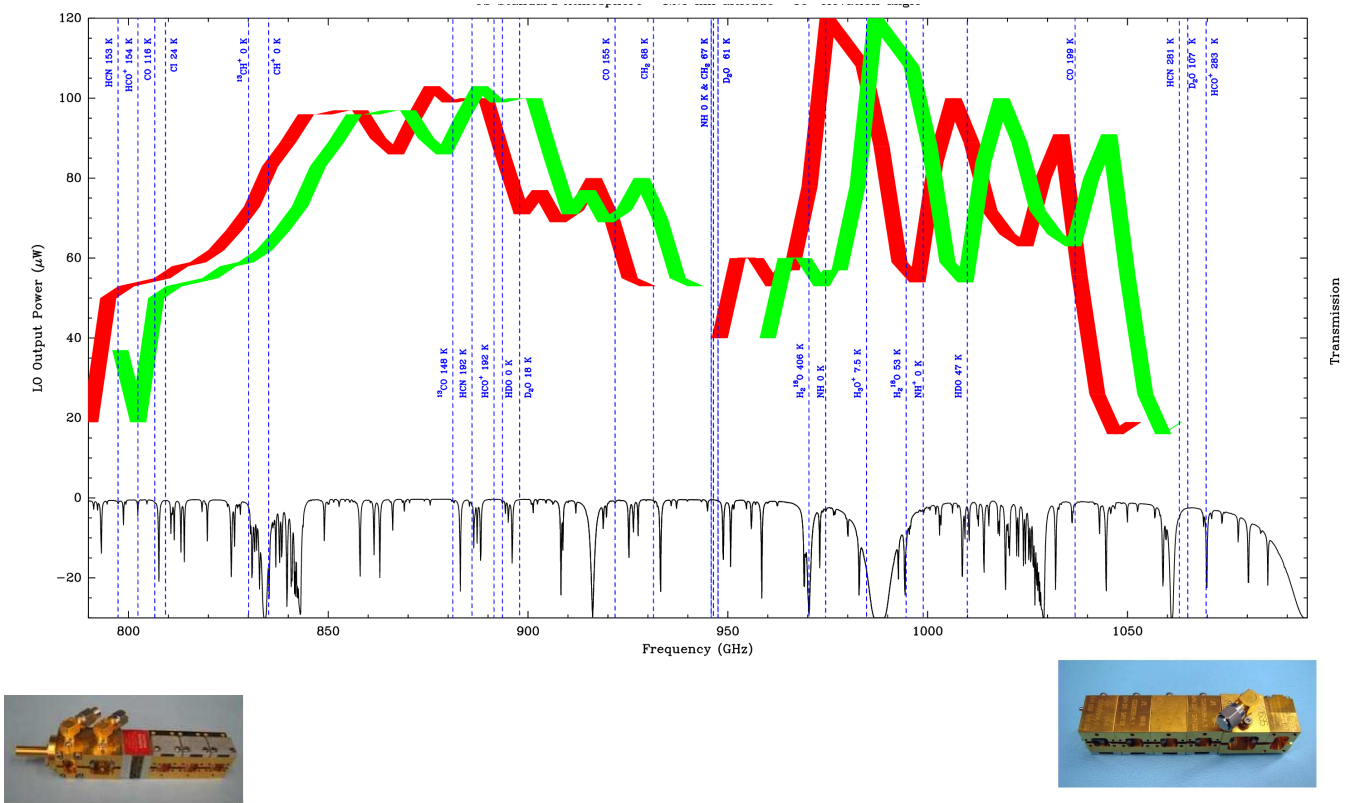


Fig. 15. Frequency coverage of the 1 THz band and the 900 and 1000 GHz LOs. The format of the diagram is similar to that in Figure 14. The high frequency portions of the multiplier chains are shown below the main figure, the 900 GHz to the left and the 1 THz on the right.

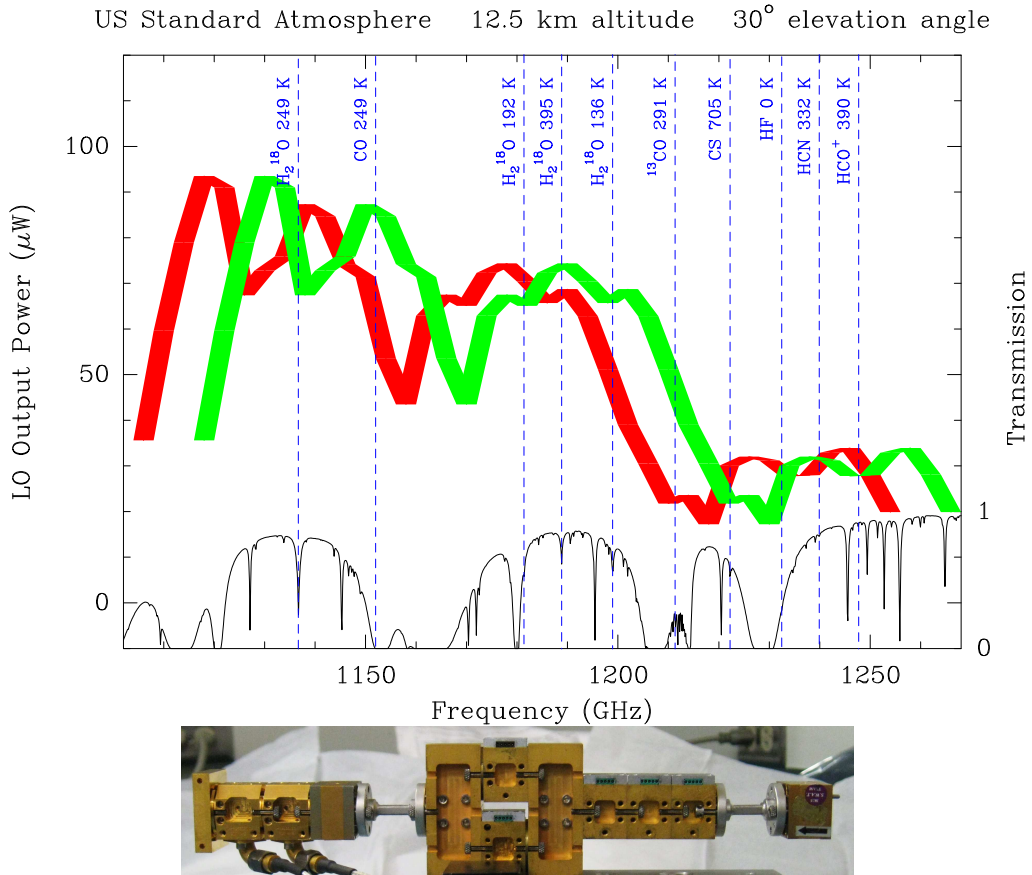


Fig. 16. Frequency coverage of the 1.2 THz band and the high frequency portion of the multiplier chain for the 1.2 THz LO. The format of the diagram is similar to that in Figure 14.

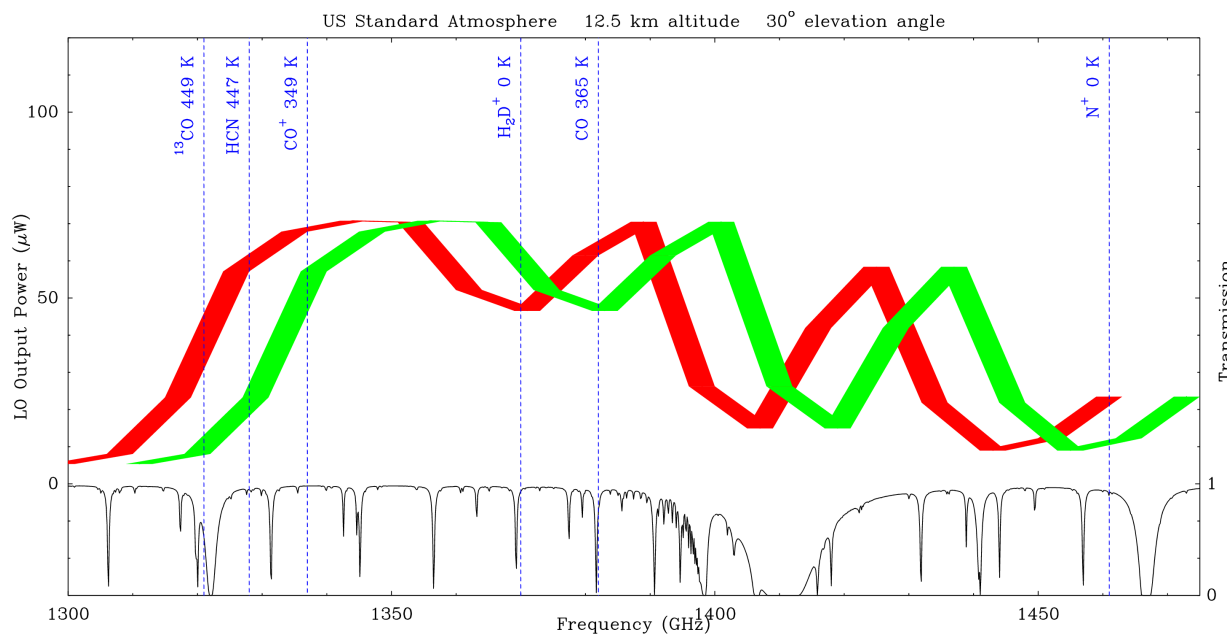


Fig. 17. Frequency coverage of the 1.4 THz LO. The format of the diagram is similar to that in Figure 14.

Session S6: Schottky Diodes and Mixers

TeraHertz Schottky-Diode Balanced Mixers

Neal R. Erickson¹ and Thomas M. Goyette²

¹*Astronomy Department, University of Massachusetts, Amherst, MA, USA*

²*Submillimeter-wave Technology Laboratory, University of Massachusetts, Lowell, MA, USA*

Contact: neal@astro.umass.edu

Abstract— We report on a very high performance THz balanced mixer/upconverter using a Schottky diode MMIC chip. Using an optically pumped laser at 1561 GHz as an LO source with a coupled power of about 1.5 mW, and 1.5 mW input at an IF frequency of 10 GHz, we obtained a sideband output power of 45 μW (sum of two sidebands). As a mixer, at an LO of 1561 GHz, we measured a mixer noise temperature of ~3000 K DSB. At the same frequency, used as a 16th harmonic mixer the conversion loss is ~55 dB. The design bandwidth is 1250-1650 GHz, and scaled devices have been fabricated for all frequencies through 3.5 THz, but the higher frequency designs have not been tested.

I. INTRODUCTION

In the THz range there is a need for room temperature mixers to act as both downconverters and upconverters using laser local oscillators. In these applications the relatively high LO power required by Schottky diodes is not a problem. This paper reports on a high performance THz balanced waveguide mixer built using a planar diode MMIC. This development was motivated by a need for a frequency agile sideband generator at 1.5 THz which would use a laser as one input and a 5-40 GHz microwave synthesizer as the other.

II. MIXER AND MMIC DESIGN

The mixer developed in this work is similar to one used for proof of concept testing [1], and is based on crossbar waveguide mixers [2] that have been made for many years in the mm-wave bands. Fig 1 shows the basic circuit, with two diodes in series in the signal waveguide driven at their center point by the LO. This LO port is also the IF output which must be split off from the LO. With separate LO and signal ports, no diplexer is required at the mixer input, and there is high isolation between these ports. A particular advantage of this geometry is that the two diodes are in parallel to the IF port, halving the IF impedance. Given that single diode mixers typically have 100-150 Ω IF impedances, this reduction eliminates the need for an IF matching circuit. The off-chip IF circuit is simply a 50 ohm line.

The MMIC chip designed for the mixer is shown in Fig 2, and its placement in the mixer in Fig 3. The device is built on 3 μm thick GaAs with beam lead contacts for ground, IF and bias. The fragile substrate is completely suspended by the beam leads. At the end of the LO waveguide probe a high impedance line continues along the axis of the waveguide through the backshort, forming the IF port. This creates little disturbance to the THz input circuit and there is little loss of power into the IF port. A thin SiN layer is used between metal layers to produce a bypass capacitor on the bias port, and to add a low impedance section of line to the IF port to improve the LO rejection.

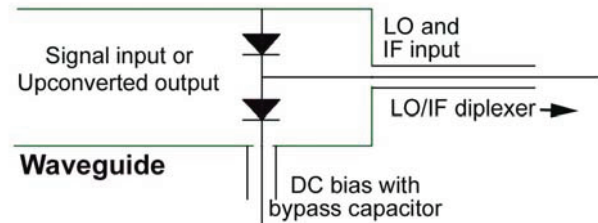


Fig. 1 Schematic diagram of a balanced mixer with LO/IF input on the right and signal input waveguide on the left.

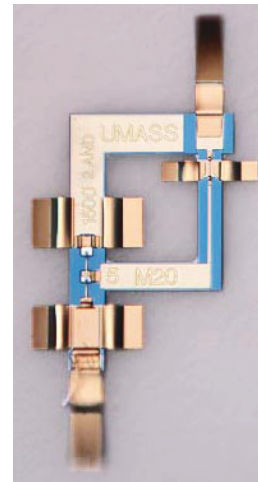


Fig. 2 Photograph of the diode used in the mixer. Overall height of the 1.5 THz device (with leads) for is 570 μm.

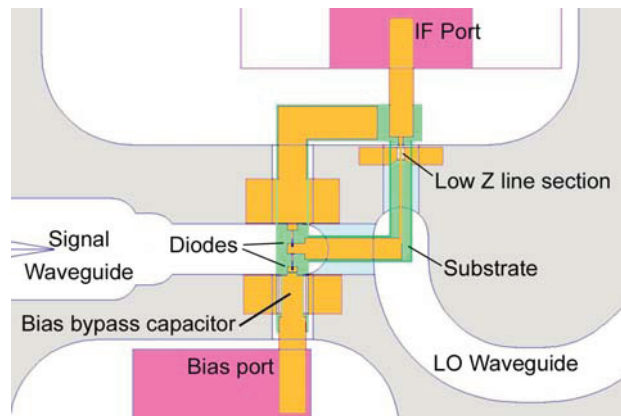


Fig. 3 Balanced mixer cross section. The MMIC substrate is shown in green, metal in gold. Both waveguides transition to diagonal horns on opposite sides of the block.

Two diode-MMIC wafers were fabricated at JPL using the very successful membrane process developed for Hershel HIFI [3]. The wafers had epi-layer doping of $5 \times 10^{17}/\text{cm}^3$ and 2×10^{17} with identical circuit layouts. Variations of the design were scaled to as high as 3.5 THz, but tests reported here are of only the 1.5 THz design. Simulations of the performance of these designs indicate a relatively flat RF fractional bandwidth of 25%. Upconverted power is limited by the input power which is very constrained in a circuit with just two anodes, since the anodes must be very small for proper impedance matching. The required capacitance $C_j(0)$ is 1 fF at 1.5 THz yielding an anode diameter of $0.5 \mu\text{m}$ (scaling downward with increasing frequency). However, it is practical to add anodes in series, as has been done with multiplier circuits [4]. In principle, using two anodes in series increases the maximum input power by a factor of four, assuming that the failure mechanism is related to power density within the device. This scaling comes about because for the same impedance level, each device can have twice the area if two devices are in series. In the case of failure due to heating, the scaling is much less obvious, since it depends on thermal pathways within the complete circuit, not just local device properties, but there is still some significant advantage. Four-anode devices were fabricated but the anode size was only 1.5 times larger so the maximum power in this case should only increase a factor of three.

The best results were obtained with the 5×10^{17} doping devices, but this wafer yield is quite low, $\sim 35\%$ for 2-anode devices, and the yield seems to be near zero for 4-anode devices. The wafer with 2×10^{17} doping works acceptably at 1.5 THz, but it is clear that the doping is too low. This wafer has a high yield of 2-anode devices and 30% yield of 4-anode devices.

As is apparent from Fig 2, these are very small devices. While the GaAs membrane can not be touched, the beam leads can be handled safely, and installation in the block is done by positioning the device with a micro-manipulator. Once positioned, conductive epoxy is applied to the IF and bias port leads. Because of the small contact area this can result in a high contact resistance, and a solder contact would be preferred, but is much more difficult to produce.

The block was machined in brass as an E-plane split-block using conventional tools with a CNC micro-milling machine [5] and the block was then gold plated. Both waveguides are $80 \times 160 \mu\text{m}$, stepping up to square cross section before transitioning to diagonal feedhorns on both input and output ports. The diagonal aperture sizes of each were 1.5 mm. Details of the block are shown in Figs 3 and 5. The diode was installed with the beamleads clamped between the halves of the block. The IF port used a K type connector to allow tests up to 40 GHz, but in fact no dimension or circuit capacitance inherent to the design limits the bandwidth below ~ 150 GHz. For practical reasons of testing and machining, the input waveguide was bent to align with the axis of the output guide. This adds LO loss but this is not a concern with laser sources.

III. UPCONVERSION RESULTS

Upconversion tests were done using an optically pumped laser at 1561 GHz, with an available power level of >10 mW and a variable attenuator before the mixer input. The IF was 10 GHz from a synthesizer. For the tests with the 5×10^{17} doping devices, only 2-anode devices were available. Four mixers were assembled with these devices. These were driven with a laser power of ~ 1.5 mW (as measured by a coupling aperture comparable to that of the feed horn). Diodes were forward biased in operation, with the conversion efficiency rising with bias up to 1 mA (which was the maximum used). With an IF power of 1.5 mW, the output power from the best device in the two sidebands is $45 \mu\text{W}$ with only $5 \mu\text{W}$ of LO feedthrough (~ 25 dB LO-RF isolation). The feedthrough power was measured with the IF signal off, but there is the possibility that the feedthrough may increase with IF applied. In previous tests with a similar mixer a very narrow band FPI etalon was used to separate the LO from the sideband signals. Use of this filter showed that there was no change in LO feedthrough with the IF applied. The THz input and output power were measured with a waveguide calorimeter (Erickson Instruments PM4) [6] built in WR10 waveguide with no transition between the horn and the waveguide in the sensor. The size of the horns and WR10 waveguide are fairly similar so coupling was expected to be good. For two other devices taken from very nearby on the wafer, output power was within 10%, while the fourth device from another region produced only $18 \mu\text{W}$.

Fig 4 shows the power output vs IF drive power at the maximum laser power used of ~ 1.5 mW. Output power is compressed by ~ 1 dB at 1 mW IF level, but is still increasing up to the maximum applied. There is the potential for higher output power, particularly with increased laser power, but diode failure due to heating is likely within a factor of 1.5 higher input. RF dissipation within the diodes is difficult to estimate from diode bias since most of the THz input power is lost in parasitic resistances. Simply summing all the input power is the only way to estimate dissipation, which is ~ 4 mW at the maximum output.

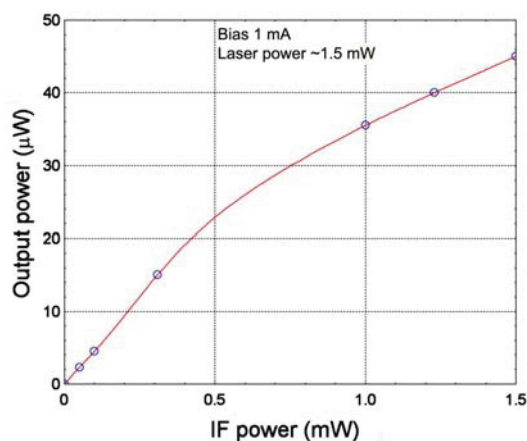


Fig. 4 Output power vs 10 GHz IF drive with laser power of 1.5 mW. The solid line is a spline fit, with no physical model.

Tests at other offset frequencies show the same power output for an IF range of 2 to 40 GHz, with IF coupling nearly flat across this band. The RF bandwidth is predicted to be 1250-1650 GHz, but no other frequencies have been tested.

The devices with 2×10^{17} doping showed significantly poorer performance. A 2-anode device showed significant saturation effects at 1 mA bias, and best output power was at 0.5 mA. The power output saturated at $13 \mu\text{W}$, with an LO power of 1 mW and an IF power of 1 mW. The 4-anode devices worked better, but still required a bias of 0.5 mA although optimum LO and IF power increased to 2 mW and 4 mW respectively. At this drive level the output peaked at $37 \mu\text{W}$, and began to decrease with increasing drive. LO-RF isolation with 4-anodes is excellent, just $2 \mu\text{W}$ feedthrough, or ~ 30 dB LO-RF isolation.

Perfect LO to RF isolation can never be obtained with this type of mixer because of the essential mechanical asymmetry between the anode and cathode of a planar diode. Isolation should be better at lower frequencies because the asymmetry couples to evanescent modes which become more important with increasing frequency. The 4-anode version of the design has much better isolation because the individual devices are smaller, and thus couple to even higher modes.

A comparison between the 2-anode and 4-anode mixers with 2×10^{17} doping shows that the output increases a factor of 3 with twice the anode number, as is expected for the anode sizes used. With similar scaling, 4-anode mixers with 5×10^{17} doping should produce an output power $\sim 150 \mu\text{W}$.

IV. DOWNCONVERTER RESULTS

This device has been tested as a conventional mixer downconverter only at 1561 GHz. The IF source was replaced by a 3 GHz IF amplifier with a noise temperature of ~ 150 K. The mixer was the same one giving best results as an upconverter. With an estimated LO power of 1 mW and a bias current of 1 mA, a Y factor of 1.050 was measured with room temperature and liquid nitrogen cooled loads. This yields a complete receiver noise temperature of 4500K DSB. Assuming a typical noise contribution of a mixer diode ~ 300 K, the estimated mixer noise temperature is 3000 K DSB, and the conversion loss ~ 10 dB. This is not an optimized result, with DC bias and LO power only roughly adjusted. The DC resistance of the IF contact to the MMIC is ~ 9 ohms, adding 1.4 dB to the conversion loss if capacitive bypassing of this resistance is not significant at 3 GHz. This noise is substantially lower than any other Schottky mixer results at a similar frequency, and is less than would be expected based on lower frequency results with waveguide mixers.

Other types of mixers built for this frequency range all require cooling. THz Schottky mixers show noise reduction by only a factor of two [7] when cooled due to the high doping of the diodes, with no further reduction in the noise below ~ 50 K. Therefore the best achievable receiver noise with this mixer might be ~ 1600 K DSB, but since the diode noise dominates, similar noise may be achieved up through a very high IF. A state-of-the-art waveguide HEB mixer at 1350 GHz has a receiver noise temperature ~ 1200 K [8], but

has much more restricted IF bandwidth of ~ 3 GHz, so this Schottky mixer may be very competitive, particularly in applications requiring wide bandwidth. Its reduced cooling requirements are another advantage, and many years of experience with Schottky diode mixers at lower frequencies has shown them to have the best dynamic range and stability of any type of receiver.

V. HARMONIC MIXING

At these frequencies a quantum cascade laser could be the LO, leading to a simple all solid state receiver with wide frequency coverage through use of the >100 GHz wide IF. QCL's can easily produce >1 mW output power, and can operate at ~ 50 K. Although output mode control can still be a problem, solutions are emerging that should produce good quality beams, and single frequency operation. A remaining challenge with QCL lasers is a means of locking their frequency since their free running stability is poor. At mm wavelengths, sources are typically measured by comparison to a microwave reference via harmonic mixing. This has not been possible in the THz range due to the need for high harmonics and the resulting very high conversion loss which typically increases as ~ 3 dB per harmonic. Using one of these mixers, we attempted to measure a 1561 GHz laser mixed with an LO near 39 GHz ($N = 40$) but no signal was detected implying a conversion loss >120 dB (consistent with $L_c \sim 3\text{dB} \cdot N$). To overcome this limitation complex multiplier chains [9] have been used to produce a reference signal which is mixed with the laser in a fundamental HEB mixer but this complexity is almost too great to justify the use of a laser LO. However, this new mixer can harmonic mix with a very high LO, reducing the harmonic number N to below 20 and the conversion loss to ~ 60 dB.

To test this application, a WR 10 waveguide was added to one mixer, coupling to the IF microstrip line, but leaving the coaxial IF port functional for low frequencies, as shown in Fig 5. The waveguide port is fairly well matched from 75 to ~ 100 GHz, although only about half the power couples toward the mixer chip since there is no filter structure in the microstrip line.

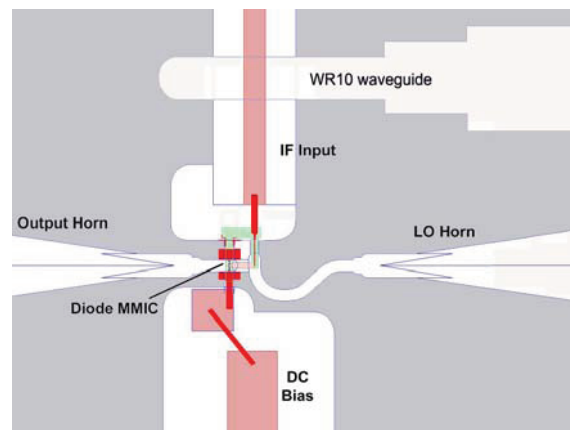


Fig. 5 Layout of the mixer block showing the added WR10 waveguide which allows low frequencies to couple from the mixer to the coaxial IF port at the top of the block. This waveguide is bent to offset it from the LO feedhorn.

With this wideband port we mixed the 1561 GHz laser with an LO at 97.4 GHz. This LO was in turn derived from a commercial x8 active multiplier chain plus synthesizer. ($N = 16$ for the mixer). The inefficient coupling is not a concern since the WR10 source produced more power (10 mW) than the diodes can survive. While setting up the test with a 2-anode mixer, one of the diodes was burned out but the test was continued with the surviving diode, and the mixer still worked well. The measured conversion loss was ~ 55 dB and the S/N on a spectrum analyser was ~ 40 dB in 10 kHz resolution BW (and 300 Hz video BW). With 2 working diodes the conversion process should be more efficient since it favours even or odd harmonics (depending on the input port). With an LO in the 150-200 GHz range, harmonic mixing up to ~ 3 THz should be practical.

VI. CONCLUSIONS

Planar Schottky diode MMIC's can serve as efficient upconverters and low noise mixers well into the THz range, offering room temperature operation. The balanced mixer design separates the LO and IF ports, making an extremely simple, compact receiver requiring no LO/signal diplexer, and having no restriction on IF bandwidth. With cooling their noise temperature may be competitive with HEB mixers in applications requiring wide IF bandwidth and high stability. These mixers should be feasible throughout the THz range and devices have already been fabricated which may operate up to 3.5 THz. LO requirements are within the power available from QCL's, and the combination should form very simple receivers. Harmonic mixers using the same design have low conversion loss and can serve to provide the frequency comparison needed to lock the QCL.

ACKNOWLEDGMENT

The authors wish to thank R. Grosslein for machining the blocks and R. Erickson for the assembly. The diodes were fabricated by Imran Mehdi's group at JPL. M. Coulomb of the UMass Lowell Submillimeter Technology Lab assisted in the tests.

REFERENCES

- [1] N. Erickson, "A Schottky-Diode Balanced Mixer for 1.5 THz," *19th International Symposium on Space Terahertz Technology*, pp. 221-223, Apr 08, Groningen.
- [2] S. Maas, *Microwave Mixer 2nd Eds*, pp 291-293, Artech House, 1993.
- [3] A. Maestrini, J. Bruston, D. Pukala, S. Martin and I. Mehdi, "Performance of a 1.2 THz Frequency Tripler Using a GaAs Frameless Membrane Circuit," *IEEE MTT-S Int'l Microwave Symposium* (Phoenix), pp. 1657-1660, May 2001.
- [4] B.J. Rizzi, T.W. Crowe and N.R. Erickson, "A High-Power Millimeter-Wave Frequency Doubler Using a Planar Diode Array," *IEEE Microwave and Guided Wave Lett.* vol 3, pp. 188-190, 1993.
- [5] G. Narayanan, N. Erickson, R. Grosslein, "Low Cost Direct Machining of Terahertz waveguide Structures," *Tenth International Symposium on Space Terahertz Technology*, pp. 518-528, Mar. 99.
- [6] N. Erickson, "A Fast and Sensitive Submillimeter Waveguide Power Meter," *Tenth International Symposium on Space Terahertz Technology*, pp. 501-507, Mar. 99.
- [7] P.F. Goldsmith, H.R. Fetterman, B.J. Clifton, C.D. Parker and N.R. Erickson, *Cryogenic Operation of Submillimeter Quasioptical Mixers*, International Journal of IR and MM Waves, vol 2, pp. 915-924, 1981.
- [8] D. Meledin, et al, "A 1.3 THz Balanced Waveguide HEB Mixer for the APEX Telescope," *IEEE Trans Microwave Theory Tech.*, vol MTT 57, pp. 89-98, 2009.
- [9] A.M. Baryshev, P. Khosropanah, W. Zhang, W. Jellema, J.N. Hovenier, J.R. Gao, T.M. Klapwijk, D.G. Paveliev, B.S. William, S. Kumar, Q. Hu, J.L. Reno, B. Klein, J.L. Hesler, "Phase-locking of a 2.7-THz quantum cascade laser to a microwave reference," *20th International Symposium on Space Terahertz Technology*, pp. 49-52, Apr 09, Charlottesville.

Full Waveguide Band Schottky Mixers for Terahertz Applications

K. Hui, J.L. Hesler and T.W. Crowe

Virginia Diodes Inc., Charlottesville, USA (Crowe.vadiodes.com)

Abstract

Although diode mixers have been supplanted by cryogenically cooled SIS and HEB mixers for ultra low-noise radio-astronomical purposes; Schottky mixers are still the best solution for most other scientific and commercial applications. Their room temperature operation, broad signal and IF frequency bandwidths and overall robust operation, coupled with their modest LO power requirements and relative sensitivity make them ideal for atmospheric studies and modern test and measurement systems, such as VNA frequency extenders. This paper will discuss the ongoing development of low-noise Schottky mixers that operate across complete waveguide bands without LO power tuning and without DC bias requirements. These subharmonically pumped mixers are being developed to achieve very compact and easy to operate receiver systems that are ideal for planetary missions. As an example, the figure shows the measured mixer noise temperature of a WR1.9SHM being developed as a prototype for a proposed atmospheric probe for Venus. The goal is to cover the frequency band from 440-590GHz with only a few milliwatts of LO power (220-295GHz) and a noise temperature of less than 2,000K, DSB. Results for an optimized version of this mixer will be presented at the conference.

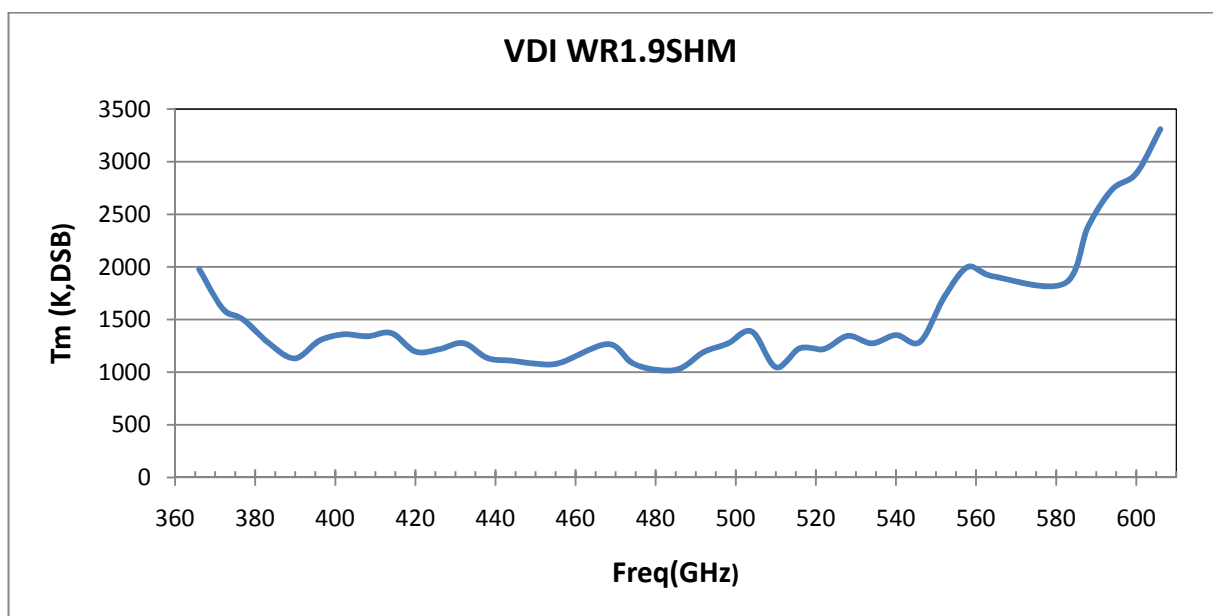


Fig. 1. The measured sensitivity of a broadband WR1.9SHM design with flat LO power across the band. The mixer designs being pursued use no DC bias and require no LO power adjustments as the frequency is tuned across the band. The final mixer design will be optimized for the VESPER frequency band of 440-590GHz.

This effort is primarily funded through a NASA / GSFC SBIR contract (#NNX09CA57C), "Schottky Heterodyne Receivers with Full Waveguide Bandwidth."

An 874 GHz fundamental balanced mixer based on MMIC membrane planar Schottky diodes

B. Thomas¹, A. Maestrini², J. Gill¹, C. Lee¹, R. Lin¹, I. Mehdi¹ and P. de Maagt³

¹NASA- Jet Propulsion Laboratory, California Institute of Technology,

4800 Oak Grove Drive, PASADENA, CA, 91101, USA. Email: Bertrand.C.Thomas@jpl.nasa.gov

²Observatoire de Paris, LERMA, University P&M Curie, Paris-VI. 77 avenue Denfert-Rochereau, 75014 Paris, France

³European Space and Technology Center (ESA/ESTEC), Noordwijk 2201 AG, The Netherlands.

Abstract— We present here the design, fabrication and test of a novel 874 GHz Fundamental Balanced Mixer based on MMIC membrane planar Schottky diodes. The device includes an integrated DC bias circuit in order to reduce the amount of LO power required to pump the mixer. The mixer performance are best DSB mixer noise temperature of 2660 K at 865.8 GHz and best DSB mixer conversion losses of 8.02 dB at 862.2 GHz for room temperature operation. When cooled to 120 K ambient temperature, the best DSB mixer noise temperature drops down to 1910 K. Although at least 1 mW of LO power is required to optimally pump the mixer, performance are still acceptable with only 0.5 mW. To the authors' knowledge, these results are state-of-the-art.

INTRODUCTION

The remote sensing of stratospheric ice clouds is of key interest in understanding the hydrological cycle of climate systems for life on Earth. Several missions have been proposed that would monitor globally the ice water content of cirrus clouds using passive sub-millimeter radiometer instruments up to 874 GHz [1]. Therefore, highly sensitive heterodyne receivers operating at room temperature in the sub-millimeter wave range are needed for such applications. Development of compact and broadband receivers in this frequency range can also benefit THz imaging applications by providing higher resolution compared to lower frequency systems [2].

Sub-harmonic mixers working up to 874 GHz [3] have already been demonstrated. Previous studies have shown that improved performance can be obtained from fundamental mixers over sub-harmonic types. Recent breakthroughs in power generation from amplifier-multiplier based solid-state sources up to 900 GHz [4] allow for enough LO power to pump a biasable fundamental mixer, as demonstrated here.

We present the design, development and characterization of a fully monolithic 835-900 GHz biasable fundamental balanced mixer (FBM) using GaAs Schottky diode MMIC developed at JPL. The mixer is pumped by a powerful compact LO chain based on solid-state power combined amplifiers and multipliers, resulting in the highest frequency all solid-state compact broad band heterodyne receiver operating at room temperature with state-of-the-art performance. The front-end has been tested at both room and cryogenic temperatures (120 K) using a dedicated cryogenic test system.

874 GHz FUNDAMENTAL BALANCED MIXER ARCHITECTURE

The topology of the 835-900 GHz fundamental balanced mixer is based on a cross-bar balanced architecture recently used at higher frequencies [5][6]. For the present design, both diodes are located inside the RF waveguide in a series configuration across the central suspended stripline, as illustrated in Fig. 1&2. Airbridges are used to connect the mesas and Schottky contacts to the central stripline and lateral grounding beamleads. Another beamlead at the end of the circuit is used to connect the MMIC to an IF circuit. A DC bias line and a MIM capacitor are used to bias the diodes in series while providing an efficient IF, LO and RF ground.

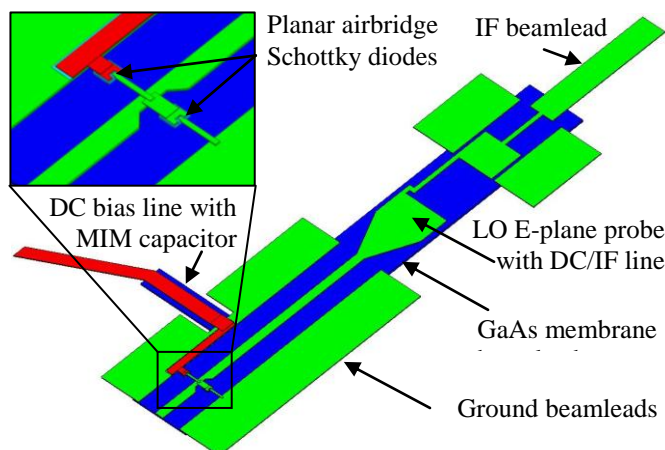


Fig.1. 3-D view of the 874 GHz Fundamental Balanced Mixer MMIC device, featuring a pair of planar Schottky diodes in balanced configuration on a thin GaAs membrane, gold beamleads and DC MIM capacitor.

The LO signal is coupled via a bowtie E-plane probe with integrated DC/IF line to the diode. This transition is adapted from a previous design that uses an integrated DC bias line [8]. The length of the narrow line connecting the bowtie antenna is optimized to prevent any resonance in the desired LO band. The bandwidth of this bowtie-type transition is also improved by adding narrow steps inside the LO waveguide as demonstrated in [9].

DESIGN METHODOLOGY

This section describes the methodology employed to design the 835-900 GHz fundamental balanced mixer, including the determination and optimization of the diodes

geometrical and electrical parameters.

Linearisation of the ideal mixer. Non-linear circuit simulation of an ideal pair of Schottky diodes is performed using the Harmonic Balance code of the ADS Software Suite [10]. The goal is to determine the anode size of the diodes in order to get the best mixer conversion losses, lowest RF and LO input return losses. The IF signal is fixed at 5 GHz. With an estimated LO power of 0.5 mW reaching the diodes, the mixer conversion losses are minimized by tuning the bias voltage and ideal embedding impedances. Assuming an epilayer doping concentration N_D of $5.10^{17} \text{ cm}^{-3}$, it is found that best conversion losses are obtained for anode area A of approximately $0.4 \mu\text{m}^2$, a bias voltage V_{DC} of 1.3 V, and ideal embedding impedances Z_{LO} of approximately $17 + j.50$ for the LO at 870 GHz, Z_{RF} of approximately $90 + j.200$ for the RF at 875 GHz, and Z_{IF} of 200 Ω for the IF at 5 GHz. The resulting electrical parameters used at room temperature for the Schottky diode model are a zero voltage capacitance of 1 fF, a saturation current of 2.10^{-13} A, barrier height of 0.73 V, ideality factor of 1.4, and series resistance of 30 Ω .

Synthesis of the mixer circuit. Three-dimensional electromagnetic (EM) simulations of the different parts of the mixer circuit are simulated separately using HFSS (from Ansys [11]) and exported as S-parameter Touchstone files into ADS. These parts include the RF and LO waveguides-to-stripline transitions, diode cells, high-low suspended stripline transitions and DC/IF transmission lines. Using ADS, a linear simulation bench of the mixer circuit is built which includes the S-parameter files, RF and LO diode's impedance ports obtained previously, electrical transmission lines and the waveguide ports. This bench has two separate sub-circuits: one for the RF signal propagating from the waveguide to the diodes' port with a TE_{10} mode, and the other for the LO signal propagating with a TEM mode. The resulting coupling efficiency from waveguides to both diode ports is predicted to be approximately 80 % between 840 and 910 GHz for the RF, and 40 to 45 % between 850 to 900 GHz for the LO.

Prediction of the mixer performance. A set of non-linear simulations is performed to fine tune the circuit and predict the performances of the mixer. For the conversion loss calculation, the standard ADS model of the Schottky diode [11] is used. For the mixer noise temperature calculation, the standard ADS model includes thermal and shot noise sources, but does not include any other sources that account for hot electron noise. As this effect can become significant at sub-millimeter wave frequencies for small anode devices, an additional noise source is added in series with the standard ADS Schottky model [12].

Simulations show that the mixer should work with a Local Oscillator power of only 0.5mW and a bias voltage of 1.4V for the two diodes in series. For 1 mW of input LO power and a fixed bias voltage of 1.2 V, DSB mixer conversion losses are 8.5 dB, and DSB mixer noise temperature of 2000 K are predicted between 850 and 910 GHz. This estimation includes additional 0.7 dB of losses for the feedhorn, and 1.2 dB of insertion losses for the IF transformer,

connector and cable. Results are shown in Fig. 4 as continuous lines. The predicted RF/LO isolation ranges from 29 dB up to 33 dB between 830 and 900 GHz.

874 GHz FBM FABRICATION AND MOUNTING

The circuit is based on a thin GaAs membrane and uses beamleads for connections and handling [7] as shown in Fig. 2. The Schottky contacts, defined using E-beam lithography, are connected to the circuit via air-bridges. The JPL MMIC membrane Schottky process described in [7] is specially suited for the realization of fundamental balanced mixer at these frequencies. Indeed, the thin membrane prevents excessive dielectric loading of the waveguides and channels, the beamleads allow for a precise grounding, centering and DC/IF connection of the MMIC to the block and DC/IF circuits. The on-chip MIM capacitor allows to DC bias the mixer with minimum RF/LO fields disturbance. Finally the MMIC process reduce the uncertainties associated with handling and placing the device inside the block.

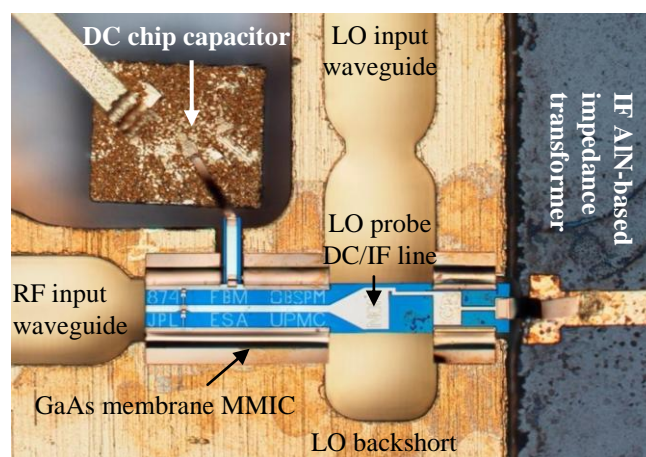


Fig.2: View of the 835-900 GHz fundamental mixer circuit mounted inside the lower half of the mechanical block, including a MMIC mixer device (center) mounted with DC chip capacitor (top) and IF transformer (right), DC bias, ground and IF gold beam-leads.

External chip capacitors are used for the DC bias and further filtering of any unwanted IF residue. The IF signal is output through an IF impedance transformer to the K-type connector. The IF transformer circuit is designed to improve the Voltage Standing Wave Ratio between the mixer and the external first low noise Amplifier in the 2-11 GHz range. A view of the IF transformer mounted inside the lower half of the mechanical block is shown in Fig. 3. It consists of a meandering line to match from 200 Ω to 50 Ω in 4-sections impedance steps. The circuit is based on gold microstrip lines deposited on a 1.27 mm thick Aluminum Nitride substrate. This enables to keep return losses above 10 dB and insertion losses below 1 dB over a relatively broad bandwidth 2-11 GHz. The DC bias chip capacitors are connected with thermo-compressed bond wires to a SMA-type glass bead.

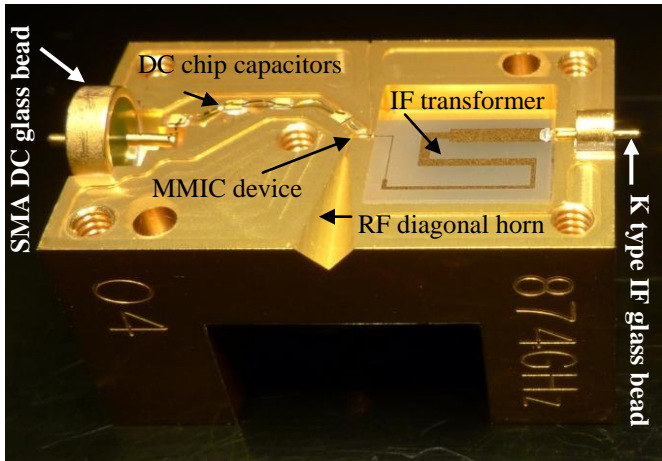


Fig.3: View of the lower half of the mechanical split-block, showing from left to right the SMA-type DC glass bead, DC chip capacitors, the IF impedance transformer and the K-type IF glass bead.

SMA flange launcher connector is mounted afterwards to the block. The IF circuit is connected to a K-type glass bead via a stripline stress relief contact inserted on the tip of the glass bead and silver-epoxy glued on the ending of the microstrip line section.

874 GHz FBM TESTING

The 874 GHz Fundamental Balanced Mixer has been tested at room temperature and at cryogenic temperatures using the test set-up described in [12]. The mixer is pumped by a W-band Agilent source linked to an Agilent E8257D synthesizer. The LO signal is then amplified outside the cryogenic test chamber using a series of power combined W-band power amplifiers. The 2-4 GHz IF amplification and filtering chain is described in [13]. The output power of the IF chain was measured using an Agilent total power sensor N8482A linked to a N1912A power meter.

The first multiplier chains used inside the test chamber to generate the 830-900 GHz LO signal is a medium power multiplier chain featuring a dual-chip power combined 300 GHz tripler and single-chip 900 GHz tripler. The characteristics of this LO chain is described in [14][4]. It outputs an LO power ranging from 0.3 to 0.6 mW at ambient temperature from 840 to 930 GHz. The complete multipliers/mixer front-end receiver is very compact and is shown in Fig. 4. Measured performance are shown in Fig.5. As illustrated in Fig.5, a DSB mixer noise temperature of 3000-4000 K and DSB mixer conversion losses of 10.5 to 11 dB in the range 847-885 GHz are measured at room temperature.

A second high power LO chain featuring a quad-chip 300 GHz power combined tripler and dual-chip 900 GHz power combined tripler outputting over 1 mW of power at room temperature in the 840-900 GHz range and up to 2 mW when cooled at 120 K has been used. Details concerning the LO chain can be found in [15]. Measured mixer performance for 295 K and 120 K ambient temperature operation is shown in Fig.6.

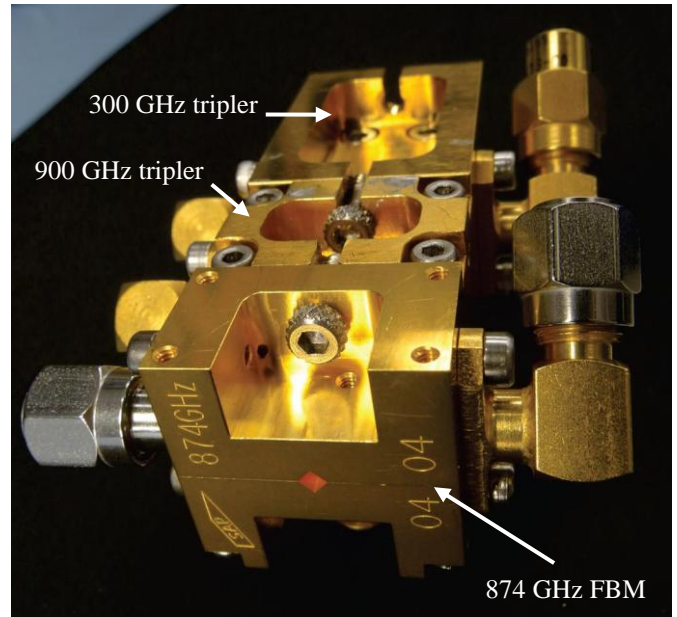


Fig.4: Photo of an entire 874 GHz receiver front-end including the 874 GHz Fundamental Balanced Mixer (foreground), a 900 GHz single-chip tripler (middle), and a dual-chip 300 GHz power combined tripler (background).

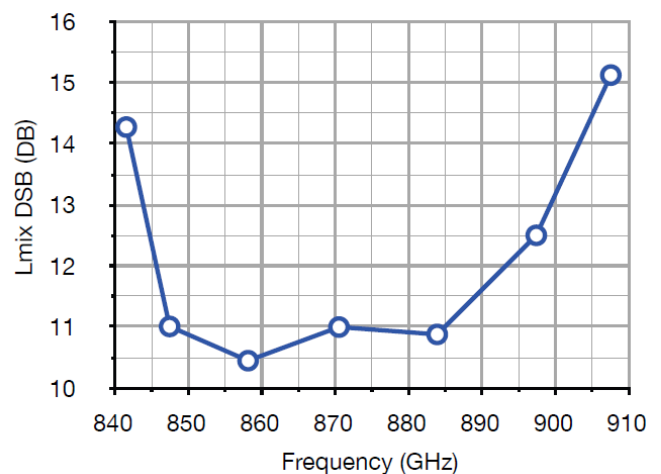
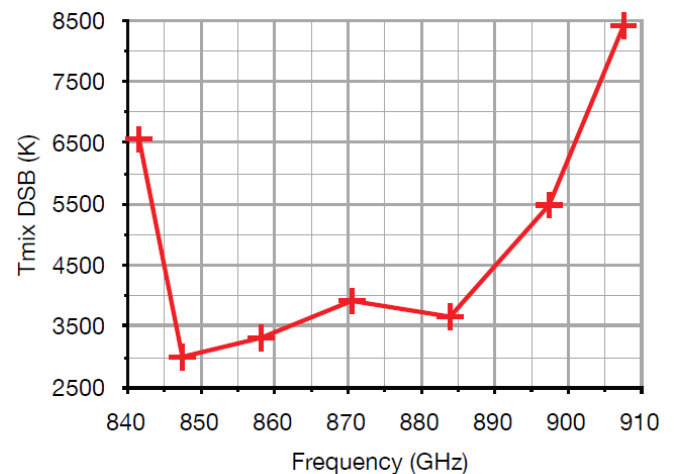


Fig.5: 874 GHz FBM mixer performance at room temperature using a medium power LO chain in the range 840-930 GHz. Top curve shows the DSB mixer noise temperature, lower curve shows the DSB mixer conversion losses VS center RF frequency.

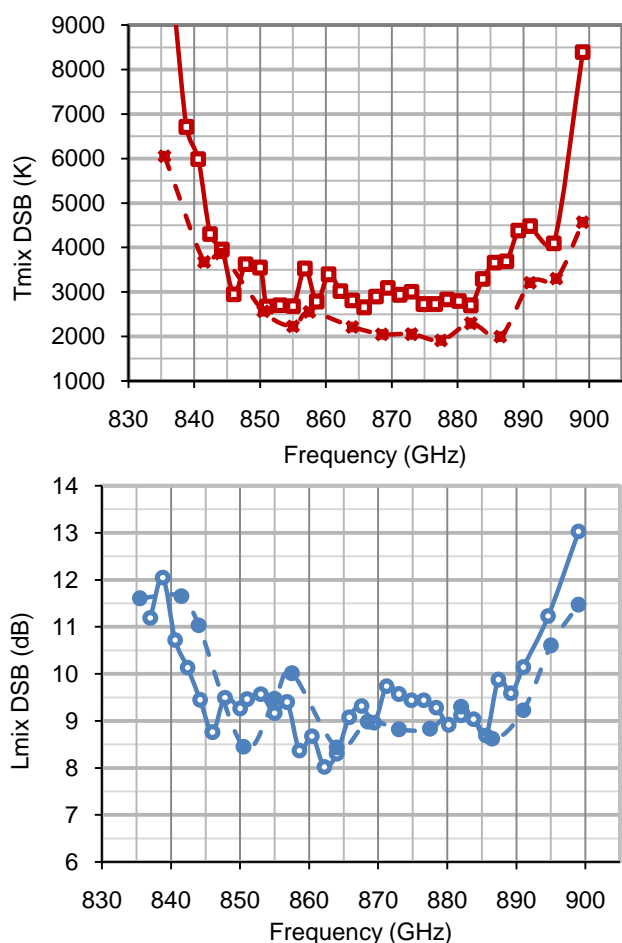


Fig.6: 874 GHz FBM mixer performance at 295 K (empty dotted curves) and 120 K (full dotted curves) ambient temperature operation using a high power LO chain in the range 840-930 GHz. Top curves show the DSB mixer noise temperature, lower curves show the DSB mixer conversion losses VS center RF frequency.

As shown in Fig.6, The best mixer noise temperature measured at room temperature is 2660 at 865.8 GHz, with DSB mixer conversion losses of 9.08 dB. The best DSB mixer conversion losses measured at room temperature is 8.02 dB at 862.2 GHz, with corresponding DSB mixer noise temperature of 3021 K. If the mixer performances are corrected for IF external cable losses (0.64 dB), DSB mixer noise temperature and conversion losses drops to 2330 K at 865.8 GHz, and 7.38 dB at 862.2 GHz respectively. DSB mixer noise temperature and conversion losses are below 4000 K and 10.5 dB resp. from 845 GHz to 888 GHz. At 120 K of operating temperature, the best DSB mixer noise temperature measured is 1910 K at 877.5 GHz, with DSB mixer conversion losses of 8.84 dB. The best DSB mixer conversion losses observed is 8.44 dB at 864 GHz, with corresponding DSB mixer noise temperature of 2213 K. DSB mixer noise temperature and conversion losses are below 3000 K and 10 dB resp. from 847 GHz to 890 GHz.

It is interesting to notice that, for room temperature operation, the mixer still works relatively well with only 0.5 mW of LO power in average, and a bias voltage increased to 1.4 V, as shown in Fig.5. A maximum of 2 dB

degradation of the DSB conversion losses is measured by going from 1 mW to 0.5 mW of LO power.

CONCLUSIONS

The design, fabrication and test of a 874 GHz fundamental balanced mixer based on MMIC membrane planar Schottky diodes has been presented. It exhibits state-of-the-art performance at room temperature and cooled to 120 K. Although at least 1 mW is required to optimally pump this mixer, performance degrades nicely with only 0.5 mW.

ACKNOWLEDGMENT

The authors wish to acknowledge the help and support of Dr. Peter Siegel. The company SAP-France is also acknowledged for the high quality block manufacturing.

This work was partly funded by ESA under contract nb. ESTEC/RFQ/3-12604/08/NK/FM and carried out at the Jet Propulsion Laboratory, California Institute of Technology, under contract from NASA, and at Observatoire de Paris.

REFERENCES

- [1] S.A. Buehler, "CIWSIR: A Proposed ESA Mission to Measure Cloud Ice Water Path," proceedings of the Int. TOVS Study Conf., ITSC-XV Program, Maratea, Italy, 4-10 October 2006.
- [2] K.B. Cooper *et al.*, "Penetrating 3-D Imaging at 4- and 25-m Range Using a Submillimeter-Wave Radar", IEEE Trans. on Microwave Theory and Techniques, Vol. 56, No.12, pp. 2771-2778, Dec. 2008.
- [3] B. Thomas *et al.*, "Design of an 874 GHz Biasable Sub-Harmonic Mixer Based on MMIC Membrane Planar Schottky Diodes", Proceedings of the 33rd Int. Conf. on IR, Millimeter, and Terahertz Waves, Pasadena, CA, USA, September 2008.
- [4] I. Mehdi *et al.*, "Broadband sources in the 1-3 THz range", proceedings of the 34th Infrared and Millimeter Wave and 17th THz Electronics Conference, Busan, Korea, Sept. 2009.
- [5] E. Schlecht *et al.*, "First Wideband 520-590 GHz Balanced Fundamental Schottky Mixer", proceedings of the 18th Int. Symp. on Space THz Technology, Pasadena, CA, USA, pp. 296, March 2007.
- [6] N. Erickson and T. Goyette, "TeraHertz Schottky-Diode Balanced Mixers", Proc. of SPIE conf. Vol. 7215, 721508, pp.1-5, Feb. 2009.
- [7] S. Martin *et al.*, "Fabrication of 200 to 2700 GHz multiplier devices using GaAs and metal membranes", Microwave Symp. Digest, 2001 IEEE MTT-S, Vol. 3, pp.1641 - 1644, 2001
- [8] C. Risacher *et al.*, "Waveguide-to-microstrip transition with integrated bias-T", IEEE Microwave and Wireless Components Letters, Volume 13, Issue 7, pp. 262-264, 2003.
- [9] J.W. Kooi *et al.*, "A Full-Height Waveguide to Thin-Film Transition with Exceptional RF Bandwidth and Coupling Efficiency", Int. Journal of Infrared and Mm Waves, Vol. 24, No. 3, pp. 261-284, March 2003.
- [10] Advanced Design System 2009, Agilent Technologies, 395 Page Mill Road, Palo Alto, CA 94304, USA.
- [11] High Frequency Simulation Software, V12.0, Ansoft Corporation, 225 West Station Square Drive, Suite 200, Pittsburgh, PA 15219, USA.
- [12] B. Thomas *et al.*, "Terahertz cooled sub-harmonic Schottky mixers for planetary atmospheres", proceedings of the 5th ESA workshop on Millimetre Wave Technology and Applications, Noordwijk, The Netherlands, May 2009.
- [13] J. Treuttel *et al.*, "A 380 GHz sub-harmonic mixer using MMIC foundry based Schottky diodes transferred onto quartz substrate", proceedings of the 20th Int. Symp. on Space Terahertz Technology, Charlottesville, VA, April 2009.
- [14] A. Maestrini *et al.*, "In-Phase Power-Combined Frequency Triplers at 300 GHz", IEEE Microwave and Wireless Component Letters, Vol. 18, no. 3, pp. 218-220, March 2008.
- [15] A. Maestrini *et al.*, "A 0.9 THz Frequency Multiplied Source with milliwatts of power" submitted to IEEE Trans. on Microwave Theory and Techniques, October 2009.

183 GHz Mixer on InGaAs Schottky Diodes

I. Oprea^{1,3}, A. Walber², O. Cojocari^{1*}, H. Gibson², R. Zimmermann², and H. L. Hartnagel³

¹ACST GmbH, Darmstadt, Germany

²RPG Radiometer Physics GmbH, Germany

³Technische Universität Darmstadt, Darmstadt, Germany

*Contact: cojocari@acst.de, phone +49-6151-162762

Abstract— This work reports on experimental results of a 183 GHz sub-harmonically pumped mixer based on InGaAs anti-parallel diode pair. The diode structure provides extremely low parasitic capacitance of about 2.5 fF. Roughly estimated series resistance junction capacitance and ideality factor 10Ω, 4fF/anode and 1.2, respectively. The optimal LO-Power is as low as 0.34 mW, whereas usable performance can be achieved even with less than 0.2 mW.

I. INTRODUCTION

The Schottky junction is a generic technology, needed not only in space instruments but in practically all millimeter and sub-millimetre equipment, with the imaging evolving fast to become the primary area of application. During the last years the rapid progress in the development of Schottky technology has allowed efficient heterodyne receiver systems at frequencies up to 1.5 THz [1]–[3]. As the applications require a constant rise of the operation frequency, the expense of LO power used to drive the diode to the needed conductance is still a concern. A reduction of the LO frequency and thus the LO power requirements is possible by using subharmonically pumped mixers (SHM), where normally the LO is one half the RF frequency. GaAs antiparallel Schottky Diodes used in subharmonic mixer unfortunately require a significant DC bias or high LO power to drive the diode to an optimum conversion performance. Since it is difficult to bias diodes in this way the low Schottky barrier height of InGaAs material reduces the required LO power relative to diodes based on GaAs [4], [5]. Schottky barriers formed from $\text{In}_x\text{Ga}_{1-x}\text{As}$ have a height that decreases with increasing indium mole fraction. A lower barrier height means that a smaller LO Power is required to effectively pump the diode. The higher electron mobility in InGaAs in comparison to GaAs should play a role in minimising the series resistance which will reduce the conversion losses especially at higher frequencies. InGaAs mixers are also very interesting for potential use in integrated InP based millimetre and submillimetre wave receivers with state-of-the-art noise performance.

II. ANTI-PARALLEL DIODE PARAMETER DETAILS

The anti-parallel diode (APD) was fabricated by so-called Film-Diode process, which has been particularly developed at ACST for THz devices and circuits. The diode structure is based on the Quasi-vertical diode design, developed at Technical University of Darmstadt [6] and represents a discrete Schottky structure suitable for hybrid integration. In contrast to traditional planar structures, Film-Diode

fabrication implies two-side processing of the semiconductor wafer, which implies a more complex fabrication, but is more flexible concerning the reduction of structure parasitics. In turn this provides a better potential for improving performance and allows operation at higher frequencies. The APD mixer diodes use an $\text{In}_{0.53}\text{Ga}_{0.47}\text{As}$ active layer with a doping level of $8 \times 10^{16} \text{ cm}^{-3}$ which is lattice matched grown on an InP substrate. Recently Schlecht [7] discussed the principle of an $\text{In}_{0.25}\text{Ga}_{0.75}\text{As}$ based Schottky mixer, but no experimental results have been shown. Moreover the epitaxial growth of material with this indium mole fraction will not be lattice matched to InP and have much stress.

The structures have 1.2 μm anodes in diameter and estimated zero bias junction capacitance per anode is about 4fF. The employed Film-Diode approach uses a transferred membrane substrate process which provides for strongly reduced structure parasitics. The shunt capacitance of APD diodes is as low as 2.5fF. The series resistance R_s is extracted from simple I-V measurements and is slightly higher than expected. The high value of R_s , approximately 10Ω, can be caused by the wafer layout which was not optimised for mixing applications. On the other side the ideality factor η is 1.2 and is comparable to GaAs diodes. The calculated Schottky barrier height is around 0.21 eV and is about one quarter of the value for similar GaAs diodes. Figure 1 shows the typical I-V curves of an InGaAs and GaAs diode measured on-wafer. The typical turn-on voltage ($1 \mu\text{A}$) for fabricated InGaAs diodes is below 50 μV , which is drastically reduced in comparison to GaAs diodes.

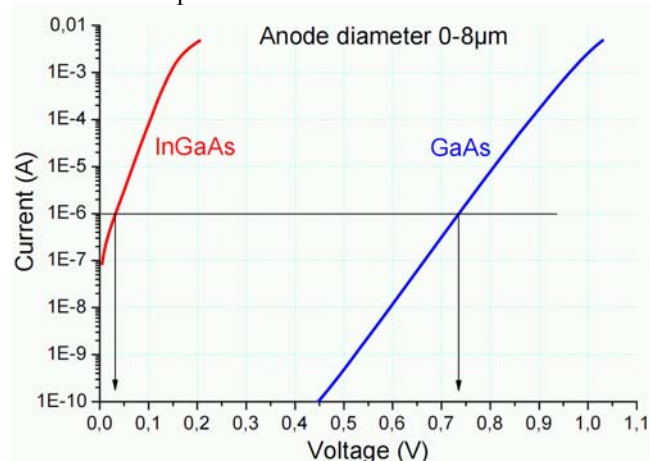


Fig. 1. Measured I-V Curves of InGaAs and GaAs Schottky Diodes

III. SUBHARMONIC MIXER PERFORMANCE

Since the InGaAs material was available for comparison with GaAs, no new mixer block was designed. A similar mixer block was used as for 183 GHz ALMA subharmonic mixers developed by RPG. The employed mixer block was originally designed for ACST GaAs diodes, which typically exhibits state-of-the-art performance of



$T_{mix} \leq 450K$. The mixer design is very similar to [8] but employs discrete diode mounting. A small picture of the SHM is inserted on the left. The waveguides for RF and LO signals are fabricated from quartz and the diode is soldered using indium solder. The double sideband (DSB) noise temperature T_{sys} and conversion loss L_c of the mixer were measured using the standard Y-Factor measurement technique. One target at room temperature and another one immersed in liquid nitrogen are used at RPG as hot and cold load, respectively. The results are summarised in Fig. 2.

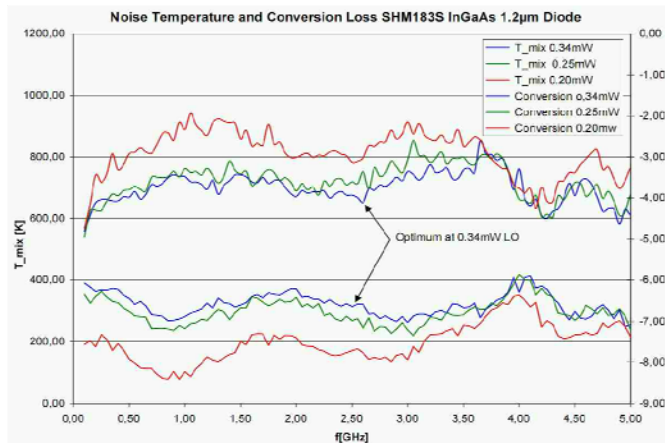


Fig.2. IF Plot showing conversion loss (right) and noise temperature of mixer for different LO powers.

The shown data is raw data from the power measurements and is not corrected for losses or mismatches in any way. It includes waveguide losses as well as the IF amplifier noise contribution. Although the measured mixer temperature is higher in comparison to state-of-the-art performance, it is still rather good and acceptable for many applications. Moreover, this can probably be improved by the optimization of wafer layout and mixer design. It has to be pointed out, however, that the optimal LO-power is as low as 0.34mW, whereas usable performance can be achieved even with less than 0.2mW. This value is at least one order of magnitude lower than typically required for GaAs-diodes.

Table 1 summarizes the sub-harmonic mixer parameter. In contrast to InGaAs mixer results, also the results for GaAs mixer are included (the values in green are the best achieved).

TABLE I

	T_{mix}	L_c (DSB)	LO
InGaAs	700 K	-6.6 dB	0.34 mW
GaAs	500 K (450 K)	-6.0 dB (-5.7 dB)	3.0 mW (2.2 mW)

As can be seen the mixer noise temperature, as well as the conversion efficiency is inferior to the results achieved with GaAs. However, this can be explained by the high value of R_s , which may result from the 70 nm thick active layer of the used wafer. The zero bias capacitance is slightly too high for 183 GHz which also may limit the performance of the mixer.

IV. CONCLUSIONS

The first test performed by using InGaAs antiparallel diode structures in a sub-harmonically pumped mixer, where no DC bias was required, is extremely encouraging. The receiver performance is only slightly worse than with a GaAs diode, but the Local Oscillator requirements are drastically reduced. Due to recent advances of millimetre wave power generation technology, the obtained results may be considered insignificant. However, this approach may open new perspectives for higher frequencies, where LO power is still a concern.

ACKNOWLEDGMENT

The authors would like to acknowledge the ESA/ESTEC for supporting this study under contract No: 21628-08-NL-GLC.

German Research Foundation (DFG) is acknowledged for support within the framework of Research Training Group 1037 "Tunable integrated components in microwave technology and optics" (TICMO).

REFERENCES

- [1] E. Schlecht, J. Gill, R. Dengler, R. Lin, R. Tsang, and Mehdi, "A Unique 520-590 GHz Biased Subharmonically-Pumped Schottky Mixer", *IEEE Microwave Wireless Components Letters*, Vol. 17, No. 12, pp. 879-881, Dec. 2007.
- [2] B. Thomas, A. Maestrini, D. Matheson, I. Mehdi and P. de Maagt, "Design of an 874 GHz Biasable Sub-Harmonic Mixer Based on MMIC Membrane Planar Schottky Diodes," in *Proc. of 33rd Conf. IRMMW-THz*, 2008.
- [3] N. R. Erickson, "A Schottky-Diode Balanced Mixer for 1.5 THz", in *Proc. of 19th International Symposium on Space Terahertz Technology*, pp. 221-223, 2008.
- [4] U. V. Bhapkar, T.A. Brennan, R.J. Mattauch, "InGaAs Schottky Barrier Mixer Diodes for minimum Conversion Loss and low Power Requirements at Terahertz Frequencies," in *Proc. of Second International Symposium on Space Terahertz Technology*, pp. 371-388, 1991.
- [5] P. Marsh, D. Pavlidis, K. Hong, "InGaAs-Schottky Contacts Made by In Situ Plated and Evaporated Pt - An Analysis Based on DC and Noise Characteristics," *IEEE Trans. On Electron Devices*, vol. 45, NO. 2, February 2008.
- [6] A. Simon, Konzeption und Technologieentwicklung von Schottkydioden für Anwendungen im Terahertzbereich, *Doctoral Thesis*, (Shaker Verlag, Aachen), 1996.
- [7] E. Schlecht and R. Lin, "Schottky Diode Mixers on Gallium Arsenide Antimonide or Indium Gallium Arsenide," in *Proc. of 19th International Symposium on Space Terahertz Technology*, pp. 221-223, 2008.
- [8] J. Hesler, "The Design and Analysis of Antiparallel Schottky Diode Mixers," in *Proc. of International Conference on Terahertz Electronics [8th]*, Darmstadt, Germany, 28-29 September, 2000.

A 530-600 GHz silicon micro-machined integrated receiver using GaAs MMIC membrane planar Schottky diodes

B. Thomas¹, C. Lee¹, A. Peralta¹, J. Gill¹, G. Chattopadhyay¹, S. Sin¹, R. Lin¹ and I. Mehdi¹

¹NASA- Jet Propulsion Laboratory, California Institute of Technology,
4800 Oak Grove Drive, PASADENA, CA, 91101, USA. Email: Bertrand.C.Thomas@jpl.nasa.gov

Abstract— We present here a novel integrated receiver architecture called Radiometer-On-a-Chip (ROC) that uses a combination of MMIC amplifier, GaAs Schottky multiplier and mixer devices and silicon micro-machining techniques. The novel stacking of micro-machined silicon wafers allows for the 3-dimensional integration of the W-band power amplifier, a 280 GHz tripler and a 560 GHz sub-harmonic mixer in an extremely compact package. Preliminary results give a DSB mixer noise temperature of 4860 K and DSB mixer conversion losses of 12.15 dB at 542 GHz. Instantaneous 3 dB RF bandwidth extends from 525 to 585 GHz. To the authors' knowledge, this is the first demonstration of an all integrated silicon micro-machined receiver front-end at these frequencies.

INTRODUCTION

The sub-millimeter wave range (300 GHz – 3 THz) is rich in emission and absorption lines of various molecular species (i.e. CH₄, CO, H₂O, HCN, etc...) whose detection and mapping are important to understand the atmospheric circulation of telluric planets (Venus, Earth, Mars), outer planets (Jupiter, Saturn) and their moons (i.e. Europa, Titan). Sub-millimeter wave spectrometers with very high spectral resolution have been flown for Earth remote sensing up to 2.5 THz. However, their use in planetary exploration has been severely restricted due to their large mass and power requirements. Conventional approach prevents them from fitting in the mass and power budgets of most platforms.

To tackle that problem, we present here a novel Radiometer-On-Chip (ROC) architecture that uses a combination of GaAs MMIC Schottky diodes and silicon micromachining techniques. Due to the unique arrangement of active components together with silicon micro-machined waveguide structure in a stacked configuration, three-dimensional radiometer circuits can now be conceived and are presented here. First, a W-band amplifier module based on this technology utilizing pHEMT based MMICs has been designed, fabricated and tested. The design of the Si-packaged amplifier is shown here. Second, the development of an integrated 530-600 GHz silicon micro-machined ROC is discussed later. The 530-600 GHz ROC features an integrated 265-300 GHz tripler and 530-600 GHz sub-harmonic mixer based on MMIC GaAs membrane planar Schottky diodes. Preliminary measurement results are presented. This novel approach allows the reduction of the heterodyne receiver front-end elements (Local Oscillator generation based on frequency multiplication/amplification, sub-harmonic and/or fundamental mixers, IF Low Noise Amplifiers and DC bias circuits) by an order of magnitude in mass compared to conventional metal milling.

ROC ARCHITECTURE CONCEPT

The ROC architecture is based on the stacking of Silicon micro-machined wafers together with MMIC GaAs devices, and is shown in Fig.1. Two stages can be identified: the 1st one including components operating at W-band and the second one for the 300-600 GHz components. The first stage is made of the 1st and 2nd Si-layer. It includes a W-band Power Amplifier (PA) MMIC device in between. The 2nd wafer also act as a spacing layer between the first stage (PA) and the third stage. The second stage is made of the 3rd and 4th Si-layer. It includes a 265-300 GHz MMIC GaAs membrane Schottky tripler and a 530-600 GHz MMIC GaAs membrane Schottky sub-harmonic mixer in between. Each layer interfaces with the next one through waveguides opening on the flat of the Si wafers. The LO signal is input via a W-band input waveguide. The RF signal is input via an RF feed-horn. The IF signal is output via a micro-coaxial connector on the top of the 4th layer.

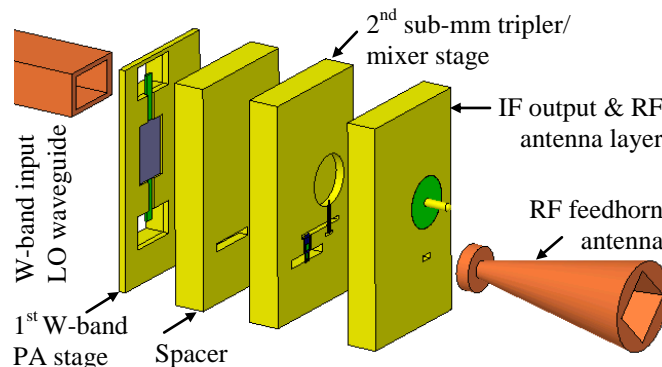


Fig.1. Radiometer-On-a-Chip concept, including an input W-band waveguide, a W-power amplifier stage, an integrated 300 GHz tripler - 600 GHz sub-harmonic mixer stage, and a 600 GHz RF feed-horn antenna.

Although this approach is meant to integrate both stages at the same time, each stage has first been designed and implemented individually in order to characterize them separately. Therefore, in the following sections, additional Si-layers are used for each stage in order to interface them with standard metal waveguide flanges required for testing.

DESIGN OF A W-BAND POWER AMPLIFIER

First, a W-band Power Amplifier MMIC based on GaAs pHEMT technology is packaged in a novel silicon micro-machined block. The MMIC devices are similar to the one previously used in classical metal packages [1]. These MMIC devices are interfaced with W-band waveguide via H-plane probe transitions described in [2]. These transitions are chosen to have the input/output waveguide interfaces with external waveguides on the flat surface of the wafers as shown in Fig.1. However, in order to use common screw holes and dowel pin holes of standard waveguide flanges (UG387) for the input and output waveguides, it is necessary to re-align the input/output waveguides of the amplifier module. For that purpose, two waveguide H-bends derived from [3] are used at the input and output. One-step H-bends are chosen instead of two-steps bends described in [3] mainly for ease of fabrication. It has been shown using 3-D electromagnetic simulations (HFSS [4]) that the return losses of the transition from the microstrip lines to the input/output waveguides including the double bends are below -12 dB between 75 and 108 GHz, which is acceptable for W-band amplifier stage. The resulting 3-D hollow waveguide and channel structures is shown in Fig.2. They are shown together with the split lines of the four Si-wafer used.

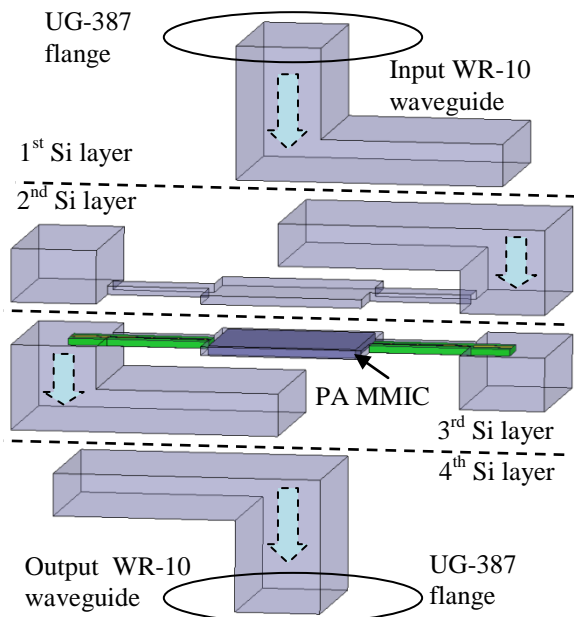


Fig.2: 3-D view of the W-band Si micro-machined Power Amplifier stage showing the hollow waveguide and channel structure (left hand side), and the four silicon micro-machined layers constituting the module and including a UG-387 flange for the input and output waveguides connections.

The final W-band Si PA module is shown in Fig.3. The overall dimensions are 20 x 25 x 4 mm³. It weighs less than 5 grams. As presented in a companion paper [5], the performance is similar to a metal packaged amplifier module using the similar devices. A typical output power between 30 and 80 mW has been measured between 92 and 104 GHz.

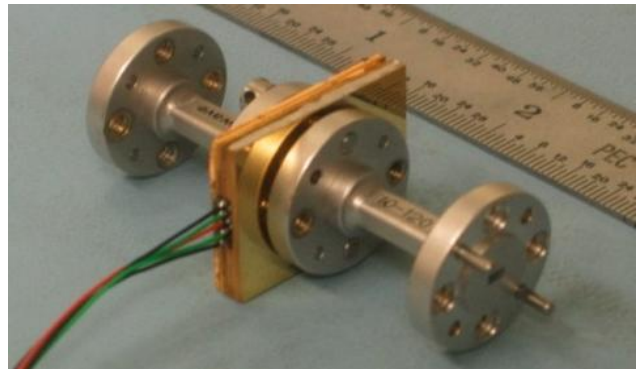


Fig.3: Photo of an W-band Si micro-machined power amplifier module with integrated DC bias board. The dimensions of the Si part are 20x25x4 mm³.

A 530-600 GHz INTEGRATED TRIPLER/SUB-HARMONIC MIXER

The second stage of the ROC is an integrated 265-300 GHz tripler and 530-600 GHz sub-harmonic mixer using MMIC planar Schottky diode devices.

A view of the second stage is shown in Fig.4. It is made of four micro-machined silicon layers stacked on top of each other (only the 2 bottom layers are visible in Fig.4). The tripler W-band input waveguide and 560 GHz RF input waveguide are aligned to use common screw holes and dowel pin holes of the UG-387 flanges, as previously described for the PA stage. Additional 1 mm diameter holes are included as dowel pin holes to align the four silicon layers precisely. K-type glass beads are used for the DC connection of the tripler, and the IF connection of the mixer. The IF microstrip to K-connector transition is taken from [6]. The only modification is that an SSMA flange launcher connector is used instead of a K flange launcher to reduce the footprint on the Si-wafer. A 2-10 GHz IF impedance matching circuit on AlN substrate is also included between the mixer and the output connector. It allows one to match the high impedance of the mixer diodes to the 50 Ω impedance of the 1st LNA.

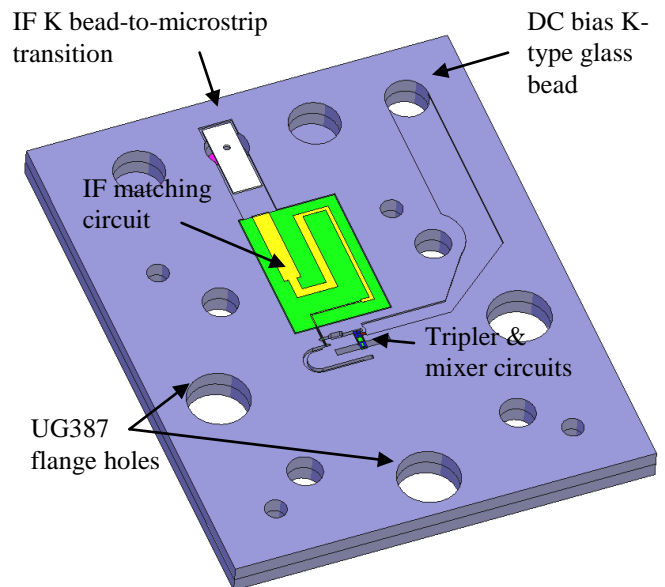


Fig.4: 3-D view of the two bottom layers of the integrated 280 GHz tripler/560 GHz sub-harmonic mixer stage of the ROC. It includes DC and IF K-type connectors for the tripler bias and mixer IF output, a 2-10 GHz IF matching circuit, and two tripler and sub-harmonic mixer MMICs.

The 300 GHz MMIC Schottky device used for the tripler has been described previously [7]. In order to adapt it to the Si micro-machining architecture, the input and output waveguide matching network has been re-designed. As a result, the nominal operating bandwidth of the tripler is re-tuned for 265-310 GHz, compared to the initial 260-340 GHz bandwidth [7]. The 530-600 GHz sub-harmonic mixer features a GaAs membrane MMIC device with a pair of planar Schottky diodes arranged in balanced configuration, as described in [8]. The MMIC sub-harmonic mixer (SHM) is biasless. Details about the simulation procedure employed for the design of the 280 GHz tripler and the 560 GHz sub-harmonic mixers can be found in [9][10]. Both devices are first simulated separately, and then simulated together in ADS to compute the overall performance and maximize the matching between the tripler and mixer stage at LO frequencies (265-300 GHz). Detailed view of the 280 GHz tripler/ 560 GHz sub-harmonic mixer circuit is shown in Fig.5. As shown in Fig.5, the W-band input LO signal enters from the top and the RF signal enters from the bottom of the Silicon wafers stack.

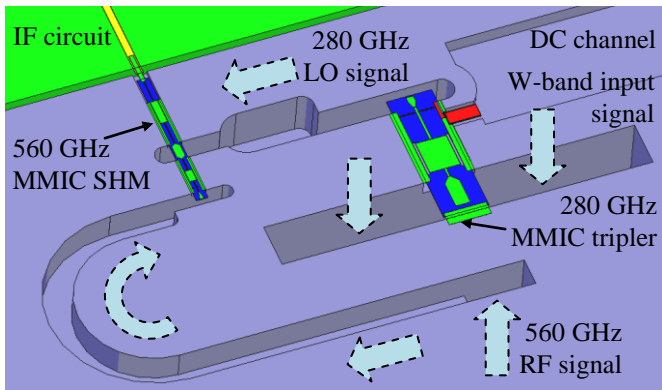


Fig.5: Detailed 3-D view of the 280 GHz tripler / 560 GHz sub-harmonic mixer stage. The tripler is a balanced 6-anodes GaAs Schottky MMIC similar to [7]. The sub-harmonic mixer is a balanced 2-anodes GaAs membrane Schottky MMIC scaled from [8].

Simulations show that an input power between 2 mW and 3 mW is enough to pump the mixer, and that 30-50 mW of input power at W-band is necessary to pump the combined tripler/mixer.

Tripler/mixer stage fabrication

The second stage of the ROC has been fabricated using DRIE micromachining techniques to etch the waveguides and channels in four 750 μm thick silicon layers. The details of the fabrication process are described in a companion paper [5]. The Silicon layers, once etched, are gold plated. Devices are mounted on the two bottom layers. Due to the fact that the RF waveguide is opened in the bottom, it is possible to precisely align optically the RF feed-horn with the RF waveguide opening of the two bottom Si layers and glue it in place before closing the Si block. A photo of the mounted second ROC stage is shown in Fig.6. As illustrated in Fig.6, the four Si layers are sandwiched between the W-band input LO waveguide and the 560 GHz RF feed-horn antenna. The

feedhorn antenna used for the test is a corrugated type. A small additional plate on the back of the wafers (the W-band input side) allows to press the SSMA connector flat on the front side of the wafers (RF input side).

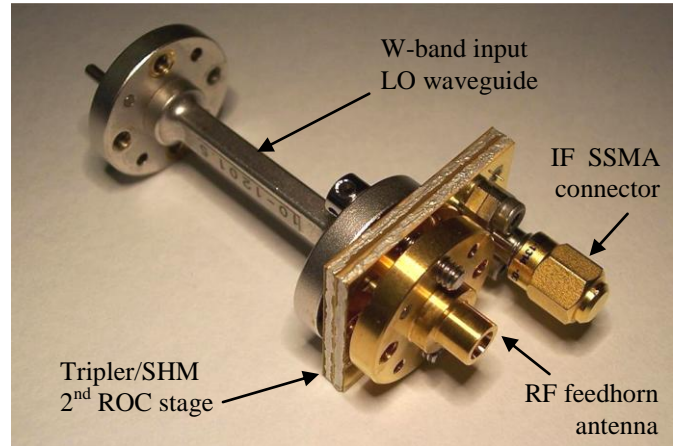


Fig.6: Photo of the second stage of the ROC, including 280 GHz tripler and 560 GHz sub-harmonic mixer MMICs. It also includes an SSMA IF connector and K-type glass bead DC bias connection. The overall dimensions of the Si block are 20x25x3 mm³.

The overall dimensions of the silicon micromachined tripler/mixer stage is 20x25x3 mm³. Without the feedhorn, SSMA and input waveguide, it weighs less than 5 grams.

Preliminary test results

Preliminary tests on the second stage of the ROC are very encouraging. The tripler/mixer stage is pumped with an Agilent W-band source and a classical driver/power amplifier stage. The IF output is fed into an automatic mixer measurement IF amplification and detection test set-up. A classical Y-factor measurement was performed using a room temperature and liquid nitrogen cooled calibration load. The IF bandwidth is 30 MHz centered around 4 GHz. No correction for IF mismatch was included.

Preliminary test results give a DSB mixer noise temperature of 4860 K and DSB mixer conversion losses of 12.15 dB at 540 GHz center RF frequency. The 3 dB instantaneous RF bandwidth extends from 525 to 585 GHz. The amount of input power necessary at W-band to pump optimally the mixer is measured between 30 and 50 mW, in accordance with the predictions.

It is expected that the performance of the ROC will improve with a better control of the surface roughness of the waveguides.

A 560 GHz COMPLETE ROC FRONT-END

A complete silicon micro-machined ROC module including the first W-band PA stage and the second tripler/mixer stage has been assembled and is shown in Fig.7. The overall dimensions of this front-end is 25x25x8 mm³ for the silicon parts, and weighs less than 10 grams. This corresponds to a reduction of approximately 50 in size and mass compared to traditional metal machined receiver front-ends.

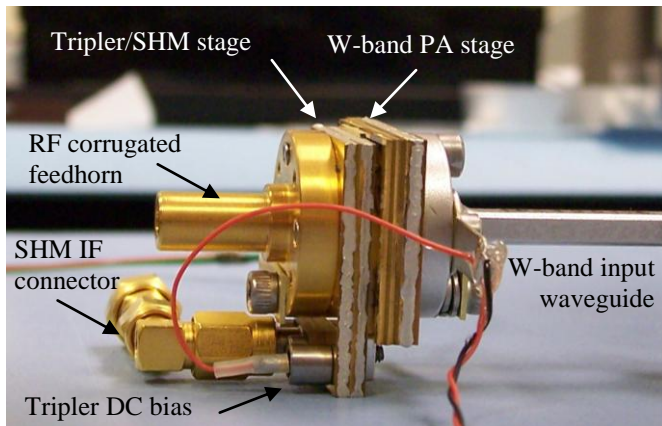


Fig.7: Photo of a fully assembled ROC front-end module, including the silicon micro-machined PA and tripler/mixer stages. The overall dimensions of the silicon parts of the ROC is $25 \times 25 \times 8 \text{ mm}^3$.

Tests are on-going in order to fully characterise this ROC front-end module.

CONCLUSIONS

As a proof-of-concept, a silicon micro-machined W-band amplifier module and a 530-600 GHz integrated sub-harmonic mixer/tripler based on the same approach have been demonstrated. This novel silicon-based architecture allows for the 3-D integration of amplifier, multiplier and mixer MMICs in a extremely small package. This architecture is also readily extendable to two dimensional array of receivers, paving the way for the development of large focal plane array type instruments. This novel architecture is expected to reduce the size, mass and power consumption of heterodyne receivers onboard future missions dedicated to the remote sensing of planets' atmospheres and surfaces, as well as for astrophysics.

ACKNOWLEDGMENT

The authors wish to acknowledge the help and support of Dr. Peter Siegel. We also would like to thank Dr. Alain Maestrini for providing very useful information concerning the design of the tripler.

This work was carried out at the Jet Propulsion Laboratory, California Institute of Technology, under contract from the National Aeronautic and Space Administration.

REFERENCES

- [1] Samoska, et al., "MMIC Power Amplifiers as Local Oscillator Drivers for FIRST," *Proc. SPIE* vol. 4013, pp. 275-284, 2000.
- [2] Y.-C. Leong and S. Weinreb, "Full Band Waveguide-to-Microstrip Probe Transitions", *IEEE MTT Symposium Digest*, pp. 1435-1438, 1999.
- [3] A.R. Kerr, "elements for E-plane Split-Block Waveguide Circuits", *ALMA Memo 381*. website: <http://www.mma.nrao.edu/memos/>
- [4] High Frequency Simulation Software, V12.0, Ansoft Corporation, 225 West Station Square Drive, Suite 200, Pittsburgh, PA 15219, USA.
- [5] C. Lee, B. Thomas, G. Chattopadhyay, A. Peralta and I. Mehdi, "Silicon Micromachining Technology for Passive THz Components", accepted for publication in the proceedings of the 21st Int. Symp. on Space THz Technology, Oxford, England, 23-25 March 2010.
- [6] M. Morgan and S. Weinreb, "A millimeter-wave perpendicular coax-to-microstrip transition," *IEEE MTT-S Intl. Microwave Symp. Digest*, pp. 817-820, Seattle, WA, 2002.
- [7] A. Maestrini, C. Tripon-Canseliet, J. Ward, H. Javadi, J. Gill, G. Chattopadhyay, E. Schlecht, and I. Mehdi, "Multi-Anode Frequency Triplers at Sub-Millimeter Wavelengths", proceedings of the 16th International Symposium on Space Terahertz Technology, paper P5-3, Göteborg, Sweden, 2-4 May 2005.
- [8] B. Thomas, A. Maestrini, D. Matheson, I. Mehdi and P. de Maagt, "Design of a 874 GHz Biasable Sub-Harmonic Mixer Based on MMIC Membrane Planar Schottky Diodes", Proceedings of the IR and Millimeter Wave Conference – Terahertz electronics IRMMW-THz 2008, Caltech, Pasadena, CA, USA, September 2008.
- [9] A. Maestrini, J. Ward, J. Gill, H. Javadi, E. Schlecht, C. Tripon-Canseliet, G. Chattopadhyay and I. Mehdi, "A 540-640 GHz High Efficiency Four Anode Frequency Tripler", *IEEE Transactions on Microwave Theory and Techniques*, Vol. 53, pp. 2835-2843, September 2005.
- [10] B. Thomas, B. Alderman, D. Matheson and P. de Maagt "A Combined 380 GHz Mixer/Doubler Circuit based on Planar Schottky Diodes", *IEEE Microwave & Wireless Components Letters*, Vol.18, No.5, May 2008, pp-353-355.

Electro-Thermal Model for the Design of Schottky Diode Based Circuits

Jesús Grajal, Carlos-Gustavo Pérez and Beatriz Mencía.

Dept. Signals, Systems and Radiocommunications
Technical University of Madrid, Spain
Email: jesus@gmr.ssr.upm.es

Abstract

The planar GaAs Schottky diode frequency multiplier is a critical component for the local oscillator for submillimeter wave heterodyne receivers. They provide low mass, electronic tunability, broad bandwidth, long life time, and room temperature operation. The use of a W-band (75GHz – 110 GHz) power amplifier followed by one or more frequency multipliers is the most common implementation of submillimeter-wave sources from 200 GHz to 2000 GHz.

Recently, W-band GaN-based MMIC power amplifiers and power-combined GaAs power amplifiers have provided the possibility of generating watt level powers at W-band. As more power at W-band is available to the multipliers, the power handling capability of multipliers becomes more important. High operating temperature due to the high input power leads to degradation of conversion efficiency.

Therefore, electro-thermal models have to be used to optimize the performance of the devices themselves but also the multipliers. We have developed a circuit simulator that couples the embedding circuit with a numerical physics-based electro-thermal model for Schottky diodes. This model takes into account both the electrical limiting transport mechanisms and also self-heating. The thermal characteristics are taken into account by adding the heat conduction equation to an existing physics-based electrical model based on the drift-diffusion theory. This additional equation applies conservation of energy to the composite system consisting of electrons, holes, and phonons.

Thermal phenomena are strongly affected by 3D propagation effects, and are relevant on lengths much larger than what is needed for an accurate electrical description. This property makes a direct numerical solution of the coupled electro-thermal problem unnecessary. An accurate and efficient approach is thus required, based on the full numerical solution of the transport equations coupled to the heat transfer equation in a reduced volume. This reduced volume includes all areas of the device where electrical effects take place. Thermal effects from the excluded device volume are accounted for by using appropriate thermal transport boundary conditions, derived based on a lumped approximation of heat transfer in the corresponding areas.

This tool can be used to design appropriate Schottky diodes taking into account not only geometrical aspects but also different materials (GaAs diode on diamond, GaN diode on SiC). However, the main objective is to develop high performance Schottky-based circuits working at millimeter bands and above based on simulation tools with increasing capabilities.

Session S7: Calibration and Measurements

ALMA Front-End Verification Using a Dry Cold Load

Yoonjae Lee¹, Brian Ellison¹, Peter Huggard¹, Mark Harman¹, Abdelhakim Boughriet¹, Wojciech Bartynowski¹, Matthew Oldfield¹, Nigel Morris¹, Peter Hekman², and Gie Han Tan²

¹Science and Technology Facilities Council, Rutherford Appleton Laboratory, Chilton, Didcot, OX11 0QX, UK

²European Organisation for Astronomical Research in the Southern Hemisphere (ESO)

Karl-Schwarzschild-Straße 2, 85748 Garching bei München, Germany

*Contact: yoonyae.lee@stfc.ac.uk; phone +44-(0)1235-44-6846, brian.ellison@stfc.ac.uk; phone +44-(0)1235-44-6719

Abstract— Several techniques for measuring the radiometric temperature (brightness) of a refrigerated dry calibration load for ALMA front-end verification are presented. The brightness of the load including the effects of the cryostat window is estimated using different techniques and compared at frequencies up to 1 THz. The measured results are compared with those obtained by a conventional calibration technique using the ALMF front-end. The estimated brightness shows a good agreement at lower ALMA bands (below 400 GHz) with increased deviation at higher frequencies. Measured noise temperatures of the ALMF front-end using a wet LN₂ load and the dry cold load are also presented.

I. INTRODUCTION

Noise temperature is one of the crucial parameters that describe the performance of a high sensitivity cooled receiver. The noise performance of a receiver can be characterised by performing a relative measurement using thermal calibration loads with the radiated noise power or radiometric temperature known *a priori*. For a reference radiometric temperature, thermal calibration loads commonly use high emissivity absorbing materials immersed in liquid cryogen (wet load), which provides stable radiometric temperatures at stationary state. However, owing to the difficulties in handling of the wet load, the measurement could be cumbersome when the receiver under test needs to be measured repeatedly at different orientations. Verification of the Atacama Large Millimetre/submillimetre Array (ALMA) front-end [1] requires such a task, for which use of a closed cycle refrigerator cooled load inside a vacuum container, *i.e.*, a dry cold load shown in Fig. 1 is proposed. This will reduce the need for a liquid Nitrogen (LN₂) load and will ensure stable load temperature during measurement. Key requirements of the dry cold load for the characterisation of the ALMA receivers include a constant stable brightness temperature over a wide bandwidth up to 1 THz, polarisation insensitiveness, high emissivity, mechanical stability, etc.

For an ideal blackbody load (emissivity = 1), the radiometric temperature (brightness) of the load is identical to its physical temperature. The reflection from the load will add the same fraction of radiation from the surrounding environment to its original brightness, hence results in a modified overall radiometric temperature. Owing to the presence of the window and metallic surroundings in the dry cold load, the accurate estimation of the load brightness is

challenging. The most significant factor that affects the performance of the dry load is the window characteristics, which are described by absorption and reflection coefficients.

In this paper, several techniques for estimating the brightness of the dry cold load by using a network model, Fourier transform spectroscopy and receiver calibration are presented.

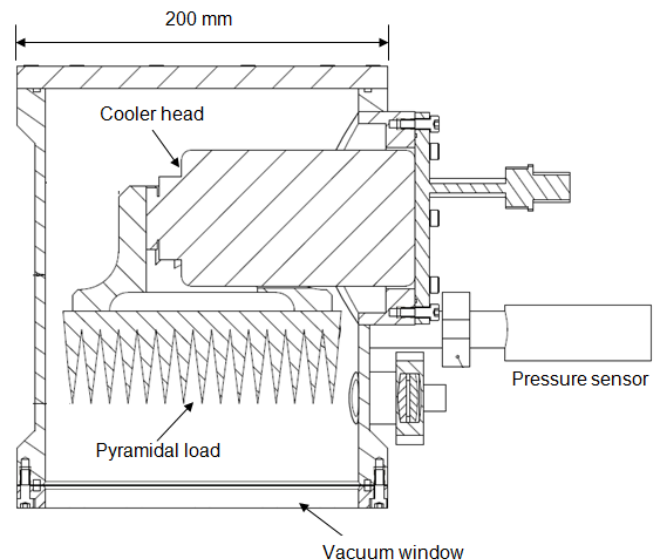


Fig. 1 Cross section of dry cold load

II. LOAD DESIGN

The calibration target for the dry cold load shown in Fig. 3 is manufactured by the Rutherford Appleton Laboratory (RAL) and is based on a pyramidal absorber fabricated from cast epoxy that is loaded with ferrite to provide good absorption properties at microwave and millimetre-wave frequencies [2]. A corresponding pyramidal aluminium backing structure ensures that the surface of the absorber is no more than 2 mm from the aluminium, providing good thermal coupling between the absorber and the heat sink. The target load is mounted in a cryostat and cooled by a commercial cold head (Cryo Tiger T2114). The performance of the cooler is independent of orientation. To maintain a vacuum a 119 mm window of Mylar sheet with 23 μ m thickness is used and this is backed (without using glue) by

50 mm of expanded polystyrene foam (FLOORMATE 700-A, Dow Chemical Co.) fitted in an aluminium frame attached to the cryostat for mechanical support. The geometry and photo of the dry cold is shown in Figs. 1 and 2, respectively.

The backscatter of the calibration target has been measured using a millimetrewave VNA. The maximum reflectance of the target was searched and recorded for the angle of incidence varied between -10° and $+10^\circ$. The overall reflectance of the target was measured around -40dB at most frequencies within the band (75 - 360 GHz) as shown in Fig. 4. The polarisation sensitivity of the calibration target is also tested by rotating the target with a fixed incident polarisation (vertical electric field). The measured results showed that the target does not show significant variation in the maximum reflectance for different polarisations at normal incidence.

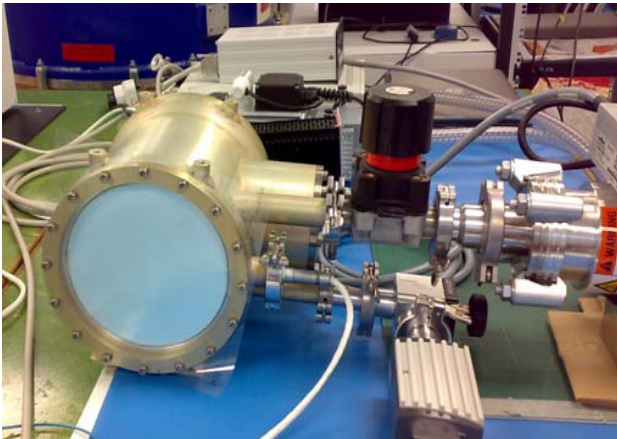


Fig. 2 Dry cold load connected to a vacuum pump and cooler

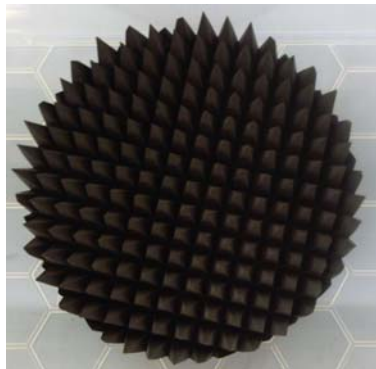


Fig. 3 Calibration target manufactured by RAL

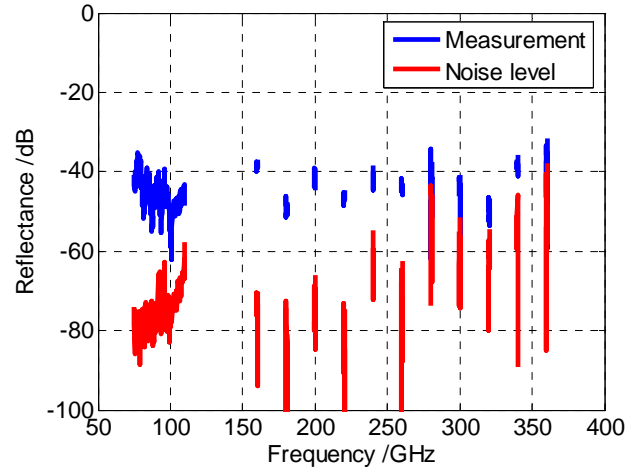


Fig. 4 Measured reflectance of the calibration target

III. WINDOW PROPERTIES

Effects of the vacuum window on load performance must be minimal and provide transparent radiometric characteristics to the calibration target. Several low-loss materials have been investigated and it was found that combination of insulating foam commonly used for construction material and a Mylar sheet showed desirable performance. The window material introduces reflective and absorptive properties, which alter the effective brightness of the calibration load. Fig. 5a shows the simulated reflectance of commercially available Mylar sheets with different thicknesses. The insertion loss of the Mylar sheet is primarily due to reflection from the material. Fig. 5b shows the transmittance of the foam material measured using a Fourier transform spectrometer (FTS) [3].

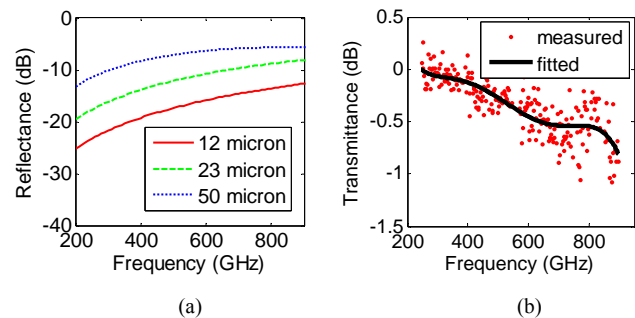


Fig. 5 Characteristics of the window material: (a) simulated reflectance of Mylar, (b) measured (FTS) transmittance of expanded polystyrene foam

IV. EFFECTIVE RADIOMETRIC TEMPERATURE

If the radiometric temperature of the load is known, the overall effective brightness of the load, including the window effects, can be calculated using a microwave network model [4]. The window material is characterised by absorption and reflection coefficients and represented using the S-parameters. The overall brightness of the load is calculated using the model shown in Fig. 6. The S-parameters used for

the investigation were extracted from reflectance and transmittance of the window materials shown in Fig. 5.

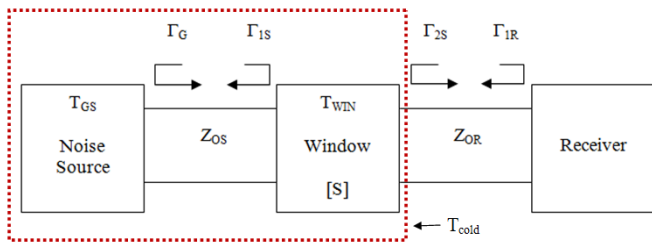


Fig. 6 Microwave network model of cold load problem (T_{GS} : radiometric temperature of the target, T_{WIN} : radiometric temperature of the window, T_{cold} : radiometric temperature of the cold load, Z_{OS} : characteristic impedance of the medium between the target and the window, Z_{OR} : characteristic impedance of the medium between the window and the receiver, Γ_G : reflection coefficients of the target, Γ_{IS} : reflection coefficients of the window, Γ_{2S} : reflection coefficient of the window, Γ_{IR} : reflection coefficients of the receiver, [S]: S-parameter of the window)

Owing to a low thermal conductivity of the window material, the temperature gradient within the window is ignored in the model and a uniform ambient temperature is used; however, in reality, the contribution of the reflection and absorption of the window to the overall radiometric temperature must be weighted by the temperature gradient within the window.

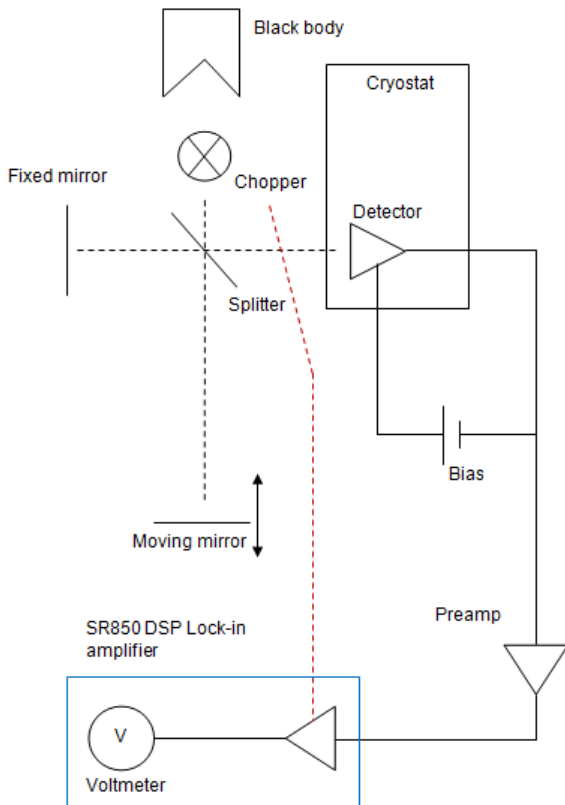


Fig. 7 Fourier Transform Spectrometer set-up

Direct observation of the radiated noise power from the load at upper ALMA bands (200 GHz – 1 THz) was performed using a Fourier transform spectrometer (FTS) and the detected power from the dry cold load was compared with those from an ambient and an LN₂ load. A cooled InSb hot electron bolometer detector system (QFI/2BI, QMC Instruments, Ltd.) was used for the measurement. For the reference load, microwave absorbing materials (Eccosorb® AN-72) [5] at ambient temperature and immersed in LN₂ were prepared. The radiometric temperature used for the LN₂ load is 77.35 K over the observed frequency. The reflection from the LN₂ load was ignored, but the true radiometric temperature of the LN₂ load is slightly higher than 77.35 K. The input of the detector was chopped at 680 Hz against the ambient load and the detector output was measured using a lock-in amplifier (SR-850, Standard Research Systems). The overall diagram of the set-up is shown in Fig. 7. The detected spectra for different loads are plotted in Fig. 8. The results were accumulated over eight times of measurements in order to reduce measurement noise. The radiometric temperature of the load is calculated by comparing the detector output of two reference loads (ambient and LN₂ loads). Effects of the optics (lens) at the load side are subtracted from the results. The performance of the dry cold load was found to be almost identical up to 250 GHz showing very similar radiometric temperature compared with the physical temperature of the target and beyond 250 GHz, the brightness gradually increases. There were several atmospheric absorption lines observed in the measured spectrum, and the measurements at those frequencies were ignored. The calculated brightness of the load based on the FTS measurements was fitted by a polynomial and compared later with results obtained by other techniques.

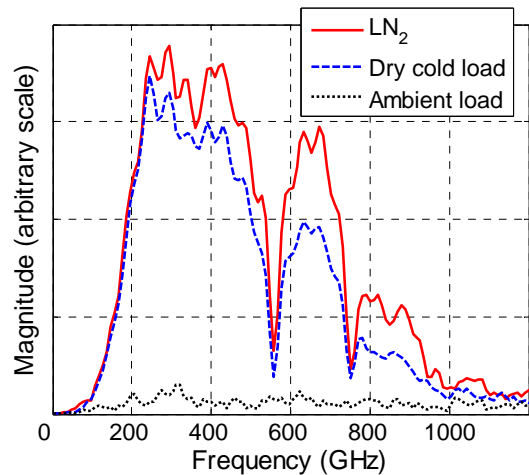


Fig. 8 Radiation spectra measured using FTS

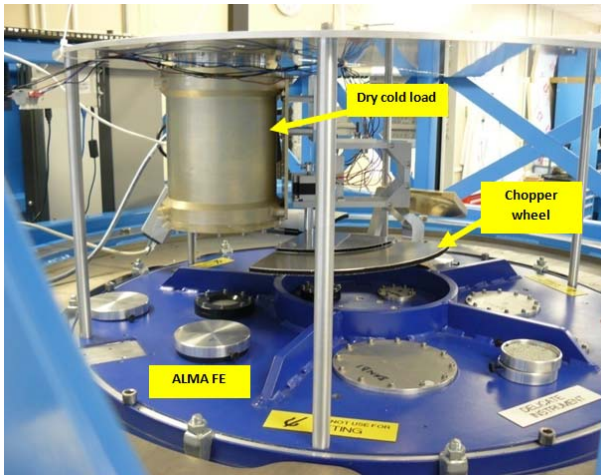


Fig. 9 Dry cold load installed at ALMA Front-End for receiver noise measurement

Finally, the brightness of the cold load was measured using the ALMA front-end receiver at Band 6 (221-265 GHz) and Band 9 (614-710 GHz). Fig. 9 shows the dry cold load installed on the ALMA front-end cryostat with chopper assembly. The standard Y-factor method was used to calculate the radiometric temperature of the load. For the calibration load, a cone of AN-72 absorbing material soaked in LN₂ and a sheet of AN-72 at ambient temperature were used. The radiometric temperatures estimated and measured by three different methods were plotted together in Fig. 10 for comparison. Good agreement was observed among three methods at lower frequencies, whereas some discrepancies, but with reasonable agreement in the trend, were noted at higher frequencies. These discrepancies are attributed to increased errors in the measured material properties used in the model and the assumptions made for the window, *e.g.*, temperature profile.

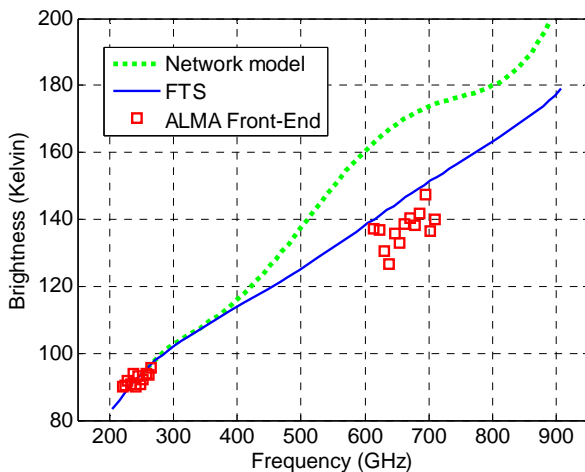


Fig. 10 Comparison of estimated and measured brightness

The receiver noise temperature of ALMA front-end at Band 9 was measured again using both the dry cold load and compared with the cartridge group data in Fig. 11.

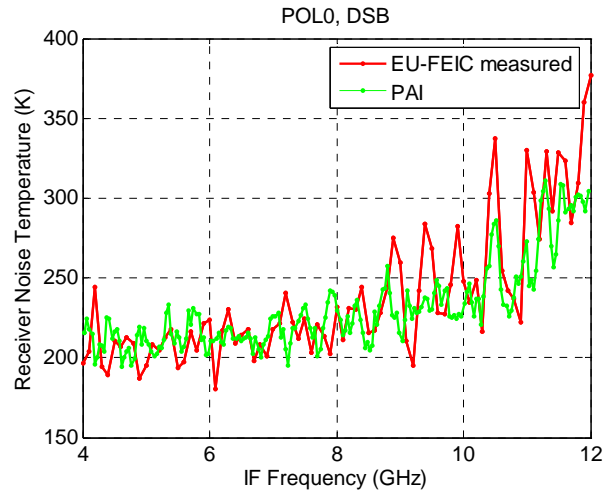


Fig. 11 Comparison of receiver noise temperatures (Band 9 LO = 614 GHz) measured at ALMA European Front-End Integration Centre (EU-FEIC) and reported in Preliminary Acceptance In-house (PAI) test results at cartridge group

V. CONCLUSIONS

The radiometric temperature of the dry cold load with a vacuum window has been measured using several techniques. A microwave network model based on the transmission and reflection characteristics of the window material is used to estimate the effective brightness of the dry cold load. The radiation spectrum of the dry cold load was directly compared with the liquid Nitrogen cooled and the ambient loads using the Fourier transform spectroscopy technique, and the effective brightness was calculated. Finally, the dry cold load was calibrated using the ALMA front-end. The performance of the dry cold load investigated by different techniques showed a good agreement in the estimated brightness. The FTS technique can be very effective for characterising calibration targets over a broad frequency range.

REFERENCES

- [1] R. L. Brown, W. Wild, and C. Cunningham, "ALMA – the Atacama large millimetre array," *Advances in Space Research*, 2004, 34, pp. 555-559.
- [2] A. Murk, A. Duric, and F. Patt, "Characterization of ALMA calibration targets," *19th International Symposium on Space Terahertz Technology*, (ISSTT), Groningen, April 2008.
- [3] M. N. Afsar, "Dielectric measurements of millimetre-wave materials," *IEEE Trans. Microwave Theory and Tech.*, 1984, 32, pp. 1598-1609.
- [4] T. Y. Otoshi, "The effect of mismatched components on microwave noise-temperature calibrations," *IEEE Trans. Microwave Theory and Tech.*, 1968, 16 (9), pp. 675-686.
- [5] <http://www.eccosorb.com/file/832/eb-10%20eccosorb%20an%20.pdf>

Development of Conical Calibration Targets for ALMA

Axel Murk^{*}, Pavel Yagoubov[†], Richard Wylde[‡], Graham Bell[‡], Irena Zivkovic^{*}

^{*}Institute of Applied Physics
University of Bern
Email: murk@iap.unibe.ch

[†]European Southern Observatory
ALMA Front End Division
Email : pyagoubo@eso.org

[‡]Thomas Keating Ltd.
Email : r.wylde@terahertz.co.uk

Abstract

We present the design and test results of the hot and the ambient calibration targets for the Atacama Large Millimeter Array (ALMA). The targets have to cover a very wide frequency range from 31 to 950GHz and the hot target has to be heated up to 90°C. The required absolute radiometric accuracy of the ambient and hot targets is +/- 0.3K and +/- 0.5K (at 70°C) respectively. In order to meet these requirements different contradictory design aspects had to be considered. One of the most important parameters for a high quality blackbody calibration target is an overall emissivity close to unity. The requirement on the emissivity depends on the temperature difference between the target and its environment. Even in the worst case the ALMA requirements for the absolute accuracy of the ambient and hot targets will be met with emissivities of 0.999 and 0.998 respectively, which corresponds to a total scattering of -30dB and -27dB. In addition the coherent backscatter of the target has to be significantly smaller than these values since it can lead to standing waves between the receiver and the target and thus to a significant error on the radiometric calibration. Although not quantified explicitly in the ALMA requirements, we identified as a design goal a coherent backscatter of -56dB for the hot and -60dB for the ambient target. The second parameter which determines the absolute calibration accuracy is the temperature gradient across the target aperture or within the absorber material. Especially for the hot target there will be always a certain difference between the sensors that read the physical temperature and the effective surface temperature of the absorber.

To meet the stringent accuracy requirements the ALMA calibration targets have a folded conical geometry. The absorbing material is attached to a metal backing and consists of a multilayer composition of different absorber grades which is tuned for the most critical frequency bands of operation. We present the overall design of the calibration targets, ray-tracing simulations of the multilayer absorber cones, as well as experimental results. These include reflection measurements between 30-700GHz with a vector network analyzer, radiometric tests with a 91GHz radiometer and an assessment of the thermal gradients under different operating conditions using distributed temperature sensors and an IR camera.

Harmonic Mixers for VNA extenders to 900GHz

Hugh J.E. Gibson¹, Achim Walber², Ralph Zimmerman², Byron Alderman³, Oleg Cojocari⁴

¹ *Gibson Microwave Design EURL, Antony, France / RPG*

² *RPG Radiometer Physics GmbH, Meckenheim, Germany*

³ *SFTC Rutherford Appleton Laboratory, Oxon, UK*

⁴ *ACST GmbH, Darmstadt, Germany*

Contact: gibson@radiometer-physics.de

Abstract— Harmonic mixers for high frequencies have been available for many years but conversion loss has always been relatively high and usually with many dips in the frequency response. There are many devices covering the lower waveguide bands, but relatively little above 110GHz. As part of Rohde & Schwarz's new line of VNA extenders, Radiometer Physics (RPG) has designed a new range of waveguide harmonic mixers, covering from 24.5 to 900GHz with excellent performance. Part of this work includes complete redesign and fabrication of extremely low parasitic anti-parallel mixer diodes by two independent, competing groups: RAL and ACST. These diodes can also be used to make excellent sub-harmonic mixers (2nd harmonic of the LO) with high sensitivity. We also outline the use of a wideband stripline filter, using a "photonic band gap" structure and an unconventional waveguide transition for the RF signal coupling.

I. INTRODUCTION

Recent years have seen an increasing interest in extremely high (sub-mm) frequencies by the microwave industry. The technology to reach these high frequencies has only recently moved from the exotic to main-stream. Use of sub-mm instrumentation includes high-resolution security scanners [1], quality control of thin materials [1], atmospheric ice-cloud studies by satellite [2] or high-altitude balloon or aircraft [3], and ultra secure high-speed data links. Test equipment for these sub-millimetre wavelengths (>300GHz) has previously been limited to over-moded versions of lower frequency devices, with poor performance. Radiometer Physics has developed a new range of high-performance, broadband, balanced mixers and frequency sources, which are used to make test equipment to enable sub-millimetre engineers to use the same methods as millimetre or microwave engineers. These individual devices will be discussed, as well as the test equipment that can be built from them. Several other groups (Oleson OML, Virginia Diodes) are developing similar test equipment for this rapidly expanding field and interest in sub-mm wavelengths is certain to increase.

II. HARMONIC MIXERS

A key to using spectrum analysers and Vector Network Analysers (VNA) at sub-millimetre (sub-mm) frequencies is the development of high performance harmonic mixers, which have good conversion efficiency, flat frequency response, and stable characteristics to allow unchanging

calibration. These specifications can be achieved with mixers having the following characteristics:

1) Low Harmonic Number

Many harmonic mixers for sale today were designed more than 25 years ago, when the maximum Local Oscillator (LO) frequency was usually less than 6 GHz. This severely limits performance, as a very high harmonic number is required to reach sub-mm frequencies. A key to our harmonic mixer results is keeping the harmonic number low, which implies a high LO frequency. Modern VNAs and spectrum analysers have internal oscillators which often exceed 15GHz and are much better suited for high frequency extender use. A low harmonic number allows a very uniform conversion efficiency curve, which is less prone to LO power or temperature variations. For extremely high frequencies, the harmonic number of the mixer can further be reduced by multiplying the LO before use in the harmonic mixer. This is nowadays quite simple, with a large range of GaAs MMIC devices to provide multiplication and amplification. We can, for example, pump a 800GHz mixer using the 8th harmonic (at 100GHz) and employ a x6 multiplier (16.67GHz initial LO frequency). Such a system is usually packaged as a module which includes all additional amplifiers, multipliers and power supplies.



The small insert photo on the left shows such a receive system, in this case allowing the 110-170GHz waveguide band to be covered but using only the 4th harmonic at the mixer by providing an additional x4 for the externally applied LO. This enables better performance to be achieved than using x16 directly.

2) Good Input Match

All harmonic mixers using a harmonic more than 4 (including the latest ones developed here) have a terrible RF input return loss of typically -2 to -4 dB. This is often compensated for by fitting the harmonic mixers with lossy absorbing material, but is accompanied by a loss in sensitivity and performance unrepeatability. Our approach is different; instead of using an absorber, or another lossy device, we fit each harmonic mixer with an RPG-made full-band, low-loss Faraday rotation isolator, (based on [4]), fitted

as close to the mixer as possible. This solves the problem of the input return match as well as providing a good termination for unwanted harmonic signals generated at the mixer. Return loss is maintained at better than -16dB and the behaviour of the harmonic mixer is now entirely decoupled from the input waveguide flange match. Calibration data is provided for the mixer plus isolator combination and can be applied with high accuracy.

3) Control of Harmonics

In the design of the Agilent 11970 harmonic mixer, HP engineers discovered just how severe a problem unwanted harmonics can be [5]. We have already spoken about unwanted harmonics in the input waveguide in 2) but harmonics also travel back down the LO port. Controlling how these frequencies are terminated is similarly critical to producing a mixer with a flat frequency response. We use balanced designs for all the mixers which have many advantages, including cancellation of LO amplitude noise in the IF. The balanced design also means that the even LO harmonic components remain in a “virtual loop” in the anti-parallel diode and mix with the incoming signal. No filtering of any sort is required for the even harmonics.

The odd harmonic RF currents however do not cancel in the anti-parallel diode pair, but are strongly generated and travel away from the diodes. The third harmonic is especially strong and needs proper termination. This is of course rather difficult to achieve in practise as the stripline circuitry must be small for the high input frequency but large enough to create a 3rd harmonic filter (at a very much lower frequency). If the substrate is made too wide or thick, it starts to exhibit narrow-band ‘substrate’ modes which cause unpredictable behaviour. We have used a combination of stub-filters and new, photonic-band gap (PBG) filters to achieve extremely wideband filters in a very compact form, such that the reflections of the 3rd and 5th harmonics do not have enough electrical length to cause interference problems, but realised on quartz, with dimensions that are appropriate for the high input frequency.

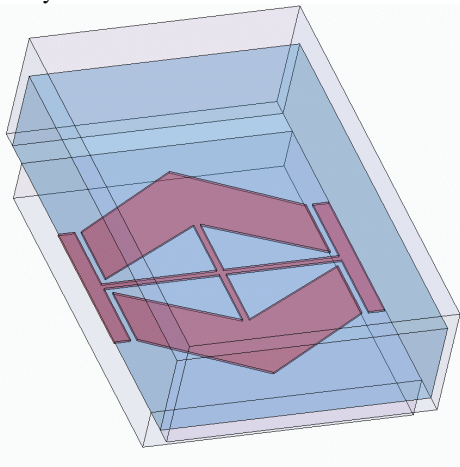


Fig 1 HFSS model of “PBG” low-pass filter

The filter structure illustrated uses a quartz substrate, with dimensions of only 180um wide x 160um long x 35 um high;

unusually small for a 200GHz LPF. A transmission and reflection plot of this design is shown in Fig 2.

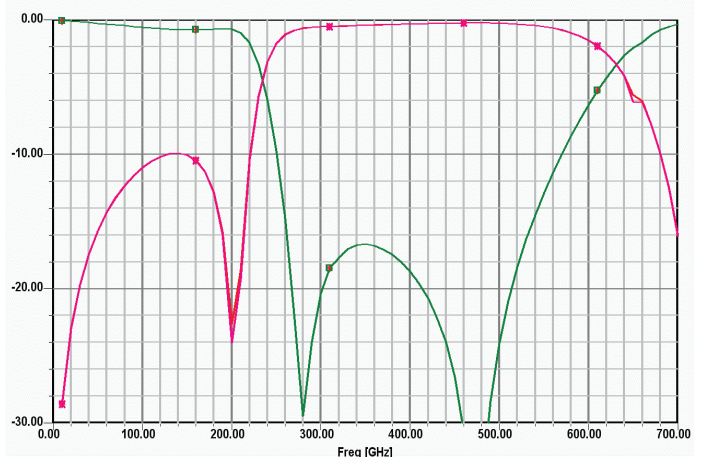


Fig2 S21(red) and S11(green) plot of Fig 1 (dB scale)

4) Novel Waveguide Transition Structure

To keep electrical lengths to an absolute minimum on the RF input side of the diode pair, a modified version of a standard rectangular waveguide to stripline transition (using a paddle probe extending approximately 1/2 way into the waveguide) was used. The design easily covers a whole waveguide band.

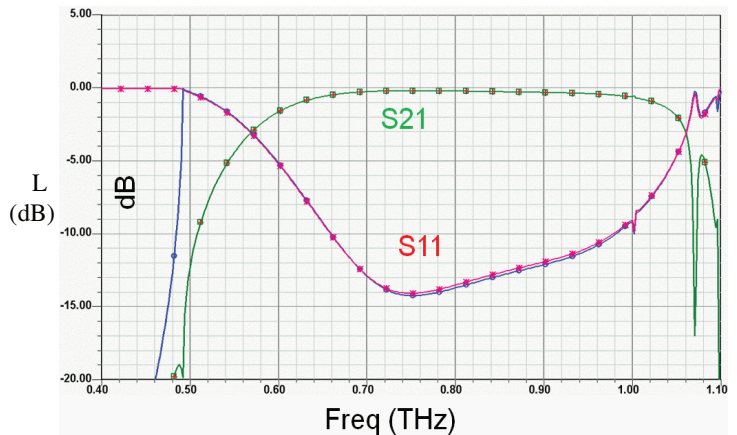


Fig 3 HFSS simulation of performance of the transition.

This transition has the new feature of a bond-wire forming a short to the waveguide back-short wall. The design is extremely tolerant to the dimensions of the short and there is an added advantage that the waveguide is not reduced-height. The short is necessary to drive the diodes against a ground for the LO frequency.

5) Anti-parallel Diode Redesign

Anti-parallel diodes which have low parasitic reactance are critical to providing good performance at high frequencies. Keeping junction capacitance (Cj0) down is also important to maintain a low conversion loss. The dependence of conversion loss (L) on Cj0 in an anti-parallel mixer has been previously studied [6].

Unfortunately, all the presently available anti-parallel diodes for general sale have too high a value of C_{j0} and too high parasitic reactance for high-performance use much above 300GHz. They are also physically too large to fit on strip-line substrate which is appropriate for 900GHz.

We have two collaborators: RAL and ACST, who have independently fabricated GaAs anti-parallel diodes that are of a new design, suitable for mixer use up to near 1THz. Two different approaches have been applied to the parasitic reactance question, both of which have been proven to work extremely well for harmonic mixers. In both cases, a key feature is reducing the parasitic capacitances of the diode, but also reducing the inductance of the beam-lead anode fingers, which we believe has been slightly overlooked in previous anti-parallel diodes. Details of these two diode designs will soon be released by the manufacturers (ACST GmbH Germany and SFTC RAL, UK)

6) Design Method

Designs were created and analysed using a mixture of Ansoft HFSS and AWR Microwave Office. HFSS is used to model the 3-D structure and diodes. An S-parameter file is then exported to Microwave Office for non-linear harmonic balance analysis. Accurate simulations are extremely tricky due to the high harmonic content and harmonic interactions.

III. RESULTS

TABLE I

Freq (GHz)	Harmonic Mixer parameters		
	Harmonic number	max/min Conversion loss (dB) SSB	LO power
26.5-40	3 *	13dB to 17dB	+13dBm
75-110	8	16 to 26dB	+15dBm
75-110	6	15dB to 25dB	+15dBm
75-110	7 *	18dB to 27dB	+10dBm
110-170	12	24dB to 35dB	+14dBm
140-220	16	30dB to 42dB	+12dBm
220-325	16	32dB to 50dB	+11dBm
400-560	6**	25dB to 35dB	+12dBm
650-780	8**	39dB to 43dB	+12dBm
680-780	10**	45dB to 50dB	+12dB
810-835	8***	24dB	+10dBm

*Indicates a cross-bar mixer, operation on ODD harmonic

** Unit sold by RPG includes a x6 active multiplier

*** Narrow band unit optimised for 820GHz

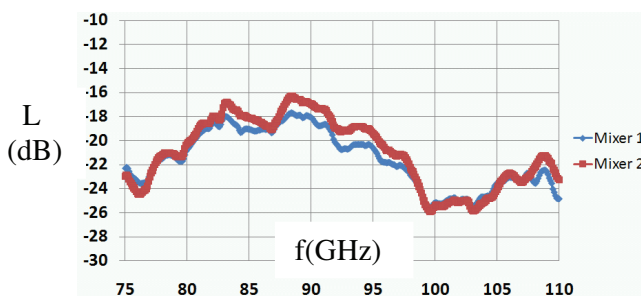


Fig 4 Conversion Loss (L) measurement of two mixers (WR10 mixer, 8th harmonic). Data point every 0.1GHz

Fig 4 shows high frequency resolution measurements of two, identical WR10 (75-110GHz) harmonic mixer, using the 8th harmonic. The conversion efficiency is good (-20dB on average), shows minimal structure and the mixer-to-mixer performance is very repeatable.

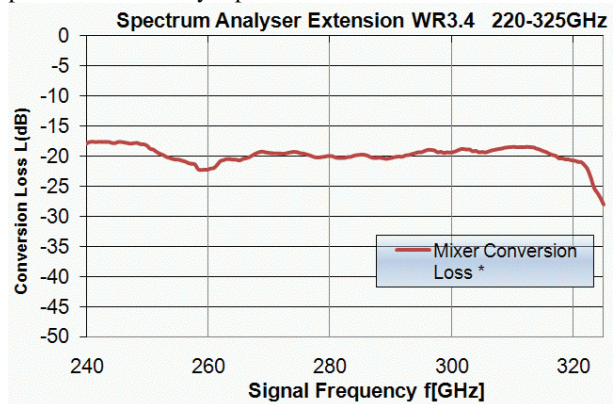


Fig 5 Conversion Loss (L) measurement of a WR3.4 mixer using the 4th harmonic, showing remarkably flat response.

All conversion loss curves for normal products can be viewed on RPG's web site, under "New Product line: Spectrum Analyser solutions" [7].



Fig. 6 A packaged harmonic mixer includes a replaceable waveguide test-port adaptor, an internal isolator and a LO/IF diplexer. IF and LO have separate SMA connectors.

These new mixers in table 1 show excellent performance compared to previous designs. Especially good is the result at 820GHz which is, however, narrow band and highly optimised. The 820GHz mixers have been built into an array.

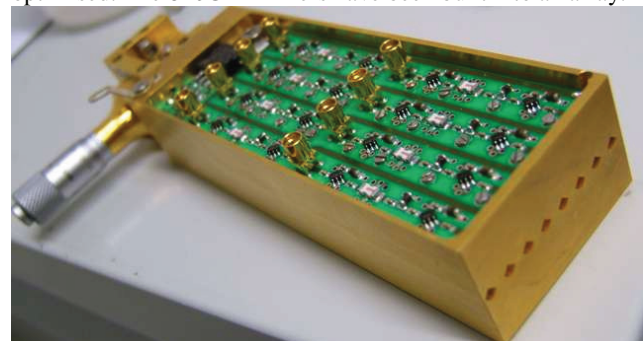


Fig 7 Packaged 820GHz harmonic mixers with feed horns, IF amplifiers and common WR10 LO port.

Using the previous generation of anti-parallel diodes in the 820GHz mixer, conversion efficiencies of around -45dB were obtained for a similar setup, so the new result shows a 20dB improvement! This conversion efficiency is exceptionally good given the frequency, and is very important for achieving a good dynamic range. The 820 GHz mixer is intended for use in a 32-element FMCW radar array for the examination of closed containers with a fast frame rate of 10 f.p.s. (project TERAcam). It is quite easy to integrate these mixers into a linear array and feed them with a common, high power LO source. Fig 7 shows a photo of eight such mixers in a working, stackable system, with a common WR10 LO input, ready for integration.

The rest of the harmonic mixers are designed to cover an entire waveguide band and some compromises have been made for bandwidth. Mixers up to 900GHz have been designed and are in the process of being tested. Testing is presently hampered by the unavailability of test equipment, calibration standards and wideband test sources.

These new mixers and wideband sources (also newly developed at RPG) are integrated into the latest Rohde & Schwarz VNA ZVA-Z series extenders and provide excellent dynamic range, calibration stability and accuracy. With two extenders (Fig 8) a complete set of accurate S-parameters can be measured, with a dynamic range of > 110dB (10Hz bandwidth) across the entire WR10 waveguide band.



Fig 8 Rohde & Schwarz ZVA-Z110 VNA setup for WR10.

IV. SUB-HARMONIC MIXERS

It is also possible to use these new, low-parasitic antiparallel diodes in “normal” sub-harmonic mixers (LO is $\frac{1}{2}$ the RF frequency). The results of early tests are very encouraging. For the highest frequencies, this has required a slight re-design of the existing mixer blocks, as the electrical length of the new-style anode beam-leads is significantly shorter than the older diode (less phase shift). The transmission line path length on both sides of the diode therefore had to be slightly lengthened to compensate and bring the design back to the optimum point. Tests at 424GHz and 660GHz have been made with the following results:

TABLE II

Freq (GHz)	Sub-Harmonic Mixer parameters		
	Tsys	Conversion loss (dB) DSB	LO power & diode type
410-450	1700K	7.2dB	5mW ACST
650-670	2400K	8.0dB	4mW ACST

Tsys is calculated directly from Y-factor measurements, without any extra corrections, so it also includes losses of waveguide and horn as well as the IF amplifier noise contribution. The 660GHz measurement is especially good, and uses a novel waveguide transition. Three 660GHz mixers with similar performance have been manufactured, with consistent Tmixer of around 1700K.

V. CONCLUSIONS

Using new diodes and careful mixer design, the performance of harmonic mixers at sub-mm wavelengths has improved substantially. There are still challenges to be overcome, including the design and production of low-loss, wideband isolators, directional couplers, wideband sources and calibration methods at the highest frequencies. However, big improvements have already been made. Many of these new components are being used to construct new ranges of test equipment, including spectrum analyser and Vector Network Analyser extenders, offering previously unavailable performance, stability and dynamic range.

ACKNOWLEDGMENT

This research and development has been possible with funding from Rohde & Schwarz, and for the diodes with funding from ESA-ESTEC. Realisation of the mixers and the new form of the diodes owes much to separate discussions between Byron Alderman (RAL), Oleg Cojocari(ACST) and Hugh Gibson. Both ACST and RAL plan to market these new diodes, so they should soon be available for purchase. Much of the design work was influenced by papers of J. Hesler and T. Crowe of Virginia Diodes, Charlottesville, VA USA and Neal Erickson of UMASS USA. Harmonic mixer design was assisted by previous papers of HP/Agilent [5].

I would also like to acknowledge the craftsmanship of Achim Walber, Jan Oelrichs, Marko Schwarze and Ralf Henneberger, the fine-mechanic team at RPG lead by Marc Warnke and the wealth of experience of Ralph Zimmerman.

REFERENCES

- [1] Synview GmbH, Glaskopfweg 17, 61479 Glashütten, Germany, Available at : <http://www.synview.com/>
- [2] ESA-Eumetsat Post-EPS satellite Available: <http://www.eumetsat.int>
- [3] MARSCHALS Upper-Troposphere Limb sounder Available at: www.ssttd.rl.ac.uk/mmt/documentsfordownload/MARSCHALS.pdf
- [4] Erickson, N. “Very Low Loss Wideband Isolators for mm-Wavelengths” 2001 IEEE MTT-S Digest p. 1175-1178
- [5] R.J. Matreci, F.K. David Signal Analysis Division, Hewlett-Packard. “Unbiased, Sub-Harmonic Mixers for Millimeter wave spectrum analysers” IEEE MTT-S Digest 1983 p 130 - 132
- [6] Kenji Itoh, Mitsuhiro Shimozawa, “Fundamental Limitations of Conversion Loss and Output Power on an Even Harmonic Mixer with Junction Capacitance” IEEE MTT-S Digest 2001 p.1333 – 1336 Available: http://www.radiometer-physics.de/rpg/pdfs/SAM-Overview_all_mixers.pdf
- [7] Available: http://www.radiometer-physics.de/rpg/pdfs/SAM-Overview_all_mixers.pdf

Session S8:

Earth Observations

Performance of JEM/SMILES in orbit

Satoshi Ochiai^{*}, Kenichi Kikuchi[†], Toshiyuki Nishibori[†], Takeshi Manabe[‡],
Hiroyuki Ozeki[§], Kazuo Mizukoshi[†], Fumiaki Ohtsubo[¶], Kazuyoshi Tsubosaka[†],
Yoshihisa Irimajiri^{*}, Ryota Sato[†], and Masato Shiotani^{||}

^{*}National Institute of Information and Communications Technology, Tokyo, Japan, Email: ochiai@nict.go.jp

[†]Japan Aerospace Exploration Agency, Ibaraki, Japan

[‡]Osaka Prefecture University, Osaka, Japan

[§]Toho University, Chiba, Japan

[¶]Advanced Engineering Services Co. Ltd., Tsukuba, Japan

^{||}Kyoto University, Kyoto, Japan

Abstract—Superconducting Submillimeter-Wave Limb-Emission Sounder (SMILES) has successfully started in-orbit operation. The results of the ground tests and in-orbit performance measurements are described and compared in this paper. We found that the in-orbit performance is fully satisfy the specifications and SMILES data has sufficient quality for atmospheric science study. The system noise temperature in orbit is consistent with that measured in the ground test if the result of the ground test is modified correctly. The measured system noise temperature measurement is also influenced by the receiver gain nonlinearity. There is still a room for improvements, for example nonlinearity correction, in Level 1B processing of SMILES,

I. INTRODUCTION

Superconducting Submillimeter-Wave Limb-Emission Sounder (SMILES), which was jointly developed by National Institute of Information and Communications Technology (NICT) and Japan Aerospace Exploration Agency (JAXA), was launched in September 2009 and successfully started observations of the Earth's atmosphere. The original proposal for SMILES mission was made by the former organizations of NICT and JAXA, that is Communications Research Laboratory (CRL) and National Space Development Agency (NASDA) respectively, and accepted by NASDA in 1997 [1]. Since the late 1990s we have developed SMILES payload whose main part is 640-GHz band superconducting receivers with a space-qualified 4-K mechanical refrigerator to cool SIS mixers. Although the launch date of SMILES to the International Space Station (ISS) was significantly delayed from the expected date in early stage of development, the revised schedule after the critical design review of SMILES in 2006 was kept without large delay. We did not have any critical problem in the integration of the flight model, the ground tests, the launch and the installation on the ISS. Soon after SMILES was attached to the Exposed Facility (EF) of Japanese Experiment Module (JEM or Kibo), the SMILES 4-K cooler was turned on and is continuously running up to now without any serious problem. The receivers are also stable. SMILES shows satisfactory performance in orbit and continues to produce excellent observation data of atmosphere just as we had designed. The objectives of the SMILES mission are an engineering demonstration of the submillimeter

limb-emission sounding with the superconducting technology in space, and scientific observation of the spatial and temporal distributions of global atmospheric properties in stratosphere [2].

By applying very low noise receiver performance to Earth's limb-emission sounding, it becomes possible to study detailed stratospheric chemistry and other atmospheric science more precisely than before. Many stratospheric radicals and molecules can be observed by SMILES. Chlorine monoxide, ClO, is one of the important components in halogen chemistry of stratosphere. The MLS [3] and Odin/SMR [4] have long records of ClO observations. SMILES will add the more detailed observations including mid-latitude or background low-level concentrations, and diurnal variations. SMILES will also provide the observations of chlorine related species such as HCl and HOCl. Bromine monoxide, BrO, is another important halogen radical in the stratosphere. Global observation of stratospheric BrO is, however, very limited in the past. The submillimeter observation of BrO is not necessarily easy. The limb-emission intensity from BrO is far weaker than that from ClO, and is in the order magnitude of 0.1 K, that is less than the SMILES instantaneous sensitivity of 0.3 K. Nevertheless, some early studies on the retrieval from the SMILES data show that the height profiles of BrO can reasonably be retrieved. There are many emission lines of radicals and molecules in the atmosphere in the SMILES band. In addition to the halogen species, observations of those constituents, such as O₃, O₃ isotopes, HO₂, HNO₃, CH₃CN, are expected to contribute to the atmospheric science.

In this paper we describe an overview of the SMILES instrument with the results of ground tests carried out before launch. in-orbit performance is compared with the ground test results in section IV. example of the observed spectra are shown in section V. In this section, pointing issue of the SMILES antenna related to the attitude of SMILES is also discussed. In section VI the SMILES products, Level 1 product in particular, are introduced.

II. OVERVIEW OF SMILES

The Kibo module (JEM), that is a Japan's contribution to the International Space Station (ISS), was constructed on the



Fig. 1. Japanese Experiment Module (JEM) in the International Space Station (ISS). The right half of the photo is the Exposed Facility (EF). The ISS flies downward of the photo. The second from the left in three payloads attached on the front side of the EF is SMILES. (photo courtesy of NASA)



Fig. 2. SMILES (right) on the EF Pallet. The pallet was launched via H-II Transfer Vehicle (HTV) and carries to the EF. The left of SMILES is US HREP. The photo was taken in May 2009.

ISS in 2008 and 2009. The Exposed Facility (EF), which is a part of JEM, has an ability to accommodate 9 payloads for the experiments utilizing exposed environment and for observations of the Earth or the space. Currently 4 experiment payloads are being operated in the EF. SMILES is one of the EF payloads (Fig. 1). The orbit of the ISS is almost circular with an inclination of 51.6° to the Equator, and is non-sun-synchronous with a precession of one circle per about 71 days or one rotation per 2 months against the sun. The altitude of the ISS is 330 to 380 km above the surface.

The SMILES payload has a size of $0.8 \text{ m(W)} \times 1.0 \text{ m(H)} \times 1.8 \text{ m(D)}$ (Fig. 2), weighs approximately 480 kg, and consumes an electric power of 320 to 600 W. Heat to be wasted from SMILES is not radiated but removed by a fluid coolant, Fluorinert, supplied by JEM.

The SMILES mission instrument consists of an antenna, an antenna feed system, two SIS receivers for 624.25 – 626.39 GHz and 649.03 – 650.37 GHz, IF amplifier chains,

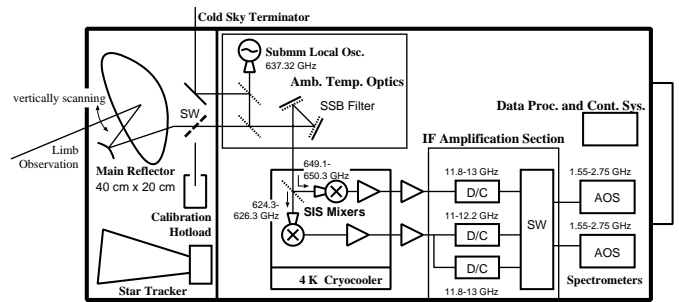


Fig. 3. Block diagram of SMILES

two acousto-optical spectrometers, and other components such as the attitude detection system. In addition to the mission instrument, the SMILES system includes a data processing and control system, an electric system, a thermal control system, and interfaces to JEM. Fig. 3 shows block diagram of SMILES.

An offset Cassegrain antenna with an elliptical aperture of $400 \text{ mm} \times 200 \text{ mm}$ is employed to resolve the tangent atmosphere with a vertical resolution of about 3 km. The antenna is mechanically scanned by a stepping actuator in the direction of elevation. The scanning is started at the elevation angle where the equivalent geometric tangent height of the line-of-sight is about -10 km, and moved upward in an angular rate of 0.1125 deg/s for 30 s. At the end of each 30-s scanning the antenna is pointed at the tangent height of 100 km typically. Then antenna is quickly moved to the tangent height of about 200 km in 2.5 s for the purpose of cold calibration. In addition, frequency calibration, hot calibration, and antenna rewinding are sequenced in a scan cycle. The total antenna scan cycle completes in 53 s. The hot-load calibration system consists of the calibration hot load (CHL) and a mechanical switch mirror between the tertiary and the fourth mirrors in the antenna feed system. The CHL, which is a three dimensional Eccosorb CR-110 based absorber and specially prepared for SMILES, shows a return loss far less than -60dB. The details of the antenna feed system, which consists of an antenna beam transmission system (TRN), an ambient temperature optics (AOPT), and a cryogenic optics, are described elsewhere [5][6].

The SMILES SIS mixer employs PCTJ-type Nb/AlOx/Nb junctions in a waveguide-mount following a corrugated horn [7]. SMILES has a single submillimeter local oscillator at 637.32 GHz. The two sidebands of the atmospheric signal are separated in the quasi-optics circuit using a pair of frequency-selective polarizers (FSPs) [8], and are fed to two SIS mixers respectively. The SIS mixers are cooled down to 4.3 K by a Helium JT-cycle cooler precooled by a two-stage Stirling-cycle cooler. HEMT amplifiers operating in a frequency band of 11 to 13 GHz are installed on both stages of the Stirling cooler. The temperatures of those two stages are about 16 K and 75 K, The cooling capacity of the JT cooler is 20 mW at 4.5 K. The cooling system consumes an electric power of 120 to 304 W, which is supplied with 120 V DC by JEM. The weight is about 82 kg (cryostat 24 kg, compressors and circuits 33 kg, electronics 25 kg). Designed lifetime of the

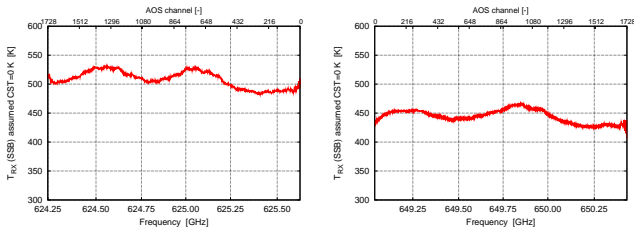


Fig. 4. Ground measured SSB system noise temperature of the SMILES receivers. The system noise temperature is converted into one with an image termination (Cold Sky Terminator (CST) in Fig. 3) of almost 0 K, while the corrections of the atmospheric attenuation and the receiver gain compression are not applied.

cooler is one year.

The SMILES backend is two acousto-optical spectrometers (AOSs). Each AOS has a bandwidth of about 1.3 GHz. The frequency resolution is typically 1.4 MHz. The CCD images of 1728 pixels are integrated every 0.5 s. The SMILES mission data file (or Level 0), which is processed every 53 s by the data processing and controlling section of SMILES, contains two AOS data for 46-s measurements (the data during rewinding the antenna are discarded). The size of the mission data file is 659 kB, so that the averaged data transfer rate from SMILES is about 100 kbps.

The SMILES was launched aboard the HTV Demonstration Flight via the Test Flight of the H-IIB launch vehicle on 11th September 2009. After the HTV arrived on the ISS, SMILES was attached to the EF of JEM on 25th September 2009 (JST). The atmospheric observation in a normal operation sequence started in the middle of October 2009.

III. MAJOR RESULTS OF GROUND TESTS

The performance of the SMILES flight model was measured in the ground tests. The ground tests include measurements of the antenna beam pattern, the receiver noise temperature, the receiver stability, the sideband separation ratio, the gain linearity, and the frequency response of the spectrometers.

The results of the antenna beam pattern measurements by a near-field phase retrieval method show that the 3-dB beamwidths of the far-field pattern of the SMILES antenna are estimated to be 0.893° and 0.173° in elevation and azimuth respectively, and no remarkable unwanted sidelobe peaks are observed [5].

The system noise temperature of the SMILES receiver was measured using an ambient temperature absorber and a large liquid-nitrogen bath in front of the main reflector and another ambient and liquid-nitrogen temperature absorbers in the beam from the Cold-Sky Terminator (CST). The measured system noise temperature is translated into the estimated system noise temperature assuming the incoming emission from the CST to be 2.7 K. The result is shown in Fig. 4. The corrections of the atmospheric attenuation and the receiver gain compression are not applied in the result of Fig. 4. The system noise temperature is found to satisfy the initially targeted value of 500 K.

The receiver stability was measured during the thermal-vacuum tests of the SMILES system. Because the calibration

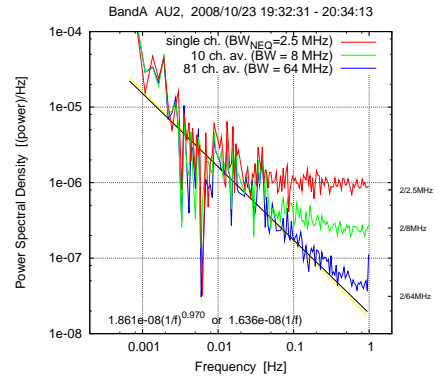


Fig. 5. Ground measured power spectrum density (PSD) of the SMILES output, of single channel (red), which has a noise equivalent bandwidth of about 2.5 MHz, of the average of 10 channels (green), which has a bandwidth of about 8 MHz, and of the average of 81 channels (blue), 64 MHz. The PSD was measured during thermal-vacuum tests of the SMILES system.

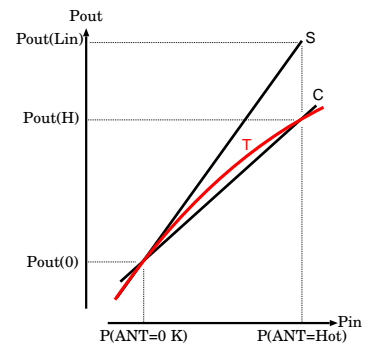


Fig. 6. Definition of the nonlinearity. Curve T (red line) is a measured input-output relationship of the receiver. Line C shows slope of the hot-cold calibration. Line S shows is the tangent of Curve T at infinitesimal input. nonlinearity is the difference of slopes between S and C.

cycle of SMILES is 53 s the stability about the time scale of less than 1 min is important. The power spectrum density (PSD) of the SMILES AOS output was measured during the low-temperature soak test of the thermal-vacuum tests of the SMILES system. An example of the results is shown in Fig. 5. The result shows that the receiver output fluctuation in the shorter time interval than about 15 s is consistent with the radiometric noise of a noise-equivalent bandwidth of 2.5 MHz, and that the random drift (1/f noise) in the longer time interval than about 15 s exceeds the radiometric noise. In Fig. 5 the PSDs for the signals of wider bandwidths are also shown. With the rather slow data sampling interval of 0.5 s, which was restricted by available data transmission rate for EF payloads, the noise in continuum emission level cannot be reduced by expanding the bandwidth beyond the noise level at a bandwidth of 100 MHz.

The sideband separation ratio was measured in the tests of ambient temperature optics (AOPT) and submillimeter receiver assembly. The rejection ratio of image band is confirmed to be less than -20dB.

The gain linearity of the receiver system was measured with

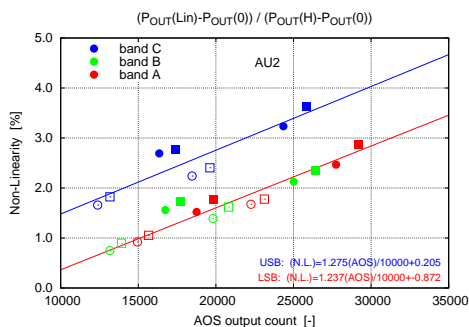


Fig. 7. Measured nonlinearity, nonlinearity is a function of the input signal level. Band A and Band B are lower sideband of submillimeter SIS mixer, and share the same chain of amplifiers. Band C is upper sideband.

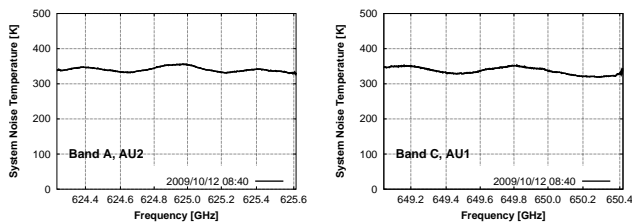


Fig. 8. SSB system noise temperature of the SMILES receivers in orbit. The examples of the system noise temperature shown in this figure were measured on 12th October 2009, when the 4-K stage temperature was at about 4.33 K.

the fully assembled SMILES flight model. The perturbation method using a quasi-optical network described in [9] is applied to measure the linearity. A quasi-optical network is prepared on the beam from CST. The linearity measured with our setup is that of the image band signal. We believe there is no large difference between linearity responses in USB and LSB in our mixer. nonlinearity is defined as the difference of slopes between line S and line C in Fig. 6. The measured nonlinearity is shown in Fig. 7. The figure shows that the nonlinearity is a linear function of the output signal level. This suggests the nonlinearity of the receiver can be corrected in the data processing chain properly.

IV. INSTRUMENTAL PERFORMANCE IN ORBIT

The initial checkout phase lasted for 6 weeks. We found there was no serious problem on the SMILES hardware in orbit. Each component was confirmed that it satisfied the specifications during the former half of the initial checkout. In the latter half SMILES has almost been shifted into the normal observation mode. In this section we discuss the system noise temperature, the gain stability, and the gain linearity of in-orbit SMILES, and comparisons between the ground tests and in-orbit measurements of those performances.

The system noise temperature of the SMILES receivers is being measured every 53 s in the normal calibration sequence. An example of the system noise temperature is shown in Fig. 8. The system noise temperature has varied up and down with an amplitude of about 10%_{p-p} in 6 months since October 2009. The system noise temperature is strongly depends on the temperature of the 4-K stage, that is the temperature of the SIS mixer. Fig. 9 shows the relationship between the system

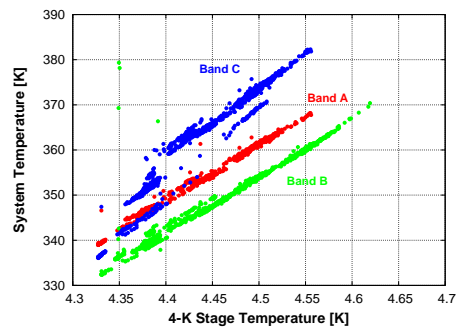


Fig. 9. Relationship between the system noise temperature and the temperature of the 4-K stage. The system noise temperature of Band A and Band B are well correlated to the 4-K stage temperature.

noise temperature and the temperature of the 4-K stage. The system noise temperature of Band A and Band B are well correlated to the 4-K stage temperature with an approximate slope of 125 K/K. The relationship between the system noise temperature of Band C and the 4-K stage temperature are not aligned on a single line. Three different states can be seen in the plots of Band C in Fig. 9. In each state the relationship can be expressed by a line with a slope of 150 K/K. Operational parameters have ever been changed twice which correspond to those differences between groups. One of them is change of the AOS heater control from on to off. This disabling of the heater caused the gain increment of the amplifier in the AOS. It is possible that the apparent system noise temperature was increased by a deterioration in the nonlinearity due to the gain increment. Another change was the operation voltage of the Stirling compressor. The change of the relation between the 4-K stage temperature and Stirling stages temperatures (16 K and 75 K) affects the system noise temperature. The same changes are also observed in the system temperature of Band A and Band B. These bands, however, suffered relatively small effects because the nonlinearity are relatively small as is compared with Band C as shown in Fig. 7.

Fig. 8 can be compared with Fig. 4. The in-orbit system noise temperatures are found to be less than those measured in the ground measurements shown in Fig. 4 by 100 –170 K and 100 –110 K for Band A and Band C, respectively. The main reason of these difference is the atmospheric attenuation of submillimeter waves in the ground measurements of the system noise temperature. The results shown in Fig. 5 are not corrected for the atmospheric attenuation. By taking the atmospheric attenuation into account, the ground system noise temperature should be reduced by 120 K and 50 K in Band A and Band C, respectively. The wing of the water vapor line at 620 GHz makes the attenuation in Band A much larger than in Band C. The second reason of the difference is the nonlinearity. While the cold temperature for the Y-factor measurement is almost 0 K in in-orbit, the liquid nitrogen was used as a cold load in the ground measurement. This makes signal the signal level different so that the system noise temperatures in the ground and in-orbit may, we estimate, differ by 4 – 31 K. The third reason is the 4-K stage temperature. Due to the difference of the 4-K stage temperature between the

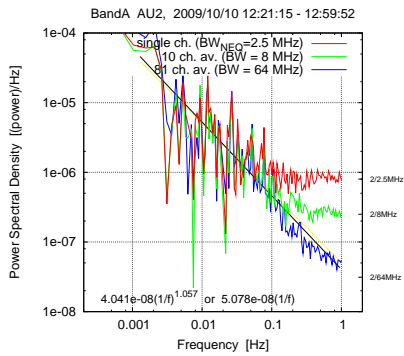


Fig. 10. Power spectrum density (PSD) of the SMILES output in orbit. The colored lines mean the same with Fig. 5. The stability was measured in orbit during SMILES sees the cold space without atmospheric observation.

two measurements the system noise temperature in the in-orbit measurement should be 4 K higher than the ground measurement. There may be other unknown effects such as the reflection on the surface of the liquid nitrogen. From those reasons the system noise temperatures measured on the ground and in orbit are almost consistent.

The gain stability was measured in orbit as it was measured in the thermal vacuum tests on the ground. The results is shown in Fig. 10. In the measurement of Fig. 10 SMILES sees the space while in the measurements of Fig. 5 both of the main beam and the CST beam see the ambient temperature terminations. It must be cautioned that the stability shown in Fig. 5 is the sum of DSB receiver and the emissions from the two ambient temperature black bodies. Because the emission from the black body is very stable, the drift noise ($1/f$ part) in Fig. 5 should be multiplied by 4 or 5 when comparing with the in-orbit measurements. Considering this correction the stability is not changed before and after the launch.

The gain linearity itself cannot be measured in orbit. The system noise temperature consistency described previously gives us some suggestion for estimating the gain linearity in orbit. The gain linearity is not currently corrected in the SMILES data processing. The correction will be applied in the next version of the SMILES Level 1 data.

V. OBSERVED ATMOSPHERIC SPECTRA

SMILES is continuously operated since the middle of October as long as the operation is allowed. Nominally SMILES scans the atmosphere every 53 s and makes about 1600 vertical scans per day. Fig. 11 shows an example of observed spectra. Because SMILES has two AOS units, only two bands are observed in one scan. The remarkable thing of the SMILES spectra is not only that the random error is sufficiently low but that we never observe any ripples or undulations larger than the noise level in the spectra. When the spectra are integrated, a gentle undulation of less than 0.5 K will be found in the frames in the beginning of the scan. Because the calibration frames are located in the end of the scan, the effect of small

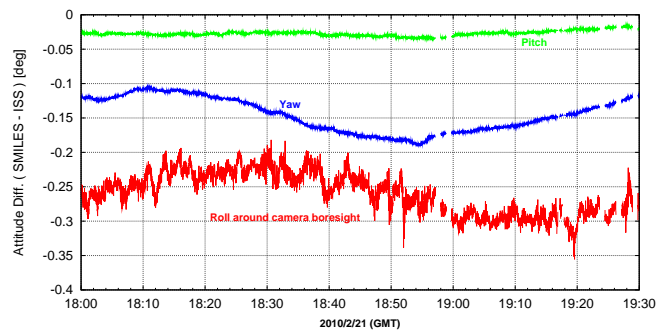


Fig. 12. Difference of the SMILES attitude measured by SMILES star tracker against the ISS attitude. The span of the figure is 90 min., in which the ISS circles the Earth.

gain instability accompanied gain nonlinearity would appear in those frames. This small undulation is enough lower than the specification.

To retrieve the height profiles of atmospheric compositions the tangent height knowledge of the observed spectra is essentially important. The tangent heights imposed in Fig. 11 are approximations. The random error of the tangent height knowledge should be less than 350 m, ie. 0.01 deg. in the elevation angle. The attitude of SMILES is measured by a star tracker. One of three axes of the star tracker output has poor precision comparing with other axes. Because the direction of the star tracker bore sight was not optimized we must use partly the poor axis to derive the tangent height from the attitude. Fig. 12 shows an example of the difference of the SMILES attitude measured by SMILES star tracker against the ISS attitude. The roll attitude is poorer than others. From other axes we know SMILES, or probably JEM, vibrates slowly against the ISS. The JEM vibration is synchronized with the orbital motion and irregularly perturbed with a small amplitude. The smoothing of the roll axis attitude is necessary to get a better tangent height knowledge.

VI. SMILES PRODUCTS

The observed data at about 1600 locations of 2 AOS bands are processed every day. SMILES products include Level 1B, Level 2, and Level 3 data. Level 2 data and partially Level 1B data are now internally distributed to the researchers whose theme was adopted by JAXA as a proposal to the SMILES research announcement. Level 3 is in preparation. Those data is scheduled to be open to the public from one year after the launch.

Level 1B data is the calibrated limb emission spectra with ancillary data, such as frequencies, system noise temperature, locations of tangent points, time. Level 2 data is the retrieved height profiles of radicals and molecules at each observed location [10]. The nonlinearity correction and the attitude correction discussed in this paper will be reflected in the future version of Level 1B.

VII. CONCLUSIONS

SMILES works very healthy since the launch and installation on the ISS in September 2009. SMILES produces steadily

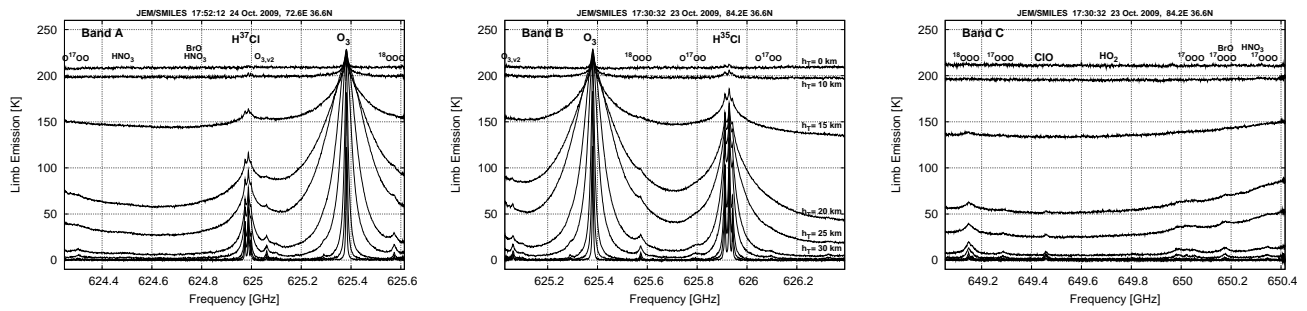


Fig. 11. Examples of observed spectra by SMILES. SMILES integrates the atmospheric emission for 0.5 s. Each line in this figures shows the spectra of 0.5 s observation. One spectral band has 1728 frequency channels.

atmospheric limb-emission observation spectra which are with sufficiently low noise and almost free from standing waves. The system noise temperature and the gain stability of the SMILES receiver show consistent results between in-orbit and the pre-launch tests. Although the effect of the receiver gain nonlinearity is rather complicated under several operational conditions, we are preparing to make a correction in the future Level 1B products as well as a correction in the star tracker attitude data. Quality of SMILES data almost meets the specification, and is being improved furthermore.

ACKNOWLEDGMENT

The authors would like to thank J. Inatani (National Astronomical Observatory of Japan), H. Masuko (NICT), M. Seta (Tsukuba Univ.) for their contributions to this mission in earlier stage.

REFERENCES

- [1] H. Masuko, S. Ochiai, Y. Irimajiri, J. Inatani, T. Noguchi, Y. Iida, N. Ikeda, and N. Tanioka, "A Superconducting Sub-millimeter Wave Limb Emission Sounder (SMILES) on the Japanese Experimental Module (JEM) of the Space Station for Observing Trace Gases in the Middle Atmosphere," *8th Int'l Symp. Space Terahertz Technol.*, (Cambridge, MA), Mar. 1997.
- [2] SMILES Science Team and SMILES Mission Team, *JEM/SMILES Mission Plan, Ver. 2.1*, NASDA and CRL, Nov. 2002. available at http://smiles.nict.go.jp/Mission_Plan/.
- [3] <http://mls.jpl.nasa.gov/>, and references in the pages.
- [4] J. Urban, N. Lautié, E. Le Flochmoën, C. Jiménez, P. Eriksson, J. de La Noë, E. Dupuy, M. Ekström, L. El Amraoui, U. Frisk, D. Murtagh, M. Olberg, and P. Ricaud, "Odin/SMR limb observations of stratospheric trace gases: Level 2 processing of ClO, N₂O, HNO₃, and O₃," *J. Geophys. Res.*, 110(D14), D14307, 2005.
- [5] T. Manabe, T. Nishibori, K. Mizukoshi, F. Ohtsubo, and S. Ochiai, "Measurements of the Offset-Cassegrain Antenna of JEM/SMILES Using a Near-Field Phase-Retrieval Method in the 640 GHz Band," *21st Int'l Symp. Space Terahertz Technol.*, (Oxford, UK), Mar. 2010.
- [6] T. Manabe, T. Fukami, T. Nishibori, K. Mizukoshi, and S. Ochiai, "Measurement and Evaluation of Submillimeter-Wave Antenna Quasioptical Feed System by a Phase-Retrieval Method in the 640-GHz Band," *IEICE Trans. Commun.*, vol. E91-B, no. 6, pp. 1760-1766, June, 2008.
- [7] K. Kikuchi, Y. Fujii, W.L. Shan, and J. Inatani, "Repeatability and Reliability of the 640 GHz SIS Mixer for JEM/SMILES," *14th Int'l Symp. Space Terahertz Technol.*, (Tucson, Az), Apr. 2003.
- [8] T. Manabe, J. Inatani, A. Murk, R. Wylde, M. Seta, and D.H. Martin, "A New Configuration of Polarization-Rotating Dual-Beam Interferometer for Space Use," *IEEE Trans. Microwave Theory and Techniques*, 51(6), 1696-1704, 2003.
- [9] A. Murk, K. Kikuchi, and J. Inatani, "Linearity Measurements of the 640 GHz SIS Mixer for JEM/SMILES," *16th Int'l Symp. Space Terahertz Technol.*, (Goeteborg, Sweden), May 2005.
- [10] C. Takahashi, S. Ochiai, and M. Suzuki, "Operational retrieval algorithms for JEM/SMILES Level 2 Data Processing System," *J. of Quantitative Spectroscopy & Radiative Transfer*, 111, 160-173, 2010.

ISMAR: Towards a Sub Millimetre-Wave Airborne Demonstrator for the Observation of Precipitation and Ice Clouds

Brian Moyna^{*}, Clare Lee[†], Janet Charlton[§], Ian Rule[†], Robert King[†], Matthew Oldfield^{*} and Ville Kangas[‡].

^{*}Space Science & Technology Department
Rutherford Appleton laboratory
Email: brian.moyna@stfc.ac.uk

[†]The Met Office
Email: clare.lee@metoffice.gov.uk

[§]Sula Systems Ltd.
Email: jcharlton@sula.co.uk

[‡]European Space Agency
Email: ville.kangas@esa.int

Abstract

A strong interest is emerging for satellite observations of clouds and rain at millimetre and sub-millimetre wavelengths. The motivations are twofold: Firstly, there is a lack of information on the characteristics of ice clouds. On average, approximately 20% of the globe is covered by high clouds, with substantial impact on the global radiative budget depending on the optical properties of the ice particles. No existing satellite instrument is capable of observing the large variety of ice cloud properties. The visible and thermal domains are essentially sensitive to the thin cirrus (particles with sizes below $\sim 50\mu\text{m}$ diameter) whereas the available microwave measurements below 190 GHz are limited to the observations of large ice particles (larger than $\sim 200\mu\text{m}$) present in deep convective clouds. Millimetre and sub-millimetre observations could fill the gap and provide information on the intermediate ice cloud types and crystal habits. Secondly, there is a need for observations for now-casting of extreme weather events. Microwave measurements show a more direct relation with precipitation than visible and infrared observations. However, so far passive microwave instruments are only available on low orbit satellites and the temporal sampling of the same area is limited, even in the case of a satellite constellation (with eight over-flights per day in the case of the Global Precipitation Measurement from a constellation of satellites). Geostationary satellites offer the possibility of quasi-continuous coverage of large portions of the Earth. The main difficulty is to obtain adequate spatial resolutions from a geostationary orbit, with an antenna of a reasonable size. One solution is thus to observe at higher frequencies than currently measured today from operational satellites i.e. the sub-millimetre wave range.

Two projects have been submitted to ESA in recent years as Next Earth Explorer core missions: (a) The Cloud Ice Water Sub-millimeter Imaging Radiometer (CIWSIR), which is dedicated to the observations and characterization of ice clouds from a polar orbit, focusing on climate studies and (b) The Geostationary Observatory for Microwave Atmospheric Sounding (GOMAS), the key objective of which is the estimation of precipitation with a high temporal sampling, for now-casting. Although neither of these missions has yet been selected, several technical and scientific preparatory activities are underway in Europe to allow these mission concepts to mature.

This paper reports on one of these preparatory activities; the design of a sub-millimetre wave airborne demonstrator for both ice cloud and precipitation observations which will be able to prove the feasibility of the scientific principles of both the CIWSIR and GOMAS missions. The paper will describe a demonstrator design based upon the new Met Office International Sub Millimetre-wave Airborne Radiometer (ISMAR) which is now under development with a first test flight scheduled for November 2010.

Laboratory and Ground Testing Results from ATOMMS: the Active Temperature, Ozone and Moisture Microwave Spectrometer

E. Robert Kursinski¹, Abram Young¹, Angel Otarola¹, Michael Stovern¹, Brian Wheelwright¹, Dale Ward¹, Kate Sammler¹, Robert Stickney¹, Christopher Groppi*², Sarmad Al Banna¹, Michael Schein¹, Steve Bell¹, Willy Bertiger³, Mark Miller³, Herb Pickett³

¹University of Arizona, Tucson, AZ 85721 USA

²School of Earth and Space Exploration, Arizona State University, Tempe, AZ 85287 USA³NASA Jet Propulsion Laboratory, Pasadena, CA 91109

*Contact: cgroppi@asu.edu, +01-480-965-6436

Abstract— ATOMMS represents a new class of active, airborne, limb-viewing spectrometer that is a cross between Global Positioning System (GPS) occultations and NASA's Microwave Limb Sounder. ATOMMS will characterize atmospheric water vapour and ozone by actively probing the absorption lines at 22.2 GHz, 183.3 GHz and 195 GHz, respectively. Two instrument packages are being constructed for NASA's WB-57F high altitude research aircraft, now equipped with precise WAVES gimballed pointing systems. One aircraft will generate multiple tones near the 22 GHz water line and 183 GHz to 204 GHz absorption lines and transmit them across the Earth's limb through the atmosphere to receivers on a second aircraft. Flight paths of the two aircraft begin over the horizon, with the two aircraft flying at 65 kft altitude. This creates a rising occultation geometry as the aircrafts fly towards each other. ATOMMS provides the sensitivity, vertical spatial resolution and accuracy needed to satisfy key monitoring needs for temperature, pressure, moisture and ozone. The 100 to 200 m ATOMMS vertical resolution will far surpass the 1 to 4 km vertical resolution of present state-of-the-art satellite radiometers opening a window into atmospheric scales previously inaccessible from space. Predicted precisions of individual ATOMMS temperature, pressure and moisture profiles are unprecedented at ~0.4 K, 0.1% and 1-3% respectively, extending from near the surface to the flight altitude of ~20 km. ATOMMS ozone profiles precise to 1-3% will extend from the upper troposphere well into the mesosphere. Other trace constituents such as water isotopes can be measured with performance similar to that of ozone. The ATOMMS experiment is a pathfinder experiment for eventual implementation on a constellation of satellites. Space observations from multiple satellites in precessing orbits will allow for global spatial coverage and increased altitude coverage. Our long term goal is a constellation of approximately a dozen small spacecraft making ATOMMS measurements that will provide dense, global coverage and complete cloud-penetration and diurnal sampling every orbit.

The ATOMMS instruments have been completed and are now undergoing extensive laboratory and ground testing. We report on the laboratory testing results including the differential amplitude and phase stability of the instrument and systems integration testing. We will also report on ground testing experiments, where the ATOMMS instruments, located on two building tops, were used to measure atmospheric water vapour

content. Comparison measurements were made using in-situ hygrometers. Further ground-based tests are planned to exercise the full ATOMMS system, including the GPS-based positioning and time correction system, accelerometer system and dual-one-way phase correction system. We will also discuss planned instrument upgrades to be implemented in preparation for air-to-ground and air-to-air flights on the WB-57F aircraft.

INTRODUCTION

For more than ten years, our group has been developing an atmospheric remote sensing system called the Active Temperature, Ozone and Moisture Microwave Spectrometer (ATOMMS). ATOMMS combines the best features of the GPS radio occultation (RO) [1], [2] and the Microwave Limb Sounder (MLS) [3] techniques by actively probing via radio occultation the 22 GHz and 183 GHz water vapour lines; the latter observe via passive emission by the MLS, and the Ozone emission line near 195 GHz. Our analysis shows that ATOMMS will profile tropospheric and middle atmosphere water vapour and middle atmosphere ozone to 1-5%, temperature to 0.5K, and geopotential heights to 10-20 m, all with ~200 m vertical resolution, in both clear and cloudy air. This unprecedented performance will improve significantly with averaging. Because the occultation signal source is observed immediately before or after each occultation, ATOMMS is self-calibrating, which eliminates long-term drift. These capabilities will fulfil crucial needs for climate change monitoring, research and policymaking.

ATOMMS OVERVIEW

ATOMMS limb-viewing occultation system, promising unprecedented performance, will likely become a key observing system in the Global Climate Observing System (GCOS). We have nearly completed a pair of ATOMMS instrument for the WB-57F high altitude aircraft to aircraft demonstration of its performance.

The ATOMMS instrumental configuration is depicted in Fig. 1. The ATOMMS system consists of 5 elements:

1. The ATOMMS microwave instruments with 13 GHz, 22 GHz and 183 GHz transmitters and receivers,
2. ATOMMS precise positioning system which is a combination of hardware consisting of a GPS receiver and a 3 axis precision accelerometer on each aircraft combined with precise positioning system software from JPL,
3. The two WB57F aircraft,
4. The WAVE gimbal built by SRI for NASA that points the ATOMMS microwave instrument and
5. The ATOMMS retrieval software system under development at the University of Arizona.

During an occultation, each ATOMMS microwave transmitter radiates several monochromatic signal tones that pass through the atmosphere to the receiver on the opposite side of the atmosphere which digitizes and records the signals. We have designed the ATOMMS transmitters and receivers to simultaneously sample water vapor at both the 22 and 183 GHz lines to create the dynamic range needed to profile water vapor from the surface into the mesosphere as well as measure ozone at 195 GHz in the upper troposphere and middle atmosphere. The ATOMMS signal processing system later derives the phase and amplitude of the signals and combines them with the precise knowledge of the transmitter and receiver positions (from the ATOMMS precise positioning subsystem) and physical constraints such as the hydrostatic equation to derive profiles of atmospheric moisture, ozone, temperature and pressure.

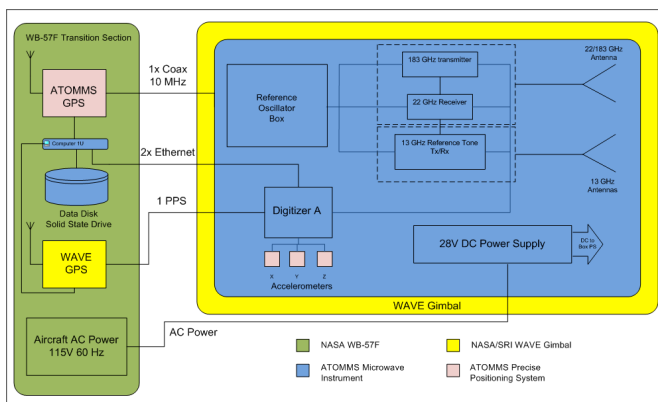


Figure 1: Block diagram of the ATOMMS A aircraft. With the exception of the 22 & 183 GHz transmitter and receiver pairs, ATOMMS B is identical.

Accuracy and Vertical Resolution of Temperature and Water Vapour Profiles

ATOMMS unique observations & parameter retrievals are very well suited for monitoring climate change and will provide a new window into the atmosphere strongly constraining thermodynamic & dynamic processes needed to assess and improve the realism of climate models. The unprecedented combination of performance includes

- High *precision* profiles of temperature to 0.4 K, water vapor to 1-10% and geopotential height to ~10-20 m extending through the free troposphere to the mesopause and ozone to 1-10% through the middle atmosphere, whose *accuracy* should be

better by an order of magnitude or more when many profiles are averaged.

- ~200 m vertical resolution, as demonstrated by GPS occultation missions, that exceeds the vertical resolution of passive systems (e.g., AIRS, IASI, AMSU and MLS) by approximately an order of magnitude or more,
- Self calibration because ATOMMS measures differential absorption and the signal sources are measured immediately before or after each occultation which eliminates drift and should provide absolute accuracy,
- Retrievals in both clear and cloudy conditions with performance in clouds expected to be within a factor of 2 of clear sky performance, thus eliminating clear sky biases that plague other remote sensing systems.
- Full sampling of the diurnal cycle every orbit with a satellite constellation like the COSMIC GPS RO mission,
- Refinement of the spectroscopy from orbit [4],
- ATOMMS ability to estimate the climate state independent of atmospheric models, an achievement that is simply not possible with passive radiometric sensors (e.g. [5]), and yet is fundamental to both determining the true climate state and quantifying climate and weather model performance and realism.

A more complete description of ATOMMS and its improvements on the state of the art can be found in [6].

ATOMMS provides the combined vertical resolution and precision critical to resolving the 1.5 km scale height of water vapor and fundamental vertical structure such as ubiquitous layering in the troposphere with vertical scales of a few hundred meters [7]. Only RO can globally determine temperature and lapse rates at the sharp vertical scales at which they vary and can do so in both clear and cloudy conditions. While accurate GPS-RO temperatures are limited to the upper troposphere (by moisture) through the mid-stratosphere (by the ionosphere), ATOMMS will accurately determine temperature and vertical stability from the free troposphere through the mesosphere. Another key point is that GPS-RO measures temperature *or* water vapor, not both. GPS-RO has shown some of the potential for RO observations to measure water vapor in the warmer regions of the lower and middle troposphere with accuracies of 0.2 – 0.5 g/kg [8]. ATOMMS will extend this dynamic range by orders of magnitude to precisely profile water vapor over mixing ratios ranging from several percent in the lower troposphere to a few ppm at the mesopause while simultaneously profiling temperature to sub-Kelvin precision over the same altitude interval. With averaging, we anticipate the absolute accuracies will be better by an order of magnitude or more (depending on spectroscopy which we will refine with ATOMMS).

Upper Troposphere / Lower Stratosphere Retrievals

ATOMMS offers a means to significantly improve our ability to globally measure temperature, water vapor and

ozone behavior in the climatically critical upper troposphere and lower stratosphere (UTLS). Despite the crucial roles this region plays in determining how our climate will change in the future, its behavior has been and continues to be poorly observed, particularly on a global scale. To place ATOMMS in context, a basic conundrum for understanding and predicting climate change has been that our ability to measure water vapor and temperature in the upper troposphere (UT) under all sky conditions has been close to nil. The existing observational techniques all have very different types of uncertainties, errors and resolutions. When comparisons have been made, they have not agreed very well. This region is critical for climate because changes in temperature as well as changes in the water and ozone concentrations here will produce large changes in the outgoing long wave radiation that cools the Earth. UT temperature changes are also indicative of how realistic models are in transporting added heat from additional greenhouse gases from the surface up to the upper troposphere. There has been an issue for quite some time as to whether model simulations at the surface in relation to the free troposphere are realistic. For instance, a primary feedback is water vapor above 500 mb. It appears climate models have a tendency to produce more water vapor in the upper troposphere in response to increased greenhouse gas concentrations and surface warming than may be occurring in the real world. Unfortunately we really don't know whether or not this is true because the water vapor and temperature observations in the upper troposphere are simply not good enough.

Retrievals can be made in the presence of most clouds

Earth is at least two-thirds cloud covered [9] such that data sets from remote sensing systems with limited ability to penetrate clouds such as IR probing systems like AIRS [10] & IASI [11] and even MLS will be incomplete and dry-biased. This limits the ability to measure and understand processes that control climate and aid in weather prediction as well as detect and attribute the cause of climate change. GPS experiments have demonstrated the ability of radio occultations to make observations and retrievals in both clear and cloudy conditions (see for instance [12] and references therein). Coincident cloud observations and ATOMMS-derived relative humidity in and around clouds will establish the relation between cloud properties and relative humidity at scales typically resolved by models. Other important issues include the frequency and amount of supersaturation and supercooled mixed phase clouds, all important but poorly observed and understood phenomena sorely waiting for new critical, globally distributed, observational constraints. One can see from these discussions that once deployed in orbit, ATOMMS will provide something approaching a global field campaign for studying convection at the scales of GCMs.

ATOMMS DEVELOPMENT STATUS

A. ATOMMS Microwave Instrument

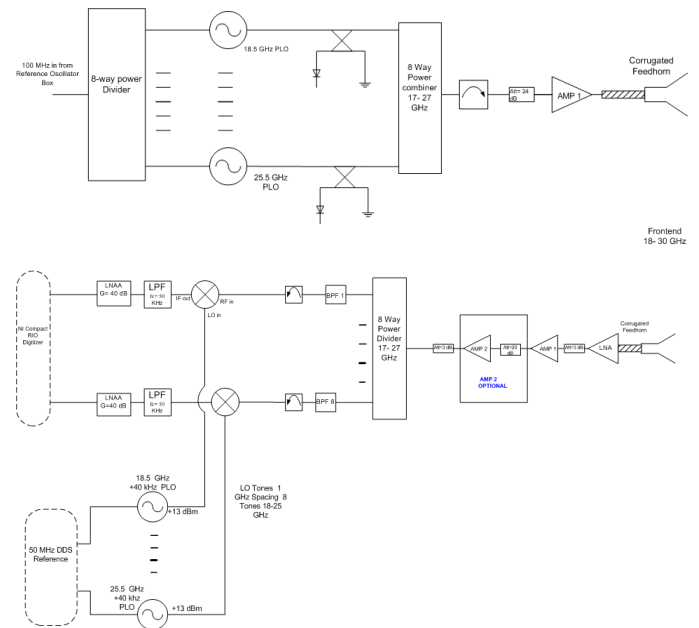


Figure 2: The ATOMMS 22 GHz transmitter (top) and receiver (bottom) subsystems. Two of the eight channels are shown in each block diagram for clarity.

The ATOMMS microwave instrument has been designed to take advantage of off-the-shelf telecommunications technology whenever possible, particularly for the 22 GHz channel. The basic instrument design uses very similar circuits for all channels. Figure 2 shows the block diagram of the 22 GHz transmitter and receiver. The transmitter uses eight separate phase locked YIG oscillators to generate the tones. These tones are individually power-monitored before they are power combined. A single amplifier then amplifies these eight tones to a level of ~100 mW per tone. Since ATOMMS measurements are effected by differential amplitude noise, a common power amplifier is used for all tones to attenuate differential amplitude fluctuations. The receiver amplifies all eight received tones simultaneously for the same reason. The amplified signal is then power divided into eight channels. Bandpass filters in each channel isolate a single received tone. These tones are then mixed with LO signals generated by YIG phase locked oscillators fed with a reference from a DDS synthesizer. This synthesizer is used to offset the frequency of the LO, generating a ~ 40 kHz IF frequency. The low frequency IF is then low pass filtered and amplified with a low noise audio frequency amplifier. The IF is then fed into a National Instruments Compact RIO real-time data acquisition system, where the time domain waveform is digitized and recorded. This data acquisition system has been shown to operate at ambient pressure in the WB-57F in previous experiments. The 13 GHz reference tone transmitter and receiver are identical to the 22 GHz system, but with a single transmitted and received tone rather than eight.

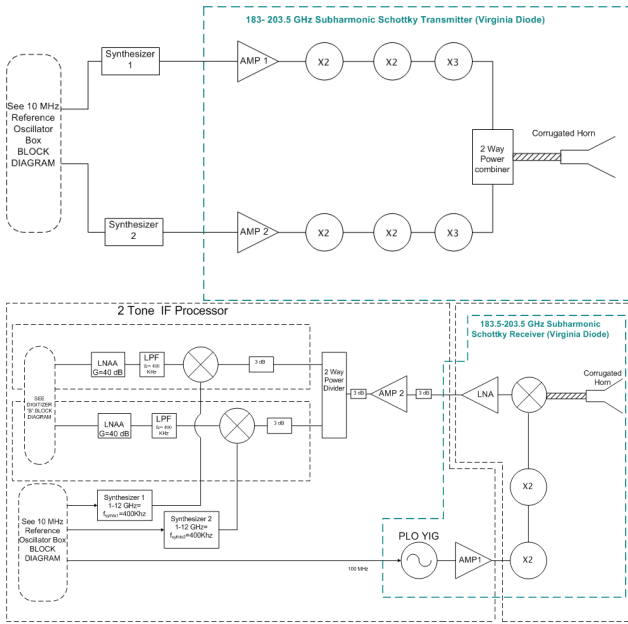


Figure 3: The ATOMMS 183 GHz transmitter (top) and receiver (bottom) system block diagrams.

The 183 GHz subsystem is based on a two tone transmitter and subharmonically pumped Schottky mixer receiver front end from Virginia Diodes. The transmitters each provide 40 mW of power from 180-203.5 GHz, and are power combined using a waveguide magic tee. Power monitoring diodes before the magic tee record the transmitted power level of each channel, for later removal of differential amplitude effects. After power combining, the transmitted power is ~20 mW per tone. The subharmonically pumped Schottky receiver has a measured noise temperature of ~1100K, and is flat across the band. A low noise amplifier with a 1-12 GHz bandwidth relays the IF signal to a downconverter module. The receiver IF downconverter is identical in architecture to the 22 GHz receiver system with the exception that tunable synthesizers are used to generate the LO signals rather than fixed tuned oscillators. Block diagrams of the 183 GHz subsystem are shown in figure 3. Figure 4 shows the 183 GHz transmitter system mounted to the ATOMMS-A rear plate.

The ATOMMS antenna system uses a pair of coaxially mounted feedhorns to illuminate a single 30 cm diameter high density polyethylene lens, anti-reflection grooved for operation at 183 GHz. [13].

A detailed link budget simulated the performance of the instrument using realistic antenna parameters and estimated losses. This link budget was used to specify all the components of the ATOMMS transmitter and receiver systems. Transmitter and receiver pairs are mounted in opposite aircraft, with each aircraft containing a transmitter for one band and the receiver for the other band. This balances both the data acquisition and power needs for each instrument.

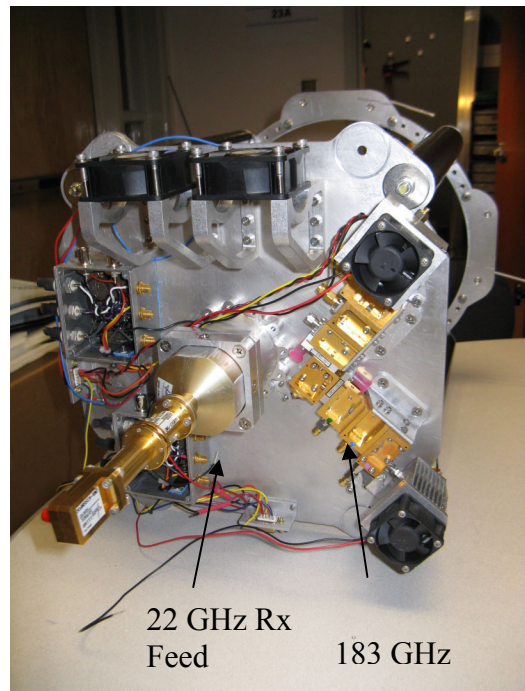


Figure 4: The ATOMMS 183 GHz transmitter system and 22 GHz receiver feed.

The ATOMMS instrument package mechanical aspects are as highly engineered as the electronics. Past experience in flying complex research instruments in the WB-57F aircraft have shown that a fairly sophisticated minimum level of integration of structure, power, thermal, vibration, low pressure and various other design factors are required to build a successful instrument. The ATOMMS instrument design, shown in figure 5, was engineered down to the level of fasteners, connectors and wiring using 3D Computer Aided Drafting (CAD) software before any manufacturing. Figure 6 shows the ATOMMS-A instrument, completely assembled and awaiting system testing.

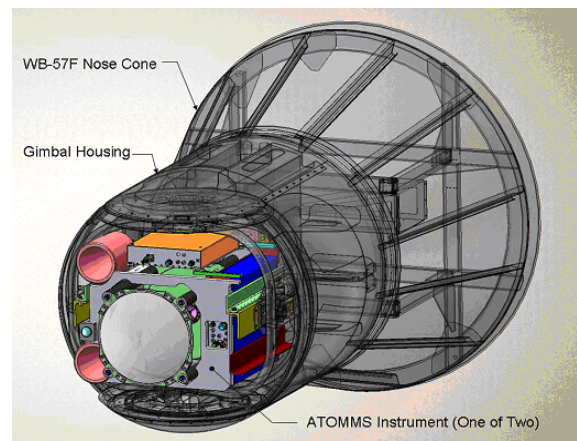


Figure 5: A 3D CAD model of one of the ATOMMS instruments in the SRI WAVE gimbal. The ATOMMS instrument was completely built in CAD before any fabrication took place.

Data acquisition duties are handled by National Instruments Compact RIO systems. These small chassis can be loaded with up to eight multifunction interface modules to

handle science signal and housekeeping digitization, digital I/O and accelerometers readout. Each Compact RIO system communicates with a PC over two dedicated Ethernet cables. These PCs are mounted in a partially pressurized part of each aircraft, just behind the moving portion of the gimbal. Each PC is equipped with large capacity solid state hard drives, and runs Labview Realtime OS. These computers receive the data collected by the Compact RIO system mounted directly on the ATOMMS instruments and record the data to disk. They also are responsible for collecting the GPS observables from the JPL provided GPS receiver used as part of the Precise Positioning System.

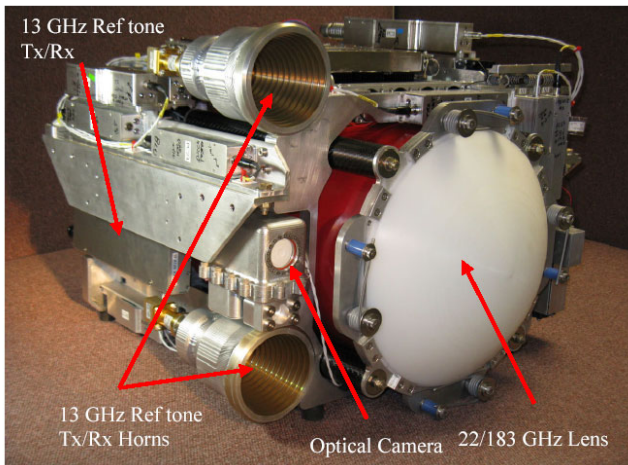


Figure 6: The fully assembled ATOMMS A instrument. Visible components are labeled. The 183 GHz Tx and 22 GHz Rx modules are not visible.

B. Precise Positioning System

The ATOMMS system will profile atmospheric temperature, humidity and pressure. Air temperature and barometric pressure, in a dry atmosphere, are derived from a profile of refractivity that is derived from a profile of bending angle derived in turn from a profile of Doppler shift versus time (see for instance [14]). The determination of the atmospheric absolute humidity profile requires the analysis of the vertical profile of atmospheric water vapour [15], and this is the most important contribution of ATOMMS when compared to the GPS-RO technique that probes only the real part of the atmospheric index of refraction.

In the aircraft to aircraft occultations, the atmospheric Doppler shift is much smaller than for the spacecraft occultation case because the aircraft move much slower (~200 m/sec) than the spacecraft (several km per second). At the uppermost altitudes, just below the altitude of the aircraft, the atmospheric bending angle is quite small. Therefore the atmospheric Doppler shift is quite small. In order to precisely determine atmospheric temperature and pressure, the ATOMMS system must measure very small bending angles at high altitudes. The system goal is to estimate the motion of the aircraft to an accuracy of 0.1 mm/sec.

Over the course of the experiment design, we refined our understanding of the necessity of this goal and how to achieve this small error. The ATOMMS Precise Positioning System consists of accelerometers and GPS receiver on each

aircraft. Positions can be estimated very accurately from the GPS receiver data about every 100 seconds. In profiling the atmosphere via the ATOMMS occultations, we determined that we will use integration times of ~10 seconds or less. To achieve the high vertical resolution and performance over these short intervals, we determined that low-noise and very accurate accelerometers must be used. Essentially the precise reconstruction of the time-varying aircraft positions and velocities will integrate the acceleration measured by the accelerometers to obtain the velocities of the two ends of the ATOMMS instrument. The GPS receiver data will essentially be used to estimate the bias and scale factor of the accelerometers. Extremely low-noise accelerometers (Endevco Model 86), developed for seismic research, were selected for the ATOMMS experiment after extensive analysis by the ATOMMS team at the University of Arizona and JPL.

High performance GPS receivers have been selected that could satisfy the ATOMMS requirements that were also familiar to JPL. The receivers already in the WB-57F aircraft were deemed insufficient to deliver the quality of phase data needed. JPL suggested a high performance Ashtech receiver that they use for other applications.



Figure 7: The WAVE system mounted on the nose of a WB-57F. ATOMMS will replace the optical telescope in this system. A microwave transparent radome will replace the front skin and optical window.

C. NASA/Southern Research Institute (SRI) WAVE Gimbal Pointing System

The ATOMMS experiment takes advantage of NASA's WB-57F Ascent Video Experiment (WAVE) system, designed to optically image the space shuttle during launch. This system is a complete replacement nose for the WB-57F, containing a 2-axis gimballed pointing system capable of 0.25 degree pointing accuracy (see figure 7). The system also contains an optical telescope with a high definition video camera and recorder. The ATOMMS microwave sensors replace this optical imaging package, but still use the replacement nose and gimbal. The optical window will be replaced with a microwave-transparent radome manufactured by Nurad corporation.

ATOMMS does present several challenges for pointing and integration with the WAVE system. The ATOMMS instrument must be adequately balanced, and within weight limits for the gimbal. More importantly, ATOMMS is not an imaging detector, so pointing cannot be done with image recognition. In addition, the atmospheric attenuation effects we wish to measure will not allow pointing based on feedback from the microwave signal strength. Any atmospheric fluctuations would be interpreted as a pointing error, and would cause the pointing loop to become unstable. We have therefore developed, jointly with Southern Research Institute (SRI) a pointing system based on GPS coordinates. As a development effort with NASA, SRI has already proven the capability to point and track a known GPS coordinate to far better than 0.25 degree accuracy in level flight. This accuracy has been demonstrated by SRI on several WB-57 test flights with the WAVE optical sensor. Using an optical camera co-mounted with the ATOMMS instrument, we can calibrate this GPS pointing system using SRI's existing algorithm to allow ATOMMS to also point to within 0.25 degrees of a known GPS coordinate. The ATOMMS microwave beam will be measured in the lab relative to the center of this optical camera to compensate for any fixed pointing offset.

The next challenge was to predict the GPS coordinate for each aircraft, and provide that information to the other aircraft to allow them to point at each other. This will be done with a combination of a pre-computed flight plan based on GPS waypoints and times, and pseudo-real time updates of position provided by an Iridium phone data link between aircraft. Because of the slow speed and unreliability of the Iridium link, the primary location information will be the flight plan, which the pilots will attempt to fly as accurately as possible. Meeting the waypoint locations accurately is not a large challenge for the pilots, but timing arrival at those waypoints is a significant challenge. Therefore, the Iridium link will be used to provide time shifts along the flight path rather than for full position and time information. The code for this implementation has been written by SRI and is now undergoing testing.

D. ATOMMS Retrieval System

Retrieval Software

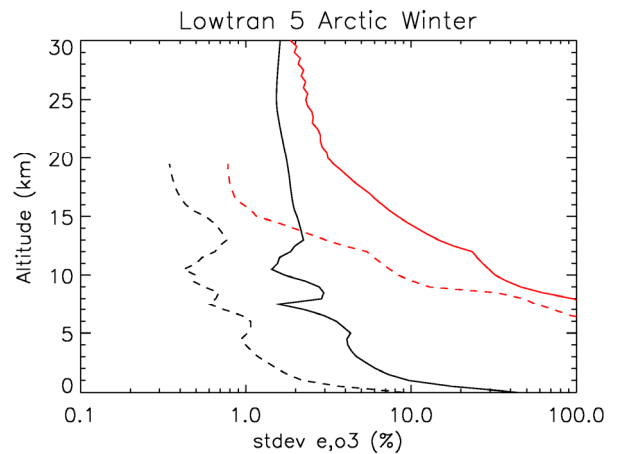
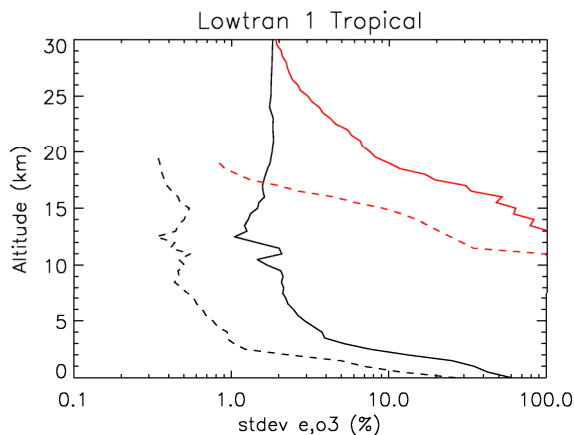


Figure 8. Standard deviation of simulated errors of H₂O vapor (black) and O₃ (red) from satellite (solid) and aircraft occultations (dashed). top: arctic winter conditions. bottom: tropical conditions.

Prior to this project, we developed simulations to investigate the accuracy of retrievals for an ATOMMS-type instrument in a satellite-to-satellite geometry. We have been adapting this code to perform retrievals in the MRI aircraft to aircraft geometry. We have used this code to understand how instrumental parameters, such as SNR and antenna gain pattern, will affect retrieval accuracy. We have also developed an improved method to deal with liquid water clouds distributed inhomogeneously along the occultation signal path. We developed a two relaxation dielectric model of liquid water for simulating ATOMMS retrievals when liquid clouds are present [16].

ATOMMS will retrieve the atmospheric profile of index of refraction using the method proven to work for GPS occultations, modified for the aircraft geometry. JPL has agreed to provide the JPL GPS occultation processing software to the UA that we will modify for the ATOMMS processing. Simulated errors based on this retrieval technique for water and ozone are shown in figure 8.

Atmospheric Turbulence

Amplitude scintillations (“twinkling of a star”) are an unwanted source of amplitude variation that reduces the accuracy of how well we can isolate the absorption on the ATOMMS signals. To better understand this error, Angel Otarola’s recently defended dissertation research [17] focused on atmospheric turbulence and its impact on the ATOMMS observations. We have coupled this effort to the retrieval system development to understand the impact these variations will have on the accuracy of the ATOMMS retrievals.

We have developed a relation between the scintillations due to the real part of the wet refractivity variations that allows us to estimate the magnitude of the scintillations due to water vapor knowing the average of the wet-component of atmospheric air refractivity [17]. Using high resolution radiosonde data, we have developed an understanding of the spectrum of turbulent variations in the vertical coordinate in particular the spectral transition from homogeneous turbulence at smaller scales to a different spectral dependence of turbulence at larger scales.

Prior to this work, the impact of turbulent variations in the imaginary component of refractivity has thus far been ignored by the radio occultation community. We are working towards generalizing the equations that describe the impact of turbulence variations in the real part of the index of refraction to include the contributions of the imaginary variations. This work is important because we now realize that the simple two tone amplitude ratioing method described by [4] will not work as well for the imaginary contributions. The two tone method cancels the real contributions well because of their weak frequency dependence, but does not perfectly cancel the contributions due to the imaginary component. Based on this new understanding, we feel that it is essential that we simultaneously measure more than two tones at our high band frequencies (180 – 203 GHz) to diagnose and minimize the effects of turbulence on our retrievals.



Figure 9: View of the Gould Simpson building from AME building. ATOMMS transmitter is shown in right side of the figure on the AME roof. The insert in the lower left shows the ATOMMS receiver on the 11th floor roof of Gould Simpson.

ATOMMS GROUND TESTING

ATOMMS has been undergoing ground testing experiments at 183 GHz for several months. The ATOMMS data is clearly tracking the water vapour variations observed by the rooftop hygrometer of the University of Arizona Department of Atmospheric Sciences.

A. Introduction

ATOMMS is a differential absorption measurement system that will profile water vapour, temperature, pressure and ozone from orbit. The water vapour content is derived from the frequency dependence of the absorption and knowledge of the spectroscopy.



Figure 10: ATOMMS receiver on Gould-Simpson looking back at the transmitter on AME located in the white circle. Photograph taken on the morning of March 12, 2010. The cement beam above the ATOMMS receiver is in front of and above the ATOMMS receiver and is part of a façade that encircles the entire building.

Presently we are testing the “high band” portion of the ATOMMS instrument prototype that probes the 183 GHz water line. In these tests, signals are transmitted from the 8th floor rooftop of the Aeronautics and Mechanical Engineering (AME) building along an 820 m path to the 11th floor rooftop of the Gould-Simpson (GS) building on the University of Arizona campus. The view from the AME building of the transmitter looking toward the receiver on the Gould-Simpson building is shown in figure 9. The view from the receiver to the transmitter is also shown in figure 10. The map of the geometry is shown in figure 11.

B. Phase stability testing

Measurements of the 13 GHz transceiver systems set the phase noise floor for the ATOMMS instrument. The bidirectional 13 GHz system is used for the dual-one-way phase correction system, allowing the data from each aircraft to be phase locked after the fact. Since ATOMMS IF data is recorded as a time series with Nyquist sampling, timing errors between the two aircraft can be corrected after flight. The data from the 13 GHz system is the reference for this process. Figure 13 shows the Allan variance of the phase for the 13 GHz system. With integration times of 0.5s or longer, the phase noise introduced by the 13 GHz electronics is well below the 0.1mm/s velocity specification for ATOMMS.

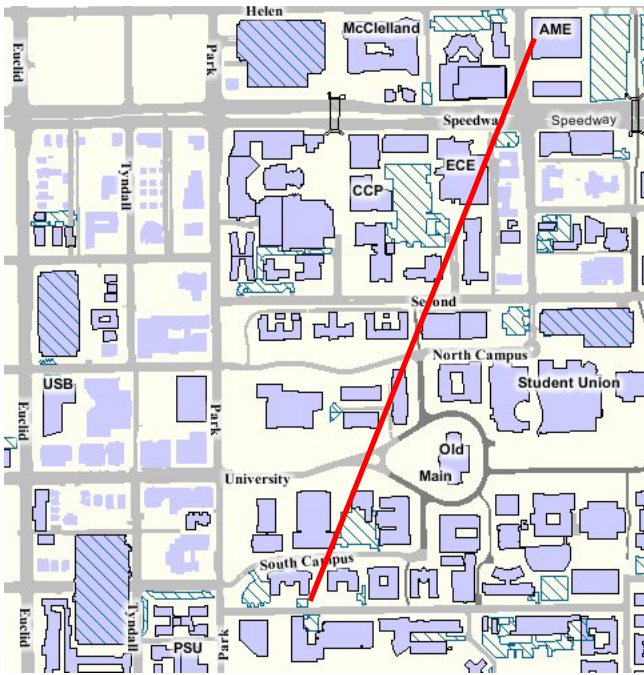


Figure 11: Map of University of Arizona showing the ATOMMS rooftop geometry. Path length is 820 m.

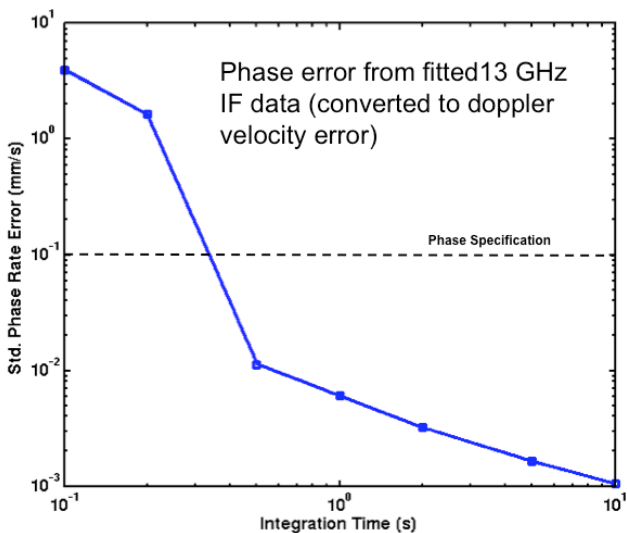


Figure 12: Allen variance plot of ATOMMS phase noise converted to velocity error. The total phase error budget is shown by the dotted line. For integration times of less than 1s, the 13 GHz system is an order of magnitude below the phase error specification.

C. ATOMMS Atmospheric Measurements

The ATOMMS ground based testing described above has allowed us to estimate the water vapour content integrated along the 820m line of sight though fitting of the measured 183 GHz absorption line profile. These data have then been compared to a fast capacitive hygrometer located near one of the ATOMMS instrument packages. These first results are shown in figure 14. Given an expected ~10% error in the water vapour content as measured with the hygrometer, the correlation between the two sets of data is encouraging.

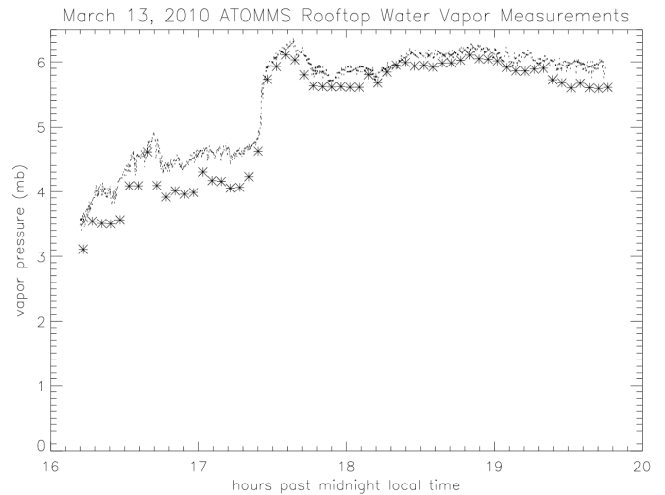


Figure 13: Water vapour data from March 13, 2010 on the University of Arizona campus. Asterisks are water vapour derived from ATOMMS measurements. The fine dots are 5 second partial pressure derived from the capacitive hygrometer on the roof of Physics and Atmospheric Sciences (PAS) building just east of the Gould-Simpson building (see map above).

CONCLUSION

ATOMMS offers a unique and unprecedented capability for measuring key atmospheric variables fundamental to climate independently from models and other climatological assumptions. The ATOMMS aircraft to aircraft occultations offer the best way to demonstrate and assess the ATOMMS concept and its performance without the very costly step of placing at least one if not both of the instruments in orbit. Assuming the aircraft demonstrations prove successful, they will pave the way for support from the larger science community for the ATOMMS concept and a NSF/NASA/NOAA spacecraft mission and a major new global research instrument for atmospheric science. Recent ground based testing shows ATOMMS is capable of measuring amplitudes and frequencies to the required accuracy, a crucial step in the evolution of this instrument.

ACKNOWLEDGEMENTS

ATOMMS is supported by the NSF Major Research Instrumentation Program under award ATM-0723239.

REFERENCES

Kursinski et al., 1996, Initial results of radio occultation observations of Earth's atmosphere using the global positioning system, *Science*, 271, 1107-1110.
 Waters, J.W., 2006, The Earth Observing System Microwave Limb Sounder (EOS-MLS) on the AURA Satellite, *IEEE Transactions on Geoscience and Remote Sensing*, 44, No 5, 1075-1092.
 Ware R. et al., 1996, GPS sounding of the atmosphere from low-orbit: Preliminary results, *Bulleting Of The American Meteorological Society*, 77(1), 1377-1416.
 Kursinski, E. R. et al. (2004), *An Active Microwave Limb Sounder for Profiling Water Vapor, Ozone, Temperature, Geopotential, Clouds, Isotopes and Stratospheric Winds, in Occultations for Probing Atmosphere and Climate (OPAC-1)*, Springer-Verlag, Berlin, p. 173 - 188, 2004.
 Rodgers, C., 2000, *Inverse methods for atmospheric sounding: Theory and Practice*, World Scientific.
 Kursinski, E. R., D. Ward, A. Otarola, K. Sammler, R. Frehlich, D. Rind, C. Groppi, S. Albanna, M. Shein, W. Bertiger, H. Pickett and M. Ross,

- (2008b), The Active Temperature Ozone and Moisture Microwave Spectrometer (ATOMMS), in ECMWF/EUMETSAT GRAS SAF Workshop Proceedings on The Applications of GPS Radio Occultation Measurements. June 2008.
- Newell, R.E., V. Thouret, J.Y.N. Cho, P. Stoller, A. Marengo, and H.G. Smit, Ubiquity of quasi-horizontal layers in the troposphere, *Nature*, 398, 316-319, 1999.
- Kursinski, E. R. and G. A. Hajj, A comparison of water vapor derived from GPS occultations and global weather analyses, *J. Geophys. Res.*, 106, 1113-1138, 2001.
- Rossow, W.B. and R.A. Schiffer, Advances in understanding clouds from ISCCP, *Bull. Amer. Meteor. Soc.*, 80, 2261-2288, 1999.
- Aumann H.H., Chahine M.T., Gautier C., Goldberg M.D., Kalnay E., McMillin L.M., Revercomb H., Rosenkranz P.W., Smith W.L., Staelin D.H., Strow L.L., and Susskind J., 2003, *IEEE Trans. in Geo. and Rem. Sens.*, 41, 2, 253-264.
- Blumstein, D. et al., 2004, IASI instrument: technical overview and measured performances, in: *Society Of Photo-Optical instrumentation Engineers (SPIE) Conference Series*, edited by: Strojnik, M., Vol. 5543.
- Anthes, R.A. et al., 2008, The COSMIC/FORMOSAT-3 mission: Early results, *Bulleting of the American Meteorological Society*, 89(3), 313-333.
- Sarmad. H. AlBanna, Chris Groppi, Chris Walker, Michael Schein, Steve Bell, Brian Wheelwright, Christian Drouet d'Aubigny, Abram Young, Dathon Golish, E. Robert Kursinski, Angel Otarola, Dale Ward, Kate Sammler, Willy Bertiger, Mark Miller, Herb Pickett, *A Single 30 cm Aperture Antenna Design for the Operation of 2 Widely Separated Frequency Bands for the Active Temperature, Ozone and Moisture Microwave Spectrometer (ATOMMS)*, Proceedings of the 20th International Symposium on Space Terahertz Technology, 2009.
- Fjelbo, G.A., Kliore, A.J., Eshleman, V.R., 1971, The neutral atmosphere of Venus studied with the Mariner V radio occultation experiments, *The Astronomical Journal*, 76(2), 123-140.
- Kursinski, E.R. et al., 2002, A microwave occultation observing system optimized to characterize atmospheric water, temperature, and geopotential height via absorption, *Journal Of Atmospheric and Oceanic Technology*, 19, 1897-1914.
- Otárola A. (2007), *The Complex Permittivity of Pure Liquid Water From Microwave Frequencies Up To 1.5 THz*, Master Thesis, Department of Atmospheric Sciences, University Of Arizona, Prof. E.R. Kursinski.
- Otárola, A., Kursinski, E.R., Ward, D., Frehlich, R., On the structure constant of the wet component of atmospheric index of refraction, *Radio Science* (submitted).

TELIS: TERAHERTZ and subMMW LIMB Sounder – Project Summary After First Successful Flight

Manfred Birk^{1*}, Georg Wagner¹, Gert de Lange², Arno de Lange², Brian N. Ellison³, Mark R. Harman³, Axel Murk⁴, Hermann Oelhaf⁵, Guido Maucher⁵ and Christian Sartorius

¹ German Aerospace Center (DLR), Germany

² Netherlands Institute for Space Research (SRON), The Netherlands

³ Rutherford Appleton Laboratories (RAL), United Kingdom

⁴ University Bern, Switzerland

⁵ Karlsruhe Institute of Technology (KIT), Germany

*Contact: manfred.birk@dlr.de, phone +49-8153-28-3084

Abstract— The TELIS instrument is a balloon-borne cryogenic three-channel heterodyne spectrometer for limb sounding of stratospheric trace gases. The instrument is flown on the MIPAS gondola together with the MIPAS-B Fourier-transform spectrometer of the Institute of Meteorology and Climate Research (IMK) of the Karlsruhe Institute of Technology (KIT). The MIPAS gondola is equipped with a precise GPS-aided inertial navigation system providing attitude and heading data of the gondola movements with 128 Hz that are also used as input for the TELIS pointing system. TELIS was developed by a European consortium involving research institutions, universities and industrial partners.

Thermal emission radiation is coupled in by a 26x13 cm dual offset Cassegrain telescope controlled to maintain constant tangent height during measurement. Radiometric calibration is achieved by a blackbody and deep space view. The radiation is divided into three channels by means of a polarizer and a dichroic. Within a special lightweight cryostat three complete heterodyne receivers are kept at liquid helium temperature: THZ channel, 1750-1890 GHz, hot electron bolometer mixer, DLR; SIR channel, 480-650 GHz, integrated receiver, SIS mixer, SRON (see poster ‘TELIS instrument performance analysis’); subMMW channel, 497-504 GHz, SIS mixer, RAL. A digital autocorrelator spectrometer with 4 GHz bandwidth and ca. 2 MHz resolution serves as backend shared among the channels.

The first successful flight was in March 2009 and the second in January 2010, both launched from Esrange near Kiruna, Sweden. Calibrated spectra are so far only available as quicklook data. Sideband ratios have been characterized. The radiometric accuracy of the autocorrelator is under investigation (see poster ‘Characterisation of the TELIS autocorrelator spectrometer’).

This paper will present the instrument as well as first results from the flight campaigns.

I. INTRODUCTION

In order to investigate stratospheric trace gas distributions associated with ozone destruction and climate change, TELIS (TERahertz and submillimetre LIMb Sounder) has been developed, a new state-of-the-art balloon-borne three channel (500, 480-650, 1800 GHz for RAL, SRON and DLR respectively) cryogenic heterodyne spectrometer. The instrument applies state-of-the-art superconducting heterodyne technology operated at 4K and is designed to be

compact and lightweight, while providing broad spectral coverage within the submillimetre and far-infrared spectral range, high spectral resolution and long flight duration (~24 hours during a single flight campaign). The TELIS instrument is operated together with the MIPAS-B Fourier Transform spectrometer on the same balloon platform. MIPAS was developed by the Institute of Meteorology and Climate Research of the Karlsruhe Institute of Technology, Germany, and has completed 18 successful flights (see e.g. [1] and references cited therein). The combination of TELIS and MIPAS instruments covers all relevant atmospheric species:

TELIS species (limb sounding: height range 10-40 km, altitude resolution 2 km)

DLR: **OH**, **HO₂**, **HCl**, NO, NO₂, O₃, H₂O, **O₂** (pointing, temperature), HOCl, H₂¹⁸O, H₂¹⁷O, HDO

RAL: **BrO**, ClO, O₃, N₂O

SRON: ClO, **BrO**, O₃, **HCl**, HOCl, H₂O, HO₂, NO, N₂O, HNO₃, CH₃Cl, **HCN**, H₂¹⁸O, H₂¹⁷O, HDO, **O₂** (pointing, temperature)

MIPAS-B species (incomplete list)

Ozone relevant: O₃, NO, NO₂, HNO₃, HNO₄, N₂O₅, ClO, ClOOCl, HOCl, ClONO₂, BrONO₂

Water isotopologues: HDO, H₂¹⁶O, H₂¹⁷O, H₂¹⁸O

Tracers: N₂O, CH₄, CO, SF₆, CF₄, CCl₄, CFC-11, CFC-12, CFC-113, HCFC-22, CH₃Cl

Short-lived source gases: NH₃, acetone, PAN, H₂CO

NMHCs: C₂H₆, C₂H₂

Species involved in cloud physics: H₂O, HNO₃, NH₃, OCS, ...

Cirrus cloud parameters: extinction, volume, bulk composition, coarse size dist.

The species marked in red are measured by TELIS alone and are thus complementary to the MIPAS observations. Several species can be used for cross validation. In case of the water isotopologues the DLR channels measures strong isolated lines which are suited for MIPAS/ENVISAT validation.

II. TELIS INSTRUMENT OVERVIEW

Fig. 1 shows the block diagram of the TELIS instrument. Three heterodyne receivers are installed inside the cryostat fabricated by RAL which is lightweight and has two optical benches (ca. 30 cm diameter), one below and one above the helium vessel. The 480-650 GHz channel developed by Netherlands Institute of Space Research (SRON) utilizes the Super-Integrated-Receiver (SIR) combining the Superconductor-Isolator-Superconductor (SIS) mixer and its quasi-optical antenna, a superconducting phase-locked Flux Flow Oscillator (FFO) acting as LO and SIS Harmonic Mixer (HM for FFO phase locking [2],[3]). The 500 GHz channel developed by Rutherford Appleton Laboratory (RAL) is a highly compact heterodyne receiver. It uses a fixed tuned SIS mixer, with a junction provided by the Institut de Radioastronomie Millimetrique, France and a solid state LO [4]. The 1.8 THz channel [5] uses a solid state local oscillator and a hot electron bolometer as mixer.

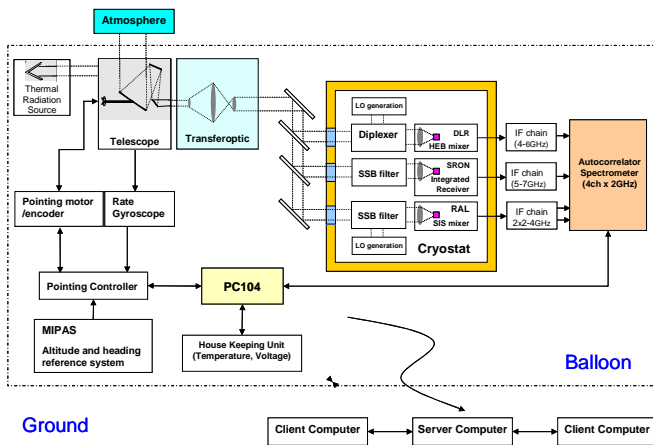


Fig. 1 Block diagram representing the TELIS instrument

The atmospheric signal is transmitted from the telescope through the front-end transfer optics where the signals are separated and coupled into each channel through dedicated windows. For radiometric calibration a cone-shaped blackbody [6] is used together with an up-looking spectrum (ca. 65° elevation angle). The input of the channels is switched to the warm blackbody by a flip mirror between telescope and transfer optics. For on-ground operation, a second flip mirror is installed to couple radiation from a cold load (Dewar lined with Eccosorb filled with liquid nitrogen). The telescope was designed to yield 2 km vertical resolution at 500 GHz. To avoid edge taper effects the vertical size of the mirror is 4ω . The size of primary of the dual offset Cassegrain is 26 cm in vertical and 13 cm in horizontal direction. The anamorphicity is introduced by a cylindrical tertiary. The RAL channel signal path is separated by means of a polarizer (manufactured by RAL) which transmits the SRON and DLR beams. SRON and DLR beams are further separated by a dichroic filter plate (also manufactured by RAL) transmitting 84-93% of the THz spectral signal to the DLR channel.

The telescope is positioned by a limited angle torque motor powered by an H-bridge. The angle is measured with a high-accuracy angular encoder. Furthermore, the angle

change with respect to a space-fixed coordinate system is measured with a rate gyro. A real time processor controls the telescope using a digital control loop to keep an earth-fixed pointing angle of the telescope. Data for this control to relate the gondola and earth-fixed systems is supplied by the AHRS (attitude and heading reference system) of MIPAS. The AHRS is a precise GPS-aided inertial navigation system with gyros and accelerometers providing attitude and heading data of the gondola movements with 128 Hz. The pointing stability is 1' peak-to-peak in absence of large gondola oscillations. For a single measurement the pointing angle is held constant.

The Intermediate Frequency (IF) output of each channel is fed to a digital autocorrelator spectrometer developed by the OMNISYS company (Sweden), having a resolution of about 2 MHz and two independent spectrometers with an input frequency range of 2 GHz each. The total bandwidth is either shared by DLR and SRON channels or entirely dedicated to the RAL channel, which uses a 14 GHz to 18 GHz IF downconverted to two separate 2 GHz channels.

All devices of the TELIS instrument are controlled by a computer (based on PC/104). Device drivers running in a Linux environment control the hardware. Communication between flight and ground segment servers is done via telemetry supporting TCP/IP. The ground server uses a MySQL database to store all sent and received commands and data. The data received from the instrument are raw autocorrelation as well as housekeeping data, e.g. temperatures, voltages, pointing data.

During flight, the TELIS instrument is powered by lithium sulfuryl chloride batteries offering high energy density. The instrument is also surrounded with PE foam insulation and heat from the autocorrelator unit is transferred to a radiator plate by ammonia-filled heat pipes. Table 1 contains summary details about the instrument. Figure 2 shows the optical module of TELIS including the telescope, blackbody unit, transfer optics, and cryostat (blue). The autocorrelator unit (Figure 3) contains IF pre-amplifiers for SRON and DLR channel and an IF box which converts channel outputs to 1.75-3.75 GHz for the autocorrelator. This box also controls the autocorrelator and variable attenuators. The local oscillator synthesizer for the 1.8 THz channel (output frequency ca. 16 GHz), the autocorrelator, and the DC/DC power supply for all components on this unit are also on this plate which is mounted on the back of the optical module. Beside the optical module, there are four small racks: digital rack, analogue rack, battery rack, and a rack controlling the SRON channel. All racks are stored in compartments (40x40x25 cm) of the gondola structure.

TABLE I
TELIS SPECIFICATIONS

Dimensions optical module	120 x 70 x 72 cm
Total mass	140 kg
Total power consumption	240 W
Liquid helium	15 l
Liquid nitrogen	7 l

Telescope	
Size	26 cm vertical x 13 cm horizontal
Design	Dual offset Cassegrain, anamorphic
Field of View	Ca. 2 km FWHM at tangent point
Spectrometer	
Type	Digital autocorrelator, 1.5 bit
Bandwidth	2 x 2 GHz
Resolution	2 MHz
Measurement cycle	
Duration	30-50 s
Calibration	Hot load + deep space view
Measurement time per microwindow	10-20 min
DLR Channel	
Frequency range	1750-1890 GHz
LO power	>200 nW
Noise temperature	3000-4000 K DSB
Mode	Double sideband
SRON Channel	
Frequency range	480-650 GHz
Noise temperature	200 K DSB
Mode	Double sideband
RAL Channel	
Frequency range	497-504 GHz
Noise temperature	2000 K DSB
Mode	Double sideband

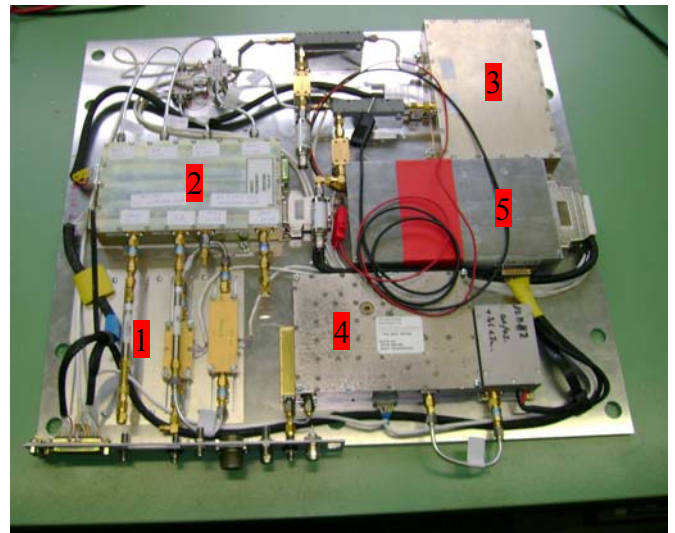


Fig. 3 Autocorrelator unit. Pre-amplifiers (1), IF box (2), autocorrelator (3), LO synthesizer (4), power supply (5).

III. CHARACTERIZATION

A. Radiometric accuracy

Gas cell measurements offer a radiometric check of the entire system. Opaque lines of ambient temperature gas have a known line contrast when measured against a cold background. By adjusting the total pressure atmospheric signals can be simulated. In the case of unknown sideband ratio opaque lines may be selected with a difference frequency in the range $2 \times IF_{lower}$ to $2 \times IF_{upper}$, where IF_{lower} and IF_{upper} are the IF boundary frequencies. The local oscillator can then be adjusted to position the lines from both sidebands at the same IF frequency. Thus, the IF signal represents the sum of both sidebands and the radiometric accuracy can be investigated without knowing the sideband ratio.

Cell measurements (OCS for SRON channel, methanol for DLR channel) showed radiometric errors in the autocorrelator (see Fig. 4). The errors affect the signal intensity and signal spectral shape. Radiometrically calibrated spectra with broad spectral signatures, similar to the shapes in the calibration spectra, do not show any errors. When the spectrum to be calibrated has a spectral shape which differs from that of the calibration measurements errors occur depending on the difference of calibration and target spectral shape. The OCS spectra in Fig. 4 could be fitted by using a multiplicative and additive correction in radiance in each of the 500 MHz autocorrelator segments. The scalar increased from narrow to broad lines from 0.8 to 1.0. To characterize the spectrometer, identical measurements were performed with an FFT spectrometer for comparison. A final analysis is in progress.

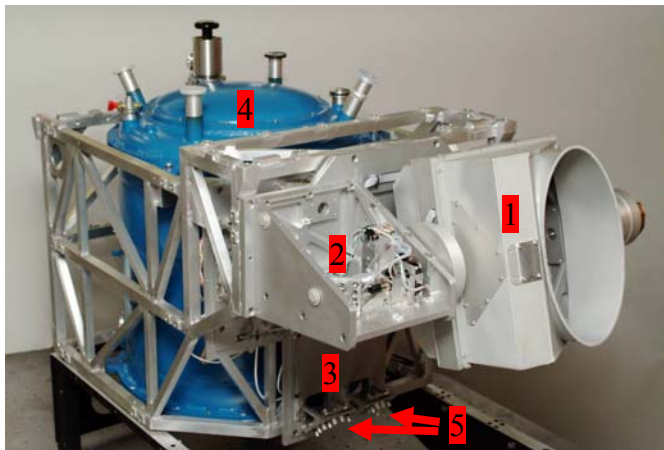


Fig. 2 Optical module of TELIS. The module is based on a welded aluminium frame. The oval opening on the right belongs to the telescope (1) and has about the size of the primary which is behind the opening. The blackbody unit (2) with the flip mirrors and one imaging mirror is left of the telescope. The warm blackbody itself is under the unit and cannot be seen. The transfer optics plate (3) is between telescope, blackbody unit, and cryostat (blue vessel, 4). The only elements of the transfer optics which can be seen are the coupling mirrors (5) to the RAL and SRON channels.

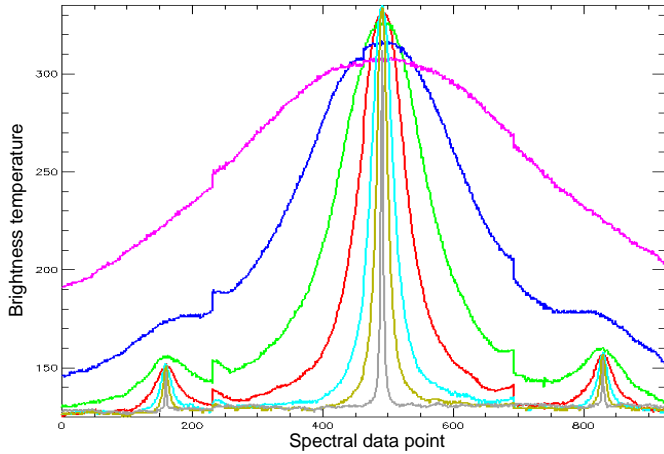


Fig. 4 Measured OCS spectra at different gas pressures. There was a saturated line in each sideband. All lines should peak at 300 K (gas temperature) and there should be no steps in the line profile.

A method was developed to measure sideband ratios using a high resolution Fourier-transform spectrometer (6 m maximum optical path difference, corresponding to 30 MHz resolution). The heterodyne channel is used as detection unit of the FT-spectrometer and the IF power diode output is fed into the Fourier-transform analogue electronics. Several iterations were required to optimize the procedure and to obtain reproducible results. With this method the sideband ratios of both the DLR and SRON channel were measured. Figure 5 shows an example of the spectral dependence of the sideband ratio for two independent measurement campaigns (new positioning of detector unit). Worst case differences of 10% occur. On average, the method is accurate to 5%. The spectral shape indicates that some small interference (Fabry-Perot) effects are still present in the optics of the heterodyne spectrometer.

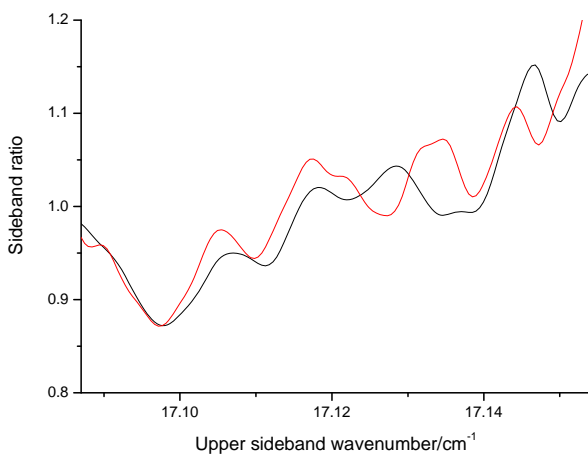


Fig. 5 Example of sideband ratio from two different measurement campaigns

B. Antenna beam profile

The influence of the telescope on the beam profile was measured by Fürholz and Murk [7]. The azimuthally collapsed antenna beam profile (ACAP) of the entire system

was measured according to a method developed by Pickett [8]. For this a copy of the telescope was built omitting the tertiary and using a mercury arc lamp slit source where the arc is imaged into the focal plane of the telescope copy equipped with a well-defined slit. Antenna beam profiles are measured by placing the telescope copy in front of the telescope, and recording the total IF power as function of telescope angle. A typical beam profile of the SRON channel is shown in Fig. 6.

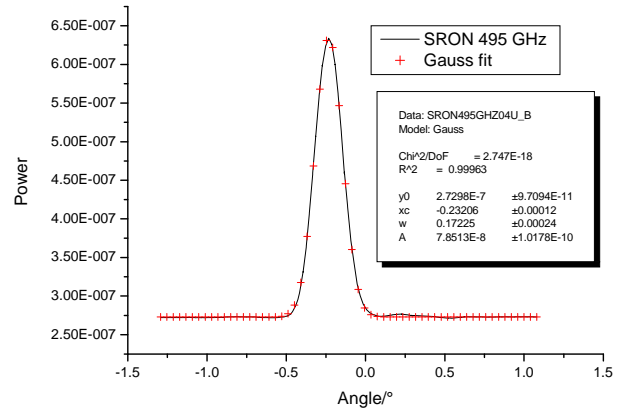


Fig. 6 SRON ACAP at 495 GHz and fitted Gauss profile. The ω is 0.17° corresponding to 0.2° FWHM corresponding to a width of 1.8 km at a distance of 550 km (typical distance sensor to lowest tangent point).

IV. CAMPAIGNS AND RESULTS

TELIS participated in two successful campaigns, one in March 2009 and the second in January 2010. Both campaigns were in Esrang near Kiruna, Sweden. The flight altitude was between 30 and 35 km. In contrast to the MIPAS Fourier-Transform spectrometer the different species to be measured cannot be simultaneously covered since they require different local oscillator settings. The optimum LO frequency was determined by simulating the double sideband spectra using standard atmospheric trace gas profiles and the HITRAN spectroscopic database. The selection criterion was to have mostly isolated lines for the target species. The different spectral regions to be covered are called microwindows. The different microwindows were tested in the same cryostat cooling cycle as the flight itself was performed. In case of the THz channel it was confirmed that the optical path difference setting for the diplexer (Martin Puplett interferometer) did not drift between characterisation and flight outside the specification. The diplexer setting influences the sideband ratio and is selected for optimum transmittance of the atmospheric signal.

A single microwindow was measured for a time period of about 10-20 minutes. The measurement sequence includes individual atmospheric measurements and the calibration measurements (hot load, up-looking 65°). The atmospheric measurements consist of a series tangent spectra (spaced by 1.5 or 2 km) from 10 km to flight altitude, 2 up-looking spectra 6° and 12° . Each spectrum was measured for 1.5 s, calibration spectra were measured about every 30 s. The

measured data are directly transmitted to the ground and processed to so-called “quick look” products. Fig. 7 shows a computer screen with quick look data. On the left DLR and on the right SRON results are shown. The upper graphs shows power spectra, the next single calibrated spectra and the lower co-added spectra for all tangent heights and up-looking angles.

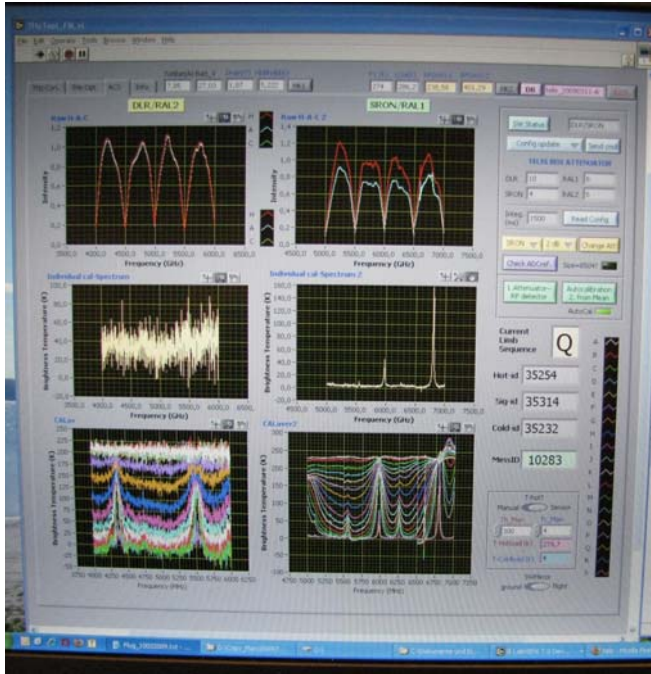


Fig. 7 Example of quick look data

Figure 8 shows an example for the THz co-added spectra for the OH microwindow together with model calculations. It can be seen that the modelled baseline is significantly lower than the measured one. Investigations on the reason are in progress. It was found that the noise temperature which was usually of order 3000-4000 K increased in the flight up to 7000 K. This happened during both flights. However, during the first flight, and when the instrument was bathed in sunlight and warming up, the noise temperature decreased to the nominal values. The likely cause of this effect is ice formation on the tertiary telescope mirror which, in turn, introduces increased attenuation in the signal path. Whether the increase in noise temperature is correlated with the large baseline values observed in the measured spectrum is still under investigation.

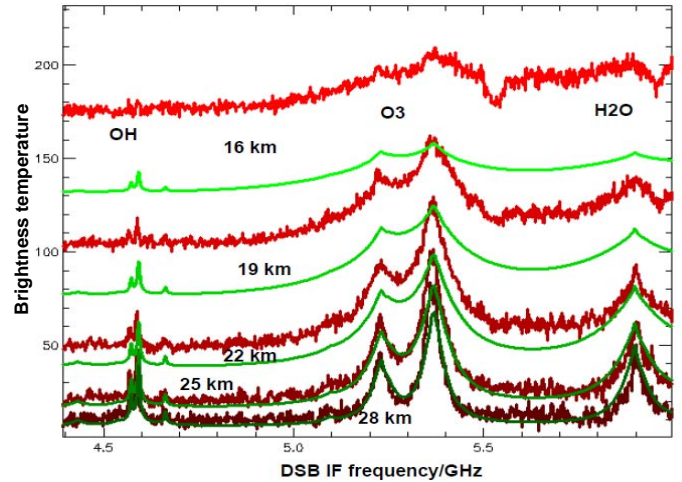


Fig. 8 Measured (shades of red) and modelled (shades of green) double sideband quick look spectra of THz channel OH microwindow at 16, 19, 22, 25 and 28 km tangent altitude

Figure 9 and 10 show spectra measured with the SRON channel during the recent flight. These spectra are very important in improving our understanding of atmospheric chemistry. In Figure 9 the time dependence of the ClO signal can be seen, with the most recent flight located inside the polar vortex during perturbed chemistry. Since MIPAS measures ClOOCl, both instruments MIPAS and TELIS can measure the time dependence of the most relevant chlorine species in perturbed chemistry which would finally quantitatively close open issues about the polar ozone hole. Figure 10 shows, also for the first time, a subMMW measurement of BrO in the polar vortex. To date in situ and UV remote measurements have provided contradictory results regarding the bromine budget. This new measurement will help to quantify the atmospheric bromine content and its consequent impact upon the global ozone budget.

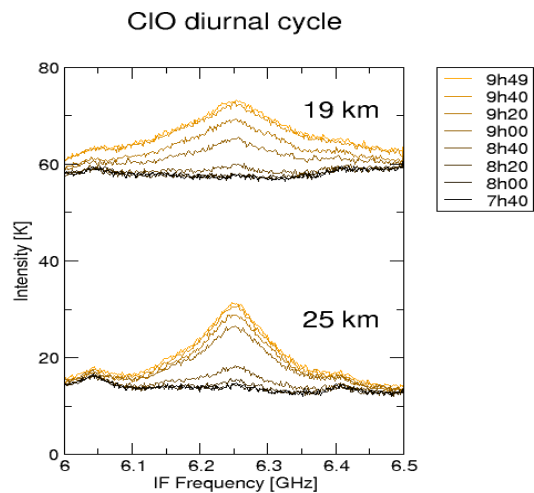


Fig. 9 The perturbed chemistry diurnal cycle of ClO recorded by the SRON channel of the TELIS instrument during the 2010 flight from Kiruna. The quick look spectra measured at 19 and 25 km tangent altitude are shown at intervals of 20 minutes

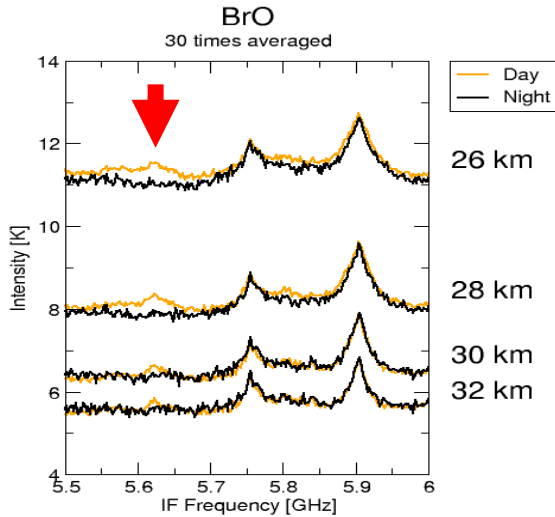


Fig. 10 BrO recordings by the SRON channel of the TELIS instrument during the 2010 flight from Kiruna. The quick look spectra measured at 26, 28, 30, and 32 km tangent altitude are shown.

V. OUTLOOK

The next step is the generation of calibrated spectra which requires the correction of the autocorrelator error, the implementation of sideband ratios and the solution of the problem of too high baselines in SRON and DLR channel. Scientific exploitation of the data will help to improve atmospheric models and the data quality of remote sensing instruments.

TELIS is currently being modified to allow installation on the new German HALO research aircraft.

REFERENCES

- [1] Friedl-Vallon, F., Maucher, G., Seefeldner, M., Trieschmann, O., Kleinert, A., Lengel, A., Keim, C., Oelhaf, H., and Fischer, H., *Design and characterization of the balloon-borne Michelson Interferometer for Passive Atmospheric Sounding (MIPAS-B2)*, Appl. Opt., 43, 3335-3355, 2004.
- [2] Yagoubov, P. et al., *Superconducting Integrated Receiver on Board TELIS*, in proc 19th International Symposium on Space Terahertz Technology, Groningen, 28-30 April 2008, pp. 268-275.
- [3] Hoogeveen, R. W. M., Yagoubov, P. A., de Lange, A., Selig, A. M., Koshelets, V. P., Ellison, B. N., Birk, M., *Superconducting integrated receiver development for TELIS*, SPIE Proceedings Vol. 5978 (2005) 59781F.
- [4] Ellison, B. N., et al., *Development of a compact sub-millimetre wave SIS receiver for terrestrial atmospheric sounding Infrared and Millimeter Waves*, proc. 12th. International Conference on Terahertz Electronics. (2004), pp. 445-446.
- [5] Suttiwong, N., Birk, M., Wagner, G., Krocka, M., Wittkamp, M., Haschberger, P., Vogt, P. and Geiger, F., *Development and characterization of the balloon-borne instrument TELIS (TERahertz and Submm Limb Sounder): 1.8 THz receiver*, Proc. 19th ESA Symp. on European Rocket and Balloon Programmes and Related Research (Bad Reichenhall) 2009, in press.
- [6] Murk A., Wylde R., Spurrett R., Fürholz P., Kämpfer N., *Blackbody Calibration Targets with Ultralow Reflectivity at Submillimeter Wavelengths*, 4th ESA Workshop on Millimetre-Wave Technology and Applications, Volume WPP-258, pp. 359-364, 2006.
- [7] Fürholz, P. and Murk, A., *Phase-Corrected Near-Field Measurements of the TELIS Telescope at 637 GHz*, IEEE Transactions on Antennas and Propagation, Volume 57, Issue 9, Sept. 2009, pp. 2518-2525.
- [8] Pickett, H.M., *Microwave Limb Sounder THz module on Aura*, IEEE Transactions on Geoscience and Remote Sensing, Volume 44, Issue 5, May 2006, pp. 1122-1130.

Session S9: Superconducting Mixers

1.4 THz SIS mixer using Nb and Al tuning circuit

A. Karpov¹, D. Miller¹, J. A. Stern², F. Rice¹, H. G. LeDuc², J. Zmuidzinas^{1,2}

1 California Institute of Technology, Pasadena, CA 91125, USA,
Email: Karpov@submm.caltech.edu

2 Jet Propulsion Laboratory, Pasadena, CA 91109, USA

Abstract

The 1.4 THz SIS mixer is prepared for a heterodyne spectrometer CASIMIR aimed for the stratospheric observatory SOFIA. One of goals of this work is to supply a low noise spectrometer for the studies of the H₂D⁺ 101 - 000 line around 1370 GHz.

We report on the development of a new version of a THz band SIS mixer. In order to reduce the loss in the matching circuit of the mixer we are using Nb/Al microstrip circuit with the Silicon dioxide dielectric layer. The low loss in the circuit using SiO₂ dielectric layer should provide a significant improvement compared to the previously used mixer circuits with SiO dielectric. The mixer is using a quasi optical design in order to couple the SIS junctions with the telescope beam. The mixer chip with a planar double-slot antenna is mounted at the back side of a Silicon lens. The SIS junction normal resistance to the area product RNA is about 6 Ohm per micron square. At the target frequency of about 1.4 THz the on-chip coupling is expected to be better than 70%. With this level of the circuit loss the expected receiver noise may be close to 4-5 hv/k. The receiver design bandwidth is 1300 – 1500 GHz, about 200 GHz wide.

The mixer test with SiO and SiO₂ dielectric in the circuit will be reported.

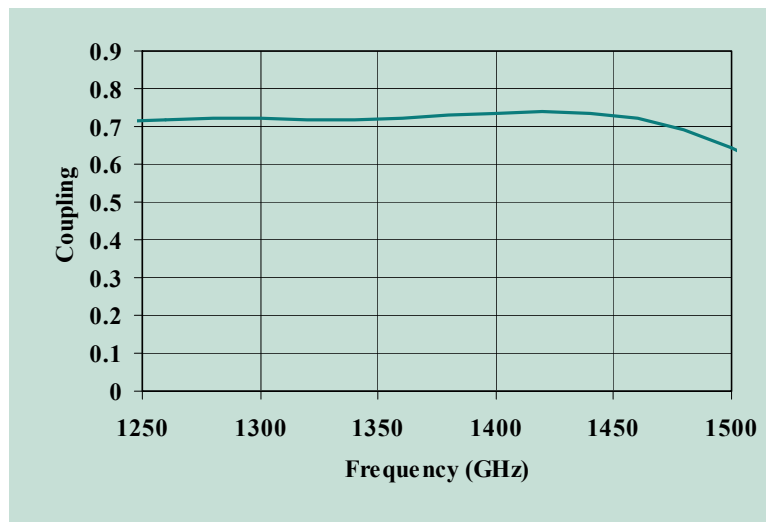


Figure 1. The expected SIS mixer coupling to the signal source in the 1.3-1.5 THz range is better than 70%.

Designs of Broadband Unilateral Finline SIS Mixers Employing 15 μm Silicon-On-Insulator Substrate at THz Frequencies

Boon-Kok Tan^{*‡}, Ghassan Yassin^{*}, Paul Grimes^{*} and Karl Jacobs[†]

^{*}Department of Physics (Astrophysics), Denys Wilkinson Building, Keble Road, Oxford, OX1 3RH, UK.

[†]KOSMA, I. Physikalisches Institut, University of Cologne, Germany.

[‡]Contact: tanbk@astro.ox.ac.uk, phone +44 1865 273303

Abstract—We present the design of two niobium single-ended Superconductor-Insulator-Superconductor (SIS) mixers optimized to work in the frequency range of 600–700 GHz. A key feature of this new mixer design is the utilization of a unilateral finline taper. This transition is significantly easier to design and simulate than the previously employed antipodal finline, and more importantly it simplifies the chip fabrication considerably since the fins do not overlap at any stage. RF power propagating in the finline is coupled to the microstrip either directly from the slotline to microstrip, or more efficiently via a coplanar waveguide (CPW). Another novel feature of our design is the fabrication of the mixer chip on a very thin silicon substrate which will be achieved using Silicon-On-Insulator (SOI) technology. This will allow easy matching of the incoming signal from the feed horn to the loaded waveguide and allows the lightweight mixer chip to be held in the E-plane of the waveguide using gold beam leads, eliminating the need for a deep groove in the waveguide wall. These new features yield a significantly shorter chip and allow wider RF bandwidth since the excitation of higher order modes in the groove has been avoided. The mixer block is extremely simple, composing a smooth-walled horn and a waveguide section without any complicated mechanical features. In this paper, we present the details of the mixer chip, including various transition sections, tuning circuits and mixer block designs, supported by electromagnetic simulations. We describe the design procedure in detail and predict the full mixer performance using the SuperMix software package.

I. INTRODUCTION

The next generation of astronomical instrument requires a mixer design that is suitable for large format imaging array architecture. The mixer should be easy to produce, repeatable, broadband and compatible with planar circuit technology. At submillimetre wavelengths, the finline-tapered mixer design which is compact and easy to fabricate offers a very attractive option to satisfy this requirement. Finline mixers do not require complicated waveguide structures and do not rely on mechanical tuners, i.e. backshorts or E-plane tuners. All the superconducting circuitry is fabricated using planar circuit technology. They have wide RF bandwidth and the large substrate area makes integrating additional mixer circuits elegant and simple.

One essential feature of the finline mixer is that the entire mixer, from the feed horn to the IF output of the mixer chip, lies along the same axis. The mixer chip is held along the E-plane of a split-block waveguide with a groove on the

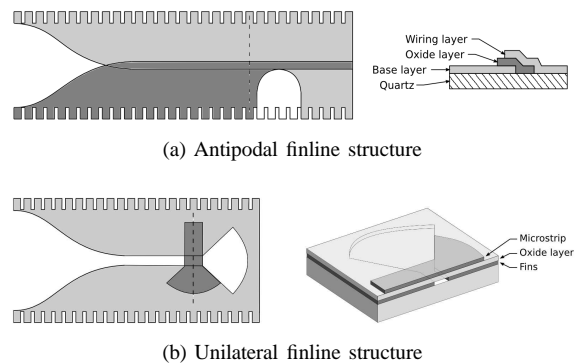


Fig. 1. Finline diagram.

waveguide wall. The RF propagation path is oriented to the axial axis of the feed horn. This greatly simplifies the design of a closed-packed imaging array, since the size of the whole mixer is completely defined by the footprint of the horn aperture. This becomes even more attractive at higher frequency.

Traditionally, finline mixers use antipodal fins to couple RF signal from the waveguide to the microstrip line containing the miniature SIS tunnel junction. As shown in Figure 1(a), the metallisation for the base and the wiring layer is in the form of two niobium fins separated by 400 nm of oxide. The whole arrangement is deposited on a conventional 220 μm thick quartz substrate, which can occupy a substantial space in the waveguide. The resulting dielectric loading losses which increases with frequency makes this traditional finline mixers design less attractive at higher frequency band.

An antipodal finline mixer chip comprise of three distinct sections: the non-overlapping fins, the overlapping regions and the microstrip line. The first section tapers down smoothly the high impedance of an unloaded waveguide to match that of a superconducting microstrip line. This also transforms the RF from the waveguide mode into microstrip mode. When the fins starts to overlap, it behaves more like a parallel-plate waveguide with the effective width equal to the overlap region. The overlapping width is widened until it is large enough to ignore the fringing effects. This then slowly tapered to the required width of the microstrip line by a semicircular cutout, as shown in Figure 1(a). This technology had been fabricated and tested by Yassin et. al. [1], [2], [3] at various submillimeter bands.

They demonstrated state-of-the-art performance, comparable to the more conventional probe-coupled waveguide mixer.

Despite the excellent performance of an antipodal finline mixer, there are some shortcomings. The need of overlapping region makes the mixer chip longer, and is susceptible to shorting during the fabrication process. The electromagnetic behaviour of the mixer is also very difficult to simulate, making it hard to design. To overcome these difficulties, we have developed a new waveguide-to-planar circuit transition that replace the antipodal fins with a unilateral finline taper. Unilateral finline mixer retain all the above-mentioned advantages of an antipodal finline mixers, but have no overlapping taper region. This yield a shorter mixer chip, and hence reduce the losses and enable more devices to be fabricated on the same wafer. This will significantly reduce the time needed to produce a large number of mixer chips for a focal plane array.

As seen from Figure 1(b), the unilateral fins transform the RF power from the waveguide mode into a slotline without any additional complicated structures. The narrow slotline on the other hand provides a natural band-pass filter to prevent the IF signal entering the mixer chip. The transition from slotline to microstrip or coplanar waveguide (CPW) can be done easily and are broadband as well. This design is straightforward and its electromagnetic behaviour can be easily simulated using conventional software package like HFSS or well-understood algorithms such as the Optimum Taper Method or Spectral domain analysis [4]. This has already been demonstrated in conjunction with Transition-Edge Sensors (TES) for CLOVER project [5] (fabricated at University of Cambridge [6]) and shown to works very well.

Another novelty of our new mixer design is that the entire superconducting circuit is deposited on a $15\ \mu\text{m}$ thick silicon substrate using the Silicon-On-Insulator (SOI) technology, which was not available until recently. This allows the thin mixer chip to be positioned across the split-block waveguide without a supporting groove in the waveguide wall, avoiding the excitation of higher order modes. The chip is simply supported by gold beam leads deposited on the substrate. Thin substrate decreases the dielectric loading losses, and allows the finline mixer design to be extended well into the THz regime. SOI technology also allows the mixer chip to be shaped into any desirable form using photolithography rather than dicing. This leaves more freedom in designing the matching notches, which are used to match the impedance of the air-filled waveguide to the loaded waveguide for broadband performance.

In this paper, we lay out the design of our unilateral finline mixer in Section II, and proceed to discuss in detail each component building up to the final mixer design. We emphasize the RF design procedure of the various transitions, the tuning circuit and the RF choke in this section. The IF matching transformers design is explained in Section III and we study the heterodyne performance of the complete mixer design predicted by the SuperMix[10] in Section IV. The design of the mixer block and its feed horn is presented in the subsequent section, before we conclude our paper.

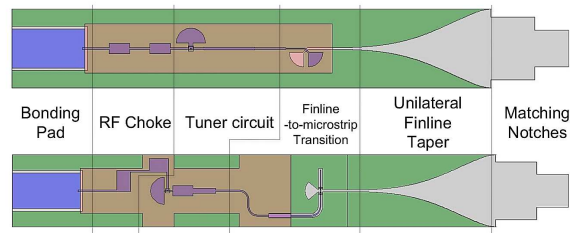


Fig. 2. Overview of the unilateral finline mixer design, with two different types of finline-to-microstrip transition, showing the different components that make up the complete mixer chip.

TABLE I
GENERAL MATERIAL AND DIMENSION OF OUR SIS MIXER CHIPS.

Structure	Material	Dimension
SIS junction	Nb/AIO _x /Nb	$1\ \mu\text{m}^2$
Substrate	Silicon	$15\ \mu\text{m}$
Ground plane	Niobium	$250\ \text{nm}$
Dielectric layer	Silicon monoxide	$475\ \text{nm}$
Signal layer	Niobium	$400\ \text{nm}$
Waveguide	Aluminium	$320 \times 160\ \mu\text{m}$

II. MIXER DESIGNS

Figure 2 shows the basic components that make up our finline mixer chip. It comprises 6 major sections, following the direction of the RF signal propagation: a 2-step matching notch, unilateral finline taper, finline-to-microstrip transition, superconducting tuning circuit, RF chokes and an IF bonding pad. We have designed two different mixer layouts, differing mainly by the way used to couple power from the finline to the microstrip. The first design employ a direct slotline-to-microstrip transition (herein after known as the direct-mixer) and the second utilize an intermittent coplanar waveguide (CPW) section to better match the impedance of the slotline and the microstrip (herein after known as the CPW-mixer). Our mixers are designed to work in conjunction with a circular Nb/AIO_x/Nb SIS tunnel junction with the total area of $1\ \mu\text{m}^2$. This corresponds to a normal resistance of approximately $20\ \Omega$ and junction capacitance of $75\ \text{fF}$, leading to $\omega R_n C \simeq 1$ at $650\ \text{GHz}$. Table I summarizes the material and dimensions of the common structures used in both mixer designs.

The mixer design procedure is rather straightforward, using various commercially or freely available software packages, and is summarized as follow:

- 1) Finline taper designed using FinSynth [7] or HFSS.
- 2) Transition from finline to microstrip, mixer tuning circuit, IF choke and other superconducting circuits using Ansoft Designer and HFSS.
- 3) Superconductivity was included by inserting surface inductance to the perfect conductor structure in HFSS
- 4) Complete mixer chip simulation in HFSS.
- 5) Mixer performances verified using SuperMix by feeding the scattering matrices of electromagnetic components from HFSS.

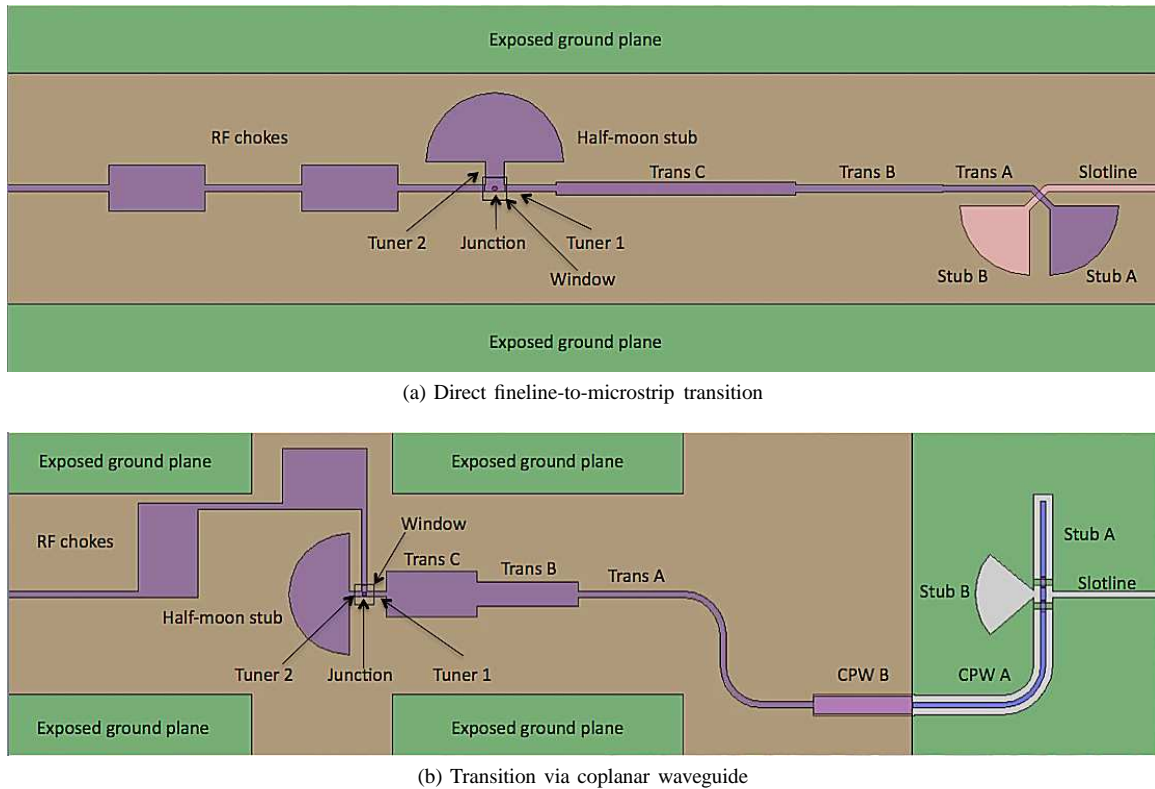


Fig. 3. Two different types of unilateral finline SIS mixer employing SOI substrate.

A. Finline-to-microstrip transition

Complex superconducting planar circuits are usually fabricated in microstrip because this type of transmission line confines the frequency independent TEM fields between the strip and the ground plane well. Once the RF power is converted into the microstrip mode, the back of the finline chip need not be surrounded by waveguide anymore, hence all additional circuitry can be elegantly incorporated. The transition from the slotline at the output of the unilateral finline to the microstrip can be realized either through direct coupling across the dielectric layer, or more efficiently via intermittent CPW sections. We have designed our mixers using both types of transition. The advantage of the latter option is that it offers a wide range of impedance that can be matched to the relatively high impedance of the unilateral finline. The drawback is that this design is slightly more complicated. Both designs share the same tuning circuit and utilize similar fabrication steps, and can be fabricated on a single wafer. Figure 3 shows the design of the planar circuit for both mixer chips in detail, and the critical dimensions are tabulated in Table II and III. The "exposed ground plane" in the figure is where the gold beam leads will be deposited to earth the chip. The oxide layer around the junction, about $10 \times 10 \mu\text{m}$ in area, is deposited with only about half of the thickness of the rest of the area. This is to ensure the wiring layer had a good contact with upper layer of the SIS junction.

1) *Direct finline-to-microstrip transition (3a)*: This layout is simple and elegant, however the flexibility in design is much restricted by the lateral dimensional limitation of photolithography in fabricating the slotline and microstrip. The narrow-

est slotline feasible with modern photolithography is about $2.5 \mu\text{m}$, which is about 70Ω on a $15 \mu\text{m}$ silicon substrate. This is much higher than the smallest microstrip feasible, i.e. $3 \mu\text{m}$ wide microstrip is only about 20Ω . Hence, this mismatch must be included in the design of the transformer section leading to the junction. The incoming slotline is terminated by a 90° radial stub of approximately $\lambda_g/4$ in radius, forcing the RF power to couple to the microstrip. The microstrip line is also terminated by a similar radial stub to provide a short to the incoming RF signal. The advantage of this simple structure is that the RF path is aligned along with the central axis of the mixer chip, and different layers of material are clearly separated, easing the fabrication process.

2) *Transition via coplanar waveguide (3b)*: The impedance of a CPW can be easily adjusted to match that of the slotline and microstrip, since the characteristic impedance of a CPW is largely dependant on the ratio between the width of the central strip and the width of the gaps. The central strip and the ground plane can be fabricated simultaneously in one photolithography step to ensure better symmetrical alignment. We first transform the slotline to a CPW via an extended CPW stub and a radial slotline stub. Two air-bridges are deployed at both side of the slotline, across the CPW, to make sure that the ground planes are equipotential. One slight complication in this design compared to the previous one is that to achieve a low impedance CPW without a very wide central strip, the gap width has to be very small. This ultra-narrow gap can be achieved with a quasi-CPW structure (Section CPW B shown in Figure 3(b)), where the central strip and the ground plane are separated by the thin oxide layer. The gap is defined by

TABLE II

CRITICAL DIMENSION OF THE TUNING CIRCUITS, INCLUDING THE FINLINE-TO-MICROSTRIP TRANSITION, FOR DIRECT TRANSITION MIXER DESIGN. ALL DIMENSION IN μM .

	Stub A	Stub B	Halfmoon Stub	Slotline	Trans A	Trans B	Trans C	Tuner 1	Tuner 2	RF Chokes
Width/Radius	30	30	30	3.0	2.5	3.5	5.5	3.0	8.5	20/3
Length/Angle	90°	90°	180°	50.0	38.5	64.0	104.5	26.5	11.5	42.0

TABLE III

CRITICAL DIMENSION OF THE TUNING CIRCUITS, INCLUDING THE FINLINE-TO-MICROSTRIP TRANSITION, FOR CPW-MIXER DESIGN. ALL DIMENSION IN μM .

	Stub A	Stub B	Halfmoon Stub	Slotline	CPW A	CPW B	Trans A	Trans B	Trans C	Tuner 1	Tuner 2	RF Chokes
Width/Radius	2.5	31.0	30.0	3.0	2.5	8.5	3.0	12.0	23.0	2.5	2.5	30/3
Length/Angle	48.0	80°	180°	60.0	111.5	49.0	155.0	50.0	45.0	10.0	7.0	42.0
CPW gap width	3.5				3.5	1.0						

the effective distance between the edge of the central strip to the ground. Since the central strip and the ground plane of this quasi-CPW section is deposited using two different steps of photolithography, this avoids the problem of short being caused by the ultra-narrow gap. One disadvantage of this structure is that it might cause misalignment of the central strip that leads to imbalanced CPW.

B. Tuner circuit

Conventionally, the tuning circuit used to tune out the junction capacitance is narrow band, determined primarily by the $\omega R_n C$ constant. The standard method is simply to utilize an inductive strip with an end-stub [8] to tune out the capacitance at a particular frequency. Utilizing the twin-junction method [9] with a microstrip to transform the complex impedance of one junction to the complex conjugate of the other one, can provide a broader band performance, but often with the difficulty that both junctions to be fabricated identically. In the following section, we explain in detail our tuner circuit design methodology which can provide a broad band performance by using only a planar circuit structure with a single SIS junction.

Our tuner circuit is composed of mainly four parts: an inductive strip with a half-moon stub, an inductive strip before the junction, a multi-sections transformer and an RF choke. The dimensions of the various components are tabulated in Table II and III.

In order to match the junction impedance across a broader bandwidth, we make use of two inductive strips, tuned at slightly different frequencies, to provide two poles in the matching circuit. The first utilizes a short microstrip section terminated with a half-moon stub acting as a short. Assuming the load impedance of the half-moon stub is close to zero, the length and the width of this inductive strip can be calculated using the standard transmission line equation simplified to

$$l = \frac{1}{Z_0 \beta \omega C}, \quad (1)$$

where Z_0 is the characteristic impedance of the microstrip line, determining the width of the line, and l is the length of the microstrip line in electrical wavelength, which can be easily converted to actual dimension.

The second pole in the matching circuit make use of another short microstrip line before the junction to tune out

the residual impedance at a slightly different frequency (most of the junction impedance had been tuned out by the first inductive strip). Again, the length and width of this microstrip line can be calculated using the standard transmission line equation.

$$Y_s = \frac{Y_l + iY_0 \tan \beta l}{Y_0 + iY_l \tan \beta l} \quad (2)$$

where Y_s is the source impedance, Y_l is the load impedance, which is the residue impedance at the tuned frequency, Y_0 is the characteristic impedance of the line and βl is the propagation constant. By enforcing the imaginary part of Y_s to zero, the length of the strip can thus be obtained in terms of βl . The value of Y_0 can be chosen arbitrarily to determine the width of the line. Combining both inductive strips in conjunction with the junction, the reactance is tuned to zero twice, giving the two poles for better matching.

At this stage, a 3-step transformer is deployed to match the final load impedance (consist of the junction and the two inductive strips) to the input impedance of the slotline. The initial dimension of the transformer can be estimated by standard quarter-wavelength steps, or of Chebyshev design. The transformer matches the Z_0 of the slotline to the real part of the load impedance at the central frequency. The final dimension of transformer can be optimized using conventional software package like HFSS to include various other effects such as the superconducting surface impedance etc.

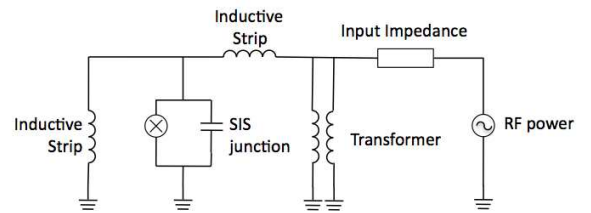


Fig. 4. Electrical diagram of the RF tuning network for our finline mixers.

Figure 4 shows the electrical network representation of our tuning circuit, and Figure 5 illustrates an example using the above method. Figure 5(a) shows the result of using an inductive strip with the half-moon stub to tune out the capacitance of the junction at the first frequency (i.e. 750 GHz in this case). Figure 5(b) shows the result of tuning using the

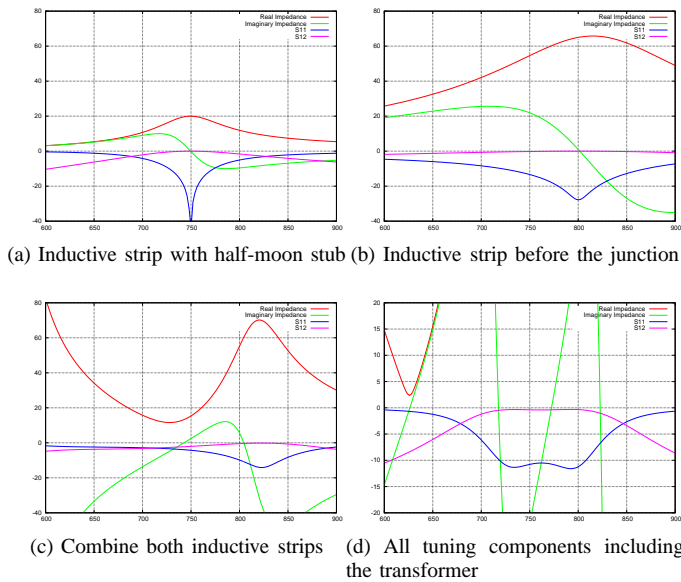


Fig. 5. Example illustrates how each component in the tuning circuits works toward a broadband performance.

second inductive strip to tune out the residual impedance at slightly higher frequency (800 GHz in this case). As can be seen in Figure 5(c), when both the inductive strips are used, there are two poles in the reactance curve that cross the zero axis at the two tuned-out frequencies. Figure 5(d) shows the wide band performance of the tuner after matching the real part of the load impedance to the slotline using the transformer, which exhibit a twin-peaks feature. In this example, the tuning band is tuned slightly higher, as the superconducting surface impedance tends to shift the tuned frequency band downward. It should be noted that this simple circuit representation only gives a preliminary estimation of the required dimension of various parts. The final design is often simulated and optimised in a 3-D electromagnetic simulators such as HFSS to include effects of thickness, superconducting surface reactance, dielectric tangential loss, etc.

C. RF choke

The RF choke is made of alternating high and low impedance $\lambda_g/4$ sections of microstrip to provide high rejection to the RF signal over the operating band. This avoids RF signal leaking into the IF path and ensure that most of the RF power is coupled to the SIS junction. The width of the high and low impedance sections are chosen so as not to be too narrow or so wide to induce high IF capacitance. We combine all these components into planar circuit together with the unilateral finlines and SOI substrate to simulate the electromagnetic behaviour of the complete mixer chip. Figure 6 shows the return loss and the insertion loss of the complete RF design predicted by HFSS. Both designs have about 100 GHz bandwidth across 600 GHz to 700 GHz band. The power coupled to the junction is better than -0.5 dB in both case, across the operating bandwidth. Outside the design band, the performance of the CPW-mixer deteriorates more slowly compare to the direct-mixer. This is mostly due to the

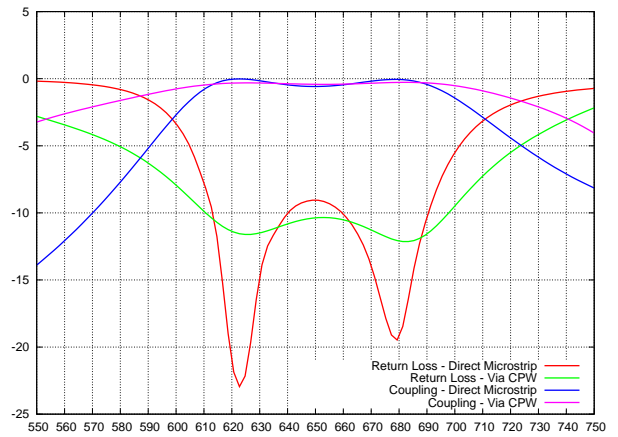
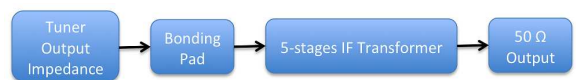


Fig. 6. HFSS simulation shows that the tuner design exhibit broad bandwidth, with about 100 GHz centered at 650 GHz.

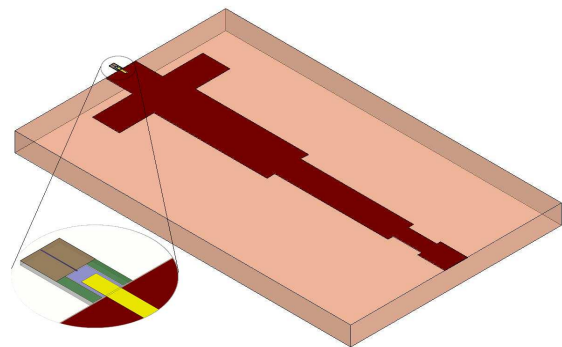
severe mismatch of the slotline to microstrip away from the central frequency band.

III. IF TRANSFORMER DESIGN

The physical structure of planar circuits and the finline of the mixer chip will be seen as a lumped RLC load at the IF band, which is not purely resistive. We thus represent the output impedance of the mixer chip as an RLC circuit, and match this load to the 50 Ω input impedance of the low-noise amplifier (LNA), to provide wide IF bandwidth operation. Given that the physical dimensions of both of the mixer designs are similar, the IF impedance would not be very much different, and hence only one IF transformer design is explored. The design procedure are fairly simple, with standard transformer design methodology, and can be optimized using conventional circuit design packages. We use HFSS to provide the flexibility to include more realistic structures such as the bonding pad and the gold beam leads. This is to make certain that we include the effective inductance induced by these structures in the design of the matching transformer.



(a) Flowchart of IF transformer design.



(b) Diagram of IF transformer.

Fig. 7. IF transformer to match the output complex impedance of the mixer chip to the 50 Ω IF output.

TABLE IV
ALL DIMENSION IN MM. IF TRANSFORMER DIMENSION. THE IF TRANSFORMER WILL BE THE SAME FOR BOTH MIXER DESIGN.

	Sect 1	Sect 2	Sect 3	Sect 4	Sect 5	Sect 6	Pocket size
Width	1.00	3.68	1.38	0.86	0.51	0.76	7.0
Length	0.90	0.90	3.76	3.75	0.94	0.9 0	11.15

Figure 7 shows the various components included in the IF transformer design. The following steps summarize the complete design procedure for the IF transformer after the RF part of the mixer design is complete:

- 1) Obtain the output impedance of the mixer chip seen from the IF port from Ansoft Designer's circuit or SuperMix package
- 2) At the frequency where the real part of the impedance is zero, find the reactance and estimate the value of the capacitor or inductor
- 3) Represent the RF mixer chip as an RLC equivalent
- 4) Use Designer or any other simple circuit simulation package to design the impedance matching transformer
- 5) Include the gold beam leads and the bonding pads in HFSS to optimize the transformer design
- 6) Export the scattering matrix into SuperMix to verify the final full mixer heterodyne IF performance

Table IV lists the dimension of the IF transformer used in our mixer design. As can be seen from Figure 8, HFSS calculated that the return loss to be less than -10 dB from about 2 to 12 GHz. This matches very well with our LNA's bandwidth, and is wide enough for most astronomical requirements.

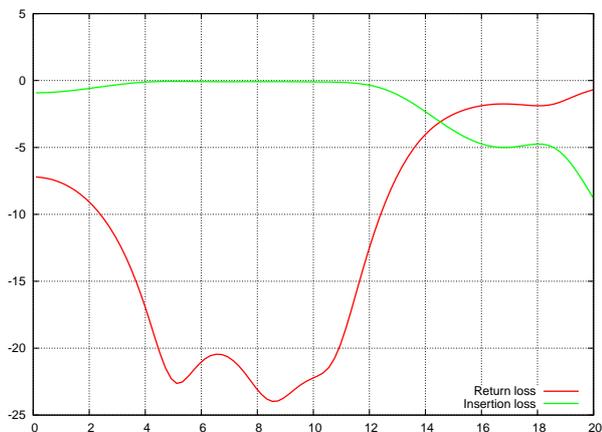


Fig. 8. HFSS simulation shows that the transformer had better than -15 dB return loss from 4 GHz to 12 GHz IF band.

IV. SUPERMIX SIMULATION RESULTS

To verify and understand the heterodyne mixing behaviour of the mixer, we exported the scattering matrices of all the components computed using electromagnetic software package, mainly from HFSS, to SuperMix. In this way, we combine both the more accurate description of electromagnetism behaviour by the electromagnetic package, and make use of SuperMix to predict the superconducting mixer heterodyne performance, such as noise temperature and gain. The dimension obtained from the electromagnetic design can also

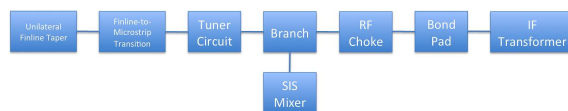


Fig. 9. Flow chart shows the various components included in the SuperMix simulation.

be input directly to SuperMix as various circuit components for cross-checking purpose, and both methods generally give similar results.

Figure 9 shows all the components included in our SuperMix circuits, and Figure 10 and 11 show the results of the calculation. Both mixer designs yield very flat RF gain response across the operating band. The IF gain is also stable across the desired IF bandwidth. The noise temperature of both mixers is estimated to be lower than 50 K across the whole design band. Again, CPW-mixer design yield a slightly wider RF band, agreeing with the performance predicted by HFSS. These results will serve as a good guideline to better understand the experimental measurement of the real mixer.

V. MIXER BLOCK AND FEED

The mixer block to house the SOI finline mixer is extremely simple. As shown in Figure 12, only a straight rectangular waveguide is needed, with a pocket for the IF board to be sit on. At the front of the rectangular waveguide is a cone-shaped circular-to-rectangular transition to make sure that the signal from the feed horn is coupled to the mixer chip efficiently. This can be done by simply drilling a 10° opening cone at the inlet of the split-block after the waveguide and other component have been machined. This 10° smooth-cone transition have been demonstrated to work with HARP-B mixers [11] and HFSS simulations predict that the return loss across the band would be less than -20 dB, as shown in Figure 13.

The mixer block will be connected to a smooth-walled horn [12] designed using genetic algorithm. These horns shows good circularity and low side-lobes level, comparable to conventional corrugated horns. They are easy to manufacture and time/cost saving, which is important for multi-pixel focal plane array applications.

VI. CONCLUSION

We have presented the design of a broadband unilateral finline SIS mixer at 650 GHz utilizing SOI technology. The design results in a tunerless, elegant yet fully integrated planar circuits, and an easy-to-fabricate mixer chip and block. A smooth-walled horn that is manufactured by a simple drilling technique, will be used to feed the signal to the mixer. The use of planar circuit technology ensures that a large number of mixers can be produced in short time and reduces the tolerances between mixer chips. This shall greatly improves the performance and reduces the cost of constructing large-format mixer arrays. The performance was fully simulated using rigorous electromagnetic methods, exported into SuperMix package, and the heterodyne performance has been reported. The chip design will be fabricated at KOSMA, University of Cologne and the experimental measurement of the mixer performance will take place soon.

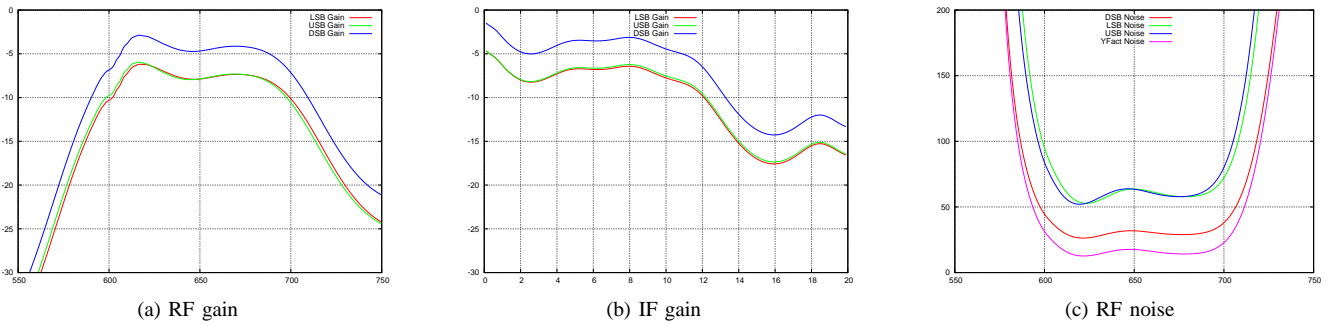


Fig. 10. SuperMix simulation results of direct-mixer chip.

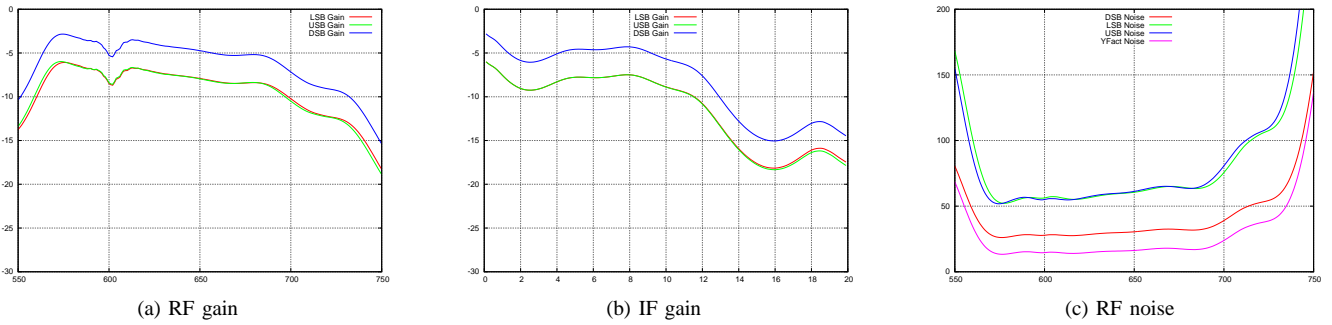


Fig. 11. SuperMix simulation results of CPW-mixer chip.

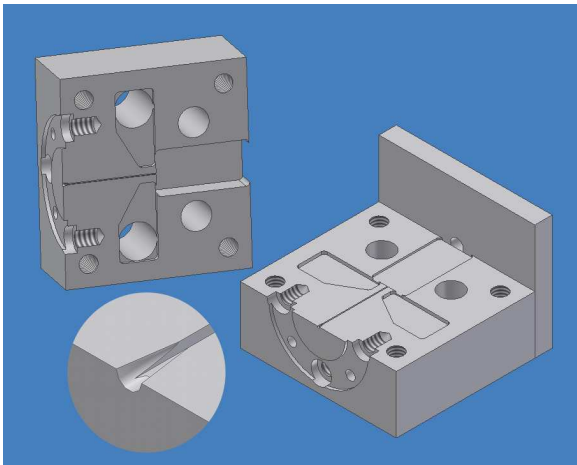


Fig. 12. The drawing of the block that will be used to house the mixer chip. The two butterfly-wing-structure are used to hold the metal that couple the magnetic field from the coil to suppress the Josephson current. It will be fed from the two poles on top of the mixer block. The IF output will be tapped from the IF board using standard SMA connector at the back of the mixer block.

ACKNOWLEDGMENT

The project is part of a program in collaboration with the Detector Physics group at Cambridge and KOSMA, University of Cologne, and is partially funded by AMSTAR+.

REFERENCES

[1] G. Yassin, R. Padman, S. Withington, K. Jacobs, and S. Wulff. Broadband 230 GHz finline mixer for astronomical imaging arrays. *Electronics Letters*, 33:498–500, March 1997.

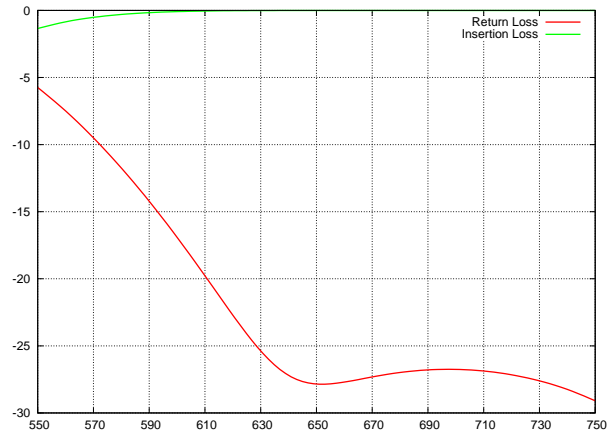


Fig. 13. Return loss and insertion loss for the circular to rectangular waveguide with an opening angle of 10° . The input throat opening of the 700 GHz smooth-walled horn is 408 μm .

[2] G. Yassin, S. Withington, M. Buffey, K. Jacobs, and S. Wulff. A 350-GHz SIS antipodal finline mixer. *IEEE Transactions on Microwave Theory Techniques*, 48:662–669, April 2000.

[3] Kittara P., Jiralucksanawong A., Yassin G., Wangsuya S., and Leech J. The design of Potter horns for THz applications using a genetic algorithm. *Int. J. Infrared Milli. Waves*, 28:1103–1114.

[4] Yassin G., Grimes P. K., King O.G., and North C. E. Waveguide-to-planar circuit transition for millimetre-wave detectors. *Electronics Letters*, 44(14).

[5] L. Piccirillo, P. Ade, M. D. Audley, C. Baines, R. Battye, M. Brown, P. Calisse, A. Challinor, W. D. Duncan, P. Ferreira, W. Gear, D. M. Glowacka, and et. al. The CIOVER experiment. In *Society of Photo-Optical Instrumentation Engineers (SPIE) Conference Series*, volume 7020 of *Society of Photo-Optical Instrumentation Engineers (SPIE) Conference Series*, August 2008.

[6] M. D. Audley, R. W. Barker, M. Crane, R. Dace, D. Glowacka, D. J. Goldie, A. N. Lasenby, H. M. Stevenson, V. Tsaneva, S. Withington,

- P. Grimes, B. Johnson, G. Yassin, L. Piccirillo, G. Pisano, W. D. Duncan, G. C. Hilton, K. D. Irwin, C. D. Reintsema, and M. Halpern. TES imaging array technology for C₁OVER. In *Society of Photo-Optical Instrumentation Engineers (SPIE) Conference Series*, volume 6275 of *Society of Photo-Optical Instrumentation Engineers (SPIE) Conference Series*, July 2006.
- [7] C. North, G. Yassin, and P. Grimes. Rigorous Analysis and Design of Finline Tapers for High Performance Millimetre and Submillimetre Detectors. In A. Hedden, M. Reese, D. Santavicca, L. Frunzio, D. Prober, P. Piitz, C. Groppi, & C. Walker, editor, *Seventeenth International Symposium on Space Terahertz Technology, held May 10-12, 2006 at Observatoire de Paris, LERMA. Paris, France., p.284-287*, pages 284–287, May 2006.
- [8] K. Jacobs, U. Kotthaus, and B. Vowinkel. Simulated performance and model measurements of an SIS waveguide mixer using integrated tuning structures. *International Journal of Infrared and Millimeter Waves*, 13:15–26, January 1992.
- [9] V. I. Belitskii, M. A. Tarasov, S. A. Kovtoniuk, L. V. Filippenko, and O. V. Kaplunenko. Low noise completely quasioptical SIS receiver for radioastronomy at 115 GHz. *International Journal of Infrared and Millimeter Waves*, 13:389–396, April 1992.
- [10] J. Ward, F. Rice, G. Chattopadhyay, and J. Zmuidzinis. SuperMix: A Flexible Software Library for High-Frequency Circuit Simulation, Including SIS Mixers And Superconducting Elements. In T. W. Crowe & R. M. Weikle, editor, *Proceedings of the Tenth International Symposium on Space Terahertz Technology, held March 16-18, 1999, at the University of Virginia, Charlottesville, VA USA. Organized by University of Virginia, Applied Electrophysics Laboratory. Organizing committee: Thomas W. Crowe and Robert M. Weikle. 1999, p.268*, pages 268–+, March 1999.
- [11] H. Smith, R. E. Hills, S. Withington, J. Richer, J. Leech, R. Williamson, H. Gibson, R. Dace, P. G. Ananthasubramanian, R. W. Barker, R. Baldwin, and et. al. HARP-B: a 350-GHz 16-element focal plane array for the James Clerk Maxwell telescope. In T. G. Phillips & J. Zmuidzinis, editor, *Society of Photo-Optical Instrumentation Engineers (SPIE) Conference Series*, volume 4855 of *Society of Photo-Optical Instrumentation Engineers (SPIE) Conference Series*, pages 338–348, February 2003.
- [12] P. Kittara, J. Leech, G. Yassin, B. K. Tan, A. Jiralucksanawong, and S. Wangsuya. High performance smooth-walled feed horns for focal plane arrays. In W. Wild, editor, *Proceedings of the Nineteenth International Symposium on Space Terahertz Technology, held April 28-30, 2008, in Groningen. Edited by Wolfgang Wild. Sponsored by SRON, Netherlands Institute for Space Research, TUDelft, Delft University of Technology, and the University of Groningen. 2008, p.346*, pages 346–+, April 2008.

An SIS unilateral finline mixer with an ultra-wide IF bandwidth

Yangjun Zhou^{*†}, Jamie Leech^{*}, Paul Grimes^{*} and Ghassan Yassin^{*}

^{*}*Dept. of Physics, University of Oxford, UK*

[†]Contact: yangjun.zhou@physics.ox.ac.uk, phone 0044+01865273433

Abstract—In this paper, we will present the design and the simulation of a 230GHz finline Ultra-wide IF Bandwidth SIS mixer. This mixer will be used in a novel millimeter-wave heterodyne interferometer: GUBBINS. GUBBINS is designed to demonstrate high surface brightness mm-wave interferometry at modest spatial and spectrum resolution. Its observational targets are the spectrum of the Sunyaev-Zel'dovich effect in the brightness galaxy cluster[3]. The archetype of the mixer design described here is an antipodal finline SIS mixer designed by Paul Grimes in Oxford Experimental Cosmology group in 2008[1]. Here several improvement and modification are made to simplify the design and fabrication, and also enhance the IF bandwidth. An unilateral finline replaces the complicated antipodal finline. No RF bandpass filter is needed after finline. The tuning circuit design presented here aims to achieve wider RF coupling bandwidth, even though only a single junction is used. A multi-stage IF transformer follows the IF bonding pad matching the IF output of the mixer to the input of the IF amplifier, as well as reducing the impact of the parasitical capacitance introduced by the RF finline and RF radial stub.

I. INTRODUCTION

In recent years, considerable astronomical research has been focused in the millimeter and submillimeter band. The increasing sensitivity of the millimeter and submillimeter receiver enables the observation of fainter astronomical target, e.g the cosmic microwave background radiation. A novel heterodyne interferometer telescope- GUBBINS (220GHz Ultra-BroadBand INterferometer for S-Z) is under construction in Oxford, with the aim of observing galaxy clusters via the Sunyaev-Zel'dovich effect and demonstrating high surface brightness mm-wave interferometer at modest spatial and spectral resolutions.

The observation of the continuous source, like cosmic microwave background, requires extremely high brightness sensitivity. The sensitivity of a receiver does not only depend on the noise performance, but also on the available instantaneous bandwidth over which detected power is integrated. In a heterodyne receiver, the instantaneous bandwidth is determined by the IF bandwidth. Also, wide IF bandwidth mixers allow spectroscopic observations to detect several spectral lines simultaneously. But wide IF bandwidth SIS mixers are still rare currently because several key design challenges are waiting to be solved. Wide RF bandwidth signal has to be coupled into SIS junction efficiently, while the IF signal generated in the SIS junction should not leak into the RF circuit of the mixer. The SIS junction must see a reasonably constant embedding impedance throughout the IF bandwidth. This enables the IF

signal to be well coupled from the junction to the input of cold IF amplifier over a wide IF bandwidth.

The finline mixer chip introduced here is not sensitive to mixer block fabrication tolerance, hence ease the requirement for the precision of the mixer block. The large chip area also allows elegant integration of complicated planar circuit onto a single chip. The SIS finline mixer design presented below is an improved unilateral finline design based on a direct transition from slotline to microstrip, mounted on a $60\mu\text{m}$ silicon substrate. The silicon substrate reduces the impedance difference between finline slot and microstrip transmission line, which acts to improve the scattering parameter performance. The designed includes the following components:

- A silicon substrate with 2-stage rectangular notch at the front end, used to transfer the signal from unloaded waveguide to loaded waveguide. The mixer chip is mounted in the E-plane split mixer block, supported by grooves in the waveguide wall.
- A unilateral finline transition to couple the signal from loaded waveguide to microstrip transmission line, where the SIS junction is fabricated. Quarter wavelength serrations are added to each side of the finline to prevent RF power propagating in the grooves.
- A multi-stage microstrip tuning circuit around the SIS junction to tune out the parasitical capacitance of the SIS junction over a very wide RF bandwidth. A 5-stage RF choke is integrated in the tuning circuit to prevent RF signal leaking into the IF output port.
- At the rear of the chip, the IF bonding pad is used to transmit the IF signals from the mixer to the IF transformer using several aluminium bond wires. It is carefully simulated in HFSS to present inductance as low as possible and good transmission performance over a wide IF bandwidth.
- A five-stage quarter-wave microstrip transformer is incorporated onto the IF connection bonding pad to match the mixer output to the 50ohms SMA connector and IF amplifier input over the 2-20 GHz IF band.

A. Mixer design

The mixer is fed by a waveguide diagonal horn which couples into a unilateral finline taper, the taper then couples the signal into a microstrip line which contains the superconducting tunnel junction[4]. The device is fed by a miniature microstrip line, the field of which does not interact

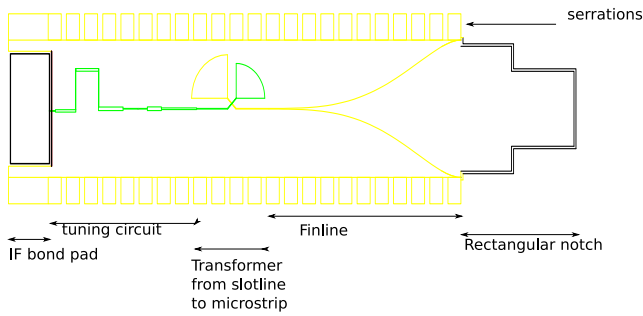


Fig. 1. AutoCAD photo of an ultra-wide IF bandwidth finline SIS mixer chip. The RF signal is coupled from free space from the right and the IF signal leaves from the IF bond pad, on the right.

with the waveguide mode, thus neither back-short or E-plane tuner is needed. The mixer chip will be fabricated on $60\mu\text{m}$ silicon substrate and uses a $200/10/100$ nm thick NB-AIOx-Nb trilayer, a 490 nm thick SiO dielectric evaporated separately in two layers, 240nm and 250nm , with a dielectric constant of 5.8 and 400nm thick Nb wiring layer.

A schematic of diagram of the mixer chip in shown in Fig.1. In the following section , we will introduce the detail of each Mixer component.

1) *Transmission line:* The finline mixer is deposited on a $60\mu\text{m}$ silicon substrate which supports the structure in the E-plane of a rectangular waveguide. The wafer is supported in a groove which runs along the sides of the waveguide. Waveguide dimension is standard WR-4 , $550\mu\text{m} \times 1100\mu\text{m}$. Impedance matching between the loaded waveguide and free space is achieved by a 2-step binomial multisection notch shown in Fig. 1. The length of each step is approximately one quarter of the guide wavelength at that section and the impedance of each step can be determined by the binomial formulars(eq. 1) given the impedance of waveguide Z_0 and microstrip Z_L [2]. The widths of each step are optimized in the HFSS software.

$$[tp] \ln \frac{Z_{n+1}}{Z_n} = 2^{-N} C_n^N \ln \frac{Z_L}{Z_0} \quad (1)$$

As stated in the previous paper[1], a lot of care has to be taken in the fabrication of antipodal finline to avoid the narrow spikes that can potentially AC-short the chip , especially at the stage when the fins start to overlap with each other. To overcome this difficulty, A newly developed unilateral finline transition is used to couple the RF power into the mixer chip[5][6][7]. An important advantage of this design is that it provides an extremely wide bandwidth transition from the waveguide impedance to a low microstrip impedance. For Nb film with 500nm thickness deposited on $60\mu\text{m}$ silicon substrate, an impedance of approximately 36Ω is obtained with a finline gap of $2.5\mu\text{m}$. A microstrip bridge with a width of $2.2\mu\text{m}$ is deposited across the slotline on a 490nm thick layer of SiO and terminated by a shorted quarter-wave radial stub. The finline itself is also terminated by a quarter-wave radial stub which forms a RF short. The quarter-wave radial stub of finline shorts the signals to the microstrip bridge, and then the radial stub of the microstrip shorts the signal again and then directs the signals to the $2.2\mu\text{m}$ microstrip line.

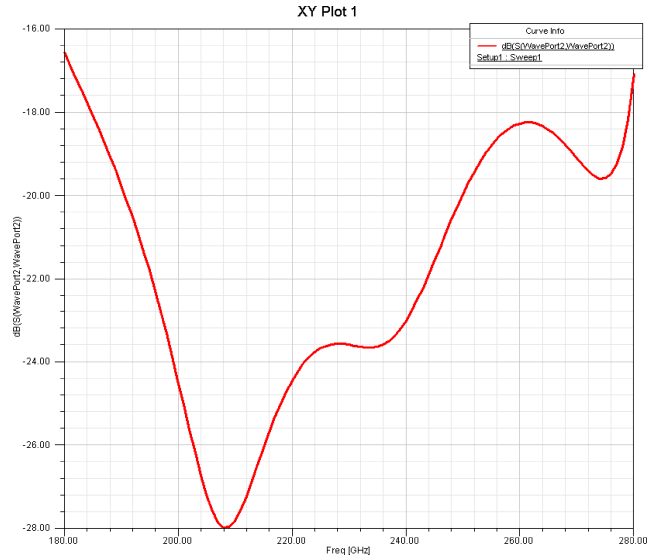
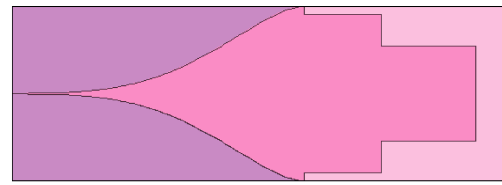


Fig. 2. (Top)HFSS model of the unilateral finline.(Bottom)The scattering parameter of such unilateral finline across RF bandwidth.

In the calculation of the unilateral finline taper, the Optimum Taper Method is used[5], which takes a maximum allowed returned loss for the taper (e.g. -30dB), and then calculates the corresponding cutoff frequency profile along its length. Transverse resonance method is used to give the relationship between the cutoff frequency , the slot width and the propagation constant. Because the cutoff frequency of unilateral finline is right above the IF frequency range, no RF bandpass filter is needed after the finline, which reduces the length of the chip, hence the loss. Figure 2 shows the computed scattering parameter of an unilateral finline taper deposited on a $60\mu\text{m}$ silicon substrate using HFSS software. We found that the bandwidth of the finline taper is restricted by the 2-stage rectangular notch , rather than the finline taper itself.

2) *Tuning circuit:* The RF choke is integrated in the tuning circuit design. We have designed three tuning circuits of different sizes, using the same design method and roughly the same performance, but with various dimensions . Here only one designed will be illustrated and introduced in detail. The schematic diagram of the tuning circuit is shown in Figure 3, with 20Ω , $1\mu\text{m}^2$ SIS junction with a critical current density of $14\text{KA}/\text{cm}^2$ and a specific capacitance of $75\text{fF}/\mu\text{m}^2$. It is a single junction tuned out by two series microstrip stub located before and after the junction, each tuned at two different frequency, giving a wide RF coupling. The $2.5\mu\text{m}$ wide microstrip transmission line deposited on 490nm thickness SiO dielectric layer presents an impedance of roughly 20Ω , ideal for the the coupling to the 20Ω SIS junction. Before

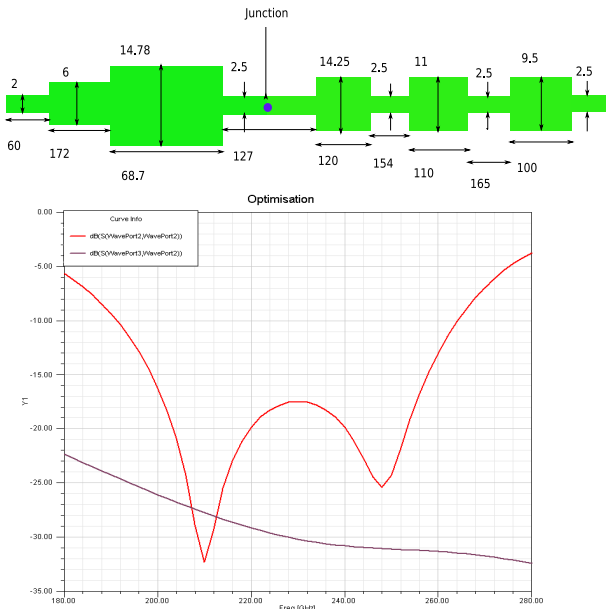


Fig. 3. (Top)Diagram of the tuning circuit with the integrated RF choke. Dimensions are in μm and the SIS junction is shown as a purple dot. The 7-step stubs after the junction are the RF choke. (Bottom) HFSS calculated scattering parameter of the tuning circuit. The red line represents the return loss while the purple line represent the insertion loss.

the SIS junction, a 3-stage Chebyshev transformers is used to realize impedance matching between $2.2\mu m^2$ microstrip line and the SIS junction.

After the SIS junction, 6-stepped width section RF chokes are added to block the unnecessary RF signals leaking into the IF port. The first section of the RF choke also acts as the microstrip stub termination in the tuning circuit.

3) *IF connection and transformer:* The IF signal generated in the SIS junction is transmitted to the wiring layer bond pad at the rear of the chip. This bond pad is connected to the IF transformer through three $50 \mu m$ diameter aluminium bond wires. The 5-step IF transformer is fabricated on $254 \mu m$ thick Roger’s Duroid 6010 substrate. The bonds are kept as short as possible to minimize the inductance of the bond wires. At each side of the chip, there are two bond wire providing a ground connection to the mixer block. The gap between the wiring layer and the ground layer is optimized in HFSS to achieve good performance in the IF coupling(Figure 4).

A five step quarter-wave microstrip transformer is designed following the IF bond pad connection to match the mixer output to the 50Ω SMA connector over 2- 20GHz IF band. The finline and large area stub on the chip will introduce considerable parasitical capacitance. Thus the width and length of the first section of the IF transformer is optimized in Ansoft Designer to enable a good match between the complex output impedance of the SIS mixer chip and the 50Ω IF amplifier(Figure 5).

II. SIMULATED MIXER PERFORMANCE

As well as the HFSS simulations shown above, the mixer designs have been extensively simulated by the software based on Caltech’s SuperMix simulation library. In this section , we

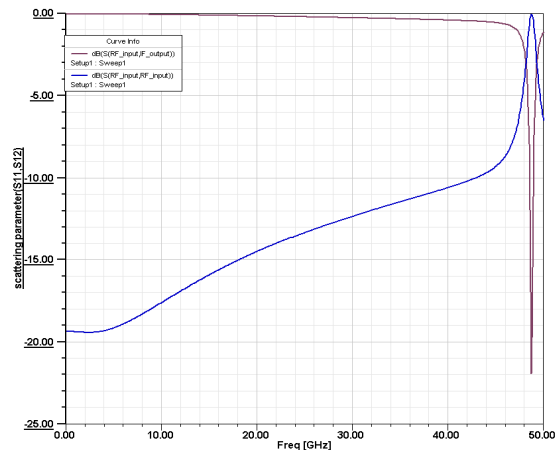
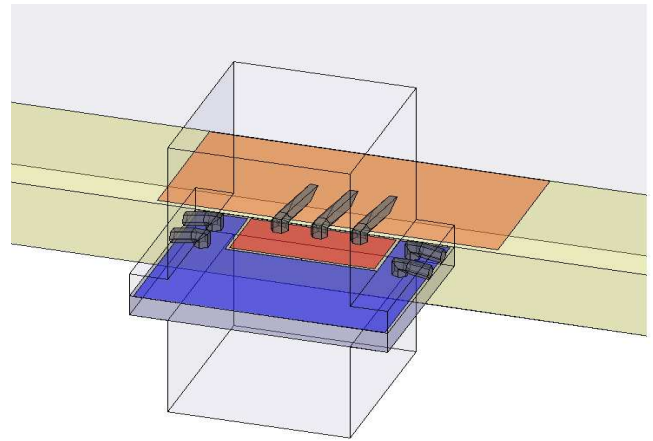


Fig. 4. (Top)HFSS model of the IF bond pad.Bond wires are shown in grey. The blue pad is the ground plane while the red pad is the bonding pad. The orange pad connected to the bonding pad by grey wire is part of the IF transformer.(Bottom)HFSS calculated scattering parameter of the IF connection,normalized to the mixer output impedance of 20Ω)

will present simulation results for the whole chip, including unilateral finline ,tuning circuit, IF bond pad and IF transformer along RF bandwidth, IF bandwidth and various DC bias point. But other receiver components , like the cryostat window, IR shields and the LO injection beamsplitter are not included. The mixer performance along the RF band for the single junction design is present in Figure 6 and the performance along the IF band for the single junction design is presented in Figure 7. In these RF simulation, the mixer is biased at a fixed voltage $2.2mV$ and pumped by a fixed LO power of $40nW$, while the performance calculated at a fixed IF frequency of $10GHz$. In the IF simulation, the voltage bias point and pumped level are the same with the RF while, but the RF frequency is set to be $230GHz$.

III. CONCLUSION

We have designed a novel silicon-substrate unilateral finline mixer which is expected to exhibit wide RF coupling bandwidth and ultra wide IF bandwidth of 2-20GHz. The application of the novel unilateral finline allows wide RF signal

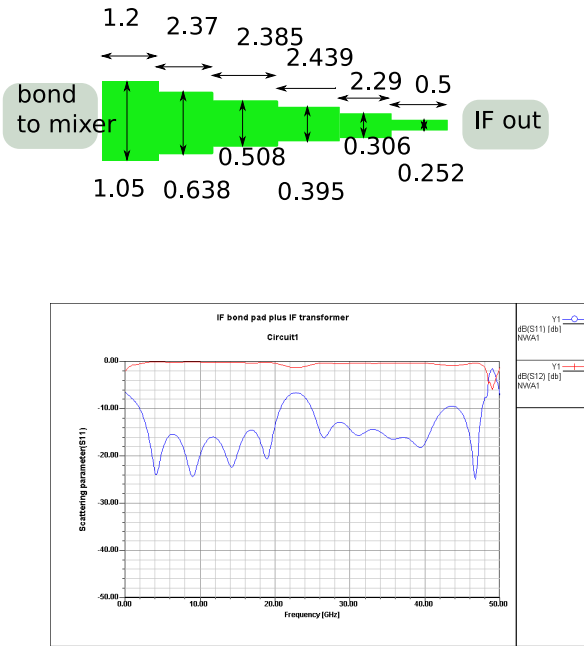


Fig. 5. (Top) Combined scattering parameter of the IF bond pad and the 6-step IF transformer, normalized to 20 Ω at the input end and 50 Ω at the output SMA of amplifier. The dimension shown is in unit of mm. It is calculated by the Ansoft designer. The scattering parameter of IF bond pad is exported from the HFSS simulation. (Bottom) Diagram of the IF output transformer, fabricated on 254 μm thick Duroid 6010LM. The unit in the diagram is μm and the left hand side of the IF transformer is connected to the IF bond pad and the right hand side is connect to the output SMA.

coupling , elegant integration of complicated planar circuit as well as minimum parasitical capacitance. The simulation result from SuperMix demonstrates both the wideband RF and IF operation could be achieved by this high performance mixer.

REFERENCES

[1] Paul K.Grimes, Ghassan Yassin, Karl Jacobs and Jamie Leech, “ Design of SIS finline mixers with ultra-wide IF bandwidths”, in *Proc. 19th Int. Symp. Space THz Tech., Groningen,2008*
 [2] Microwave Engineering, Third Edition, David M.Pozar, ISBN:0-471-32282-2
 [3] P.K. Grimes, C. Holler, M.E. Jones, O.G. King, J. Leech, A.C. Taylor and G. Yassin, “A novel heterodyne interferometer for millimeter and submillimeter astronomy” in *Proc. 19th Int. Symp. Space THz Tech., Groningen,2008*

[4] G.Yassin, P.K. Grimes, O.G. King, and C. E. North, “Waveguide-to-planar circuit transition for millimeter-wave detectors”, *arXiv806.0255v2 [astro-ph] 7Sp 2008*
 [5] Chris North, Ghassan Yassin, Paul Grimes, Rigorous analysis and design of finline tapers for high performance millimeter and submillimeter detectors, 17th International Symposium on Space Terahertz Technology, P2-24
 [6] G. Yassin, S. Withington, Electromagnetic models for superconducting millimeter-wave and submillimeter-wave microstrip transmission line, *J.phys.D: appl. Phys*, vol.28, pp,1083-1991, Apr.1995
 [7] C.Schieblich, J.K.Piotrowski, “Synthesis of Optimum finline tapers using dispersion formulas for arbitrary slot widths and locations”, *IEEE, Trans, Microwave theory Tech, Microwave theory Tech*, pp,981-985, Sept,1980

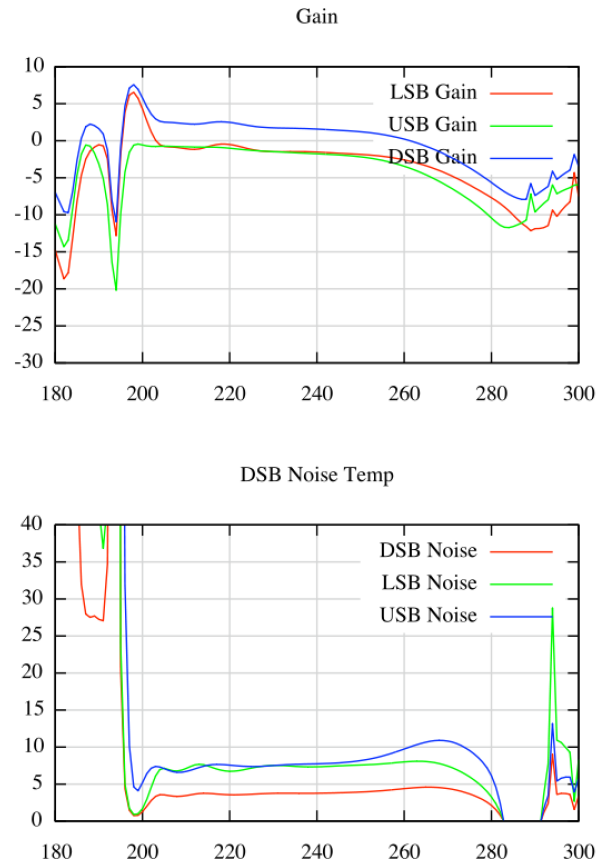


Fig. 6. Supermix calculated mixer conversion gain and noise temperature against the LO frequency the entire mixer chip. The mixer is biased at a fixed bias voltage of 2.2mv and pumped with a fixed LO power of 40nw. The IF frequency is 5GHz.

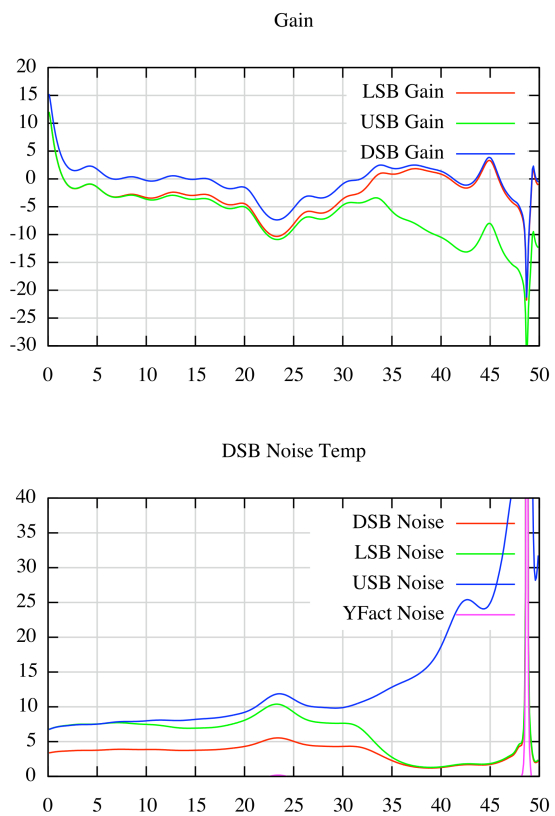


Fig. 7. SuperMix calculated mixer conversion gain (top) and noise temperature (bottom) against IF frequency. The mixer is biased at 2.2mv and pumped by 40nw of LO power at frequency of 230Ghz.

A 1.5 THz waveguide HEB mixer using silicon-on-insulator substrates for the Stratospheric Terahertz Observatory

Jonathan Kawamura¹, Anders Skalaré¹, Jeffrey Stern¹ and Edward Tong²

¹Jet Propulsion Laboratory
California Institute of Technology
Pasadena, California 91109 USA

²Smithsonian Astrophysical Observatory
60 Garden Street
Cambridge, Massachusetts, 02138 USA

Abstract

The Stratospheric Terahertz Observatory (STO) is a long-duration balloon-borne telescope that will initially map the Galaxy in two key spectroscopic lines, C+ at 1.9 THz and N+ at 1.46 THz [1], using two arrays of superconducting hot-electron bolometer receivers. We are currently fabricating the lower frequency mixers for this project, and 4 units will be built and assembled to form an array. The basic mixer design is similar to the one developed for the receiver operating in Chile [2], with one key difference: instead of using quartz for the mixer substrate material, we use silicon-on-insulator (SOI) wafers, with which it is possible to obtain final chip thickness of only a microns. The use of very thin silicon permits us to easily scale the mixer design to higher frequencies, and at the same time to take advantage of the fact that superconducting nitride films for mixer applications grow best on crystalline silicon than on quartz or amorphous membranes. The final devices, which are 6 microns thick, are robust and easily mounted into a channel that spans across a waveguide in the waveguide block. With a prototype mixer which uses a corrugated feed, we measured a receiver noise temperature of 1050 K (DSB) at 1.398 THz with an intermediate frequency of 1.5 GHz, using a laser local oscillator source. We are presently scaling the design to 2.7 THz.

REFERENCES

- [1] C. Walker, et al., "The Stratospheric Terahertz Observatory (STO), An LDB experiment to investigate the life cycle of the interstellar medium" 19th International Symposium on Space Terahertz Technology, Groningen, Netherlands (2008)
- [2] E. Tong, et al, "A 1.5 THz hot-electron bolometer receiver for ground-based terahertz astronomy in northern Chile," Proc. SPIE 6373 (2006)

Gain bandwidth and noise temperature of NbN HEB mixers with simultaneous phonon and diffusion cooling

Anna Maslennikova, Ivan Tretyakov, Sergey Ryabchun, Matvey Finkel, Natalia Kaurova, Boris Voronov, and Gregory Gol'tsman

Department of Physics and Information Technology
Moscow State Pedagogical University
29 Malaya Pirogovskaya St, Moscow, 11992, Russia
Email: annamaslennikova@rplab.ru

Abstract

The space observatory Millimetron will be operating in the millimeter, sub-millimeter and infrared ranges using a 12-m cryogenic telescope in a single-dish mode, and as an interferometer with the space-earth and space-space baselines (the latter after the launch of the second identical space telescope). The observatory will allow performing astronomical observations with an unprecedented sensitivity (down to nJy level) in the single-dish mode, and observations with a high angular resolution in the interferometer mode. The total spectral range $20\ \mu\text{m} - 2\ \text{cm}$ is separated into 10 bands. HEB mixers with two cooling channels (diffusion and phonon) have been chosen to be the detectors of choice of the system covering the range from 1 THz to 6 THz as the best detectors in terahertz receivers.

This type of HEB has already shown good work in the terahertz range. A gain bandwidth of 6 GHz at an LO frequency of 300 GHz and a noise temperature of 750 K at an LO frequency of 2.5 THz are the best values for HEB mixers with two cooling channels [1]. Theoretical estimations predict a bandwidth up to 12 GHz. Reaching such good result demands more systematic and thorough research.

We present the results of the gain bandwidth and noise temperature measurements for superconducting hot-electron bolometer mixers with two cooling channels. These characteristics of the devices of lengths varying from 50 to 200 nm were measured for the purposes of Millimetron at frequencies of 600 GHz, 2.5 THz, and 3.8 THz. For gain bandwidth measurements we use two BWO's operating at 600 GHz: one as the signal and the second as the LO. The noise temperature measurements were performed using a gas discharge laser as the LO and blackbodies at 77 K and 295 K as input signals.

The devices studied consist of 3.5-nm-thick NbN bridges connected to thick (10 nm) high conductivity Au leads fabricated *in situ*. This method of fabricating devices has already proved promising by opening the diffusion cooling channel. [2] Fig. 1 shows a SEM photograph of a log-spiral antenna with an HEB at its apex.

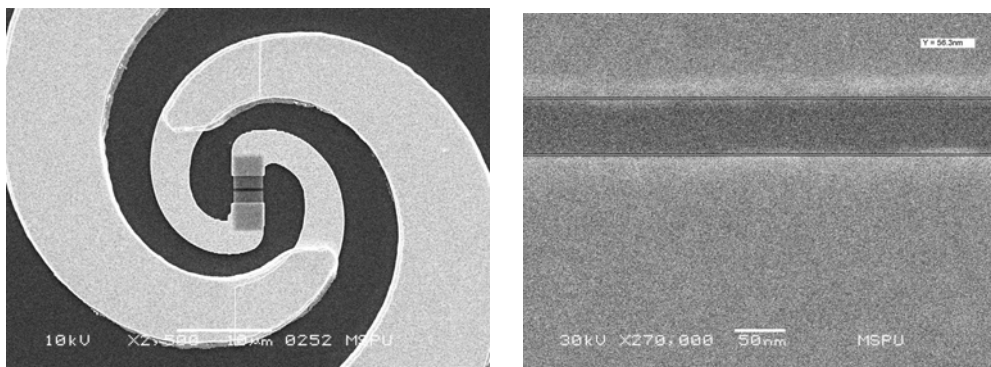


Fig. 1. Left: a SEM photograph of a log-spiral antenna with an HEB at its apex; right: a close-up of the HEB at the antenna apex.

[1] S. A. Ryabchun, I. V. Tretyakov, M. I. Finkel, S. N. Maslennikov, N. S. Kaurova, V. A. Seleznev, B. M. Voronov, and G. N. Gol'tsman, NbN phonon-cooled hot-electron bolometer mixer with additional diffusion cooling, Proc. of the 20th Int. Symp. Space. Technol., Charlottesville, Virginia, USA, April 20 – 22, 2009.

[2] S. A. Ryabchun*, I. V. Tretyakov, M. I. Finkel, S. N. Maslennikov, N. S. Kaurova, V. A. Seleznev, B. M. Voronov and G. N. Goltsman, Fabrication and characterisation of NbN HEB mixers with *in situ* gold contacts, Proc. of the 19th Int. Symp. Space. Technol., Groningen, The Netherlands, April 28-30, 2008

Noise Temperature and Beam Pattern of a Quasioptical Heterodyne Receiver based on NbN Hot Electron Bolometer Mixer at 5.25 THz

W. Zhang^{1,2,#}, P. Khosropanah¹, J. R. Gao^{1,3,*}, T. Bansal^{1,3}, T. M. Klapwijk³, W. Miao², and S. C. Shi²

¹*SRON Netherlands Institute for Space Research, Groningen, the Netherlands*

²*Purple Mountain Observatory, National Astronomical Observatories of China, Chinese Academy of Sciences, China*

³*Kavli Institute of Nanoscience, Delft University of Technology, Delft, The Netherlands*

#Contact: wzhang@mail.pmo.ac.cn, phone +86-25-83332229

*Contact: J.R. Gao@tudelft.nl, phone +31-15-2781370

Abstract—We report the measured sensitivities of a superconducting NbN hot electron bolometer (HEB) heterodyne receiver at 5.25 THz. The terahertz (THz) radiation is quasi-optically coupled to the HEB mixer with a lens and a spiral antenna. Using a measurement setup with black body calibration sources and a beam splitter in vacuum, and an antireflection coated Si lens, we obtained a double sideband (DSB) receiver noise temperature (T_{rec}^{DSB}) of 1150 K, which is 4.5 times $h\nu/k$ (the quantum limit). In addition, the measured far field beam patterns of the integrated lens antenna from 2.5 THz to 5.3 THz show collimated beams that make it reliable to measure T_{rec}^{DSB} using the vacuum setup. Our experimental results in combination with an antenna-to-bolometer coupling simulation suggest that the HEB mixer can work well at least up to 6 THz, suitable for next generation of high-resolution spectroscopic space telescopes and, in particular, for the detection of the neutral atomic oxygen (OI) line at 4.7 THz.

I. INTRODUCTION

Superconducting hot-electron bolometer (HEB) mixers are so far the most sensitive heterodyne detectors at THz frequencies above 1.5 THz. The HEB mixers based on NbN or NbTiN superconducting films have been successfully used to detect spectral lines up to 2 THz from ground based [1-3] and space [4] telescopes. The performances, such as the low double sideband (DSB) T_{rec}^{DSB} of 1300 K at 4.3 THz [5], an intermediate frequency (IF) gain bandwidth of 3 GHz and noise bandwidth of ~5 GHz [6], low local oscillator (LO) power of 50-500 nW [7], and a long Allan variance stability time [1], have been reported by different research groups. They become the choice of the detector in the upper THz frequency range (3-6 THz) for high resolution spectroscopic observations for astronomy. One example is the fine-structure line of neutral atomic oxygen OI ($^3P_1-^3P_2$) at 4.7448 THz, which is a major coolant of dense interstellar medium and is a vital tool for probing the physical conditions of massive young stars [8]. The OI line has been recorded by a Schottky heterodyne receiver flying on the Kuiper Airborne Observatory [9]. However, the sensitivity of the receiver used is very poor and is 75000 K at 4.7 THz. The sensitivity of a

receiver, i.e. T_{rec}^{DSB} , is a crucial parameter that defines the minimal detectable line amplitude and also the observation time.

The far field beam pattern of a quasi optical HEB mixer, governed by a lens/antenna combination and radiation frequency, is also an important performance parameter for a practical receiver. The beam pattern of a spiral antenna at 5 THz is not known, which motivates us to investigate that. Besides, we also notice that the beam patterns are crucial for measuring T_{rec}^{DSB} when hot/cold loads with a limited surface area are used, which is the case in our vacuum setup.

The aim of this work is to demonstrate experimentally the ultimate sensitivity of an NbN HEB mixer at the high-end of THz frequency range. Here we use a similar HEB mixer and measurement setup as reported earlier at 4.3 THz [5]. However, we extend the LO frequency to 5.25 THz. We report T_{rec}^{DSB} of 1150 K at 5.3 THz. In addition, the coupling efficiency between spiral antenna and bolometer is simulated. The far field beam patterns of the mixer were measured at several frequencies up to 5.3 THz.

II. HEB DEVICE AND MEASUREMENT SETUP

The HEB mixer used consists of 2 μm wide, 0.2 μm long, and 5.5 nm thick NbN bridge on a highly resistive Si substrate. The NbN thin film was produced by a group at Moscow State Pedagogical University (MSPU), Russia. The details of the NbN film can be found in [10]. The bridge is connected to the antenna by Nb (10 nm)/Au (50 nm) superconducting bilayer contact pads [11]. Prior to deposition of the contact pads, Ar ion etching is applied to clean the surface of NbN, eliminating contact resistance between NbN and contact pads. Such contact structures allow RF and DC power being dissipated only in the NbN bridge, thus there are no RF loss and no additional noise contribution due to the contact interface. The antenna is an on-chip self-complementary spiral antenna that is made of a 170 nm thick Au layer. It has a tight winding design with an inner diameter

of 6.6 μm close to the NbN bridge [Fig.1(a)]. The HEB has a low-temperature normal-state resistance (R_N) of 83 Ω , a critical temperature of 9.3 K, and a critical current of 210 μA at 4.2 K.

We apply the same vacuum measurement setup as described in [5] except for a different heat filter [12] and without bandpass filter. The HEB chip is glued to the backside of Si elliptical lenses [13] without and with an antireflection coating, mounted in a mixer unit that is placed in a 4.2-K liquid helium cryostat. As calibration sources, a blackbody at 295 K is used as the hot load and another one at 77 K as the cold load. The two loads can be selected by rotating a mirror. The radiation from the hot/cold load is combined with that from the LO by a 3- μm Mylar beam splitter. Before reaching the HEB, the radiation passes through the heat filter at 4.2 K that blocks infrared radiation. There is no window on the cryostat and all these components are in the same vacuum [14]. Therefore the radiation does not suffer from the absorption due to water in the air and due to the window.

The LO is an optically pumped FIR ring laser, operated at a frequency of 5.2456 THz using CH_3OD gas, which is pumped by 9R08 CO_2 line. We choose this frequency because it provides enough amount of power in the frequency range of our interest. The LO power coupled to the mixer is regulated by rotating a wire grid in front of the gas laser

The IF signal, resulting from the mixing of the LO and the hot/cold load signal, first passes through a bias-T, a circulator, and then a cryogenic low noise amplifier (Berkshire 1.3-1.7 GHz) operated at 4.2 K, followed by room-temperature amplifiers. This signal is filtered at 1.5 GHz within a band of 80 MHz. Between each two components in the IF chain, an attenuator is added to avoid standing waves. The entire IF chain has a gain of about 80 dB and a noise temperature of 7 K.

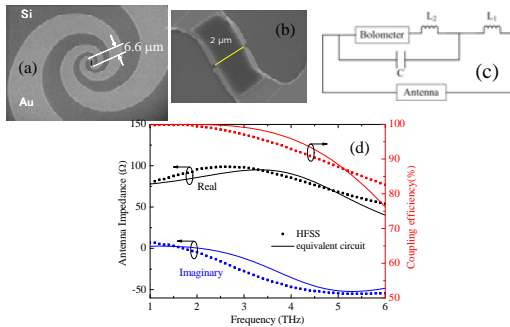


Fig. 1 (a) SEM picture of a tight winding spiral antenna with an inner diameter of 6.6 μm ; (b) SEM picture of the NbN bridge with a length of 0.2 μm and a width of 2 μm ; (c) Equivalent circuit of the whole antenna structure, which includes parasitic inductance and capacitance; (d) Simulated impedances of the spiral antenna versus frequency using HFSS and using the equivalent circuit (left axis) and calculated coupling efficiency between bolometer and antenna versus frequency (right axis).

III. SIMULATION OF THE ANTENNA IMPEDANCE AND THE COUPLING

To predict the impedance of the antenna and further calculate the coupling efficiency for the radiation power from

the antenna to the HEB at the upper THz frequencies, we model the antenna using a three dimensional electromagnetic field simulator HFSS based on finite element method [15]. We assume that an RF signal is excited at the slit between two contact pads of the HEB, which is called lumped gap source. The Si substrate with a refractive index $n_{\text{Si}}=3.42$ is set to be much thicker than the wavelength (λ) of the radiation and is treated as the half infinite space. All the surfaces are taken as radiation boundary. The scattering parameters are extracted from the electromagnetic field distribution. From the complex reflection coefficient (S_{11}) and its characteristic impedance (Z_0), the input impedance (Z_{antenna}) of the spiral antenna can be given as [16]:

$$Z_{\text{antenna}} = Z_0 \frac{1 - S_{11}}{1 + S_{11}} \quad (1)$$

Fig. 1(d) shows the simulated Z_{antenna} of the spiral antenna as a function of frequency between 1 and 6 THz. At lower frequencies the impedance is real and has a value close to 75 Ω , as expected for an equiangular spiral antenna [17]. But with increasing the frequency the reactive part appears and increases to -50 Ω at around 5 THz. The reactance can be explained by a parasitic effect that is due to the presence of a transition structure, namely the contact-pad structure between the HEB and the two arms of the spiral [see Fig.1(b)]. This leads to deformation of RF current and thus inductive and capacitive parasitic effects [18]. One can describe this by assuming an equivalent circuit that is shown in Fig.1(c). The transition structure acts as a series inductance L_1 to the antenna resistance R_{antenna} , and the slit between contact pads can be represented as a parallel capacitance C . Furthermore, the difference in the width between bolometer and contact pads causes current crowding which can be described as a series inductance L_2 . Using this argument together with the following parameters: $R_{\text{antenna}}=75 \Omega$, $L_1=2.34 \text{ pH}$, $L_2=0.7 \text{ pH}$, and $C=0.45 \text{ fF}$, we can obtain a very similar impedance for the antenna as predicted by HFSS. The result is also plotted in Figure 1(d) for comparison.

Given that our HEB impedance is constant [19], equal to R_N , the coupling efficiency η can be calculated based on the impedance match:

$$\eta = \frac{4Z_{\text{HEB}} \text{re}(Z_{\text{antenna}})}{|Z_{\text{HEB}} + Z_{\text{antenna}}|^2} \quad (2)$$

The calculated η is also given in Fig. 1(d). We find that η is nearly 100 % at the frequencies below 3 THz, while above this value it decreases, but decreases gradually with increasing frequency. Even at the highest frequency of 6 THz, it is still more than 80 %, suggesting that our particular spiral antenna with the tight winding design can work well up to at least 6 THz and even beyond this frequency. For comparison, Fig. 1(d) shows also the calculated coupling efficiency based on the simple equivalent circuit. The result suggests that the simple model is able to qualitatively explain the frequency dependence of η .

IV. CHARACTERIZING AN ANTI-REFLECTION COATED LENS

It is known that when a Si lens is used to couple THz radiation from the free-space to an antenna, a considerable amount of optical loss is due to reflection because of the high reflective index of Si, n_{si} . This loss can be minimized by coating an anti-reflection layer with a thickness of quarter wavelength ($\lambda/4n_{AR}$) and with a refractive index $n_{AR} = \sqrt{n_{si}} = 1.85$. Parylene C is a known coating material since it has a refractive index (n_{PC}) of 1.65, which is close to the optimum value [20].

To measure the ultimate T_{rec}^{DSB} at 5.25 THz, we apply an existing Si lens coated with a Parylene C. The coating layer has a thickness of 10.9 μm and was originally designed for 4.3 THz [5]. To find its transmission at 5.25 THz, we prepared a double-side polished Si wafer coated with a Parylene C layer of the same thickness (10.9 μm) on both sides and measured the power transmission as a function of frequency by a Fourier transform spectrometer. The measured result is shown in Fig. 2. A good theoretical fit to the measured data is found when the coating layer is assumed to be 10.93 μm thick and $n_{PC}=1.634$. Based on the data and analysis, the transmission for the coated lens as a function of frequency is calculated and also depicted in Fig. 2. At 5.25 THz the transmission reaches 92 %, which is 22 % higher compared to that of an uncoated lens. We also find that at the designed frequency (4.3 THz), the transmission reaches its maximum of 97 %.

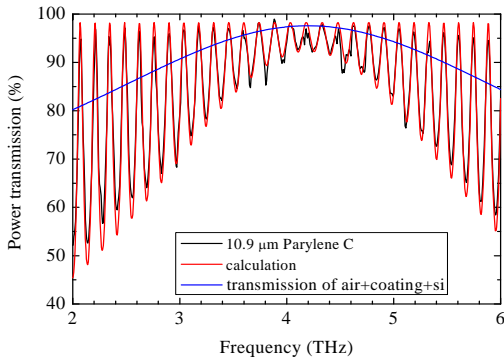


Fig. 2 Measured and theoretical power transmission of a double-side polished Si wafer coated with a Parylene C layer on both sides. The Si wafer and Parylene C coating layer are 2 mm and 10.9 μm thick, respectively.

V. EXPERIMENTAL RESULTS

A. R-T Curve and Pumped I-V Curves

The resistance of a similar HEB from the same fabrication run has been measured as a function of temperature. The result is shown in the inset of Fig. 3. It is featured by three superconducting transitions. The lowest transition T_{c1} of 6 K is associated to the Au/Nb/NbN contact structures; the middle transition T_{c2} of 8 K is associated to the NbN under Au (thick) antenna layer; and the highest transition T_{c3} of 9.3 K is due to the NbN bridge. The resistance above T_{c3} is about 83 Ω , making a good impedance match possible with the spiral antenna. It is important to mention that in our case when the HEB is operated in the optimal biasing point, the contacts are in the superconducting state. More discussions

of the superconducting transitions in such structures can be found elsewhere [11].

A typical set of I-V curves of the HEB with different LO power levels at 5.25 THz, recorded at 4 K, are shown in Fig. 3. With increasing LO power level, the superconductivity of the NbN bridge becomes gradually suppressed, showing a transition from the superconducting state to normal. The measured curves can be explained by a nonuniform distribution model for a HEB [21]. The optimum operating region, where the lowest T_{rec}^{DSB} can be obtained, is indicated in the I-V plot. This region is centered around a bias voltage of 0.6 mV and a current of 34 μA . The optimum LO power in the HEB is about 150 nW, obtained by the isothermal technique [22]. The LO power required for HEB is known to be proportional to the volume and the T_{c3} of the HEB.

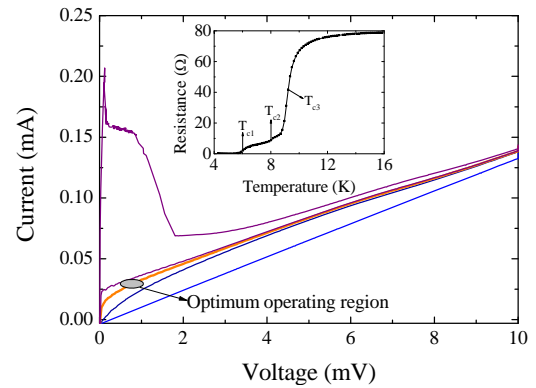


Fig. 3 A set of current-voltage curves of the NbN HEB mixer at 4.2 K and at different LO power, where the optimum operating region is indicated. The inset shows the DC resistance versus temperature of a very similar HEB, which was measured in the low current limit.

B. Receiver Noise Temperature at 5.25 THz

We start with a measurement in which the HEB is mounted on the uncoated Si lens and T_{rec}^{DSB} is characterized in a conventional way. We measured the output power of the receiver, $P_{out,hot}$ and $P_{out,cold}$, responding to the hot and cold load as a function of bias voltage under a constant, but optimum LO power. The results are plotted in Fig. 4. T_{rec}^{DSB} is obtained by the Y-factor method and using the equivalent temperatures for the blackbody at 295 K and 77 K according to Callen-Welton definition [23]. T_{rec}^{DSB} as a function of bias voltage is also plotted in Fig. 4. The lowest T_{rec}^{DSB} (black dot line) is roughly 2000 ± 500 K. The uncertainties are mainly caused by the LO power fluctuation and drift.

It has been well established that a HEB with a wideband antenna and low LO power requirement can suffer from the direct detection effect due to broadband blackbody radiation [24]. An additional demonstration of the direct detection effect in this particular experiment will be given in the subsection C. As a result, a measured T_{rec}^{DSB} is usually higher than it should be [25]. This effect can be corrected out by adjusting LO power such that the DC current of the HEB is the same responding to the hot and cold loads. For comparison, the receiver output power data after adjusting

LO power are also shown in Fig. 4. For clarity a 2 dB positive offset in the vertical direction is introduced in the plot. The measured lowest T_{rec}^{DSB} becomes 1500 ± 300 K, which is on average 25% lower than what measured previously.

By applying a different characterization method [5] we can measure directly T_{rec}^{DSB} , without suffering from the direct detection and the instability of the gas laser as well. At the bias voltage of 0.6 mV we measure the receiver output power as a function of bias current, which is the result of varying LO power. Two such data sets are recorded, $P_{out,hot}(I)$ responding to the hot load and $P_{out,cold}(I)$ to the cold load. The Y factor can be obtained by $Y(I) = P_{out,hot}(I)/P_{out,cold}(I)$ at the same current using the fitted polynomial curves. The calculated T_{rec}^{DSB} as a function of bias current is plotted in Fig. 5 and shows a broad minimum at the bias current of around $34 \mu\text{A}$ and the lowest value of 1550 ± 50 K. This is in good agreement with the value measured in the conventional way, but after correcting the direct detection effect. The advantage is the high accuracy. Furthermore, the mixer conversion loss is found to be 8.9 dB.

Now we measure T_{rec}^{DSB} of the same HEB, but mounted on the coated Si lens. Again, we measure at the optimum bias voltage of 0.6 mV. The data are added in Fig. 5. For clarity, the receiver output power data as a function of current, responding to hot/cold loads, have an offset positively by 2 dB. The lowest T_{rec}^{DSB} obtained is 1150 ± 40 K, which is about 23 % lower than the value (1550 K) measured previously using the uncoated lens. This difference is consistent with what is expected from using anti-reflection coating.

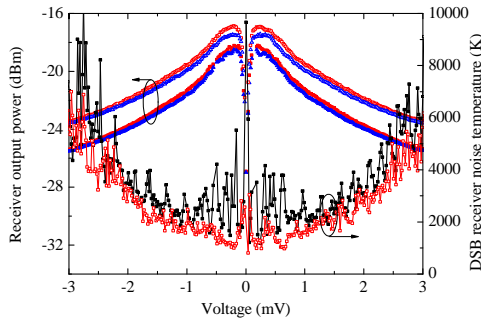


Fig. 4 Measured receiver output power (left axis) responding to the hot and cold load at optimum LO power as a function of bias voltage. One set of data are measured with fixed LO power level, and another set (2 dB positive offset for clarity) by adjusting LO power such that the current is the same for hot and cold loads. The resulted DSB receiver noise temperatures are also plotted vs. bias voltage (right axis).

C. Direct Detection

Fig. 6 shows measured receiver output power, together with the DC current of the HEB, as a function of time over a period of 150 seconds, during which the hot and cold loads are manually switched after roughly each 5 seconds. The HEB in this case is mounted on the coated lens. The bias voltage is fixed at 0.8 mV and the LO power set at the optimal value. The periodic jumps of ≤ 0.3 dB in the output

power between the hot and cold load should reflect directly how large the Y-factor is. However, the actual value is affected by the direct detection effect [25]. This effect is demonstrated by the observed jumps in the current, which is about $1.2 \mu\text{A}$ in amplitude. In principle, the direct detection effect can be minimized or eliminated by reducing the blackbody radiation power, for example, by adding a narrow bandpass filter in front of the mixer [24].

The absolute value of the bias current corresponding to either the hot or cold load varies less than 2 % during the measurement period in Fig. 6, which indicates reasonable power stability of the 5.25 THz lasing line.

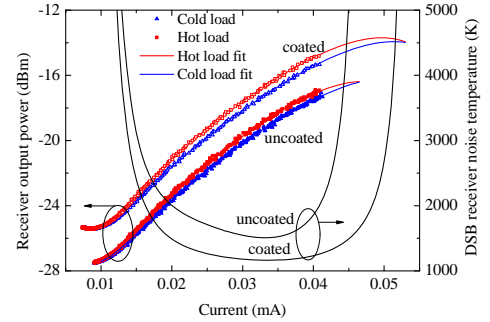


Fig. 5 Measured receiver output powers at the optimum bias voltage of 0.6 mV (dots) and the polynomial fit (lines) responding to the hot and cold load as a function of bias current of the HEB, which is varied by changing the LO power (left axis). One set of data are measured using uncoated lens and another set of data (2 dB positive offset for clarity) are measured using a coated lens. The resulted DSB receiver noise temperature curves are also shown as a function of bias current of the HEB (right axis).

D. Beam Patterns of the Lens/Antenna

The far-field beam patterns of the same HEB mixer on the uncoated Si lens are measured at several frequencies from 2.5 to 5.3 THz using a computer controlled setup as described previously [26]. We apply the same gas laser as a signal source to measure the beams of the mixer. The HEB cryostat is placed on a rotation/tilt table in the far-field of the gas laser, which has a linearly polarized electrical field in the vertical direction. The center of the spiral antenna is located in the axis of the rotation.

The HEB is heated to a temperature which is slightly below the superconducting transition temperature of the NbN bridge T_{c3} . It is voltage biased and the current changes due to the modulated incident power are measured as a function of the angle of rotation/tilt by a lock-in amplifier. The tilt movement is referred to as vertical scan and the rotation as horizontal scan. The dynamic range of the setup is about 20 dB. The antenna is positioned in such a way that the direction along the NbN bridge width is about 30 degrees counter clockwise from the vertical direction of the setup.

Fig. 7 shows the beam patterns, measured in both horizontal and vertical directions of the integrated lens/antenna at 2.5 THz, 4.3 THz and 5.3 THz. The main lobes are similar in horizontal and vertical scans, which indicate that our beam patterns are close to rotational symmetry. The full width half maximum (FWHM) at 5.3 THz is 0.6 degree, which is similar to 0.55 degree at 4.3 THz, but smaller than 0.9 degree at 2.5 THz. At such high

frequencies the beam pattern of integrated lens antenna is diffraction limited, which scales with the wavelength and the effective aperture. The main beam becomes narrower from 2.5 to 4.3 THz due to wavelength, while it is almost the same between 4.3 THz and 5.3 THz, indicating the effective aperture at 5.3 THz is smaller. The difference in the side lobes is likely due to combination of antenna misalignment, IF feed structure and the measurement setup. Especially at 5.3 THz the beam profile in vertical scan has a large shoulder [see Fig. 7(c)], the reason for which is unclear yet. The first side lobes at 2.5 THz, 4.3 THz and 5.3 THz occur at -13, -11 and -7 dB, respectively, which increases with increasing the frequency [27]. The physical reasons of this are the internal reflection and surface roughness [28], [29]. Although the beam patterns are not ideally Gaussian, the measured beam patterns of the lens/antenna combination confirm the collimated beam, which is crucial to correctly measure T_{rec}^{DSB} using the vacuum setup.

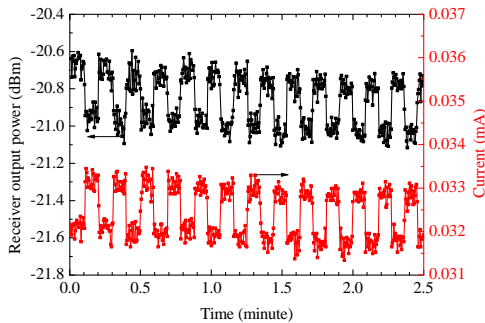


Fig. 6 Measured receiver output power, together with the bias current of the HEB, is measured as a function of time over a period of 150 seconds, during which the hot and cold load are manually switched after roughly each 5 seconds.

VI. CONCLUSIONS

We have demonstrated a highly sensitive NbN HEB mixer at 5.25 THz using a spiral antenna coupled NbN HEB. We measured the lowest T_{rec}^{DSB} of 1150 K at 5.25 THz. It is worthwhile to note that the sensitivity at 5.3 THz is about 65 times better than the Schottky diode mixer at 4.7 THz [9]. We also present the far-field beam pattern of the mixer at 5.25 THz, which shows a collimated beam with the side lobe occurring roughly at -7 dB level. With further improvement of the beam pattern, such a mixer together with recently developed THz quantum cascade lasers as LO should allow constructing new receivers [30] for detecting OI line at 4.7 THz for future airborne and space-borne telescopes.

ACKNOWLEDGMENT

We acknowledge E.L. Kollberg and K.S. Yngvesson for stimulating discussions on the equivalent circuit of the antenna, L. de Jong, W. M. Laauwen, and J. N. Hovenier for their technical support, and W. Horinga for the FTS transmission measurement. The work was supported by the NSFC under Grant Nos. 10803021 and 10621303, and by China Exchange Programme executed by KNAW and CAS,

and by the AMSTAR+ project of RadioNet under FP7 and N.W.O.

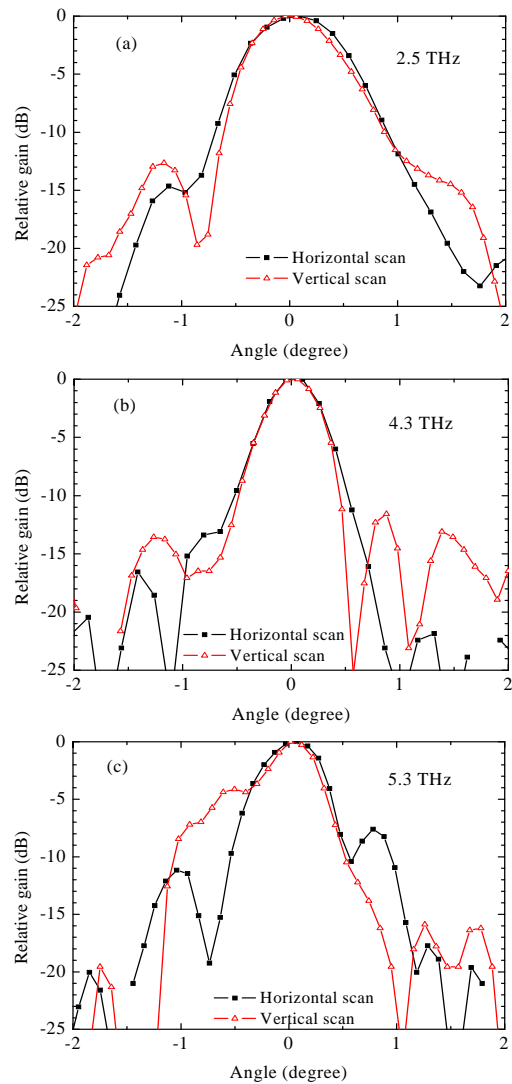


Fig. 7 Measured far field beam patterns of the HEB mixer on the uncoated Si lens, which are the same as used for the sensitivity measurements, at 2.5 THz (a), 4.3 THz (b), and 5.3 THz (c). The scans are made for both horizontal and vertical directions. The horizontal scan is indicated by black solid square+line; while the vertical scan by red hollow triangle+line.

REFERENCES

- [1] D. Meledin, A. Pavolotsky, V. Desmaris, I. Lapkin, C. Risacher, V. Perez, D. Henke, O. Nystrom, E. Sundin, D. Dochev, M. Pantaleev, M. Fredrixon, M. Strandberg, B. Voronov, G. Goltzman, and V. Belitsky, *IEEE Trans. Microwave Theory Tech.* **57**, 89 (2009).
- [2] J. Kawamura, R. Blundell, C.-Y. Tong, D. Papa, T. Hunter, G. Goltzman, S. Cherednichenko, B. Voronov, and E. Gershenson, *Proceedings of 9th International Symposium on Space Terahertz Technology*, Pasadena, California, USA, 17-19 March 1998 (unpublished), pp. 35-43.
- [3] M. C. Wiedner, G. Wieching, F. Biela, K. Rettenbacher, N. H. Volgenau, M. Emprechtinger, U. U. Graf, C. E. Honingh, K. Jacobs, B. Vowinkel, K. M. Menten, L.-A. Nyman, R. Gusten, S. Philipp, D. Rabanus, J. Stutzki, and F. Wyrowski, *A&A.*, **454**, L33 (2006).
- [4] S. Cherednichenko, V. Drakinskiy, T. Berg, P. Khosropanah, and E. Kollberg, *Review of Scientific Instruments*, **79**, 0334501 (2008).
- [5] P. Khosropanah, J. R. Gao, W. M. Laauwen, M. Hajenius, and T. M. Klappwijk, *Appl. Phys. Lett.* **91**, 221111 (2007).

- [6] J. W. Kooi, J. J. A. Baselmans, J. R. Gao, T. M. Klapwijk, M. Hajenius, P. Dieleman, A. Baryshev, and G. de Lange, *J. Appl. Phys.* **101**, 044511 (2007).
- [7] S. Cherednichenko, P. Khosropanah, E. Kollberg, M. Kroug, H. Merkel, *Physica C*, **372-376**, 407 (2002).
- [8] R. Gusten, P. Hartogh, H.-W. Hubers, U. Graf, K. Jacobs, H.P. Poser, F. Schafer, R. Schieder, R. Stark, J. Stutzki, P. Van der Wal, and A. Wunsch, *Proc. SPIE*, **4014**, 23 (2000).
- [9] R. T. Boreiko and A.L. Betz, *ApJ*, **464**, L83 (1996).
- [10] J. R. Gao, M. Hajenius, F. D. Tichelaar, T. M. Klapwijk, B. Voronov, E. Grishin, G. Gol'tsman, C. A. Zorman and M. Mehregany, *Appl. Phys. Lett.* **91**, 062504 (2007),
- [11] T. Aggarwal, P. Khosropanah, W. Zhang, F. D. Tichelaar, J. R. Gao, and T. M. Klapwijk, *Proceedings of 19th International Symposium on Space Terahertz Technology*, Groningen, The Netherlands, 28-30 April 2008 (unpublished), pp.398-402.
- [12] The heat filter has an upper cutoff frequency of 6 THz and 0.8 dB loss at 5.25 THz and is produced by QMC Ltd.
- [13] HEB chip is placed on the backside of an elliptical Si lens, which is governed by the equation of $(x/a)^2+(y/b)^2=1$ with a major radii $b=5.228$ mm and a minor radii $a=5$ mm. The extension from geometric center of the elliptical lens is 1.229 mm and the Si substrate of the HEB chip is 340 μ m thick.
- [14] Vacuum unit consists of a beam splitter (which is changeable), a hot and cold load, and a rotating mirror. The beam splitter (3- μ m Mylar) with a diameter of 22 mm is 35 mm away from the cryostat (the position of the window if it is there). The hot and cold load with diameters of 30 mm are 140 mm and 230 mm, respectively, away from the cryostat.
- [15] 3D Full-wave Electromagnetic Field Simulation, see <http://ansoft.com/products/hf/HFSS/>.
- [16] W. Zhang, C.-Y. Edward Tong, and S. C. Shi, *IEEE Microwave & Wireless Components Letts.* **13**, 376 (2003).
- [17] J. D. Dyson, *IRE Trans. Antennas and Propagation*, **7**, 181 (1959).
- [18] P. Focardi, A. Neto, W. McGrath, *IEEE Trans. Microwave Theory Tech.* **50**, 2374 (2002).
- [19] E. L. Kollber, K. S. Yngvesson, Y. Ren, W. Zhang, P. Khosropanah, and J. R. Gao, (unpublished).
- [20] H.-W. Hüber, J. Schubert, A. Krabbe, M. Birk, G. Wagner, A. Semenov, G. Goltsman, B. Voronov and E. Gershenzon, *Infrared Physics & technology*, **42**, 41 (2001).
- [21] R. Barends, M. Hajenius, J. R. Gao, and T.M. Klapwijk, *Appl. Phys. Lett.* **87**, 263506 (2005).
- [22] H. Ekstrom, B. Karasik, E. Kollberg, and S. Yngvesson, *IEEE Trans. Microwave Theory Tech.* **43**, 938 (1995).
- [23] A. R. Kerr, *IEEE Trans. Microwave Theory Tech.* **47**, 325 (1999).
- [24] M. Hajenius, J. J. A. Baselmans, A. Baryshev, J. R. Gao, T. M. Klapwijk, J. W. Kooi, W. Jellema, and Z. Q. Yang, *J. Appl. Phys.* **100**, 074507 (2006).
- [25] J. J. A. Baselmans, A. Baryshev, S.F. Reker, M. Hajenius, J.R. Gao, T.M. Klapwijk, B. Voronov, and G. Goltsman, *J. Appl. Phys.* **100**, 084510 (2006).
- [26] P. Yagoubov, W.J. Vreeling, and P.de Korte, *Proceedings of 12th International Symposium on Space Terahertz Technology*, San Diego, California, 14-16 February 2001(unpublished), pp.193-199.
- [27] H.-W. Hüber, A. D. Semenov, H. Richter, J. Schubert, S. Hadjiloucas, J. W. Bowen, G. N. Goltsman, B. M. Voronov, and E.M. Gershenzon, *Proceedings of 12th International Symposium on Space Terahertz Technology*, San Diego, California, 14-16 Feb 2001, pp.286-296.
- [28] M. J. M. van der Vorst, P. J. I. de Maagt, A. Netto, A. L. Reynolds, R. M. Heeres, W. Luinge, and M. H. A. J. Herben, *IEEE Trans. Microwave Theory Tech.* **49**, 1118 (2001).
- [29] A. D. Semenov, H. Richter H.-W. Hübers, B. Gunther, A. Smirnov, K. S. Il'in, M. Siegel and J. P. Karamarkovic, *IEEE Trans. Microwave Theory Tech.* **55**, 239 (2007).
- [30] J. R. Gao, J. N. Hovenier, Z. Q. Yang, J. J. A. Baselmans, A. Baryshev, M. Hajenius, T. M. Klapwijk, A. J. L. Adam, T. O. Klaassen, B. S. Williams, S. Kumar, Q. Hu, and J. L. Reno, *Appl. Phys. Lett.* **86**, 244104, 2005.

Session S10: THz Systems and Planetary Missions

The Background-Limited Infrared Submillimeter Spectrograph (BLISS) for SPICA

C.M. Bradford*, on behalf of the BLISS-SPICA study team

*Jet Propulsion Laboratory, Caltech, Pasadena, CA

Email: bradford@submm.caltech.edu

Abstract

With the advent of new large-format far-IR / submm arrays, imaging surveys are revealing hundreds of thousands of dusty galaxies from the first half of the Universe's history when the bulk of star formation and black hole growth likely occurred. The key to studying these objects is spectroscopy in the rest-frame mid- to far-IR. Fine-structure and molecular transitions in this waveband are largely unaffected by dust extinction and the suite of lines provides redshifts and reveals the properties of the embedded stellar and black-hole energy sources. We have developed BLISS to provide a breakthrough capability for far-IR survey spectroscopy at wavelengths between JWST and ALMA. SPICA's large cold aperture allows mid-IR to submm observations which are limited only by the natural backgrounds, and BLISS-SPICA is 6 orders of magnitude faster than the spectrometers on Herschel and SOFIA in obtaining full-band spectra. The sensitivity allows study of galaxies at all epochs back to the first billion years after the Big Bang ($z \sim 6$), making BLISS-SPICA the ideal platform for spectroscopic follow-up for the wide variety of sources now being discovered with far-IR and submm imaging.

BLISS provides instantaneous coverage from 38–433 μm using ten grating spectrometer modules coupling 2 sky positions in 5 wavelength bands. The instrument is cooled to 50 mK for optimal sensitivity with an on-board magnetic refrigerator. The detector package is 4224 silicon-nitride micro-mesh leg-isolated bolometers with superconducting transition-edge-sensed (TES) thermistors, read out with a cryogenic time-domain multiplexer. All technical elements of BLISS have heritage in mature scientific instruments, and many have flown. We are now engaged in a design study to optimize performance while accommodating SPICA's constraints, including the stringent cryogenic mass budget. We present our progress in all key aspects: 1) science requirements and the opto-mechanical instrument architecture, 2) detector and readout approach, and 3) sub-K cooling approach, including mitigation of magnetic interference.

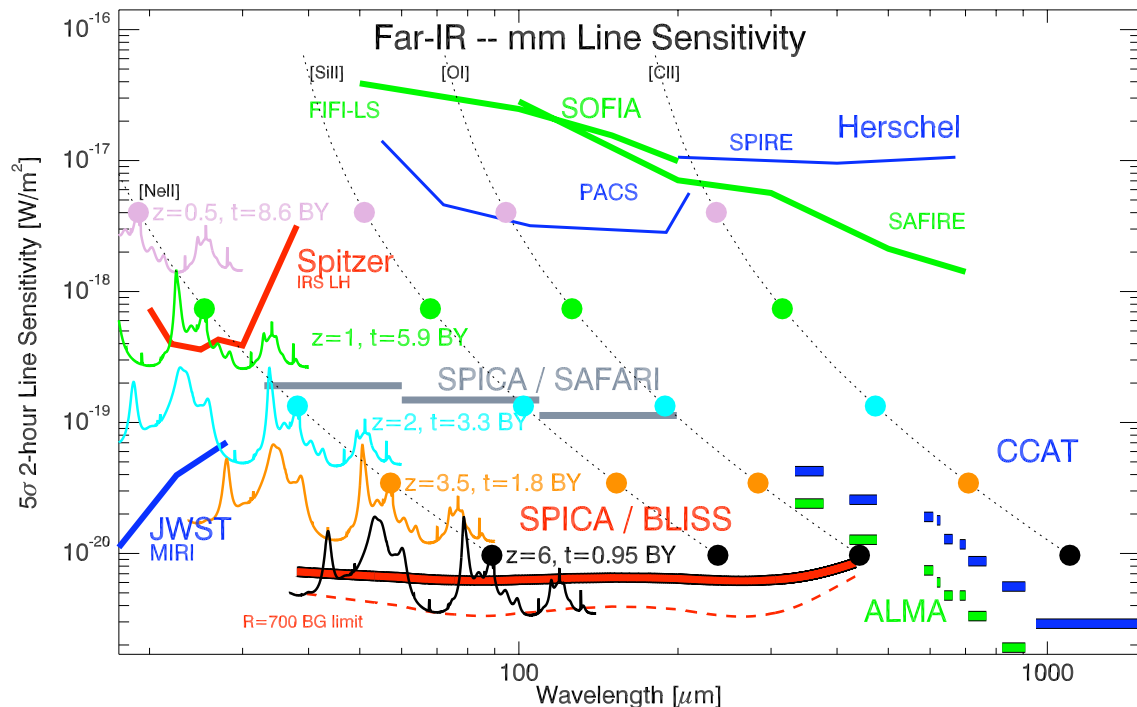


Figure 1. BLISS-SPICA is 100–1000 times more sensitive than present-day far-IR facilities for spectroscopy. Observing speed scales as the inverse square of the plotted sensitivity. The dashed curved at bottom is the photon background limit, the heavy curve above it is the BLISS design sensitivity. Fine-structure line intensities are shown as dots colored to denote redshift (and age of the Universe), assuming $L_{\text{line}}=10^9 L_{\odot}$. BLISS also has excellent sensitivity to broad features such as the PAH bands—a redshifted $L=10^{12} L_{\odot}$ galaxy template is plotted, with flux scaled to show the BLISS sensitivity when binned to $R=60$.

Gas cell measurement using a 2.9 THz heterodyne receiver based on a quantum cascade laser and a superconducting hot electron bolometer

Y. Ren^{1,2,3,*}, J.N. Hovenier¹, R. Higgins⁴, J.R. Gao^{1,5}, T.M. Klapwijk¹, S.C. Shi², A. Bell⁶, B. Klein⁶, T-Y. Kao⁷, S. Kumar⁷, Q. Hu⁷, and J. L. Reno⁸

¹*Kavli Institute of NanoScience, Delft University of Technology, The Netherlands*

²*Purple Mountain Observatory (PMO), Chinese Academy of Sciences, Nanjing, China.*

³*Graduate School, Chinese Academy of Sciences, China*

⁴*National University of Ireland, Maynooth, Ireland*

⁵*SRON Netherlands Institute for Space Research, The Netherlands*

⁶*Max-Planck-Institut für Radioastronomie (MPIfR), Bonn, Germany*

⁷*Department of Electrical Engineering and Computer Science, Massachusetts Institute of Technology, Cambridge, U.S.A.*

⁸*Sandia National Laboratories, Albuquerque, NM 87185-0601, U.S.A.*

*Contact: y.ren@tudelft.nl, phone +31-15-278 6113

Abstract— Superconducting heterodyne receiver has played a vital role in the high resolution spectroscopy applications for astronomy and atmospheric research up to 2THz. NbN hot electron bolometer (HEB) mixer, as the most sensitive mixer above 1.5THz, has been used in the Herschel space telescope for 1.4-1.9THz and has also shown an ultra-high sensitivity up to 5.3THz. Combined a HEB mixer with a novel THz quantum cascade laser (QCL) as local oscillator (LO), such an all solid-state heterodyne receiver provides the technology which can be used for any balloon-, air- and space-borne heterodyne instruments above 2THz. Here we report the first high-resolution heterodyne spectroscopy measurement using a gas cell and using such a HEB-QCL receiver. The receiver employs a 2.9THz metal-metal waveguide QCL as LO and a NbN HEB as a mixer. By using a gas cell filled with methanol (CH₃OH) gas in combination with hot/cold blackbody loads as signal source, we successfully recorded the methanol emission line around 2.918THz. Spectral lines at different pressures and also different frequency of the QCL are studied.

I. INTRODUCTION

High-resolution spectroscopy, as a technology to study the rotational lines from ions, atoms and molecules, plays a vital role in atmospheric and astronomical research at terahertz frequency in space. Heterodyne spectroscopy based on superconducting heterodyne receiver provides the most promising performance for its nearly quantum limited sensitivity and ultra high spectral resolution ($\nu/\Delta\nu > 10^6$, where ν is the frequency). A superconducting HEB mixer has shown a superior sensitivity up to 5.3THz [1]. Availability of suitable local oscillator sources (LOs) above 2THz becomes the only limiting factor for the future applications. Thanks to the recently developed terahertz QCLs [2], we have a promising candidate. THz QCLs, compared with other sources such as solid state THz sources based on multipliers and optically pumped gas lasers, they show advantages with regard to the output power, frequency coverage, compactness,

and power consumption. Until now, THz QCL has demonstrated performances such as covering almost the whole THz frequency range [3], peak emission power over 100mW [4] and maximum operating temperature 190K in pulse mode [5]. It has been proved to be a suitable source for various applications such as sensing, imaging [3], gas phase spectroscopy [6], and LO for a heterodyne receiver [7,8]. Besides, THz QCL has exhibited excellent power stability [7], phase-lock capability [9], and narrow intrinsic linewidth [10], which meet essentially the requirements as a LO. Many experiments have been reported to demonstrate the suitability of a QCL as LO, however, no truly heterodyne spectroscopic measurement using a QCL as LO has been reported until now. In this paper we present the first high resolution spectroscopic measurement at 2.9THz using a gas cell containing methanol and using a double sideband heterodyne receiver based on a THz QCL as LO and a NbN HEB as mixer.

II. THZ QCL

The QCL used in this experiment is a metal-metal waveguide QCL, developed by Qing Hu's group at MIT. It is based on resonant phonon scattering as described in reference [11]. The active region contains 176 GaAs/Al_{0.15}Ga_{0.85}As quantum well modules. The 40 μ m wide ridge waveguide was cleaved at both ends to form a 1.18mm long Fabry-Perot cavity, and it is fabricated using a copper-to-copper thermocompression wafer bonding technique. The QCL is indium soldered on a copper mount and is mounted on the cold stage of a helium-flow cryostat. As shown in Figure 1, the QCL emits a single-mode emission line at 2.918THz in continuous wave mode. The spectrum was measured using a Fourier-transform Spectrometer (FTS) [12]. Latter has a spectral resolution of 0.7GHz, which is much larger than the intrinsic linewidth of the QCL, typically in the range of 6-30KHz. In the current measurement, we used a free-running

QCL (namely without any stabilization on the phase/frequency and the amplitude), Based on the previous experience [9], due to the jitter we expect a linewidth of less than 1MHz in practice. The QCL provides a maximum output power of 1mW in the CW mode and at a temperature of 30K. Although the laser can be operated up to about 100K, in our experiment we operated the laser at the lowest temperature (~30K).

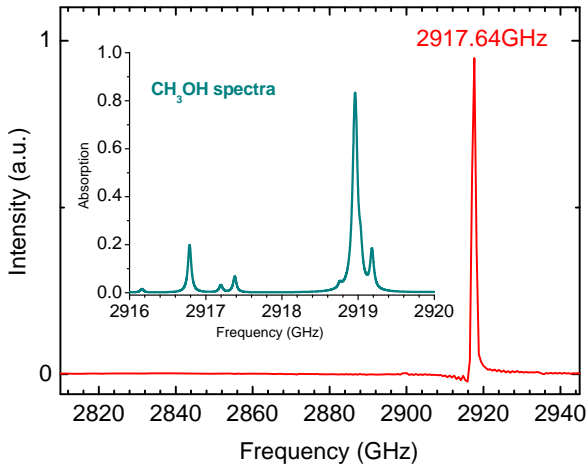


Fig. 1 Measured emission spectrum of a THz quantum cascade laser biased at 16.44V at a bath temperature around 30K in CW mode. It is measured with a FTS with a resolution of 0.7GHz. The inset shows simulated methanol (CH_3OH) spectrum [15] for a 0.5m optical path length and gas cell pressure of 5.9mBar between 2916 and 2920GHz.

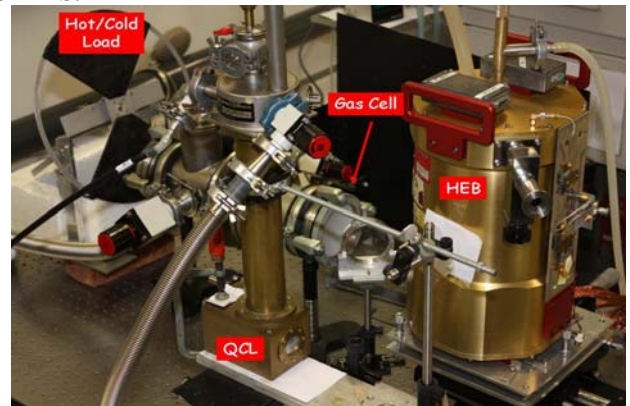
III. HEB MIXER

We use a NbN HEB mixer, which consists of a $2\mu\text{m}$ wide, $0.2\mu\text{m}$ long, and 5.5nm thick NbN bridge [13]. The bridge is connected with a tight winding spiral antenna, which is made of a 170nm thick Au layer, and has an inner diameter of $6.6\mu\text{m}$. This special design expands the cut off frequency up to 6THz [14]. The HEB has a low-temperature normal-state resistance (R_N) of 83Ω , a critical temperature of 9.3K, and a critical current of $210\mu\text{A}$ at 4.2K. In a separate experiment [1], the mixer has shown superior sensitivities across the frequency range of 1.6-5.3THz, from which the receiver noise temperature ($T_{N,\text{rec}}$) around 2.9THz is expected to be 1000K [1].

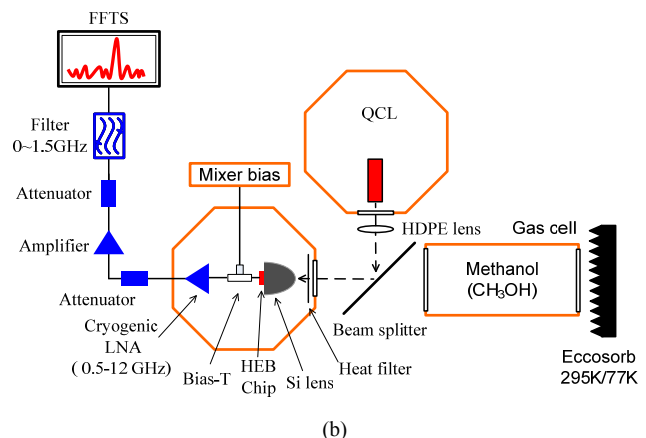
IV. MEASUREMENT SETUP

The spectroscopic measurement setup is shown in Figure 2. We use two separate L-He cryostats for QCL and HEB mixer, respectively. For coupling the THz radiation from free space to the antenna of the HEB mixer, we used an elliptical silicon lens without anti-reflection coating. The lens is placed in a metal mixer unit, which is mounted on the 4.2K cold plate of the cryostat. The THz radiation beam from the QCL firstly passes through the high-density polyethylene (HDPE) window of the QCL's cryostat and then is focused with a HDPE ($f=26.5\text{mm}$) lens. As signal source, it is a combination of a gas cell and hot/cold blackbody loads. The gas cell is a

50cm long cylinder with an inner diameter of 10cm (at room temperature). It has two HDPE windows with a thickness of 1.5mm at two ends of the gas cell. The blackbody load is defined as a hot load at 295K and as a cold load at 77K. The gas we used is methanol (CH_3OH), from which a few absorption lines are expected in the vicinity of the LO frequency [15]. The expected spectral lines with different strength are plotted in the inset of figure 1. By applying three valves for methanol gas (two) and vacuum pump (one), the gas pressure inside the cell can be controlled relatively accurately. The gas pressure in the cell is measured by a gas-independent gauge [16]. The methanol emission lines and the QCL signal are combined by a $3\mu\text{m}$ thick Mylar beam splitter and are fed further into the HEB mixer. The intermediate frequency (IF) signal is amplified first using a wide band low noise amplifier (0.5-12GHz) at 4.2K, and then followed by a room-temperature amplifier with 13dB attenuator in between. As back-end spectrometer, we used a Fast Fourier Transform Spectrometer (FFTS) [17], which is developed by MPIfR in Bonn. This FFTS provides 8192 channels for the frequency range of 0 to 1.5GHz, and thus gives a spectral resolution of 183KHz. In order to match the optimal input signal intensity required by the FFTS a 6dB attenuator is employed, and to avoid aliasing effect a 1.5GHz low pass filter is added before the FFTS.



(a)



(b)

Fig. 2 Picture (a) and Schematic view (b) of the heterodyne gas cell measurement setup.

V. RESULTS

Before we perform spectroscopic measurement, we calibrated the sensitivity of the whole system at the optimal operating point (bias and LO power) for the HEB mixer. We measured first the receiver noise temperature for the case where the hot/cold loads are positioned just after the beam splitter, and found it to be 2500K. When the hot/cold loads are positioned after the gas cell, which is evacuated, the receiver (system) noise temperature increases to 3800K. The difference between these two can be attributed to the loss due to two windows ($2 \times 0.9\text{dB}$) of the gas cell and the additional loss due to the air in the optical pass. The value of 2500K is higher than other measurement [1], that can be attributed to the losses due to the window of HEB cryostat and the air, to non-optimised IF chain due to the use of the wide band low noise IF amplifier, and to the direct detection effect. To measure the spectral lines of methanol, we used the same method as described in reference. 18. We record three IF noise power traces using the FFTS, which are: 1) the spectrum $S_{emp77}(f)$ when the cold load is behind the evacuated gas cell; 2) $S_{gas77}(f)$ when the cold load is behind the filled gas cell; 3) $S_{gas300}(f)$ when the hot load is behind the filled gas cell. All three traces are recorded when the HEB is operated at its optimal operating point. Each trace is measured by the FFTS with an integration time of 5 second. The brightness of the methanol emission lines in terms of temperature is calculated according to the following expression:

$$T_{gas}(f) = T_{cold} + (T_{hot} - T_{cold}) \frac{S_{gas77}(f) - S_{emp77}(f)}{S_{gas300}(f) - S_{emp77}(f)} \quad (1)$$

where all the temperatures are the effective temperatures defined by the Callen-Welton form [19] because of the THz frequency .

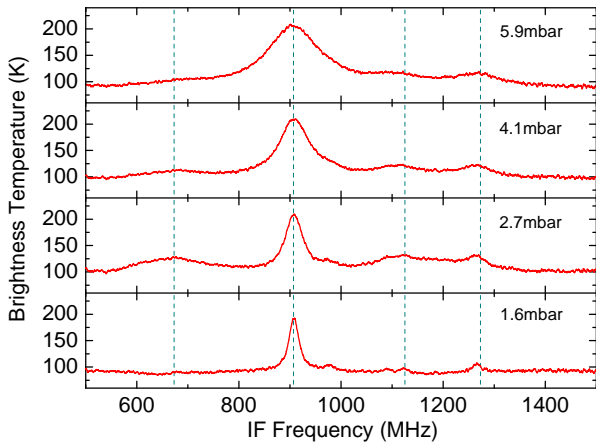


Fig. 3 Measured line spectra of methanol (CH_3OH) gas within the IF range between 0.5 and 1.5GHz. The QCL’s frequency is 2918.053GHz and the gas cell pressure varies from 1.6mBar to 5.9mBar. The dash line indicates positions of the theoretical simulated methanol lines.

By varying the gas pressure we are able to measure the methanol spectral lines at different pressures. Figure 3 shows such a set of spectra within the IF frequency range between 0.5 to 1.5GHz and with increased pressures varying from

1.6mBar to 5.9mBar. A relatively strong methanol emission line is found at an IF frequency of 907MHz, which is assumed to be the methanol line at 2918.96GHz in the upper sideband (USB) with respect to the LO frequency, as shown in the inset of figure 1. Since our receiver measures double sideband, we should see lines from both the upper side band and lower side band (LSB). Three relatively weak lines, as shown in the inset of figure 1, were also successfully detected. Those are at 673MHz (lower sideband, LSB), 1125MHz (USB) and 1273MHz (LSB), respectively. Having done such a comparison, we can also derive the QCL’s frequency that is 2918.053GHz, which agrees well with the frequency measured by FTS.

Since the frequency of the QCL can be tuned slightly by varying its bias voltage, we can make use of this to have an additional check for the correspondence between the expected spectral of methanol and the measured ones. As shown in figure 4, the measured spectra are indeed varied by changing the bias of the QCL. A detailed analysis shows that all those spectra correspond well to the predicted emission lines in the inset of figure 1. We find a tuning coefficient for this specific QCL to be about 550MHz/V. It is known that this is a compromise between the “red shift” caused by the thermal tuning and the “blue shift” due to the Stark effect by the bias [9].

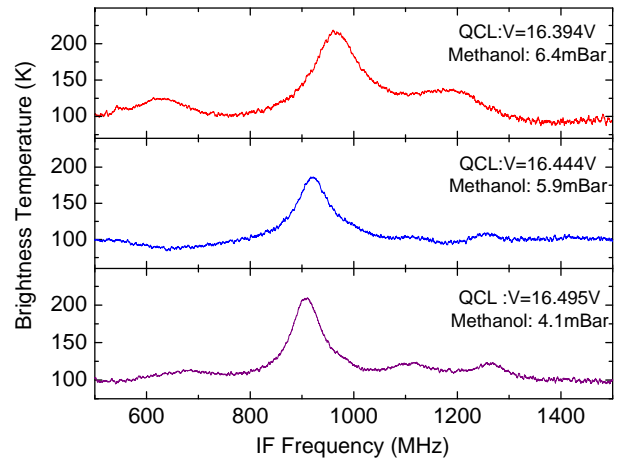


Fig. 4 Line spectra of methanol (CH_3OH) gas within the IF range between 0.5 and 1.5GHz measured with different the bias voltage to the QCL. The different bias varies the QCL frequency a bit. Although the pressure is slightly different, the key point is the change of line positions.

We have fitted the measured strong line at 907 MHz using a Lorentzian line profile. The result is shown in figure 5, the reasonable fitting quality suggests that measured line profile is Lorentzian. Theoretically, besides the pressure broadening, there are two main factors to determine the intrinsic methanol line profile. One is natural broadening and the other is Doppler broadening. The natural broadening process and pressure broadening both will give a Lorentzian line profile. For the second case, the Doppler broadening effect will impose a full width at half maximum (FWHM) of 200 KHz and should give a Gaussian line profile. Obviously this does not apply to our experiment. So in our case we should expect

a Lorentzian line profile and this is what we saw experimentally.

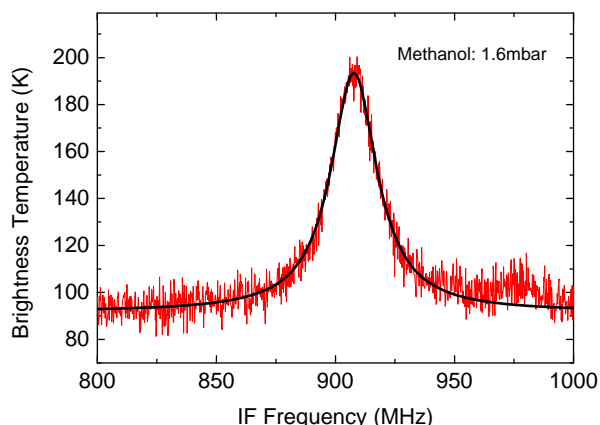


Fig. 5 Measured line spectra of methanol (CH_3OH) gas at 2918.96GHz, where the gas cell pressure is 1.6mBar. Also shown is a Lorentzian profile fitting.

Using the strong line measured at pressures from 1 to 6.5mBar, we can determine the pressure broadening coefficient by plotting FWHM as a function of the methanol pressure. We find it to be $15 \pm 2 \text{ MHz/mBar}$. This value is considerably lower than what expected by the model [15]. One hypothesis is that we might have leakage of the air into the gas cell. Because of the leakage, we are able to obtain the exact methanol spectra, but not correct pressure broadening coefficient. By the time we are writing this paper, we have discovered the leakage in one of the valves in our setup, which controls methanol into the gas cell. With the improved setup we have taken new methanol spectra successfully. However, a detailed analysis of the data is needed and is also planned.

VI. SUMMARY

In conclusion we have for the first time succeeded in demonstrating high-resolution heterodyne spectroscopic measurement using a double side band heterodyne receiver based on a THz quantum cascade laser as local oscillator and a NbN HEB as mixer. The QCL is operated in a free running mode and emits LO signal at 2918.053GHz. Within an IF bandwidth of 0.5 - 1.5GHz we observed 4 methanol lines. One of them is a relatively strong line at 2918.96GHz. Our gas cell measurement is a crucial demonstration of the QCL as LO for practical heterodyne instruments. Together with other recent progresses, such as the wide tuning range of THz QCL ($\sim 100\text{GHz}$) [20], phase locking, and pumping a HEB mixer when a QCL is operated at 60-70K, THz QCL is in principle ready for building a real instrument at the super-THz frequencies.

ACKNOWLEDGMENT

We acknowledge W. Zhang and P. Khosropanah for their support to make the HEB mixer ready for this experiment. The work was partly supported by China Exchange Programme executed by KNAW and CAS, and by the AMSTAR+ project of RadioNet under FP7, and NWO.

REFERENCES

- [1] W. Zhang, P. Khosropanah, J.R. Gao, E. L. Kollberg, K. S. Yngvesson, T. Bansal, R. Barends, and T. M. Klapwijk, "Quantum noise in a terahertz hot electron bolometer mixer," *Applied Physics Letter* **96**, 111113 (2010).
- [2] R. Köhler, A. Tredicucci, F. Beltram, H. E. Beere, E. H. Linfield, A. G. Davies, D. A. Ritchie, R. C. Iotti, and F. Rossi, "Terahertz semiconductor-heterostructure laser," *Nature*, **417**, 156 (2002).
- [3] B. S. Williams, "Terahertz quantum-cascade lasers," *Nature photonics*, **1**, 517 (2007).
- [4] A. W. M. Lee, Q. Qin, S. Kumar, B. S. Williams, Q. Hu, and J. L. Reno, "High-power and high-temperature THz quantum-cascade lasers based on lens-coupled metal-metal waveguides," *Opt. Lett.* **32**, 2840 (2009)
- [5] S. Kumar, Q. Hu, and J. L. Reno, "186 K operation of terahertz quantum-cascade lasers based on a diagonal design," *Appl. Phys. Lett.* **94**, 131105 (2009).
- [6] H.-W. Hübers, S.G. Pavlov, H. Richter, A.D. Semenov, L. Mahler, A. Tredicucci, H.E. Beere, and D.A. Ritchie, "High-resolution gas phase spectroscopy with a distributed feedback terahertz quantum cascade laser," *Appl. Phys. Lett.* **89**, 061115 (2006).
- [7] J.R. Gao, J.N. Hovenier, Z.Q. Yang, J.J.A. Baselmans, A. Baryshev, M. Hajenius, T.M. Klapwijk, A.J.L. Adam, T.O. Klaassen, B.S. Williams, S. Kumar, Q.Hu, and J.L. Reno, "Terahertz heterodyne receiver based on a quantum cascade laser and a superconducting bolometer," *Appl. Phys. Lett.* **86**, 244104 (2005).
- [8] H.-W. Hübers, S. G. Pavlov, A. D. Semenov, R. Köhler, L. Mahler, A. Tredicucci, H. E. Beere, D. A. Ritchie, and E. H. Linfield, "Terahertz quantum cascade laser as local oscillator in a heterodyne receiver," *Opt. Express* **13**, 5890 (2005).
- [9] P. Khosropanah, A. Baryshev, W. Zhang, W. Jellema, J. N. Hovenier, J. R. Gao, T. M. Klapwijk, D. G. Paveliev, B. S. Williams, S. Kumar, Q. Hu, J. L. Reno, B. Klein, and J. L. Hesler, "Phase locking of a 2.7 THz quantum cascade laser to a microwave reference," *Opt. Lett.* **34**, 2958 (2009)
- [10] A. Barkan, F. K. Tittel, D. M. Mittleman, R. Dengler, P. H. Siegel, G. Scalari, L. Ajili, J. Faist, H. E. Beere, E. H. Linfield, A. G. Davies, and D. A. Ritchie, "Linewidth and tuning characteristics of terahertz quantum cascade lasers," *Opt. Lett.* **29**, 575 (2004).
- [11] B. S. Williams, H. Callebaut, S. Kumar, Q. Hu, and J. L. Reno, "3.4-THz quantum cascade laser based on longitudinal-optical-phonon scattering for depopulation," *Appl. Phys. Lett.* **82**, 1015 (2003).
- [12] ABB Bomen Inc., St-Laurent, Canada
- [13] M. Hajenius, J.J.A. Baselmans, J.R. Gao, T.M. Klapwijk, P.A.J. de Korte, B. Voronov and G. Gol'tsman, "Low noise NbN superconducting hot electron bolometer mixers at 1.9 and 2.5THz," *Supercond. Sci. Technol.*, vol. **17**, 224 (2004).
- [14] A.D. Semenov, H. Richter, H.-W. Hübers, B. Günther, A. Smirnov, K.S. Il'in, M. Siegel, and J.P. Karamarkovic, "Terahertz performance of integrated lens antennas with a hot-electron bolometer," *IEEE Trans. Microwave Theory Tech.* **55**, 239 (2007).
- [15] R. Higgins, et al., 21st International Symposium on Space Terahertz Technology (ISSTT 2010), Oxford.
- [16] MKS Instruments, Inc. <http://www.mksinst.com/product/category.aspx?CategoryID=72>.
- [17] B. Klein, I. Krämer, S. Hochgürtel, R. Güsten, A. Bell, K. Meyer, and V. Chetuk, "Fast Fourier Transform Spectrometer," 20th International Symposium on Space Terahertz Technology (ISSTT 2009), Charlottesville.
- [18] S. Ryabchun, C.-Y. Tong, S. Paine, Y. Iobanov, R. Blundell, and G. Gol'tsman, "Temperature resolution of an HEB receiver at 810 GHz," *IEEE Trans. App. Supercond.* **19**, 293 (2009)
- [19] H. B. Callen, and T. A. Welton, "Irreversibility and Generalized Noise," *Phys. Rev.* **83**, 34 (1951).
- [20] Q. Qin, B. S. Williams, S. Kumar, J. L. Reno, and Q. Hu, "Tuning a terahertz wire laser," *Nature photonics*, **3**, 732 (2009)

A flexible quasioptical input system for a submillimeter multi-object spectrometer

Paul F. Goldsmith* and Michael Seiffert*

*Jet Propulsion Laboratory

California Institute of Technology

4800 Oak Grove Drive

Pasadena, CA 91109

Email: Paul.F.Goldsmith@jpl.nasa.gov

Abstract

We present a conceptual design for the input optical system for a multi-object spectrometer operating at submillimeter wavelengths, which is well suited for use on the Cornell Caltech Atacama Telescope (CCAT) or any other large single-dish telescope having a large field of view. The "Mirror MOS" is based on a sequence of mirrors that enable low-loss propagation of beams from selected positions distributed throughout the focal plane to the spectroscopic receiver inputs. Unlike the majority of millimeter and submillimeter focal plane arrays built to date, the key requirement for a multi-object spectrometer is not to get full sampling of a region of the sky, but to be able to observe selected sources that are sparsely distributed over the relatively large area imaged to the focal plane. The approach we describe here should be useful for observations of distant galaxies which have a relatively low density on the sky, but which are very weak so that simultaneous observation of many sources results in a significant improvement in telescope productivity. It is assumed that the candidate sources have been previously identified, so that their coordinates are known. Our concept is based on assigning a patrol region to each of the receivers, which have inputs distributed over the focal plane of the telescope. The input to each receiver can be positioned at any point within this patrol region. This approach, with only 4 reflections, offers very low loss. In many cases, a set of flat mirrors can be used, but employing focusing optics can make the system more compact. A further advantage of using beam transformation is that a Gaussian beam optical system can be designed to produce frequency-independent illumination of the telescope, which is an important advantage for very broadband systems such those required for determination of redshifts of submillimeter galaxies. We have made calculations of the expected efficiency of such a Mirror MOS system with a range of patrol region parameters, receiver number, and source density, and find that ~ 80 percent utilization can be expected for redshift determination from CO lines and reasonable estimates of submillimeter galaxies observed with a 25 m telescope observing in the 1mm atmospheric window.

Wide-band heterodyne submillimetre wave spectrometer for planetary atmospheres

Erich Schlecht

Jet Propulsion Laboratory, California Institute of Technology
 Contact: Erich.Schlecht@jpl.nasa.gov, phone +01-818-354-4887

Abstract— We present calculations and measurements on a passive submillimetre wave spectroscopic sounder to gather data on the thermal structure, dynamics and composition of the upper atmosphere of a planet, e.g. the stratosphere of Jupiter, or the entire thickness of the atmosphere of Mars. The instrument will be capable of measuring *wind speeds, temperature, pressure, and key constituent concentrations* in the stratosphere of the target planet. This instrument consists of a Schottky diode based front end and a digital back-end spectrometer. It differs from previous space-based spectrometers in its combination of wide tunability (520-590 GHz), and rapid frequency switching between widely spaced lines within that range. This will enable near simultaneous observation of multiple lines, which is critical to the reconstruction of atmospheric pressure and density versus altitude profiles. At the same time frequency accuracy must be high to enable wind speeds to be determined directly by measurement of the line's Doppler shift.

I. INTRODUCTION

Recently, NASA and ESA have turned their attention to an Outer Planet Flagship Mission (OPFM) to the Jupiter system, focusing on Ganymede, Europa and other Galilean moons, as well as Jupiter, and to the Saturn system focusing on the Titan. Both studies call for inclusion of a submillimeter spectrometer. The Jupiter measurements will greatly expand on those from the Juno mission currently being built, the prime target being Jupiter's stratosphere. Titan measurements would concentrate on the upper atmosphere dynamics of hydrocarbon chemistry. Another possible target for a submillimetre wave spectrometer is Mars, whose atmosphere is thin enough to be observed all the way to the surface.

Submillimetre spectral observations of these planets' atmospheres will allow multiple physical properties of the atmosphere to be measured as a function of altitude and latitude/longitude:

- Concentration of various critical gases of interest
- Pressure
- Temperature
- Wind Velocity

Fig. 1a shows a planet limb sounding observation, where the radiometer observes the atmosphere against the cold dark background of space. Fig. 1b shows a simulated line intensity profile for HCN (531.7 GHz) at two different altitudes over Titan and several mixing ratios (ratio of HCN to all gases). The 100 km lines are dominated by pressure broadening, the 500 km line is entirely Doppler broadened. In between, the line shape is a combination known as the Voigt profile. By

examining these line profiles as a function of h_T , the minimum limb observation altitude, a model of the concentration/temperature/pressure profiles can be determined.

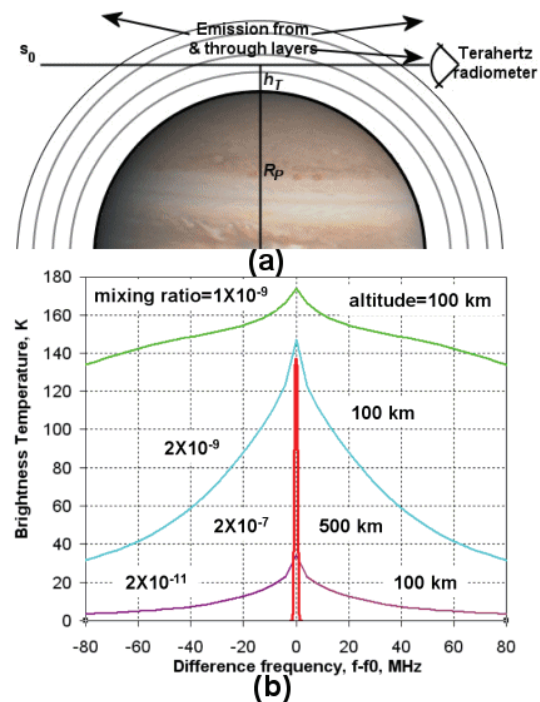


Fig. 1. (a) Limb sounding spectrometer configuration frequency. (b) A few spectral line profiles for HCN at Titan.

In order to retrieve separate the signal pressure profile from the concentration profile, it is necessary to observe more than one line of the relevant gas species. Because of the rapid movement of the spacecraft at Mars or Titan, the spectrometer needs to switch rapidly from one to the other while integrating the signal to produce near simultaneous measurements before the spacecraft motion degrades the measurement. Wind velocity determination uses the Doppler effect to determine the relative radial velocity between the spacecraft and the spot in the atmosphere being observed.

This paper examines the affect of system additive noise, phase noise, and line-to-line frequency switching on the quality of the measurement of the line profile and the line frequency accuracy.

II. SYSTEM ADDITIVE NOISE

The system under consideration is depicted in the block diagram of Fig. 2. The signal from the planet enters at the left, and is mixed in the mixer with a locally generated LO signal. The LO is derived from the ultra-stable oscillator (USO) primary frequency reference, and generated by a synthesizer at a frequency range around 30 GHz. From the synthesizer, the signal frequency is multiplied by the active millimetre wave/submillimetre wave chain by a factor of 18 to the signal frequency. The mixer IF output is amplified and converted to the range of 0-125 MHz, digitized, and analysed by an FFT-type discrete Fourier transform (DFT) spectrum analyser, followed by additional signal processing to be described later.

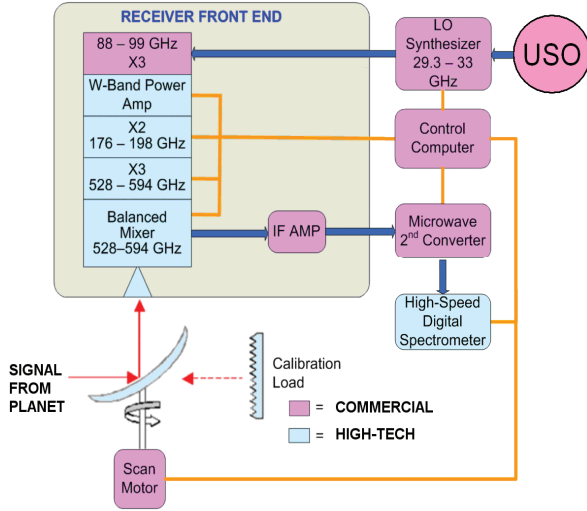


Fig. 2. Block diagram of spectrometer.

White noise from both the background of the observation and the mixer's thermal and shot noise enters the system, where it adds to the desired signal, resulting in measurement uncertainty. This additive noise affects both the frequency estimate and the amplitude profile determination of the spectral line.

A. Effect of system noise on frequency estimate

The effect of Gaussian additive noise on the frequency estimate of a single line (less than a channel bandwidth wide) has been analyzed by [1, 2] for the idealized case of an infinitely narrow sinusoidal CW line. The minimum possible frequency uncertainty, known as the Cramers-Rao lower bound (CRLB) [3] on the variance is given as:

$$\text{var}\{\hat{\omega}_1\} = \frac{6\sigma^2}{\hat{A}^2 N(N^2 - 1)} \quad (1)$$

\hat{A} is the amplitude estimate, σ^2 is the Gaussian noise voltage variance, and N the total number of points in the measurement. In the nomenclature of [1], the frequencies are normalized to the inter-sample time, T :

$$\hat{\omega}_1 = 2\pi\hat{f}T$$

To express the frequency uncertainty in terms of the system temperature, T_{sys} , some identities must be used. The total noise power σ^2 , is the product of the total noise power density, kT_{sys} , times the Nyquist bandwidth, $1/(2T)$, i.e.

$$\sigma^2 = \frac{kT_{\text{sys}}}{2T}. \quad (2)$$

As for most spectrometers $N^2 \gg 1$ so the CRLB frequency variance can be expressed as

$$\text{var}\{\hat{f}\} = \frac{3kT_{\text{sys}}}{4\pi^2 N^3 T^3 \hat{A}^2}. \quad (3)$$

For a DFT spectrometer, the channel bandwidth is the inverse of the total measurement time for each spectrum, $B_C = 1/(NT)$. In the measurement mode anticipated for the planetary spectrometer, successive measurements will have their power spectral densities summed [4]. Assuming these measurements are not correlated, frequency variance will be reduced the number of spectra averaged together, N_S . With this in mind, define the total integration time as:

$$\tau_I = N_S NT = \frac{N_S}{B_C} \quad (4)$$

Finally the frequency uncertainty (deviation) is expressed as the square root of the variance,

$$\Delta f = \sqrt{\text{var}\{\hat{f}\}} = \sqrt{\frac{3kT_{\text{sys}}B_C^2}{4\pi^2 \hat{A}^2 \tau_I}} = \sqrt{\frac{3B_C}{2\pi^2 \tau_I} \frac{1}{\text{SNR}}}, \quad (5)$$

where the last expression expresses the deviation in terms of the channel signal to noise ratio defined as the ratio of the line power ($\hat{A}^2/2$) to the channel noise power:

$$\text{SNR} = \frac{\hat{A}^2}{2kT_{\text{sys}}B_C} \quad (6)$$

Usually the only variable than can be manipulated for any particular measurement is the integration time, the others being set by practical considerations.

B. Effect of system noise on line profile estimate

The total power in a "limited-bandwidth" channel is given by Rice (Dover, etc.), who derived it in the context of a band-limited square law device:

$$P = \sigma_C^2 + \frac{\hat{A}^2}{2}, \quad (7)$$

which is the sum of the CW power and the channel noise power. The channel noise power, σ_C^2 , is the total noise power σ^2 divided by the number of frequency channels:

$$\sigma_C^2 = \frac{\sigma^2}{N/2} = kT_{\text{sys}}B_C,$$

using the results from the previous section.

The variance of P [5, eq 4-16] is, again taking into account averaging over N_S records,

$$\text{var}\{P\} = \frac{\sigma_C^2}{N_S} (\sigma_C^2 + \hat{A}^2). \quad (8)$$

Note that if the channel contains pure noise, $\hat{A} = 0$ and the deviation for a single measurement ($N_S=1$) is 100% of the power, i.e. σ_C^2 . On the other hand, if $\hat{A}^2 \gg \sigma_C^2$, the deviation

is much higher, $\sigma_C \hat{A}$, since the power is the square of the sum of the line voltage and noise voltage. Expressing the channel power in terms of T_{sys} gives, for the power estimate deviation,

$$\Delta P \equiv \text{dev}\{P\} = \sqrt{\text{var}\{P\}} = \sqrt{\frac{kT_{sys}B_C}{N_S} (kT_{sys}B_C + \hat{A}^2)}. \quad (9)$$

For $\hat{A} \sim 0$, the “signal” as well as the noise has a white spectrum, and it is sensible to define the power estimate deviation in terms of noise equivalent temperature difference:

$$\Delta P = k\Delta T_{eq}B_C$$

Putting this into (6) with $\hat{A} = 0$, and using (2) to replace N_S results in the radiometer equation:

$$\Delta T_{eq} = \frac{T_{sys}}{\sqrt{B_C\tau_l}} \quad (10)$$

Conversely, For $\hat{A}^2 \gg \sigma_C^2$ it is more sensible to express the result as a relative power deviation,

$$\frac{\Delta P}{P} = \frac{2\sqrt{\text{var}\{P\}}}{\hat{A}^2} = \sqrt{\frac{4kT_{sys}B_C}{N_S\hat{A}^2}} = \sqrt{\frac{2}{B_C\tau_l} \frac{1}{SNR}}, \quad (11)$$

with the last equivalence applying to the DFT spectrometer and including equations (4) and (6).

III. PHASE NOISE

In addition to the effect of AM noise on the frequency and line profile uncertainty, the effect of phase noise can be determined, in order to establish that the local oscillator

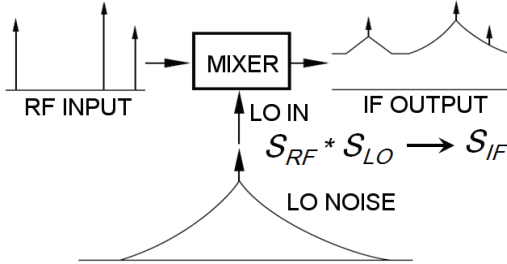


Fig. 3. LO Phase noise convolves with spectral lines to distort them.

does not degrade the measurement accuracy further. As depicted in Fig. 3, the LO phase noise profile is mixed with the input signal, polluting it. Since the mixer operates like a time domain multiplying element, the IF output is the product of the LO and RF signals in the time domain. Since the phase noise is described statistically in the frequency domain, the RF signal must be converted to frequency domain and, by the convolution theorem, the total signal is the convolution of the two. The phase-noise distorted IF signal is [3, p503] –

$$S_{IF}(f) = \int_{-\infty}^{\infty} S_{LO}(f-f')S_{RF}(f')df' \quad (12)$$

For example, if the LO were a perfect sinusoid at frequency F_{LO} , its Fourier transform would be $S_{LO}(f) = \delta(f + F_{LO}) + \delta(f - F_{LO})$ and the IF signal would simply be a phase shifted version of the RF and image.

One problem presented by the phase noise is distortion of the RF signal. If a strong line is close to a weak one, the phase noise will spread out the line, increasing the chance of it interfering with the weak one.

Besada [6] came up with a similar criterion based on an effective spectrometer channel filter. He noted that the output of one channel of the spectrometer would be:

$$S_{IF}(f) = |H(f)|^2 \int_{-\infty}^{\infty} S_{LO}(f-f')S_{RF}(f')df', \quad (12a)$$

similar to equation (12) but including the filter transmission function $H(f)$. The total channel output power is then given by an additional integration:

$$P = \int_{-\infty}^{\infty} |H(f)|^2 \left[\int_{-\infty}^{\infty} S_{LO}(f-f')S_{RF}(f')df' \right] df.$$

Now reverse the order of integration:

$$P = \int_{-\infty}^{\infty} S_{RF}(f') \left[\int_{-\infty}^{\infty} S_{LO}(f-f')|H(f)|^2 df \right] df'$$

which is a convolution of the RF signal with the IF channel response:

$$S_{CHAN}(f) = \int_{-\infty}^{\infty} S_{LO}(f-f')|H(f')|^2 df'. \quad (13)$$

This is just equation (12) substituting the RF line profile SRF with the channel profile, $|H(f)|^2$. Note that all of these spectral densities are two sided, integrated from $-\infty$ to $+\infty$. Hence, they should be determined from the normal one-sided density by dividing by two. Also, $S_{LO}(f)$ is assumed even in f .

The convolution of equation (13) can be used to calculate the distortion of the filter profile of the spectrometer channel, $|H(f)|^2$ in the output response, S_{CHAN} by the phase noise, S_{LO} . If S_{LO} were an ideal delta function S_{CHAN} would be the same as $|H(f)|^2$. In order to determine S_{LO} it is necessary to determine the effect of multiplication of the LO signal source up to the submillimetre wave signal frequency on the known (specified) low frequency LO source. According to the simple model proposed by Walls and DeMarchi [7, 8] the phase noise of a typical source can be divided into a central “carrier” where the carrier is sharply peaked at low Fourier frequencies $< f_p$, and the pedestal continues relatively flat out to some much higher frequency B . f_p might be around 1 kHz,

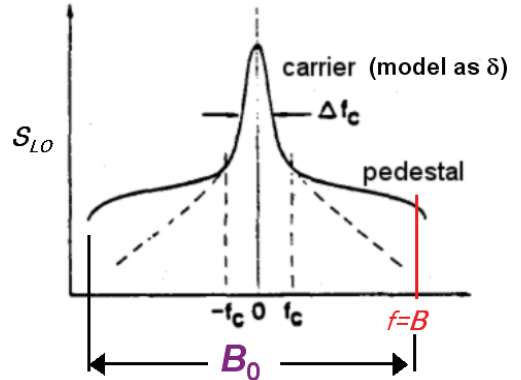


Fig. 4. LO phase noise spectrum, showing carrier in center and “pedestal”. Based on [9].

B around 1000 kHz. See Fig. 4. As long as f_p is much smaller than the channel bandwidth (as in our case) the phase noise effect can be parameterized in terms of the total phase variance of the pedestal region, defined as:

$$\Phi_p = \int_0^{\infty} S_{\phi}^p(f)df, \quad (14)$$

where the parameter $\Phi_p \equiv \langle \phi_p^2 \rangle$ is the total integrated phase error in the pedestal and the sub- or superscript p refers to the pedestal. (Note that Walls and Dimarchi have the integration carried out from f_p , though Bava starts at 0. Since the pedestal has almost no power in the low-frequency-offset carrier region, the difference is inconsequential.)

Since multiplication into the submillimetre wave range by a factor of N increases the phase noise by N^2 , the normal small angle approximation where $S_{LO} = S_\phi$ is longer valid. Instead, the normalized carrier power (carrier power to total power) can be approximated:

$$P_c = \exp(-\Phi_p), \quad (15a)$$

Then the normalized pedestal power is:

$$P_p = 1 - P_c = 1 - \exp(-\Phi_p). \quad (15b)$$

At low phase noise levels ($\Phi_p \ll 1$) $P_c \approx 1$ and $P_p \approx \Phi_p$. As the phase noise levels increase with multiplication to higher frequencies, signal power is transferred from the carrier to the pedestal, broadening it. The model assumes that S_ϕ is not affected by multiplication, other than the general $20\log N$ increase:

$$S_\phi^p(f) = \frac{S_\phi^p(0)}{1+(f/B)^2} = \frac{2\Phi_p}{\pi B} \frac{1}{1+(f/B)^2}, \quad (16)$$

assuming the pedestal exhibits a Lorentzian frequency dependence with 3-dB half-width bandwidth B , though exponents other than 2 could also be used.

To calculate the effect of phase noise on the power in the spectrometer channels, we want to determine S_{LO} . Walls and DeMarchi noted that the pedestal at frequencies well below its bandwidth followed a simple law:

$$S_{LO}^p(0) = \frac{2P^2}{\pi B \Phi_p}$$

Assume the pedestal has continues to exhibit a Lorentzian frequency profile at high phase noise levels with a two-sided

bandwidth $\Delta\nu_p$, the complete power spectrum of the pedestal can be determined by combining the three previous equations and noting that S_{LO} integrated from 0 to ∞ gives the total pedestal power P_p :

$$S_{LO}^p(f) = \frac{2P^2}{\pi B \Phi_p} \left[\frac{1}{1+(2f/\Delta\nu_p)^2} \right] \quad (17)$$

with the full-width bandwidth of:

$$\Delta\nu_p = 2B \frac{\Phi_p}{1 - \exp(-\Phi_p)}$$

Note that for small values of the total phase error, Φ_p , $S_{LO} \rightarrow S_\phi$, and $\Delta\nu_p \rightarrow 2B$. The model is valid until approximately half the average power *density* is in the pedestal so that

$$\exp(-\Phi_p) = \frac{\Delta\nu_p}{\Delta\nu_c}$$

where the carrier linewidth, $\Delta\nu_c$ is defined by [7, eqn (19)]:

$$\int_{\Delta\nu_c/2}^{\infty} S_\phi^c(f) df = \ln 2$$

More generally, if the carrier noise profile can be modelled as $S_\phi(f) = K_\alpha f^{-\alpha}$, where K_α is determined from the magnitude of S_ϕ at some frequency then,

$$\Delta\nu_c = 2 \left(\frac{\alpha-1}{\ln 2} K_\alpha \right)^{1/(\alpha-1)}$$

A. Effect of phase noise on spectrometer channel amplitudes

Fig. 5(a) shows a generic frequency synthesizer phase noise spectrum S_ϕ at 30 GHz, as well as the frequency multiplied version at 540 GHz, with $N=18$. The pedestal S_{LO} is also shown. In addition, S_ϕ and pedestal S_{LO} for a synthesizer with 20 dB worse phase noise is shown (multiplied only) demonstrating the widened pedestal for $\Phi_p = 12$. Shown in Fig. 5(b) are the dependencies on total phase error of the carrier power, pedestal power and S_{LO} pedestal bandwidth relative to S_ϕ pedestal bandwidth.

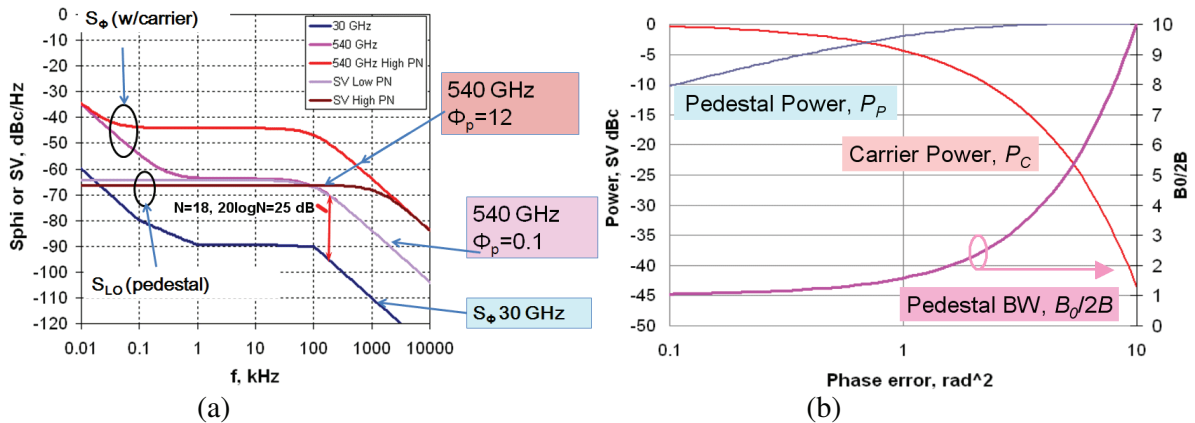


Fig. 5. (a) Synthesizer phase noise at 30 GHz compared to phase noise when multiplied to 540 GHz. For comparison, multiplied noise of a synthesizer with 20 dB more noise is shown. (b) Dependence of carrier power, pedestal power and pedestal bandwidth on phase error.

The results of the convolution calculation in equation (13) are shown in Fig. 6, demonstrating the distortion of the

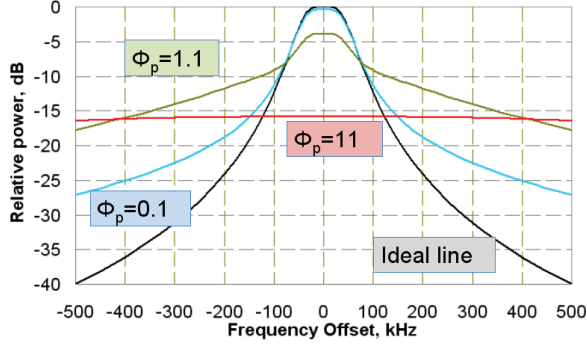


Fig. 6. Spectrometer profile distortion due to phase errors of 0.1, 1.1 and 11 rad² compared to the ideal line.

spectrometer line profile due to three levels of total phase error. The $\Phi_p = 0.1$ line is faithful to the ideal down to about -10 dB, but the $\Phi_p = 1.1$ line has leaked half the power of the channel into its neighbours. The $\Phi_p = 12$ profile is only barely recognizable as a channel filter response.

These results argue that that the phase error should be less than about 0.1 rad² to yield accurate line profiles.

A. Effect of phase noise on frequency estimation

To estimate the effect of phase noise on frequency measurement over some period of time, several frequency uncertainty measures can be used. One that is commonly adopted is the Allan or two-measurement variance, defined as:

$$\left(\frac{\Delta f}{\nu_0}\right)^2 \equiv \sigma_y^2(\tau) = \frac{1}{2} \langle [\bar{y}_{k+1}(\tau) - \bar{y}_k(\tau)]^2 \rangle, \quad (18)$$

where $\bar{y}_k(\tau) = \bar{\nu}_k / \bar{\nu}_0$ is the k th normalized frequency measurement averaged over time τ , and $\bar{\nu}_0$ is the frequency average over all measurements. Over long periods of time (tenths of seconds on up) the Allan variance can be determined from sequential time interval (phase) measurements. For shorter intervals, the Allan variance can be calculated directly from the phase noise spectrum [9]:

$$\begin{aligned} \sigma_y^2(\tau) &= \frac{2}{(\pi\tau\nu_0)^2} \int_0^{f_h} S_\phi(f) \sin^4(\pi\tau f) df \\ &= \left(\frac{2}{\pi\tau\nu_0}\right)^2 \int_0^{f_h} \mathcal{L}(f) \sin^4(\pi\tau f) df \end{aligned} \quad (19)$$

In oscillator and synthesizer phase noise specifications and measurements, the phase noise density is often expressed using the symbol \mathcal{L} , to match what would be observed on a spectrum analyzer. Since S_ϕ includes the phase noise in both sidebands, $\mathcal{L} = S_\phi/2$ [10]. To model the LO phase noise spectrum we break it into segments with fixed power frequency dependencies:

$$S_\phi(f_{1,k} < f < f_{2,k}) = 2\mathcal{L}_k \left(\frac{f_k}{f}\right)^{\alpha_k} \quad (20)$$

where \mathcal{L}_k is the phase noise at a reference frequency f_k with a frequency dependence of $f^{-\alpha}$ over the frequency range stretching from $f_{1,k}$ to $f_{2,k}$. In the literature [9, 11] the values of the integral in equation (1b) are tabulated for single values of α assuming that they stretch from 0 to infinity. More complicated formulae can be derived for finite length segments, each segment having an Allan variance of:

$$\sigma_{y,\alpha}^2(\tau) = \frac{2}{(\pi\tau\nu_0)^2} \int_{f_1}^{f_2} 2\mathcal{L}(f_r) \left(\frac{f}{f_r}\right)^\alpha \sin^4(\pi\tau f) df$$

The oscillator phase noise spectrum can then be fit approximately by a piecewise $f^{-\alpha}$ series and integrated from 0 to some high frequency limit, f_h .

As an alternative, equation (19) can be integrated directly. However, at frequencies above $10/\tau$ or so, the sine factor in (19) oscillates so rapidly that it is difficult to integrate numerically. To solve this problem, the integral can be divided up into a region with frequencies below $10/\tau$, integrated with the full integrand, and a region above $10/\tau$, where the oscillatory integrand is approximated by its average, $3/8$.

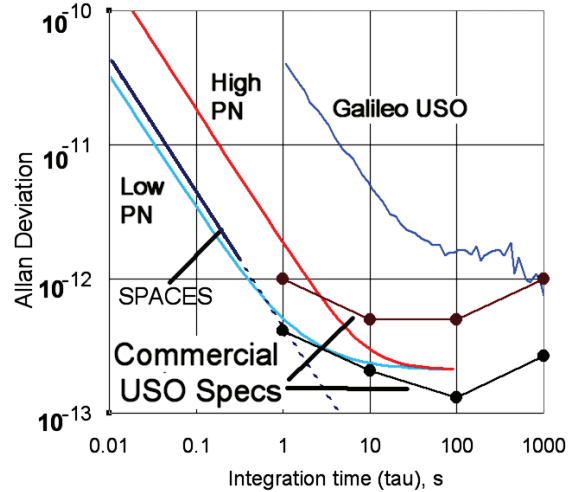


Fig. 7. Frequency Allan deviation due to high ($\Phi_p = 11$) and low ($\Phi_p = 0.1$) phase noise sources, compared to several USOs and the breadboard measurements.

Fig. 7 shows the result of the integration for two values of multiplied synthesizer phase error, 0.1 and 11 rad². For comparison some modern commercial USOs and the 1970s era Galileo-Jupiter USOs are also plotted. The broken trace labelled SPACES is calculated from the 540 GHz phase noise measurement on the breadboard spectrometer described later.

These numbers can be compared to the frequency accuracy required to achieve the desired wind velocity resolution. The Doppler relative frequency shift is the velocity divided by the speed of light, c , the velocity resolution ΔV is given by:

$$\Delta V = c \frac{\Delta f}{\nu_0}$$

For a typical desired wind velocity resolution of 3 m/s, the frequency must be accurate to 10^{-8} . Note that all traces in

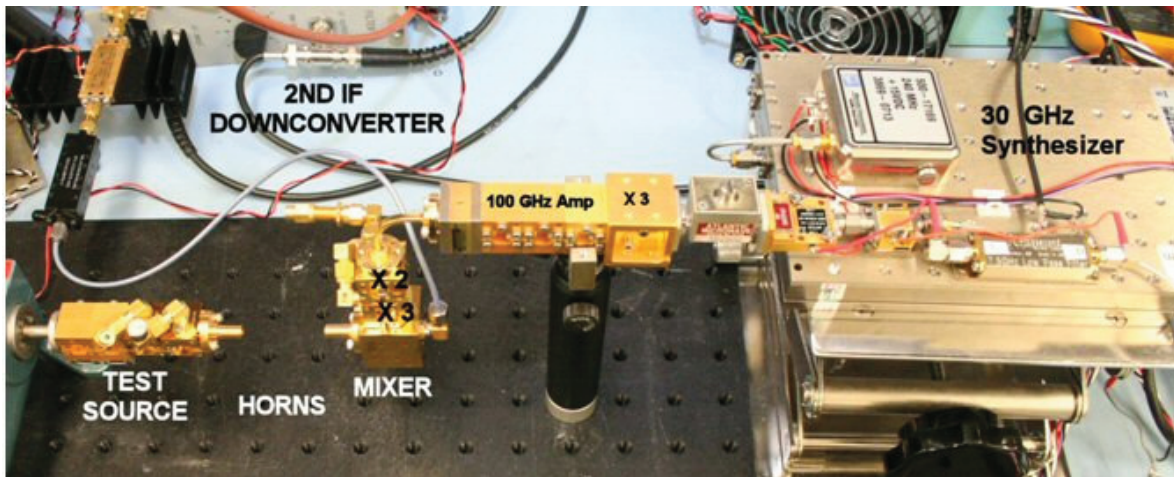


Fig. 8. Submillimeterwave Planetary Atmospheric Chemistry Exploration Sounder (SPACES) laboratory breadboard.

Fig. 7 are well below the range of 10^{-8} on these time scales. On longer time scales the frequency accuracy is dominated by the long term drift of the USOs. Over those time scales (years) other methods can be used to ensure that the USO frequency is determined and corrected for.

A synthesizer that satisfies the total phase error $\Phi_p < 0.1 \text{ rad}^2$ requirement discussed earlier will meet frequency accuracy requirements of 10^{-8} as long as the measurement is made for longer than a millisecond or so.

One further point to note: the segment of the Allan deviation dominated by synthesizer phase noise ($\tau < 1$ second) has a $1/\tau$ integration time dependence, as opposed to the $\tau^{-1/2}$ dependence predicted by the white AM noise equation (5) presented earlier.

IV. BREADBOARD MEASUREMENTS

To demonstrate that the planetary submillimetre wave spectrometer will work according to the requirements described above, a laboratory breadboard version has been built under a NASA Planetary Instrument Design and Development and Program contract. The breadboard is depicted in Fig. 8, which shows the synthesizer to the right, the front end multiplier chain and mixer in the middle facing the test source which made of an Agilent synthesized signal

generator and sub millimeter chain at the middle left. Behind the test source is the 5 GHz IF second downconverter, which feeds a 0-125 MHz digitizer board that is part of the control computer, a standard PC to the right, out of the picture.

The digitization occurs at 250 Megasamples/second, and the spectra are generated by an FFT software algorithm, including a Hanning window to reduce side lobe generation. The LO synthesizer operates in the 30 GHz band, and is followed by an attenuator and a frequency tripler to raise the frequency to 100 GHz, where the signal is amplified to feed the X2X3 Schottky multiplier chain [12] to pump the mixer. The mixer is a balanced fundamental type [13, 14].

In these tests, the 540 GHz test signal is received at a frequency of 70 MHz. A single 4096-frequency spectrum using 32.8 μs of data and channel width of 30.5 kHz appears in Fig. 9. This is zoomed in to the region around 70 MHz, and it and the approximate signal-to-noise ratio of 20 dB is marked.

To assess the effect of switching frequencies rapidly, a continuous measurement was made for 6.3 seconds while switching LO frequencies approximately every 21 ms between 540 and 570 GHz, yielding 3.15 seconds of data for each frequency. In order to process these spectra, the line amplitude and frequency must be estimated from the FFT spectra.

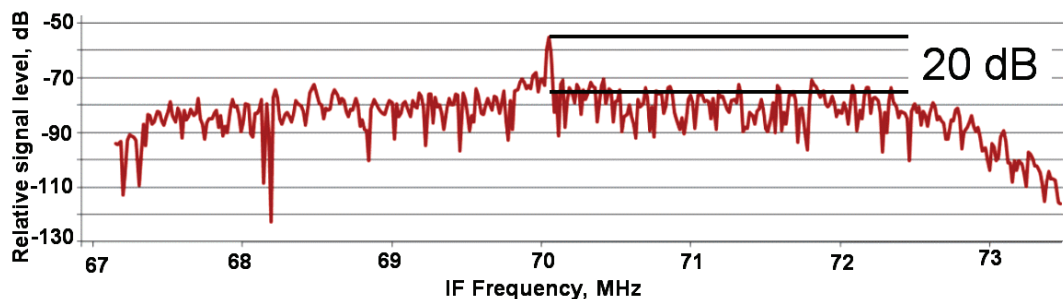


Fig. 9. A portion of a single spectrum showing the test signal at the 70 MHz 2n IF frequency.

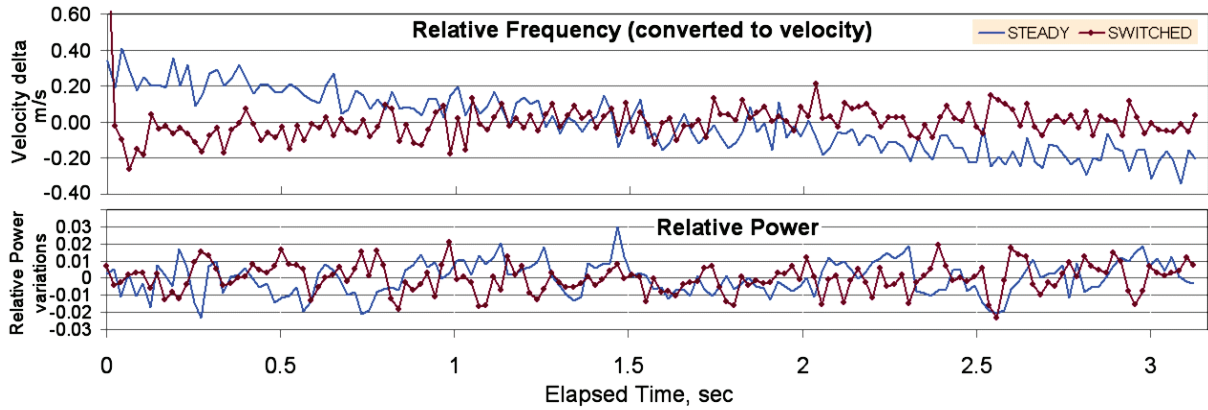


Fig. 10. Relative frequency (converted to velocity) and power plots over 3.15 seconds of observation.

A. Frequency and channel power estimators

In order to estimate the frequency and power in the CW test signal this an interpolation algorithm was used on the FFT data [15-17] starting with the amplitudes calculated from the spectrometer having N_C channels, $|X_k|$, $k=1..N_C$.

1. Find maximum magnitude peak, $|X_k|$, and the largest adjacent sample, $|X_{k+\alpha}|$, where $\alpha = \pm 1$.
2. Define: $\gamma = \frac{|X_{k+\alpha}|}{|X_k|}$
3. Calculate δ , the frequency offset from the center of the k th channel. For a DFT spectrometer with a Hanning window: $\delta = \alpha \frac{2\gamma - 1}{1 + \gamma}$.
4. The frequency estimate is given by $f_T = (k + \delta)B_C$, where B_C is channel bandwidth.
5. For Hanning windowed data the amplitude estimate [15]:

$$X_T = \frac{\pi\delta}{\sin \pi\delta} (1 - \delta^2) |X_k|$$

A three-point interpolator calculated from the peak magnitude, $|X_k|$ and the two adjacent frequency magnitudes, $|X_{k-1}|$ and $|X_{k+1}|$ could be used [16, 18]. However, [17] notes that with reasonable SNR, this does not add substantially to the accuracy. The three-point interpolator was tried, but yielded results that differed by only a few percent from the two-point interpolator above.

B. Measurement results

Fig. 10 shows the 3.15 seconds of accumulated relative frequency and power data, comparing the switched data with a steady (unswitched) data set taken without changing LO frequency. For comparison to the 3 m/s velocity resolution requirement described earlier, the frequency data have been converted from frequency deviations to “velocity” deviations via multiplication by the speed of light, $3X10^8$ m/s. Each point is the average of the frequency (or power level) over the entire 18 ms record between switches. (The first 3 ms of data after each frequency switch is deleted to allow the synthesizer to settle on the new frequency).

Two things are apparent: first, there is a secular drift in both data sets, but more pronounced in the switched data. This is due to the unfortunate fact that the synthesizer has its own TCXO reference, and is not lockable to the main system reference as are the test generator and 5 GHz 2nd downconverter. As the synthesizer generates a fair amount of heat during the test, the lower amount of drift during the switched test is almost certainly due to the fact that the system stabilized during the steady test, which was performed directly preceding the switched test.

A second observation: other than the drift, there is no apparent difference between the steady and switched data.

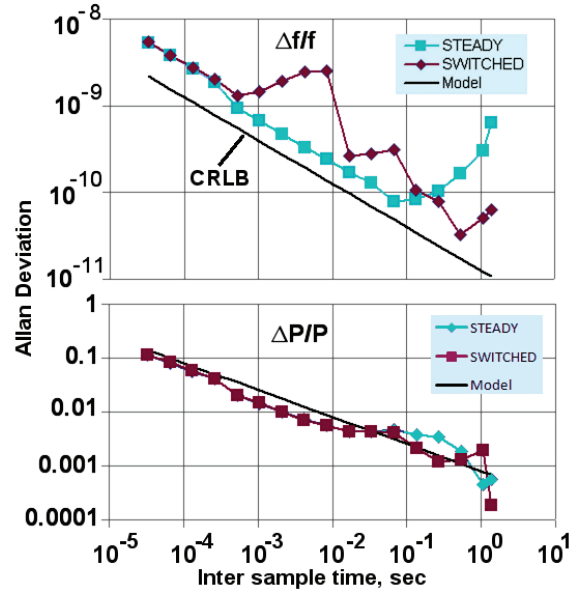


Fig. 11. Allan deviation comparison for frequency (top) and power (bottom).

The Allan deviation data depicted in Fig. 11 show a different story. As with the plots of Fig. 10, the relative power deviation shows very little difference between switched and steady data sets. However, the frequency deviation data show a large difference, especially in the

regime between about a half millisecond and 10-20 ms. A close up of the frequency deviation data during several switching sequences (Fig. 12) indicates the source of the problem. The frequency synthesizer requires longer than 2.5 ms to settle on the new frequency after switching, requiring about 10 ms instead. The original specification on the synthesizer was 100 ms. This variation would seem to compromise the use of frequency switching to accommodate the science requirements. However, the use of longer integration times between switching (100 ms) is acceptable (at Mars, at least), which eliminates the problem, as long as

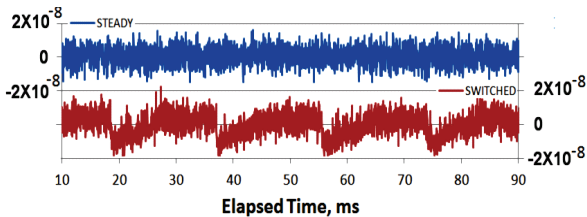


Fig. 12. Close up of frequency measurement over several switching cycles comparing steady and switched data.

the settling time is accounted for.

Plotted with the measured Allan deviation is the results of equations (5) and (11) earlier for the deviations due to system AM white noise, using $BC=30.5$ kHz and $SNR=100$ (20 dB). The fact that the dependence of the frequency deviation on time follows a $\tau^{-1/2}$ confirms the earlier prediction that frequency (and power) deviations are dominated by the AM white noise. The CRLB falls below the measurements, most likely because the simple DFT interpolation algorithm trades maximal likelihood estimation for speed and simplicity [17].

Finally, a phase noise measurement was made of the LO system, both at 30 GHz and 540 GHz. See Fig. 13. These are quick, somewhat rough measurements and should be considered uncalibrated, since the effect of the test oscillator has not been separated from that of the spectrometer. Nevertheless, the synthesizer measurement matches the specification (shown as diamonds) fairly closely. The calculated phase errors at 30 GHz and 540 from equation (15) are 0.00189 and 0.621 rad² respectively; the compare value at 540 GHz to the 30 GHz error multiplied by the square of the multiplication ratio: $0.00189 \times 18^2 = 0.621$, indicating model consistency.

V. CONCLUSIONS

Several key points about the submillimeter wave planetary atmospheric spectrometer have been demonstrated. The LO synthesizer total integrated phase noise error at the signal frequency should be < 0.1 radian². As long as this difficult to meet (considering lower power and mass demands) is met, the phase noise is much less critical to frequency accuracy for measurement times greater than about 1 millisecond. Likewise, USOs are stable ($\Delta f/f_0 < 3 \times 10^{-8}$) for integration times of 0.1 sec or longer, but long term (10 years) stability is a problem that needs to be considered during mission planning. Finally, frequency switching works fine if the

observation time is much longer than synthesizer settling time.

ACKNOWLEDGMENT

I would like to acknowledge the efforts of: Robert Lin for mixer and LO measurements; Pete Bruneau for machining the blocks; Mark Allen (Science Co-I) and Sam Gulkis for guidance on science requirements; John Gill and Choonsup Lee for device fabrication; Imran Mehdi, Peter Siegel as leaders of our team.

This work was performed at Jet Propulsion Laboratory/California Institute of Technology under contract to the National Aeronautics and Space Administration. © 2010 California Institute of Technology. Government sponsorship acknowledged.

REFERENCES

- [1] M.D. Macleod, "Fast Nearly ML Estimation of the Parameters of Real or Complex Single Tones or Resolved Multiple Tones," *IEEE Trans. Signal Processing*, pp 141-148, Vol. 46, No. 1, Jan. 1998.
- [2] D. C. Rife, and R. R. Boorstyn, "Single tone parameter estimation from discrete-time observations," *IEEE Trans. Inform. Theory*, vol. IT-20, pp. 591-598, 1974.
- [3] S. M. Kay. *Fundamentals of Statistical Signal Processing: Estimation Theory*, Prentice Hall, Englewood Cliffs, NJ, 1993.
- [4] W.H. Press, S. A Teukolsky, W.T. Vetterling, B.P. Flannery, *Numerical Recipes in C++*, Cambridge University Press, Cambridge, 2002.
- [5] S.O. Rice, "Mathematical analysis of random noise," Bell System Tech. J., Vols. 23, 24, reprinted in *Selected Papers on Noise and Stochastic Processes*, ed. Nelson Wax, Dover, New York, 1954.
- [6] J.L. Besada, "Influence of local oscillator phase noise on the resolution of millimeter-wave spectral-line radiometers," *IEEE Trans. Instrum. Meas.*, IM-28, no. 2, June 1979.
- [7] F.L. Walls and A. DeMarchi, "RF Spectrum of a Signal after Frequency Multiplication; Measurement and Comparison with a Simple Calculation," *IEEE Trans. Instrum. Meas.*, IM-24, no. 3, Sept. 1975.
- [8] E. Bava, A. DeMarchi, A. Godone, "Spectral analysis of synthesized signals in the mm wavelength," *IEEE Trans. Instrum. Meas.*, IM-26, no. 2, June 1977.
- [9] S.R. Stein, "Frequency and Time - Their Measurement and Characterization," Ch. 12 of *Precision Frequency Control*, Vol. 2, edited by E.A. Gerber and A. Ballato pp. 191-416, Academic Press, New York, 1985.
- [10] D. Allan, H. Hellwig, P. Kartaschoff, J. Vanier, J. Vig, G.M.R. Winkler, and N.F. Yannoni, "Standard terminology for fundamental frequency and time metrology," *Proceed. 42nd Annual Freq. Control Symp.*, 1988.
- [11] J.A. Barnes et al, "Characterization of frequency stability," *IEEE Trans. Instrum. Meas.*, IM-20, no. 2, May 1971.
- [12] A. Maestrini, J. Ward, J. Gill, H. Javadi, E. Schlecht, C. Tripon-Canseliet, G. Chattopadhyay and I. Mehdi, "A 540-640 GHz High Efficiency Four Anode Frequency Tripler," *IEEE Trans. Microwave Theory Tech*, Vol. 53, pp. 2835-2843, Sept. 2005.
- [13] E. Schlecht, J. Gill, R. Dengler, R. Lin, R. Tsang, and I. Mehdi, "First wideband 520-590 GHz balanced fundamental Schottky mixer," presented at the Eighteenth International Symposium on Space Terahertz Technology, Pasadena, CA, Mar. 2007, available at <http://www.nrao.edu/meetings/issst/papers/2007/2007296000.pdf>
- [14] E.T. Schlecht, J.J. Gill, R.H. Lin, R.J. Denge, and I. Mehdi, "A 520-590 GHz Crossbar Balanced Fundamental Schottky Mixer," to be published in *IEEE Microw. Wireless Compon. Lett.*
- [15] T. Grandke, "Interpolation algorithms for discrete fourier transforms of weighted signals," *IEEE Trans. Instrumentation and Measurement*, Vol. IM-32, pp 350-355, June 1983.

- [16] J. Schoukens, R. Pintelon, and H. Van hamme, "The interpolated fast fourier transform: a comparative study," *IEEE Trans. Instrumentation and Measurement*, Vol. 41, No. 2, pp 226-232, June 1983.
- [17] I. Santamaria, C. Pantaleon and J. Ibanez, "A comparative study of high-accuracy frequency estimation methods," *Mechanical Systems and Signal Processing* Vol. 14, No. 5, pp 819-834, 2000.
- [18] [18] D.C. Rife and G.A. Vincent, "Use of the discrete Fourier transform in the measurement of frequencies and levels of tones," *Bell Syst. Tech. J.*, vol. 49, pp. 197-228, Feb. 1970.

ORTIS - ORbiter Terahertz Infrared Sounder

B.N. Ellison(1), P.G.J. Irwin(2), S.B. Calcutt(2), S. Rea(1), B. Alderman(1), N. Bowles(2),
R. Irshad(2) and J. Hurley(2)

(1) Rutherford Appleton Laboratory, Didcot, OX11 0QX, UK

(2) Atmospheric, Oceanic, and Planetary Physics, University of Oxford, Clarendon
Laboratory, Parks Rd, Oxford, OX1 3PU, UK,

Abstract

Accurate measurement of the temperature, composition and dynamics of Jupiter's atmosphere is one of the main scientific goals of ESA's and NASA's Outer Planet Mission proposals. Infrared remote sounding provides a powerful tool for achieving these objectives and was used by Voyager/IRIS and Cassini/CIRS, but is insensitive to some altitudes and gases. The sub-millimetre wavelength (terahertz) region of the electromagnetic spectrum, which has not been significantly exploited to date in the discipline of planetary science, provides unique spectral information over a range of atmospheric pressures and, when combined with infrared data, is a powerful in situ planetary atmospheric sounder.

We will describe a novel low mass and low power consumption combined terahertz/IR instrument proposed for inclusion on the Jupiter Ganymede Orbiter that will greatly improve our understanding of the atmosphere of Jupiter. Through the combination of high spectral resolution 2.2THz spectroscopy ($R=10^6$) and low-spectral resolution IR radiometry, the entire temperature profile of the Jovian atmosphere from 0.6 to 10^{-3} bar can be evaluated (filling in the currently unmeasured levels between 0.1 and 0.01 bar). In addition, the tropospheric and stratospheric composition can be determined (especially water vapour) and observations of the Doppler shifting of sub-millimetre lines can also be used to measure horizontal wind speeds.

Oral presentation preferred.

Session S11:

Direct Detectors II

A TES Focal Plane for SPICA-SAFARI

Philip D. Mauskopf^{1*}, P. A. R. Ade¹, J. Beyer², M. Bruijn³, J. R. Gao³, D. Glowacka⁴, D. Goldie⁴, D. Griffin⁵, M. J. Griffin¹, H. F. C. Hoevers³, P. Khosrapanah³, P. Kooijma³, P. A. J. De Korte³, D. Morozov¹, A. Murphy⁶, C. O'Sullivan⁶, M. Ridder³, N. Trappe⁶, H. Van Weers³, J. Van Der Kuur³, S. Withington⁴

¹*School of Physics and Astronomy, Cardiff University, CF24 3AA, UK*

²*Physikalisch-Technische Bundesanstalt, Berlin, Germany*

³*SRON Netherlands Institute for Space Research, Utrecht, the Netherlands*

⁴*Cavendish Laboratory, University of Cambridge, Cambridge, UK*

⁵*Submillimetre Astronomy Group, Rutherford Appleton Laboratory, UK*

⁶*Department of Physics, National University of Ireland in Maynooth, Ireland*

*Contact: mauskopf@astro.cf.ac.uk, phone +44-2920-876 170

Abstract— We describe the design of a focal plane array assembly incorporating transition edge superconducting bolometers (TES) for the SAFARI instrument aboard the SPICA satellite. SPICA consists of a 3.5 metre telescope actively cooled to a temperature of < 7 K, designed to be diffraction limited at a wavelength of $3 \mu\text{m}$. The active cooling of the telescope reduces its emission to a level below the astrophysical background power level over the entire wavelength range of operation ($\sim 4 - 210 \mu\text{m}$). This represents a reduction in loading at far-infrared (FIR) wavelengths of more than a factor of 10,000 over the 50 K HERSCHEL telescope. SAFARI is a proposed FIR instrument for SPICA consisting of an imaging Fourier Transform Spectrometer (FTS) covering the wavelengths from $34 - 210 \mu\text{m}$ with science goals of furthering our understanding of planetary system formation, the life cycle of dust and gas in the galaxy and the formation of galaxies.

The SAFARI wavelength coverage is divided into 3 bands in the focal plane covering the wavelength ranges from $35 - 60 \mu\text{m}$, $60 - 110 \mu\text{m}$, and $110 - 210 \mu\text{m}$. Each band requires a 2D focal plane array of $0.5 f\lambda$ spaced pixels covering a $2' \times 2'$ field of view. The total number of pixels in all three bands is approximately 6000. In order to take advantage of the reduction in background power provided by the cooled telescope, SAFARI requires detectors with a combination of low optical NEP ($\sim 2 \times 10^{-19} \text{ W}/\sqrt{\text{Hz}}$) and high optical efficiency. There are several detector technologies that have been under development to meet these requirements including Kinetic Inductance Detectors (KIDs), Transition Edge Superconducting bolometers (TES), Silicon bolometers, Ge:Ga photoconductors and Quantum Well detectors. We describe the conceptual design of a TES focal plane array including the detector array, coupling optics, cold electronics and interconnections and mechanical and thermal design. We also describe the results of measurements of performance of single pixel prototypes as well as small prototype arrays and compare these results with the required performance.

I. INTRODUCTION

Roughly half of the light emitted by stars is reabsorbed and emitted in the Far Infrared (FIR) by diffuse interstellar dust and gas. Detection of this FIR emission from our own galaxy and from distant galaxies provides information about galaxy formation and evolution and complements observations in other wavebands. For example, the integrated brightness of FIR *continuum* emission from cold (~ 30 K) interstellar dust in galaxies is correlated to the rate of star formation [1]. However, because interstellar dust also

absorbs starlight, many of the galaxies which are bright in the FIR and undergoing periods of rapid star formation are highly obscured and difficult to detect in the optical. In addition to continuum emission from dust, there are a large number of spectral lines in the FIR which can be used as diagnostics for physical properties of molecular and atomic gas in galaxies as well as galaxy type, evolutionary phase and redshift. Many galaxies are expected to have FIR lines with intensities on the order of $F_{\text{line}} = 1.5 \times 10^{-18} \text{ W}/\text{m}^2$ over the redshift range from $z = 0.1-5$ [2], [3]. In comparison, the typical optical/NIR H α line, which is a primary target of the next generation of spectroscopic surveys for measurements of large scale structure, has an intensity of $F_{\text{line}} = 1.5 \times 10^{-20} \text{ W}/\text{m}^2$ for a similar galaxy number density ($\sim 10,000$ per square degree) and redshift range [4].

For an instrument with detectors sensitive enough to count individual photons, the survey speed and flux limit are determined by the photon statistics or photon count rate. The photon count rate from H α and Ly α line emission in a 1 square meter collecting area is approximately 0.1 – 1 photons per second for bright sources at high redshifts. In comparison, the photon count rate from FIR line emission from similar sources is much higher, on order 100 – 1000 photons per second. Therefore, in principle, imaging and spectroscopic surveys should be much more efficient in the FIR than in the optical/NIR.

However, there are several challenges to observing in the FIR. First the earth's atmosphere is much less transparent in the FIR than in the optical with narrow transmission windows at the long wavelength edge of the spectrum orders of magnitude worse than the atmospheric transmission in the optical. This means that the only way to cover a wide band is from space. Second, blackbody emission from any object at a temperature greater than a few degrees Kelvin will add a large background level of FIR power, swamping the astronomical sources and drastically increasing the base photon noise level. To avoid this, the entire telescope must be cooled to less than 10 K. Third, the low energy of the FIR photons means that it is challenging to design and fabricate detectors sensitive enough to be limited by the photon noise from astronomical sources. Finally, the current state of the art for FIR focal plane array sizes is on order of 1000-10000 pixels compared to megapixel to gigapixel arrays now used in the optical.

There have been a number of space-borne telescopes and instruments developed to explore the FIR universe including: IRAS, COBE, IRTS, ISO, Spitzer and HERSCHEL. IRAS performed an all-sky survey in the FIR and made a large number of new discoveries including a new class of ultraluminous infrared galaxies (ULIRGs). The FIRAS and DIRBE instruments on COBE were used to make the first measurement of the spectrum of the unresolved FIR extragalactic background ([5], [6]). ISO, Spitzer and HERSCHEL have in turn resolved more and more of this background into individual sources (e.g. [7], [8], [9]) and begun to spectroscopically characterize these sources.

In this paper, we describe the conceptual design of a focal plane array based on transition edge superconducting bolometers (TES) for the SAFARI instrument: a Fourier Transform Spectrometer (FTS) in the focal plane of a cooled FIR space telescope (SPICA). SAFARI is designed to perform FIR spectroscopic surveys over the wavelength range from 34 – 210 μm with a sensitivity limited by photon noise from astronomical sources.

II. BASIC TES PRINCIPLES AND REQUIREMENTS

One of the most commonly used incoherent detectors in long-wavelength astronomy is the bolometer. A bolometer consists of a broad band radiation absorber that converts incident electromagnetic energy into heat, which is then detected using a sensitive thermometer; both the absorber and the thermometer are thermally isolated from the surrounding environment by a micro-miniature structure of some kind. Bolometers have been used as detectors in ground-based submm astronomical instruments such as UKT14, SCUBA, BOLOCAM, SHARC, on balloon-borne experiments such as BOOMERANG, Top Hat and MAXIMA, and on space-based instruments such as IRAS, IRTS and FIRAS; they are due to be flown in the upcoming PLANCK-HFI and HERSCHEL-SPIRE and HERSCHEL-PACS instruments. In these devices, the absorber consists of a thin metal film, which is impedance matched to the incoming radiation, and the thermometer comprises a doped semiconductor, which has a resistance that depends on temperature.

A. TES detectors

The Transition Edge Sensor (TES) is a bolometer that uses a thin superconducting film, biased in the middle of its superconducting transition, as the sensitive thermometer. When voltage-biased, an increase in the temperature of the superconducting film results in an increase the resistance, which in turn reduces the current flowing in the bias circuit. The small change in bias current is monitored by a low-impedance, low-noise Superconducting Quantum Interference Device (SQUID) amplifier. Both the TES and the SQUID are planar superconducting devices, and can be lithographically mass produced to form large-format imaging arrays. Each sensor requires a total of 6 wires, and so for large arrays, some degree of cold multiplexing is required in order to minimize the thermal loading and complexity of the control electronics. SQUIDS can be used to achieve the multiplexing, as well as the first stage of amplification.

In the phonon-limit, which with care can be achieved experimentally, the NEP of a TES is given by

$$NEP = \sqrt{4\gamma k_B T^2 G} \text{ Watt}/\sqrt{\text{Hz}} \quad (1)$$

where $\gamma \approx 0.5$, k_B is Boltzmann's constant, T is the TES operating temperature, and G the thermal conductance of the link between the TES and the heat bath. Clearly, according to (1), there is a trade-off between the operating temperature, T , and the thermal conductance of the device, G , which is dependent on both the geometry of the isolating legs and their temperature. In reality, however, the saturation power of the detector also falls as G falls, and therefore it is necessary to reduce both the temperature and the thermal conductance to achieve a detector that both has low noise and that can be used to detect significant levels of power before saturation sets in. For a TES with $T=100$ mK, requiring a bath temperature T_0 of about 50 mK, a sensitivity of 2×10^{-19} W/ $\sqrt{\text{Hz}}$ sets a requirement on G of $\leq 2 \times 10^{-13}$ W/K. Low-dimensional SiN structures are capable of achieving thermal conductances in this range.

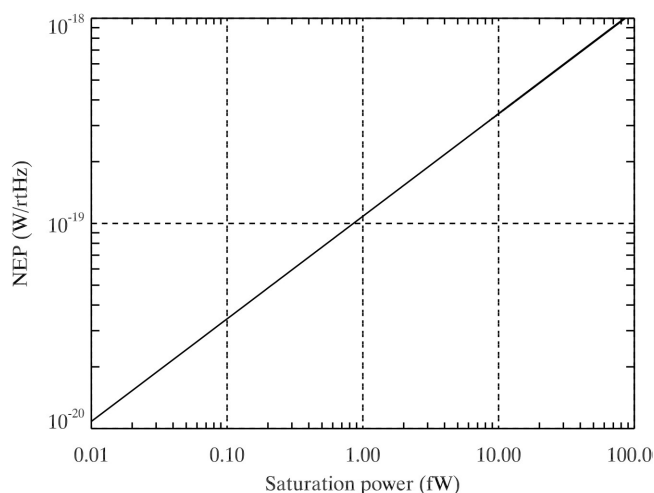


Fig. 1 Noise equivalent power (NEP) from phonon fluctuations vs. saturation power for a TES detector with $T_C=100$ mK, $T_B=50$ mK and power law index, $n=2.5$. The saturation power is defined as $P_{SAT} = \kappa(T_C^n - T_B^n)$ and the phonon $NEP^2 = 4\gamma\kappa n\kappa T_C^{n+1}$. For the SAFARI goal sensitivity of $NEP = 2-3 \times 10^{-19}$ W/ $\sqrt{\text{Hz}}$ the saturation power is 4 - 8 fW.

1) Signal dynamic range:

The instantaneous dynamic range of a detector is the maximum change in power that can be detected divided by the noise in one second of integration. At equilibrium, the bias power supplied to the TES is well described by $P = \kappa(T_C^n - T_B^n)$, with κ a constant, and $2 < n < 4$, depending on temperature and heat transport mechanism. The differential thermal conductance, $G = dP/dT$, is therefore equal to $G = n\kappa T^{n-1}$. Both the signal dynamic range and NEP are functions of G . For a TES with $T = 100$ mK, $T_0 = 50$ mK, $r = 0.2$, $n = 2.6$, and NEP of 10^{-18} W/ $\sqrt{\text{Hz}}$, the signal dynamic range is 7×10^4 $\sqrt{\text{Hz}}$, falling to about 7×10^3 $\sqrt{\text{Hz}}$ for device operating at the same temperature, but with an NEP of $\sim 10^{-19}$ W/ $\sqrt{\text{Hz}}$.

2) Imaging dynamic range and saturation power:

The imaging dynamic range of a TES detector refers to the maximum signal power that is able to be measured by the detector without saturating divided by the minimum signal power coming from a combination of emission from the instrument and the sky. If a TES is designed to have a phonon-NEP a factor α (typically 2-3) times lower than the photon noise for the minimum signal power case then the saturation power is determined by the base temperature, T_B , the TES transition temperature, T_C , index of thermal conductivity, n , and frequency of observation, ν , to be approximately $P_{SAT} \sim GT_C/n \sim P_{MIN}h\nu/(\alpha^2nk_B T_C)$.

The imaging dynamic range is the ratio of $P_{SAT}/P_{MIN} \sim h\nu/(\alpha^2nk_B T_C)$. For $\alpha = 3$, $n = 2$, $T_C = 100$ mK and $\nu = 3$ THz (100 μm), this ratio is about a factor of 100. If we only require that the detector noise be equal to the photon shot noise in the minimum loading condition then the saturation power increases by an order of magnitude.

3) Speed of response:

The effective time-constant τ_{eff} of a TES-based bolometer is given by $\tau_{eff} = C/(G(1+\mathcal{R}))$, where C is the heat capacity of the TES and its absorber, G its heat conductance to the bath, and \mathcal{R} its electro-thermal feedback loop gain. We recall that to achieve a detector NEP of $2-3 \times 10^{-19}$ W/ $\sqrt{\text{Hz}}$, with a detector operating at a T_C of 100 mK, we require a thermal conductance $G \leq 2 \times 10^{-13}$ W/K. To estimate the heat capacity we use the following arguments: a 100 x 100 μm^2 Ti/Au thermometer has a normal state heat capacity of 8×10^{-15} J/K; half way up the transition this will be 1.4×10^{-14} J/K. The C/G time constant will therefore be about 100 ms. Experience with Ti/Au TES for X-ray and even low- G TES for IR applications suggests that the ETF-loop gain \mathcal{R} is somewhere around 20 – 200. Thus, a realistic pixel speed for a 100 mK detector would be 1 - 5 ms.

4) Heritage:

The rapid development of TESs over the last decade has led to their widespread use on ground-based and balloon-borne mm-wave and submm-wave telescopes such as SCUBA2 [10], ACT [11], SPT [12], APEX [13], EBEX [14] and SPIDER [15]. Experience with TES technology in these instruments has increased its technology readiness level, and has paved the way for use on future space missions. To be suitable for the next generation of space missions, however, it is necessary to increase the sensitivity by at least two orders of magnitude and to configure the devices in medium and large-format imaging arrays. In addition, it must be possible to multiplex the detector signals, and to qualify the systems and components for use in a space environment.

Existing TES detectors developed for ground-based applications have NEPs of approximately 10^{-17} W/ $\sqrt{\text{Hz}}$. This NEP requirement ensures background limited sensitivity in an environment with radiation loading levels characteristic of a transmissive 250 K atmosphere. In space applications, where the background loading is considerably lower than the best terrestrial sites, particularly if cooled-aperture telescopes are used, the required NEP drops to on order 10^{-19} W/ $\sqrt{\text{Hz}}$. While it is technically feasible to manufacture single TESs

having this sensitivity, it is challenging to create an ultra-low-noise TES technology that can be engineered into complete imaging arrays, with the required optical packing and uniformity of performance.

B. SAFARI requirements

SAFARI is a FIR imaging Fourier Transform Spectrometer (FTS) that will be mounted on the SPICA telescope. One of the science goals of SAFARI is characterize the properties of star forming galaxies and active galactic nuclei using their FIR spectra to help determine the overall history of galaxy formation and evolution in the universe. Other science goals include characterizing the evolutionary steps in forming discs of gas and dust around young stars and tracing the behavior of water ice and other materials with strong signatures in the FIR not observable from the ground. The baseline requirements for the instrument are [16]:

1) **Wavelength coverage:** The full-wavelength coverage of the SAFARI instrument is 35 – 210 μm , and will be split into three bands, covering the wavelength ranges given in Table 1.

2) **Pixel size/spacing:** Fully filled Nyquist sampling ($0.5F\lambda$) at the band centre (given in Table 1). Ideally the camera focal ratio should be as small as possible and the lower value pixel sizes are preferred. So $f/20$ is required with $f/10$ as a goal.

3) **Matrix size:** Detector arrays with sufficient pixels to fully sample a field of view of $2' \times 2'$ at the mid-wavelength of each of the three waveband

4) **Detector sensitivity:** The photon NEP per pixel for a reference sky background level given in Table 1 referred to absorbed power is 4×10^{-19} W $\text{Hz}^{-1/2}$. Therefore, in order to not significantly degrade the sensitivity in a deep integration, the detector optical NEP (referred to incident power per $0.5F\lambda$ pixel) goal is $< 3 \times 10^{-19}$ W $\text{Hz}^{-1/2}$.

5) **Detector/read-out electronics bandwidth:** Detector arrays/read-out electronics with bandwidths appropriate for implementation in an imaging Fourier-Transform-Spectrometer, i.e. a signal bandwidth > 20 Hz, an instantaneous dynamic range > 1000 , and multiplexed read-out with at least 32 pixels per amplifier chain.

6) **Saturation level:** The detectors are required to be able to observe sources with a brightness of 1 Jy without saturation. This corresponds to power levels of 3-7 fW depending on the wavelength band.

TABLE I
SAFARI REQUIREMENTS

Band μm	$F\lambda/2$ pixel size (f/20) μm	Estimated FIR power W	Number of pixels
35-60	480	1.4×10^{-17}	64×64
60-110	840	2.4×10^{-17}	38×38
110-210	1600	4.5×10^{-17}	20×20

III. SAFARI TES FOCAL PLANE CONCEPTUAL DESIGN

The SAFARI TES conceptual design consists of 3 focal plane array (FPA) units for the 3 SAFARI bands. Each FPA unit has a 150 mm diameter footprint and is 65 mm high not including a stray light/magnetic shielding forebaffle with a total mass of 1.3 kg. Each FPA has optical, mechanical, thermal and electrical interfaces to the main instrument assembly. In addition, the TES detectors require a sub-K cooler unit to provide 50 mK and 300 mK heat sinks to meet the system requirements.

An FPA contains: i) the detector chip and associated coupling optics (horn array), ii) electrical interconnections and readout electronics components and iii) supporting infrastructure including a light-tight housing incorporating optical filters, magnetic shielding, a thermal/mechanical isolation system and feed-throughs for cold fingers and a wiring harness. A schematic of the focal plane is shown in figure 2.

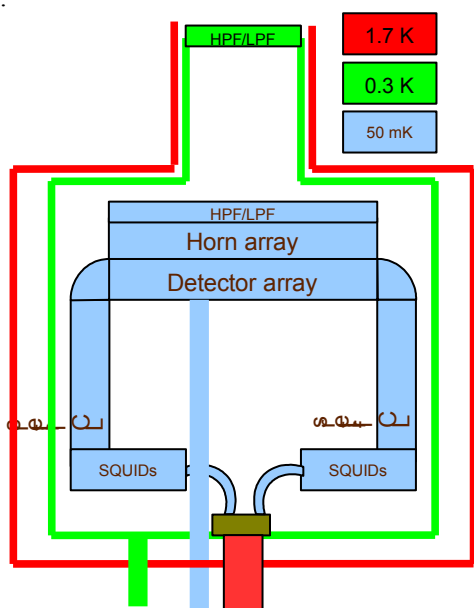


Fig. 2 Schematic of TES FPA design showing nested 50 mK, 300 mK and 1.7 K structures.

A. Detector chip and coupling optics

The detector chip is an integrated array of TES detectors, each consisting of a TES thermometer connected to an absorbing metal film on a silicon nitride island. The TES thermometer and absorber are thermally isolated from a silicon frame by long narrow legs. Light is collected and concentrated onto the absorbers with a close packed array of square horns (figure 2). Behind each detector is a metallized integrating cavity. There is a small gap ($< 50 \mu\text{m}$) between the horn and the suspended absorber and a similar gap between the absorber and the front surface of the cavity. A high pass/low pass filter pair is mounted on the front of the horn array. The horn plate and detector mount are aligned to within $\pm 10 \mu\text{m}$.

B. Electrical interconnections and readout electronics

The readout electronics for the SAFARI TES detectors makes use of frequency division multiplexing (FDM) and

SQUID amplifiers to minimize the power consumption at the cryogenic temperature stages without degrading the detector performance. The detector and signal chain are schematically shown in figure 4. The schematic is shown for a set of pixels that can be multiplexed by one amplifier chain. In this scheme the AC-biased detector pixels play the role of amplitude modulators (AM) in the FDM read-out.

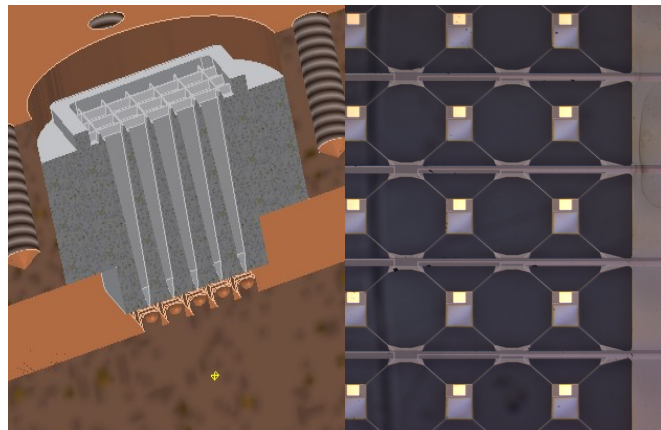


Fig. 3 Left: Schematic of 5×5 horn array and integrating cavities. Right: Photograph of a section of a TES detector array chip.

Frequency division multiplexing requires that the detectors are AC-voltage biased at different frequencies. The AC-bias currents are generated digitally in an FPGA or ASIC and converted to analogue by means of a DAC. Incoming radiation absorbed by the detector(s) amplitude-modulates these AC-bias currents, which are subsequently band pass filtered (LC-filters) and summed. The sum-signal is amplified by a combination of a cold SQUID-amplifier and a warm low-noise amplifier.

The standard procedure to read-out a SQUID is to use a feedback loop, called a flux-locked loop (FLL). This maintains the SQUID at a fixed operating point by canceling changes in flux due to variations in current through the input coil by applying a current through a feedback coil. In this way, the SQUID response is linearized and the dynamic range enhanced. The FLL-gain that can be achieved is a function of the delay in the interconnecting cables and the bandwidth required. A key constraint in SAFARI/SPICA is the distance between the warm control electronics and the cold SQUID-amplifiers of at least 4.5 m, resulting in a roundtrip delay equivalent to 8 m which corresponds to 60 ns. For a critically damped FLL, the product of unity gain bandwidth f_1 and (cable) delay time t_d is $f_1 t_d = 0.08$. The unity gain bandwidth achievable for SAFARI is therefore at best only 1.4 MHz. So very moderate gains 2 - 4 are possible in the 350 - 750 kHz band.

A better approach is to make use of baseband feedback. This feedback is generated by the digital electronics at a narrow frequency band around each AC-carrier frequency. This type of feedback has a very large gain at the carrier frequency, so that the carriers are almost totally suppressed at the SQUID-amplifier input, which reduces the required dynamic range of the amplifier chain. The output signal from

the amplifier chain is de-modulated to recover the individual signals for each pixel in the chain. The detectors, filters, and sum point are all at cryogenic temperatures. The AC-bias generators, demux electronics, and signal processing are all at ambient temperature.

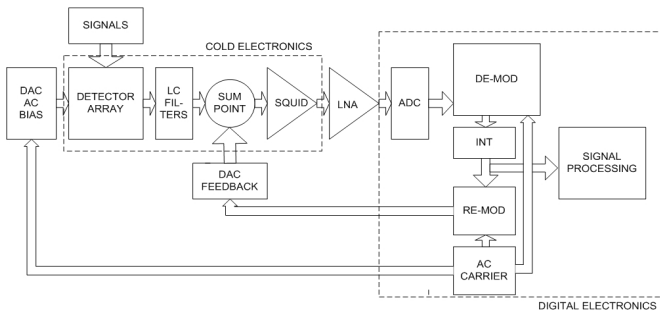


Fig. 4 Schematic of detector and signal read-out chain for one amplifier channel used to read-out multiple pixels. One of the dotted lines indicates the part of the circuit inside the cryostat (cold electronics), the other indicates the warm digital electronics.

The number of channels that can be multiplexed in a given frequency band with FDM depends on the quality factor, Q , of the LC filters and the centre frequency, f_0 . The minimum frequency spacing is roughly, $\Delta f \sim 10 f_0 / Q$. For 1 MHz centre frequency and $Q \sim 4000$ this corresponds to approximately 2.5 kHz spacing. The SAFARI baseline design is for 5 kHz spacing and therefore a total bandwidth of 800 kHz for 160 channels.

The TES detector array is connected to the readout electronics through a set of superconducting traces deposited on a curved substrate which allows the cold electronics chips to be mounted at 90 degrees to the detector array. The low operating resistance of the TES detectors means that low loss (zero resistance) interconnections are required between the TES detectors and the cold electronics components (LC filters and SQUIDS). The baseline for these interconnects is to use Aluminum wire bonds. In this case, the area required for the interconnections determines the size of the M-band and S-band FPA footprint. Another option is to use Indium bump bonds which have a potentially smaller footprint than the wire bonds.

C. Mechanical structure and environmental shielding

The 50 mK and 300 mK stages are mechanically supported in a nested structure by kevlar suspension units arranged in isometric 3 point mounts (figure 5). The suspension is designed to have its lowest mechanical resonance at > 250 Hz. The 50 mK stage supports the detector chip, horn array, LC filter chips and first stage SQUID amplifiers. The 300 mK stage acts as a light-tight shield and superconducting magnetic shield. An additional 1.7 K cryoperm magnetic shield surrounds the 300 mK shield. The 300 mK and 1.7 K shields also include long forebaffles for rejection of stray light and attenuation of external magnetic fields.

The estimated thermal loads from the mechanical supports, dissipation in the cold electronics and wiring harness at the different temperature stages are given in Table II.

TABLE II
CRYOGENIC POWER DISSIPATION

Band	Power Dissipation (μ W)						
	50 mK stage			300 mK stage		1.7 K stage	
	SQUIDS	wiring	kevlar	wiring	kevlar	SQUIDS	wiring
LW	0.01	0.02	0.04	0.1	2.1	0.24	1.2
MW	0.02	0.11	0.04	0.5	2.1	0.8	6.4
SW	0.05	0.27	0.05	1.3	2.1	2.16	16
Total	0.08	0.4	0.13	1.9	6.3	3.2	23.8

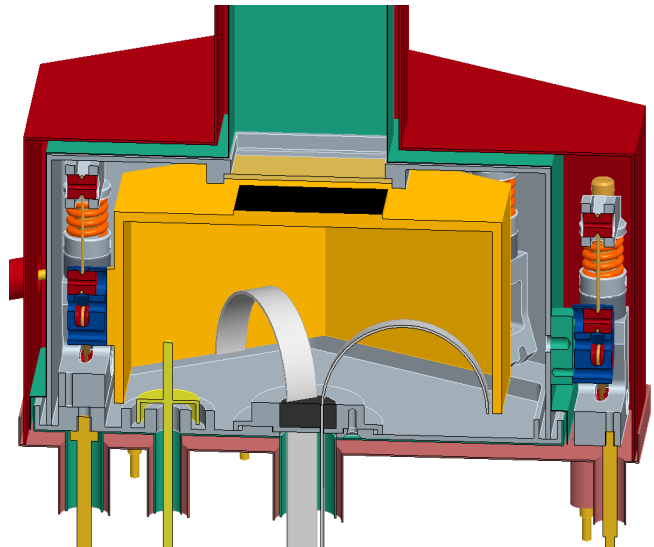


Fig. 5 Schematic of the mechanical assembly of a TES FPA unit. The outer shield is the 1.7 K shield, then the 300 mK shield and at the center the 50 mK mounting surface. Kevlar suspension units are visible on either side of the structure – the unit on the left supports the 50 mK structure from the 300 mK structure and the unit on the right supports the 300 mK structure from the 1.7 K structure. The detector chip mounts on the top of the 50 mK structure with the LC filters and SQUID chips mounting on the side walls. Feedthroughs for the wiring harness and the 50 mK and 300 mK cold fingers are also shown.

IV. CURRENT STATUS

A. Pixel design

1) Optical coupling:

The size and spacing of pixels in the focal plane is determined by the wavelength of operation, λ , the focal ratio, f , of the optics and the sampling of the image. For Nyquist sampling, the pixels should be spaced by $f\lambda/2$. One challenge for Nyquist sampled FIR arrays is to make the TES pixels small enough to meet the requirements for pixel spacing while having the necessary thermal isolation to achieve the required sensitivity. This is most difficult at the shortest wavelengths since the pixel spacing scales with wavelength while the sensitivity requirement is roughly independent of wavelength. Constraints on the fabrication of thermally isolating supports determine the minimum pixel spacing for a given sensitivity, image plane focal ratio and pixel filling factor and operating temperature. For a sensitivity of 2×10^{-19} W/ \sqrt Hz, fully filled arrays of free-space absorbers similar to SCUBA2 and HERSCHEL-PACS are ruled out for all SAFARI and FIRI bands for operating temperatures of > 50 mK by limits of standard photolithographic fabrication techniques.

A second challenge for FIR TES detectors is to achieve the required time constants in detectors which incorporate broadband absorbers covering the SAFARI bands. This is most difficult at the longest wavelengths because the absorber size and heat capacity scale with wavelength for a given optical coupling scheme.

Multimoded concentrators and/or lenses can reduce the requirements on absorber size and filling factor while maintaining Nyquist sampling. Traditional horn-coupled arrays such as in HERSCHEL-SPIRE [17] are more sparsely sampled and have theoretically a smaller mapping speed for a fixed focal plane area but with a significant reduction in the number of required pixels and pixel spacing. Collecting horns have been used to couple to photoconductive FIR detectors in the ISO-LWS [18] and HERSCHEL-PACS [19] instruments with high filling factor and coupling efficiency.

We use a similar concept as the baseline design for the optical coupling to a SAFARI pixel consisting of an input collecting horn which feeds a hemispherical cavity containing a detector with a planar absorber with impedance matched to free space ($377 \Omega/\text{square}$). This design is based on experience with standard wide band 4 K bolometers used for FTS spectroscopy. However, the size of the horns required for SAFARI is much smaller than has been used in any previous instrument. For example, the horns for the short wavelength band of SAFARI have large apertures of less than $500 \mu\text{m}$ and small apertures of close to $50 \mu\text{m}$. Fabrication of a large 2-D array of these horns for the SAFARI focal plane is challenging.

2) Thermal isolation:

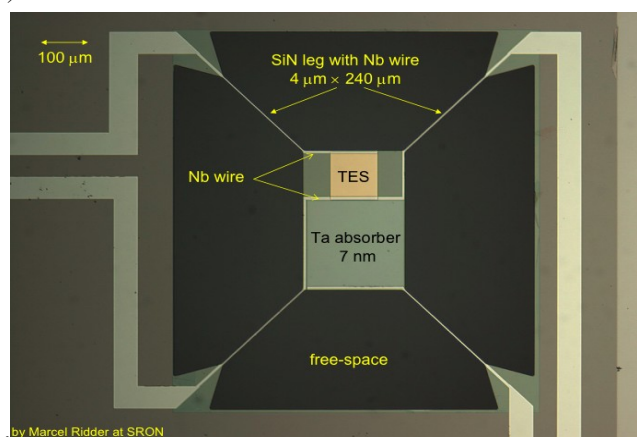


Fig. 6 Photograph of a TES detector with thermally isolating straight legs fabricated from silicon nitride (SiN). The membrane thickness is $1 \mu\text{m}$, the width of the legs is $4 \mu\text{m}$ and the length of the legs is $240 \mu\text{m}$. Also visible at the top of the central SiN island is a $100 \mu\text{m} \times 100 \mu\text{m}$ Ti/Au TES (yellow) and Nb superconducting contacts (light grey). On the bottom part of the island is a $200 \mu\text{m} \times 200 \mu\text{m}$ Ta absorber (dark grey) on the central SiN island.

The use of a collecting horn to focus incoming radiation on a spot a fraction of the pixel area in size allows space around the thermally isolated island containing the absorber and thermometer for a thermally isolating mechanical support structure. There are two different designs for the geometry of the thermal isolation which have been fabricated and tested: i) absorbers suspended on thin and narrow straight legs of silicon nitride (Figures 6 and 7) and ii)

absorbers suspended on ring-type structures of silicon nitride (Figure 8).

Both designs have the capability of meeting the requirement for the thermal conductance. The straight leg geometry has the advantage of a high mechanical resonant frequency but requires the use of thin ($\sim 200 \text{ nm}$) membranes of SiN and narrow ($\sim 2 \mu\text{m}$) beams to achieve the required thermal isolation. The device shown in figure 6 has a measured transition temperature of 108 mK and a measured thermal conductance of 3 pW/K (saturation power level of 80 fW) [20].

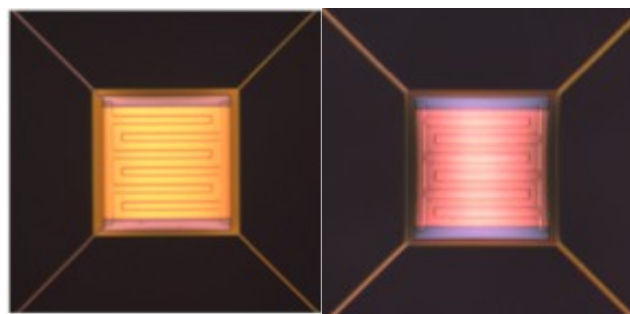


Fig. 7 Photographs of TES detectors with thermally isolating straight legs fabricated from 200 nm thick silicon nitride (SiN). The image at the left is a $100 \text{ mm} \times 100 \text{ mm}$ Mo/Au (yellow) with interdigital Au bars. The image at the right is a $100 \text{ mm} \times 100 \text{ mm}$ Mo/Cu TES with the same geometry. The width of the legs in the left hand picture is 2 mm and the width of the legs in the right hand picture is 4 mm . Both have legs with length 420 mm .

The ring-type geometry allows for the use of thicker SiN membranes and wider beams while achieving the required thermal isolation within the S-band pixel spacing. The device shown in figure 7 has a measured transition temperature of 155 mK and a measured thermal conductance of 1.6 pW/K (saturation power level of 40 fW).

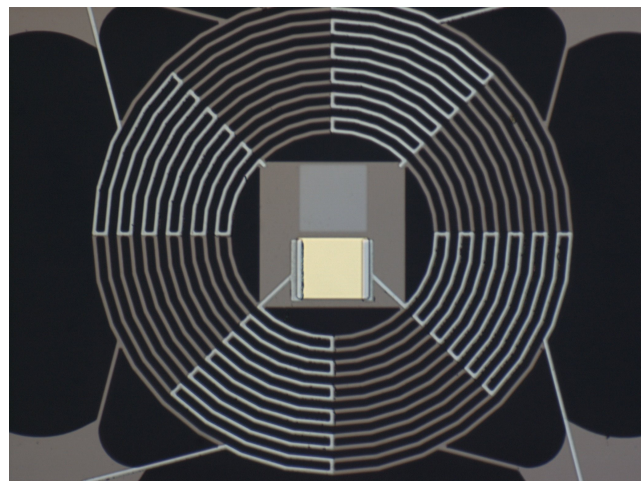


Fig. 8 Photograph of a TES detector with thermally isolating ring structure fabricated from silicon nitride (SiN). The membrane thickness is $1 \mu\text{m}$, the width of the legs is $4 \mu\text{m}$ and the spacing between rings is $8 \mu\text{m}$. The diameter of the inner ring is approximately $200 \mu\text{m}$ and the diameter of the outer ring is $450 \mu\text{m}$. Also visible at the bottom of the central SiN island is a $100 \mu\text{m} \times 100 \mu\text{m}$ Ti/Au TES (yellow) and Nb superconducting contacts (light grey). On the bottom part of the island is a $200 \mu\text{m} \times 200 \mu\text{m}$ Ta absorber (dark grey) on the central SiN island.

B. Fabrication

Detectors have been fabricated at SRON and Cambridge with a variety of geometries and TES materials (Ti/Au, Mo/Cu, Mo/Au). Pixels with both straight legs and ring-type thermal isolation have been fabricated with high (>95%) yield. The transition temperatures and normal resistances of the Ti/Au and Mo/Cu TES thermometers show good uniformity with variations smaller than 2% over sub-array test chips.

C. Dark testing

Dark characterization of the detectors involves measurements of the TES transition temperature, thermal conductance (G) of the silicon nitride suspension, thermal response time to electrical pulses, complex impedance as a function of frequency and characterization of the noise power spectrum. Devices have been characterized in test-beds at SRON and Cambridge. The Cambridge cryogenic system consists of a pulse tube cooler, He-7 sorption cooler, and miniature dilution fridge with a 70 mK operating temperature. The SRON test bed consists of an Oxford instruments Kelvinox dilution refrigerator with a 25 mK base temperature. Both test beds incorporate light-tight enclosures and light-tight feedthroughs for the signal wires and use SQUID-based readout electronics.

A NIST TDM multiplexer chip was used for the thermal conductance (G) measurements at Cambridge, together with multi-channel electronics (MCE) developed by the University of British Columbia. This system was used to test sub-arrays of 16 detectors simultaneously. Measurements of thermal conductance at SRON were done with single pixel DC biased and AC biased SQUID readout electronics. Measured thermal conductances for devices with straight legs and ring structures which fit within the SAFARI pixel spacing ranged from 0.1 – 1 pW/K, spanning the SAFARI requirement of 0.2 pW/K.

Noise and complex impedance data were obtained using single channel SQUID-based amplifiers operated in a flux locked loop (FLL). A basic schematic of a single stage SQUID amplifier with a DC bias resistor chain is shown in figure 9. Data from the complex impedance measurements (figure 10) were used to extract the TES properties including loop gain and thermal transfer function. Data from devices with straight legs and rings were well fit to a thermal model dominated by a single time constant which ranged from 50 μ s to 15 ms depending on the device geometry and thermal conductance. Devices with thermal conductances less than or equal to 0.2 pW/K were measured to have time constants of 7-15 ms and loop gains of $\mathfrak{R} \sim 100$ -200.

The shape of the measured noise spectra agrees well with predictions from the parameters extracted from the complex impedance measurements. The corresponding NEP values calculated from the noise spectra agree with the predictions from the measured thermal conductances using a value of $\gamma=1$ in equation (1). For example, an NEP of 4×10^{-19} W/ $\sqrt{\text{Hz}}$ was measured for a straight leg device with $G = 0.3$ pW/K, $T_c=100$ mK and a time constant of 7 ms. This is consistent with other measurements of noise from low-G TES detectors [21]. In addition, the time constant

measurements indicate that these detectors do not have significant excess heat capacity compared to what is expected from the TES materials properties.

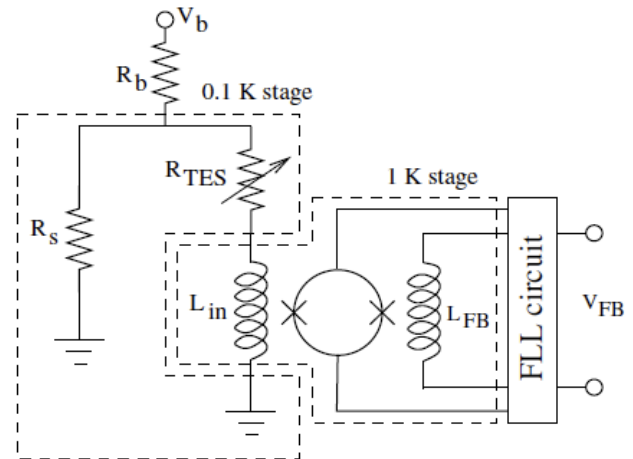


Fig. 9 Schematic of a DC biased TES with SQUID amplifier. For low values of the shunt resistor, $R_s \ll R_{TES}$, a constant voltage bias is applied across the TES with a value of $V_{TES} \sim V_b R_s / R_b$.

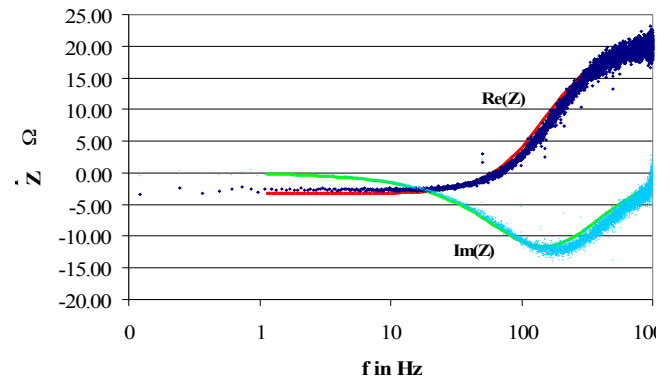


Fig. 10 Complex impedance measurement for a low-G SAFARI TES with straight legs. Real (dark blue dots) and imaginary (light blue dots) parts of the impedance and fits using $\alpha_I = 240$ and $\beta_I = 1.8$

D. Optical testing

Optical tests of TES detectors were performed in a test bed at Cardiff equipped with an adiabatic demagnetization refrigerator (ADR) with a 70 mK operating temperature. The readout electronics consist of a PTB XF-16 SQUID read out with a Magnicon XXF room temperature preamplifier and FLL. The SQUID is mounted on the 100 mK plate as close to the detector as possible. The SQUID noise has been measured to be less than 6 pA/ $\sqrt{\text{Hz}}$ at frequencies above 1 Hz. The SQUID is configured to read out a single pixel DC and up to 15 pixels AC through lithographed LC filters with central frequencies between 1 and 2 MHz. Because of the high frequencies used for the AC readout, a baseband feedback system is required to operate the AC channels.

The detector chips are mounted on a gold plated copper mount which has a set of raised metal squares with machined hemispherical cavities inset. These serve as integrating cavities for the optical absorbers suspended on the silicon nitride island next to the TES. The raised metal squares are $500 \mu\text{m} \times 500 \mu\text{m}$ and $450 \mu\text{m}$ in height above the flat

surface of the mounting plate. They occupy the space behind the TES where the silicon substrate has been etched away with a gap of 50 μm between the front surface of the wafer and the front surface of the raised metal cavity (figure 11).

Copper clad aluminum wires were epoxied with stycast into small (1 mm) holes around the edge of the chip in the bottom of the mounting plate. These form a set of light-tight superconducting feedthroughs. Each TES is connected to two of the feedthroughs via aluminum wire bonds attached to niobium pads on the chip. Superconducting niobium titanium wires are soldered to the copper clad aluminum wires on the outside of the light-tight optical cavity connecting the TES to the SQUID. The measured parasitic impedance when the TES is superconducting is less than 2 m Ω .

A horn plate was attached to the top of the detector mount, sealing the chip inside a light-tight cavity with the exception of the horn aperture. For the tests reported here, we used a conical horn designed for the short wavelength band of SAFARI (S-band) with a large aperture of 450 μm and a small aperture of 46 μm . The horn was fabricated by electroforming copper onto a smooth steel mandrel. The position of the horn aperture was referenced to a set of dowel pins pressed into the mounting plate to an accuracy of < 10 μm . The exit aperture (small aperture) of the horn was positioned within 50 μm of the optical absorbing element along the axis of propagation of light down the horn.

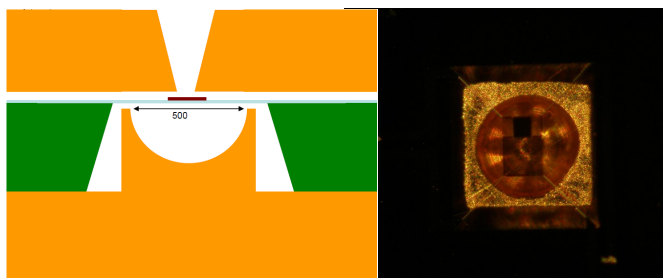


Fig. 11 Left: schematic of detector mounted in the optical test-bed. In yellow is the gold-plated copper mounting plate (bottom) and horn plate (top). In green is the silicon substrate. The silicon nitride is light blue and the TES is dark red. Right: photograph of a TES detector mounted in front of the integrating cavity.

We mounted a set of high pass and low pass metal mesh filters [22] directly on the horn plate and another set on the 100 mK shield to define a detector bandpass covering a range of wavelengths from 30 – 60 μm . The average transmission of the filter stack over this wavelength range is estimated to be approximately 0.7 from measurements of the individual filters at 4 K.

We used two thermal sources to optically characterize the detectors: a fast, small area (1 mm \times 1 mm) source with an 8 ms time constant which was a copy of the optical calibrator used in the HERSCHEL-SPIRE instrument [23] and a slow, large area blackbody calibrator (14 mm diameter) with a 10 second time constant and calibrated thermometer. The fast calibrator was used for first-light testing and for estimating the TES detector response time. The large area calibrator was used for optical efficiency measurements. Both sources were mounted on the 4 K radiation shield 10 mm away from the optical apertures in the 1 K and 100 mK shields. Figure 12

shows a time trace of the response of a detector to modulation of the fast blackbody calibrator.

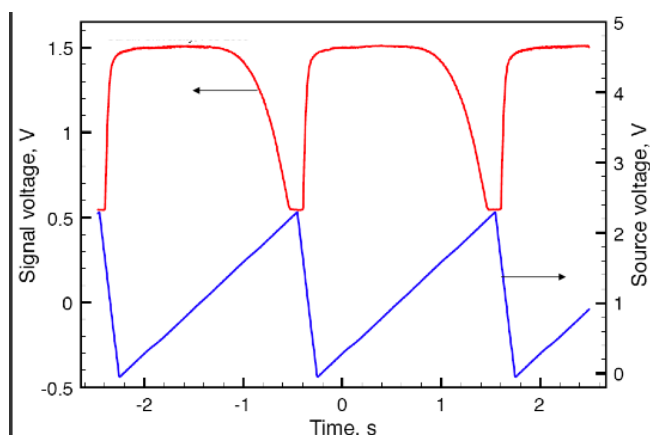


Fig. 12 Current through the TES detector (red) vs. time during a modulation of the temperature of the fast optical calibrator. The voltage applied to the calibrator is shown in blue. TES current is a maximum when the calibrator is off and the TES is superconducting. As the calibrator heats up, the TES current drops exponentially until the TES is normal (the flat part of the curve at the minimum current). As the temperature of the blackbody increases from 4 K to 40 K in the Wien limit of the blackbody radiation law the optical power incident on the detector increases exponentially.

The optical efficiency of the absorber, horn and integrating cavity assembly was estimated by comparing the power absorbed by the detector with the incident power from the blackbody. We measured the absorbed power by the change in electrical power dissipated in the TES when biased on the transition at different blackbody temperatures. We then estimated the incident power at the entrance to the horn by integrating the blackbody intensity over the passband defined by the optical filters. From these measurements, we estimate an absorbing efficiency of 0.7 ± 0.2 . The accuracy of the measurement is limited by uncertainty in the temperature and emissivity of the blackbody and in the shape of the high pass filter edge. Measured values of absorbed power vs. blackbody temperature are shown in figure 13.

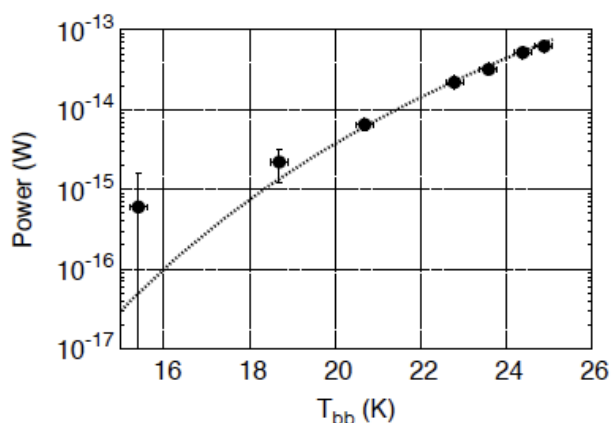


Fig. 13 Power absorbed by a detector vs. temperature of the blackbody calibrator. The uncertainty in the absorbed power is 1.5 fW. The error in the blackbody temperature is 0.2 K. The dashed line is the predicted emission as a function of blackbody temperature multiplied by an efficiency factor of 0.7.

Another way to measure the absorbed power and the optical frequency response of the TES is by detecting the photon noise from the optical source. Photon noise is a modulation of the optical signal due to the random arrival time of individual photons. Photon shot noise is the dominant contribution to photon noise in the low photon occupation number limit, $\eta \ll 1$. The occupation number, η , is defined for blackbody radiation as

$$\eta = \frac{1}{e^{h\nu/k_B T} - 1} \quad (2)$$

where T is the blackbody temperature and ν is the electromagnetic frequency of the radiation. Shot noise has a white noise spectrum with an amplitude given by

$$NEP^2 = \int d\nu 2B_\nu h\nu \text{ W}^2/\text{Hz} \quad (3)$$

where B_ν is the frequency dependent intensity of the absorbed radiation. This formula can be approximated by

$$NEP \sim \sqrt{2P_0 h \nu_0} \text{ W}/\sqrt{\text{Hz}} \quad (4)$$

where P_0 is the optical power detected and ν_0 is the emission-weighted frequency of the absorbed power. For our measurements, the emission-weighted frequency of the absorbed power is close to the low frequency edge of the filter pass band, $\nu_0 = 5$ THz and therefore the optical signal from the blackbody is in the low photon occupation number limit for blackbody temperatures, $T \leq 100$ K.

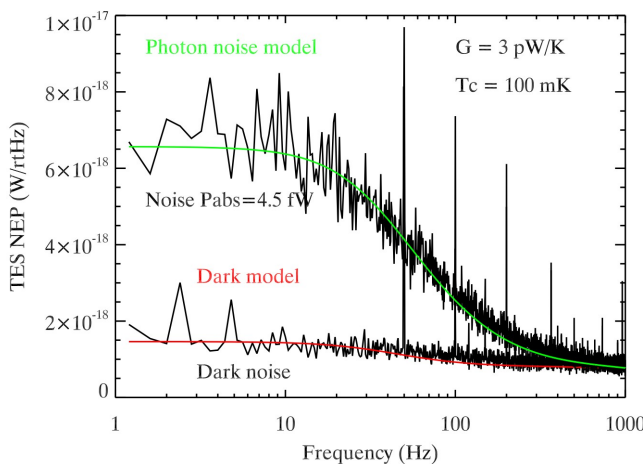


Fig. 14 Noise spectral densities for a TES detector under different loading conditions. The lower curve is the measured noise spectrum for the detector with the blackbody source off. The raw noise data has been converted to NEP using the measured responsivity to electrical power. The upper curve is the measured noise spectrum for the same detector with the blackbody source at 20 K. The increase in noise below 200 Hz can be attributed to photon shot noise for an absorbed power of 4.5 fW. This is consistent with the absorbed power measured from the TES IV curves.

We detected photon noise in all of the optical noise measurements as an excess detector noise at low frequencies which increases in amplitude as the blackbody temperature is increased. We fit a single pole frequency response curve to the measured noise spectrum to determine the TES optical time constant. We also determine the absorbed power from the amplitude of the photon noise and use this as a consistency check for the absorbed power measured from the TES electrical dissipation (figure 14).

V. CONCLUSIONS

This paper presents an outline of the conceptual design of a TES detector-based focal plane array for the SAFARI instrument on the SPICA satellite and reports on design, fabrication and testing of prototype subsystems. There are a number of challenges remaining in the realization of a final focal plane system which meets the SAFARI requirements including: design and fabrication of the detectors and coupling optics, integration of the cold FDM readout electronics, design and implementation of warm low-power digital electronics and minimization of disturbances to the operation of the detectors including stray light, magnetic fields, temperature fluctuations and mechanical vibrations. Achieving photon noise limited sensitivity in a large format focal plane array on a cooled space platform will enable large area FIR spectroscopic surveys.

ACKNOWLEDGMENT

We acknowledge support from an ESA-TRP contract 22359/09/NL/CP and support from STFC in the UK.

REFERENCES

- [1] R. C. Kennicutt, "Star Formation in Galaxies Along the Hubble Sequence," *Annual Review of Astronomy and Astrophysics*, vol. 36, pp. 189-232, 1998.
- [2] L. Spinoglio, M. Magliocchetti, S. Tommasin, A. M. Di Giorgio, C. Gruppioni, G. De Zotti, A. Franceschini, M. Vaccari, K. Isaak, F. Pozzi and M.A. Malkan, "Spectroscopic Cosmological Surveys in the Far-IR," in *Proc. Workshop 'The Space Infrared Telescope for Cosmology & Astrophysics: Revealing the Origins of Planets and Galaxies'*, 6-8 July 2009, Oxford, United Kingdom
- [3] G. J. Stacey, S. Hailey-Dunsheath, T. Nikola, T. E. Oberst, S. C. Parshley, D. J. Benford, J. G. Staguhn, S. H. Moseley, C. Tucker, "ZEUS: The Redshift(z) and Early Universe Spectrometer," in *From Z-Machines to ALMA: (Sub)millimeter Spectroscopy of Galaxies*, 2006.
- [4] J. E. Geach, A. Cimatti, W. Percival, Y. Wang, L. Guzzo, G. Zamorani, P. Rosati, L. Pozzetti, A. Orsi, C.M. Baugh, C. G. Lacey, B. Garilli, P. Franzetti, J. R. Walsh and M. Kummel, "Empirical H emitter count predictions for dark energy surveys," *Monthly Notices of the Royal Astronomical Society*, vol. 402, pp. 1330-1338, 2009.
- [5] D.J. Fixsen, E. Dwek, J. C. Mather, C. L. Bennett, and R. A. Shafer, "The Spectrum of the Extragalactic Far Infrared Background from the COBE Firas Observations," *The Astrophysical Journal*, vol. 508, pp. 123-128, 1998.
- [6] J.-L. Puget, A. Abergel, J.-P. Bernard, F. Boulanger, W. B. Burton, F.-X. Desert and D. Hartmann, "Tentative detection of a cosmic far-infrared background with COBE," *Astronomy and Astrophysics*, v.308, p.L5, 1996.
- [7] S. Oliver, M. Rowan-Robinson and W. Saunders, "Infrared background constraints on the evolution of IRAS galaxies," *Monthly Notices of the Royal Astronomical Society*, vol. 256, pp. 15-22, 1992.
- [8] H. Dole, et al., "FIRBACK: III. Catalog, Source Counts, and Cosmological Implications of the 170 μm ISO+ Deep Survey," *Astronomy and Astrophysics*, vol. 372, pp. 364-376, 2001.
- [9] S. J. Oliver, et al., "HerMES: SPIRE galaxy number counts at 250, 350 and 500 μm ," *Astronomy and Astrophysics*, vol. 518, 2010.
- [10] X. Gao, et al., "Automatic setup of SCUBA-2 detector arrays," in *Proc. of SPIE*, vol. 7020, pp. 702025-702027, 2008.

- [11] D. Swetz, et al., "The Atacama Cosmology Telescope: The receiver and instrumentation," submitted to *ApJS*, astro-ph/1007.0290, 2010.
- [12] J. Carlstrom, et al., "The 10 meter South Pole telescope," submitted to *PASP*, astro-ph/0907.4445, 2010.
- [13] D. Schwan, et al., "The Apex-SZ instrument," submitted to *Review of Scientific Instruments*, astro-ph/1008.0342v1, 2010.
- [14] B. Reichborn-Kjennerud, "EBEX: A balloon-borne CMB polarization experiment," in *Proc. SPIE*, astro-ph/1007.3672, 2010.
- [15] B. Crill, et al., "SPIDER: A balloon-borne large-scale CMB polarimeter," in *Proc. SPIE*, vol. 7010, 2008.
- [16] B. Swinyard, et al., "The space infrared telescope for cosmology and astrophysics: SPICA A joint mission between JAXA and ESA," *Experimental Astronomy*, vol. 23, pp. 193-219, 2009.
- [17] M. J. Griffin, et al., "The Herschel-SPIRE instrument and its in-flight performance," *Astronomy and Astrophysics*, vol. 518, 2010.
- [18] P. E. Clegg, et al., "The ISO Long Wavelength Spectrometer," *Astronomy and Astrophysics*, vol. 315, p.L38-L42, 1996.
- [19] A. Poglitsch, et al., "The Photodetector Array Camera and Spectrometer (PACS) on the Herschel Space Observatory," *Astronomy and Astrophysics*, vol. 518, 2010.
- [20] D. Morozov, et al., "Ultrasensitive TES bolometers for space based FIR astronomy," in *AIP Conference Proceedings*, vol. 1185, pp. 48-51, 2009.
- [21] M. Kenyon, P. K. Day, C. M. Bradford, J. J. Bock and H. G. LeDuc, "Ultra-sensitive transition-edge sensors (TESs) for far-IR/submm space-borne spectroscopy," in *AIP Conference Proceedings*, vol. 1185, pp. 56-59, 2009.
- [22] P. A. R. Ade, G. Pisano, C. Tucker, S. Weaver, "A review of metal mesh filters," in *Proc. of SPIE*, vol. 6275, pp. 62750U, 2006.
- [23] P. Hargrave, T. Waskett, T. Lim, B. Swinyard, "Performance of flight-model on-board calibration sources on Herschel-SPIRE," in *Proc. of SPIE*, vol. 6275, pp. 627514, 2006.

Cold-Electron Bolometer Array Integrated with a 350 GHz Cross-Slot Antenna

Mikhail A. Tarasov^{1,2,*}, Leonid S. Kuzmin¹, Natalia S. Kaurova¹, Ernst A. Otto^{1,3}, Ghassan Yassin³, and Paolo de Bernardis⁴

¹*Chalmers University of Technology, Gothenburg, Sweden*

²*Kotel'nikov Institute of Radio Engineering and Electronics of Russian Academy of Sciences, Moscow, Russia*

³*Oxford University, Oxford, United Kingdom*

⁴*Rome University, Italy*

*Contact: tarasov@chalmers.se, phone +46-31-7725479

Abstract— Two series/parallel arrays of Cold-Electron Bolometers (CEB) with Superconductor-Insulator-Normal (SIN) tunnel junctions were integrated in orthogonal ports of a cross-slot antenna. The receiving system was designed for polarisation measurements in a 350 GHz frequency band with JFET readout at the BOOMERanG-FG balloon telescope. Each orthogonal array consists of 10 cold-electron bolometers connected in parallel for RF signal and in series for DC signal. The array was designed to increase the output resistance by a factor of 10^2 in comparison to a single CEB, for matching with JFET readout while maintaining the same conditions for RF coupling. The dynamic resistance of such array is $1\text{ M}\Omega$ at the bias point of maximal response. For the input microwave signal bolometers are connected in parallel. This provides matching to the $30\text{ }\Omega$ input impedance of a cross-slot antenna on Si substrate. The array of bolometers has a saturation power 10 times higher than a single bolometer. This significantly increases the dynamic range. With a measured temperature response of $8.8\text{ }\mu\text{V}/\text{mK}$, a total absorber volume of $0.08\text{ }\mu\text{m}^3$, and an output noise of about $11\text{ nV}/\text{Hz}^{1/2}$, we estimated the dark electrical noise equivalent power as $\text{NEP}=6\cdot 10^{-18}\text{ W}/\text{Hz}^{1/2}$ at 280 mK. The optical response was measured using both hot/cold loads and a backward wave oscillator as sources of radiation.

I. INTRODUCTION

One of the goals is of current Cosmology experiments is to detect the B-mode of the polarization of the Cosmic Microwave Background (CMB), which is believed to be generated by primordial gravitational waves. Several cosmology instruments (e.g. BOOMERanG [1], EBEX, BICEP, QUIET, B-POL) are being designed to measure it. We describe here development of a bolometer system with a JFET readout for the 350 GHz channel of the BOOMERanG-FG balloon telescope.

The optimal detector for this purpose would be the Cold-Electron Bolometer (CEB) based on strong electron cooling of the absorber [2-4]. The concept is based on combination of several functions in a SIN tunnel junction: RF capacitive coupling and effective thermal isolation [3], electron cooling [5], and temperature sensing. The responsivity of a CEB is extremely high, due to the small volume of the absorber and the very low temperature. The CEB can reach remarkable sensitivities of $\text{NEP}\sim 10^{-19}\text{ W}/\text{Hz}^{1/2}$ for space-borne telescopes with small optical power load [2]. A high sensitivity of the Cold-Electron Bolometer (CEB) with nanoscale absorber has been observed at 100 mK with a

power load of 20 fW; the NEP was below $2\cdot 10^{-18}\text{ W}/\text{Hz}^{1/2}$ [6]. For balloon and ground-based telescopes the CEB sensitivity could be dominated by photon noise of the signal itself, under relatively high optical power loads [7]. We therefore expect that these detectors will be key components for the future European space-mission B-Pol [8], which will follow existing balloon-borne and ground based CMB polarimeters.

At present there are three competing types of incoherent superconducting detectors for space applications. The first and the most developed is the Transition Edge Sensor (TES) [9] with a bias point at the center of the transition of a superconducting strip. The second is the Kinetic Inductance Detector (KID) [10] with a high frequency bias at the resonance frequency. The third is the Cold Electron Bolometer (CEB), with a bias point below the energy gap voltage of a Superconductor-Insulator-Normal metal (SIN) tunnel junction. The CEB is coupled to an antenna through the capacitance of the tunnel junctions, and could be fabricated on planar substrates. CEBs have several advantages over TESs:

- an effective electron cooling of the detector by the readout current for the CEB, in contrast to the heating of the detector by the readout current for the TES. This means that the operating temperature and noise of a CEB are lower than for a TES
- the increased saturation power, due to the ability to remove incoming power from the absorber by effective electron cooling.
- temperature stability is not as important for CEBs as for TESs, because CEBs are based on removing the incoming signal by tunnelling, and the e-ph contribution is rather small.
- the CEB could be matched to $\text{M}\Omega$ noise impedances of a simple JFET readout (as required by BOOMERanG) in contrast to the TES demanding low-ohmic SQUID readout.

The advantage of CEBs versus TESs is increased when measuring under high background power loads. For example, the dc bias power for a TES should be not less than the maximum signal power, and such bias brings additional thermodynamic noise. The readout for a TES is based on a SQUID amplifier, which is extremely sensitive to external magnetic fields and microphonics. The flexibility of CEBs allows the use of already available readout electronics, based on either semiconductor JFETs, or MOSFETs, or superconducting SQUIDS. In the first case the proper output

matching can be achieved by series array of CEB bolometers [7], that as is described in this paper. For the second case proper output matching can be achieved by using a single CEB with SIN tunnel junction, or a parallel array of CEBs.

II. CEB ARRAY COMPARED TO SINGLE CEB

The CEB concept has been proposed as the main detector for the 350 GHz channel of BOOMERanG [1]. The requirement is to develop a CEB array with a JFET readout for 90 channels. The NEP of the CEB should be less than photon noise for an optical power load of 5 pW, and the cross-polar response should be at least 25 dB below the copolar one, for observations of CMB and foregrounds polarization. Simulations showed that it is impossible to satisfy these requirements with single CEB plus JFET readout, for both current-biased [7] and voltage biased modes [11]. A novel concept of a series/parallel array of CEBs in current-biased mode has been proposed, offering effective matching to a JFET amplifier under high power load [7] (Fig. 1). The main innovation of the CEB array, in comparison to a single CEB [2-4, 6], is the distribution of power between N CEBs, and the increased dynamic range. An effective distribution of power is achieved by a parallel RF connection of CEBs, which couple to the RF signal through additional capacitances (Fig. 1). The response is increased, because the CEB is sensitive to the level of power, and the power is decreased N times for the individual CEBs, resulting in a proportional decrease of absorber overheating and saturation.

Also the background power is divided among single absorbers, decreasing overheating and increasing the responsivity of the array. The amplifier noise becomes less important, since the responsivity of the array has been multiplied. On the other hand, the increase of the number of bolometers leads to an increase of the absorber volume and corresponding electron-phonon noise. The optimisation of this circuit for a given power load and JFET amplifier is shown in Fig. 2. The optimal number of CEBs is around 10, when total noise is becoming less than photon noise of the incoming signal. This number was used for the design of the device.

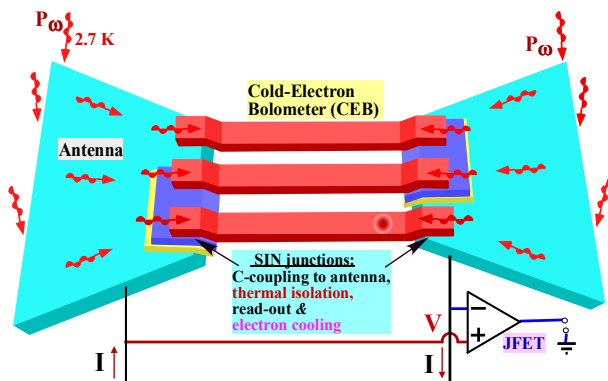


Fig. 1. Schematic of an array of three CEBs with series connection for DC bias and parallel connection for RF. This solution was devised to match a JFET readout. For RF signals the CEBs are connected in parallel through the additional capacitances between the superconducting islands and the antenna.

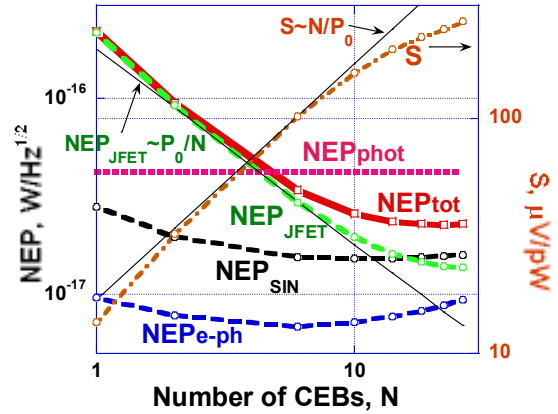


Fig. 2. NEP components and photon NEP versus number of CEBs in the array. The optical power load is $P_0=5$ pW, $I_{JFET}=5$ fA/Hz^{1/2}, $V_{JFET}=3$ nV/Hz^{1/2}, $R=1$ kΩ, $A=0.01$ μm³. The responsivity S is also shown to illustrate the effect of CEB number. Thin lines show asymptotics for S and NEP_{JFET} [7].

III. EXPERIMENTAL TECHNIQUE

The layout design of CEB array has been optimized for polarization measurements in a 345 GHz frequency band for CMB and foregrounds polarisation measurements with the balloon-borne telescope BOOMERANG. Bolometers are integrated in a cross-slot antenna that is placed in the centre of a 7x7 mm chip on oxidized Si substrate. Antenna design is similar to [12]. Each orthogonal array consists of 10 CEBs connected in series for dc bias and readout. A picture of the antenna is presented in Fig. 3. The dark narrow slots are covered with an Al capacitive layer. Each part of the antenna contains 5 CEBs that are connected in series for each polarisation, making an array of 10 CEBs for vertical and 10 CEBs for horizontal polarization components. The NIS tunnel junctions of CEBs are made of CrAl/AlOx/Al trilayer. An advanced shadow-evaporation technique was used for fabrication of the CEB [13]. A detailed SEM view of a half an array with 5 absorbers and 10 tunnel junctions is presented in Fig. 4.

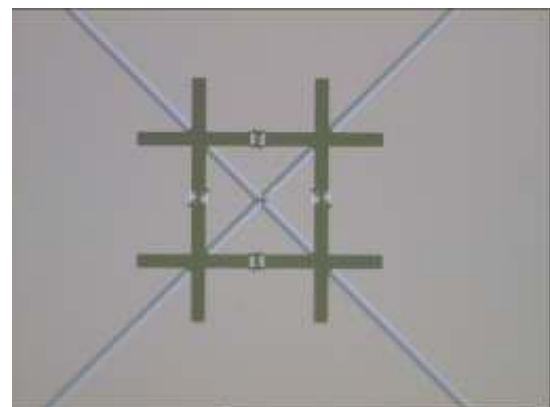


Fig. 3. Optical image of a cross-slot antenna.

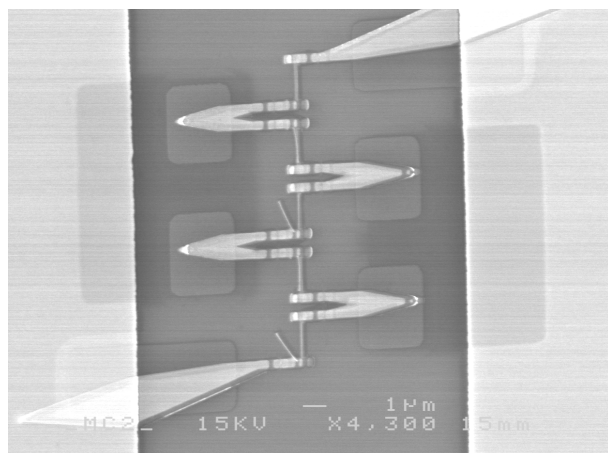


Fig. 4. SEM image of a half of array consisting of 5 absorbers and 10 SIN tunnel junctions.

Each array was protected against external interferences by four on-chip CrPd resistors with 12 nm Cr and 3 nm Pd [13]. The Pd layer was added to improve contact with the top layer of the bolometer structure. Current lead resistors have a value of 2 MΩ and voltage lead resistors have a value of 150 kΩ each.

Such a chip with antenna is attached to an extended Si lens with antireflection coating, or to the horn antenna for simple measurements with a cold radiation source. The lens is facing the optical window through low-pass filters at two temperature stages, as is shown in Fig. 5 .

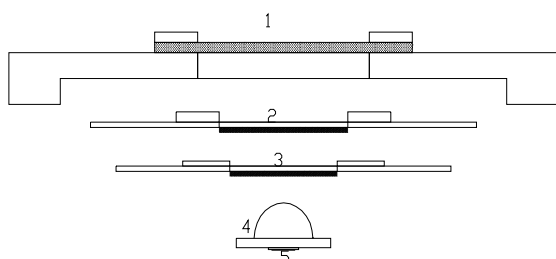


Fig. 5. Schematics of the quasioptical beam path in the cryostat. (1) - Teflon window, (2) - first low-pass filter, (3) - second low-pass filter, (4) - Si extended hyper-hemisphere lens, (5) - sample chip.

To suppress overheating by IR radiation, the optical window is protected by low-pass filters (LPF). Commercial low-pass multi-mesh filters from QMC Instruments™ provide attenuation over 10 dB above the cut-off frequency of 100 cm⁻¹ for LPF W97s and above 33 cm⁻¹ for LPE B694. Filters were placed at the openings in the radiation shields at the 70 K and 3 K temperature stages. With these filters, however, we measured significant overheating of the cold stage, and reduced holding time for the He3 sorption cooler. Usual low-pass filters for 30 cm⁻¹ is array of metal film squares 300 μm sides on thin dielectric support like KAPTON™. Metal squares are radiation heated from the warmer side of cryostat and as a result their equilibrium temperature is some average between hot and cold sides. It

means that such filter is a source of thermal radiation above the cut-off frequency. A band-pass filter consisting of cross-shaped holes in a metal film can be better from the overheating point of view, because it can be anchored thermally very well to the radiation shield, and its equilibrium temperature is the same as the shield. In our case we solved the problem placing neutral density filters (NDF) with attenuation about 6 dB in front of each LPF. As a result IR radiation was suppressed; the temperature of self irradiation is the same as the radiation shield and no visible overheating of the cold stage or reduction of holding time was measured.

IV. MEASUREMENT RESULTS

The IV characteristic of the array of ten SINIS cold-electron bolometers, together with the voltage response to temperature differences are presented in Fig. 6. It clearly demonstrates the sum gap voltage of 20 SIN junctions. The resistance ratio of subgap resistance to normal resistance for this array is over 500, close to the theoretical estimates for a temperature of 280 mK. The voltage at a 0.1 nA bias current together with the dynamic resistance at zero bias versus temperature are presented in Fig. 7. The maximum voltage response to temperature is 8.8 μV/mK.

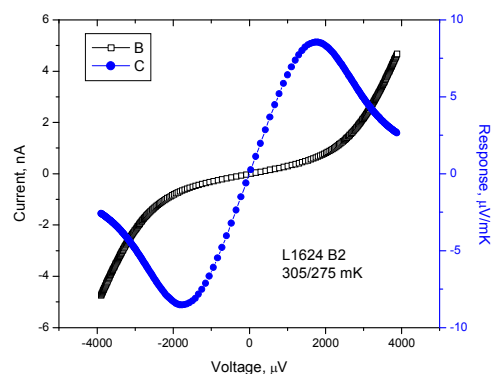


Fig. 6. IV curve and voltage response for a temperature difference of 305-275 mK

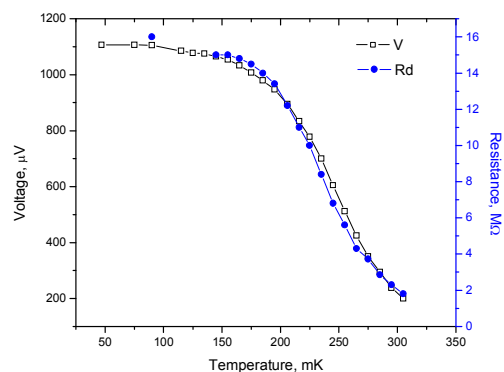


Fig. 7. Voltage across the array of 10 bolometers, for a bias current 0.1 nA, versus temperature of the array. The maximum responsivity is 8.8 μV/mK. Dynamic resistance at zero bias is for comparison.

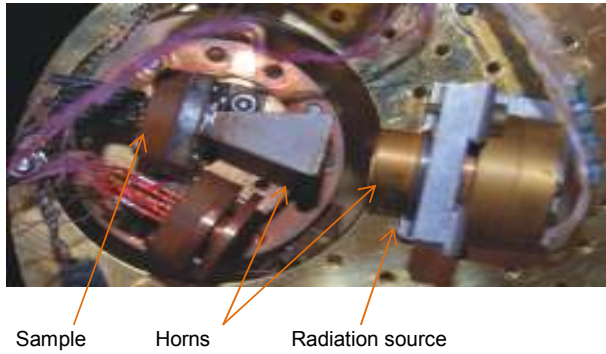


Fig. 8. Bottom view of the open cryostat, with the sample on the 300 mK stage and the radiation source on the 3 K stage

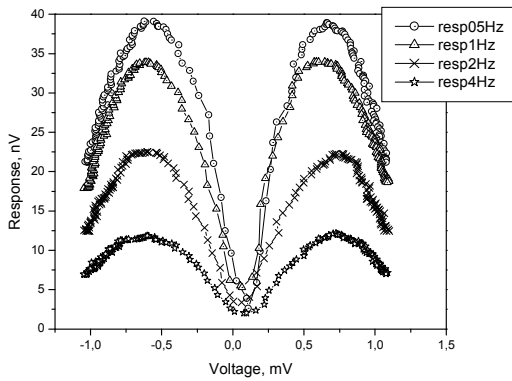


Fig. 9. Voltage response of the bolometer array to radiation emitted from a source modulated at 0.5 Hz, 1 Hz, 2 Hz, 4 Hz, versus dc bias voltage of the array.



Fig. 10. Photo of rotatable aperture with Cu shield at one side and 10 dB NDF at other side. Below is the magnet by which we can precisely rotate the aperture, to place Cu shield, NDF, or OPEN between the bolometer and the window.

We measured the response of this array to microwave radiation emitted by a cryogenic thermal radiation source (Fig. 8, 9). The source was mounted on the 2.8 K stage; it consists of a NiCr film on a thin sapphire substrate, and was attached to a horn directing radiation to the bolometer unit with its own horn at 280 mK. Such source is relatively slow and its modulation depth decreases increasing the modulation frequency, so the measured signal amplitude decreases from 40 nV to 10 nV when the frequency rises from 0.5 Hz to 4 Hz. The temperature increase of the radiation source is estimated to be about 1 K, so the emitted power in the 100 GHz bandwidth is of the order of 1 pW. Microwave losses due to beam mismatch, reflection from Si substrate back side, mismatch of horns are estimated to be above 30 dB.

For correct optical measurements, and to get an additional calibration of the bolometer input, we installed inside the cryostat a holder with a Cu foil opaque screen, a 10 dB NDF, and an open aperture. The holder can be rotated by an external magnet while the experiment is cold. A photo of this setup being tested at room temperature is presented in Fig. 10; the measured signal is shown in Fig. 11.

The measured temperature sensitivity is 17 $\mu\text{V}/\text{K}$ and the optical noise equivalent temperature difference is $\text{NETD}=0.65 \text{ mK}/\text{Hz}^{1/2}$. Similar response dependencies were measured with hot/cold load at 300/77 K in front of the optical window.

For NEP estimations we measured the output noise of the array using a MOSFET OPA111 instrumentation amplifier as input IC. The corresponding NEP can be calculated from the available data on array parameters. For theoretical estimations of such bolometer array performance we can take the power flow determined only by electron-phonon interaction $P=\Sigma v(T^5-T_0^5)$ so that $G=dP/dT=5\Sigma vT^4$. In this case the responsivity is $S=dV/dP=(dV/dT)/(dP/dT)=(dV/dT)/G$. The volume of the absorber for our array of 10 bolometers is $v=10^{-19} \text{ m}^3$ and for aluminium $\Sigma=1.2*10^9 \text{ Wm}^{-3}\text{K}^{-5}$; so the thermal conductivity is $G=3.6*10^{-12} \text{ W/K}$ at 280 mK phonon temperature. Taking the measured bolometer output voltage noise of $v_n=11 \text{ nV}/\text{Hz}^{1/2}$ in the white noise region, and a temperature response of $dV/dT=8.8*10^{-3} \text{ V/K}$ (see Fig. 6) we can estimate the minimum noise equivalent power $\text{NEP}=v_n/S=6*10^{-18} \text{ W}/\text{Hz}^{1/2}$. For practical power load of 5 pW at 345 GHz, the photon contribution to NEP can be estimated as $\text{NEP}_{\text{phot}}=(2P_0hf)^{1/2}=4.8*10^{-17} \text{ W}/\text{Hz}^{1/2}$. Taking into account the experimental values of noise and response, we can plot the dark NEP of our bolometer array, see Fig. 12, 13.

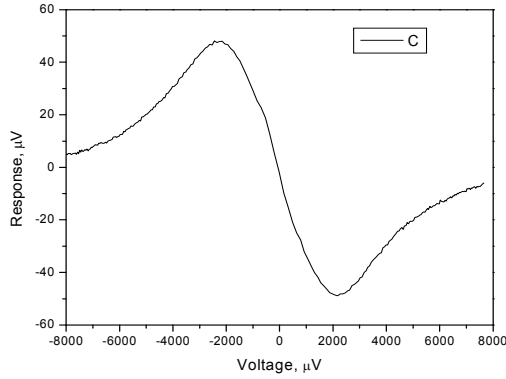


Fig. 11. Voltage response to changing aperture from Cu foil to NDF 10 dB attenuator at 3 K.

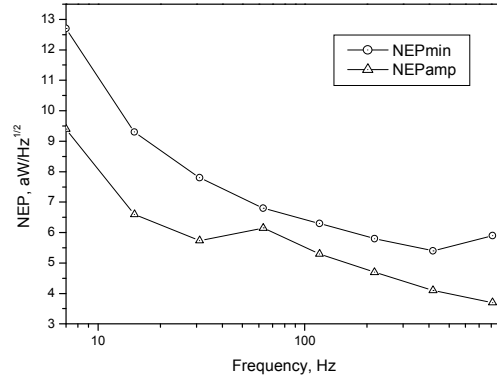


Fig. 13. The minimum Noise Equivalent Power (NEP) from Fig. 14 and the contribution due to the amplifier.

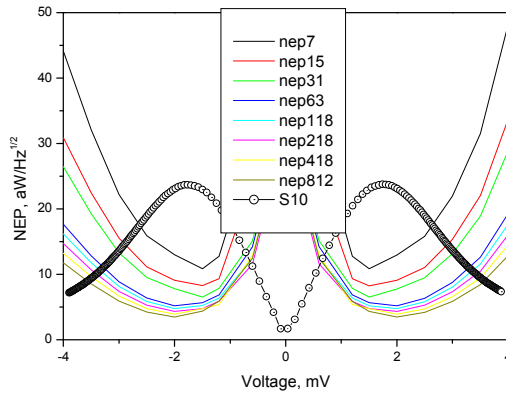


Fig. 12. The Noise Equivalent Power (NEP) and absolute value of response for the series array of 10 bolometers.

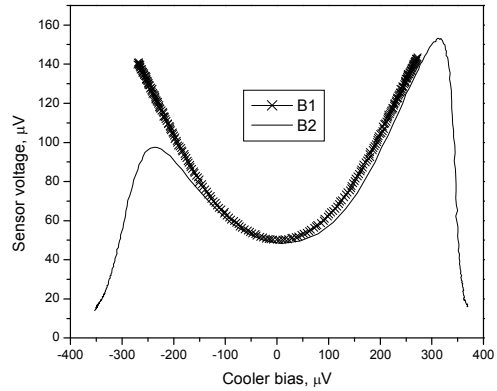


Fig. 14. The electron cooling measured by the voltage across small-area sensor junctions, versus the voltage across the bolometer junctions that serve as electron coolers.

Optical NEP can be also estimated from Fig. 11. The incoming power P_{sig} at the signal frequency $f=350$ GHz within the bandwidth of the cross-slot antenna $\Delta f=100$ GHz is calculated from Planck formula

$$\Delta P = \frac{hf}{\exp(hf/kT) - 1}$$

so that $P_{sig} = \Delta P * \Delta f = 10^{-13}$ W. The response for this signal is $50 \mu V$ so the responsivity is $S = dV/dP = 5 * 10^8$ V/W. For an output noise of $V_n = 11$ nV/Hz^{1/2} we obtain the total optical $NEP = V_n/S = 2.2 * 10^{-17}$ W/Hz^{1/2}.

We also observe the effect of electron cooling. On the same chip we have a test structure comprising a single bolometer of the same shape as in the array and with the absorber connected to another pair of SIN sensor junctions. Applying the bias voltage to the bolometer part we can sense the resulting electron temperature in the absorber. The results of such a measurement are presented in Fig. 14. The maximum increase in sensor voltage is about $105 \mu V$. Taking into account the calibration curve for sensor junctions with $dV/dT = 1.08 \mu V/mK$ one can estimate the cooling effect as 97 mK. So we can expect a maximum cooling of -97 mK at the corresponding bias point of 3 mV, for the series array of 10 bolometers. Maximum response for array is observed at a bias voltage of 2 mV, that corresponds to a $200 \mu V$ bias voltage for each single bolometer, like in Fig. 14. At this voltage we have an increase of the sensor voltage by $49 \mu V$, that corresponds to cooling down by 45 mK, i.e. from the base temperature of 276 mK down to 230 mK.

The effectiveness of connecting bolometers in a series array and electron cooling can be illustrated by direct optical measurements of dynamic range. For such experiment we use Backward Wave Oscillator (BWO) that operates in a frequency range of 250-380 GHz for anode voltages in the range 1100-3800 V. A calibrated polarisation grid attenuator was used for accurate control of the incident power. Inside the cryostat besides the 20 dB NDF cold attenuator at the optical window we also use our cold rotatable stage with opaque Cu window, 10 dB NDF, and open aperture. A photo of a room-temperature setup is presented in Fig.15. The measured output voltage dependence on signal attenuation is presented in Fig. 16.



Fig. 15. The backward wave oscillator (to the right), the polarisation grid attenuator (in the center), and the optical window of He3 cryostat (to the left) in the experiment to measure the dynamic range of the bolometer.

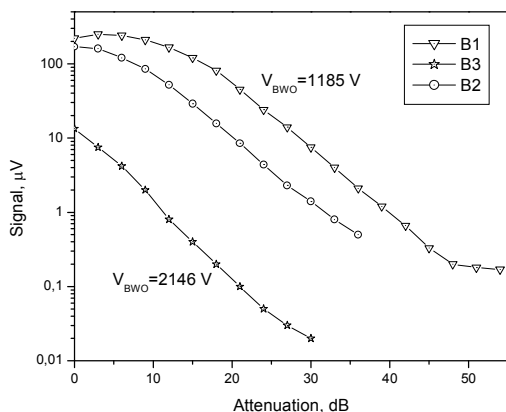


Fig. 16. The output voltage dependence on incoming signal attenuation for 242 GHz and 292 GHz radiation from backward wave oscillator.

Accuracy of such measurements is limited by mechanical instabilities and leak of power through NDF. Nevertheless even in this experiment the dynamic range is over 30 dB. If we take the lower signal level equal to amplifier noise of $11 \text{ nV/Hz}^{1/2}$ and saturation level as presented in Fig. 16 of $200 \text{ } \mu\text{V}$ both measured with integration time 1 s, this results in a full dynamic range of bolometer array over 43 dB.

V. CONCLUSIONS

Optical response with $\text{NEP} = V_n/S = 2.2 \cdot 10^{-17} \text{ W/Hz}^{1/2}$ at 345 GHz, temperature response $dV/dT = 8.8 \text{ } \mu\text{V/K}$, power response $dV/dP = 8.6 \cdot 10^8 \text{ V/W}$, optical $\text{NETD} = 0.65 \text{ mK/Hz}^{1/2}$; dark $\text{NEP} = 6 \cdot 10^{-18} \text{ W/Hz}^{1/2}$, and dynamic range over 30 dB were measured at $T = 280 \text{ mK}$ for a series array of cold-electron bolometers integrated in a cross-slot antenna. Electron cooling by 45 mK at maximum response bias point improves the NEP of such detector and increases the dynamic range.

ACKNOWLEDGMENT

This work was supported by Swedish agencies: VR, Rymdstyrelsen, STINT, Swedish Institute, by RFBR under grant 09-02-12272-OFIM, and Russian ministry of sciences under contract 02.740.11.5103.

REFERENCES

- [1] S. Masi et al, "Instrument, Method, Brightness and Polarization Maps from the 2003 flight of BOOMERanG", 2006, *Astronomy and Astrophysics*, 458, 687-716, astro-ph/0507509
- [2] L. Kuzmin, "Ultimate Cold-Electron Bolometer with Strong Electrothermal Feedback", *Proc. of SPIE conference*, vol. 5498, pp 349-361, June 2004.
- [3] L. Kuzmin "On the Concept of a Hot-Electron Microbolometer with Capacitive Coupling to the Antenna", *Physica B: Condensed Matter*, vol. 284-288, 2129 (2000).
- [4] L. Kuzmin and D. Golubev, "On the concept of an optimal hot-electron bolometer with NIS tunnel junctions" *Physica C*, vol. 372-376, pp 378-382 (2002).
- [5] M. Nahum, T. M. Eiles, and J. M. Martinis, "Electronic microrefrigerator based on a normal-insulator-superconductor tunnel junction". *Appl. Phys. Lett.*, vol. 65, 3123 (1994).
- [6] A. Agulo, L. Kuzmin, M. Tarasov, "Attowatt sensitivity of the Cold-Electron Bolometer". Proceedings of the 16th Int. Symp. On Space Terahertz Technol., ISSTT2005, pp 147-152, Gothenburg, Sweden, May 2005.
- [7] Leonid Kuzmin, "Array of Cold-Electron Bolometers with SIN Tunnel Junctions for Cosmology Experiments". *Journal of Physics: Conference Series (JPCS)*, vol. 97, 012310 (2008).
- [8] Leonid Kuzmin, Ghassan Yassin, Stafford Withington, and Paul Grimes. "An Antenna Coupled Cold-Electron Bolometer for High Performance Cosmology Instruments", *Proc. of the 18th ISSTT*, pp 93-99, Pasadena, March 2007.
- [9] K. Irwin "An application of electrothermal feedback for high-resolution particle detectors". *Applied Physics Letters*, vol. 66, p.1998, (1995).
- [10] N. Grossman, D. G. McDonald, and J. E. Sauvageau, "Far-infrared kinetic-inductance detectors". *IEEE Trans. Magn.*, vol. 27, 2677 (1971).
- [11] Leonid Kuzmin, "A Superconducting Cold-Electron Bolometer with SIS' and Josephson Tunnel Junctions", *Journal of Low Temperature Physics*, **151**, pp. 292-297 (2008).
- [12] G.Chattopadhyay, F.Rice, D.Miller, H.G.LeDuc, and J.Zmuidzinas, "A 530-GHz balanced mixer", *IEEE Microwave Guide Wave Lett.*, vol. 9, pp. 467-469, Nov. 1999.
- [13] Leonid Kuzmin. "Self-Aligned Shadow-Evaporation Technology for Large Area Tunnel Junctions and Nanoabsorbers". PCT Patent, to be filed (August 2010).
- [14] L.S. Kuzmin, Yu.V. Nazarov, D.B. Haviland, P. Delsing and T. Claeson. "Coulomb Blockade and Incoherent Tunneling of Cooper Pair in Ultra-Small Junctions Affected by strong Quantum Fluctuations", *Phys. Rev. Lett.* Vol.67, 1161 (1991).

Development of a MKID camera for APEX

Heyminck, S.¹, Klein, B.¹, Güsten, R.¹, Kasemann, C.¹, Baryshev, A.², Baselmans, J.², Yates, S.², and Klapwijk, T.M.³

¹Max-Planck Institut für Radioastronomie
²SRON, Netherlands Institute for Space research
³Delft University of Technology

Email: heyminck@mpifr-bonn.mpg.de

Abstract

Based on our reconfigurable FPGA spectrometer technology, we have developed a read-out system, operating in the frequency domain, for arrays of Microwave Kinetic Inductance Detectors (MKIDs). The readout consists of a combination of two digital boards: A programmable DAC-/FPGA-board (tone-generator) to stimulate the MKIDs detectors and an ADC-/FPGA-unit to analyze the detectors response. Laboratory measurement show no deterioration of the noise performance compared to low noise analog mixing. Thus, this technique allows capturing several hundreds of detector signals with just one pair of coaxial cables.

This readout technology together with the encouraging performance of the MKID detectors developed by SRON over the last years, initiated the construction of a large MKID camera for the APEX 12m telescope.

As a pathfinder camera, we developed a camera with up to 81 pixels, depending on the detector chip used, during the last year. This system, currently being tested in the lab, will have its first telescope run at APEX in early spring 2010.

We will report about the system, its performance as verified in the lab and, if possible on the time-scale of the conference, the first results from the field tests at the telescope.

An Update on MUSIC: A Kinetic Inductance Detector Camera for Sub/Millimeter Astrophysics at the Caltech Submillimeter Observatory

M. I. Hollister*, N. G. Czakon*, P. K. Day†, R. Duan*, J. Gao ‡, J. Glenn§, S. Golwala*, H. LeDuc†, P. R. Maloney§, B. Mazin¶, H. T. Nguyen†, O. Noroozian*, J. Sayers†, J. Schlaerth§, S. Siegel*, J. E. Vaillancourt ||, A. Vayonakis*, P. Wilson†, and J. Zmuidzinas*

* California Institute of Technology, Pasadena, CA 91125

Email: mih@caltech.edu

†Jet Propulsion Laboratory, Pasadena, CA 91109

‡National Institute of Standards and Technology, Boulder, CO 80305

§CASA, University of Colorado, Boulder, CO 80303

¶University of California, Santa Barbara, CA 93106

||SOFIA/USRA, NASA Ames Research Center, Moffet Field, CA 94035

Abstract—MUSIC (Multiwavelength Sub/millimeter kinetic Inductance Camera, formerly the MKID Camera) is a new facility-class instrument for submillimeter- and millimeter-wave astrophysics at the Caltech Submillimeter Observatory (CSO) on Mauna Kea, Hawaii. The instrument utilizes microwave kinetic inductance detectors (MKIDs), coupled to slot-line antennae through lithographic bandpass filters, offering simultaneous imaging in four bands between 2 mm and 850 μm with 576 spatial pixels. The MKID technology naturally leads to implementation of a frequency-division multiplexing scheme, with several hundred detectors read out through a pair of coaxial connections and a single cryogenic HEMT amplifier. Room-temperature readout is handled with commercial software-defined radio techniques. MUSIC is a collaborative project between the California Institute of Technology, the Jet Propulsion Laboratory, the University of Colorado at Boulder and the University of California, Santa Barbara, and is due for commissioning in late 2010. This paper presents an overview of the project, and an update on the current status and latest results.

I. INTRODUCTION

The development of large-format instruments with arrays of incoherent detectors for astronomy at millimeter and submillimeter wavelengths has proved to be extremely challenging. However, in the last few years considerable success has been realized through the use of transition-edge sensor (TES) bolometers [1] multiplexed with SQUID arrays [2], with instruments such as SCUBA-2 on the James Clerk Maxwell Telescope [3] producing first results. However, such focal planes present considerable technical challenges in implementation.

We report on the progress towards deployment of a new instrument for millimeter wave astronomy from the Caltech Submillimeter Observatory (CSO), Mauna Kea, Hawaii. MUSIC, the Multicolor Submillimeter kinetic Inductance Camera (formerly the MKID Camera), use microwave kinetic inductance detectors, or MKIDs, a novel superconducting detector that overcomes many of the complexities associated with

SQUID multiplexing systems for TES detectors. This paper discusses a number of the key design features of the MUSIC instrument, in addition to a summary of the current status of the project.

II. MICROWAVE KINETIC INDUCTANCE DETECTORS

MKIDs are a type of superconducting detector in which the energy absorbed from an incoming photon breaks Cooper pairs. The physics of MKIDs have been extensively discussed elsewhere [4], and only an overview will be presented in this work.

For alternating currents, superconductors have a non-zero impedance since the Cooper pairs can be accelerated by an electric field, allowing energy to be stored in or extracted from the kinetic energy of the paired electrons. The inertia of the Cooper pairs contributes to what is known as the kinetic inductance.

At finite temperatures below the transition temperature, T_c , a small fraction of electrons are thermally excited out of paired states to produce a surface impedance, Z_s . The surface impedance of a pure superconductor is imaginary since the inductive response of the Cooper pairs is lossless. The free electrons, or “quasiparticles”, produce a real component in Z_s , analogous to the skin effect in a normal metal. Cooper pairs are bound by electron-phonon interaction with a binding energy $\approx 3.5kT_c$, where k is the Boltzmann constant. Photons with energy greater than this binding energy can break Cooper pairs, causing an increase in the quasiparticle density and a change in Z_s .

To use this effect as a photon detector, thin films of aluminium and niobium are used to construct LC resonant circuits. When a photon is absorbed, the change in $\Re(Z_s)$ due to quasiparticle production increases the attenuation of the feedline, while the change in $\Im(Z_s)$ reduces the phase velocity (Fig. 1). These changes are measured as a change in Q and in the resonant frequency.

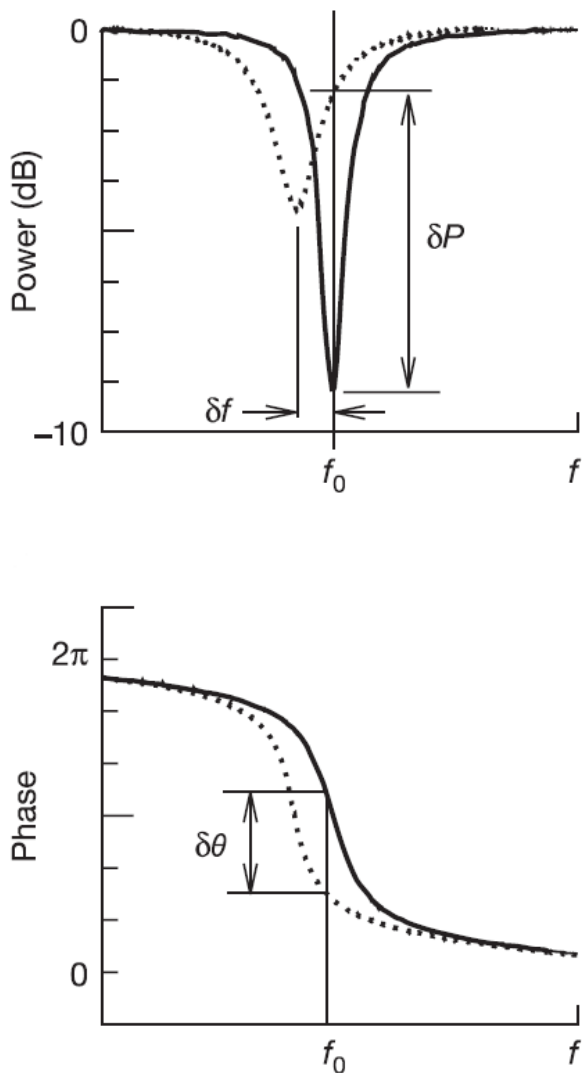


Fig. 1. Illustration of the MKID detection principle. On resonance, the LC circuit loads the feedline, producing a dip in transmission. Absorption of a photon produces quasiparticles, increasing the surface impedance, resulting in a frequency shift of the resonance and a broader, shallower dip. Both effects contribute to a change in amplitude and phase of the microwave transmission. Figure adapted from Ref. [4].

The readout scheme for MKIDs uses homodyne mixing to measure the complex transmission of a microwave probe signal. An MKID is excited at its resonance frequency, while the output of the detector is amplified with a cryogenic HEMT and room-temperature electronics. The output signal is demodulated using a copy of the input signal with an IQ mixer, producing a recovered signal that has in-phase and quadrature components.

Away from resonance, the transmission of the LC circuit is close to unity, so multiple resonators with slightly different frequencies may be coupled to a single transmission line. The quality factors of these resonators is high ($> 10^4$), allowing resonant frequencies to be closely spaced. Sufficient control over resonant frequency for submillimeter detectors has been demonstrated to allow resonance spacing of as little as a few MHz.

TABLE I
MUSIC OBSERVING BANDS.

Band	Band center / GHz	Band width / GHz
0	150	36
1	226	48
2	293	35
3	349	19

The MKID design currently under development for submillimeter radiation is a hybrid design using niobium and aluminium. A schematic of the design is shown in Fig. 3a. Radiation is coupled into an aluminium strip where the pair-breaking occurs. The aluminium section forms part of an inductive meander. The capacitive section of the resonator is a niobium interdigitated design that displays advantageous noise properties over previous designs [5]. The resonator is capacitively coupled to a coplanar waveguide transmission line that carries the microwave probe signal. Current MKID designs have resonant frequencies between 3 and 4 GHz.

III. INSTRUMENT DESCRIPTION

MUSIC implements a focal plane of antenna-coupled MKID resonators, filling a field-of-view of 14 arcminutes at the Cassegrain focus of the 10.4 m Leighton telescope of the Caltech Submillimeter Observatory. The key features of the instrument design are discussed in more detail in the following sections.

A. Focal plane

Development of MKIDs for submillimeter astronomy at Caltech has adopted an antenna-coupled scheme. Radiation is coupled from the telescope to broadband planar slot antennae. [6] A binary summing network combines the received power from the antenna slots, and then feeds this power to the MKID resonators. In the case of the MUSIC implementation, lithographic filters define the final bandpass of the resonators, allowing multiple MKIDs to be connected to a single antenna to form a multicolor spatial pixel. The final focal plane design will have four observing bands between $850 \mu\text{m}$ and 2 mm well-matched to the atmospheric transmission windows from the summit of Mauna Kea. Details of the bands are summarized in Table I, while Fig. 2 shows the 4 MUSIC bands overlaid on an atmospheric transmission plot for the summit of Mauna Kea with 1.68 mm of water vapor (the historical median at CSO). As may be seen, the bandpasses are well-matched to the atmospheric windows between 100 and 380 GHz.

Current prototype arrays have 36 spatial pixels in a 6×6 layout, each with three resonators operating in bands 1–3. A fourth, dark resonator is also included. This resonator is coupled to the transmission feedline, but not to the antenna. Four of these spatial pixels on an early prototype 36-pixel array are shown in Fig. 3b. Also shown here is the transition from the CPW feedline on the array to a microstrip line. The resonant frequencies on these arrays have a target spacing of 5 MHz, such that the 144 resonators fit within two ~ 400 MHz

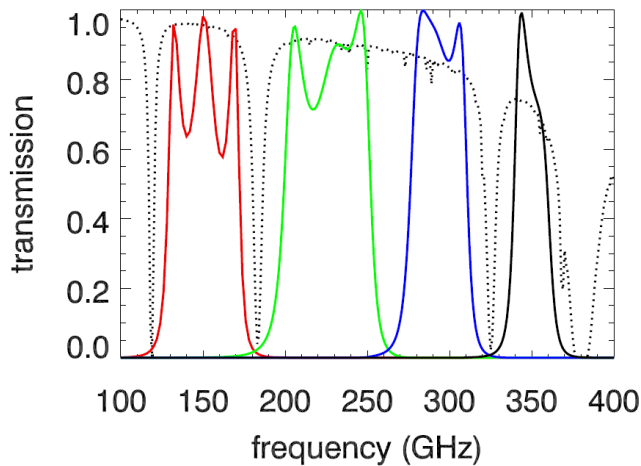


Fig. 2. Simulated bandpasses of the four MUSIC observing bands (solid lines) overlaid on an atmospheric transmission plot (broken line) for the summit of Mauna Kea at 1.68 mm water vapor. Figure adapted from Ref. [7].

blocks of readout bandwidth, a limit set by the readout electronics discussed later in this section. The arrays are back illuminated, with an antireflection coating provided by a fused silica tile tuned to $\lambda/4$ at 1 mm. Concerns over heating in the AR tiles from absorbed optical power have prompted a move to Z-cut single crystal quartz as a substitute.

The MUSIC focal plane will be formed from a mosaic of octant tiles, each approximately 66×34 mm, with 72 spatial pixels and 288 resonators per tile. Each octant is essentially two arrays of 36 pixels fabricated on a single wafer. The frequency spacing of the resonators will be reduced over the prototype arrays such that each block of 36 pixels is placed within the bandwidth of one readout module. The full focal plane therefore has a total of 576 spatial pixels, and 2304 illuminated resonators. Additional dark resonators may also be included.

B. Cryomechanical design

The MUSIC cryostat is based on a modified system built by High Precision Devices,¹ cooled by a Cryomech² PT-415 pulse tube cooler, providing stages at 50 K and 4 K for radiation shielding, infrared filtering and heat sinking. A Chase Cryogenics³ two-stage ³He sorption refrigerator provides sub-Kelvin stages: an intermediate heat sinking stage at ~ 0.36 K and the focal plane heat sink at ~ 0.25 K. An overview of the cryostat is shown in the CAD solid model in Fig. 4a.

The 4-K space is a cylindrical volume of ~ 450 mm diameter and 850 mm in height. Due to the sensitivity of the MKIDs to changes in the magnetic field environment (for example, as the cryostat moves through the Earth's field as the telescope scans in azimuth), the focal plane hardware is enclosed by a cylindrical shield of high-magnetic permeability material. In the past, the material most commonly used for such cryogenic shields was Cryoperm-10, a mu-metal annealed to maximize its magnetic permeability at ~ 4 K produced

by Vacuumschmelze GmbH, in Germany and primarily distributed through Amuneal Manufacturing Corp.⁴ The shield in MUSIC is fabricated from a new material, Amumetal 4K, produced exclusively for Amuneal and displaying improved shielding properties over Cryoperm-10 at considerably reduced cost. The high-permeability shield for MUSIC comprises a double-walled cylinder of 1 mm-thick material with an outside diameter of 358 mm and length 625 mm. Further shielding is provided by a niobium superconducting can, heat sunk at the intermediate sub-K stage inside the high-permeability shield. A CAD cross-section of the magnetic shield and enclosed hardware is shown in Fig. 4b.

The cold hardware structure is supported from the 4-K cold plate by a truss composed of carbon fiber-epoxy composite rods. Although this truss is not intended to be thermally isolating, the carbon fiber supports have a higher Young's modulus and much lower density than materials such as aluminium alloys and copper, and are considerably less expensive. Carbon fiber trusses with cooling provided by copper straps therefore offer an inexpensive and extremely stiff structural support for instrument cold hardware. The total mass supported from this truss is ~ 40 kg, while the deflection of the support structure under gravity, as predicted using finite-element analysis, is ~ 50 μ m. The mass of the cold structures has been minimized through the extensive use of aluminium alloys with copper thermal straps for critical cooling paths, rather than bulk fabrication using copper.

The sub-K stages are also supported by trusses of reinforced carbon fiber. Although the thermal conductivity of carbon fiber-epoxy composites are higher than traditional low temperature structural materials such as Vespel (see, for example, Ref. [8]), the higher Young's modulus allows smaller cross-sectional areas to be used. Furthermore, carbon fiber composites may be obtained at a fraction of the price of Vespel.

C. Optomechanical design

MUSIC is intended to be mounted at the Cassegrain focus of the CSO, the position currently utilized by the Bolocam instrument. However, in order to maximize the instrument field of view, the tertiary mirror assembly (a system of movable mirrors designed to allow instruments at the Nasmyth foci to be selected) and relay optics were redesigned, increasing the field of view from 8 arcminutes as in the current configuration to at least 14 arcminutes. The field of view is then limited by the aperture in the telescope primary reflector. The new relay optics from the secondary focus are essentially a scaled-up version of the existing Bolocam relay optics, with two flat mirrors to fold the optical path, and an elliptical mirror to form an image of the primary. All mirrors are of order 1 m in size and machined from aluminium alloy.

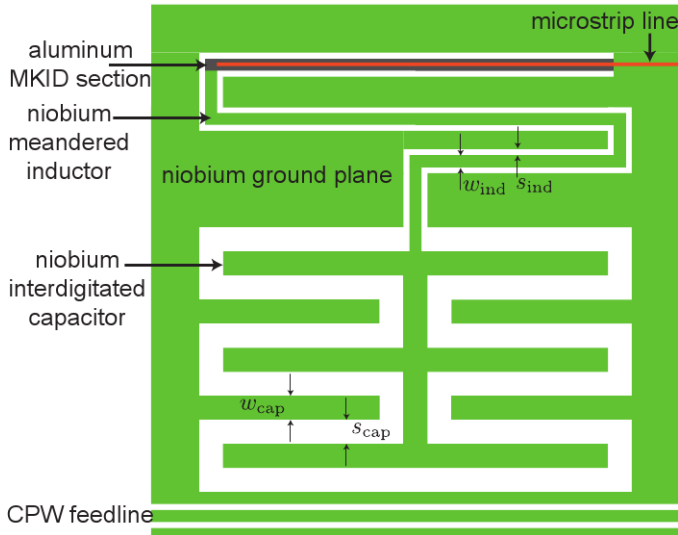
Within the cryostat, a cold stop is positioned at the image formed by the elliptical mirror to define the illumination of the primary. The lyot stop is sized such that ~ 9 m of the 10.4 m telescope primary is illuminated. This illumination is chosen such that point-source sensitivity is maximized while limiting the primary spillover power to $< 1\%$ in all four bands. Rays are

¹<http://www.hpd-online.com>

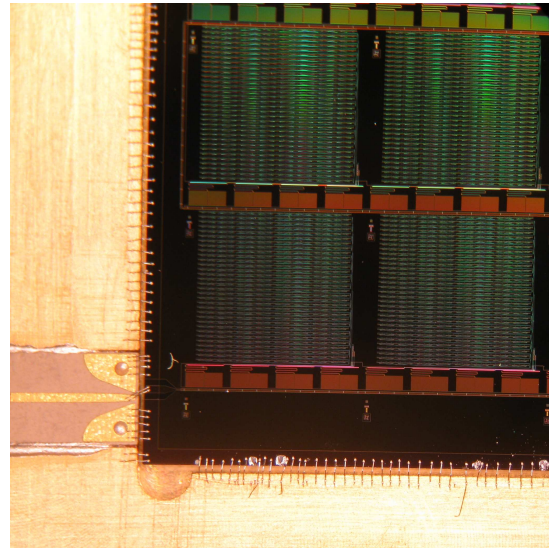
²<http://www.cryomech.com>

³<http://www.chasecryogenics.com>

⁴<http://www.amuneal.com>

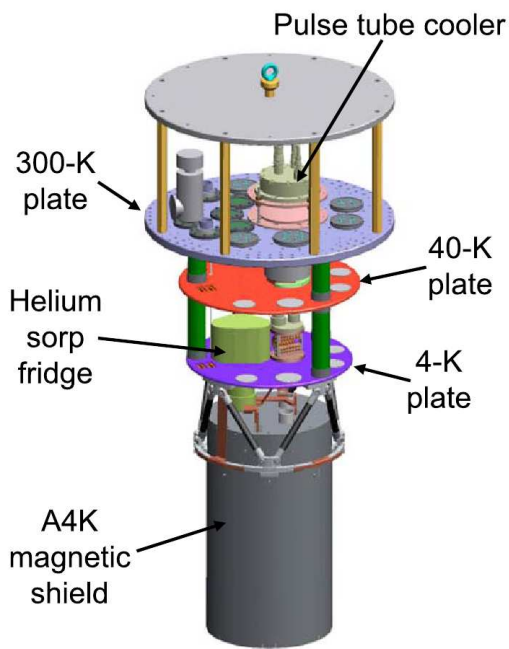


(a) Schematic of an MKID resonator with an interdigitated capacitor architecture. See text for further details. Figure adapted from Ref. [5]

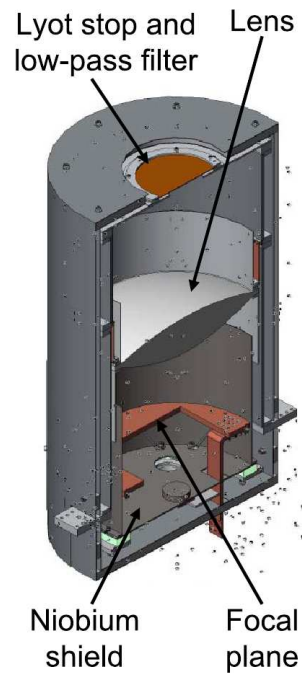


(b) Image of a prototype array. Four spatial antenna pixels may be seen, each coupled to 4 MKID resonators. Also seen here is the transition from on-chip CPW feedline to microstrip (lower left corner of image).

Fig. 3. Microwave kinetic inductance detectors for submillimeter wavelengths.



(a) Overview model of the MUSIC cryostat cold hardware.



(b) Cross-section of the MUSIC magnetic shield showing the sub-K stages and the cold optics.

Fig. 4. CAD solid models of the MUSIC instrument.

focused to the focal plane by a cold lens 275 mm in diameter and ~ 65 mm-thick at its center. This lens is machined from ultra high-molecular weight polyethylene (UHMWPE), with an antireflection coating of Porex⁵ porous teflon attached by melting thin intermediate layers of low-density polyethylene. The coating is tuned to a wavelength of 1 mm. The path length from the lyot stop to the focal plane is over 450 mm, while the final image at focal plane has a diameter of ~ 130 mm. The overall optical efficiency of the system ranges from ~ 8 to $\sim 13\%$ in the four observing bands. This low efficiency is dominated by spillover at the cold stop, and the fact that the antennae only couple to a single polarization.

Infrared filtering in MUSIC is achieved with a combination of capacitive metal-mesh and dielectric filters. The cryostat has a UHMWPE vacuum window. The relatively high thermal conductivity of polyethylene compared to Zotefoam, a cross-linked block foam commonly used as a window in millimeter-wave instruments, means that the window does not passively cool to any great extent. Combined with the large surface area (the window aperture is ~ 300 mm), the result is a large radiative load on the first infrared blocking filters. In order to reduce this loading, the outermost filter on the 50-K radiation shield is a polypropylene IR shader produced by QMC Instruments Ltd.⁶ [9]. Further filtering is provided by a pair of 16 mm-thick PTFE discs, with Porex AR coating as described previously.

At the 4-K shield, further infrared rejection is provided by a pair of 6 mm-thick AR-coated PTFE discs sandwiching a 3 mm-thick Fluorogold (glass loaded teflon) filter with 250 mm clear apertures. Finally, a 125 mm diameter QMC metal-mesh low pass filter at the lyot stop defines the high-frequency edge of the passband at 405 GHz (13.5 cm^{-1}).

D. Readout

As described previously, the MUSIC focal plane is composed of a mosaic of octant tiles. Each of the 8 tiles requires an input and output coaxial cable. Semirigid coaxial cables are used throughout the cryostat. From the room temperature flange to the 4-K cold plate, the coaxes are single lengths of 0.086" stainless steel, approximately 500 mm long, with a copper clamp approximately half way along the cable for heat sinking at the 50-K cold plate. The stainless steel coaxes are terminated with SMA connectors, fabricated by welding rather than soldering in order to increase cryogenic reliability. The stainless steel coaxes connect to a bulkhead at the 4-K cold plate, which includes fixed attenuators (typically 30dB on the input coaxes and 1dB on the output).

On the cold side of the 4-K plate, the input coaxial lines transition to 0.064" NbTi semirigid cables, providing thermal isolation between the 4-K plate and the intermediate heat sinking stage at ≤ 0.4 K, where the coax is again heat sunk using an attenuator (typically 10dB). NbTi coax is used between the intermediate heat sink and the focal plane, terminating is adaptors from SMA to GPO blindmate connectors⁷ for the final connections to the focal plane.

⁵<http://www.porex.com/>

⁶<http://www.terahertz.co.uk/>

⁷Corning Gilbert, <http://www.corning.com/gilbert>

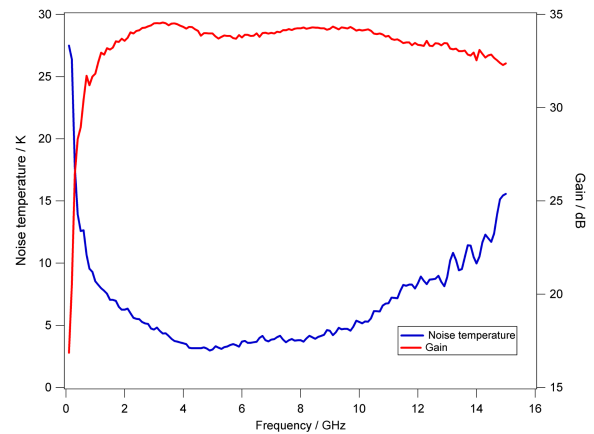


Fig. 5. Typical noise and gain performance of a broadband cryogenic HEMT LNA of the type used for MUSIC, measured at 15 K. Data courtesy of H. Mandi and S. Smith (California Institute of Technology).

The output coaxes from the focal plane are again NbTi. After the intermediate heat sink stage, the coaxes connect to cryogenic HEMT amplifiers mounted on the 4-K cold plate (one amplifier per output cable). The final connection from the HEMTs to the 4-K bulkhead is made with 0.086" copper coax. The HEMTs are provided by S. Weinreb's group at Caltech, and at the MUSIC resonator frequencies typically provide a gain of 30–40dB and a 5 K noise temperature, with $\sim 30 \mu\text{W}$ power dissipation. Typical performance data at 15 K for one of the MUSIC HEMTs is shown in Fig. 5.

E. Room-temperature electronics

The analog homodyne readout scheme described in § II for a single resonator is clearly not practical for the implementation of an MKID array. Readout of multiple resonators can be achieved using a system to generate a comb of probe signals simultaneously [10]. Large-bandwidth, high-speed digital-to-analog converters are used to play back a predefined waveform at audio frequencies. The I and Q components of the probe signal are generated independently, and are mixed and upconverted to the resonator band at GHz frequencies. The frequency comb is passed through the cryostat to excite the resonators, then mixed back down to audio frequencies. The individual resonator responses recovered using an FPGA as a channelizer, demodulating the signal at each comb frequency to determine the response of each resonator. A simplified block diagram of this system is shown in Fig. 6. The electronics are designed in modules, since current limitations on fast ADCs limit the bandwidth of a single unit to approximately 500 MHz, so multiple copies of the electronics are required to read out large focal planes.

Two different systems have been developed for resonator readout. The first is a commercial system from Omnisys Instruments AB in Sweden. In parallel, a project led by UC-Santa Barbara is developing an open source FPGA readout system based on the ROACH platform developed by the CASPER group at UC-Berkeley. This open source readout uses largely commercial software-defined radio techniques from the telecommunications industry to produce a generic

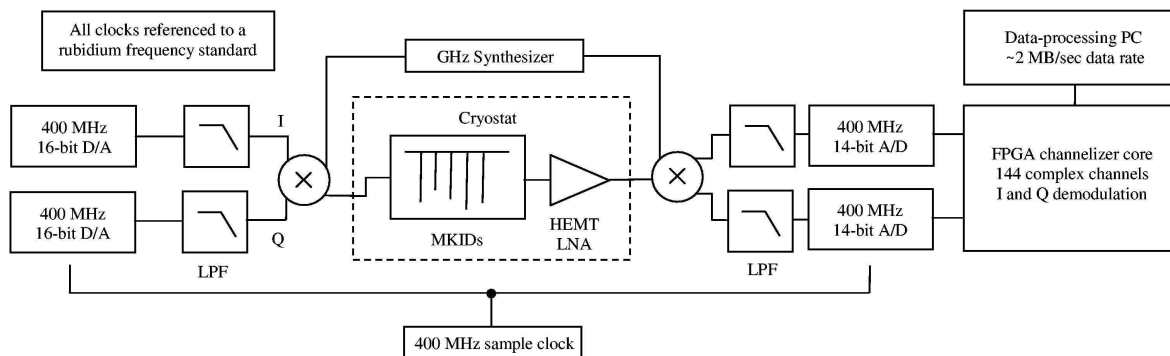


Fig. 6. Simplified block diagram for a multiple resonator MKID readout system. A frequency comb at audio frequencies is played back from memory using fast DACs. The I and Q components are combined with an upconverting mixer and based through the cryostat. The signal is then mixed back to audio frequencies and the individual resonator responses are recovered by Fourier transforms of the I and Q components.

readout system for superconducting resonators. The system is modular, so is easily upgradable, and the open source nature of the firmware programming allows extensive customization. At present, prototype modules of each system are under evaluation.

IV. CURRENT STATUS AND TIMELINE

Development of arrays and the integration of camera hardware has been separated in order to allow parallel development tracks. At present, the cold hardware for the MUSIC cryostat has been fully fabricated, and the process of assembly and integration is due to commence shortly. Although the base cryostat has been operational for over a year, the dewar has so far been used for unrelated testing and for cryogenic testing of HEMT amplifiers.

Array testing and development has primarily been conducted using a smaller cryostat, that has also served as a prototype instrument for testing arrays on-sky at the CSO. This cryostat, known as DemoCam, has been used for extensive lab testing, and in 2007 was used for the first astronomical demonstration of MKIDs using a 16 pixel, 2 color array [11]. Based on lessons learned during that engineering run, a number of modifications were implemented in the cryostat, in addition to an upgrade to a 36-pixel, 3 color focal plane in preparation for a second engineering run. One of the key changes in advance of this second run was the installation of a high-permeability magnetic shield to counteract the observed response of the MKID resonators to changes in the magnetic field environment during telescope scans. Measurements made during the 2007 engineering run showed resonator frequency responses to magnetic fields of order 100 kHz/Gauss. Lab measurements of the resonator response with the new shielding installed has indicated a reduction of response of 4 orders of magnitude. More extensive shielding integrated with the MUSIC cryostat and focal plane is expected to reduce this effect by a further 2 orders of magnitude.

Preparations are currently underway for a second engineering run at CSO with the improved demonstration camera and a 36 pixel, 3 color focal plane. This run will also be an on-sky test of the CASPER/ROACH-based readout electronics. Based

on lab measurements carried out with the current array, it is expected that sensitivities at or very close to the background limit will be demonstrated during this run.

With the successful conclusion of this second run, array development will continue with the first fabrication of 72 pixel, 4 color arrays for the MUSIC focal plane. It is not anticipated that this development will be a technically challenging process, since the new arrays will simply be a scaled version of the current generation of 36-pixel arrays. However, there will likely be issues with fabrication yield that will be overcome through process iteration. Modifications at the CSO in preparation for the new instrument will be carried out during the annual maintenance shutdown in July, with MUSIC anticipated for deployment for initial commissioning towards the end of 2010.

V. SUMMARY

This paper has discussed details of the MUSIC project - a new sub/millimeter array camera intended for use at the Caltech Submillimeter Observatory as a replacement for the current Bolocam instrument. In parallel with the assembly and integration of the camera, array development has been ongoing in a prototype instrument known as DemoCam. It is expected that commissioning of MUSIC will begin in late 2010, pending in part the successful conclusion of a telescope engineering run with DemoCam.

ACKNOWLEDGMENT

The MUSIC project is supported by NSF grant AST-0705157 to the University of Colorado, NASA grant NNGC06C71G to the California Institute of Technology, the Gordon and Betty Moore Foundation, and the JPL Research and Technology Development Fund.

REFERENCES

- [1] K. D. Irwin, *An application of electrothermal feedback for high resolution cryogenic particle detection*, *Applied Physics Letters* 66, pp. 1998-2000 (1995).
- [2] J. A. Chervenak, K. D. Irwin, E. N. Grossman, J. M. Martinis, C. D. Reintsema and M. E. Huber, *Superconducting multiplexer for arrays of transition edge sensors*, *Applied Physics Letters* 74, pp. 4043-4046 (1999).
- [3] W. Holland, M. MacIntosh, A. Fairley, D. Kelly, D. Montgomery, D. Gostick, E. Atad-Ettinger, M. Ellis, I. Robson, M. Hollister, A. Woodcraft, P. Ade, I. Walker, K. Irwin, G. Hilton, W. Duncan, C. Reintsema, A. Walton, W. Parkes, C. Dunare, M. Fich, J. Kycia, M. Halpern, D. Scott, A. Gibb, J. Molnar, E. Chapin, D. Bintley, S. Craig, T. Chylek, T. Jenness, F. Economou and G. Davis, *SCUBA-2: a 10,000-pixel submillimeter camera for the James Clerk Maxwell Telescope* in *Proceedings of the SPIE* 6275, (2006).
- [4] P. K. Day, H. G. Leduc, B. A. Mazin, A. Vayonakis and J. Zmuidzinas, *A broadband superconducting detector suitable for use in large arrays*, *Nature* 425, pp. 817-821 (2003).
- [5] O. Noroozian, J. Gao, J. Zmuidzinas, H. G. LeDuc and B. Mazin, *Two-level System Noise Reduction for Microwave Kinetic Inductance Detectors* in *The Thirteenth International Workshop on Low Temperature Detectors*, 2009.
- [6] P. K. Day, H. G. Leduc, A. Goldin, A. Vayonakis, B. A. Mazin, S. Kumar, J. Gao and J. Zmuidzinas, *Antenna-coupled microwave kinetic inductance detectors*, *Nuclear Instruments and Methods in Physics Research A* 559, pp. 561-563 (2006).
- [7] J. Sayers, N. G. Czakon, P. K. Day, T. P. Downes, R. Duan, J. Gao, J. Glenn, S. R. Golwala, M. Hollister, H. LeDuc, P. R. Maloney, B. Mazin, H. T. Nguyen, O. Noroozian, J. Schlaerth, S. Siegel, J. E. Vaillancourt, A. Vayonakis, P. Wilson and J. Zmuidzinas, *In preparation* (2010).
- [8] M. C. Runyan and W. C. Jones, *Thermal conductivity of thermally-insulating polymeric and composite structural support materials between 0.3 and 4 K*, *Cryogenics* 48, pp. 448-454, (2008).
- [9] P. A. R. Ade, G. Pisano, C. Tucker and S. Weaver, *A review of metal mesh filters* in *Proceedings of the SPIE* 6275 (2006)
- [10] B. A. Mazin, P. K. Day, K. D. Irwin, C. D. Reintsema and J. Zmuidzinas, *Digital readouts for large microwave low-temperature detector arrays*, *Nuclear Instruments and Methods in Physics Research A*, 559, pp. 799-801 (2006).
- [11] J. Schlaerth, A. Vayonakis, P. Day, J. Glenn, J. Gao, S. Golwala, S. Kumar, H. Leduc, B. Mazin, J. Vaillancourt and J. Zmuidzinas, *A Millimeter and Submillimeter Kinetic Inductance Detector Camera*, *Journal of Low Temperature Physics*, 151, pp. 684-689 (2008).

Design and readout of large MKID arrays for submillimeter astronomy

J. A. Schlaerth^{*}, O. Noroozian[†], N. G. Czakon[†], P. K. Day[‡], T. Downes[†], R. Duan[†], Js. Gao[§], J. Glenn^{*}, S. Golwala[†], M. I. Hollister[†], H. G. LeDuc[‡], P. R. Maloney^{*}, B. A. Mazin[¶], H. T. Nguyen[‡], J. Sayers[‡], S. Siegel[†], J.E. Vaillancourt^{||}, A. Vayonakis[†], and J. Zmuidzinas[†]

^{*}CASA

University of Colorado, Boulder, CO 80309

Email: james.schlaerth@colorado.edu

[†]California Institute of Technology, Pasadena, CA, 91125

[‡]Jet Propulsion Laboratory, Pasadena, CA, 91109

[§]National Institute of Standards and Technology, Boulder, CO, 80305

[¶]University of California, Santa Barbara, CA 93106

^{||}NASA Ames Research Center, Moffet Field, CA 94035

Abstract

Microwave Kinetic Inductance Detectors (MKIDs) are superconducting microresonators useful as detectors for sub/millimeter and far-infrared cameras, as well as instruments in optical and x-ray wavelengths. A probe sine wave at the resonance frequency can detect a change in frequency and microwave loss due to submillimeter optical load as a phase or amplitude change. These detectors may be coupled to light through on-chip, phased-array antennas. A single antenna may feed several detectors with different bandpasses defined by on-chip lumped-element filters. The resonators are easily frequency multiplexed by tuning the resonance frequencies, so hundreds of detectors can be read out while coupled to a single feedline.

The deployment and operation of ground-based, background-limited detectors in close-packed arrays present significant challenges in both readout strategy and array design. The initial designs consisted of simple coplanar waveguide microwave resonators with aluminum absorptive sections. The first change has been to substitute the capacitive portion of the resonator with a large interdigitated capacitor (IDC) to reduce its noise contribution. While their low-noise characteristics have been demonstrated, these detectors had not yet been tested on array-scale devices. We present results from arrays of detectors designed for sub/millimeter imaging, tested for their optical response characteristics. In particular, we address challenges of microwave inter-resonator coupling, out-of-band resonator optical sensitivity, and noise reduction in the latest device designs. We show the results of stepped-impedance filters in preventing direct pickup of wide-band radiation, and new frequency spacing to limit crosstalk between resonators. We show direct comparison between older-design coplanar waveguide resonators and new IDC resonators under optical load, demonstrating the noise reduction and comparable responsivity. In addition, we show results of the probe signal readout power that maximizes signal-to-noise.

Poster Session P1: Astronomical Telescopes

Pico Veleta Atmospheric Noise Limits At Millimeter Wavelengths

Dominic J. Benford^{*}, Dale J. Fixsen^{*,†}, Samuel Leclercq[‡] and Johannes G. Staguhn^{*,§}.

^{*} Observational Cosmology Laboratory
NASA / Goddard Space Flight Center
Email: Dominic.Benford@nasa.gov

[†] University of Maryland at College Park
Email: dale.j.fixsen@nasa.gov

[‡] IRAM – Grenoble
Email: leclercq@iram.fr

[§] Johns Hopkins University
Email: johannes.g.staguhn@nasa.gov

Abstract

In November 2007 and October 2008, we demonstrated a new camera for the 2 mm wavelength band, GISMO (Goddard IRAM Superconducting 2 Millimeter Observer), at the IRAM 30 m telescope in Spain. Based on a novel superconducting transition edge sensor bolometer array, GISMO features a compact optical design that should provide rapid imaging in its band. We detail the calculations made for GISMO to determine the atmospheric emission optical loading and resultant photon noise in the 2 mm band at Pico Veleta, and show confirming measurements obtained during the observing runs.

Poster Session P2: Direct Detectors

Comparative Performance of Mo/Cu vs. Mo/Au Transition Edge Sensors for Space Science Applications

D. M. Glowacka¹, D. J. Goldie¹, and S. Withington¹

¹ *Detector and Optical Physics Group, Cavendish Laboratory, University of Cambridge, JJ Thomson Avenue, Cambridge, UK CB3 0HE*

*Contact: glowacka@mrao.cam.ac.uk, phone +44-1223-764089

Abstract—The performance of Transition Edge Sensors (TES) based on Mo/Cu and Mo/Au is assessed. We have fabricated a number of TES bolometers from Mo/Cu and Mo/Au allowing TESs to be fabricated on free-standing micromachined membranes. The low stress conditions allow very thin SiN_x to be used for the membranes, which helps with achieving low-conductance thermal links and low heat capacity. Long-term stability against inter-diffusion is an intrinsic feature of Mo/Cu, but suitable passivation is needed to achieve long-term stability against corrosion. The Mo/Au bilayer does not need a passivation, Mo/Au TESs also show improved chemical, electrochemical and thermal stability compared to other bilayer combinations. The transition temperature of both Mo/Cu and Mo/Au is reproducible, sharp and tuneable over the whole range of temperatures need for space applications. The bolometer can be produced using standard lithographic techniques without any degradation of performance.

INTRODUCTION

The rapid development of TESs over the last decade has led to their widespread use on ground-based and balloon-born mm-wave and submm-wave telescopes. Experience with TES technology in these instruments has increased its technology readiness level, and has paved the way for use on future space missions such as B-POL, SPICA and FIRI [1-3]. The next generation of space missions covering the mm-wave to far-infrared bands will require large-format arrays of extremely low-noise detectors and the sensitivity should increase by at least two orders of magnitude. The current TES detectors developed for ground-based applications have NEPs of around 10⁻¹⁷ WHz^{-1/2} [4-8]. In space applications, where the background loading is considerably lower than the best terrestrial sites the required NEP drops to on order 10⁻¹⁹ WHz^{-1/2}. While it is technically feasible to manufacture single TESs having this sensitivity, it is challenging to create an ultra-low-noise TES technology that can be engineered into complete imaging arrays, with the needed optical packing and uniformity of performance.

DETECTOR FABRICATION

Our TESs consist of superconducting Mo/Cu or Mo/Au bilayers that sit on a silicon nitride membrane isolated from a heat bath by thin legs with different widths and lengths. We are using Nb as a bias connection (Fig. 1, 2).

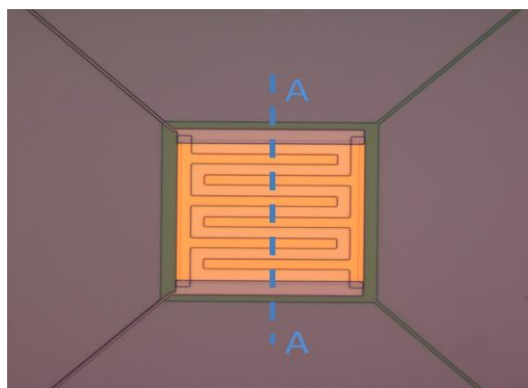


Fig. 1. A single Mo/Au TES with thick Au banks and fingers partially across the TES. The SiN_x island is 200nm thick. The dashed line A-A refers to Fig. 3

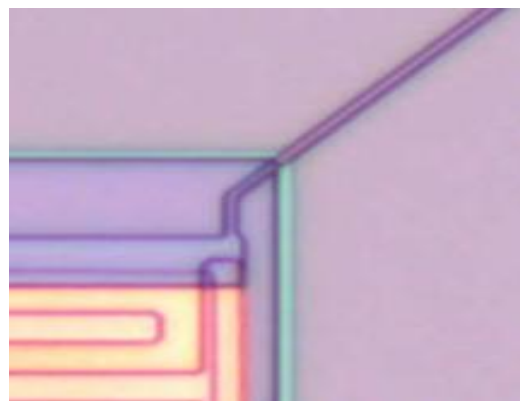


Fig. 2. Mo/Cu TES with 1μm SiN_x (200nm thick) legs, 1μm Nb connection and SiO₂ passivation layer.

The devices are fabricated on 50mm, 225 μm thick $\langle 100 \rangle$, double-side polished Si wafers. These wafers have a 50 nm thermal oxide and 200 nm of low-stress SiN_x , formed by low-pressure chemical vapour deposition, on both sides. Ultimately the silicon nitride becomes a suspended membrane, produced by back-side etching of the supporting silicon substrate, to give the required thermal isolation.

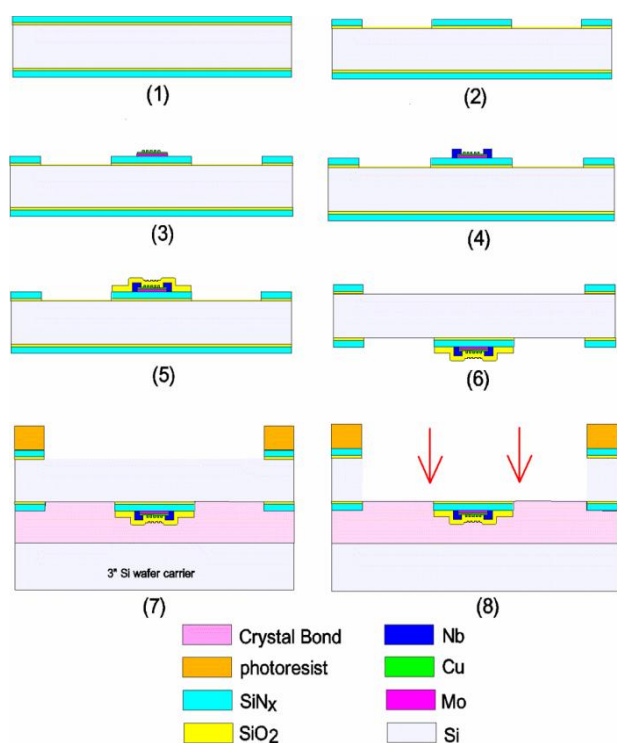


Fig. 3. Schematic process flow for device fabrication. Cross-section along the dashed line shown Fig. 1.

Device fabrication starts with a Reactive Ion Etch (RIE) of the SiN_x using CHF_3 gas to outline the devices and define the membrane and legs (Fig. 3.2). The bilayer is deposited by dc magnetron sputtering with a base pressure of $\sim 1 \times 10^{-9}$ Torr, and consists of a Mo layer followed by a Cu or Au layer deposited in quick succession to prevent any oxidation of the interface. The bilayer is then patterned by wet etching the Cu in a 5% solution of ammonium persulfate and water. The gold is etched in commercial Gold Etchant (iodine plus potassium iodide). Then the Mo is etched in commercially prepared aluminium etch. Additional normal metal Cu or Au banks and zebra stripes [9] are added by sputtering through a photoresist lift-off stencil covering the edges of the bilayer (Fig. 3.3) [10]. The bias connection of Nb, is then deposited and patterned by lift-off (Fig.3.4). The SiO_2 is used as a passivation layer for Cu. The SiO_2 layer is removed from unwanted areas by lift-off (Fig.3.5). The device is then ready for the RIE silicon nitride etching on the back of the wafer

and bonding face down to a carrier wafer (Fig. 3.6 and Fig. 3.7). The last step is the fabrication of the suspended membrane, which requires removal of the supporting Si from the window using Deep Reactive Ion Etching, thus leaving the TES membrane suspended on nitride legs.

RESULTS AND CONCLUSIONS

We have developed deposition and processing techniques for Mo/Cu and Mo/Au TES detectors. The same geometry was used to fabricate Mo/Cu and Mo/Au TESs (Fig. 4).

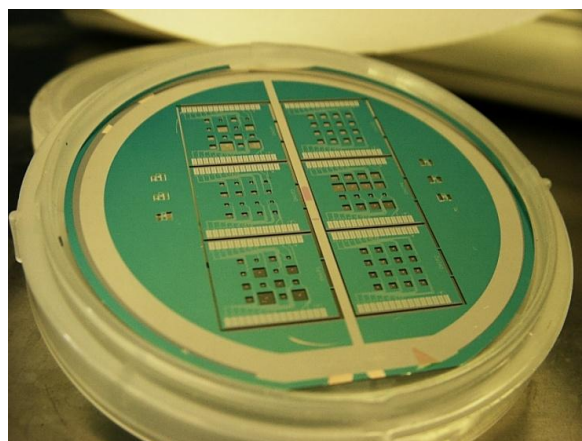


Fig. 4. Completed wafer

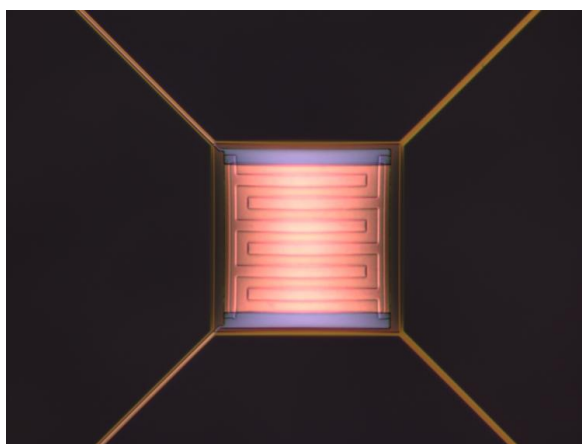


Fig. 5. A single Mo/Cu TES on 200nm SiN_x membrane suspended on 4.2 μm width and 420 μm length legs.

We measured the superconducting-resistive transition of 40nm Mo/30nm Cu and 40nm Mo/30nm Au. In both cases the transition is reproducible and sharp. Fig. 6 and Fig. 7 show a typical resistive transition for the process devices.

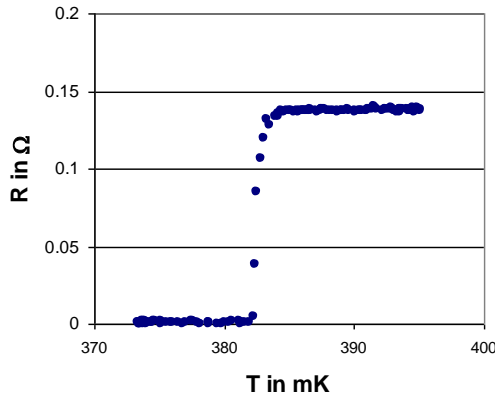


Fig. 6. Typical resistive transition of Mo/Cu (40/30nm) TES

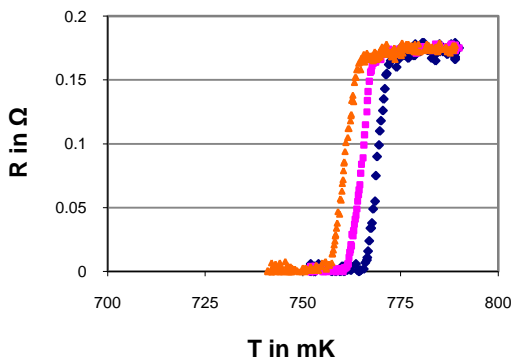


Fig. 7. Resistive transition of a Mo/Au (40/30nm) TES

We fabricated devices with different Mo/Cu bilayer layup, 40nm/30nm, 40nm/81nm and 40nm/106nm. The transition temperature is 382mK, 210mK and 122mK respectively. Typical T_c for Mo/Au (40nm/30nm) is 765mK. For different thicknesses of Cu and Au layers we measured the electrical conductivity (Fig. 8) which is related to the thermal conductivity through the Wildemann-Franz law. High thermal conductivity reduces noise due to internal thermal fluctuations [11].

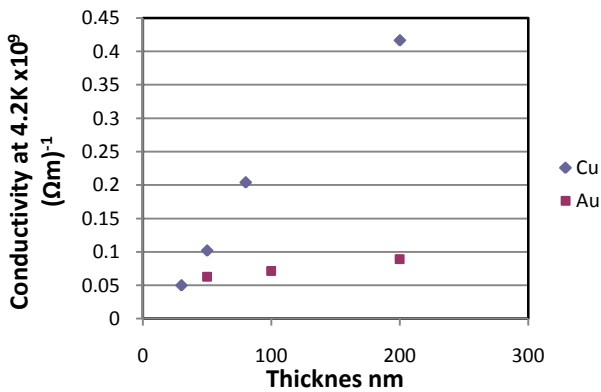


Fig. 8. Conductivity for different thicknesses of Cu and Au layers.

Mo/Cu and Mo/Au TESs are an establish technology and suitable for space application. Low stress Mo/Cu and Mo/Au bilayer films allow TESs to be manufacture on free-standing micromachined membranes. Long term stability against inter-diffusion is an intrinsic feature of Mo/Cu and Mo/Au bilayer [12]. Mo/Au shows long term-stability against corrosion. For Mo/Cu to achieve this stability it needs suitable passivation, in our case SiO₂, although can be difficult to get good adhesion to Cu. The transition of Mo/Cu and Mo/Au is reproducible, sharp and tunable over the whole range of temperatures needed for space applications. The bolometers can be produced using standard lithographic techniques without any degradation of detector performance. Mo/Au TESs are extremely rugged devices and they can withstand extraordinary – including prelaunch – environments. This is a consideration specific to space application.

REFERENCES

- [1] P. De Bernardis, et al., “B-Pol: detecting primordial gravitational waves generated during inflation”, *ESA Cosmic Vision, Experimental Astronomy*, online First 92008)
- [2] T. Onaka, et al., “A 3.5m space infrared telescope for mid-and far-infrared astronomy,” *Advances in Space Research* **36**, pp 1123-1127 (2005).
- [3] FIRI proposal for Cosmic Vision, <http://arxiv.org/ftp/arxiv/papers/0707/0707.1822.pdf>
- [4] M. D. Audley, et al., “A large-format TES array for submillimetre astronomy”, *Proceedings of the 10th International Workshop on Low Temperature Detectors. Nuclear Instruments and Methods in Physics Research Section A: Accelerators, Spectrometers, Detectors and Associated Equipment Volume 520, Issues 1-3, 11 March 2004*, pp. 479-482 (2004)
- [5] B. Maffei, et al., 2005, *EAS Publ. Ser. Vol. 14, Dome C Astronomy and Astrophysics Meeting*. EDP Sciences, Les Ulis, p. 251
- [6] J. Fowler, “*The Atacama Cosmology Telescope Project*”, *Proc. SPIE* vol. 5498, p. 1-10 (2004)
- [7] J. Ruthl, et al., “*The South Pole telescope*”, *Proc. SPIE*, vol. 5498, p. 11-29
- [8] J. Mehl, et al., “*TES Bolometer Array for the APEX-SZ Camera*”, *Journal of Low Temperature Physics*, 151, p. 697 (2008)
- [9] S. J. Smith, et al., “*Characterizing the Superconducting-to-Normal Transition in Mo/Au Transition-Edge Sensor Bilayers*”, *J Low Temp Phys*, 151, pp. 195-200, (2008)
- [10] G. C. Hilton, et al., “*Microfabricated Transition-Edge X-ray Detectors*”, *IEEE Trans. Applied Superconductivity*, vol. 11, pp. 739-742, (2001)
- [11] D. J. Goldie, et al., *Modeling and reduction of excess noise in transition edge sensor detectors*, *Proceedings of the SPIE*, vol. 7020, 70200L, (2008).
- [12] N. Tralshawala, et al., “*Fabrication of Mo/Au Transition-Edge Sensors for X-ray Spectrometry*”, *IEEE Trans. on Applied. Superconductivity*, vol. 11 pp. 755-758 (2001)

Cold-Electron Bolometer Integrated with a Unilateral Finline

Ernst A. Otto^{1,2*}, Mikhail A. Tarasov^{2,3}, Paul K. Grimes¹, Leonid S. Kuzmin², and Ghassan Yassin¹

¹ Oxford University, Oxford, United Kingdom

² Chalmers University of Technology, Gothenburg, Sweden

³ Kotel'nikov Institute of Radio Engineering and Electronics of Russian Academy of Sciences, Moscow,

*Contact: otto@chalmers.se, phone +46-31-7725173

Abstract— The Cold-Electron Bolometer (CEB) is a very sensitive millimetre-wave detector which is easy to integrate with planar circuits. CEB detectors have other important features such as high saturation power and very fast response. We have designed, fabricated and tested CEB detectors integrated across the slot of a unilateral finline on silicon substrate. Bolometers were fabricated using e-beam direct-write trilayer technology. The CEB performance was tested in a He³ sorption cryostat HELIOX-AC-V at a bath temperature of 280 mK. To reduce the background power radiation overheating the optical window in the cryostat was equipped with two low-pass filters with cut-off frequency 33 cm⁻¹ and 100 cm⁻¹ and 2 neutral density filters with 10 db attenuation each. DC IV curves were measured in a current bias mode, optical response was measured by irradiating samples with a microwave signal from IMPATT diode at 110 GHz modulated at 127 Hz. These tests were conducted by coupling power directly into the finline chip. The signal response was measured using a lock-in amplifier. The bolometer dark electrical noise equivalent power is estimated to be about NEP=5·10⁻¹⁶ W/Hz^{1/2}.

I. INTRODUCTION

A new generation of bolometric detectors is needed for advanced telescopes for sub-mm imaging, CMB polarization experiments and far-infrared spectroscopy. One candidate technology is the capacitively coupled Cold-Electron Bolometer (CEB) [1]-[4]. The CEB can be used with both JFET [3] and SQUID readout [1, 2] systems, both of which are now well developed for use in astronomical instruments. JFET readout systems have been used with NTD semiconductor bolometers on ground based, balloon borne and space based instruments. SQUID readout and multiplexing have been developed for TES (Transition-Edge Sensor) bolometers [1] and used in both ground and balloon based instruments. Our goal is to develop CEBs that can be read by a JFET or SQUID, so that the performance of the two systems can be compared.

The CEB is a planar antenna-coupled superconducting detector with high sensitivity and high dynamic range. A unique feature of this device is electron cooling by SIN tunnel junctions with strong electro-thermal feedback [5]. The CEB devices considered here consist of a normal metal absorber coupled to superconducting electrodes via SIN tunnel junctions at each end of the absorber. RF power from the antenna is capacitively coupled through the SIN tunnel junctions into the absorber. The absorbed power heats

electrons above the Fermi level and the hottest electrons eventually tunnel through junction oxide barrier.

The cooling of the device as a result of removing the hot electrons from the absorber increases dynamic range of the system, thus substantially increasing the detector saturation power. This is to be contrasted with the operation of the TES where a biasing constant voltage source heats the device to keep it near the transition temperature. It has already been shown [1-3] that a cold-electron bolometer with strong electrothermal feedback can potentially give state of the art noise performance in presence of a realistic background power load. The time constant of CEB could be considerably reduced by the loop gain of negative electrothermal feedback to the level of 10 ns which is several orders of magnitude shorter than that for TES detectors. The CEB is therefore a very promising device for future space telescopes due to fast response, high sensitivity and low noise.

II. CEB DEVICE MODEL

The operation of CEB can be described using the heat balance equation [1, 2]:

$$P_{cool}(V, T_e, T_{ph}) + \Sigma \Lambda (T_e^5 - T_{ph}^5) + \frac{V^2}{R_j} + I^2 R_{abs} + C_A \frac{dT}{dt} = P_0 + \delta P(t) \quad (1)$$

The right hand side represents the total power injected into the device.

The first term in the left hand side of the equation (1) $P_{cool}(V, T_e, T_{ph})$ is the cooling power of the SIN tunnel junction, where T_e and T_{ph} are, respectively, the electron and phonon temperatures of the absorber. The second term $\Sigma \Lambda (T_e^5 - T_{ph}^5)$ is the heat flow from the electron to the phonon subsystems in the absorber with Σ being the material constant and Λ is the volume of the absorber; $C_A = \Lambda \gamma T_e$ is the heat capacity of the absorber; R_j is the subgap resistance of the tunnel junction; R_{abs} the resistance of the absorber; $P(t)$ the incoming RF power.

The power flowing in and out of the CEB may be separated into two parts; a time independent term,

$$\Sigma \Lambda (T_{e0}^5 - T_{ph}^5) + P_{cool0}(V, T_{e0}, T_{ph}) = P_0,$$

and a time dependent term,

$$(\partial P_{cool} / \partial T + 5 \Sigma \Lambda T_e^4 + i \omega C_A) \delta T = \delta P \quad (2)$$

The term $G_{cool} = \partial P_{cool}/\partial T$ is the effective cooling thermal conductance of the SIN junction that gives rise to the negative electrothermal feedback (ETF). When it is large, it reduces the temperature response δT because cooling power, P_{cool} , compensates for the change of signal power in the bolometer. The term $G_{e-ph} = 5\Sigma\Lambda Te^4$ is the electron-phonon thermal conductance of the absorber. From Eq. (2) we define an effective complex thermal conductance which controls the temperature response of CEB to the incident signal power

$$G_{eff} = G_{cool} + G_{e-ph} + i\omega C_{\Lambda} \quad (3)$$

In contrast with TES, the effective thermal conductance of the CEB is increased by the effect of electron cooling (negative ETF).

In what follows we will assume that the SIN tunnel junction is voltage-biased, and that the current is measured by a SQUID. The sensitivity of the device is then characterized by the current responsivity S_I , which is the ratio of the current change and the change in the power load of the bolometer,

$$S_I = \frac{\partial I}{\partial P_{\omega}} = \frac{\partial I/\partial T}{G_{cool} + G_{e-ph} + i\omega C_{\Lambda}} = \frac{\partial I/\partial T}{G_{cool}(L+1)[1+i\omega\tau]} \quad (4)$$

where $L = C_{cool}/G_{e-ph} \gg 1$ is ETF gain and

$$\tau = \frac{C_{\Lambda}}{G_{e-ph}(L+1)} = \frac{\tau_0}{L+1} \quad (5)$$

is an effective time constant, with $\tau_0 = C_{\Lambda}/G_{e-ph}$ ($\tau_0 \sim 10 \mu\text{s}$ at 100 mK).

The strength of the electrothermal feedback is estimated as:

$$L(\omega) = \frac{G_{cool}}{G_{e-ph}(1+i\omega\tau)} = \frac{\partial I/\partial T}{G_{cool} + G_{e-ph} + i\omega C_{\Lambda}} \quad (6)$$

The noise properties of the detector are characterized by the NEP, which is the sum of three different contributions:

$$NEP_{total}^2 = NEP_{e-ph}^2 + NEP_{SIN}^2 + \delta I^2/S_I^2 \quad (7)$$

$$\text{where } NEP_{e-ph}^2 = 10k_B\Sigma\Lambda(T_e^6 + T_{ph}^6) \quad (8)$$

is the noise associated with electron-phonon interaction. NEP_{SIN}^2 is the noise of the SIN tunnel junctions, and the last term $\delta I^2/S_I^2$ is the noise of a SQUID (or other) current amplifier with δI expressed in $\text{pA}/\text{Hz}^{1/2}$.

The noise of the SIN tunnel junctions, NEP_{SIN} , has three components: shot noise $2eI/S_I^2$, the fluctuations of the heat flow through the tunnel junctions, and the anticorrelation term between these two processes [1]:

$$NEP_{SIN}^2 = \delta P^2 - 2\frac{\delta P_{\omega}\delta I_{\omega}}{S_I} + \frac{\delta I_{\omega}^2}{S_I^2} \quad (9)$$

III. DESIGN OF CEB AND UNILATERAL FINLINE

The detector reported here uses a CEB with SIN tunnel junctions as a detector of an incoming radiation propagated through a 97 GHz WR-10 waveguide and a finline taper (Figure 1). The integrated circuit comprises a finline with a CEB device deposited across the fins. The CEB chip will be inserted into the E-plane of a rectangular waveguide block designed for 97 GHz frequency and fabricated by the Oxford Physics workshop (Figure 2). The devices are fabricated using the trilayer direct-write technology presented in [6, 7]. This approach is suitable for low-frequency applications as it allows for large size tunnel junctions, which are difficult to fabricate using traditional shadow evaporation technique. The latter is more suitable for higher frequencies (350 GHz and above) as smaller tunnel junctions are required and can be more easily fabricated in that technology. The next step of our work will be fabrication of parallel-series arrays of CEBs to overcome the amplifier noise of a JFET-readout system [8].

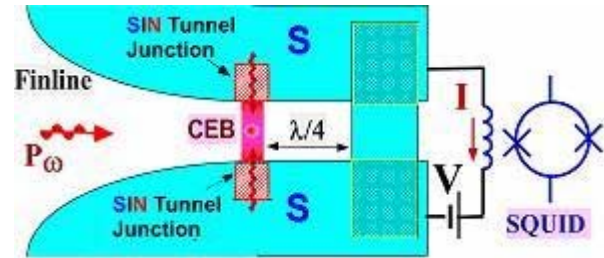


Fig. 1. A Cold-Electron Bolometer (CEB) coupled to a finline with SQUID readout

The SQUID readout can be used the same as for TES bolometers with typical SQUID sensitivity of $1 \text{ pA}/\text{Hz}^{1/2}$. The relatively moderate dynamic resistance of CEB ($\sim 1\text{k}\Omega$) should be matched to the low noise equivalent resistance of SQUID.

An attractive readout option is to use a JFET-readout, which can operate at room temperature. For this type of readout system, a higher dynamic resistance at the CEB output is desirable, which can be readily achieved using a parallel-series array [8]

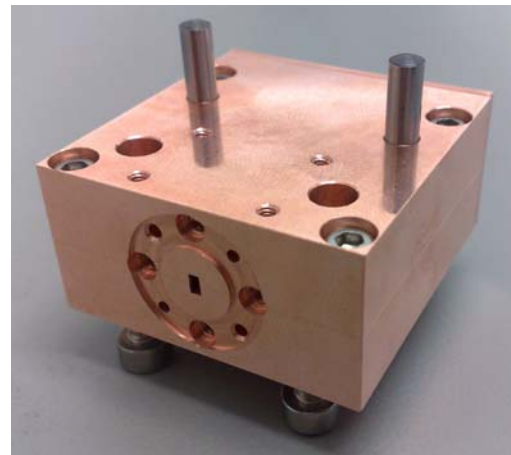


Fig. 2. Photo of a waveguide mount.

The performance of a cold-electron bolometer suitable for above described detector has already been analyzed in [1], at a frequency range centered at 70 GHz.

Assuming the presence of the typical background power load ($P_0 = 0.2$ pW per polarization component), the results of simulation are presented in Fig. 3.

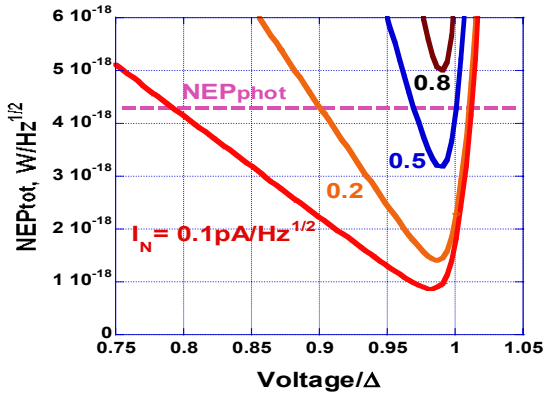


Fig. 3 Total NEP of the CEB with SIN tunnel junction for the 70 GHz channel, with a SQUID noise current from 0.1 pA/Hz^{1/2} and 0.8 pA/Hz^{1/2}. R=0.2 kOhm, S=2μm², Vol=0.03μm³, power load $P_0 = 0.2$ pW, T=100 mK. The $NEP_{phot} = 4.3 \cdot 10^{-18}$ W/Hz^{1/2} is shown by dashed line [1].

In Fig. 3, the photon shot noise at power load P_0 is given by

$$NEP_{phot} = \sqrt{2P_0 hf} \tag{10}$$

For a detector centred at 70 GHz, the photon noise at power load $P_0 = 0.2$ pW is estimated as $NEP_{phot} = 4.3 \cdot 10^{-18}$ W/Hz^{1/2}.

Fig. 3 shows the results of a simulation of a CEB with a single SIN junction, with realistic parameters for the tunnel junction and absorber, and values of SQUID noise from 0.1 pA/Hz^{1/2} to 0.8 pA/Hz^{1/2}. It has been shown theoretically [1] that the level of NEP_{phot} can be achieved for SQUID noise lower than 0.5 pA/Hz^{1/2}

IV. ANALYSIS OF CEB-FINLINE IC

We have analyzed electromagnetic behaviour of the CEB-finline integrated circuit using Ansoft Designer and HFSS software. An equivalent circuit for the CEB was simulated with an ideal transmission line in Ansoft Designer software (Figure 4). In this model, the incoming signal propagates through a transmission line of electrical length of 360° and the power is fed into the CEB represented here by RLC tank circuit assuming matched terminals. The end of the transmission line is shorted at a distance called here “back short distance”. This value was set first to $\lambda/4$ and then optimised in order to achieve the best matching between the characteristic impedance of the transmission line and the input impedance of the RLC circuit over the band of interest.

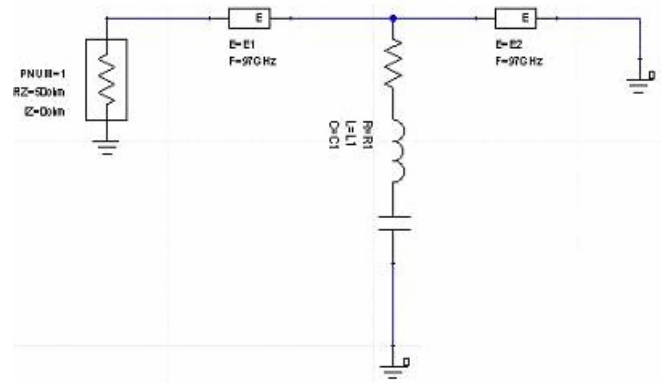


Fig. 4. Equivalent circuit used for simulations in Ansoft Designer.

Next we used HFSS to simulate a finline CEB with finline slot widths between 2 and 10 microns, deposited on silicon or quartz. The CEB itself was represented by an equivalent RLC circuit. The profile of the finline taper was designed using an optimum taper technique, implemented in the *Finsynth* software described in [9].

Simulations performed in Ansoft Designer and HFSS showed that most reliable matching can be achieved using tunnel junctions of 1.5×1.5 to 2×2 microns area, which correspond to capacitance values of 100-200 fF. For Si substrate, the optimum values obtained for the inductance and the resistance are 2.4 pH and 45 Ω respectively. For a quartz substrate, the corresponding values were 2.6 pH and 70 Ω. Simulations also showed that using a back short distance of 225-250 μm and 5 μm slot width a reflection coefficient down to -20 dB can be achieved for Si, while the result is rather insensitive to small variations in absorber resistance and inductance values. S_{11} for Si and quartz are shown in Figure 5a and 5b respectively. Similar values (-18 dB) were obtained for quartz substrate at a backshort distance of 500 μm (Figure 5b). Based on these simulations, we decided to fabricate a CEB-finline structure at 5 μm width on silicon substrate; using quartz substrate is still an option.

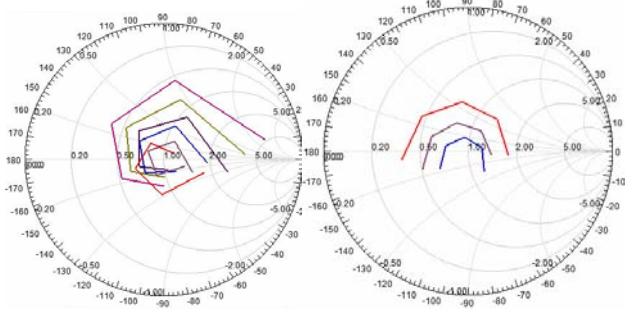


Figure 5. Reflection coefficient for Si substrate(a) and quartz (b)

V. FABRICATION

The CEB-finline samples have been fabricated using e-beam lithography in direct-write mode using the trilayer technology principle of fabricating tunnel junctions proposed by L. Kuzmin and described in [6, 7]. First, gold contact pads and wires have been patterned using e-beam exposure and thermal evaporation. Then finlines have been patterned in the same way and finally the Cold-Electron Bolometer structures have been fabricated in the middle of the finline using the trilayer process [6, 7]. As the last step, the Cu-Au layer has been removed by Ion-Beam Etching on the top of the trilayer structure. The photo of the fabricated CEB on finline is shown in Figure 6.

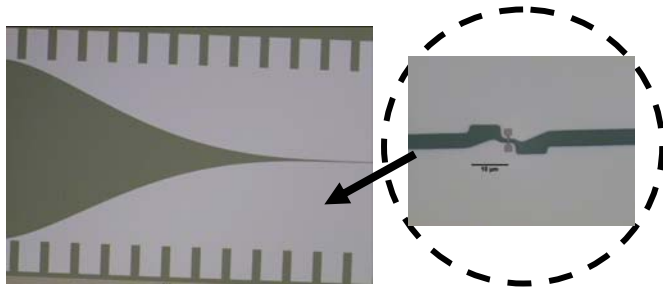


Fig. 6. Photo of finline with CEB across the slot.

VI. MEASUREMENT RESULTS AND ANALYSIS

Testing of the CEB-devices was carried out at Chalmers University of Technology using an Oxford Instruments HELIOX-AC-V He³ sorption cryostat, which can reach a base temperature of 280mK. In order to keep the optical power load on the detectors to acceptable levels, two low-pass filters with cut-off frequencies of 33 cm⁻¹ and 100 cm⁻¹ and two neutral density filters with 10dB attenuation each were mounted over the windows in the radiation shields inside the cryostat.

DC current-voltage characteristics of the CEB devices were measured in the fixed current bias mode, using a differential bias circuit with room temperature amplifiers and bias resistors. This circuit uses a driver circuit with bias resistance switchable in a range from 100kOhm to 10GOhm, and AD743 BiFET based first stage amplifiers with input voltage noise of around 4nV/√Hz. I-V curves were taken at several bath temperatures between 286mK and 356mK.

The voltage to temperature response, $S_{V/T} = dV/dT$ of CEB is calculated by comparing the I-V curves at different bath temperatures. The IV curve of the fabricated device is shown in Figure 7. Voltage response to the temperature versus bias voltage is shown in Figure 8.

Noise measurements were made using a lock-in amplifier referenced to a signal generator to make a spot measurement of the noise power at the voltage output of the bias system at 127Hz, using a 24dB/oct filter. The measured total voltage noise is shown as a function of bias voltage in fig. 9.

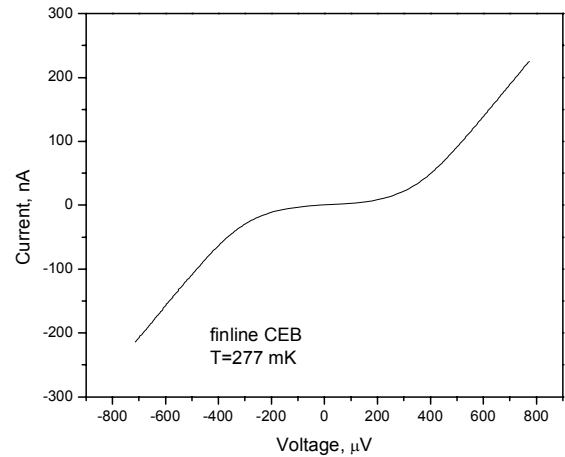


Fig. 7. The IV curve of CEB at temperatures 277 mK.

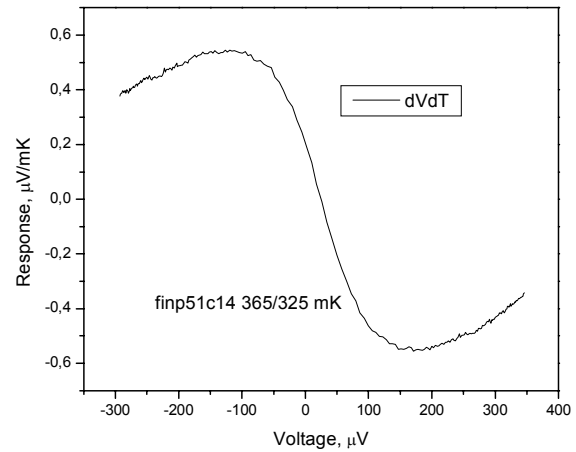


Fig. 8. Voltage response of the CEB with changing temperature versus bias voltage.

Preliminary optical tests of the bolometers were performed at 110 GHz with IMPATT diode as a signal source. The optical response was measured using lock-in amplifier. A photo of the experimental setup is presented in Fig. 10. Measurements were performed by mounting the CEB-finline chip on a sample holder not far away from the cryostat window and illuminating it from the outside. In this experiment, a small amount of optical power from a 110GHz

IMPATT diode with a horn was coupled into the finline which when mounted in free space behaves somewhat like a Vivaldi antenna, loaded on one side by the dielectric of the substrate. The output of the IMPATT diode was modulated at 127Hz and the bolometer response detected via a lock-in amplifier, at three levels of signal power. The measured optical response is shown in fig. 11.

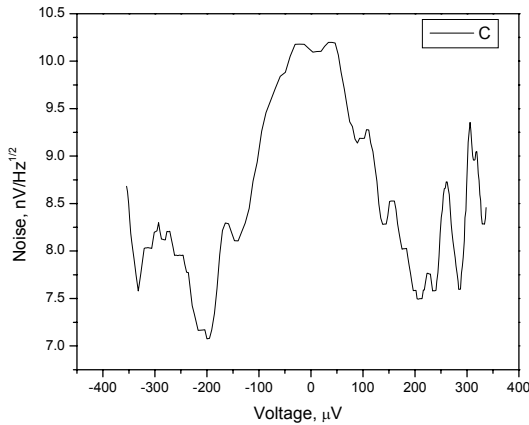


Fig. 9. Noise of CEB at 127 Hz.

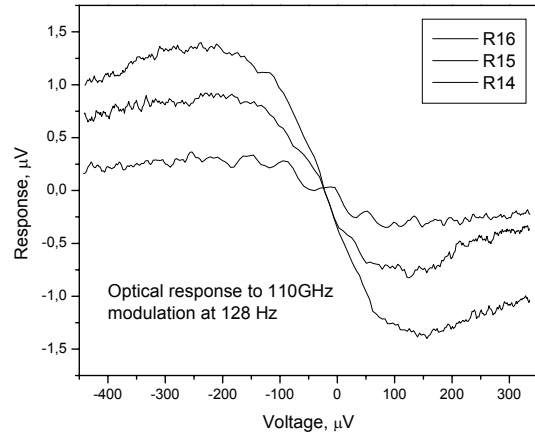


Fig. 11. Voltage response of bolometer to the incoming signal at 110 GHz at three levels of signal power

Taking into account the above experimental data we can estimate the dark NEP as follows. Voltage response is $S_v = dV/dP = (dV/dT)/G$, thermal conductivity due to electron-phonon interaction $G_{e-ph} = 5\Sigma vT^d$. Another component of thermal conductivity is due to thermal flow by electrons:

$$G_i = \frac{dP_i}{dT} = \frac{d}{dT} \left(kT \frac{I}{e} \right) = \frac{kI}{e}$$

For the sample with two SIN tunnel junctions of $1.5 \times 1.5 \mu\text{m}^2$, absorber thickness of 50 nm, volume of absorber is $2 \cdot 10^{-19} \text{ m}^3$, material parameter $\Sigma = 3 \cdot 10^9 \text{ Wm}^{-3}\text{K}^{-5}$ for copper, at temperature of 280 mK the thermal conductivity due to electron-phonon interaction can be estimated as $G_{e-ph} = 1.84 \cdot 10^{-11} \text{ W/K}$. At bias current of 20 nA thermal conductivity due to thermal flow by electrons will be $G_{e-ph} = 1.6 \cdot 10^{-12} \text{ W/K}$, which yields the total thermal conductivity of $2 \cdot 10^{-11}$. Taking the maximum experimental value for bolometer output noise of $10 \text{ nV/Hz}^{1/2}$ (including the amplifier noise) and temperature response 0.5 mV/K we can get the rough estimation $\text{NEP}_{\text{bias}} = 5 \cdot 10^{-16} \text{ W/Hz}^{1/2}$.

For reduced volume of absorber and in the voltage bias mode with SQUID readout the dark NEP of CEB can achieve rather promising level. For most of practical cases the NEP will be determined by a background power load that is about $P_{bg} = 5 \text{ pW}$ and for our signal frequency 100 GHz it corresponds to

$$\text{NEP}_{\text{phot}} = \sqrt{2P_{bg} E_{\text{quant}}} = \sqrt{2P_{bg} hf} = 2.4 \cdot 10^{-17} \text{ W/Hz}^{1/2}.$$

We expect improvements in the fabrication and design of this device and its bias circuit to yield improved responsivity [9, 10]. Fig. 12 shows the calculated NEP and current responsivity anticipated for a device with a responsivity a few times better than our estimated value for the measured device. These results are obtained by simulation using advanced CEB models and assuming a SQUID readout.

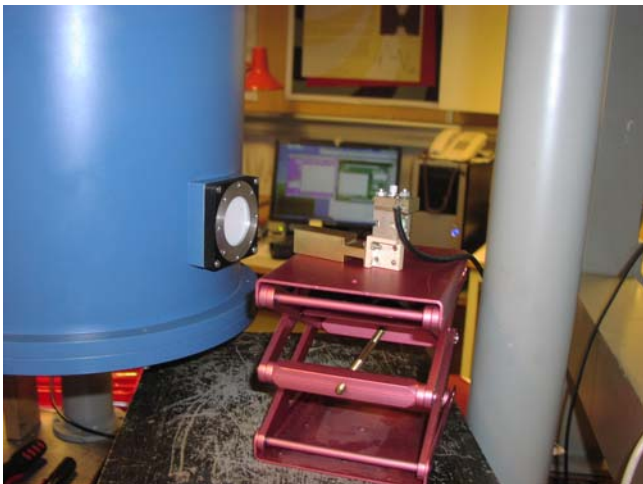


Fig. 10. IMPATT diode source irradiating sample at 110 GHz through optical window

We have also measured the detector's optical response to CW signals at 110 GHz, directly coupled to the finline chip.

ACKNOWLEDGMENT

This work was supported by Swedish agencies: VR, Rymdstyrelsen, STINT, Swedish Institute.

REFERENCES

- [1] L. Kuzmin, G. Yassin, S. Withington, and P. Grimes "An Antenna Coupled Cold-Electron Bolometer for High Performance Cosmology Instruments" Proc. of the 18th ISSTT, pp 93-99, Pasadena, March 2007
- [2] D. Golubev and L. Kuzmin, "Nonequilibrium theory of a hot-electron bolometer with normal metal-insulator-superconductor tunnel junction," *J. Applied Physics*, vol. 89, pp. 6464-6472, June 2001.
- [3] L. Kuzmin, P. Mauskopf, and D. Golubev, "Superconducting cold - electron bolometer with JFET readout for OLIMPO balloon telescope", *Journal of Physics*, vol. 43, pp. 1298-1302, 2006.
- [4] L. Kuzmin, I. Agulo, M. Fominsky, A. Savin, and M. Tarasov, "Optimisation of electron cooling by SIN tunnel junctions", *Superconductor Science and Technology*, vol. 17, pp. 400-405, 2004.
- [5] L. Kuzmin "Ultimate Cold-Electron Bolometer with Strong Electrothermal Feedback", *Proc. of SPIE conference "Millimeters and Submillimeter Detectors"*, **5498**, p 349, Glasgow, June 2004.
- [6] E. Otto, M. Tarasov, and L. Kuzmin, "Direct-write trilayer technology for Al-Al₂O₃-Cu superconductor-insulator-normal metal tunnel junction fabrication" *J. Vac. Sci. Technol. B* 25 (4), Jul/Aug 2007 p. 1156-1160
- [7] E. Otto, M. Tarasov, et al "An array of 100 Al-Al₂O₃-Cu SIN tunnel junctions in Direct-write trilayer technology" *Supercond. Sci. Technol.* **20** (2007) 1155-1158
- [8] L. Kuzmin, "An Array of Cold-Electron Bolometers with SIN Tunnel Junctions and JFET readout for Cosmology Instruments" *Journal of Physics: Conference Series (JPCS) EUCAS-2007, Brussels*;
- [9] C. E. North, G. Yassin and P. K. Grimes "Rigorous Analysis and Design of Finline Tapers for High Performance Millimetre and Submillimetre Detectors", 17th Int. Symp. on Space THz Tech., 284, (2006)
- [10] L. Kuzmin. "Self-Aligned Shadow-Evaporation Technology for Large Area Tunnel Junctions and Nanoabsorbers". PCT Patent, to be filed (2010).

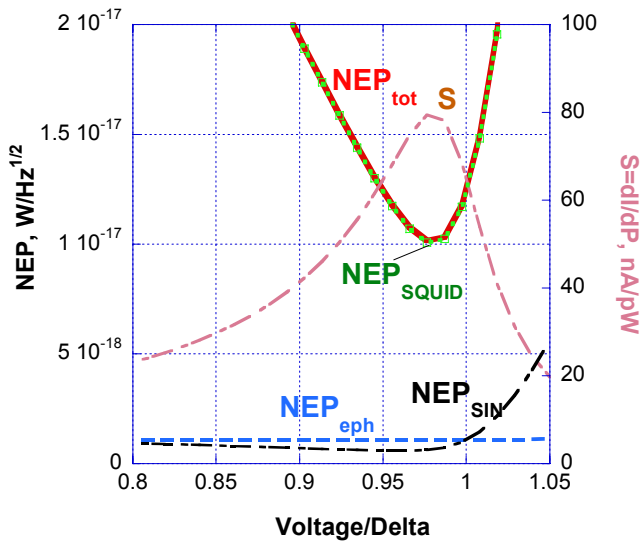


Fig. 12. Simulated NEP components and responsivity S for improved parameters of the CEB, power load of 20 fW, and SQUID noise current of 0.8 pA/Hz^{1/2}.

VII. CONCLUSIONS

The analysis of a Cold-Electron Bolometer deposited across a unilateral finline on a planar substrate has been presented. The detector can be a potential candidate for the next space cosmology missions and can also be of interest to ground-based experiments as a result of the simplicity of its integration to planar circuit technology, high saturation power and fast response.

We have fabricated finline coupled CEBs using direct-writing of the detector structures. We have estimated the dark noise equivalent power for devices in the current biased mode operating at 300mK and read by room temperature op-amp electronics as NEP=5·10⁻¹⁶ W/Hz^{1/2}.

Ultra-sensitive Transition-edge Sensors for Far-Infrared Spectroscopy on SPICA

A. D. Beyer^{1,2}, M. Kenyon^{1,2}, J. Bueno^{1,2,3}, P. M. Echternach^{1,2}, J.J. Bock^{1,2}, C.M. Bradford^{1,2}

¹California Institute of Technology, Pasadena, CA 91125, USA

²Jet Propulsion Laboratory Pasadena, CA 91109, USA

³Currently at Centro de Astrobiología (CSIC-INTA) Madrid, Spain

*Contact: beyer@caltech.edu, phone 1-626-434-6868

Abstract—We report progress in the fabrication of low-thermal conductance (G) transition-edge sensors (TESs) for SPICA. The TESs are silicon-nitride (Si-N) micro-mesh bolometers patterned into grid absorbers suspended by thin support beams. We are prototyping TESs for the Background Limited Far-Infrared Sub-millimeter Spectrograph (BLISS) far-infrared (IR) grating spectrometer, for which the photon-noise-limited noise-equivalent power (NEP) goal is $3 \times 10^{-20} \text{ W/Hz}^{1/2}$ and the NEP requirement is $10^{-19} \text{ W/Hz}^{1/2}$. The NEP sets the thermal conductivity (G) for a 65 mK operating temperature to be $G=4 \text{ fW/K}$ for the NEP goal and $G=45 \text{ fW/K}$ for the NEP requirement. We report measurements of our progress toward meeting the requirement and goal G values. Additionally, BLISS requires the TESs to be sufficiently fast with an effective response time of $\tau_{\text{eff}} \leq 100 \text{ ms}$. For the NEP requirement and $G=45 \text{ fW/K}$, the heat capacity (C) of the TES absorbers should be on the order of 10 fJ/K , which we demonstrate here. In addition to building TESs and TES absorbers and support beams for BLISS, we can also manufacture TES absorbers and support beams suitable for the Spica FAR-infrared Instrument (SAFARI). We investigate the effect of a dry XeF_2 etch versus a wet KOH etch on the C and G properties of BLISS-like and SAFARI-like absorbers and support beams.

I. INTRODUCTION

Instrumentation and technology for infrared (IR) and sub-millimeter (mm) observations are enabling the next generation of investigations into the origins of galaxies, stars, planets, and life. In order to push forward the capabilities of far-IR/sub-mm spectroscopic instrumentation, we are building ultra-sensitive transition-edge sensors (TESs). Additionally, we are evaluating fabrication techniques for producing the absorbers, support beams, and bilayer thermistors, which are the building blocks of TESs. Our goal is to produce TESs suited to meet the requirements of the Background Limited far-Infrared/Sub-mm Spectrograph (BLISS). The fabrication techniques used to build the BLISS TESs could also be adapted to suit the Spica FAR-infrared Instrument (SAFARI). Therefore, our TES detector technology is broadly designed for use with far-IR spectroscopy on the SPace Infrared telescope for Cosmology and Astrophysics (SPICA), a Japan Aerospace eXploration Agency (JAXA) led mission with ESA participation proposed for a 2018 launch.

II. BLISS DESIGN

BLISS is a space-borne, broadband grating spectrometer used for far-IR/sub-mm spectroscopy. It is divided into five bands spanning $38 \mu\text{m}$ - $433 \mu\text{m}$. BLISS uses ultra-sensitive TESs as detectors. The detectors are required to exhibit a noise equivalent power $\text{NEP} = 10^{-19} \text{ W/Hz}^{1/2}$, to have a fast effective response time $\tau_{\text{eff}} \leq 100 \text{ ms}$, and to be scalable to more than 10^3 pixels. To be truly background limited, the NEP goal of BLISS is $3 \times 10^{-20} \text{ W/Hz}^{1/2}$. The read out of the TES arrays is accomplished using a time-domain multiplexer scheme [1]. With $>10^3$ pixels in the current design, BLISS will have a resolving power of $R \equiv \lambda/\Delta\lambda \sim 700$ in each of the five bands. The combination of the goal NEP and resolving power $R \sim 700$ will allow observations that are background limited by the zodiacal and galactic cirrus diffuse astrophysical backgrounds in the far-IR/sub-mm spectrum.

The TESs use a membrane-isolated architecture consisting of a bilayer superconducting thermistor as the TES film, a mesh Si_xN_y (Si-N) absorber, and Si-N isolation legs suspending the bilayer and absorber from a Si-N on Si substrate. The architecture is shown in Fig. 1A. The bilayer thermistor is either a Mo/Au or Ti/Au bilayer, with the superconducting transition temperature T_C tuned by the proximity effect. We choose a value of $T_C = 65 \text{ mK}$ because BLISS will utilize a space-qualified cryocooler capable of achieving a base temperature of 50 mK .

The five bands of BLISS are designed to accommodate 1D or quasi-1D arrays of TESs to detect the output of the gratings in each band. The five bands and their span are listed in Table 1. A 1D array of TESs for the longest wavelength band fabricated at the Microdevices Laboratory (MDL) at the Jet Propulsion Laboratory (JPL) is shown in Fig. 1B. Fig. 1B illustrates the pixel dimensions Δx and Δy listed in Table 1 for the longest wavelength band of BLISS. The TESs are arranged in a 1D array to detect the outputs of machined gratings for the three longest wavelength bands of BLISS. This geometry is known as the WaFIRS geometry and has been utilized in Z-spec at the Caltech Submillimeter Observatory. The other two bands use quasi-1D arrays of TESs and cross-dispersed echelle grating modules to spread the incoming radiation out for detection. More details on the grating spectrometer design and echelle module design may be found in [2]. Ultimately, each TES in a given array will be read out by a time-domain Superconducting Quantum

Interference Device (SQUID) multiplexer (MUX). In this architecture, the wiring layer of the TESs runs from the TES films to the first-stage SQUID input coils in the MUX design [1].

The mesh absorbers on the TESs are designed to maximize the absorption of far-IR/sub-mm radiation. A schematic cross-section of the absorber architecture is shown in Fig. 1C. Each beam of the mesh absorber is suspended a distance x above the underlying substrate, and the substrate has a thickness denoted as y . The beams of the mesh absorber are a distance d apart, and a bilayer of Ti/Au with

width w is deposited on top of the beams. The effective impedance of the absorber is given by $R_{\text{eff}} = d/w R_F$, where R_F is the sheet resistance of the Ti/Au bilayer on top of the rungs. The Ti/Au thickness is tuned so that R_{eff} matches the impedance of the incoming radiation for maximal optical efficiency. A metal backshort at a distance of $\lambda/4$ is deposited on the backside of the Si underneath the absorber to increase optical coupling. The incoming radiation will be polarized parallel to the absorber beams to further enhance optical efficiency.

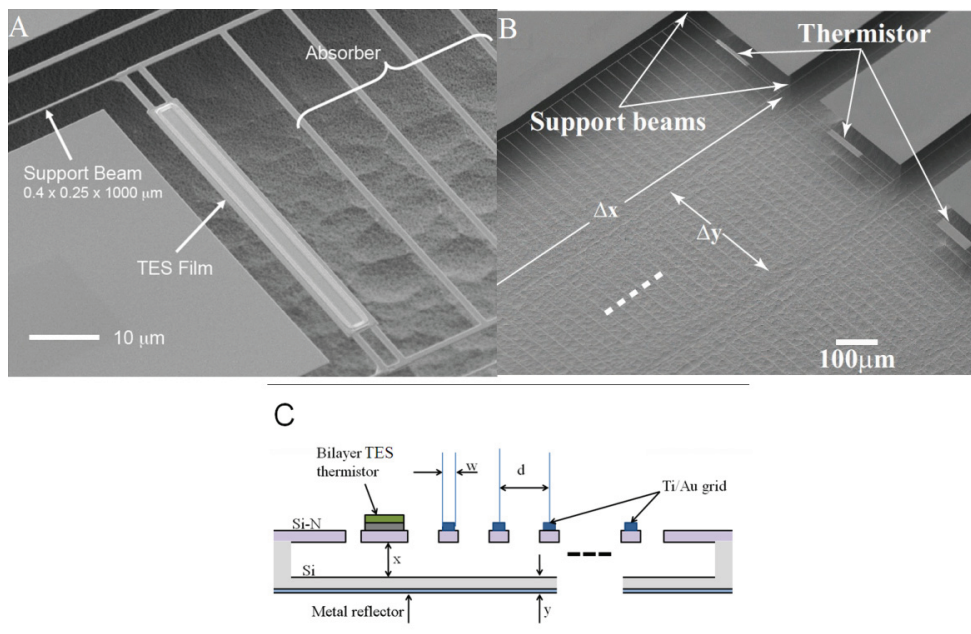


Fig. 1: BLISS TES and TES array: (A) Scanning electron microscope (SEM) image of a single BLISS TES in the longest wavelength band. The support beams, absorber, and TES film are shown. The TES is a bilayer thermistor of Mo/Au or Ti/Au for BLISS. (B) An SEM image of a 1D array of BLISS TESs in the longest wavelength band. The pixel dimensions Δx and Δy of Table 1 are illustrated here. (Figure reproduced from [5].) (C) Side-view schematic of a BLISS TES illustrating dimensions and components of the mesh absorbers. The height x and thickness y are controlled using double silicon-on-oxide (SOI) wafers.

TABLE 1: DIMENSIONS OF BLISS DETECTION BANDS

Band	λ_{\min} (μm)	λ_{\max} (μm)	Pixel Δx (μm)	Pixel Δy (μm)
1	38	67	306	193
2	67	116	535	337
3	116	180	873	140
4	180	280	1353	216
5	280	433	2097	336

The expected NEP due to the thermal impedance of the Si-N support beams is given by $NEP = \sqrt{4k_B T_C^2 G}$ [3]. Here k_B is Boltzmann's constant and G is the thermal conductance of the support beams. To meet the NEP requirement of BLISS, G should equal 45fW/K at the target $T_C=65\text{mK}$. To meet the NEP goal, G should equal 4fW/K at 65mK. The longest wavelength band shown in Fig. 1A has straight support beams 1mm long by $0.4\mu\text{m}$ wide by $0.25\mu\text{m}$ thick. The

support beams for the three longest wavelength bands are straight beams, whereas the two remaining bands use meander beams in order to meet the different packing requirements for the quasi-1D arrays in the echelle modules.

The effective response time τ_{eff} goal of 100ms or less is dictated by the heat capacity C of the TES absorbers. The thermal time constant $\tau_0 = C/G$, and

$$\tau_{\text{eff}} = \tau_0 / (1 + P_J \alpha / G T_C) , \quad (1)$$

where P_J is the Joule power through the TES film and $\alpha = d \log R / d \log T$ is a measure of the sharpness of the superconducting transition. The value of τ_{eff} may be from 10-100 times smaller than τ_0 when the TES is voltage-biased in negative electrical thermal feedback (ETF) operation [4]. The time-domain MUX architecture will be voltage-biased to control the BLISS arrays; therefore, the BLISS goal for τ_{eff} will be met if C is between 45-450fJ/K for the NEP

requirement G of 45fW/K at 65mK . If $G=4\text{fW/K}$ at 65mK for the NEP goal, C should be between $4\text{-}40\text{fJ/K}$.

Modifications in the BLISS TES architecture can be made to produce TESs suitable for SAFARI, which is a Fourier transform spectrograph. The NEP and τ_{eff} requirements for the detectors on SAFARI are: $\text{NEP} \leq 10^{-19} \text{W/Hz}^{1/2}$ and $\tau_{\text{eff}} \leq 10\text{ms}$. Solid Si-N membrane absorbers are used instead of the mesh absorbers of BLISS, and the detectors are arranged in 2D arrays. The slightly higher NEP goal permits thicker support beams to be used in a membrane-isolation TES structure. Given the NEP goal, the value of G should be less than or equal to 45fW/K at 65mK . Assuming a 10-100 reduction in τ_{eff} compared to τ_0 , C will need to be on the order of 1fJ/K for SAFARI TESs.

III. FABRICATION

A. Composite BLISS TESs

Micromachining and lithographic patterning processes are used to produce TESs. Each TES consists of a bilayer thermistor, a Si-N absorber, Si-N support beams, a wiring layer, and a substrate supporting the membrane-isolated TES. The TESs are constructed at JPL using 100mm $\langle 100 \rangle$ Si wafers. In the future, the TESs will be fabricated using double silicon-on-oxide (SOI) wafers. Silicon-oxide (SiO_2) layers buried in the SOI wafers will be used to control the front and backside etch depths, shown as dimensions x and y in Fig. 1C.

A layer of low-stress Si-N with controllable thickness is first grown on top of a wafer using low pressure chemical vapor deposition. Low stress is important to prevent warping of the Si-N structures when the Si underneath them is released. The silicon underneath the Si-N structures is removed using a dry XeF_2 gas-etch or a wet KOH etch. A layer of photoresist (PR) is used to protect the top Si-N surfaces from the etchants. The PR is cleaned off after the devices are released from the silicon underneath the Si-N. Additionally, a layer of SiO_2 left behind from the growth of Si-N protects the underside of the Si-N for the devices prepared using a dry XeF_2 gas-etch.

The thermistor consists of a bilayer of Mo/Au or Ti/Au deposited onto the Si-N, and the wiring layer is deposited on top of the Mo/Au or Ti/Au thermistor and runs along the support beams to bond pads. Additionally, the size of the thermistor is patterned to produce a thermistor with the desired normal state resistance to match the designs of the time-domain multiplexer for controlling the TES arrays.

B. Si-N Test Structures for BLISS and SAFARI

The NEP and τ_{eff} for BLISS and SAFARI depend strongly on the values of G and C that can be obtained from the Si-N absorbers and support beams. Therefore, we have fabricated noise thermometry test devices that can be used to test the effect of different fabrication processes on the value of G and C for BLISS-like and SAFARI-like absorber and support beam architectures. Our BLISS-like noise thermometry device has support beams with a cross section that is typically $0.25\mu\text{m}$ thick by $0.4\mu\text{m}$ wide, and the absorber is a

micromesh grid absorber with fill factor of 10%, as shown in Fig. 2A. The rungs are $1\mu\text{m}$ wide and are spaced $10\mu\text{m}$ apart for this absorber. In contrast, our SAFARI-like noise thermometry device has larger cross section support beams that are typically $1\mu\text{m}$ thick and $5\mu\text{m}$ wide. The SAFARI-like absorber is a solid membrane absorber, as shown in Fig. 2B, and it is $1\mu\text{m}$ thick.

The SAFARI-like noise thermometry devices are released using either a dry XeF_2 etch or a wet KOH etch, whereas the narrow beams and spider-web like structure for the BLISS-like devices have been fabricated using the XeF_2 release process. In the mesh-absorber design for BLISS TESs, wet etching could result in the absorber and support beams becoming stuck together. Additionally, the absorbers and support beams could break from a wet etch process. Future designs to prevent the sticking and breaking of beams could incorporate additional Si-N separation beams. The separation beams would keep the support and absorber beams apart and prevent breakage. The separation beams could later be removed by cutting them with a laser.

The layer of PR that protects the top surfaces of the noise thermometry devices during etching is removed by either an O_2 deep reactive ion etch (DRIE) or by rinsing in warm isopropyl alcohol and acetone. The mesh absorber has SiO_2 underneath the Si-N, while the solid absorber does not.

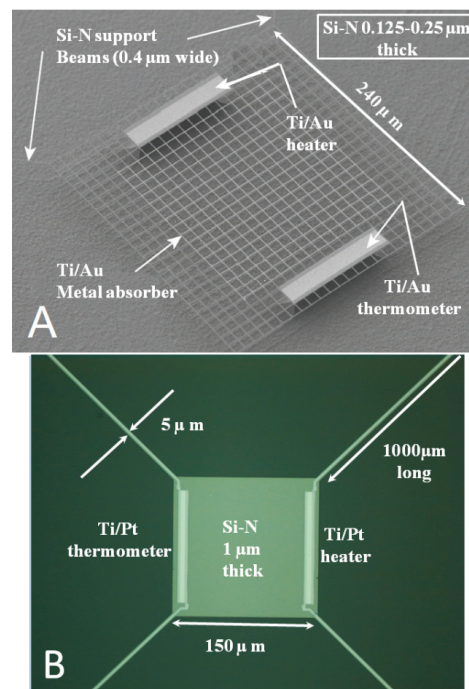


Fig. 2: SEM images of noise thermometry devices for determining thermal properties of Si-N: (A) The BLISS-like noise thermometry absorber device. The support beams are typically $0.4\mu\text{m}$ wide \times $0.25\mu\text{m}$ thick \times $1000\mu\text{m}$ long. The mesh has a 10% fill factor. (Image reproduced from [5].) (B) The solid membrane noise thermometry absorber device has support beams that are $5\mu\text{m}$ wide \times $1\mu\text{m}$ thick \times $1000\mu\text{m}$ long. The support beams and solid membrane absorber reproduce an architecture used in SAFARI TESs.

Two resistors composed of Ti/Pt or Ti/Au are lithographically defined on opposite sides of the noise thermometry devices to provide resistors. The resistors are used as a heater and a thermometer. The heater is hooked up to a current source, and the thermometer is wired up to a SQUID input coil to measure the current noise of the resistor. A wiring layer is deposited on top of the resistors to provide electrical links to the SQUID and bias line, with the wiring layer running along the support beams.

IV. EXPERIMENTAL PROCEDURE

We measured C and G values for the two noise thermometry devices in a ^3He - ^4He Janis dilution refrigerator with a base temperature of 15mK. The devices were mounted onto a gold-plated copper plate attached to the mixing chamber of the refrigerator and surrounded by an enclosed Nb shielding can. The thermometer was connected by wire bonds to NbTi superconducting wires. The NbTi wires passed through Nb capillaries to the input coil of a SQUID for readout of the thermometer current response and power spectral density. The heater resistor was connected via wire bonds to a lossy coaxial bias line connection.

The Nb can served to prevent optical dark power from reaching the test devices and to shield from magnetic pickup. To pump out any excess ^3He exchange gas or air inside the Nb can, we employed a meandered pump-out port filled with bronze mesh. The bronze mesh served to prevent optical dark power from leaking through the pump-out port to the devices, while still maintaining throughput for pump-out.

Attenuators, filters, and lossy coaxial cables helped to prevent electrical dark power from passing down the bias line to the device, as shown in Fig. 3A. Lossy coaxial cables were inserted between the room temperature bias input port and the device input port. We also inserted a 30dB or 30dB+10dB attenuator in series at the 1K pot stage between the coaxial cable from room temperature and the device. Two mini-circuits low-pass filters with roll-off at 300 MHz and 1.9 MHz were inserted into the lossy coaxial line prior to connection to the device. The mini-circuits were held at the mixing chamber temperature T_{mx} .

The thermometer resistance was calibrated by varying T_{mx} and observing the Johnson noise current detected by the SQUID. The electron temperature can be calculated from the Johnson noise current formula

$$S_I = 4k_B T_e / R_{\text{th}}, \quad (2)$$

where T_e is the electron temperature, R_{th} is the thermometer resistance, and S_I is the power spectral density of the Johnson noise current sensed by the SQUID.

Experimentally, the thermal conductance G is determined by applying a small change in bias power to the heater resistor and measuring the resulting ΔT on the thermometer for a fixed T_{mx} . Quantitatively, $G = \Delta P / \Delta T$. Here ΔP is the small change in bias power.

If no dark power P_D reaches the noise thermometry devices, a linear relationship between T_{mx} and T_e will be observed at all temperatures. Any dark power P_D impinging upon the device will cause a deviation in T_e from T_{mx} . The

expected deviation is

$$T_e - T_{\text{mx}} \approx P_D / G(T_{\text{mx}}). \quad (3)$$

Given the small G values of the noise thermometry devices and TESs, the dark power would ideally be below 1fW. Using all the measures described above, we found the dark power was around 0.22fW for a 30dB+10dB or 0.6fW for a 30dB attenuator in our experimental setup, as shown in Fig. 3B.

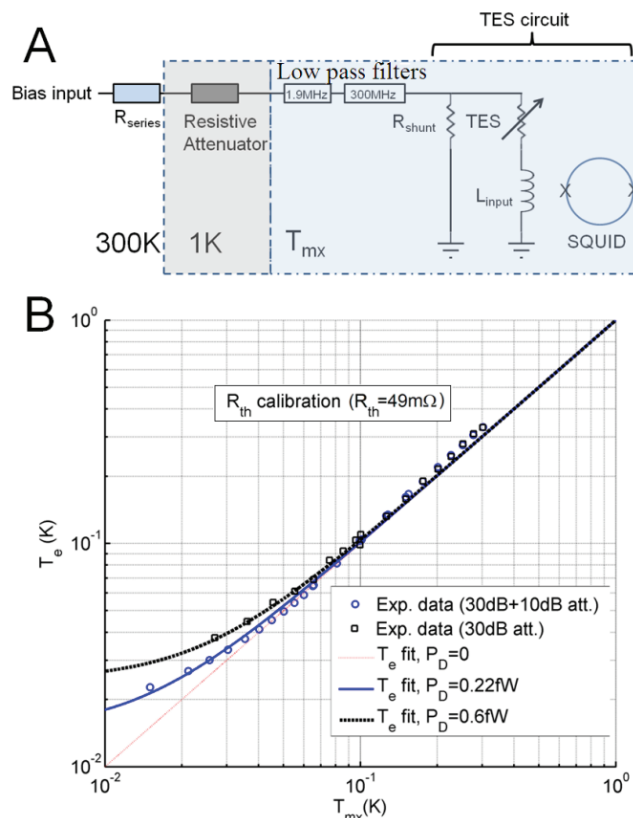


Fig. 3: (A) Experimental setup for noise thermometry measurements. (B) Measurement of electron temperature T_e vs. mixing chamber temperature T_{mx} . The dark power is below 1fW in our experimental setup.

Once the values of $G(T)$ are determined, $C(T)$ is measured by applying a small heat pulse to the heater resistor and observing the decay time τ_0 at different mixing chamber temperatures. The measurement is operated without ETF; therefore, $C(T) = \tau_0(T) \times G(T)$.

V. RESULTS AND DISCUSSION

Table 2 shows thermal and performance properties obtained from our measurements of the two Si-N absorber geometries prepared under different fabrication techniques at $T=100\text{mK}$.

In addition, we have included Si-N properties obtained from similar geometries for comparison in the literature [5]-[7]. The values shown for [5] are for $T=60\text{mK}$, and the values shown for [7] are for $T=113\text{mK}$. To obtain the NEP values at $T=65\text{mK}$, the values of G have been extrapolated to $T=65\text{mK}$ using $G \sim T^{1/2}$ for mesh absorbers [5] and $G \sim T^{3/2}$ for solid absorbers.

TABLE 2: THERMAL PROPERTIES OF Si-N AT 100MK

A comparison of the Si-N heat capacity (C), surface specific heat (c_s), thermal conductance (G), expected heat capacities for bands 3-5 of BLISS, and estimated thermal time constant τ_0 in band 4 (based on the assumption of $G=4fW/K$). We prepared mesh-absorber BLISS-like noise thermometry devices (Fig.2A) and solid-membrane-absorber SAFARI-like noise thermometry devices (Fig.2B) using different fabrication processes. Selected results from the literature are also included for comparison.

No.	Type	Process	Bilayer (nm/nm)	G (fW/K)	C_{Si-N} (fJ/K)	c_s (aJ/(K· μm^2))	$C_{Band 3}$ (fJ/K)	$C_{Band 4}$ (fJ/K)	$C_{Band 5}$ (fJ/K)	τ_0 (Band 4) (s)	NEP (W/Hz ^{1/2}) at 65mK
1	Solid	wet KOH etch; IPA/Acetone	Ti/Pt (2/50)	1500	3	0.04	1.0	1.5	2.4	0.39	4.3×10^{-19}
2	Solid	wet KOH etch; IPA/Acetone	Ti/Pt (2/50)	1000	6	0.08	2.0	3.1	4.8	0.77	3.5×10^{-19}
3	Solid	XeF ₂ dry etch; O ₂ DRIE	Ti/Pt (2/50)	450	146	1.98	50.0	76.5	119	19.12	2.3×10^{-19}
4	Solid	XeF ₂ dry etch; IPA/Acetone	Ti/Pt (2/50)	1000	171	2.32	58.5	89.6	139	22.40	3.5×10^{-19}
5	Mesh	XeF ₂ dry etch; IPA/Acetone +O ₂ DRIE	Ti/Au (2/50)	130	89	3.06	77.2	118.2	184	29.55	1.6×10^{-19}
[5]	Mesh	XeF ₂ dry etch; O ₂ DRIE	Ti/Au (2/50)	54	98	3.98	100.4	153.7	239	38.43	1.1×10^{-19}
[6]	Solid	DRIE	Mo/Au	5500	50	1.02	25.7	39.4	61.2	9.85	8.2×10^{-19}
[7]	Solid	wet KOH etch	Ti/Au	320	1.4	0.03	0.8	1.2	1.8	0.29	1.8×10^{-19}

Due to the fact that metals have a larger specific heat than Si-N, we have calculated the heat capacity contribution $C_{bilayer}$ of the different bilayers to the total heat capacity, C_{tot} . We obtained the heat capacity of the Si-N according to $C_{Si-N} = C_{tot} - C_{bilayer}$. To calculate $C_{bilayer}$, we used $\gamma_{Ti} = 3.35 \text{ mJ}/(\text{mol} \cdot \text{K}^2)$, $\gamma_{Au} = 0.729 \text{ mJ}/(\text{mol} \cdot \text{K}^2)$, and $\gamma_{Pt} = 6.8 \text{ mJ}/(\text{mol} \cdot \text{K}^2)$ [8].

The NEPs shown in Table II are expected to be on the order of $10^{-19} \text{ W/Hz}^{1/2}$ for $T_C = 65 \text{ mK}$ for both solid and mesh devices based on the values of G . Despite the scatter in G values for the solid devices, the values are consistently on the order of 10-100 fW/K—except for the solid device in [6]. This device is connected to the substrate bath via perforations in the Si-N, which explains the larger value of G , and is designed for soft X-ray spectroscopy instead of far-IR spectroscopy. The mesh devices have smaller G values than the solid devices because their support beams are thinner than those of the solid devices. Device 5 and the average result from mesh devices in [5] differ in G because the support beams were twice as long in [5] as in device 5. Taking all these factors into consideration, neither the etchant nor the PR removal steps affect G much. As can be seen, G is converging toward the BLISS/SAFARI requirements.

The strongest effects due to process can be seen in the values of C in Table 2. The values of C for the wet etch are on the order of 1 fW/K at 65 mK, whereas the C values for the XeF₂ etch are on the order of 10-100 fW/K for both solid and mesh absorbers. Table 2 indicates that the type of process for removing PR did not change the C values significantly for

either type of absorber; therefore, we conjecture that the differences are due to the type of etchant based on the solid membrane results. Wet KOH etching seems to produce solid membranes with lower C than XeF₂.

As described in the Section III, we have not produced mesh devices using the wet etch process. However, mesh devices prepared using XeF₂ showed similar values of C to solid absorber devices. This result is surprising because the surface area of solid absorbers is $45,600 \mu\text{m}^2$, whereas that of the mesh absorbers is $28,275 \mu\text{m}^2$. A simple scaling of surface area would predict a smaller value of C in mesh devices.

The values of C for the solid and mesh absorbers etched with XeF₂ could be similar if the edges and top/bottom surfaces of the devices have different specific heat values per surface area. (It has been shown that the Si-N thickness does not affect C for mesh devices [5].) This scenario could result because the top and bottom surfaces of the devices were protected during XeF₂ etching, whereas the edges were not. Using the values of C from devices 4 and 5 and the edge and top/bottom surface areas, we calculate the edge specific heat to be $6.5 \text{ aJ}/\mu\text{m}^2$ and the top/bottom surface specific heat to be $2 \text{ aJ}/\mu\text{m}^2$. Both results are on the order of $1 \text{ aJ}/\mu\text{m}^2$, similar to a value observed in [9]. The interaction of XeF₂ with the SiO₂ protecting the bottom surface of the mesh devices could also explain the discrepancy.

For the solid membrane devices, we estimate the specific heat to be $0.1 \text{ aJ}/\mu\text{m}^2$ by ignoring the edges. This value is the same order of magnitude of specific heat expected for

amorphous materials such as vitreous silica, which has a specific heat equal to $0.22\text{aJ}/\mu\text{m}^2$ [10].

We can then conjecture that the use of XeF_2 is correlated with added C in our investigation. Randomly distributed populations of two-level systems explain the specific heat values observed in amorphous materials, such as vitreous silica [11]. Therefore, it is possible that the XeF_2 is introducing additional TLS into our Si-N, possibly through diffusion of F_2 into the Si-N. Again, the XeF_2 interacting with SiO_2 could also be responsible for the excess specific heat. For $T > 1\text{K}$, the type of SiO_2 used as a substrate for growing Si-N does affect the specific heat of Si-N produced [12]. Different SiO_2 growth techniques and the interaction with XeF_2 could be investigated. However, our values of C differ by two orders of magnitude devices from Si-N grown in the same way. Therefore, the major difference appears to be due to the type of etch. We are continuing to investigate these issues, but we find that the C values measured are within the requirements for far-IR spectroscopy instruments on SPICA, such as BLISS or SAFARI.

VI. CONCLUSIONS

Meeting the demands of far-IR spectroscopy detectors for SPICA requires TES detectors with G and C values to meet the $\text{NEP} = 10^{-19}\text{W}/\text{Hz}^{1/2}$ requirement and $\tau_{\text{eff}} \leq 100\text{ms}$ requirements. Our values of G are approaching the $45\text{fW}/\text{K}$ needed to meet the requirement NEPs of BLISS and SAFARI at 65mK , and we are developing methods to reach the NEP goal of $3 \times 10^{-20}\text{W}/\text{Hz}^{1/2}$ for BLISS. Our demonstrated values of C for the mesh-absorber noise thermometry devices are on the order of $10\text{fJ}/\text{K}$, which is necessary to meet the τ_{eff} requirement for TESs on BLISS. Similarly, the demonstrated values of C for the solid-membrane-absorber noise thermometry devices are on the order of the $1\text{fJ}/\text{K}$, which is necessary to meet the τ_{eff} requirements for TESs on SAFARI. Finally, we may be able to reduce C further for BLISS TESs with different fabrication techniques.

ACKNOWLEDGMENT

A.D. Beyer thanks the Caltech Moore Foundation for financial support. This research was carried out at the Jet Propulsion Laboratory, California Institute of Technology, under a contract with the National Aeronautics and Space Administration.

© 2010 California Institute of Technology. Government sponsorship acknowledged.

REFERENCES

- [1] Piet. A.J. de Korte *et al.*, "Time-division superconducting quantum interference device multiplexer for transition-edge sensors," *Rev. Sci. Instr.*, Vol. 74, pp. 3807-3815. Aug. 2003.
- [2] C.M. Bradford *et al.*, "BLISS for SPICA: Far-IR at the background limit," in Vol. 375, *Proc. of From Z-Machines to ALMA: (Sub)Millimeter Spectroscopy of Galaxies Conference (SPIE)*, Charlottesville, Virginia, United States, 2006, pp. 199-210.
- [3] J. C. Mather, "Bolometer noise: nonequilibrium power" *Applied Optics*, Vol. 21, pp. 1125-1129. March 1982.
- [4] K.D. Irwin, "An application of electrothermal feedback for high resolution cryogenic particle detection," *App. Phys. Lett.*, Vol. 66, pp. 1998-2000. April 1995.
- [5] M. Kenyon, P.K. Day, C.M. Bradford, J.J. Bock, and H.G. Leduc, "Ultra-sensitive transition-edge sensors (TESs) for space-borne far-IR/submm spectroscopy," *Proc. of 13th International Workshop on Low-Temperature Detectors*, Stanford, California, United States, 2009, pp. 56-59.
- [6] Megan E. Eckart *et al.*, "Experimental results and modeling of low-heat-capacity TES Microcalorimeters for Soft-X-ray Spectroscopy," *Proc. of 13th International Workshop on Low-Temperature Detectors*, Stanford, California, United States, 2009, pp. 430-433.
- [7] P. Khosropanah *et al.*, "Low Thermal Conductance Transition Edge Sensor (TES) for SPICA," *Proc. of 13th International Workshop on Low-Temperature Detectors*, Stanford, California, United States, 2009, pp. 42-47.
- [8] Charles Kittel, *Introduction to Solid State Physics*, Sixth edition. New York: John Wiley & Sons, Inc. 1986, pg. 141.
- [9] Warren A. Holmes *et al.*, "Initial test results on bolometers for the Planck high frequency instrument," *Applied Optics*, Vol. 47, pp. 5996-6008. Nov. 2008.
- [10] R. C. Zeller, R.O. Pohl, "Thermal conductivity and specific heat of noncrystalline solids," *Phys. Rev. B.*, Vol. 4, pp. 2029-2041. May 1971.
- [11] W.A. Phillips, "Two-level states in glasses," *Rep. Prog. Phys.* Vol. 50, pp. 1657-1708. Feb. 1987.
- [12] B.L. Zink, F. Hellman, "Specific heat and thermal conductivity of low-stress amorphous Si-N membranes," *Solid State Comm.* Vol. 129, pp. 199-204. Jan. 2004.

Optical NEP in Hot-Electron Nanobolometers

Boris S. Karasik^{1*} and Robin Cantor²

¹*Jet Propulsion Laboratory, California Institute of Technology, Pasadena, California, CA 91109, USA*

²*STAR Cryoelectronics, 25-A Bisbee Court, Santa Fe, NM 87508, USA*

*Contact: boris.s.karasik@jpl.nasa.gov, phone +1-818-393 4438

Abstract—For the first time, we have measured the optical noise equivalent power (NEP) in titanium (Ti) superconducting hot-electron nanobolometers (nano-HEBs). The bolometers were $2\mu\text{m}\times 1\mu\text{m}\times 20\text{nm}$ and $1\mu\text{m}\times 1\mu\text{m}\times 20\text{nm}$ planar antenna-coupled devices. The measurements were done at $\lambda = 460\ \mu\text{m}$ using a cryogenic black body radiation source delivering optical power from a fraction of a femtowatt to a few 100s of femtowatts. A record low NEP = $3\times 10^{-19}\ \text{W/Hz}^{1/2}$ at 50 mK has been achieved. This sensitivity meets the requirements for SAFARI instrument on the SPICA telescope. The ways for further improvement of the nano-HEB detector sensitivity are discussed.

I. INTRODUCTION

Recently, an interest to ultrasensitive submillimeter/FIR detectors has been driven due to the astrophysics community and space agencies' plans to launch telescopes with cryogenically cooled primary mirrors where the thermal emission from the telescope would be largely eliminated. Several concepts of such telescopes (SAFIR [1-2], SPECS [2], CALISTO [3], FIRI [4], SPICA [5]) have been proposed and studied. Moderate resolution spectroscopy ($\nu/\delta\nu \sim 1000$) would be the most demanding application requiring the detector NEP to be less than $10^{-19}\ \text{W/Hz}^{1/2}$ in the most of the submillimeter/FIR spectral range in order for the photon shot noise to dominate the detector noise. The SPICA mission led by the Japanese space agency [6] is currently seen as the most feasible opportunity to realize such a sensitive astronomical platform. There are two instruments considered for far-IR spectroscopy on SPICA. An ESA led SAFARI instrument would use a Fourier Transform Spectrometer in the 30-210 μm wavelength range [7]. The detectors for SAFARI should have an NEP = $3\times 10^{-19}\ \text{W/Hz}^{1/2}$. Another instrument (BLISS) [8], which is under study in the US, is a grating spectrometer operating in the 35-433 μm range. The detector sensitivity goal here (NEP = $3\times 10^{-20}\ \text{W/Hz}^{1/2}$) is non-precedent and requires an improvement of the state-of-the-art by 2-3 orders of magnitude.

II. ULTRASENSITIVE FIR BOLOMETERS

Several approaches have been pursued in order to demonstrate an NEP $\sim 10^{-19}$ - $10^{-20}\ \text{W/Hz}^{1/2}$ in the FIR. They include kinetic inductance detectors [9-10], quantum dot detector [11] and bolometers with a superconducting transition-edge sensor (TES) thermometer. Because of the relatively simple underlying physics and long application heritage, the latter look more promising at the moment for meeting new sensitivity challenges.

Thermal energy fluctuation (TEF) (aka phonon) noise is dominating in a well-optimized bolometer and the corresponding NEP contribution is:

$$\text{NEP}_{\text{TEF}} = (4k_{\text{B}}T^2G)^{1/2}, \quad (1)$$

where G is the effective thermal conductance. G is commonly used as a benchmark when different bolometric devices are compared. A more traditional version of the TES bolometer uses a suspension made from thin and narrow Si_3N_4 to thermally isolate the radiation absorber and the TES thermometer from the heat sink. Here an impressively low thermal conductance has been achieved in geometrically isolated structures in [12]. At 65 mK (probably the lowest critical temperature one may expect for a practical space TES detector), $G \approx 30\ \text{fW/K}$ was measured that corresponds to $\text{NEP}_{\text{TEF}} = 8\times 10^{-20}\ \text{W/Hz}^{1/2}$. Similarly low NEP_{TEF} were obtained in the following works from the same group [13-14] where SiN mesh structures optimized for better radiation absorption and smaller time constant were used.

Another group [15] has achieved a fully functioning bolometer using a MoAu TES and a Ta radiation absorber suspended with long and narrow SiN beams. The TEF noise NEP has been reported to be $1.3\times 10^{-18}\ \text{W/Hz}^{1/2}$ at $\approx 100\ \text{mK}$. Similar detectors have been tested optically yielding the total NEP = $2\times 10^{-18}\ \text{W/Hz}^{1/2}$ at $\lambda \approx 30$ - $60\ \mu\text{m}$ [15-16].

Our approach is to use the electron-phonon decoupling mechanism in a small TES in order to achieve an ultralow NEP [17]. In this case, a SiN membrane is not needed and the TES is fabricated directly on Si or sapphire substrate. When a TES is made from a thin ($<100\ \text{nm}$) superconducting film, the temperature of electrons becomes greater than the phonon temperature when the radiation or current heating is applied. The phonon temperature remains close to that of the substrate since non-equilibrium thermal phonons escape from the film very fast. The characteristic time in this case is the electron-phonon energy relaxation time $\tau_{\text{e-ph}}$, which depends on the temperature but does not depend on the device volume. In turn, the effective thermal conductance $G_{\text{e-ph}} = C_{\text{e}}/\tau_{\text{e-ph}}$ (C_{e} is the electron heat capacity) is proportional to the volume, so NEP_{TEF} decreases in smaller devices. The practically useful device size is $\sim \mu\text{m}$ or less so the device contacts should be made from a superconducting material with large T_{C} in order to employ the Andreev reflection mechanism confining the electron thermal energy inside the device volume.

We have been using Ti hot-electron TES's in our work though some other materials (e.g., Hf, Ir, W) might be suitable too. Although the electron-phonon interaction

strength varies to some degree between these materials the most important consideration is the availability of the fabrication technique leading to small devices with low T_C and large enough sheet resistance $R_s = 20\text{-}50\ \Omega$. The latter is important for a good rf impedance match between the device and a microantenna or a waveguide which are the only ways to couple a subwavelength-size nano-HEB device to FIR radiation.

In our recent work [18], we pushed the device size to submicron (device volume of about $10^{-21}\text{-}10^{-20}\ \text{m}^3$) and measured an extremely low thermal conductance $G_{e\text{-ph}}$. In comparison to the phonon conductance in SiN, the electron-phonon conductance in a metal has stronger temperature dependence. In fact, we achieve $G_{e\text{-ph}} = 0.3\ \text{fW/K}$ at 65 mK that corresponds to $\text{NEP}_{\text{TEF}} = 9 \times 10^{-21}\ \text{W/Hz}^{1/2}$. However, the very small TES devices studied in [18] did not have large enough critical current so they were not very useful for the noise studies or optical measurements. In the following works [19-20] somewhat larger size devices ($6\ \mu\text{m} \times 0.4\ \mu\text{m} \times 56\ \text{nm}$ and $2\ \mu\text{m} \times 0.15\ \mu\text{m} \times 60\ \text{nm}$) were used where a sufficiently large critical current along with $T_C = 330\text{-}350\ \text{mK}$ was achieved due to an increased film thickness. Electrical noise and $G_{e\text{-ph}}$ have been studied as functions of temperature yielding an electrical $\text{NEP} \approx 2 \times 10^{-20}\ \text{W/Hz}^{1/2}$ at 60 mK along with $\tau_{e\text{-ph}} \approx 0.5\ \text{ms}$.

Although investigation of the electrical and thermal characteristics of bolometers is an important development step, the ultimate goal is optical demonstration of the detector sensitivity. In this work, we present the first results on the optical NEP measurements in Ti nano-HEBs coupled to planar antennas using an adequately low-power (femtowatt) radiation source. Besides the absolute NEP figures, an interesting feature in the detector response manifesting the presence of the photon shot noise was observed. The ability of the bolometer to detect photon noise is an independent confirmation of the validity of the optical power calibration scale in our setup.

III. DEVICES AND EXPERIMENTAL SETUP

A. Devices

Our current device fabrication process is different from what was used in [18]. For this work, the nano-HEB devices were fabricated on c-axis sapphire using magnetron sputtering of Ti target and were patterned using optical lithography and ion beam milling. A 650 GHz twin-slot planar antenna structure was formed afterwards by means of the lift-off process using an NbTiN/Au bi-layer. This type of antenna with coplanar waveguide (CPW) impedance tuning sections has been well characterized and used by many groups since our original work [19]. NbN HEB mixers on the Herschel's HIFI use similar antennas but at THz frequencies. The critical temperature in NbTiN was greater than 10 K even in the presence of Au so it served as the Andreev reflection contact material as well. The device parameters are listed in Table I. R_N in the Table is the device normal resistance.

Figure 1 shows a close-up of Ti device #1 in the center of the CPW structure. The real part of the antenna impedance

derived from the HFSS modelling was $\sim 30\text{-}40\ \Omega$ at the resonance frequency of 650-670 GHz depending on the gap size between the CPW lines in the middle of the structure. Therefore, the impedance match should be very good for the device normal resistance values in Table I. The choice of the central frequency was driven by the trade-off between the intention to use the highest possible frequency and the size of the gaps between the central line in the CPW and the ground plane achievable using available optical lithographic equipment. The use of high frequency was important in order to achieve a better control over the radiation power emitted by a cryogenic black body calibration source (see next subsection). Beside the devices with twin-slot antennas many spiral antenna-coupled devices were fabricated on the same wafer, which have not yet been tested.

TABLE I
PARAMETERS OF TI NANO-HEBS

Device	Substrate	Length \times Width ($\mu\text{m} \times \mu\text{m}$)	Thickness (nm)	T_C (mK)	R_N (Ω)
1	sapphire	2.0×1.0	20	357	45
2	sapphire	1.0×1.0	20	360	28

That the normal metal resistivity $\rho = 45\text{-}55\ \mu\Omega\ \text{cm}$ of our films was similar to that of [20] for same film thickness. The T_C in found in [20] was, however, much smaller ($\sim 100\ \text{mK}$). Transport and superconducting properties of our large area films and small devices will be addressed in a separate work in the future.

B. The Setup

All the measurements were performed in a dilution refrigerator. A dc SQUID was used as the readout. The devices were biased via a $1\text{-}\Omega$ resistor connected in series with the device and with the SQUID input coil. The resistor was situated in the vicinity of the device on the mixing chamber. The SQUID amplifier was placed at the 1-K pot of the dilution refrigerator and was connected to the device circuit via a magnetically shielded superconducting twisted pair. The device assembly was in an rf tight superconducting shield in order to avoid overheating of the device by uncontrolled rf interferences and noise. The bias lines and the

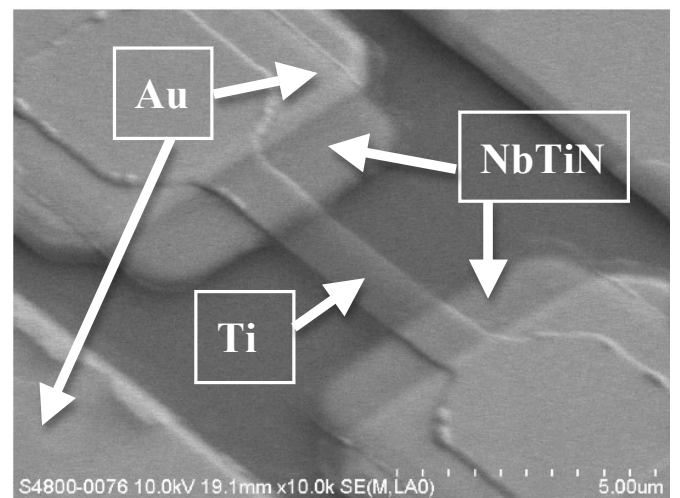


Fig.1. SEM image of a $2\ \mu\text{m} \times 1\ \mu\text{m}$ Ti nano-HEB device (device #1 from Table I) in the center of the CPW structure of the planar antenna.

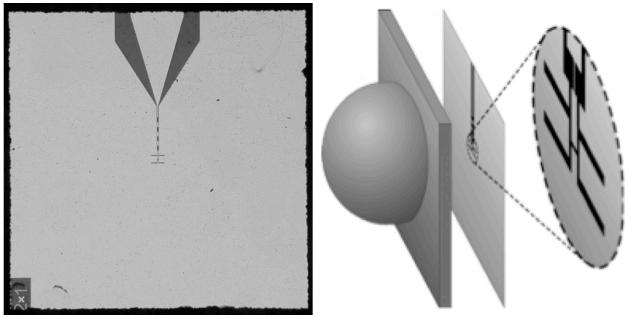


Fig.2. Detector chip layout and its attachment to the lens. The chip size is 5 mm × 5 mm. The lens diameter is 12 mm and is out of scale on this figure.

SQUID wires were fed through custom low-pass filters (LPF), which were built from discrete element LPFs placed inside metal tubes filled with lossy microwave absorbing compound. The SQUID noise ($\sim 2 \text{ pA/Hz}^{1/2}$) and bandwidth ($\sim 70 \text{ kHz}$) were calibrated in a separate experiment using the Johnson noise of a 1- Ω resistor at different temperatures.

In order to perform measurements at different temperatures below T_C a small superconducting solenoid with an iron core was mounted near the bolometer. The perpendicular field created by the solenoid was enough to suppress T_C down to 50 mK with the solenoid current not exceeding 100 mA. The entire experimental volume was surrounded by a Cryoperm-10[®] magnetic shield immersed in liquid He4.

Optical NEP was measured using a black body source made from a metal disc in which a thermometer and a small heater were embedded. The emitting surface was machined into an array of small pyramids and was painted with an FIR absorbing paint whose high (97%) absorptivity was validated by both direct measurements of the reflection at around 600 GHz and comparison with the emissivity of foamed Eccosorb used as the standard calibration target for a heterodyne receiver. This black body assembly was weakly coupled to the 1K pot of the dilution refrigerator so its temperature T_{BB} could be controlled with a better than 0.1 K precision from 1.5 K to 10 K.

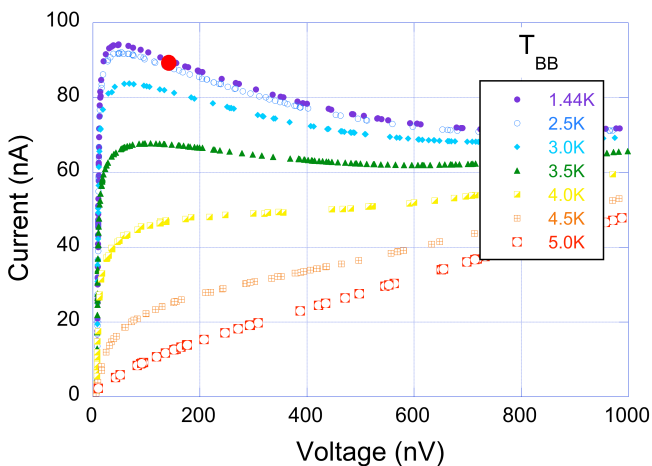


Fig. 3. IV characteristics at 355 mK (no magnetic field) under optical loading from the blackbody. $T_{BB} = 5 \text{ K}$ corresponded to $\approx 160 \text{ fW}$ of the radiation power emitted into a single mode through the filter bandwidth. The red circle denotes the operational point where the device was biased in the absence of radiation power.

The detector chip was glued to the backside of a 12-mm diameter lens made from the high-purity high-resistivity Si ($\rho > 10 \text{ k}\Omega \text{ cm}$) thus forming a hybrid antenna (Fig. 2) with a well-defined and narrow diffraction limited beam. In order to define the optical bandwidth a bandpass (10% fractional bandwidth) mesh filter centred at 650 GHz was used [21]. The filter transmission spectrum $\text{Tr}(\nu)$ was characterized prior to the experiment using an FTS. We assumed that our hybrid antenna couples only into a single radiation mode and therefore the amount of radiation power P_{rad} incident on the detector can be calculated as follows:

$$P_{\text{rad}} = \int_0^\infty \frac{\text{Tr}(\nu) h\nu d\nu}{0 \exp(h\nu/k_B T_{\text{BB}}) - 1} \quad (2)$$

In practice, a black body temperature range $T_{\text{BB}} = 1.5\text{-}5 \text{ K}$ was sufficient to observe the entire evolution of the detector output signal and of the noise up to the full saturation of the output ($R \approx R_N$).

IV. EXPERIMENTAL RESULTS

A. Procedures

The experimental procedure for determination of NEP consisted of the measurements of bias current I as function of T_{BB} varied in small 0.25 K steps and of the output system noise i_n . The corresponding optical power was calculated using Eq. 2. From the initial part of the $I(P_{\text{rad}})$ dependence, detector responsivity $S_I = \Delta I/P_{\text{rad}}$ was calculated. Then the small signal optical NEP was found as $i_n(P_{\text{rad}}=0)/S_I$.

We also measured IV characteristics of the devices as function of temperature and radiation power. From the IVs taken and different temperatures, the effective thermal conductance corresponding to the device electron temperature T_e can be extracted. This procedure is based on the assumption that the device resistance is a single-valued function of the electron temperature $R(T_e)$. Then from the

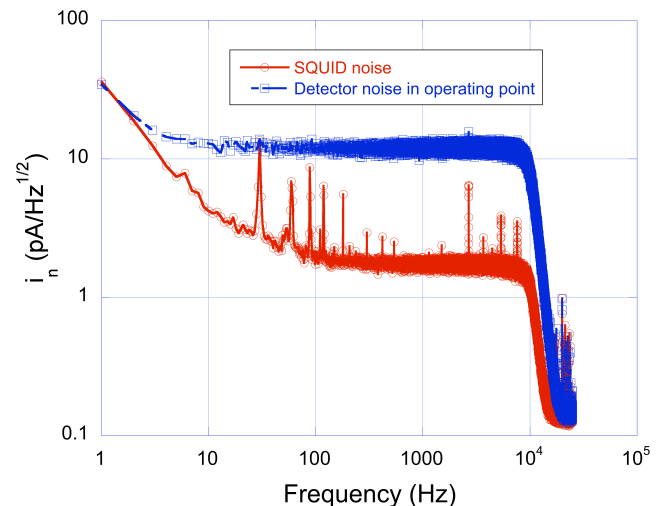


Fig. 4. Output noise at the bias point of Fig. 3 at 355 mK and SQUID noise. The latter was measured when the device was in the normal state (large resistance, small Johnson noise). A sharp cut-off at 10 kHz is due to the external bandwidth limiting filter.

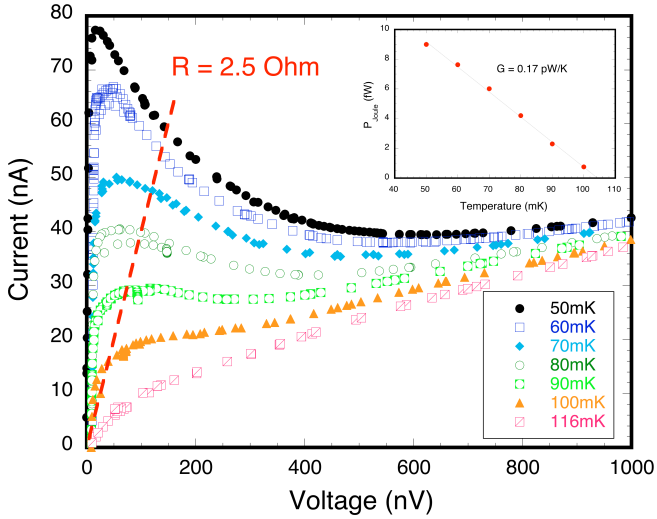


Fig. 5. IV characteristics in the 50-116 mK temperature range used for determination of the thermal conductance (see inset). The bias point was at the crossing of the 50-mK IV curve at the 2.5-Ohm resistance line.

heat balance equation one can obtain:

$$(P_{\text{Joule}1} - P_{\text{Joule}2}) = G(T_2 - T_1), \quad (3)$$

where P_{Joule} is the Joule power dissipated in a given bias point. Thermal conductance G derived in this way was used to calculate NEP_{TEF} . Equation 3 assumes that $T_2 - T_1 \ll T_1$, T_2 but can be easily generalized for a non-linear case.

In a similar fashion, the optical coupling efficiency η can be derived from the IVs taken at a fixed bath temperature but when P_{rad} is varied. In this case, the following equation holds:

$$P_{\text{Joule}1} - P_{\text{Joule}2} = \eta(P_{\text{rad}2} - P_{\text{rad}1}). \quad (4)$$

The coupling efficiency derived from Eq. 4 was crosschecked with the ratio $\text{NEP}_{\text{TEF}}/\text{NEP}$, which should yield the same η value.

B. The Data

Here we present the detailed data only for device #2. More details for device # 1 can be found in [23]. Figure 3 demonstrates optical loading of the device by the 650 GHz

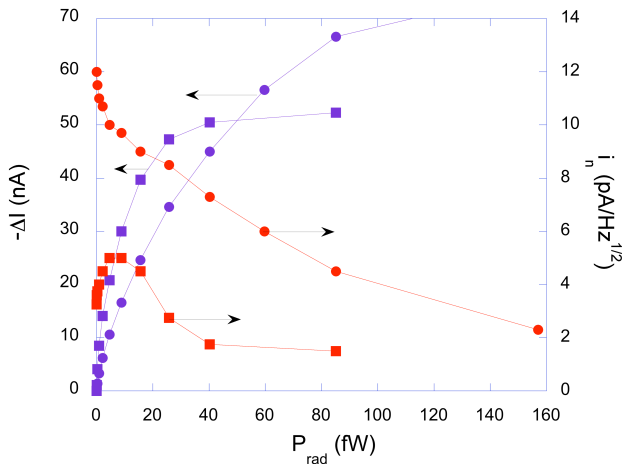


Fig. 6. Experimental data used for determination of optical NEP. Round symbols: $T = 355$ mK; square symbols: $T = 50$ mK.

radiation. From these IVs, an optical coupling efficiency $\eta = 40-80\%$ was estimated. The large error margin is due to the fact that η happened to depend on the particular $R = \text{constant}$ line along which the data were taken (see Eq. 4).

Figure 4 demonstrates the detector output noise at the operating point of Fig. 3. The noise spectrum is very flat in this 10-kHz bandwidth. A $1/f$ -noise below a few Hz originates in the SQUID. Its origin is still unknown.

Figure 5 shows IV characteristics when a certain magnetic field was applied. From these data, the thermal conductance was obtained. P_{Joule} vs T dependence in the inset in Fig. 5 shows that the electron temperature for this resistance was $T_e = 105$ mK. The broad transition in magnetic field was likely the reason for the output noise at 50 mK to be much smaller than that at 355 mK (see Fig. 6). Since T_e is substantially greater than $T = 50$ mK a slightly different expression from Eq. 1 should be used for determination of NEP_{TEF} :

$$\text{NEP}_{\text{TEF}} \approx (2k_B T_e^2 G)^{1/2}. \quad (5)$$

Equation 5 is valid in a strong non-equilibrium case reflecting the fact that the contribution of the fluctuation of energy at the bath temperature is negligible compared to the fluctuation of energy at the electron temperature.

For $T = 355$ mK, NEP_{TEF} was determined in similar fashion, i.e., using IVs at different temperatures. However, the temperature range where IVs differ from each other was much more narrow ($T_e = 367$ mK). This is because the natural superconducting transition in the absence of the magnetic field is relatively narrow (within 10 mK). In this case the difference between T and T_e is not so significant so the fluctuations at both temperatures contribute to NEP_{TEF} .

Finally, optical NEP was determined at both 50 mK and 355 mK by measuring the change of current vs radiation power and the output noise at the same time (see Fig. 6). We found an order of magnitude difference in the NEP at these two temperatures (see Table II). Saturation of ΔI vs P_{rad} naturally occurs much sooner at 50 mK than at 355 mK. The output noise also behaves differently. Whereas the noise at 355 mK monotonically decreases with P_{rad} , the noise at 50 mK exhibits a peak at some power range below 20 fW. We speculate that the origin of this peak may be in the detection of fluctuation of power in the impinging radiation. This photon shot noise is characterized by

$$\text{NEP}_{\text{phot}} = (2P_{\text{rad}} h\nu)^{1/2}. \quad (6)$$

When the detector becomes sensitive enough to detect this fluctuation ($\text{NEP} \sim \text{NEP}_{\text{phot}}$) the output noise-like signal increases as square root of P_{rad} . Eventually, S_1 drops and the output noise decreases. This effect could not be seen at 355 mK since a much greater $P_{\text{rad}} \sim 100$ fW is needed to make NEP_{phot} large enough to be detected. But at such high power the detector is already saturated.

Another argument in favor of this explanation is the comparison between the P_{rad} scales for the devices with different sensitivity. Figure 7 shows the output noise vs P_{rad} for both devices. Device #1 was operated at 100 mK but the electron temperature was about 150 mK [23]. Also device #1

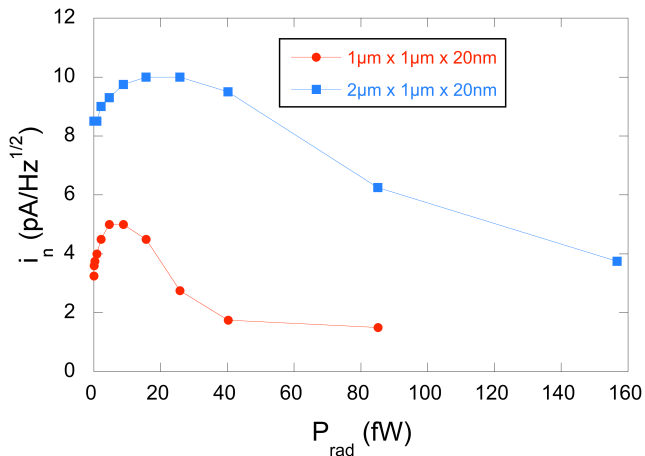


Fig. 7. Output noise for both devices #1 and #2 in magnetic field at temperatures well below T_c .

is at least 2 times larger in volume than device #2. As a result, it had optical NEP = 1.4×10^{-18} W/Hz^{1/2}, that is, a factor of 4-5 greater than the NEP in device #2. One can see from Fig. 7 that the position of the noise peak and the radiation power required to saturate the detector was correspondingly greater for device #1

V. DISCUSSION

Table II summarizes the main results of this study. The NEP data look very encouraging especially for device #2, which is already meeting the sensitivity requirements for SAFARI on SPICA. This NEP is an order of magnitude smaller than the closest competing TES approach using SiN membranes [15-16] has demonstrated. The optical coupling efficiency found from the ratio of NEP_{TEF} and NEP correlates with η derived from the shift of IV curves under optical loading. To be fair, the η value may be slightly overestimated given the fact that the Si lens did not have any AR coating. This is, however, quite understandable: these are very first measurements and more work is needed to tweak the measurement procedures. We are planning on using an additional high-pass 600 GHz filter with a sharp cut-off in order to eliminate any possible leak of the out-of-band radiation power at the long-wavelength wing of the mesh filter. Also, devices with spiral antennas will be tested to study the effect of different antenna types. Such devices will be eventually needed for FIR applications of this detector ($\lambda < 100 \mu\text{m}$) where slot antennas can be difficult to fabricate.

TABLE II
NEP DATA

Device	T_c (mK)	NEP (aW/Hz ^{1/2})	NEP _{TEF} (aW/Hz ^{1/2})	NEP _{TEF} /NEP
1	150	1.4	1.0	0.71
	357	8.6	6.3	0.73
2	105	0.30	0.23	0.77
	367	3.0	2.5	0.83

Another important issue is a comparison of the achieved NEP with the expectations for this type of detectors. Since the optical NEP came close to NEP_{TEF}, the latter can be used

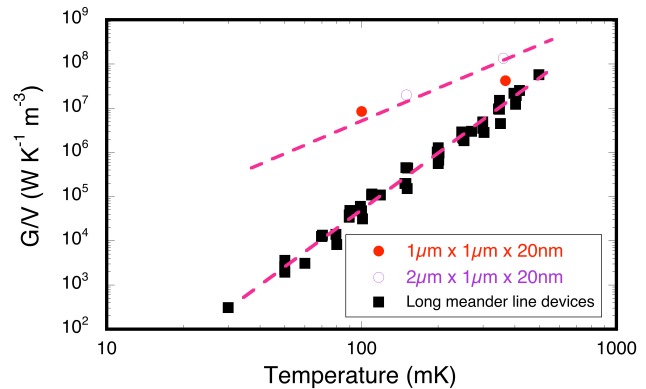


Fig. 8. Thermal conductance in large and small hot-electron bolometers normalized to the device volume. Round symbols are the data for the devices of Table I. Long meander data are from [-].

for comparison since it is easy to estimate from the material parameters. In our original paper [17] we predicted that NEP in $1 \mu\text{m} \times 1 \mu\text{m}$ size nanobolometers at 100 mK should be at least $\sim 10^{-20}$ W/Hz^{1/2}. The best current NEP_{TEF} is an order of magnitude worse. Comparison with the large area devices gives some clue on what might be wrong with the small devices. Figure 8 shows a normalized by volume electron-phonon thermal conductance measured in 4 long-meander-line devices (some up to 10 cm long) over the years [24-25]. They were all fabricated on sapphire using either e-beam evaporation or magnetron sputtering. Amazingly, all the data points closely follow one universal line that is a strong indication of the electron-phonon nature of G in these devices, which should be proportional to the volume. When the G-data for devices #1 and #2 are plotted on the same graph it becomes apparent that there is an excessive thermal conductance in these device especially at low temperature where magnetic field was used. The excessive thermal conductance is 100-time greater than should be due to the electron-phonon interaction alone. We suspect that the reason for that might be in the unfavorable configuration of metal layers in the device contact areas. As seen in Fig. 1, the projection of top Au layer overlaps with Ti being separated by NbTiN. When a perpendicular magnetic field is applied it suppresses T_c in Ti. The field is not sufficient to destroy superconductivity in NbTiN which has $T_c > 10$ K. However, the field may create a lot of magnetic vortices in the NbTiN layer. These vortices have normal metal core, which would connect the Ti layer with the Au layer thus creating a channel for cooling of hot electrons via electron diffusion.

The next iteration of the devices will not have the Au layer which is redundant for the purpose of low electromagnetic loss. NbTiN by itself should be a good enough rf conductor at 650 GHz.

This quick fix may help to get even better NEP data relatively soon. However, in a long run, one need to get rid of the magnetic field which is unacceptable for the detectors operating in large (1000s pixels) arrays. We see several options for reducing T_c to about 100 mK. The simplest approach is to keep reducing the films thickness. However the transition region between “high” (~ 300 mK) and “low” (~ 100 mK) T_c may be narrow so a large scattering of device-to-device parameters can happen. Another approach is implantation of ⁵⁵Mn⁺ ions into ready devices or into bare Ti

films. This has been demonstrated to be a reasonably well controlled process [26] and we plan to try it within next few months with devices similar to those of Table I. A similar technique has been also used successfully for tuning TC in W using $^{56}\text{Fe}^+$ ions [27]. One more option is to synthesize some binary alloys (like, e.g. AlMn [28]), which will require a significant material development effort. We should mention that bi-layer materials commonly used for membrane supported TES will not work here because of their low resistivity making it impossible to match the device R_N to the antenna impedance.

Finally, some SQUID based multiplexing technique should be made compatible with the hot-electron nano-HEBs. There may be multiple solutions here depending on what sensitivity and, correspondingly, what operating temperature is targeted. For the most sensitive applications when $T = 50\text{--}100\text{ mK}$, the time constant in nano-HEB devices would be $\sim 0.5\text{--}1\text{ ms}$ [23]. If it turns out that the thermal conductance in these devices will be eventually reduced to the value of large area Ti films then $\tau_{e\text{-ph}} = 0.6\text{ ms}$ at 100 mK and $\tau_{e\text{-ph}} = 2.5\text{ ms}$ at 65 mK . This is derived using the Sommerfeld constant value $\gamma = 315\text{ J m}^{-3}\text{ K}^{-2}$ and the data of Fig. 8. There needs to be some design study in order to understand if the well-established time-domain multiplexing (TDM) technique can be used. However, the recently demonstrated GHz frequency domain multiplexing (FDM) using microwave SQUIDS [29-30] should work well not only at 100 mK but also at $300\text{--}400\text{ mK}$ where $\tau_{e\text{-ph}}$ is in the μs range. This technique is still emerging but should soon become suitable for reading large arrays.

VI. CONCLUSIONS

In conclusion, a significant progress has been made in the development of the nano-HEBs based detector technology resulting in the first optical demonstration of the state-of-the-art detector sensitivity in FIR. The current generation of the detectors together with the microwave SQUID readout is suitable for building a detector array with $NEP \sim 10^{-17}\text{ W/Hz}^{1/2}$ operating in a He3 dewar. Such systems can be used for photometry, polarimetry, or CMB studies from balloons or SOFIA airplanes.

The obtained record low $NEP = 3 \times 10^{-19}\text{ W/Hz}^{1/2}$ is a good news for the low-background spectroscopy in space where no adequate detectors have existed so far. This already meets the sensitivity goals for the SPICA/SAFARI instrument. The future R&D work will address the ways of getting optical NEP down to $10^{-20}\text{ W/Hz}^{1/2}$ by means of controllable T_C reduction in Ti nano-HEB devices and also by making the devices smaller (submicron). A significant improvement of the existing optical setup will be required in order to control the fW level optical power with sufficient precision.

ACKNOWLEDGMENT

This research was carried out at the Jet Propulsion Laboratory, California Institute of Technology, under a contract with the National Aeronautics and Space Administration. The authors are grateful to D. Harding and S. Pereverzev for the help with optical NEP setup and cryogenic filters, to N. Llombart for the help with HFSS modelling, and

to J. Kawamura for many fruitful discussions and for providing a superconducting solenoid.

REFERENCES

- [1] <http://safir.jpl.nasa.gov>
- [2] D. Leisawitz, "NASA's far-IR/submillimeter roadmap missions: SAFIR and SPECS," *Adv. Space Res.*, vol. 34, 631-636, 2004.
- [3] P. F. Goldsmith, M. Bradford, M. Dragovan, C. Paine, C. Sattera, W. Langer, H. Yorke, D. Benford, and D. Lester, "CALISTO: The cryogenic aperture large infrared space telescope observatory," *Proc. SPIE*, 2008, vol. 7010, paper 701020.
- [4] F. P. Helmich and R. J. Ivison, "FIRI—A far-infrared interferometer," *Exp. Astron.*, vol. 23, 245-276, 2009.
- [5] T. Nakagawa, "SPICA: space infrared telescope for cosmology and astrophysics," *Adv. Space Res.*, vol. 34, 645-650, 2004.
- [6] T. Nakagawa, "The next-generation infrared space mission: SPICA," *Proc. SPIE*, 2010, vol. 7731, paper 773100.
- [7] B. Swinyard, T. Nakagawa, H. Matsuhara, D. Griffin, M. Ferlet, P. Eccleston, A. di Giorgio, J. Baselmans, J. Goicoechea, K. Isaak, P. Maukopf, L. Rodriguez, F. Pinsard, W. Raab, L. Duband, N. Luchier, N. Rando, A. Heras, T. Jagemann, N. Geis, S. Vives, "The European Contribution to the SPICA Mission," *Proc. SPIE*, 2008, vol. 7010, paper 701001.
- [8] C.M. Bradford, M. Kenyon, W. Holmes, J. Bock, T. Koch, "Sensitive far-IR survey spectroscopy: BLISS for SPICA," *Proc. SPIE*, 2008, vol. 7020, paper 702010.
- [9] A.V. Sergeev, V. V. Mitin, and B. S. Karasik, "Ultrasensitive hot-electron kinetic-inductance detectors operating well below the superconducting transition," *Appl. Phys. Lett.*, vol. 80, 817-819, Feb. 2002.
- [10] P. K. Day, H. G. LeDuc, B. A. Mazin, A. Vayonakis, and J. Zmuidzinas, "A broadband superconducting detector suitable for use in large arrays," *Nature*, vol. 425, 817-821, Oct. 2003.
- [11] S. Komiyama, O. Astafiev, V. Antonov, T. Kutsuwa, and H. Hirai, "A single-photon detector in the far-infrared range," *Nature*, vol. 403, 405-407, Jan. 2000.
- [12] M. Kenyon, P. K. Day, C. M. Bradford, J. J. Bock, and H. G. LeDuc, "Progress on background-limited membrane-isolated TES bolometers for far-IR/submillimeter spectroscopy," *Proc. SPIE*, 2006, vol. 6275, paper 627508.
- [13] M. Kenyon, P. K. Day, C. M. Bradford, J. J. Bock, and H. G. LeDuc, "Ultra-sensitive transition-edge sensors (TESs) for far-IR/submm space-borne spectroscopy," *AIP Conf. Proc.*, 2009, vol. 1185, p.56-59.
- [14] A. D. Beyer, M. E. Kenyon, P. M. Echternach, B.-H. Eom, J. Bueno, P. K. Day, J. J. Bock, and C. M. Bradford, "Characterizing SixNy absorbers and support beams for far infrared/submillimeter transition-edge sensors," *Proc. SPIE*, 2010, vol. 7741, paper 774121.
- [15] D. Morozov, P. D. Maukopf, P. Ade, M. Bruijn, P. A. J. de Korte, H. Hoevers, M. Ridder, P. Khosropanah, B. Dirks and J.-R. Gao, "Ultrasensitive TES bolometers for space based FIR Astronomy," *AIP Conf. Proc.* 2009, vol. 1185, p. 48-51.
- [16] D. Morozov, private communication.
- [17] B. S. Karasik, W. R. McGrath, M. E. Gershenson, and A.V. Sergeev, "Photon-noise-limited direct detector based on disorder-controlled electron heating," *J. Appl. Phys.*, vol. 87, 7586-7588, 2000.
- [18] Wei, J., Olaya, D., Karasik, B.S., Pereverzev, S.V., Sergeev, A.V. and Gershenson, M.E., "Ultra-sensitive hot-electron nanobolometers for terahertz astrophysics," *Nature Nanotechnol.*, vol. 3, 496-500, 2008.
- [19] B. S. Karasik, M. C. Gaidis, W. R. McGrath, B. Bumble, and H. G. LeDuc, "Low Noise in a Diffusion-Cooled Hot-Electron Mixer at 2.5 THz," *Appl. Phys. Lett.*, vol. 71, 1567-1569, 1997.
- [20] J. Vangrunderbeek, C. Van Haesendonck, and Y. Bruynseraede, "Electron localization and superconducting fluctuations in quasi-two-dimensional Ti films," *Phys. Rev. B*, vol. 40, 7594-7601, Oct. 1989.
- [21] <http://www.virginidiodes.com/>
- [22] B. S. Karasik, S. V. Pereverzev, D. Olaya, J. Wei, M. E. Gershenson, and A. V. Sergeev, "Noise Measurements in Hot-Electron Titanium Nanobolometers," *IEEE Trans. Appl. Supercond.*, vol. 19, 532-535, 2009.
- [23] B. S. Karasik, S. V. Pereverzev, D. Olaya, M. E. Gershenson, R. Cantor, J. H. Kawamura, P. K. Day, B. Bumble, H. G. LeDuc, S. P. Monacos, D. G. Harding, D. Santavica, F. Carter, and D. E. Prober.

- “Development of the nano-HEB array for low-background far-IR applications,” *Proc. SPIE*, 2010, vol. 7741, paper 774119.
- [24] M. E. Gershenson, D. Gong, T. Sato, B. S. Karasik, and A. V. Sergeev, “Millisecond Electron-Phonon Relaxation in Ultrathin Disordered Metal Films at Millikelvin Temperatures”, *Appl. Phys. Lett.*, vol. 79, 2049-2051, 2001.
- [25] J. Wei, “Hot-electron effects, energy transport and decoherence in nano-systems at low temperatures”, *Ph. D. thesis*, New Brunswick, New Jersey, Jan. 2007
- [26] B. A. Young, J. R. Williams, S. W. Deiker, S. T. Ruggiero, B. Cabrera, “Using ion implantation to adjust the transition temperature of superconducting films,” *Nucl. Instr. Meth. Phys. Res. A*, vol. 520, 307–310, 2004.
- [27] B. A. Young, T. Saab, B. Cabrera, J. J. Cross, R. M. Clarke, and R. A. Abusaidi, “Measurement of T_c suppression in tungsten using magnetic impurities,” *J. Appl. Phys.*, vol. 86, 6975-6978, Dec. 1999.
- [28] S. W. Deiker, W. Doriese, G. C. Hilton, K. D. Irwin, W. H. Rippard, J. N. Ullom, L. R. Vale, S. T. Ruggiero A. Williams, and B. A. Young, “Superconducting transition edge sensor using dilute AlMn,” *Appl. Phys. Lett.*, vol. 85, 2137-2139, Sep. 2004.
- [29] B. S. Karasik, P. K. Day, J. H. Kawamura, B. Bumble, and H. G. LeDuc, “Multiplexing of Hot-Electron Nanobolometers Using Microwave SQUIDs,” *AIP Conf. Proc.*, 2009, vol. 1185, p. 257-260.
- [30] B. S. Karasik, P. K. Day, J. H. Kawamura, S. P. Monacos, B. Bumble, H. G. LeDuc, and R. Cantor, “Demonstration of Multiplexed Operation of Hot-Electron Detectors Using MSQUIDs,” this *Symp. Proc.*

Focal Plane Array of Thermo-Electric Bolometers

Sumedh Mahashabde¹, Leonid Kuzmin¹, Mikhail Tarasov¹, Peter Day², and Jonas Zmuidzinas³

¹Chalmers University of Technology, S-41296 Gothenburg, Sweden,

²Jet Propulsion Laboratory, Pasadena, California 91107, USA

³California Institute of Technology, 320-47, Pasadena, CA 91125, USA

e-mail: leonid.kuzmin@chalmers.se

Abstract— Novel concepts of the parallel and series array of Thermo-Electric Bolometers (TEB) with Superconductor-Insulator-Normal (SIN) Tunnel Junctions [1] have been proposed and realized for a distributed focal plane antenna. The arrays are developed for a pixel design based on arrays of TEBs coupled to a distributed slot antenna or dipole antenna [2] similar to array of Cold-Electron Bolometers (CEB) [3,4].

Two variants of the CEB arrays have been considered for both types of antenna on bulk substrate.

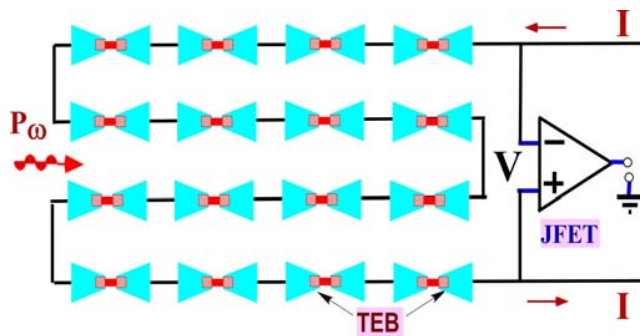


Fig 1. A distributed single polarization dipole antenna with a series array of TEBs and a JFET readout. This dipole antenna will be sensitive only to horizontal component of RF signal.

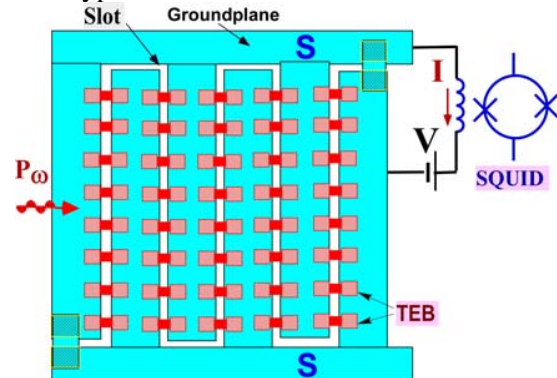


Fig 2. A distributed single polarization slot antenna with a parallel array of TEBs and a SQUID readout.

The series connection of TEBs with SIN tunnel junctions in current-biased mode [2] is optimal for dipole antennas. Estimations of the TEB noise with JFET readout have shown an opportunity to realize NEP less than photon noise for typical power load.

The parallel connection of CEBs with SIN tunnel junctions in voltage-biased mode [3] is optimal for a slot antenna. Remarkable progress in performance is expected from implementation of a new technology for fabrication of the CEB and SQUID on the same chip in one vacuum circle.

The design of 2x2 pixels for dipole and slot antennae has been realized for 350 GHz. The samples were fabricated using shadow evaporation technique on Si substrate. Results of DC and RF measurements will be reported at the conference.

1. Leonid Kuzmin, "Thermo-Electric Charge-to-Voltage Converter based on SIN Tunnel Junction", submitted to Applied Physics Letters (December 2009)
2. Peter K. Day et al., "Far-infrared imager-polarimeter using distributed antenna-coupled transition-edge sensors, 5498, pp 856-875, SPIE, 2004.
3. Leonid Kuzmin, "Array of Cold-Electron Bolometers with SIN Tunnel Junctions for Cosmology Experiments", Journal of Physics: Conference Series (JPCS), 97, 012310 (2008).
4. Leonid Kuzmin, "Distributed Antenna-Coupled Cold-Electron Bolometers for Focal Plane Antenna", Proc. of the 19th ISSTT, pp 154-158, Groningen, April 2008.

Poster Session P3: Earth Observation

TELIS SIR channel performance analysis

Gert de Lange^{1*}, Oleg Kiselev³, Pavel Yagoubov², Hans Golstein¹, Arno de Lange¹, Bart van Kuik¹, Joris van Rantwijk¹, Ed de Vries¹, Johannes Dercksen¹, Ruud Hoogeveen¹, Manfred Birk⁴, Georg Wagner⁴, Andrey Ermakov³, Valery Koshelets³

1 SRON Netherlands Institute for Space Research, the Netherlands

2 ESO, Garching, Germany

3 Institute of Radio Engineering and Electronics (IREE), Moscow, Russia

4 DLR Oberpfaffenhofen, Germany

* Contact: gert@sron.nl, phone +31-50-363 4074

Abstract

The TELIS (Terahertz and sub-millimeter limb sounder) instrument is a three-channel heterodyne receiver developed for atmospheric research. TELIS is mounted together with the MIPAS-B2 instrument on a balloon platform of the Institute for Meteorology and Climate Research of the Karlsruhe Institute of Technology. TELIS can observe both in the sub-millimeter range (480-650 GHz) and at 1.8 THz, while MIPAS-B2 observes trace-gases in the thermal infrared window. Results are used to refine and constrain numerical chemical transport models.

The SRON contribution to TELIS is the 480-650 GHz Superconducting Integrated Receiver (SIR) channel. This is a unique superconducting on-chip heterodyne receiver, consisting of a double dipole antenna, a SIS mixer, a flux-flow Local Oscillator, and a superconducting harmonic mixer used for phase locking of the LO-signal. The lowest noise temperature of the receiver is 120 K DSB, measured over the full IF bandwidth (2 GHz).

The first successful flight campaign with TELIS/MIPAS was in March 2009 from Kiruna (Sweden). The SIR channel was operating well during the 11 hour flight. Many hundreds of limb scan data have been taken at different frequency settings. This has shown the stable remote operation of the SIR receiver in harsh environmental conditions. The data is currently further analyzed and in order to get reliable level 2 data processing we have further characterized the channel properties after return of the instrument to the laboratory. Especially the Side Band Ratio of the channel is of importance and we have performed detailed analysis of this with a high resolution Bruker Fourier Transform Spectrometer. A new flight with TELIS is scheduled for winter 2010, again from Kiruna.

We will present data of the first flight, details of the channel characterization and possibly new results on the second flight of the instrument.

High Performance component development at RAL for the ISMAR instrument

Manju Henry, Byron Alderman, Brian Moyna, Simon Rea, Hosh Sanghera, Dave Matheson

Space Science and Technology Department
 Rutherford Appleton Laboratory, Chilton, Oxfordshire OX11 7RQ
 Email: manju.henry@stfc.ac.uk

Abstract

The source/mixer components required for the 325 GHz receiver channel has been developed at RAL for the International Sub-millimetre Air-Borne radiometer (ISMAR), new instrument for FAAM aircraft. We report here the design and development of the high performance components required for this receiver channel. The source operating at 162.5 GHz is based on RAL GaAs schottky varactor diodes in anti-series configuration mounted inside the waveguide as shown in the photograph Fig. 1a. The doubler gives a conversion efficiency ~30% and 3dB BW >15% (Fig. 1b).

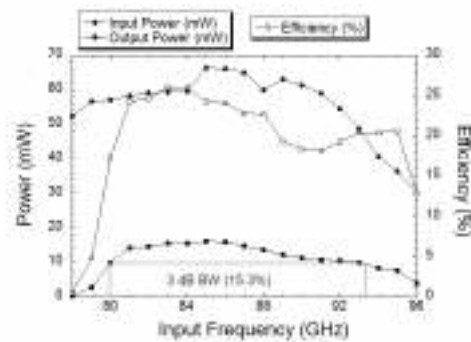


Figure 1 (a) Photograph of the 162 GHz doubler inside the split block waveguide (b) doubler efficiency plot

The double side band sub-harmonic mixer at 325 GHz is designed using RAL anti-parallel GaAs schottky mixer diodes. The mixer shows an excellent conversion loss ≤ 6.5 dB over a wider IF band (0.7 GHz to 11 GHz) for an optimum pump power of 3 mW. The performance is achieved using suspended substrate technology for the diode/matching circuits in order to reduce high frequency losses.

IF Band (GHz)	Tm (K)	L (dB)	Optimum LO power (mW)
0.7-2.3	1181	5.9	3.0
2.3-4.7	1142	6.1	3.0
8-11	1254	6.5	3.0

Figure 2 Mixer performance for the 325 GHz ISMAR receiver channel over the required IF band (0.5-11 GHz).

Characterisation of the TELIS autocorrelator spectrometer

P. Vogt^{*}, M. Birk^{*}, G. Wagner^{*}, F. Geiger^{*}, G. de Lange[†], H. Golstein[†], O. Kiselev[†], A. Emrich[‡].

^{*}Remote Sensing Technology Institute
DLR
Email: Peter.Vogt@dlr.de

[†]SRON
Email: G.de.Lange@sron.nl

[‡] Omnisys Instruments AB
Email: ae@omnisys.se

Abstract

The balloon borne cryogenic heterodyne spectrometer TELIS allows limb sounding of the Earth's atmosphere within the submillimeter and far-infrared spectral range. The instrument was developed by a consortium of major European institutes that includes the Space Research Organisation of the Netherlands (SRON), the Rutherford Appleton Laboratory (RAL) in the United Kingdom and the Deutsche Zentrum für Luft- und Raumfahrt (DLR) in Germany (lead institute). TELIS offers three channels (450-650 GHz, 499-503 GHz, 1.79 – 1.870 THz) and utilises state-of-the-art superconducting heterodyne technology [1].

As a spectrometer a 3-level autocorrelator with complex I-Q-sampling technique is used. It offers the advantage of low energy consumption, being light weight and has a resolution better than 2.5 MHz. A similar spectrometer without I-Q-technique has been successfully used on the ODIN satellite [2].

During gas cell characterization measurements of the TELIS autocorrelator spectrometer however, discrepancies occurred between measured and expected spectra. To investigate and quantify the observed errors, the TELIS autocorrelator spectrometer was referenced against a well known FFT spectrometer [3] in simultaneous measurements. In order to generate well controlled input signals, a 50 Ohm load plunged into temperature stable slush-baths ranging from 77 K to 273 K has been used. The obtained input signal was split, processed and simultaneously fed into both spectrometer inputs for spectral intercomparison. We will show and discuss the obtained experimental results for radiometric characterisation of the TELIS autocorrelator spectrometer.

REFERENCES

- [1] DEVELOPMENT AND CHARACTERIZATION OF THE BALLOON BORNE INSTRUMENT TELIS (TErahertz and Submm Limb Sounder): 1.8 THz RECEIVER, N. Suttiwong, M. Birk, G. Wagner, M. Krocka, M. Wittkamp, P. Haschberger, P. Vogt, F. Geiger, in Proceedings in press, 19th ESA Symposium on European Rocket and Balloon Programmes and Related Research, 07. - 11. Juni 2009, Bad Reichenhall, Germany.
- [2] H. L. Nordh, F. von Schéele, U. Frisk, K. Ahola, R. S. Booth, P. J. Encrenaz, Å. Hjalmarson, D. Kendall, E. Kyrölä, S. Kwok, A. Lecacheux, G. Leppelmeier, E. J. Llewellyn, K. Mattila, G. Mégie, D. Murtagh, M. Rougeron, and G. Witt, "The Odin orbital observatory", in A&A 402, L21–L25 (2003).
- [3] Klein, B., Philipp, S.D., Güsten, R. et al., "A new generation of spectrometers for radio astronomy: Fast Fourier Transform Spectrometer", 2006, Proc. of the SPIE, Millimeter and Submillimeter Detectors and Instrumentation for Astronomy III. Vol. 6275, pp. 627511.

Poster Session P4: Novel Devices and Measurements

On-Wafer Penetration Depth Measurements of Superconducting Films

Michael E. Cyberey*, Robert M. Weikle and Arthur W. Lichtenberger
University of Virginia Microfabrication Laboratories, VA, USA

*Contact: mc8qr@virginia.edu

Abstract— An on-wafer measurement technique allowing measurement of a superconducting film's penetration depth without post device-fabrication separation of the chips has been investigated. Coplanar waveguide (CPW) probes and a CPW to microstrip transition are utilized, allowing the use of commercially available LakeShore® CPX-1.5K cryogenic CPW probing station capable of microwave measurements to 50 GHz. The use of CPW probes allows for rapid prototyping and is nondestructive to the device wafers, and hence compatible with many device fabrication technologies. Measurement techniques utilizing resonant microwave circuits have been reported [1],[2], but require mounting to custom-made test fixtures and are not performed on-wafer, but instead on individual diced devices. However, such a dicing requirement is incompatible with our ultra-thin Si, Au beam-lead chip architecture [3]. In addition to a traditional resonant circuit measurement technique, a technique that uses on-wafer calibration standards is discussed. The on-wafer calibration eliminates possible effects introduced by the testing setup and potentially offers additional advantages such as a size reduction and a direct measurement of RF loss. The designs and results for both measurement techniques are reported for NbTiN films.

I. INTRODUCTION

Superconducting circuits have found broad application in THz electronics, with energy gap materials allowing operation at higher frequencies. Precise knowledge of the films' magnetic penetration depth is useful in the optimization of material quality and integral to RF circuit design.

With regard to the material quality of sputtered films, there are multiple variables which may require optimization. For larger energy gap superconductors, such as NbN and NbTiN, normal-state resistivity, stress, and transition temperature have been used as figures of merit for optimization [4],[5]. Using BCS theory, the penetration depth of a film can be approximated from these measurements using the relation [4]

$$\lambda_l (nm) \approx 105 \left[\frac{\rho (\mu\Omega - cm)}{T_c (K)} \right]^{(\frac{1}{2})} \quad (1)$$

where λ_l is the London penetration depth, ρ is the normal-state resistivity, and T_c is the transition temperature. A direct measurement of penetration depth can therefore also be used as a figure of merit. Having test structure designs compatible with normal device fabrication processes will alleviate the need to require separate material test wafers.

The use of resonant circuits though the microstrip resonator technique is a proven method for the measurement of the penetration depth of thin films [1]. One typical

drawback is the necessity to dice devices and mount them in a custom fixture. This requirement limits the usability when fabrication techniques require thinning of the whole wafer. In an attempt to address this limitation, new resonators based on those published by Lea [2] are designed and adapted for use with a cryogenic CPW probing station. The use of such a system ensures testing can be performed on-wafer and non-destructively.

Although this method can be adapted to cryogenic probing, it still has fundamental limitations in terms of size requirements. The method relies on measuring the resonant frequencies which only occur at multiples of half wavelengths of the fundamental resonance. As such, transmission lines must be wavelengths in length, consuming valuable area on actual device-containing wafers. As the wavelengths decrease with increasing measurement frequency, a trade-off between the decrease in required resonator length and increased system losses at high measurement frequency occurs. Through the use of a CPW probing station, the resonators have been tested up to 50 GHz to show the upper limit of the practical measurement frequency using our probe station.

To further reduce the required physical size of test structures, a method of determining the penetration depth without the need for long transmission lines is investigated. Through the use of on-wafer TRL standards, the phase velocity can be directly determined from the phase of the de-embedded S-parameters. Since the phase velocity is determined from S-parameters across all and not only certain resonant frequencies, the need to fabricate lines of multiple wavelengths is removed. An on-wafer set of TRL standards was designed and fabricated. The TRL standards set a reference plane after a CPW to microstrip transition. In theory, when such a calibration is implemented the phase velocity can be determined solely from the calibration standards and no additional devices.

II. EXPERIMENTAL METHODS AND DESIGN

A. Penetration Depth Calculations

The impedance of a superconducting microstrip line differs from that of an ideal lossless line of zero resistance. The penetration depth affects the impedance of the superconducting microstrip line through the change in kinetic inductance introduced by cooper pairs. The solutions for the inductance and capacitance of a superconducting microstrip line have been published by W.H. Chang [6] as

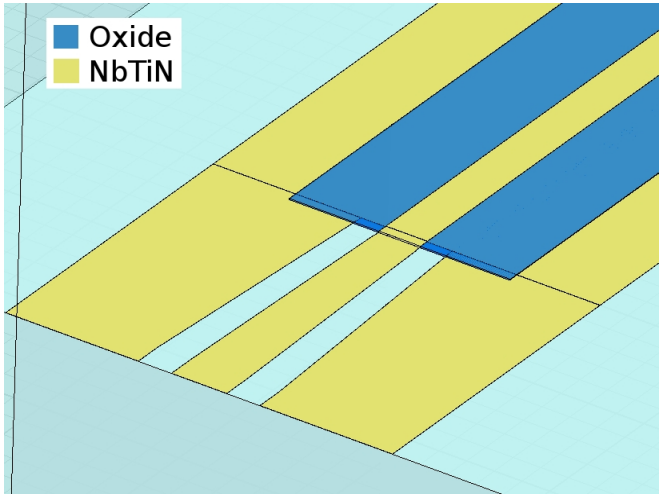


Fig. 1 A screenshot from HFSS® showing a portion of the 3D model before design simulations. The CPW line is shown as well as the abrupt transition to microstrip. The device is symmetric about the center of the microstrip line.

$$L = \frac{\mu_0}{WK} \left[h + \lambda_1 \left(\coth\left(\frac{t_1}{\lambda_1}\right) \dots \right. \right. \quad (2)$$

$$\left. \left. \dots + \frac{2p^{1/2}}{r_b} \operatorname{csch}\left(\frac{t_1}{\lambda_1}\right) + \lambda_2 \coth\left(\frac{t_2}{\lambda_2}\right) \right]$$

and

$$C = \frac{\epsilon \epsilon_0 W}{h} K \quad (3)$$

where W is the center conductor line width, h is dielectric thickness, t_1 , λ_1 and t_2 , λ_2 are the thickness and the penetration depth of the center conductor and ground plane respectively. The factors K , r_b and p take into account fringing fields and are determined by the microstrip geometries. These factors are included in Chang's paper [6].

Noting that only the inductance per unit length is a function of penetration depth and that for our design both metal layers are the same, $\lambda_1 = \lambda_2 = \lambda_i$; the phase velocity is simply

$$v_p = \frac{1}{\sqrt{(L(\lambda_i)C)}} \quad (4)$$

Once phase velocity of a microstrip line is measured, Matlab® is used to solve Eqs. 2-4 for the penetration depth.

B. Resonator Device Design

The design of the first device relies on the microstrip resonator technique to determine phase velocity and calculate the penetration depth. The details of the resonance measurement technique have been covered in detail by Langley [1] and Lea [2]. Our design consists of a low impedance $\sim 1 \Omega$ microstrip line connected at both ends by a 50Ω CPW line designed to be probed by a $150 \mu\text{m}$ pitch 50Ω CPW probe. The impedance mismatch at the abrupt CPW to microstrip transition introduces the reflections necessary to measure distinctive resonant frequencies. Fig 1 displays the

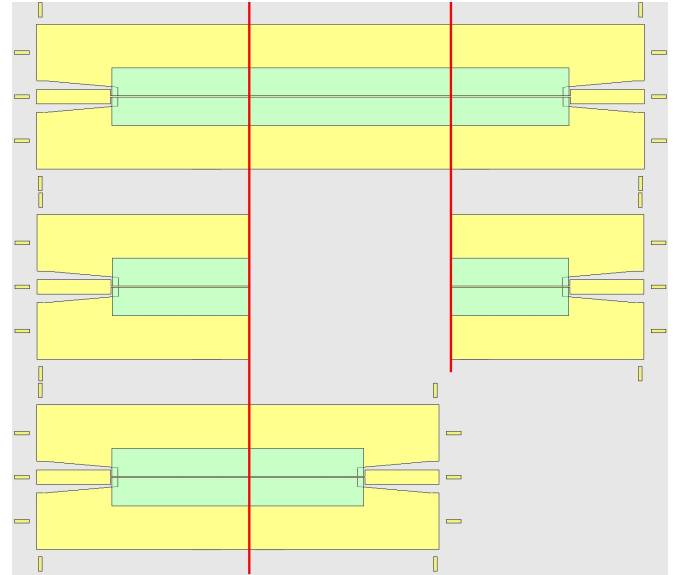


Fig. 2 The Line, Reflect, and Through standards from top to bottom, respectively. All standards contain alignment keys to aid with repeatable placement of CPW probes. The reference planes are displayed as the solid vertical lines.

design including the abrupt CPW to microstrip transition. Multiple lengths of line ranging from 5 mm to 3.5 cm have been included in the design.

C. TRL Calibration / Direct Phase Measurement

The phase velocity of a transmission line of know length is simply

$$v_p = \frac{\omega l}{\theta} \quad (5)$$

Where ω is the angular frequency, θ is the phase difference across the line, and l is the length of the line. If the measurement system can be de-embedded, phase can be directly measured. Once the phase velocity is determined using Eq. 5, penetration depth can be calculated from Eqs. 2-4. Since a CPW probe is used and a CPW to microstrip transition is to be employed, an on-wafer calibration is required to de-embed the probes and transition.

A set of on-wafer TRL standards was designed and fabricated. The standards set a reference plane for phase measurement after the CPW to microstrip transition. Fig 2 displays the calibration standards and outlines the location of the reference plane. The standards utilize a zero-length through, a 90° line at the center frequency, and a zero-length short for the reflect. The short is created by physically connecting the center-conductor of the microstrip line to the ground plane though a hole defined in the dielectric layer. Through the use of the NIST StatistiCAL® algorithm [9], the measured response of the standards is used to de-embed the entire measurement system before this reference plane.

Unlike the previous resonator design where high reflections are desirable, the design of the CPW to microstrip transition is such to allow minimal reflections to enable maximum power transmission across the entire frequency band. To reduce reflections, a smaller microstrip line width

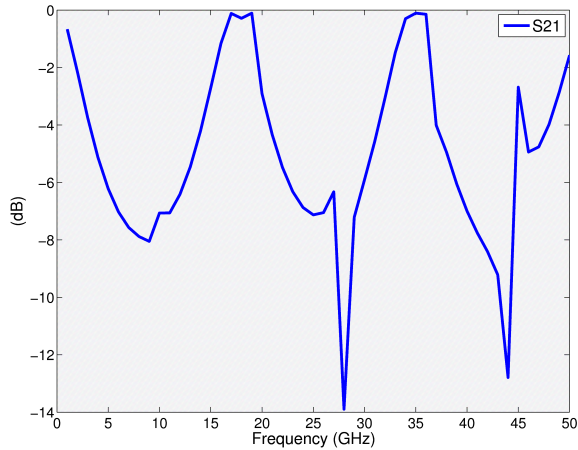


Fig. 3 HFSS simulation results for the CPW to microstrip transition are shown above. S_{21} is shown from 1 to 50 GHz and less than 8 dB attenuation is seen through most of the band.

is employed to increase the impedance. The CPW line is also tapered to gradually reduce the 50 Ω input impedance at the probing location and provide a better match at the transition. The design was simulated using HFSS® to verify minimal reflections and a transmission coefficient with less than -10 dB attenuation. The superconductivity of the thin films was taken into account by noting the surface impedance of a superconducting film of thickness t is

$$Z_s = (j\omega\mu_0\lambda_l) \frac{e^{\frac{t}{\lambda_l}} + \frac{Z_n - j\omega\mu_0\lambda_l}{Z_n + j\omega\mu_0\lambda_l} e^{-\frac{t}{\lambda_l}}}{e^{\frac{t}{\lambda_l}} - \frac{Z_n - j\omega\mu_0\lambda_l}{Z_n + j\omega\mu_0\lambda_l} e^{-\frac{t}{\lambda_l}}} \quad (6)$$

$$\approx j\omega\mu_0\lambda_l \coth\left(\frac{t}{\lambda_l}\right)$$

where Z_n is the impedance of free space and $Z_n \gg j\omega\mu_0\lambda_l$ [7]. Using this approximation, surface impedance boundaries for the films were set in HFSS. Fig 3 shows the results of the simulation, a transmission coefficient of >-8 dB is seen across the majority the band from 1-50 GHz. In addition to the calibration standards, additional lines of 1-3 cm in length were included for comparison.

D. Equipment

All aspects of fabrication were performed in the University of Virginia Microfabrication Laboratories. The designs were directly exported from HFSS to CAD format and were transferred to chrome plated photo-masks using a Heidelberg DWL 66 Laser Mask Writer.

DSP silicon wafers (50 mm diameter with 1500 Å thermal oxide) were chosen as the carrier substrate. The NbTiN films were deposited by reactive sputtering of NbTi through an Ar/N₂ plasma. The details of the NbTiN deposition and system used are previously covered in detail [5]. The oxide layers were deposited by RF diode sputtering of a 5 in quartz target. The substrate was mounted using high vacuum grease

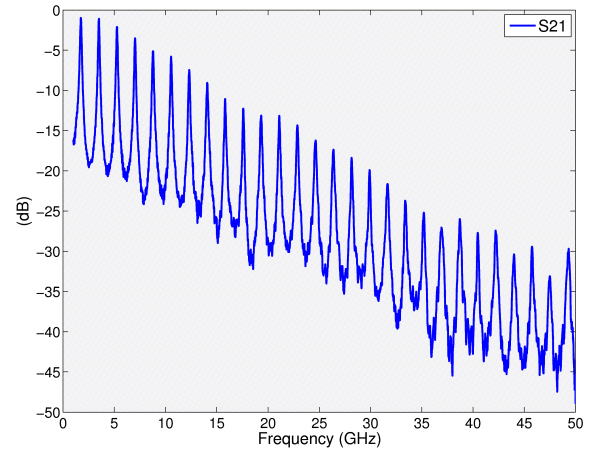


Fig. 4 The clear resonant peaks of S_{21} are seen from 1 to 50 GHz.

to a water-cooled grounded platter with a target-substrate separation of 1.5 in.

Film stress was measured by use of an optical profilometer which measures the change in wafer curvature after a deposition is completed. Film resistivity was recorded using the four point probe technique. All film thicknesses were measured using a Dektak® 8 stylus profiler. Dielectric constant of the oxide was determined by measuring the capacitance of multiple capacitors fabricated on-wafer alongside devices. The capacitance was measured using a Wayne Kerr LCR meter connected to the DC probes of the CPX cryostat.

The RF measurements were performed in a LakeShore CPX 1.5K Flow Cryostat equipped with two Picoprobe® CPW microwave probes. All S-parameters were measured and recorded using mwavepy [8] and an HP8510C VNA. A full two port first tier calibration was performed before connecting the VNA to the cryostat. Raw first tier calibrated data was recorded and the subsequent TRL calibration was applied as a second tier calibration using the NIST StatistiCAL calibration package. Temperatures were monitored using a LakeShore Model 340 Temperature Controller and a DT-670 temperature sensor located on the cryostat's stage. Apiezon N® grease was used as a thermal interface material between the substrate and stage.

We found that during the time of testing, the cryostat was equipped with one incorrect model probe. Testing was possible using this probe, but as a result of probe geometries, repeatable and reliable contact was difficult to achieve. This has little effect on uncalibrated resonator measurements but can play a critical role in the accuracy of the calibrated device measurements.

III. RESULTS

A. Resonator Measurements

Five resonators with lengths ranging from 5 mm to 3.5 cm were tested. A sweep from 1 to 50 GHz using 8001 data points was recorded. Noting the limitation of the HP8510C to record a maximum of 801 data points, this was achieved by breaking the sweep into smaller bands and stitching

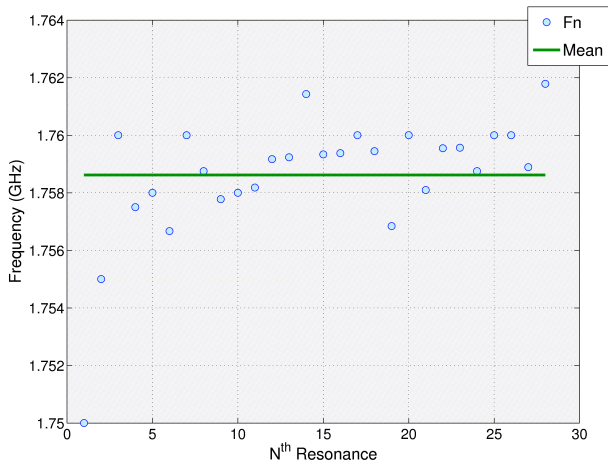


Fig. 5 The fundamental resonances, F_n , and their mean plotted across the N^{th} order resonance from which they were determined. The standard deviation is 2.2 MHz and the RMS error is 0.12%.

together 10 separate scans. Fig 4 shows the resulting S_{21} measurements and the sharp resonant peaks of the 3.5 cm long resonator. The fundamental resonances were determined at each peak by dividing the frequency of the n^{th} peak by n . This method was chosen over simply measuring the difference in peak locations in order to reduce measurement error. If we model the measured frequency, f_{meas} , as the actual frequency, f , plus an uncertainty term, e , the fundamental frequency, f_{meas}/n , has the uncertainty reduced by a factor of n .

$$\frac{f_{\text{meas}}}{n} = \frac{(f + e)}{n} = \left(\frac{f}{n}\right) + \left(\frac{e}{n}\right) \quad (7)$$

Fig 5 shows the measured fundamental resonances, as well as their mean, plotted across the n^{th} order. The standard deviation to the mean is only 2.2 MHz. This reduction in the uncertainty leads to a standard deviation which is less than the frequency spacing, 6.1 MHz, of the scan. The RMS error of the fundamental resonance is a remarkably low 0.12%.

Using the results of the 5 resonators, an average penetration depth of 281 nm with a standard deviation of only 2.9 nm was calculated. Using the NbTiN film's measured resistivity of 107 $\mu\Omega\text{-cm}$ and measured transition temperature of 14.45 K, BCS theory (Eq. 1) predicts a penetration depth of 285 nm, in good agreement with the measured values.

B. TRL Measurements

TRL measurements were recorded over a range of 3-23 GHz, which is the designed bandwidth of the single line TRL calibration. All TRL calibration standards were measured as well as lines of varying length. The calculated penetration depth of 281 nm, from the previous resonator measurements, was used to predict the calibrated response. The response was then compared with this theoretical prediction to first give qualitative evidence the calibration is working correctly. Fig 6 shows this agreement and one can see that around 20 GHz, the calibration begins to fail. TRL calibrations are only valid within a limited bandwidth,

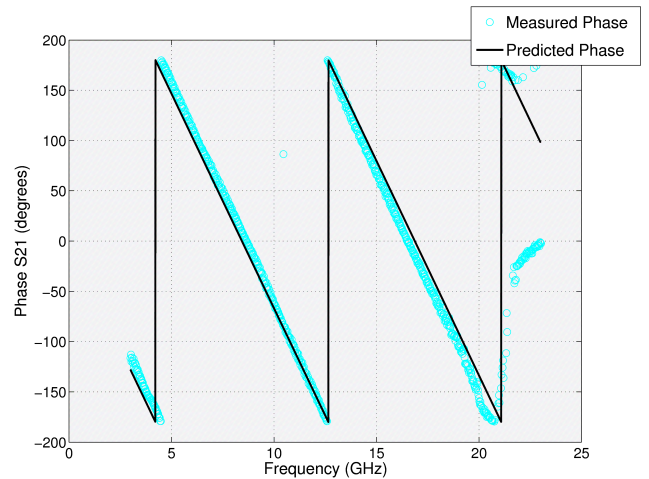


Fig. 6 The measured phase plotted alongside the phase predicted using the calculated penetration depth from the resonator measurements. Agreement is seen across the band until around 20 GHz, where it is believed the TRL calibration reaches the upper limit of its bandwidth.

determined by the length of the line standard, and this is near the upper limit. For this reason, only data below 20 GHz was used for the penetration depth calculations. For the quantitative results, the calibrated results were used to solve for the phase velocity as shown in Eq. 5. Three of the five measured lines gave usable results and a penetration depth of 284 nm with a standard deviation of 9.5 nm was calculated.

IV. CONCLUSIONS AND FUTURE WORK

Two methods of measuring penetration depth have been investigated. Through the use of CPW probes and a cryogenic probing station, both methods introduce a method of non-destructively measuring penetration depth on-wafer. A notable benefit of using CPW probes is the ability to rapidly test multiple devices. Previous methods through the use of dip-sticks and dicing of individual devices can take hours to test a single device. Another benefit is that the on-wafer devices can be incorporated to any mask set that includes at least two superconducting layers and one oxide layer. Both test structures can also be fabricated on the same wafer and tested side-by-side in the same testing setup.

The CPW-adapted resonator measurement has been shown to provide results which agree well with each other, as well as BCS theory. This method provides accurate on-wafer penetration depth measurements and has shown consistency up to 50 GHz.

The phase measurement devices produced results for penetration depth that agreed well with both the resonator measurements and BCS theory. When directly compared to the resonator measurements, they did have a standard deviation nearly 3 times larger and only 3 of the 5 tested devices showed usable results. With regard to these disparities, it should be noted that during the time of testing, an incorrect model probe had been provided by LakeShore and had to be used. The physical difference of the incorrect model resulted in difficulty with repeatable probe placement. Such repeatable placement is an integral part of any calibration scheme.

The motivation of pursuing calibrated measurements can be seen in the simplicity of Eq. 5. Phase velocity, and hence penetration depth, can be extracted from the TRL standards themselves with no additional devices. The calibrated phase information of the line standard can be used to determine the phase velocity when such a calibration is perfected. The line standard for TRL calibrations is generally only a quarter-wavelength at center frequency, a much shorter length when compared to the multiple-wavelength long lines required for resonance measurements. An additional benefit is that penetration depth results can be obtained from any wafer where TRL standards are already present, such is the case for many wafers containing superconducting microwave circuits.

For future work, accurate resonance measurements at frequencies up to 50 GHz will allow the testing of resonator devices of reduced size. Further work and improvements will be made to the probe station in efforts to increase the accuracy of TRL calibrations. The TRL calibration will be retested, including additional calibration standards designed for higher frequencies. It is also believed RF loss can be seen in the magnitude of the transmission coefficient of a transmission line inserted between our two reference planes. This idea will also be tested in future work.

ACKNOWLEDGMENT

The authors thank Alex Arsenovic for his helpful critiques, Theodore Reck for his help in photo-mask fabrication, and J. M. Beatrice for his work as UVML Facility Manager.

REFERENCES

- [1] B. W. Langley, S. M. Anlage, R. F. W. Pease, and M. R. Beasley, "Magnetic penetration depth measurements of superconducting thin films by a microstrip resonator technique," *Review of scientific instruments*, vol. 62, pp. 1801-1812, July 1991
- [2] Lea, Dallas Millard, Jr., "Integrated test structures for characterization of thin films for superconductor-insulator-superconductor devices and circuits," PhD Dissertation, University of Virginia, 1996
- [3] R.B. Bass *et. all*, "Ultra-Thin Silicon Chips for Submillimeter-Wave Applications," in *ISSTT'04*, 2004, paper 10.3, pp. 392
- [4] T. Matsunaga, H. Maezawa, and T. Noguchi, "Characterization of NbTiN Thin Films Prepared by Reactive DC-Magnetron Sputtering," *IEEE transactions on applied superconductivity*, vol.13, NO. 2, pp. 3284-3287, June 2003
- [5] T. W. Cecil, M. E. Cyberey, R. E. Matthews, J. Z., and A. W. Lichtenberger, "Development of Nb/Al-AIN/NbTiN SIS Junctions With ICP Nitridation," *IEEE transactions on applied superconductivity*, vol.19, NO. 3, pp. 409-412, June 2009
- [6] W. H., Chang, "The inductance of a superconducting strip transmission line," *Journal of applied physics*, vol. 50, issue. 12, pp. 8129-8134, Dec. 1979
- [7] A. R. Kerr, "Surface Impedance of Superconducting and Normal Conductors in EM Simulators," *MMA Memo*. No. 245 Jan. 1999
- [8] (2010) mwavepy – Project Hosting. [Online]. Available: <http://code.google.com/p/mwavepy/>
- [9] D. F. Williams, J. C. M. Wang, and U. Arz, Member, "An Optimal Vector-Network-Analyzer Calibration Algorithm," *IEEE transactions on microwave theory and techniques*, vol. 51, NO. 12, Dec. 2003

Terahertz imaging with a highly-sensitive quantum dot detector

S. Spasov¹, S. Pelling¹, R. Davis¹, V. Antonov¹, L.V. Kulik², and S. Kubatkin³

¹Physics Department of Royal Holloway
University of London
Email: spas.spasov@rhul.ac.uk

²Institute of Solid State Physics, RAS,
Chernogolovka, Russia

³Department of Microtechnology and Nanoscience (MC2),
Chalmers University of Technology, S-41296 Göteborg, Sweden

Abstract

We report on an application of photon counting detector in the sub-terahertz range of electromagnetic waves for imaging of natural and stimulated radiation emitted by free standing objects. The detector is assembled from a GaAs/AlGaAs quantum dot, electron reservoir and quantum point contact (QPC). Its operation relies on photon-to-plasmon and plasmon-to-charge conversion, followed by charge measurement in a single-shot mode. Individual photons excite plasma waves in the quantum dot, with a resonance frequency determined by the shape of the QD confining potential. The plasma wave decays subsequently by single-particle electron-hole excitations, which change the electrostatic potential stepwise in the close proximity to the QD. The potential steps are probed with the QPC operating as a sensitive electrometer. A studied object is placed on a two-dimensional translating stage. Its emission is projected through an optical window onto the detector attached to a 1K cold finger in a cryostat. Subsequently translating the stage in two space directions we are able to map the distribution of the emitted radiation. The presented technique has a potential for imaging of objects passively radiated in the sub-terahertz range.

Single Wall Carbon Nanotube (SWCNT) Devices as THz Detectors and Mixers

Enrique Carrion**, Martin Muthee**, Zuoqing Chen, John Nicholson, Eric Polizzi, and Sigfrid Yngvesson

Department of Electrical and Computer Engineering, Univ. of Massachusetts, Amherst, MA01003, USA

*Contact: ecarrion@ecs.umass.edu, yngvesson@ecs.umass.edu; phone (US) (413) 545-0771

** These authors contributed equally to this paper

Abstract—In this paper we present a review of the progress that our group has done in the development of Carbon Nanotube based devices as THz detectors. We describe new techniques for fabrication of log periodic antennas, as well as for better control of the placement and selection of the CNTs. The new THz detector devices utilize single tubes (or a few single tubes in parallel), and have potential for increased responsivity by about two orders of magnitude, compared with the devices based on CNT bundles that we reported on at the ISSTT 2009. The new devices are initially characterized being characterized as microwave detectors in order to study and optimize the two detection modes (“diode”-type, and bolometer type) that we have identified. We plan to utilize the best CNT devices as heterodyne detectors, down-converting in a two-laser experiment from different terahertz frequencies to the GHz range. Further, we present new results of time-dependent simulations of the THz response of a single carbon nanotube. We use time-dependent density functional theory and obtain a value for the kinetic inductance that agrees with accepted theoretical/experimental values

I. INTRODUCTION

Our first paper at the ISSTT symposia on the topic of Terahertz detection in carbon nanotubes (CNTs) was presented at ISSTT2005 [1]. We also discussed the topic of microwave and terahertz detection in CNTs in ref. [2], as well as a later ISSTT symposia. Our group reported the first terahertz detection in bundles containing m-SWCNTs [3], up to 2.5 THz, at ISSTT2008 and ISSTT2009. The SWCNT bundles were coupled to log-periodic antennas similar to those used to couple to NbN HEBs. CNTs are a promising medium for future terahertz detectors based on some general features based on their small diameters (1-2 nm) which lead to very low heat capacity and low capacitance. They can also have nearly ideal transport properties (ballistic transport) for both electrons and phonons. Detection in m-SWNTs can occur due to two basic mechanisms: (1) a diode type mechanism demonstrated at microwaves in [4]-[10]; (2) bolometer type modes, similar to that in HEBs and other terahertz bolometers. Both types of modes will be discussed below. We present advances in device fabrication that have enabled us to realize antenna-coupled SWCNT devices that contain a single SWCNT, or just a few SWCNTs. We have demonstrated excellent microwave detection in such tubes, and discuss how these results can be translated to enable realization of future terahertz SWCNT detectors with enhanced responsivity. We also present unique results from

time-dependent simulations of the THz response of SWCNTs, relevant for the development of such detectors.

II. DEVICE FABRICATION

As described at earlier ISSTT symposia, we fabricated the CNT devices by the dielectrophoresis (DEP) method. We refer to [11] and our earlier ISSTT papers for a general description of the method. We employed two types of log-periodic toothed antennas, fabricated by lift-off UV lithography in sputtered films of either gold or palladium, see Figure 1. The latest antennas utilize e-beam evaporation for the gold film deposition. In the initial stages of working out optimized processes for DEP we often employed standard low-resistivity silicon substrates. We then changed to high-resistivity substrates for actual devices to test at microwaves or at terahertz. All silicon substrates were oxidized with typical oxide thickness of 350 nm.

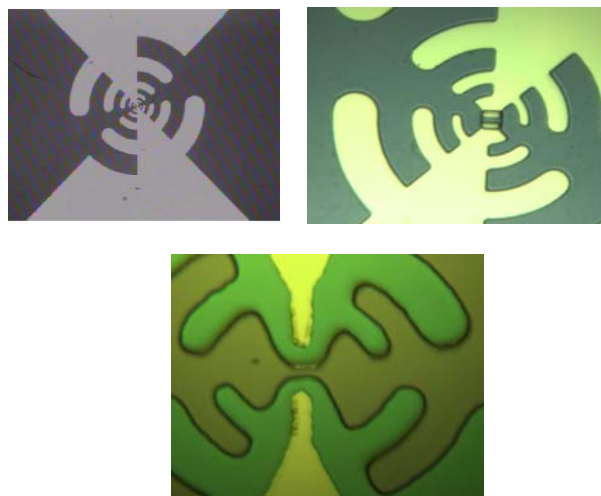


Figure 1. Different terahertz log-periodic antennas used in this work: LPA2 (top left); LPA3 (top right) and LPA4 (bottom).

Antenna LPA2 (Figure 1, top left) has a 1 μm gap and an estimated upper frequency limit of 3.5 THz. The LPA2 design is identical to one we used in our earlier NbN HEB work [12]. We were also concerned about minimizing the thermal conductance, and therefore fabricated antennas that had an etched trench in the silicon oxide in the gap region. Antennas of type LPA2 were employed as etching mask for

RIE etching of the trench. We term LPA2 antennas with a trench “LPA3”. Antenna LPA4 is a new design that was employed to facilitate DEP deposition of tubes with improved contacts, see Figure 1 (bottom). In one version, an antenna with about a 9 μm gap (but without “side teeth”; yellow in Figure 1) was first fabricated and DEP was performed to place tubes in its well-defined gap. A second (log-periodic) antenna (green in Figure 1) was then aligned and fabricated on top of the first one, thus establishing *contact from the top side* of the CNTs. Typically, the bottom antenna was made from gold and the top one from palladium. Palladium is known to produce the best contacts to CNTs, especially when it is applied from the top, and we have confirmed this in our work. A different version of LPA4 was later fabricated by using the same mask (the one with the smaller gap in Figure 1) for both the bottom and the top antenna. The photo resist for the top antenna was exposed differently which produced an antenna with a smaller gap that overlapped that of the bottom antenna along all edges.

Results from our earlier work are shown in Figure 2. During this period we employed CNTs that were present in bundles, even after long ultrasonication [13]. The bundles also contained a surfactant, that affects the quality of the contacts negatively. The SEM pictures show how the edges of the antennas were “flaked up” which made DEP difficult to perform successfully. Another problem at this stage was that the tubes were deposited outside the main gap of the antennas. Attempt to avoid this by etching a window over that gap (as shown in Figure 2, top left) and then performing DEP were only partially successful, but should succeed after further experimentation.

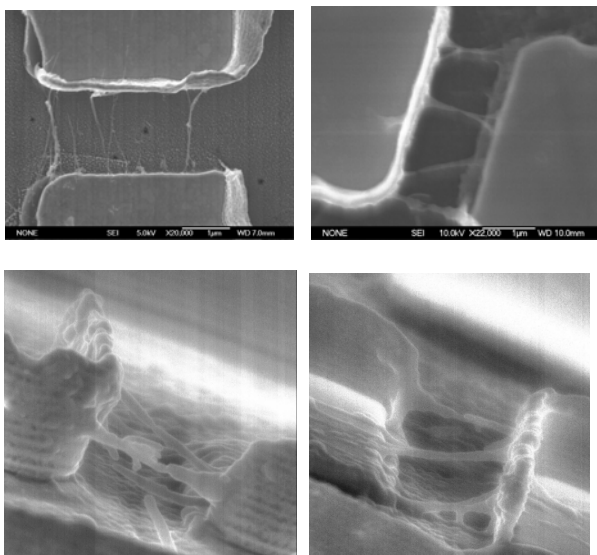


Figure 2. SEM pictures of devices with CNT bundles, using antenna LPA2. The bottom pictures are taken at a slanted angle to show the etched trench below the bundles, as well as the flaking of the gold edges.

The IV-curves of all bundle devices were of the “Zero-Bias Anomaly (ZBA) type, and dominated by the contacts, as described in our earlier papers (see Figure 3).

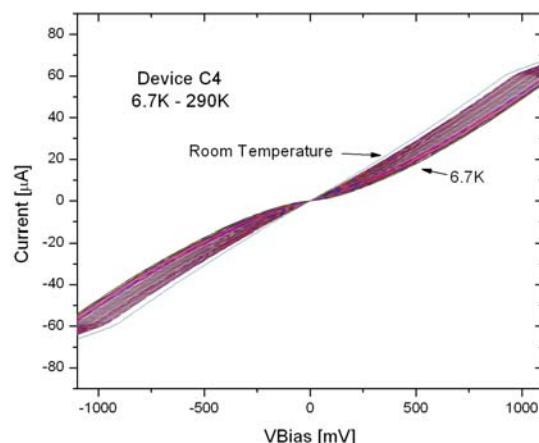


Figure 3. IV-curves for a typical CNT bundle device.

To fabricate single tube devices with better contacts we switched to a different CNT manufacturer [14]. These tubes had been dispersed in water effectively by the manufacturer and did not include any surfactant. The procedures for the DEP were re-optimized in order to emphasize single tubes with good contacts. Important elements in the new process are the use of a very low concentration of the tubes in the solution (ng/mL), and selection of an antenna gap that matches only the longest of the tubes in the solution. While other methods have also been employed elsewhere for placing single SWCNTs on contacts, we believe the method described here is unique, and relatively simple to implement. We monitor the DC resistance simultaneously through a bias tee. The DEP process is halted when the dc resistance is sufficiently low. All devices were annealed in air at 200 $^{\circ}\text{C}$ for two hours which decreased the contact resistance. As the result of the improved DEP process we were able to contact single SWCNTs to the LPA4 antenna. An example (device F2) is shown in Figure 4. The tube was measured by AFM to have a diameter of 1.5 nm, clearly identifying it as a single tube. We also note that DEP preferentially aligns metallic tubes, as versus semiconducting ones, which was confirmed based on the IV-curves for our devices.

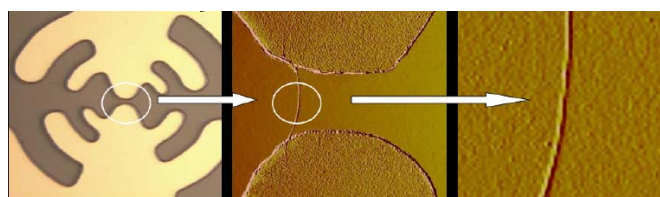


Figure 4. Example of a single SWCNT, contacted to an LPA4 antenna. The two frames in the center and to the right were imaged in an AFM.

Even though the SWCNT in the device in Figure 4 was placed from the top of the antenna contacts, it had improved contact resistance as shown by an IV-curve that “saturated” at higher voltages, see Figure 5. The saturation occurs because most of the bias voltage is developed across the SWCNT, rather than just the contacts, in this case. The resistance increases at higher voltages due heating of the

electrons in the tube and consequent optical phonon emission.

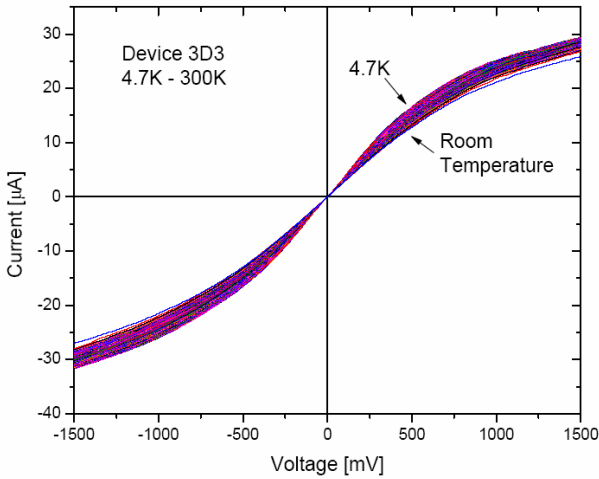


Figure 5. IV-curves at temperatures from 4.7 K to 300 K for device 3D3.

Further improvement of the contact resistance has been achieved by implementing the bottom/top antenna method described above. Figure 6 shows an IV-curve at 300 K for a device of this type, fabricated very recently.

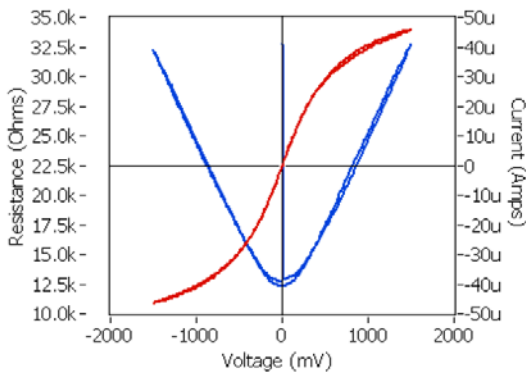


Figure 6. IV-curve (red) and resistance versus voltage (blue) for a device made with a bottom gold LPA4 antenna and a top palladium LPA4 antenna. The device was measured at 300 K.

III. FURTHER DC DEVICE CHARACTERIZATION

We performed further measurements of the device resistance versus temperature in order to explore the height of the contact barriers. In the AFM picture of Figure 7 we can identify one single tube and one bundle, containing two tubes. The resistance of this device while varying both the bias voltage and the temperature is displayed in a 3-D diagram in Figure 8. It is clear that there are two regions: (i) for low T and low V, the contact resistance begins to dominate; (ii) for higher T and V the contact resistance plays only a minor role. This type of studies are being used to optimize the device processing in the direction of pushing the contact effects toward lower T/V. For this particular device,

the contact resistance may be neglected above about 200 K. The best low barrier contact devices we are aware of fabricated by other groups have negligible contact resistance effects above about 20 K [5,6,15].

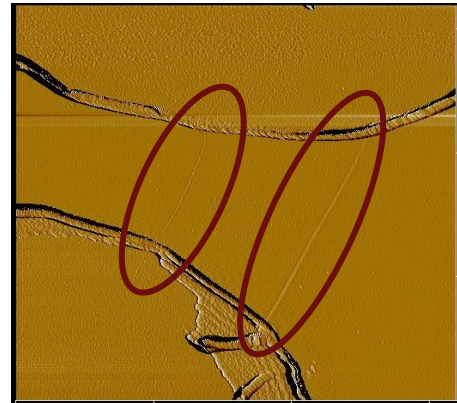


Figure 7. AFM picture of device 3D3

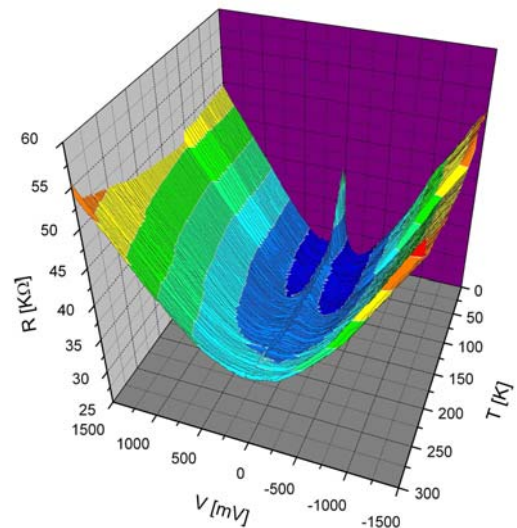


Figure 8. A 3-D plot of the resistance vs bias voltage and temperature for device 3D3.

IV. MICROWAVE DETECTION MEASUREMENTS

Microwave (MW) detection in the devices was measured by feeding a MW signal through a coaxial cable to the device, which was mounted in a liquid helium dewar. This method allows us to perform both microwave and terahertz measurements on a particular device without changing the setup. Our experimental setup was described in our previous ISSTT papers. We identified two different processes for MW detection:

- (1) *The “diode” process.* This detection mode is similar to that occurring in any semiconductor diode, except for the trivial difference that our IV-curves are symmetric between positive and negative bias voltages. As in our previous work, we model the SWCNT as shown in Figure 9.

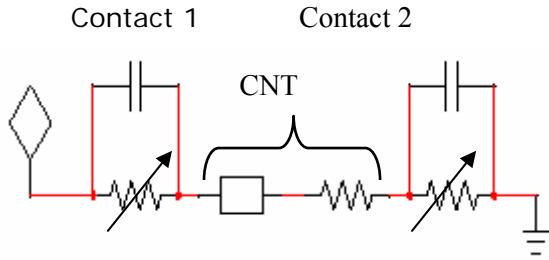


Figure 9. The circuit model for a single SWCNT.

In the diode mode, we utilize the nonlinearity of the contact resistances in Figure 9, the IV-curve for the entire device is well described by this model, while neglecting the intrinsic SWCNT resistance. These IV-curves are similar to the ones in Figure 3). We find the responsivity from:

$$S_V = (1/4)R \frac{d^2 I}{dV^2} \frac{V_{MW}^2}{P_{MW}} \quad (1)$$

Here, $R = V/I$ is the device resistance at the operating point, V_{THz} is the MW voltage at the device terminals and P_{THz} is the available power from the MW source. S_V has units of V/W.

2) For the *bolometer mode*, the expression is

$$S_V = \frac{V_0 * b}{G_{th}} \quad (2)$$

where V_0 is the bias voltage, $b = (1/R)(dR/dT)$ and G_{th} the thermal conductance. As shown in Figure 10, the diode mode occurs in the lowest voltage range, and the bolometer mode at higher bias voltages.

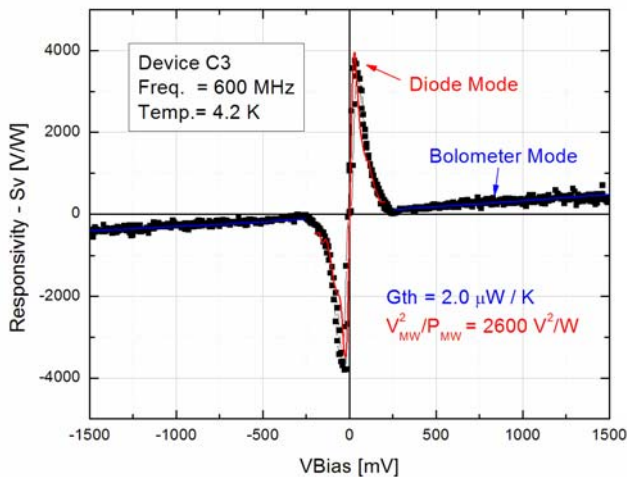


Figure 10. Responsivity versus bias voltage for device C3 at 4.2 K.

The device in Figure 10 has one the highest responsivities for either mode, about 4,000 V/W in the diode mode and 500

V/W in the bolometer mode. The response is quite flat with frequency up to 3 GHz, the highest frequency of the source used at the moment. We can predict the *ideal response* in the bolometer mode from Eq. (2), using $R(T)$ and G_{th} for an optimum device [5,6,15], see Figure 11.

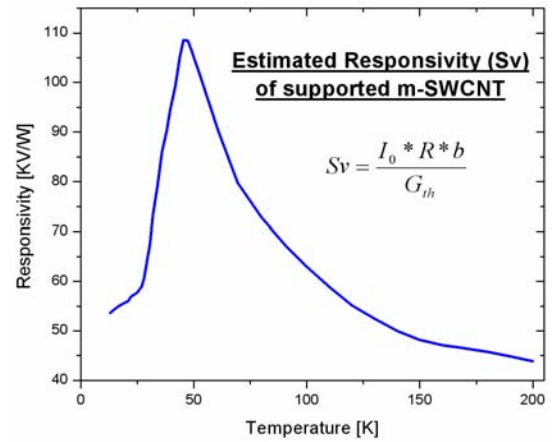


Figure 11. Predicted optimum responsivity for a single CNT in the bolometer mode.

What is noteworthy in Figure 11 is the fact that the responsivity depends only very slowly on the temperature, at least up to 200 K. For a more realistic device, we must include estimated coupling losses due to the high resistance of the device, 18 dB, which reduces the maximum S_V to about 2,000 V/W. This excellent responsivity should also occur at terahertz frequencies provided that the coupling loss were the same. We will discuss the THz coupling loss further below. The measured MW responsivities for devices C3 (Figure 10) and F2 agree well with this theory. The maximum responsivity (500 V/W) is less than for the optimum device primarily because the contact barriers are higher. MW measurements of the type described here enable us to optimize the device fabrication, particularly in terms of the contact barriers, as reflected in the IV-curves.

We plan to perform heterodyne measurements using two lasers for a device that has been optimized in this manner. We can estimate the conversion gain (G_C) in the heterodyne mode from the responsivity in the direct detector mode [17]:

$$G_C \approx 2S_V^2 P_{LO} / R_L \quad (3)$$

Here, P_{LO} is the local oscillator power and R_L the load resistance at the IF. With even a moderately good $S_V = 1,000$ V/W, $P_{LO} = 10^{-6}$ W, and $R_L = 100 \Omega$, we estimate a conversion gain of -17 dB. **Since the responsivity can potentially be much higher the prospects for realizing a very efficient mixer are excellent. Moreover, the predicted temperature dependence of the responsivity (Figure 11) is very slow, showing the potential for operation at least up to about 100K.** Eq. (3) assumes that the IF output is matched to the IF amplifier and this would require a matching circuit. Alternatively, some IF mismatch

may be tolerated, or for example traded against using higher LO power.

An estimate of the LO power can best be obtained by using the already measured typical IV-curves. We find a P_{LO} of about 1 μ W or less.

V. TERAHERTZ COUPLING TO SWCNTs

We have simulated the coupling loss for an m-SWCNT, expressed in terms of the S-parameter S11 in dB, using a circuit model similar to that in Figure 9. The tube was assumed to be 1 μ m long. The circuit model assumes a particular version of the Luttinger-Tomonaga plasmon model, which as mentioned earlier is not yet experimentally verified. Questions related to the terahertz model for SWCNTs and the resulting coupling loss are the most significant questions that still require much research in the field of terahertz SWCNT detectors. It is encouraging to note that substantially reduced coupling loss is predicted at the plasmon resonance frequencies based on our present understanding of such models.

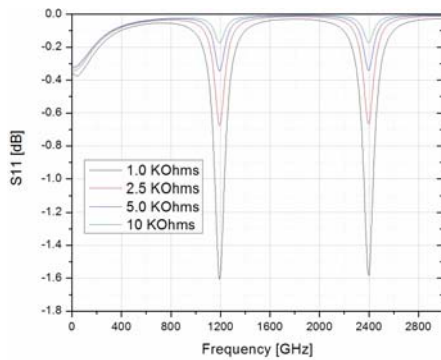


Figure 12. Simulated coupling loss for a metallic SWCNT at THz frequencies. Four different values for the SWCNT intrinsic resistance were assumed, as marked.

VI. TIME-DEPENDENT DFT SIMULATIONS

Another objective of this study consists in performing reliable modeling and simulations of the CNT electron dynamics in order to supplement the high-frequency electronics experiments. Our primary focus has been concerned with setting up a robust and efficiency time-dependent density functional theory (TDDFT) simulation-based framework which we can address the numerical challenges arising from large scales related to both space and time.

For addressing the electronic structure calculations of large-scale atomistic systems such as long CNTs, we have proposed a new modelling approach which benefits from well-suited combinations of specific mathematical and numerical algorithms that exploit fully the potentiality of real-space mesh techniques in achieving linear scaling performance [18]. As compared to traditional approaches, our DFT technique applied to CNTs allows order of magnitude speed-up and is applicable to both pseudopotential

approaches and all-electron calculations. To address the problem of long time period required to capture the behavior of the electron dynamics in the THz regime, we have developed a numerical procedure that goes beyond perturbation theory or linear response. Accurate, robust and scalable time dependent simulations are indeed difficult, if not impossible, to achieve using conventional modeling approaches. Our technique consists of performing directly the integration of the time evolution operator (i.e. time ordered exponential) along with the spectral decomposition of the time dependent Hamiltonian at each time step. The expression of the evolution operator is given as follows:

$$\psi(t) = \hat{U}(t, 0)\psi_0 = \mathcal{T} \exp \left\{ -i \int_0^t d\tau \hat{H}(\tau) \right\} \psi_0$$

Our in-house FEAST eigenvalue solver [19,20] (which is more efficient and scalable than other conventional eigenvalue solvers) can be used to speed up the spectral decompositions and evaluate the exponential at each small time step $d\tau$. In our work [21], we have also proposed a new Gaussian quadrature scheme to minimize the integration error on the Hamiltonian. This scheme provides a good trade off between computational consumption and numerical accuracy, meanwhile unitary, stability and time reversal properties are well preserved.

Here, we are applying this TDDFT framework to the simulation of a (5,5) CNT whose end sections are wrapped around two electrodes, with no charge transfer, producing an AC voltage at the THz frequency (see Figure 13).

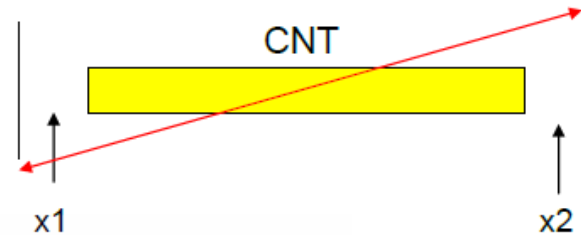


Figure 13. Simulation set-up with an isolated CNT in contact with two electrodes (no charge transfer) producing an AC voltage at the THz frequency.

The time variation of the electron density calculated at the two specific positions x1, x2 in Figure 13 is represented in Figure 14.

We estimate the kinetic inductance (L_K) of this tube from the basic definition that sets $\frac{1}{2} L_K I^2$ equal to the kinetic energy. The latter can be obtained directly from our simulation. The kinetic inductance we find this way is 3.6pH/nm which is in agreement with experimental and theoretical estimation results of 8pH/nm [22] and 4pH/nm [16]. We note that the kinetic inductance is an important circuit parameter in the transmission line model in Figure 9, that was referred to in our discussion of the plasmon phenomena in SWCNTs.

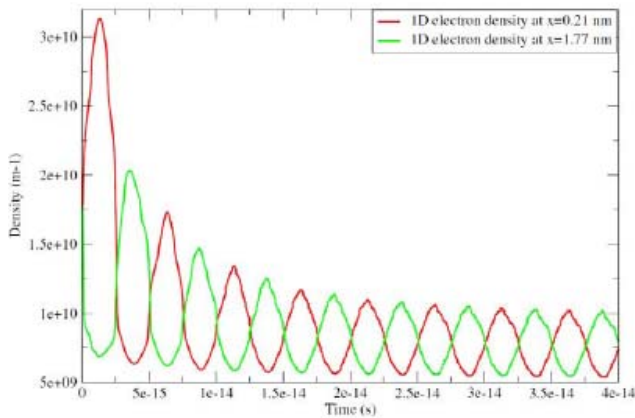


Figure 14. Time variation of the cross-sectional average of the electron density obtained at positions x_1 , x_2 . The CNT is only 2nm long here, and after a few periods the signal becomes periodic.

ACKNOWLEDGEMENT

This work was supported by grants from the US National Science Foundation, grant numbers ECS-0508436 and ECS-0725613.

REFERENCES

- [1] K.S. Yngvesson, "A New Hot Electron Bolometer Heterodyne Detector Based on Single-Walled Carbon Nanotubes," *16th Intern. Symp. Space Terahertz Technol.*, Göteborg, Sweden, May 2005, p. 531.
- [2] K.S. Yngvesson, "Very wide bandwidth hot electron bolometer heterodyne detectors based on single-walled carbon nanotubes," *Applied Phys. Lett.*, vol. **87**, p. 043503 (2005).
- [3] K. Fu, R. Zannoni, C. Chan, S.H. Adams, J. Nicholson, E. Polizzi and K.S. Yngvesson, "Terahertz detection in single wall carbon nanotubes," *Appl. Phys. Lett.*, **92**, 033105 (2008). For further details, see K. Fu, "Metallic Carbon Nanotubes, Microwave Characterization and Development of a Terahertz Detector," *M.Sc. thesis, University of Massachusetts, Amherst, MA* (2008).
- [4] F. Rodriguez-Morales, R. Zannoni, J. Nicholson, M. Fischetti, K. S. Yngvesson, and J. Appenzeller, *Appl. Phys. Lett.* **89**, 083502_2006_.
- [5] D.F. Santavicca and D. Prober, "Terahertz Resonances and Bolometric Response of a Single Walled Carbon Nanotube", paper 1646, 33rd Intern. Conf. Infrared, Millimeter and Terahertz Waves, Sept. 2008, CalTech, Pasadena, CA.
- [6] D.F. Santavicca, J. Chudow, A. Annuciata, L. Frunzio, D. Prober, M. Purewal and P. Kim, "Terahertz resonances on a single-walled carbon nanotube," Intern. Workshop on Optical Terahertz Science and Technol., Santa Barbara, CA, March 7-11, 2009. Also, see D.F. Santavicca, Ph.D. Thesis, Yale Univ., Dec. 2009.
- [7] H.M. Manohara, E.W. Wong, E. Schlecht, B.D. Hunt, and P.H. Siegel, *Nano Lett.*, **5**, 1469 (2005).
- [8] S. Rosenblatt, H. Lin, V. Sazonova, S. Tiwari, and P.L. McEuen, *Appl. Phys. Lett.* **87**, 153111 (2005).
- [9] A. A. Pesetski, J.E. Baumgardner, E. Folk, J. Przybysz, J. D. Adam, and H. Zhang, *Appl. Phys. Lett.*, **88**, 113103 (2006).
- [10] M. Tarasov, J. Svensson, L. Kuzmin, and E. E. B. Campbell, *Appl. Phys. Lett.*, **90**, 163503 (2007).
- [11] R. Krupke and F. Hennrich, *Adv. Eng. Mater.* **7**, 111_2005.
- [12] E. Gerecht, C. Musante, Y. Zhuang, K. Yngvesson, T. Goyette, J. Dickinson, J. Waldman, P. Yagoubov, G. Gol'tsman, B. Voronov, and E. Gershenzon, *IEEE Trans. Microwave Theory Techn.*, vol. **47**, pp. 2519-2527, (1999).
- [13] Cheap Tubes, Brattleborough, VT, USA.
- [14] CNTRENE from Brewer Science, Rolla, MO, USA.
- [15] M. S. Purewal, B. H. Hong, A. Ravi, B. Chandra, J. Hone, and P. Kim, "Scaling of Resistance and Electron Mean Free Path of Single-Walled Carbon Nanotubes", *Phys.Rev.Lett.* **98**, 186808 (2007).
- [16] P. J. Burke, "Luttinger Liquid Theory as a Model of the Gigahertz Electrical Properties of Carbon Nanotubes," *IEEE Trans. Nanotechnol.* **1**, 129 (2002).
- [17] B.S. Karasik and A.I. Elantiev, Proc. 6th Intern. Symp. Space Terahertz Technol., Pasadena, CA, March 1995, pp. 229-246.
- [18] D. Zhang, E. Polizzi, *Linear scaling techniques for first-principle calculations of large nanowire devices*, 2008 NSTI Nanotechnology Conference and Trade Show. Technical Proceedings, Vol. 1 pp12-15 (2008).
- [19] E. Polizzi, *Density-Matrix-Based Algorithms for Solving Eigenvalue Problems*, *Phys. Rev. B*. Vol. 79, 115112 (2009).
- [20] <http://www.ecs.umass.edu/~polizzi/feast>
- [21] Z. Chen *Efficient modeling techniques for time-dependent quantum system with applications to Carbon nanotubes.*, MS thesis, UMass Amherst (2010).
- [22] Zhang, M., Huo, X., Chan, PCH, Liang, Q., and Tang, ZK. *Radio-frequency transmission properties of carbon nanotubes in a field-effect transistor configuration*. *IEEE Electron Device Letters* 27, 8, 668-670 (2006).

THz Vector Network Analyzer Measurements and Calibration

Jeffrey L. Hesler*, Yiwei Duan, Brian Foley and Thomas W. Crowe
Virginia Diodes Inc., Charlottesville, USA

*Contact: hesler@vadiodes.com

Abstract— Virginia Diodes is developing a series of Vector Network Analyzer extenders to cover waveguide bands from WR-10 (75-110 GHz) up to WR-1.0 (750-1100 GHz). This article discusses the basic configuration of the VDI extenders, and shows examples of several systems. Several measurement examples are discussed, including the measurement of waveguide loss, interface mismatch, and loads. Initial measurements of a WR-1.2 (600-900 GHz) extender are presented, showing a typical dynamic range of 85 dB.

I. INTRODUCTION

Vector Network Analyzers (VNAs) are used to accurately measure the complex scattering parameters for a wide variety of devices in different environments, and are a key measurement instrument in the microwave and millimeter-wave frequency ranges. The accuracy of the VNA is achieved by using high quality signal sources and receivers, as well as sophisticated calibration methods that have been developed to eliminate systematic errors.

Virginia Diodes (VDI) is developing a series of modules that can be used to extend the frequency range of modern VNAs up to THz frequencies. This article describes the basic layout and operation of these VNA Extenders. In addition, measurements of waveguide components in the WR-1.5 (500-750 GHz) band are presented.

II. FREQUENCY EXTENDER CONFIGURATION

A schematic of VDI's frequency extender configuration is shown in Fig. 1. The extender consists of a transmitter followed by back-to-back directional couplers. A receiver is attached to each of the couplers; one to sample the outgoing signal (i.e. the Reference Mixer) and one for the incoming/returning signal (i.e. the Measurement Mixer). The two VNA drive signals (one for the transmitter and one for the receivers) are offset by a fixed amount to generate IF signals at a constant frequency, which are then measured by the VNA.

The transmitter consists of an amplifier followed by a series of full waveguide band frequency multipliers. Back-to-back directional couplers at the transmitter output are used to route the signal power. One coupler samples the outgoing power and the second samples the input power that is received from the test port. This input power may be either a signal transmitted by this module and reflected off of the device under test (S11) or a signal transmitted by a separate module through the DUT (S21, for example). Each receiver consists of an amplifier and multipliers that generate the LO

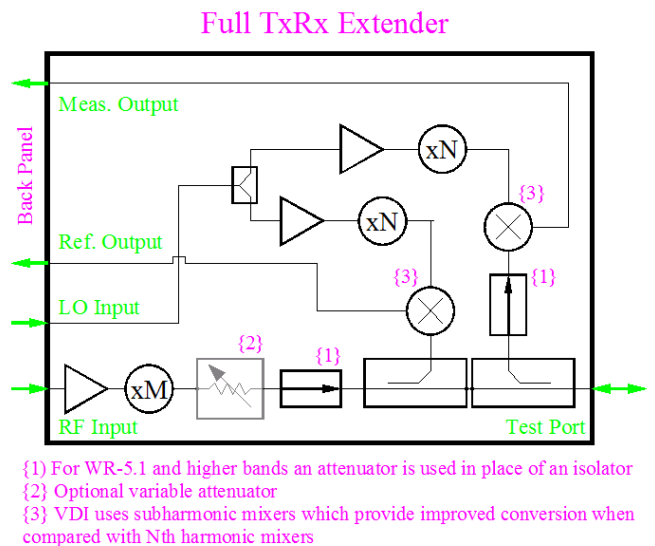


Fig. 1. VDI TxRx frequency extender configuration.

drive power and finally a subharmonic mixer, which gives high sensitivity and suppresses LO noise. The Reference mixer sets the amplitude and phase reference for the system, and the Measurement signal provides information about the Device Under Test (DUT).

For full two-port measurements (i.e. measurement of all four S-parameters) two TxRx Extenders are used. For one-path two-port measurements (i.e. measurement of S11 and S21 only), one TxRx Extender and one Rx Extender (consisting of a single receiver) can be used.

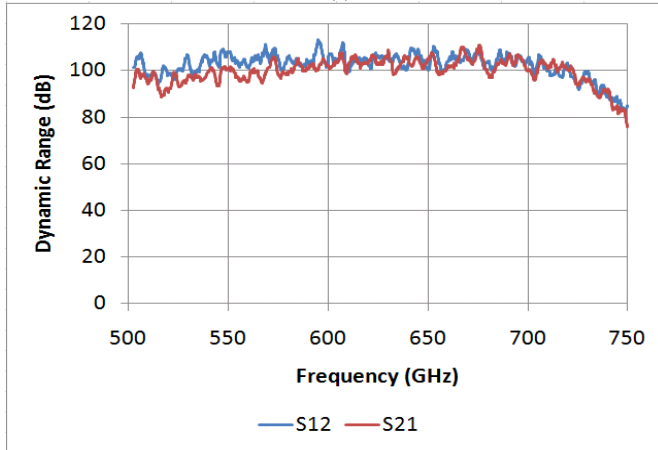
III. WR-1.5 (500-750 GHz) MEASUREMENTS

A pair of VNA Extenders to WR-1.5 (500-750 GHz) are shown in Fig. 2. The multipliers and mixers in the extenders rely on VDI's series of full waveguide band THz Schottky diode components, e.g. doublers, triplers, and subharmonic mixers. These components produce high output power and low conversion loss, yielding state-of-the-art sensitivity and bandwidth for the extenders. In addition to these components, a full line of directional couplers and other waveguide components have been developed. The WR-1.5 extenders have an average dynamic range of 100 dB (with 10 Hz bandwidth), and a test port power of -25 dBm (typ.).

For calibration a TRL method was used, with a flush connection for the Thru, a $\frac{1}{4}$ wave delay for the Line, and short circuits for the Reflects. Measurements of the full two-



(a)



(b)

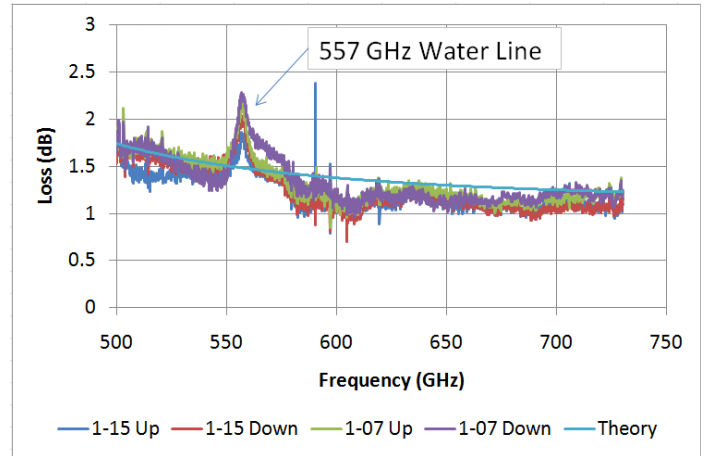
Fig. 2. (a) Photograph and (b) measured dynamic range of a WR-1.5 VNA Extender.

port S-parameters were performed using a pair of TxRx heads.

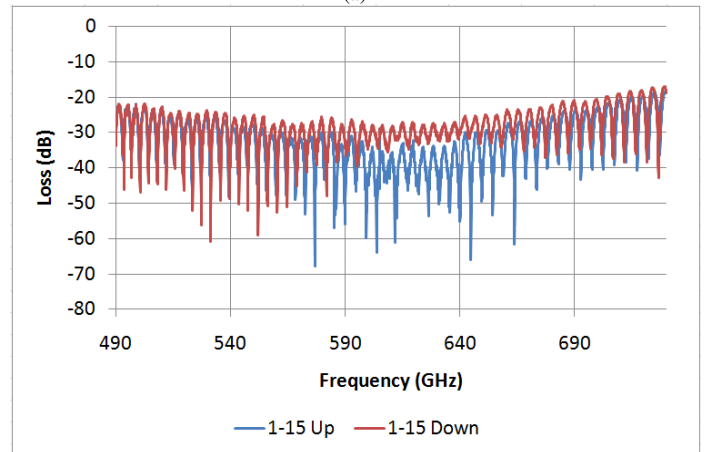
Fig. 3 shows measurements of a 25 mm long section of straight WR-1.5 waveguide. The return loss is dominated by reflections from the waveguide interface at each end, which introduces standing waves in the S21 measurement. The reflections from the two interfaces can be seen clearly in the time-domain data, shown in Fig. 4. The measured waveguide loss (Fig. 3(a)) matches the calculated loss of smooth-walled gold-plated waveguide, indicating the quality of the machining and gold. Similar loss measurements at other submillimeter bands have found that the loss for VDI waveguide ranges from 1-1.5 times the theoretical limit. The measurement disturbance at 557 GHz is caused by the strong water line at that frequency.

Fig. 5 shows a measurement of the loss of a 90 degree H-plane bend (length ~ 20.7 mm). The loss for this waveguide is about 5 times the calculated “ideal” loss. The dominant reason for the high loss is that the waveguide (made in two pieces) is split in the H-plane. The waveguide measured in Fig. 3 was split in the E-plane, which has less loss because there are no currents crossing the split.

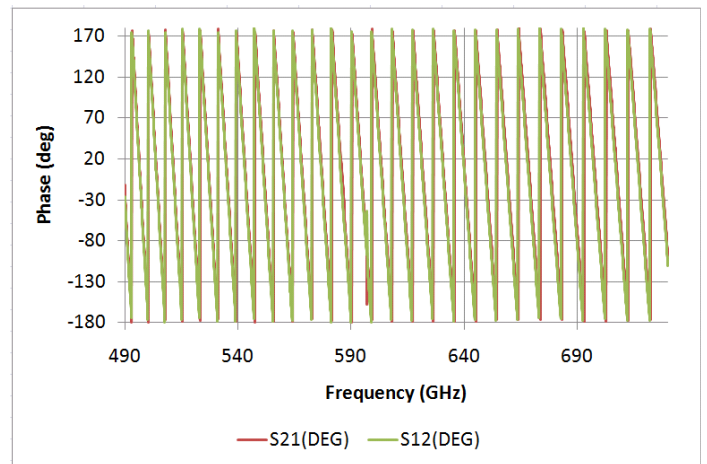
Fig. 6 shows the return loss of a WR-1.5 waveguide load in both the frequency and time-domain. The ripples in the return loss measurement (Fig. 6(a)) are caused by reflections between the waveguide interface and the waveguide termination. The return loss of the interface mismatch and of the termination are seen to be comparable.



(a)



(b)



(c)

Fig. 3. (a) Insertion loss, (b) Return loss, and (c) transmission phase for a 25 mm long straight waveguide section. The standing wave pattern is reflections from the waveguide interface at each end of the block. The notation “up” and “down” refers to the waveguide orientation of the UG-387/U-M flange, which can be re-connected after a rotation of 180 degrees. Ideally the curves for “up” and “down” should be identical, and differences indicate alignment issues between the waveguide and the alignment dowels.

IV. WR-1.2 (600-900 GHz) DEVELOPMENT

Work is underway to develop extenders to above 1 THz. As an example, the dynamic range of a WR-1.2 prototype is shown in Fig. 7. A non-optimal drive chain was used for this measurement, and so the system frequency range is shifted

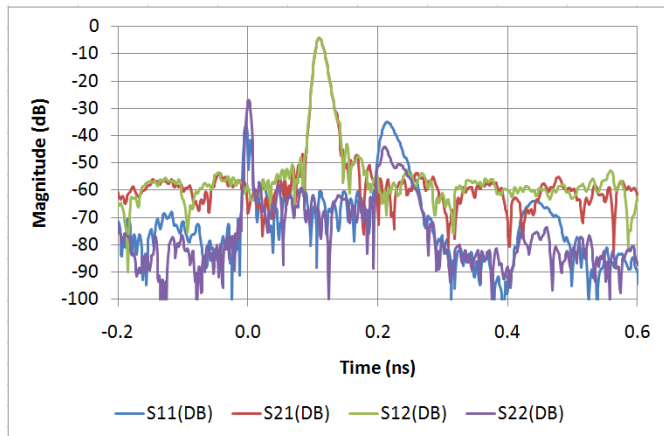


Fig. 4. Time domain measurement of a 25 mm long section of WR-1.5 straight waveguide

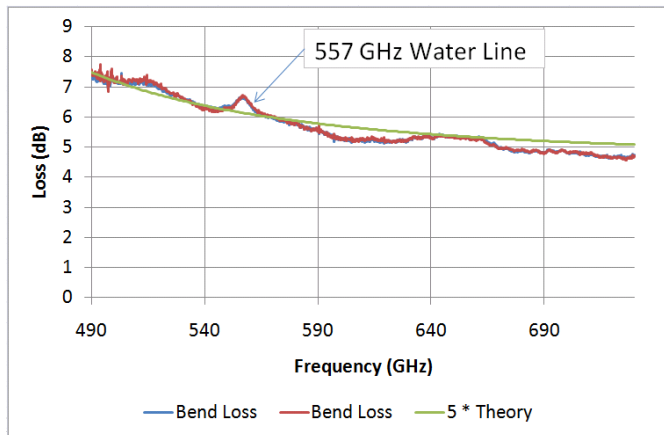


Fig. 5. Insertion loss for an H-plane bend, length ~ 20.7 mm.

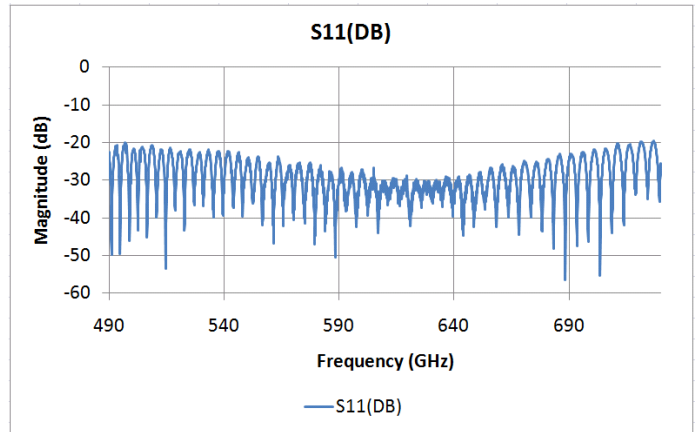
higher in the waveguide band. Even so, this extender demonstrates excellent dynamic range up to 950 GHz. Work is underway to develop a drive chain that better matches the standard WR-1.2 waveguide band. Calibration standards have also been successfully developed for this band, and calibrated measurements will be performed once the system has been optimized. A WR1.0 system (750-1,100GHz) is also under active development.

V. CONCLUSIONS

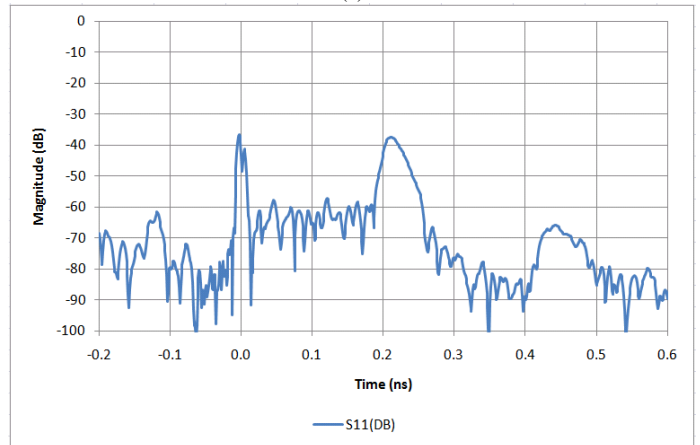
Frequency extenders with high dynamic range have been developed up to 750 GHz, and research is underway to develop calibrated VNA measurements up to 1,100 GHz. Initial measurements have demonstrated dynamic range of 85 dB (typ.) up to 950 GHz. These extenders have excellent amplitude and phase stability, and can be used to perform accurate measurements up to THz frequencies.

VI. ACKNOWLEDGEMENTS

This development has been supported by various SBIR contracts for THz Transmitters and Receivers (Army DAAD19-02-C-0013), Broadband Receivers (NASA GSFC NNX09CA57C), and Modular Frequency Extenders (DHS N10PC20044).



(a)



(b)

Fig. 6. S11 measurements of waveguide load.

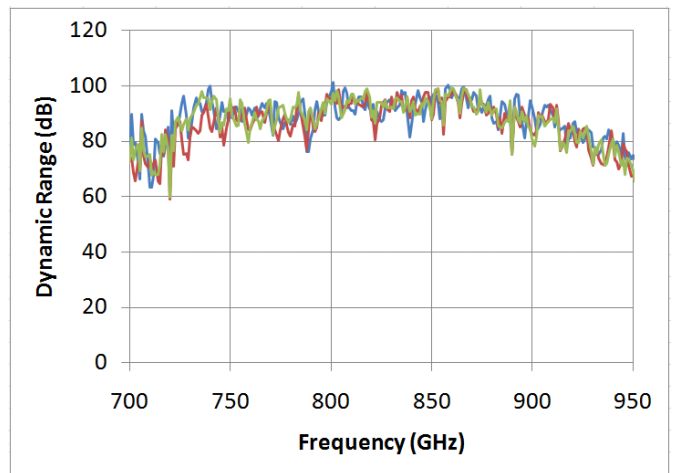


Fig. 7. Measured dynamic range of a WR-1.2 VNA Extender.

Development of Microwave and Terahertz Detectors Utilizing AlN/GaN High Electron Mobility Transistors

L. Liu^{1,2,*}, B. Sensale-Rodriguez¹, Z. Zhang¹, T. Zimmermann¹, Y. Cao¹, D. Jena¹, P. Fay¹, and H. Xing¹

¹Department of Electrical Engineering, University of Notre Dame, Notre Dame, IN 46556, USA

²Advanced Diagnostics and Therapeutics Initiative, University of Notre Dame, Notre Dame, IN 46556, USA

*Contact: lliu3@nd.edu, phone 1-574- 631- 1628

Abstract—We report our work on development of microwave and terahertz detectors using AlN/GaN high electron mobility transistors. Microwave measurements ($f = 10 - 40$ GHz) using AlN/GaN HEMTs as detectors have been performed and the results have shown that the device work in non-resonant mode at room temperature with a responsivity roughly proportional to f^{-2} at low frequencies. Measured responsivity as a function of gate bias also shows reasonable agreement with theory and published results. Initial calculation results show that an AlN/GaN HEMT with 0.15 μm gate length works in the resonant mode when it is cooled down to 77K. The fundamental resonant frequency increases from 200 GHz to 3.2 THz with gate-to-source voltage swing of 0.01 V to 2.0 V. The drain-to-source voltage response also increases with increasing of the gate-to-source voltage swing. We plan to integrate the AlN/GaN HEMT devices broadband lens-coupled antennas and low-pass filters for tunable plasma wave THz detectors.

I. INTRODUCTION

High sensitivity, cost-effective and frequency-tunable terahertz (THz) detectors have many applications in astronomy, imaging, spectroscopy and biosensing. Current solid-state all-electronic THz detectors are mainly based on bolometers, Schottky diodes, and pyroelectric or photoconductive devices, and these detectors either have fixed operation frequencies and narrow band, or are ‘broadband’ but require spectrometers or equivalent for spectrum analysis. Frequency-tunable detectors are desired in many systems for realizing all-electronic tunability instead of using gratings or moving mirrors that are bulky and prone to mechanical failure.

Dyakonov and Shur [1] have shown that plasma waves in a high electron mobility transistor (HEMT) channel have nonlinear properties, and can be utilized for tunable terahertz detection. A HEMT, when biased with gate-to-source voltage ($V_{gs} - V_{th}$, V_{th} is the threshold voltage) and illuminated by electromagnetic radiation, can generate a constant drain-to-source voltage due to the asymmetry boundary conditions at the drain and source. For a HEMT (with effective electron mass, m) with an effective gate length L , the plasma wave resonates at,

$$f = \frac{1}{4L} \sqrt{e(V_{gs} - V_{th}) / m} \quad (1)$$

and its odd harmonic frequencies. The quality factor of the resonance is determined by $s\tau/L$, where s is the plasma wave velocity, and τ is the momentum relaxation time. If $s\tau/L > 1$, the HEMT works in the resonant mode, and the detection frequency can be tuned by the gate-to-source biasing, according to (1). If $s\tau/L < 1$, the HEMT then works as a non-resonant broadband THz detector.

To date, THz detectors using HEMTs have been demonstrated in various GaAs and GaN based devices [2, 3]. However, in most of the experiments performed, THz radiation was directly focused on devices without any coupling antennas, resulting in limited detector responsivity. In addition, the plasma wave in an GaAs HEMT corresponds to a plasma resonant frequency up to ~ 10 THz. AlN/GaN nano-scale heterojunctions offer better structures with very large tunable frequency range up to ~ 100 THz due to their extraordinarily high carrier concentration and high carrier mobility. Thus, THz detectors using AlN/GaN HEMTs can have much broader tunable frequency range and better sensitivity.

In this work, we report our initial work on development of microwave and THz detectors using AlN/GaN HEMT devices. We have performed microwave measurements (10-40 GHz) using AlN/GaN HEMTs as detectors. The results have shown that the device works in non-resonant mode at room temperature with a responsivity roughly proportional to f^{-2} at low frequencies, which agrees well with the theoretical prediction. Measured responsivity as a function of gate bias also shows reasonable agreement with the theory and published results [4]. Measurements at W-band using Agilent 110 GHz vector network analyser (VNA), and at 200 GHz and 600 GHz using VDI (Virginia Diodes, Inc.) solid-state source will be performed to characterize the device behaviours at higher frequencies. Initial calculation results show that an AlN/GaN HEMT with 0.15 μm gate length works in the resonant mode when it is cooled down to 77K. The fundamental resonant frequency increases from 200 GHz to 3.2 THz with the gate-to-source voltage swing ($V_{gs} - V_{th}$) varies from 0.01 V to 2.0 V. The drain-to-source voltage

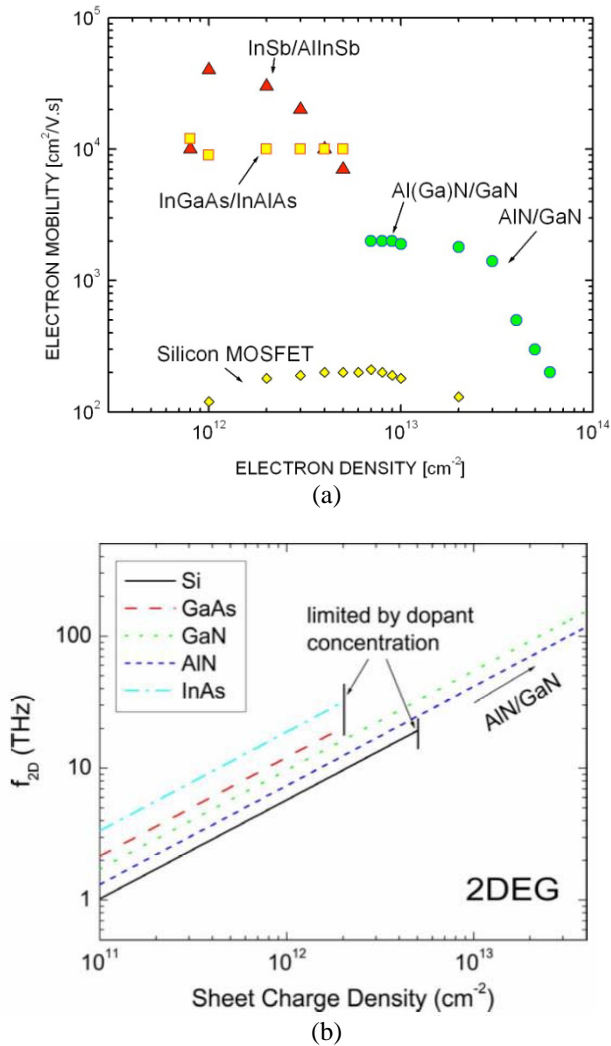


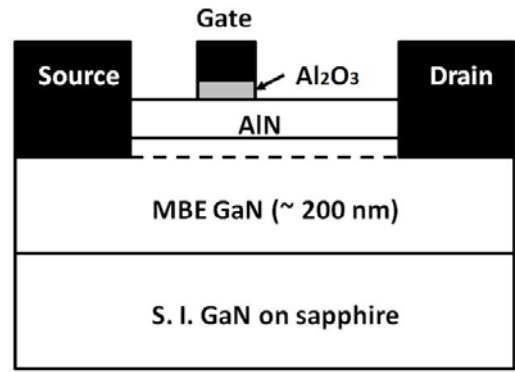
Fig. 1 (a) Carrier density and mobilities measured on AlN/GaN structures grown at Notre Dame in comparison with other 2DEG system [5], and (b) calculated corresponding plasma wave frequency in AlN/GaN HEMT devices and other semiconductors.

response also increases with increasing of the gate-to-source voltage swing.

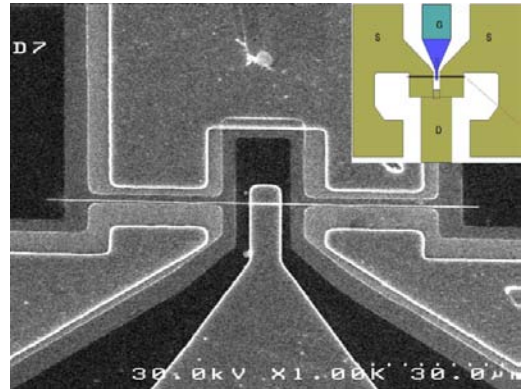
II. ALN/GAN HEMT DEVICES

High performance HEMT devices are desired in realizing tunable THz detectors. AlN/GaN HEMTs offer the advantages including simultaneously high 2-D electron-gas density (2DEG) and high carrier mobility, high current density, low sheet resistance and high transconductance [5-7].

As shown in Fig. 1 (a), nitride-based heterostructures have the extremely high 2DEG densities compared to other HEMT technologies. The fundamental upper limit of the polarization-induced 2DEG density at Al(Ga)N/GaN heterojunctions is nearly $6 \times 10^{13}/\text{cm}^2$, which is achievable only when the barrier layer is AlN, due to the maximum polarization (spontaneous and piezoelectric) difference between the AlN barrier and the underneath GaN layer [6]. At such a high 2DEG density, the carrier mobility is usually degraded. However, a window is observed in which the



(a)



(b)

Fig. 2 (a) Schematic of the AlN/GaN HEMT structure, and (b) SEM image of the device contact geometry.

AlN/GaN heterostructures have both high mobility ($1600 \text{ cm}^2/\text{V}\cdot\text{s}$) and high 2DEG density, resulting in highly sensitive THz detectors in a wide frequency range. According to (1), the resonant frequency is proportional to the square root of the 2DEG electron concentration. Fig. 1(b) shows the calculated plasma resonant frequencies in various semiconductors. The 2DEG formed at an AlGaAs/GaAs HEMT corresponds to a frequency up to 10 THz, while an AlN/GaN HEMT can attain much higher frequency up to 100 THz.

Fig. 2(a) shows the typical schematic of the AlN/GaN HEMT structure. The ultrathin AlN/GaN heterojunctions were grown at the University of Notre Dame using the process described in [6] using a Veeco Gen 930 plasma-assisted MBE system. The process starts from the growth of a 200 nm unintentionally doped (UID) GaN buffer layer, followed by a 3.5 nm UID AlN barrier. The device isolation mesa is fabricated using a BCl_3/Cl_2 reactive ion etch (RIE) process and Ti/Al/Ni/Au stacks were deposited to obtain ohmic contacts. The gates were defined using e-beam lithography. A 3 nm Al_2O_3 gate dielectric was deposited followed by a Ni/Au gate metal layer. Fig. 2(b) shows the SEM image of the device contact geometry for RF probing measurement. The fabricated AlN/GaN HEMT devices resulted in a typical carrier concentration of $2.75 \times 10^{13}/\text{cm}^2$, a

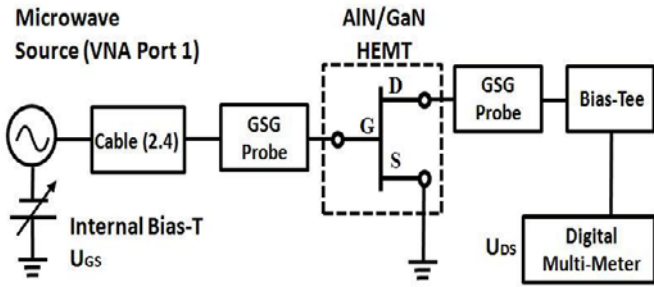


Fig. 3 AIN/GaN Detector measurement setup for microwave frequencies from 0.1 GHz to 40 GHz, the microwave power is provided by an Agilent 8722D vector network analyser.

carrier mobility of $1367 \text{ cm}^2/\text{V}\cdot\text{s}$, and a device sheet resistance of $\sim 166 \Omega/\square$.

III. MICROWAVE MEASUREMENT

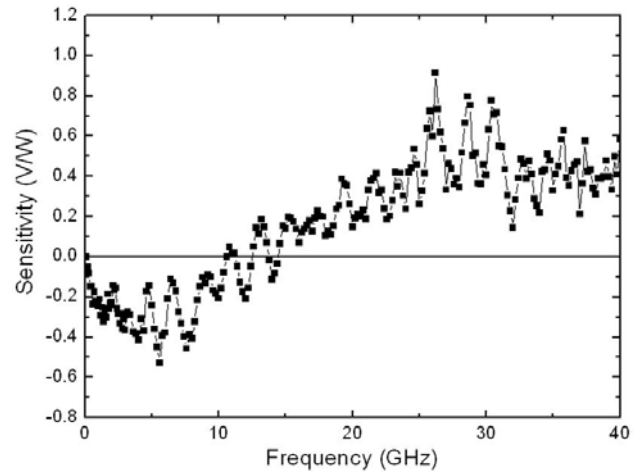
On the basis of the Dyakonov and Shur theory [1], a 2D electron fluid detector operates in a non-resonant regime at low frequencies when $f \rightarrow 0$. The detector responsivity, R , is determined by [1]:

$$R = \frac{|U_{ac}|^2 \pi^2 L^4}{P 6u^2 (U_{gs} - U_{th})^3} f^2, \quad (2)$$

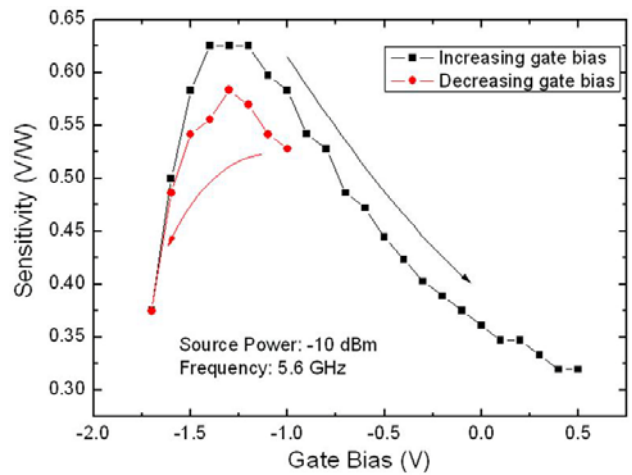
where U_{ac} is the microwave amplitude applied to the gate, P is the available microwave power, and u is the channel electron mobility.

To verify this, we have performed microwave measurement using AIN/GaN HEMTs as detectors, in the frequency range of 0.1 GHz to 40 GHz. The device for this study has a nominal gate length of $2 \mu\text{m}$, a gate width of $25 \mu\text{m}$, a measured threshold voltage of -3 V , and a carrier mobility of $\sim 1300 \text{ cm}^2/\text{V}\cdot\text{s}$. Fig. 4 shows the microwave measurement setup where the microwave power was provided by an Agilent 8722D vector network analyser. This allowed the input reflection coefficient to be measured when the incident RF frequency was swept from 0.1 to 40 GHz. The HEMT device was placed on a microwave probe station platform and fed by a GSG (Ground-Signal-Ground) microwave probe (see inset of Fig. 2 (b)), where the device gate was connected to the S-finger and the source was connected to the ground. The gate-to-source voltage was applied through the Agilent 8722D internal bias-T (Port 1). The device drain was connected to another GSG probe followed by the second bias-T (external), and the device DC response (i.e. the drain-to-source voltage, U_{ds}) was measured using a digital multimeter at the bias-port of the second bias-T. In this measurement, the output RF power from the VNA Port 1 (P_0) was fixed at -10 dBm , and the detector responsivity, R , is defined as $R = U_{ds}/P_0$. The intrinsic responsivity of the detector can be corrected on the basis of the reflection measurement (S_{11}) at Port 1.

Fig. 4 shows the initial microwave measurement results using AIN/GaN HEMTs as detectors. Impedance matching



(a)



(b)

Fig. 4 Microwave measurement results: (a) measured frequency dependence of detector responsivity (gate-to-source voltage swing -1 V), and (b) measured gate bias dependence of detector responsivity.

was not performed for this initial test, and the input reflection coefficient of the detector was found to be quite large (S_{11} average -0.05 dB) and a strong function of frequency over the entire frequency range (10-40 GHz). The cable loss of the measurement system was first measured, and then the device response was taken with gate biasing of -1 V . After cable loss (0-4 dB, depends on frequency) correction, the detector responsivity as a function of frequency is shown in Fig. 4(a). From nearly 15 GHz, the measured responsivity increases from 0 to 1 V/W (at 26 GHz) and then becomes relatively flat, with an average around 0.5 V/W . The responsivity is roughly proportional to f^2 at low frequencies (15-26 GHz), which agrees well with theoretical prediction. The behaviour at frequencies higher than 26 GHz will be discussed in the later section. At frequencies lower than 15 GHz, negative responsivities were measured, which is not well understood at this time. Taking into account of the large reflection at the input port, the intrinsic responsivity of the AIN/GaN HEMT as a microwave detector will be in the

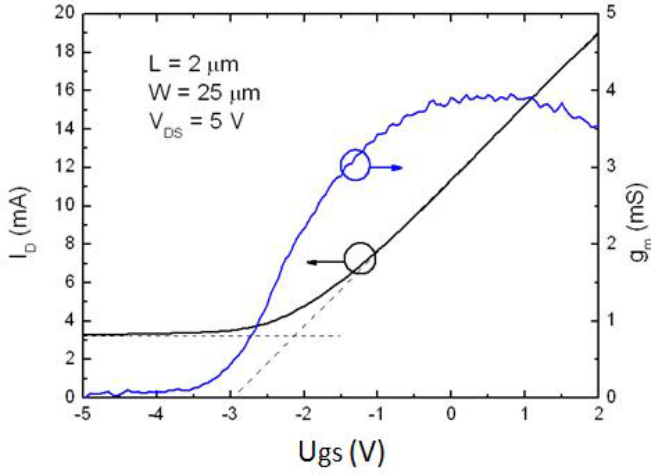


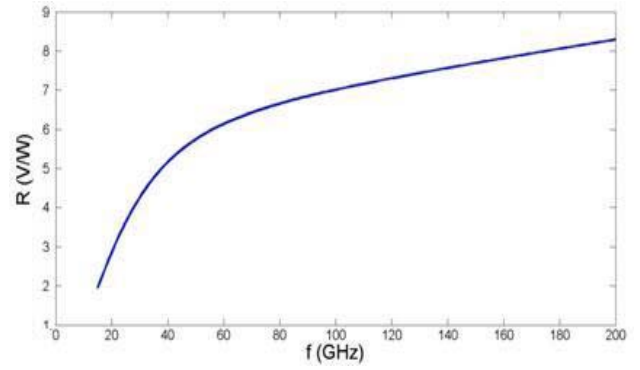
Fig. 6 DC I-V transfer curves for the AlN/GaN HEMT device under test.

range of 0-10 V/W. Measured responsivity as a function of gate bias at 5.6 GHz is shown in Fig. 4 (b). The responsivity increases with decreasing gate biasing voltage when $U_{gs} > -1.6$ V, and decreases rapidly when $U_{gs} < -1.4$ V. The detector theory in (2) and [1] only valid at $U_{gs} > -1.4$ V. The gate bias dependence of the responsivity shows reasonable agreement with the theory and published results [4]. We attribute the discrepancy to the relatively low quality of the device in this study. As shown in Fig. 5, the DC I-V transfer curves for the AlN/GaN HEMT device under test show relatively large drain current leakage (~ 3 mA) after pinch-off (i.e. $U_{gs} < -3$ V), and relatively small transconductance. Better devices will be utilized in the future measurement.

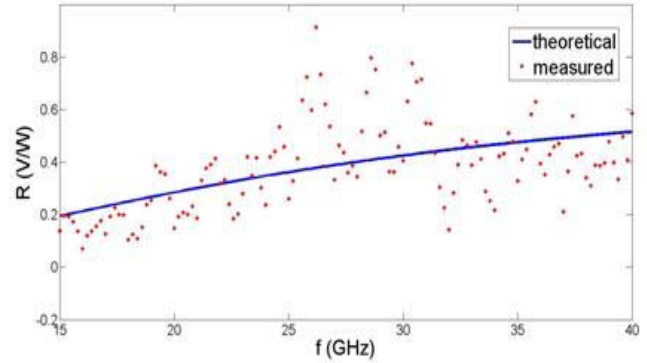
IV. ALN/GAN HEMT THZ DETECTORS

At terahertz frequencies, the plasma wave in a HEMT device resonates at fundamental frequency and its odd harmonics (see equation (1)). If $\sigma\tau/L > 1$, the HEMT works in the resonant mode, and the detection frequency can be tuned by the gate-to-source biasing, according to (1). If $\sigma\tau/L < 1$, the HEMT then works as a non-resonant broadband THz detector. On the basis of the Dyakonov and Shur theory [1], we have solved the 2D electron fluid equations in an AlN/GaN HEMT channel.

Nonresonant THz Detectors: For the AlN/GaN HEMT device under test in this study, we use $m_e = 0.2 m_0$ (where m_e is the effective mass and m_0 is the electron mass), gate length $L = 2 \mu\text{m}$, and carrier mobility $u = 1300 \text{ cm}^2/\text{V}\cdot\text{s}$ (room temperature). Fig. 6 (a) shows the calculated detector responsivity (gate biasing -1 V) over the frequency range of 0 to 200 GHz. The responsivity increases rapidly at frequencies lower than 80 GHz, and then increases much slower at higher frequencies. The curve is quite smooth and no resonance is observed, demonstrates that the device works in a nonresonant mode ($\sigma\tau/L \sim 0.02 \ll 1$). We compare the calculated results with the measurement data from 15 GHz to 40 GHz by taking into account of the large reflection at port 1, as shown in Fig. 6 (b). The agreement between theory and measurement is quite good at this microwave frequency range.



(a)



(b)

Fig. 6 Nonresonant AlN/GaN HEMT detector: (a) calculated detector responsivity, and (b) comparison between theory and measurement. The HEMT device under study (theory) has a gate length of $2 \mu\text{m}$, and a carrier mobility of $1300 \text{ cm}^2/\text{V}\cdot\text{s}$ (room-T). In addition, we use $m_e = 0.2 m_0$ for GaN systems.

Resonant THz Detectors: A THz HEMT detector is predicted to have much higher responsivity when it works in the resonant mode [1]. In order to have a resonant mode THz AlN/GaN detector, the value of $\sigma\tau/L$ must be greatly increased. Since the momentum relaxation time τ is determined by,

$$\tau = um_e / e \quad , \quad (3)$$

the device can be cooled down to lower temperatures for higher carrier mobility. For GaN systems, u can be significantly increased from $\sim 1000 \text{ cm}^2/\text{V}\cdot\text{s}$ at room-T to $\sim 6500 \text{ cm}^2/\text{V}\cdot\text{s}$ at 77 K. In addition, the device effective gate length L should be decreased. Our calculation shows that an AlN/GaN HEMT with $0.15 \mu\text{m}$ gate length at 77 K has resonant features on its frequency dependent responsivity curves. As shown in Fig. 7 (a), the fundamental resonant frequency of an cooled AlN/GaN HEMT (77 K, $0.15 \mu\text{m}$ gate length) with 0.01 V gate-to-source voltage swing ($V_{gs} - V_{th}$) is nearly 200 GHz, and its third harmonic frequency is 600 GHz. As shown in Fig. 7 (b), the fundamental resonant frequency increases from 200 GHz to 3.2 THz with the gate-to-source voltage swing varies from 0.01 V to 2.0 V. The drain-to-source voltage response also increases with increasing of the gate-to-source voltage swing. These

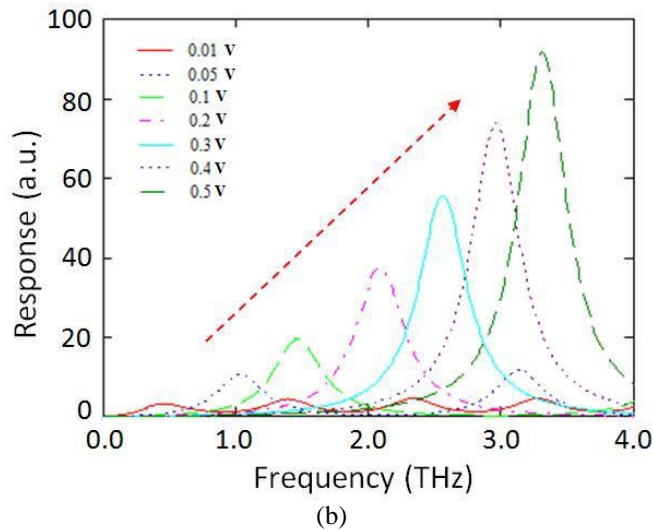
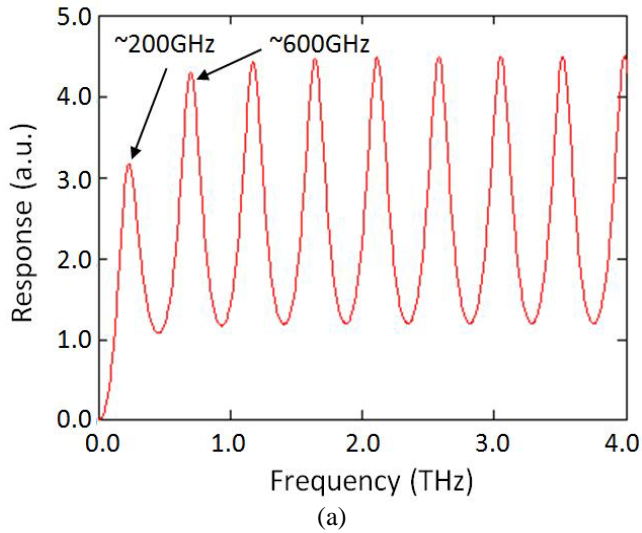


Fig. 7 Resonant AlN/GaN HEMT detector: (a) calculated detector response ($V_{gs}-V_{th} = 0.01$ V) as a function of frequency, and (b) the detector response at various gate-to-source voltage swing. The HEMT device under study (theory) has a gate length of $0.15 \mu\text{m}$, and a carrier mobility of $6300 \text{ cm}^2/\text{V}\cdot\text{s}$ (77 K). We use $m_e = 0.2 m_0$ for GaN systems in this calculation.

features are very attractive at THz region. Measurements at 180-220 GHz and 570-630 GHz are currently under way. The AlN/GaN HEMT devices will soon be integrated with broadband lens-coupled antennas [8] and low-pass filters for tunable plasma wave THz detectors.

V. CONCLUSIONS

We have performed microwave measurement (0.1-40 GHz) using AlN/GaN HEMTs as detectors. The results have

shown that the device works in non-resonant mode at room temperature with a responsivity agrees well with the theoretical prediction. Measured responsivity as a function of gate bias also shows reasonable agreement with the theory and published results. Room temperature responsivity measurement at W-band using Agilent 110 GHz vector network analyser (VNA), and at 200 GHz and 600 GHz using VDI (Virginia Diodes, Inc.) solid-state source are currently underway. Initial calculation results show that an AlN/GaN HEMT with $0.15 \mu\text{m}$ gate length works in the resonant mode when it is cooled down to 77K. The fundamental resonant frequency increases from 200 GHz to 3.2 THz with the gate-to-source voltage swing ($V_{gs}-V_{th}$) varies from 0.01 V to 2.0 V. The drain-to-source voltage response also increases with increasing of the gate-to-source voltage swing. The AlN/GaN HEMT devices are planned to be integrated with broadband lens-coupled antennas and low-pass filters for tunable plasma wave THz detectors.

ACKNOWLEDGMENT

The authors would like to thank their colleagues in the Nano Materials and Devices Laboratory and the High Speed Electronic Devices and Circuits Laboratory at the University of Notre Dame. This work is funded by the Office of Naval Research (Dr. Paul Maki).

REFERENCES

- [1] M. Dyakonov, and M. S. Shur, "Shallow water analogy for a ballistic field effect transistor, new mechanism of plasma wave generation by DC current," *Phys. Rev. Lett.*, vol. 71, no. 15, 1993.
- [2] W. Knap, *et al.*, "Nonresonant detection of terahertz radiation in field effect transistors," *J. Appl. Phys.*, vol. 91, no. 11, 2002.
- [3] A. Wl Fatimy, *et al.*, "Resonant and voltage-tunable terahertz detection in InGaAs/InP nanometer transistors," *Appl. Phys. Lett.*, 89, 131926, 2006.
- [4] R. M. Weikle, II, J.-Q. Lü, M. S. Shur, and M. I. Dyakonov, "Detection of microwave radiation by electronic fluid in high electron mobility transistors," *Electron. Lett.*, vol. 32, no. 23, 1996.
- [5] D. Deen, T. Zimmermann, Y. Cao, D. Jena, and H. G. Xing, "2.3 nm AlN/GaN high electron mobility transistors with insulated gates," *Phys. Solid. Stat. (c)*, vol. 5, no. 6, 2008.
- [6] T. Zimmermann, D. Deen, Y. Cao, J. Simon, P. Fay, D. Jena, and H. G. Xing, "AlN/GaN insulated gate HEMTs with 2.3 A/mm output current and 480 mS/mm transconductance," *IEEE Electron. Device Lett.*, vol. 29, no. 7, 2008.
- [7] H. Xing, T. Zimmermann, D. Deen, Y. Cao, D. Jena, and P. Fay, "Ultrathin AlN/GaN heterostructure based HEMTs," *International Conference on Compound Semiconductor Manufacturing Technology*, Chicago, USA, Apr. 2008.
- [8] L. Liu, J. L. Hesler, H. Xu, A. W. Lichtenberger, R. M. Weikle, II, "A quasi-optical broadband terahertz detector utilizing a zero bias Schottky diode," submitted to *IEEE Microwave and Wireless Components Letters*.

Poster Session P5: Optics and Waveguides

A Waveguide Orthomode Transducer for 385-500 GHz

A. Navarrini¹, C. Groppi², and G. Chattopadhyay³

¹*INAF-Cagliari Astronomy Observatory, Italy*

²*ASU School of Earth and Space Exploration, USA*

³*NASA-Jet Propulsion Laboratory, USA*

* Contact: navarrin@ca.astro.it, phone +39-070-711 80 218

Abstract— We describe the design, construction, and performance of a waveguide Orthomode Transducer (OMT) for the 385-500 GHz band. The OMT is based on a symmetric backward coupling structure and has a square waveguide input (0.56x0.56 mm²) and two single-mode waveguide outputs: a standard WR2.2 waveguide (0.56x0.28 mm²) and an oval waveguide with full-radius corners. The OMT is rescaled from a lower frequency design that was developed for the 3 mm band; it was optimized using a commercial 3D electromagnetic simulator.

The OMT consists of two mechanical blocks in split-block configuration that were fabricated using conventional CNC milling machine. A first prototype copper alloy OMT employing standard UG387 flanges at all ports was fabricated and tested. From 385 to 500 GHz the measured input reflection coefficient was less than -10 dB, the isolation between the outputs was less than -25 dB, the cross polarization was less than -10 dB, and the transmission was \approx 2 dB at room temperature for both polarization channels.

The effects of misalignment errors in the OMT performance were studied using electromagnetic simulation.

A second OMT version utilizing custom made mini-flanges and much shorter waveguides was designed and will be tested soon. This novel OMT is more tolerant to misalignment errors of the block halves and is expected to have much improved performance over the first prototype.

I. INTRODUCTION

An Orthomode Transducer (OMT) is a passive device that separates two orthogonal linearly polarized signals within the same frequency band. An OMT has three physical ports but exhibits properties of a four-port device because the input common port, usually a waveguide with a square or circular cross-section, provides two electrical ports that correspond to the independent orthogonal polarized signals. In modern radio-astronomy receivers, requirements of the OMT are a high cross-polarization discrimination between the orthogonal signals, low insertion loss, and a good match of all electrical ports over relative bandwidths of 30% or wider. Several asymmetric OMTs have been designed to cover

bandwidths of less than 30% [1]-[2]. Highly symmetric structures are required to avoid the excitation of higher order modes and achieve broad bandwidth (up to 40% or wider.)

Because the small dimensions and tight tolerances pose a significant challenge for the fabrication and assembly of the parts, only few broadband OMT designs have been demonstrated to work well at frequencies greater than \approx 100 GHz. These designs are based on: *a*) the two-fold symmetric Bøifot junction [3]-[6] adopted for ALMA Band 3 (84-116 GHz) and Band 6 (211-275 GHz); *b*) the four-fold symmetric turnstile junction [7]-[9] adopted for CARMA 200-270 GHz and Clover 75-110 GHz; *c*) the double ridged Bøifot-type junction [10]-[11] adopted for ATNF 70-117 GHz and for ALMA Band 4 (125-163 GHz), Band 5 (163-211 GHz), and Band 8 (385-500 GHz); *d*) the reverse-coupling waveguide junction [12]-[13] adopted for the 84-116 GHz band of the Sardinia Radio Telescope.

In particular, the highest frequency range for which a broadband OMT has been developed and employed in a large project is the 385-500 GHz of ALMA Band 8 [14]; the OMT is based on a double ridged Bøifot-type junction.

Alternative OMT designs based on finline [15] or planar structures have also been proposed for use at millimetre and submillimetre wavelengths.

Here, we present the design and performance of two waveguide OMT prototypes for the 385-500 GHz band which are based on a symmetric reverse-coupling architecture. The first OMT prototype, presented in Sec. II, utilizes standard UG387 flanges and has long input and output waveguide sections. The second OMT prototype, presented in Sec. III, utilizes custom made mini-flanges, has much shorter input and output waveguides, and is more tolerant to misalignment errors of the mechanical blocks.

II. FIRST OMT PROTOTYPE

A. Architecture of the first OMT prototype

The design of our first 385-500 GHz OMT is directly rescaled from the lower frequency device developed for the 3 mm band (84-116 GHz band) presented in [13]. Our 385-500 GHz waveguide OMT, illustrated in Fig. 1, is based

on a reverse-coupling structure and consists essentially of: *a*) a $0.56 \times 0.56 \text{ mm}^2$ square waveguide input (Port 1) that transitions to a full-height WR2.2 ($0.56 \times 0.28 \text{ mm}^2$) rectangular waveguide through a two-section transformer; the transformer is followed by a 90 deg E-plane rectangular-to-oval waveguide bend; *b*) two symmetric 90° waveguide hybrid couplers on the sidearms utilizing reactively terminated ports (dual-side backward coupler); *c*) an E-plane 180° waveguide hybrid (Y-junction) to recombine the out-of-phase signals from the two backward coupling structures.

The OMT single-mode waveguide outputs are: *a*) an oval waveguide with full-radius corners and external cross-section $0.62 \times 0.28 \text{ mm}^2$ for Pol 1 (Port 2); *b*) a standard WR2.2 rectangular waveguide for Pol 2 (Port 3.)

The square waveguide input propagates two orthogonal linear polarized signals Pol 1 and Pol 2 associated, respectively, with the TE_{10} and TE_{01} fundamental modes, when the wavelength is below the cut-off value $\lambda_c(TE_{10})=2a=1.12 \text{ mm}$ (frequencies above $\nu_c=267.67 \text{ GHz}$.) Besides the fundamental modes, higher order modes can propagate in the square waveguide in the 385-500 GHz frequency band of interest. These are the TE_{11} and TM_{11} that have the same cut-off frequency of $\nu_c=378.55 \text{ GHz}$. In theory, these modes can be excited by the discontinuity created by the apertures (slots) of the sidearms. However, their excitation can be avoided as long as the two-fold symmetry of the structure is maintained. The adopted symmetry enables broadband operation allowing to achieve a relative bandwidth for the device larger than ~30 %.

The symmetric coupling structure in the common square waveguide arm splits, with opposite phases, the incoming Pol 2 signal in the two rectangular waveguide sidearms. Signal coupling to each sidearm is obtained with a broadband 90° hybrid coupler realized as a 3-dB E-plane branch-line coupling structure with four branches. The four 0.10 mm wide apertures through the broad walls of the waveguide sidearms are equally spaced of 0.072 mm (see details in Fig. 2.) The branches have a length of 0.178 mm. The through port and the coupled port of each hybrid are terminated with reactive loads for Pol 2. In the common arm, the reactive load is provided by a two-section transformer polarization discriminator that reflects back all Pol 2 power in the 385-500 GHz frequency range of design. Indeed, the output rectangular waveguide section of such transformer has size $0.56 \times 0.28 \text{ mm}^2$ that cuts off the propagation of the TE_{01} mode associated with Pol 2 to frequencies above $\nu_c(TE_{01})=535.34 \text{ GHz}$, outside our operating range. On the other hand, the orthogonal polarization, Pol 1, is relatively unaffected by the presence of both the branch-line apertures in the two sidearms and of the common arm two-section transformer. Each section of such transformer is approximately a quarter wavelength long. Therefore, Pol 1 is well matched to the output and is fully coupled (forward coupling) to an E-plane 90 deg bend transition that brings out, orthogonal to the main arm, the oval cross section port; the oval waveguide is easy to machine with an end-mill and can be attached to a standard WR2.2 waveguide producing a

negligible power reflection (return loss >38 dB across 385-500 GHz.)

The two Pol 2 signals emerging backward with -3 dB power from the sidearms of the reverse-coupling structure travel through two symmetric waveguide paths. Each Pol 2 signal travels through a 180 deg WR2.2 waveguide E-plane bend (0.96 mm inner diameter), a straight waveguide section (length of 2.2 mm), and a 90 deg waveguide E-plane bend (0.85 mm inner diameter;) the two Pol 2 signals are recombined by an E-plane Y-junction power combiner with standard WR2.2 output whose axis is coincident with the one

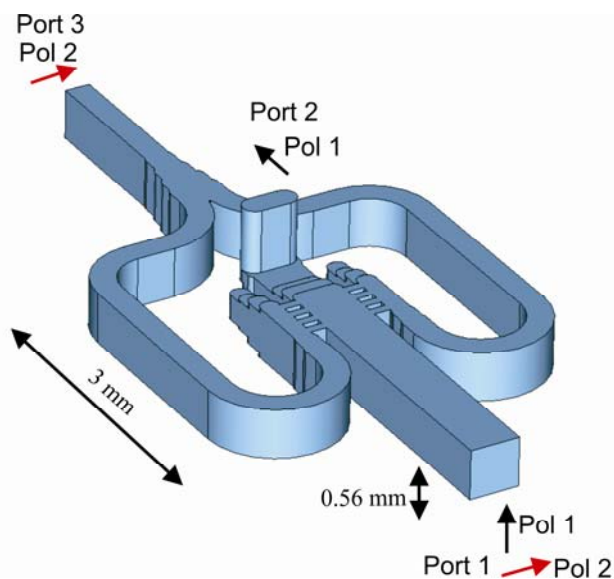


Fig. 1. Internal view of the symmetric dual-side backward coupler OMT.

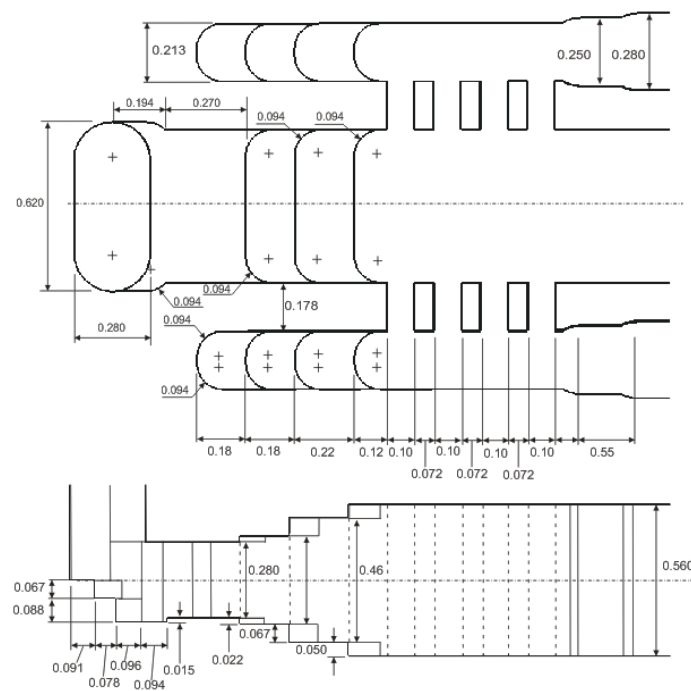


Fig. 2. Cutout views with dimensions (in mm) of the symmetric backward couplers of Fig. 1. The structure was optimized for operation in the 385-500 GHz band.

of the square waveguide input. The combiner is based on a design by Kerr [16].

In the rectangular waveguide sidearms, the reactive loads for Pol 2 are provided by a short circuited three-step H-plane discontinuity (two transformer sections.) The transformer sections have the same physical length and height in the sidearms and in the common arm to guarantee that Pol 2 sees the same impedance when looking toward the through and coupled ports of the hybrids. This allows the split Pol 2 signals, which are reflected backward by the reactive loads, to recombine out-of-phase in the common arm (thus providing a destructive interference with low reflection at the common port) and in-phase in the two opposite sidearms. The constructive interference of the backward waves provides a coupling of -3 dB to each rectangular output port. Pol 2 signals at these two ports are 180° out-of-phase to each other because the E-field signal at the common square input couples to the two sidearm hybrids in opposite directions. The rectangular waveguide sidearms have a reduced height in the coupling section of the hybrids (0.213 mm rather than full 0.280 mm) in order to increase the bandwidth of the device.

The waveguide steps of the two-section transformers have round corners (radius 0.094 mm) to allow easy machining of the parts with an end-mill. Each reduced-height rectangular waveguide sidearm carrying the reverse-coupled -3 dB Pol 2 signal is transformed to a standard WR2.2 full-height 0.56×0.28 mm² waveguide at the hybrid signal output. This is accomplished by a single-section quarter-wave transformer, 0.55 mm long.

The electrical performance of the OMT was optimized using the commercial electromagnetic simulator CST Microwave Studio¹ based on the finite integration technique.

B. Electromagnetic simulation of the first OMT prototype

The first OMT prototype has long input and output waveguides (see Fig. 3) with lengths, respectively 11.3 mm and 10.8 mm. This OMT utilizes standard UG387 flanges. The physical length of the waveguide circuit of the OMT from input to output ports is approximately 14 mm for Pol 1 and 31 mm for Pol 2.

The simulation results for the reflected amplitude of the two independent fundamental modes TE₁₀ (Pol 1) and TE₀₁ (Pol 2) at the square waveguide input of the device of Fig. 3 are illustrated in Fig. 4. The reflection coefficient is below -17 dB for both polarizations over the entire band of interest.

The simulated transmission losses at 300 K and at 4 K of the two polarization channels of the OMT are shown in Fig. 5. In the simulation, we assumed the waveguide conductor to have perfectly smoothed walls with conductivities $\sigma=4.26 \cdot 10^7 \Omega^{-1}m^{-1}$ at 300 K (same as the dc conductivity of Gold) and $\sigma=10.0 \cdot 10^7 \Omega^{-1}m^{-1}$ at 4 K. The simulated transmissions are about -0.35 dB for Pol 1 and about -1 dB

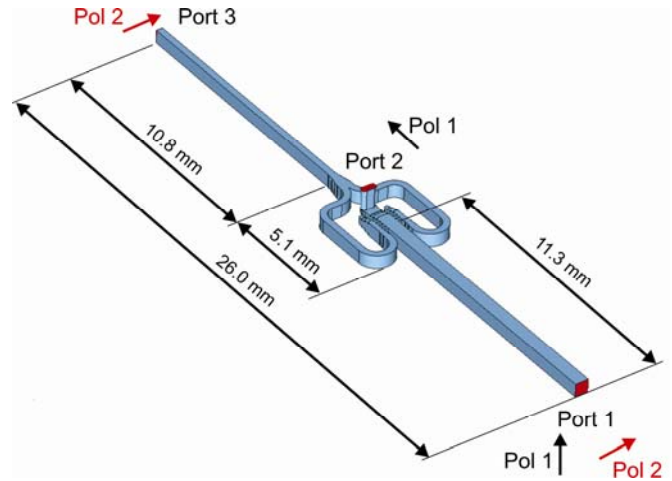


Fig. 3. Full view of the inner parts of the first OMT prototype showing the long square waveguide input (11.3 mm) and rectangular waveguide output (10.8 mm) of the reverse-coupling structure. The oval waveguide has a length of only 1 mm.

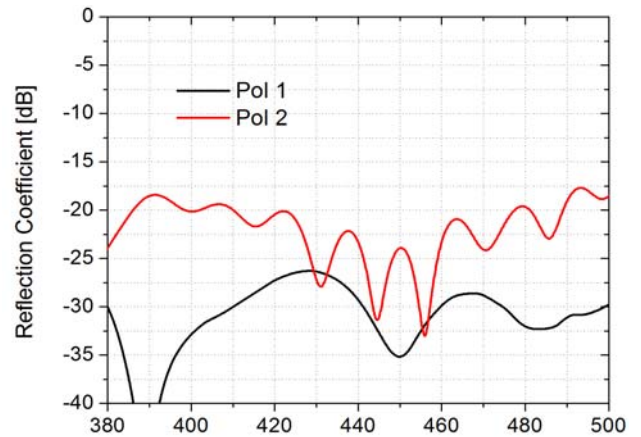


Fig. 4. Simulated reflection coefficient at the common waveguide port of the three-port device illustrated in Fig. 3.

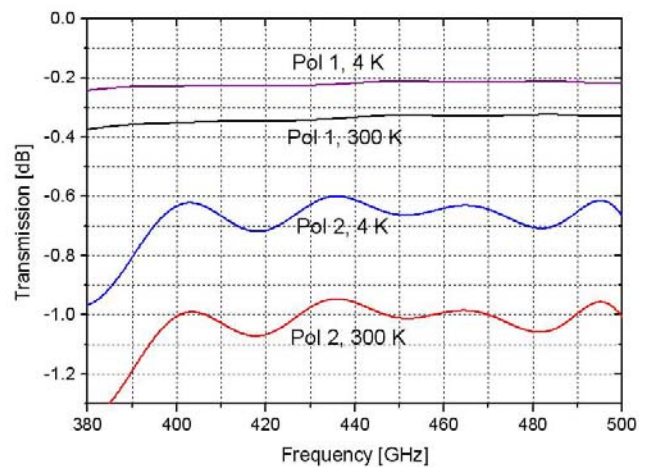


Fig. 5. Simulated transmissions of the full OMT illustrated in Fig. 3.

¹ CST Microwave Studio, Darmstadt, Germany.

for Pol 2 at 300 K. Under these assumptions the losses at 4 K reduce to $(4.26/10)^{0.5} \approx 64\%$ of the 300 K values.

To evaluate the contribution to the OMT insertion loss due to the input and output waveguide sections of the device, we simulated the loss of a straight section of a 11.3 mm long $0.56 \times 0.56 \text{ mm}^2$ square waveguide and of a 10.8 mm long WR2.2 waveguide. The simulation results across 385-500 GHz, shown in Fig. 6, indicate that the losses at 300 K are $\approx 0.2 \text{ dB/cm}$ and $\approx 0.3 \text{ dB/cm}$ for, respectively the square waveguide and the WR2.2 waveguide. Therefore, in the OMT, more than half of the room temperature insertion loss of Pol 1 is due to the square waveguide input, and about half of the insertion loss of Pol 2 is due to the square waveguide input plus rectangular waveguide output.

The cross-polarization and isolation levels of the OMT is expected to be zero ($-\infty \text{ dB}$) for the perfectly symmetric model of Fig. 3. The extremely low but finite value (less than -100 dB) obtained from simulation is due to the numerical rounding off errors in the computation.

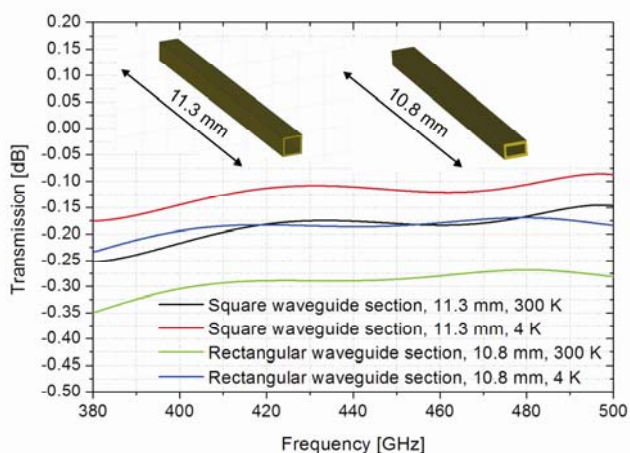


Fig. 6. Simulated transmissions loss of 11.3 mm long square waveguide (cross-section $0.56 \times 0.56 \text{ mm}^2$) and 10.8 mm long WR2.2 rectangular waveguide (cross-section $0.56 \times 0.28 \text{ mm}^2$) at 300 K and 4 K.

C. Mechanical blocks of the first OMT prototype

The OMT consists of two mechanical blocks and is fabricated by splitting the structure of Fig. 3 along the E-plane of the side-coupled rectangular waveguides. The device has external dimensions $19 \times 26 \times 28 \text{ mm}^3$ and accepts standard UG387 flanges at all ports. A circular pocket (diameter 20 mm, depth 8.5 mm) is machined into one of the blocks to reduce the oval waveguide to a length of only 1 mm. Photographs of the assembled OMT and of the two unassembled OMT blocks are shown, respectively in Fig. 7 and Fig. 8. The blocks were fabricated in 145 Copper alloy (unplated) using a Kern Micro numerically controlled milling machine at University of Arizona.

Photographs of the internal details of the blocks are shown in Figs. 9-10. The blocks were aligned using two precision $1/16''$ diameter dowel pins. The tolerances for the waveguide channels in the two blocks and of the alignment between the blocks were specified at $\pm 5 \mu\text{m}$. The blocks are bolted together by four 4-40 stainless steel screws.

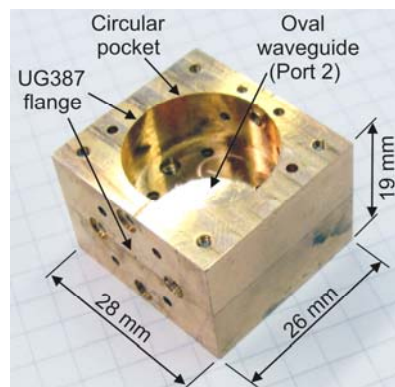


Fig. 7. Photograph of the assembled OMT (first prototype) with UG387 flanges at all ports.

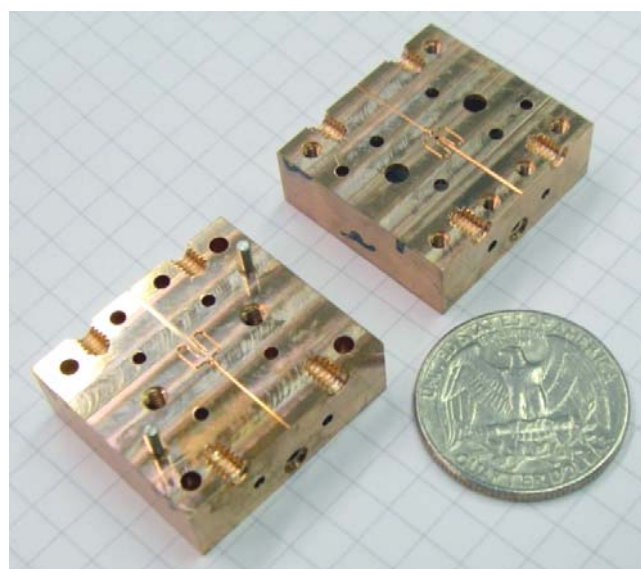


Fig. 8. Photograph of the two unassembled blocks of the first OMT prototype showing the internal waveguide circuitry.

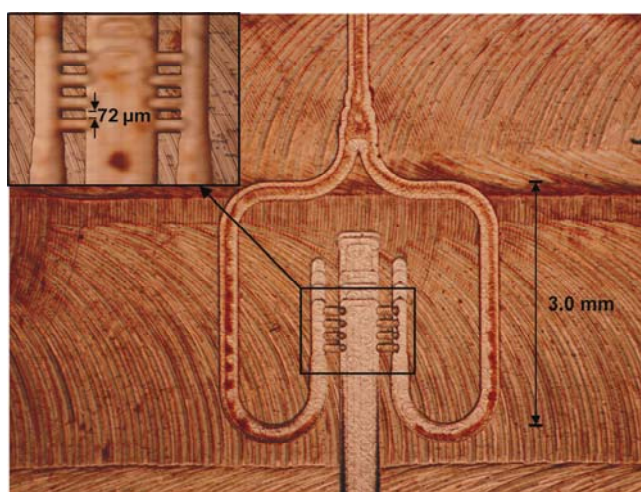


Fig. 9. Photograph of the internal details of one of the OMT blocks showing the dual-backward coupler waveguide circuitry and the three metal "teeth" between branch-line slots on both sidearms (close-up view.) The oval waveguide is also visible on the right.

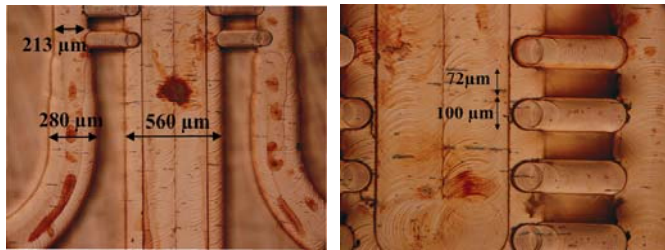


Fig. 10. Detail of the three metal “teeth” between branchline slots of one of the coupler sidearms.

D. Experimental results of the first OMT prototype

The OMT was tested at JPL (Jet Propulsion Laboratory) using a Vector Network Analyser (VNA) consisting of a HP8510C Network Analyser and submillimeter-wave OML test set extensions. The VNA was calibrated at the WR2.2 rectangular waveguides outputs of the extension heads using two-port calibrations with WR2.2 calibration kit. The calibration procedure was used to remove systematic instrumental effects and to calibrate out the response of the instrument up to the chosen calibration planes (see Fig. 11.) Additional measurement of two pairs of identical back-to-back WR2.2 waveguide-to-square waveguide transition² (3/4” long, linearly tapered from one end to the other, with UG387 flanges at both sides) allowed to calibrate out their individual effects and to derive the S-parameters of the OMT at the physical ports of the device.

A schematic of the Pol 2 transmission test setup is shown in Fig. 11. The square waveguide input of the OMT was attached to the WR2.2 waveguide port of the network analyser (Port 1) through the WR2.2 waveguide-to-square waveguide transition. The transition was oriented to excite the Pol 2 in the OMT. The WR2.2 waveguide output of the OMT was attached to the second WR2.2 waveguide port of the analyser (Port 2.) The oval waveguide of the OMT was terminated with a matched WR2.2 waveguide. The transmission measurement of the other polarization channel was obtained with a setup similar to the one in Fig 11 but with WR2.2 waveguide-to-square waveguide transition rotated by 90 deg to excite Pol 1 at the OMT input and with waveguide matched load and second port of the analyser swapped at the OMT outputs. A photograph of the transmission test setup of Pol 1 is shown on Fig. 12.

The measured transmissions of the OMT are illustrated in Fig. 13. The average measured transmission of the OMT is ≈ -1.7 dB for Pol 1 and ≈ -2.2 dB for Pol 2, much larger in overall level of the values predicted by simulation (see Fig. 5.)

The reflection coefficient at the OMT input port was measured for both polarizations by terminating the OMT outputs with WR2.2 matched loads. The amplitude of the measured reflection is below -10 dB for both polarization channels (Fig. 14.)

An estimate of the isolation was obtained by measuring the transmissions from the OMT output ports with its square waveguide input port open to free space. This gives an upper

limit of the isolation of the device. The measured isolation is below -25 dB (Fig. 15.)

The cross-polarization of the OMT is the transmission from one polarization channel at the square waveguide input to the unwanted output channel when the other two electrical ports (of the four electrical ports device) are terminated into a matched load. We estimated the cross-polarization of the OMT by using a transmission setup similar to the one in Fig. 12, where the square waveguide-to-rectangular waveguide transition is connected to VNA port 1 to inject one polarization signal at the OMT square waveguide input port, the VNA port 2 is connected to the “unwanted” OMT output, and the second OMT output is terminated into a WR2.2 matched load. The measured cross polarization level is below -10 dB across the band of interest (Fig. 16.)

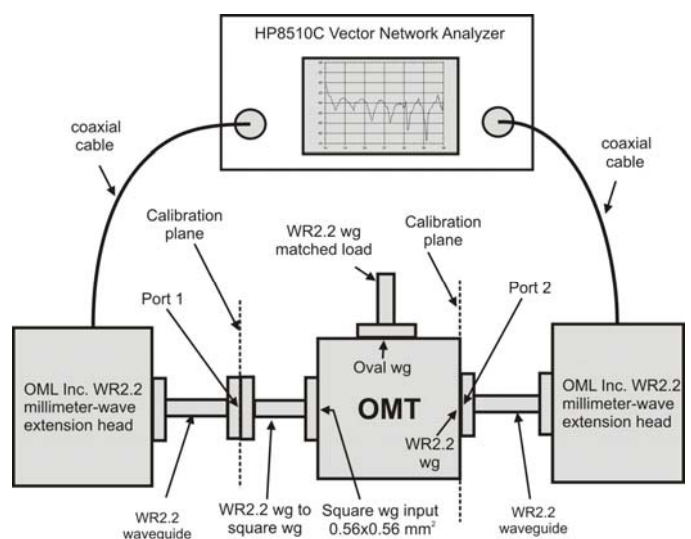


Fig. 11. S-parameter measurement of the OMT with the vector network analyser. The particular configuration refers to the transmission measurement of Pol 2.



Fig. 12. Photo of the OMT during Pol 1 transmission measurement with the vector network analyser.

² Radiometer Physics GmbH, Germany.

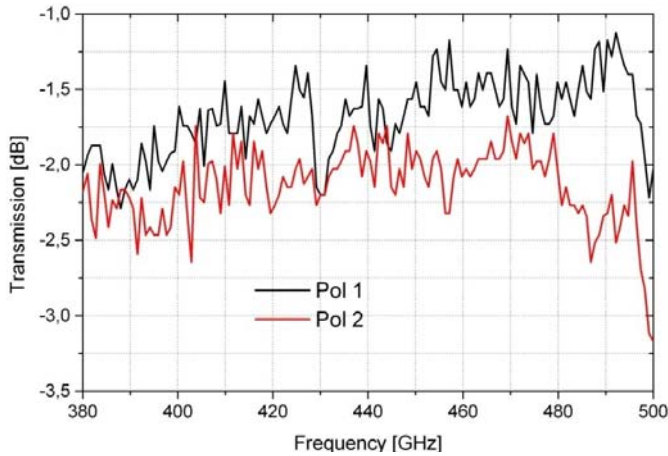


Fig. 13. Measured transmissions of the first OMT prototype (at room temperature.)

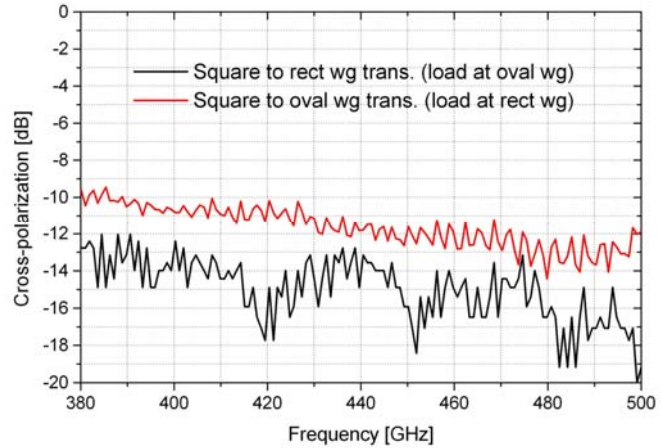


Fig. 16. Measured cross-polarization of the first OMT prototype.

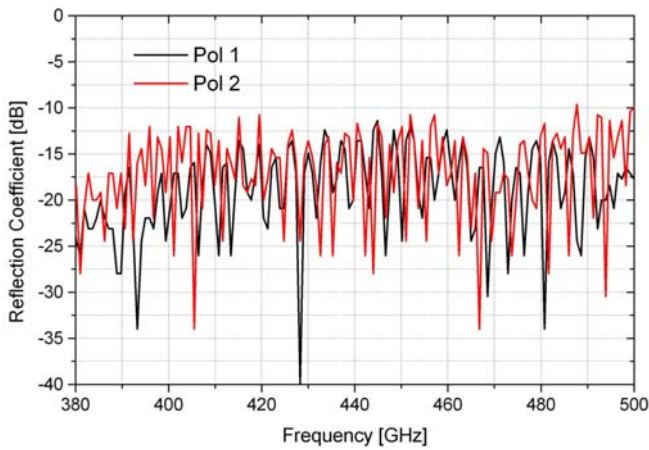


Fig. 14. Measured input reflections of OMT (first prototype.)

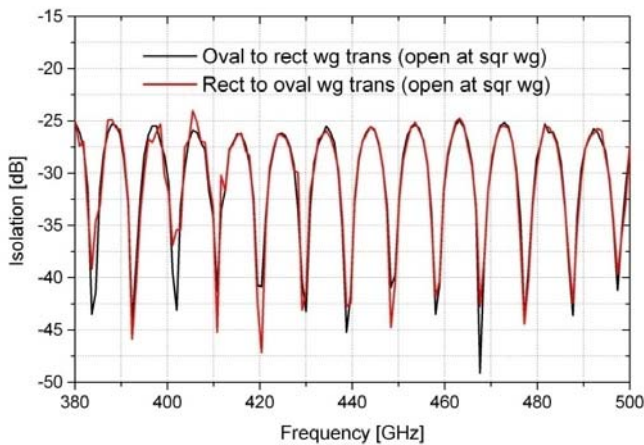


Fig. 15. Measured upper limit of the isolation of the OMT (first prototype): transmission between output ports with square waveguide input open to free space.

E. Electromagnetic simulation of misaligned square waveguides

The measured performance of the first OMT prototype are clearly inferior to what expected from the electromagnetic simulation of the “ideal” device of Fig. 3. As a first step to understand the observed differences between simulation and measure, we estimated, using simulation, the contribution to the cross-polarization due to a lateral misalignment δ of a square waveguide section of length l (see Fig. 17) as it would result from a lateral shift of two block halves. The cross-polarization is, in this case, the coupling between Pol 1 at one end and Pol 2 at the other end of the square waveguide.

The cross-polarization was simulated for misaligned square waveguides with cross-section $0.56 \times 0.56 \text{ mm}^2$ (guided wavelength $\lambda_g \approx 0.86 \text{ mm}$ around the central frequency of 440 GHz.) We used waveguide lengths $l=11.3 \text{ mm}$ (same as the input waveguide section of the OMT, $\approx 13 \lambda_g$), $l=2 \text{ mm}$ ($\approx 2.3 \lambda_g$), and lateral misalignments δ of 2 and 5 μm .

The simulation results are shown in Fig. 18. We can see that for $l=11.3 \text{ mm}$, even a misalignment as small as $\delta=5 \mu\text{m}$ generates a cross-polarization level of $\approx -10 \text{ dB}$, which is of the same level of the one measured in the OMT. Reducing the square waveguide length down to $l=2 \text{ mm}$ decreases the cross-polarization level to $\approx -25 \text{ dB}$ (using the same $\delta=5 \mu\text{m}$.) If we could reduce the misalignment to $\delta=2 \mu\text{m}$ in a waveguide with $l=2 \text{ mm}$ the cross-polarization would decrease to $\approx -33 \text{ dB}$.

Therefore, for a given misalignment δ , the cross-polarization level is greater for a longer waveguide, while for a given waveguide length l , the cross-polarization level is greater for a larger misalignment.

In conclusion, the cross-polarization level can be minimized by choosing the shortest possible square waveguide length at the OMT input.

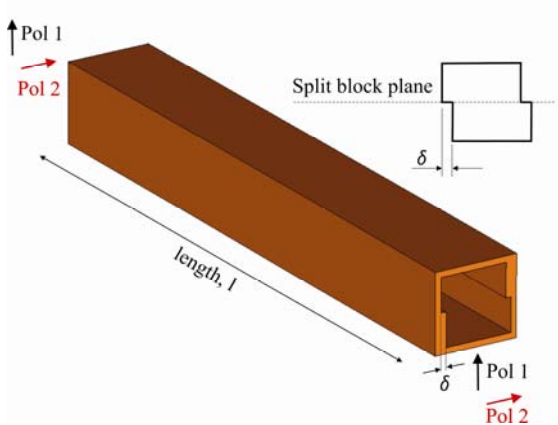


Fig. 17. Square waveguide of length l with lateral misalignment δ along the E-plane of Pol 2.

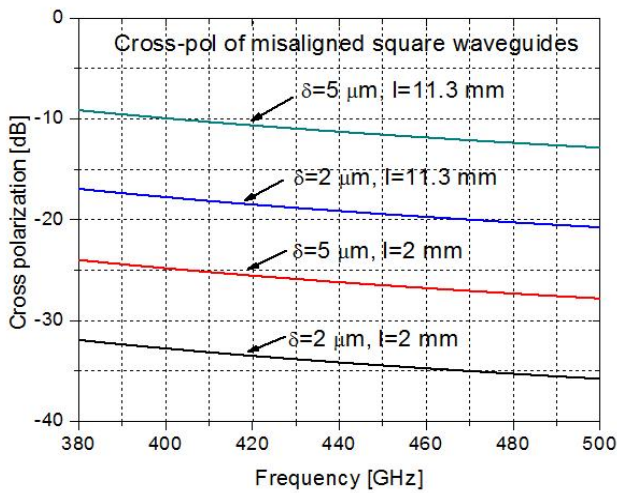


Fig. 18. Simulated cross-polarization of $0.56 \times 0.56 \text{ mm}^2$ square waveguides, $l=11.3 \text{ mm}$ and $l=2 \text{ mm}$ long, with lateral misalignments δ of $2 \mu\text{m}$ and $5 \mu\text{m}$.

F. Electromagnetic simulation of misaligned OMT (first prototype)

We performed electromagnetic simulation of a full structure of the first OMT prototype, as in Fig. 3, where the two OMT block halves are laterally misaligned of $\delta=2 \mu\text{m}$ and $5 \mu\text{m}$.

The simulation result for the transmissions of the two polarization channels with OMT blocks misaligned by $5 \mu\text{m}$ is shown in Fig. 19. The transmissions, of order -1 dB and -1.7 dB for, respectively Pol 1 and Pol 2, are considerably worse than those expected from the perfectly aligned device (see Fig. 5), and are quite close to the measured values (see Fig. 13.)

The simulated input reflection of the OMT, misaligned by $5 \mu\text{m}$, is shown in Fig. 20. As we can see, except for a relatively small increase in reflection of Pol 1, the overall levels remain below -20 dB across most of the band, similar to the simulated value of the perfectly aligned device (see Fig. 4.)

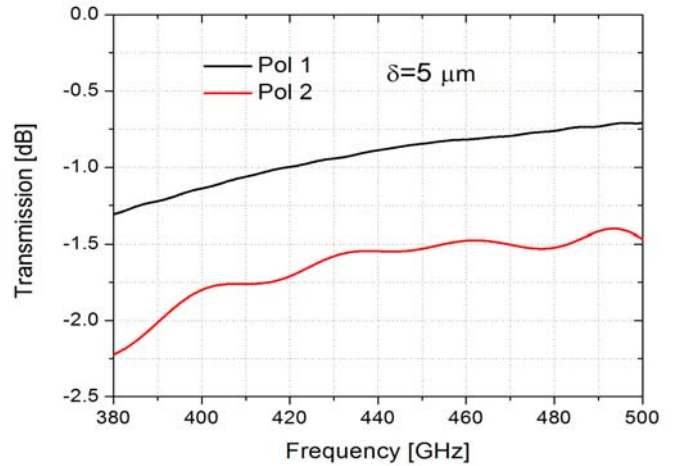


Fig. 19. Simulated transmissions of the first OMT prototype of Fig. 3 with lateral misalignments $\delta=5 \mu\text{m}$. We assumed the waveguide conductor to have perfectly smoothed walls with conductivities $\sigma=4.26 \cdot 10^7 \Omega^{-1} \text{ m}^{-1}$ (300 K.)

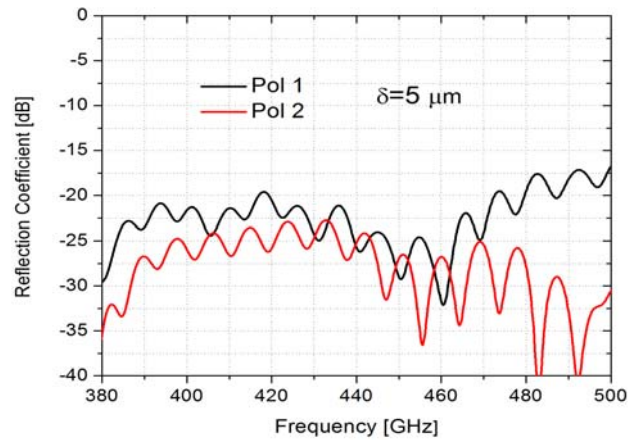


Fig. 20. Simulated input reflection coefficient of the first OMT prototype of Fig. 3 with lateral misalignments $\delta=5 \mu\text{m}$.

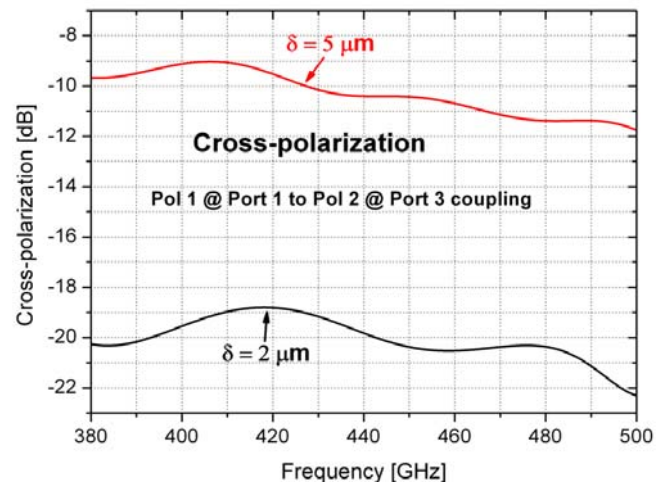


Fig. 21. Simulated cross-polarization of the full OMT of Fig. 7 with lateral misalignments δ of $2 \mu\text{m}$ and $5 \mu\text{m}$.

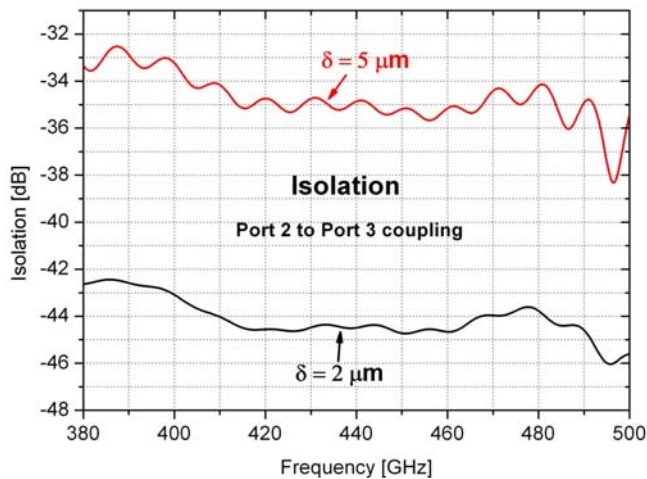


Fig. 22. Simulated isolation of the full OMT of Fig. 7 with lateral misalignment δ of 2 μm and 5 μm .

The results of the electromagnetic simulation for the cross-polarization and isolation of the OMT misaligned of $\delta=2$ and 5 μm are shown, respectively in Fig. 21 and Fig. 22. With a misalignment of $\delta=5 \mu\text{m}$, the cross-polarization is approximately -10 dB, similar in overall level to the measured value as well as to the value resulting from the simulation of a 11.3 mm long square waveguide laterally misaligned by the same δ . This implies that, in a laterally misaligned OMT, most of the cross-polarization is due to the misalignment of the common square waveguide of the device rather than to the misalignment of the remaining parts (i.e. of the reverse-coupling structure.)

The simulated isolation is of the order of -35 dB when $\delta=5 \mu\text{m}$. Both cross-polarization and isolation decrease, respectively to ≈ -20 dB and ≈ -44 dB if $\delta=2 \mu\text{m}$.

In addition to the effects of misaligned block halves of the OMT, the cross-polarization level also depends on the misalignment of square waveguide joints [17] between OMT input and its connecting element (for example a square waveguide-to-rectangular waveguide transition used for test or a feed-horn used in a radioastronomy receiver.) The measured cross-polarization value of the OMT is due to the combined effects of the various misalignments as well as of the internal mechanical imperfections and small asymmetries in the OMT structure.

III. SECOND OMT PROTOTYPE

The simulation results presented in Sec. II E and F indicate that the OMT performance can be considerably improved by decreasing the length of the square waveguide input section of the device. Therefore, we decided to design a second OMT prototype with an input waveguide length l as short as possible. We adopted custom made mini-flanges at all ports and were able to reduce l to 2 mm. In the new design, shown in Fig. 23, the oval waveguide output was moved further away from the input. A shorter output waveguide (4.8 mm long) was also used. The physical length of the waveguide circuit of the new OMT from input to output ports is approximately 6.5 mm for Pol 1 and 20 mm for Pol 2,

respectively 46% and 65% of the lengths used in the first OMT prototype.

The alignment pins and screw holes of the mini-flange are on a 7.11 mm (0.28") bolt circle. A slightly modified Y-junction 180° power combiner and additional waveguide bends in the sidearms are used to conveniently route the signals and avoid mechanical interference between the mini-flange pins and screws with the waveguide circuit.

A 3D drawing of the mechanical blocks of the new OMT prototype is shown in Fig. 24. The external dimensions of the OMT are the same as in the first prototype.

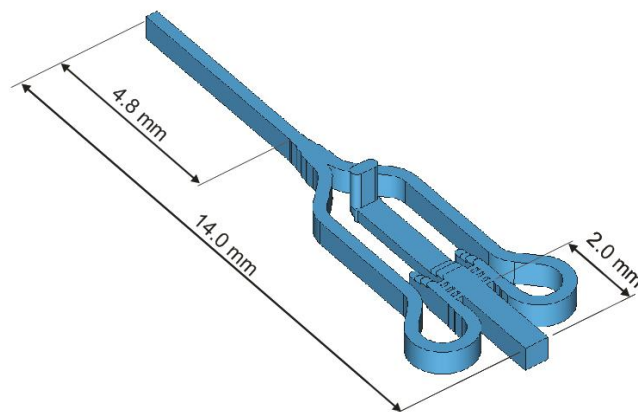


Fig. 23. Internal view of the new OMT design (full view) with short square waveguide input (2.0 mm long) and output (4.8 mm.) Custom-made mini-flanges are adopted at all ports in order to reduce the length of the waveguide sections (see Fig. 24.)

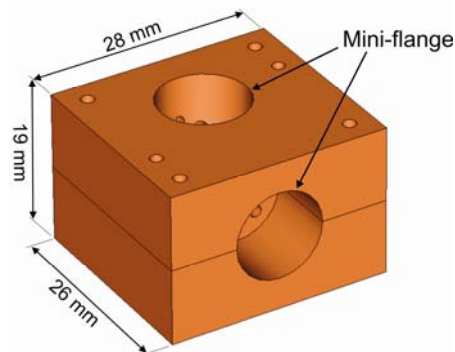


Fig. 24. Mechanical design of the second OMT prototype employing mini-flanges at all ports. The external dimensions are 19×26×28 mm³.

The results of electromagnetic simulation of the second OMT prototype are shown in Figs. 25-27. Three different cases were analysed with OMT block halves laterally misaligned of: $\delta=0 \mu\text{m}$ (perfectly aligned OMT), $\delta=2 \mu\text{m}$, $\delta=5 \mu\text{m}$.

The simulated input reflections (Fig. 25) depend weakly on δ and are below -17 dB across the 385-500 GHz band.

Fig. 26 shows the simulated transmission of the device, which is about -0.25 dB for Pol 1 and about -0.65 dB for Pol 2. In particular, the transmission is greater than in the first OMT prototype and depends much more weakly on δ (see Fig. 5 and Fig. 19 for comparisons.) This is a considerable advantage of this new design.

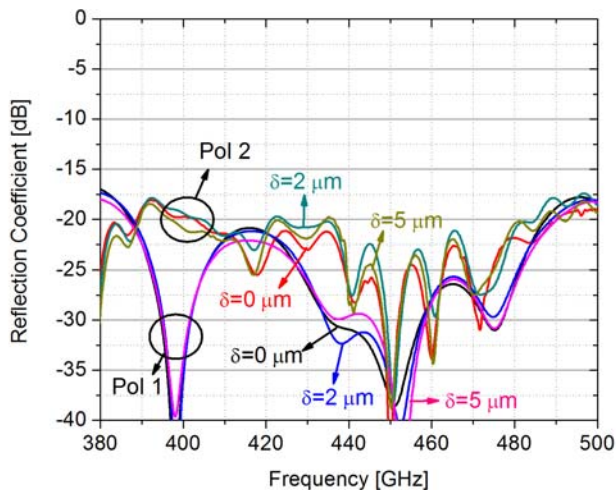


Fig. 25. Simulated input reflection coefficient of the second OMT prototype of Fig. 23 with lateral misalignments $\delta=0, 2,$ and $5 \mu\text{m}$.

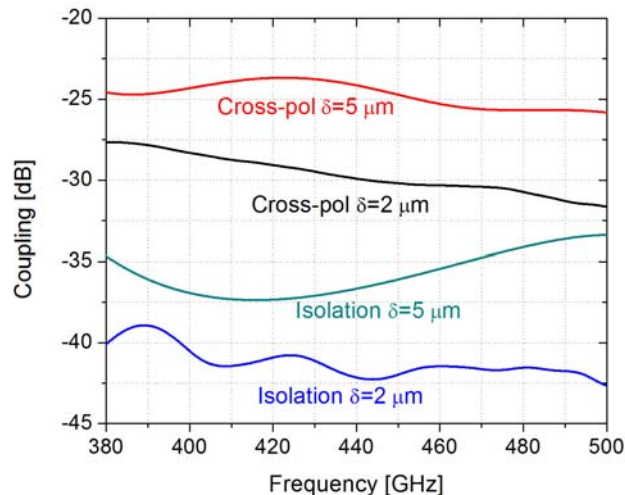


Fig. 27. Simulated cross-polarization and isolation of the second OMT prototype of Fig. 23 with lateral misalignments $\delta=2$ and $5 \mu\text{m}$.

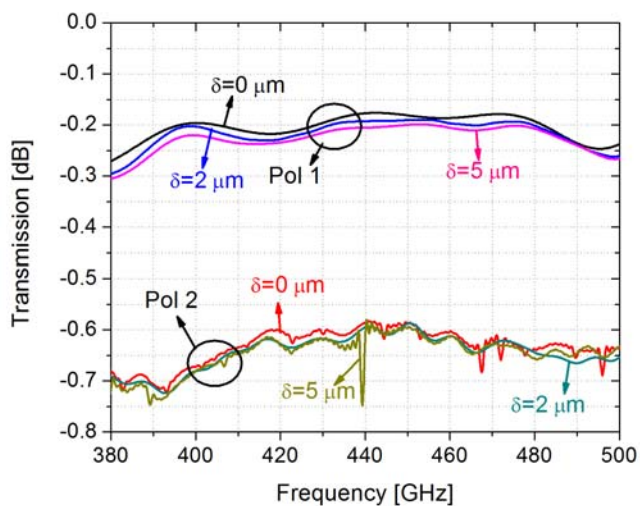


Fig. 26. Simulated transmission of the second OMT prototype of Fig. 23 with lateral misalignments $\delta=0, 2,$ and $5 \mu\text{m}$. We assumed the waveguide conductor to have perfectly smoothed walls with conductivities $\sigma=4.26 \cdot 10^7 \Omega^{-1}\text{m}^{-1}$ (300 K.)

The simulated cross-polarization and isolation of the OMT are shown in Fig. 27. With a misalignment $\delta=5 \mu\text{m}$ the cross-polarization is approximately -25 dB, much lower than in the first OMT prototype, where a value of approximately -10 dB was predicted (see Fig. 21.) The cross-pol would reduce to ≈ -30 dB with $\delta=2 \mu\text{m}$. The simulated isolation is of order -35 dB and -42 dB for, respectively $\delta=2 \mu\text{m}$ and $5 \mu\text{m}$.

Ideally, if we could reduce the length of the square waveguide input of the OMT in Fig. 23 from 2 mm to zero (which would be impossible to fabricate) the predicted cross-polarization level with a lateral misalignment $\delta=5 \mu\text{m}$ between block halves would reduce to approximately -30 dB.

VII. CONCLUSIONS

We have presented the design, construction, and test of a 385-500 GHz waveguide OMT based on a symmetric reverse-coupling structure. The OMT was fabricated in split-block technique using a numerically controlled milling machine.

The OMT was tested at JPL using a sub-mm VNA. The measured room temperature insertion loss was approximately 2 dB, the reflection was less than -10 dB, the isolation was less than -25 dB, and the cross-polarization level was less than -10 dB for both polarization channels.

Electromagnetic simulation of the OMT, obtained with a commercial software, predicted considerably better performance.

We investigated the effects of misalignments between OMT block halves using simulation and found that even a small alignment error of $5 \mu\text{m}$ can explain most of the measured effects.

Starting from the first prototype, we designed a second OMT that has shorter input and output waveguides and is much more tolerant to misalignment errors. The second OMT prototype is expected to have considerably improved performance over the first prototype. The new OMT is being fabricated and will be tested soon.

REFERENCES

- [1] G. Chattopadhyay, B. Philhour, J. E. Carlstrom, S. Church, A. Lange, and J. Zmuidzinas, "A 96-GHz Ortho-Mode Transducer for Polatron", *IEEE Microwave and Guided Wave Letters*, vol. 8, no. 12, pp. 421-423, Dec. 1998.
- [2] A. Dunning, S. Srikanth, and A.R. Kerr, "A Simple Orthomode Transducer for Centimeter to Submillimeter Wavelengths", *Proceedings of the 20th International Symposium on Space Terahertz Technology*, Charlottesville, Apr. 2009, pp. 191-194.
- [3] A. M. Boïfot, E. Lier, T. Schaug-Pettersen, "Simple and Broadband Orthomode Transducer," *Proceedings IEE*, 1990, vol. 137, n. 6, pp. 396-400.

- [4] E. J. Wollack and W. Grammer, "Symmetric Waveguide Orthomode Junctions," *Proceedings of the 14th International Symposium on Space Terahertz Technology*, Tucson, Arizona, Apr. 2003, pp.169-176.
- [5] G. Narayanan and N. Erickson, "Full-Waveguide Band Orthomode Transducer for the 3 mm and 1mm Bands," *Proceedings of the 14th International Symposium on Space Terahertz Technology*, Tucson, Arizona, Apr. 2003, pp. 508-512.
- [6] A. Navarrini and M. Carter, "Design of a Dual Polarization SIS Sideband Separating Receiver Based on Waveguide OMT for the 275-370 GHz Frequency Band," *Proceedings of the 14th International Symposium on Space Terahertz Technology*, Tucson, Arizona, Apr. 2003, pp. 159-168.
- [7] A. Navarrini and R. L. Plambeck, "A Turnstile Junction Waveguide Orthomode Transducer," *IEEE Trans. Microwave Theory Tech.*, vol. 54, n. 1, pp. 272-277, Jan. 2006.
- [8] A. Navarrini A. Bolatto, R. L. Plambeck, "Test of 1 mm Band Turnstile Junction Waveguide Orthomode Transducer", *Proceedings of the 17th International Symposium on Space Terahertz Technology*, Paris, France, May 10-12, 2006, pp. 99-102.
- [9] G. Pisano, L. Pietranera, K. Isaak, L. Piccirillo, B. Johnson, B. Maffei, S. Melhuish, "A Broadband WR10 Turnstile Junction Orthomode Transducer," *IEEE Microwave and Wireless Components Letters*, vol. 17, n. 4, pp. 286-288, April 2007.
- [10] G. G. Moorey, P. Axtens, M. Bowen, A. Dunning, R. Gough, G.R. Graves, H. Kanoniuk, "A 77-117 GHz cryogenically cooled receiver for radioastronomy," *Workshop in Applications of Radio Science (WARS2006)*, Leura, NSW, 15-17 Feb. 2006.
- [11] S. Asayama, "Double-Ridged Orthomode Transducer for ALMA Band 4 receiver," *Technical Memo of National Astronomical Observatory of Japan NINS*, 27 Feb. 2007.
- [12] O. A. Peverini, R. Tascone, G. Virone, A. Olivieri, R. Orta, "Orthomode Transducer for Millimeter-Wave Correlation Receivers," *IEEE Trans. Microwave Theory Tech.*, vol. 54, n. 5, May 2006, pp. 2042-2049.
- [13] A. Navarrini, R. Nesti, "Symmetric reverse-coupling waveguide orthomode transducer for the 3 mm band," *IEEE Trans. Micr. Theory and Tech.*, vol. 57, n. 1, Jan 2009, pp. 80-88.
- [14] M. Kamikura, M. Naruse, S. Asayama, N. Satou, W. Shan, and Y. Sekimoto "Development of a 385-500 GHz Orthomode Transducer (OMT)," *Proceedings of the 19th International Symposium on Space Terahertz Technology*, Groningen, The Netherlands, Apr. 2008, pp 557-562.
- [15] C. Groppi, C. Y. Drouet d-Aubigny, A. W. Lichtenberger, C. M. Lyons, C. K. Walker, "Broadband Finline Ortho-Mode Transducer for the 750-1150 GHz Band," *Proceedings of the 16th International Symposium on Space Terahertz Technology*, Chalmers, May 2005, pp. 513-518.
- [16] A. R. Kerr, "Elements for E-plane Split-Blocks Waveguide Circuits," National Radio Astronomy Observatory, *ALMA Memo* No. 381, Jul. 2001.
- [17] A. R. Kerr, "Effects of misalignment of square waveguide joints," National Radio Astronomy Observatory, *EDTN 211*, 12 March 2009. Available at: <http://www.gb.nrao.edu/electronics/edtn/edtn211.pdf>

Automated CNC Micromachining for Integrated THz Waveguide Circuits

Christopher E. Groppi^{1*}, Brian Love², Matthew Underhill¹, Christopher Walker²

¹Arizona State University School of Earth and Space Exploration, Tempe, AZ 85287, USA

²Steward Observatory, University of Arizona, Tucson, AZ 85721, USA

*Contact: cgroppi@asu, phone +31-50-363 4074

Abstract— Computer Numerically Controlled (CNC) machining of splitblock waveguide circuits has become the primary method of constructing terahertz waveguide circuits. The majority of these circuits have been made on traditional CNC machining centers or on custom-made laboratory machining systems. At both the University of Arizona and Arizona State University, we have developed techniques for machining splitblock waveguide circuits using purpose-built ultra high precision CNC machining centers designed for micromachining. These systems combine the automation of a traditional CNC machining center, including a high capacity toolchanger, workpiece and tool metrology systems and a large work volume, with the precision of custom laboratory systems. The systems at UofA and ASU are built by Kern Micro and deliver typical measured dimensional accuracies of 2-3 microns. Waveguide surface finish has been measured with a Veeco white light interferometric microscope to be Ra~75 nm. Tools of sizes between 25 microns and 10mm are available, with toolchanger capacities of 24-32 tools.

The automated toolchanger and metrology systems allow a metal blank to be machined into the final part in one machining cycle, including both micromachining operations and traditional machining operations. This allows for perfect registration between all block features, in addition to very short cycle times. Even the most complicated blocks have machining cycle times of no more than a few hours. Workpiece and tool metrology systems also allow for fast setup times and straightforward part re-work. In addition, other high-throughput techniques such as palletization are enabled for the simultaneous manufacture of large numbers of blocks.

Using these machines, we have successfully produced waveguide circuits at frequencies ranging from W-band to 2.7 THz, including highly integrated blocks. The Supercam project relied on these machines to produce integrated 8-pixel SIS mixer array units with integrated low noise amplifiers, bias tees and blind mate connectors. In addition, the 64-way corporate power divider used for LO multiplexing was machined using these techniques. This system consists of 17 split-block circuits containing E-plane power dividers, waveguide twists, diagonal horns and all associated flanges. The final system consists of a single WR-3 UG-387 input and an 8x8 array of 11mm aperture diagonal feedhorn outputs. This is one of the largest submillimeter waveguide circuits ever constructed. Future large focal plane arrays and other applications requiring highly integrated waveguide circuits will critically depend on this type of highly automated micromachining technology.

We present the capabilities and machining process used with these machining centers, along with several waveguide circuits that were manufactured with this process including measured results from these circuits. Future directions for improving manufacturing quality and automation for large focal plane arrays will be discussed, including the use of palletization, in-situ metrology, and automatic workpiece changers. Using these techniques, construction of the necessary waveguide blocks for even kilopixel class heterodyne array receivers should be realizable in a manageable time with high part yield and relatively low incremental cost.



Figure 1: The Kern Model 44 (left) and Kern MMP (right) micromilling systems used at Arizona State University and the University of Arizona.

MICROMILLING SYSTEMS

The state of the art Kern micromilling systems at ASU (Model 44) and the University of Arizona (MMP) allow for the automated production of terahertz waveguide and quasioptical components with micron level accuracy and nanometer scale surface roughness (See figure 1). Both machines are equipped with laser tool measurement systems and strain-gauge touchprobes which allow the measurement and control of both tool sizes (both diameter and length) and workpiece location to the micron level. These machines are capable of maintaining their rated accuracies over their entire work volume, which enables very large integrated terahertz circuits to be produced, while maintaining dimensional accuracy and splitblock alignment. Both machines are 3-axis fully CNC controlled systems and are equipped with large capacity toolchangers. This allows all machining operations (both standard and micromachining) to be completed in one clamping, eliminating the need to align micromachined features to traditionally machined components. This

dramatically increases productivity while maintaining the best possible quality. Future upgrades to 5-axis machining are possible with both machines.

These machines are capable of cutting traditional waveguide block materials (brass, copper, and aluminum) as well as more exotic materials including stainless steel, hardened steel, ceramics and silicon. Their high precision and large work volumes also make them particularly well suited to the production of terahertz optical components, optical systems and precision mechanical components.

TABLE I
MICROMILLING SYSTEM SPECIFICATIONS

	Kern Model 44	Kern MMP
Positioning accuracy	+/- 0.5 micron	+/- 1.0 micron
Surface Finish	Ra<0.1 microns	Ra<0.2 microns
Work Volume	300x280x250mm	250x220x200mm
Max workpiece mass	50kg	30 kg
Spindle	Vector controlled 50 krpm	Vector controlled 40 krpm
Toolchanger	32 positions	24 positions
Tool measurement	Laser diameter and length	Laser diameter and length
Workpiece setting	Touchprobe	Touchprobe
Cutting lubricant	Temperature controlled cutting fluid	Oil mist lubrication system

MICROMACHINING PROCESS

The micromachining process at the UofA and ASU combines electromagnetic design, mechanical design, CAM programming, machining, metrology, assembly and RF testing in one location. This allows for rapid progress from design to finished, working components, and also allows for multiple design cycles for the refinement and optimization of complex THz circuits. The CAM system used with both processes (Openmind Hypermill) is integrated into the CAD package used for design. This system automatically updates CAM programming when the solid model is changed in the CAD package. Toolpaths are calculated to an accuracy of 0.1 microns.

MICROMACHINED TERAHERTZ COMPONENTS

The Kern MMP at the University of Arizona was originally purchased to fabricate the waveguide structures for the Supercam 64 beam array receiver [1]. The Supercam 8-pixel mixer module is shown in figure 2. The block consists of eight single ended SIS waveguide mixers, with integrated diagonal horns. LNA modules, IF and bias distribution and electromagnets are all contained in this single, large (160x50x11mm) waveguide splitblock. All waveguide, feed and classical machining is done in a single clamping per side

in the Kern MMP. 20 tools, and approximately 4 hours of machine run time are required to complete a single splitblock half.

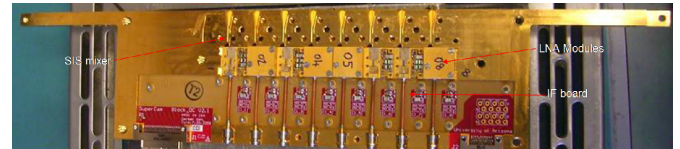
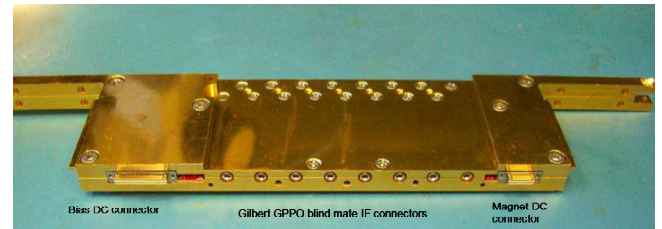


Figure 2: The Supercam 8-pixel mixer module. The single splitblock contains 8 single ended SIS mixers, 8 low noise amplifier modules, 8 electromagnets, and all DC and IF distribution circuitry.

LO power multiplexing for Supercam is also accomplished using a micromachined waveguide structure. The 64-way LO power divider shown above-left consists of 17 separate waveguide splitblocks with custom interface flanges. The first waveguide splitblock consists of 7 WR3 E-plane Y-splitters in a binary tree. This tree of splitters divides the output of a single Virginia Diodes LO chain by 8, with equal waveguide pathlength for each output port (see figure 3). The output ports end with splitblock waveguide twists. This block's 8 output ports then meet 8 additional waveguide splitblocks. These blocks have an identical tree of 7 E-plane Y-splitters, but the output ports end with diagonal feedhorns (see figure above-right). The diagonal feedhorns are then extended with another set of splitblocks to reach 11mm aperture size. The final block achieves even pixel-to-pixel splitting of LO power to within 10%, with a total loss of 2 dB compared to a lossless divider [2].

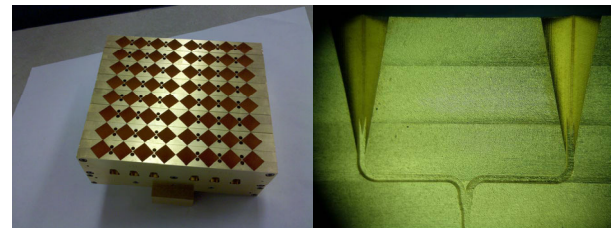


Figure 3: The completed Supercam LO power divider (left) and a close up photo of one of the E-plane Y-junctions inside the splitter (right).

In addition to Supercam, many other waveguide components have been produced. The spatial filter shown in figure 4 was designed to improve the beam quality of a 2.7 THz QCL [3]. This is currently the highest frequency waveguide structure to be designed, fabricated and tested using our micromachining process.

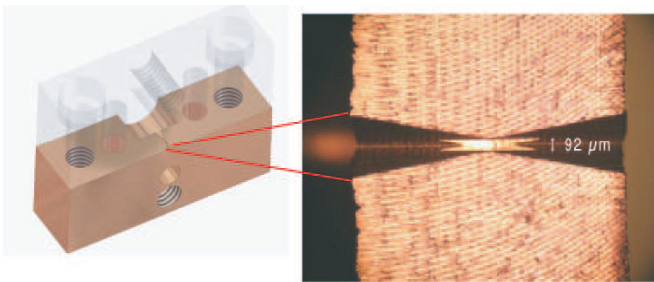


Figure 4: A solid model and photo of a 2.7 THz spatial filter made at the University of Arizona using the micromachining process described in this paper.

Highly integrated THz waveguide circuits are possible to fabricate using our micromachining process. The 660 GHz sideband separating mixer shown in figure 5 is fabricated from a splitblock containing two branch line directional LO couplers, 1 branch line hybrid coupler, two SIS mixers, an integrated diagonal LO feedhorn and associated IF circuitry and magnets [4]. The 1.45 THz mixer shown in figure 6 was fabricated using a 25 micron diameter cutter [5]. The b-dimension of the waveguide is 42 microns. Feature depths are 18 microns for the waveguide backshort and 8 microns for the device channel. The coupler slot shown below right was cut with a 100 micron tool with a 5.5:1 aspect ratio.

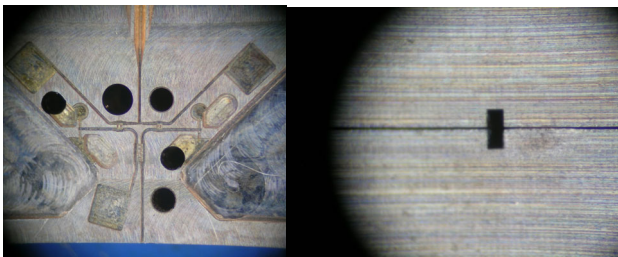


Figure 5: A 660 GHz sideband separating mixer block (left), and the splitblock alignment of the two halves of this block (right). The size of the full-height waveguide is 145x310 microns, with +/- 2 micron splitblock alignment.

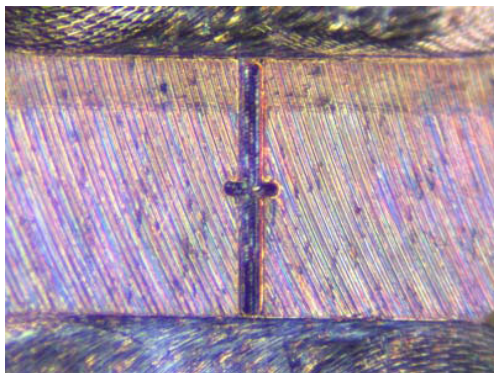


Figure 6: A 1.4 THz HEB mixer block for the Stratospheric Terahertz Observatory experiment. The dimensions of the waveguide backshort are 160x42 microns, with a 18 micron depth. Features were machined with a 25 micron diameter endmill.

METROLOGY

Metrology is a critical component to any micromachining process. High performance waveguide circuits are impossible

to successfully fabricate without the ability to measure micron-level dimensions and nanometer scale surface roughnesses. Both micromilling systems are equipped with laser tool measurement systems and touchprobe systems which allow the measurement of tool length and diameter to the micron level, and the location and rotation of the workpiece to the same level of precision. Combined with the exceptional positioning accuracy of the machine axes, these systems allow on-the-part accuracies of ~2um. Structure dimensions can then be measured to micron accuracies using a 3-axis measurement microscope with photographic capability. At the University of Arizona, a Veeco white light interferometric microscope is available to measure surface roughnesses. Typical surface roughness is Ra~75 nm. An example of such a waveguide is shown in figure 7.

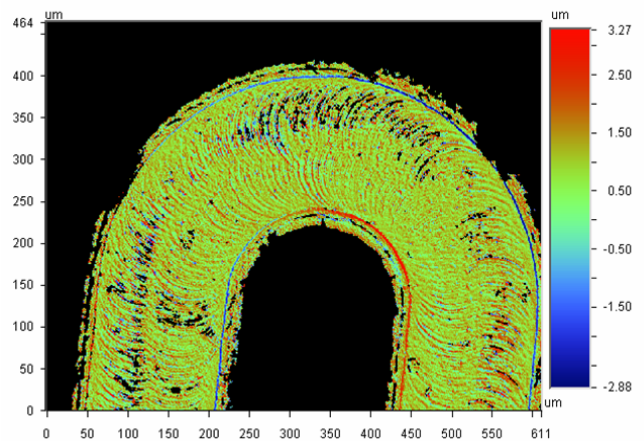


Figure 7: A white light interferometric microscope image of the floor of a 350 GHz waveguide. The measured surface roughness is Ra~75 nm.

FUTURE DIRECTIONS

Automation techniques used for decades in classical machining systems can now be applied to high precision micromachining. Rather than producing one or a few waveguide blocks at a time, automation systems can allow the production of hundreds of blocks at a time without user intervention. The Kern Evo's toolchanger can be expanded to up to 96 tools. The System 3R workpiece chuck allows straightforward palletization of workpieces, and allows the removal and reinstallation of the chuck with a precision of 2um or better. The chuck can be combined with an automatic workpiece changer to allow the automated loading and unloading of pallets. Combined with the laser tool metrology system and workpiece touchprobe, very large numbers of THz waveguide blocks could be produced economically and quickly. Future instruments with large (~1000) pixels are feasible using these production techniques, in addition to the expansion of THz technology to the private sector.

REFERENCES

[1] Groppi, C.E., Walker, C.K., Kulesa, C., Golish, D., Kloosterman, J, Puetz, P., Weinreb, S., Kuiper, T., Kooi, J., Jones, G., Bardin, J., Mani, H., Lichtenberger, A., Cecil, T., Hedden, A., Narayanan, G. SuperCam: a 64 pixel heterodyne imaging spectrometer, Millimeter and Submillimeter Detectors and

- Instrumentation for Astronomy IV, Edited by Duncan, William, Holland, Wayne, Withingtonm Stafford, Zmuidzinas, Jonas, Proc. SPIE 7020, 26, 2008.
- [2] Christopher Groppi, Christopher Walker, Craig Kulesa, Dathon Golish, Jenna Kloosterman, Sander Weinreb, Glenn Jones, Joseph Barden, Hamdi Mani, Tom Kuiper, Jacob Kooi, Art Lichtenberger, Thomas Cecil, Patrick Puetz, Gopal Narayanan, Abigail Hedden, Testing and Integration of Supercam, a 64-Pixel Array Receive for the 350 GHz Atmospheric Window, 21st International Symposium on Space Terahertz Technology, in press, 2010.
- [3] Abigail Hedden, Patrick Pütz, C. d'Aubigny, Dathon Golish, Christopher Groppi, Christopher Walker, Benjamin Williams, Qing Hu, John Reno, Micromachined Spatial Filters for Quantum Cascade Lasers, 17th International Symposium on Space Terahertz Technology, P2-11, 2006.
- [4] F.P. Mena, J. Kooi, A.M. Baryshev, C.F.J. Lodewijk, T.M. Klapwijk, R. Hesper, W. Wild, RF Performance of a 600 - 720 GHz Sideband- Separating Mixer with All-Copper Micromachined Waveguide Mixer Block, 19th International Symposium on Space Terahertz Technology, pp. 90-92, 2008.
- [5] J. Kawamura, A. Skalare, J. Stern, E. Tong, C. Groppi, THz waveguide HEB mixer using Silicon-on-Insulator substrates for STO, 21st International Symposium on Space Terahertz Technology, in press, 2010.

Silicon Micromachining Technology for Passive THz Components

Choonsup Lee, Bertrand Thomas, Goutam Chattopadhyay, Alex Peralta, Robert Lin, Cecile Jung, and Imran Mehdi

Abstract— Silicon micromachined terahertz passive components such as silicon washers, waveguide blocks for W-band (75-110 GHz) power amplifiers, and waveguides for 325-500 GHz band have been designed, microfabricated, and characterized. Based on these results, an integrated 600 GHz silicon micromachined Radiometer-On-a-Chip (ROC) has been demonstrated for the first time. It reduced in mass by an order of magnitude compared to the conventional metal machining.

Index Terms—Silicon micromachining, Radiometer-On-a-Chip (ROC), waveguide, silicon washer.

I. INTRODUCTION

There is an increasing interest in the millimeter and submillimeter wave frequency range for various applications such as compact range radar, terahertz imaging, and the space [1-2]. The frequency bands for these applications are in the range of 300 GHz to 3 THz corresponding to a wavelength of 1 mm to 100 μm which silicon micromachining can contribute significantly. At submillimeter wave frequency range, the hollow waveguide has been used due to the low loss, and manufactured by conventional milling and drilling machines. However, at frequencies above 500 GHz, waveguides become so small (less than 0.3 by 0.15 mm) that conventional machining technique becomes extremely difficult, expensive, and/or impossible to manufacture. Thus, silicon micromachining technique have been attempted to make passive components below 100 GHz. [3]. Silicon micromachining technique is capable of achieving micron feature size with excellent process control such as high aspect-ratio, uniformity, and surface quality. While there have been several demonstrations of waveguide circuits fabricated with silicon micromachining and other techniques, few if any of these circuits have been subjected to any significant electrical testing [3-4]. In this paper, we have demonstrated THz passive components such as silicon washer, waveguide blocks for W-band amplifiers, and waveguides for the 325-500

GHz band, and applied it to 600 GHz ROC for the first time ever.

II. IMPLEMENTATION AND RESULTS

A common hurdle to date to test these components has been the eventual interface of the Si pieces with the metallic waveguide. We have developed a silicon washer where the surface of the Si wafer is used to make the Si-metal interface. It showed the same behavior as metal washer (Figure 1).

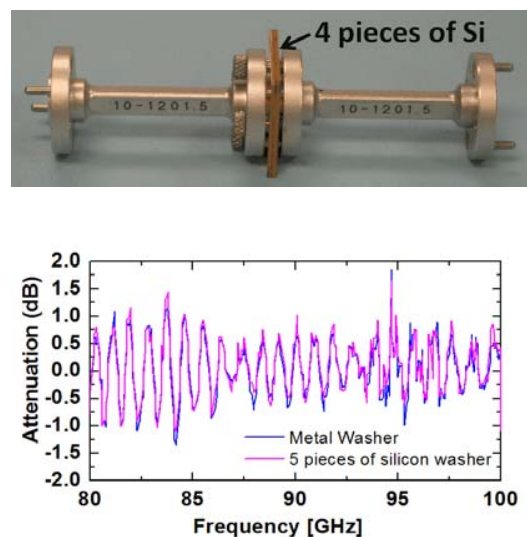
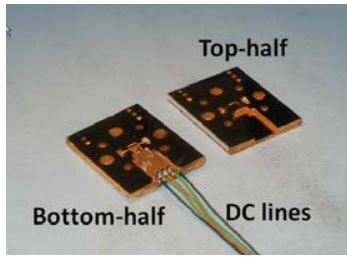


Figure 1. Measured attenuation data plot of both 2.5 mm-thick metal and 2.5 mm-thick silicon washers. Si washer is composed of 4 pieces of wafers. It shows almost identical behavior.

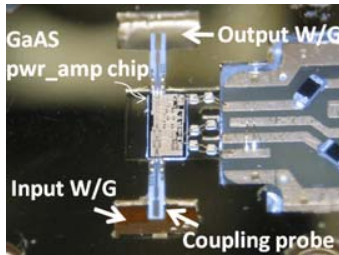
Subsequently, we have designed and microfabricated a silicon based W-band (75-110 GHz) power amplifier module (Figure 2). This circuit is based on a stack of four Si wafers and provides the standard UG-387 flange for interface to metallic waveguides. The performance of the silicon block is similar to a block fabricated using conventional metal machining (Figure 3).

The research described in this paper was carried out at the Jet Propulsion Laboratory, California Institute of Technology, under a contract with the National Aeronautics and Space Administration.

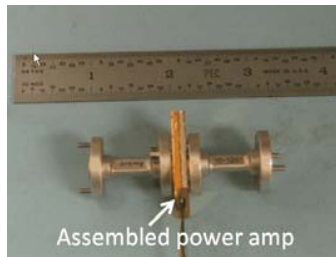
C. Lee, B. Thomas, G. Chattopadhyay, A. Peralta, R. Lin, C. Jung, and I. Mehdi are with the Jet Propulsion Laboratory, Pasadena, CA 91109 USA (Choonsup.Lee@jpl.nasa.gov)



(a)



(b)



(c)

Figure 2. (a)View of top and bottom half of the silicon blocks. (b) It shows the GaAs power amplifier sitting on the channel in silicon micromachined waveguide. (c) Photograph of assembled GaAs power amplifier using silicon micromachined waveguide block.

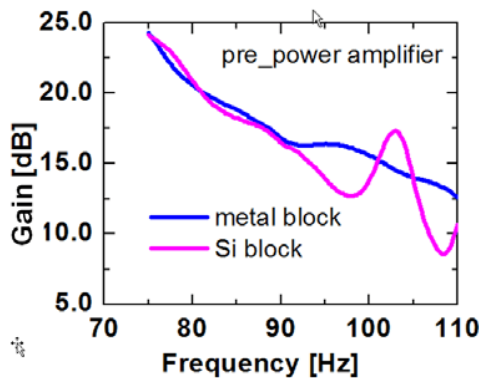


Figure 3. Measured data plot of GaAs pre-power amplifiers assembled in both metal and silicon blocks. It shows similar behavior.

The pre-power amplifier assembled in metal module and the power amplifier assembled in silicon module are connected in a cascade (Figure 4). We have demonstrated over 140 mW at 94 GHz from the cascaded power amplifiers (Figure 4).

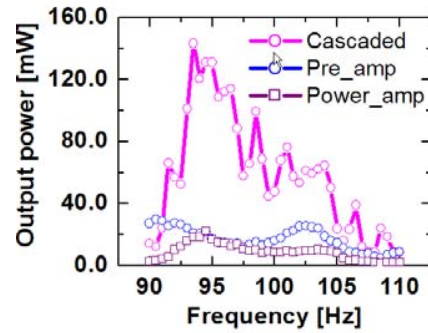
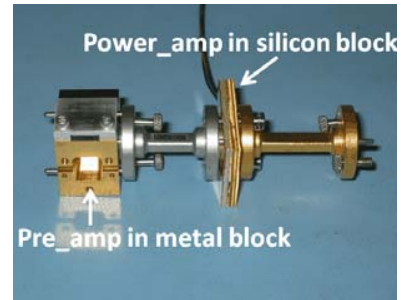
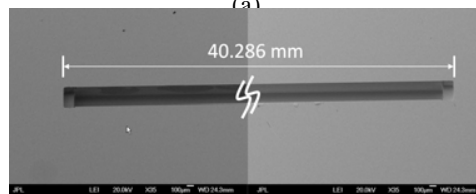


Figure 4. (left) Photograph of cascaded pre-amplifier and power amplifier (right) Measured output power of cascaded power amplifiers. Over 140 mW has been achieved.

Furthermore, we have developed silicon micromachined waveguide components in WR-2.2 (325-500 GHz) band (Figure 5). We used a 40mm straight section of waveguide with two two-step H-plane bends bringing the waveguide flanges on top surface of the silicon. We measured approximately 5-6 dB of loss at 350 GHz for the guide, which also includes 8 mm of waveguide length of the testing fixture (Figure 5). These results are consistent with theoretical simulations and demonstrate that this approach can be used for building passive THz components.



(b)



(c)

Figure 5. SEM images of 325-500 GHz waveguide. (a) bottom half of Si waveguide (b) top half of Si waveguide. (c) assembled waveguide.

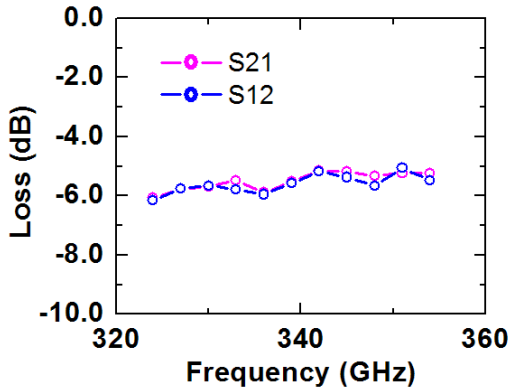


Figure 6. Measured data plot of 325-500 GHz waveguide block. The loss is about 5-6 dB according to HFSS simulation. It matches the measurement results.

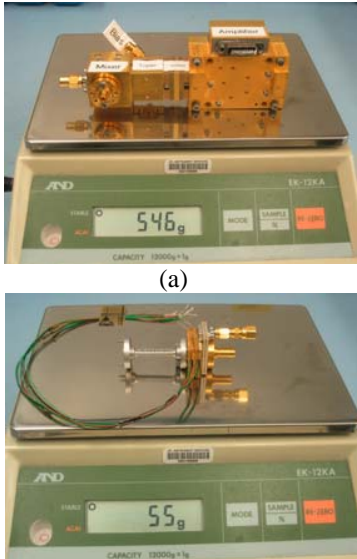


Figure 7. (a) Conventional machined 600 GHz receiver (b) silicon micromachined 600 GHz receiver. It reduces an order of magnitude in weight.

Finally, we have applied silicon micromachining techniques to build a 600 GHz integrated heterodyne receiver. Double Side Band (BDS) receiver noise temperature of 4200 K and 13 dB conversion losses have been measured at 540 GHz. It dramatically reduced both mass and size (Figure 7).

III. CONCLUSION

This is the very first demonstration of a novel receiver using silicon micromachining techniques. This architecture will open the new door for the development of large arrays of receivers in the sub-millimeter wave range.

REFERENCES

- [1] P. H. Siegel “THz technology,” IEEE Trans. Microw. Theory Tech., 50, 3 (2002)
- [2] Peter de Maagt, Janet Charlton, “Terahertz Space Applications and Technology,” J. IEEE MTT-S (2005)
- [3] J. P. Becker, J. R. East, and L. P. B. Katehi, “Performance of Silicon Micromachined Waveguide at W-band,” Electron. Lett., vol. 38, p. 638 (2002)
- [4] G. Chattopadhyay, J. Ward, H. Manohara, R. Toda, and R. Lin, “Silicon Micromachined Components at Terahertz Frequencies for Astrophysics and Planetary Applications,” ISSTT (2008)

Performance of Planar Ortho-Mode Transducers for CMB satellite missions

Jin Zhang¹, Philip Mauskopf¹, Stafford Withington², David Goldie², Dorota Glowacka²

¹Astronomy Instrumentation Group
Cardiff University, UK
Email: Jin.Zhang@astro.cf.ac.uk

²Cavendish Laboratory
University of Cambridge, UK
Email : stafford@mrao.cam.ac.uk

Abstract

Planar waveguide E-field probes have been used in a number of millimeter wave instruments although usually for single polarization detection in rectangular waveguide. The coupling efficiency of these types of probes is found to be high over the full waveguide bandwidth. Because of the advantages in integration, scalability and mass of planar OMTs compared to external waveguide OMTs, a planar OMT coupled to a corrugated horn is a good option for future CMB polarisation missions such as B-Pol. We estimate the performance of planar OMTs where the signals from the probes are combined after detection (power combination) and before detection (field combination) and show that under ideal circumstances the two methods give equivalent performance over a 20% bandwidth. However, field combination suppresses coupling to higher order waveguide modes and therefore enables wider bandwidth operation (up to 40%).

We present a design of an ortho-mode transducer (OMT) to separate two orthogonal linearly polarized signals traveling in a circular waveguide in the frequency band from 190-250 GHz band using 4 probes in circular waveguide. In this design, the power in each linear polarisation is divided between two opposite probes. A field combiner (hybrid coupler) combines the signals from the probes on opposite sides of the waveguide before detection using planar microstrip structures. We use Ansoft/HFSS 3-D electromagnetic simulation software and the Agilent Advanced Design System (ADS) to evaluate the performance of the design and to determine the optimal probe geometry and feed impedance. The main questions have been investigated for this technology are coupling efficiency and cross-polarization response, achievable bandwidth, and scalability.

VNA-Calibration and S-Parameter Characterization of Submillimeter Wave Integrated Membrane Circuits

Huan Zhao^{1,2}, Aik-Yean Tang^{1,2}, Peter Sobis^{1,3}, Tomas Bryllert^{1,2}, Klas Yhland^{1,4}, Jörgen Stenarson^{1,4}, Jan Stake^{1,2}

¹GigaHertz Center, ²Physical Electronics Laboratory,

Department of Microtechnology and Nanoscience, Chalmers University of Technology, SE-41296, Sweden

³Omnisys Instruments AB, V. Frölunda, Sweden

⁴SP Technical Research Institutes of Sweden, Borås, Sweden

Abstract—A TRL-calibration kit enabling S-parameter characterization of membrane circuits has been developed for the WR-03 band. The TRL-design features 3 μm thick GaAs membrane circuits packaged in E-plane split waveguide blocks. Membrane filters have been characterized after the calibration.

I. INTRODUCTION AND BACKGROUND

There is a strong need for development of compact receivers operating in the submillimeter wave band for earth observation instruments, space science missions as well as THz imaging systems. However, as circuit operating frequency increases, the difficulty of assembly increases as chip dimensions and alignment tolerances shrink. Furthermore, the high frequency circuits are usually limited by the thickness of the support substrate. To overcome these drawbacks, membrane supported monolithic integrated circuits (MICs) have been proposed and show promising results. However, little has been reported about the S-parameter characterization of membrane circuits. Although this is significant for circuit modeling and design verification.

We have developed membrane *thru-reflect-line* (TRL) calibration standards to characterize membrane circuits in the WR-03 waveguide band (220-325 GHz) [1,2]. In this paper, we have improved the design of the contacting surfaces to the beam lead and to improve ground connection and alignment tolerance. TRL calibration is performed based on an optimized design of the TRL standards. S-parameter of passive circuits are presented.

II. DESIGN AND METHOD

We designed the membrane TRL standards and circuits using a three-dimensional electromagnetic simulator (Ansoft HFSS) and a linear circuit simulator (Agilent ADS). The design principle of the TRL standards is described in [3]. In our design, all standards have the same waveguide to planar interface in each end, as shown in Fig.1 (a). The *thru* and *line* standards have a length of 600 μm and 850 μm respectively, with a same nominal characteristic impedance of close to 100 Ω and a phase difference of 90 degrees at 300 GHz. An *open* standard was chosen as it has a very good response characteristic and should be less sensitive and more reliable than a *short*, which has a stronger dependence on mounting tolerances and perfect ground contact. To minimize the number of different mechanical blocks, the same mechanics as for the *line* standard were used for both the *open* and all the DUTs. The epitaxial structure and the membrane circuit fabrication are described in [2].

The design of E-plane block is shown in Fig.1 (b). A 26 mm long reference waveguide (waveguide thru) was designed for evaluation of the waveguide loss. A modified block with decreased contact surface was designed to improve the contact to the beam lead.

Fig.2 shows schematic pictures of planar view and cross section view of the membrane circuits in blocks. The beam leads provide electrical contact as well as mechanical support, making the membrane circuits suspend in the air. The membrane circuits were designed to have a self aligning structure with a tolerance of maximum 20 μm movement in the split-plane. After the first achievement of this work, we found this tolerance can be decreased to 10 μm .

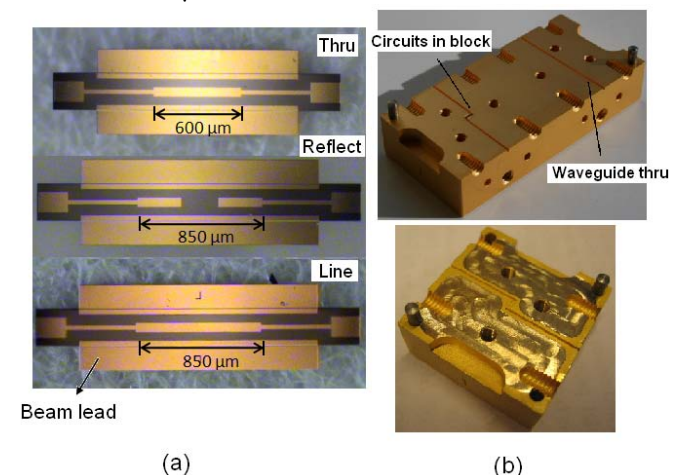


Fig.1. Microscope pictures of the membrane calibration standards (a) Photos of the blocks (b).



Fig.2. Schematic pictures of planar view and cross section view of the circuits in blocks.

For the WR-03 test set, Oleson Microwave Labs (OML) V03VNA2-T/R frequency extension modules with an Agilent E8361A PNA S-parameter test set are used.

III. VNA CALIBRATION

Calibration was first performed with waveguide TRL standards from OML to verify our membrane TRL standard

design. Once calibrated, the reference planes were set at the flange of the two frequency extenders. First, the flange thru (flanges directly connected) and the waveguide thru were measured, as shown in Fig.3. S_{21} of the waveguide is approximately -0.7 dB. Then the membrane standards were measured. As shown in Fig.4, S_{21} of the membrane *thru* and the membrane *line* is approximately -1 dB, respectively. These results indicate that the loss in a 2 mm long membrane is less than 0.3 dB. The ripples seen in S_{11} , are most likely due to imperfect repeatability of the flange connections and inequality assembly. S_{11} of the membrane *reflect* is about -0.7 dB. S_{12} of the membrane *reflect* is below -40 dB, so that the two ports are well isolated even though only one reflect standard is used for calibration.

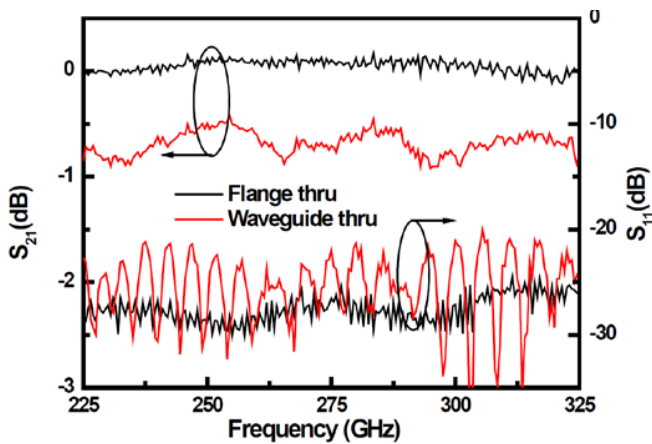


Fig.3. S_{21} and S_{11} of the flange thru and the waveguide thru.

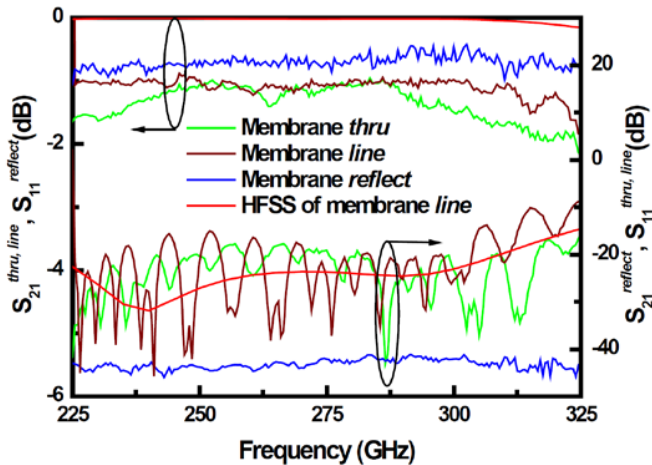


Fig.4. S_{21} and S_{11} of the membrane standards and simulation of membrane *line*.

Then we use membrane TRL standards for calibration. The reference plane is set in the middle of the *thru* after calibration. The membrane *thru* shows an insertion loss magnitude and an insertion loss phase variations within ± 0.01 dB and ± 1 degree respectively without reconnection. Then, each membrane standard was reconnected and measured to check the repeatability. Small differences are observed in both magnitude and phase measurements between the two ports for all the standards.

IV. RESULTS

Figure 5 shows S-parameter characterization of a ring resonator filter after the calibration and comparison to simulation. Measured S_{12} and S_{21} are almost identical. A 5 GHz frequency shift, between the simulation model and circuit measurements, corresponding to 1.5 % of the resonance frequency was observed.

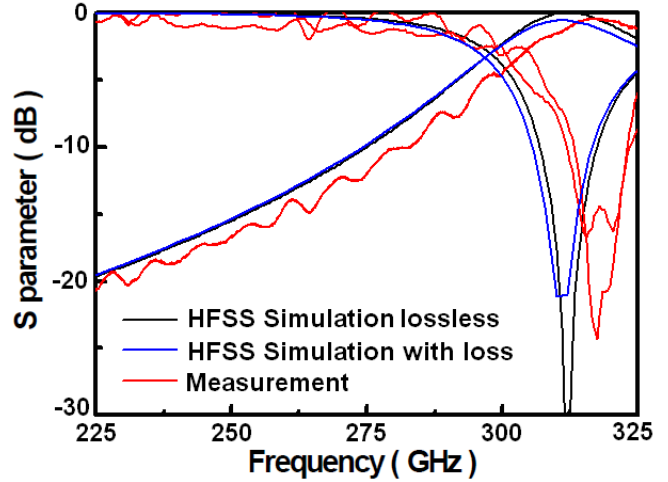


Fig.5. S-parameter characterization of a 300 GHz ring resonator filter.

Figure 6 shows S-parameter characterization of a stub filter after the calibration and comparison to simulation. Measured S_{12} and S_{21} are almost identical. A 10 GHz frequency shift, between the simulation model and circuit measurements was observed.

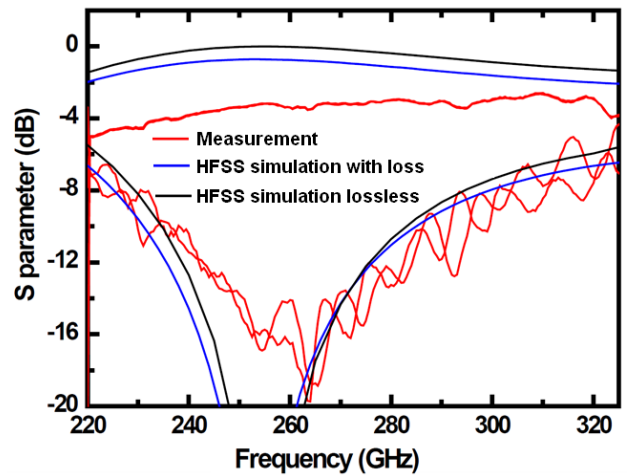


Fig.6. S-parameter characterization of a 250 GHz stub filter.

REFERENCES

- [1] H. Zhao, A. Y. Tang, P. Sobis, V. Drakinskiy, T. Bryllert, J. Stake "Characterization of GaAs membrane circuits for THz heterodyne receiver applications", 21st International Symposium on Space Terahertz Technology, Oxford, UK, March, 2010
- [2] H. Zhao, A. Y. Tang, P. Sobis, T. Bryllert, K. Yhland, J. Stenarson, J. Stake "TRL-calibration and S-Parameter Characterization of Membrane Circuits for Submillimeter Wave Frequency", submitted to IEEE Microwave and Wireless Components Letters, 2010
- [3] "Applying the 8510 TRL calibration for Non-coaxial Measurement", Agilent Application note 8510-8A.

Revisiting the ALMA Band 1 Optics Design

P. Zorzi¹, D. Henke², S. Claude², P. Mena¹, L. Bronfman³, and J. May³

¹*Department of Electrical Engineering, Universidad de Chile, Santiago, Chile*

²*NRC Herzberg Institute of Astrophysics, Victoria, Canada.*

³*Astronomy Department, Universidad de Chile, Las Condes, Chile*

*Contact: pzorzi@ing.uchile.cl, phone +56-2-9780691

Abstract— In this paper, we revisit the optics design for the ALMA Band 1 cartridge as presented previously by M. Carter and report on progress made towards that end. Since the layout of the ALMA cartridges is not optimised for the lowest frequency band, certain design trade-offs must be made; most importantly the use of a re-focusing lens is required to avoid blocking other bands and the ALMA calibration device assembly. Furthermore, we are motivated to analyse the optics design because close to half of the receiver noise budget is consumed by the optics, mostly due to truncation, reflection, and dielectric loss of the lens and infrared filters. Any small improvement in the optics is worthwhile as its contribution is cascaded through the receiver. Also of significance, the antenna and cryostat layout has changed since the original reports and that related to Band 1 must be clarified and updated.

I. INTRODUCTION

The Atacama Large Millimetre Array (ALMA) will be the largest millimetre and sub-millimetre radio telescope in the world. It is under construction in the Altiplano region of northern Chile, specifically in the Chajnantor Plateau. This is an extremely dry site at 5000 m altitude. Consequently it is one of the best sites on earth for the measurement of millimetre/sub-millimetre radiation from astronomical sources. ALMA combines an array of 66 antennas designed for continuum and spectroscopic measurements of the early Universe. It will also reveal new information about the birth of stars, planets, and galaxy formations with an angular resolution accuracy of 1". Moreover, it will provide high sensitive and precision imaging between 30 and 950 GHz in 10 bands at the Southern Hemisphere.

Each telescope will have a common cryostat that was specially designed to house all ten receiver bands. The dimensions of this cryostat are 0.97 m in diameter and a 0.62 m in height. Each receiver are designed to measure total power and dual linear polarization state of the received signal at a given frequency. They will be built in a cylindrical structure called *cartridge* which is divided in three section-levels cooled down to 4, 15 and 110 K, respectively. This telescope will be fully functional in about 2012. ALMA Band 1 will offer many unique scientific research capabilities related to the field of radio astronomical observation for low centimeter wavelength ranges. There are several important radio astronomical studies that can be made at this frequency band. Among them, the most interesting ones are the Cosmic Microwave Background radiation (CMB) anisotropies studies, high-resolution Sunyaev-Zel'dovich (SZ) effect

imaging of cluster gas at all redshifts, gravitational lenses survey and monitoring, and mapping the cold Inter Stellar Media (ISM) matter at intermediate and high redshift.

The aim of paper is to provide information about the different aspects that involve the design, optimization and construction of a suitable optical system for the 31-to-45GHz receiver that will be part of the prototype receiver for Band 1 of ALMA. Three optical layouts will be presented: (1) a single HDPE lens that also acts as vacuum window – this is the original configuration[**1,2**], (2) two lenses forming a Gaussian beam telescope where the first lens is cooled, and (3) a single room temperature lens, but using a separate thinner vacuum window, giving more freedom to the choice of material for the lens. In each scenario, the feed is represented as an optimum gain horn and first-order Gaussian beam analysis, i.e., quasioptics, has been used to model the system. Each system is optimized for frequency independent illumination of the secondary and aperture efficiency, and then put into context through a comparison of the predicted receiver noise. Focus efficiency has been placed at a lower priority since it is assumed that the secondary can be refocused.

Progress on component development, including a comparison of different feedhorn designs and modelling will be summarised. There is also considerable interest in either extending or shifting the existing frequency range of 31-45 GHz towards 50 GHz, and consideration of the impact concerning the optics will be provided.

II. OPTICAL DESIGN

We started our work rechecking and updating some of the antenna and cryostat layout dimensions presented in [**1**] and [**2**] for the ALMA Band 1 optics. Our work continued with finding an optimum gain horn design that fit the ALMA cassegrain antenna specifications between 31 to 45 GHz frequency band. Once this was achieved, we proceeded to analyse the Gaussian beam propagation [**3**] between the horn and the antenna subreflector at those frequencies, using a thin lens approximation optical design. When a -12.3dB edge taper (this value gives the best ALMA antenna aperture efficiency for our quasioptical system design) for a frequency independent illumination at the subreflector were achieved in the simulations (i.e. when the Gaussian beam radius at the sub reflector is constant at any frequency) then we retrieved from the optimizations result the values of the lens focal distance, its separation from the horn, and the beam radius of

the propagating beam between the lens and the subreflector. Thereby, the lens thickness was derived using a bi-hyperbolic lens design, which preserve the face of the propagating beam [3] when pass through the lens. Finally, the total noise contribution of the optics was estimated for each one of the proposed optical configuration.

A. Optical layout dimensions

In this section we present the final layout location and dimension of the different optical parameters for this band. Those values are of importance when estimating the truncation losses and the edge taper of the receiving signal when using quasioptical beam analysis. In Table 1 are summarized the most relevant optical parameters that we used in all our different simulations.

TABLE 1
BAND 1 UPDATED OPTICAL DIMENSIONS

PARAMETER	VALUE
Distance dewar top center to subreflector rim center	5.99380 m
Distance dewar top center to subreflector apex	5.88287 m
Angle horn to subreflector apex	2.48 deg.
Optimal horn z-distance to dewar top	93 mm
Optimal horn x,y-distance to dewar center	263.6 mm
15 K and 110 K stage z-distance to dewar top	83 mm, 51 mm
15 K and 110 K stage clearance aperture diameter	40 mm, 60 mm
Dewar-top hole clearance diameter	110 mm

B. The Feedhorn

Figure 1 shows two different horn profile geometries that we studied. The first horn design was proposed by M. Carter [4]. In the same figure a similar horn geometry but with a simpler corrugation design is presented. This corresponds to our own horn design, which was developed using the concepts from reference [5]. Its final geometry was optimized using Ansoft HFSS electromagnetic software [6]. Both have the same aperture diameter and total length, but horn 1 has a variable pitch-to-width ratio while for the second horn this parameter is constant.

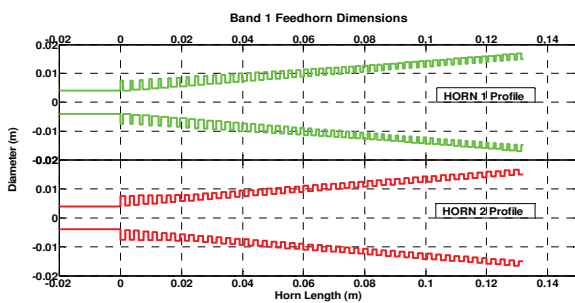


Fig. 1 Corrugated horn 1 and 2 geometries.

C. Bi-Hyperbolic Lens Design

An important part of the work was to use different dielectric materials in the simulations to find the one that minimizes the lens thickness and therefore the dielectric losses of the same. Table 1 presents the material properties used for the different investigated optical layout

configurations and their optical components. The IR-filters dimensions and properties are also included in this table. Those filters have already being designed by the IRAM for all the ALMA receiver bands [7].

TABLE 2
OPTICAL COMPONENT DIELECTRIC PROPERTIES

Dielectric Material for:	Material	Souranding Temp. (K)	Refractive index n	Tan loss (e-004)
Lens:	HDPE*	300, 15	1.5259	2.73
	Quartz*	300	2.1056	0.45
	Silicon*	300	3.4165	4.00
Vac.Window:	Quartz*	300	2.1056	0.45
	SolidPTFE	110	1.5000	3.00
IR Filter:	Gore-Tex	15	1.2000	2.00

* Refractive index and tan-loss values where averaged from well know experimental measured data taken from [3] and [8].

D. Studied Optical Configurations

The technical specifications of the ALMA Band 1 cartridge and cryostat design are presented in [2] and [9]. In both documents is stated that the use of a re-focusing lens device is required to avoid blocking the other receiver bands. That lens will be located between the top of the dewar and the antenna calibration system assembly. Since in the ALMA antennas there will not be moving optical parts, besides the subreflector, the design of the all the ALMA bands optical setups must be frequency independent (i.e. the illumination at the subreflector must approximately be constant for all wavelengths). Thus the antenna efficiency will be maximized. According to [10], the edge taper must be of about 12.3 dB. The studied optical system configuration that we present in this paper consisted in 3 single lens system layouts and a 2-lens optical system. The details of those layouts are the following:

1) Optical layout 1: In this configuration a single HDPE lens at 300 K was used. The lens optimal simulation result gave us a diameter was of 20 cm and the total thickness was 5.72 cm. The single lens used here acts also as a vacuum window.

2) Optical layout 2: Two HDPE lens system. A small one placed inside the cryostat 15 K stage, and the second one locate between the top of the dewar and the ALMA calibrator device at 300 K.

3) Optical layout 3: As in the first optical layout, this system also uses a single lens at 300 K but now we assume that this is made of quartz instead. A quartz vacuum window is also used at the top of the dewar.

4) Optical layout 3: Here, the quartz lens used in the previous layout was replaced with a silicon lens design. It also has a quartz vacuum window at 300 K.

III. SIMULATION RESULTS

A. Horn Radiation and Phase Patterns

In Figure 2 the simulated radiation pattern performances for horn 1 and horn 2 at 38 and 50 GHz are shown. Figure 3 shows their respective return losses from 30 GHz up to 50 GHz.

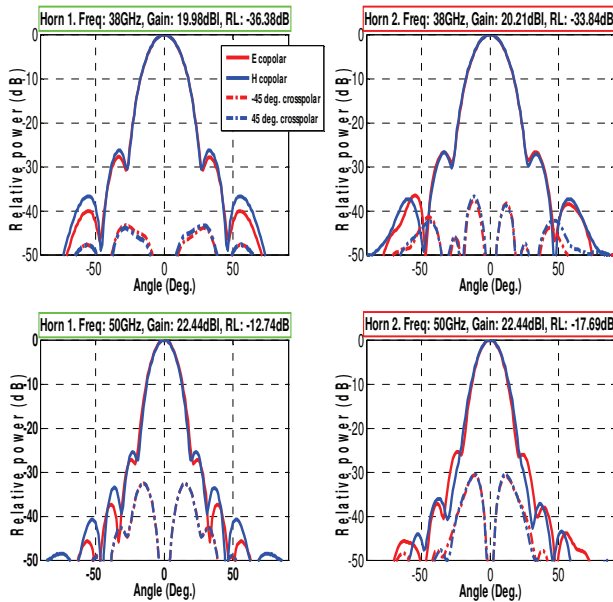


Fig. 2 CST [11] and HFSS simulated radiation patterns of the corrugated conical horn 1 and 2, at 38 and 50 GHz.

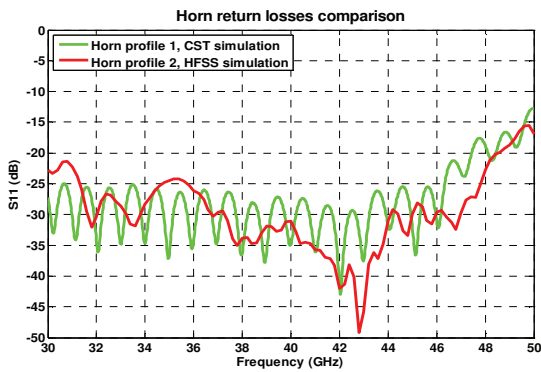


Fig. 3 Simulated return loss for the corrugated conical horn 1 and 2 between 30 to 50 GHz

The simulated radiation patterns and return losses results shows that horn 1 and 2 have very similar shapes. Although, the cross-polarization levels of horn number 1 are better than the ones obtained with the second horn. Figure 3 shows the far-field phase pattern of horn 1 at different frequencies.

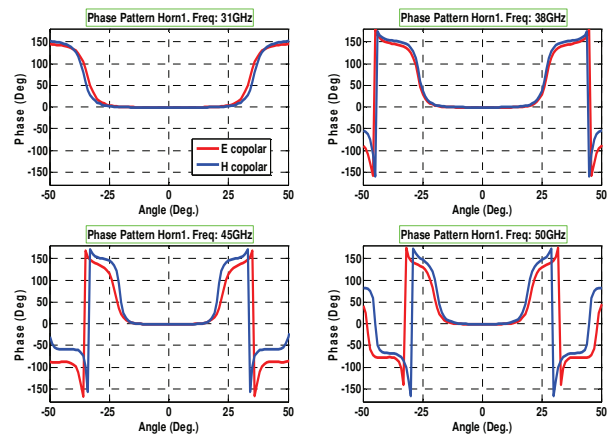


Fig. 4 CST Microwave Studio Simulated far-field phase patterns for the corrugated conical Horn 1 at 31.1, 38, 45, and 50 GHz.

B. Quasioptical Beam Analysis

Quasi-optics analysis of ALMA Band 1 system was carried out using thin lens approximation for the focusing elements. Further on, in this design we optimized very carefully the system total gain and its total noise contribution, taking into account the lens dimensions, its refractive index, thickness, focal distance, and as well as the IR filters dimensions, and material properties. The final simulation results were based on the horn 1 design presented in this paper and the geometry of the ALMA Cassegrain antenna, which details can be found in [2]. The final simulated results for the 4 different layouts are presented in Table 3. In Figure 3 the Gaussian beam propagation of the fundamental mode for the optical layout 1 is shown at 31.3, 38, and 45 GHz.

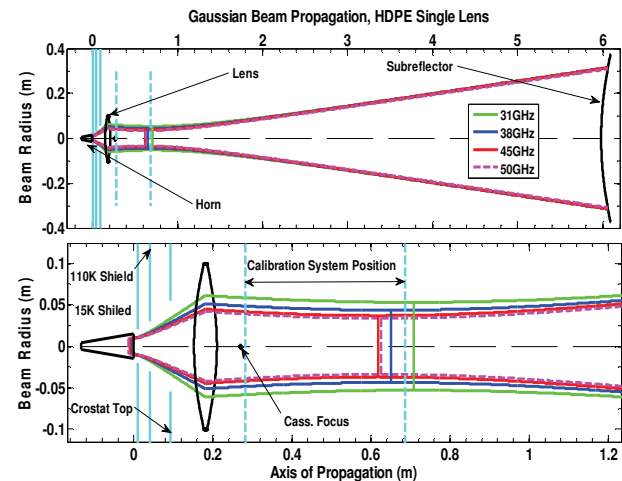


Fig. 5 Gaussian beam propagation between the horn and the antenna subreflector (top) and a magnified view of the same closed to the horn-lens part (bottom).

TABLE 3
BAND OPTICAL PARAMETERS FOR THE DIFFERENT LAYOUTS

	Layout 1	Layout 2	Layout 3	Layout 4
Lens 1.				
Material:	HDPE	HDPE	Quartz	Silicon
Distance to horn [m]:	0.1812	0.2620	0.1812	0.1812
Focal length [m]:	0.1750	0.1778	0.1750	0.1750
Diameter [m]:	0.2000	0.2076	0.2000	0.2000
Thickness [m]:	0.0578	0.0598	0.0325	0.0194
Vacuum Window.				
Material:	None	None	Quartz	Quartz
Distance to horn [m]:	None	None	0.0930	0.0930
Diameter [m]:	None	None	0.1100	0.1100
Thickness [m]:	None	None	0.00065	0.00065
Lens2.				
Material:	None	HDPE	None	None
Distance to horn [m]:	None	0.0700	None	None
Focal length [m]:	None	0.0382	None	None
Diameter [m]:	None	0.0782	None	None
Thickness [m]:	None	0.0379	None	None
Edge Taper [dB].				
31GHz	-12.32	-12.43	-12.32	-12.32
38GHz	-12.33	-12.51	-12.33	-12.33
45GHz	-12.34	-12.58	-12.34	-12.34
50GHz	-12.35	-12.35	-12.35	-12.35

E. Total Gain and Noise Estimations

After optimizing the illumination efficiency of each one of the optical system layouts, we estimated the total noise contribution of each one optical layout configurations. The gain and noise contribution related to the beam truncations, dielectric losses, and reflection losses of the lens and IR-Filters were included in the overall noise calculations. Truncation and reflection termination temperatures were taken as average of both sides. The reflection losses in the lenses and IR-filters were modelled assuming perfect surface matching. Therefore those losses were estimated to be of about -20 dB for the lens cases and -25 dB for the IR-filters. Focus efficiency of the antenna has been placed at a lower priority since it is assumed that the secondary can be refocused. Figure 6 shows the total optic noise contributions estimated for each one of the systems.

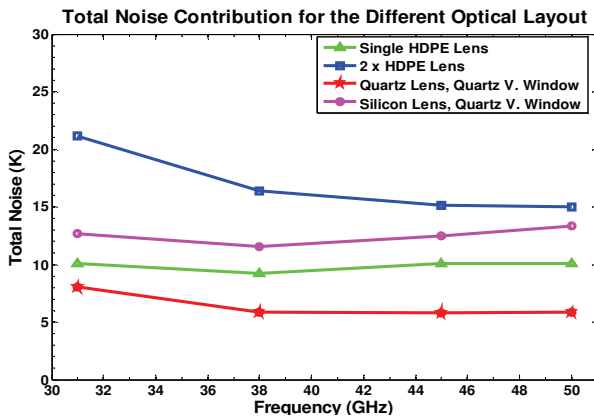


Fig. 6 Total noise estimation of the 4 different studied optical layouts.

Layout 3 (quartz lens + quartz vacuum window) provides the lowest system noise contribution. From the practical and economic point of view, layout 1 (single HDPE lens design) is a more competitive system since it is easier to construct with a CNC machine.

F. Surface matching of the lens

The lens reflection losses were modeled with CST Microwave Studio [11] using straight grooves and hole patterns. According to the preliminary results, a hole pattern gives the same performance for both linear polarisations. The simulation results of straight grooves surface matching is presented in Figure 7, while Figure 8 shows the results of the lens hole patterns surface matching. Their corresponding profiles geometries are shown in Figure 8.

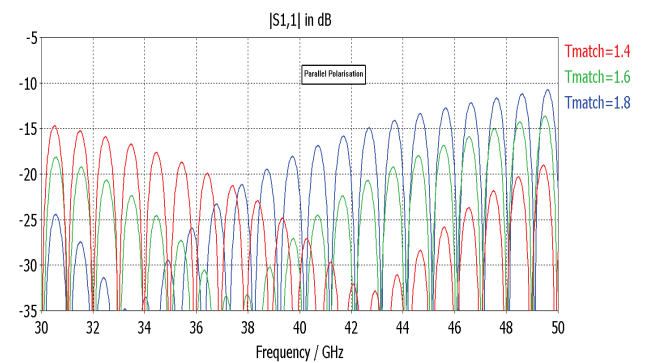


Fig. 7 Straight grooves surface matching between 30 to 50 GHz.

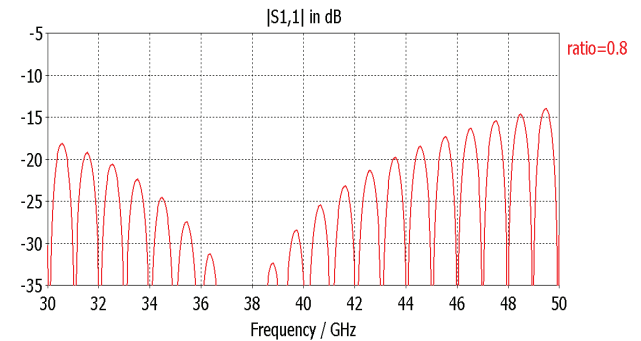


Fig. 8 Hole patterns surface matching between 30 to 50 GHz

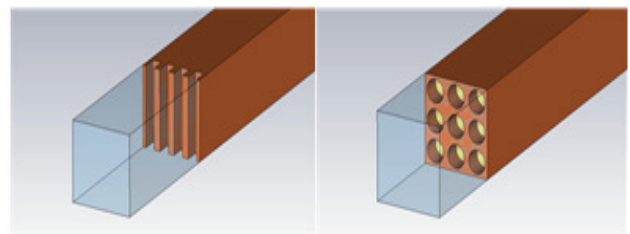


Fig. 8 Straight groove and hole pattern profile geometries.

IV. CONCLUSIONS AND FUTURE WORK

We have found that the dimensions of the optical parameters as proposed in the ALMA project book were not completely correct. When comparing the horn simulation results designed by M. Carter with our own simpler horn design, we found that both designs have rather similar characteristics although Carter's have slight better cross polarization. The quartz lens optical design (layout 3) gave the best noise performance of all the 4 different optical configuration layouts presented in this paper. However, the single HDPE lens design, originally proposed by ALMA, continues to provide a good noise performance given the layout constraints of the cryostat. Moreover, the main advantage of using a HPDE lens with an antireflection surface matching (e.g. with a machined hole pattern geometry) is that it is easier and less expensive to construct using a CNC lathe machine than using a lens made of quartz.

Before constructing and testing the HDPE lens or the quartz lens, a physical optics analysis of both configurations will be completed using Zemax. This will help to optimize the final shape and optical parameters of the lens. Also, the first horn prototype is being constructed now and will be tested soon.

ACKNOWLEDGMENT

Part of this work received support from the Center of Excellence in Astrophysics and Associated Technologies

(PBF 06), and from the ALMA-CONICYT Fund for the Development of Chilean Astronomy (Projects 31080003 and 31080004).

REFERENCES

- [1] J. W. Lamb, "Low-Noise, High-Efficiency Optics Design for ALMA Receivers," *IEEE Trans Antennas Propagat.*, vol. 51, pp. 2035-2047, 2003.
- [2] "ALMA Front-end Optics Design Report," FEND-40.02.00.00-035-B-REP, March 30, 2007, ALMA EDM. [Online] <http://edm.alma.cl>.
- [3] P. F. Goldsmith, *Quasioptical Systems: Gaussian Beam Quasioptical Propagation and Applications*. New York: IEEE Press, 1998.
- [4] "ALMA Front End Optics Design Report, Appendix 1, Band 1 Optics Measurements", FEND-40.02.00.00-035-B-REP, July 19, 2007. ALMA EDM. [Online] <http://edm.alma.cl>.
- [5] C. Granet and G. L. James. *Design of Corrugated Horns: A Primer*. IEEE Antennas and Propagation Magazine, Vol. 47, No. 2, April 2005.
- [6] High Frequency Structure Simulator (HFSS), version 11, Ansoft Corporation, Pittsburgh, PA, USA.
- [7] "ALMA Front End Optics Design Report Appendix 11 Window and IR-Filter Measurements" FEND-40.02.00.00-035-B-RE, July 15, 2008. [Online] <http://edm.alma.cl/>
- [8] J. W. Lamb, "Miscellaneous data on materials for millimeter and submillimeter optics," *Int. J. Infrared Millim. Waves*, vol. 17, no. 12, pp. 1997-2034, Dec. 1996.
- [9] H. Rudolf, M. Carter, and A. Baryshev, "The ALMA Front End Optics—System Aspects and European Measurement Results". *IEEE TRANSACTIONS ON ANTENNAS AND PROPAGATION*, VOL. 55, NO. 11, NOVEMBER 2007.
- [10] J. Lamb et al., "ALMA receiver optics design". ALMA Memo #362, 2001.
- [11] © 2010 CST Computer Simulation Technology AG. All rights reserved

Towards Standardized Waveguide Sizes and Interfaces for Submillimeter Wavelengths

N. M. Ridler^{1*}, R. A. Ginley², J. L. Hesler³, A. R. Kerr⁴, R. D. Pollard⁵, D. F. Williams²

¹National Physical Laboratory (NPL), Teddington, UK

²National Institute of Standards and Technology (NIST), Boulder, CO, USA

³Virginia Diodes, Inc, Charlottesville, VA, USA

⁴National Radio Astronomy Observatory (NRAO), Charlottesville, VA, USA

⁵University of Leeds, Leeds, UK

*Contact: nick.ridler@ieee.org, phone +44-208-943-7116

Abstract—This paper describes an activity that has begun recently to develop an international standard for rectangular metallic waveguides and their interfaces for frequencies of 110 GHz and above. The IEEE's Microwave Theory and Techniques Society (MTT-S) is sponsoring the development of this standard. The MTT-S Standards Committee has set up the P1785 Working Group tasked with undertaking the work that is necessary to write this standard. This paper describes the work to date of this Working Group and the future activities that will be necessary to complete the standard.

Index terms—Waveguides, rectangular waveguides, millimetre-wave, submillimeter-wave, waveguide flanges, waveguide interfaces

I. INTRODUCTION

At the present time, no international document standards exist for defining sizes and interfaces for rectangular metallic waveguides used at submillimeter wavelengths (i.e. at frequencies above 325 GHz). Some proposals for sizes and interfaces have been published in recent years (e.g. [1-7]) but these have not yet been adopted by any of the international standards-making bodies (e.g. ISO, IEC, IEEE). This situation was recognized recently by the IEEE Standards Association, and this has led to a project being initiated to put in place an IEEE standard for both waveguide sizes (i.e. the aperture dimensions) and their associated interfaces (e.g. flanges) suitable for use at all frequencies above 110 GHz. Although standards already exist for waveguides in the 110 GHz to 325 GHz range (see, for example, [8, 9]), these waveguides will also be included in the new IEEE standard to allow their tolerances to be re-evaluated in the context of contemporary manufacturing capabilities.

The development of the new standard is being sponsored by the Standards Committee of the IEEE's Microwave Theory and Techniques Society (MTT-S). A working group has been set up (and assigned the project number P1785) that will write the standard and ensure that it is published in a timely manner. This working group held its first meeting during the International Microwave Symposium (IMS) in Atlanta, GA, USA, in June 2008. The working group has since met a further three times (i.e. approximately every six months), with the next meeting scheduled to take place during IMS in Anaheim, CA, USA, in May 2010

(www.ims2010.org). Membership of the P1785 Working Group is open to all persons with an interest in this area, and membership to the P1785 Working Group can be achieved by attending at least one, or more, of the working group meetings. The working group currently has 22 members.

It is envisaged that the standard will be published in two parts: one part dealing with waveguide dimensions and recommended frequency bands; the other part dealing with waveguide interfaces (including flanges). The working group is already making good progress with Part 1 of the standard and it is likely that a first draft will be available for public comment during 2011.

This paper gives a review of all the activities of the P1785 Working Group. The paper describes the progress of the working group to date – specifically, the work on defining frequency bands and waveguide aperture dimensions. This includes a review of the waveguide size scheme that has been provisionally chosen for inclusion in the IEEE standard. The paper also describes the planned working group activities for the future, including: the other remaining steps needed to complete Part 1 of the standard; and, information about waveguide interfaces to be included in the standard. More information about the standard, and the activities of the P1785 Working Group, can be found at: <http://grouper.ieee.org/groups/1785>.

II. PROGRESS TO DATE

Much of the first two meetings of the P1785 Working Group, in June and December 2008, were concerned with defining the general scope of the standard and the level of detail for the information to be included in the standard. It was also agreed during these early discussions that metric units¹ (i.e. millimeter and micron) will be used in the standard, rather than the Imperial units (i.e. inch and mil) that had been used in the existing MIL standard [8]. Similarly, although no official standard for frequency bands and waveguide dimensions currently exists for frequencies above 325 GHz, it was recognised that a significant amount of scientific work is already taking place at these higher frequencies. Much of this work has used the proposed

¹ Following the International System of units (i.e. *Système International d'unités*, abbreviated to **SI**).

frequency bands given in [3] – see, for example, [10] and [11]. These waveguide bands use an extension of the WR naming convention given in the MIL standard [8], leading to waveguide names such as WR-2.8, WR-2.2, etc. However, the dimensions of these waveguide bands are defined in terms of Imperial units² and so do not meet the agreed requirement that the IEEE standard will use dimensions defined in terms of metric units.

At the third P1785 Working Group meeting (in Boston, MA, USA, in June 2009), a great deal of attention was given to the subject of defining the waveguide frequency bands and aperture sizes. This led to the setting up of a dedicated sub-group, within the P1785 Working Group, tasked with recommending to the main P1785 Working Group potential schemes for defining waveguide frequency bands and aperture sizes. This sub-group³, with membership from the USA and Europe, communicated regularly using email and teleconferencing. Over a period of six months or so, the sub-group developed a series of potential waveguide schemes that fitted, to a greater or lesser degree, some generally agreed design criteria. However, it also became clear that no unique waveguide scheme existed that perfectly met all the design criteria. The ten design criteria that were established during this process are described below.

A. Frequency bands

The frequency bands (i.e. the suggested lower and upper frequencies of each waveguide band) should:

1. Be memorable (i.e. use whole numbers);
2. Form two contiguous interleaved series (i.e. should not contain gaps or overlaps in the frequencies covered by each series);
3. Be easily extendable from lower frequencies to higher frequencies (i.e. mapping from one decade to the next);
4. Agree with the existing values for WR-10 to WR-03, as given in the MIL standard [8].

B. Waveguide dimensions

It was soon agreed that a ratio of 2:1 would be used to describe the relationship between the waveguide aperture width and height (i.e. the ratio of the broad- to narrow-wall dimensions). Therefore, it was only necessary to define the waveguide broad-wall dimension (called the ‘width’, by convention). The waveguide widths should:

5. Where appropriate, be effectively identical (within stated tolerances) to sizes WR-10 to WR-03, as given in the MIL standard [8];
6. Where appropriate, be very similar to sizes WR-2.8 to WR-1.0, as given in [3];
7. Avoid fractional micron values (i.e. $x.y$ microns).

² The number 2.8 in the name WR-2.8 refers to the defined broad-wall dimension of the waveguide, i.e. (2.8×10) mil = 28 mil.

³ The members of the subgroup were Jeffrey Hesler, Anthony Kerr, Roger Pollard, Nick Ridler and Dylan Williams.

C. Related quantities

In addition to the above, the waveguide scheme should provide, for all bands:

8. Relatively uniform fractional bandwidths;
9. Approximately constant k -factors⁴ (where $k_1 \approx 1.25$ and $k_2 \approx 1.90$);
10. Similar ratios of cut-off frequencies (or, equivalently, waveguide widths) for adjacent bands.

The subgroup developed a spreadsheet to assist in the development and evaluation of candidate waveguide schemes. The spreadsheet included plots of size deviations from current standards, worst-case reflection coefficients due to these size deviations, cutoff-frequency ratios, fractional bandwidths, and k -factors. This spreadsheet will soon be made available at: <http://grouper.ieee.org/groups/1785>. The spreadsheet and design criteria discussed above were used to establish a short-list of three candidate waveguide schemes⁵ that were presented subsequently to the P1785 Working Group for discussion, followed by a vote.

The first scheme was derived from [3]. It retained the familiar WR names and recommended operating bands currently being used, but used metric sizing. This scheme resulted in excellent compatibility with existing practice and retained familiar nomenclature and operating bands while providing a metric framework for dimensions. The disadvantages were seen to be an irregularity in the progression of the scheme, fractional numbers in the nomenclature and significant variations in the mismatch and k -factor spread.

The second scheme was developed within the subgroup itself [12], and used the names WM n , where n was an integer or half integer denoting the waveguide size. This resulted in names of the form WM 0, WM 0.5, WM 1, WM 1.5, etc, keeping names short and making it easy to identify neighbouring bands. Sizes for WM 0 to WM 2.5 were chosen from a table to correspond closely to existing standards, but above WM 2.5, the waveguide width, a , is determined by rounding $10^{(-2n/11)} \times 2540 \mu\text{m}$ to three significant digits. This formula-based approach ensured a uniform and unlimited geometric progression of center frequencies with exceptionally uniform operating bandwidths to simplify the development of certain instrumentation and even allowed for the natural definition of quarter-band sizes when necessary, while keeping deviations from established bands below the measureable limits of today’s instrumentation and standards. However, the scheme did break from the convention of using the waveguide sizes themselves as names, changing the current nomenclature style by having numbers increasing with decreasing waveguide size, and adjusted recommended operating frequency bands somewhat from existing practice.

⁴ These k -factors are the multipliers used to establish the suggested minimum frequency, f_{\min} , and maximum frequency, f_{\max} , from the cutoff-frequency, f_c , for each waveguide band: $f_{\min} = k_1 \times f_c$; $f_{\max} = k_2 \times f_c$.

⁵ Two of these schemes were derived from [3] and [6], along with a third scheme proposed in [12].

The provisional scheme eventually selected, following a discussion and vote by the P1785 Working Group, is shown in Table 1, where *a* and *b* refer to the width and height dimensions of the waveguides, respectively.

TABLE I
PROPOSED FREQUENCY BANDS AND WAVEGUIDE DIMENSIONS FOR THE IEEE STANDARD

Name	<i>a</i> (μm)	<i>b</i> (μm)	<i>f_c</i> (GHz)	<i>f_{min}</i> (GHz)	<i>f_{max}</i> (GHz)
WM-2540	2540	1270	59.014	75	110
WM-2032	2032	1016	73.767	90	140
WM-1651	1651	825.5	90.790	110	170
WM-1295	1295	647.5	115.75	140	220
WM-1092	1092	546	137.27	170	260
WM-864	864	432	173.49	220	330
WM-710	710	355	211.12	260	400
WM-570	570	285	262.97	330	500
WM-470	470	235	318.93	400	600
WM-380	380	190	394.46	500	750
WM-310	310	155	483.53	600	900
WM-250	250	125	599.58	750	1100
WM-200	200	100	749.48	900	1400
WM-164	164	82	913.99	1100	1700
WM-130	130	65	1153.0	1400	2200
WM-106	106	53	1414.1	1700	2600
WM-86	86	43	1743.0	2200	3300

This scheme, which is based on [6], was produced as follows:

- (i) use the existing MIL series [8] as the basis;
- (ii) scale widths by dividing by 10;
- (iii) express the resulting widths using rounded metric units, i.e. microns.

Minor adjustments have been made to the widths in three bands (but keeping the frequency bands the same) to make the ratios of cut-off frequency values between bands closer to the ideal value of $10^{(1/11)} \approx 1.233$ without appreciably increasing the mismatch when connected to the corresponding waveguides given in [3]. The scheme also uses a suggested upper frequency for the WM-864 band of 330 GHz (rather than 325 GHz), and an associated suggested lower frequency of 330 GHz for the WM-570 band.

In terms of meeting the above design criteria, the frequency bands:

- 1. Are memorable, i.e. the suggested minimum and maximum frequencies are ten times the values for the MIL frequency bands [8] used for the decade below (with the exception that 325 GHz has been changed to 330 GHz), thus giving full backward compatibility with existing waveguide bands;
- 2. Link together as two contiguous, interleaved, series:
 - (i) WM-710, WM-470, WM-310, etc; and,
 - (ii) WM-570, WM-380, WM-250, etc;

- 3. Are extendable to higher frequencies (i.e. smaller waveguide sizes) as follows:
 - a. use the waveguide sizes that are unshaded in Table 1;
 - b. divide mechanical dimensions by 10;
 - c. multiple frequencies by 10;
 - d. rename the waveguide accordingly.

For example, the next two sizes in this series (derived from WM-710 and WM-570) are shown in Table 2;

TABLE II
EXTENDED FREQUENCY BANDS AND WAVEGUIDE DIMENSIONS FOR THE IEEE STANDARD

Name	<i>a</i> (μm)	<i>b</i> (μm)	<i>f_c</i> (GHz)	<i>f_{min}</i> (GHz)	<i>f_{max}</i> (GHz)
WM-71	71	35.5	2111.2	2600	4000
WM-57	57	28.5	2629.7	3300	5000

- 4. Are identical with the MIL standard bands [8] in the overlap region, shaded in Table 1, with the exception that 325 GHz has been changed to 330 GHz.

Similarly, the waveguide dimensions (i.e. the widths):

- 5. Are within 0.05% of MIL standard widths [8] in the overlap region, shaded in Table 1. This produces a worst-case mismatch (i.e. return loss) when connecting to the corresponding MIL standard bands [8] of -70 dB (not including mismatch due to waveguide tolerances);
- 6. Are within 3% of the widths given in [3]. This produces a worst-case mismatch (i.e. return loss) when connecting to the corresponding bands in [3] of -35 dB (not including mismatch due to waveguide tolerances);
- 7. Do not use fractional micron values (until the series has been extended to include WM-16.4, i.e. for the frequency range 11 THz to 17 THz!)

Similarly, for the related quantities for all bands:

- 8. Ratios of minimum to maximum frequency vary between 1.47 and 1.57, indicating that all bands have relatively uniform bandwidths;
- 9. *k*-factor values are relatively constant, ranging from $1.20 \leq k_1 \leq 1.27$ and $1.83 \leq k_2 \leq 1.91$;
- 10. Ratios of cut-off frequencies for adjacent bands vary between 1.19 and 1.27 and so are considered similar.

Finally, a new naming convention has been developed for these waveguide bands. Since the sizes are defined in terms of metric units, the letters WM are used to indicate that the size refers to **Waveguide using Metric** dimensions. These letters are followed by a number that indicates the size (in microns) of the waveguide broad wall dimension. Table 3 gives a comparison between these new names and the names of related waveguides in the existing MIL standard [8]. Table 4 gives a comparison between the new names and the nearest waveguides given in [3] (i.e. the 'extended MIL' bands).

TABLE III
COMPARISON BETWEEN NEW IEEE AND EXISTING MIL WAVEGUIDE NAMES

MIL name	New IEEE Name	f_{\min} (GHz)	f_{\max} (GHz)
WR-10	WM-2540	75	110
WR-08	WM-2032	90	140
WR-06	WM-1651	110	170
WR-05	WM-1295	140	220
WR-04	WM-1092	170	260
WR-03	WM-864	220	330

TABLE IV
COMPARISON BETWEEN NEW IEEE AND 'EXTENDED MIL' WAVEGUIDE NAMES

'Extended MIL' name	New IEEE Name	f_{\min} (GHz)	f_{\max} (GHz)
WR-2.8	WM-710	260	400
WR-2.2	WM-570	330	500
WR-1.9	WM-470	400	600
WR-1.5	WM-380	500	750
WR-1.2	WM-310	600	900
WR-1.0	WM-250	750	1100

This naming convention can easily accommodate 'specialized' (i.e. custom made) waveguide bands, should they be needed, simply by giving the WM letters followed by the broad wall dimension of the custom made waveguide, expressed in microns.

III. FUTURE ACTIVITIES

A. Other waveguide size information

Having chosen a scheme for defining the frequency bands and the waveguide dimensions, this information will be contained in a table in Part 1 of the IEEE standard. It is envisaged that this table will also contain some additional information about each waveguide size. For example, it will be useful to specify tolerances on the critical mechanical dimensions of the waveguide. It has already been discussed within the P1785 Working Group that perhaps two 'grades' of waveguide quality may be given, based on the specified tolerances of the critical dimensions – a 'precision' grade, based on the best achievable tolerances using state-of-the-art manufacturing techniques, and a 'general' grade, that will be realisable using more routine manufacturing techniques.

Other specification parameters for the waveguides are also likely to be given – for example, typical attenuation per unit length, typical mismatch due to waveguide tolerances, etc.

B. Waveguide interfaces

The other main topic that will be covered by this IEEE standard is the definition of suitable interfaces for waveguides used above 110 GHz. It is widely recognised that the popular waveguide interfaces used at millimetre-wave frequencies up to 110 GHz (for example, MIL-DTL-3922/67D [13], also known as UG-387) will not be suitable for use at these higher frequencies. This is

because waveguide misalignment, due to tolerances on the critical dimensions of the interfaces, will cause unacceptably large reflections in these smaller waveguide sizes when fitted with such interfaces.

Instead, the suitability of alternative interface designs will be investigated for use with the waveguide sizes specified in the IEEE standard. There are already several interface designs that could be included in the standard. These include:

1. A precision version of UG-387, with tighter tolerances and anti-cocking mechanisms [3]. This could also include additional alignment pins directly above and below the waveguide aperture [1];
2. A miniature flange (the so-called Grammer miniature flange) [3] that has been developed by NRAO for use with the ALMA project⁶;
3. A 'plug-and-socket' style of interface [4];
4. A ring-centered flange (see [5] and [7]), of similar dimensions to the UG-387 flange (i.e. with an outer diameter of approximately 19 mm);
5. A miniature ring-centered flange [5], of similar dimensions to the Grammer miniature flange (i.e. with an outer diameter of approximately 12.7 mm).

It is likely that several different types of waveguide interface will be included in the standard so that users can select a suitable design for their particular application (including frequency range).

IV. CONCLUSIONS

This paper has described an on-going activity to develop an international standard for waveguides and their interfaces for use at frequencies of 110 GHz and above. The work to date on defining the frequency bands and waveguide dimensions has been described in detail. It is hoped that potential users of these waveguides will study these proposed frequency bands and waveguide sizes and comment on their suitability for their applications.

The plans for the future development of the standard have also been described. This has included a description of some waveguide interfaces that may be included in the standard. As before, it is hoped that potential users of these interfaces will study these proposed designs and comment on their suitability. Any such comments, either on frequency bands, waveguide sizes or waveguide interfaces, should be sent to: nick.ridler@ieee.org. Comments concerning the proposed frequency bands and waveguide sizes should be sent before May 2010, since this is when the P1785 Working Group will make a decision on whether to accept these proposed frequency bands and waveguide sizes.

ACKNOWLEDGMENTS

The funding for Mr Ridler's involvement with this activity is provided by the National Measurement Office of the UK government's Department of Business, Innovation and Skills. The National Radio Astronomy Observatory is a facility of

⁶ ALMA is the Atacama Large Millimeter / submillimeter Array, www.alma.nrao.edu.

the National Science Foundation operated under cooperative agreement by Associated Universities, Inc.

REFERENCES

[1] C. Oleson and A. Denning, "Millimeter Wave Vector Analysis Calibration and Measurement Problems Caused by Common Waveguide Irregularities", *Proc. 56th ARFTG Microwave Measurement Conf.*, Boulder, CO, USA, December 2000.

[2] J. S. Ward, "New Standards for Submillimeter Waveguides", *Proc. 17th Int. Symp. on Space THz Tech.*, Paris, France, May 2006.

[3] J. L. Hesler, A. R. Kerr, W. Grammer and E. Wollack, "Recommendations for Waveguide Interfaces to 1 THz", *Proc. 18th Int. Symp. on Space THz Tech.*, Pasadena, CA, USA, March 2007.

[4] Y. S. Lau and A. Denning, "An Innovative Waveguide Interface for Millimeter Wave and Sub-millimeter Wave Applications", *Proc. 69th ARFTG Microwave Measurement Conf.*, Honolulu, HI, USA, June 2007.

[5] A. R. Kerr and S. Srikanth, "The Ring-centered Waveguide Flange for Submillimeter Wavelengths", *Proc. 20th Int. Symp. on Space THz Tech.*, Charlottesville, VA, USA, April 2009.

[6] N. M. Ridler, "Recommendations for Waveguide Sizes at Submillimeter Wavelengths", *Proc. 73rd ARFTG Microwave Measurement Conf.*, Boston, MA, USA, June 2009.

[7] H. Li, A. R. Kerr, J. L. Hesler, H. Xu, R. M. Weikle II, "A Ring-centered Waveguide Flange for Millimeter- and Submillimeter-wave Applications", accepted for publication, *IEEE MTT-S International Microwave Symposium*, Anaheim, CA, USA, May 2010.

[8] MIL-DTL-85/3C, "Waveguides, rigid, rectangular (millimetre wavelength)", October 2005.

[9] IEC 60153-2, "Hollow metallic waveguides. Part 2: relevant specifications for ordinary rectangular waveguides", 2nd edition, 1974.

[10] C. Oleson, A. Denning and Y. Lau, "325 to 500 GHz Vector Network Analysis System", *Proc. 66th ARFTG Microwave Measurement Conf.*, Washington, DC, USA, December 2005.

[11] L. Samoska et al, "A Submillimeter-wave HEMT Amplifier Module with Integrated Waveguide Transitions Operating Above 300 GHz", *IEEE Trans. Microwave Theory Tech.*, vol. 56, pp. 1380-1388, June 2008.

[12] D. F. Williams, "A Split-Geometric Scheme", private email communication, 11 February 2010.

[13] MIL-DTL-3922/67D, "Flanges, waveguide (contact), round, 4 hole (millimeter)", December 2009.

THz Waveguide Couplers Using Quartz Micromachining

Jeffrey L. Hesler^{1,*} and Arthur W. Lichtenberger²

¹Virginia Diodes Inc., Charlottesville, USA

²University of Virginia, Dept. Of Electrical & Computer Engineering, Charlottesville, USA

*Contact: hesler@vadiodes.com

Abstract— A series of waveguide couplers using a novel configuration have been designed and measured from WR-5.1 (140-220 GHz) to WR-1.5 (500-750 GHz). The coupling is achieved using a microstrip quarter-wave coupled line, allowing for coupling factors from 7 dB to 11 dB and directivity of better than 20 dB. The coupling circuits consist of a quartz circuit micromachined into an “H” shape to transition from microstrip to waveguide. Measurement of the couplers showed good agreement between the simulations and experiment. The measured insertion loss ranges from 2 dB at WR-5.1 to 5 dB at WR-1.5.

I. INTRODUCTION

Waveguide directional couplers are an essential piece of test equipment at microwave and mm-wave frequencies, and a variety of coupler designs are available up to about WR-10 (75-110 GHz). Above WR-10 there are fewer options, in part because scaling designs to the THz region can be challenging. Several groups have reported coupler designs extending into the THz region, using either traditional machining or lithographic micro-machining techniques [1]–[4]. The fabrication of these THz couplers is quite challenging, which has tended to limit the widespread use of these elements.

This article describes a novel waveguide coupler that uses a microstrip quarter-wave coupled line coupler connected to waveguide using microstrip-to-waveguide probes. The design has low loss, wide bandwidth, flat coupling factor, compact size, and moderate directivity. Because of its compact size and the use of an E-plane split, the coupler can be integrated with other E-plane split components. The coupling factor is determined by the circuit design, with no change in the block design required. The basic design can be scaled to above 1 THz using conventional machining techniques.

II. COUPLER DESIGN AND FABRICATION

The coupling is accomplished using microstrip quarter-wave coupled lines, as shown in Fig. 1(a). Using this design, a flat coupling factor can be achieved over a full waveguide bandwidth. In order to couple the microstrip into waveguide, the lines are bent and separated into 4 separate microstrip channels, as shown in Fig. 1(b). Microstrip loss at THz is significantly higher than waveguide loss, and so it is desired

to launch into waveguide as soon as possible. The microstrip is transitioned to waveguide using a conventional E-plane waveguide-to-microstrip probe. The bends and transitions were found to have little effect on the performance of the coupler, which is shown in Fig. 1(c). The coupling is flat to within 0.5 dB over the full waveguide band, and the directivity is predicted to be 20 dB or better.

The coupler circuit needs to be H-shaped, and so it cannot be diced using a standard dicing-saw. To form the circuits into the correct shape, an ICP-RIE micromachining process was used to etch the quartz. Fig. 2(a) and 2(b) show close-ups of the circuits during and after the fabrication process. This circuit is then mounted into an E-plane split machined block, and is then ready for testing, as shown in Fig. 2(c).

III. MEASUREMENT OF A WR-2.2 COUPLER

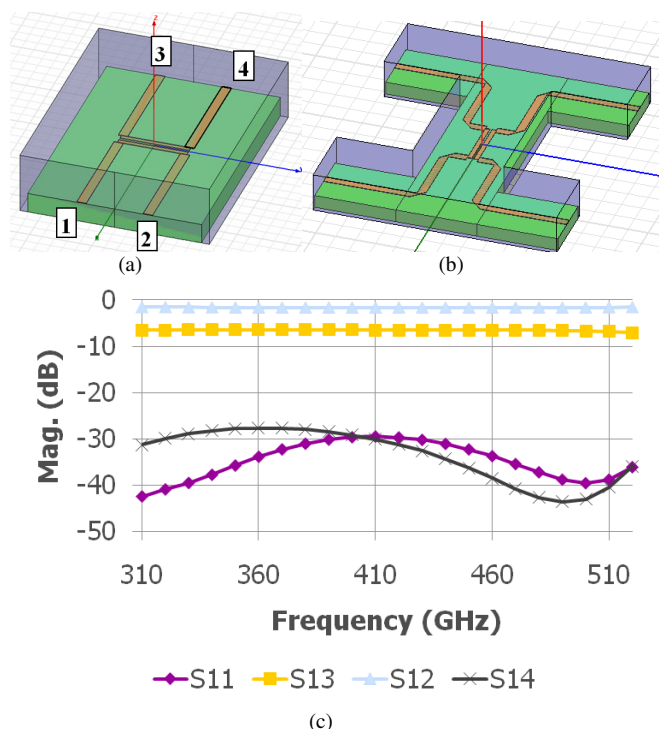


Fig. 1. (a) Schematic of the microstrip quarter-wave coupled line, (b) Schematic showing the separation of the 4 microstrip lines into separate channels, and (c) HFSS simulation of the coupler performance.

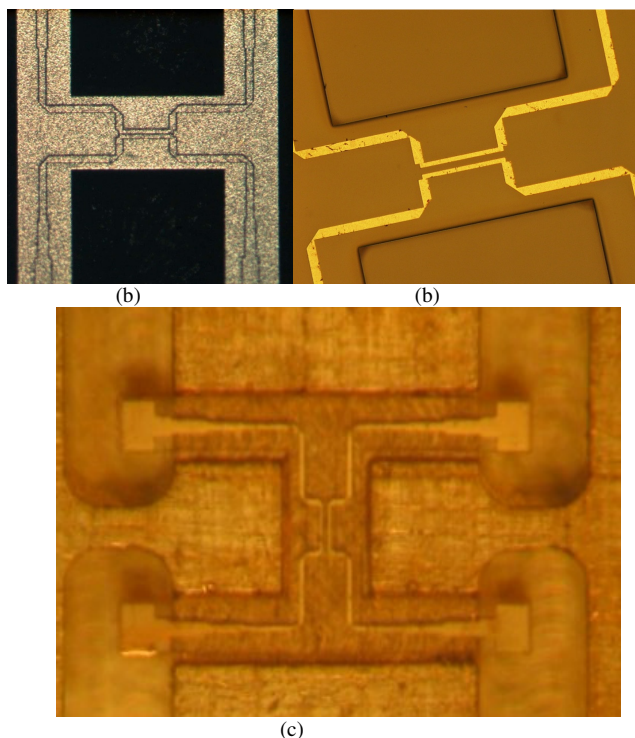


Fig. 2. (a) Photograph of the circuit during fabrication, with the metal etch mask still on the circuit, (b) the coupler section of a completed H-circuit, and (c) the H-circuit mounted into an E-plane split block.

Initial testing of the couplers has been performed using a THz source and a calorimeter, using a substitution method to normalize the source & calorimeter responses. The measured performance of a WR-2.2 coupler (330-500 GHz) is shown in Fig. 3. The WR-2.2 coupler was an early prototype, and had excess waveguide length, and thus its insertion loss was about 4 dB. Reducing the length is predicted to allow a reduction in insertion loss to less than 3 dB. A WR-3.4 (220-330 GHz) coupler was designed that has a more optimum waveguide length, and for a coupling factor of 8.5 dB the insertion loss was 2.5 dB, consisting of 1 dB of waveguide/circuit loss and 1.5 dB of input power coupled to Port 3. The length of waveguide inside the block is ~23 mm, and assuming a waveguide loss of .025 dB/mm yields a conductor loss of 0.6 dB, leaving 0.4 dB loss for the coupler itself.

Measurements of the directivity were difficult given the limited dynamic range of the test system, but indicated a value in the range 20 dB where sufficient test power was available. Additional testing using a heterodyne VNA extender system is underway, and is expected to allow full measurement of the coupler directivity even for the highest frequency coupler.

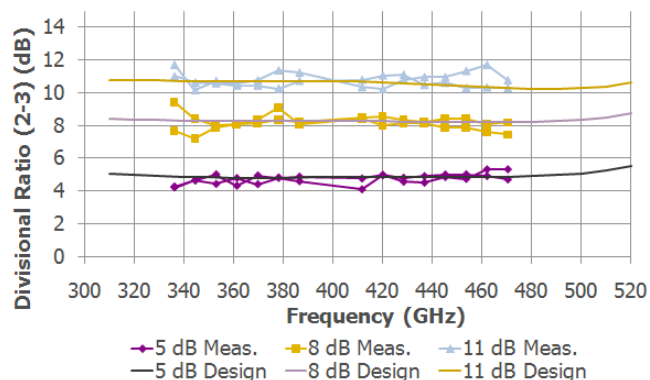


Fig. 3. Measured performance for six WR-2.2 (330-500 GHz) couplers, two each of 5 dB, 8 dB, and 11 dB designs. The divisional ratio is the ratio of power measured at Port 2 and Port 3 of the coupler when power is input into Port 1. The coupling factor is equal to the divisional ratio plus the coupler insertion loss.

IV. CONCLUSIONS

A series of manufacturable THz waveguide couplers have been designed, and have exhibited very flat coupling factor and low insertion loss over a full waveguide band. These couplers are now being used routinely for measurements at VDI.

Regarding future work, the directivity of these couplers can possibly be improved by using a “wiggly-line” coupler [5] to help balance the even and odd mode phase velocities. Also, there are a wide variety of microstrip couplers, splitter, and hybrid designs that can be placed in the same basic housing, and so this basic technology can have wide applications in THz test and measurement.

REFERENCES

- [1] N. R. Erickson, “High Performance Dual Directional Couplers for Near-mm Wavelengths,” *IEEE Microw. Wireless Comp. Lett.*, vol. 11, no. 5, pp. 205-207, May 2001.
- [2] R. Monje, V. Belitsky, V. Vassilev, “A Novel Design of Broadband Waveguide Directional Couplers and 3-dB Hybrids”, *Microwave Symposium Digest, IEEE IMTT-S*, San Francisco, California USA, 11-16 June 2006.
- [3] A. R. Kerr and N. Horner, “A Split-block Waveguide Directional Coupler,” *ALMA Memo #432*, <http://www.alma.nrao.edu/memos/>, 26 Aug 2002.
- [4] D. Meledin, A. Pavolotsky, V. Desmaris, I. Lapkin, C. Risacher, V. Perez, D. Henke, O. Nystrom, E. Sundin, D. Dochev, M. Pantaleev, M. Fredrixon, M. Strandberg, B. Voronov, G. Goltsman and V. Belitsky, “A 1.3 THz Balanced Waveguide HEB Mixer for the APEX Telescope,” *IEEE Trans. Microw. Theory Tech.*, vol. 57, no. 1, pp. 89-98.
- [5] A. Podell, “A High Directivity Microstrip Coupler Technique,” *1970 International Microwave Symposium Digest, G-MTT Symposium*, pp. 33-36, 1970.

Design and Analysis of Active Frequency Selective Surfaces with Organic Semiconductor

Hansheng Su^{1*}, Xiaoming Liu¹, Daohui Li¹, Xiaodong Chen¹, C. G. Parini¹ and T. Kreouzis²
¹*School of Electronic Engineering and Computer Science, Queen Mary University of London,*

Mile End road, London E1 4NS, UK

²*Physics Department, Queen Mary, University of London, London, Mile End road, E1 4NS, United Kingdom*

*Contact: hansheng.su@elec.qmul.ac.uk, phone +44-207 882 3620

Abstract—Frequency selective surfaces (FSS) have been studied for many years and widely used in different fields ranging from microwave engineering to optical system. Recently, Active Frequency Selective Surfaces (AFSS) having tunable or reconfigurable frequency response received more and more attention. In this study, a new means of active FSS is reported. By printing the unit elements of FSS on an organic semiconductor, the optically controlled frequency response is achieved. The transmission performance of FSS under optical illumination and non-illumination is simulated and compared, the simulated tunable range is 12GHz. The tunable performances of FSS under different illumination densities were also investigated and consecutive transmission performance movement is achieved. Finally, the photo lithography fabrication procedure is mentioned.

I. INTRODUCTION

Frequency Selective Surfaces (FSS) are well known for their filtering characteristics at microwave, millimetre wave and infrared frequency. In the earth observation application, in order to reduce mass and volume, multichannel instruments generally employ a single reflector antenna, and Frequency Selective Surfaces are used as dichroic mirrors to separate or combine beams at different frequencies.

There are two basic types of FSSs: dipole and slot arrays [1]. The dipole FSSs are composed of multilayered arrays of metal patches of arbitrary shape (typically dipoles, rings and crosses) embedded in a stratified dielectric medium. The dipole FSSs usually exhibit band-stop performance. The slots FSSs are composed of single or multiple thick metal screens perforated periodically with arbitrary shape holes (typically squares, circles and crosses). The slots FSSs are mostly used as band-pass filters. The dipole and slot arrays with elements of identical shape are defined as complementary arrays.

Key features in the performance of the Frequency Selective Surfaces include low insertion loss for the transmission and reflection bands, wide operating bandwidth, high cross-polar discrimination (XPD) and so on. These transmission and reflection characteristics depend on the shape and size of the patches or apertures, on the lattice geometry and element periodicity, and on the electrical properties of the substrate material.

Many numerical methods have been used to analyse FSS, such as equivalent circuit model method and modal method. Each method has its own merits and drawbacks. Among these numerical techniques, the Periodic Method of Moments (PMM) is one of the most popular methods for analysing

planar, multi-layered periodic structure [2]. In this paper, the electrical performance of the Frequency Selective Surfaces have been analysed by using a frequency selective surface analysis tool based on PMM theory. This frequency selective surfaces analysis tool can analyse the dipole and slot arrays with arbitrary element shape.

In the paper, we demonstrate the feasibility of a new active control strategy which exploits variable dielectric property of organic semiconductor under the optical illumination. This paper is organised as follows. Section 2 introduces the passive FSS and active FSS, and describes the related works on active FSS. Section 3 presents the organic semiconductor and demonstrates the operating theory of active FSS on organic semiconductor. Section 4 shows the design and analysis results of the optical controlled FSS on organic semiconductor. Section 5 presents the fabrication procedures. Section 6 concludes the study.

II. PASSIVE FSS AND ACTIVE FSS

In most FSS applications, the geometry and material parameters are designed to produce a static frequency response, these FSS are passive FSS. However, for a variety of applications, it would be more attractive to have an electronically controllable property for the selection of frequency as well as FSS reflection and transmission characteristics, these FSS are active FSS or tunable FSS.

A. Passive FSS

For the most part of the applications using these FSS structures require only passive printed conductors on a dielectric substrate or metal screen with holes. In these cases, no possibility exists to change the frequency or polarisation characteristics of the FSS once designed and manufactured.

Two passive FSS are shown in the Fig. 1 and Fig. 2, respectively. Fig. 1 is a two-layer slot type FSS [3], it is designed to transmit at 54GHz and reflect at 89GHz, the element is rectangular slot. Six plastic rings were used to adjust the separation between the two layers of FSS. This FSS has wide transmission band and -1dB insertion loss at 54GHz. Fig. 2 is a single copper plate FSS [4]. It is designed to transmit at 89GHz and reflect at 54GHz. This copper plate is perforated with circular holes on an equilateral triangular lattice. -0.27dB measured insertion loss is achieved at 89GHz.

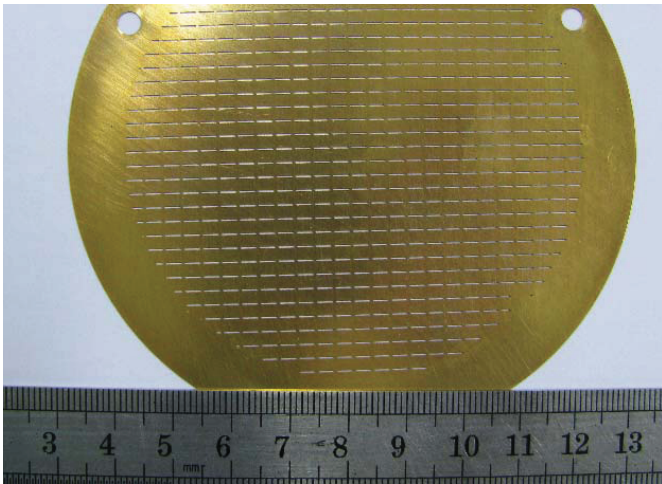


Fig. 1 Photo of 54GHz two-layer FSS

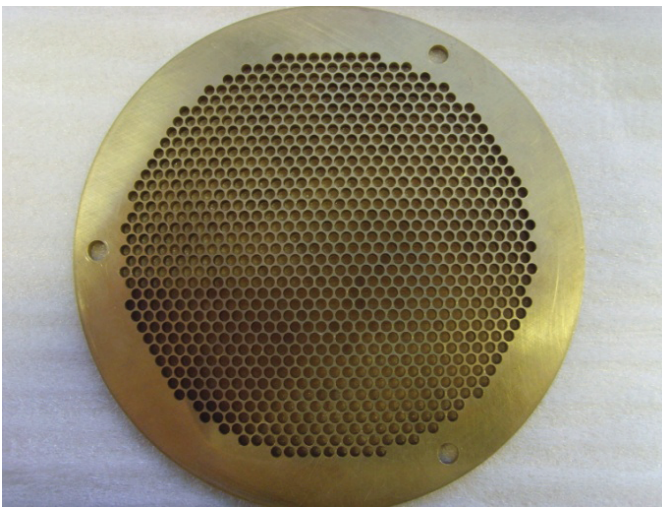


Fig. 1 Photo of 89 GHz single-layer FSS

B. Active FSS

The frequency properties of active FSSs can be varied with time. For example, at a particular time the FSS could be switched from a reflecting to a totally transparent structure or alternatively the transmission performance or reflection performance could be varied with time. Many research efforts have been paid to investigate to active and tunable FSS. T. K. Chang et al. have proposed an active FSS incorporating switched PIN diodes [5]. The PIN diodes placed in a square loop element could be used to switch the basic geometry of the elements and fundamentally change the frequency characteristics. However, there are very high biased currents due to the PIN diodes.

T. K. Chang et al. have reported the results obtained for frequency selective surfaces printed on ferrite substrates which are biased with a DC magnetic field [6]. Biasing the substrate changes its permeability, which in turn changes the frequency characteristics of the FSS so that the resonance frequency may be continuously varied or the surface switched from reflection to transmission. However, the dielectric loss of the ferrite substrates is very high.

W. Hu et al. have proposed a frequency selective surface which exploits the dielectric anisotropy of liquid crystals to

generate an electronically tunable bandpass filter response at D Band (110–170 GHz) [7]. The device consists of two printed arrays of slot elements which are separated by a 130- μm thick layer of liquid crystals. A 3% shift in the filter passband occurs when the substrate permittivity is increased by applying a control signal of 10 V. However, it needs special structure to seal the liquid crystal.

Bernhard. Schoenlinner et al. have proposed a switchable low-loss RF MEMS ka-band FSS [8]. In this paper, a switchable frequency-selective surface was developed at 30 GHz using RF micro-electro-mechanical systems (MEMS) switches on a 500- μm -thick glass substrate. However, the complicate structures make the fabrication difficult.

III. ORGANIC SEMICONDUCTOR

Organic semiconductors are any organic material that has semiconductor properties [9]. Organic semiconductor polymers have been the focus of many studies because they have shown many advantages, such as easy fabrication, mechanical flexibility and tunable optical properties.

In recent years, the potential application of poly(3-hexylthiophene) (P3HT) in polymer electronics and optoelectronic applications has gained significant attention [10]. The reason is that its relatively high drift mobility and optical absorption properties. An important characteristic of P3HT is its small band gap. It has been reported to be approximately 1.9 eV, and its corresponding absorption in the visible peaks between 450 and 600 nm. It is thus possible to photogenerate charges within the dielectric, and these charges are able to move reasonably rapidly.

The optically controlled frequency response can be achieved by printing the unit elements of FSS on an organic semiconductor, as shown in Fig. 3. When the organic substrate is being illuminated by the light source whose photon energy is greater than the band gap energy of the semiconductor material, an electron-hole plasma region will be induced. This leads to the permittivity different from that of the non-illuminated region. As a result, the dielectric property of organic material will be changed through these activated regions, and then the transmission and reflection performance of the FSS on top of the organic material will be changed. So the performance of FSS can be controlled by the intensity of the optical illumination.

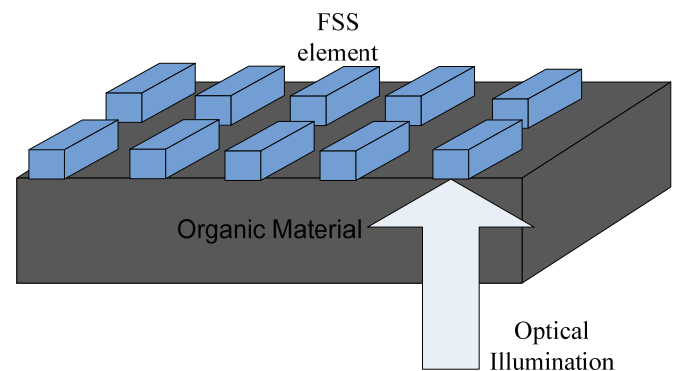


Fig. 2 Optical controlled FSS employing organic semiconductor

IV. DESIGN AND ANALYSIS RESULTS

In this paper, the tunable performance of 54GHz slot type FSS on P3HT polymer was studied. The geometry and dimensions of rectangular element of FSS is shown in Fig. 4. The unit is millimetre.

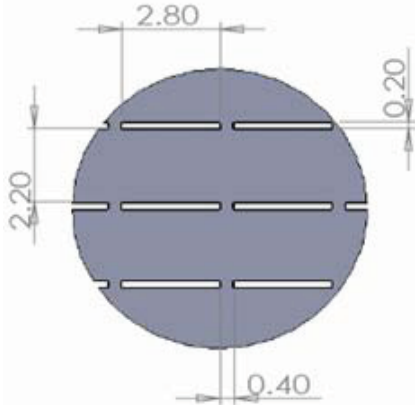


Fig. 4 Geometry of rectangular element

A. Tunable responses between optical illumination and non-illumination

The illuminated P3HT polymer will have a complex permittivity different from that of nonilluminated material. So the tunable response of FSS can be achieved by switching from optical illumination to non-illumination. In this study, we investigate the tunable performance of two-layer FSS with P3HT polymer. The accurate permittivity of P3HT under illumination is difficult to calculate, so we just use the empirical value: $\epsilon_r = 3.17$, $\tan \delta = 0.02$, for non-illumination; $\epsilon_r = 2.72$, $\tan \delta = 0.12$, for illumination. Fig. 5 shows the comparison of transmission performance between illumination and non-illumination. The simulation was performed by PMM method with the inclusion of dielectric loss. From the results, we can see the transmission performance is changed obviously due to the optical illumination. The tunable range is 12GHz and the peak insertion loss is increased from 0dB to -4.77dB due to the mismatch when the FSS under illumination.

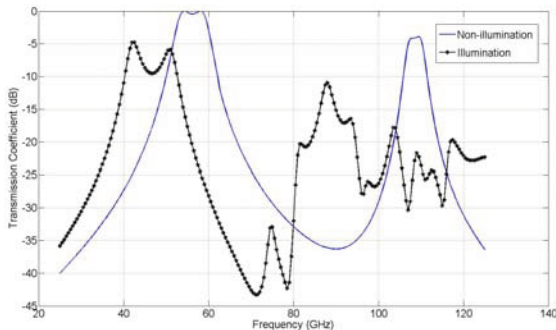


Fig. 5 Comparison of transmission performance between illumination and non-illumination

B. Tunable responses by different intensity of optical illumination

In fact, the permittivity property of P3HT is varied under the different density of optical illumination. At microwave frequency the permittivity varies between 2.2 and 3.2. In this study, the tunable performances of single layer FSS under different illumination density were investigated. The simulated results without the inclusion of dielectric loss are shown in the Fig. 6. It can be seen from the results that a consecutive transmission performance movement is achieved under the different density of optical illumination.

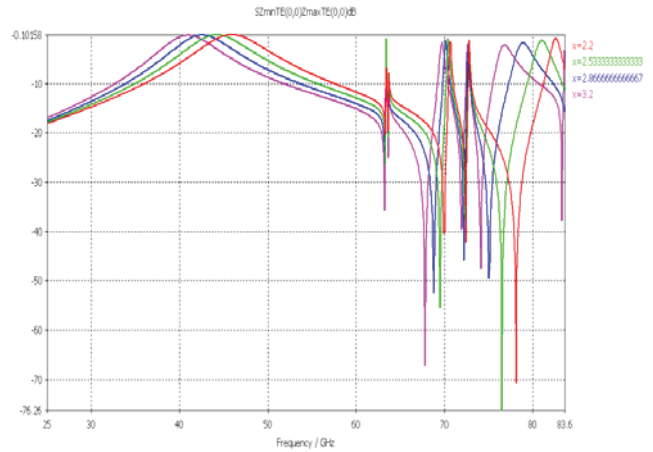


Fig. 6 Tunable transmission performance by different intensity of optical illumination

V. FABRICATION

The active FSS was fabricated by photo lithography technology. Photo lithography is a process used in micro fabrication to selectively remove parts of a thin film or the bulk of a substrate. It uses light to transfer a geometric pattern from a photo mask to a light-sensitive chemical photo resist, or simply "resist," on the substrate.

The main stages of photo lithography fabrication are shown in the Fig.7.

- 1) A 150 nm thick aluminium layer was deposited over the glass substrate in the evaporation chamber.
- 2) The photo-resist solution (light-sensitive chemical) was spin coated on the aluminium covered substrate, the photo-resist solution is S1818. There are two types of photo-resist: positive and negative. For positive resists, the resist exposed with UV light is to be removed. Negative resists behave in just the opposite manner, that remains on the surface wherever it is exposed, and the developer solution removes only the unexposed portions. Here, we use positive photo-resist.
- 3) After heated in the oven, the substrate was exposed to UV lights with photo mask in between. The exposed part of photo-resist is etched.
- 4) The aluminium pattern was developed by developer solution (25% NAOH, 75% distilled water).
- 5) The remaining photo-resist was removed by developer solution.

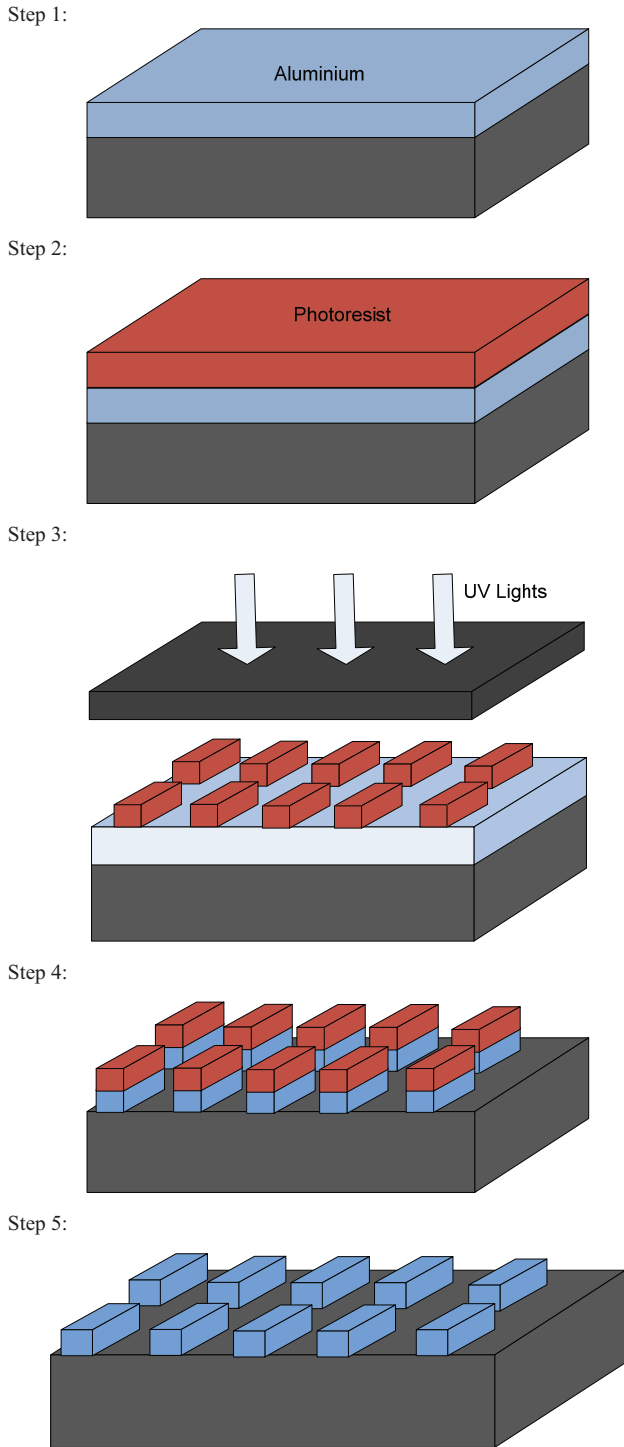


Fig. 7 The fabrication steps of photo lithography

The microscope pictures of samples were checked. From the microscope pictures, we can see the edge of aluminium element is quite straight and some air bubbles exist under the aluminium because of the clean procedure. The variation in thickness of aluminium element is another problem. The depth-profile of the aluminium was checked with profilometer, as shown in the Fig. 3. The thickness is varied between 1400Å to 1500Å. The fabrication tolerance can be improved by modifying the evaporation temperature and exposing time under UV light.

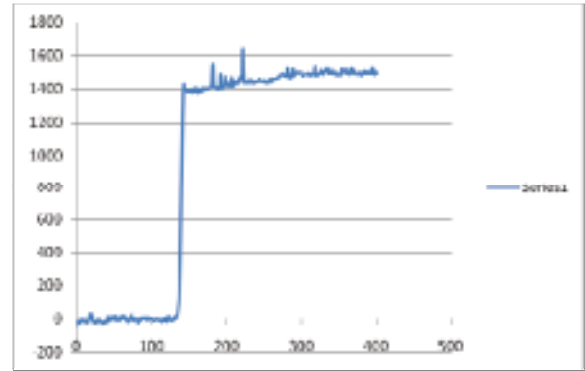


Fig. 8 Depth profiles of aluminium

VI. CONCLUSIONS

In this study, the feasibility of a new active control strategy which exploits variable dielectric property of organic semiconductor under the optical illumination is investigated. The optically controlled frequency response is achieved through simulation. The transmission performance of FSS under optical illumination and non-illumination is simulated and compared, the simulated tunable range is 12GHz. The tunable performances of FSS under different illumination density were also investigated and consecutive transmission performance movement is achieved. The active FSS was fabricated by photo lithography technology. Profilometer was used to check the depth-profile of the aluminium and the thickness is varied between 1400Å to 1500Å.

REFERENCES

- [1] Munk, B.A.: Frequency Selective Surfaces: Theory and Design. John Wiley & Sons, Inc., New York, (2000).
- [2] Wu, T. K.: Frequency Selective Surface and Grid Array. John Wiley & Sons, Inc., New York, (1995).
- [3] J. Yu, S. Liu, L. Xu, H. Su, X. Liu, Q. Wei, Y. Mai, X. Chen, J. Miao and M. Bai, "Study of A Two-Layer Dichroic for Quasi-Optical Network", Microwave and Optical Technology Letters, In Press, 2010.
- [4] Hansheng Su, Xiaoming Liu, Liang Xu, Daohui Li, Xiaodong Chen, C. Rieckmann, R. Donnan, C. Parini, Junsheng Yu, Jungang Miao, "Experimental Assessment of Periodic Method of Moments Design Accuracy for Quasi Optical Networks," 2ndUK/Europe-China Workshop on Millimetre Waves and Terahertz Technologies, Rutherford Appleton Laboratory, 19th to 21st October 2009.
- [5] Chang, T. K., Langley, R. J., Parker, E. A.: Active frequency-selective surfaces. In Proc. IEEE Microwaves, Antennas Propag., vol. 143, pp. 62–66, Feb. (1996)
- [6] Chang, T. K., R. J. Langley, and E. A. Parker, Frequency-selective surfaces on biased ferrite substrates," Electronics Letters, Vol. 30, No. 15, 1193–1194, 1994.
- [7] [1] W. Hu, R. Dickie, R. Cahill, H. Gamble, Y. Ismail, V. Fusco, D. Linton, N. Grant, S. Rea, "D Band Tunable Frequency Selective Surface Based on Liquid Crystals," IEEE Microwave and Wireless Components Letters, Dec 2006
- [8] [5] B. Schoenlinner, A. Abbaspour-Tamijani, L. C. Kempel, and G. M. Rebeiz, "Switchable low-loss RF MEMS ka-band frequency-selective surface," IEEE Trans. Microw. Theory Tech., vol. 52, no. 11, pp. 2474–2481, Nov. 2004.
- [9] Hagen Klauk, Organic Electronics: Materials, Manufacturing, and Applications, Wiley, 2006.
- [10] Hongyan Tang, Robert Donnan, T. Kreouzis, "Optically Controlled Phase Shifter Employing Organic Semiconductor poly-(3-hexylthiophene) (P3HT)", Applied Physics Letters, 91, 202101 (2007).

Poster Session P6: Receivers

Construction of a Heterodyne Receiver for Band 1 of ALMA

N. Reyes¹, P. Zorzi¹, C. Jarufe¹, P. Altamirano², F. P. Mena^{1*}, J. Pizarro², L. Bronfman², J. May², C. Granet³, and E. Michael¹

¹Electrical Engineering Department, Universidad de Chile, Av. Tupper 2007, Santiago, Chile

²Astronomy Department, Universidad de Chile, Camino El Observatorio 1515, Santiago, Chile

³BAE Systems Australia Ltd, 40-52 Talavera Road, North Ryde 2113, Australia

*Contact: pmena@ing.uchile.cl, phone +56-2-978 4888

Abstract— In this paper we present the construction and test results of several parts (horn, orthomode transducer, RF amplifier, and waveguide filter) towards the fabrication of a prototype heterodyne receiver for Band 1 of ALMA (31–45 GHz).

I. INTRODUCTION

The Atacama Large Millimeter Array (ALMA) is the largest millimeter array ever constructed. Every one of its constituent antennas will cover the spectroscopic window allowed by the atmospheric transmission at the construction site with ten different bands. Despite being declared as a high scientific priority, Band 1 (31–45 GHz) was not selected for construction during the initial phase of the project. Universidad de Chile has started a program for the construction of a prototype receiver for Band 1 of ALMA. The overall design has been presented elsewhere [1]. Here we present the construction and testing results of several of its parts.

II. LAYOUT OF THE RECEIVER

For the sake of completeness we reproduce in Fig. 1 the basic layout of the receiver we plan to construct [1]. The incoming RF signal is coupled with the horn via a lens (Sec. III-A). The signal is then divided in its polarization components in an orthomode transducer (Sec. III-B). Each polarization signal is amplified in two consecutive high electron-mobility transistors (HEMT) cooled at 20 K (Sec. III-C). Finally, the amplified signals are filtered to suppress the lower sideband (Sec. III-D) and mixed in separate Schottky diodes.

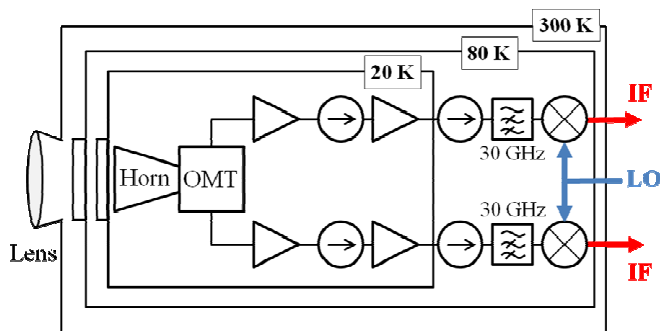


Fig. 1 Layout of the RF components of the receiver proposed for Band 1 of ALMA. All these components will be inside the cryostat and mounted in the so-called cold-cartridge assembly.

III. CONSTRUCTION AND RESULTS

A. Corrugated Horn

The details of the optical system design (lens-horn) are presented in an accompanying paper [2]. We have constructed an optimized spline-profile corrugated horn in the split-block technique (Fig. 2). Simulations indicate that it has similar performance to a normal corrugated horn but has the advantage of being almost half its size. For its characterization we are building a beam-pattern measurement set up.

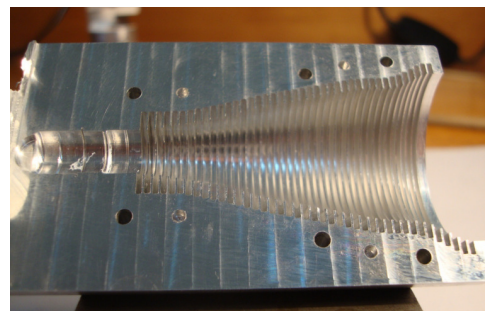


Fig. 2 One half of the optimized spline-profile corrugated horn constructed as a split-block.

B. Orthomode Transducer

We have scaled the orthomode transducer (OMT) introduced by Asayama for Band 4 of ALMA [4]. It has been constructed as a split-block made out of three parts (Fig. 3). Its performance is excellent as demonstrated in Fig. 4.

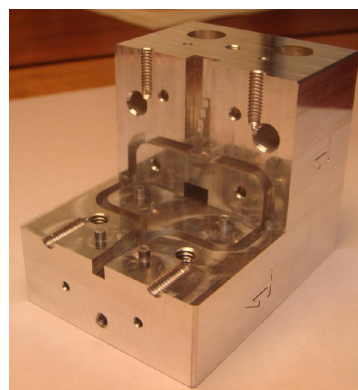


Fig. 3 Orthomode transducer constructed in the split-block technique.

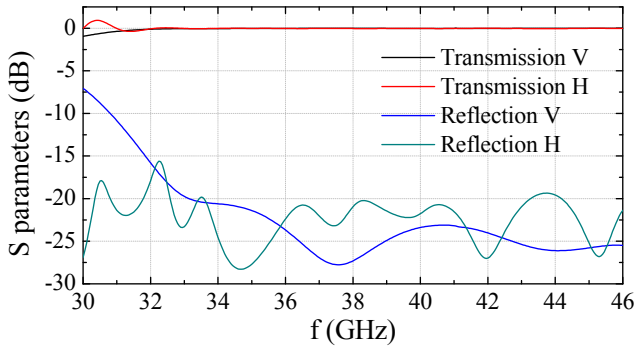


Fig. 4 S-parameters of the orthomode transducer.

C. RF amplifier

For amplification we will use chips based on high electron mobility transistors. In a first attempt to test our packaging capabilities, we have integrated commercial amplifiers [3] into a split block (Fig. 5). As demonstrated in Fig. 6 the results are excellent and in accordance with the original specifications of the commercial chips.



Fig. 5 Commercial chip packed in a split block.

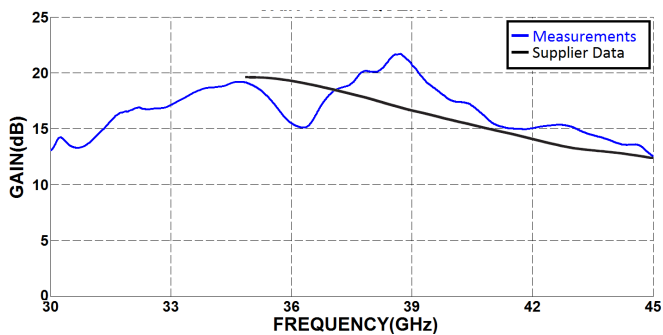


Fig. 6 Gain of the packaged amplifier.

D. Filter for Lower-Sideband Suppression

An important part in the system we are proposing is a filter that suppresses the lower sideband. We designed and constructed a waveguide-base filter as shown in Fig. 7. The results presented in Fig. 8 are in excellent agreement with the simulations.

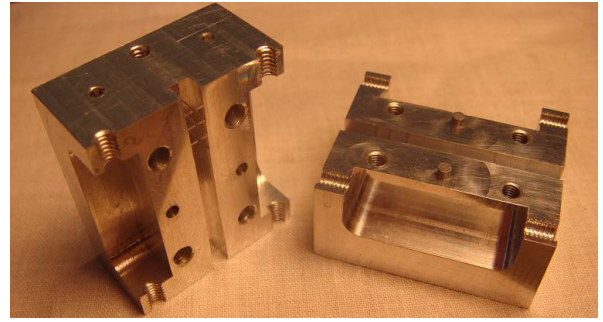


Fig. 7 Filter for lower band suppression.

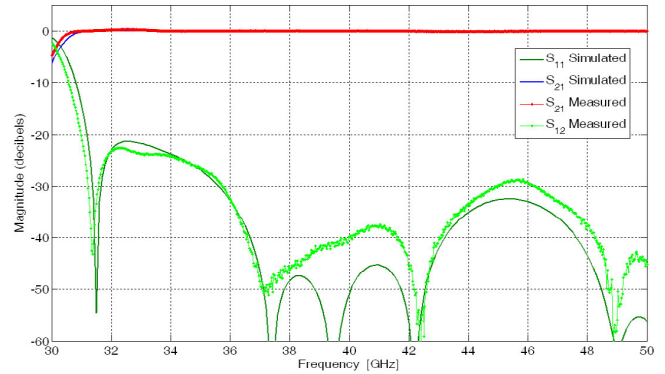


Fig. 8 S-parameters of the filter.

IV. CONCLUSIONS AND FUTURE WORK

We are currently working on fabricating and testing several parts of a heterodyne receiver for Band 1 of ALMA. So far, they show excellent response in accordance with the simulations. Our next step is to start with the integration of the receiver.

ACKNOWLEDGMENT

This work received support from the Center of Excellence in Astrophysics and Associated Technologies (PBF 06).

REFERENCES

- [1] N. Reyes, P. Zorzi, F. P. Mena, C. Granet, E. Michael, L. Bronfman, and J. May, "Design of a Heterodyne Receiver for Band 1 of ALMA," in *Proc. ISSIT'09*, 2009, paper P8D, p. 311.
- [2] P. Zorzi, D. Henke, S. Claude, F.P. Mena, L. Bronfman, and J. May, "Revisiting the ALMA Band 1 optics design," presented in *ISSIT'10*, 2010, paper P5-6.
- [3] *GaAs HEMT MMIC low noise amplifier (HMC-ALH376)*, Hitite, 2008.
- [4] S. Asayama, "Double-ridged Orthomode Transducer for ALMA Band 4 receiver," NAOJ internal MEMO, 2007.

Testing and Integration of Supercam, a 64-Pixel Array Receive for the 350 GHz Atmospheric Window

Christopher Groppi^{1*}, Christopher Walker², Craig Kulesa², Dathon Golish², Jenna Kloosterman², Sander Weinreb³, Glenn Jones³, Joseph Barden³, Hamdi Mani³, Tom Kuiper⁴, Jacob Kooi³, Art Lichtenberger⁵

¹*School of Earth and Space Exploration, Arizona State University, Tempe, AZ 85287 USA*

²*Steward Observatory, University of Arizona, Tucson, AZ 85721 USA*

³*California Institute of Technology, Pasadena, CA 91125, USA*

NASA Jet Propulsion Laboratory, Pasadena, CA 91109

⁵*University of Virginia, Charlottesville, VA 22904 USA*

*Contact: cgroppi@asu.edu, +01-480-965-6436

Abstract— We report on laboratory testing and telescope integration of SuperCam, a 64 pixel imaging spectrometer designed for operation in the astrophysically important 870 micron atmospheric window. SuperCam will be used to answer fundamental questions about the physics and chemistry of molecular clouds in the Galaxy and their direct relation to star and planet formation. The Supercam key project is a fully sampled Galactic plane survey covering over 500 square degrees of the Galaxy in ¹²CO(3-2) and ¹³CO(3-2) with 0.3 km/s velocity resolution.

SuperCam will have several times more pixels than any existing spectroscopic imaging array at submillimeter wavelengths. The exceptional mapping speed that will result, combined with the efficiency and angular resolution provided by the HHT will make SuperCam a powerful instrument for probing the history of star formation in our Galaxy and nearby galaxies. SuperCam will be used to answer fundamental questions about the physics and chemistry of molecular clouds in the Galaxy and their direct relation to star and planet formation. Through Galactic surveys, particularly in CO and its isotopomers, the impact of Galactic environment on these phenomena will be realized. These studies will serve as “finder charts” for future focused research (e.g. with ALMA) and markedly improve the interpretation, and enhance the value of numerous contemporary surveys.

In the past, all heterodyne focal plane arrays have been constructed using discrete mixers, arrayed in the focal plane. SuperCam reduces cryogenic and mechanical complexity by integrating multiple mixers and amplifiers into a single array module with a single set of DC and IF connectors. These modules are housed in a closed-cycle cryostat with a 1.5W capacity 4K cooler. The Supercam instrument is currently undergoing laboratory testing with four of the eight mixer array modules installed in the cryostat (32 pixels). Work is now underway to perform the necessary modifications at the 10m Heinrich Hertz Telescope to accept the Supercam system. Supercam will be installed in the cassegrain cabin of the HHT, including the optical system, IF processing, spectrometers and control electronics. Supercam will be integrated with the HHT during the 2009-2010 observing season with 32 pixels installed.

The system will be upgraded to 64 pixels during the summer of 2010 after assembly of the four additional mixer modules is completed.

I. SUPERCAM INSTRUMENT DESCRIPTION

A. Instrument Design

The enormous complexity of even a small discrete heterodyne array suggests a more integrated approach is needed for larger systems [1]. At the heart of SuperCam are 8 pixel, linear integrated arrays of low-noise mixers. Each mixer array contains low-noise, MMIC IF amplifier modules with integrated bias tees. Eight of these mixer modules are then stacked to produce the final 64 pixel array.

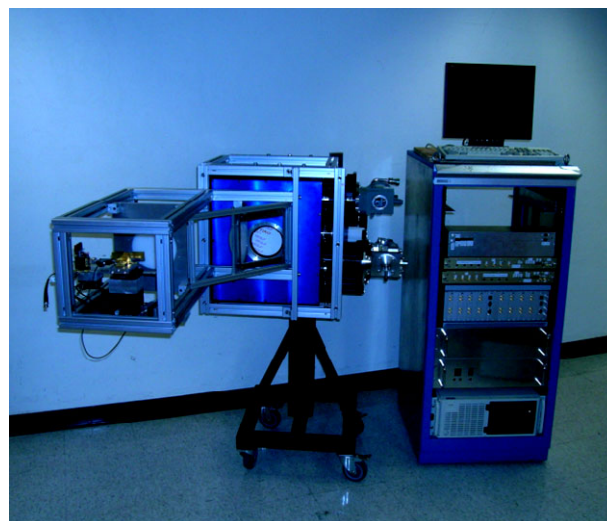


Figure 1: The SuperCam cryostat, LO optics and support electronics.

B. Cryogenics

The SuperCam system with attached LO optics, frontend support electronics and backend electronics is shown in Figure 1. The cryostat was constructed by Universal Cryogenics in Tucson, Arizona, USA. Light from the

telescope enters the cryostat through a 150 mm diameter AR coated, crystalline quartz vacuum window and passes through a Teflon coated crystalline quartz IR filter on the 40 K radiation shield before illuminating the 4 K mixer array. The Teflon layers on this filter serve as both the IR blocking filter and the antireflection coating. SuperCam uses a Sumitomo SRDK-415D cryocooler. The cooler has 1.5 W of thermal capacity at 4.2 K and 45W at 40K with orientation-independent operation. The operating temperature of the cryocooler is stabilized by the addition of a helium gas pot on the 2nd stage. A CTI cryogenics CTI-350 coldhead supplements the cooling of the 40K shield, and provides 12K heatsinking for the 64 stainless steel semi-rigid IF cables. The addition of this second coldhead permits the use of moderate lengths of standard coaxial cable while maintaining low heat load at 4K. Annealed and gold plated copper straps with a flex link connect the 4K cold tip to the cold plate, with less than a 0.2K temperature differential. Tests using heaters on the 4K cold plate, and system tests using prototype 1x8 mixer modules demonstrate adequate performance of the cryogenic system with the expected heat load from all 64 pixels.

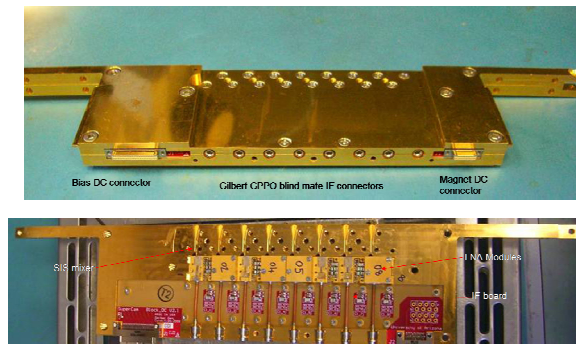


Figure 2: A completed SuperCam 1x8 mixer module, fully assembled (top) and with the top cover removed (bottom).

C. Mixer Array

The SuperCam 64 beam focal plane is constructed from eight linear array modules with eight pixels each. Each pixel consists of a sensitive, single ended SIS mixer optimized for operation from 320-380 GHz. The array mixers utilize SIS devices fabricated on Silicon-On-Insulator (SOI) substrates, with beam lead supports and electrical contacts. The waveguide probe and SIS junction are based on an asymmetric probe design currently in use at the Caltech Submillimeter Observatory in their new facility 350 GHz receiver. The 1x8 mixer subarrays are constructed from tellurium copper using the splitblock technique. Stainless steel guide pins and screws are used to ensure proper alignment and good contact between parts. Figure 2 shows a photograph of a production gold plated tellurium copper 1x8 mixer array fabricated at the University of Arizona. This block meets all design specifications, with 3 μm dimensional accuracy for all waveguide circuits. A diagonal feedhorn extension block is bolted to the front of the mixer array assembly, extending the diagonal horns to 11mm aperture size. This eliminates the need for dielectric lenses and their

associated manufacturing and alignment difficulties. The energy in the horn passes through a 90° waveguide bend before reaching the device. The waveguide environment is designed around full height rectangular waveguide, with a fixed quarter wave backshort. The SIS device is suspended and self-aligned above the stripline channel via eight small beamlead supports. The hot beamleads are tack-bonded with a wirebonder to the MMIC module input pads. Ground beamleads are glued to the mixer block using Epo-tek H20E conductive epoxy. The mounting method is designed such that the block can be opened repeatedly without disturbing the SIS devices. Single devices can be removed and replaced without disturbing neighboring devices. The mixer blocks were fabricated at the University of Arizona using a Kern MMP micromilling machine purchased for this project. This numerically controlled mill can fabricate structures to micron accuracy with a high level of automation. A SuperCam 1x8 module can be produced in ~8 hours of machine run time. All mixer blocks have been machined and gold plated. To date 4 modules (32 pixels) have been assembled and tested.

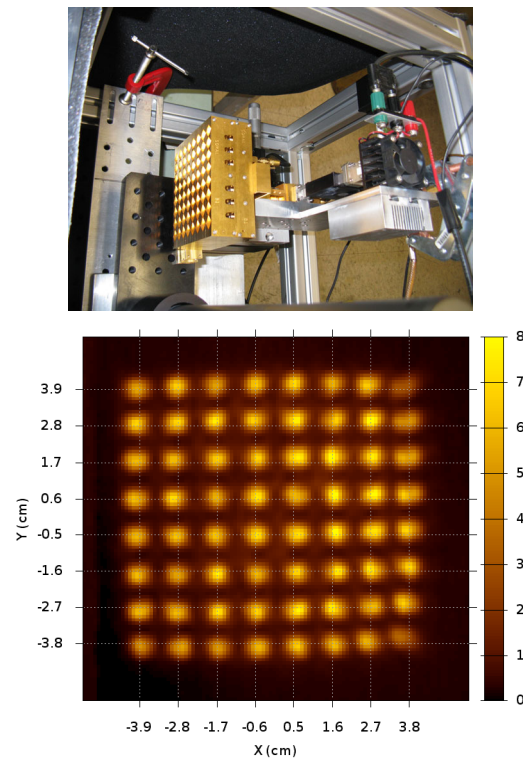


Figure 3: SuperCam 64-way waveguide LO power divider (top) and measured power pattern from this divider (bottom). Amplitude scale is linear. Power is evenly divided to the +/- ~10% level. Some asymmetrical barrel distortion is evident, due to optical misalignment in the test setup.

D. Local Oscillator

With an array receiver, LO power must be efficiently distributed among pixels. Depending on the mechanical and optical constraints of the array, a balanced distribution can be achieved using quasioptical techniques or waveguide injection. With the quasioptical approach, dielectric beam splitters or holographic phase gratings are used to divide the

LO energy between array pixels. We have chosen to use a hybrid waveguide/quasioptical LO power injection scheme. The LO power for the array will be provided by a single solid-state, synthesizer-driven source from Virginia Diode Inc. The active multiplier chain consists of a high power solid-state amplifier followed by a series of tunerless, broadband multipliers. The output of the chain is coupled to an eight-way waveguide corporate power divider with splitblock machineable waveguide twists. Each of the eight outputs provides the drive power for a 1x8 subarray via an identical 8 way corporate divider with diagonal waveguide feedhorn outputs. Figure 3 shows the complete 64-way power divider constructed with the Kern micromilling machine at the University of Arizona. The power pattern of this divider and its injection optics is also shown in Figure 3. Power division is equal to the ~10% level.

operation, low noise, high stability, and no heating effects on the SIS device. Modules have been integrated into both single pixel and 1x8 array mixers, and have shown performance as good or better than expected with connectorized amplifiers. No heating effects are visible, although care must be taken to avoid oscillation due to feedback.

In addition to the LNA modules, the Caltech group has designed and constructed a warm IF system for SuperCam that will condition the IF signal for use with the SuperCam Array Spectrometer (Figure 5). This IF system consists of a single large microwave printed circuit board with 8 channels of signal conditioning mounted in a modular chassis. The module contains a 5 GHz gain stage, switchable filters for both 250 MHz and 500 MHz bandwidth modes, baseband downconversion and baseband amplification.

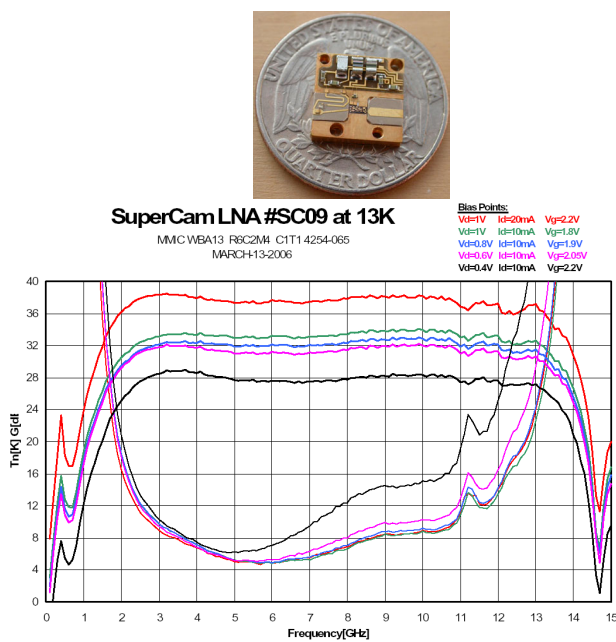


Figure 4: A SuperCam MMIC amplifier module (top), and typical measured results at 13K bath temperature (bottom) for several bias points. Amplifier noise remains low for bias powers as low as 6 mW. Gain remains above 30 dB.

E. IF/Bias Distribution System

The IF outputs from the SIS devices are bonded directly to the input matching networks of low-noise, InP MMIC amplifier modules located in the array mixers. These amplifier modules have been designed and fabricated by Sander Weinreb's group at Caltech. The IF center frequency of the array is 5 GHz. The MMIC chip is contained in an 11mm x 11mm amplifier module that contains integrated bias tees for the SIS device and the amplifier chip. The module achieves noise temperature of ~5 K and delivers 32 dB of gain while consuming only 8 mW of power. An example is shown in Figure 4, with measured gain and noise data at 4 mW through 20 mW power dissipation. Noise remains virtually unchanged down to 6 mW power dissipation, while gain is reduced modestly (Figure 4). Several tests have been performed with these modules to ensure oscillation free



Figure 5: The inside of a SuperCam IF processor. This module provides amplification, programmable attenuation, passband filtering and total power detection for 8 channels.

F. Array Spectrometer & Interfaces

The SuperCam spectrometer delivers 64 channels at 250 MHz/channel with 250 kHz resolution, or 32 channels at 500 MHz with 250 kHz resolution. The system will be capable of resolving lines in all but the coldest clouds, while fully encompassing the Galactic rotation curve. The system is easily extendible to deliver 64, 500 MHz bandwidth channels or 32, 1 GHz bandwidth channels. This leap in spectrometer ability is driven by the rapid expansion in the capabilities of high speed Analog to Digital Converters (ADCs) and Field Programmable Gate Arrays (FPGAs). The SuperCam spectrometer, built by Omnisys AB of Sweden, is based on a polyphase filterbank architecture. High speed ADCs digitize the incoming RF signal at 8 bits resolution, preventing any significant data loss as with autocorrelation based schemes. A polyphase filterbank spectrometer is implemented on a FPGA. In our board architecture, 4 ADCs feed a single Xilinx Virtex 4 FPGA on each spectrometer board. Each board can process 4, 500 MHz IF bandwidth signals or two 1 GHz IF bandwidth signals at 250 kHz resolution. These systems are fully reconfigurable by loading new firmware into the FPGAs. In addition, the spectrometer can be easily expanded to increase bandwidth. We have received an 8 board system capable of processing 64x250 MHz, 32x500

MHz or 16x1GHz IF signals (Figure 6 bottom). In the 64x250 MHz mode, we power combine two IF signals into one spectrometer input. Stability testing shows the spectrometer is capable of delivering a spectroscopic Allan time of ~650s, including the effects of the IF processor described above (Figure 6 top).

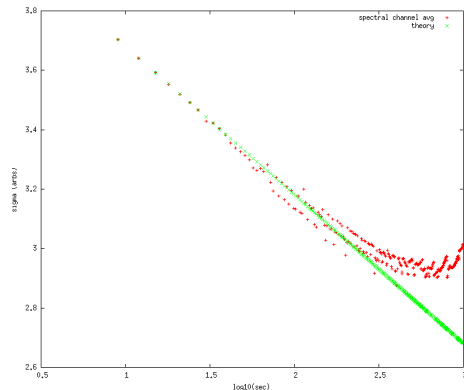


Figure 6: Measured Allan variance of the Supercam spectrometer system, including the Caltech IF processor. Allen time is 650s (top). The Supercam spectrometer system, built by Omnisys AB (bottom). This single 3U crate can process 16 GHz of IF bandwidth at 250 kHz spatial resolution. It consumes less than 200W of AC power.

The electrical and mechanical interfaces between the HHT and Supercam have been streamlined to the most necessary and simple interfaces possible (Figure 7).

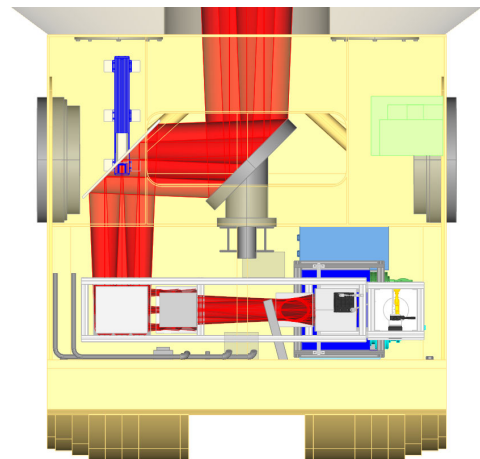
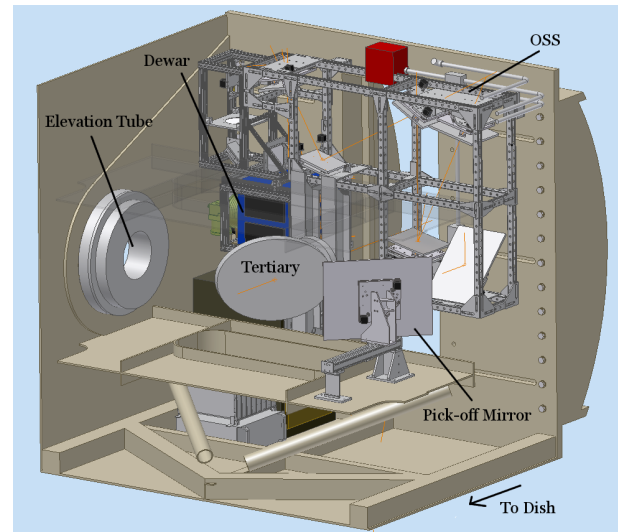


Figure 8: The SuperCam optical design viewed from behind the primary reflector, (top), and viewed from the top (bottom). The apex room is transparent to visualize the design. The beam bundles are displayed in red.

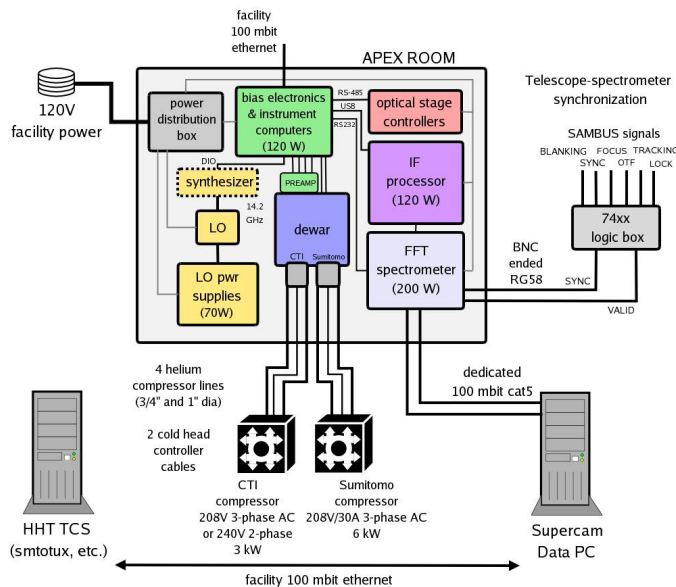


Figure 7: Schematic of the streamlined interface between Supercam and the HHT: only power, cryogenic lines, digital control signals, and ethernet are needed.

G. Optics

The existing secondary mirror of the Heinrich Hertz Telescope provides an $f/13.8$ beam at the Nasmyth focus. The clear aperture available through the elevation bearing prevents the possibility of a large format array at this position. To efficiently illuminate a large format array like SuperCam, the telescope focus must fall within the apex room located just behind the primary. A system of re-imaging optics located in the apex room transforms the f number of the telescope to $f/5$ (Figure 8). Since the physical separation between array elements in the instrument focal plane scales as $2f\lambda$, lower $f/\#$'s serve to reduce the overall size of the instrument. The reimaging optics are composed of two offset parabolas and several flat mirrors. All the reimaging optics can be mounted on a single modular optical frame. This frame can be completely constructed, aligned and tested off the telescope, disassembled into modules and reassembled in the apex room. All electronics, including the

backend, are located in the apex room. The cryostat and optics frame have been designed using finite element analysis to minimize gravitational deflection, and the calculated deflections have been fed into the tolerancing of the optical design. The optical system was initially designed and optimized with Zemax, and was then verified by BRO research using their ASAP physical optics package. The system’s efficiency exceeds 80% for all pixels, and has been verified to be robust to alignment and fabrication tolerances.

H. Data Pipeline

A schematic of the SuperCam data pipeline is shown in Figure 9. The spectrometer will have a dedicated, 1Gb ethernet connection to a data acquisition-spectrometer (DAS) control PC. The DAS PC will have two ethernet cards and a RAID5 array for local data storage and fault tolerance. Five 750 GB drives in a RAID0/1 array will provide >3 TB of storage. During the Galactic Plane survey the data rate will be 400 GB/day. The DAS disk array will provide at least a week of raw storage at 90% duty cycle. The DAS PC will stream the raw data to a background process that will be responsible for regriding the data into a more manageable format; approximately 200 GB for the entire SuperCam Galactic plane survey. The data processing task will also be responsible for determining the quality of the data and flagging bad OTF scans that need to be repeated. Quality will be assessed by evaluating the RMS noise after subtracting the baseline from each spectrum and comparing with that expected from Tsys. The data processing task will spool preprocessed data images to the telescope control computer(s) for the observer to see, upon request. The HHT telescope control computer in return will send data acquisition requests to the DAS PC, thus closing the communications loop.

II. LABORATORY TESTING

For testing the SuperCam mixer design in the laboratory, we designed two single pixel mixers. The first design used an existing SIS junction design from the DesertStar 7-pixel array [2], but incorporated the Caltech designed MMIC module. This work was reported in other papers [3, 4]. We determined that the SIS receiver with integrated MMIC amplifier worked as well as a receiver with a separate connectorized amplifier and cryogenic amplifier, and resulted in no heating effects at the SIS device from the close proximity of the amplifier. We later designed a second single pixel amplifier that is an exact copy of a single pixel of the 1x8 mixer array design discussed in section I.B. This mixer was designed to test the self-aligning beam-lead-on-SOI SIS devices that will be used in the SuperCam array, as well as the compact, low power electromagnet, MMIC amplifier module and extended diagonal feedhorn. This mixer was extensively tested for noise performance across the band. Its frequency response was measured using a Fourier Transform Spectrometer and stability measurements made using the complete backend system (Figure 6 top).

32 pixels (4 mixer modules) have been undergoing extensive laboratory tests. Representative DC IV and total

power curves measured using one of these mixers is shown in Figure 10. Noise temperature measurements of 27 pixels are presented in Figure 11. The average noise temperature is ~100K across the measured band (LO limited to 330 to 365 GHz).

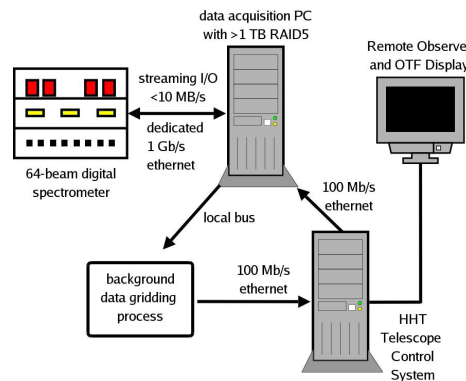


Figure 9: Schematic of SuperCam data pipeline.

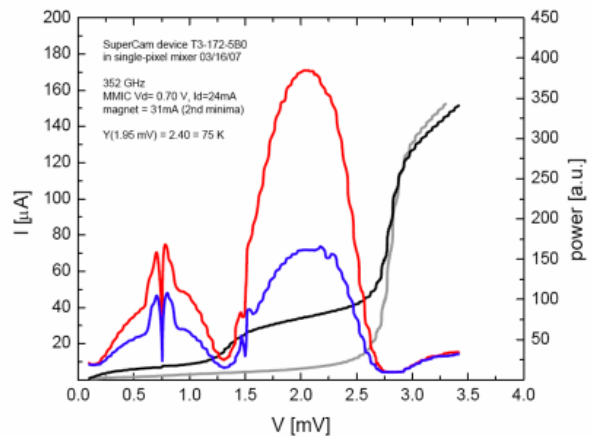


Figure 10: A representative pumped and pumped IV curve from a Supercam mixer element with hot and cold IV curves. Measured uncorrected noise temperature is 75K.

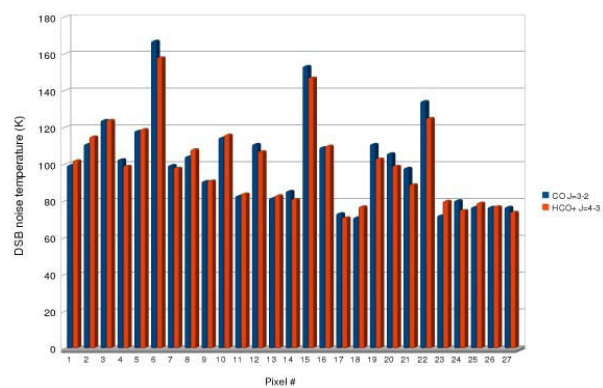


Figure 11: Uncorrected receiver temperature from the 27 out of 32 operating pixels in Supercam now, at LO frequencies for CO(3-2) and HCO+(4-3). Pixels 6, 16 and 22 are affected by issues with LO pumping or LNA performance.

III. SCHEDULE

SuperCam is rapidly nearing completion. All key components have been designed, machined, manufactured, and tested. Four modules (32 pixels) are in the SuperCam cryostat now. Four more will be delivered by July 2010. SuperCam will then be mounted on the HHT with a full complement of 64 pixels. Routine observations with SuperCam will begin on the HHT by the end of 2010.

REFERENCES

- [1] Walker, C. K., Groppi, C., d'Aubigny, C., Kulesa, C., Hungerford, A., Jacobs, K., Graf, U., Schieder, R., & Martin, C., 2001, PoleSTAR: A 4-Pixel 810 GHz Array Receiver for AST/RO, "Proceedings of the 12th International Symposium on Space Tera- Hertz Technology", San Diego, CA, Eds. Mehdi & McGrath, JPL.
- [2] Groppi, C. E. et al. 2003, "DesertSTAR: a 7 pixel 345 GHz heterodyne array receiver for the Heinrich Hertz Telescope", SPIE, 4855, 330.
- [3] Puetz, P., Hedden, A., Gensheimer, P., Golish, D., Groppi, C., Kulesa, K., Narayanan, G., Lichtenberger, A., Kooi, J., Wadefalk, N., Weinreb, S., Walker, C., 345 GHz Prototype SIS Mixer with Integrated MMIC LNA, Int. J. Infrared Milli. Waves, 27, 1365, 2006.
- [4] J. W. Kooi, C.K. Walker, and J. Hesler, "A Broad Bandwidth Suspended Membrane Waveguide to Thin Film Microstrip Transition", 9th Int. Conference on Terahertz Electronics, 15th – 16th October 2001.

Integrated Setup for THz Receiver Characterization

O. Nyström^{1,*}, H. Rashid¹, B. Billade¹, E. Sundin¹, M. Fredrixson¹, G. Johnsen¹, I. Lapkin¹, D. Meledin¹, M. Strandberg¹, R. Finger², A. Pavolotsky¹, V. Desmaris¹, and V. Belitsky¹

¹Chalmers University of Technology, Group of Advanced Receiver Technology, Gothenburg, SWEDEN

²University of Chile, Santiago, CHILE

*Contact: olle.nystrom@chalmers.se, phone +46-31-772 1838

Abstract — A highly versatile measurement setup has been built that allows complete characterization of the ALMA Band 5 cartridge. The measurement setup includes all necessary hardware and largely achieves automatic measurements for the system noise and sideband rejection with in-built optimization procedures. The measurement setup additionally comprises measurements of the receiver saturation, phase and amplitude stability, as well as optical beam characterization.

I. INTRODUCTION

The Atacama Large Millimeter/sub-millimeter Array (ALMA) is a partnership of Europe, Japan, and North America, in cooperation with the Republic of Chile. ALMA will initially be composed of 66 high-precision antennas with a possible extension in the future [1]. The ALMA site is located at an altitude of 5000 m in the Atacama desert in northern Chile.

The ALMA Band 5 receiver channel is a dual polarization, sideband separation (2SB) SIS-receiver [2] and covers the frequency range 163-211 GHz that includes the 183 GHz water absorption line. The presence of the water absorption line in the receiver RF band makes ground based observations challenging. However, the scientific drive for the development of the ALMA Band 5 cartridge is to observe the water line in space whereas the extremely dry, high-altitude site in the Atacama desert allows observations even at these frequencies. Apart from observing the water, the second drive for the Band 5 development is to detect highly red shifted galaxies, which falls in the specified frequency range [3].

The presence of the strong absorption line within ALMA B5 RF- band implies additional challenges in the receiver characterization, since the water vapour introduces substantial RF - loss affecting the accuracy of the measurements. The ALMA B5 characterization takes place in the laboratory in Gothenburg, Sweden, located at sea level, with a typical humidity of 70-90 % [4]. In order to preclude the humidity to affect the accuracy of the measurements, the RF-part of the setup is enclosed in a cabinet, constantly flushed with dry nitrogen. The enclosing of the measurement setup requires a highly compact layout, which was realized using a layered design. The layout of the measurement setup is described in section II. Section III-V of this paper describes different parts of the measurement setup, i.e. noise/sideband-rejection measurements and optimization, gain saturation, phase-stability, and optical characterization.

II. MEASUREMENT SETUP LAYOUT

The measurement setup has been built with focus to be compact and to allow largely automatic measurements and optimization of the receiver performance of the ALMA B5 Cartridge. The 183 GHz water absorption line is situated in the middle of the receiver's RF - band and introduces substantial RF - loss affecting the accuracy of the measurements. Consequently, the RF-part of the setup is enclosed inside a cabinet, which is constantly flushed with dry nitrogen in order to minimize the effect of the water vapour on the accuracy of the measurements. The layout of the measurement setup is shown in Fig. 1.

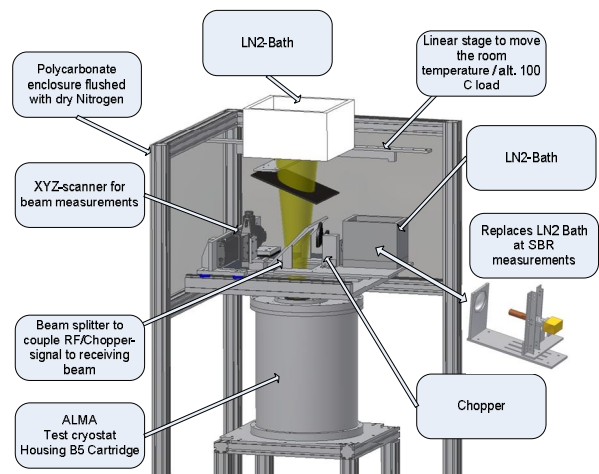


Fig. 1 Layout of measurement setup used for ALMA B5 cartridge characterization. The scanner, CW-source, and the hot/cold loads are placed in “layers” above the RF window allowing a compact setup and, to a large extent, automatic measurements.

Reduction of the water vapour in the enclosure allows the cold (77 K) LN2 load to be placed above the cryostat window at a sufficient distance to facilitate the use of hot loads: 290 K for the noise measurement setup (Y-factor measurements) and 373 K load for the dynamic range characterization, which are located in between the cryostat window and the cold load. Appropriate loads for the different measurements are inserted with computer controlled linear stages. The top plate of the cryostat accommodates the beam scanner for optical characterization that is placed in the “layer” below the loads. The use of computer controlled linear stages allows easy reconfiguration of the setup for different type of measurements.

III. NOISE AND SIDEBAND REJECTION MEASUREMENTS

We use standard Y-factor measurement technique where the receiver input is either exposed to 77 K load, the load being manufactured as described in [5] and immersed into liquid nitrogen, or to a hot load. A Mylar beam-splitter is used to inject the CW test signal in the main beam with background loaded to the cold facility load while performing the noise and sideband rejection (SBR) tuning of the receiver. The hot (room temperature) load is inserted into the receiver beam by a computer controlled linear stage; this allows simultaneous measurements and optimization for sideband rejection and noise temperature. The optimization routine finds the optimum settings with the LO-control voltage (LO-power) and the mixer bias settings as variables.

The Mylar beam-splitter (at 300 K) introduces some, but insignificant loss in the cold load signal path; our estimation predicts that the effective load temperature should not exceed 90 K and is corrected through calibration. By performing the sideband rejection measurements with a CW pilot signal with a background of approximately 90 K, we minimize potential problems with the SIS mixer saturation. The sideband rejection measurement follows the approach proposed in [6]. Fig. 2 shows a picture of the setup in SBR configuration.

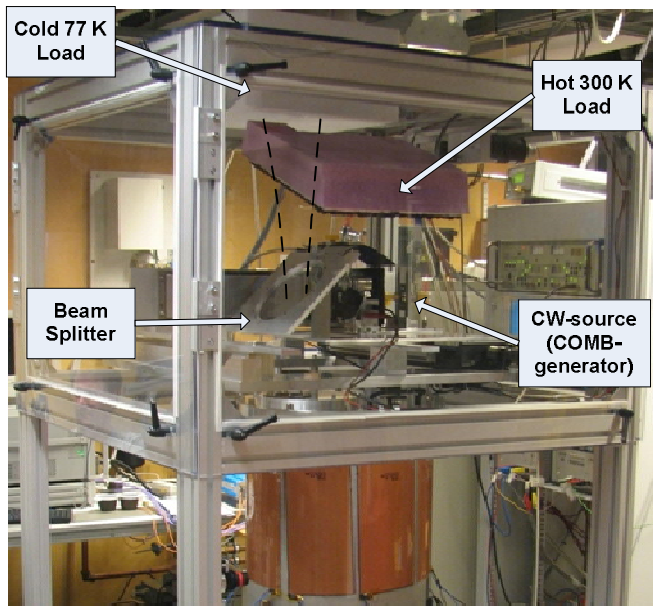


Fig. 2 Measurement setup in configuration for noise and sideband rejection measurement and optimization.

IV. GAIN SATURATION MEASUREMENTS

SIS-mixers are selected as detectors for receivers in radio-astronomy due to their extremely high sensitivity, resulting from high non-linear behavior (non-linear at voltages in the order of 1mV). A drawback of this behavior is that a SIS-mixer might saturate at input power levels from blackbody radiation at temperatures just above room temperature. The ALMA specifications require that the large signal gain compression shall be less than 5 % measured with 77 K load at the RF input port and the situation when a 373 K load is placed at the same RF input port [7].

Reference [8] outlined how the large signal gain compression, GC_{ls} , between two input levels can be determined by measuring the differential gain at the same input levels. Fig. 3 and Fig.4, from [8], illustrate how the large signal gain compression and the differential gain are defined; 1) T_{sys} (Receiver temperature + T_{in}) vs. P_{out} and 2) T_{in} vs. P_{out} . The large signal gain compression is defined as G_0/G_1 and the differential gain is defined as dP_{out}/dP_{in} . Further, [8] shows that; 1) the large signal gain is different (due to the redefinition of the origin); 2) the differential gains and gain compression is the same; 3) the large signal gain compression has the same value; 4) $GC_{ls} = \frac{1}{2} GC_{diff}$.

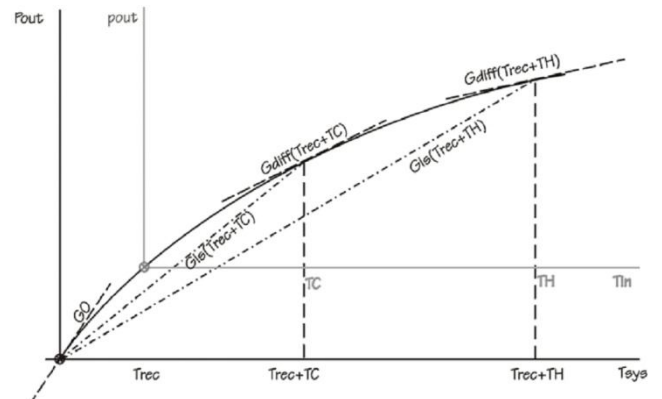


Fig. 3 The large-signal and differential gain is illustrated at two different input temperatures at the input of the receiver (P_{out} vs. T_{sys}). The input considered is $T_{rec}+T_{in}$, i.e. T_{sys} [8].

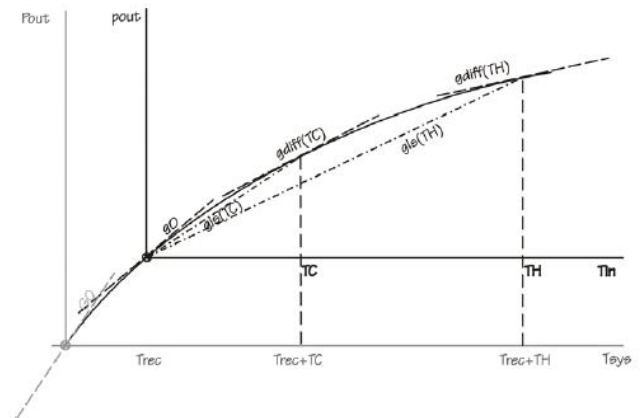


Fig 4 The large-signal and differential gain is illustrated at two different input temperatures at the input of the receiver (P_{out} vs. T_{in}). The input considered is T_{in} only [7].

In our setup, a setup similar to what is presented in [8]; the receiver beam is coupled via the beam-splitter in straight direction to a hot/cold (373K/100K) load to allow alternating the input power between these two levels. The side-beam coupled via the beam-splitter to a signal, which is modulated between the ambient/cold loads by a chopper. This procedure allows measurements of the small signal gain compression at the operating points set by the main hot/cold loads. The principle of the gain saturation setup is shown in Fig. 5 and Fig. 6 shows a picture of the laboratory setup.

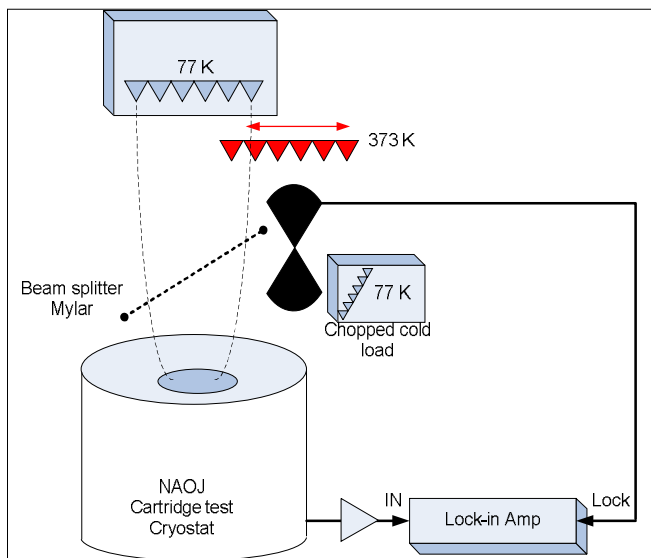


Fig. 5 Layout of gain compression measurement setup. A modulated signal is introduced through beam-splitter allowing measurements of differential gain around operating points set by the main hot/cold loads.

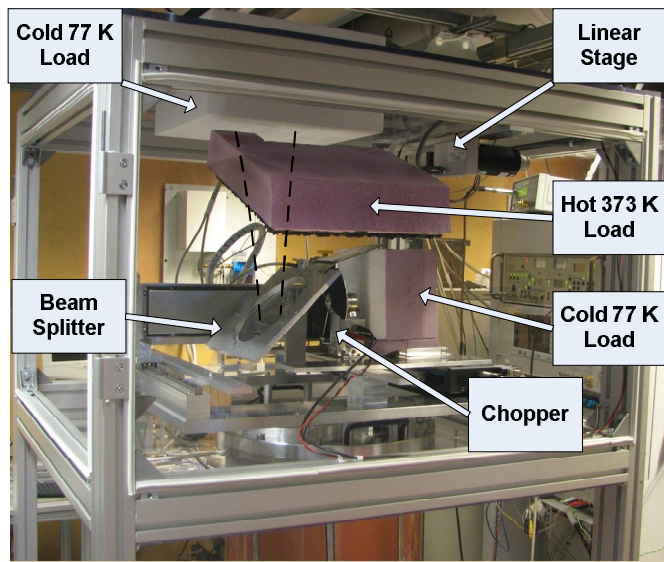


Fig. 6 Picture of the laboratory setup for saturation measurements.

V. BEAM CHARACTERIZATION AND PHASE STABILITY MEASUREMENTS

The receiver optics characterization (beam-pattern measurements) are performed using vector field, both phase and amplitude, measurements. A three axis scanner, allowing compensation for standing waves with its 3rd axis, is used to scan a test RF-source across the receiver input beam. In this setup, a vector network analyser is employed as a single frequency source together with a circuitry, generating necessary frequencies. The circuitry consists of comb-generators, filters, and amplifiers forming a homodyne receiver in order to produce perfectly phase-coherent RF- and LO- signals by taking advantage of different harmonics [9]. The advantage of employing the VNA in combination with the additional circuitry is that such circuitry produces phase

coherent LO and RF signals and removes errors due to initial phase fluctuations in the VNA. The very same setup is also utilized in phase-stability measurements. A schematic of the circuitry is shown in Fig. 7 and a picture of the scanner setup mounted on the cartridge test cryostat is shown in Fig. 8.

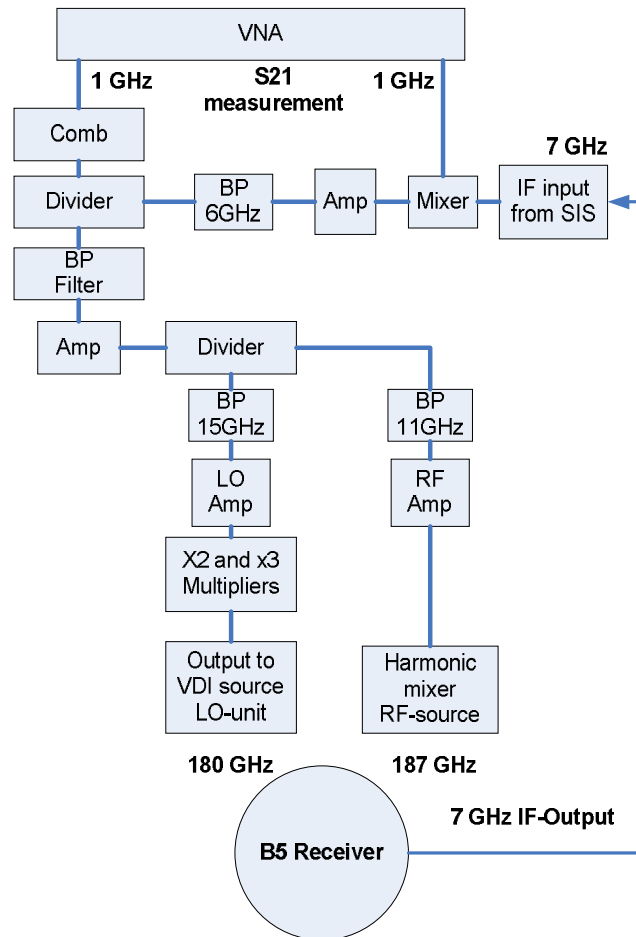


Fig. 7 Schematic of the circuit allowing phase coherent beam scanning. The circuitry is also used in phase stability measurements.

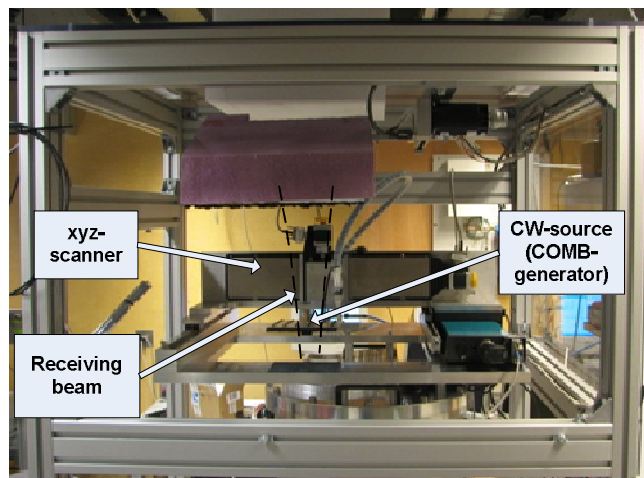


Fig. 8 Picture of the beam scanning setup with the scanner mounted on the cryostat top plate.

Measurements are performed at 168 GHz, 187 GHz, and 210 GHz, thus verifying the optical performance across the frequency band of the receiver. This reflects some limitation of the system in so far as only certain discrete frequencies across the RF – band can be used, since the generated harmonics, producing RF- and LO- signals, must generate an IF signal within the 4-8 GHz range. Figures 9-10 show the measured beam data at 168 GHz.

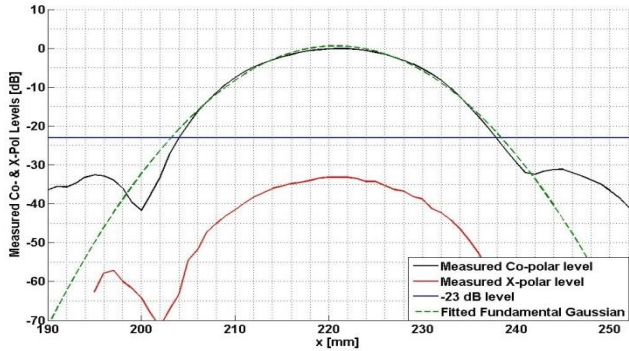


Fig 9 Measured beam, X-cut with Co- and Cross-polar levels in dB, at 168 GHz.

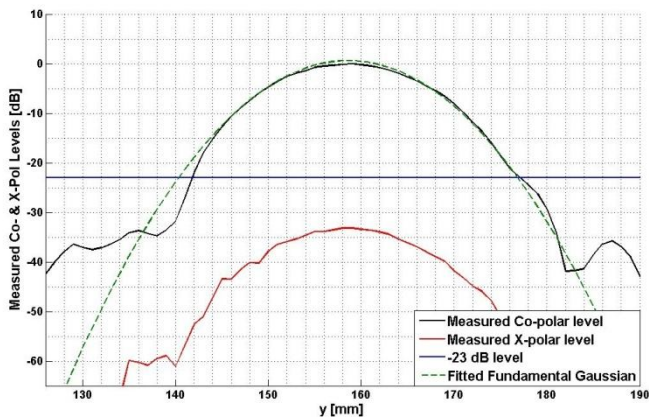


Figure 10 Measured beam, Y-cut with Co- and Cross-polar levels in dB, at 168 GHz.

The measured cross-polarization levels show in Fig 9- Figure 10, exhibit a more Gaussian like shape instead of the characteristic two-lobe shape expected for the cross polar beam pattern. The reason for this is most likely due to a small yaw- angle between the receiving horn and the probe, thus the polarization alignment is not correct and a small part of the co-polar field will be present in the cross-polar pattern. Since the cross polar levels are very low (below -23 dB), compared to the co-polar on axis value, it is sufficient with just a small percentage of the co-polar field to end up with the Gaussian shape of the cross-polar pattern instead of the two lobe pattern. The alignment (yaw-alignment) of the measurement setup will be investigated and the cross polarization will be remeasured.

The beam pattern, horn and mirrors, was previously measured in a room temperature setup using an Agilent VNA with frequency extension modules, results are shown in Fig 11 and Fig 12, where the measured data is displayed together with GRASP [10] and MODAL [11] physical optics

(PO) simulation data. The GRASP and MODAL simulations were performed by M. Whale at NUI Maynooth. The scans are performed at a distance corresponding to the focal plane of the telescope and the measured and simulated data has a correspondence of >99%. The fact that warm optics measurements show nearly 100 % agreement to the simulated data gives confidence that the optics performance is well within specifications and demonstrates the accuracy of the measurements.

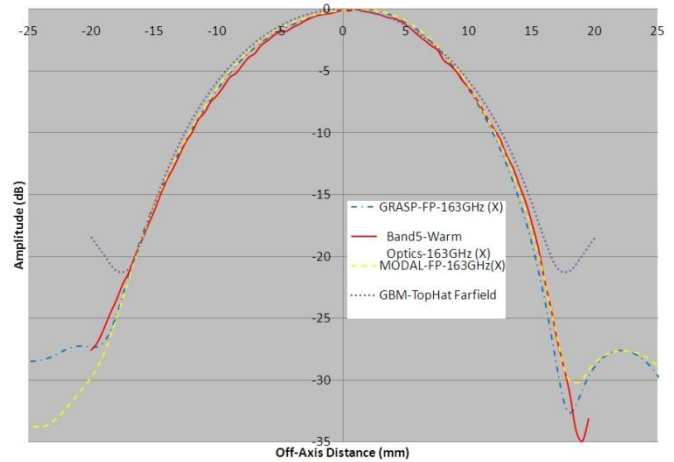


Fig 11 Measured beam pattern, at the focal plane, of the horn and two mirrors at room temperature compared to PO simulations in GRASP and MODAL. The figure shows the x-cut at 163 GHz.

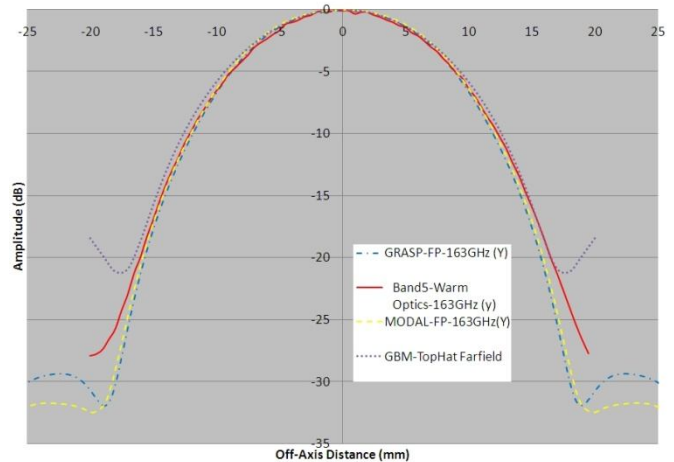


Fig 12 Measured beam pattern, at the focal plane, of the horn and two mirrors at room temperature compared to PO simulations in GRASP and MODAL. The figure shows the y-cut at 163 GHz.

In order to reduce the scan time, which can have a duration exceeding 12 h for dense scans with standing wave compensation, i.e. two measurements $\lambda/4$ apart in z-direction for each point, an on-fly measurement procedure is being implemented. The on-fly measurement reduces the scan time significantly to approximately 40 minutes. The on-fly measurements require high dynamic range and the procedure has been tested successfully with the room temperature setup where the dynamic range of the system is in the order of 80 dB. On-fly measurements will be tested also for cold

measurements for the frequency points where the dynamic range allows. On-fly measurements have the advantage of removing vibrations, due to starts and stops at each point, which otherwise requires a short delay in between measurement samples in order to allow vibrations to decay. The results of the measurements will be compared to the stepped scans for verification.

VI. CONCLUSIONS

We have presented a setup for complete characterization of a 2SB and dual-polarization receiver built in a compact design. The layered layout, i.e. scanner and loads at different distances along the beam, is used. The entire RF-part of the setup is enclosed in a cabinet flushed with dry nitrogen, reducing the water vapour content and substantial RF-loss compromising the accuracy of the measurements. The presented setup allows largely automated measurements and optimization of the noise and sideband rejection performance of the receiver. By introducing appropriate loads with computer controlled linear stages and applying a CW signal via beam splitter for SBR measurements, Y-factor and sideband rejection measurements can be done simultaneously with significantly decreased time needed for complete receiver characterization.

ACKNOWLEDGMENT

The authors would like to acknowledge Mark Whale, NUI Maynooth for help with PO simulations, Douglas Henke, HIA-NRC (former GARD member) for interesting discussions regarding the layout of the system, and Sven-Erik Ferm for machining excellent mechanical parts.

REFERENCES

- [1] ALMA Observatory Website, Available: www.almaobservatory.org.
- [2] B. Billade "Design of Dual Polarization Sideband Separation Mixer for ALMA Band 5", Thesis for licentiate of engineering, ISBN/ISSN:1652-9103, Gothenburg 2009
- [3] ALMA Band 5 Workshop, "Science with ALMA Band 5 (163-211GHz)", Available: <http://web.oa-roma.inaf.it/meetings/AlmaBand5/Home.html>
- [4] Onsala Space Observatory webpage, Available: <http://www.oso.chalmers.se/~weather/index.html#humidity>
- [5] T.O. Klaassen, et. al., "Absorbing coatings and diffuse reflectors for the Herschel platform sub-millimetre spectrometers HIFI and PACS", 2002 IEEE Tenth Int. Conf. on Terahertz Electronics Proc. 2002.
- [6] A. R. Kerr, et. al., "Sideband Calibration of Millimeter-Wave Receivers", ALMA Memo #357, March 2001
- [7] G.H. Tan, "Band 5 Cartridge Technical Specifications", Doc. nr: FEND-40.02.05.00-001-A-SPE, 2005.
- [8] Lazareff, Mahieu, "Band 7 Cartridge Test Report Gain Saturation", Doc.: FEND-40.02.07.00-013-B-PRO, IRAM 2006.
- [9] O. Nyström, et. al., "A Vector Beam Measurement System for 211-275 GHz", Proc. EuCAP 2006, France, (ESA SP-626, October 2006) ISBN/ISSN: 92-9092-937-5.
- [10] TICRA, webpage available: <http://www.ticra.com/what-we-do/software-descriptions/grasp/>
- [11] University of Ireland, Maynooth, IRLAND.

SNS: Analytic Receiver Analysis Software Using Electrical Scattering Matrices

Oliver G. King*[†]

*California Institute of Technology, MC 249-17, 1200 E. California Blvd., Pasadena, CA, 91125

[†]Contact: ogk@astro.caltech.edu

Abstract—SNS is a MATLAB-based software library written to aid in the design and analysis of receiver architectures. It uses electrical scattering matrices and noise wave vectors to describe receiver architectures of arbitrary topology and complexity. It differs from existing freely-available software mainly in that the scattering matrices used to describe the receiver and its components are analytic rather than numeric. This allows different types of modeling and analysis of receivers to be performed.

Non-ideal behavior of receiver components can be parameterized in their scattering matrices. SNS enables the instrument designer to then derive analytic expressions for the signal and noise at the receiver outputs in terms of parameterized component imperfections, and predict their contribution to receiver systematic errors precisely. This can drive the receiver design process by, for instance, allowing the instrument designer to identify which component imperfections contribute most to receiver systematic errors, and hence place firm specifications on individual components. Using SNS to perform this analysis is preferable to traditional Jones matrix-based analysis as it includes internal reflections and is able to model noise: two effects which Jones matrix analysis is unable to describe.

SNS can be used to model any receiver in which the components can be described by scattering matrices. Of particular interest to the sub-mm and terahertz frequency regime is the choice between coherent and direct detection technologies. Steady improvements in mm and sub-mm Low Noise Amplifiers (LNAs) mean that coherent receivers with LNAs as their first active element are becoming increasingly competitive, in terms of sensitivity, with bolometer-based receivers at frequencies above ~ 100 GHz.

As an example of the utility of SNS, we use it to compare two polarimeter architectures commonly used to perform measurements of the polarized Cosmic Microwave Background: differencing polarimeters, an architecture commonly used in polarization sensitive bolometer-based polarimeters; and pseudo-correlation polarimeters, an architecture commonly used in coherent, LNA-based, polarimeters. We parameterize common sources of receiver systematic errors in both architectures and compare them through their Mueller matrices, which encode how well the instruments measure the Stokes parameters of the incident radiation. These analytic Mueller matrices are used to demonstrate the different sources of systematic errors in differencing and correlation polarimeters.

I. INTRODUCTION

Many fields of astrophysics aim to measure increasingly faint signals. For instance, there is great interest at present in detecting and characterizing the B-mode [1] of the polarized Cosmic Microwave Background (CMB). The strength of this signal is not yet determined by theory, but a strong upper limit is 170 nK [2], a tiny fraction of the CMB total intensity signal (~ 2.7 K).

An instrument built to detect very faint signals will almost certainly be heavily affected by systematic errors. It is increasingly important to be able to model the effects of receiver systematic errors on the measured signal, and on the receiver sensitivity. We want to be able predict the level of receiver systematic errors, show their impact on the gathered data, and make quantitative comparisons between different receiver architectures.

Previous analytic and semi-analytic approaches to characterizing systematic effects in receivers have usually employed Jones matrices to describe receiver components and Mueller matrices to characterize the effects of receiver systematics on the observed Stokes parameters [3], [4]. The use of Jones matrices to describe individual receiver components has several shortcomings. Only the forward path of the signal through the instrument is modeled – internal scattering caused by reflections from poorly matched components is not included; and Jones matrix modeling is unable to describe component noise, and hence receiver sensitivity. Modeling a receiver with a full analytic description of the outputs and sensitivity in terms of individual component parameters allows us to identify which parameters of each component in a receiver are most important, and concentrate our efforts on improving them.

This paper introduces a technique and software for developing full analytic descriptions of receiver outputs and sensitivities in terms of lab-measurable errors in individual components. In this technique components are modeled by electrical scattering matrices. When describing a network of components with Jones matrices the forward-path cascaded response can be obtained through simple matrix manipulation and multiplication. The scattering matrix formulation does not share this simplicity of calculation: only the case of cascaded 2-port devices is amenable to a relatively simple analytic solution. This paper describes an algorithm for calculating the response of arbitrarily connected networks of components. We present software which implements this algorithm, and apply it to two common polarimeter architectures: differencing polarimeters, and pseudo-correlation polarimeters.

This software allows us to make robust analytic comparisons of receiver architectures. Errors in individual receiver components can be parameterized and propagated into the description of the receiver performance, e.g. the instrument Mueller matrix. We hence have a powerful tool for guiding the instrument design process and diagnosing the causes of non-ideal instrument behavior.

II. ELECTRICAL SCATTERING MATRICES

We model the behavior of individual receiver components, and the full receiver, using electrical scattering matrices. The electrical scattering matrix (hereafter referred to as the scattering matrix) is a representation of a network using the ideas of incident, reflected, and transmitted waves. It provides a complete description of an N -port network as seen at its N ports. A significant advantage of modeling receiver components with scattering matrices is that *noise* can easily be included in the modeling. The noise produced by a device is modeled with a noise wave vector; see e.g. [5].

Consider the arbitrary N -port network shown in Figure 1a. We denote the incident wave at port i by V_i^+ , the reflected wave by V_i^- , and the noise wave produced by the network at that port by c_i . These quantities are related by the scattering matrix \mathbf{S} and noise wave vector \mathbf{c} as follows:

$$\begin{bmatrix} V_1^- \\ V_2^- \\ \vdots \\ V_N^- \end{bmatrix} = \begin{bmatrix} S_{11} & S_{12} & \cdots & S_{1N} \\ S_{21} & & & \vdots \\ \vdots & & & \\ S_{N1} & \cdots & & S_{NN} \end{bmatrix} \begin{bmatrix} V_1^+ \\ V_2^+ \\ \vdots \\ V_N^+ \end{bmatrix} + \begin{bmatrix} c_1 \\ c_2 \\ \vdots \\ c_N \end{bmatrix} \quad (1)$$

The noise wave voltages c_i of an N -port network are complex time-varying random variables characterized by a correlation matrix \mathbf{C}

$$\begin{aligned} \mathbf{C} &= \langle \mathbf{c} \otimes \mathbf{c}^\dagger \rangle \\ &= \begin{bmatrix} \langle |c_1|^2 \rangle & \langle c_1 c_2^* \rangle & \cdots & \langle c_1 c_N^* \rangle \\ \langle c_2 c_1^* \rangle & & & \vdots \\ \vdots & & & \\ \langle c_N c_1^* \rangle & \cdots & & \langle |c_N|^2 \rangle \end{bmatrix} \end{aligned}$$

where the angle brackets indicate time averaging, \dagger indicates the conjugate transpose operation, and \otimes indicates the outer product (or Kronecker product). The diagonal terms of \mathbf{C} give the noise power deliverable at each port in a 1 Hz bandwidth. The off-diagonal terms are correlation products. The noise correlation matrix \mathbf{C} for a passive network is determined from its scattering matrix \mathbf{S} by [6]

$$\mathbf{C} = kT(\mathbf{I} - \mathbf{S}\mathbf{S}^\dagger) \quad (2)$$

where k is Boltzmann's constant, T is the physical temperature of the network, and \mathbf{I} is the identity matrix. The noise correlation matrix for an active network can be determined by measurement or modeling.

III. SOLVING ARBITRARY NETWORKS

Consider the arbitrarily connected network of N -port networks shown in Figure 1b. We need an algorithm to calculate the scattering matrix \mathbf{S} and noise wave vector \mathbf{c} which describe the connected network. The algorithm derived here is an extension of the algorithm described in [7], with added noise wave vector manipulation. Similar algorithms are used numerically in SUPERMIX [8].

First, let us consider the effect of connecting together ports k and m of an N -port network described by Equation 1. Connecting the ports means that $V_k^+ = V_m^-$ and $V_k^- = V_m^+$. Manipulation of rows k and m of Equation 1 then gives us the expressions

$$V_m^- = \sum_{i \neq k, m} \frac{S_{mi}}{1 - S_{mk}} V_i^+ + \frac{S_{mm}}{1 - S_{mk}} V_k^- + \frac{c_m}{1 - S_{mk}} \quad (3)$$

$$V_k^- = \sum_{i \neq k, m} \frac{S_{ki}}{1 - S_{km}} V_i^+ + \frac{S_{kk}}{1 - S_{km}} V_m^- + \frac{c_k}{1 - S_{km}} \quad (4)$$

By substituting Equations 3 and 4 into each other we can obtain expressions for V_m^- and V_k^- . Substituting these expressions into Equation 1 we can obtain a new expression for the reflected wave V_i^- :

$$\begin{aligned} V_i^- &= \sum_{j \neq k, m} \left[S_{ij} + \frac{(1 - S_{km})(1 - S_{mk})}{(1 - S_{km})(1 - S_{mk}) - S_{kk}S_{mm}} \right. \\ &\quad \left(\frac{S_{ik}S_{mj}}{1 - S_{mk}} + \frac{S_{ik}S_{mm}S_{kj}}{(1 - S_{mk})(1 - S_{km})} \right. \\ &\quad \left. \left. + \frac{S_{im}S_{kj}}{1 - S_{km}} + \frac{S_{im}S_{kk}S_{mj}}{(1 - S_{km})(1 - S_{mk})} \right) \right] V_j^+ \\ &\quad + c_i + S_{ik} \left(\frac{(1 - S_{km})c_m + S_{mm}c_k}{(1 - S_{km})(1 - S_{mk}) - S_{kk}S_{mm}} \right) \\ &\quad + S_{im} \left(\frac{(1 - S_{mk})c_k + S_{kk}c_m}{(1 - S_{km})(1 - S_{mk}) - S_{kk}S_{mm}} \right) \end{aligned} \quad (5)$$

From Equation 5 we obtain replacement expressions for the elements S_{ij} of \mathbf{S} and the noise waves c_i :

$$\begin{aligned} S_{ij}^{\text{new}} &= S_{ij} + A \left[S_{ik}S_{mj}(1 - S_{km}) + S_{ik}S_{kj}S_{mm} \right. \\ &\quad \left. + S_{im}S_{kj}(1 - S_{mk}) + S_{im}S_{mj}S_{kk} \right] \end{aligned} \quad (6)$$

$$\begin{aligned} c_i^{\text{new}} &= c_i + A \left[(S_{im}S_{kk} + S_{ik}(1 - S_{km}))c_m \right. \\ &\quad \left. + (S_{ik}S_{mm} + S_{im}(1 - S_{mk}))c_k \right] \end{aligned} \quad (7)$$

$$\text{where } A = \frac{1}{(1 - S_{km})(1 - S_{mk}) - S_{kk}S_{mm}}$$

Rows and columns k and m are then removed from \mathbf{S} and rows k and m are removed from \mathbf{c} to create the scattering matrix and noise vector which describe the new $(N - 2)$ -port network.

A. Algorithm

To obtain the scattering matrix and noise wave vector which describe the arbitrarily connected network shown in Figure 1b begin by forming the scattering matrix and noise wave vector which describe the unconnected network:

$$\mathbf{S} = \begin{bmatrix} \mathbf{S}_1 & \mathbf{0} & \cdots & \mathbf{0} \\ \mathbf{0} & \mathbf{S}_2 & & \vdots \\ \vdots & & & \\ \mathbf{0} & \cdots & & \mathbf{S}_N \end{bmatrix}, \mathbf{c} = \begin{bmatrix} \mathbf{c}_1 \\ \mathbf{c}_2 \\ \vdots \\ \mathbf{c}_N \end{bmatrix} \quad (8)$$

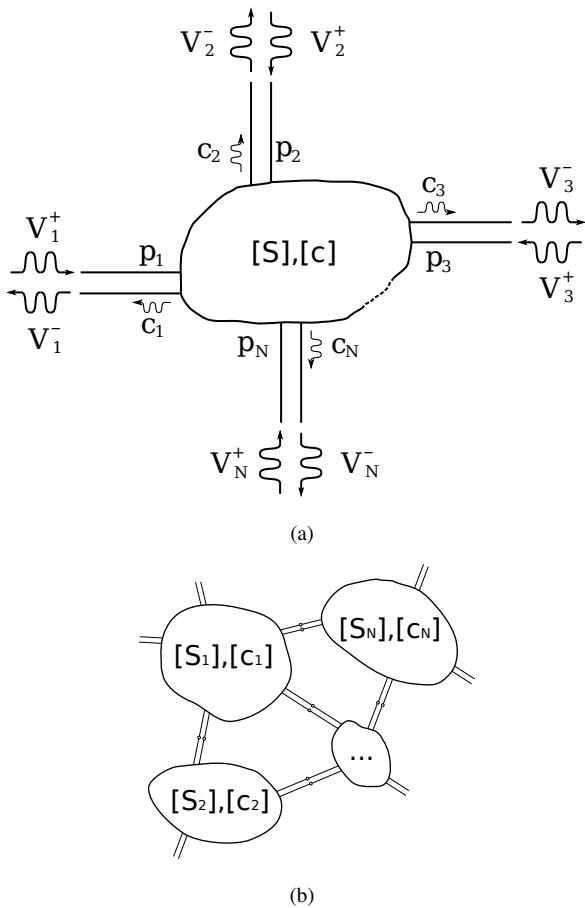


Fig. 1. (a) An arbitrary N -port network. The total signal at each port p_i consists of an incident signal V_i^+ , a reflected signal V_i^- , and a noise signal c_i . The reflected signal V_i^- is a weighted sum of the incident signal at port i and transmitted signals from the other ports of the network, the coefficients of the sum being the elements of the network scattering matrix \mathbf{S} . The noise signals are given by the noise wave vector \mathbf{c} . (b) An arbitrarily connected network of N -port devices.

We then successively form each connection in the network. For each connection, find the rows and columns k and m of \mathbf{S} and \mathbf{c} in Equation 8 which correspond to the ports being connected. Use the replacement formulae given by Equations 6 and 7 to adjust the \mathbf{S} matrix and \mathbf{c} vector. Remove rows and columns k and m from \mathbf{S} , and rows k and m from \mathbf{c} . Repeat for each remaining connection until we are left with the scattering matrix \mathbf{S} and noise vector \mathbf{c} which describe the fully connected network.

IV. SOFTWARE IMPLEMENTATION

We have derived an algorithm in §III-A for finding the scattering matrix and noise wave vector which describe an arbitrarily connected network. We need to be able to apply it to arbitrary receivers with parameterized scattering matrices describing the receiver components and obtain analytic expressions for the outputs and noise in terms of the component parameters.

The algorithm must be implemented in a programming language with the ability to manipulate symbolic algebraic expressions. This programming language must also support

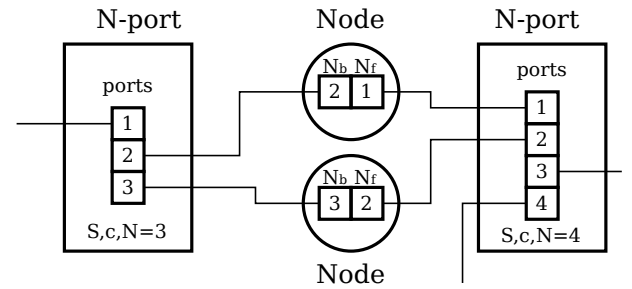


Fig. 2. Schematic showing the nature of node and N -port objects and how they connect to each other in the software.

pointers (or equivalent data structure) to allow the creation of a navigable network. We implemented the algorithm in MATLAB¹, which has a powerful and well developed symbolic algebra toolbox. While it does not have a native pointer data type (as of version R2008b), a third party open-source pointer library² adds this capability. The software package we developed to perform this modeling is called SNS³.

A. Representing a Network

A network is represented by nodes and N -port objects, as shown in Figure 2. They are both pointer objects. Each N -port object contains an array of references to the nodes connected to each of its N ports, a scattering matrix \mathbf{S} , a noise wave vector \mathbf{c} , and a variable N , the number of ports of the object.

Each node object contains two pointers; these refer to the N -port objects the node connects to in the “forward” and “backward” directions, and which port number the connection is made to (N_{fp} and N_{bp} respectively). Note that the forward and backward directions are completely arbitrary; they are merely a helpful concept when trying to visualize the operation of the algorithms which act on the network.

The network is constructed by creating all the node and N -port objects using functions called `makeNode()` and `makeNport()`, assigning scattering matrices and noise wave vectors to the N -port objects, and connecting each node to its forward and backward N -port objects. A `connectNode` function hides the complexity of assigning references to the appropriate array locations and assigning the appropriate port numbers to variables.

Nodes are classified into four types: input, output, central, and terminated. We want to calculate the performance of a network in terms of the response seen at the outputs due to signals presented at the inputs. The central and terminated nodes are removed by the network-solving program.

Once all the objects have been created, assigned matrices and vectors, and connected, it suffices to describe the network by the four arrays of nodes. Due to the fully connected nature of the network representation it is possible to start at any node and navigate to any other node by following the appropriate links between objects.

¹<http://www.mathworks.com/>

²<http://code.google.com/p/pointer/>

³Download at <http://www.astro.caltech.edu/~ogk/SNS/>

B. Solving a Network

The network-solving program accepts four arrays of nodes: the inputs, outputs, central nodes, and terminated nodes. It returns the scattering matrix and noise wave vector for the connected network, where the central and terminated nodes have been removed through application of the algorithm described in §III-A.

The first step the software performs is to remove the terminated nodes, if there are any. The software assumes that the terminations are perfectly matched and at a common physical temperature. It modifies the object scattering matrices to remove the terminated nodes, and adds the noise terms produced by the terminated nodes to the noise wave vectors.

The network *sans* terminated nodes is then passed to a recursive network shrinking program. This program begins with the first central node and applies the algorithm given by Equations 6 and 7 to a sub-network consisting of the two N -port objects connected to that particular node. A new N -port object is created and assigned the resulting scattering matrix and noise wave vector. All the nodes which were connected to the now-defunct N -port objects are reconnected to this new N -port object at the appropriate ports. A new network is formed by excluding the central node just considered and the program is recursively called on this new network. This continues until there are no more central nodes, at which point the scattering matrix and noise wave vector of the single remaining N -port object are returned.

Applying the algorithm in this fashion, rather than to the entire network at once, means that the size of the matrix \mathbf{S} in Equation 8 is kept small, speeding up computation. This is not an optimum solution to network shrinking, but we have found it to be significantly faster than applying the algorithm to the full unconnected network for networks of more than a few N -port objects.

The description given above glosses over the significant complexity in keeping track of which nodes should be connected where, and certain configurations of nodes and N -port objects which would cause the default implementation of the algorithm to fail. The majority of the code is dedicated to performing these functions; only a small fraction of the code actually carries out the calculations described by the algorithm.

C. Example Code Listing

To illustrate the operation of the program consider the network shown in Figure 3. It is represented in software by connected lists of nodes and N -port objects, as shown in the following code listing:

```
% Matrices S1, S2, S3, S4, S5 and vectors c1, c2, c3, c4, c5 assumed to
% have been previously defined using symbolic algebra library.
% Make the N-port objects
P1 = makeNport(); P2 = makeNport(); P3 = makeNport();
P4 = makeNport(); P5 = makeNport();
% Assign scattering matrices and noise vectors
P1.S = S1; P2.S = S2; P3.S = S3; P4.S = S4; P5.S = S5;
P1.c = c1; P2.c = c2; P3.c = c3; P4.c = c4; P5.c = c5;
% Make the nodes which connect the N-port objects
In1 = makeNode(); In2 = makeNode(); On1 = makeNode();
On2 = makeNode(); Tn1 = makeNode(); Cn1 = makeNode();
Cn2 = makeNode(); Cn3 = makeNode();
Cn4 = makeNode(); Cn5 = makeNode();
% Connect nodes to N-ports
connectNode(In1, [1, 1, P1, 1]); connectNode(In2, [1, 1, P1, 4]);
connectNode(Cn1, P1, 2, P3, 1); connectNode(Cn2, P1, 3, P4, 1);
connectNode(Cn3, P3, 2, P2, 1); connectNode(Cn4, P4, 2, P2, 4);
connectNode(Cn5, P3, 3, P5, 1); connectNode(Tn1, P2, 3, [1, 1]);
connectNode(On1, P5, 2, [1, 1]); connectNode(On2, P2, 2, [1, 1]);
% Build arrays of nodes
inputs = {In1 In2}; outputs = {On1 On2};
```

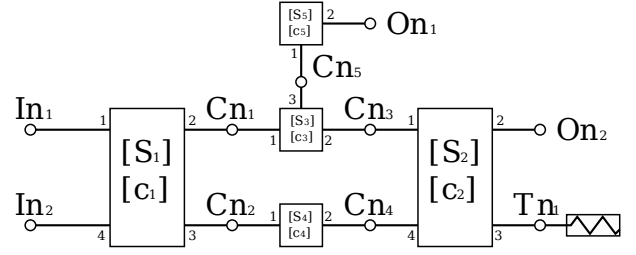


Fig. 3. An arbitrary network of N -port devices to illustrate the software. Nodes are indicated by open circles, N -port devices by rectangles. N -port device i is described by scattering matrix \mathbf{S}_i and noise wave vector \mathbf{c}_i . Input nodes to the network are In_i , central nodes Cn_i , terminated nodes Tn_i , and output nodes On_i .

```
cnodes = {Cn1 Cn2 Cn3 Cn4 Cn5}; tnodes = {Tn1};
% Pass arrays of nodes to network calculator
[S, c] = getScatteringRecursive(inputs, outputs, cnodes, tnodes);
```

The `getScatteringRecursive` program performs the actions described in §IV-B, and returns the scattering matrix \mathbf{S} and noise wave vector \mathbf{c} for the resulting 4-port object. Nodes In_1 , In_2 , On_1 , and On_2 are connected sequentially to ports 1 to 4 of this object.

V. POLARIMETRY

The example presented in the coming section, §VI, compares two receiver architectures commonly used to measure linear polarization at radio to sub-mm wavelengths. This section provides necessary background information by sketching a brief summary of polarization. It shows how a receiver may be described by a Mueller matrix, and shows how to derive a receiver Mueller matrix from the scattering matrix produced by the software described in §IV.

A. Brief Summary of Polarization

An electromagnetic signal is said to be polarized if there is some lasting amplitude or phase relation between its orthogonal modes. The coherency vector [9] captures this relation:

$$\mathbf{e} = \left\langle \begin{bmatrix} E_x(t) E_x^*(t) \\ E_x(t) E_y^*(t) \\ E_y(t) E_x^*(t) \\ E_y(t) E_y^*(t) \end{bmatrix} \right\rangle = \langle \mathbf{E} \otimes \mathbf{E}^* \rangle$$

Here \mathbf{E} is the complex vector of the orthogonal modes $E_x(t)$ and $E_y(t)$ of the signal, $\langle \dots \rangle$ indicates time averaging, and \otimes indicates the outer product.

If the signal \mathbf{E} is acted on by an object described by a Jones matrix \mathbf{J} , i.e. $\mathbf{E}_{out} = \mathbf{J}\mathbf{E}$, then the new coherency vector is given by

$$\mathbf{e}_{out} = (\mathbf{J} \otimes \mathbf{J}^*) \mathbf{e} \quad (9)$$

The polarization state of a signal is usually described by the Stokes parameters, I , Q , U , and V . I describes the total intensity of the signal, Q and U describe the linear polarization

state, and V describes the circular polarization state. The Stokes vector \mathbf{e}^S is obtained from the coherency vector \mathbf{e} by

$$\mathbf{e}^S = \begin{bmatrix} I \\ Q \\ U \\ V \end{bmatrix} = \mathbf{T}\mathbf{e} \quad (10)$$

$$\text{where } \mathbf{T} = \begin{bmatrix} 1 & 0 & 0 & 1 \\ 1 & 0 & 0 & -1 \\ 0 & 1 & 1 & 0 \\ 0 & -i & i & 0 \end{bmatrix} \quad (11)$$

We see that \mathbf{T} is a coordinate transformation of the coherency vector to the abstract Stokes frame.

The Stokes parameters are a convenient and powerful way of the describing the state of polarization of an electromagnetic signal. From Equation 10 we have:

$$\begin{aligned} I &= \langle |E_x(t)|^2 \rangle + \langle |E_y(t)|^2 \rangle \\ Q &= \langle |E_x(t)|^2 \rangle - \langle |E_y(t)|^2 \rangle \\ U &= 2\langle \Re\{E_x(t)E_y^*(t)\} \rangle \\ &= \langle E_x(t)E_y^*(t) \rangle + \langle E_x^*(t)E_y(t) \rangle \\ V &= 2\langle \Im\{E_x(t)E_y^*(t)\} \rangle \\ &= -i[\langle E_x(t)E_y^*(t) \rangle - \langle E_x^*(t)E_y(t) \rangle] \end{aligned} \quad (12)$$

a) *Mueller Calculus*: Suppose that a signal defined by the complex electric field vector \mathbf{E} and coherency vector \mathbf{e} is modified by an object described by the Jones matrix \mathbf{J} . From Equations 9 and 10 we see that the output signal $\mathbf{E}_{out} = \mathbf{J}\mathbf{E}$ will be described by the Stokes vector

$$\begin{aligned} \mathbf{e}_{out}^S &= \mathbf{T}(\mathbf{J} \otimes \mathbf{J}^*)\mathbf{T}^{-1}\mathbf{e}^S \\ &= \mathbf{M}\mathbf{e}^S \end{aligned}$$

The matrix $\mathbf{M} = \mathbf{T}(\mathbf{J} \otimes \mathbf{J}^*)\mathbf{T}^{-1}$ is called the Mueller matrix. It represents the action of the object characterized by Jones matrix \mathbf{J} in the Stokes vector space.

Mueller calculus is a matrix method for manipulating Stokes vectors. We denote the Mueller matrix elements as

$$\mathbf{M} = \begin{bmatrix} M_{II} & M_{IQ} & M_{IU} & M_{IV} \\ M_{QI} & M_{QQ} & M_{QU} & M_{QV} \\ M_{UI} & M_{UQ} & M_{UU} & M_{UV} \\ M_{VI} & M_{VQ} & M_{VU} & M_{VV} \end{bmatrix}$$

Mueller matrices are a convenient means of describing the action of an astronomical polarimeter. Of particular interest are the M_{QI} and M_{UI} parameters, which describe the leakage of the total intensity I into the measured linear polarization vector components. Much of the radio and mm/sub-mm spectrum is only slightly linearly polarized, hence non-zero values of M_{QI} and M_{UI} can imply serious contamination of the measured linear polarization vector by the total intensity signal.

B. Deriving Receiver Mueller Matrix

Say we have calculated the scattering matrix which describes the behavior of a receiver. For polarimeters, a natural way of expressing the receiver's performance is with a Mueller matrix. We need to translate the receiver scattering matrix into

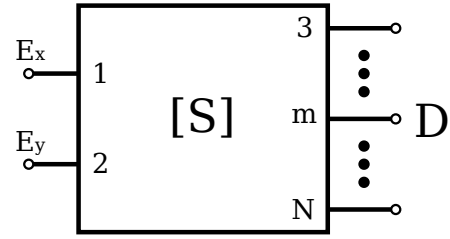


Fig. 4. A arbitrary receiver, where orthogonal linear polarizations $E_x(t)$ and $E_y(t)$ are presented at inputs 1 and 2 respectively. D is the output at port m . The receiver is described by scattering matrix \mathbf{S} .

a Mueller matrix which describes the action of the receiver on the Stokes vector of the incident electromagnetic signal.

Consider the arbitrary receiver shown in Figure 4. Orthogonal linear polarizations $E_x(t)$ and $E_y(t)$, representing either signals in transmission lines, orthogonal modes in waveguide, or orthogonal modes in free-space, are connected to ports 1 and 2 of the receiver respectively. Receiver output D is connected to port m . The receiver is described by the scattering matrix \mathbf{S} .

The output $E_m(t)$ seen at port m is given by (assuming that the connections to ports 3 to N are reflectionless):

$$E_m(t) = S_{m1}E_x(t) + S_{m2}E_y(t)$$

The power contained in the signal $E_m(t)$ is then measured. At radio wavelengths this is often achieved through the use of a square-law detector diode. At mm and sub-mm wavelengths a bolometer might be used. The measured power P_D is given by:

$$\begin{aligned} P_D &= \alpha \langle E_m(t)E_m(t)^* \rangle \\ &= \alpha \left[\langle |E_x(t)|^2 \rangle |S_{m1}|^2 + \langle |E_y(t)|^2 \rangle |S_{m2}|^2 \right. \\ &\quad + \langle E_x(t)E_y^*(t) \rangle S_{m1}S_{m2}^* \\ &\quad \left. + \langle E_x^*(t)E_y(t) \rangle S_{m1}^*S_{m2} \right] \end{aligned} \quad (13)$$

where $\langle \dots \rangle$ indicates time averaging, α is a proportionality constant dependent on the power detection method, and we assume that the instrument scattering matrix parameters are constant during the average time period. Now let

$$\begin{aligned} P_D &= M_{DI}I + M_{DQ}Q + M_{DU}U + M_{DV}V \\ &= M_{DI}(\langle |E_x(t)|^2 \rangle + \langle |E_y(t)|^2 \rangle) \\ &\quad + M_{DQ}(\langle |E_x(t)|^2 \rangle - \langle |E_y(t)|^2 \rangle) \\ &\quad + M_{DU}\langle E_x(t)E_y^*(t) + E_x^*(t)E_y(t) \rangle \\ &\quad - iM_{DV}\langle E_x(t)E_y^*(t) - E_x^*(t)E_y(t) \rangle \end{aligned} \quad (14)$$

where we have used the definition of the Stokes parameters given in Equation 12.

By comparing Equations 13 and 14 we can obtain the contribution of each Stokes parameter to the power measured

at output D:

$$\begin{aligned}
 M_{DI} &= \frac{\alpha}{2} \{|S_{m1}|^2 + |S_{m2}|^2\} \\
 M_{DQ} &= \frac{\alpha}{2} \{|S_{m1}|^2 - |S_{m2}|^2\} \\
 M_{DU} &= \frac{\alpha}{2} \{S_{m1}S_{m2}^* + S_{m1}^*S_{m2}\} \\
 M_{DV} &= \frac{i\alpha}{2} \{S_{m1}S_{m2}^* - S_{m1}^*S_{m2}\}
 \end{aligned} \quad (15)$$

We can derive the receiver Mueller matrix by applying this technique to all the outputs of the receiver.

VI. POLARIMETER ARCHITECTURE COMPARISON

Two basic types of architectures are used to measure the polarization of an electromagnetic signal: differencing polarimeters, an architecture commonly used in polarization sensitive bolometer-based polarimeters [10]; and pseudo-correlation (or correlation) polarimeters, an architecture commonly used in coherent, LNA or mixer based, polarimeters such as QUIET [11].

Differencing polarimeters measure the difference in power between orthogonal linear modes of the electromagnetic signal; see the definition of Q in Equation 12 for inspiration. Correlation, or pseudo-correlation, architectures measure the polarization state by measuring the correlation between orthogonal modes. Correlation polarimeters are required to preserve the phase of the incident signal. They are hence only feasible if coherent (i.e. phase-preserving) amplifiers or mixers are available.

The choice of which architecture to use for a particular experiment is often dominated by sensitivity considerations. At low frequencies ($< \sim 60$ GHz) the availability of low-noise coherent amplifiers has favored correlation architectures [12]. At higher frequencies, the fundamental quantum limits that amplifier noise is subject to has favored direct detection technologies such as bolometers, and hence differencing polarimeter architectures, for continuum polarimetry experiments. However, continuing improvement in coherent amplifier technology at high frequencies has pushed their performance closer to the quantum limit, e.g. [13]. As coherent amplifier technology improves, sensitivity may no longer be the deciding factor between technologies, and hence architectures.

Differencing and correlation architectures measure the polarization information of the incident signal in very different ways, and hence suffer from different sources of systematic error. A careful analysis of the fundamental strengths and weaknesses of each architecture is needed. SNS is well suited to perform this analysis. In this section we use SNS to derive receiver Mueller matrices for examples of these two polarimeter architectures. This analysis highlights the different sources of systematic error in these architectures.

A. Differencing Polarimeters

An example of a differencing polarimeter architecture is shown in Figure 5 (right). The powers in orthogonal linear modes D_1 and D_2 are detected and differenced to obtain one of the linear polarization parameters. Differencing polarimeters have a much simpler architecture than pseudo-correlation

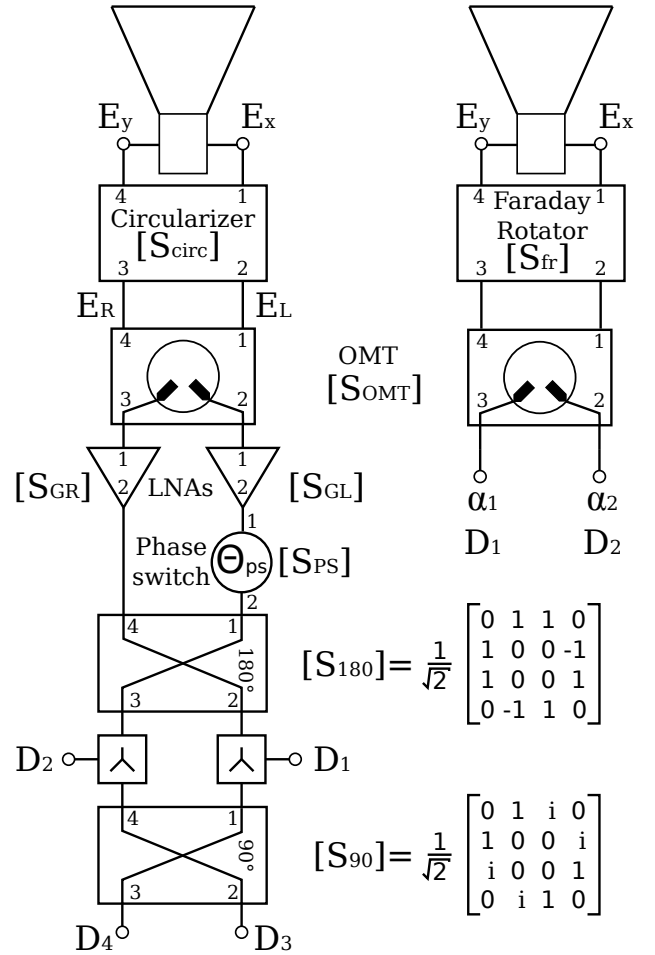


Fig. 5. Examples of two commonly used polarimeter architectures. (left) A pseudo-correlation polarimeter. (right) A differencing polarimeter. Orthogonal waveguide modes E_x and E_y are circularized or rotated, and extracted from waveguide by an orthomode transducer (OMT). In the pseudo-correlation architecture the signals are further processed. The powers in signals D_1 to D_4 are detected and processed to obtain the Stokes parameters, as explained in the text.

polarimeters. However, they measure only a single linear Stokes parameter; a duplicate receiver oriented at 45° to the first is needed to measure the second linear Stokes parameter.

B. Pseudo-correlation Polarimeters

An example of a pseudo-correlation polarimeter architecture is shown in Figure 5 (left). The Stokes parameters of linear polarization in a circular basis are given by:

$$\begin{aligned}
 E_l(t) &= \frac{1}{\sqrt{2}} [E_x(t) - iE_y(t)] \\
 E_r(t) &= \frac{1}{\sqrt{2}} [E_x(t) + iE_y(t)] \\
 Q &= 2 \langle \Re \{ E_l(t) E_r^*(t) \} \rangle \\
 U &= -2 \langle \Im \{ E_l(t) E_r^*(t) \} \rangle
 \end{aligned} \quad (16)$$

Pseudo-correlation polarimeters measure the linear Stokes vector by correlating circular polarization signals E_l and E_r with (D_3 and D_4) and without (D_1 and D_2) a 90° phase shift.

The powers in signals D_1 to D_4 are detected and combined to obtain the linear Stokes parameters.

While the architecture of a pseudo-correlation polarimeter is more complex than that of a differencing polarimeter, it does provide some significant advantages. For instance, both linear polarization parameters can be measured with a single optical assembly, providing twice the information for the same focal plane area occupied.

C. Parameterized Scattering Matrices

Some of the components in the receivers shown in Figure 5 have parameterized scattering matrices. While it is possible to describe every component in a receiver with a suitable parameterized scattering matrix, the resulting analytic expressions for the outputs soon become too complicated to be useful when written down.

In this analysis the components are assumed to be perfectly matched, i.e. the diagonal elements of the parameterized scattering matrices are zero.

1) *Circularizer*: The circular phase shifter translates orthogonal linear polarizations into orthogonal circular polarizations. It introduces a 90° phase shift into one orthogonal linear mode, and is oriented at 45° to the OMT linear axis.

A possible parameterization of the circularizer's scattering matrix as shown in Figure 5 is:

$$\mathbf{S}_{circ} = \frac{L_c}{\sqrt{2}} \begin{bmatrix} 0 & 1 & 1 & 0 \\ 1 & 0 & 0 & -e^{i(\frac{\pi}{2}+\theta_c)} \\ 1 & 0 & 0 & e^{i(\frac{\pi}{2}+\theta_c)} \\ 0 & -e^{i(\frac{\pi}{2}+\theta_c)} & e^{i(\frac{\pi}{2}+\theta_c)} & 0 \end{bmatrix}$$

Here L_c^2 is the insertion loss of the circularizer, and θ_c is the error in the 90° phase shift. The circularizer is assumed to be otherwise perfect.

2) *Faraday Rotator*: The Faraday rotator shown in the differencing polarimeter in Figure 5 is a component sometimes used in PSBs [14]. It modulates the measured polarization signal by introducing a variable rotation to the plane of linear polarization of the incident signal. A similar effect can be achieved with a rotating birefringent half-waveplate, or a wire grid.

The scattering matrix for the rotator considered here is:

$$\mathbf{S}_{fr} = \begin{bmatrix} 0 & \cos(\theta_{ps}) & \sin(\theta_{ps}) & 0 \\ \cos(\theta_{ps}) & 0 & 0 & -\sin(\theta_{ps}) \\ \sin(\theta_{ps}) & 0 & 0 & \cos(\theta_{ps}) \\ 0 & -\sin(\theta_{ps}) & \cos(\theta_{ps}) & 0 \end{bmatrix}$$

Here $2\theta_{ps}$ is the time-dependent linear plane rotation introduced by the Faraday rotator.

3) *OMT*: The OMT extracts orthogonal linear modes from the waveguide. The scattering matrix parameterization considered here is:

$$\mathbf{S}_{OMT} = \begin{bmatrix} 0 & D_x & d_{yx} & 0 \\ D_x & 0 & 0 & d_{xy} \\ d_{yx} & 0 & 0 & D_y \\ 0 & d_{xy} & D_y & 0 \end{bmatrix}$$

Here D_x and D_y measure the insertion loss for each orthogonal mode, while d_{xy} and d_{yx} measure the leakage of one mode

into the other. From conservation of energy considerations in a passive component we have the constraints $|D_x| = |D_y| = |D|$, $|d_{xy}| = |d_{yx}| = |d|$, and $|D|^2 + |d|^2 = L_{omt}^2$, where L_{omt}^2 is the insertion loss of the OMT. The parameters may have arbitrary phase.

4) *LNAs and Phase Switch*: The scattering matrices for the LNAs in the pseudo-correlation polarimeter are given by:

$$\mathbf{S}_{L,R} = \begin{bmatrix} 0 & 0 \\ G_{L,R} & 0 \end{bmatrix}$$

Here G_L and G_R are the complex voltage gains of the left and right circular polarization amplifiers respectively.

The phase switch in the pseudo-correlation polarimeter modulates the phase of one of the signal arms relative to the other. Its scattering matrix is given by:

$$\mathbf{S}_{ps} = \begin{bmatrix} 0 & e^{i\theta_{ps}} \\ e^{i\theta_{ps}} & 0 \end{bmatrix}$$

Here θ_{ps} is the time-dependent phase shift introduced by the phase switch, usually shifting between 0° and 180° .

D. Polarimeter Mueller Matrix Elements

We now build a connected model of each polarimeter in SNS using the matrix parameterizations given in §VI-C. We use Equation 15 to obtain expressions for the powers measured at each receiver output in terms of the incident signal Stokes parameters.

For the ideal pseudo-correlation polarimeter, i.e. where all the components are perfect, the outputs are:

$$\begin{aligned} P_{D_1} &= \frac{1}{2}I - \frac{1}{2}U \\ P_{D_2} &= \frac{1}{2}I + \frac{1}{2}U \\ P_{D_3} &= \frac{1}{2}I - \frac{1}{2}Q \\ P_{D_4} &= \frac{1}{2}I + \frac{1}{2}Q \end{aligned} \quad (17)$$

Here we have assumed that $\theta_{ps} = 0$ and $\alpha = 1$. To measure the Stokes parameters we take $Q_m = P_{D_4} - P_{D_3}$, $U_m = P_{D_2} - P_{D_1}$, and $I_m = \frac{1}{2}(P_{D_1} + P_{D_2} + P_{D_3} + P_{D_4})$.

For the ideal differencing polarimeter the outputs are:

$$\begin{aligned} P_{D_1} &= \frac{1}{2}I + \frac{1}{2}\cos(2\theta_{ps})Q - \frac{1}{2}\sin(2\theta_{ps})U \\ P_{D_2} &= \frac{1}{2}I - \frac{1}{2}\cos(2\theta_{ps})Q + \frac{1}{2}\sin(2\theta_{ps})U \end{aligned} \quad (18)$$

Which linear Stokes parameter we measure depends on the plane rotation introduced by the Faraday rotator, and is given by $L_m = P_{D_1} - P_{D_2} = \cos(2\theta_{ps})Q - \sin(2\theta_{ps})U$. The measured total intensity is $I_m = P_{D_1} + P_{D_2}$.

The Mueller matrix parameters of particular interest in CMB polarization studies are: M_{II} , M_{QQ} , and M_{UU} , the diagonal elements of the Mueller matrix; M_{QI} and M_{UI} , the leakage of the total intensity signal into the (generally) small linear polarization signal; and M_{QU} and M_{UQ} , which measure the rotation of the linear polarization vector by the receiver.

These Mueller matrix parameters for the pseudo-correlation polarimeter are:

$$\begin{aligned}
 M_{II} &= \frac{L_c^2 L_{omt}^2}{2} \left[|G_L|^2 + |G_R|^2 \right] \\
 M_{QQ} &= L_c^2 |G_L G_R| \left[|D|^2 \cos(\theta_3) + |d|^2 \cos(\theta_4) \right] \\
 M_{UU} &= L_c^2 |G_L G_R| \left[\cos(\theta_c) \{ |D|^2 \cos(\theta_3) - |d|^2 \cos(\theta_4) \} \right. \\
 &\quad \left. - \sin(\theta_c) |Dd| \{ \sin(\theta_1) + \sin(\theta_2) \} \right] \\
 M_{QI} &= L_c^2 |G_L G_R| |Dd| \left[\cos(\theta_2) + \cos(\theta_1) \right] \\
 M_{UI} &= L_c^2 |G_L G_R| |Dd| \left[\sin(\theta_1) - \sin(\theta_2) \right] \\
 M_{QU} &= L_c^2 |G_L G_R| \left[\cos(\theta_c) \{ |D|^2 \sin(\theta_3) - |d|^2 \sin(\theta_4) \} \right. \\
 &\quad \left. + \sin(\theta_c) |Dd| \{ \cos(\theta_2) - \cos(\theta_1) \} \right] \\
 M_{UQ} &= -L_c^2 |G_L G_R| \left[|D|^2 \sin(\theta_3) + |d|^2 \sin(\theta_4) \right] \quad (19)
 \end{aligned}$$

$$\begin{aligned}
 \text{where } \theta_1 &= \theta_{D_y} - \theta_{d_{xy}} - (\theta_{G_L} - \theta_{G_R} + \theta_{ps}) \\
 \theta_2 &= \theta_{D_x} - \theta_{d_{yx}} + (\theta_{G_L} - \theta_{G_R} + \theta_{ps}) \\
 \theta_3 &= \theta_{D_x} - \theta_{D_y} + (\theta_{G_L} - \theta_{G_R} + \theta_{ps}) \\
 \theta_4 &= \theta_{d_{xy}} - \theta_{d_{yx}} + (\theta_{G_L} - \theta_{G_R} + \theta_{ps})
 \end{aligned}$$

Here $X = |X|e^{i\theta_X}$. We have implicitly assumed that the responses of all the power detectors are equal and stable.

To keep the comparison between the architectures reasonable, we need to include varying power detection sensitivity in the differencing polarimeter. Let the power detection proportionality constants (see Equation 13) be α_1 and α_2 for outputs 1 and 2 respectively. We also need to decide on the rotation angle of the Faraday rotator to specify which linear Stokes parameter we actually measure. Let $\theta_{ps} = \pm 45^\circ$ (i.e. Stokes U). We then obtain the Mueller matrix parameters:

$$\begin{aligned}
 M_{II} &= \frac{L_{omt}^2}{2} \left[\alpha_1 + \alpha_2 \right] \\
 M_{UU} &= \frac{\sin(2\theta_{ps})}{2} \left[\alpha_1 + \alpha_2 \right] \left[|D|^2 - |d|^2 \right] - \cos(2\theta_{ps}) |Dd| \\
 &\quad \left[\alpha_1 \cos(\theta_{D_x} - \theta_{d_{xy}}) - \alpha_2 \cos(\theta_{D_y} - \theta_{d_{yx}}) \right] \\
 M_{UI} &= \frac{L_{omt}^2}{2} \left[\alpha_1 - \alpha_2 \right] \\
 M_{UQ} &= \frac{\cos(2\theta_{ps})}{2} \left[\alpha_2 - \alpha_1 \right] \left[|D|^2 - |d|^2 \right] - \sin(2\theta_{ps}) |Dd| \\
 &\quad \left[\alpha_1 \cos(\theta_{D_x} - \theta_{d_{xy}}) - \alpha_2 \cos(\theta_{D_y} - \theta_{d_{yx}}) \right] \quad (20)
 \end{aligned}$$

1) *Discussion:* One of the greatest sources of systematic error in polarimeters is leakage of the total intensity signal into the measured linear polarization amplitude, $P = \sqrt{Q^2 + U^2}$. The fractional contribution to P from total intensity leakage, $\Delta P_I = M_{PI}/M_{II}$, is given by:

$$\Delta P_I = \frac{\sqrt{M_{QI}^2 + M_{UI}^2}}{M_{II}}$$

Assume that we have two differencing polarimeters oriented such that they measure Q and U respectively, identical except for their values of α . The “ Q ” polarimeter has values

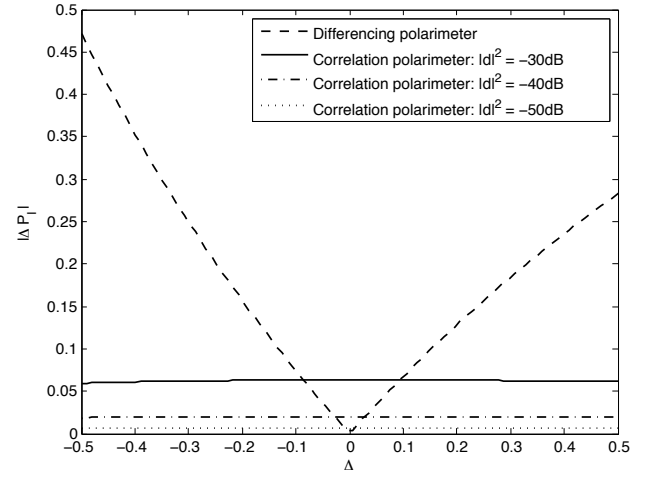


Fig. 6. Comparison of the effect of imbalance on the fractional total intensity to polarization leakage for pseudo-correlation and differencing polarimeter architectures. For the pseudo-correlation architecture, $\Delta = \Delta|G|^2$. For the differencing architecture $\Delta = \Delta\alpha$. $|d|^2$ is the OMT cross polarization.

α_1, α_2 , while the “ U ” polarimeter has α_3, α_4 . For the pseudo-correlation and differencing polarimeters we then have:

$$\begin{aligned}
 \Delta P_I^c &= \frac{2\sqrt{2}|G_L G_R|}{|G_L|^2 + |G_R|^2} |d| \sqrt{(1 - |d|^2)(1 + \cos(\theta_1 + \theta_2))} \\
 \Delta P_I^d &= 2 \frac{\sqrt{(\alpha_1 - \alpha_2)^2 + (\alpha_3 - \alpha_4)^2}}{\alpha_1 + \alpha_2 + \alpha_3 + \alpha_4}
 \end{aligned}$$

As a simplification, assume that $\Delta\alpha = (\alpha_1 - \alpha_2)/\alpha_2 = (\alpha_3 - \alpha_4)/\alpha_4$, and let $\Delta|G|^2 = \frac{|G_L|^2 - |G_R|^2}{|G_R|^2}$. Take the worst-case phase scenario, where $\cos(\theta_1 + \theta_2) = 1$. We now have:

$$\Delta P_I^c = 4|d| \sqrt{1 - |d|^2} \frac{\sqrt{1 + \Delta|G|^2}}{2 + \Delta|G|^2} \quad (21)$$

$$\Delta P_I^d = \frac{\sqrt{2}\Delta\alpha}{2 + \Delta\alpha} \quad (22)$$

Equations 21 and 22 are plotted in Figure 6. Several attributes are noteworthy: ΔP_I is independent of the OMT cross polarization $|d|^2$ for the differencing polarimeter, but is heavily dependent on the power sensitivity imbalance $\Delta\alpha$; ΔP_I is almost independent of gain imbalance $\Delta|G|^2$ for the pseudo-correlation polarimeter, but is dependent on the OMT cross polarization.

Figure 6 clearly illustrates the difference between the polarimeter architectures in terms of total intensity to polarization leakage. Correlation polarimeters are very insensitive to what is generally the most unstable parameter in a coherent receiver: fluctuating LNA gain. They are moderately sensitive to OMT cross polarization $|d|^2$. The comparatively high sensitivity of differencing polarimeters to power detection imbalance can be reduced if $\Delta\alpha$ is stable and well-known; the data can then be corrected and the leakage of I into P reduced. Phase switching can also be used to reduce this leakage.

E. Pseudo-Correlation Polarimeter Noise Temperature

A very powerful benefit of using scattering matrices to model receivers is the ability to perform noise analysis. We

specify parameterized noise wave vectors for the pre-LNA components and ignore any noise produced by the components “down stream” of the LNAs, as their contribution will be negligible if the LNA gain is high.

If the noise wave vector of the pseudo-correlation polarimeter is given by \mathbf{c} , then the noise power measured at the output D_i in a 1 Hz bandwidth is given by $P_i = \alpha \langle c_j c_j^* \rangle$, where c_j is the noise wave vector element corresponding to output D_i .

Suppose that component k of M total components has N ports, and is specified by the scattering matrix \mathbf{S}^k and the noise wave vector \mathbf{c}^k . c_j is given by:

$$c_j = \sum_{k=1}^M c_j^k, \text{ where } c_j^k = \sum_{i=1}^N b_i^k c_i^k$$

Noise waves from different devices are not correlated: $\langle c_i^k (c_j^m)^* \rangle = 0$ for $k \neq m$. So, P_i is given by:

$$P_i = \alpha \sum_{k=1}^M P_i^k$$

where $P_i^k = \sum \sum (\mathbf{C}^k \cdot (\mathbf{b}^k \otimes (\mathbf{b}^k)^\dagger))$

Here \mathbf{C}^k is the noise correlation matrix for component k , \cdot is the matrix dot product, \mathbf{b}^k is the vector $[b_1^k \dots b_N^k]^T$, \otimes is the outer product, and \dagger is the hermitian conjugate. The $\sum \sum$ indicates a sum over all the matrix elements.

The noise correlation matrices for the passive pre-LNA components are obtained using Equation 2. To get the noise correlation matrices for the LNAs we make two simplifications to the HEMT noise correlation matrix model in [5]: first, the off-diagonal terms of an LNA noise correlation matrix ($\langle c_1 c_2^* \rangle$ and $\langle c_1^* c_2 \rangle$) are much smaller than the diagonal terms so we take them to be zero. Second: $\langle |c_2|^2 \rangle \simeq |S_{21}|^2 \langle |c_1|^2 \rangle \simeq k |S_{21}|^2 T_N$, where T_N is the amplifier noise temperature and k is Boltzmann’s constant.

Receiver noise temperature is referenced to the input. We consider the receiver temperature T_i at output D_i to be the temperature of a thermal source seen equally at each input which produces the same total output noise power in a noiseless receiver:

$$P_i = \alpha \left(\sum_{j=1}^{N_{in}} |S_{ij}|^2 \right) T_i$$

$$\therefore T_i = \frac{\sum_{k=1}^M P_i^k}{\sum_{j=1}^{N_{in}} |S_{ij}|^2} \quad (23)$$

Here N_{in} is the number of inputs to the receiver, and \mathbf{S} is the receiver scattering matrix.

Applying this technique to the pseudo-correlation polarimeter we derive the receiver temperatures for the outputs D_1 to

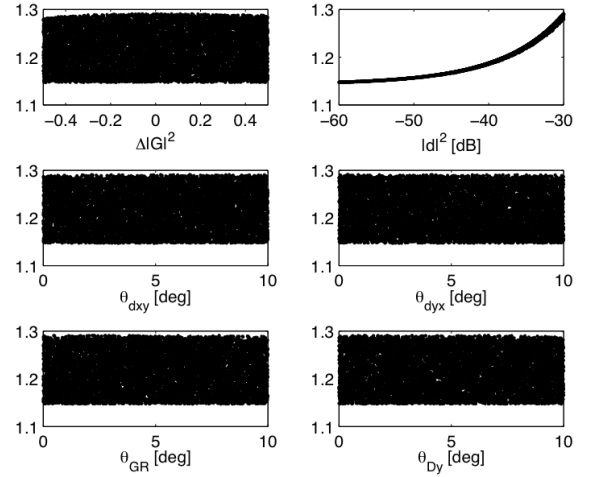


Fig. 7. Plots of T_1/T_N against various parameters. We see that the receiver is most sensitive to the cross polarization, $|d|^2$, and is negligibly sensitive to the other parameters. We assume $T_N = T_P = 15$ K. See text for details.

D_4 :

$$T_1 = T_c + \frac{T_p}{L_c^2} \left[\frac{G}{E-F} - 1 \right] + \frac{T_N}{L_c^2} \left[\frac{G}{E-F} \right]$$

$$T_2 = T_c + \frac{T_p}{L_c^2} \left[\frac{G}{E+F} - 1 \right] + \frac{T_N}{L_c^2} \left[\frac{G}{E+F} \right]$$

$$T_3 = T_c + \frac{T_p}{L_c^2} \left[\frac{G}{E-H} - 1 \right] + \frac{T_N}{L_c^2} \left[\frac{G}{E-H} \right]$$

$$T_4 = T_c + \frac{T_p}{L_c^2} \left[\frac{G}{E+H} - 1 \right] + \frac{T_N}{L_c^2} \left[\frac{G}{E+H} \right] \quad (24)$$

where $T_c = T_p \left[\frac{1}{L_c^2} - 1 \right]$

$$G = |G_L|^2 + |G_R|^2$$

$$E = (|G_L|^2 + |G_R|^2) L_{omt}^2$$

$$F = 2|G_L G_R| |Dd| \left[\cos(\theta_1) + \cos(\theta_2) \right]$$

$$H = 2|G_L G_R| |Dd| \left[\sin(\theta_1) - \sin(\theta_2) \right]$$

Here we have assumed that the amplifiers have noise temperature T_N , and that the circularizer and OMT are at a physical temperature of T_p . θ_1 and θ_2 are given in Equation 19.

1) *Discussion*: Which parameters in the multiparameter expression for T_1 in Equation 24 have the greatest impact on the receiver temperature? The most obvious are L_c^2 and L_{omt}^2 , the insertion losses of the circularizer and OMT respectively. Setting those aside, how do the other parameters affect the receiver temperature?

The minimum value that T_1 can have is T_N . Our sensitivity impact metric is then $T_1/T_N \geq 1$. We fix $L_c^2 = -0.1$ dB and $L_{omt}^2 = -0.2$ dB, and set $|G_R| = 1$, $|G_L| = \sqrt{1 + \Delta|G|^2}$, $\theta_{G_L} = 0$, and $\theta_{D_x} = 0$ (only relative phases matter here). This leaves us with six parameters: $|d|^2$, $\Delta|G|^2$, θ_{G_R} , θ_{D_y} , $\theta_{d_{xy}}$, and $\theta_{d_{yx}}$.

We generate random sets of physically realistic values for these parameters, and evaluate the metric T_1/T_N for each set. We plot T_1/T_N against each parameter under consideration

in Figure 7. It is immediately clear that the most important parameter in this set is $|d|^2$. Discarding the least important parameters we now have:

$$\begin{aligned} T_1 &\simeq \frac{1}{L_c^2 L_{omt}^2 - 2|d|\sqrt{L_{omt}^2 - |d|^2}} - T_p \\ &\simeq \frac{T_p(1 - L_c^2 L_{omt}^2) + T_N}{L_c^2 L_{omt}^2} \text{ since } |d|^2 \ll L_{omt}^2 \end{aligned} \quad (25)$$

This simplified expression for T_1 is exactly what we would derive using a conventional noise temperature analysis, indicating that the software has calculated the noise temperature correctly.

VII. CONCLUSIONS

We have presented SNS, a MATLAB-based software library written to aid in the design and analysis of receiver architectures. It uses electrical scattering matrices and noise wave vectors to describe receiver architectures of arbitrary topology and complexity.

We use SNS to compare two polarimeter architectures commonly used to perform measurements of the polarized CMB: differencing polarimeters, an architecture commonly used in PSB-based polarimeters; and pseudo-correlation polarimeters, an architecture commonly used in coherent polarimeters. This analysis highlights the differing sources of systematic error in these architectures: I to P leakage in pseudo-correlation polarimeters is almost immune to gain imbalance, but sensitive to OMT cross polarization; while I to P leakage in differencing polarimeters is immune to OMT cross polarization, but very sensitive to power detection imbalance.

We show how SNS can be used to calculate analytical expressions for the receiver noise temperature of arbitrary receivers. Analytic expressions for the receiver temperature of a pseudo-correlation polarimeter are derived, and are found to be consistent with those obtained from conventional receiver temperature calculations.

ACKNOWLEDGMENTS

Thanks go to Dr Paul Grimes for helpful discussions and pointers to papers, to Prof. Mike Jones for helpful suggestions, support and motivation, and to Nikolai Yu. Zolotykh for developing the `pointer` library for MATLAB. OGK

acknowledges the support of a Dorothy Hodgkin Award in funding his studies while a student at Oxford, and the support of a W.M. Keck Institute for Space Studies Postdoctoral Fellowship at Caltech.

REFERENCES

- [1] M. Zaldarriaga and U. Seljak, "All-sky analysis of polarization in the microwave background", *Physical Review D (Particles)*, vol. 55, p. 1830, Jan 1997.
- [2] L. Page, G. Hinshaw, E. Komatsu, M. R.olta, D. N. Spergel, C. L. Bennett, C. Barnes, R. Bean, O. Doré, J. Dunkley, M. Halpern, R. S. Hill, N. Jarosik, A. Kogut, M. Limon, S. S. Meyer, N. Odegard, H. V. Peiris, G. S. Tucker, L. Verde, J. L. Weiland, E. Wollack, and E. L. Wright, "Three-year Wilkinson Microwave Anisotropy Probe (WMAP) observations: Polarization analysis", *The Astrophysical Journal Supplement Series*, vol. 170, p. 335, May 2007.
- [3] W. Hu, M. M. Hedman, and M. Zaldarriaga, "Benchmark parameters for CMB polarization experiments", *Physical Review D*, vol. 67, p. 43004, Feb 2003.
- [4] L. O'Dea, A. Challinor, and B. R. Johnson, "Systematic errors in cosmic microwave background polarization measurements", *Monthly Notices of the Royal Astronomical Society*, vol. 376, p. 1767, Apr 2007.
- [5] S. Wedge and D. Rutledge, "Wave techniques for noise modeling and measurement", *Microwave Theory and Techniques, IEEE Transactions on*, vol. 40, no. 11, pp. 2004–2012, 1992.
- [6] —, "Noise waves and passive linear multiports", *Microwave and Guided Wave Letters, IEEE Transactions On*, vol. 1, no. 5, pp. 117–119, 1991.
- [7] G. Filipsson, "A new general computer algorithm for S-matrix calculation of interconnected multiports", *11th European Microwave Conference*, pp. 700–704, 1981.
- [8] J. Ward, F. Rice, G. Chattopadhyay, and J. Zmuidzinis, "Supermix: a flexible software library for high-frequency circuit simulation, including SIS mixers and superconducting elements", *Tenth International Symposium on Space Terahertz Technology: Symposium Proceedings*, pp. 268–281, 1999.
- [9] J. P. Hamaker, J. D. Bregman, and R. J. Sault, "Understanding radio polarimetry. I. Mathematical foundations", *Astronomy and Astrophysics Supplement*, vol. 117, p. 137, May 1996.
- [10] W. C. Jones, T. E. Montroy, B. P. Crill, C. R. Contaldi, T. S. Kisner, A. E. Lange, C. J. Mactavish, C. B. Netterfield, and J. E. Ruhl, "Instrumental and analytic methods for bolometric polarimetry", *Astronomy and Astrophysics*, vol. 470, p. 771, Aug 2007.
- [11] L. Newburgh and QUIET Collaboration, "QUIET: The Q/U Imaging Experiment", *American Astronomical Society*, vol. 215, p. 549, Jan 2010.
- [12] J. Zmuidzinis, "Progress in coherent detection methods", *The Physics and Chemistry of the Interstellar Medium*, p. 423, Aug 1999.
- [13] T. C. Gaier, "Coherent radiometers for cosmic microwave background polarization detection", *Polarimetry in Astronomy. Edited by Silvano Fineschi. Proceedings of the SPIE*, vol. 4843, p. 296, Jan 2003.
- [14] B. G. Keating, "Faraday rotation modulators for mm-wavelength polarimetry", *CMBPol White Papers*, pp. 1–12, Jul 2008.

Water Vapor Radiometer for ALMA: optical design and verification

Sergey Cherednichenko¹, Anders Emrich² and Tully Peacocke³.

¹Dept. of Microtechnology and Nanoscience
Chalmers University of Technology, Göteborg, Sweden
Email: serguei@chalmers.se

²Omnisys Instruments AB, V.Frölunda, Sweden

³Experimental Physics, National University of Ireland Maynooth, Kildare, Ireland

Abstract

Atacama Large Millimeter wave Array (ALMA) is being built at a high altitude Atacama Desert in Chile. It will consist of 50 12m telescopes with heterodyne instruments to cover a large frequency range from about 30GHz to nearly 1THz. In order to facilitate the interferometer mode of operation all receivers have to be phase synchronized. It will be accomplished by phase locking of all local oscillators from a single reference source. However, a noticeable part of the phase error is caused as the signal propagates through the Earth atmosphere. Since this effect originates from the fluctuations of water vapors, it can be accounted for by carefully measuring the spectral width of one of water vapor resonance absorption lines. This will be done with a submillimeter heterodyne radiometer, Water Vapor Radiometer (WVR) [1]. WVR will measure the sky brightness temperature in the beam path of every telescope across the 183GHz water line with a spectral resolution of about 1GHz.

Accuracy of the calculated optical delay is determined by the combination of the radiometric accuracy of the WVR and of the errors originated in the WVR illumination of the telescope. We will describe major challenges in the design of the WVR to comply with the stringent requirements set to the WVR. Several approaches to simulate the quasioptical waveguide which brings the signal from the telescope's subreflector to the mixer horn, were used: fundamental mode Gaussian beam propagation, combined ray tracing with diffraction effects (using package ZEMAX), and a full vector electromagnetic simulations (using GRASP). The computational time increases rapidly from the first method to the last one. We have found that ZEMAX results are quite close to the one from GRASP, however obtained with nearly instant computation, which allows multiple iterations during system optimization. The beam pattern of the WVR and of WVR with the optical Relay (used to bring the signal from the telescope's main axis to the WVR input window) was measured by a scalar beam scan at four planes in the far field. The experimental results correspond to the simulated ones with a high accuracy. The WVR illuminates the telescope subreflector with a spillover of less than 1.5% while maintaining high aperture efficiency. We developed an approach to calculate the beam center position at the subreflector (with is at 6m from the WVR) from our test data (at maximum 2m from the WVR) in order confirm the maximum beam deviation does not exceed 20mm, i.e. 1/15 of the beam width.

REFERENCES (OPTIONAL)

- [1] A. Emrich, S. Andersson, M. Wannerbratt, P. Sobis, S. Cherednichenko, D. Runesson, T. Ekebrand, M. Krus, C. Tegnader, U. Krus, "Water Vapor Radiometer for ALMA", in Proc. of 20th International Symposium on Space Terahertz Technology, April 2009, Charlottesville, USA, p. W3B.

Calibration of the Herschel HIFI Instrument using Gas Cell Measurements

Ronan D. Higgins^{*§}, David Teyssier[†], John C. Pearson[‡], Christophe Risacher^{**} and Neil A. Trappe^{*}

^{*} Dept. of Experimental Physics, National University of Ireland, Maynooth,
Co. Kildare, Ireland

[†]Herschel Science Centre,
European Space Astronomy Centre (ESAC), 28691 Villanueva de la C nada, Madrid, Spain.

[‡]Jet Propulsion Laboratory,
California Institute of Technology, Pasadena, CA 91109, USA

^{**} SRON (Netherlands Institute for Space Research),
Landleven 12, 9747 AD, Groningen, the Netherlands

[§]Email: daniel.r.higgins@nuim.ie

Abstract—The Heterodyne Instrument for the Far-Infrared (HIFI) was launched aboard the Herschel space telescope on the 14th of May 2009. HIFI’s frequency range is spread over 7 mixer bands. Bands 1-5 (480-1270 GHz) use Superconducting-Insulator-Superconducting (SIS) mixer technology while bands 6 & 7 (1410-1910 GHz) use Hot Electron Bolometer (HEB) mixer technology. HIFI is a double sideband instrument and hence contains both the upper and lower sideband of the down converted sky signal. The gain in the upper and lower sideband is not always equal. This effect introduces a calibration uncertainty that must be understood in order to achieve the HIFI calibration goal of 3%.

To determine the frequency dependent sideband ratio for each mixer band, a gas cell test set up was developed [1]. During the instrument level testing a number of simple (¹²CO, ¹³CO and OCS) and complex (CH₃CN and CH₃OH) molecules were observed using the HIFI instrument. Using a radiative transfer model with the measured pressure and optical path length of the gas cell and molecular line parameters taken from the JPL and HITRAN catalogs, model spectra can be generated. By comparing the generated spectra with the observed spectra the sideband gain can be determined.

In this paper we present the analysis of ¹²CO gas cell data in bands 1 & 2 and the application of the

determined side gain ratios to flight data.

I. INTRODUCTION

HIFI is a one of three instruments on board the Herschel Space Observatory. Using heterodyne techniques it provides very high spectral resolution ($R = \nu/\Delta\nu \geq 10^6$ – 10^7) from 480–1270 GHz and 1410–1910 GHz for two polarizations. This high resolution promises to open a new window on the chemistry and kinematics of the cold universe [2].

The heterodyne technique achieves high resolution spectra by beating the sky signal with an instrument produced monochromatic signal of a similar frequency close to the sky frequency of interest. This local signal is typically known as the local oscillator (LO) signal. The two signals are added together at the mixer which reacts to the beat frequency of the two signals. This down converted signal is known as the intermediate frequency (IF). Depending on the mixer characteristics a 2.4 to 4GHz band of the sky signal is down converted either side of the LO frequency, these bands are known as the sidebands.

HIFI’s frequency coverage is spread over 7 bands. Each band has two mixer blocks which detect orthogonal polarizations. Each mixer is coupled to two LO chains covering approximately half of the

mixer band frequency coverage. HIFI uses two types of mixing elements. Bands 1-5 (480–1270 GHz) use Superconductor-Insulator-Superconductor (SIS) technology and bands 6 & 7 use Hot-Electron-Bolometer technology to mix sky and LO signals. Both technology use superconducting techniques to downconvert the signal albeit via different mechanisms, for a review of mixer technology see [3].

HIFI aims to have unprecedented calibration accuracy for a heterodyne instrument. A major source of calibration error in ground based telescope is atmospheric perturbations. By going to space HIFI opens up new parts of the sub-mm spectrum but also the vacuum of space removes a large calibration error. The main calibration errors in HIFI will be from the telescope optics and the instrument itself. The main sources of calibration error for HIFI come from internal standing waves, hot and cold load coupling and temperature and mixer sideband gain ratio. Standing waves manifest themselves in numerous ways in a heterodyne systems and can be seen on the spectra baseline but also more subtly in the mixer sensitivity due to internal reflection in the LO mixer cavity, see [4] for a review.

Side band gain ratio is a bi-product of the HIFI mixer set up. The HIFI mixers are double side band (DSB) mixers and hence have an upper and lower side band in the down converted spectra. The separation of side bands in the mixer setup is a common component in ground based telescope however at the time of HIFI development the technique was still in a development phase. HIFI separates the sideband in the data processing pipeline. Using the principle that by changing the LO frequency spectral lines in the upper and lower side band move in opposite directions it is possible to deconvolve DSB spectra into its SSB (single side band) components, see [5]. For wide band spectrometers such as HIFI the change in gain across the upper and lower side bands can introduce a significant calibration error. The side band gain effect can be removed during the deconvolution process however knowledge of the side band gain ratio is required.

This paper discusses the gas cell tests undertaken during instrument level testing (ILT) phase to determine the side band gain variation across the HIFI frequency coverage. The effect of side band ratio on calibration accuracy will be discussed in section 2. The gas cell set-up will be discussed in section 3. Section 4 details the gas cell line fitting and the extraction of the side band ratio from this data. Finally section 5 details the application of side band

ratio to flight data taken during the performance verification phase of HIFI.

II. CALIBRATION ERRORS

As HIFI aims for unprecedented calibration accuracy in a heterodyne system all efforts were made in the instrument level tests to quantify and understand the sources of calibration error in the system. 2 of the main sources of calibration error within HIFI are standing waves and the mixer sideband ratio.

A. Standing waves

Standing waves are a common feature in radio and sub-mm telescopes as the telescope and instrument optics are comparable with the radiation wavelength. Standing waves occur when a signal is reflected between 2 surfaces. The reflected signal interferes with the incoming signal. Depending on the phase of the signal when reflection occurs, the interference can be constructive or destructive. When this interference is viewed from a broadband perspective it appears as sinusoidal intensity variation with frequency. From the period of this modulation one can determine the distance between 2 reflecting surfaces as follows:

$$d = c/2P \quad (1)$$

where P is the standing wave period in frequency, c is the speed of light and d is the distance between the 2 surfaces.

The main source of standing waves in ground based telescopes is from the secondary mirror. This was considered in the design of the Herschel secondary mirror and the inclusion of scattering cone has almost completely removed this effect. However even though great efforts were made to reduce standing waves they are still seen in the HIFI internal optics. Standing waves are seen in both the sky and local oscillator signal paths.

Standing waves in the sky path, be it from the calibration loads or the sky, appear as a modulation on the spectrometer output. The problem is complicated further by the double side band nature of HIFI. The standing wave in figure 1 is the result of the interference between the standing wave in the the upper and lower sideband signal.

Standing waves in the LO path are not as apparent as those in the sky signal path but can have a detrimental effect on certain observing modes such as frequency switch modes [6]. Standing waves in the LO path modulate the LO power and hence the sensitivity of the mixer. Figure 2 shows the effect of a standing wave on the mixer pump level. A fraction

of the LO power is reflected between the LO unit and mixer causing a modulation in the LO power and hence mixer sensitivity. The effect of standing waves in the LO signal path is discussed in detail in [4].

The standing wave seen in the HEB bands is of another form. Like the sky path standing wave it is seen as a broadband modulation on the spectrum baseline however the origin of the reflection cavity is not in the instrument optics but in the IF electrical amplification chain. Due to an impedance mismatch between the HEB mixer and the first amplifier not all of the signal is transmitted and some is reflected back and forth between the 2 component along 182mm of coaxial cable. In bands 1-5 an electrical isolator is present absorbing any reflected signal. However due to a late design change in IF bandwidth for the HEB band no suitable isolator was available and hence reflected signal become a problem. In an ideal system the standing waves would cancel in the calibration routine. However the HEB impedance is a very sensitive to small fluctuations in LO and sky power which change the standing wave shape and leads to a residual between the On and Off phases. The impedance of HEB and the proposed solution to remove this standing wave is discussed in reference [7].

Correcting baselines for the standing wave effects seen in figure 1 is a typical chore of a radio astronomer and a number of tools are available for this task. However complete removal of all standing wave effects is not entirely possible. Standing waves from the temperature loads can limit the absolute temperature calibration possible and the standing wave amplitude must be taken as a calibration error.

B. Side band ratio

As stated previously, HIFI is a double side band instrument and contains signal from both the upper and lower sideband. The basic HIFI calibration contains 4 different observation phases, (On source, Off source, Hot load, cold load) which when combined together in equation 2 remove the systematic effects (assuming the instrument is stable over the course of the data acquisition) and return a temperature calibrated DSB spectra.

$$\frac{On - Off}{Hot - Cold} \quad (2)$$

In an ideal mixer with an equal gain in both sidebands, the spectral line intensity for an unconfused line (i.e. not blended with a line from the other side band) can be calculated simply by multiplying the

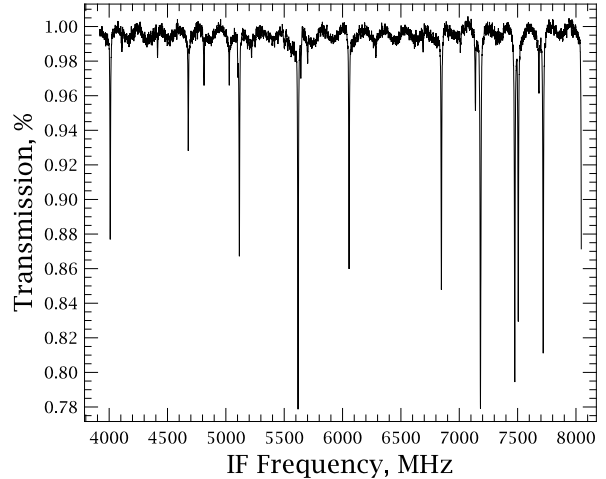


Figure 1. Plot of Methanol data taken at 645.999 GHz showing a 170 MHz period standing wave corresponding to internal reflection in a cavity of length ~ 88 cm

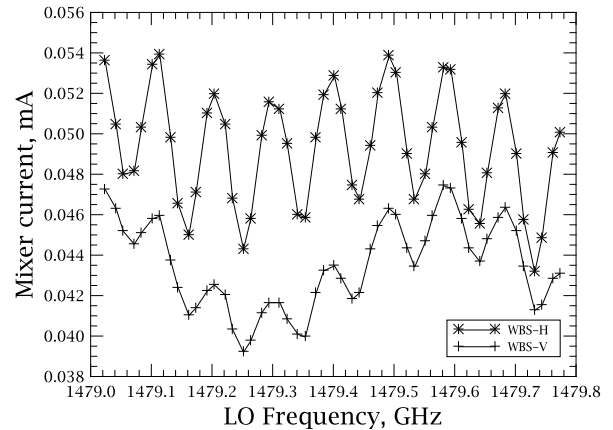


Figure 2. Plot of mixer currents for both H and V mixers. For this test the LO power is kept constant and the LO frequency is changed. In the mixer current vs. LO Frequency plot 2 standing waves are apparent, a 92MHz modulation corresponding to a distance between the LO source unit and the mixer focus and a 680 MHz period standing wave corresponding to an reflection between the diplexer rooftop mirror and the mixer focus.

line intensity by 2. However the gain response across a mixer band is not necessarily uniform.

HIFI observes 2 sidebands of 4.0 (bands 1-5) or 2.4 GHz (bands 6 & 7) either side of the LO Frequency. At the upper end of the IF band a 16 GHz frequency difference is seen between the LSB and USB frequency channel summing together to make a single IF channel. A slope in the gain across the side bands can introduce a calibration error when converting DSB intensity to SSB intensities, see figure 3. As HIFI has a large IF band width this effect becomes significant. The effect must be understood

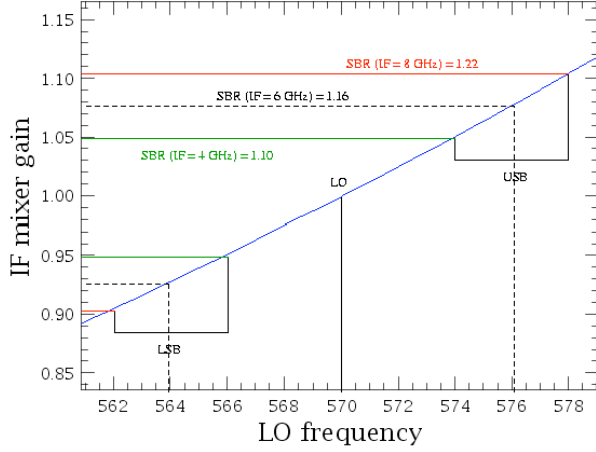


Figure 3. Example of linear mixer gain variation and the resulting side band ratios. The term SBR (side band ratio) is defined as USB gain divided by the LSB gain

in order to determine the calibration accuracy and eventually correct in the data processing pipeline.

The topic of intensity calibration is covered in detail in reference [8].

III. GAS CELL TEST SETUP

A. Principles

Gas cell tests were used by the SWAS satellite [9] and the Odin satellite [10] in their ground testing. SWAS in particular used a gas cell set up to demonstrate a side band gain ratio of unity. The IF bandwidth of SWAS of 1.4 GHz is considerably less than HIFI and hence would be less susceptible to side band gain imbalances.

The basic concept of a gas cell calibration of a heterodyne receiver is to observe well understood molecules (known line frequencies, intensities, pressure broadening parameters) and then using a radiative transfer model generate a model line profile. By comparing the model line profile with the observed line profile it is possible to extract the instrumental effects.

A gas cell observation follows that of a standard observation detailed in equation 2. A typical observation observes the hot and cold calibration loads through both the filled and empty gas cell. By forming a ratio of filled and empty observations one can extract the side band ratio. For a single spectral line in the lower side band, the filled and empty phases of the gas cell observation would be as follows:

$$S_{filled} = G_u(J_h - J_c) + G_l(J_h - J_c)e^{-\tau} \quad (3)$$

$$S_{empty} = G_u(J_h - J_c) + G_l(J_h - J_c) \quad (4)$$

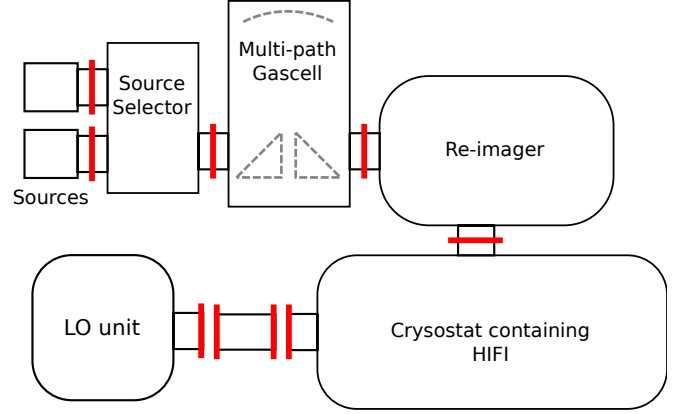


Figure 4. Gas test setup

where G_u and G_l are the frequency dependent upper and lower side band gain respectively, J_h and J_c are the effective hot and cold load temperature of a black body of temperature T at a given frequency. The $e^{-\tau}$ term represents the line opacity at the line center, see section IV. By rearranging equations 3 and 4 the side band ratio is given by:

$$R_G = \frac{G_l}{G_u} = \frac{1 - S_{filled}/S_{empty}}{S_{filled}/S_{empty} - e^{-\tau}} \quad (5)$$

For gases where the line intensity is saturated, $\tau \gg 1$, the above equation can be reduced to $S_{empty}/S_{filled} - 1$. For a gain balanced mixer S_{empty}/S_{filled} for a saturated line = 0.5 or an absorption line half the continuum level in a normalized spectra, see figure 6.

In the data processing pipeline the side band gains are applied to the DSB intensity to convert to single side band intensity. In an ideal gain balanced mixer this is simply a case of multiplying the intensity by two. Where the mixer sideband is not equal the intensity must be dividing by the side band gain factor which is defined for the upper side band as:

$$G_{ssb} = \frac{1}{1 + R_G} \quad (6)$$

and the lower side band gain factor is defined a $1 - G_{ssb}$, see reference [8].

B. Design

The design of the HIFI gas cell set up is detailed in reference [1]. The gas cell set up chosen was based on the recommendations from the SWAS gas cell setup [11]. The gas cell has a multi path optical set up which maximizes the optical path length while keeping the volume of the gas cell to minimum for ease of installation. The gas cell has a path length of

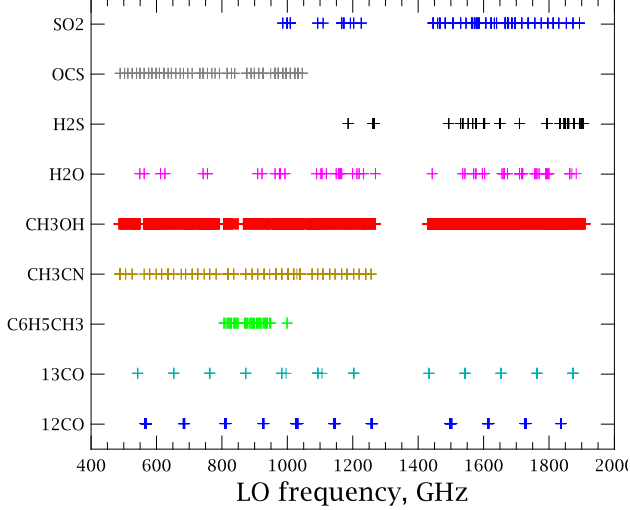


Figure 5. Summary plot showing LO frequency coverage of each gas used in the gas cell test campaign

128cm which is contained in a cylindrical vessel of 15 cm diameter and 50cm height.

As HIFI has a large frequency coverage one single molecule will not provide saturated lines at all frequencies. For the HIFI gas cell a range of molecules were observed and hence the effect of cross contamination was considered in the material choice for the gas cell. A glass gas cell design was chosen over a metal one as certain molecules would stick to the metal walls particularly water. The gas cell was designed to operate at low pressures around 1 millibar. The final gas cell test set up showing the calibration loads, re-imager, LO and HIFI cryostat is shown in figure 4.

C. Calibration gases

The choice of gases for the test campaign was a trade off between a number of criteria. For side band measurement a saturated line was necessary. This limited the gas choice to molecules with line intensities of 10^{-2} to 10^{-3} in units of $\text{nm}^{-2}.\text{MHz}$. Lab safety was also considered and possible corrosive effects on the gas cell itself. Figure 5 summarizes the frequency coverage of the final gas choices.

IV. GAS CELL LINE FITTING

A. Line profile theory

The line profile seen in figure 6 is best described using a voigt profile. The voigt profile is a convolution of a lorentzian and gaussian profile. The lorentzian profile describes the line broadening effect due to the gas pressure and its half width half

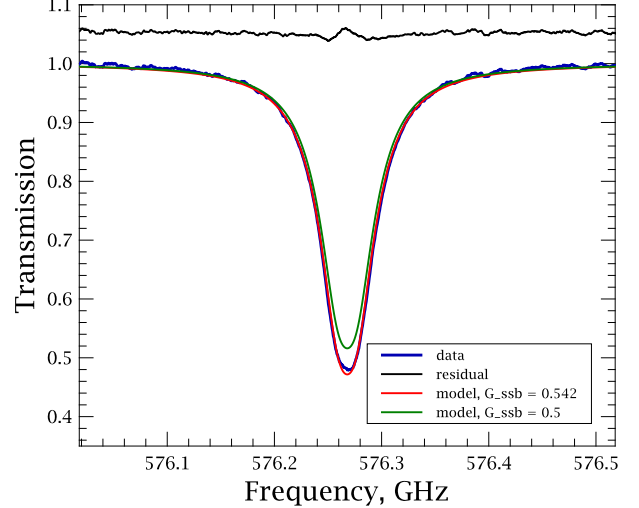


Figure 6. ^{12}CO gas cell data at 570.4 GHz (highlighted in blue on the left). Green line shows spectral line fit for a balanced mixer ($G_{ssb} = 0.5$), red line shows the fitted profile where $G_{ssb} = 0.542$

maximum is defined by the:

$$\delta\nu_L = \gamma_{self} P \quad (7)$$

where γ_{self} is the pressure broadening parameter MHz/mbar and P , the gas cell pressure, is in mbar. γ_{self} is taken from the HITRAN database [12]. The gaussian profile describes the broadening effect due to the thermal motion of the gas. The width of a gaussian profile is derived from the Boltzmann equation and is a function of the gas temperature and the line frequency. The half width half maximum is defined as:

$$\delta\nu_D = \frac{\nu_0}{c} \sqrt{\frac{2(\ln 2)kT}{m}} \quad (8)$$

where ν_0 is the line frequency, c is the speed of light, k is Boltzmann constant, T is the gas temperature and m is the molecular weight. The convolution of these 2 profiles gives the distribution of energy for that molecular transition. The integrated area of the voigt profile for that transition is then equal to the integrated intensity taken from the HITRAN or JPL catalogs for that line. The peak absorption is then defined as:

$$\alpha_{max} = \frac{I_{ba}}{\pi\delta\nu_L + \sqrt{\frac{\pi}{\ln 2}} \frac{P}{kT}} \quad (9)$$

where I_{ba} is the integrated intensity taken from the catalog. Using α_{max} the unit voigt profile peak is scaled. Combining the scaled voigt with the exponential opacity broadening effect (Beer-Lambert law)

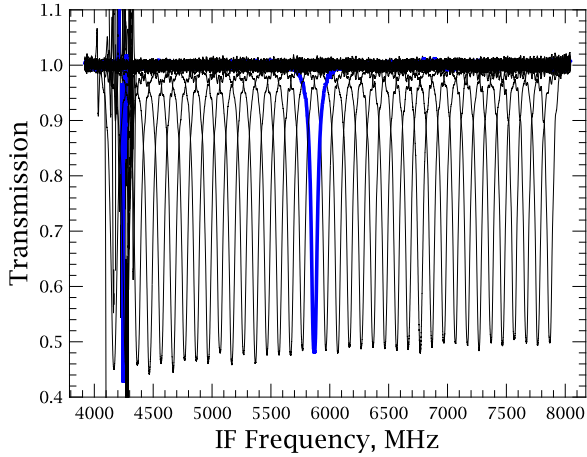


Figure 7. Plot of ^{12}CO (5-4) data taken with the V polarization wide band spectrometer (WBS) backend between 568.4 to 572.1 GHz in steps of 0.1 GHz at an average gas cell pressure of 6.5mbar. Traces of LO spurious signals can be seen between the LO frequencies of 570.7 and 568.4 GHz around the IF frequency of 4.3GHz. The spectra highlighted in blue is shown in more detail in figure 6

due to gas column length, the final line profile profile peak is:

$$e^{\alpha_{max}V(\nu-\nu_0,\delta\nu_D,\delta\nu_L)L} \quad (10)$$

where L is the gas cell column length. The residual between this line profile and the observed line is taken to be the side band gain ratio.

B. Line profile fitting

Figure 6 shows a example of the line fitting routine. The green profile shows the line profile for a balanced mixer while the red profile shows line profile where the side band gain is left as a free parameter which is fitted to match the observed line profile. The resulting side band ratio factor is 0.542, see equation 6.

Figure 7 shows an overview of the ^{12}CO 576.268 GHz spectral line for a range of LO Frequencies between 568.4 and 572.1 GHz. Each of spectra was fitted with a model spectral line where the side band gain was a free parameter. The resulting fitted side band ratio factor versus LO Frequency is shown in figure 8.

Note that the band 1b data presented here is an exceptional example with a large side band gain difference over 4GHz. This extreme example was chosen to demonstrate the gas cell method and is not typical of the side band ratio determined from ^{12}CO line fitting in other bands.

V. CORRECTION OF FLIGHT DATA

The main goal of the gas cell test campaign was to determine the side band ratio across each mixer band and eventually correct flight data for this effect. The main assumption made was that the side band ratio is an inherent part of the mixer set up and should remain the same over the instrument life time. The example presented here is an extreme side band ratio compared with other LO frequencies in HIFI. A 10% change in gain is seen across over 4 GHz of the IF band. This makes it an ideal region to compare the lab data presented here with a comparable spectral scan observed in space.

During the first performance verification phase of HIFI in July 2010 a number of spectral scan observations on strong sources were taken. Figure 9 shows a ^{12}CO line tracked across the IF band in steps of 0.4 GHz between the LO frequencies 568.535 and 571.932 GHz. In this plot it is apparent that the same slope in gain seen in the gas cell data is seen in the flight. Ideally the spectral line intensity should be the same across the IF band, however in figures 7 and 9 the line intensity is seen to decrease across the IF band indicating a side band gain imbalance. More significantly is that the slope in gain across the IF seen in flight data is consistent with that seen in the gas cell data.

Figure 10 shows the peak line intensity of the data show in figure 9 and also the peak line intensities when the side band gain shown in figure 8 is applied. From this plot one can see that before the gain correction is applied the peak intensity scatter is $\sim 10\%$ while after gain correction it is greatly reduced to $\sim 3\%$.

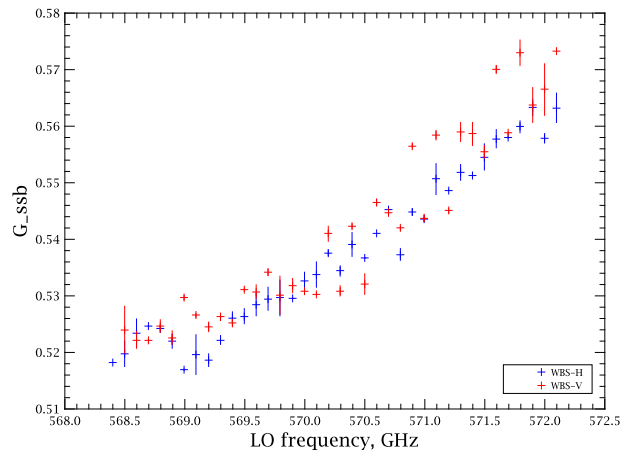


Figure 8. Fitted $G_{s,sb}$ for each line profile shown in figure 7 versus LO Frequency

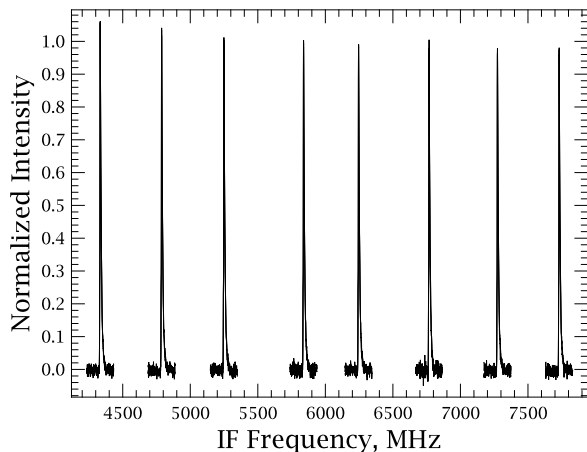


Figure 9. Flight data spectral scan showing the ^{12}CO (5-4) line for a range of LO frequencies from 568.535 to 571.932 GHz

VI. CONCLUSIONS

In this paper, the concept of calibrating a double side band heterodyne spectrometer using a gas cell test set up was described. It was shown how to generate a model spectra using radiative transfer methods taking into account the optical path length, gas pressure and temperature coupled with the JPL and HITRAN line catalogs. We described how by comparing model spectra to observed spectra the side band ratio at that IF frequency could be extracted. Using this extracted side band ratio data we showed that for the LO frequency range from 568 to 572 GHz the amount of scatter in a flight data could be reduced from the $\sim 10\%$ to $\sim 3\%$.

VII. FUTURE WORK

The data covered in this paper is only a small fraction of the total data taken during the gas cell campaign, see figure 5. Future work will involve the expansion of the methods demonstrated here to ^{12}CO and ^{13}CO in other mixer bands. The final goal of this work is to analyze the large CH_3OH and CH_3CN dataset taken and generate a more complete picture of the side band gain ratio, thereby improving the overall calibration accuracy of HIFI and finally helping produce exceptional science data.

VIII. ACKNOWLEDGMENTS

A portion of this research was performed at the Jet Propulsion Laboratory, California Institute of Technology, under contract with the National Aeronautics and Space Administration.

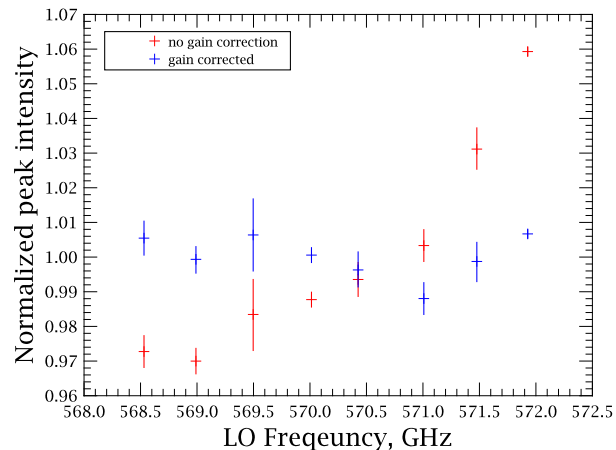


Figure 10. Peak line intensity with and without gain correction. Notice the variation in intensity scatter is reduced from 10% to 3%

REFERENCES

- [1] D. Teyssier, E. Dartois, D. Deboffle, J. Crusaire, Y. Longval, F. Boulanger, and M. Pérault, "A Multi-path Far-Infrared and Sub-millimetre Gas Cell for Spectral Tests of Herschel-HIFI," in *15th International Symposium of Space Terahertz Technology, Northampton, Massachusetts, 2004*, pp. 306–312.
- [2] T. de Graauw, N. Whyborn, F. Helmich, P. Dieleman, P. Roelfsema, E. Caux, T. Phillips, J. Stutzki *et al.*, "The Herschel-Heterodyne Instrument for the Far-Infrared (HIFI):instrument and pre-launch testing," in *Space Telescopes and Instrumentation 2008: Optical, Infrared, and Millimeter*, J. M. Oschmann, Jr., M. W. M. de Graauw, and H. A. MacEwen, Eds., vol. 7010, no. 1. SPIE, 2008, p. 701004. [Online]. Available: <http://link.aip.org/link/?PSI/7010/701004/1>
- [3] J. Zmuidzinas and P. Richards, "Superconducting detectors and mixers for millimeter and submillimeter astrophysics," *Proceedings of the IEEE*, vol. 92, no. 10, pp. 1597–1616, Oct. 2004.
- [4] O. Siebertz, C. Honingh, T. Tils, C. Gal, M. Olbrich, R. Bieber, F. Schmuelling, and R. Schieder, "The Impact of Standing Waves in the LO path of a Heterodyne Receiver," in *18th International Symposium of Space Terahertz Technology, California Institute of Technology, Pasadena, California, 2007*, pp. 117–122.
- [5] C. Comito and P. Schilke, "Reconstructing reality: Strategies for sideband deconvolution,"

- A&A, vol. 395, pp. 357–371, Nov. 2002.
- [6] J. Kooi and V. Ossenkopf, “HIFI Instrument Stability as Measured during the Thermal Vacuum Tests of the Herschel Space Observatory,” in *20th International Symposium of Space Terahertz Technology, Charlottesville, Virginia, 2009*, p. 69.
 - [7] R. D. Higgins and J. W. Kooi, “Electrical standing waves in the HIFI HEB mixer amplifier chain,” in *Society of Photo-Optical Instrumentation Engineers (SPIE) Conference Series*, ser. Society of Photo-Optical Instrumentation Engineers (SPIE) Conference Series, vol. 7215, Feb. 2009.
 - [8] V. Ossenkopf, “The Intensity Calibration Framework for HIFI,” *ALMA Memo 442*, Jan. 2003.
 - [9] V. Tolls, G. J. Melnick, M. L. N. Ashby, E. A. Bergin, M. A. Gurwell, S. C. Kleiner, B. M. Patten, R. Plume *et al.*, “Submillimeter Wave Astronomy Satellite Performance on the ground and in orbit,” *ApJS*, vol. 152, pp. 137–162, May 2004.
 - [10] U. Frisk, M. Hagström, J. Ala-Laurinaho, S. Andersson, J. Berges, J. Chabaud, M. Dahlgren, A. Emrich *et al.*, “The Odin satellite. I. Radiometer design and test,” *A&A*, vol. 402, pp. L27–L34, May 2003.
 - [11] R. Schieder, “The usefulness of a gas cell for performance testing,” Tech. Rep. SWAS/TM-4027, 1993.
 - [12] L. S. Rothman, I. E. Gordon, A. Barbe, D. C. Benner, P. F. Bernath, M. Birk *et al.*, “The HITRAN 2008 molecular spectroscopic database,” *Journal of Quantitative Spectroscopy and Radiative Transfer*, vol. 110, pp. 533–572, Jun. 2009.

Poster Session P7: Schottky Diodes

Harmonic Generation and Noise in GaAs and GaN Schottky Diodes

Diego Pardo^{1*}, Jesús Grajal², Beatriz Mencía³, Susana Pérez⁴, Javier Mateos⁵ and Tomás González⁶
^{1, 2, 3} *Universidad Politécnica de Madrid, Dept. Señales, Sistemas y Radiocomunicaciones, Madrid, Spain*
^{4, 5, 6} *Universidad de Salamanca, Dept. Física Aplicada, Salamanca, Spain*
 *Contact: dpardo@gmr.ssr.upm.es, phone +34 91-336- 73-58

Abstract— A semiconductor simulation tool based on Monte Carlo techniques has been used to analyse the performance of frequency multipliers in the millimetre-wave frequency range. Both power generation and noise properties have been compared for GaAs and GaN-based doublers. GaN could be an interesting option for frequency multiplication: efficiencies around 15 % can be reached for state-of-the-art carrier mobilities and noise performance is better than in GaAs-based doublers.

I. INTRODUCTION

Development of terahertz technologies is being conditioned by the small number of compact, powerful and tunable THz sources working at room temperature. GaAs Schottky multiplier chains have been widely used for LO power generation at millimeter wave band. However, to obtain the power levels required for applications in the terahertz region, several GaAs Schottky barrier diodes (SBDs) must work in a balanced configuration in the first multiplication stages, to prevent a single diode from entering into a breakdown regime. The set of SBDs that can be integrated in a microstrip line suspended within a transmission wave-guide supposes a limit in the available power in multiplication stages at higher frequencies.

In recent years GaN has become a promising material for high power, high temperature and high frequency applications, mainly due to its wide direct band gap, which results in a high breakdown field, and its high peak and saturated electron drift velocity. The main inconvenient of GaN in comparison to GaAs is its lower electron mobility.

The objective of this paper is to compare noise properties and harmonic generation of GaAs and GaN SBDs for multipliers by means of Monte Carlo (MC) simulations. This method is fundamental in high frequency and high power regimes of non-linear devices, where predictions of other simulation techniques differ from experimental results. As a reference to this study, a 200 GHz doubler is considered. In section II, we described the structure of the simulated diode and the main features of our MC simulator. Section III is devoted to the analysis of the electrical characteristics and the intrinsic noise sources in static conditions. In section IV, we analyse the RF and noise performance of a 200 GHz doubler based on GaAs and GaN diodes. Section V summarizes the main conclusions and future trends of our work.

II. DEVICE STRUCTURE AND MONTE CARLO SIMULATOR

The simulated Schottky diode selected has an epilayer length of 350 nm with a doping concentration of $1 \times 10^{17} \text{ cm}^{-3}$. The length of the substrate is 500 nm, with a doping concentration $2 \times 10^{18} \text{ cm}^{-3}$. The length of the substrate has been shorter as compared to the typical values of fabricated devices in order to reduce the computational cost of the Monte Carlo method. The anode area is $36 \mu\text{m}^2$. The ideal barrier height is 0.99 V for GaAs and 1.20 V for GaN diodes, respectively. The performance of the diodes has been evaluated at 300 K.

Calculations are performed by using an ensemble MC simulator three dimensional in momentum space, which is self-consistently coupled with a one dimensional Poisson solver. The effect of degeneracy is accounted for by locally using the classical rejection technique, where the electron heating and nonequilibrium screening effects are introduced by means of the local electron temperature. The ohmic contact is modelled as a surface that injects carriers in thermal equilibrium with the lattice (in order to maintain the neutrality in the region very close to the contact), according to Fermi-Dirac statistics; in addition any carrier reaching the contact leaves the device. On the other hand, Schottky contact is simulated as a perfect absorbent surface. Scattering mechanism included in the Monte Carlo simulation are ionized impurities, acoustic phonons, polar and non-polar optic phonons and intervalley mechanism, for both semiconductors materials. The band structure is modelled as a conduction band with three spherical non-parabolic valleys. The charge density is updated every 0.5 fs and devices are divided into equal cells of 20 Å long. The number of simulated carriers is around 10^5 .

Noise study is carried out from the analysis of the noise spectra of current fluctuation calculated from the Correlation Function (CF) and Fast Fourier Transform method (FFT) as reported in [1].

III. STATIC CHARACTERIZATION

In this section we analyse the diode configuration presented previously under forward bias conditions. Firstly, current-voltage (I-V) and capacitance-voltage (C-V) characteristics are presented. Secondly, we study the intrinsic noise behaviour.

A. I-V and C-V relations

Fig. 1 shows GaAs and GaN I-V curves. Two main regions are observed in these curves. Accordingly to the

thermionic emission theory, a non-linear conductance region is found for voltages lower than the built-in potential, (V_{bi} , around 0.95 V for GaAs and 1.11 V for GaN diodes); and a purely resistive region for higher bias voltages.

By comparing GaAs and GaN curves, we conclude that the I-V non-linearity is similar for both semiconductor diodes. In fact, an approximation of these curves to the exponential rule $I(t) \sim \exp(\alpha V)$ gives $\alpha \sim 27$, (ideality factor $n \sim 1.4$) for GaAs and $\alpha \sim 23$ ($n \sim 1.7$) for GaN diodes.

References [2] and [3] present simulations and measurements of electron transport for these semiconductors, showing higher mobility values for GaAs than GaN.

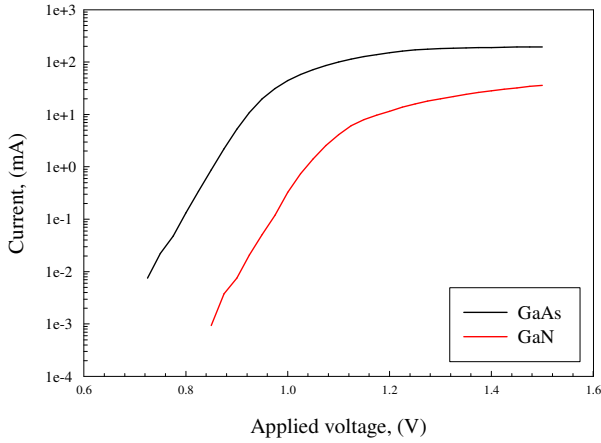


Fig. 1 Current-voltage curves for GaAs and GaN Schottky diodes, calculated with MC method

Fig. 2 shows capacitance-voltage curves, obtained as variations in the average number of carriers inside the diode with the applied voltage.

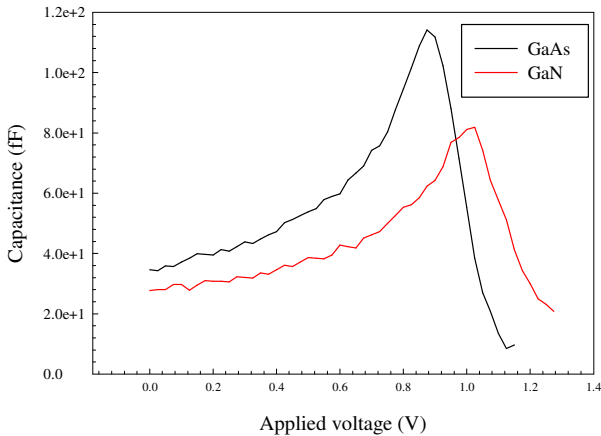


Fig. 2 Capacitance-voltage relation for GaAs and GaN Schottky diodes, obtained from MC method

For $V < V_{bi}$, C-V curves follow the known law $C/C_g = 1/(1 - V/V_{bi})^{1/2}$, where $C_g = \epsilon A/L$ is the SBD geometric capacitance. Differences between GaAs and GaN SBDs capacitance are originated by differences in relative permittivity ($\epsilon_r(\text{GaAs})/\epsilon_r(\text{GaN}) \sim 1.45$).

B. Noise under forward bias conditions

Spectral density of current fluctuations for GaAs and GaN diodes is shown in fig. 3 and fig. 4 respectively, under forward bias.

Three main features are observed in the spectral density of these Schottky diodes: a low frequency plateau and two high frequency peaks.

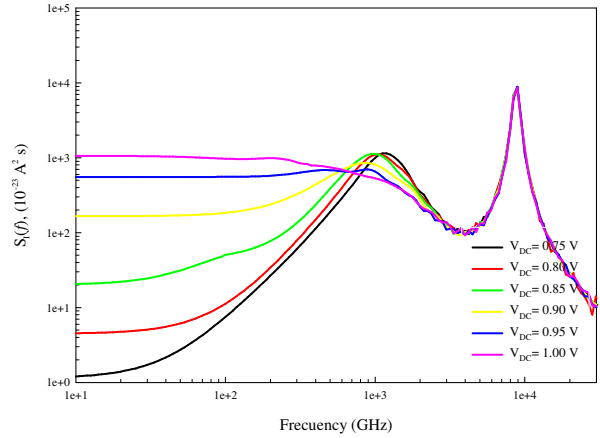


Fig. 3 Spectral density for current fluctuations in GaAs Schottky diode

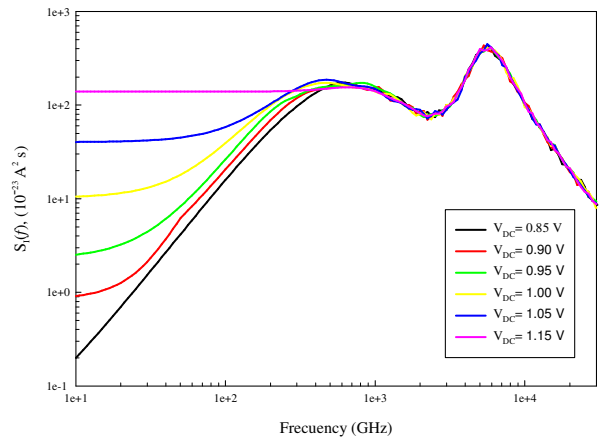


Fig. 4 Spectral density for current fluctuations in GaN Schottky diode

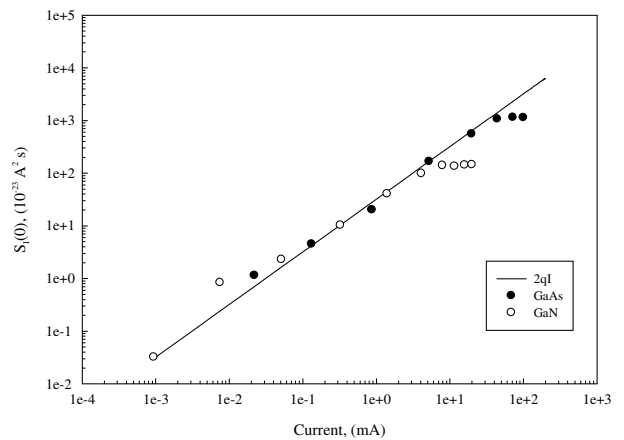


Fig. 5 Low frequency spectral density for GaAs and GaN diodes, as a function of current

The low frequency plateau observed under barrier-limited transport is in good agreement with the shot-noise law $S_I(0)=2qI$, as is shown in fig. 5. This noise component is due to carriers crossing randomly the Schottky barrier. With the increase of DC bias over flat-band regime, shot noise is replaced by thermal noise, [1].

The first high-frequency peak is related to returning carriers, i.e. carriers that approximate the Schottky barrier with insufficient kinetic energy to surmount it, and come back to neutral region of the semiconductor. According to the analytic theory presented in [4], the noise of these carriers is zero at zero frequency, rising as f^2 , reaches a maximum, and then disappears. This peak displaces slightly to lower frequencies as DC bias increases. Although the low frequency plateau due to shot noise takes lower values for GaN than GaAs diodes, this peak is located at about 0.6 THz for GaN and about 1 THz for GaAs, resulting in an excess noise influence over the level of the plateau for GaN diodes in the sub- THz region, under barrier transport.

The frequency associated to these carriers is defined by the inverse of the characteristic time of a carrier entering into the space-charge region and returning to the neutral region. So, a reduction in the depletion region by, for example, an increase in the doping of the epilayer translates this peak to higher frequencies.

The second high-frequency peak observed in the spectral density is caused by fluctuations in the carrier's velocity for the in-homogeneity of the $n-n^+$ (epilayer-substrate) homojunction, which lead to electric field fluctuations via Poisson equation. The frequency of this peak is found between the plasma frequencies of the epilayer and the substrate, [5]. So, it is placed about 8.8 THz and 5.7 THz for the GaAs and GaN diodes respectively. From fig. 6, when the doping of the substrate is the same of the epilayer, so the $n-n^+$ in-homogeneity does not exist, the plasma peak disappears. Since plasma peak is independent of DC bias, results of fig. 6 have been obtained for $V_{DC}=0.75$ for GaAs and $V_{DC}=0.90$ V for GaN.

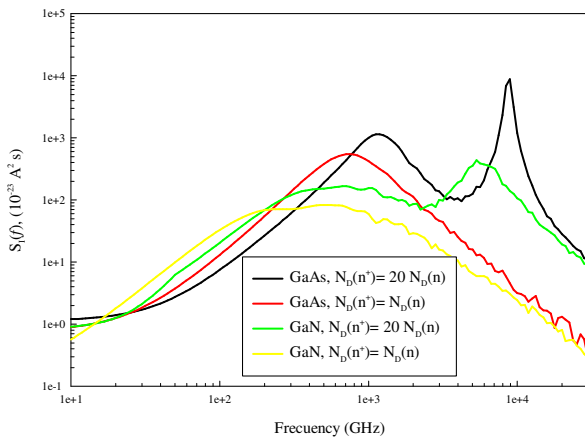


Fig. 6 Spectral density for GaAs and GaN diodes, with and without $n-n^+$ in-homogeneity

IV. 200 GHz DOUBLER

Frequency doubler operation based on GaAs and GaN diodes is analysed in this section.

A. Harmonic generation

To generate harmonics, GaAs and GaN diodes are excited with a sinusoidal voltage $V(t)=V_0+V_1 \sin(2\pi ft)$, of frequency $f=100$ GHz. The breakdown voltage for the GaAs diode is $V_{bd} \sim 12.5$ V, [6]. In order to prevent a single diode from entering into the breakdown regime, the bias point for the GaAs diode is $V_0= -5$ V. The amplitude V_1 is 6 V, to avoid the conduction regime at the maximum voltage swing. The time domain response $I(t)$ obtained from the simulation can be transformed into the frequency domain by means of Fourier Transform, and the impedance of the GaAs diode at the fundamental frequency evaluated: $Z(f_0)= (6.38- 91.43j) \Omega$. This correspond to an input power of $P(f_0)= 13.7$ mW. To evaluate the efficiency of the 200 GHz GaAs doubler we need to know the impedance at the second harmonic imposed by the external circuit, and this value it is not obtained directly for our calculations. By this end, harmonic balance simulations are used and a result for the impedance of the second harmonic for optimum harmonic extraction is obtained: $Z(2f_0)= (11.4+44j) \Omega$. So, the power delivered at the second harmonic is $P(2f_0)= 3.7$ mW. The efficiency of the doubler is evaluated as $\eta= P(2f_0) / P(f_0)= 27\%$, similar to the efficiency presented by [6].

For GaN diode, the breakdown voltage is over 82 V, [6]. This is one of the advantages of GaN versus GaAs diodes, because now the biasing of a single GaN diode can be $V_0= -15$ V. At 100 GHz enough power is available and the amplitude of the sinusoidal excitation is chosen at $V_1= 16.2$ V, to maximize the non linear capacitance swing. The impedance of the GaN diode at the fundamental frequency and the power available are $Z(f_0)= (6- 167j) \Omega$ and $P(f_0)= 28.3$ mW, respectively. Also to calculate the impedance for the second harmonic the harmonic balance simulations are used, given a value of $Z(2f_0)= (8.49+78.05j) \Omega$. Finally the calculated conversion efficiency of a single GaN doubler is $\eta= 2.3$ mW/28.3 mW= 8.1%.

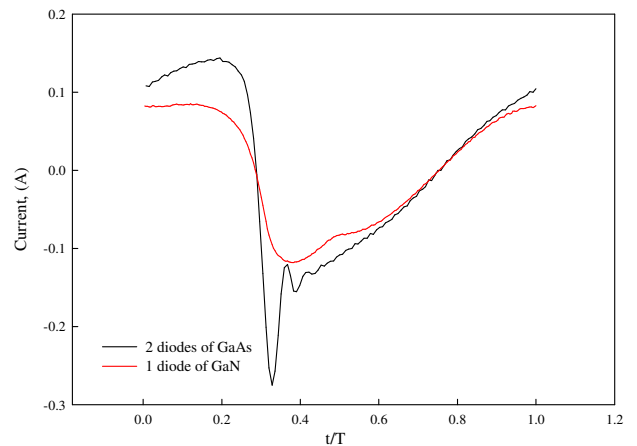


Fig. 7 Time dependence of the current response for the 100 GHz periodic excitation, for two GaAs diodes in parallel configuration and a single GaN diode

These values of conversion efficiencies for both diodes are in good agreement with the results presented in [6] using a drift-diffusion model coupled to a harmonic balance simulator. Optimized structures for the GaN-based doubler

with state-of-the-art experimental mobility characteristics suggest that efficiencies above 15% can be reached for 200GHz doublers.

Two GaAs diodes are required to support an input power of 28 mW (power delivered to the GaN doubler based on one diode). To simplify the following analysis, we suppose that the two GaAs diodes are arranged in a parallel configuration. Fig. 7 and fig. 8 show current response and harmonic amplitude for two GaAs diodes in parallel configuration and a single GaN diode. Thanks to the high breakdown potential of GaN, high power excitations can be applied to a single diode, resulting in amplitudes for the second ($m=2$) and third ($m=3$) harmonics of the current of the same order of magnitude as the two GaAs diode configuration.

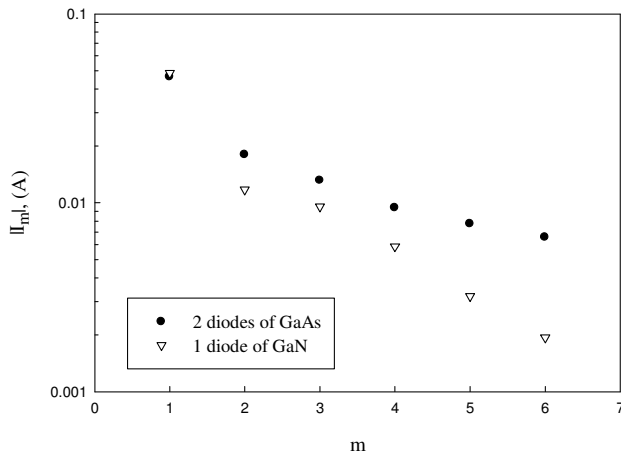


Fig. 8 Harmonics amplitude of the current for two GaAs diodes in parallel configuration and a single GaN diode, at frequency $f=100$ GHz. m represents the order of the harmonic.

B. Intrinsic noise for the 200 GHz doubler

Fig. 9 shows the main features of spectral density of current fluctuations for the two GaAs diodes in parallel configuration and the single GaN diode, under periodic large-signal operation. Additionally to the noise spectrum, the fundamental and second harmonics are also included. It is important to take into account that the two peaks represent the power of the fundamental and second harmonic, measured in dBW, while the noise level represents power per Hertz, so to obtain the noise power delivered to an impedance, it must be integrated in a given frequency range. According to power values presented in previous subsection, the relative power of two GaAs diodes in parallel configuration respect to a single GaN diode, delivered to the second harmonic is 5.1 dB.

The noise spectral density for the two GaAs diodes configuration has been obtained as two times the noise spectrum of a single GaAs diode, supposing incorrelation between both GaAs diodes.

Noise properties for the GaN-based doubler are better than for the GaAs-based doubler. Only near GaN plasma peak, about 4 THz, GaN spectral density is higher than GaAs.

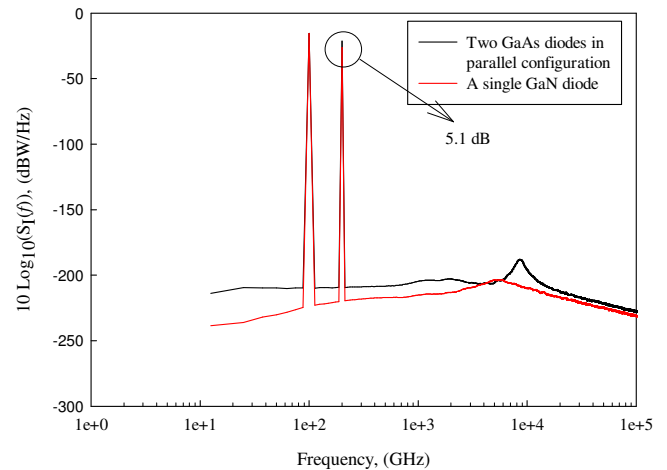


Fig. 9 FFT of fluctuations in current history obtained from MC method, together power for the fundamental and second harmonics

V. CONCLUSIONS

We have presented an analysis on noise features and harmonic generation for GaAs and GaN multipliers based on Monte Carlo method. This study presents electric considerations, which can be obtained with other semiconductor simulation models like drift-diffusion, but in addition Monte Carlo simulation let us analyse also the noise properties of devices and circuits.

Noise performance obtained from Monte Carlo method indicates that GaN presents lower levels of noise than GaAs in all frequency spectrum. In future works, analysis of noise in mixers, and the optimisation of the Schottky device structure for noise reduction will be performed.

ACKNOWLEDGMENT

This work was supported by the Junta de Castilla y Leon, Spanish National Research and Development Program under projects GR270, SA019A08, TEC2007-61259/MIC, TEC2008-02148, TeraSense (Consolider- Ingenio 2010, CDS2008-00068), RooTHz (European Commission- ICT-2009-243845).

REFERENCES

- [1] S. Pérez, T. González, P. Shiktorov, E. Starikov, V. Gružinskis, L. Reggiani, L. Varani and J. C. Vaissière, "Noise in Schottky-barrier diodes: from static to large-signal operation," in *Proc. of the SPIE*, 2004, vol. 5470, pp. 322-36.
- [2] B. E. Foutz, S. K. O'Leary, M. S. Shur and L. F. Eastman, "Transient electron transport in wurtzite GaN, InN and AlN," *J. Appl. Phys.* vol. 85, no. 11, pp. 7727-7734, 1999.
- [3] F. Schwierz, "An electron mobility model for wurtzite GaN," *Solid-State Electronics*, vol. 48, no. 6, pp. 889-895, June 2005.
- [4] M. Trippe, G. Bosman and A. Van Der Ziel, "Transit-time effects in the noise of Schottky-barrier diodes," *IEEE Trans. Microwave Theory Tech*, vol. 34, no. 11, pp. 1183-1192, 1986.
- [5] E. Starikov, P. Shiktorov, V. Gružinskis, L. Varani, J. C. Vaissière, J. P. Nougier and L. Reggiani, "Monte Carlo calculation of noise and small-signal impedance spectra in submicrometer GaAs n^+nn^+ diodes," *J. Appl. Phys.* vol. 79, no. 1, pp.242-252, Jan. 1996.
- [6] J. V. Siles and J. Grajal, "Capabilities of GaN Schottky multiplier for LO power generation at millimeter-wave bands," in *Proc. ISSIT*, 2008, pp.504-507.

Physics-Based Modeling Aspects of Schottky Diodes for Circuit Design Above 1 THz

José V. Siles*, Jesús Grajal* and Aldo Di Carlo†
(Contact: jovi@gmr.ssr.upm.es)

*Dept. Signals, Systems and Radiocommunications, Technical University of Madrid, Madrid, Spain

†Dept. Electronic Engineering, Optolab, University of Rome II Tor Vergata, Rome, Italy

Abstract—This work analyzes some of the physical aspects that must be dealt with for terahertz circuit design based on Schottky diodes beyond 1 THz. The high operation frequencies and the small dimensions that will be required for the devices make it essential to employ physics-based numerical simulators for the device optimization. We present an overview of the possible alternatives and discuss the most adequate ones considering both accuracy and simulation time. As a reference, we employ a Monte Carlo simulator because it provides a numerical solution to the Boltzmann Transport Equation. Since high doping levels will be necessary at these frequencies, the MC analyses should be based on Fermi-Dirac statistics. An efficient method for the inclusion of Fermi-Dirac statistics in MC simulators for non-homogeneous devices is also outlined and the effects of using Fermi-Dirac statistics instead of Maxwell-Boltzmann in Schottky diode models are analyzed.

I. INTRODUCTION

In the recent years, great advances are being made in millimeter-wave solid-state sources resulting in a rapid increase of the available local oscillator (LO) power at frequencies around 100 GHz. Current state-of-the-art LO sources can provide around 400 mW at W-band, and up to several watts can be achieved in the near future [1]. This clearly opens the possibility for the development of LO sources and mixers based on Schottky diodes beyond 2 THz. However, the traditional methods widely employed by designers so far, which are generally based on simple analytical diode models, will not be appropriate for THz circuit design beyond 1-2 THz. At these frequencies, even the validity of those physical models based on simplifications of the Boltzmann Transport Equation (BTE), like Drift-Diffusion (DD) and Hydro-Dynamic models (HD), has to be confirmed.

Therefore, accurate physics-based semiconductor models must be employed for the next generation of both Schottky diode based LO sources and frequency mixers at the THz range. The high operation frequency, the small dimensions that will be required for these devices (with epilayer thicknesses of 100 nm or less) and the high doping concentrations necessary to mitigate carrier velocity saturation will make it crucial to employ very accurate models accounting for the limiting physical mechanisms connected with these device characteristics. However, computational cost must also be accounted for and a trade-off between accuracy and simulation time has to be found.

The goal of this paper is to analyze some of the physical aspects that must be dealt with for terahertz circuit design

based on Schottky diodes beyond 1 THz. The main approach consists in using an harmonic balance simulator coupled with a physics-based drift-diffusion model to analyze the device in a self-consistent way together with the embedding circuit [2]. In order to check this approach beyond 1 THz (with short devices and high doping concentrations) we employ a Monte Carlo (MC) simulator as a reference because it provides a numerical solution to the BTE [3]. Moreover, the MC device analysis should be based on Fermi-Dirac statistics in order to account for the semiconductor degeneracy. Fermi-Dirac statistics needs to be implemented by using the energy moment distribution function $f(k)$ at every instant of time instead of the equilibrium Fermi-Dirac distribution function to well control the energy transitions during the MC simulation [4]. Thus, non-equilibrium conditions can be well accounted for during high-frequency RF simulations using MC. An efficient method for the inclusion of Fermi-Dirac statistics in MC simulators for non-homogeneous devices is outlined and the effects of using Fermi-Dirac statistics instead of Maxwell-Boltzmann within the Schottky diode analysis are presented.

It is important to remark that the use of MC device models for terahertz circuit design with harmonic balance methods is prohibitive due to its high computational cost. However, it allows to evaluate and improve other physics-based models that might work reasonably well at THz frequencies with an affordable computational cost.

II. SCHOTTKY DIODE MODELING FOR THz CIRCUIT DESIGN. ACCURACY AND SIMULATION TIME.

The selection of the most adequate method for semiconductor device simulation depends on two important factors: Accuracy and simulation time. Generally, the more complex the selected model, the higher the computational cost will be. Hence, it is important to choose an adequate approach for the device under study and to appreciate its limits and range of validity. So far the most widely employed method for millimeter-wave and submillimeter-wave Schottky diode based circuit design consist of an harmonic balance (HB) circuit optimization using either simple analytical models available in commercial simulators [5] or more complex physics-based numerical models [2], [6], [7]. In either case, the computational cost of the employed device model acquires a major significance because of the iterative nature of the HB methods, which involves several executions of the nonlinear analysis of the device.

The accuracy in the device simulation is normally determined by how accurately carrier transport is described [3]. Analytical device models based on equivalent circuits (generally included in commercial simulators such as ADS from Agilent) assume that the capacitance and current are function of the present value of the internal voltage. For Schottky diodes, this quasi-static approach has been proved to be valid only up to a few hundred GHz [8] so some empirical adjustments are often necessary for submillimeter-wave circuit design [9]. The advantage of analytical models is their very low computational cost.

The key advantage of physical-based numerical models over analytical ones lies in the fact that they are self-consistent and no empirical adjustment is necessary. Most widely used physical models for semiconductor devices are those based on the Boltzmann Transport Equation, which can be used either directly or through its moments [10]. The BTE formulation (Eq. 1) assumes that the electron dynamics are described by a distribution function $f = f(\vec{r}, \vec{p}, t)$, where \vec{p} is the momentum and \vec{r} is the position of the particle. The term $\partial f / \partial t|_{coll}$ has to do with the variation of the distribution function as a consequence of particle collisions inside the device. Once the distribution function f is known, all the parameters of interest (carrier drift velocities, energy distribution, diffusion coefficients, etc.) can be derived from it. However, finding the exact solution to the Boltzmann's equation is a very difficult task, so approximate approaches are generally employed to simplify the problem [10].

$$\partial f / \partial t + \vec{v} \cdot \nabla_r f + \partial \vec{p} / \partial t \cdot \nabla_p f = \partial f / \partial t|_{coll} \quad (1)$$

On the one hand, HD numerical models consist of the first three moments of the BTE that give respectively the continuity equations, the current flow equations and the energy balance equations for both electrons and holes. The current flow equations are introduced in the continuity equations resulting in four equations that together with Poisson's equation and the corresponding boundary conditions, define the HD method. Hence, the HD method involves the numerical solving of five coupled nonlinear partial differential equations [3]. On the other hand, DD numerical models consider only the two first moments of the BTE (*electron conservation* and an approximate form of the *momentum conservation*). In this case, only three coupled nonlinear partial differential equations must be numerically solved to simulate the device [11]. However, neglecting *energy conservation* prevents DD models from reproducing nonlocal effects such as the velocity overshoot. This may represent a problem at high frequencies because velocity overshoot might increase the current and modify the high frequency performance of the semiconductor device [3].

In contrast to DD and HD models that are based on simplifications of the BTE, MC simulation provides a numerical solution to the BTE. Thus, all the simplifying approximations can be removed and the real shape of the distribution functions can be computed. In addition, MC simulation accounts for the *scattering* mechanisms occurring inside the device and may include a more detailed physical description of the energy band structure [3], [12].

A rough estimation of the valid operation ranges for the different available physics-based model was given by M. Lundstrom in [3] (see Fig. 1). Nevertheless, the actual validity of a specific model has to be verified for the device and operation conditions under study. Obviously, the best way for this task is by direct comparison between measurements and simulation results [2]. However, MC results are in very close agreement with experimental results [3] and can be employed to validate other device models.

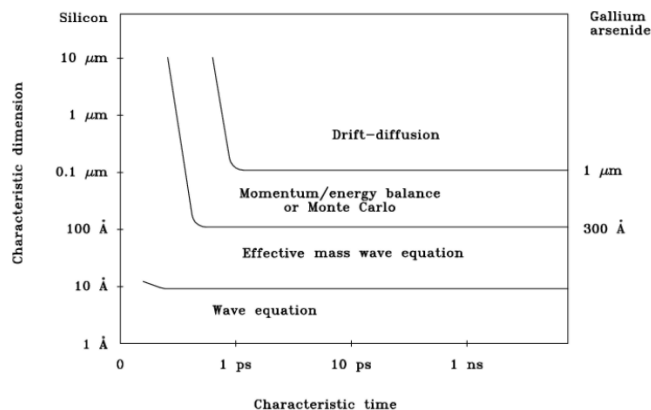


Fig. 1. Estimation of the valid operation range of physics-based semiconductor models by M. Lundstrom [3].

Unfortunately, the excessive simulation time required for MC simulations makes it prohibitive to use MC analysis for the optimization of THz circuits like frequency mixers and multipliers. This is shown in Table I with a comparison between HB simulation times employing both physics-based MC and DD Schottky diode models. Single analysis refers to a Schottky multiplier/mixer simulation for a single operation point whereas circuit optimization involves the joint optimization of all the design parameters (embedding impedances, epilayer thickness and doping, anode area, bias, etc.) in order to maximize the performance at a certain input power and frequency. Note that the computational cost for mixer analysis is much larger than for multipliers. The reason for this is that the time-domain nonlinear response of the diode has to be analyzed along one period of the intermediate frequency resulting in a larger number of voltage samples [13]. Moreover, HB mixer analysis involves a larger number of frequencies, and thereby more HB iterations, because of the necessity to account for both LO and RF harmonics and their intermodulation products [13].

In order to illustrate the usefulness of MC simulators to test other device models, Fig. 2a shows the evolution of the electron velocity as a function of the epilayer thickness for a typical Schottky diode used at millimeter/submillimeter wavelengths. It can be noticed the important increase in the velocity overshoot as the device shrinks from 480 nm to 90 nm according to MC simulations. As already discussed, velocity overshoot is not taken into account in DD models. The difference between MC results (solid curves) and DD results (dashed curves) becomes more evident as the device shrinks. Therefore, DD models seems *a priori* inadequate for terahertz

TABLE I
ANALYSIS AND OPTIMIZATION TIME FOR SCHOTTKY DIODE BASED MIXERS AND MULTIPLIERS USING HARMONIC BALANCE TOGETHER WITH EITHER A MC DEVICE MODEL OR A DD DEVICE MODEL.

	CIRCUIT	Single Analysis	Circuit Optimization (for 1500 analyses)
DD Enhanced DD	MULTIPLIER	0.5 min	~ 12.5 h
	MIXER	40 min	~ 1000 h
MC	MULTIPLIER	140 min	~ 3500 h
	MIXER	3500 min	~ 87500 h

• Simulation Platform: Intel P4 3.0 GHz with 4 GB RAM
 • Circuit optimization times are indicative (referred to a full optimization involving the analysis of 1500 different operation points)

	Time per Voltage Sample	# Voltage samples (per HB iteration)	# HB iterations (per analyzed operation point)	# Electrons (MC simulation)
MULTIPLIERS	DD → 0.006 s	256	~ 20	~ 50000
MIXERS	MC → 1.620 s	~ 5000	~ 80	(in this work)

circuit design were epilayer thicknesses of the order of 100 nm will be employed. These results are also in agreement with the range of validity predicted in Fig. 1. Moreover, not accounting for velocity overshoot has a notable impact on the simulated Schottky diode I-V curves, which is manifest by the early current saturation in DD results with regard to MC results (Fig. 2b).

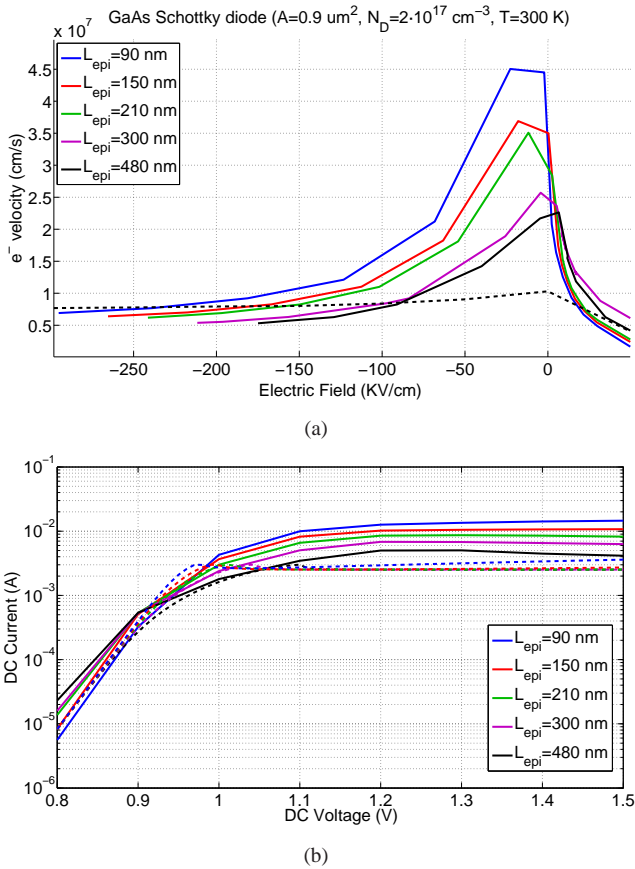


Fig. 2. MC analysis of the limitations of DD models with device shrinkage: Velocity overshoot (a) and I-V curves (b). MC analysis (solid curves) and DD analysis (dashed curves).

Nevertheless, velocity overshoot occurs at the flatband regime and these operation conditions are not reached in general for Schottky diode based multipliers. On the contrary, minimum conversion losses for Schottky mixers are obtained when flatband voltages are slightly exceeded [14]. Hence, traditional DD simulations are not longer adequate for mixer design due to the limitations shown in Fig. 1. As discussed before, HD models do not experience these limitations but imply the numerical solution of a five-equation system (two more than in DD models), which increases the computational cost. We proposed in [15] an intermediate approach consisting in using MC simulation to redefine the mobility-field characteristics and recombination velocity used in DD Schottky diode models beyond flatband. As illustrated in Fig. 3, our enhanced DD model overcomes the problems shown in Fig. 2 and extends the validity of traditional DD models to submicron devices without adding any extra simulation time.

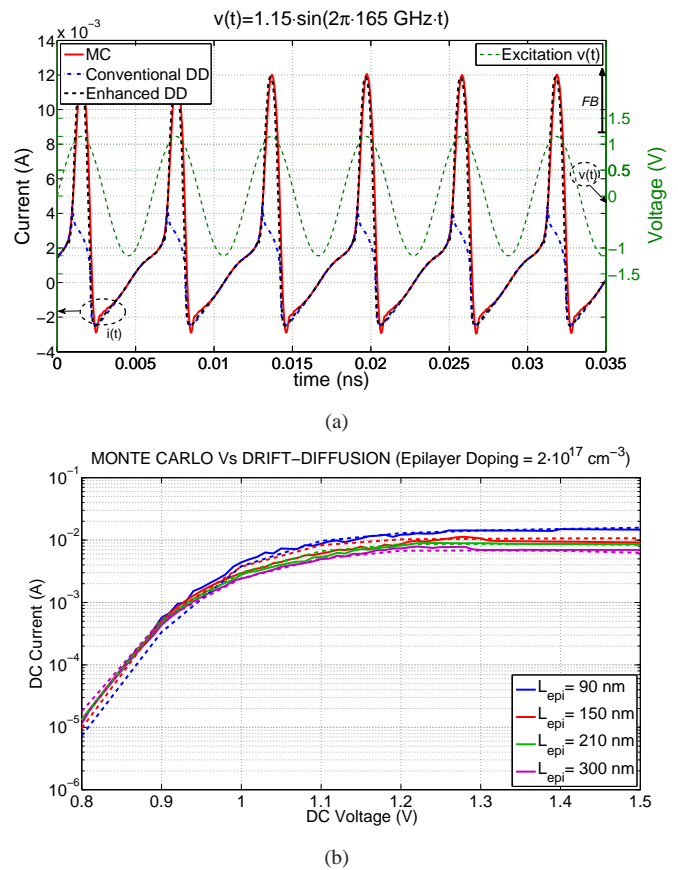


Fig. 3. MC analysis of the performance of our enhanced DD model presented in [15]: RF current response to a 165 GHz voltage excitation for MC, DD and enhanced DD (a), and I-V curves obtained with MC -solid lines- and DD -dashed lines- (b).

The use of a HB circuit simulator together with our enhanced DD model offers a good trade-off between accuracy and simulation time and might be employed as a first attempt to well optimize Schottky-based circuits beyond 1-2 THz. MC simulations can be used not only to check the validity of the approach but also to analyze other aspects like the evolution of the electron temperature within the device as exemplified in Fig. 4.

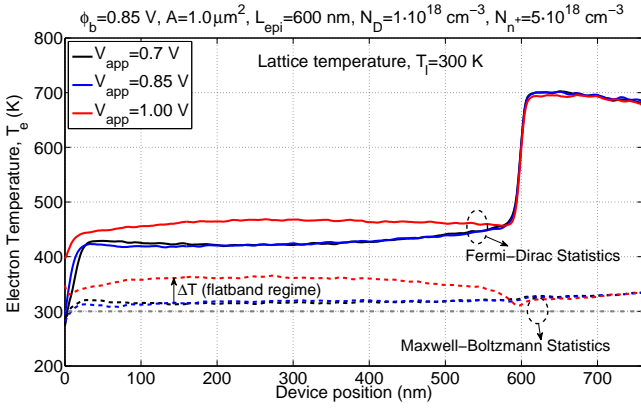


Fig. 4. Electron temperature (T_e) obtained by means of MC simulation (Maxwell-Boltzmann and Fermi-Dirac statistics). Electron temperature is equal to lattice temperature in DD simulations (300 K in this case).

It is important to remark that the electron temperature (T_e) actually represents the average random kinetic energy of the electrons. This corresponds to a temperature only for a non-degenerate Maxwellian distribution function (Maxwell-Boltzmann statistics). For Fermi-Dirac statistics, this quantity accounts for an increase in the electrochemical potential due to degeneracy plus a real-temperature effect [4]. Noise can be as well easily analyzed with MC simulation since it is inherent to MC simulators [16].

III. AN EFFICIENT IMPLEMENTATION OF FERMI-DIRAC STATISTICS ON SCHOTTKY DIODE MC SIMULATORS

MC simulators have a semiclassical nature as they simulate the electron as a classical particle affected by *scattering* mechanisms whose probabilities are obtained according to principles from quantum mechanics. The electrons within the semiconductor behave like *fermions* and consequently the Pauli Exclusion Principle should be included. In this case, the electronic states are described by the Fermi-Dirac statistics instead of by Maxwell-Boltzmann statistics. For MC analysis at terahertz frequencies, where Schottky diodes with highly doped epilayers are necessary, semiconductor degeneracy has to be taken into account. For GaAs, degeneracy occurs for doping levels higher than $4 - 5 \cdot 10^{17} \text{ cm}^{-3}$.

The MC code employed herein has been developed at the Tor Vergata University of Rome (Italy). It consists of a band structure with three valleys at the conduction band (the central valley Γ , and the two satellite valleys L and X), and three valence bands (heavy-holes, light-holes and spin-orbit). Spherical constant-energy surfaces are assumed and non-parabolicity correction factors are applied for the calculations [12]. The following scattering events are included: acoustic phonon interaction, polar-optical phonon interaction, electron-plasmon interaction, impurity scattering, electron-hole scattering, intervalley scattering and impact ionization.

The implementation of Fermi-Dirac statistics presented in this section is based on the rejection method proposed by P. Lugli and D.K. Ferry in 1985 for homogeneous devices [4]. MC simulation allows to know the distribution function even in the transient phase. Hence, the actual Fermi-Dirac

distribution function $f(\mathbf{k})$, which evolves during the MC simulation (i.e. in RF simulations), can be computed at every instant of time during the MC simulation and employed to control the accepted/rejected energy transitions according to Pauli Exclusion Principle. This technique avoids to use the analytical expression for the equilibrium Fermi-Dirac distribution function (only valid *a priori* in the stationary regime). The method described in this work is an extension of [4] to ensemble MC simulation of heterostructure devices (e.g. Schottky diodes) and performs well even when weighted particles and particle multiplication/cut algorithms are considered within the MC simulation. Note that the use of weighted particles (i.e. one particle represents several electrons) improves MC convergence.

The key point of the algorithm is the adequate normalization of the distribution function $f(\mathbf{k})$ by the maximum number of allowed states (N_c) to properly allow/reject the electron moment transitions after each scattering event [4]. The probability of an electronic transition from state \mathbf{k} to state \mathbf{k}' is proportional to the probability that the final state \mathbf{k}' is unoccupied: $P(\mathbf{k}, \mathbf{k}') \propto f(t, \mathbf{k}')/N_c(t)$. Since $N_c(t)$ depends on the electron concentration n , independent distribution functions are considered for each device layer i (epilayer, n^+ -layer and buffer in the case of Schottky diodes):

$$N_c(t, i) = \frac{2 \cdot \Omega_c(t, i) \cdot V(t, i)}{8 \cdot \pi^3} \quad (2)$$

$\Omega_c(t, i) = \Delta k_x(t, i) \cdot \Delta k_y(t, i) \cdot \Delta k_z(t, i)$ being the unitary \mathbf{k} -space volume cell for the MC simulation and $V(t, i) = N_{electrons}(t, i)/n(i)$ being the effective volume in layer i (N_c is derived from the Heisenberg Uncertainty Principle). The index t in the previous equations indicates that these parameters are dynamically recalculated during the MC analysis in order to improve the efficiency of the algorithm. On the one hand, at least 50 particles are always guaranteed for each \mathbf{k} -space mesh cell in order to have an accurate enough calculation of the distribution function. Hence, the mesh cell volume $\Omega_c(t, i)$ is dynamically recalculated each time the distribution function is re-evaluated. In addition, maximum and minimum values for the electron moment (k_x, k_y, k_z) are monitored along the analysis in order to well determine the limits for the dynamical definition of the \mathbf{k} -space mesh. To avoid unwanted effects when particles with different weights are present in the simulation, especially at the interphases between layers, the effective volume and the number of allowed states are made dependant in the proposed algorithm on the average weight of the electrons within the layer.

On the other hand, the efficiency of the algorithm in terms of simulation time depends on how often the distribution function is recalculated. Fig. 5 shows the performance of the proposed algorithm as a function of the number of MC iterations (N_{FD}) between re-evaluations of the distribution function. It can be seen that good results are obtained for N_{FD} values below 100 MC iterations. Obviously, considering $N_{FD} > 1$ implies that some energy states become slightly overpopulated for small periods of time throughout the analysis. The MC simulation itself rapidly corrects these anomalies so the effect is not noticeable in the overall MC simulation. For $N_{FD} > 200$,

overpopulated energy states are not longer under control and the algorithm fails as can be seen in Fig. 5. Note that a very good accuracy is achieved for $N_{FD} = 50$ with almost no extra time added to the simulation with regard to the use of Maxwell-Boltzmann statistics (see Table II).

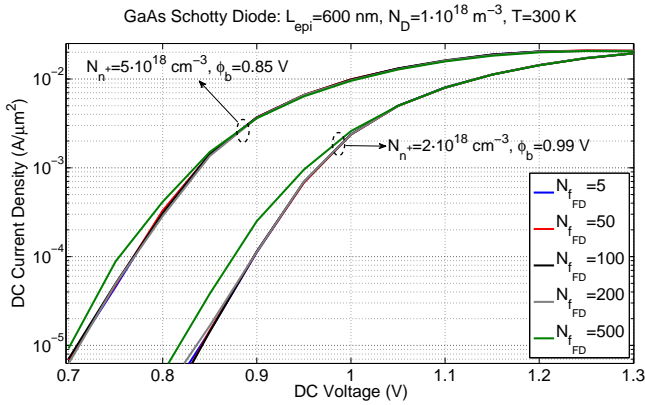


Fig. 5. Fermi-Dirac Monte Carlo I-V Curves as a function of the number of MC iterations N_{FD} between recalculations of the of the distribution function.

TABLE II
FERMI-DIRAC MONTE CARLO SIMULATION TIME AS A FUNCTION OF THE NUMBER OF MC ITERATIONS N_{FD} BETWEEN RECALCULATIONS OF THE OF THE DISTRIBUTION FUNCTION.

	# MC iteration between re-evaluation of Fermi-Dirac distribution function	Time to perform 1000 MC iterations
Monte Carlo (Maxwell-Boltzmann)	----	54 sec
Monte Carlo (Analytical Fermi-Dirac)	----	58 sec
MC (Dynamic Fermi-Dirac) THIS WORK	500	59 sec
	50	62 sec
	5	90 sec
	2	130 sec

To conclude this section, Fig. 6 shows a comparison between the I-V curves obtained with both Maxwell-Boltzmann statistics (blue curves) and Fermi-Dirac statistics (red curves) for two Schottky diodes with epilayer dopings of $1 \cdot 10^{18} \text{ cm}^{-3}$ and n^+ - layer dopings of $2 \cdot 10^{18} \text{ cm}^{-3}$ and $5 \cdot 10^{18} \text{ cm}^{-3}$. From these results, it is evident that Fermi-Dirac statistics must be accounted for in order to well determine the I-V response of highly-doped Schottky diodes. Note that when a low-doped homogeneous diode ($N_D = 1 \cdot 10^{16} \text{ cm}^{-3}$) is simulated, both Fermi-Dirac and Maxwell-Boltzmann statistics yield the same results since the semiconductor is not degenerated in this case. It can be observed in Fig. 7 that for low dopings similar distribution functions are obtained with both statistics. However, if the doping is increased to $N_D = 1 \cdot 10^{18}$ (degenerate conditions) the MC results obtained with each of the statistics differ significantly. In the case of the Fermi-Dirac statistics, the Pauli exclusion principle forces a large portion of the electrons located in the lower-energy states to move towards higher energy states so the energy distribution function tends to broaden and diminish in comparison to the Maxwell-Boltzmann distribution.

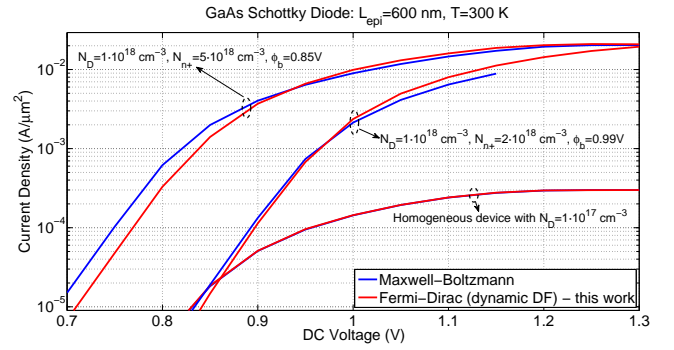


Fig. 6. Performance of the proposed Fermi-Dirac implementation: Monte Carlo simulated I-V curves.

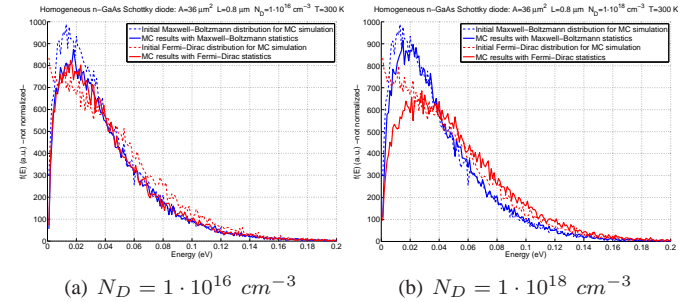


Fig. 7. Resultant energy distribution functions for a low-doped layer (non-degeneracy case) -left- and a highly-doped layer (degeneracy case) -right-. MC results with Maxwell-Boltzmann statistics (blue curves) and Fermi-Dirac statistics (red curves). Dashed lines represent the initial distribution functions employed for the MC simulations.

IV. PHYSICAL SCHOTTKY-BASED CIRCUIT DESIGN BEYOND 1 THZ

To exemplify those aspects that have been dealt with in the previous sections, we present here a brief study on the theoretically achievable performance of Schottky based frequency doublers at 2.4 THz and 4.8 THz. The analysis is performed by means of the HB circuit simulator coupled with the physics-based enhanced DD model described in [2], [15]. In order to investigate the adequacy of this approach beyond 1 THz we have firstly compared the predicted Schottky diode responses obtained with both the MC and the DD Schottky diode model. A sinusoidal voltage excitation, $V = -2 + 2.85 \cdot \sin(\omega t)$, has been considered since it provides a good representative case where the diodes are driven covering almost the whole range between breakdown and forward conduction. It can be noticed in Fig. 8 that the results are quite similar with both simulators. For example, peak to peak amplitudes and waveform slopes are identical. A certain difference can be appreciated at the maximum current peaks. Nevertheless, the general good agreement leads us to think that the considered method may represent a good approach to well estimate the achievable multiplier performances at these frequency ranges. Note that both Maxwell-Boltzmann and Fermi-Dirac statistics provides similar results for these specific devices.

It is well known that for multiplier design above 1-2 THz, where the available input power is very low to provide a sufficient voltage swing of the nonlinear C-V curve, best per-

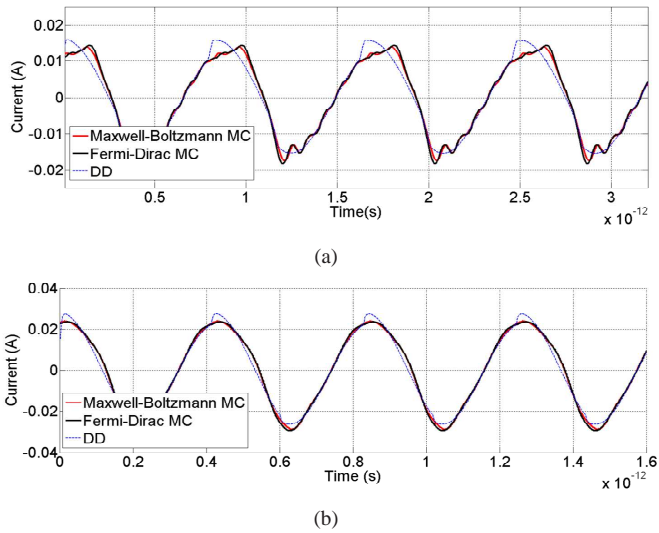


Fig. 8. MC and DD Schottky diode model response to a voltage excitation of 1.2 THz(a) and 2.4 THz (b): $V = -2 + 2.85 \cdot \sin(\omega_0 t)$ Volts ($T=300$ K). GaAs Schottky diodes feature: $A = 0.5 \mu\text{m}^2$, $L_{\text{epi}} = 100\text{nm}$, $N_D = 1 \cdot 10^{18} \text{cm}^{-3}$, $N_{n^+} = 5 \cdot 10^{18} \text{cm}^{-3}$.

formance will be obtained for biasless or slightly forward bias designs because of the higher nonlinearity of the capacitance under these circumstances. High doping concentrations ($5 \cdot 10^{17} \text{cm}^{-3}$ or higher) need to be considered to mitigate the effect of carrier velocity saturation leading to very short space charge regions. Hence, epilayer thicknesses must be as shorter as possible to reduce the contribution of the non-depleted region of the epilayer to the overall series resistance [2].

Simulation results for a 2.4 THz Schottky diode doubler and a 4.8 THz doubler are respectively shown in Figs. 9 and 10. We have considered an epilayer thickness of 100 nm for the 2.4 THz doubler and a 75 nm epilayer for the 4.8 THz doubler. Epilayer doping concentrations from $5 \cdot 10^{17} \text{cm}^{-3}$ to $1 \cdot 10^{18} \text{cm}^{-3}$ are analyzed. The n^+ -layer doping is $5 \cdot 10^{18} \text{cm}^{-3}$ in all the cases. Two important conclusions can be derived from these results. On the one hand, worse results are obtained when using a $1 \cdot 10^{18} \text{cm}^{-3}$ doping level due to the reduction of the space charge region that causes an increase in the series resistance. On the other hand, a very precise definition of the optimum values for the design parameters is mandatory, especially for the 4.8 THz doubler.

For the 2.4 THz doubler, a maximum efficiency of 4 % could be theoretically achieved for a $0.5 \mu\text{m}^2$ anode area assuming a 1 mW input power per anode ($R_s = 35\Omega$, $C_{j0} = 1.16 \text{fF}$). For the 4.8 THz doubler much lower anode areas are necessary due to the lower available input power ($40 \mu\text{W}$ per anode assumed in this work). We have assumed a minimum limit for the anode area of $0.2 \mu\text{m}^2$ ($R_s = 80\Omega$, $C_{j0} = 0.47 \text{fF}$) and tried to compensate the high required input power by varying the DC bias voltage (towards forward conduction). Note that the peak efficiency is obtained at a lower input power as bias voltage is increased. For 0.8 V, the efficiency drops due to the change between varactor and varistor modes of operation as shown in Fig. 10. This transition coincides with an increase in both the real part and the imaginary part of

the optimum resistance at the fundamental frequency (shown impedances are matched for each analyzed input power). This factor is also responsible of the fast degradation of the doubler efficiency beyond a certain input power level.

2.4 THz Doubler: $\phi_b = 0.86$ V, $L_{\text{epi}} = 100$ nm, $N_{n^+} = 5 \cdot 10^{18} \text{cm}^{-3}$, $T = 300$ K

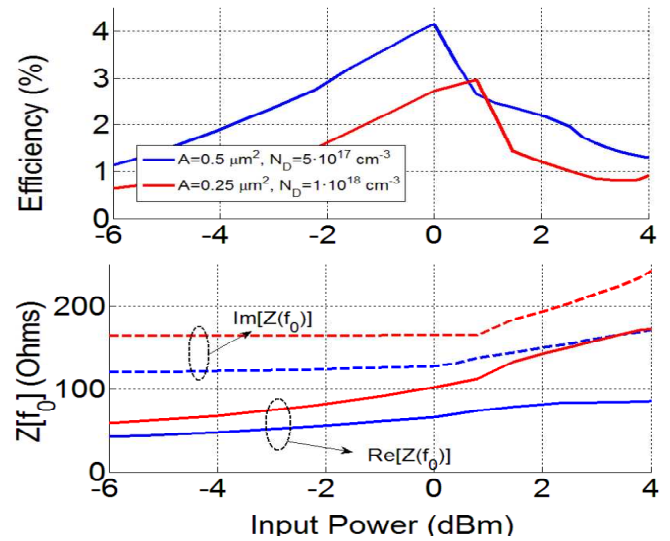


Fig. 9. Theoretically achievable performance for Schottky doublers at 2.4 THz for a 2 mW input power at 1.2 THz (1 mW per anode) and 300 K. Impedances are referred to a single anode (impedances seen from device terminals).

4.8 THz Doubler: $\phi_b = 0.86$ V, $L_{\text{epi}} = 75$ nm, $N_{n^+} = 5 \cdot 10^{18} \text{cm}^{-3}$, $T = 300$ K

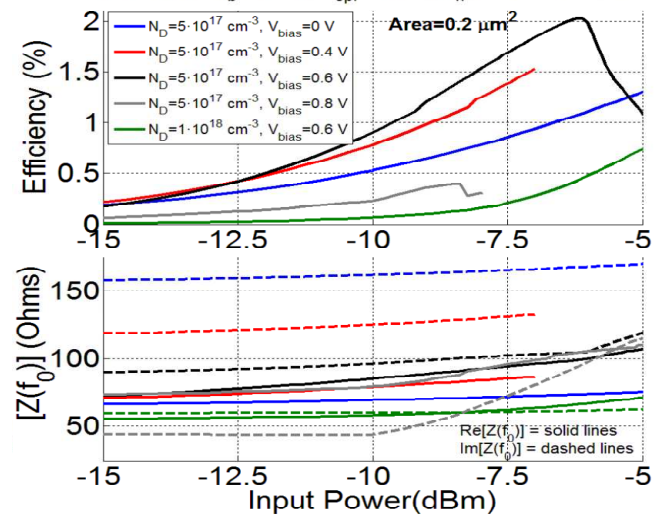


Fig. 10. Theoretically achievable performance for Schottky doublers at 4.8 THz for a $80 \mu\text{W}$ (-11 dBm) input power at 2.4 THz ($40 \mu\text{W}$ per anode) and 300 K. Impedances are referred to a single anode (impedances seen from device terminals).

To summarize, the low available input power and the circuit sensitivity makes it essential to utilize very accurate device models able to well determine the correct device impedances and properly optimize the circuits. Due to the high sensitivity of the circuit optimization, tuning elements like using DC bias to compensate possible circuit imbalance will not be effective

if the employed model for the circuit design does not guarantee a sufficient accuracy.

Once the device has been optimized by means of HB simulation, MC codes can be employed to evaluate additional aspects like the evolution of the electron temperature within the device. To exemplify this, Fig. 11 shows that the electron temperature remains almost constant (and equal to the lattice temperature: $T_e = T_l = 300K$) along the RF current cycle. However, electron temperature within the active layer vary between 400K and 700K for the 2.4 THz case, and from 350K to 400K for the 4.8 THz due to the lower input power. For these analyses, the MC simulator has been driven with the actual voltage RF waveforms at the Schottky diode terminals resulting from the HB simulation (assuming 1 mW/anode at 2.4 THz and 40 μW /anode at 4.8 THz).

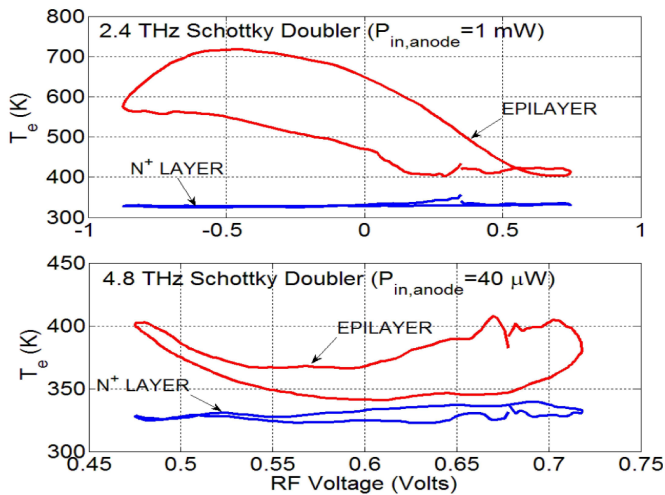


Fig. 11. MC simulation of the RF electron temperature for the analyzed 2.4 THz and 4.8 THz doublers over the RF voltage swing.

V. CONCLUSION

The use of harmonic balance simulators together with accurate physics-based device models represents the most appropriate way for terahertz circuit design since both the external circuit and the device structure can be simultaneously optimized in a self-consistent way. In this work we have briefly discussed several available device models and its suitability for Schottky based circuit design and optimization beyond 1 THz in terms of accuracy and computational cost. Our harmonic balance simulator featuring an enhanced DD model with improved definition of the mobility-field characteristics offers a good trade-off between simulation time and accuracy. According to HB simulation results, a theoretically achievable performance of $\sim 4\%$ might be achieved for 2.4 THz doublers, and $\sim 2\%$ for 4.8 THz doublers. MC simulation results have been used to give confidence to the results obtained with this approach. Moreover, an efficient implementation of Fermi-Dirac statistics in the MC simulator has been presented and

the impact of using Fermi-Dirac statistics instead of Maxwell-Boltzmann statistics in the simulation of highly-doped n-GaAs Schottky diodes has been discussed.

ACKNOWLEDGMENT

This work was supported by the Spanish National Research and Development Program under projects TEC2008-02148 and TeraSense (Consolider-Ingenio 2010, CSD2008-00068).

REFERENCES

- [1] J. S. Ward, G. Chattopadhyay, J. Gill, H. Javadi, C. Lee, R. Lin, A. Maestrini, F. Maiwald, I. Mehdi, E. Schlecht, and P. Siegel, "Tunable broadband frequency-multiplied terahertz sources," *33rd International Conference on Infrared, Millimeter and Terahertz Waves*, September 2008.
- [2] J. V. Siles and J. Grajal, "Physics-based design and optimization of Schottky diode frequency multipliers for THz applications," *Accepted for IEEE Transactions on Microwave Theory and Techniques, Special Issue on "THz Technology: Bridging the Microwave-to-Photonics Gap"*, 2010.
- [3] M. S. Lundstrom, *Fundamentals of carrier transport*. Addison-Wesley, 1990.
- [4] P. Lugli and D. K. Ferry, "Degeneracy in the ensemble Monte Carlo method for high-field transport in semiconductors," *IEEE Transactions on Electron Devices*, vol. ED-32, no. 11, pp. 2431–2437, November 1985.
- [5] A. Maestrini, J. S. Ward, J. J. Gill, H. S. Javadi, E. Schlecht, C. Tripon-Canseliet, G. Chattopadhyay, and I. Mehdi, "A 540-640 GHz high-efficiency four-anode frequency tripler," *IEEE Transactions on Microwave Theory and Techniques*, vol. 53, no. 9, pp. 2835–2843, September 2005.
- [6] R. E. Lipsey, S. H. Jones, J. R. Jones, T. W. Crowe, L. F. Horvath, U. V. Bhaskar, and R. J. Matlack, "Monte Carlo harmonic-balance and drift-diffusion harmonic-balance analyses of 100-600 GHz Schottky barrier varactor frequency multipliers," *IEEE Transactions on Electron Devices*, vol. 44, no. 11, pp. 1843–1850, November 1997.
- [7] J. Grajal, V. Krozer, E. Gonzalez, F. Maldonado, and J. Gismero, "Modelling and design aspects of millimeter-wave and submillimeter-wave Schottky diode varactor frequency multipliers," *IEEE Transactions on Microwave Theory and Techniques*, vol. 48, no. 4, pp. 700–711, April 2000.
- [8] S. A. Maas, *Non-linear Microwave Circuits*. Artech-House, Inc. Boston-London, 1993.
- [9] N. Erickson, "Diode frequency multipliers for terahertz local-oscillator applications," *In Proc. SPIE Advanced Technology MMW, Radio and Terahertz Telescopes*, pp. 75–84, March 1998.
- [10] S. Selberherr, *Analysis and Simulation of Semiconductor Devices*. Springer-Verlag, Wien-New York, 1984.
- [11] P. J. C. Rodrigues, *Computer-aided analysis of nonlinear microwave circuits*. Artech-House, Inc. Boston-London, 1997.
- [12] C. Jacoboni and P. Lugli, *The Monte Carlo method for semiconductor device*. Springer-Verlag Wien New York, 1989.
- [13] J. V. Siles, J. Grajal, V. Krozer, and B. Leone, "A CAD tool for the design and optimization of Schottky diodes mixers up to THz frequencies," *In Proc. of the 16th International Symposium on Space Terahertz Technology*, pp. 477–482, May 2005.
- [14] T. W. Crowe, W. L. Bishop, D. W. Porterfield, J. L. Hesler, and R. M. Weikle II, "Opening the Terahertz window with integrated diode circuits," *IEEE Journal of Solid-State Circuits*, vol. 40, no. 10, pp. 2104–2110, October 2005.
- [15] J. V. Siles and J. Grajal, "Design of submillimeter schottky mixers under flat-band conditions using an improved drift-diffusion model," *IEEE Microwave and Wireless Component Letters*, vol. 19, no. 3, pp. 167–169, March 2009.
- [16] J. G. Adams, T. W. Tang, and L. E. Kay, "Monte carlo simulation of noise in GaAs semiconductor devices," *IEEE Transactions on Electron Devices*, vol. 41, no. 4, pp. 575–581, April 1994.

Design and Fabrication of 190-GHz Dual-Chip Single-Waveguide Schottky Doublers

José V. Siles^{1,2}, Alain Maestrini², Byron Alderman³, Steven Davies⁴, Hui Wang³ and Tapani Närhi⁵

¹Dept. Signal, Systems and Radiocommunications
Technical University of Madrid, Spain
Email: jovi@gmr.ssr.upm.es

³Dept. Millimetre-Wave Technology
Rutherford Appleton Laboratory, UK
Email: byron.alderman@stfc.ac.uk

²Université Pierre et Marie Curie–Paris 6 &
Observatoire de Paris, LERMA, France
Email: alain.maestrini@obspm.fr

⁴Department of Physics
University of Bath, UK
Email: s.r.davies@bath.ac.uk

⁵European Space Agency (ESA/ESTEC), Email: tapani.narhi@esa.int

Abstract

The next generation of Schottky multipliers will take advantage of the high power already available from driver amplifiers (up to 500 mW in the 70-113 GHz band) and of the several watts expected at 100 GHz from MMIC amplifiers based on GaN transistors [1]. Power-combining strategies consisting in using several chips on a single split-waveguide multiplier block [2,3] will make it possible to handle the high LO power provided by state-of-the-art LO sources at 100 GHz, and thereby to increase the available LO power at terahertz frequencies.

In this work, we will present the design of power-combined 190-GHz Schottky-diode doublers using United Monolithic Semiconductor (UMS) BES Schottky process based on the dual-chip single-waveguide topology described in [3]. The doublers feature two MMIC chips with a series array of 6 planar Schottky diodes each, integrated into a 50- μm -thick GaAs substrate. A bias-less design was chosen to accommodate the mixer-optimized UMS BES Schottky diodes that feature short epilayers and subsequently relatively low breakdown voltages. Two designs have been made. The first one consists of two symmetrical circuits that incorporate beam-leads ground connections and a cross-shape 50- μm -thick substrate for lowering the dielectric load. This version of the doubler requires several post processing steps after the completion of the nominal UMS BES process. These steps are performed at the University of Bath and at the Rutherford Appleton Laboratory (RAL). The second version of the doubler does not require post processing steps. It features two symmetrical circuits implanted on a 50- μm -thick rectangular substrate and no beam leads are employed.

The first design with post-processing is expected to achieve $\sim 10\%$ efficiency over a 15% 3-dB bandwidth, whereas 7-10% efficiency over a 12% 3-dB bandwidth is predicted for the second design without post-processing. The MMIC chips for both 190-GHz doublers have been already delivered by UMS and the multiplier blocks are now under process at RAL. RF measurements of the doublers are planned for the beginning of 2010. This work was supported by the European Space Agency and the CNES.

REFERENCES

- [1] J. S. Ward, G. Chattopadhyay, J. Gill, H. Javadi, C. Lee, R. Lin, A. Maestrini, F. Maiwald, I. Mehdi, E. Schlecht and P. Siegel, "Tunable broadband frequency-multiplied terahertz sources," *33rd International Conference on Infrared, Millimeter and Terahertz Waves*, Sep. 2008.
- [2] A. Maestrini, J. S. Ward, C. Tripon-Canseliet, J. Gill, C. Lee, H. Javadi, G. Chattopadhyay and I. Mehdi, "In-phase power-combined frequency triplers at 300 GHz," *IEEE Microwave and Wireless Component Letters*, vol. 18, no. 3, pp. 218-220, Mar. 2008.
- [3] J. V. Siles, A. Maestrini, B. Alderman, S. Davies, and H. Wang, "A novel dual-chip single-waveguide power combining scheme for millimeter-wave frequency multipliers," *20th International Symposium on Space Terahertz Technology*, pp. 205-209, Apr. 2009.

Parameter Extraction and Geometry Optimisation of Planar Schottky Diodes

Aik Yean Tang^{1,2}, Peter Sobis¹⁻³, Vladimir Drakinsky², Huan Zhao^{1,2} and Jan Stake^{1,2}.

¹GigaHertz Centre,

²Physical Electronics Laboratory,
Department of Microtechnology and Nanoscience,
Chalmers University of Technology.
Email: aik-yeen.tang@chalmers.se

³Omnisys Instruments AB, SE-421 30 Göteborg, SWEDEN.

Abstract

The continuous interests in terahertz (300 GHz to 10 THz) applications have generated technology pressure in the search of reliable, room temperature operational and compact sources and detectors. Various terahertz sources such as optically pumped lasers, backward wave oscillators, and direct multiplied sources have been explored [1]. For direct multiplied sources, the GaAs-based Schottky diode is one of the most critical devices in heterodyne receivers operating at millimetre and sub-millimetre wavelengths.

The importance of Schottky diode could be seen from the meticulous efforts in the diode technology advancement. This includes the evolvement of the whisker contact to the surface channel planar diode technology [2] as well as the circuit integration of the discrete Schottky diodes. For high frequency applications, the performance of a GaAs Schottky diode is limited by the parasitic elements [3] and the losses due to skin effects [4]. Thus, systematic studies of the Schottky diode parasitic elements and high frequency losses are very crucial in meeting the design goals.

In the search of optimised diode performance, several studies on diode modelling have been performed [5], [6]. In this paper, we present a systematic method to estimate the diode geometry dependent parasitic elements and skin effect losses for diodes operating up to 400 GHz. Different diode geometries, such as pad-to-pad distance, buffer layer thickness and semi-insulating etch depth have been investigated. The equivalent circuit based method as in [7] has been used, where the parasitic elements are extracted through the least square error fitting of the S-parameters simulated in Ansoft HFSS simulator to the lumped equivalent circuit. Simulations are performed with the semi-insulating substrate of 3 μm (for the case of integrated diode on the membrane) and 10 μm (for the case of discrete diode). In addition, high frequency losses are investigated with the similar method, by using lossy conductors and adding a frequency dependent resistor in the lumped equivalent circuit. Analysis of the simulation and measurement results will be presented.

REFERENCES

- [1] E.R. Mueller, "Terahertz radiation: Applications and Sources", *Industrial Physicist*, vol. 9, pp. 27-29, August-September 2003.
- [2] W. Bishop, K. McKinney, R. Mattauch, T. Crowe, and G. Green, "A Novel Whiskerless Schottky Diode for Millimeter and Submillimeter Wave Application," *IEEE MTT-S International Microwave Symposium Digest*, pp. 607-610, 1987.
- [3] T.W. Crowe, "GaAs Schottky barrier mixer diodes for the frequency range 1-10 THz," *International Journal of Infrared and Millimeter Waves*, vol. 10, pp. 765-777, Jul. 1989.
- [4] K. Bhaumik, B. Gelmont, R. Mattauch, and M. Shur, "Series impedance of GaAs planar Schottky diodes operated to 500 GHz," *IEEE Transactions on Microwave Theory and Techniques*, vol. 40, pp. 880-885, 1992.
- [5] J.L. Hesler, "Planar Schottky diodes in submillimeter-wavelength waveguide receivers," Ph.D. dissertation, School of Elect. Eng., University of Virginia, 1996.
- [6] H. Xu, G.S. Schoenthal, L. Liu, Q. Xiao, J.L. Hesler, and I. Weikle, "On Estimating and Canceling Parasitic Capacitance in Submillimeter-Wave Planar Schottky Diodes," *Microwave and Wireless Components Letters, IEEE*, vol. 19, pp. 807-809, 2009.
- [7] A.Y. Tang, V. Drakinskiy, P. Sobis, J. Vukusic, and J. Stake, "Modeling of GaAs Schottky diodes for terahertz application," *34th International Conference on Infrared, Millimeter, and Terahertz Waves*, Busan, Korea: 2009.

A 664 GHz Sub-Harmonic Schottky Mixer

Paul Wilkinson⁽¹⁾, Manju Henry⁽²⁾, Hui Wang⁽²⁾, Hoshiar Sanghera⁽²⁾, Byron Alderman⁽²⁾, Paul Steenson⁽¹⁾ and David Matheson⁽²⁾

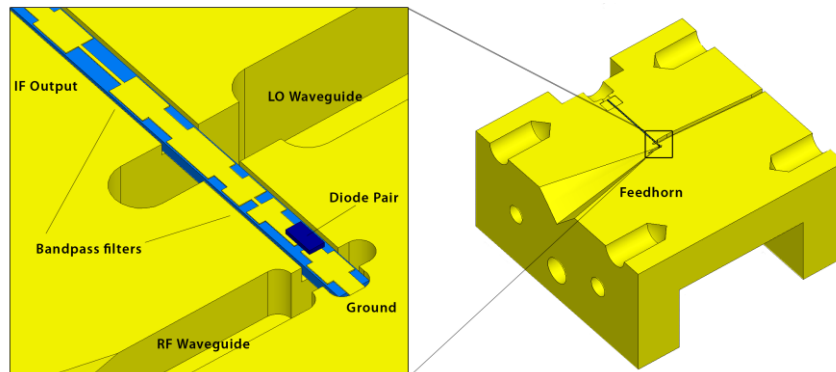
⁽¹⁾ Institute of Microwaves and Photonics
School of Electronic and Electrical Engineering
University of Leeds, Leeds, LS2 9JT
Email: sms4prw@leeds.ac.uk

⁽²⁾ Millimetre-Wave Technology
Space Science and Technology Department
STFC Rutherford Appleton Laboratory
Harwell Science and Innovation Campus
Didcot, OX11 0QX

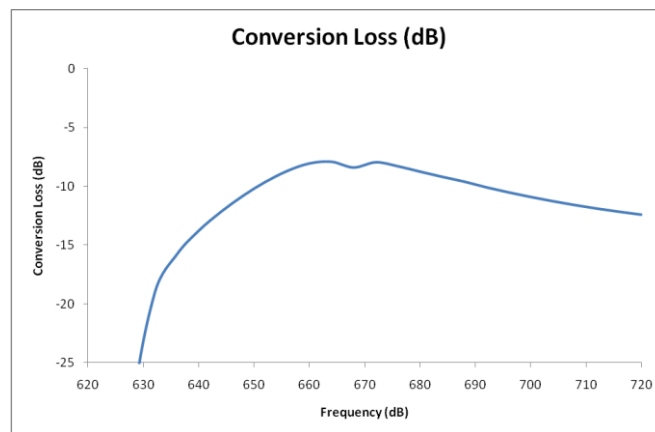
Abstract

This paper presents the design and simulation of a novel fixed-tuned sub-harmonic mixer operating at a central frequency of 664 GHz. The mixer is based on a discrete anti-parallel pair of Schottky diodes fabricated at the STFC Rutherford Appleton Laboratory and flip-chip mounted onto a quartz based microstrip circuit. A double-sideband conversion loss of better than 10 dB is simulated with 4.2 mW of local oscillator power across an RF range of 650-690 GHz, with a minimum of 8 dB at 663 GHz.

The Following is a 3d model of the mixer block complete with integrated diagonal feedhorn.



Simulated performance is shown in the graph below and experimental results will be presented at the symposium.



Design of a Combined Tripler-Subharmonic Mixer at 330 GHz for Multipixel Application Using European Schottky Diodes

J. Treuttel, A. Maestrini, B. Alderman, H. Wang, D. Matheson, P. De Maagt,

Abstract—We present the development of an integrated heterodyne receiver at 330 GHz featuring a balanced tripler and a sub-harmonic mixer embedded on the same substrate. The receiver block has one face dedicated to the feed aperture, and the opposite face to the local oscillator input and the intermediate frequency output. By utilizing only opposite faces this configuration makes building of a full two-dimensional array possible through stacking receiver elements. Moreover, the size of the receiver block is minimised by a small spacing between the mixer and its local oscillator circuit. The input signal of the multiplier stage is between 55 and 60 GHz where high power sources are more commonly available than at sub-millimeter frequencies. A preliminary design and its analysis are described in order to enlight problematics related to circuits composed of several non-linear elements. Packaging constraints are also discussed here since the spacing between two horn antennas is limited by the physical size of the local oscillator and IF connectors on the back face of the pixel.

Index Terms—Frequency Tripler, Sub-harmonic mixer, Heterodyne arrays, Spurious signal, Submillimeter-wave.

I. INTRODUCTION

Theoretical studies of atmospheric sounding from space borne instruments have shown that sub-millimeter wave radiometry offers new perspectives for the characterization of clouds and rain on a global scale. Moreover, the non-ionizing properties of sub-millimeter and terahertz radiation and the relatively low power levels generally required make its use safe for bio-medical diagnostics. Sub-millimeter radiation also has the remarkable property of having only moderate attenuation while propagating through non-polar materials such as paper, wood, glass, plastic or ceramic, and is demonstrably useful for security screening, explosives and contraband detection. The list of applications at millimeter and sub-millimeter wavelengths continues to grow as new fields emerge through the development of increasingly mature technology. Several of these developments are focused on technologies for heterodyne focal plane arrays, in order to ally higher sensitivity, greater mapping speed and large-scale mapping ability [1]. In this context, more widespread use of array receivers will be

encouraged by the availability of integrated components with appropriated packaging. In particular, Schottky array elements give the advantage that they will work at ambient temperatures. The current work is part of a program dedicated to Schottky diode receiver array development, conducted at the Rutherford Appleton Laboratory and held in collaboration with the Observatory of Paris. The motivation for building these receivers is the applications in atmospheric sensing particularly observations of cirrus cloud at Sub-millimeter frequencies (EUMETSAT post-EPS and EU/ESA GMES Sentinel programmes).

A. Circuit Configuration

The main issue for the development of heterodyne receiver array is the integration of components at a high level with special care given to power transmission and dissipation. Mass production, repeatability, miniaturization, and the use of MMICs are also key issues for arrays fabrication. To resolve these questions, it is necessary to optimize the interface between the mixers and the local oscillator unit.

Two different configurations can be used to integrate the mixer and the frequency multiplier; either integrate the mixer and multiplier that are based on separate substrate via waveguide component [2] or combine the mixer and the frequency multiplier on a single substrate [3]. The optimum performance

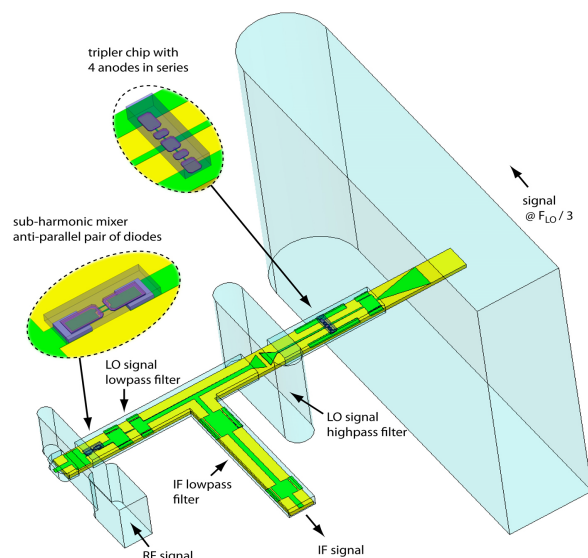


Fig. 1. HFSS view of the preliminary combined tripler/subharmonic mixer design. The high pass filter is not included in the presented results.

J. Treuttel is with Observatoire de Paris, LERMA, 75014 Paris, FRANCE and STFC, Rutherford Appleton Laboratory, Didcot, OX11 0QX, UK. E-mail: j.treuttel@obspm.fr

A. Maestrini is with Universite Pierre et Marie Curie Paris 6.

B. Alderman is with Rutherford Appleton Laboratory, Didcot, OX11 0QX.

H. Wang is with Rutherford Appleton Laboratory, Didcot, OX11 0QX.

D. Matheson is with Rutherford Appleton Laboratory, Didcot, OX11 0QX.

P. DeMaagt is with ESA/ESTEC, Keplerlaan1, 2200 AG Noordwijk ZH, The Netherlands.

of the mixer and the frequency multiplier generally require respectively different epitaxial doping layer of the substrate not possible in the combined circuit case. Nevertheless, the integration of a mixer and multiplier on a single substrate offers a simpler assembly work and higher integration level, which are suitable for large array development.

The block presented in this paper features a combined circuit composed of a balanced tripler and a sub-harmonic mixer integrated within the same circuit. The input signal of the multiplier stage is between 55 and 60 GHz where high power sources are more commonly available than at sub-millimeter frequencies. At E band, commercially available power sources¹ are reaching 27 dBm so make it possible to pump four integrated receivers with the same source.

Both multiplier and mixer are unbiased, which means in the tripler case working in the varistor mode, therefore with limited efficiency. It allows to reduce the number of connectors and also favors easier operation than with biased circuits. The mixer and multiplier circuits are balanced. For the tripler, this leads to an impedance close to pure reactance at the second (idler) harmonic of the input signal [4]. If we consider 20 dBm power at the multiplier input for each of the receiver, the tripler predicts to reach efficiency of 2 to 4 percents enough to pump the mixer.

The IF band is set in the 9-21 GHz band fitting specifications of the PREMIER mission (Process Exploration through Measurements of Infrared and millimetre-wave Emitted Radiation). The preliminary design uses separate flip-chip mounted planar Schottky diodes components to perform the two functions. The electrical parameters of the RAL Schottky diode model considered in the simulations for the mixer diodes are an anode diameter of 1.2 μm , a series resistance of 12 Ω , a zero voltage junction capacitance of 8 fF, a saturation current of 2 fA, an ideality factor of 1.2 and a built-in potential of 0.6 V. The parameters for the tripler diode chosen here are an anode diameter of 2.2 μm , a zero voltage junction capacitance of 6 fF, a series resistance of 4 Ω , a saturation current of 3.10-13 A, an ideality factor of 1.2, a built-in potential of 0.8 V and a breakdown voltage of 8 V.

B. Design methodology

The combined circuit includes six non-linear elements that need to be matched at three different frequencies. The fundamental input source needs to be coupled evenly to the four tripler diodes, the third harmonic generated by these diodes needs to be perfectly coupled to the diodes mixer, and the mixer diodes should be matched optimally at RF frequencies. These conditions have to be fulfilled during a same simulation optimization run.

This type of circuit might present converging issues when performing an harmonic balance simulation with the standard parameters found in ADS software [5]. This is particularly true when it is simulated over a large bandwidth. The methodology for optimizing the circuit in order to reach an optimal conversion loss consists in several steps which have been described in [3]. As a first step, the tripler and mixer diodes

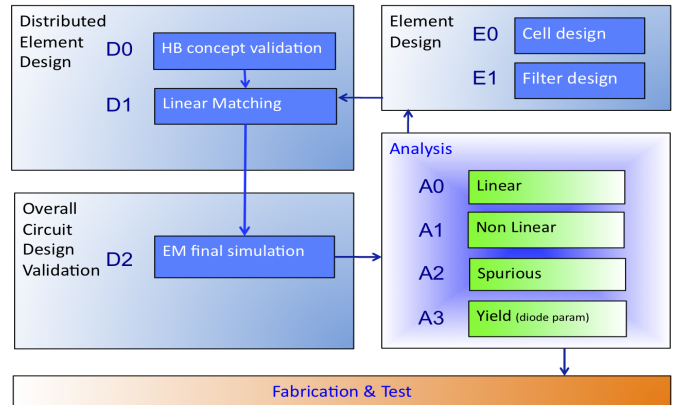


Fig. 2. Design and Analysis methodology for circuits composed of multiple non-linear elements.

optimum impedances are found using the ADS harmonic balance program during two separated simulations. During these simulations, we consider realistic input power conditions (respectively estimated at 20 dBm at multiplier stage input frequency for the tripler diodes and at 2 dBm at LO frequency signal for the mixer diodes). The values of the impedances are found to be $Z_{RF} = 53 + jx43$ and $Z_{LO} = 91 + jx137$ for the mixer diodes and $Z_{in} = 37 + jx3$ and $Z_{LO} = 21 + jx1$ for the tripler diodes. A second step consists in modelling each sub-circuit with a 3D-EM software (Ansys HFSS) and using the resulting Sparameter files for an optimization of the distributed circuit in Agilent ADS. The transmissions coefficients are optimized (D1) to reach an ideal of magnitude of 0.7 for the RF input port to the mixer diode ports, 0.5 for the LO input signal to the tripler diode ports and 0.3535 for the tripled signal to each of the mixer diodes. Adapted weighting factors are applied for each of the matching during the optimization. When the non-linear matching reach the desired coupling with an optimal tuning, one can verify the results with a harmonic balance routine.

Despite a good tuning at our frequencies of interest, the large number of non-linear components makes the circuit model complex and susceptible to harmonic mixing products. We will describe the analysis undertaken in order to cross-check the conversion loss results to the circuit linear matching value and its spurious responses.

C. Circuit Analysis

The result of a preliminary design gives the opportunity of better understanding phenomenon occurring in a circuit susceptible to high harmonic mixing products. A 3D EM simulation of the total circuit over the full bandwidth with HFSS is performed. Special care is given to the convergence of the solution at different frequency. Several frequency sweeps are put together in a same S-parameters 11-ports matrix (6 for the mixer and tripler diodes, 4 for the RF and inut signal through waveguides and 1 for the IF output matching).The matrix is then used in an ADS analysis following the three steps given in Fig.2 and decribed hereafter.

¹see <http://virginiadiodes.com>

1) *Overall circuit linear analysis (steps D2 and A0)*: The linear analysis gives information on the overall circuit matching between the different ports. This result can be compared to the optimization performed in step D1. The matching has slightly shifted from the one found in the distributed model. The RF and input backshorts can be reoptimized for the non linear analysis.

2) *Overall circuit non linear analysis (steps D2 and A1)*: This simulation is performed using the ADS diode model with the parameters given in paragraph A. The previous 11-ports matrix is used to take into account ohmic losses at all frequencies between 100 and 360 GHz (case 1) and 21 GHz and 360 GHz (case 2). The conversion loss is found for case 1 to be a very flat conversion loss between 6 and 7 dB with resonances at 315 and 345 GHz. When the lower frequencies are taken into account at the mixer diode level (case 2), the conversion loss average falls to a 10 dB level with resonances around 326 GHz and 345 GHz. The resonance peaks can be explained by local unbalance seen in the interaction between the tripler diodes or in the magnitude transmission diagram of the input signal overloaded at the center diodes ports and lacking at the extremity diodes ports. The tripler should be reviewed to avoid such effects (step E0). This comparison also highlights the importance of isolating the mixer diode from the frequency band outside the LO band. As a result, a filter element fulfilling this band requirement should be designed (step E1). The spectrum of the fundamental and mixing product signals and their power levels seen by the mixer diodes are given during a spurious analysis simulated at the central frequency point.

3) *Overall circuit spurious signal analysis (steps D2 and A2)*: Spurious signal generation is an issue in non linear circuits. Studies have been conducted to see the effect of parasitic spurious signal at different frequencies coming from bias line or RF port leakage on frequency multiplier output [6]. In our case we consider the spurious generated from intermixing product of the signals inside the circuit, and no outside signal interference is considered. This analysis is particularly useful to determine if unwanted harmonics or mixing product are within the IF band and see the different power levels at frequencies of interest. For this simulations, we have taken a two tone simulation with respectively 1 and 6 harmonics for the RF and input signals and an intermixing order of 7. This minimum order level has been set for accuracy and stability considerations. A significant increase in the signal power level at the fundamental input frequency lands on each of the mixer diodes compared to when ideal isolation is done. This signal appears to be the principal cause of the 3dB degradation of the mixer average performances observed in the non linear analysis.

D. Circuit preliminary performances and main considerations for the final design

The trend of the curve is given with a moving average algorithm to be 10 dB over 12 percent bandwidth for a circuit where the input signal is taken into account at the mixer diodes level.

A second version of the design should consider the effects highlighted during the preliminary design analysis. The main issue is that a good isolation of the signal at the fundamental input frequency propagating in a TEM mode towards the mixer is needed. We note that in similar combined circuit where the isolation is performed by geometric means as in [3] this problem is bypassed by a natural mode selection. The determination of the maximum acceptable power level helps to determine further needed rejection. A study is currently undertaken to integrate a high pass filter with a rejection ≥ 10 dB illustrated in Fig.1.

E. Connector Analysis

The combined circuit described in the first part has the advantage of having the possibility of being integrated in a block where one face of the pixel contains the feed aperture, and the opposite face can be dedicated to the local oscillator input and the intermediate frequency output. The attractiveness of this configuration is that a full two-dimensional array ($n \times m$ elements, where n and $m \geq 2$) is possible.

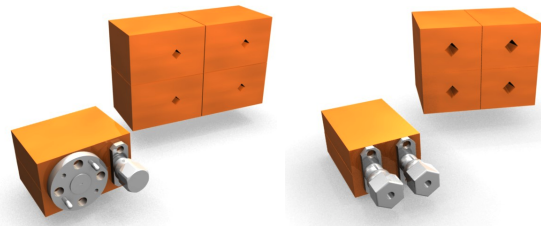


Fig. 3. On-scale pixel block for $n \times m$ arrays. The spacing of the feed horn is 22 x 32 mm (left) and 16 x 22 mm (right).

The specifications of future instrument are a beam spacing of a few wavelengths of the array frequency. In this heterodyne Schottky receiver array, the feedhorn spacing is limited by the physical size of the back connector and standard flange. This leads us to difficult packaging constraints as the wavelength of sub-millimeter frequency signal are on the order of one millimeter. A first solution with an array constituted of different connector type could help reducing the beam spacing. An other solution currently being studied is using a LO/IF diplexer. Indeed, this option give the possibility to have a pixel with only one connectors at its back face, dedicated to the fundamental E band input and the IF output. This solution could be used to a larger scale if injecting the fundamental input signal through V connectors.

II. CONCLUSION

The single pixel receiver block described here includes a combined circuit tripler / sub-harmonic mixer circuit at 330 GHz. The large number of non-linear components makes the circuit model complex and susceptible to harmonic mixing products. The design methodology is described in order to enlight the effect of unwanted signal landing on the mixer, and local unbalance at multiplier level. Predicted performance of a preliminary design suggests a DSB conversion loss with an average value of 10 dB over 12 percents bandwidth with

a 20dBm input power at E band. An analysis of packaging constraints is also provided since the spacing between two horn antennas is limited by the physical size of the local oscillator and IF connectors on the back face of the pixel.

ACKNOWLEDGMENT

This work is being conducted with the ESA program ESA RFQ3-12346/08/NL/ST. The authors would like to thank Thibault Vacelet for drawing the scaled version of the mono-pixel concept with different connector types.

REFERENCES

- [1] G.Narayanan, N. Erickson, and A. W. Lichtenberger, "Integrated Terahertz Heterodyne Focal Plane Array Receivers," *Proc. Far-IR, Sub-MM, and MM Detector Technology Workshop*, April 2002.
- [2] H.Wang, A.Maestrini, B.Thomas, B.Alderman, and G.Beaudin, "Development of a Two-Pixel Integrated Heterodyne Schottky Diode Receiver at 183 Ghz," pp. 490–493, April 2008.
- [3] B.Thomas, B.Alderman, D.Matheson, and P. Maagt, "A Combined 380 GHz Mixer/Doubler Circuit Based on Planar Schottky Diodes," *IEEE Microwave and Wireless Component Letters*, vol. 18, pp. 353–355, May 2008.
- [4] A.Maestrini, J. Ward, J. Gill, H.S.Javadi, E.Schlecht, C.Tripon-Canseliet, G.Chattopadhyay, and I.Mehdi, "A 540-640 GHz High Efficiency Four Anode Frequency Tripler," *IEEE Transactions on Microwave Theory and Techniques*, vol. 53, September 2005.
- [5] Agilent Technologies, Inc. 2000-2009, 5301 Stevens Creek Blvd., Santa Clara, CA 95052 USA, *Advanced Design System 2009 Update 1*.
- [6] G.Chattopadhyay, E.Schlecht, F.Maiwald, R. Dengler, J. Pearson, and I.Mehdi, "Frequency Multiplier Response to Spurious Signal and its Effect on Local Oscillator Systems in Millimeter and Submillimeter Wavelengths," *SPIE Astronomical Telescopes and Instrumentation*, vol. 4855, pp. 480–488, August 2002.

Poster Session P8: Superconducting Mixers

Microwave-assisted Measurement of the Frequency Response of Terahertz HEB mixers with a Fourier Transform Spectrometer

Yury V. Lobanov^{1,*}, Cheuk-yu E. Tong¹, Abigail S. Hedden¹, Raymond Blundell¹, and Gregory N. Gol'tsman²

¹Harvard-Smithsonian Center for Astrophysics, Cambridge, USA

²Moscow State Pedagogical University, Moscow, Russia

*Contact: ylobanov@cfa.harvard.edu, phone +1-617-496-7667

Abstract— We describe a novel method of operation of the HEB direct detector for use with a Fourier Transform Spectrometer. Instead of elevating the bath temperature, we have measured the RF response of waveguide HEB mixers by applying microwave radiation to select appropriate bias conditions. In our experiment, a microwave signal is injected into the HEB mixer via its IF port. By choosing an appropriate injection level, the device can be operated close to the desired operating point. Furthermore, we have shown that both thermal biasing and microwave injection can reproduce the same spectral response of the HEB mixer. However, with the use of microwave injection, there is no need to wait for the mixer to reach thermal equilibrium, so characterisation can be done in less time. Also, the liquid helium consumption for our wet cryostat is also reduced. We have demonstrated that the signal-to-noise ratio of the FTS measurements can be improved with microwave injection.

I. INTRODUCTION

The Fourier Transform Spectrometer (FTS) is widely used to characterize the frequency response of Hot Electron Bolometer (HEB) mixers operating in the Terahertz frequency range [1]-[4]. In such measurements, the HEB mixer is operated as a direct detector of the thermal source which powers the FTS. Appropriate operating conditions (i.e. bias voltage and current) are typically set by heating the HEB device to an elevated temperature around its critical temperature, T_c . This eliminates the need of a THz source to pump the HEB mixer.

It has previously been demonstrated that the injection of microwave radiation can be used to replace some of the required LO power in a THz HEB mixer [5]-[6]. This opens the possibility of performing FTS measurements of an HEB mixer operating at liquid helium temperature by applying microwave radiation. Given that a large number of scans and long integration time are needed for high spectral resolution measurements, the microwave injection method allows us to avoid the effects of any long term thermal instability associated with raising the bath temperature with a heater. In addition, there is no need to wait for the mixer to reach thermal equilibrium and liquid helium consumption in our wet cryostat is also reduced.

Our experiments show that the I-V characteristics of an HEB mixer pumped with microwave radiation differ significantly from those obtained with thermal biasing. This

is in line with prior observations which have shown that the NbN film responds differently to microwave radiation [7]. In spite of the differences, we will show in this paper that the FTS data sets obtained when microwave radiation is applied compare very well to the spectra obtained when the device is heated.

In addition, we report on the observed families of current-voltage characteristics obtained when various amounts of heat, microwave, or terahertz radiation are applied to the mixer.

II. EXPERIMENTAL SETUP

The FTS used in our experiments is based on the Martin-Puplett interferometer and is housed in a vacuum chamber to avoid any atmospheric losses, as is shown in Fig. 1.

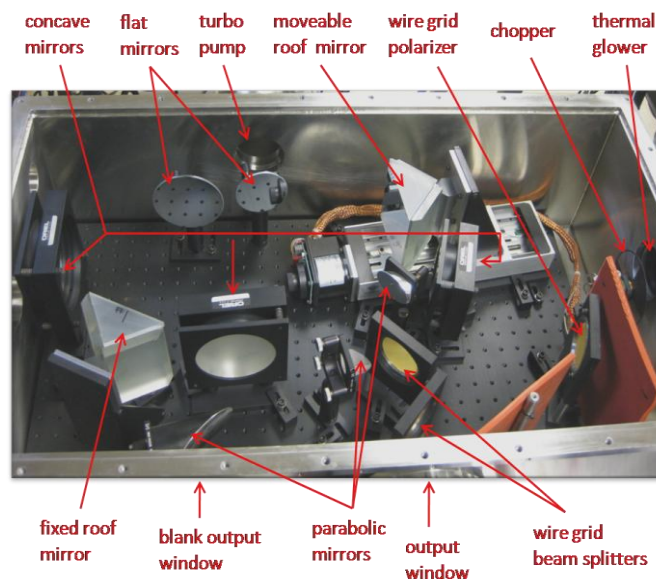


Fig. 1 A photograph of the FTS instrument

Details of the FTS instrument have been described previously [8]. A thermal glower acts as a broadband thermal source. Its radiation is chopped at a frequency of 37 Hz and divided by a wire grid polarizer made from 25 μm gold plated tungsten wires into two beams. The translation stage on which the movable roof-top mirror of the FTS is mounted

provides a maximum displacement of 15 cm that produces spectral resolution of about 1 GHz. However, in our experiments, we generally limit our scan length to ~ 2 cm, corresponding to a spectral resolution of about 8 GHz.

As shown in Fig. 2, the cryostat housing the HEB mixer is positioned in front of the FTS chamber, with its anti-reflection coated crystalline quartz window facing the 0.5 mm Teflon output window of the FTS. This Teflon window imposes a small frequency dependent attenuation over the target frequency range of 0.5 – 1.5 THz.

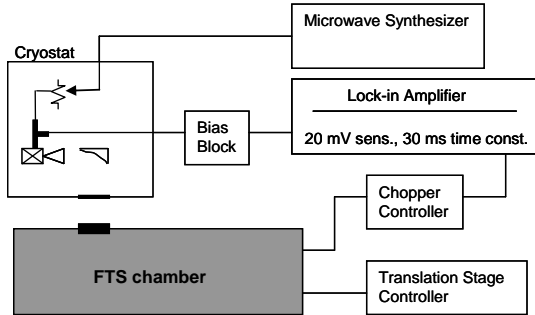


Fig. 2 Schematic diagram of the experimental setup

In these experiments, the HEB mixer measured was mounted in a 0.8 THz mixer block equipped with a corrugated horn feed [9]-[10]. A resistive heater and a diode thermometer, attached to the mixer block, allowed us to vary and measure the temperature of the block. Fig. 3 shows the layout inside the cryostat.

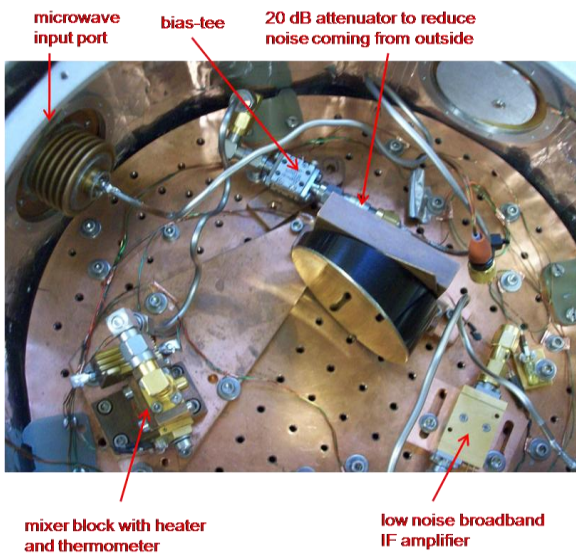


Fig. 3 Cryostat layout

The mixer block was connected to a bias-tee through which DC bias was applied. This was followed either by a low noise cryogenic amplifier for Y-factor characterization or by a 20 dB attenuator, which limits broadband noise, and a stainless steel semi-rigid cable is used to connect to the microwave input port of the cryostat.

An Agilent analog signal generator (Agilent Technology, E8257D) was used to produce a microwave tone up to 40 GHz for microwave injection.

III. I-V CURVES OF HEB MIXERS

In our experiments, we used 800 GHz waveguide HEB mixers produced by the technological group of the MSPU. These mixers employ a ~ 3.5 nm thick NbN film produced by standard methods of photo- and e-beam lithography. Basic properties of the devices are presented in Table I. Devices #1 and #2 belong to two different batches and although their processing was similar, they differ in some features such as I-V and R(T) characteristics.

TABLE I
BASIC PROPERTIES OF THE HEB MIXERS USED FOR EXPERIMENTS

Device	Characteristics of the mixers			
	Size of the active element	Critical temperature	Critical current	R_N
#1	$0.13 \times 1.2 \mu\text{m}$	10 K	220 μA	$\sim 130 \Omega$
#2	$0.12 \times 1.5 \mu\text{m}$	11 K	210 μA	$\sim 60 \Omega$

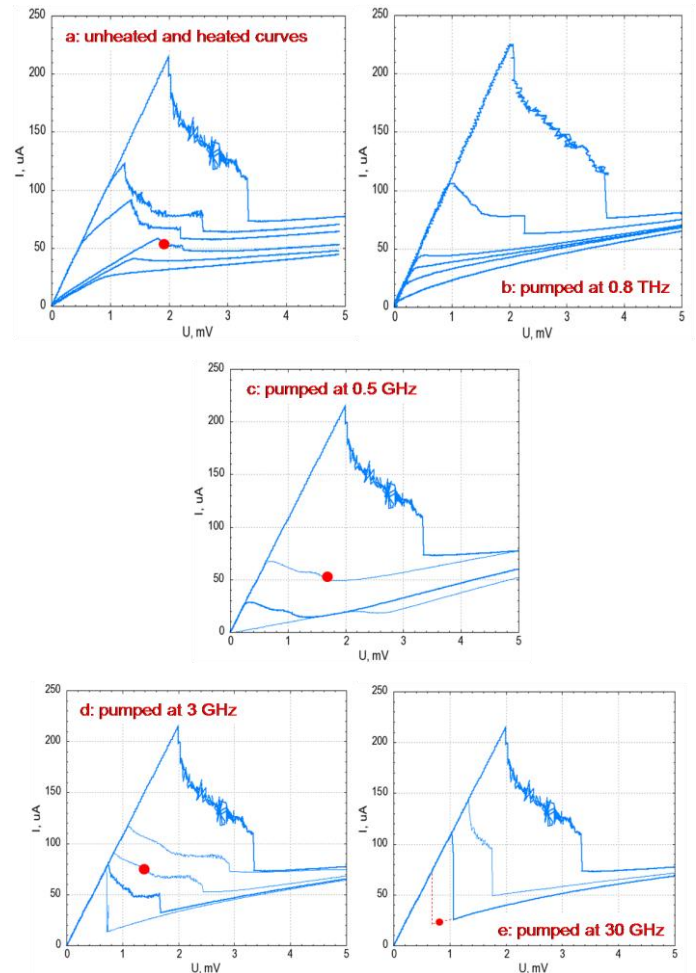


Fig. 4 Families of I-V curves of the HEB mixer (device #1): (a) unheated and heated curves; unpumped and pumped curves for incident radiation of (b) 0.8 THz; (c) 0.5 GHz; (d) 3 GHz; and (e) 30 GHz.

Red dots (·) represent bias points at which the FTS measurements were made. Dashed (---) line shows hysteresis when I-V curve was recorded.

We have studied the I-V characteristics of the two mixers measured with varying amounts of applied heat, terahertz radiation or microwave radiation. Four families of curves are plotted in Fig. 4.

It can be seen that the I-V curves produced by increasing the temperature of the mixer block (Fig. 4-a) most resemble those obtained by pumping the HEB mixer with 0.8 THz radiation that is above the gap frequency of the NbN film (Fig. 4-b). This explains why FTS measurement with thermal biasing can be used to derive the frequency response of HEB mixers. The curves produced by microwave injection (Fig. 4-c – Fig. 4-e) are marked by current switching between the superconducting state and the normal state of the NbN film. At the low end of the frequency range, the switching occurs at the much lower bias voltages. This phenomenon will be reported elsewhere [11].

IV. FTS MEASUREMENT RESULTS AND DISCUSSION

For each family of curves shown in Fig. 4-a, 4-c – 4-e, we have selected bias points marked by red dots in the figure, at which FTS measurements were performed. These bias conditions were chosen to generate the maximum signal-to-noise ratio (SNR) in the interferograms. Fig. 5 shows interferograms obtained after averaging 4 scans at each of the bias points. It should be noted that for injection at 30 GHz the best bias point is found to be on a hysteretic branch of the I-V curve close to a current switching bias setting (shown with the red dashed (---) line in the figure).

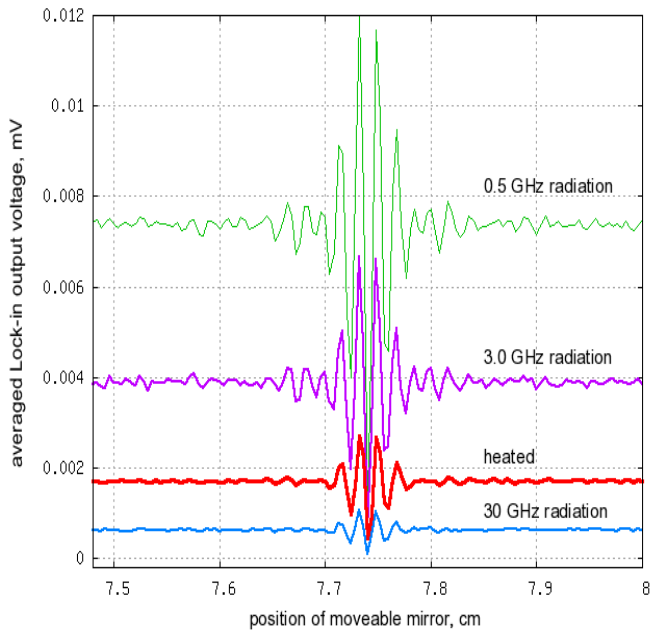


Fig. 5 Interferograms, each an average of 4 scans, for HEB mixer #1. The 4 interferograms from top to bottom were obtained when the device was pumped at 0.5 GHz, pumped at 3.0 GHz, heated, and pumped at 30 GHz respectively.

We noted that the higher direct responsivities associated with these optimal bias settings are related to regions of negative differential resistance around the bias points.

However, in some negative resistive regions, the intrinsic noise of direct detection tends to be higher, especially near current switching regions exhibited with high frequency microwave pumping.

Referring to Fig. 5, the best SNR was obtained when a low frequency microwave radiation was used to pump the HEB mixer. The application of heat produced SNR that was intermediate between radiation injected at 3 GHz and 30 GHz. In spite of the difference in sensitivity the central fringes of the four interferograms are largely identical when normalized. In Fig. 6, we display a pair of normalized interferograms for comparison.

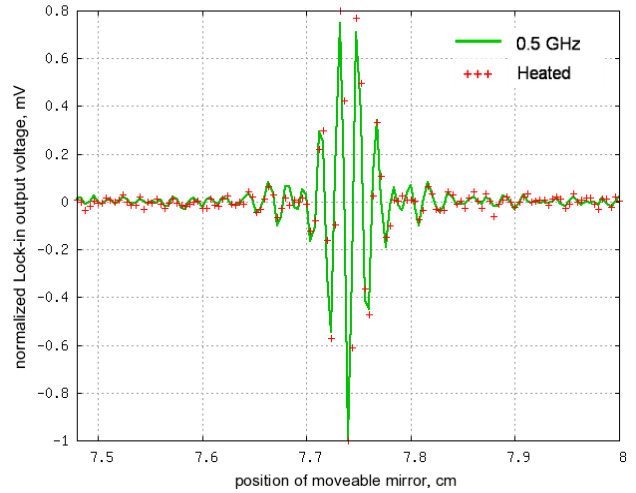


Fig. 6 Normalized response of the FTS when 0.5 GHz microwave radiation is applied (green line) or when heated (red marks +++).

Standard techniques [12] of data apodization of the interferograms with a Hann window followed by a discrete Fourier Transform were used to derive the frequency response of the HEB mixers. In Fig. 7, we compare the normalized power spectra, or frequency response, of HEB mixer #1, obtained when heat or microwave radiation was applied.

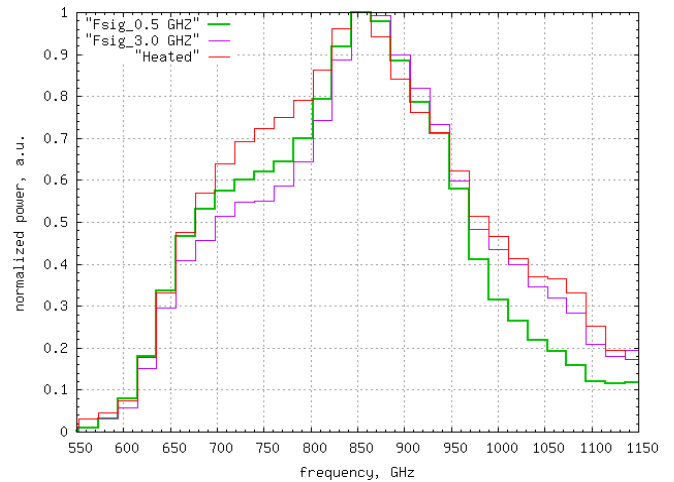


Fig. 7 Normalized power spectra for HEB mixer #1, obtained either through application of 0.5 GHz, or 3 GHz radiation or by heating the device.

In each curve, the spectral resolution is ~ 8 GHz, and the spectral response is centered at about 820 GHz. Furthermore, the shape of the spectral response obtained under different conditions remains constant. Fig. 8 displays a pair of normalized power spectra for mixer #2. Here the responses are a little different, but both show a significant dip at 760 GHz, which we attribute to attenuation from an atmospheric water line. Again, the mixer response to 33 GHz radiation agrees quite well to that obtained by mixer heating.

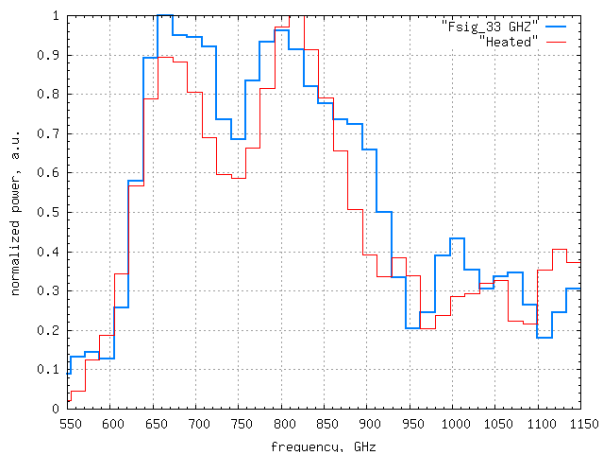


Fig. 8 Normalized power spectra for HEB mixer #2, obtained either through application of 30 GHz radiation or by heating the device.

V. CONCLUSIONS

We have successfully used microwave radiation to study the input bandwidth of HEB mixers with the help of an FTS. Our experiments demonstrate a certain equivalency between applying heat and microwave radiation for setting an appropriate pumping level of the HEB mixer in an FTS measurement.

We have carefully compared FTS data observed when microwave radiation or heating was used and found that microwave pumping can also reproduce the normalized power spectra derived from heating the device. In particular, we have shown that by lowering the injected microwave frequency, a higher responsivity can be achieved for certain bias points, usually associated with noticeable negative differential resistance.

Finally, we have compared I-V curves of HEB mixers pumped by a 0.8 THz LO source or applying heat to those

obtained under different amounts of applied microwave radiation. We notice that in the microwave regime below the superconducting gap frequency, the I-V curves are marked by current switching between the superconducting and normal states.

ACKNOWLEDGMENT

The authors would like to thank S. Paine for helping with FTS setup and the technological group of the Moscow State Pedagogical University for device processing.

REFERENCES

- [1] E. Gerecht, *et al.*, "New results for NbN phonon-cooled hot electron bolometric mixers above 1 THz," *IEEE Trans. Applied Supercond.*, vol. 9, pp. 4217-4220, June, 1999.
- [2] D. Loudkov *et al.*, "Broadband Fourier Transform spectrometer (FTS) measurements of spiral and double-slot planar antennas at THz frequencies," in *Proc. 13th Int. Symp. Space THz Tech.*, pp. 373-382, 2002.
- [3] D. Loudkov, C.E. Tong, R. Blundell, N. Kaurova, E. Grishna, B. Voronov, and G. Gol'tsman, "An investigation of the performance of the superconducting HEB mixer as a function of its RF embedding impedance", *IEEE Trans. Appl. Supercond.* vol.5, pp. 472-475, June 2005.
- [4] J. Baubert *et al.*, "FTS measurement of a 2.5 THz double-slot antenna on SiO₂/Si₃N₄ membrane", *Proc. 16th Int. Symp. On Space THz Techn.*, pp. 260-264, 2005.
- [5] S. Ryabchun, C.E. Tong, R. Blundell, R. Kimberk, and G. Gol'tsman. "Study of the effect of microwave radiation on the operation of HEB mixers in the THz frequency range," *IEEE Trans. Appl. Supercond.*, vol. 17, No. 2, pp.391-394, 2007.
- [6] S. Ryabchun, C.E. Tong, R. Blundell, R. Kimberk, and G. Gol'tsman., "Stabilization of a terahertz Hot-Electron-Bolometer mixer with microwave feedback control," *Proc. 18th Int. Symp. Space THz Tech.*, pp. 193-198, 2007.
- [7] S. Ryabchun, C.E. Tong, R. Blundell, and G. Gol'tsman, "Stabilization scheme for Hot Electron Bolometer receivers using microwave radiation" *IEEE Trans. Appl. Supercond.*, vol.19, pp.14-19, Feb., 2009
- [8] J. Kawamura, S. Paine, and D. C. Papa, "Spectroscopic measurements of optical elements for submillimeter receivers," *Proc. 7th Int. Symp. Space THz Tech.*, pp. 349-355, 1996.
- [9] C.-Y. Tong, D. Meledin, R. Blundell, N. Erickson, J. Kawamura, I. Mehdi and G. Gol'tsman "A 1.5 THz hot-electron bolometer mixer operated by a planar diode based local oscillator", in *Microwave Symposium Digest*, IEEE MTT-S., pp. 751-754, 2003.
- [10] D. Meledin, C.E. Tong, R. Blundell, N. Kaurova, K. Smirnov, B. Voronov, and G. Gol'tsman., "The sensitivity and IF bandwidth of waveguide NbN HEB mixers on MgO buffer layers over crystalline quartz", *Proc. 13th Int. Symp. Space THz Tech.*, pp. 65-72, 2002.
- [11] Y. Lobanov *et al.*, "Large signal frequency response of an HEB mixer: from DC to terahertz", submitted to *Applied Supercond. Conf.*, 2010.
- [12] P. R. Griffiths, and J. A. de Haseth, *Fourier Transform Infrared Spectrometry*, 2nd ed., Wiley-Interscience, 2007.

Superconducting devices for radioastronomy; First steps in Chile: SNS-junction fabrication

V. Conte*, J. L. Giordano^{†§}, J. Luzuriaga[‡], J. Zárata[‡] and H. Pastoriza[‡]

*Applied Sciences Ph.D. Program, Universidad de Talca, Chile

[†]Applied Sciences Department, Universidad de Talca, Chile

[‡]Comisión Nacional de Energía Atómica, Centro Atómico Bariloche, 8400-S.C. de Bariloche, Argentina

[§]Contact: giordano@utalca.cl, phone +56 75 201709

Abstract—We present results of the microfabrication of Josephson Junctions (JJs) of Superconductor-Normal-superconductor (SNS) type, as a first step in the acquisition of the know-how of superconducting devices applied to radioastronomy. A two-junction SQUID was built using a Nb/Al bilayer deposited on a Si wafer. The procedure needs only one mask and a single UV exposure (i.e., one photolithography step). We show the micrograph and the observed non linear characteristic I - V curve at 4K of the first device fabricated in the framework of ALMA Grant 31090010.

I. INTRODUCTION

Almost 50 years ago, using the tunnel quantum effect and the BCS theory Josephson predicted the tunneling of Cooper pairs between two superconductors (S) through an ~ 1 nm insulating barrier (I) [1]. This was the starting point of the development of Superconducting Tunneling Junctions (STJs) for sensitive superconducting quantum interference device (SQUID) magnetometers, detectors and mixers for astronomical applications.

The Atacama Large Millimeter Array (ALMA, 1995-2012) radio telescope is an array of 64 antennas of 12 m-diameter to observe the Universe from the Atacama desert (Chile) at 5 km altitude, where the sky is exceptionally dry and clear. This facility will be the world's most extensive superconducting receiver system with 10 bands in the 31.3 - 950 GHz ($= 9.6 - 0.3$ mm) range providing detailed images from galaxies, stars and planet formation and will be useful for testing cosmological models. Superconducting devices are essential for mm-submm radioastronomy, and measurements of most ALMA bands are only possible by the use of STJ-based detectors [2].

We present here the first experimental results of the ALMA Grants 31070019, 31080012 and the current 31090010, devoted to research and training on superconducting devices for astronomical applications, and also to develop the relevant know-how on Superconductivity in Chile, via Ph.D. theses focused on the new technologies used in radio telescopes. Additionally, this project intends to strengthen the scientific collaboration among local groups and research centers abroad, specifically Caltech/JPL (USA) and Centro Atómico Bariloche (CAB, Argentina).

II. THEORETICAL BACKGROUND

In 1962 Brian Josephson, then a twenty-two year old graduate student, made a remarkable prediction [1] that two superconductors separated by a thin insulating barrier should give rise to a spontaneous (zero voltage) DC current.

The lossless tunneling current was found to depend upon the difference between the phases of the condensate wave functions for the superconductors on each side of the barrier as

$$I(t) = I_c(T) \sin \phi(t) \quad (1)$$

where ϕ is the phase difference and $I_c(T)$ is the maximum current that can be driven through the junction without dissipation.

When a DC potential V_0 is present across the barrier, ϕ varies in time as:

$$\frac{d\phi}{dt} = 2eV_0/\hbar \quad (2)$$

A Josephson Junction can be described in terms of *weak links*. The weak link can be an insulating layer (SIS junction), as Josephson originally proposed, or a normal metal layer (SNS junction) made weakly superconductive by the so-called *proximity effect* (in which Cooper pairs from a superconducting metal diffuse into the normal metal).

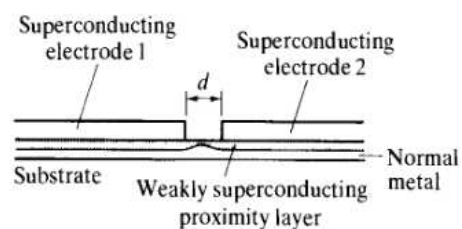


Fig. 1. Proximity effect SNS Josephson junction [3].

In the SNS junction, the normal metal coherence length ψ_n sets the length scale and I_c falls with the thickness d of the normal region as $e^{-\psi/d}$ [3].

We can consider a Josephson junction with a I - V characteristic given by (1) to be in parallel with a capacitor C and a shunt resistance R . If we connect this junction in series with a current source as is shown in Fig. 2, we can analyze the system using the so called resistively and capacitively shunted junction (RSJC Model) where R is the resistance in

the finite voltage regime, while C reflects the capacitance of the electrodes.

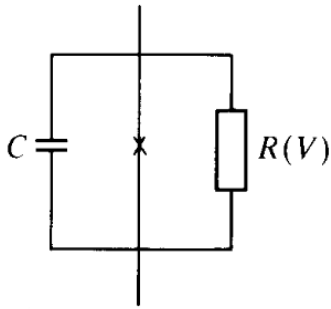


Fig. 2. Equivalent circuit of a Josephson junction by the RSJC model [3].

Within the RSJC model, the time dependence of the phase ϕ is given by the voltage resulting from the parallel distribution of the bias current I in the 3 channels of Fig. 2.

$$I = I_c \sin \phi + V/R + CdV/dt \quad (3)$$

Using (2) and (3) and for a small capacitance C the system is overdamped. The resulting (scaled) I - V dependence is shown in Fig. 3.

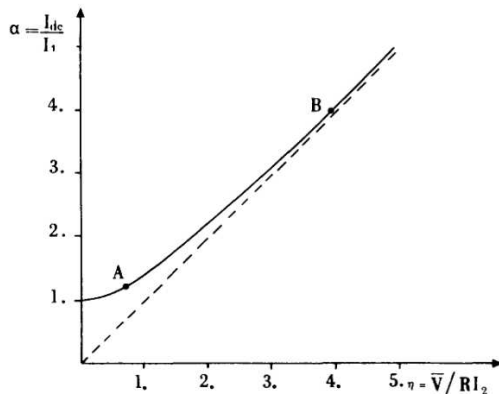


Fig. 3. Overdamped characteristic curve [4].

III. SAMPLES FABRICATION

We have built proximity effect SNS junctions, using the technique of UV Photolithography to define a circuit on a thin film bilayer of aluminium (Al) and niobium (Nb) using a Cr metalized glass plate as photo mask, containing the pattern. The bilayer was deposited by magnetron sputtering on a single crystal Si wafer.

The samples were made at the Centro Atómico Bariloche by the following microfabrication process:

- 1) Metallic Layers Deposition: After reaching a pressure of 10^{-7} Torr, the Ar plasma is turned-on at 50 mTorr. First an Al thin film is grown on the Si substrate by RF magnetron sputtering. Then without breaking the vacuum, a Nb thin film is grown on top of the Al by DC magnetron sputtering. Deposition ratios were 40 nm/min

for Al, using 50 W of RF power and 80 nm/min for Nb using 100 W of DC power, both at pressures of 10 mTorr.

- 2) Resist Application: Spin-coating was used to form a thin layer of UV-sensitive photo resin (positive Microposit 1400-31). This was soft-baked at 90 °C for 120 seconds. The sample was exposed for 5 seconds to UV light through the photo mask. Then we removed the more soluble (UV-exposed) regions by using microposit developer, and after this the sample was hard-baked at 120 °C for 120 seconds.
- 3) Dry Plasma Etching: The metallic layers not covered by the resist are removed using Reactive Ion Etching (RIE) with SF_6 gas.
- 4) Stripping: Removal of resist with acetone.
- 5) Electrical contacts: Four-point contacts were made using epoxy with silver particles (Epotek) and gold wires.

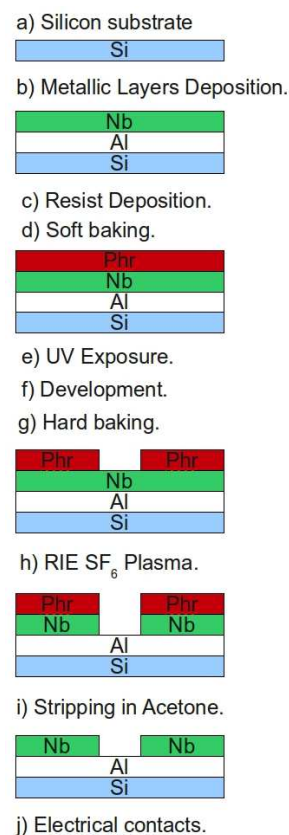


Fig. 4. Fabrication process.

IV. EXPERIMENTAL WORK

We characterized the metallic deposition rate of the sputtering machine by using an UV-Lithography-based technique using the following steps: 1) Photolithography with positive photo resin over Si wafer. 2) Sputtering. 3) Lit-Off with acetone. 4) Measurement in optical profiler (OP).

To measure the resin thickness with the OP, gold or silver were sputtered on the surface.

The etching rate was measured by producing a step in the film by attacking an uncovered region with RIE, using SF_6

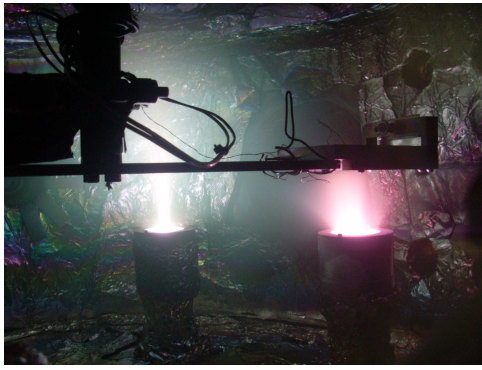


Fig. 5. Photograph of the bi-layer fabrication with niobium (left) and aluminum (right) sources by magnetron DC/RF sputtering under argon atmosphere.

reactive gas. The electrical power used was 300 W at 10 mTorr (for Plasma generation) and 70 W (bias power for acceleration against the sample). The step height was measured using the OP.

The T_c of the Nb/Al bi-layer is determined from the magnetization vs temperature curve measured with a SQUID magnetometer in Zero Field Cooling (ZFC) and Field Cooling (FC) temperature sweeps (Fig. 6).

The patterned sample (Fig. 8) was mounted in a cryostat (Fig. 7) and the I - V characteristic was measured at 4 K in zero applied magnetic field (Fig.9).

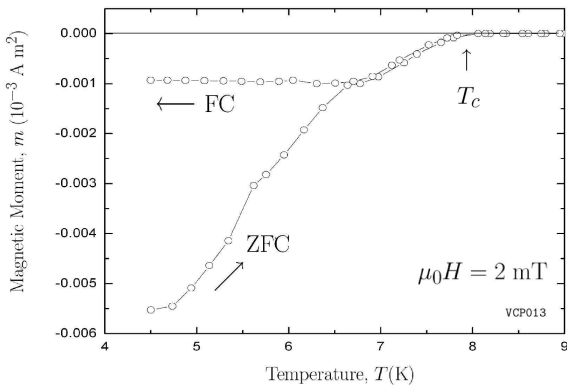


Fig. 6. Magnetization $m(T)$ vs temperature of the Nb (200 nm)/Al (200 nm) bi-layer control sample. The measured T_c is 7.8 K

V. CONCLUSIONS

The result $T_c \sim 8$ K shows the acceptable quality of the Nb (S) layer. According to the Resistively Shunted Junction (RSJ) model [4], [5] the characteristic curve qualitatively corresponds to a junction with negligible capacitance. Quantum interference experiments applying magnetic field on the double SNS-junction loop are being prepared. We are beginning to build SNS junctions, as a starting point in the study of superconducting devices for radioastronomy. The construction and testing of new SNS and SIS junctions in a complete detection system is being planned.

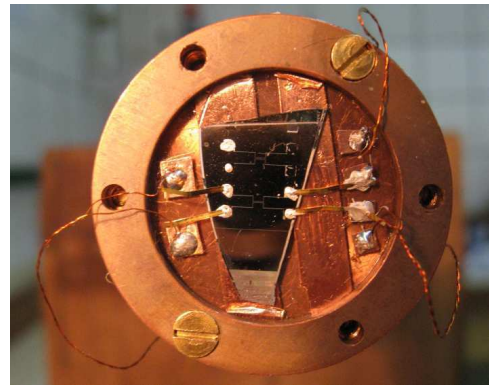


Fig. 7. Sample mounted on the cold finger.

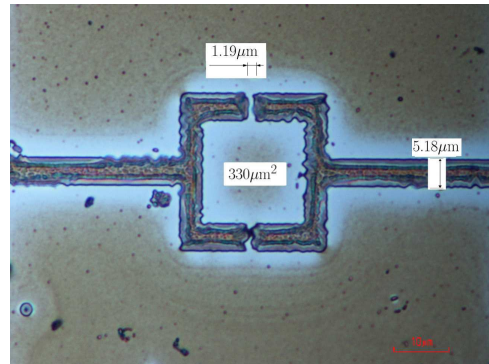


Fig. 8. Micrograph of the first sample. The patterned Nb layer can be seen. The two gaps form the SNS junctions, the Al layer below provides the normal metal path between the superconducting strips. This circuit forms a two slit SQUID.

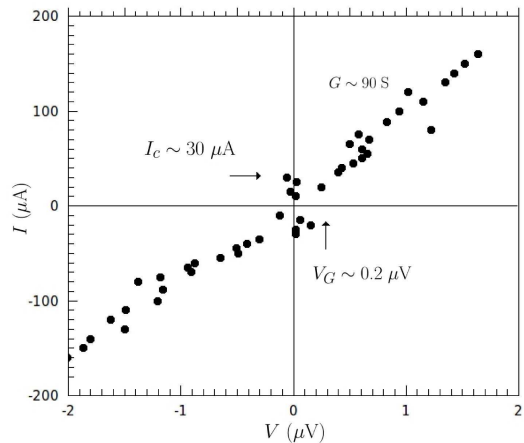


Fig. 9. I - V characteristic curve of the sample at 4K and zero magnetic field showing the damped characteristic as in Fig. 3 [4]

ACKNOWLEDGMENTS

The authors would like to thank ALMA Fund for the Development of Chilean Astronomy, Grants 31080012 and 31090010. We also thank Dr. Jonas Zmuidzinas (CALTECH and JPL at Pasadena, CA, USA) for his scientific support and stimulating discussions. University of Talca for partial support and VCs Ph.D. scholarship. VC also thanks to Gladys Nieva, Julio Guimpel and Ignacio Artola for technical assistance.

REFERENCES

- [1] Josephson B. D. "Possible new effects in superconducting tunneling" *Phys. Lett.* 1, 251, 1962 & Anderson P.W. and Rowell J. M. "Probable Observation of the Josephson Superconducting Tunneling Effect" *Phys. Rev. Lett.* 10, 230, 1963
- [2] Zmuidzinas J. and Harris P. L. "Superconducting Detectors and Mixers for Millimeter and Submillimeter Astrophysics" *Proceedings of the IEEE* 92 1597-1616, 2004
- [3] Tinkham M. *Introduction to Superconductivity* 2nd Ed. Dover, 1996
- [4] Barone A. and Paternò G. *Physics Applications of Josephson Effect* John Wiley & Sons, 1982
- [5] Van Duzer T. and Turner C. W. *Principles of Superconductive Devices and Circuits* 2nd ed. NJ: Prentice-Hall, 1999

Upgrading the SMA 600 GHz Receivers

A. Hedden^{1*}, E. Tong¹, R. Blundell¹, D.C. Papa¹, M. Smith¹, C.E. Honingh², K. Jacobs², P. Pütz², S. Wulff², S. Chang³, and Y. Hwang³

¹Harvard Smithsonian Center for Astrophysics, Cambridge, MA 02138, USA

²I. Physikalisches Institut der Universität zu Köln, 50937 Köln, Germany

³Academia Sinica Institute of Astronomy and Astrophysics, Taipei, Taiwan

*Contact: ahedden@cfa.harvard.edu, phone +1-617-495-7487

Abstract— We present the results of an ongoing effort to improve the sensitivity of the Submillimeter Array (SMA) 660 GHz receivers, including upgrades to the local oscillator (LO) units, improved telescope–receiver coupling optics, and upgraded 660 GHz mixers and receiver inserts. New tunerless varistor multiplier chains have resulted in increased local oscillator (LO) power across the frequency band ($> 10 \mu\text{W}$) and have enabled the upgrade of receiver coupling optics inserts, including the use of a fine (400 lines-per-inch) metal mesh as an RF/LO diplexer. This has resulted in a decrease in overall system complexity and an improvement of about 0.5 dB in signal beam transmission. This work has focused on improving the performance of the double sideband (DSB) SIS receivers designed for operation in the 630-700 GHz frequency range. In collaboration with University of Köln (KOSMA), a new batch of 660 GHz Nb/Al-AIOx/Nb SIS devices with end-loaded stub integrated tuning structures was designed and fabricated. We present an overview of this work and a summary of performance achieved both in a laboratory liquid helium cooled cryostat and in the SMA cryostat environment. First-light SMA observations with an upgraded 600 GHz receiver insert are shown.

I. INTRODUCTION

The Submillimeter Array (SMA) is the world's first operational interferometric telescope for submillimeter-wave astronomy. It is an eight-element array of 6 meter antennas with baselines ranging between 25 and 500 m resulting in high resolution observational capabilities (e.g., 5 to 0.25 arcseconds at 350 GHz). Each antenna contains a cryostat that houses heterodyne receivers covering four frequency bands including 180-250 GHz, 266-355 GHz, 320-420 GHz, and 600-700 GHz [1-2] (Fig.1). Polarization diplexing enables simultaneous observations with low and high frequency receiver pairs. An IF bandwidth of 4-6 GHz in dual frequency operation mode and 4-8 GHz with single frequency operation is now achievable with recent upgrades. The move to wider IF operation and the need for improvement in receiver sensitivity, especially for the high frequency bands where atmospheric transmission is comparatively poor, has prompted an ongoing effort to upgrade the 600 GHz SMA receivers.

We present results of the 600 GHz receiver upgrade work, including outfitting the 600 GHz LO units with new tunerless varistor multipliers capable of delivering more output power across the frequency band, upgrading the telescope – receiver coupling optics to eliminate the Martin-Puplett RF/LO diplexer and improve signal transmission, and the development and characterization of new SIS devices

optimized for performance over the 630-700 GHz frequency range. Details of the main focal points of the upgrade work are presented in II. Measurement setup details and the results of laboratory characterization of new SIS mixers both in a liquid helium cooled test cryostat and in the SMA cryostat are provided in III and IV. A brief summary of this work is given in V.



Fig. 1 SMA cryostat with upgraded 600 GHz receiver insert, LO unit, and coupling optics operating in the lab in Cambridge, MA.

II. 600 GHz RECEIVER UPGRADE PROJECT

We present a brief overview of the upgrade project including details of the SIS device design and fabrication work done in collaboration with KOSMA (A.) and upgrades to the 600 GHz LO units and optics inserts (B).

A. SIS Device Design and Fabrication

A new batch of 660 GHz Nb/Al-AIOx/Nb SIS devices with end-loaded stub integrated tuning structures were optimized and fabricated in collaboration with KOSMA. They are intended to serve as drop-in replacements for those currently in use at the telescope [3-4]. These devices incorporate the standard SMA waveguide probe optimized for performance over 600-720 GHz [5] and were designed to be used with existing mixer hardware.

Images of the 600 GHz mixer blocks and the SIS device integrated tuning structure are shown in Fig. 2. The mixer blocks sandwich the SIS device between a copper bottom piece containing a shorted waveguide cavity and a top block

incorporating a corrugated feedhorn for coupling incident radiation to the device. Overall device dimensions are $160 \mu\text{m} \times 2 \text{mm} \times 40 \mu\text{m}$ and contact to the device is achieved mechanically with two spring wires installed in the top block. Junctions were designed with an area of $0.95 \mu\text{m}^2$ and a critical current density of $12 \text{ kA}/\text{cm}^2$. The devices were fabricated on $200 \mu\text{m}$ thick crystalline quartz substrates (for improved device cooling) using e-beam lithography for the junction definition at KOSMA. Wafer runs were carried out in 2008 and 2009 and bulk wafer liquid helium diptesting performed in Köln reveals overall device-to-device uniformity (Fig. 3) with typical characteristics of $R_{\text{subgap}} / R_N = 14.9$, $V_{\text{gap}} = 2.83 \text{ mV}$, and $R_N = 22.8 \Omega$. Wafer post-processing (e.g., thinning of quartz substrates to $40 \mu\text{m}$ and device dicing) was carried out in Cambridge, MA. Subsequent diptest measurements agree well with the KOSMA bulk wafer characterization and do not reveal performance degradation.

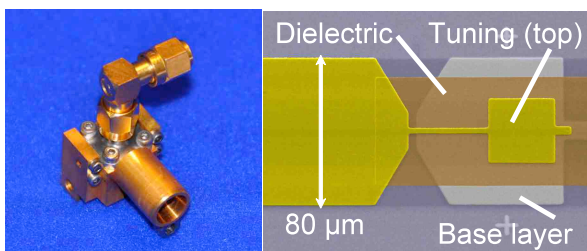


Fig. 2 *Left*: Assembled 600 GHz SMA mixer block. *Right*: SEM image of a 660 GHz SIS device fabricated at Univ. of Köln.

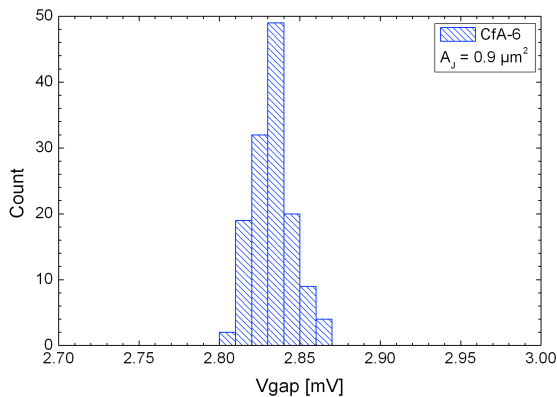


Fig. 3 Histogram of the spread in V_{gap} values measured for CfA-6 batch of 660 GHz SIS devices. The mode V_{gap} value is 2.83 mV .

B. 600 GHz LO and Optics Insert Upgrades

The original 660 GHz LO modules incorporated Gunn-oscillator driven, mechanically tuned multiplier chains with a thick Teflon lens at the output. Because of their particular topology and loss incurred by a waveguide isolator, these units were capable of delivering only about $\leq 5 \mu\text{W}$ of power across the frequency band of interest. Upgrading to a more tightly integrated Gunn-driven ($\sim 100 \text{ GHz}$, $25\text{-}35 \text{ mW}$ output power) tunerless varistor $\times 2 \times 3$ multiplier chain and reflective LO optics has resulted in decreased system complexity and increased available LO power (at least 10

μW across the $640\text{-}700 \text{ GHz}$ band) [6]. Because the signal coupling optics configuration was previously limited by the amount of available LO power (especially for high frequency operation), the original 660 GHz receiver optics inserts used a Martin-Puplett Interferometer (MPI) as an RF-LO diplexer. Drawbacks of this optics configuration include additional motorized actuators required to tune the MPI moveable roof mirror and increased RF transmission loss due to the insertion loss. Additionally, the instantaneous bandwidth limitation of the MPI is incompatible with the SMA's upgrade toward wide IF operation (e.g., $4\text{-}8 \text{ GHz}$ current capability). Increased output power availability of the upgraded 660 GHz LO units has permitted a revision of the RF-LO coupling optics. A fine metal mesh (400 lines-per-inch, $20 \mu\text{m}$ wire thickness) is used to couple the incoming signals to the receiver insert, resulting in $\sim 5\%$ LO and $\sim 95\%$ RF coupling. The new coupling optics improves the signal beam transmission by about 0.5 dB .

III. LABORATORY MEASUREMENT SETUP

We present an overview of the measurement setups used to characterize the sensitivity of the upgraded 660 GHz mixers both in a laboratory liquid helium cooled test cryostat (A) and in the SMA cryostat environment (B).

A. Liquid Helium Cryostat

A series of receiver noise measurements made in the laboratory in a liquid helium cooled IR Labs test cryostat were used to assess the sensitivity of upgraded 660 GHz mixers. Receiver Y-factor measurements were made using room-temperature (295 K) and liquid nitrogen cooled (77 K) absorber loads. These measurements were made across the $630\text{-}700 \text{ GHz}$ frequency band with a 600 GHz LO unit incorporating a Gunn oscillator driven, tuneable $\times 2 \times 3$ multiplier chain from RPG. A curved mirror was used to couple the incident signal to a wire grid diplexer oriented at a 7° angle for minimal RF signal loss (e.g., 7° corresponds to a 1.5% loss or 4.5 K at room temperature). A removable sheet metal hood was used to change between ambient and cooled absorber loads for Y-factor measurements.

A photograph of the cryostat interior is shown in Fig. 4. The vacuum window of the cryostat was a $0.1''$ thick crystalline quartz window with an $80 \mu\text{m}$ thick polyethylene anti-reflection (AR) coating. Three layers of 8 mil thick Zitec attached to the 77 K radiation shield and to the 4 K cold plate were used as infrared blocking filters and a cold mirror was used to couple incident RF and LO signals to the mixer feedhorn. The mixer and mirror share the same OFHC mount to ensure optimal signal coupling at cryogenic temperatures. A coil of Nb wire was used to generate a magnetic field used to suppress the Josephson noise of the SIS device and a $4\text{-}6 \text{ GHz}$ cryoisolator was used both to inject the device DC bias and to curb reflections between the low noise amplifier (LNA) and the mixer. The LNA is a multi-stage InP HEMT amplifier providing $\sim 25 \text{ dB}$ of gain and 3.5 K noise across the $4\text{-}6 \text{ GHz}$ IF. A room temperature IF chain consisting of a MITEQ $4\text{-}6 \text{ GHz}$ amplifier and a 5 GHz bandpass filter were used along with an HP power

meter to measure receiver total output power for Y-factor characterization.

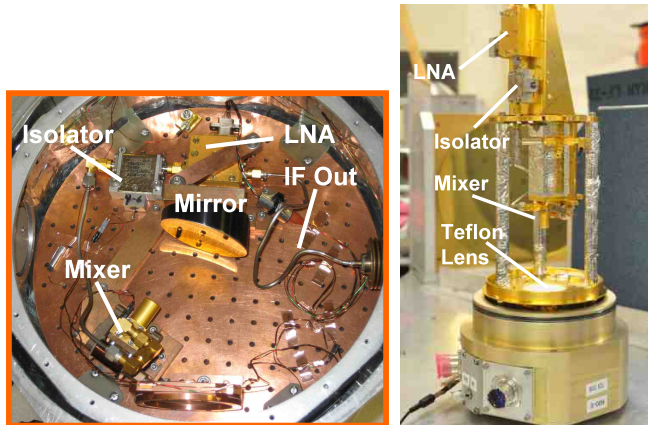


Fig. 4 *Left*: Photograph of interior of IR Labs liquid helium cryostat (4K cold plate). *Right*: Photo of upgraded 600 GHz SMA receiver insert cartridge. Vacuum window is located on the bottom along with feed-through connections. The radial o-ring vacuum seal on the cartridge is also visible.

B. Laboratory SMA Cryostat

Fig. 4 shows a photograph of an upgraded SMA 600 GHz receiver insert. The RF and LO signal (provided by the Gunn-driven solid state multiplier chain) are combined optically prior to entering the insert (see II B and Fig. 1). The RF/LO signals enter the insert through an AR-coated crystalline quartz vacuum window and pass through several layers of Zitex IR-blocking filters mounted to the 70 K radiation shield. A cooled Teflon lens (~100 K at the lens center) mounted to the 70 K shield is used to couple the incident signals to the mixer feedhorn. The SIS mixer sits at the heart of the receiver insert and during operation, the mixer mount is connected to the cold head of a closed-cycle Joule-Thomson mechanical cryocooler with multi-layered high-purity copper heat straps to minimize thermal losses. The mixer is connected via a 6” stainless steel semirigid cable to a 4-8 GHz Pamtech cryoisolator used to mitigate reflections between the mixer and a 4-8 GHz HEMT LNA, providing ~30 dB of gain and 9 K noise. Y factor measurements were accomplished by removing the central turning mirror used to couple the incident sky signal to the receiver optics insert during normal telescope operations and directing the beam across the optics cage (Fig. 1) to room temperature and liquid nitrogen cooled absorber loads.

Y-factor measurements across the IF passband were made using a sweepable, programmable Hittite 10 MHz-20 GHz signal generator to supply a 2nd LO for a room temperature mixer. A 2-18 GHz Krytar power splitter was used to supply the 4-8 GHz receiver IF to the RF input of the 2nd mixer. The signal generator was swept from 3-9 GHz in steps of 0.1 GHz and the resulting signal (2nd IF = 650 MHz) total power was detected with an HP power meter. Measurements were recorded for the receiver looking at room temperature and cooled absorber loads.

IV. RESULTS

We present the results of receiver characterization in the liquid helium cooled cryostat (A) and in the SMA cryostat environment (B).

A. Liquid Helium Cryostat Performance

A comparison of SIS DC-IV characteristics between diptest data and measurements made in the liquid helium cooled cryostat reveal that the device is operating near 4.2 K with $V_{gap} = 2.83$ mV, $R_{subgap} / R_N = 20$, and $R_N = 26 \Omega$. Using the measurement setup described in III A, a series of Y-factor measurements were made for the upgraded 660 GHz mixer in the lab test cryostat over the 630-700 GHz frequency range. These measurements resulted in Y factors spanning 1.94-2.22 (with best performance ~ 670 GHz). This corresponds to double-sideband (DSB) receiver noise temperatures of $T_{rec} = \sim 100-150$ K. Mixer conversion loss was calculated over this frequency range and resulted in ~2-5 dB conversion loss. A comparison was made with Y-factor measurements obtained using a 600 GHz SIS device from an older batch with characteristics typical of the devices currently being used at the telescope. We observed good improvement in sensitivity; T_{rec} spanned ~160-220 K for the older device in the same test cryostat measurement setup.

SMA Cryostat P-V Curves at 684 GHz:

$V_{bias} = 2.3$ mV, $I_{jcn} = 30$ uA, $Y = 1.80$, $T_{rec} = 190$ K

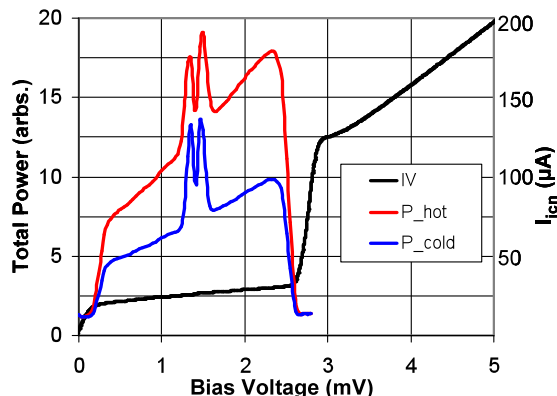


Fig. 5 Typical DC-IV curves and total power (PV) measurements made for the upgraded 660 GHz receiver insert in the lab SMA cryostat. Device bias parameters and Y-factor results are shown.

B. SMA Cryostat Performance

After characterization in the liquid helium cryostat, the same 660 GHz mixer was incorporated into an SMA receiver insert and its performance was measured in a laboratory SMA cryostat (see III B for a description of the setup). DC-IV curves taken in the SMA cryostat reveal that the device was operating at a warmer temperature (~4.8 K) than in the liquid helium cooled cryostat, with $V_{gap} = 2.80$ mV, $R_{subgap}/R_N = 16$, and $R_N = 25 \Omega$. Typical SIS device DC-IV curves and swept total power curves at 684 GHz are shown in Fig. 5. Y-factor measurements over the frequency band of interest reveal elevated noise temperatures compared with results in the liquid helium cryostat, with $T_{rec} = \sim 190-280$ K over 630-700 GHz (Fig. 6). The observed difference in sensitivity is likely attributable to multiple factors, including warmer device operating temperatures and increased IR

loading in the SMA cryostat environment (e.g., ~ 100 K Teflon lens in SMA insert vs. 4 K mirror in the test cryostat). As described in IV B, Y factor measurements were made over the 4-8 GHz IF passband for the receiver operating at 632 GHz. The results are shown in Fig. 7 and reveal that the upgraded receivers provided a wider IF coverage of up to > 7 GHz which fits into the recent IF bandwidth upgrade of the SMA. These measurements were limited by resonance effects observed at ~ 7.5 GHz with the bias tee supplying the SIS DC. The bias tee will be replaced in the future.

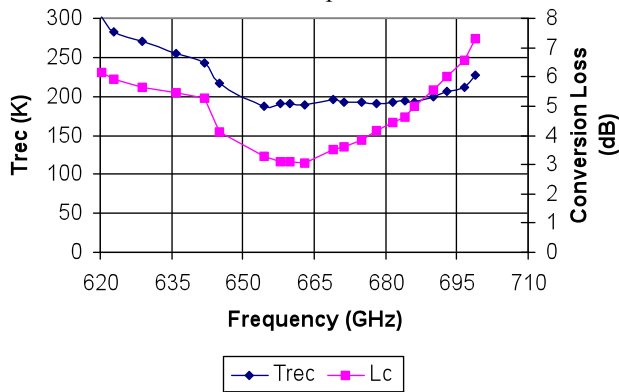


Fig. 6 Measured T_{rec} (left, blue) and mixer conversion loss (right, pink) over the 620-696 GHz frequency range for a receiver insert with an upgraded 660 GHz mixer operating in the laboratory SMA cryostat.

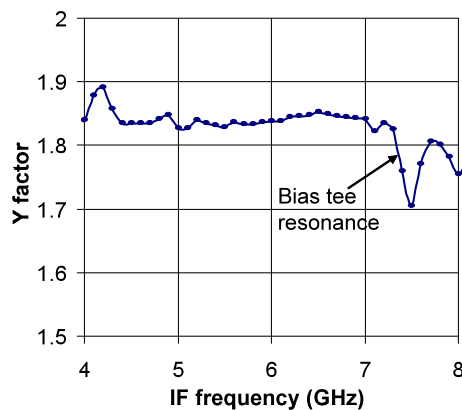


Fig. 7 Y-factor measurements made at 632 GHz over the 4-8 GHz IF passband for an upgraded 660 GHz receiver in the SMA cryostat. Measurements made from 3-9 GHz in steps of 0.1 GHz looking at a room temperature and liquid nitrogen cooled loads. Resonance effects with the bias tee used to provide SIS device bias are apparent at ~ 7.5 GHz.

C. First Results at the Telescope

New 660 GHz devices have been incorporated into several receiver inserts now at the SMA. One of these upgraded inserts has been operating at the telescope since the beginning of the 2009 fall-winter observing semester and the other was shipped for installation last week. Observations were recently made at 658 GHz toward the evolved star VX Sgr, the brightest submillimeter water maser, as part of recent 600 GHz receiver testing. The resulting spectrum representing the vector-average of all baselines with the antenna containing a new 660 GHz receiver is shown in Fig 8. Observations were made with the SMA operating in “very extended” configuration, corresponding to a maximum

baseline of 500 m and a synthesized beam of < 0.25 arcseconds during very good weather conditions (atmospheric opacity at 225 GHz ~ 0.05). The frequency resolution of the spectrum is ~ 1 MHz.

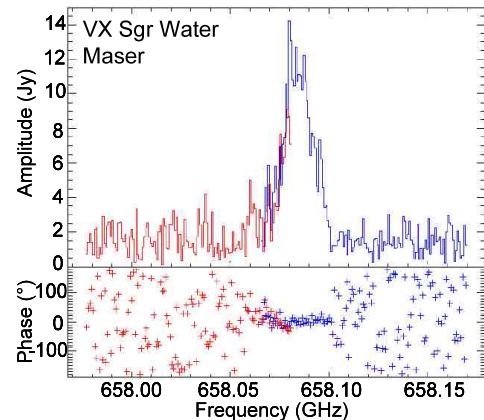


Fig. 8 Spectrum at ~ 658 GHz toward VX Sgr made with the SMA. Spectrum is vector average of all baselines containing Antenna 2 (with upgraded 660 GHz receiver insert).

V. SUMMARY

We report on the status of an ongoing project to upgrade the performance and sensitivity of the 600 GHz SMA receivers. The LO units have been upgraded with new tunerless varistor $\times 2 \times 3$ multiplier chains, resulting in increased LO output power ($> \sim 10 \mu\text{W}$) across the 640-700 GHz frequency range. This has enabled the receiver coupling optics to be upgraded. A fine metal mesh is used as an RF/LO diplexer instead of a MPI, resulting in less overall complexity and has improved signal beam transmission by ~ 0.5 dB. New SIS mixers were designed, fabricated, and characterized in collaboration with Univ. of Köln for operation in the 630-700 GHz frequency range. Results of laboratory Y-factor measurements are presented for operation in both a liquid helium test cryostat and in the lab SMA cryostat. DSB T_{rec} of 100-150 K were achieved over the design frequency range in the liquid helium cooled cryostat. This shows good improvement compared with the sensitivity of typical SIS devices currently in use at the SMA measured under the same laboratory operating conditions. Y-factor measurements made across the IF passband indicate that the upgraded receivers provide wider IF coverage, up to > 7 GHz, which fits into the recent IF bandwidth upgrade of the SMA. First-light observations with an upgraded 660 GHz SMA receiver insert are presented.

ACKNOWLEDGMENT

We wish to thank Dr. Kenneth Young (Taco) for his help observing and for the VX Sgr spectrum.

REFERENCES

- [1] R. Blundell, “The Submillimeter Array Antennas and Receivers,” *Proc. of the 15th International Symp. on Space THz Tech. ISSIT04*, April 27-29, 2004. [Online]. Available: <http://adsabs.harvard.edu/abs/2005astro.ph..8492B>
- [2] R. Blundell, “The Submillimeter Array,” 2007. [Online]. Available: <http://www.cfa.harvard.edu/sma/general/IEEE.pdf>

- [3] C.-Y.E. Tong, R. Blundell, D.C. Papa, J.W. Barrett, S. Paine, X. Zhang, J.A. Stern, and H.G. LeDuc, "A Fixed-Tuned SIS Receiver for the 600 GHz Frequency Band," *Proc. of the 6th International Symp. on Space THz Tech. ISSTT95*, pp. 295-304, (ed. J. Zmuidzinas), Pasadena, CA, March, 1995.
- [4] C.-Y.E. Tong, R. Blundell, K.G. Megerian, J.A. Stern, and H.G. LeDuc, "Quantum-limited Mixing in a Transformer-Coupled SIS Resonator for the 600 GHz Frequency Band," *Proc. of the 13th International Symp. on Space THz Tech. ISSTT02*, pp. 23-32, (ed. E. Tong), Harvard Univ., Cambridge, MA, March, 2002.
- [5] W. Zhang, C.-Y.E. Tong, and S.C. Shi, "Scaled Model Measurement of the Embedding Impedance of a 660-GHz Waveguide SIS Mixer with a 3-Standard Deembedding Method," *IEEE Microwave and Wireless Components Lett.*, vol 13, no. 9, pp. 376-378, Sept. 2003.
- [6] S. Chang, C.E. Tong, A. Hedden, Y. Hwang, and Blundell, R., "A 660 GHz Local Oscillator Subsystem: Design, Testing, and Alignment," *Microwave Conference, 2009. EuMC 2009*, pp. 834-837, Sept.2009.

Implementing a Modular 650 GHz Sideband-Separating Mixer

R. Hesper^{*}, A.M. Baryshev[†], G. Gerlofsma^{*}, F.P. Mena[§],
T. Zijlstra[‡] and M.C. Spaans^{*}

^{*} NOVA/Kapteyn Astronomical Institute, University of Groningen, The Netherlands
Email: r.hesper@sron.nl

[†] SRON Netherlands Institute for Space Research, Groningen, The Netherlands

[‡] Kavli Institute of Nanoscience, Delft University of Technology, The Netherlands

[§] Electrical Engineering Department, Universidad de Chile, Santiago, Chile

Abstract

The ALMA band 9 receiver cartridge (600-720 GHz), which currently is in full production, features two single-ended (dual sideband) SIS mixers in orthogonal polarizations. In the case of spectral line observations, the integration time to reach a certain desired signal-to-noise level can be reduced by about a factor of two by rejecting the unused sideband.

A design study for a modular sideband-separating (2SB) mixer, suitable for retrofitting with minimal impact into the existing band 9 cartridges, has been presented on this conference last year. The design builds on the monolithic proof-of-concept 2SB mixer that was developed at SRON over several years.

Here, we present the first implementation of the modular 2SB mixer concept. A mechanical prototype (omitting the RF structure) was manufactured, and several improvements were fed back into the design. After that, a full prototype was produced, using micro-milling for the RF structures. We hope to present the first noise temperature and sideband separation results of the new mixer.

Modeling SIS Junction Arrays for APEX Band 3 (385–500 GHz)

D. Henke^{1,*}, D. Meledin², R. Monje³ and V. Belitsky²

¹*NRC Herzberg Institute of Astrophysics, Victoria, Canada*

²*Chalmers University of Technology, Gothenburg, Sweden*

³*California Institute of Technology, Pasadena, USA*

*Contact: Doug.Henke@nrc-cnrc.gc.ca, phone +1-250-363-6937

Abstract— A methodology for the modeling of superconducting-insulator-superconducting (SIS) junction arrays will be presented and compared with measured results. In many cases, junction arrays (either in parallel or series) are treated as a single equivalent junction. The APEX Band 3 (385–500 GHz) receiver design has been implemented with two junctions connected in parallel via a section of inductive microstrip line. In this case, it is desirable to separately model each junction as the pumping between junctions is no longer symmetrical across the entire band. Since the performance of the SIS junction depends on its terminating network, a complicated interaction occurs when another junction is part of the embedding impedance and, therefore, there remain aspects of its performance that are difficult to analyse. A simplified model, demonstrated with MATLAB, will be given and compared with a more complete model implemented using a common circuit simulator, Agilent ADS. In both cases, each junction is represented by a quasi 5-port network determined using the quantum theory of mixing. The model is then used to predict the performance of the APEX Band 3 mixer and compared with measured results.

I. BACKGROUND AND MOTIVATION

One common topology for superconducting-insulator-superconducting (SIS) mixer design is to use parallel junctions connected by a section of inductive microstrip line. This has been referred to as the twin junction, as in [1], parallel-connected twin junctions (PCTJ) in [2] and an asymmetric “two-feed” configuration [3]. The twin junction has a wide operating bandwidth, as first proposed in [4], and improved power handling, as is common to all junction arrays. The twin junction also offers a unique advantage due to its self-terminating structure such that the dependence of the admittance of the connecting circuitry (i.e., the probe) is reduced; that is, for each junction the opposite junction is in parallel with the rest of the circuit admittance.

The twin junction may be impedance matched using values realizable with microstrip transmission line, given the SIS junction fabrication constraints. A simplified waveguide-based design approach consisting of an E-probe, microstrip quarter-wave transformer, and twin junction is outlined below:

- Choose the lowest reliable $R_N A$ for fabrication of the wafer, since lower $R_N A$ implies broader bandwidth (where $Q = \omega R_N C_J = \omega (R_N A) C_S$ is a measure of bandwidth, R_N is the normal state resistance, C_J is the junction capacitance, A is the

junction area, and C_S is the specific capacitance). A good design value is $\sim 20\text{--}30 \Omega \mu\text{m}^2$.

- Design an RF probe with the lowest achievable impedance covering the frequency range; often resulting in a value approximately 35Ω .
- Choose a suitable characteristic impedance for the microstrip quarter-wave transformer. Fabrication constraints limit the upper range of characteristic impedance of the microstrip to around 13Ω (given a single deposition process step of SiOx with a thickness between 100–300 nm and minimum Nb line widths of $\sim 5 \mu\text{m}$).
- With the given probe and quarter-wave transformer impedances, this results in a transformed impedance of a few Ohms. Since SIS junctions have an RF impedance approximately equal to R_N at these frequencies of interest, the twin junction circuit has an impedance close to $R_N/2$ at the mid-band frequency, therefore a target R_N of $\sim 6\text{--}8 \Omega$ is used and the junction size determined.
- The length of the microstrip connecting the junctions is chosen so that the input impedance of the twin circuit has a resonance centred within the band.

As can be seen from this approach, impedance matching to the probe (or coupling at RF) is emphasized. Following this methodology, a promising design for the APEX telescope receiver band 3 (385–500 GHz) was shown in [5]. It is novel, employing a key integration of the LO coupler which drives many features of the design. The coupler, in this case, also serves as the quarter-wave transformer between the probe and the twin circuit, and is a hybrid slot microstrip coupler which employs the use of slots cut into the ground plane to achieve the desired coupling. Another feature of the slots is that the LO feeding circuitry is de-coupled from the IF, reducing the IF capacitance.

Typical results of the mixer chip are shown in Fig. 1 and indicated a frequency offset in the noise performance. Several key improvements were made in the processing, described in [6], yet still the offset persisted. Furthermore, it was difficult to differentiate between the effects of the integrated LO circuitry and the matching to the twin SIS structure; this served as motivation for a more detailed look at the interaction between the two junctions.

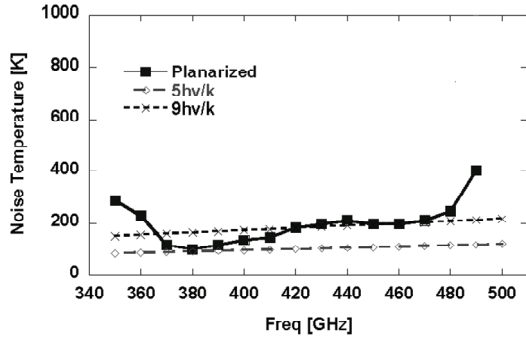


Fig. 1 Measured DSB results showing a frequency offset in performance. Figure is from [6].

II. FIRST APPROACH USING MATLAB

As pointed out in [3], the large signal response (i.e., the LO signal) is distributed between the junctions asymmetrically across the entire frequency band. Also, since the performance of the SIS junction depends on its terminating network, a complicated interaction occurs when another junction is part of the embedding impedance and aspects of its performance are difficult to analyse. How does the inevitable phase difference between the junctions affect the performance? How do the noise components of each junction combine? What is the resulting noise and signal power delivered to the IF? What role does pumping symmetry between the junctions play? To address these questions, each junction was represented using the theory outlined in [7].

The usual simplifying assumptions were made concerning the large signal analysis; a quasi 5-port analysis was used for each junction with only the fundamental of the LO considered but with the sideband harmonics terminated by the junction capacitance [8].

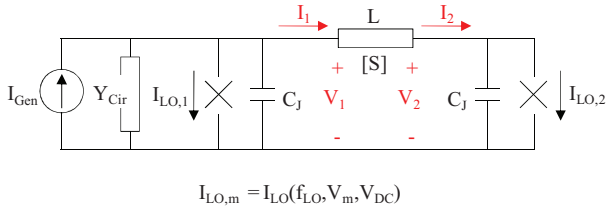


Fig. 2 Large signal view of twin circuit. V_1 and V_2 are the complex large signal voltages that determine the pumping level for each junction. I_{LO} is the complex tunneling current through each SIS junction as given in [7], I_{Gen} is the generating current source of the LO, Y_{Cir} is the admittance of the entire circuit excluding the twin circuit (e.g., the probe and transformer), C_J is the junction capacitance, and L is the s-parameter matrix describing the inductive microstrip line between the junctions.

Fig. 2 illustrates the circuit that must be solved for each LO frequency. A simplifying assumption can be made such that one may assume that I_{Gen} may be adjusted, in amplitude and phase, so that V_2 has zero phase and some initial magnitude [3]. For example, as an initial starting point, the LO pumping across *junction 2* may be set at $\alpha_2 = eV_2/hf_{LO} = 1$. Under this simplification, V_1 may be found using:

$$I_2 = Y_{CJ}V_2 + I_{LO,2} \quad (1)$$

and

$$V_1 = A(V_2) + B(I_2) \quad (2)$$

where A and B are from the ABCD matrix of the microstrip line connecting the junctions. From this it is clear that the pumping symmetry of the junctions is determined by the relationship between C_J and the length of microstrip line between the twin junctions.

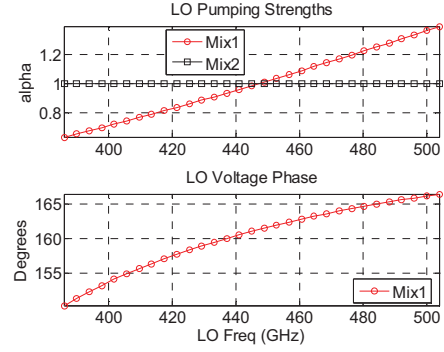


Fig. 3 Large signal voltage distribution between junctions in the twin circuit as illustrated in Fig. 2. In this case, the length of microstrip line connecting the junctions has been chosen to resonate at the middle of the band. Note that the phase difference is the LO phase across *junction 1* with respect to *junction 2*.

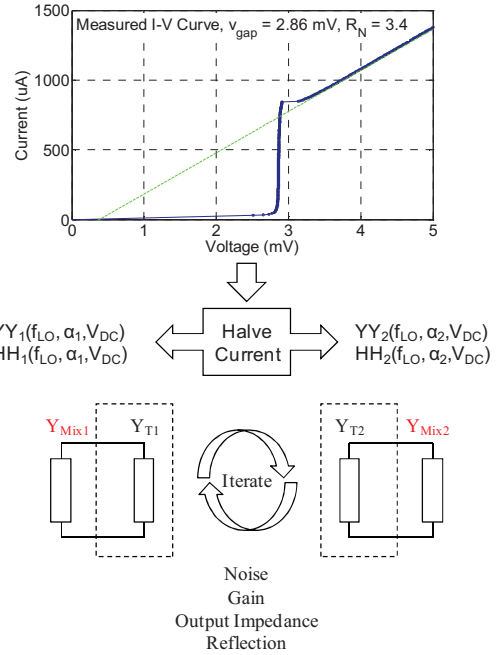


Fig. 4 Overview of the small signal modeling approach for the twin junction mixer. Beginning with a measured I-V curve, the small signal admittance and noise correlation matrices, YY and HH , are found according to the LO pumping levels (e.g. shown in Fig. 3). The small signal parameters are then calculated according to the termination matrix, Y_T , for each junction (shown in Fig. 5).

Fig. 3 shows how the relative pumping relationship between each junction undergoes a reversal above the

resonant frequency. Note that in practice, it is not possible to distinguish between the current of each junction during measurement and, in realistic tuning, as the LO power is optimised, the current through each junction is simultaneously established. In this way, it is seen that Fig. 3 is a simplification, but it is useful for analysing the pumping asymmetry and to therefore better understand the twin tuning circuitry. In paragraph III, the assumption of pumping levels is extended by constraining both junctions to a fixed value in an effort to more closely replicate practical tuning.

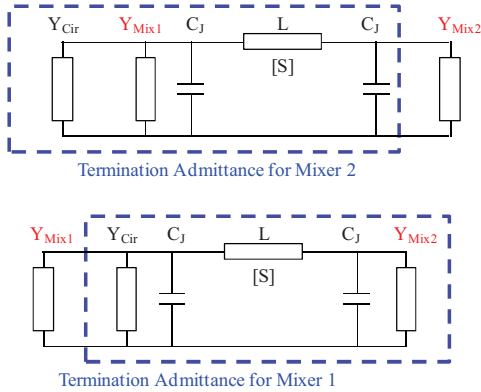


Fig. 5 Illustration of the embedding impedances, or termination matrix Y_T , of each junction within the twin junction topology. Y_{Cir} is the admittance of the entire network (i.e. the probe, choke and transformer) excluding the twin circuit. C_J is the geometric capacitance of the SIS junction, L is the inductive microstrip line connecting the junctions and Y_{Mix} is the admittance of the junction which depends on its terminating matrix. Note that circuit elements are defined for each sideband frequency.

Using the unique pumping strengths of each junction, α_1 and α_2 , the small signal analysis can be computed as shown in Fig. 4 and Fig. 5. Since the measured I-V curve includes both junctions, a new I-V curve for parallel junctions can be created by halving the current which is then used to compute the small signal noise and admittance matrices, HH and YY . The final step is to find the appropriate embedding impedance for each junction, referred to here as the termination matrix of each junction, Y_T . An iterative process was used, with R_N used as an initial guess at all sideband ports for each mixing junction. Within this initial modeling approach, only the small signal parameters delivered to each termination matrix were determined. In other words, the responses from each junction were analysed separately and not combined.

In retrospect, the following inconsistencies contributed to inaccuracies during this first approach to modeling. The phase difference of the large signal voltage between the two junctions was not used to correct the phase of the admittance matrix of *junction 1* (see below for a more complete approach). Furthermore, the measured I-V curve used for design was taken from a wafer with the best results achieved thus far; however, it was not known at the time that the resulting junction sizes were 20–30% smaller from the target due to processing. Nevertheless, the measured data fit the simulation reasonably well and a new mask set was created. An important result of the study demonstrated that the nominal line length between the junctions was previously

tuned below the middle of the band, and the length was reduced from 12.2 μm to 11.5 μm , with a prediction to shift the frequency response upwards approximately 15 GHz.

A. Design of the Mixer Chip

Of the chips with the integrated LO coupler, several options were introduced: ‘A’ designs were matched for best impedance match to the probe, and ‘B’ designs were matched with an emphasis to shift the frequency of the nominal design approximately 7% higher. Each design also included a variation of the microstrip line length between the junctions to account for a $\pm 10\%$ deviation in junction capacitance. For example, A1, A2, and A3 designs incorporated a line length of -1, 0, and +1 μm with A1 corresponding to an upwards shift in frequency. Another layout was included in the mask that did not include the LO circuitry, but instead used a single microstrip line as an impedance transformer (referred to here as ‘C’ design).

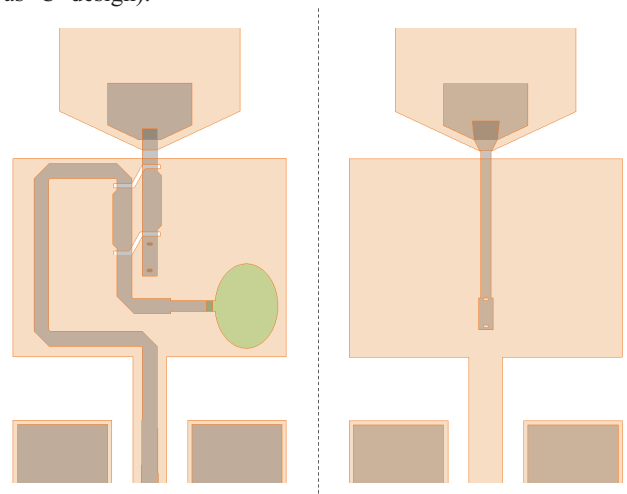


Fig. 6 Close-up of the mixer chip layout for designs ‘A’ and ‘B’ (left) that have the integrated LO coupler, and ‘C’ (right) using a single quarter-wave transformer.

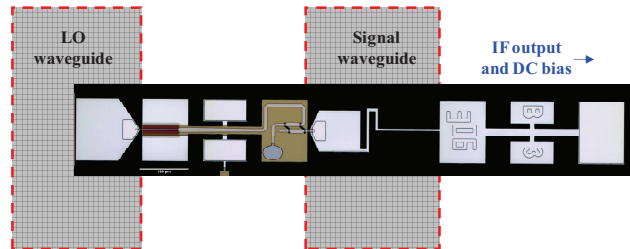


Fig. 7 Photo of the ‘B’ design incorporating the LO coupler on the chip. The dashed lines indicate the placement of the chip within the LO and RF waveguides of the mixer block.

Fig. 6 to Fig. 9 show the design and simulated results for the key components of the chip design. Two identical chokes are used to isolate the LO and IF from the signal. The signal is coupled through a probe with a high impedance line that serves as a path for both the IF output and DC biasing [9]. A bond-wire from the middle section of the RF probe serves as the DC ground (see discussion below). The LO is coupled through a separate waveguide probe and combined through a hybrid slot microstrip coupler located on the first section of

the RF choke; the coupler also acts as a quarter-wave transformer. Following the transformer is the twin circuit. The termination on the coupler is formed from Nitrogen-doped sputtered Titanium alloy as described in [10]. The surface resistivity is chosen close to that of the coupler port impedance, and a small section of inductive line is used to compensate for its capacitive nature.

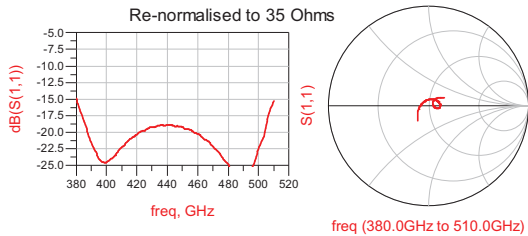


Fig. 8 Simulation of the RF probe with complete choke structure.

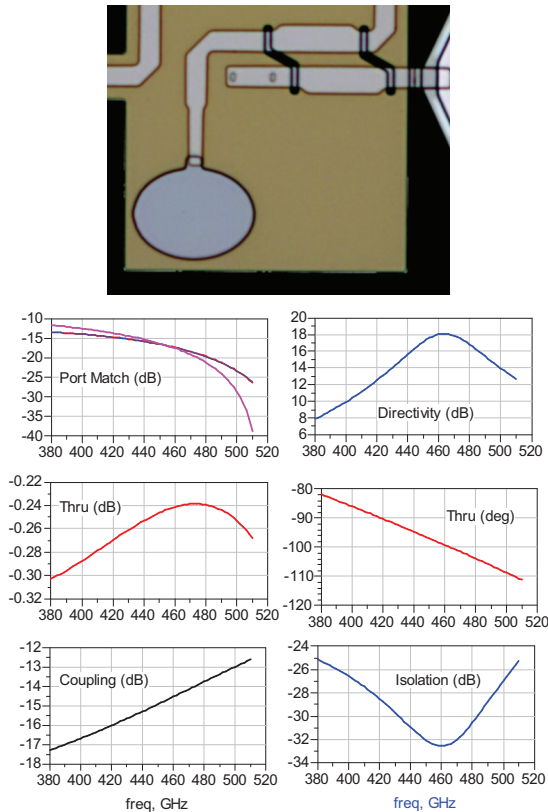


Fig. 9 Simulated response (bottom) and photograph (top) of the integrated LO coupler with resistive termination. The coupler is formed from microstrip, referenced to the first section of the RF choke, and has increased coupling from slots cut into the ground-plane. The twin junctions are shown following the coupler.

B. Measured Results and Discussion

Of those designs with the integrated LO coupler, only the ‘A’ designs were measured as the ‘B’ designs were diced slightly wider and would not fit within the mixer channel without modifying the mixer block. Despite the variations of microstrip tuning lengths, these designs continued to show a

poor response at high frequency. Considering Fig. 10, it is seen that the A1 designs appear to have a slightly better performance at high frequency, but the result is not conclusive. Note that between the A1 and A2 designs, the nominal resonant point of the twin circuit was set at 460 and 430 GHz respectively.

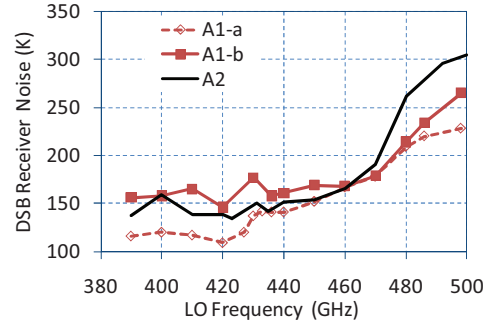


Fig. 10 Measured DSB receiver noise using the ‘A’ designs.

In an effort to understand the effects of the coupler, design ‘C’ (without the on-chip LO coupler) was tested using a micro-machined waveguide LO coupler [11]. Fig. 11 shows the substantial improvement in DSB noise when layout ‘C’ is used with the cold waveguide LO coupler.

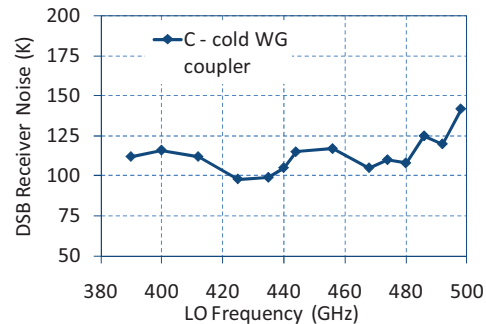


Fig. 11 Measured DSB receiver noise of ‘C’ chip layout that uses a cold waveguide LO coupler.

While it is not known the exact reason for the degradation with the integrated coupler, the difference in response deserves some discussion. One very important advantage of the ‘C’ designs is that the bonding location for the DC ground may be moved to the LO end of the RF choke. This is the ideal location to bond as here the choke is most effective in isolating the effects of the bond-wire. With the integrated coupler, bonding cannot occur on the end because of the LO probe and, due to the relatively large diameter of the bond-wire and its added asymmetry, a resonance within the choke may occur, as shown in Fig. 12. From extensive simulation, it was determined that through careful control of the length and placement of the bond-wire, the resonance could be minimized, but, in practice, this is difficult.

The measured effect of the bonding was compared between bonding on the hammer of the choke, as shown in Fig. 12, and bonding on the first section of the choke (i.e., the LO end) and is shown in Fig. 13. A clear degradation is seen due to the bonding location, but it is apparently not the sole

contributor to the troubling performance shown with the integrated coupler.

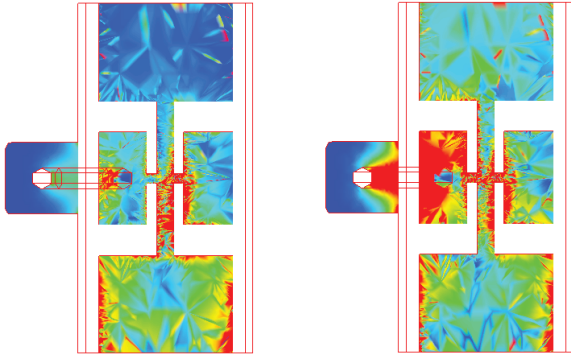


Fig. 12 Simulated surface current along the RF choke (a top view as shown placed in the mixer block channel) with a bond-wire extending from the centre-left hammer of the choke to a point on the mixer block, where the current intensity is indicated using a colour scale ranging from red (strong) to blue (minimal). The left figure shows a frequency where the bond-wire is sufficiently isolated, whereas on the right a resonance involving the bond-wire is shown at a frequency where the performance is severely degraded. The bond-wire has a diameter of 18 μm . An ideal location for the bond-wire is on the upper pad of the choke, where symmetry is preserved and maximum isolation is achieved.

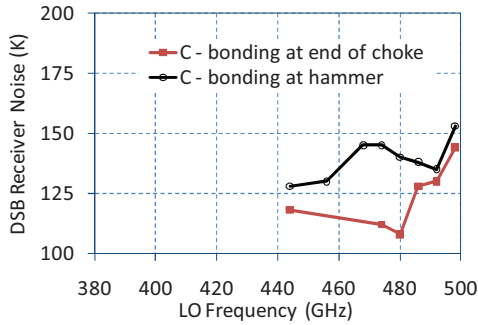


Fig. 13 Effect of bonding when bonded on the hammer as compared to the first section of the choke.

Therefore, it is quite likely that the integrated LO coupler exhibits some unexpected performance. The coupler is very sensitive to processing errors especially with respect to the slot dimensions and alignment. Furthermore, the slot widths at this frequency have a strong effect on the phase and impedance of the coupler, causing a strong slope in the coupling and off-centred input matching (as shown in Fig. 9 and by comparing the physical length of the transformer sections in Fig. 6). Because of increased LO noise coupling at these frequencies, the overall noise is impacted. Finally, there may be another unexpected effect since field lines are not well confined within slot-line modes.

III. MODELING WITH AGILENT ADS

In an effort to improve on the modeling of the SIS twin circuit (in particular to account for the large signal phase distribution between the two junctions) and to analyse the combined response delivered to the IF, the small signal noise and admittance matrices were joined into a complete circuit

using Agilent ADS [12] following a methodology similar to that described in [13] for a single junction. It is appropriate to mention here *SuperMix* (an extensive software package that is used by several groups in SIS junction array designs) that uses the theory of [7] in addition to a harmonic balance analysis of the LO [14]. One motivation within this paper is to perform a simplified analysis using a circuit simulator familiar to many designers across the industry.

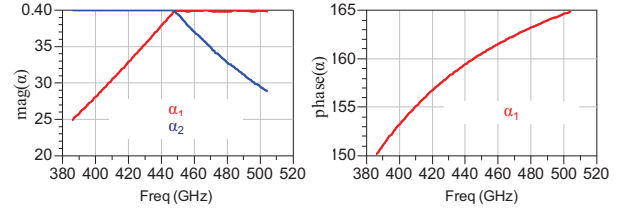


Fig. 14 Large signal pumping magnitude and phase between junctions in the twin circuit. In this case it is assumed that neither the left nor right junction may exceed some maximum pumping level (in this case 0.4).

In this setup, the pumping distribution of the LO was determined in the same manner as described above. It is important to recall that the phase of the down-converted IF signal is a function of the phase difference between the LO and RF signals at each junction. One may assume that this relative phase difference between the LO and RF is the same for each junction in the twin circuit, i.e., both the LO and RF undergo the phase change as illustrated by Fig. 3. Additionally, the spatial separation of the junctions at IF is negligible so that the down-conversions from each junction add in phase. In order for the small signal conversions to add in phase, the small signal admittance matrix of the first junction, YY_1 , must be modified according to

$$YY_{1,mn}' = YY_{1,mn} e^{j(m-n)\varphi} \quad (3)$$

where φ is the phase of the LO voltage and m and $n = 0, \pm 1, \pm 2$ representing each sideband of the 5-port network following [7]. Eq. (3) is identical to that found in [3]. Note that it is not necessary to modify the noise correlation matrix, HH_1 , since it is assumed here that the noise between the two junctions is not correlated (this is also stated in [7]).

Following the steps outlined in [13], each junction in the array was first represented as a noiseless 5-port uniquely described by its LO pumping, measured I-V curve, and DC biasing. Instead of fixing the pumping of *junction 2* to some value, it was assumed here that neither junction may exceed some maximum pumping level as shown in Fig. 14.

The small signal analysis was then set up by the following steps. The “noiseless” admittance matrix of each junction was combined with noise current sources at each sideband port, shown in Fig. 15, with magnitudes equal to

$$I_{Noise,m} = \sqrt{HH_{mm}} \quad (4)$$

with units of pA/\sqrt{Hz} . Using the noise correlation block in ADS, *NoiseCorr*, the noise currents were related according to normalized values

$$h_{mn} = 1/\sqrt{HH_{mm}HH_{nn}}, \quad m \neq n. \quad (5)$$

To form the twin circuit, the two junctions were attached at each port through a pi-network representing the junction capacitance and inductive microstrip line as seen in Fig. 16.

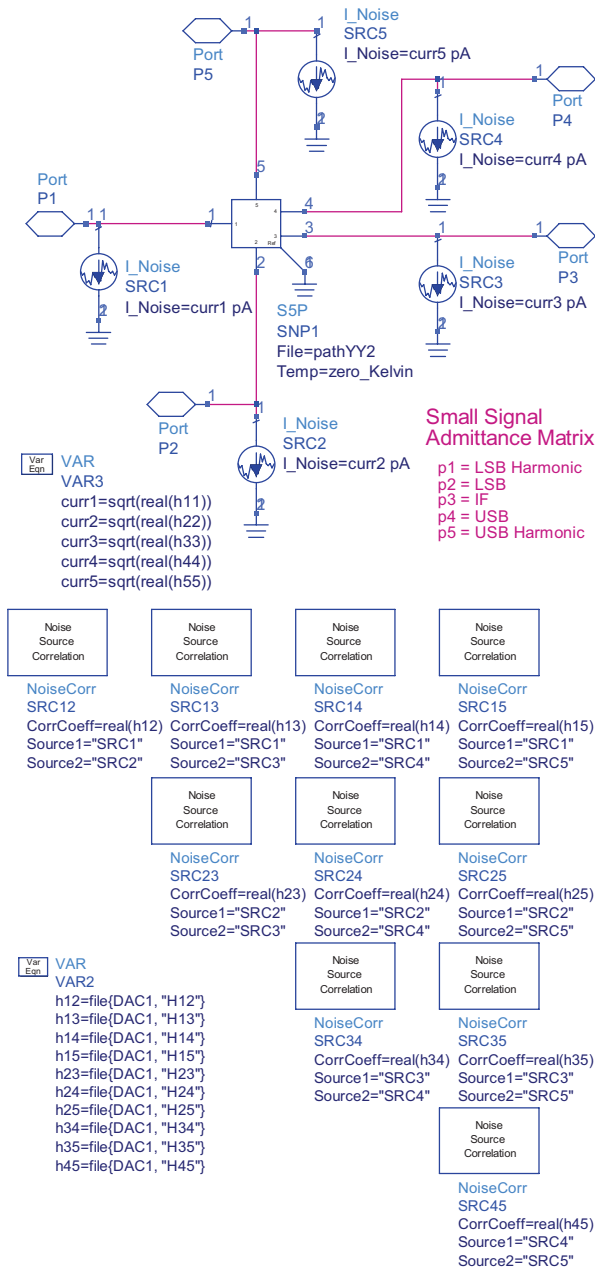


Fig. 15 Network representing each junction of the array in Agilent ADS. Noise currents are combined to the "noiseless" linear 5-port network and correlated using the *NoiseCorr* circuit block.

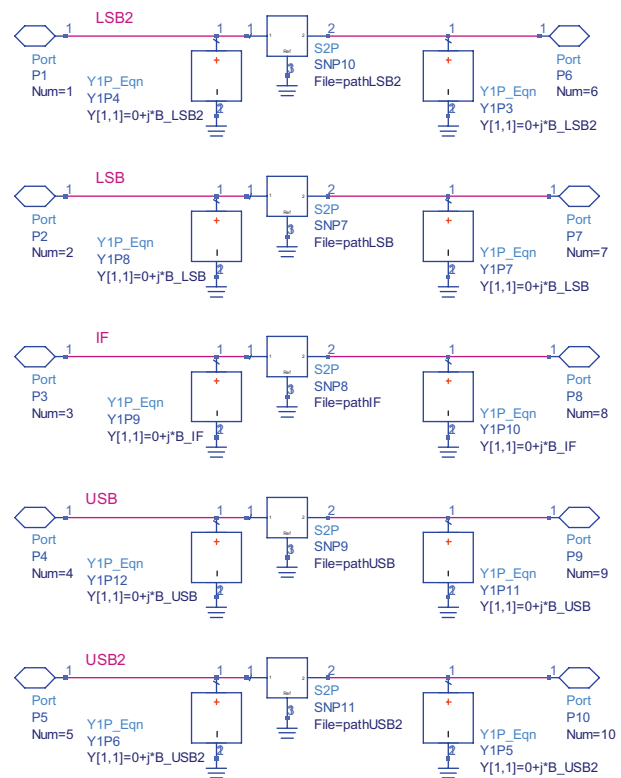


Fig. 16 Network showing the sideband port connections of each junction completing the twin circuit. Each port consists of a pi-network of the junction capacitance, determined by the susceptance calculated at each sideband frequency, along with simulated s-parameters of the inductive microstrip line.

Following the notation in [7], lower-sideband ports and admittances have been conjugated (e.g., susceptances and s-parameters have been conjugated).

The simulation was performed with respect to an LO frequency sweep, so the respective embedding impedances (i.e., probe and transformer) included a frequency offset for each sideband. Fig. 17 shows the completed twin circuit connected to ports containing the respective embedding impedance for each sideband (separately modeled).

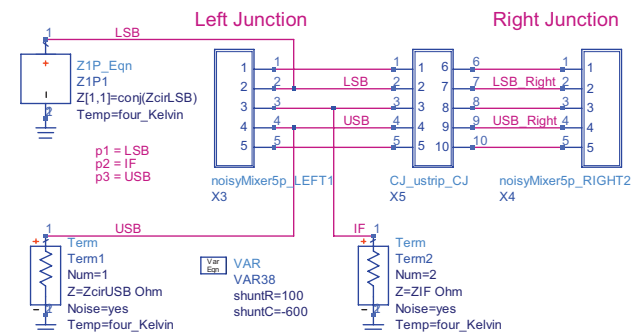


Fig. 17 Full twin mixer chip simulation showing the twin circuit connection terminated with the respective sideband impedances that contain the surrounding circuitry (e.g., the probe and transformer).

C. Comparison of Simulated and Measured Results

Following the earlier discussion above, it is appropriate to compare the measured performance with the simulation for the 'C' layout. Note that the small signal matrices have been calculated from a measured I-V curve typical of the wafer (see Fig. 5) using a 2.2 mV DC bias (the complex LO tunneling current is close to purely real at this point). It is assumed that $R_{NA} = 20 \Omega \mu\text{m}^2$ for the wafer resulting in a junction capacitance of 300 fF from junction areas of $3.0 \mu\text{m}^2$ (these were the targeted design values verified by dip testing of the wafer). As an initial (though not complete) validation step, the IF port was short-circuited; this causes the input RF admittance of each junction to appear close to a shunt resistance value of R_N . Fig. 18 shows a nice agreement with this assertion.

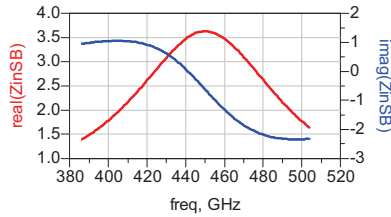


Fig. 18 Input impedance at the upper-sideband, Z_{inSB} , when the IF port is short-circuited using layout 'C'. The result closely matches that of the twin circuit if each junction is represented as a pure shunt resistance equal to R_N .

An interesting result of the simulation shows that this particular circuit appears to have high gain with moderate pumping values over the lower half of the band. Furthermore, at the higher edge of the band, conversion gain drops off and is not improved with increased LO pumping. When comparing with the measured results, the pumping should be reduced to stable levels (i.e., no generation of reflected power and negative conversion gain). Under these conditions, one can see a reasonable resemblance between the measured and simulated values when compared with Fig. 11 above. The DSB system noise has been modeled as:

$$T_{sys,DSB} = \frac{T_e}{2} + \frac{hf_{LO}}{k} + \frac{T_{IF}}{|S(2,1)|} \quad (6)$$

where T_e is the equivalent noise single-sideband noise temperature of the circuit, T_{IF} is the noise of the IF chain (taken to be 10 K), and S is the s-parameter matrix between the ports as illustrated in Fig. 17.

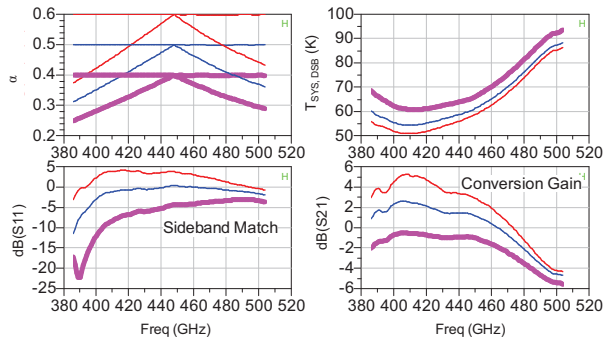


Fig. 19 Simulated results of the full mixer chip for the 'C' layout showing the dependence on LO pumping magnitude, where maximum $\alpha = 0.6$ (red), 0.5 (blue), and 0.4 (pink).

Fig. 20 indicates the noise dependence on the tuning length of the microstrip line between junctions. It is interesting to see that centred noise performance does not exactly correspond with resonating out the junction capacitances at the mid point of the band. This finding appears to be corroborated independently in [2] who found it was necessary to reduce the microstrip line length by 15%.

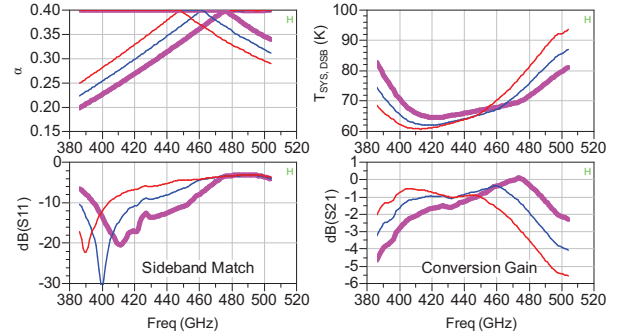


Fig. 20 Variation of the length of microstrip line between the junctions where the length is given as 11.5 (red), 11.0 (blue), and 10.5 (pink) μm . The noise performance of the twin circuit becomes centred as the resonance point is shifted towards the upper portion of the band.

IV. CONCLUSIONS

An overview of the design, measurement, and modeling of the APEX band 3 mixer chip (385–500 GHz) has been presented. It was found that the integrated coupler contributed to poor performance at higher frequency and, while the precise cause is unknown, it is speculated that it is due to the size of slots for this frequency range, or that the slots in the ground plane enhance vortex penetration in the ground Nb layer of the mixer circuitry which causes an increasing RF loss as the LO frequency rises (approaching 70% of the Nb gap frequency).

Version 'C' of the mixer has been installed at the APEX telescope ([15]), during March 2010, as the third receiver channel of the Swedish Heterodyne Facility Instrument ([16]).

A methodology for simulating SIS junction arrays with Agilent ADS has been presented and applied to the twin junction design. It is shown that the twin junction circuit is sensitive to LO pumping levels, and that for a centred noise performance across the band, the resonance point of the junction capacitance should be offset towards the upper part of the band.

ACKNOWLEDGEMENT

The authors would like to gratefully acknowledge the help and support of the members of the Group for Advanced Receiver Development (GARD) at Chalmers University of Technology, in particular: Bhushan Billade, Dr. Vincent Desmaris (micro-machining), Dimitar Dochev (IF bias-T), Sven-Erik Ferm (CNC machining), Igor Lapkin, Olle Nyström, Dr. Alexey Pavolotsky (SIS fabrication), Magnus Strandberg, and Erik Sundin (cryogenic LNA design).

REFERENCES

- [1] V. Y. Belitsky, S. W. Jacobsson, L. V. Filippenko, and E. L. Kollberg, "Broadband twin-junction tuning circuit for submillimeter SIS mixers," *Microwave and Optical Technology Letters*, vol. 10, no. 2, Oct. 1995.
- [2] W. Shan, T. Noguchi, S. Shi, and Y. Sekimoto, "Design and Development of SIS Mixers for ALMA Band 8," *IEEE Trans. Appl. Supercond.*, vol. 15, no. 2, Jun. 2005.
- [3] J. Zmuidzinas, H. G. LeDuc, J. A. Stem, and S. R. Cypher, "Two-Junction Tuning Circuits for Submillimeter SIS Mixers," *IEEE Trans. Microwave Theory Tech.*, vol. 42, no. 4, Apr. 1994.
- [4] V. Y. Belitsky and M. A. Tarasov, "SIS junction complete reactance compensation," *IEEE Trans. Magn.*, vol. 27, pp. 2638-2641, Mar. 1991.
- [5] R. Monje, V. Belitsky, C. Risacher, V. Vassilev, and A. Pavolotsky, "SIS mixer for 385–500 GHz with on-chip LO injection," *Proc. 18th Int. Symp. Space THz Tech.*, Mar. 2007.
- [6] R. Monje, "Advancement of THz integrated SIS mixers for radio astronomy," PhD thesis, Chalmers University of Technology, 2008.
- [7] J. R. Tucker and M. J. Feldman, "Quantum detection at millimeter wavelengths," *Rev. Mod. Phys.*, vol. 57, no. 4, pp. 1055-1113, Oct. 1985.
- [8] A. R. Kerr, S.-K. Pan and S. Withington, "Embedding Impedance Approximations in the Analysis of SIS Mixers," *IEEE Trans. Microwave Theory Tech.*, vol. 41, no. 4, pp. 590-594, Apr. 1993.
- [9] C. Risacher, V. Belitsky, V. Vassilev, I. Lapkin, and A. Pavolotsky, "A 275-370 GHz Receiver Employing Novel Probe Structure," *Int. Journal of Infrared and Millimeter Waves*, vol. 26, pp.867-879, Jun. 2005.
- [10] R. Monje, V. Vassilev, A. Pavolotsky, and V. Belitsky, "High quality microstrip termination for MMIC and millimeter-wave applications," *IEEE MTT-S International Microwave Symposium*, pp. 1827-1830, Jun. 2005.
- [11] V. Desmaris, D. Meledin, A. Pavolotsky, R. Monje, and V. Belitsky, "All-metal micromachining for the fabrication of submillimetre and THz waveguide components and circuits," *J. Micromech. Microeng.*, vol. 18, Jul. 2008.
- [12] ADS, Agilent Technologies, Palo Alto, CA, 2009.
- [13] A. R. Kerr and S.-K. Pan. (1999, Feb.) Mixer-Preamp Design Using MMICAD. [Online] <http://www.mma.nrao.edu/memos/>
- [14] J. Ward, F. Rice, G. Chattopadhyay and J. Zmuidzinas, "SuperMix: A flexible software library for high-frequency circuit simulation, including SIS mixers and superconducting elements", in *Proc. 10th Int. Symp. Space THz Tech.*, pp 269, 1999.
- [15] APEX. [Online] <http://www.apex-telescope.org/>
- [16] V. Belitsky et al., "Facility heterodyne receiver for the Atacama pathfinder experiment telescope," in *Proc. Joint 32nd Int. Infrared Millim. Waves Conf./15th Int. Terahertz Electron. Conf.*, Cardiff, U.K., 2007, pp. 326–328.

Superconducting Integrated THz Receivers

Valery P. Koshelets^{*}, Pavel N. Dmitriev^{*}, Andrey B. Ermakov^{*}, Lyudmila V. Filippenko^{*},
Andrey V. Khudchenko^{*}, Nickolay V. Kinev^{*}, Pavel Kudryashov^{*}, Oleg S. Kiselev^{*},
Mikhail Yu. Torgashin^{*}, Gert de Lange[†], Leo de Jong[†], Pavel A. Yagoubov[†].

^{*} The Kotelnikov Institute of Radio Engineering and Electronics, Moscow, Russia
Email: valery@hitech.cplire.ru

[†] SRON Netherlands Institute for Space Research, Groningen, the Netherlands
Email : G.de.Lange@sron.nl

Abstract

A Superconducting Integrated Receiver (SIR) [1, 2] was proposed more than 10 years ago and has since then been developed for practical applications [3]. A SIR comprises on one chip (size of 4 mm*4 mm*0.5 mm) all elements needed for heterodyne detection: a low-noise SIS mixer with quasioptical antenna, an Flux-Flow Oscillator (FFO) acting as a Local Oscillator (LO) and a second SIS harmonic mixer (HM) for the FFO phase locking. The concept of the SIR looks very attractive for many practical applications due to its compactness and the wide tuning range of the FFO. Presently, the frequency range of most practical heterodyne receivers is limited by the tunability of the local oscillator, typically 10-15% for a solid-state multiplier chain. In the SIR the bandwidth is determined by the SIS mixer tuning structure and the matching circuitry between the SIS and the FFO. A bandwidth up to 30 – 40% can be achieved with a twin-junction SIS mixer design. All components of the SIR microcircuits are fabricated in a high quality Nb-AlN/NbN-Nb tri-layer on a Si substrate [4]. The receiver chip is placed on the flat back surface of the silicon lens, forming an integrated lens-antenna.

Light weight and low power consumption combined with nearly quantum limited sensitivity and a wide tuning range of the FFO make SIR a perfect candidate for many practical applications. In particular, the SIR developed for novel balloon borne instrument TELIS (Terahertz and submillimeter LIMB Sounder) [5] covers frequency range 450 -650 GHz. As a result of recent receiver's optimization the DSB noise temperature was measured as low as 120 K for the SIR with intermediate frequency band 4 – 8 GHz. The spectroscopic Allan stability time is about 20 seconds; required spectral resolution of about 1 MHz was confirmed by gas cell measurements. Results of comprehensive phase noise measurements will be presented. Several algorithms for remote automatic computer control of the SIR have been developed and tested.

A possibility to implement the SIR for ground-based radio astronomy and future space missions will be discussed. In particular, details of the on-going project directed on development of the SIR for PORTable Submillimeter Telescope (POST), Purple Mountain Observatory, China, will be presented.

Capability of the SIR for high resolution spectroscopy has been successfully proven in a laboratory environment by gas cell measurements. Possibility to use the SIR devices for analysis of the breathed out air at medical survey will be demonstrated. Many of spectral lines very important for such survey and medical analysis are concentrated in the sub-terahertz range and can be detected by such spectrometer. There is also a large niche for applications of integrated spectrometers for the detection of radiation from the newly developed cryogenic Terahertz sources.

The work was supported by the RFBR projects 09-02-00246 and 09-02-12172.

REFERENCES

- [1] V.P. Koshelets, S.V. Shitov, L.V. Filippenko, A.M. Baryshev, H. Golstein, T. de Graauw, W. Luinge, H. Schaeffer, H. van de Stadt "First Implementation of a Superconducting Integrated Receiver at 450 GHz"; *Appl. Phys. Lett.*, vol. 68, No. 9, pp. 1273-1275 (1996).
- [2] V. P. Koshelets and S. V. Shitov, "Integrated Superconducting Receivers," *Superconductor Science and Technology*, vol. 13, pp. R53-R69 (2000).
- [3] V.P. Koshelets, A.B. Ermakov, L.V. Filippenko, A.V. Khudchenko, O.S. Kiselev, A.S. Sobolev, M.Yu. Torgashin, P.A. Yagoubov, R.W.M. Hoogeveen, and W. Wild, "Integrated Submillimeter Receiver for TELIS", *IEEE Trans. on Appl. Supercond.*, vol. 17, pp 336-342 (2007).
- [4] M.Yu. Torgashin, V.P. Koshelets, P.N. Dmitriev, A.B. Ermakov, L.V. Filippenko, and P.A. Yagoubov, "Superconducting Integrated Receivers based on Nb-AlN-NbN circuits", *IEEE Trans. on Appl. Supercond.*, vol. 17, pp.379- 382, (2007).
- [5] R.W.M. Hoogeveen, P.A. Yagoubov, G. de Lange, A. de Lange, V. Koshelets, M. Birk, B. Ellison, 2007 *Proceedings of SPIE* **6744** 67441U-1

Wideband receiver based on AlN barriers

A. Brettschneider*, T.M. Klapwijk*, T. Zijlstra*, A. Baryshev**, R. Hesper**

* Kavli Institute of NanoScience, Faculty of Applied Sciences
Delft University of Technology
Lorentzweg 1, 2628 CJ Delft, The Netherlands
** Netherlands Institute for Space Research, Postbus 800
9700 AV GRONINGEN, The Netherlands

Email: a.brettschneider@student.tudelft.nl

Abstract

In current receiver technology different device technologies are used for different frequency bands. The recent finding¹ that a plasma source can be used to create tunnel barriers with high quality I,V curves and current densities up to J_c of 100 kA/cm² creates the opportunity to cover a full band of 350 GHz potentially covering several atmospheric windows, for example Band 9 and Band 10 of ALMA.

We report on the design and technology-development of Niobium based aluminum-nitride barrier tunnel junctions with NbTiN/Al striplines.

The receiver is made by first depositing a NbTiN groundplane and covering it with a Nb/Al/AlN/Nb junction layer. This layer is etched away and covered with SiO_x except where the junctions will be. Finally the Al stripline is deposited. Deposition is done by magnetron (reactive) plasma sputtering.

For CHAMP+ we are developing both single as twin junction receivers. CHAMP+ is a sky survey telescope for band 9 and 10 of ALMA to search for interesting sub millimeter sources. These sources can be examined more detailed later by ALMA.

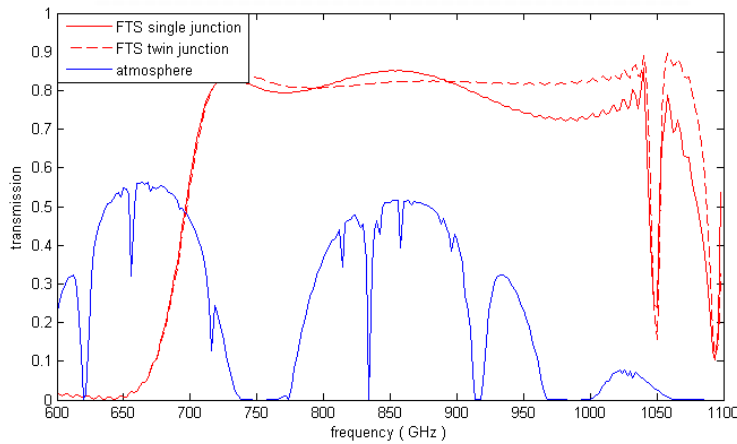


Figure 1 FTS prediction of single junction (full red line) twin junction (dashed red line) and the atmospheric transmission at Atacama (blue line).

Fig.1 shows the predictions made for a center frequency of 850 GHz. The width of the band is wide enough to cover both band 9 as well as band 10 for CHAMP+ with just 1 receiver. This would make measuring with CHAMP+ more efficient. The present design is based on a feed horn and waveguide antenna suited for frequencies of 680 GHz and higher. The dip at 1050 GHz is due to the antenna.

Results will be presented on mixers based on the current design to demonstrate the potential of the technology.

¹ T. Zijlstra, C.F.J. Lodewijk, N. Verduyssen, F.D. Tichelaar, D.N. Loudkov, T.M. Klapwijk, "Epitaxial aluminum nitride tunnel barriers grown by nitridation with a plasma source", Applied Physics Letters **91**, 2007

Development of a 1.9-THz Band Hot-Electron Bolometer Heterodyne Receiver with a Quantum Cascade Laser

H. Maezawa^{1*}, T. Yamakura², T. Koyama¹, S. Yamamoto³, S. Shiba³, T. Shiino³, N. Sakai³,
N. Nakai², M. Seta², A. Mizuno¹, T. Nagahama¹, Y. Fukui¹, Y. Irimajiri⁴, N. Sekine⁴, I. Hosako⁴

¹ Nagoya University, Furo-cho Chikusa-ku, Nagoya Aichi, Japan

² the University of Tsukuba, Department of Physics, Tsukuba, Ibaragi Japan

³ the University of Tokyo, Department of Physics, Hongo 7-3-1 Bunkyo-ku, Tokyo, Japan

⁴ National Institute of Information and Communications Technology, Japan.

*Contact: hiro@stelab.nagoya-u.ac.jp, phone +81-52-747-6314

Abstract— We are developing a superconducting Hot-Electron Bolometer (HEB) mixer receiver for the 1.9 THz frequency band. The microbridge of the HEB mixer was made at room temperature from a 6 nm thick Niobium Titanium Nitride (NbTiN) film deposited on a 20 nm-thick AlN interface layer using a helicon sputtering technique. The mixer was cooled to 4.2 K by using a vibration-free closed-cycle mechanical 4 K pulse tube refrigerator. The stability of the HEB mixer receiver was studied in the 1.5 THz band by varying the local oscillator power of a multiplier chain solid-state source with the bias voltage of the mixer fixed. The output power of the intermediate frequency (IF) signal had a maximum peak as a function of the bias current of the HEB mixer. The receiver noise temperature was minimum at around the maximum peak. It was also found that the IF signal was most stable at around the maximum peak. For future use we have performed test fabrication of stacked GaAs/Al_{0.1}Ga_{0.9}As active layers for the preparation of bound to continuum based quantum cascade lasers to be used as a 1.9 THz band local oscillator source. The result of X-ray diffraction measurements showed that the 120 repeated quantum well structures can be deposited with a molecular beam epitaxy (MBE) system within 0.78 % structural mismatch error.

Index Terms—Terahertz, Hot-electron bolometer mixer, NbTiN film, Quantum cascade laser, Radio astronomy, Atmospheric research

I. INTRODUCTION

Terahertz band heterodyne spectroscopy of ions, atoms, and molecules plays an important role in the study of the physical and chemical conditions in both astronomical targets and terrestrial and planetary atmospheres. In the millimeter/submillimeter wave bands, near quantum-noise limited superconductor-insulator-superconductor (SIS) receivers have enabled the development of highly sensitive ground-based, balloon-borne, and space-based astronomical

and atmospheric research.

The Nagoya University Southern Observatory (NUSO) has employed mm/sub-mm SIS receivers installed on instruments at Pampa la Bola in the Atacama desert, Chile (alt. 4860m), to carry out a broad range of work on both astronomical targets and terrestrial and planetary atmospheres. This work includes a large-scale survey of molecular clouds along the Galactic Plane, carried out with the NANTEN2 telescope (4m), as well as monitoring of millimeter wave band spectral lines of minor constituents in the stratosphere and mesosphere such as water vapor isotopes, ozone, NO_x species, etc [e.g. 1]. In addition, the National Institute of Information and Communications Technology (NICT) of Japan has succeeded in constructing a balloon-borne superconducting submillimeter-wave limb emission sounder (BSMILES) in the 600 GHz frequency band

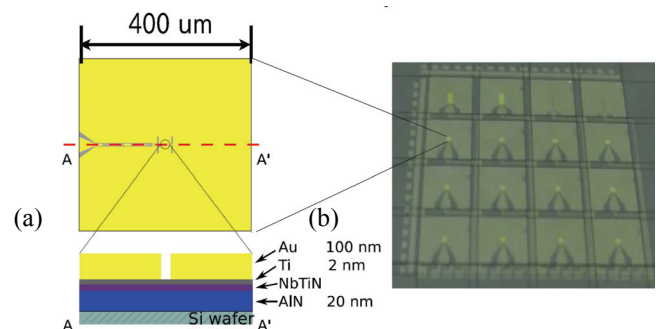


Fig. 1. (a) Cross section of the NbTiN HEB mixer. The 400μm² field is patterned by an electron beam lithography system. (b) The photograph shows a 35mm-diameter FZ Si wafer on which 16 HEB mixer chips are prepared.

[2]. Currently the University of Tsukuba is planning a project for a THz radio telescope at Dome Fuji in Antarctica. For such projects, the establishment of 1.8-2.0 THz band heterodyne sensing technology is a common thread, which will enable us to observe plasma gases such as ionized carbon and various

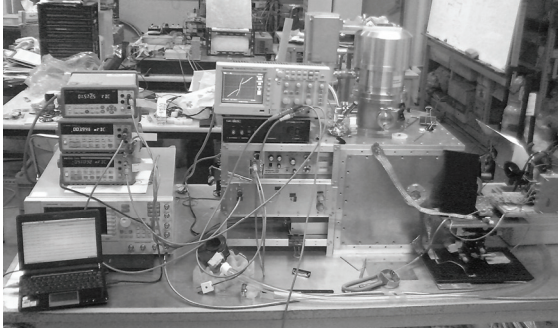


Fig. 2. Laboratory HEB mixer receiver system employing a vibration-free pulse-tube (PT) 4 K closed-cycle mechanical refrigerator.

highly excited transition lines in the interstellar medium, as well as key species involved in photochemistry, such as OH radicals in planetary atmospheres.

In THz frequency band, however, SIS mixers do not function since the energy of the incident radiation is sufficient to completely break the superconducting cooper pair electrons[3] (for niobium the energy gap is ~ 700 GHz, for instance). Therefore, superconducting hot electron bolometer (HEB) mixers have been actively studied as an alternative sensitive heterodyne detector for THz band astronomy and atmospheric applications. In principle these superconducting HEB mixers can work from millimeter frequencies to far infrared wavelength without being limited to RF frequencies.

The most widely developed THz band heterodyne detectors to date have been niobium nitride (NbN) phonon-cooled HEB mixers. An alternative is niobium titanium nitride (NbTiN) HEB mixers [4-10]. In contrast to NbN films, the hot-electron cooling mechanism of NbTiN HEB mixers is not completely understood. NbTiN HEB mixers can be easily fabricated on quartz substrate, whose low dielectric constant and toughness is useful for microfabrication processes such as the lapping of THz band waveguide mixer chips. The combination of waveguide and horn antenna provides a well-defined beam pattern. Both diffusion- and phonon-cooling mechanisms may be able to function in the microbridge of NbTiN HEB mixers made by *in-situ* deposition processes [9,11]. Further study now promises to expand the potential performance of NbTiN HEB mixers.

We are developing a 1.9 THz band NbTiN HEB mixer. Since our micromachining process for the 1.9 THz band waveguide structure is not completely established, at present we have employed a quasi-optical antenna for the experimental

development of our mixers. In addition we are now ordering a 1.9 THz band solid state multiple chain local oscillator (LO) source (Virginia Diodes Inc.). Until the delivery we are investigating the performance of our NbTiN HEB mixer by using an existing 1.5 THz band multiple chain LO source.

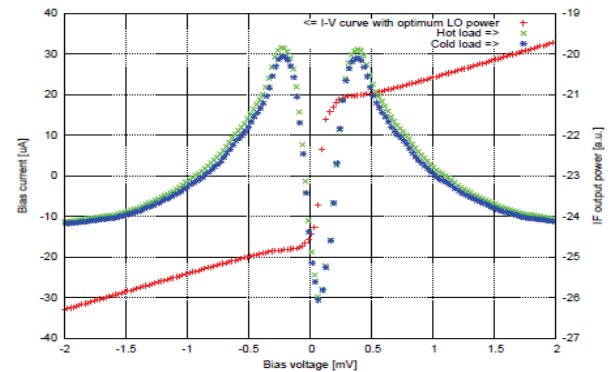


Fig. 3. I-V characteristic of HEB mixer at optimum LO power and the dependence of bias voltage on IF output power.

II. FABRICATION PROCESSES AND DESIGN OF NbTiN HEB MIXERS

A non-doped high resistivity floating zone (FZ) silicon wafer is first cleaned in deionized water with an ultrasound bath. Within a $400\mu\text{m}\times 400\mu\text{m}$ field a microbridge, RF choke filter, and twin-slot antenna are patterned with an electron-beam lithography system. An AlN interface layer is deposited by DC reactive sputtering [12], after which a NbTiN superconducting thin film is accurately deposited using a helicon sputtering technique with an NbTi (weight ratio of Nb:Ti = 4:1) alloy target in a mixture of Ar and N_2 gas at room temperature. This sputtering system was designed and purpose-built on the basis of a process simulation [13] and the field pattern is formed by a lift off process with a positive photo resist mask.

In our multi-deposition system, the sputtering room and electron-beam evaporation room are connected through a load lock room. Without breaking the vacuum, a bilayer consisting of a 2 nm-thick Ti interface layer and a 100 nm-thick Au contact/electrode layer is deposited on the NbTiN layer. This is an *in situ* technique, which minimizes the impeditive deterioration of the NbTiN film surface. The critical temperature (T_c) of a bilayer consisting of a 6 nm thick NbTiN film and a 20 nm interface AlN layer on Si wafer was found to be 3.0 K higher than the T_c of a 6 nm thick NbTiN film alone. However, in our current fabrication process the T_c of the HEB mixer is less than 10 K due to the superconducting proximity effect induced by the remnant 2 nm thick Ti interface layer.

Ground plane and IF read out coplanar patterns are determined by a photo mask aligner, and 350 nm Al layers are

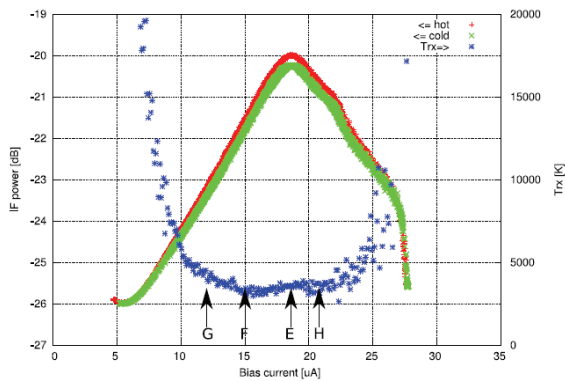


Fig. 4. Uncorrected receiver noise temperature of HEB mixer receiver and IF output power corresponding to input blackbody temperatures of hot (295 K) and cold loads (77 K) at 1.47 THz as a function of bias current with bias voltage fixed. The bias current is varied by changing the LO power. Position E shows the bias current point corresponding to the maximum peak of the IF output power, where the receiver noise temperature was minimum and insensitive to bias current levels.

deposited. Finally the length of the microbridge is defined by the electron-beam lithography system and subsequent inductively coupled plasma (ICP) etching with Ar gas. The Ti interface layer remaining on the NbTiN microbridge plays the role of the etching stopper. A cross sectional view of the HEB structures is shown in Fig. 1 (a), and a scanning electron microscope (SEM) photograph of sixteen 4mm×4mm HEB mixer chips is shown in Fig. 1 (b). In this 1.5 THz band experiment an HEB mixer employing an NbTiN microbridge of 0.3 μm in length and 0.5 μm in width was studied. The bridge size, including the thickness, was adjusted for the insufficient pumping power of our 1.5 THz band LO source and the cooling operation temperature of the mixer mount (4.2 K). Therefore this bridge size was not fully optimized for the sensitivity and the IF bandwidth of the HEB mixer.

Twin-slot antennae prepared for various frequency bands including the 0.2, 0.6, 0.8, 1.5, 1.9 and 2.5 THz bands are patterned on the basis of the design reported in [14,15]. The structure of the coplanar slot and choke filter are slightly re-designed with a high frequency structure simulator (HFSS, Ansoft inc.). The frequency responses of the HEB mixers measured by a Fourier transform spectrometer (FTS) system were in accordance with those predicted by the designs. In the FTS system a signal beam emitted from an Hg lump is collimated to the mixers by a parabolic reflector. The polarizations of the mixers were checked by tilting an inner wire grid polarizer set in the evacuated FTS chamber. The ratio of co- to cross-polarization was greater than 10dB at 1.9 THz.

IF output coplanar lines formed on Si wafer are connected to an IF Duroid microstrip circuit by bonding wires. The reflection and transmission coefficient at this connection was

designed based on the HFSS simulation. The mixer chip is attached to the bottom surface of a hyper hemisphere made of a non-doped high resistivity Si lens. This lens should be coated by anti-reflection (AR) coating in order to match the impedance

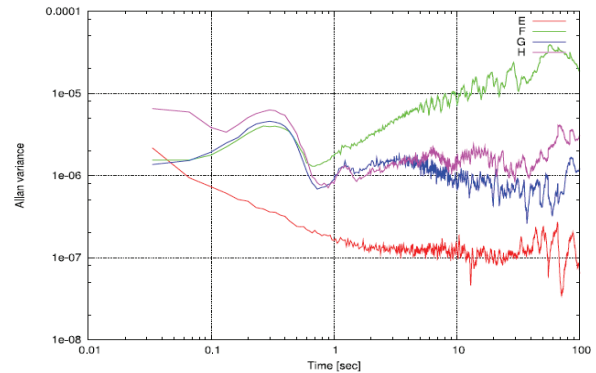


Fig. 5. Allan variance $(\sigma_A / \langle v(t) \rangle)^2$ of the 1.5 THz band NbTiN HEB mixer receiver system measured for the four bias current positions labeled in Fig.4. Except for bias current position E, corresponding to the IF maximum peak, the influence of mechanical vibration on the Allan variance can be seen below 1 second.

between the atmosphere and the lens. On Si lenses prepared for the 1.9 THz band we employ a 27 μm thick layer of Parylene-C, which is widely used for printed circuit boards (PCBs) and medical and space industry devices. However, for this experiment at 1.5 THz, we used a Si lens without AR coating.

III. MEASUREMENT SETUP

The HEB mixer chip was cooled to 4.2 K with a vibration-free pulse-tube (PT) 4 K close-cycled refrigerator (Sumitomo heavy industries, Ltd.) for which the cooling capacity and amplitude of the mechanical vibration are 0.5 W and less than 3 μm , respectively. The temperature fluctuation synchronized to inner He gas circulation is 300 mK with a period of about 1.2 seconds, which is greater than that of a Gifford McMahon 4 K close-cycled refrigerator with same cooling capacity. We inserted various interface metal materials between the mount block of the HEB mixer and the 4 K cold head, so that the temperature fluctuation at the mixer mount block was reduced to less than 2 mK.

In this measurement the beam of a 1.5 THz band multiplier chain LO source is collimated with a parabolic mirror, and is coupled with the blackbody RF signal from slabs of Eccosorb at 295 K (hot load) and 77 K (cold load) by using a polarized wire grid. Because of the insufficient power of the LO source, the RF/LO coupling efficiency is reduced to 67 % by the wire grid. The vacuum window is 25 μm -thick Kapton film. The infrared filter attached to 50 K shield panel is a Zitex G106.

In front of the HEB mixer, a band pass mesh filter is inserted to transmit only 1.5 THz band signal with a band width of 10 %. Broad band incident thermal emission ranging from millimeter

to infrared wavelengths makes it difficult to evaluate the performance of HEB mixers accurately because it induces the well-known cumbersome bolometric phenomenon known as the direct detection effect. This direct detection effect drifts the operation bias voltage and bias current, which complicates the intensity calibration of observed spectra.

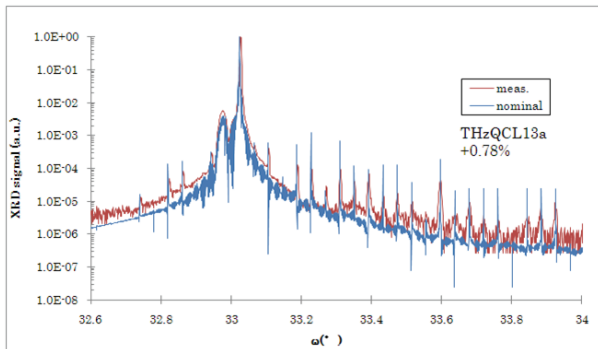


Fig. 6. X-ray diffraction measurement of the stacked GaAs/Al_{0.1}Ga_{0.9}As active layers prepared for a bound to continuum based quantum cascade laser.

For the stable bias control of the HEB mixer, we improved the Nitsuki 8842 bias control unit used for the operation of SIS mixers. The intermediate frequency (IF) signal output from the HEB mixer is connected via a bias-tee to a 1.3-1.8 GHz band isolator and a low noise HEMT amplifier made in Russia, and then amplified by two low noise HEMT amplifiers at room temperature. The equivalent noise temperature of this cryogenic LNA cooled to 4.2 K is less than 3 K. The linearity of the system is checked by variable attenuators. The frequency characteristics of the IF signal are evaluated with a spectrum analyzer. When the Allan variance of the HEB mixer receiver is measured, the IF output signal is narrowed by a frequency tunable band pass filter with 15 % bandwidth, and then monitored by a square law direct detector.

IV. MEASUREMENT RESULTS

A. Receiver noise temperature

The receiver noise temperature of the NbTiN HEB mixer was measured at 1.47 THz by using the Y-factor method on the basis of a Callen and Welton radiation law [16]. Fig. 3 shows the bias current and IF output power corresponding to the input blackbody temperatures of the hot and cold loads measured as a function of the bias voltages at the optimum LO pumping level. The maximum Y-factor is 0.3 dB at a bias voltage of 0.4 mV and a current of 20 μ A. The lowest uncorrected receiver noise temperature was 3400 K. Taking into account only our low RF/LO coupling efficiency at the wire grid splitter and the reflection loss at the surface of the Si-lens without AR coating, this receiver noise temperature is partially corrected to be about

1600 K for the 1.3-1.8 GHz IF band, which is comparable to those of other NbTiN HEB mixers reported previously [6,7]. By optimizing the microbridge dimension of the NbTiN HEB mixer using an LO source with sufficient power the noise performance will be further improved.

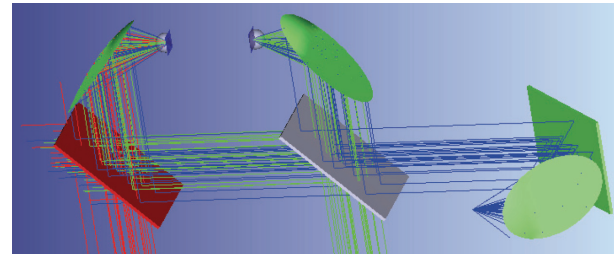


Fig. 7. Schematic optical design of NbTiN HEB mixer receiver with a THz band CW QCL LO source, where an additional superconducting HEB mixer is prepared exclusively for the phase locked loop system. The HEB mixers and the QCL are assembled on the 2nd stage (4K) and 1st stage (50 K) of our PT cryostat, respectively

B. Stability

Generally the Allan variance, $(\sigma_A / \langle v(t) \rangle)^2$, is measured to study the stability performance of the HEB mixer receiver system [e.g. 17-19]. Here $v(t)$ and σ_A present the instantaneous output voltage of a direct detector and the standard deviation (rms voltage), respectively. Firstly in this measurement the receiver noise temperature and IF output power as a function of the HEB mixer bias current were investigated by varying the LO power at 1.47 THz around the bias voltage giving the lowest receiver noise temperature. As shown in Fig. 4 we found that the maximum peak of the IF output power is a function of the bias current. The receiver noise temperature was not strongly influenced by bias current at around the IF maximum peak.

Next, we measured the IF output power at bias current levels close to those resulting in the IF maximum peak in order to calculate the Allan variance of the HEB mixer receiver. Direct detection of an IF signal with a center frequency of 1.5 GHz and a band width of 150 MHz was measured for 15 minutes with a 20 ms sampling speed by using a high speed digital multi-meter. As can be seen in Fig.5 we found that the most stable condition, where the Allan variance and time are of the order of 10^{-7} and about 10 seconds, respectively, is obtained at the bias current level marked E, which gives a moderate receiver noise temperature. This mainly seems to be because the IF output power is relatively insensitive to the bias current, that is to say, the LO power at the IF maximum peak.

The Allan variance and time obtained for bias current level E are better than those measured with a 4 K GM refrigerator as

previously reported in [10,20]. In other bias current positions such as G, F, and H, the Allan variance value and time are worse than those for position E. The convex features seen in F, G, and H data at shorter than 1 sec are due to the LO power fluctuation induced by the imperceptible mechanical vibration of the PT refrigerator. The power of LO source also drifts with the change of ambient room temperature. If the temperature of the HEB mixer bias unit, IF amplifier chain, and multiplier chain LO source were stabilized, the Allan variance and time would be further improved.

V. QUANTUM CASCADE LASER

Quantum cascade lasers (QCL) promise a continuous-wave (CW) solid-state LO source providing sufficient power for THz band heterodyne receivers. Several successful demonstrations of stabilization in the CW THz band frequency of QCLs have been reported by using electronic phase lock loop (PLL) systems employing heterodyne mixing techniques [e.g.21-23]. We are also planning to integrate a 1.8-2 THz band tunable CW QCL as a LO source in our HEB mixer receiver system, where the frequency of the QCL should be stabilized by a PLL system with a superconducting HEB mixer. In order to prepare such a QCL we have attempted the fabrication of quantum well structures by using a molecular beam epitaxy technique at the photonic device laboratory of NICT. In this fabrication the same active layer structure consisting of GaAs-wells, $\text{Al}_{0.1}\text{Ga}_{0.9}\text{As}$ -barriers, and an Si doped layer, as reported in [24], was deposited 120 times on a semi-insulating GaAs substrate. In X-ray diffraction measurements (Fig.6) the sample showed good property where the uniformity of the active layer thickness was within 0.78 %. With this grown active layer, bound to continuum based QCLs will be fabricated experimentally, and then the performance such as power, frequency, current density and operational temperature will be studied.

VI. CONCLUSION AND FUTURE WORK

In this study HEB mixers employing a 6 nm thick superconducting NbTiN microbridge with an 20 nm thick AlN interface layer and Ti/Au bilayer by an *in situ* fabrication process were prepared. The best Allan variance was obtained at the maximum peak of IF output power where the receiver noise temperature is optimum.

As shown in our previous paper both phonon- and diffusion-cooling mechanisms may function potentially in our NbTiN HEB mixers due to this *in situ* process. Based on these results, the basic characteristics and potential performance of the NbTiN HEB mixer receiver in the 1.9 THz frequency band will be investigated by optimizing the dimensions of the NbTiN microbridge and by improving the RF/LO coupling efficiency and reflection at the lens surface.

In addition we will develop a 1.9 THz band HEB mixer receiver employing a continuous-wave QCL LO source with stacked GaAs/AlGaAs layers (Fig.7).

ACKNOWLEDGMENTS

We are grateful to Dr. H. Matsuo of the advanced technology center of the National Astronomical Observatory of Japan for cooperative FTS measurements. We also extend our thanks to the technical staff at Nagoya University, K. Kobayashi and T. Kawai for the fabrication of the cryostat and wire grids. This work is supported by Grant-in-Aid for Scientific Research (B) of the Japan Society for the Promotion of Science (JSPS). This development of the NbTiN HEB mixer was carried out as a part of the doctoral thesis of T. Yamakura.

REFERENCES

- [1] Kuwahara, T., Mizuno, A., Nagahama, T., Maezawa, H., Morihira, A., Toriyama, N., Murayama, S., Matsuura, M., Sugimoto, T., Asayama, S., Mizuno, N., Onishi, T., Fukui, Y., "Ground-based Millimeter-wave Observations of Water Vapor Emission (183 GHz) at **Atacama, Chile**", *Advances in Space Research*, Volume 42, Issue 7, p. 1167-1171, 2008
- [2] Y. Irimajiri, T. Manabe, S. Ochiai, H. Masuko, T. Yamagami, Y. Saito, N. Izuka, T. Kawasaki, M. Namiki, and I. Murata, "BSMILES –A Balloon-Borne Superconducting Submillimeter-Wave Limb-Emission Sounder for Stratosphere Measurements", *IEEE Geoscience and Remote Sensing Letters*, vol.3, no.1, pp.88-92, 2006
- [3] D. C Mattis and J. Bardeen, "Theory of the Anomalous Skin Effect in Normal and Superconducting Metals", *Phys. Rev.*, Vol. 111, no. 2, pp. 412-417, Jul., (1958).
- [4] C.E. Tong, J. Stern, K. Megerian, H. LeDuc, TK Sridharan, H. Gibson, and R. Blundell. A low-noise NbTiN hot electron bolometer mixer. In *Proc. 12th Int. Symp. Space Terahertz Technology*, pp. 253–261, 2001
- [5] D. Loudkov, C.Y.E. Tong, R. Blundell, KG Megerian, and JA Stern. Performance of the NbTiN hot electron bolometer mixer with AlN buffer layer at terahertz frequency range. *IEEE Transactions on Applied Superconductivity*, Vol. 15, No. 2 Part 1, pp. 476–479, 2005.
- [6] PP Munoz, S. Bedorf, M. Brandt, T. Tils, N. Honingh, and K. Jacobs. THz Waveguide Mixers With NbTiN HEBs on Silicon Nitride Membranes. *IEEE Microwave and Wireless Components Letters*, Vol. 16, No. 11, pp. 606–608, 2006.
- [7] M. C. Wiedner, G. Wieching, F. Bielau, K. Rettenbacher, N. H. Volgenau, M. Emprechtinger, U. U. Graf, C. E. Honingh, K. Jacobs, B. Vowinkel, K. M. Menten, L.-A. Nyman, R. Gusten, S. Philipp, D. Rabanus, J. Stutzki, and F. Wyrowski, "First observations with CONDOR, a 1.5 THz heterodyne receiver," *Astronomy and Astrophysics*, vol. 454, pp. L33–L36, 2006.
- [8] Pedro Pablo Muñoz, Sven Bedorf, Michael Brandt, Thomas Tils, Netty Honingh, and Karl. Jacobs, "THz waveguide mixers with NbTiN HEBs on silicon Nitride membranes," *IEEE Microwave and Wireless Components Lett.*, vol. 16, no. 11, 2006.
- [9] L. Jiang, S. Shiba, K. Shimbo, M. Sugimura, P. G. Ananthasubramanian, H. Maezawa, Y. Irimajiri, S. C. Shi, and S. Yamamoto, "Development of 0.8 THz and 1.5 THz Waveguide NbTiN HEB Mixers," *Proc. of 19th Int. Symposium on Space Terahertz Tech.*, pp. 409-412, 2008.
- [10] L. Jiang, S. Shiba, K. Shimbo, N. Sakai, T. Yamakura, M. Sugimura, P. G. Ananthasubramanian, H. Maezawa, Y. Irimajiri, and S. Yamamoto, "Development of THz Waveguide NbTiN HEB Mixers," *IEEE Trans. Appl. Supercond.*, vol. 19, no. 3, pp.301-304, 2009
- [11] S. A. Ryabchun, I. V. Tretyakov, M. I. Finkel, S. N. Maslennikov, N. S. Kaurova, V. A. Seleznev, B. M. Voronov, and G. N. Goltsman, "Fabrication and characterization of NbN HEB mixers with *in situ* gold

- contacts,” Proc. of 19th Int. Symposium on Space Terahertz Tech., pp. 62-67, 2008.
- [12] T. Shiino, S. Shiba, N. Sakai, T. Yamakura, L. Jiang, Y. Uzawa, H. Maezawa, and S. Yamamoto, “Improvement of the critical temperature of superconducting NbTiN and NbN thin films using the AlN buffer layer”, *Supercond. Sci. Technol.* 23, 045004, 2010
- [13] H. Maezawa, T. Sato, and T. Noguchi, “Process simulation of reactive DC magnetron sputtering for thin film deposition of niobium-titanium nitride”, *IEEE Trans. Appl. Supercond.*, vol.15, no. 2, pp. 3520-3523, 2005
- [14] RA Wyss, A. Neto, WR McGrath, B. Bumble, and H. LeDuc, “Submillimeter-wave spectral response of twin-slot antennas coupled to hot electron bolometers”. proceedings of 11th Int. Symp. on Space, THz Tech., JackEast Editor, pp.379–388.
- [15] P. Focardi, A. Neto, and W. R. McGrath, “Coplanar-Waveguide-Based Terahertz Hot-Electron-Bolometer Mixers Improved Embedding Circuit Description”, *IEEE Trans. Microwave Theory Tech.*, vol. 50, no. 10, pp.2374-2383, 2006
- [16] Anthony R. Kerr, “Suggestions for revised definitions of noise quantities, including quantum effects,” *IEEE Trans. Microwave Theory Tech.*, vol. 47, no. 3, pp. 325-329, 1999.
- [17] D. W. Allan, “Statistics of Atomic Frequency Standards”, *Proc. of the IEEE*, vol. 54, no. 2, pp. 221-230, 1966.
- [18] J.W.Kooi, J.J.A.Baselmans, A.Baryshev, R. Schieder, M. Hajenius, J.R. Gao, T.M.Klapwijk, B.Voronov, G.Gol’tsman, “Stability of heterodyne terahertz receiver”, *Journal of Appl.Phys.*100,064904, 2006
- [19] T. Berg, S. Cherednichenko, V. Drakinskiy, P. Khosropanah, H. Merkel, E. Kollberg, and J. W. Kooi, “Stability of HEB receivers at THz frequencies”, *Proc. SPIE*, 21-25 Jun., Glasgow, Scotland, United Kingdom, (2004).
- [20] Ling Jiang, Wei Miao, Wen Zhang, Ning Li, Zhen Hui Lin, Qi Jun Yao, Sheng-Cai Shi, Sergey I. Svechnikov, Yury B. Vakhtomin, Sergey V. Antipov, Boris M. Voronov, Natalia S. Kaurova, and Gregory N. Gol’tsman, “Characterization of a quasi-optical NbN superconducting HEB mixer,” *IEEE Trans. Microwave Theory Tech.*, vol. 54, no. 7, 2006.
- [21] D. Rabanus, U.U. Graf, M. Philipp, O. Ricken, J. Stutzki, B. Vowinkel, M.C. Wiedner, C. Walther, M. Fischer, J. Faist, “Phase locking of a 1.5 Terahertz quantum cascade laser and use as a local oscillator in a heterodyne HEB receiver”, *Optics Express*, Vol. 17, No.3, pp.1159–1168, 2009.
- [22] J. R. Gao, J. N. Hovenier, Z. Q. Yang, J. J. A. Baselmans, A. Baryshev, M. Hajenius, T. M. Klapwijk, A. J. L. Adam, T. O. Klaassen, B. S. Williams, S. Kumar, Q. Hu, and J. L. Reno, “Terahertz heterodyne receiver based on a quantum cascade laser and a superconducting bolometer”, *Appl. Phys. Lett.* 86, 244104, 2005
- [23] H.-W. Hübers, S. G. Pavlov, A. D. Semenov, R. Köhler, L. Mahler, A. Tredicucci, H. E. Beere, D. A. Ritchie, and E. H. Linfield, “Terahertz quantum cascade laser as local oscillator in a heterodyne receiver”, *OPTICS EXPRESS*, Vol. 13, no. 15, 5890-5896, 2005
- [24] C. Walther, G. Scalari, J. Faist, H. Beere, and D. Ritchie, “Low frequency terahertz quantum cascade laser operating from 1.6 to 1.8 THz”, *Applied Phys. Lett.* 89, 231121, 2006.

Poster Session P9: THz Sources

Frequency stabilization of a THz quantum-cascade laser to a molecular absorption line

H. Richter ¹⁾, S. G. Pavlov ¹⁾, A. D. Semenov ¹⁾, L. Mahler ²⁾,
A. Tredicucci ²⁾, H. E. Beere ³⁾, D. A. Ritchie ³⁾, and H.-W. Hübers ^{1), 4)}

¹⁾Institute of Planetary Research, German Aerospace Center (DLR),
Rutherfordstr. 2, 12489 Berlin, Germany

²⁾NEST CNR-INFM and Scuola Normale Superiore,
Piazza dei Cavalieri 7, 56126 Pisa, Italy

³⁾Cavendish Laboratory, University of Cambridge, Madingley Road,
Cambridge CB3 0HE, United Kingdom

⁴⁾Institut für Optik und Atomare Physik, Technische Universität Berlin,
Hardenbergstraße 36, 10623 Berlin, Germany

Abstract

The terahertz (THz) portion of the electromagnetic spectrum bears an amazing scientific potential in astronomy. High resolution spectroscopy in particular heterodyne spectroscopy of molecular rotational lines and fine structure lines of atoms or ions is a powerful tool, which allows obtaining valuable information about the observed object such as temperature and dynamical processes as well as density and distribution of particular species. One example is the OI fine structure line at 4.7 THz. This is a main target to be observed with GREAT, the German Receiver for Astronomy at Terahertz Frequencies, which will be operated on board of SOFIA. A major challenge for a heterodyne receivers operating at this frequency is the local oscillator (LO). THz quantum-cascade lasers (QCLs) have the potential to replace the presently used gas laser LO. A major issue is the frequency stabilization of the QCL, because its free-running linewidth is several MHz.

We report on the frequency stabilization of a THz QCL to the absorption line of methanol gas at a frequency of 2.55 THz. The QCL is mounted on the first stage of a pulse tube cooler and operates at a temperature of about 50 K. The stabilization method is based on frequency modulation of the laser emission across the absorption line. The resulting derivative-like signal is used as error signal for a control loop which keeps the laser frequency at maximum absorption. The unstabilized laser has frequency fluctuations of 15 MHz which are reduced to 300 kHz (full width at half maximum) with the control loop in action. The line shape of the locked signal is Gaussian. The achieved linewidth is already sufficient for many applications. For example the frequency resolution of a typical heterodyne receiver with an acousto-optical backend spectrometer is 1.5 MHz. With a 300 kHz linewidth of the LO this increases marginally to 1.53 MHz. In addition, the stabilization scheme is robust and versatile, because it requires only an additional detector and a small gas absorption cell, while being applicable even at the highest THz frequencies due to the rich absorption spectra of molecules such as CH₃OH or H₂O.

REFERENCES

- [1] H. Richter, A. D. Semenov, S. Pavlov, L. Mahler, A. Tredicucci, H. E. Beere, D. A. Ritchie, K. Il'in, M. Siegel, and H.-W. Hübers, "Terahertz heterodyne receiver with quantum cascade laser and hot electron bolometer mixer in a pulse tube cooler", *Appl. Phys. Lett.* 93, 141108 (2008).
- [2] H. Richter, S. G. Pavlov, A. D. Semenov, L. Mahler, A. Tredicucci, H. E. Beere, D. A. Ritchie, and H.-W. Hübers "Sub-megahertz frequency stabilization of a terahertz quantum cascade laser to a molecular absorption line", submitted to *Appl. Phys. Lett.*

A 4.7-THz gas laser local oscillator for GREAT on SOFIA

H. Richter¹⁾, M. Greiner-Bär¹⁾, B. Günther¹⁾, K. Rösner¹⁾, and H.-W. Hübers^{1), 2)}

¹⁾Institute of Planetary Research, German Aerospace Center (DLR),
Rutherfordstr. 2, 12489 Berlin, Germany

²⁾Institut für Optik und Atomare Physik, Technische Universität Berlin,
Hardenbergstraße 36, 10623 Berlin, Germany

Abstract

A particularly important transition for astronomy is the OI fine structure line at 4.7 THz. It is an important cooling line of the interstellar medium and allows studying the chemical composition, the evolution, and the dynamical behavior of astronomical objects. Consequently, this transition is a main target to be observed with GREAT, the German Receiver for Astronomy at Terahertz Frequencies, which will be operated on board of SOFIA.

A major challenge for a heterodyne receiver operating at such a high frequency is the local oscillator (LO). Despite significant progress in the development of a quantum-cascade laser based LO [1] the baseline design for GREAT is an optically pumped gas laser operated at 4.7 THz. In this report we will present the design and performance of the 4.7-THz gas laser LO for SOFIA. The LO is based on a radio frequency excited CO₂ laser which has a sealed-off gas volume and which is frequency tunable by a grating. The CO₂ laser is operated on the 9P12 transition of the CO₂ molecule. The output emission is focused into the THz laser resonator. The THz laser is transversely excited. It operates on the 4.75 THz line of ¹³CH₃OH. For frequency stabilization of the CO₂ laser a small part of its output radiation is guided into a Fabry-Pérot interferometer (FPI) which serves as a length or frequency reference. In order to compensate for temperature or pressure induced drifts of the FPI length the emission of a frequency stabilized helium-neon (HeNe) laser is coupled into the FPI as well. The FPI is locked to the emission of the HeNe laser. We will present the design and the performance of the LO with respect to output power, short and long term power stability, and beam profile. The system is ready and awaits implementation in GREAT and operation on board of SOFIA.

REFERENCES

- [1] H. Richter, A. D. Semenov, S. Pavlov, L. Mahler, A. Tredicucci, H. E. Beere, D. A. Ritchie, K. Il'in, M. Siegel, and H.-W. Hübers, "Terahertz heterodyne receiver with quantum cascade laser and hot electron bolometer mixer in a pulse tube cooler", *Appl. Phys. Lett.* 93, 141108 (2008).

Development of a HBV tripler for 0.6 THz

Johanna Liljedahl*, Tomas Bryllert, Josip Vukusic and Jan Stake

Dept. of Microtechnology and Nanoscience, Chalmers University of Technology, Göteborg, Sweden

*Contact: johanna.liljedahl@chalmers.se, phone +46(0)31 772 18 75

Abstract—We report on the progress of the design of a HBV frequency tripler for 0.6 THz. The diode is based on the InGaAs/InAlAs/AlAs on InP material system, and the diode material and geometry has been optimised with regards to conversion efficiency. In designing the diode, it was found that self heating is the major limiting factor due to the poor thermal conductivity of InGaAs. The resulting HBV is a two-mesa diode from a three-barrier material, with a mesa area of $6 \times 3 \mu\text{m}^2$, and is estimated to have a 6-7% conversion efficiency and 100 - 150 K self heating at an input power of 30 mW.

I. INTRODUCTION

The trend in recent space observing projects is to cover frequencies in the terahertz (THz) gap. In many observing applications the high spectral resolution from heterodyne receivers is desired. However, when going from millimetre to sub-millimetre wavelengths there is a lack of fundamental LO sources above 200 GHz. Therefore the most commonly used and efficient solution for LO signal sources is frequency up-conversion through multiplication by non-linear semiconductor devices [1].

Today most frequency multiplier circuits are realized using Schottky diodes. Due to their high performance, balanced Schottky doublers have become standard as multiplier sources, and planar Schottky diode multipliers for the THz frequency range have been demonstrated [2].

An alternative to the Schottky diode is the Heterostructure Barrier Varactor (HBV). Ever since the invention in 1989, the HBV diode has been promising for frequency multiplication to THz frequencies [3]. Today HBV diodes are used as high power multipliers for frequencies up to and above 200 GHz [4].

The HBV consists of a wide bandgap semiconductor barrier spaced between two narrow bandgap, equally doped, semiconductor modulation layers. The C-V curve is symmetric, while the I-V curve is anti-symmetric, and these properties cause the HBV to only generate odd harmonics. Thereby, when used as a frequency tripler, there is only need for circuit matching at the in and output frequencies, and no idler matching is needed. In addition, there is no need for DC-biasing, which together with the matching requirements enables a simple and compact circuit design, making it ideal for space applications.

Another advantage is that the sandwich structure of the HBV allows stacking of several diodes for better power handling capability, and at the same time diode miniaturisation is prevented [5]. Nevertheless, the highest output frequency published for HBV diode based multipliers is 450 GHz [6]. Our aim is to push this limit further into the sub-mm region.

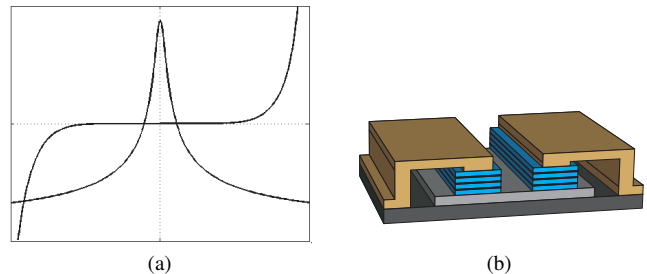


Fig. 1. (a) C-V and I-V curve for a HBV diode. C-V is symmetric while I-V is antisymmetric. (b) Model of a two-mesa HBV diode with a total of six barriers, and gold air bridges. (The model is not according to scale)

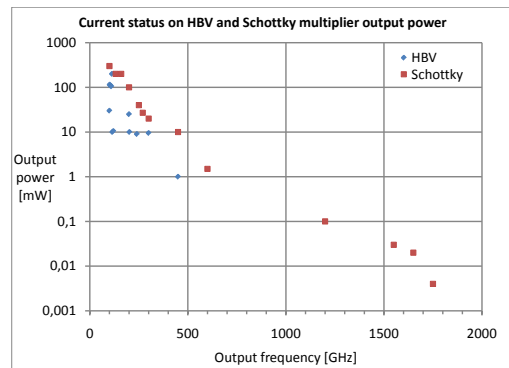


Fig. 2. Current status on output power for single diode HBV frequency multipliers and Schottky diode frequency multiplier chains [7][8][9][5].

We present the current status on the development of an HBV tripler for an output frequency of 600-700 GHz. The designed HBV is based on the InGaAs/InAlAs/AlAs epitaxially grown on InP material system. The doping and layer structure impact on the conversion efficiency has been evaluated, and consideration of the effects of self heating has been crucial when choosing an appropriate diode design. The HBV diode is implemented in a MMIC circuit containing matching and filtering elements.

II. 0.6 THz HBV TRIPLER DEVELOPMENT

In developing a 600 GHz frequency tripler there are several constraints to consider. At this high input frequency, 200-220 GHz, the available power is estimated to be less than 40 mW, which together with impedance boundaries limits the size and geometry of the diode. The high frequency makes it unsuitable for the otherwise commonly used flip chip soldering, hence the HBV frequency tripler is implemented using a monolithic

approach which offers high repeatability.

For the circuit design we decided to use conventional technology, with the advantage of having good heat sinking properties and already established designs to fall back on. The tripler will consist of a waveguide block, with waveguide in and outputs, and the matching circuit and HBV on a microstrip MMIC in a waveguide channel, coupled into the waveguides by probes.

We have limited ourselves to the use of the InGaAs/InAlAs/AlAs epitaxially grown on an InP substrate material system. The advantages of this material are the high mobility of InGaAs and the height of the energy bandgap barrier.

An effort to analytically optimise the material structure with regards to the conversion efficiency for an input frequency of 200 GHz has been made. This optimised material, material A was then compared to an already grown material, material B, to evaluate the necessity of growing a new material. The existing Material B has been verified in I-V and C-V measurements.

In comparing the two materials the effects of self heating were taken into account through FEM heat transfer modelling combined with harmonic balance simulations in ADS. In these simulations the diode geometry was investigated as well.

Finally the optimum embedding impedances for the HBV diode tripler configuration has been determined to maximise the conversion efficiency. For these simulations a 3-D model of the diodes including air bridges have been modelled in Ansoft HFSS for S-parameter extraction, combined with harmonic balance simulations in ADS.

III. MATERIAL VERIFICATION

The material in Table I, earlier introduced as Material B, has been verified in I-V and C-V measurements, see figure 3. For these measurements single mesa test diodes were fabricated with different areas and measured in a probe station with an I-V and a LCR meter. The maximum capacitance of the HBV material was measured to be $C_{max} = 0.9 \text{ fF}/\mu\text{m}^2$, and the breakdown voltage $V_{br} = \pm 19 \text{ V}$ (for 3 barriers). From the C-V measurements the doping concentration was extracted, $N_d = 1.4 \cdot 10^{17} \text{ cm}^{-3}$, which is slightly higher than the specification. The extracted value for the doping was then used when evaluating the material in harmonic balance simulations, described below.

IV. DIODE OPTIMISATION

The HBV tripler will be pumped with at a frequency of 200-220 GHz, and at this frequency the expected available input power is about 20-40 mW. Thus the diode is optimised for an input power of 30 mW. Diode parameters such as the epi-layer structure, size and geometry have been examined in order to ensure large conversion efficiency. Furthermore, the advantage of growing a new frequency optimised material, versus using a material that has already been fabricated, but is optimised for a lower frequency range, has been evaluated.

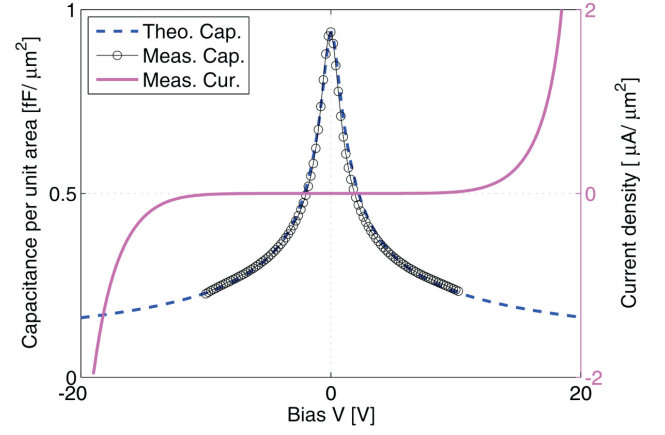


Fig. 3. I-V and C-V measurement result plus the theoretical C-V curve using the extracted doping.

A. Epi-layers

1) *Barrier*: The barrier material in the epi-layer design consists of a 3 nm thin layer of AlAs in the middle of two layers of 50 nm $\text{In}_{0.52}\text{Al}_{0.48}\text{As}$. The AlAs prevents leakage current by increasing the energy bandgap, but this barrier layer is lattice mismatched to InAlAs, so in order to keep it strained the thickness is limited. This optimum barrier design for the InGaAs/InAlAs/AlAs HBV material system is further described in [10] and [11], and has not been treated within this work.

2) *Modulation layers*: A figure of merit for a varactor diode design is the dynamic cut-off frequency [12]

$$f_c = \frac{S_{max} - S_{min}}{2\pi R_S} \quad (1)$$

It is derived from the equivalent circuit of a varactor with a variable reactance, $C(v) = \frac{1}{S(v)}$, connected in series with a resistance, R_S .

The cutoff frequency dependence of the conversion efficiency can be estimated by

$$\eta \approx \frac{100}{1 + \alpha \left(\frac{f_p}{f_c}\right)^\beta} \% \quad (2)$$

where f_p is the pumping frequency, f_c the cutoff frequency, $\alpha = 200$ and $\beta = 1.5$ [13]. So in order to achieve a high efficiency, the cutoff frequency should be maximised, which is done by maximising the difference in elastance and minimising the series resistance.

The series resistance consists of several resistance elements

$$R_S = R_{active} + R_{spread,buffer} + R_{contact} \quad (3)$$

where the resistance in the epi-layers is

$$R_{active} = \sum_n \frac{l_n}{\mu_n N_n q A} \quad (4)$$

n is the layer number, l_n the layer thickness, μ_n the layer mobility, N_n the layer doping and A the mesa area. The

spreading resistance between two mesas or mesa and contact for a single mesa diode is

$$R_{spread,buffer} = \frac{l_{buffer}}{\mu_{buffer} N_{buffer} q A_{buffer}} \quad (5)$$

and the ohmic contact resistance is

$$R_{contact} = N_m \frac{r_c}{A} \quad (6)$$

where N_m is the number of mesas and $r_c = 100 \Omega\text{-}\mu\text{m}^2$. The mobility is doping dependent and estimated according to [14].

The minimum elastance is determined by the Debye length, L_D ,

$$S_{min} = \frac{N}{A} \left(\frac{b}{\varepsilon_b} + \frac{2s}{\varepsilon_d} + \frac{2L_D}{\varepsilon_d} \right) \quad (7)$$

while the maximum elastance is determined by the maximum depletion width, w_{max} , [13]

$$S_{max} = \frac{N}{A} \left(\frac{b}{\varepsilon_b} + \frac{2s}{\varepsilon_d} + \frac{w_{max}}{\varepsilon_d} \right). \quad (8)$$

N is the number of barriers, A the diode area, b and s the barrier and spacer thickness respectively, and ε the dielectric constants for the different materials. The maximum depletion width is limited by impact ionization, which is doping dependent, and by the current saturation which can be approximated to be constant with regards to the doping level for a constant pumping frequency [13]. This means that for doping levels above a certain value the cutoff frequency is impact ionization limited and below that frequency it is limited by the current saturation. These two criteria can be combined to estimate the optimum doping level for a high cutoff frequency, see figure 4.

This model indicates that the difference in modulation layer thickness has little impact on the conversion efficiency compared to for example the number of barriers, i.e. HBV diodes stacked in series. In order to minimise the series resistance, an optimised modulation layer thickness has the same value as the maximum depletion width, and the cut-off frequency decreases for thicker layers. While the cut-off frequency increases with the number of barriers. However, as the number of barriers increase, so does the input power necessary to drive the HBV. Therefore we chose to compare conversion efficiency for HBV diodes with different geometries, made of a two-barrier material with a modulation layer thickness of 190 nm and doping of $1.4 \cdot 10^{17} \text{ cm}^{-3}$, i.e. Material A, and the three-barrier material we already have, Material B (see Table I).

B. Device geometry

In deciding the geometry of the HBV diode taking the effects of self heating into account is crucial due to the poor thermal conductivity of InGaAs. Using heat transfer FEM simulations combined with ADS harmonic balance simulations the heating in the diode active region and the conversion efficiency has been estimated, and an appropriate geometry found.

TABLE I
HBV ACTIVE LAYER MATERIAL SPECIFICATION, MATERIAL B

Layer	Material	Thickness [Å]	Doping [cm^{-3}]	Comment
1	In _{0.53} Ga _{0.47} As	2,500	10^{17}	Modulation
2	In _{0.53} Ga _{0.47} As	50	Undoped	Spacer
3	In _{0.52} Al _{0.48} As	50	Undoped	Barrier
4	AlAs	30	Undoped	Barrier
5	In _{0.52} Al _{0.48} As	50	Undoped	Barrier
6	In _{0.53} Ga _{0.47} As	50	Undoped	Spacer
7-18	... 2 × Layers 1 - 6 ...			
19	In _{0.53} Ga _{0.47} As	2,500	10^{17}	Modulation

1) *Self heating*: In the FEM heat transfer model the power distributed as a volume power source, assuming all input power is converted to heat, see Figure 5. The resulting temperature is then used to calculate the thermal resistance, R_T of the diode, and the thermal resistance is then put in to ADS harmonic balance simulations where self heating is implemented using Chalmers HBV electro-thermal model to calculate the rise in temperature under RF pumping [15]. In the heat transfer simulations the temperature dependent thermal conductivity is used for InGaAs, InP and gold.

$$\begin{aligned} \kappa_{InGaAs} &= 4.7 \cdot \left(\frac{T_0}{T} \right)^{1.375} \\ \kappa_{InP} &= 68 \cdot \left(\frac{T_0}{T} \right)^{1.48} \\ \kappa_{Au} &= 0.0586(282 - T) + 317 \end{aligned}$$

2) *Harmonic balance*: The electrical properties of the HBV are modeled in ADS with the quasi-empirical Chalmers HBV model [16]

$$V(Q) = N \left\{ \frac{bQ}{\varepsilon_b A} + 2 \frac{sQ}{\varepsilon_d A} + \text{Sign}(Q) \cdot \left(\frac{Q^2}{2qN_d \varepsilon_d A^2} + \frac{4k_B T}{q} \left(1 - \exp \left[-\frac{|Q|}{2L_D A q N_d} \right] \right) \right) \right\} \quad (9)$$

These simulations also provides a value for the optimum embedding impedances for a maximised conversion efficiency.

Different geometries have been evaluated for a fixed input power of 40 mW and pump frequency $f_p = 200 \text{ GHz}$. We have examined one and two-mesa HBV diodes, with different mesa areas, of Material A and B, to determine which geometry will give the highest conversion efficiency without exceeding the maximum temperature increase allowed, 130 – 150 K. For each geometry the efficiency improves when the area decreases, see Figure 6. However only the geometry and areas where the temperature limit has not been reached are interesting, consequently the one-mesa geometry could be ruled out immediately since the area required results in a very low conversion efficiency of the HBV diode.

The best conversion efficiency geometry was chosen, a two-mesa HBV with a mesa area of $6 \times 3 \mu\text{m}^2$, where the larger dimension sets the width of the air bridges. As can be seen in figure 6, the difference in efficiency is not very large, why we choose to use the epi-material we already have, Material B, rather than fabricate a new material.

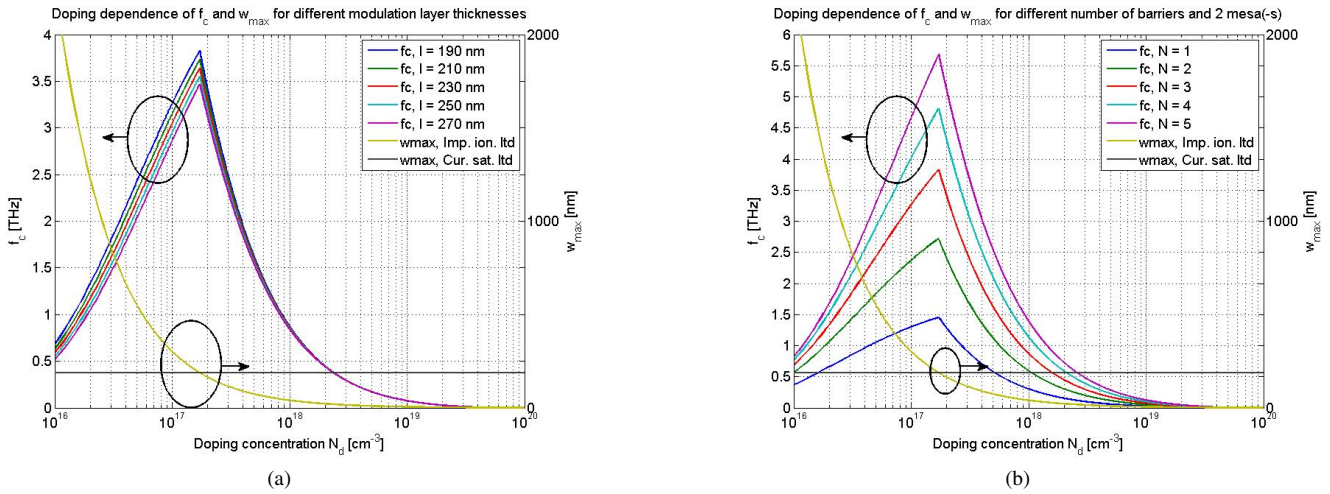


Fig. 4. Cutoff frequency and maximum depletion layer width dependence on modulation layer doping level. To the left of the intersection the cutoff frequency is current saturation limited, and to the right the cutoff frequency is impact ionization limited. $f_p = 200$ GHz, $A = 18 \mu\text{m}^2$. (a) Cutoff frequency for different thickness of the modulation layers. $N = 3$, $N_m = 2$. (b) Cutoff frequency for different number of barriers per mesa. $l = 190$ nm, $N_m = 2$.

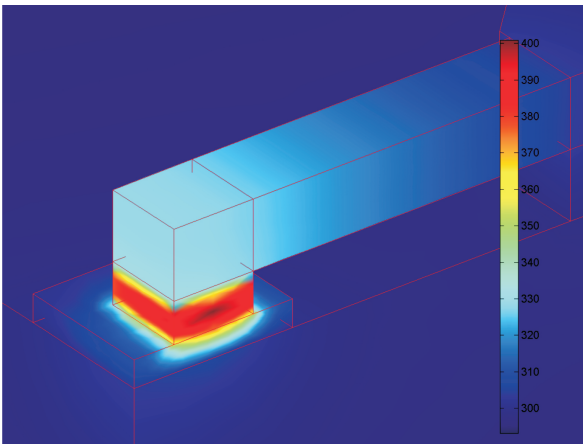


Fig. 5. Heat transfer FEM simulation of a two-mesa HBV diode. Clearly shows how the heat is concentrated in the active layers of the HBV. The image shows quarter of a diode, due to symmetry.

V. CIRCUIT

While HBV diodes for lower frequencies often are separately flip chip soldered to a circuit of another material, e.g. quartz, integration of the HBV diode on a MMIC is preferable for THz frequencies. As the frequency gets higher soldering uncertainty and losses are eliminated. This means that we are limited to a InP substrate which has a large dielectric constant, so in order to reach reasonable line widths and impedances, and to avoid waveguide modes in the substrate, the substrate needs to be thin.

We will design a classic waveguide-to-microstrip-to-waveguide circuit, with all matching elements fabricated on the microstrip MMIC. The waveguide dimensions are WR-4 at the input and WR-1.5 at the output. The channel width and height is $160 \mu\text{m}$. The design is similar to the design in [17].

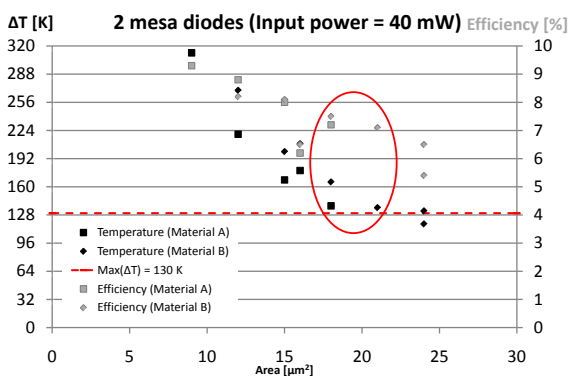


Fig. 6. Efficiency and temperature comparison of two-mesa diodes with different mesa areas and two different materials: A two-barrier material optimised for an input frequency of 200 GHz, and the 3-barrier material described in Table I. It shows that the area needs to be at least $18 \mu\text{m}^2$ to not overheat, and that the 3-barrier material we already have can be used.

A. Substrate

The most common way to thin down a substrate is either mechanically, through lapping of the back of the substrate, or through membrane technology where the back side of the substrate is etched away until a stop layer is reached deciding the substrate thickness. As InP is a brittle material there is some concern when thinning it down too thin. And as for membrane technology there are also some issues regarding the background doping of the epitaxially grown InP layer. We do not have access to Fe-doped InP epi-material, which means the membrane will be lossy.

We have decided to move forward with a $20 \mu\text{m}$ thick substrate, which we can lap down mechanically with good precision. Propagation constant simulations in Ansoft HFSS show that $20 \mu\text{m}$ is small enough to avoid waveguide modes in the substrate for strip widths smaller than about $40 \mu\text{m}$ in a waveguide $160 \mu\text{m}$ wide, but still large enough to have a reasonable tolerance.

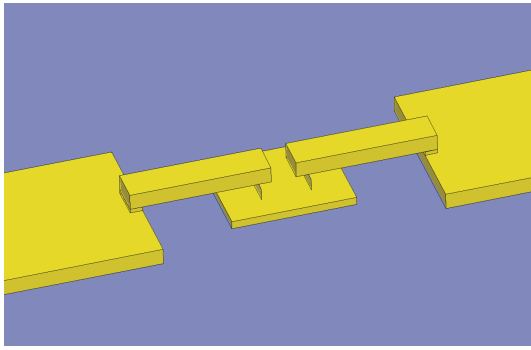


Fig. 7. HBV diode HFSS model with airbridges for deembedding optimum impedances.

B. Diode embedding impedance

The optimum HBV diode embedding impedance has been estimated in order to achieve maximum conversion efficiency at an input power of 30 mW in order to keep good efficiency over the whole 20–40 mW region. The input and output matching impedance for the fundamental tone at 200 GHz and third harmonic has been calculated in S-parameter simulations in Ansoft HFSS combined with harmonic balance simulations in ADS of the chosen geometry, a two-mesa diode of the three-barrier material (Material B). The air bridges are included in the S-parameter simulation, see Figure 7, in order to have them included in future matching circuit simulations. The HBV diode mesas are replaced with lumped ports in this simulation, and the HBV model in (9) is used in ADS. The length of the air bridges is $12 \mu\text{m}$, the width is $4 \mu\text{m}$, the mesa area is $6 \times 3 \mu\text{m}^2$, the distance between the mesas is $3 \mu\text{m}$, pump frequency $f_p = 200 \text{ GHz}$ and the input power is 30 mW. The thermal resistance put in to the device is a "worst case" thermal resistance calculated from an input power of 40 mW on the same diode area, $R_T = 4474 \text{ K/W}$.

The resulting optimum impedances at the fundamental and third harmonic, for an input frequency of 200 GHz is displayed in Figure 8. The conversion efficiency at these impedances is $\eta > 6\%$ and the self heating in the HBV diode is $100 < \Delta T < 150 \text{ K}$.

VI. CONCLUSION

A HBV frequency tripler with an output frequency of 0.6 THz is currently under development. Investigations of material and diode layout show that self heating is a major limiting factor for reaching high conversion efficiency and power levels at higher frequencies. The 3-barrier epi-material developed for operation at lower frequencies can be used for the HBV and provide a theoretical conversion efficiency of 6-7% for a 2-mesa HBV diode. At an expected input power of 30 mW this will result in a output power of about 1 mW.

The circuit developed for the tripler is a waveguide-to-microstrip MMIC-to-waveguide circuit. The matching circuitry on the MMIC is under development and when that is done the HBV tripler will be fabricated at MC2, Chalmers.

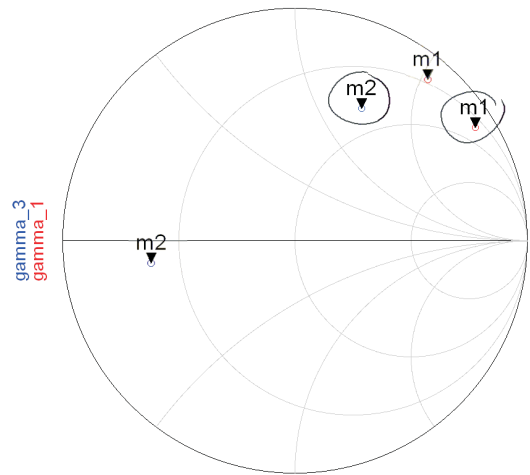


Fig. 8. HBV optimum embedding impedances for maximised efficiency at 30 mW input power and $f_p = 200 \text{ GHz}$. m1 marks the input matching impedance for fundamental tone, and m2 the output impedance at the third harmonic including and excluding (circled) air bridges.

ACKNOWLEDGMENT

The authors would like to thank the Swedish Research Council (VR) and MSB "ISSI" for funding this research.

REFERENCES

- [1] P. H. Siegel, "THz Technology: An Overview," *International Journal of High Speed Electronics and Systems*, vol. 13, no. 2, pp. 351–394, 2003.
- [2] A. Maestrini, J. Ward, J. Gill, H. Javadi, E. Schlecht, C. Tripon-Canseliet, G. Chattopadhyay, and I. Mehdi, "A 540-640-ghz high-efficiency four-anode frequency tripler," *Microwave Theory and Techniques, IEEE Transactions on*, vol. 53, no. 9, pp. 2835 – 2843, sept. 2005.
- [3] E. Kollberg and A. Rydberg, "Quantum-Barrier-Varactor Diodes for High-Efficiency Millimetre-Wave Multipliers," *Electronic Letters*, vol. 25, no. 25, pp. 1696–1698, 1989.
- [4] J. Stake, T. Bryllert, A. i. Olsen, and J. Vukusic, "Heterostructure barrier varactor quintuplers for terahertz applications," *Proceedings of the 3rd European Microwave Integrated Circuits Conference*, pp. 206 – 209, oct. 2008.
- [5] J. Vukusic, T. Bryllert, T. A. Emadi, M. Sadeghi, and J. Stake, "A 0.2-W heterostructure barrier varactor frequency tripler at 113 GHz," *IEEE ELECTRON DEVICE LETTERS*, vol. 28, no. 5, pp. 340–342, MAY 2007.
- [6] M. Saglam, B. Schumann, V. Mullerwiebus, A. Megej, U. Auer, M. Rodriguez-Girones, R. Judaschke, E. Tegude, and H. Hartnagel, "450 ghz millimetre-wave signal from frequency tripler with heterostructure barrier varactors on gold substrate," *Electronics Letters*, vol. 38, no. 13, pp. 657 –658, Jun 2002.
- [7] J. S. Ward, G. Chattopadhyay, J. Gill, H. Javadi, C. Lee, R. Lin, A. Maestrini, F. Maiwald, I. Mehdi, E. Schlecht, and P. Siegel, "Tunable broadband frequency-multiplied terahertz sources," *Infrared, Millimeter and Terahertz Waves, 2008. IRMMW-THz 2008. 33rd International Conference on*, pp. 1 – 3, sept. 2008.
- [8] J. Stake, T. A. Emadi, and J. Vukusic, "Terahertz generation by multiplication," in *Terahertz Frequency Detection and Identification of Materials and Objects*, R. E. Miles, X.-C. Zhang, H. Eisele, and A. Krotkus, Eds. Dordrecht, The Netherlands: Springer Netherlands, 2007, pp. 17–30.
- [9] V. D. Inc., "Multipliers," available: <http://www.virginiadiodes.com/>, Date: April 13 2010.
- [10] Y. Fu, J. Stake, L. Dillner, M. Willander, and E. L. Kollberg, "AlGaAs/GaAs and InAlAs/InGaAs heterostructure barrier varactors," *Journal of Applied Physics*, vol. 82, no. 11, pp. 5568–5572, Dec 1997.
- [11] T. A. Emadi, T. Bryllert, M. Sadeghi, J. Vukusic, and J. Stake, "Optimum barrier thickness study for the InGaAs/InAlAs/AlAs heterostructure barrier varactor diodes," *Applied Physics Letters*, vol. 90, no. 1, Jan 2007.
- [12] P. J. Penfield and R. P. Rafuse, *Varactor Applications*. The M.I.T. Press.

- [13] J. Stake, S. H. Jones, L. Dillner, S. Hollung, and E. L. Kollberg, "Heterostructure-Barrier-Varactor Design," *IEEE Transactions on Microwave Theory and Techniques*, vol. 48, no. 4, pp. 677–682, Apr 2000.
- [14] M. Sotoodeh, A. Khalid, and A. Rezazadeh, "Empirical low-field mobility model for III-V compounds applicable in device simulation codes," *JOURNAL OF APPLIED PHYSICS*, vol. 87, no. 6, pp. 2890–2900, MAR 15 2000.
- [15] M. Ingvarson, J. Vukusic, A. Olsen, T. Emadi, and J. Stake, "An electro-thermal HBV model," in *2005 IEEE MTT-S INTERNATIONAL MICROWAVE SYMPOSIUM, VOLS 1-4*, 2005, pp. 1151–1153.
- [16] L. Dillner, J. Stake, and E. Kollberg, "Modeling of the heterostructure barrier varactor diode," 1997, presented at the Int. Semiconductor Device Res. Symp., Charlottesville, VA.
- [17] J. Vukusic, A. Ø. Olsen, T. Bryllert, and J. Stake, "High power w-band monolithically integrated tripler," *International Conference on Infrared, Millimeter, and Terahertz Waves IRMMW 2009 Proceedings*, 2009.

Vertically Illuminated TW-UTC Photodiodes for Terahertz Generation

Claudio Barrientos Z. ^{*†}, Victor Calle^{*}, Marcos Diaz^{*}, F. Patricio Mena^{*}, Josip Vukusic [†], Jan Stake[†] and Ernest A. Michael (PI)^{*†}

^{*}University of Chile, Department of Electrical Engineering, Santiago de Chile

[†]Chalmers University of Technology, Department of Microtechnology and Nanoscience MC2, Gothenburg, Sweden

[‡]Contact: cbarrien@ing.uchile.cl, emichael@ing.uchile.cl phone +56-2-9784095

Abstract—More efficient continuous-wave photonic near-infrared mixers as terahertz sources are investigated with the motivation to develop a universal photonic local oscillator for astronomical submillimeter/terahertz receiver systems. For this, our group has developed new concepts for vertically illuminated traveling-wave (TW) photomixers. The new device called TW-Uni-Travelling Carrier photodiodes (TW-UTC PD) was simulated, modeled and shall be optical/terahertz tested at the Electrical Engineering Department of the University of Chile, whereas device fabrication is performed at the MC2 cleanroom facility at Chalmers University of technology. We are reporting on first progresses in this direction.

I. INTRODUCTION

Development of terahertz frequencies systems has been widely studied during the last years and this, has lead to a wide range of applications in astronomy, biology, medicine, imaging, communications and security. For radio astronomy applications more efficient continuous-wave photonic mixers as terahertz sources are being developed with the motivation to fabricate a universal photonic local oscillator for THz radio astronomy receivers. Two new concepts are being integrated to develop these new types of photomixers. The first concept is called large area vertical illuminated travelling-wave (TW) photomixing and the second one involves Uni-Travelling Carrier Photodiodes (UTC-PD). The final device, called TW-UTC photodiode, has been simulated and modeled and shall be optically tested in the new terahertz photonics laboratory at the Electrical Engineering Department of the University of Chile, whereas device fabrication is being conducted at the MC2 clean room facility at Chalmers University of Technology. This paper describes design and developments made so far, for a TW-UTC photomixer between 200 GHz and 2 THz.

II. VERTICAL ILLUMINATED TW-UTC PD CONCEPT

The main goal behind fabrication of these new types of photomixers is to achieve better efficiency, which is measured with higher power at high frequencies and larger bandwidth. It is well known that the main advantage of travelling-wave photodetectors (TWPD's) is to avoid the parasitic RC constant limitation of the corresponding lumped element [1], this means that bandwidth and power can be improved with TW devices. Travelling-wave photomixers can be divided in two classes

depending of the effective absorption coefficient (α) of the devices structure [2], low effective $\alpha \ll 1\mu m^{-1}$ leads to edge coupled (fiber-illuminated), whereas high absorption leads to vertically illuminated designs. In fiber illuminated devices, the output power is proportional to the square of the photocurrent and the bandwidth depends inversely on the photocarrier lifetime and electrode capacitance, therefore, photomixers have been usually designed for small areas. In order to get a higher power capability large-area travelling-wave photomixers is in our case a better option, due to in these types of devices bandwidth is not limited for the electrode capacitance and also it has higher-power handling capacity. In a general case of photomixing when a photomixer is illuminated by two single mode CW lasers beams, the THz output power may be written as [3].

$$P(\omega) = \frac{I_0^2 R_A}{2[1 + (\omega\tau_c)^2][1 + (\omega R_A C)^2]} \quad (1)$$

where $I_0 (= GV_0)$ is the photocurrent, G is the DC photoconductance, V_0 is the bias DC voltage, R_A is the antenna resistance, τ_c is the carrier life time, and C is the device capacitance. In the case of TW devices the time constant $\tau_{RC} (= R_A C)$ is ideally bypassed, thus the output power roll-off is proportional to ω^{-2} . In addition to improve even more the THz power, and achieve wide bandwidth, the carrier life time must be improved. One way to do it, is using Uni-travelling Carrier Photodiodes (UTC-PD). The main feature of the UTC-PD proposed by Ishibashi et al. [4] is that only electrons work as active carriers optimizing the $R_A C$ and transit time constants. Thus, bandwidth and output saturation current are both increased in comparison with PIN PD's and therefore higher output powers can be obtained at high frequencies [3],[4].

By using UTC-PD's as vertical illuminated travelling-wave devices, it is feasible to improve simultaneously bandwidth and output power, the latter would increase by a factor of $(1 + (\omega R_A C)^2)$. Hence output power and bandwidth in TW-UTC PD may be rewritten as,

$$P_{THz}(\omega) = \frac{1}{2} R_A \frac{I_0^2}{1 + (\omega\tau_c)^2} \quad (2)$$

$$f_{3dB} = \frac{1}{2\pi\tau_c} \quad (3)$$

Using the fact of I_0 is equal to [8]:

$$I_0 = \eta P_0 \frac{e}{h\nu} \frac{\tau_{tr}}{2} v_{e,dr} A_{ill} \quad (4)$$

where $P_0 = \sqrt{P_1 P_2}$ is the beat part of the interference of both laser powers, η is the quantum efficiency, $v_{e,dr} (= \mu_e \frac{V_0}{W})$, is the drift velocity of the electrons, $W (= W_A + W_c)$ is the spacing between the electrodes, A_{ill} is the effective illuminated area, and $\tau_{tr}/2$ is the effective life time of the photoelectrons in the photoconductive gap.

In order to optimize THz power, not only the above parameters must be tuned, we also need optimize the transit time. The travelling time in the collection layer can be defined as $\tau_c = W_c/v_d$, where W_c is the collection layer width and v_d is the drift velocity of electrons [6], thus transit time in UTC-PDs can be defined as [7].

$$\tau_{tr} = \tau_A + \tau_c = \frac{W_A^2}{3D_e} + \frac{W_A}{v_{th}} + \frac{W_c}{v_d} \quad (5)$$

where, τ_{tr} is the total transit time and τ_A is the transit time in the absorption layer, τ_c is the transit time in the collection layer, W_A , D_e and v_{th} are the absorption layer thickness, diffusivity of electrons in the absorption layer and the electron thermionic emission velocity, respectively. For absorption layer thickness larger than 100 nm (our case), transit time of electrons is dominated mainly for the first term in the equation (5), then transit time can be approximated as $\tau_{tr} \approx W_A^2/3D_e$.

III. TW-UTC PHOTOMIXER MODELLING

A. Layer Structure

The layer structure chosen for the UTC-PD is based in the optimization made for Biddut Banik et al. [7] using TCAD simulator from Synopsys (table 1). The epitaxial layer of an InGaAs/InP was optimized for 340 GHz, the simulation result predicted ≈ 1 mW of output power assuming a maximal allowable optical excitation of 0.25 W, thereby assuming $R_A \approx 50 \Omega$, the fact of bypassing the factor $(1 + \omega^2 \tau_{RC}^2)$ using TW scheme could increase the output power approximately in a factor 6 at 1 THz.

B. Antenna Integration

1) *Bow-tie slot antenna* : The UTC-PD must be integrated with antennas for THz generation and emission.

Different types of antennas such a log spiral and log periodic have been reported [7], but the impedance of those broadband antennas is low for our propose.

Due to terahertz power is proportional to antenna impedance higher impedance antennas are desirable. One of our antennas is a bow-tie slot antenna designed to reduce the reflections and minimize standings waves (Fig. 1). In this design the UTC-PD is placed in a coplanar wave guide (CPW) integrated with a slot bow-tie antenna, photomixer is back illuminated and coupled to hemispherical GaAs lens (2).

The electromagnetic performance of the scheme shown in figure 2, was optimized using CST Microwave Studio. The S_{11}

TABLE I
OPTIMIZED UTC-PD LAYER STRUCTURE FOR 340 GHz [7]

LAYER	MATERIAL	THICKNESS	DOPING
12	In _{0.53} Ga _{0.47} As	50	3e19 p+
11	In _{0.53} Ga _{0.47} As _{0.80} P _{0.20}	20	2e19 p+
10	In _{0.53} Ga _{0.47} As	125	1e18 p
9	In _{0.53} Ga _{0.47} As	8	1e15 i
8	In _{0.76} Ga _{0.24} As _{0.54} P _{0.28}	16	1e15 i
7	InP	6	1e15 i
6	InP	7	1e18 n
5	InP	150	1e16 n-
4	InP	50	5e18 n
3	In _{0.53} Ga _{0.47} As	10	1e19 n+
2	InP	500	> 2e19 n+
1	In _{0.53} Ga _{0.47} As	10	I
Sub	InP	SI	SI

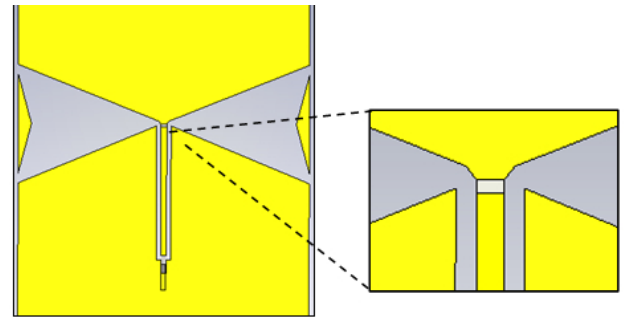


Fig. 1. Bow-tie slot antenna integrated to CPW.

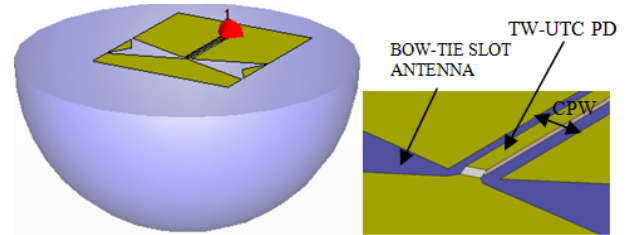


Fig. 2. Bow-tie antenna fed with CPW and integrated in a hemispherical GaAs lens.

parameter is shown in the figure 3, which is better than around -10 dB. Its oscillating shape is due to the presence standing waves which are consequences of the impedance mismatch between the CPW and the bow-tie antenna. The matching process is still under research.

2) *Butterfly metal antenna*: Due to the preferred small gap between inner and outer conductors (a larger one would just produce ohmic losses), the impedance of the CPW is below 50 Ohms.

Therefore, a metal bowtie antenna with its lower impedance around 70 Ohms matches much better than a bowtie slot which has a much higher impedance.around 150 Ohms.

It is well known that the terahertz output power is proportional to the antenna impedance and in the general case the impedance of a planar antenna is at most a few hundreds of ohms [3] and usually is bigger than the impedance of

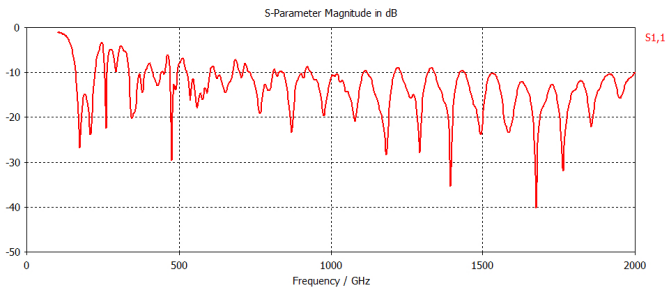


Fig. 3. S_{11} parameter for modified bow-tie slot antenna with 25° of aperture and 120 μm length.

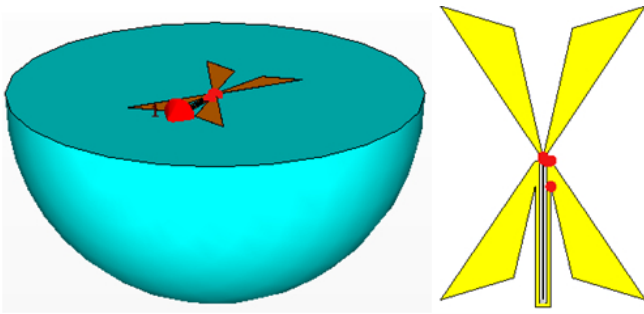


Fig. 4. Butterfly metal antenna over a GaAs lens.

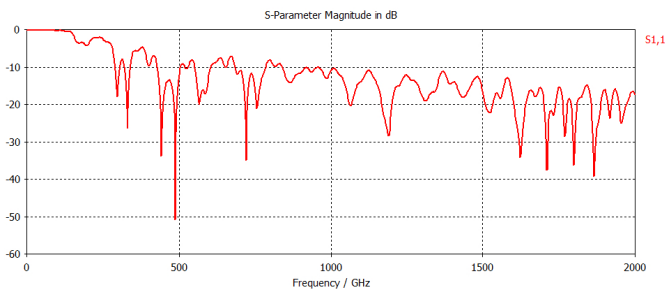


Fig. 5. S_{11} parameter for metal Butterfly antenna with mesa width of 0.5 μm , and slot lines of 2 μm .

our CPW. Thus the photomixer works under mismatched condition, therefore a lower impedance antenna is another alternative to reduce the mismatch shown in Fig. 3, where the oscillating shape of the S_{11} parameter is a consequence of this mismatch.

Antenna simulations in CST microwave studio show that the mismatch of this antenna (Fig. 5) is lower than the previous one but its drawback is that the output power shall be slower.

IV. DEVICE FABRICATION

The firsts back side illuminated TW-UTC PDs are being fabricated at Chalmers University. First devices have been developed using 150-300 μm slot bow-tie antenna integration and 600 μm CPW length structures with mesa structure width of 3 μm and slot lines of 3-6 μm . Three solvents are used in the process of wafer cleaning, acetone, methanol and IPA, all of them heated at 60°C in a sequence of 10 min, 30 s and 2 min respectively. After this step standard optical lithography is used to fabricate antenna integration and the CPW mesa structure, the first p-contact on the top of the mesa structure

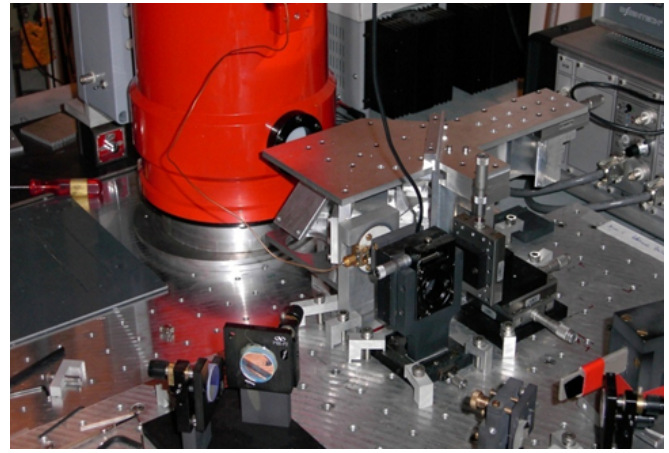


Fig. 6. Optical set-up used for 800 nm testing system.

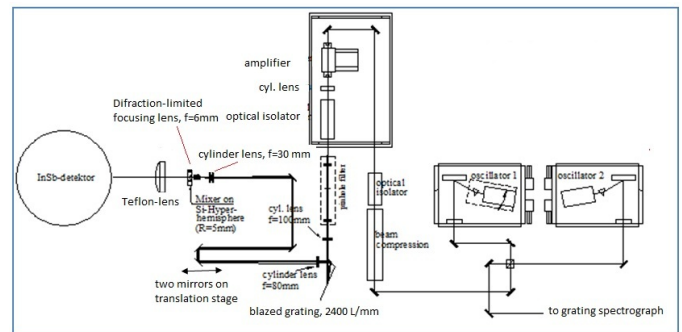


Fig. 7. Schematic of set-up used for 800 nm testing, the 1550 nm fiber system is being set up similarly.

is built using an image reversal resist AZ5214E, the contact is deposited using standard vapour deposition technique. In order to have an ohmic contact the sequence of Pt/Ti/Pt/Au was used, for the n-contact and a similar sequence of Ti/Pt/Au was used for the p-contact. For wet etching two different etches are needed, one for etching InGaAs/InGaAsP, and another for InP. The InGaAs/InGaAsP etch is $H_3PO_4:H_2O_2:H_2O$ (1:1:25), this etch is selective to InP and it stops when it reaches an InP layer, $HCL:H_3PO_4:H_2O_2$ (3:1:6) is used for InP and is also highly selective to InGaAs. The process of fabrication also uses dry etching for etching InP and InGaAs/InGaAsP, but in another part of the process. The final fabricated device shall be placed on a hyper-hemispherical Si lens, and the front part of the device will be antireflection coated for 1550 nm.

V. DEVICE TESTING SET UP

Device testing will be performed at our terahertz photonics laboratory at the Electrical Engineering Department at University of Chile Fig. 6

Schematic set-up of the optical testing system is shown in Fig. 7, the IR-optic developed by Ernest Michael [8], was designed using an optical ray-tracing software (ZEMAX). The idea is to exploit the grating dispersion to design an optical set-up with frequency independent alignment which does the proper transformation from the grating dispersion to the phase-match angle frequency dependence on the mixer.

ACKNOWLEDGMENT

We acknowledge support from the ALMA-Conicyt fund N 31080020 for Chilean Astronomy, Chilean Fondecyt fund N 1090306, and to the Physical Electronic Laboratory team of MC2-Chalmers University of Technology.

REFERENCES

- [1] K. S. Giboney, M.J.W. Rodwell, and J.E. Bowers, "Travelling-wave photodetector theory," *IEEE Trans. Microwave theory Tech*, vol 45, pp 1310-1319, Aug. 1997
- [2] Ernest A Michael, Travelling-wave photonic mixers for increased continuous-wave power beyond 1 THz, *Semiconductor Science and Technology*, vol 20, pp 164-177, Jun., 2005
- [3] Shuji Matsuura, Hiroshi Ito, *Generation of CW Terahertz Radiation with Photomixing*, *Topics in Applied Physics*, Springer Berlin, vol 97, pp 157-202, Jan 2006
- [4] T. Ishibashi et al. Uni-travelling carrier photodiodes, *Tech Dig. Ultrafast Electronics and Optoelectronics*, Incline Village, NV, pp 83-87, USA, 1997
- [5] T Ishibasi, T. Futura, H. Fushimi, S. Kodama, H. Ito, T. Nagatsuma, N. Shimizu, and Y. Migamoto, *InP/InGaAs Uni-Travelling-Carrier Photodiodes*, *IEICE Transaction on Electronics*, vol. E83-C, pp. 938-49, 2000.
- [6] Biddut Banik, Josip Vukosic, Hans Hjelmgreen, Jan Stake, Optimization of the UTC-PD Epitaxy for Photomixing at 340 GHz, *International Journal of Infrared and Millimeter Waves*, pp 914-923, 2008
- [7] Ernest A Michael, Large-area travelling-wave LT-GaAs photomixers for LO application, *Proc. SPIE*, vol 5498, 525, 2004.
- [8] Ernest A. Michael et al, Large-area traveling-wave photonic mixers for increased continuous terahertz power, *Appl. Phys. Lett.* 86, 111120, 2005

Phase-locking of Flux-Flow Oscillator by Harmonic Mixer based on SIS junction

Konstantin V. Kalashnikov^{**†}, Andrey V. Khudchenko^{**†}, Pavel N. Dmitriev, Valery P. Koshelets^{**†} and Andrey M. Baryshev[†].

^{*}The Kotel'nikov Institute of Radio Engineering and Electronics, Russian Academy of Science, 11/7 Mokhovaya St., 125009, Moscow, Russia
Email: Kalashnikov@hitech.cplire.ru

[†]SRON Netherlands Institute for Space Research, P.O. Box 800, 9700 AV Groningen, the Netherlands
Email : A.M.Baryshev@sron.nl

Abstract - A new approach to phase-locking of a Flux Flow Oscillator (FFO) [1] in a superconducting integrated receiver [2, 3] has been proposed and experimentally verified. According to this novel concept, a superconductor-insulator-superconductor (SIS) junction is implemented both for down-conversion of the FFO frequency and for formation of the signal to phase-lock the FFO to the external reference by applying the Harmonic Mixer (HM) output directly to the FFO control line. In other words, we introduce a new element of superconductive electronics, which is based on the SIS junction and works as a cryogenic harmonic phase detector (CHPD).

To realize efficient phase-locking of the FFO the HM output signal should be maximized. Value of this signal depends in a complicated way on the HM bias voltage, frequencies and powers of the local oscillator (LO) and the RF signals. We have studied the HM theoretically and calculated 3D dependences of the HM output signal power versus the bias voltage and the LO power. Results of the calculations have been compared with experimental measurements. Good qualitative and quantitative correspondence has been achieved.

For demonstration of the FFO phase-locking by the CHPD we have fabricated specially designed samples: all feedback loop elements are integrated on the same chip together with the FFO and the CHPD. The FFO frequency should be equal to a harmonic of the LO signal applied to the CHPD. Such a PLL system is expected to be extra wideband due to considerable reduction of the loop length. This concept is very promising for building of the multi-pixel SIR array.

I. INTRODUCTION: IDEA OF CRYOGENIC HARMONIC PHASE DETECTOR

A Phase Locking Loop system (PLL) based on Cryogenic Harmonic Phase Detector (CHPD) described in this report is a new way of phase stabilization of a superconducting flux flow oscillator (FFO) [1], which operates as a heterodyne source in a Superconducting Integrated Receiver (SIR) [2], [3].

The SIR circuit comprises on a single chip (size of 4 mm by 4 mm) a planar antenna integrated with an SIS (superconductor-insulator-superconductor) mixer, the FFO operating in the frequency range of 400 - 700 GHz and the second SIS harmonic mixer (HM) to phase-lock the FFO.

The block diagram of the SIR with conventional PLL system to stabilize FFO is presented in Fig. 1; this concept has been successfully used for the TELIS project [4].

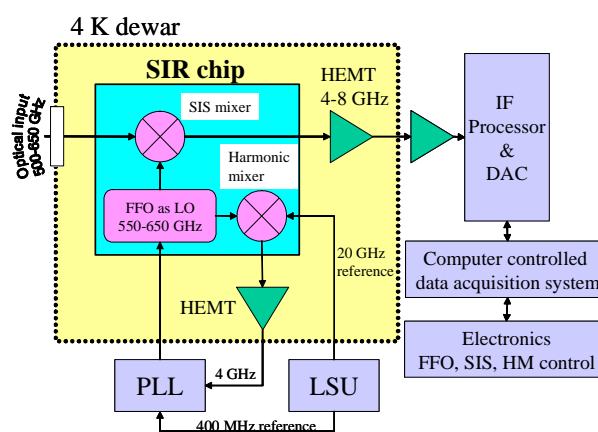


Fig. 1. Block diagram of SIR with RT PLL.

In the SIR with conventional PLL the FFO signal (frequency of about 600 GHz) is down-converted to 400MHz in the HM by mixing with n -th harmonics of the LO signal (frequency of about 20 GHz). The intermediate frequency (IF) signal is amplified and applied to a semiconductor phase detector placed outside the cryostat. The detector compares phase of this signal with one of the stable reference signal of frequency 400 MHz; the resulting error signal is applied to the FFO control line. This semiconductor PLL system has a bandwidth of about 15 MHz. Such a wideband PLL system is required because the FFO autonomous radiation spectrum has a Lorentz shape of width about few MHz. Only limited part of the FFO power can be synchronized by such a PLL system [5]. The semiconductor PLL system has to have long cables since the phase detector has to be outside the cryostat. The long cables lead to time delay, which limits the PLL synchronization bandwidth.

To overcome the problem of long cables and to synchronize the FFO power more efficiently a cryogenic PLL system has been developed [5] - [7]. Bandwidth of the cryogenic PLL system as large as 40 MHz has been realized. There are two SIS junctions in the loop of the cryogenic system. The first one works as the HM for down-convention of the FFO signal and second junction operates as a Cryogenic Phase Detector (CPD). The CPD compares the HM IF signal amplified by the HEMT-amplifier with reference oscillator signal of the same frequency (0.4 GHz [5], [6] or 4 GHz [7]). The resulting phase error signal changes the FFO control line current and adjusts the FFO frequency.

The novel concept of the FFO phase stabilization described in this report is based on employment of a single SIS junction as the HM and the phase detector simultaneously. This cryogenic harmonic phase detector (CHPD) substitutes the HM, the HEMT-amplifier and the CPD in the cryogenic PLL described above. The CHPD and all loop elements can be placed on the same chip with the FFO, which leads to loop delay reduction. Such PLL system will be ultra wideband that is important for the FFO phase-locking. A block diagram of the new PLL system is shown in Fig. 2. The signals from the FFO and the LO#1 are applied to the CHPD. The frequency of harmonic of the LO#1 signal is equal to the FFO frequency (~600 GHz). The CHPD generates output signal proportional to the phase difference between the FFO and the appropriate harmonic of the LO#1. This error signal is applied directly to the FFO control line through a low pass filter.

For demonstration of the CHPD operation we used additional SIS Mixer. This mixer operates as a HM (see Fig. 2). It is utilized for observation of the FFO radiation line spectrum and monitoring of the phase locking effect. The LO#2 frequency is chosen to obtain the intermediate frequency of this mixer of about 6 GHz.

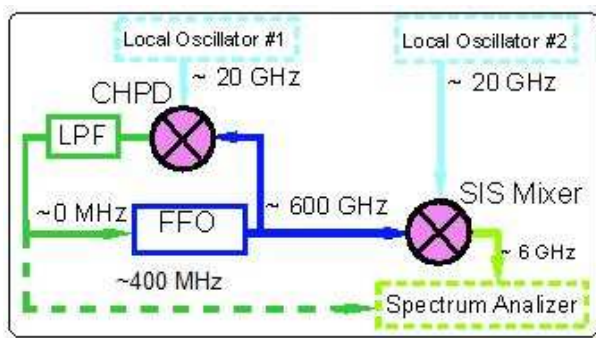


Fig. 2. Block diagram of the system for the FFO synchronization by the CHPD

II. ON THEORY OF HARMONIC MIXER

It is crucial to achieve a high-power HM output signal to demonstrate effective FFO synchronization. The experimental data shows that power of the IF signal depends in a complicated way on the HM bias voltage, frequencies

and powers of local oscillator LO and FFO signals. We have studied the HM theoretically and calculated the 3D dependences of its output signal power versus the bias voltage of SIS-junction and the LO power.

The detailed theoretical description of the SIS junction under action of microwave frequency signals is given in [8] – [10]. In [8] a simplifying assumption about the small amplitude of the input signal and shunting of the highest harmonics of the LO by junction capacitance was used. Papers [9], [10] involved the method of the SIS-junction description in general case, when the powers of input signals may be of any value. Nowadays the theory [9], [10] is the most complete; it takes into account existence of the harmonics generated by SIS-junction and influence of the external elec. The calculations of some characteristics HM on SIS based on this theory are given in [10].

We present the simpler model, which gives us the opportunity to reduce the time of HM characteristics calculation and still obtain good qualitative and quantitative agreement with the experimental data. Let us consider the model of the weakly-interacting quasi-particles under the influence of the periodic electric field without taking into account spin effects as in [11].

Wave function of a quasi-particle with energy E without applying altering electric field is $\Psi = f(x, y, z) \exp(-iEt / \hbar)$, where $f(x, y, z)$ – certain function of coordinates, i – imaginary unit, t – time, \hbar – Planck's constant. This wave function is the eigen function of a non-excited system Hamiltonian H_0 . The voltage across the junction is $V_{\omega_1} \cos(\omega_1 t) + V_{\omega_2} \cos(\omega_2 t)$ then two periodic signals of frequencies ω_1 , ω_2 and amplitudes V_{ω_1} , V_{ω_2} are applied to junction electrodes. The hamiltonian of quasi-particles system is then:

$H = H_0 + eV_{\omega_1} \cos(\omega_1 t) + eV_{\omega_2} \cos(\omega_2 t)$, where H_0 – non-excited system Hamiltonian, H – Hamiltonian of system influenced by two harmonic signals, e – charge of electron. The new wave function is

$$\Psi = f(x, y, z) \exp(-iEt / \hbar) \left(\sum_n B_n \exp(-in\omega_1 t) \right) \left(\sum_m C_m \exp(-im\omega_2 t) \right)$$

where B_n and C_m – unknown functions.

Applying this wave function to Schrödinger's equation $i\hbar \frac{\partial \Psi}{\partial t} = \hat{H} \Psi$, we obtain equations for B_n and C_m .

Solution of this Schrödinger's equation is:

$$\Psi = f(x) \exp(-iEt / \hbar) \left(\sum_n \sum_m J_n \left(\frac{eV_{\omega_1}}{\hbar\omega_1} \right) J_m \left(\frac{eV_{\omega_2}}{\hbar\omega_2} \right) \exp[-i(n\omega_1 + m\omega_2)t] \right),$$

where $J_n(\alpha)$ Bessel function n -th order

We can see that quasi-particles energy levels are split into levels described by wave functions Ψ_{nm} with energies $E + n\hbar\omega_1 + m\hbar\omega_2$; $n, m = 0, \pm 1, \pm 2, \dots$. Probability of

occupation of such levels is proportional to $J_n\left(\frac{eV\omega_1}{\hbar\omega_1}\right)J_m\left(\frac{eV\omega_2}{\hbar\omega_2}\right)$.

Quasi-particle tunnel current is provided by quasi-particles transport between SIS-junction electrodes. This current is described as complex function of current response $j(V)$, here V is a DC voltage applied to junction. The function $j(V)$ is calculated in [12]: $j(V) = iI_{dc}(V) + I_{KK}(V)$. Here $I_{dc}(V)$ is unpumped IVC of the SIS, and the $I_{KK}(V)$ relates to the $I_{dc}(V)$ as Kramers - Kronig transform.

It should be noted that the function $j(V)$ used in the calculations was measured experimentally. So the IVC of the HM contains information about the gap voltage and the current step.

The quasi-particle increases its energy by $\hbar\omega$ when the radiation quant is absorbed. This is the case identical with the applying voltage $\hbar\omega/e$ to junction. Therefore, the tunnel current is defined by function $j(V + \hbar\omega/e)$. As far as the quasi-particle is able to absorb several photons of the energy $\hbar\omega_1$ and $\hbar\omega_2$, in order to find the total tunnel current we should sum the current response functions

$j_{nm} = j\left(V + \frac{n\hbar\omega_1}{e} + \frac{m\hbar\omega_2}{e}\right)$ subject to the probability of the quasi-particle tunneling. The quasi-particle transmission probability of state Ψ_{nm} to state Ψ_{lk} is defined by the matrix element $\langle \Psi_{lk} | \Psi_{nm} \rangle$, where

$$|\Psi_{nm}\rangle = f(x)\exp(-iEt/\hbar)\left(J_n\left(\frac{eV\omega_1}{\hbar\omega_1}\right)J_m\left(\frac{eV\omega_2}{\hbar\omega_2}\right)\exp[-i(n\omega_1 + m\omega_2)t]\right),$$

$$\langle \Psi_{lk} | = g(x)\exp(-iEt/\hbar)\left(J_l\left(\frac{eV\omega_1}{\hbar\omega_1}\right)J_k\left(\frac{eV\omega_2}{\hbar\omega_2}\right)\exp[i(l\omega_1 + k\omega_2)t]\right).$$

The changing summation variable leads to:

$$I(V, t) = \text{Im} \sum_{n,m,l,k} J_n(\alpha_1)J_{n+l}(\alpha_1)J_m(\alpha_2)J_{m+k}(\alpha_2) * \exp[-i(l\omega_1 + k\omega_2)t] j\left(V + \frac{n\hbar\omega_1}{e} + \frac{m\hbar\omega_2}{e}\right),$$

$$\text{where } \alpha_i = \frac{eV\omega_i}{\hbar\omega_i}.$$

It should be noted that we can overwrite the current function in the form:

$$I(V, t) = a_0 + \sum_{l=1}^{\infty} \sum_{k=1}^{\infty} (2a_{lk} \cos((l\omega_1 + k\omega_2)t) + 2b_{lk} \sin((l\omega_1 + k\omega_2)t)).$$

This formula shows that the signals of the frequencies described as $l\omega_1 + k\omega_2$ (l and k are integers) are generated on the SIS junction. For the practical application of the

harmonic mixer the first signal frequency is close to the frequency of second signal harmonic k , i.e. $\omega_1 - k\omega_2 \ll \omega_2$.

Let us put that frequency of RF signal is $\omega_1 \equiv 2\pi f_{RF}$, and for LO signal is $\omega_2 \equiv 2\pi f_{LO}$. Then current amplitude of IF $f_{IF} = f_{RF} - nf_{LO}$ is given by

$$I_{IF} = \sqrt{a_{1k}^2 + b_{1k}^2},$$

$$a_{1k}(V) = \sum_{n,m} J_n(\alpha_1)J_m(\alpha_2) [J_{n+1}(\alpha_1)J_{m-k}(\alpha_2) + J_{n-1}(\alpha_1)J_{m+k}(\alpha_2)] * I_{dc}\left(V + \frac{n\hbar\omega_1}{e} + \frac{m\hbar\omega_2}{e}\right),$$

$$b_{1k}(V) = \sum_{n,m} J_n(\alpha_1)J_m(\alpha_2) [J_{n+1}(\alpha_1)J_{m-k}(\alpha_2) - J_{n-1}(\alpha_1)J_{m+k}(\alpha_2)] * I_{kk}\left(V + \frac{n\hbar\omega_1}{e} + \frac{m\hbar\omega_2}{e}\right).$$

The dependence of the IF signal's power versus the input signals' parameters and the bias voltage across the junction has been calculated by the presented formula. The result of such calculations is presented in Fig. 3.

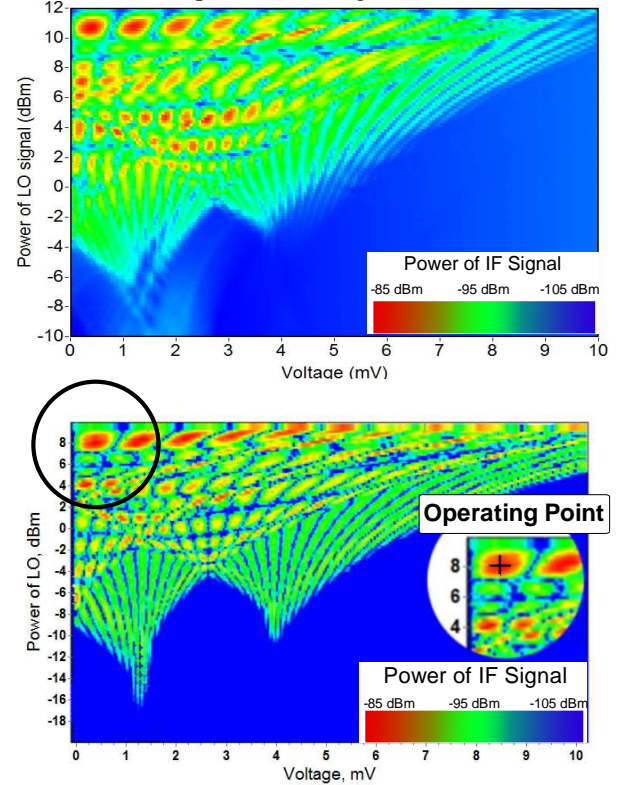


Fig. 3. Experimental (up) and theoretical (down) dependence of IF signal's power versus LO signal's power and bias voltage across the HM. The operating point with the maximum power of IF signal (-85 dBm) is shown on the theoretical dependence. The FFO frequency is 636 GHz, LO frequency - 18 GHz (the 35th harmonic of LO is used) as result frequency of IF signal is equal 6 GHz.

The experimental studying of such dependences was made. The dependence IF power versus LO power and bias

voltage was acquired. The frequency of the RF signal was 636 GHz, the LO frequency – 18 GHz. The critical current of the SIS junction was suppressed by the magnetic field. Good qualitative and quantitative correspondence has been achieved (Fig. 3). We used in experiment the Nb-AlO_x-Nb SIS junction with area of 1 μ² and gap current 90 μA. The maximal output signal power for described frequencies was obtained of about -90 dBm. Our calculations show that 5 dB larger value can be achieved at more careful adjustment.

III. EXPERIMENTAL RESULTS

A test circuit presented by the diagram in Fig. 2 has been experimentally realized. The feedback loop between the HM and the FFO was implemented in two ways: by lumped elements on a contact plate and by the microstrip lines directly on the chip.

In our experiment the FFO signal is split into two channels to pump both mixers. Each part of the signal is down-converted so that output signals frequencies are 400 MHz for the CHPD and of about 6 GHz for the SIS (Fig. 2). The IF signals are amplified and transferred to spectrum analyzers. The IF signal of CHPD is maximized by finding the optimal point (see Fig. 3). After the optimum is found, we change the frequency of the LO#1 so that the IF of the CHPD becomes “0” instead of 400 MHz (the certain n-th harmonic of LO#1 becomes equal to the FFO frequency). At the same time, the IF of the HM #2 is also changed but the FFO radiation line is still presented on spectrum analyzer screen and synchronization effect is observed.

The result of the FFO synchronization by the CHPD is shown in Fig. 4. This spectrum demonstrates the validity of the concept. The bandwidth of such a PLL system is expected to be about 100 MHz providing optimal gain in the loop. For the data presented in Fig. 4 (red curve) free running FFO linewidth is 6 MHz and such a system should phase-lock more than 90% of emitted power. Because the HM output signal is limited, the open loop gain is not large enough to demonstrate optimal synchronization. As a result, only 55% of the FFO emitted power is locked (see Fig. 4, blue curve).

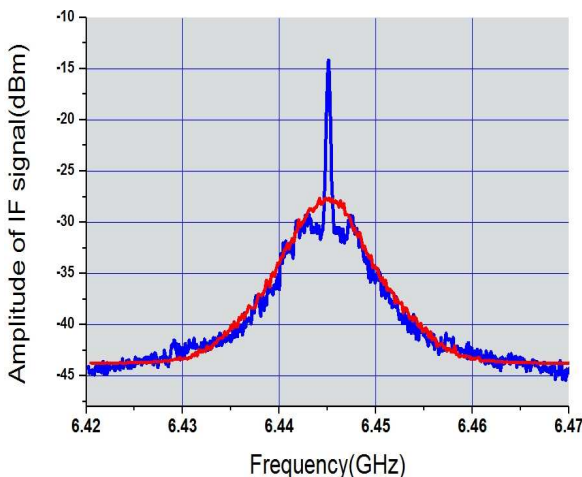


Fig. 4. Down-converting spectrum of FFO: red curve – free running line, LW = 6 MHz; blue curve – FFO is phase locked by the CHPD.

IV. SUMMARY

We propose a novel application of the SIS junction – the Cryogenic Harmonic Phase Detector (CHPD). The theoretical and experimental studies of the HM have been performed. Comparison of the theoretical and experimental data demonstrates a good qualitative and quantitative agreement. The concept of the CHPD is experimentally realized and the FFO phase locking has been obtained. The part of the phase-locked FFO power is not ultimate because output signal of HM was not large enough. This problem would be overcome by utilizing the HM with larger area. The application of a low-frequency superconductive on-chip amplifier in the feedback loop looks also very promising.

ACKNOWLEDGMENT

The authors thank Meno van den Bemt for the warm support and Michael Torgashin for fruitful and stimulating discussions.

The work was supported by the RFBR projects 09-02-00246, 09-02-12172 and Grant for Leading Scientific School 5423.2010.2.

REFERENCES

- [1] T. Nagatsuma, K. Enpuku, F. Irie, and K. Yoshida 1983 *J. Appl. Phys* **54** 3302, see also Pt. II: 1984 *J. Appl. Phys.* **56** 3284; Pt. III, 1985 *J. Appl. Phys* **58** 441, Pt. IV, 1988 *J. Appl. Phys* **63** 1130
- [2] V. P. Koshelets and S. V. Shitov, “Integrated Superconducting Receivers,” *Superconductor Science and Technology*, vol. 13, pp. R53-R69 (2000).
- [3] V.P. Koshelets, A.B. Ermakov, L.V. Filippenko, A.V. Khudchenko, O.S. Kiselev, A.S. Sobolev, M.Yu. Torgashin, P.A. Yagoubov, R.W.M. Hoogeveen, and W. Wild, “Integrated Submillimeter Receiver for TELIS”, “*IEEE Trans. on Appl. Supercond.*”, vol. 17, pp 336-342 (2007).
- [4] Gert de Lange, Dick Boersma, Johannes Dercksen, et al, “Development and Characterization of the Superconducting Integrated Receiver Channel of the TELIS Atmospheric Sounder”, *Supercond. Sci. Technol.* vol. 23, No 4, 045016 (8pp), (2010). <http://iopscience.iop.org/0953-2048/23/4/045016>
- [5] A.V. Khudchenko, V.P. Koshelets, P.N. Dmitriev, A.B. Ermakov, P.A. Yagoubov, and O.M. Pylypenko, “Cryogenic Phase Detector for Superconducting Integrated Receiver”, “*IEEE Trans. on Appl. Supercond.*”, vol. 17, pp. 606-608, 2007.
- [6] A.V. Khudchenko, V.P. Koshelets, P.N. Dmitriev, A.B. Ermakov, O.M. Pylypenko, and P.A. Yagoubov, “Cryogenic Phase Locking Loop System for Flux-Flow Oscillator”, ISST-08, vol 2, pp. 511-515, 2009.
- [7] A V Khudchenko, V P Koshelets, P N Dmitriev, A B Ermakov, P A Yagoubov and O M Pylypenko, “Cryogenic Phase Locking Loop System for Superconducting Integrated Receiver”, *Superconductor Science and Technology*, vol. 22, No8, 2009.
- [8] Tucker J. R., Feldman M. J. // *Rev. Mod. Phys.* 1985. V.57. №4. P.1055
- [9] Withington S., Kittara P., Yassin G. // *J. Appl. Phys.*, 2003. V.93. №12. P. 9812
- [10] Kittara P., Withington S., Yassin G. // *J. Appl. Phys.* 2007. V.101. №2. P.024508.
- [11] Tien P.K, Gordon J.P. // *Phys. Rev.* 1963. V. 129. №2. P. 647.
- [12] Werthamer N. R. // *Phys. Rev.* 1966. V.147. № 1. P.255

3.5 THz surface emitting distributed feedback QCL operated at 70 K as local oscillator

Y. Ren^{1,2,3,*}, P.J. de Visser¹, J.N. Hovenier¹, W.Zhang², P. Khosropanah⁴, J.R. Gao^{1,4}, T.M. Klapwijk¹, S.C. Shi², T-Y. Kao⁵, S. Kumar⁵, Q. Hu⁵, and J. L. Reno⁶

¹*Kavli Institute of NanoScience, Delft University of Technology, The Netherlands*

²*Purple Mountain Observatory (PMO), Chinese Academy of Sciences, Nanjing, China.*

³*Graduate School, Chinese Academy of Sciences, China*

⁴*SRON Netherlands Institute for Space Research, The Netherlands*

⁵*Department of Electrical Engineering and Computer Science, Massachusetts Institute of Technology, Cambridge, U.S.A.*

⁶*Sandia National Laboratories, Albuquerque, NM 87185-0601, U.S.A.*

*Contact: y.ren@tudelft.nl, phone +31-15-278 6113

Abstract— We report a set of measurements to demonstrate a new type of surface emitting distributed feedback (DFB) quantum cascade laser (QCL) operated at 3.5 THz as local oscillator by pumping a superconducting hot-electron bolometer (HEB) mixer. The second order DFB surface emitting THz QCL, based on the Bragg gratings incorporated into the waveguide, shows single mode emission at 3.555 THz, which is only 4 GHz off from the hydroxyl (OH) line. This frequency can be slightly tuned by operating current or temperature. Because of the radiation being emitted from the surface, the far-field beam is much improved, with a divergent far field beam pattern only in one direction. We also notice that in the far field beam pattern, unlike conventional metal-metal waveguide QCLs, there are no interference patterns. All these make it possible to fully pump a superconducting NbN HEB mixer with a surface emitting DFB QCL at 60 K, and even at 70 K based on the estimated power.

I. INTRODUCTION

The hydroxyl (OH) radical has been identified to be a crucial probe for problems related to the atmosphere such as global warming and ozone destruction. The OH radical has the emission lines at terahertz frequencies such as 1.8, 2.5 and 3.5THz [1]. Among them, the emission line at 3.551 THz has been identified as the best candidate for OH profile retrieval because of its brightness and isolation. With a nearly quantum noise limited sensitivity and ultra high spectral resolution ($\nu/\Delta\nu > 10^6$, where ν is the frequency), a heterodyne receiver based on a NbN HEB mixer will be ideal for detecting the OH line. Since such a mixer has shown a superior sensitivity up to 5.3 THz [2], suitable local oscillators (LO) at this particular frequency become the only obstacle. Solid state LOs based on multipliers have only been demonstrated up to 2 THz, but the output power drops severely with frequency due to reduced multiplication efficiency at high frequencies. Optically pumped FIR gas lasers are very bulky, huge power consumptive and have no strong molecular lines close to this specific frequency.

Recently developed terahertz quantum cascade lasers (QCLs) [3] become a promising candidate for LO in a heterodyne receiver. THz QCLs are based on quantum well

structures, where the photon energy can be chosen by tailoring the thickness of the coupled wells and barriers, which makes such structures ideal for generation of arbitrary wavelength radiation. It has been demonstrated that a THz QCL is a suitable source for the application of LO in a heterodyne receiver system [4]. In addition, THz QCLs have shown excellent power stability [4], phase-lock capability [5], and narrow intrinsic linewidth [6], which meet the essential requirements as LO.

Until now, most of the THz QCLs used for LO are based on a Fabry-Perot cavity. This cavity makes use of two facets as reflecting surfaces and a gain region in between. However, the edge-emission Fabry-Perot laser often gives multi-modes emission. It can generate single mode, but it is hard to control the emission frequency precisely. Furthermore, to achieve single mode lasing, the laser has to be narrow and often the width is much smaller than the wavelength. The latter causes a highly divergent beam with even strong interference fringes [7,8]. For high-resolution spectroscopy applications, it is essential to control the single mode lasing at the exact targeting frequency. Recently a surface emitting DFB THz QCL was reported [9]. By incorporating the second order Bragg gratings into the waveguide, a single mode emission is coupled out from the surface. These characteristics make surface emitting DFB QCL having the advantage in both the frequency and beam pattern in comparison with a typical metal-metal waveguide Fabry-Perot QCL. And the improved beam pattern will also lead to a better beam coupling to the HEB mixer, which is essential for high temperature operation of QCL as LO since the emission power is limited in this case. Here we demonstrate this new type of surface emitting DFB QCL, operated at 3.55THz, as local oscillator by pumping a superconducting HEB mixer.

II. THz SURFACE EMITTING DFB QCL

The surface emitting DFB QCL used in this experiment is developed by the MIT group and is described in reference. 9. The active region is based on a resonant-phonon depopulation scheme and a metal-metal waveguide is used for modal confinement. As shown in Fig.1, by introducing a

second-order Bragg grating on the top surface of the waveguide, the radiation is coupled out from the top surface. The DFB grating enables robust single-mode operation over a large operating range. By using a Pi phase-shift in the center of the grating, a single-lobed far beam pattern is obtained.

The QCL is indium soldered on a copper mount and is mounted on the cold stage of a helium-flow cryostat. The QCL consumes 4W DC power in continuous wave mode and emits a maximum output power of 1mW. This laser can also be operated at a relatively high temperature. As to be explained, the QCL working at 70K can still provide about 25% of its maximum power (Fig.2) and is estimated to have enough power to pump a HEB mixer at its optimal operating point.

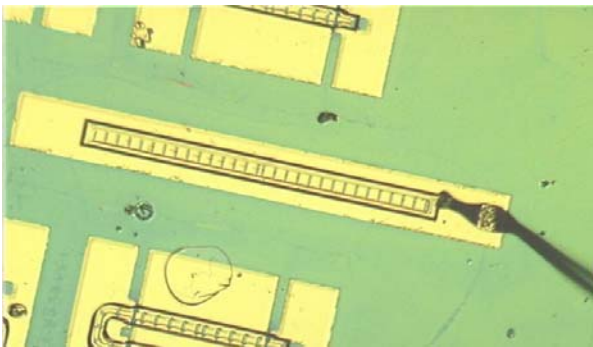


Fig. 1 Picture of a MIT surface emitting DFB QCL with a length of 754 μ m and a width of 40 μ m. Also shown is the Al wire bonding for biasing the laser

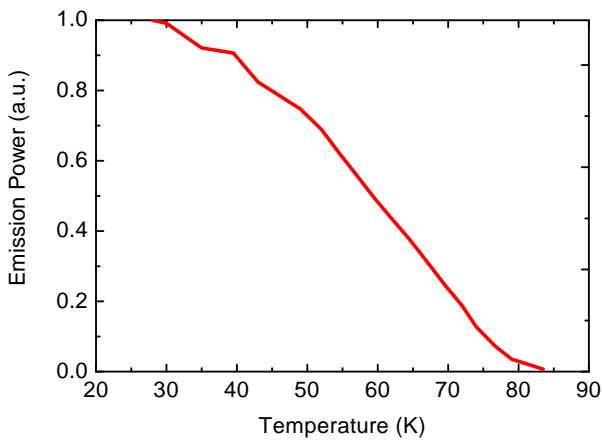


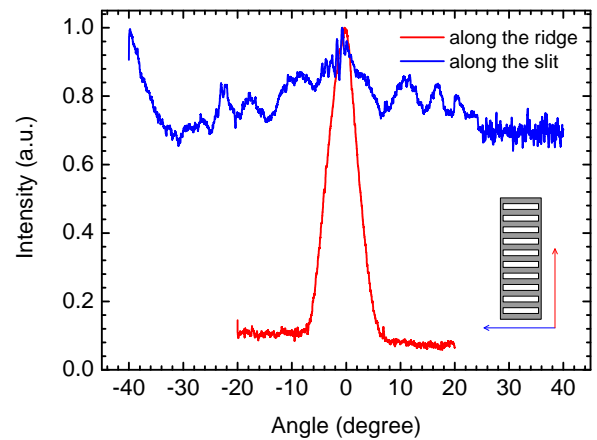
Fig. 2 Emission power of the surface emitting DFB QCL as a function of the bath temperature. The power is measured with a pyrodetector after focusing the beam by a HDPE lens ($f=26.5$ mm).

III. RESULTS

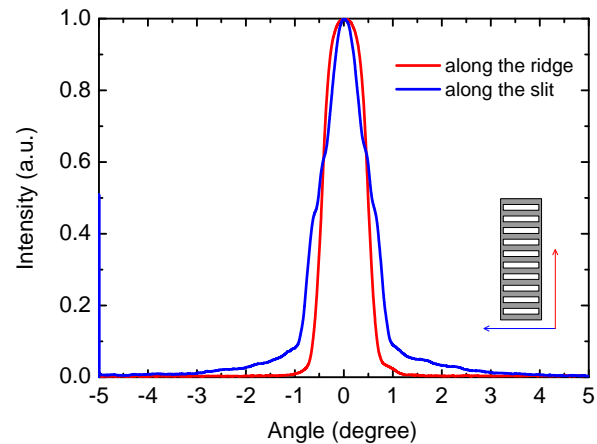
A. Far-field beam pattern

The beam pattern measurement setup was described in Ref. [10]. By using a room temperature pyrodetector and two PC controlled stepper motors, the radiation beam was measured in both horizontal and vertical directions spherically.

As shown in Fig.3a, the radiation beam was measured with the pyrodetector placed at a radial distance of 112mm. Along the laser's ridge direction, a single-lobed beam was observed, where the full width at half maximum (FWHM) is 7deg. However, along the laser's slit direction, the beam is highly divergent, which is mainly due to the subwavelength dimension in this direction. Compared with the beam patterns measured from meta-metal waveguide Fabry-Perot type QCLs [7,8], the surface emitting DFB QCL emits a directional beam in one direction. The other advantage is that there are no interference fringes in both directions. These features make it easy to couple the laser's radiation into a HEB mixer, which typically has a Gaussian beam [11]. Fig.3b shows the beam pattern measured after focusing by a HDPE lens ($f=26.5$ mm). A single-lobed beam is found in both directions, where the FWHMs are less than 1 deg.



(a)



(b)

Fig. 3 Measured far-field beam pattern of the surface emitting DFB QCL. (a) Beam pattern measured directly in front of the QCL at a distance of 112mm. (b) beam pattern measured after the radiation focused by a HDPE lens.

B. Spectra characteristics

Emission spectra were measured using a Fourier-transform spectrometer (FTS) [12] with a resolution of 0.7GHz. This value is much larger than the intrinsic linewidth of a QCL, which is typically in the range of 6-30KHz. As shown in Fig.4, by changing the bias current, the surface emitting DFB QCL shows robust single mode emission over a wide operating range, which indicates a frequency tuning range of 5GHz. With increasing the bath temperature from 30K to 70K, a frequency tuning range of around 10GHz was measured in this case. It is interesting to note that the observed frequency range can cover the particular OH line at 3.551THz. This single mode lasing together with a relative large tuning range makes surface emitting DFB laser ideal for high resolution molecular line detection.

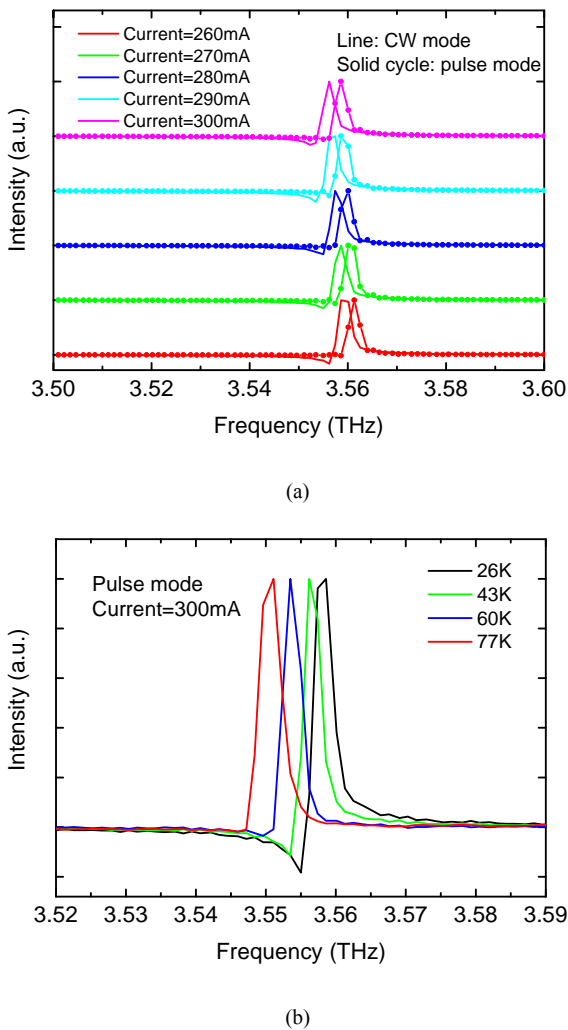


Fig. 4 (colour online) Measured emission spectra of the surface emitting DFB QCL. (a) Emission spectra measured at different bias current in pulsed and CW mode;(b) Emission spectra measured at different bath temperature in pulsed mode.

C. Coupling the radiation to the HEB mixer

We use a spiral antenna coupled NbN HEB mixer, which consists of a 2 μ m wide, 0.2 μ m long, and 5.5nm thick NbN bridge [2]. The HEB has a low-temperature normal-state

resistance (R_N) of 83 Ω , a critical temperature of 9.3K, and a critical current of 210 μ A at 4.2K.

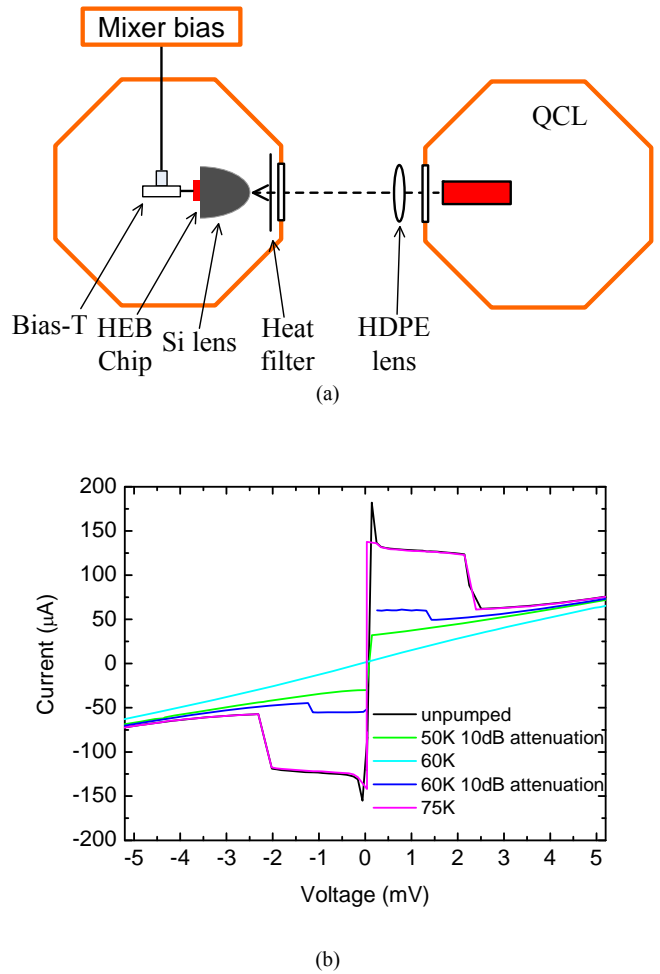


Fig. 5 (colour online) (a) Schematic view of the QCL-HEB coupling experimental setup. (b) Current-voltage characteristics of the HEB for different pumping levels caused by different operating temperature of the QCL. In some cases, an attenuation of the LO power is introduced in order to get a proper pumping curve.

As shown in Fig.5, by placing the QCL and the HEB directly face to face, and using a HDPE lens ($f=50$ mm) to focus the laser's radiation, the current-voltage characteristics of the HEB at different pumping levels are obtained. It is clearly shown that the emission power from the surface emitting DFB QCL working at 60K is enough to fully pump the HEB (bringing the HEB fully in the normal state). This enables the QCL to operate as LO with a HEB mixer in a heterodyne receiver where a thin Mylar beam splitter is used to reflect the power to the HEB [4]. Based on the pumping curve at 60 K with additional 10 dB attenuator, and using the iso-thermal method [13], the LO power absorbed at the HEB itself is estimated to be 530 nW. Taking all known losses (the HDPE window, air, heat filter, Si lens) into account, we found that 4% of total emission power from the QCL is absorbed by the HEB. Although this is still a low value, the coupling efficiency is improved by a factor of 3 compared with that obtained with a metal-metal waveguide Fabry-Perot

cavity QCL as described in Ref. 4, which is mainly due to the improved far-field beam pattern.

We did not perform the pumping measurement directly at 70 K. However, we can predict that this laser would be powerful enough to pump the HEB at 70 K. Figure 2 indicates that the output power of the QCL at 70K is about half the power generated at 60K. Based on the value of 530 nW at 60 K, we expect a power of 270nW at the HEB itself with the QCL at 70K. This value is more than the optimal LO power (140nW). Since the beam is still highly divergent in one direction, further improvement can be made by placing the QCL closer to the cryostat window and using a short focal distance lens. The possibility of operating a QCL at 70 K or above is crucial for the application in a space instrument because it is technically much easier to have such a cooler in comparison with a cooler for, e.g. 10 K.

IV. SUMMARY

In conclusion we have made a set of measurements, like the beam pattern measurement, the spectral measurement, and pumping a HEB mixer, to demonstrate that the surface emitting DFB QCL working at 3.5 THz can be used as LO in a heterodyne receiver for the OH line detection. We found that the new laser gives a better beam pattern. The QCL can fully pump a HEB mixer at 60K, suggesting that there is enough power even at 70 K. We emphasize that operating a QCL at a temperature of 70 K or above is practically important for a real instrument.

ACKNOWLEDGMENT

The work was partly supported by China Exchange Programme executed by KNAW and CAS, and by the AMSTAR+ project of RadioNet under FP7, and NWO.

REFERENCES

- [1] R.G. Prinn, J. Huang, R.F. Weiss, D.M. Cunnold, P.J. Fraser, P.G. Simmonds, A. McCulloch, C. Harth, P. Salameh, S. O'Doherty, R.H.J. Wang, L. Porter, and B.R. Miller, "Evidence for substantial variations of atmospheric hydroxyl radicals in the past two decades," *Science*, vol.292, pp.1882-1888, 2001.
- [2] W. Zhang, P. Khosropanah, J.R. Gao, E. L. Kollberg, K. S. Yngvesson, T. Bansal, R. Barends, and T. M. Klapwijk, "Quantum noise in a terahertz hot electron bolometer mixer," *Applied Physics Letter* 96, 111113 (2010).
- [3] R. Köhler, A. Tredicucci, F. Beltram, H. E. Beere, E. H. Linfield, A. G. Davies, D. A. Ritchie, R. C. Iotti, and F. Rossi, "Terahertz semiconductor-heterostructure laser," *Nature*, 417, 156 (2002).
- [4] J.R. Gao, J.N. Hovenier, Z.Q. Yang, J.J.A. Baselmans, A. Baryshev, M. Hajenius, T.M. Klapwijk, A.J.L. Adam, T.O. Klaassen, B.S. Williams, S. Kumar, Q.Hu, and J.L. Reno, "Terahertz heterodyne receiver based on a quantum cascade laser and a superconducting bolometer," *Appl. Phys. Lett.* 86, 244104 (2005).
- [5] P. Khosropanah, A. Baryshev, W. Zhang, W. Jellema, J. N. Hovenier, J. R. Gao, T. M. Klapwijk, D. G. Paveliev, B. S. Williams, S. Kumar, Q. Hu, J. L. Reno, B. Klein, and J. L. Hesler, "Phase locking of a 2.7 THz quantum cascade laser to a microwave reference," *Opt. lett.* 34, 2958 (2009)
- [6] A. Barkan, F. K. Tittel, D. M. Mittleman, R. Dengler, P. H. Siegel, G. Scalari, L. Ajili, J. Faist, H. E. Beere, E. H. Linfield, A. G. Davies, and D. A. Ritchie, "Linewidth and tuning characteristics of terahertz quantum cascade lasers," *Opt. Lett.* 29, 575 (2004).
- [7] A. J.L. Adam, I. Kašalynas, J.N. Hovenier, T.O. Klaassen, J.R. Gao, E.E. Orlova, B.S. Williams, S. Kumar, Q. Hu, and J. L. Reno, "Beam pattern of Terahertz quantum cascade lasers with sub-wavelength cavity dimensions", *Appl. Phys. Lett.* 88, 151105(2006).
- [8] E.E. Orlova, J.N. Hovenier, T.O. Klaassen, I. Kašalynas, A.J.L. Adam, J.R. Gao, T.M. Klapwijk, B.S. Williams, S. Kumar, Q. Hu, and J.L. Reno, "Antenna model for wire lasers", *Phys. Rev. Lett.* 96, 173904(2006).
- [9] S. Kumar, B.S. Williams, Q. Qin, A.W.M. Lee, Q. Hu and J. L. Reno, "Surface-emitting distributed feedback terahertz quantum-cascade lasers in metal-metal waveguides," *Opt. Express.* 15,113 (2007)
- [10] X. Gu, S. Paprotskiy, J.N. Hovenier, J. R. Gao, E. E. Orlova, T.M. Klapwijk, P. Khosropanah, S. Barbieri, S. Dhillon, P. Filloux, and C. Sirtori, "High angular resolution far-field beam pattern of a surface-plasmon THz quantum cascade laser," 19th International Symposium on Space Terahertz Technology (ISSTT 2008), Groningen.
- [11] A.D. Semenov, H. Richter, H.-W. Hübers, B. Günther, A. Smirnov, K.S. Il'in, M. Siegel, and J.P. Karamarkovic, " Terahertz performance of integrated lens antennas with a hot-electron bolometer," *IEEE Trans. Microwave Theory Tech.* 55, 239 (2007).
- [12] ABB Bomen Inc., St-Laurent, Canada
- [13] Hans Ekstrom, B.S. Karasik, E.L. Kollberg, and K.S. Yngvesson, "Conversion Gain and Noise of Niobium Superconducting Hot-Electron-Mixers," *IEEE Trans. Microwave Theory Tech.*, 43,938 (2005)

Development and Characterization of a 1.9THz LO Source

T.W. Crowe, J.L. Hesler, C. Pouzou, W.L. Bishop, G.S. Schoenthal

Virginia Diodes Inc., Charlottesville, USA (Crowe - vadiodes.com)

Abstract

Over the last several years VDI has been developing THz sources based on microwave frequency amplifiers and a cascaded series of frequency multipliers. Much of this effort has been focused on the 1.9THz frequency range, which is of significant astronomical importance and will soon be accessible from the Sofia airborne observatory. This development is now nearing completion with the successful development of sources with power levels well above ten microwatts. This effort has required the development of improved millimeter-wave varactor multipliers with better thermal grounding for greater power handling, the optimization of the THz multipliers for operation at low power levels and the development of improved assembly and testing techniques. This paper will discuss the many challenges of achieving useful sources at such high frequency, as well as review the results that have been achieved. For example, the figure below shows the measured performance of several frequency triplers to the desired frequency band. The results show significant variation from build-to-build, but very impressive power levels for the best builds.

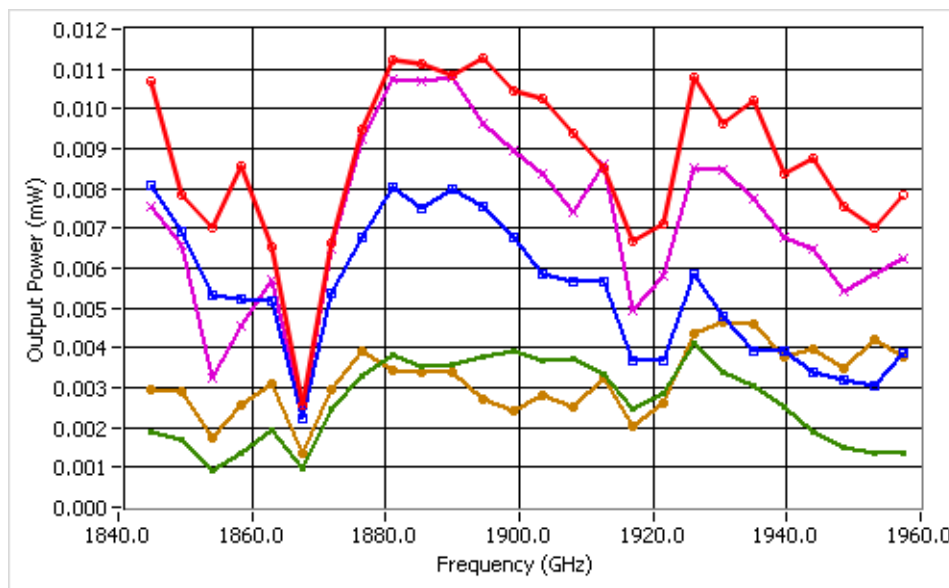


Fig. 1. The measured output power of a series of WR0.51x3 triplers to ~1.9THz at room temperature. Each of these triplers was pumped by the same lower frequency driver. Although the power level achieved for the best builds is very useful for atmospheric purposes, the variation from build to build is indicative of the challenges of developing such high frequency sources.

List of Registered Participants

Byron Alderman	Rutherford Appleton Laboratory	byron.alderman@astfc.ac.uk
Damian Audley	University of Cambridge	daudley@gmail.com
Jan Barkhof	ALMA	janbarkhof@hotmail.com
Claudio Barrientos Zúñiga	Universidad de Chile	claudio.barrientos@gmail.com
Andrey Baryshev	SRON, RuG	a.m.baryshev@sron.nl
Victor Belitsky	GARD, Chalmers University of Technology	
Graham Bell	Thomas Keating Instruments	g.bell@terahertz.co.uk
Dominic Benford	NASA / GSFC	dominic.benford@nasa.gov
Bhushan Billade	GARD, Chalmers University of Technology	
Manfred Birk	DLR	manfred.birk@dir.de
Raymond Blundell	Smithsonian Astrophysical Observatory	rblundell@cfa.harvard.edu
Charles M Bradford	California Institute of Technology	bradford@phobos.caltech.edu
Alwin Brettschneider	Delft University of Technology	a.brettschneider@student.tudelft.nl
Eric Bryerton	NRAO	ebryerto@nrao.edu
Stig Busk Soerensen	TICRA	tkb@ticra.com
Ivan Camara Mayorga	Max Planck Institut für Radioastronomie	imayorga@mpifr-bonn.mpg.de
Cecilia Cappelin	TICRA	tkb@ticra.com
Sergey Cherednichenko	Chalmers University of Technology	serguei@chalmers.se
Victor Conte	Universidad de Talca (Chile)	jlgordano@hotmail.com
Tom Crowe	Virginia Diodes Inc.	bodell@vadiodes.com
Michael Cyberey	University of Virginia	michaelecyberey@virginia.edu
Prof Peter de Maagt	European Space Agency	
Pieter de Visser	SRON / TU Delft	p.j.devisser@tudelft.nl
Michael Edgar	California Institute of Technology	mick@submm.caltech.edu
Dr Heribert Eisele	University of Leeds	imp@leeds.ac.uk
Brian Ellison	STFC-RAL	brian.ellison@stfc.ac.uk
Matthew Emery	STFC Rutherford Appleton Laboratory	matthew.emery@stfc.ac.uk
Jian-Rong Gao	SRON & Delft University of Technology	j.r.gaol@tudelft.nl
Belen Andres Garcia	Universidad Carlos III de Madrid	belens@tsc.uc3m.es
Robert D. Gehrz	University of Minnesota	gehrz@astro.umn.edu
Gerrit Gerlofsma	University Groningen / SRON	g.j.gerlofsma@sron.nl
Hugh Gibson	RPG / Gibson Microwave Design	hughgibs@yahoo.co.uk
J. Luis Giordano	Universidad de Talca (Chile)	jlgordano@hotmail.com
Dorota Glowacka	University of Cambridge	glowacka@mrao.cam.ac.uk
David Goldie	Cavendish Laboratory, Cambridge	d.j.goldie@mrao.cam.ac.uk
Paul Goldsmith	JPL/Caltech	paul.f.goldsmith@jpl.nasa.gov
Gregory Goltsman	Moscow State Pedagogical University	
Jesus Grajal	Technical University of Madrid	jesus@gmr.ssr.upm.es
Paul Grimes	University of Oxford	p.grimes1@physics.ox.ac.uk
Christopher Groppi	Arizona State University	cgroppi@asu.edu
Dr Peter Hargrave	Cardiff University	p.hargrave@astro.cf.ac.uk
Abigail Hedden	Harvard-Smithsonian Center for Astrophysics	abigail.hedden@gmail.com
Pieter Klaas Hekman	European Southern Observatory	alma_admin@eso.org
Doug Henke	HIA-NRC	doug.henke@nrc-cnrc.gc.ca
Manju Henry	STFC	manju.henry@stfc.ac.uk
Jeffrey Hesler	Virginia Diodes Inc.	bodell@vadiodes.com
Ronald Hesper	University of Groningen / SRON	r.hesper@sron.nl
Stefan Heyminck	Max Planck Institut für Radioastronomie	sheymnck@mpifr-bonn.mpg.de

Daniel Ronan Higgins	NUI Maynooth	ronan.higgins@gmail.com
Matt Hollister	California Institute of Technology	mih@caltech.edu
Netty Honingh	University of Cologne	honingh@ph1.uni-koeln.de
Heinz-Wilhelm Hübers	DLR	heinz-wilhelm.huebers@dlr.de
Peter Huggard	RAL	peter.huggard@stfc.ac.uk
Yoshihisa Irimajiri	National Institute of Information and Communications Technology	irimaji@nict.go.jp
Cecile Jung	Jet Propulsion Laboratory	cecile.d.jung@jpl.nasa.gov
Boris Karasik	JPL/Caltech	boris.s.karasik@jpl.nasa.gov
Alexandre Karpov	California Institute of Technology	karpov@submm.caltech.edu
Jon Kawamura	JPL	kawamura@jpl.nasa.gov
Dr Oliver King	Caltech	ogk@astro.caltech.edu
Teun Klapwijk	Delft University of Technology	t.m.klapwijk@tudelft.nl
Kalashnikov Konstantin	Kotel'nikov Institute of Radio Engineering and Electronics RAS	kalashnikov@hitech.cplire.ru
Jacob Kooi	California Institute of Technology	kooi@submm.caltech.edu
Valery Koshelets	Kotel'nikov Institute of Radio Engineering and Electronics	valery@hitech.cplire.ru
Torben Kronborg Bak	TICRA	tkb@ticra.com
Prof Leonid Kuzman	Chalmers University	kuzmin@chalmers.se
Yoonjae Lee	STFC Rutherford Appleton Laboratory	yoonsae.lee@stfc.ac.uk
Choonsup Lee	JPL	choonsup.lee@jpl.nasa.gov
Jamie Leech	University of Oxford	j.leech1@physics.ox.ac.uk
Christian Leinz	Max Planck Institut für Radioastronomie	cleinz@mpifr.de
Arthur W. Lichtenberber	University of Virginia	lichtenberger@virginia.edu
Johanna Liljedahl	Chalmers University of Technology	johanna.liljedahl@chalmers.se
Robert Lin	Jet Propulsion Laboratory	robert.h.lin@jpl.nasa.gov
Yury Lobanov	Harvard-Smithsonian Centre for Astrophysics	ylobanov@cfa.harvard.edu
Alain Maestrini	Observatoire de Paris	alain.maestrini@obspm.fr
Hiroyuki Maezawa	Nagoya University	hiro@stelab.nagoya-u.ac.jp
Sumedh Mahashabde	Chalmer University, Sweden	sumedh@chalmers.se
Takeshi Manabe	Osaka Prefecture University	manabe@ieee.org
Hiroshi Matsuo	ATC/NAOJ	h.matsuo@nao.ac.jp
Prof Philip Maukopf	Cardiff University	jin.zhang@astro.cf.ac.uk
Imran Mehdi	Jet Propulsion Laboratory	imran.mehdi@jpl.nasa.gov
Tetsuo Mori	Infrared Limited	tmori@infrared.co.jp
Pat Morris	Caltech	pmorris@ipac.caltech.edu
Brian Moyna	Rutherford Appleton Laboratory	brian.moyna@stfc.ac.uk
Axel Murk	University of Bern	murk@iap.unibe.ch
Prof J Anthony Murphy	NUI Maynooth	anthony.murphy@nuim.ie
Alessandro Navarrini	National Institute for Astrophysics, Italy	navarrini@ca.astro.it
Olle Nyström	GARD, Chalmers University of Technology	
Ochiai Satoshi	NICT, Japan	ochiai@nict.go.jp
Matthew Oldfield	Rutherford Appleton Laboratory	matthew.oldfield@stfc.ac.uk
Ernst Otto	University of Oxford	e.otto1@physics.ox.ac.uk
Tully Peacocke	National University of Ireland Maynooth	tully.peacocke@nuim.ie
Göran Pilbratt	European Space Agency	
Simon Rea	Rutherford Appleton Laboratory	simon.rea@stfc.ac.uk
Yuan Ren	TU Delft	y.ren@tudelft.nl
Heiko Richter	German Aerospace Center (DLR)	heiko.richter@dir.de
Nick Ridler	National Physics Laboratory	nick.ridler@npl.co.uk

Markus Roesch	IRAM	roesch@iram.fr
Erich Schlecht	Jet Propulsion Laboratory	erich.t.schlecht@jpl.nasa.gov
Wenlei Shan	Purple Mountain Observatory	shan@pmo.ac.cn
Sheng-Cai Shi	Purple Mountain Observatory	pmosis@gmail.com
José V. Siles	Technical University of Madrid	jovi@gmr.ssr.upm.es
Erich Smidt	Infrared Laboratories	esmidt@irlabs.com
Dr Spas Spasov	Royal Holloway University of London	spas.spasov@rhul.ac.uk
Jan Stake	Chalmers University of Technology	jan.stake@chalmers.se
Hansheng Su	Queen Mary, University of London	hansheng.su@elec.qmul.ac.uk
Boon Kok Tan	University of Oxford	b.tan1@physics.ox.ac.uk
Aik Yean Tang	Chalmers University	aik-yeen.tang@chalmers.se
Mikhail Tarasov	Chalmers University of Technology	tarasov@hitech.cplire.ru
David Teyssier	ESAC - European Space Agency	dteyssier@sciops.esa.int
Chris Thomas	University of Cambridge	cnt22@cam.ac.uk
Dr Bertrand Thomas	NASA - JPL	bertrand.c.thomas@jpl.nasa.gov
Edward Tong	Smithsonian Astrophysical Observatory	etong@cra.harvard.edu
Jeanne Treuttel	Rutherford Appleton Laboratory	
Menno van den Bemt	ALMA	m.van.den.bemt@sron.nl
Peter Vogt	DLR-IMF	peter.vogt@dir.de
Chris Walker	University of Arizona	cwalker@as.arizona.edu
Hui Wang	STFC-Rutherford Appleton Laboratory	hui.wang@stfc.ac.uk
Mike Wanke	Sandia National Labs	mcwanke@sandia.gov
Martina Wiedner	Observatoire de Paris	martina.wiedner@obspm.fr
Wolfgang Wild	European Southern Observatory	wwild@eso.org
Paul Wilkinson	Rutherford Appleton Laboratory	Byron.Alderman@stfc.ac.uk
Daniel Williamson	Rutherford Appleton Laboratory	Byron.Alderman@stfc.ac.uk
Prof S Withington	University of Cambridge	stafford@mrao.cam.ac.uk
Richard Wylde	Thomas Keating Instruments	
Pavel Yagoubov	ESO	pyagoubo@eso.org
Ghassan Yassin	University of Oxford	g.yassin1@physics.ox.ac.uk
Sigfrid Yngvesson	UMass Amherst	yngvesson@ecs.umass.edu
Wen Zhang	Purple Mountain Observatory	wzhang@mail.pmo.ac.cn
Dr Jin Zhang	Cardiff University	jin.zhang@astro.cf.ac.uk
Huan Zhao	Chalmers University of Technology	zhaoh@chalmers.se
Yanjun Zhou	University of Oxford	y.zhou1@physics.ox.ac.uk
Pablo Zorzi Avendano	Universidad de Chile	pzorzi@ing.uchile.cl
Neil Trappe	NUI Maynooth	neal.a.trappe@nuim.ie
Willem Jellema	SRON	W.Jellema@sron.nl
Gert de Lange	SRON	gert@sron.nl